Microstrip Antenna Design Handbook

Ramesh Garg
Prakash Bhartia
Inder Bahl
Apisak Ittipiboon

Artech House
Boston • London
www.artechhouse.com

Library of Congress Cataloging-in-Publication Data
Microstrip antenna design handbook / R. Garg ... [et al.].
p. cm. — (Artech House antennas and propagation library)
Includes bibliographical references and index.
ISBN 0-89006-513-6 (alk. paper)
1. Microstrip antennas. I. Garg, Ramesh. II. Bhartia, P. III. Bahl, Inder.
IV. Ittipiboon, A. V. Title. VI. Series.

TK7871.6 .M515 2000
621.382'4—dc21

00-059387
CIP

British Library Cataloguing in Publication Data
Microstrip antenna design handbook. — (Artech House
antennas and propagation library)
1. Microstrip antennas 2. Microstrip antennas—Design and
construction
I. Garg, R.
621.3'824

ISBN 0-89006-513-6

Cover design by Igor Valdman

685 Canton Street
Norwood, MA 02062

International Standard Book Number: 0-89006-513-6
Library of Congress Catalog Card Number: 00-059387

10 9 8 7 6 5 4 3 2 1

Contents

Foreword xix

Preface xxi

1 Microstrip Radiators 1

1.1 Introduction 1
1.1.1 Advantages and Limitations of Microstrip Antennas 2
1.1.2 Radiation Mechanism of a Microstrip Antenna 3
1.2 Various Microstrip Antenna Configurations 8
1.2.1 Microstrip Patch Antennas 8
1.2.2 Microstrip or Printed Dipole Antennas 9
1.2.3 Printed Slot Antennas 13
1.2.4 Microstrip Traveling-Wave Antennas 13
1.3 Feeding Techniques and Modeling 14
1.3.1 Coaxial Feed/Probe Coupling 16
1.3.2 Microstrip (Coplanar) Feeds 19
1.3.3 Proximity (Electromagnetically) Coupled Microstrip Feed 28
1.3.4 Aperture-Coupled Microstrip Feed 28

1.3.5 Coplanar, Waveguide Feed 29
1.4 Radiation Fields 31
1.4.1 Vector Potentials and Radiation Field Formulation 33
1.4.2 Microstrip Antenna Characteristics Calculations 40
1.5 Surface Waves and Photonic Bandgap Structures 43
1.5.1 Surface Waves 43
1.5.2 Photonic Bandgap Structures 47
1.6 Applications 54
1.6.1 Mobile and Satellite Communications Applications 57
1.6.2 Radar Antennas 66
1.6.3 Patch Applicators for Medicine 67
References 68

2 Analytical Models for Microstrip Antennas 73

2.1 Introduction 73
2.2 Transmission Line Model 78
2.2.1 Simple Transmission Line Model 80
2.2.2 Transmission Line Model With Mutual Coupling 82
2.2.3 Generalized Transmission Line Model 85
2.2.4 Lossy Transmission Line Model 88
2.3 Cavity Model 90
2.4 Generalized Cavity Model 97
2.5 Multiport Network Model 103
2.6 Radiation Fields 108
2.7 Aperture Admittance 110
2.7.1 Aperture Conductance, G_s 111
2.7.2 Edge Susceptance, B_s 116

2.8 Mutual Admittance, Y_m 118
2.8.1 Mutual Conductance, G_m 118
2.8.2 Mutual Susceptance, B_m 120
2.9 Model for Coaxial Probe in Microstrip Antennas 121
2.10 Comparison of Analytical Models 126

Appendix 2A: Theoretical Background of the Generalized Transmission Line Model 128

Appendix 2B: Eigenfunctions, Equivalent Dimensions, and Effective Permittivities for Some Patch Shapes With Separable Geometries 144

References 150

3 Full-Wave Analysis of Microstrip Antennas 157

3.1 Spectral-Domain Full-Wave Analysis 159
3.1.1 Input Impedance and Radiation Efficiency 164
3.1.2 Radiation Patterns 166
3.1.3 Numerical Evaluation of Matrix Elements and Voltage Vector 169
3.1.4 Basis Functions 174
3.1.5 Mathematical Model of Excitation 179
3.1.6 Applications of the Spectral-Domain Technique to Microstrip Antennas 185
3.2 Mixed-Potential Integral Equation Analysis 186
3.2.1 Potential Green's Functions in the Spectral Domain 187
3.2.2 Potential Green's Functions in the Space Domain 189
3.2.3 Results for Potentials for a Single-Layer Microstrip Structure 190

3.2.4 Integral Equation Solution Using Method of Moments 191
3.2.5 Applications of the MPIE Technique to Microstrip Antennas 197
3.3 Finite-Difference Time-Domain Analysis 197
3.3.1 Formulation of FDTD 199
3.3.2 Stability Criteria 203
3.3.3 Numerical Dispersion 203
3.3.4 Absorbing Boundary Conditions 205
3.3.5 Excitation and Source Modeling 214
3.3.6 Extraction of Frequency-Domain Characteristics From Time-Domain Data 217
3.3.7 Propagation in a Microstrip Line 220
3.3.8 Applications of the FDTD Technique to Microstrip Antennas 221

Appendix 3A: Derivation of Green's Functions in the Spectral Domain 224

Appendix 3B: Moment Method Solution 231

Appendix 3C: Derivation of Potential Green's Functions 234

Appendix 3D: Numerical Evaluation of Scalar and Vector Potentials 240

References 246

4 Rectangular Microstrip Antennas 253
4.1 Introduction 253
4.2 Models for Rectangular Patch Antennas 254
4.2.1 Transmission Line Model Analysis 255
4.2.2 Cavity Model Analysis 257
4.3 Design Considerations for Rectangular Patch Antennas 265
4.3.1 Substrate Selection 265

4.3.2 Element Width and Length 265
4.3.3 Radiation Patterns and Radiation Resistance 269
4.3.4 Losses and Q Factor 279
4.3.5 Bandwidth 282
4.3.6 Radiation Efficiency, e_r 285
4.3.7 Feed Point Location 287
4.3.8 Polarization 289
4.3.9 RCS of a Rectangular Patch 290
4.3.10 Effects of a Dielectric Cover 291
4.3.11 Effects of Finite Size Ground Plane 293
4.3.12 Computer-Aided Design 297
4.4 Tolerance Analysis of Rectangular Microstrip Antennas 299
4.5 Mechanical Tuning of Patch Antennas 302
4.5.1 Mechanical Tuning Using Stubs 303
4.5.2 Mechanical Tuning Based on Shorting Posts or Pins 303
4.5.3 Mechanical Tuning Using an Adjustable Air Gap 306
4.6 Quarter-Wave Rectangular Patch Antennas 306
4.6.1 Quarter-Wave Patch With Shorting Pins 308
4.6.2 Stacked Quarter-Wave Antennas 311
References 314

5 Circular Disk and Ring Antennas 317
5.1 Introduction 317
5.2 Analysis of a Circular Disk Microstrip Antenna 317
5.2.1 Cavity Model 318
5.2.2 Mode Matching With Edge Admittance 329
5.2.3 Generalized Transmission Line Model for a Circular Disk 337

7.6 Comparison of Slot Antennas With Microstrip Antennas 487
References 488

8 Circularly Polarized Microstrip Antennas and Techniques 493

8.1 Introduction 493
8.2 Various Types of Circularly Polarized Printed Antennas 493
8.2.1 Microstrip Patch Antennas 494
8.2.2 Other Types of Circularly Polarized Antennas 500
8.3 Singly Fed Circularly Polarized Microstrip Antennas 503
8.3.1 Rectangular-Type Circularly Polarized Microstrip Antennas 505
8.3.2 Circularly Polarized Circular Microstrip Antennas 513
8.4 Dual-Orthogonal Feed Circularly Polarized Microstrip Antennas 515
8.4.1 The Quadrature Hybrid 516
8.4.2 The 180-Degree Hybrid 518
8.4.3 The Wilkinson Power Divider 518
8.4.4 The T-Junction Power Divider 519
8.4.5 Design Procedure 520
8.5 Circularly Polarized Traveling-Wave Microstrip Line Arrays 520
8.5.1 Rampart Line Antenna and Crank-Type Microstrip Line Antenna 521
8.5.2 Chain Antenna 522
8.5.3 Square-Loop-Type Microstrip Line Antenna 523
8.6 Bandwidth Enhancement Techniques 524
8.6.1 Utilization of Wide-Band Microstrip Antennas 524

8.6.2 Sequentially Rotated Arrays 525
References 530

9 Broadbanding of Microstrip Antennas 533

9.1 Introduction 533
9.2 Effects of Substrate Parameters on Bandwidth 534
9.3 Selection of Suitable Patch Shape 538
9.4 Selection of Suitable Feeding Technique 538
9.4.1 Aperture-Coupled Microstrip Antennas 539
9.4.2 Transmission Line Model of Aperture Coupling 540
9.4.3 Modal Expansion Model of Aperture Coupling 544
9.5 Multimoding Techniques 551
9.5.1 Broadbanding Using Stacked Elements 552
9.5.2 Broadbanding Using Coplanar Parasitic Elements 570
9.5.3 Other Multimoding Techniques 576
9.6 Other Broadbanding Techniques 578
9.6.1 Impedance Matching 580
9.6.2 Resistive Loading 583
9.7 Multifrequency Operation 585
References 586

10 Loaded Microstrip Antennas and Applications 591

10.1 Introduction 591
10.2 Polarization Diversity Using Microstrip Antennas 592
10.3 Frequency Agile Microstrip Antennas 595
10.3.1 Varactor-Tuned Microstrip Antennas 595
10.3.2 Optical Tuning of Patch Antennas 598

10.4 Radiation Pattern Control of Microstrip Antennas 599
10.5 Loading Effect of a Short 599
10.5.1 Shorting Pin at the Radiating Edge 601
10.5.2 Shorting Pin on the Center Line of the Patch 605
10.6 Compact Patch Antennas 607
10.6.1 Compact Linearly Polarized Antennas 607
10.6.2 Compact Circularly Polarized Antennas 610
10.7 Planar Inverted-F Antenna 620
10.8 Dual-Frequency Microstrip Antennas 625
10.8.1 Dual-Frequency Slotted Patch Antennas 626
10.8.2 Dual-Frequency Dual-Linearly Polarized Microstrip Antennas 630
10.8.3 Dual-Frequency Circularly Polarized Microstrip Antennas 633
10.8.4 Dual Circularly Polarized Microstrip Antennas 636
10.9 Dual-Frequency Compact Microstrip Antennas 637
10.9.1 Pin-Loaded Dual-Frequency Antennas 637
10.9.2 Slot-Loaded Dual-Frequency Antennas 643
10.9.3 Dual-Frequency PIFA 646
References 654

11 Active Integrated Microstrip Antennas 659
11.1 Introduction 659
11.2 Classification of Active Integrated Microstrip Antennas 659
11.2.1 Oscillator Type 660
11.2.2 Amplifier Type 661
11.2.3 Frequency Conversion Type 663

11.3 Theory and Design of Active Integrated Microstrip Antenna Oscillators 666
11.3.1 One-Port Active Integrated Microstrip Antenna Oscillators 666
11.3.2 Active Patch Antennas Integrated With Diodes 668
11.3.3 Active Patch Antennas Integrated With Two-Port Devices 675
11.4 Theory and Design of Active Integrated Microstrip Antenna Amplifiers 696
11.4.1 Analysis and Design of Active Integrated Microstrip Antenna Amplifiers 697
11.4.2 Specified Gain Active Integrated Microstrip Antenna Amplifier Design 700
11.4.3 Low-Noise Active Integrated Microstrip Antenna Amplifier Design 706
11.5 Frequency Conversion Active Integrated Microstrip Antenna Theory and Design 709
11.5.1 Operational Principle of Transconductance Mixers 711
11.5.2 Self-Oscillating Mixer Active Integrated Microstrip Antennas 712
References 714

12 Design and Analysis of Microstrip Antenna Arrays 719
12.1 Introduction 719
12.2 Parallel and Series Feed Systems 719
12.2.1 Parallel Feed for One and Two Dimensions 720
12.2.2 Series Feeding of Microstrip Arrays 722
12.3 Mutual Coupling 727
12.4 Design of Linear Arrays 728
12.4.1 Linear Array Design With Microstrip Patches 728

12.4.2	Linear Array Design With Capacitively Coupled Fingers	732
12.4.3	Design of Comb-Line Arrays With Microstrip Stubs	733
12.5	Design of Planar Arrays	737
12.5.1	Infinite Arrays of Printed Dipoles	737
12.5.2	Infinite Arrays of Rectangular Microstrip Patches	742
12.5.3	Finite Planar Arrays of Printed Dipoles	746
12.6	Monolithic Integrated Phased Arrays	750
12.6.1	Design Considerations	751
12.6.2	Array Architectures	753
	References	756
	Appendix A: Substrates for Microstrip Antennas	**759**
A.1	Substrate Characteristics for Microstrip Antenna Design	759
A.1.1	Ceramic Substrates	760
A.1.2	Semiconductor Substrates	760
A.1.3	Ferrimagnetic Substrates	760
A.1.4	Synthetic Substrates	763
A.1.5	Composite Material Substrates	763
A.1.6	Low-Cost Low-Loss Substrates	763
A.1.7	Substrate Anisotropy	765
A.2	Desirable Substrate Characteristics for Antenna Fabrication	768
	References	770
	Appendix B: Design of Planar Transmission Lines and Discontinuities	**771**
B.1	Microstrip Line Design	771
B.2	Suspended and Inverted Microstrip Line Design	779

B.3	Design of Microstrip Line With a Superstrate	781
B.4	Parallel Strips Line Design	782
B.5	Strip Line Design	783
B.6	Slot Line Design	786
B.7	Coplanar Waveguide Design	789
B.7.1	CPW With an Infinitely Thick Substrate	791
B.7.2	CPW With Finite Dielectric Thickness	791
B.7.3	CPW With Finite Dielectric Thickness and Finite Width Ground Planes	791
B.7.4	CPW With Finite Dielectric Thickness and a Cover Shield	792
B.7.5	Conductor-Backed CPW With a Cover Shield	792
B.7.6	Conductor-Backed CPW	792
B.7.7	Asymmetric CPW Without Dielectric Substrate	792
B.7.8	Asymmetric CPW With Finite Dielectric Thickness	792
B.8	Coplanar Strips Design	793
B.8.1	Symmetric CPS With Infinitely Thick Substrate	793
B.8.2	Asymmetric CPS With Infinitely Thick Substrate	793
B.8.3	Asymmetric CPS With Finitely Thick Substrate	794
B.8.4	Symmetric CPS With Finite Dielectric Thickness	795
B.8.5	Asymmetric CPS With an Infinitely Wide Strip	795
B.9	Coupled Microstrip Lines Design	795
B.10	Coupled Strip Lines Design	798
B.11	Characterization of Discontinuities in Microstrip Lines	800

B.11.1	Open Ends	800
B.11.2	Gaps in Microstrips Lines	804
B.11.3	Notch	805
B.11.4	Steps in Width	806
B.11.5	Bends in Microstrips	807
B.11.6	Symmetric T-Junctions	807
B.11.7	Short-Circuited Posts in Microstrips	809
B.11.8	Shorted Ends	809
B.12	Open-End Discontinuity in Coupled Microstrip Lines	810
	References	810
	About the Authors	**813**
	Index	**817**

Foreword

For the past 20 years I have been using books written by these authors, both as textbooks for my courses at the University of Manitoba and as design guides for microwave circuits and antennas research, development, and fabrication in my consulting practice. So, naturally, I am quite honored and happy to be asked to write a foreword for their latest book on microstrip antennas.

Two of these authors, Drs. Bahl and Bhartia, wrote the first book on microstrip antennas in 1980. That book has been out of print for some time, but is considered a classic and widely used by those who still have a copy. During the two decades since, the field has matured significantly, and a number of other texts on microstrip antennas, written by different authors, and some specialized texts treating narrow aspects of microstrip antennas, such as computer-assisted design techniques or broadbanding, have also appeared. However, a comprehensive text on the subject has not appeared for some time, and this book fills that need.

I find that the authors have been very thorough in putting together this edition. To start with, one needs a good understanding of microstrip lines and other planar transmission lines, which are used as feeds. The authors cover these in an appendix, where the most recent and up-to-date design equations are presented. Next, one needs to understand substrates for antenna fabrication, and again, these are well covered in a separate appendix. Beyond this, the 12 chapters on the principal topic of microstrip antennas cover virtually all of the available subject matter in a very organized and easy-to-understand fashion, facilitating its use by the designer or researcher.

Chapter 1 covers the advantages, limitations, configurations, feeding techniques, and applications in a general fashion. Of special interest is the treatment of surface waves. Chapters 2 and 3 delve into the principal analysis tools, and

are followed by detailed chapters on design and analysis of rectangular, circular, triangular, and slot antennas. The coverage is detailed and complete, and easy to use. These chapters are followed by a number of chapters dealing with special aspects of microstrip antennas, such as circular polarization, broadbanding, and loaded and active integrated antennas, with the final chapter being on arrays.

Overall, I found that the book is well balanced and treats the material in depth or else provides adequate references for follow-up. I congratulate the authors on a text that I am confident will be a market success, and will be well received and used by the microstrip antenna community for many years to come.

Dr. L. Shafai
Professor, University of Manitoba
Winnipeg, Canada

Preface

Microstrip antennas consist of a patch of metalization on a grounded substrate. These are low-profile, lightweight antennas, most suitable for aerospace and mobile applications. Because of their low-power handling capability, these antennas can be used in low-power transmitting and receiving applications.

Microstrip antennas have matured considerably during the past 25 years, and many of their limitations have been overcome. An interesting development has been the use of aperture coupling to feed the antenna. This type of feed arrangement allows physical separation of the two functions and the use of optimal substrates for the radiator and transmission line. The characteristics of microstrip antennas can be significantly improved by using multilayered structures with thick substrates and low-permittivity materials. At present, a bandwidth of about 65% has been achieved.

Surface wave propagation is supposed to be another limiting factor affecting efficiency, upper frequency of operation, cross-coupling, and so on. However, this problem has also been addressed through the use of photonic bandgap structures. These structures are obtained by periodic loading of substrates.

Microstrip antennas are an extension of microstrip circuits. This feature has given rise to microstrip integrated active antennas in which circuit functions are integrated with the antenna function to produce compact transceivers and in spatial power combiners to overcome power limitations of solid-state devices. Many of the antenna applications for satellite links, mobile communications, wireless local-area networks, and so on, impose constraints on compactness, dual-frequency operation, frequency agility, polarization control, radiation pattern control, and so on. These functions can be achieved by suitably loading simple microstrip antennas, and hence these antennas are becoming more commonly used.

The microstrip antenna structure is becoming complex due to the inherent inhomogeneity of the dielectric materials used, multilayered dielectric structures, periodic loading of the substrate to prevent surface waves, aperture coupling of the feed to the antenna, use of a stacked configuration to achieve larger bandwidth, loading of the antenna to achieve desired antenna characteristics, and integration of circuit functions with antenna functions. Analysis techniques have kept pace with the advances described above. The analysis of complex microstrip antennas using full-wave techniques, such as the integral equation approach and FDTD, have matured sufficiently, and software that can be run on personal computers is freely available. The present text addresses almost all of the issues described above and thus should be useful for designers and research students.

Organization of the Book

This project started with the idea of producing a revised edition of the very popular book *Microstrip Antennas* by Inder Bahl and Prakash Bhartia. During this exercise it became apparent that the old structure of the book could not be maintained because of the information explosion in the area of microstrip antennas since the publication of the original book in 1980. During the period since then, the use of microstrip antennas became established, a number of new analytical and full-wave techniques were introduced, new feeding techniques became available, and microstrip active antennas revived the field of active antennas.

The focus of this book is still on design information, and the decision was made to emphasize those design approaches that have lasting value among the full-wave techniques. Out of the various models available, it was felt that the cavity model analysis is a good compromise between accuracy and complexity. As a result, the design approaches for various antenna types center around this model. Wherever design equations are available, they are included to help the reader. This approach should be useful for designers in the industry as well as for budding research scholars. The analytical and full-wave techniques are described in detail to help the user develop a sound background in microstrip antennas. The final format of the book is thus very similar to that of another popular book by the authors, *Microstrip Lines and Slotlines*.

The book is organized in 12 chapters covering various aspects of microstrip antennas: analysis techniques; prominent antenna types such as rectangular patches, circular patches, triangular patches, dipoles, and slots; circularly polarized antennas; loaded and active (integrated) antennas; broadbanding techniques; and array antennas. The subject matter common to various types of

antennas is included in the introductory chapter and in the appendixes on substrates and on the design of planar transmission lines.

The microstrip antenna is introduced in Chapter 1. This chapter describes the characteristics of microstrip antennas as a class, their advantages and limitations and their major applications in communications and radar. It also provides a comparison of the various feeding techniques, radiation mechanisms, and evaluation of radiation fields and surface waves. Surface wave propagation sets an upper limit to the capability of a microstrip antenna. The use of photonic bandgap structures is a recent answer to this problem and is also discussed.

Chapter 2 deals with the analytical models for microstrip antenna analysis. These models are the backbone of antenna design and are based on the equivalent magnetic current radiation formulation. The models included are simple transmission line and cavity models, their improved and generalized versions, and the lossy transmission line model. Virtually complete details of these models are included so that a user does not have to look elsewhere for details. The models are compared in a qualitative manner. Equivalent dimensions and effective permittivities for patch shapes with separable geometries are included for the benefit of designers.

The limitations of the analytical models in terms of approximate design, complexity of the antenna feed, multi-substrate configuration, and so on, can be taken care of through a full-wave analysis, which is discussed in Chapter 3. The most commonly used techniques, namely, spectral-domain full-wave analysis, mixed-potential integral equation analysis, and finite-difference time-domain techniques, are described in detail. About 45 references covering applications of these techniques to various types of microstrip antennas are listed to provide the reader with greater details than can be covered here.

The analysis and design of the most commonly used microstrip antennas, that is, rectangular and circular microstrip antennas, are discussed in Chapters 4 and 5, respectively. Considering its importance the rectangular patch antenna is discussed in greater detail in Chapter 4. Almost all aspects of antenna design are considered, culminating in computer-aided design techniques. Rectangular and circular patch antennas are compared in Chapter 5. The two antennas have similar characteristics. The annular ring microstrip antenna is famous for its larger bandwidth and is described in Chapter 5. A brief description of sectors of circular patches and annular rings is also included in this chapter. The semicircular disk antenna is a space saver when operated in the TM_{11} mode.

Dipoles and the triangular microstrip patch antenna are the subject of Chapter 6. A bow-tie version of the center-fed dipole can be designed to provide about 40% impedance bandwidth. The equilateral triangular microstrip patch antenna is famous for its circular polarization characteristic. Analysis of this antenna is also described in Chapter 6.

Microstrip slot antennas are complementary to microstrip dipole and patch antennas and are discussed in Chapter 7. Like the patch antenna, the slot antenna could be rectangular or circular in shape. The most famous slot antennas are the tapered slot antenna and the annular slot antenna. The tapered slot antenna is a traveling-wave antenna and produces end-fire radiation. It finds a number of applications at millimeter-wave frequencies. The annular slot antenna can be used as a vehicular antenna for mobile communications because its radiation patterns can be controlled electronically by loading the slot with a tunable capacitor. The slot antenna and the microstrip patch antenna are compared at the end of Chapter 7, where we find that the slot antenna is less sensitive to fabrication tolerances and has a larger bandwidth.

Circularly polarized microstrip antennas and techniques are described in Chapter 8. Various types of circularly polarized microstrip antennas are described. These include single fed and dual orthogonal fed. The effect of perturbation on the resonant frequency is discussed in detail and the condition for circular polarization is obtained. The techniques for increasing the circular polarization bandwidth are discussed at the end of this chapter. A square patch with four mutually orthogonal feeds and a 90° phase difference in sequence can increase the bandwidth to about 10% with an almost 0-dB axial ratio. Another approach is to use four identical patches, with sequential physical rotation and the feed phase shift also rotated sequentially. This configuration is referred to as a sequentially rotated array.

One of the serious limitations of a microstrip antenna is its impedance bandwidth. Techniques for broadbanding of microstrip antennas are described in Chapter 9. These include the proper choice of substrate, proper feeding techniques, impedance matching, and excitation of multiple modes through mutual coupling. Bandwidths of various types of broadband microstrip antennas utilizing parasitic loading techniques are compared as a function of volume occupied by the antenna. An aperture-coupled stacked microstrip antenna configuration is the most successful broadband microstrip antenna. An impedance bandwidth of about 69% has been reported.

Modern communication systems, such as those for satellite links and mobile communications, and for emerging applications, such as wireless local-area networks, often require compact antennas at low cost. In addition to compactness, the antenna may be required to provide circular polarization, as in satellite links. In some applications, operation in two or more discrete bands and an arbitrary separation of bands is desired. It is possible to achieve some of these objectives by loading the antenna. Loading is discussed in Chapter 10 in a general way to obtain characteristics such as size reduction, dual-frequency operation, polarization control, radiation pattern control, and frequency agility. The loading effects of a short and a slot are described. These

loadings are then used to obtain compactness, dual-frequency operation, dual polarization, and so on. The highlight of this chapter is the comparison of a number of compact linearly polarized microstrip antennas. A PIFA (planar inverted-F antenna) is an important compact antenna. Some of the compact circularly polarized microstrip antennas are also compared.

The field of active antennas has been revived with the advent of microstrip antennas. In these antennas, active devices are directly integrated with the antenna structure to obtain active microstrip antenna oscillators, active microstrip antenna amplifiers, and active microstrip antenna frequency converters. Analysis and design of these types of active antennas are discussed in Chapter 11. Active antennas have many potential applications in radar and communications. They can be used as a module for high-gain phased arrays and in spatial power combiners to overcome the power limitations of solid-state devices. They also have strong potential for commercial applications in wireless communications, radar, and as low-cost and compact transceivers and sensors. Design samples of a number of active antennas are included in this chapter.

Design and analysis of microstrip antenna arrays are covered in the last chapter, Chapter 12. Parallel and series feed networks are described first. The design of traveling-wave linear arrays with capacitively coupled patches and microstrip stubs is discussed next. The design of planar arrays of printed dipoles and rectangular patches is then described. Both the infinite size and finite size planar arrays are included. Design considerations and array architectures of monolithic phased arrays are touched on at the end of Chapter 12.

The authors hope that the selection of topics and their presentation will meet the expectations of the readers.

Acknowledgments

Finally, we would like to thank the persons who have helped us most. Ramesh Garg would like to thank Mr. V. S. Reddy, his research scholar, for many valuable suggestions, for serving as a memory bank, and for electronic transportation of the manuscript. Dr. Bhartia would like to thank Ms. Josie Dunn for her outstanding support in the preparation of the manuscript and Mr. Bob Gervais for redoing all the figures in a uniform format.

1

Microstrip Radiators

1.1 Introduction

The concept of microstrip radiators was first proposed by Deschamps [1] in 1953. A patent was issued in France in 1955 in the names of Gutton and Baissinot [2]. However, 20 years passed before practical antennas were fabricated. Development during the 1970s was accelerated by the availability of good substrates with low loss tangent and attractive thermal and mechanical properties, improved photolithographic techniques, and better theoretical models. The first practical antennas were developed by Howell [3] and Munson [4]. Since then, extensive research and development of microstrip antennas and arrays, aimed at exploiting their numerous advantages such as light weight, low volume, low cost, conformal configuration, compatibility with integrated circuits, and so on, have led to diversified applications and to the establishment of the topic as a separate entity within the broad field of microwave antennas. Good reviews of much of this work can be found in [5–14].

As shown in Figure 1.1, a microstrip antenna in its simplest configuration consists of a radiating patch on one side of a dielectric substrate ($\epsilon_r \leq 10$), which has a ground plane on the other side. The patch conductors, normally of copper or gold, can assume virtually any shape, but regular shapes are generally used to simplify analysis and performance prediction. Ideally, the dielectric constant, ϵ_r, of the substrate should be low ($\epsilon_r < 2.5$), to enhance the fringe fields that account for the radiation. However, other performance requirements may dictate the use of substrate materials whose dielectric constants can be greater than, say, four. Various types of substrates having a large range of dielectric constant and loss tangent values have been developed. Their

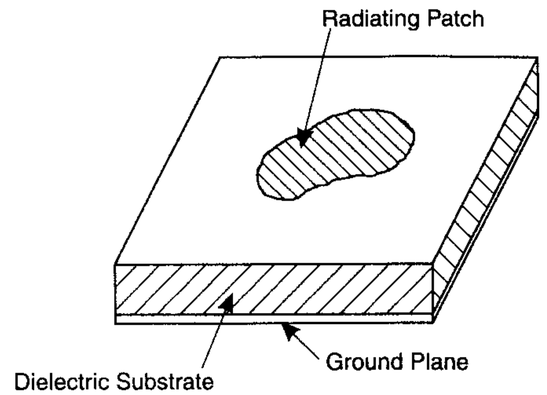

Figure 1.1 Microstrip antenna configuration.

properties are described in Appendix A. Some of these substrates are flexible in nature, which makes them suitable for conformal wraparound antennas.

1.1.1 Advantages and Limitations of Microstrip Antennas

Microstrip antennas have several advantages compared to conventional microwave antennas, and therefore many applications cover the broad frequency range from ~100 MHz to ~100 GHz. Some of the principal advantages of microstrip antennas compared to conventional microwave antennas are:

- Light weight, low volume, and thin profile configurations, which can be made conformal;
- Low fabrication cost; readily amenable to mass production;
- Linear and circular polarizations are possible with simple feed;
- Dual-frequency and dual-polarization antennas can be easily made;
- No cavity backing is required;
- Can be easily integrated with microwave integrated circuits;
- Feed lines and matching networks can be fabricated simultaneously with the antenna structure.

However, microstrip antennas also have some limitations compared to conventional microwave antennas:

- Narrow bandwidth and associated tolerance problems;
- Somewhat lower gain (~6 dB);
- Large ohmic loss in the feed structure of arrays;

- Most microstrip antennas radiate into half-space;
- Complex feed structures required for high-performance arrays;
- Polarization purity is difficult to achieve;
- Poor end-fire radiator, except tapered slot antennas;
- Extraneous radiation from feeds and junctions;
- Lower power handling capability (~100W);
- Reduced gain and efficiency as well as unacceptably high levels of cross-polarization and mutual coupling within an array environment at high frequencies;
- Excitation of surface waves;
- Microstrip antennas fabricated on a substrate with a high dielectric constant are strongly preferred for easy integration with MMIC RF front-end circuitry. However, use of high dielectric constant substrate leads to poor efficiency and narrow bandwidth.

There are ways to minimize the effect of some of these limitations. For example, bandwidth can be increased to more than 60% by using special techniques (see Chapter 9); lower gain and lower power handling limitations can be overcome through an array configuration. Surface wave-associated limitations such as poor efficiency, increased mutual coupling, reduced gain and radiation pattern degradations can be overcome by the use of photonic bandgap structures [15].

1.1.2 Radiation Mechanism of a Microstrip Antenna

We know that radiation from a microstrip line, a structure similar to a microstrip antenna, can be reduced considerably if the substrate employed is thin and has a higher relative dielectric constant [16]. Radiation from a microstrip antenna, on the other hand, is encouraged for better radiation efficiency. Therefore, thick substrates with low permittivity are used in microstrip antennas. Radiation from a microstrip antenna can be determined from the field distribution between the patch metalization and ground plane. Alternatively, radiation can be described in terms of the surface current distribution on the patch metalization. An accurate calculation of the field or current distribution of the patch is very complicated and is described in Chapter 3. However, crude approximations and simple arguments can be used to develop a workable model for a microstrip antenna. The approach presented next is based on that given in [17].

Consider a microstrip patch antenna that has been connected to a microwave source. The energization of the patch will establish a charge distribution on the upper and lower surfaces of the patch, as well as on the surface of the ground plane. This is shown in Figure 1.2 for a rectangular patch [17]. The −ve and +ve nature of the charge distribution arises because the patch is about a half-wave long at the dominant mode. The repulsive forces between like charges on the bottom surface of the patch tend to push some charges from the bottom surface, around its edges, to its top surface. This movement of charges creates corresponding current densities $\vec{J}_b$ and $\vec{J}_t$ at the bottom and top surfaces of the patch as shown in Figure 1.2. For most microstrip antennas, the ratio h/W is very small. Therefore, the attractive force between the charges dominates and most of the charge concentration and the current flow remain underneath the patch. A small amount of current flows around the edges of the patch to its top surface and is responsible for a weak magnetic field tangential to the edges. Hence, we can make a simple approximation, that the tangential magnetic field is zero and one can place magnetic walls all around the periphery of the patch. This assumption has greater validity for thin substrates with high ϵ_r. Also, since the substrate used is very thin compared to the wavelength ($h << \lambda$) in the dielectric, the field variations along the height can be considered to be constant and the electric field nearly normal to the surface of the patch. Consequently, the patch can be modeled as a cavity with electric walls (because the electric field is near normal to the patch surface) at the top and below and four magnetic walls along the edges of the patch (because the tangential magnetic field is very weak). Only TM modes are possible in this cavity. The electric field distribution for the dominant TM_{100} mode of the cavity is plotted in Figure 1.3.

The four sidewalls of the cavity represent four narrow apertures or slots through which radiation takes place. Using the Huygen field equivalence principle, the microstrip patch can be represented by an equivalent current density $\vec{J}_t$ at the top surface to account for the presence of patch metalization. The

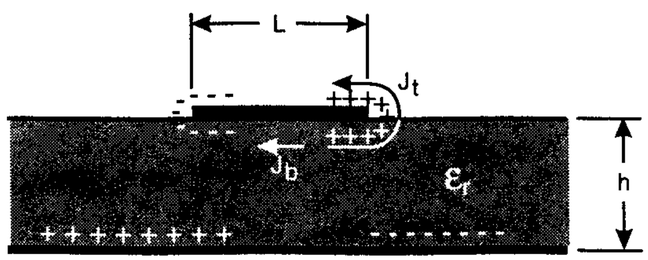

Figure 1.2 Charge distribution and current density on a microstrip antenna. (From [17]. © 1997 John Wiley. Reprinted with permission.)

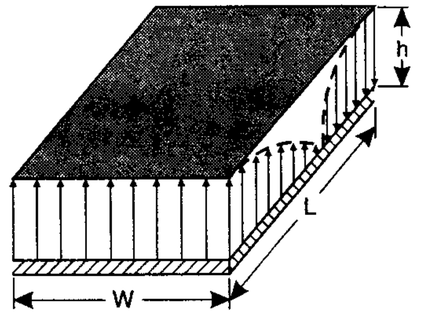

Figure 1.3 Electric field distribution for the TM_{100} mode in the microstrip cavity. (From [17]. © 1997 John Wiley. Reprinted with permission.)

four side slots are represented by the equivalent current densities $\vec{J}_s$ and $\vec{M}_s$, corresponding to the magnetic and electric fields $\vec{H}_a$ and $\vec{E}_a$, respectively, in the slots. The equivalent currents are shown in Figure 1.4(a) and are given by

$$\vec{J}_s = \hat{n} \times \vec{H}_a \tag{1.1a}$$

$$\vec{M}_s = -\hat{n} \times \vec{E}_a \tag{1.1b}$$

For thin substrates, it was shown that the patch current at the top $\vec{J}_t$ is much smaller than $\vec{J}_b$, the current at the bottom. It will be set to zero here to indicate negligible radiation from the patch current. Similarly, the tangential magnetic fields along the patch edges and the corresponding current density $\vec{J}_s$ are set to zero. Thus, the only nonzero current density is the equivalent magnetic current density $\vec{M}_s$ along the periphery of the patch. This is shown in Figure 1.4(b). The presence of the ground plane can be taken into account by the image theory, which will double the equivalent current density of (1.1b). Therefore, radiation from the patch can be ascribed to four ribbons of magnetic current (around the periphery) radiating in free space as shown in Figure 1.4(c). The new current density is given by

$$\vec{M}_s = -2\hat{n} \times \vec{E}_a \tag{1.2}$$

The slot electric field $\vec{E}_a$ for the dominant mode is shown in Figure 1.3 and is defined as

$$\vec{E}_a = \hat{z}E_0 \tag{1.3}$$

for the slots of length W and height h. Similarly, for the other two slots of length L and height h

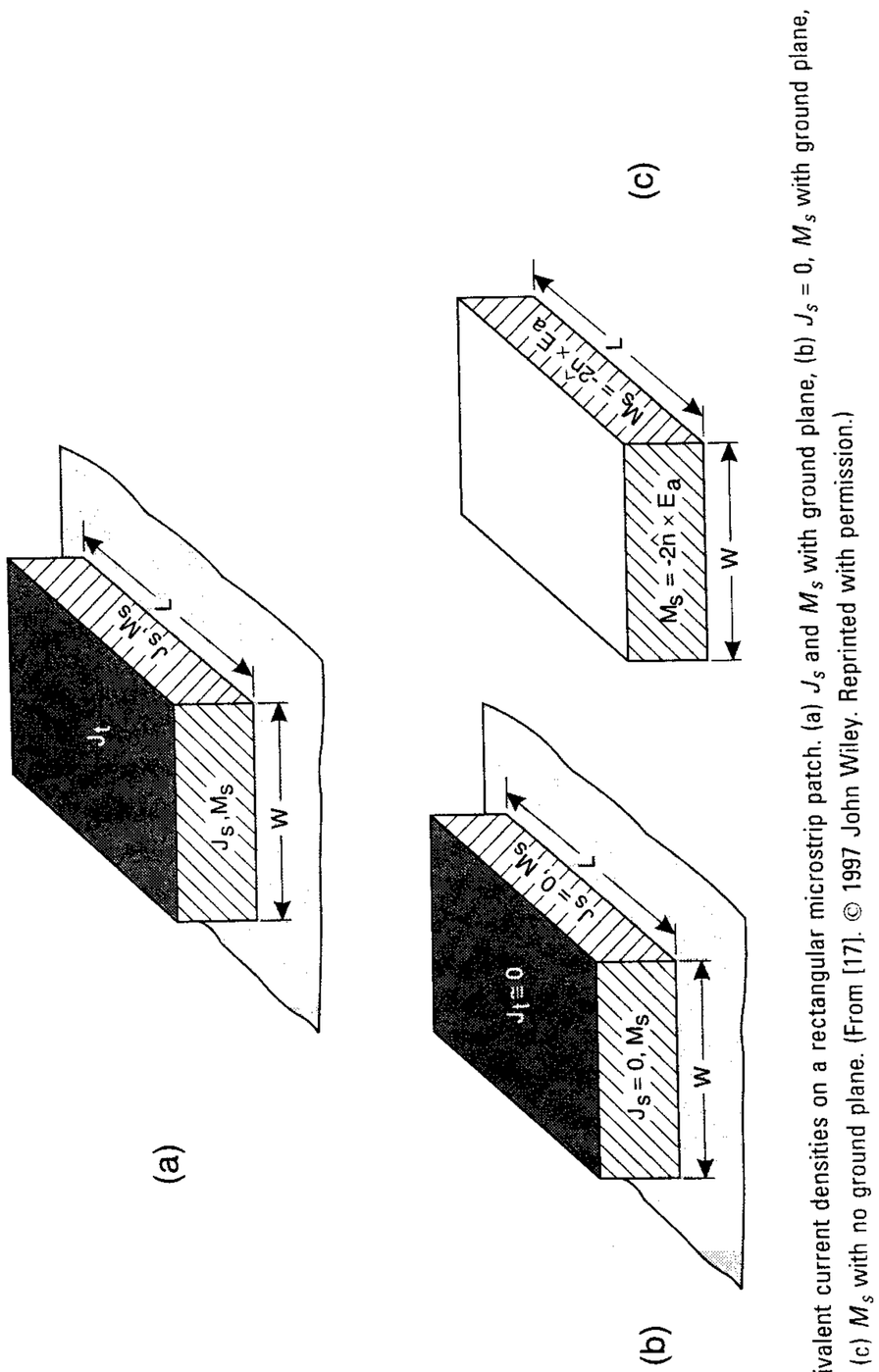

Figure 1.4 Equivalent current densities on a rectangular microstrip patch. (a) J_s and M_s with ground plane, (b) $J_s = 0$, M_s with ground plane, and (c) M_s with no ground plane. (From [17]. © 1997 John Wiley. Reprinted with permission.)

$$\vec{E}_a = -\hat{z}E_0 \sin(\pi x/L) \tag{1.4}$$

The equivalent magnetic current densities in the slots are shown in Figure 1.5 [17]. Using the equivalence principle, each slot radiates the same field as a magnetic dipole with current density $\vec{M}_s$. The radiation produced by the slots laid out along the x axis is almost zero because of equal and opposite current distributions on the slots. However, the slots along the y axis form a two-element array with the current densities of the same magnitude and phase and are separated by L, the length of the patch. Therefore, radiation from the patch can be described in terms of two vertical slots.

Vertical slots in the inhomogeneous dielectric of the microstrip antenna are difficult to analyze. Therefore, the vertical slots are replaced by two equiva-

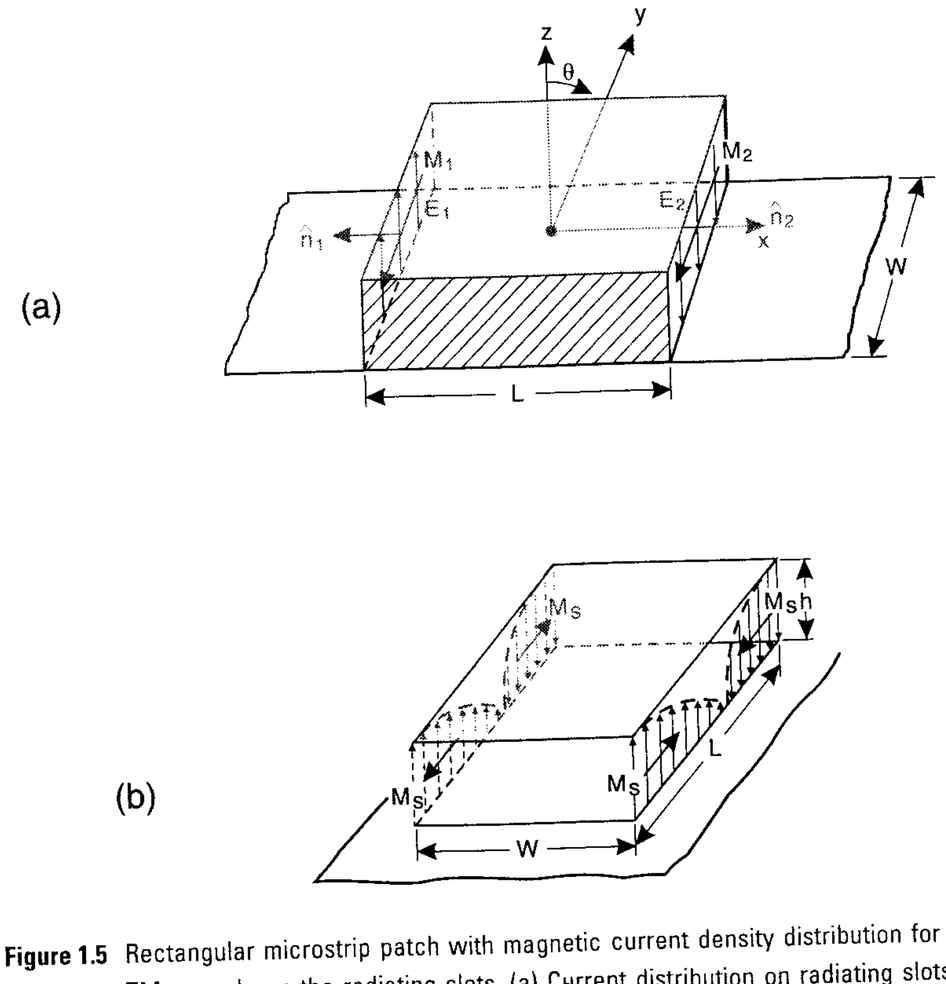

Figure 1.5 Rectangular microstrip patch with magnetic current density distribution for the TM_{100} mode on the radiating slots. (a) Current distribution on radiating slots, and (b) current distribution on nonradiating slots. (From [17]. © 1997 John Wiley. Reprinted with permission.)

lent planar slots as shown in Figure 1.6. Other microstrip antenna configurations can also be represented by equivalent slots in a similar manner.

1.2 Various Microstrip Antenna Configurations

Microstrip antennas are characterized by a larger number of physical parameters than are conventional microwave antennas. They can be designed to have many geometrical shapes and dimensions. A comprehensive list of these configurations is available [7]. All microstrip antennas can be divided into four basic catagories: microstrip patch antennas, microstrip dipoles, printed slot antennas, and microstrip traveling-wave antennas; characteristics of each are discussed next.

1.2.1 Microstrip Patch Antennas

A microstrip patch antenna (MPA) consists of a conducting patch of any planar or nonplanar geometry on one side of a dielectric substrate with a ground plane on the other side. Radiation characteristics have been calculated for a large number of patch antennas [7]. The basic configurations used in practice are shown in Figure 1.7(a). Their radiation characteristics are similar, despite the difference in geometrical shape, because they behave like a dipole. Rectangular and circular patch antennas are widely used. Typically, a patch antenna has a gain between 5 and 6 dB and exhibits a 3-dB beamwidth between 70° and 90°. Some of the other patch shapes are used for special applications. These are shown in Figure 1.7(b). In this book, the rectangular and circular geometries are discussed in Chapters 4 and 5, respectively, and the triangular geometry is described in Chapter 6.

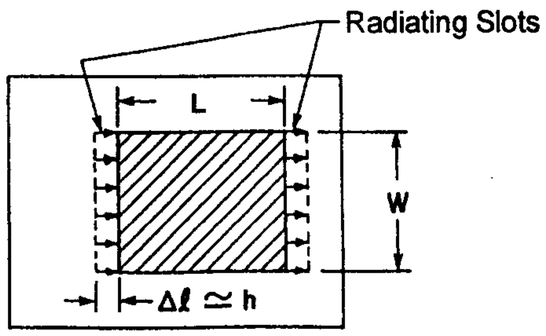

Figure 1.6 Rectangular microstrip patch antenna with equivalent horizontal radiating slots.

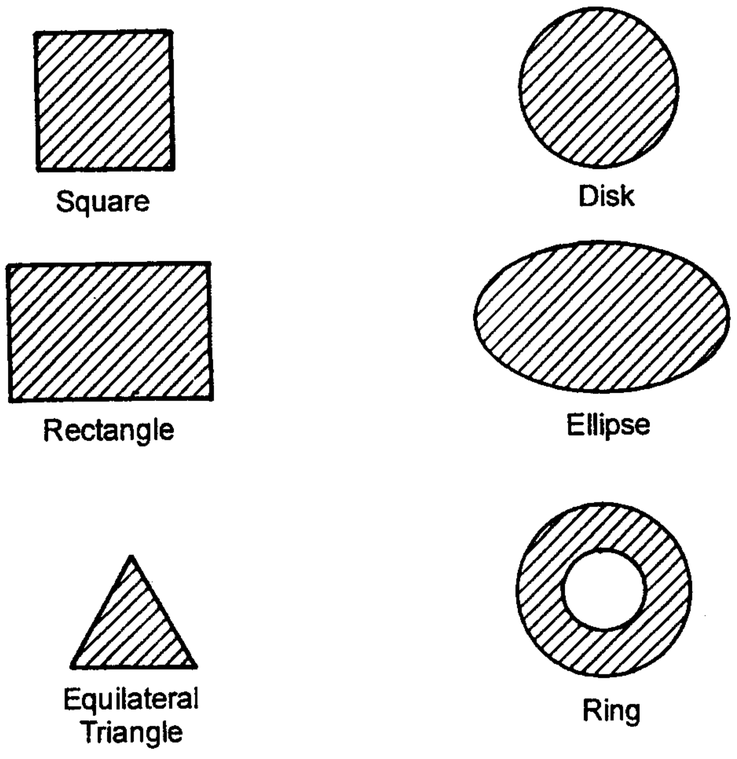

Figure 1.7 (a) Basic microstrip patch antenna shapes commonly used in practice. (b) Other possible geometries for microstrip patch antennas.

1.2.2 Microstrip or Printed Dipole Antennas

Microstrip or printed dipoles differ geometrically from rectangular patch antennas in their length-to-width ratio. The width of a dipole is typically less than $0.05\lambda_0$. The radiation patterns of the dipole and patch are similar owing to similar longitudinal current distributions. However, the radiation resistance, bandwidth, and cross-polar radiation differ widely. They have been studied extensively [7, 18]. Microstrip dipoles, Figures 1.8(a) and (b), are attractive elements owing to their desirable properties such as small size and linear polarization. The dipoles are well suited for higher frequencies for which the substrate can be electrically thick, and therefore can attain significant bandwidth. The choice of feed mechanism is very important in the microstrip dipoles and should be included in the analysis. The symmetrical folded printed dipole, Figure 1.8(c), consists of a folded dipole combined with another similar dipole (mirror image) to yield a symmetrical structure. Alternatively, this structure can be considered to be a rectangular patch with an H-shaped slot. The

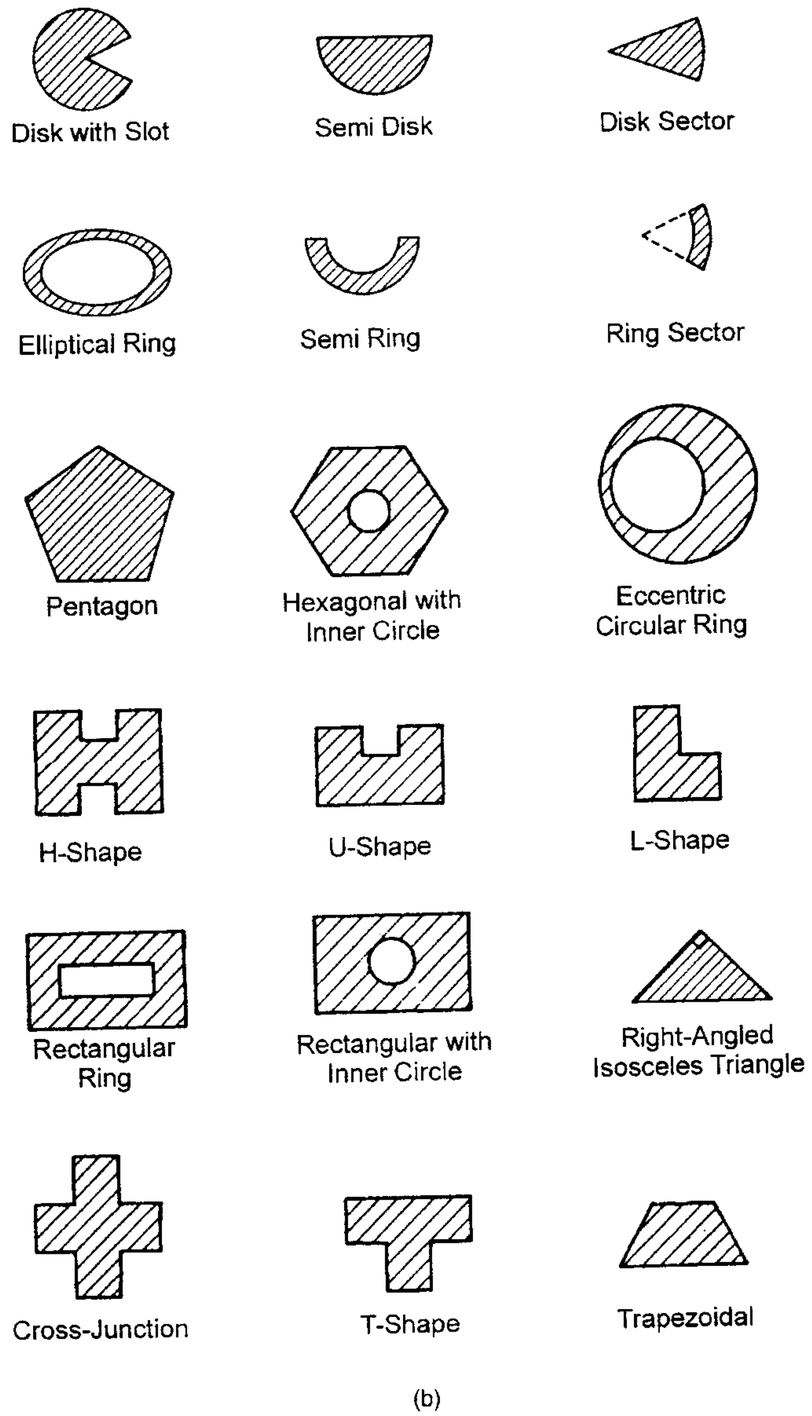

Figure 1.7 (continued).

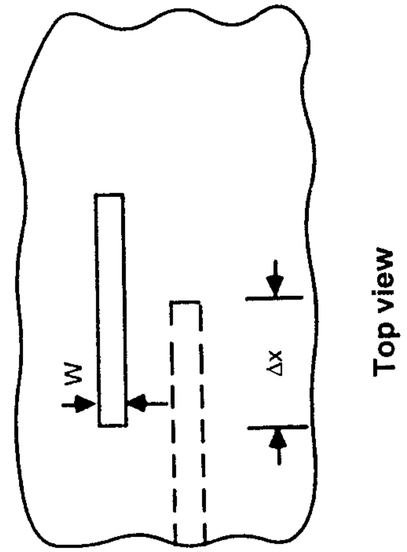

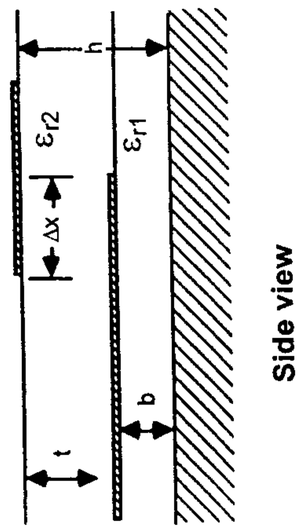

Figure 1.8 Configurations of some microstrip and printed dipoles. (a) Proximity-coupled strip dipole. (From [7]. © 1989 Peter Peregrinus. Reprinted with permission.) (b) Double-sided strip dipole and feed line. (From [11]. © 1996 Artech House. Reprinted with permission.) (c) Symmetrical folded printed dipoles. (From [18]. © 1981 Research Studies Press. Reprinted with permission.)

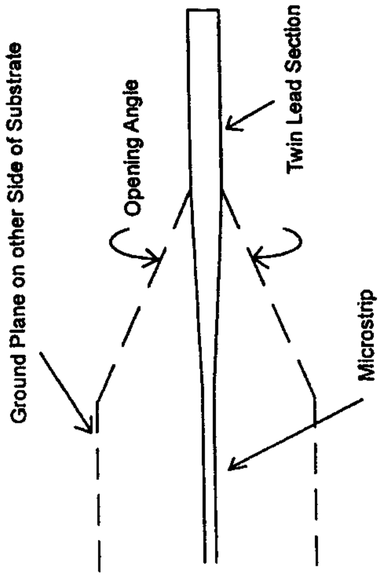

(b)

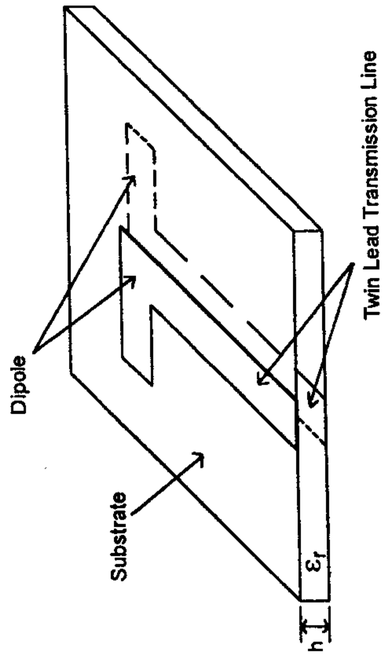

Figure 1.8 (continued).

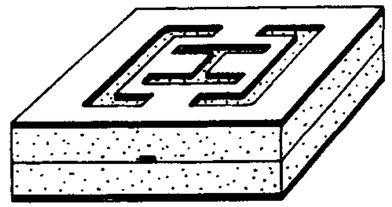

(c)

Figure 1.8 (continued).

VSWR = 2 bandwidth of this dipole can be about 16% [18]. Dipoles are studied in detail in Chapter 6.

1.2.3 Printed Slot Antennas

Printed slot antennas comprise a slot in the ground plane of a grounded substrate. The slot can have virtually any shape. Theoretically, most of the microstrip patch shapes shown in Figure 1.7 can be realized in the form of a printed slot. However, only a few basic slot shapes have been studied. These include a rectangular slot, annular slot, rectangular ring slot, and tapered slot. These are shown in Figure 1.9. Like microstrip patch antennas, the slot antennas can be fed either by a microstrip line or a coplanar waveguide. Slot antennas are generally bidirectional radiators; that is, they radiate on both sides of the slot. Unidirectional radiation is obtained by using a reflector plate on one side of the slot. Slot antennas are described in detail in Chapter 7.

1.2.4 Microstrip Traveling-Wave Antennas

A microstrip traveling-wave antenna (MTA) may consist of chain-shaped periodic conductors or a long microstrip line of sufficient width to support a TE mode. The other end of the traveling-wave antenna is terminated in a matched resistive load to avoid the standing waves on the antenna. Traveling-wave microstrip antennas can be designed so that the main beam lies in any direction from broadside to end fire. Various configurations for MTAs are shown in Figure 1.10. The tapered slot antenna is a surface wave antenna. It radiates in the end-fire direction, and is discussed in Chapter 7. Use of traveling-wave

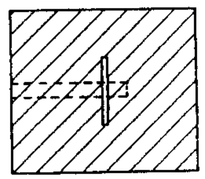

Rectangular Slot
with Microstrip Feed

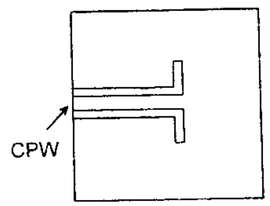

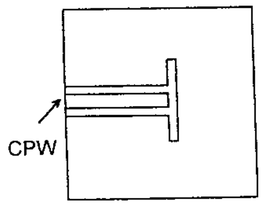

Rectangular Slot with CPW Feed

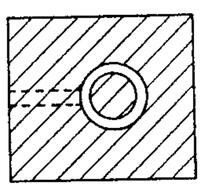

Annular Slot
with Microstrip Feed

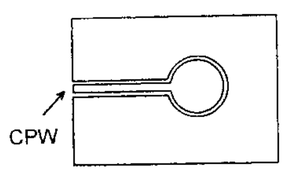

Annular Slot with CPW Feed

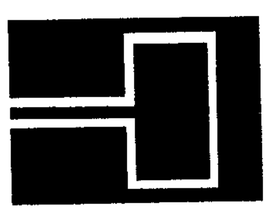

Rectangular Ring Slot

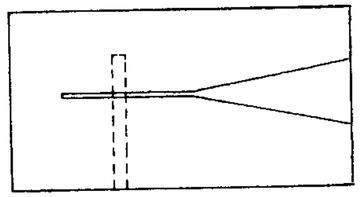

Tapered Slot

Figure 1.9 Basic printed slot antenna shapes with feed structures.

antennas such as rampart-line antenna, chain antenna, square-loop antenna, and crank-type antenna for circular polarization is described in Chapter 8.

The characteristics of microstrip patch antennas, microstrip slot antennas, and printed dipole antennas are compared in Table 1.1.

1.3 Feeding Techniques and Modeling

Microstrip antennas have radiating elements on one side of a dielectric substrate, and thus early microstrip antennas were fed either by a microstrip line or a coaxial probe through the ground plane. Since then a number of new feeding techniques have been developed. Prominent among these are coaxial feed, microstrip (coplanar) feed, proximity-coupled microstrip feed, aperture-coupled microstrip feed, and coplanar waveguide feed. These feed structures are discussed

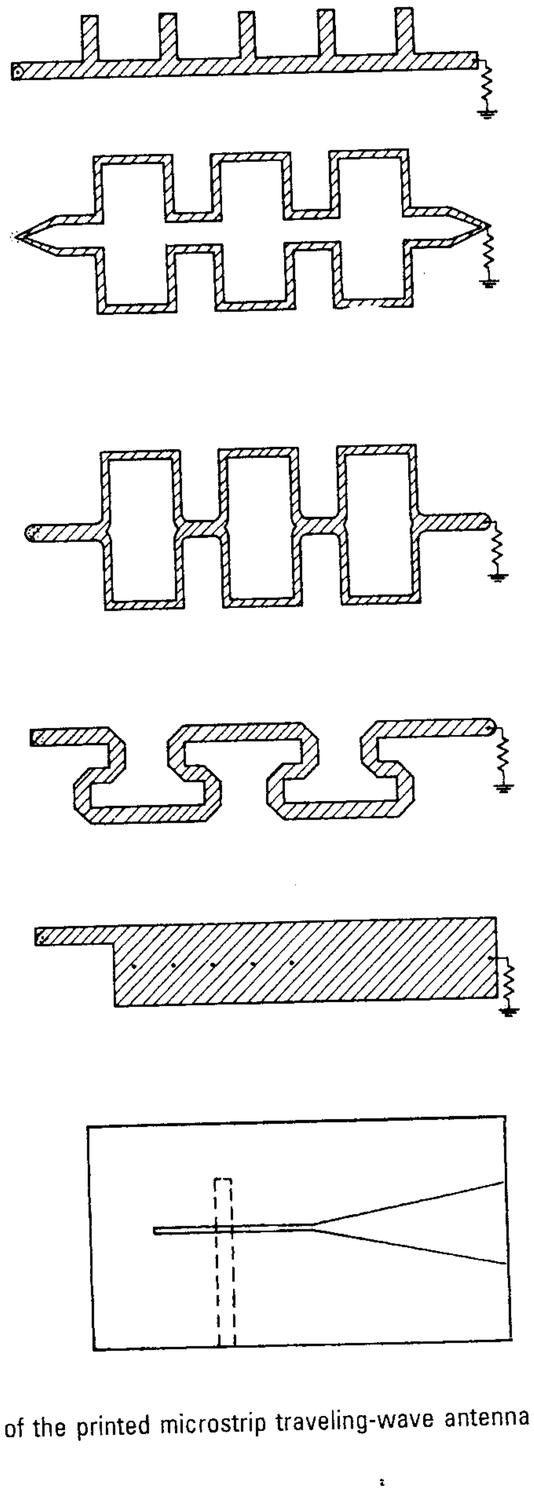

Figure 1.10 Some of the printed microstrip traveling-wave antenna configurations.

Table 1.1
Comparison of Various Types of Flat Profile Printed Antennas

Characteristics	Microstrip Patch Antennas	Microstrip Slot Antennas	Printed Dipole Antennas
Profile	Thin	Thin	Thin
Fabrication	Very easy	Easy	Easy
Polarization	Both linear and circular	Both linear and circular	Linear
Dual-frequency operation	Possible	Possible	Possible
Shape flexibility	Any shape	Mostly rectangular and circular shapes	Rectangular and triangular
Spurious radiation	Exists	Exists	Exists
Bandwidth	2–50%	5–30%	~30%

later with emphasis on the mechanism of coupling energy, equivalent circuit, and relative merits. A mathematical model for the excitation is discussed in Section 3.1. Detailed theoretical analyses of these feeds can be found in various papers [6, 7, 8, 12].

Selection of the feeding technique is governed by a number of factors. The most important consideration is the efficient transfer of power between the radiating structure and feed structure, that is, impedance matching between the two. Associated with impedance matching are stepped impedance transformers, bends, stubs, junctions, transitions, and so on, which introduce discontinuities leading to spurious radiation and surface wave loss. The undesired radiation may increase the sidelobe level and the cross-polar amplitude of the radiation pattern. Minimization of spurious radiation and its effect on the radiation pattern is one of the important factors for the evaluation of the feed. Another consideration is the suitability of the feed for array applications. Some feed structures are amenable to better performance because of the larger number of parameters available.

1.3.1 Coaxial Feed/Probe Coupling

Coupling of power through a probe is one of the basic mechanisms for the transfer of microwave power. The probe can be an inner conductor of a coaxial line in the case of coaxial line feeding or it can be used to transfer power from a triplate line (strip line) to a microstrip antenna through a slot in the common ground plane. A typical microstrip antenna using a type N coaxial connector is shown in Figure 1.11(a). The coaxial connector is attached to the back side

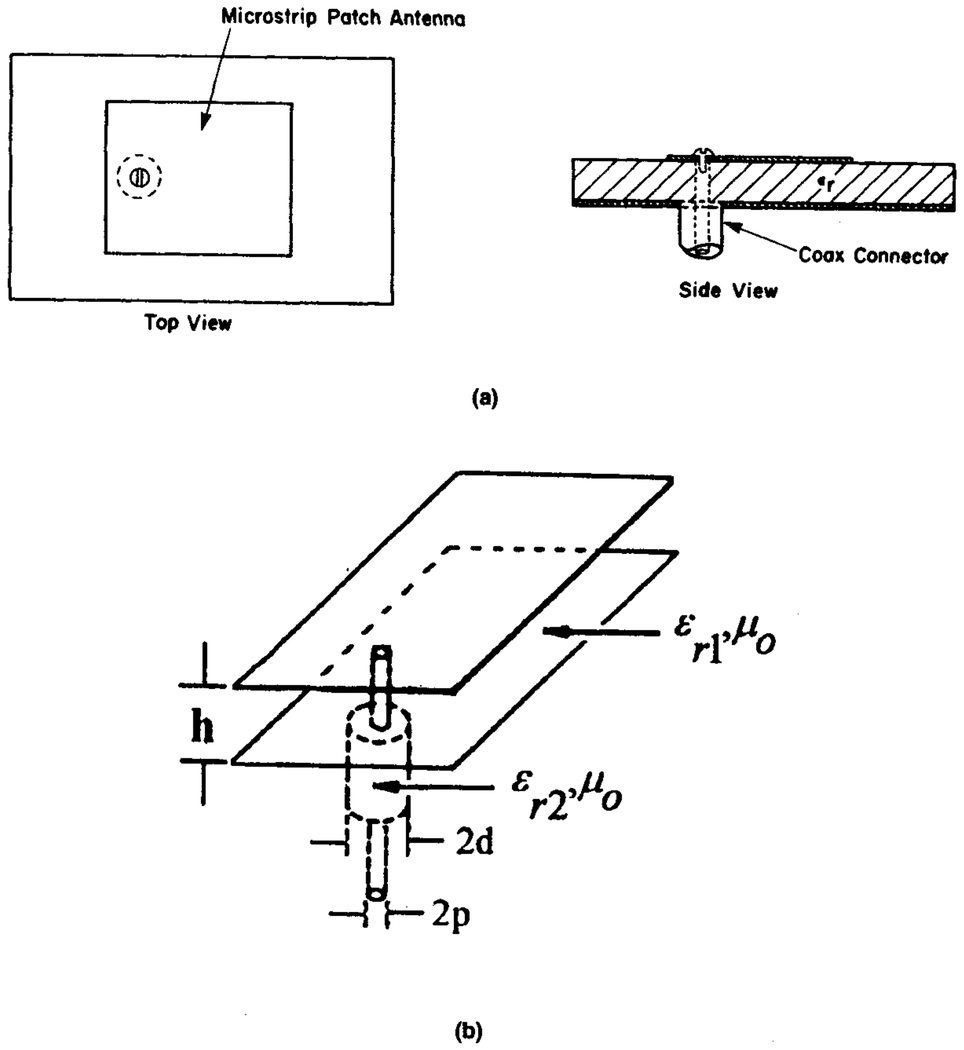

Figure 1.11 Coaxial probe feeding of a microstrip antenna and the equivalent circuit for the probe junction: (a) A typical microstrip antenna with a coaxial probe. (b) Canonical problem of a parallel plate waveguide fed by a coaxial probe. (From [19]. © 1991 IEEE. Reprinted with permission.) (c) Equivalent circuit of a microstrip antenna fed by a probe. (d) Modified equivalent circuit of (c). (From [11]. © 1996 Artech House. Reprinted with permission.)

of the printed circuit board, and the coaxial center conductor after passing through the substrate is soldered to the patch metalization. The location of the feed point is determined for the given mode so that the best impedance match is achieved. Excitation of the patch occurs principally through the coupling of the feed current J_z to the E_z field of the patch mode [12]. The coupling constant can be obtained as:

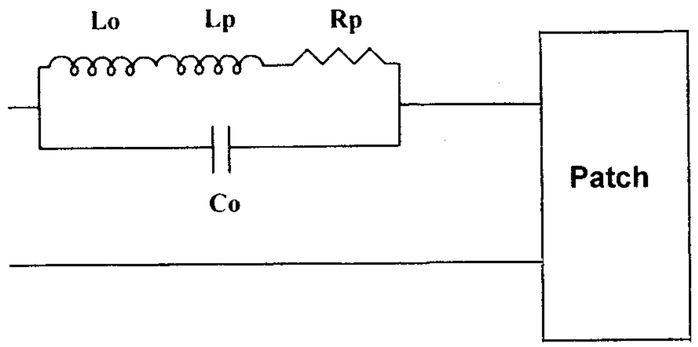

(c)

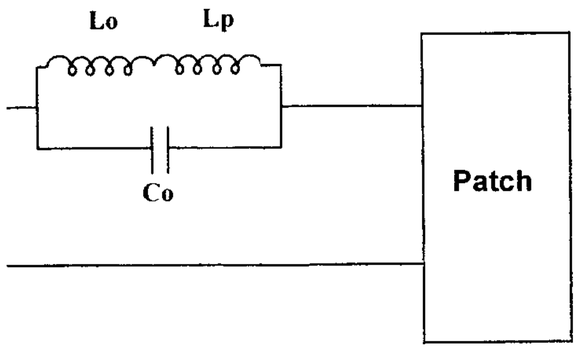

(d)

Figure 1.11 (continued).

$$\text{Coupling} \simeq \iiint_V E_z J_z \, dv \simeq \cos(\pi x_0 / L) \tag{1.5}$$

where L is the resonant length of the patch, and x_0 is the offset of the feed point from the patch edge. Expression (1.5) shows that coupling is maximum for a feed located at a radiating edge of the patch ($x_0 = 0$ or L).

Modeling of Coaxial Feed

The coaxial feed, using Huygen's principle, can be modeled by a cylindrical band of electric current flowing on the center conductor from the bottom to the top along with an annular ribbon of magnetic current in the ground plane. An idealization that simplifies the computation is to replace the electric current

cylinder by a uniform line current ribbon. To determine the probe impedance for a microstrip antenna, the canonical problem of a parallel plate waveguide fed by a coaxial line has been analyzed using the integral equation formulation [19]. The input impedance of this geometry shown in Figure 1.11(b) has been determined. In an approximate analysis, an excitation field corresponding to TEM field distribution in the annular ring about the probe gives fairly accurate results [19]. The resulting impedance can be modeled by an equivalent circuit, as shown in Figure 1.11(c). The expressions for the equivalent circuit parameters are given in Section 2.9. The modified equivalent circuit of (c) is shown in Figure 1.11(d). A number of other approaches for the analysis of a probe fed microstrip antenna are described in [20–23].

Coaxial feed has the advantage of simplicity of design through the positioning of the feed point to adjust the input impedance level. But it has several limitations. First, coaxial feeding of an array requires a large number of solder joints, which makes fabrication difficult and compromises reliability. Second, for increased bandwidth of a patch antenna, a thicker substrate is used and therefore requires a longer probe. This gives rise to an increase in spurious radiation from the probe, increased surface wave power, and increased feed inductance. However, the feed inductance can be compensated for by a series capacitor. One approach to introduce a capacitor in series with the probe is to etch out an annular slot in the patch metalization concentric with the probe [24], as shown in Figure 1.12(a). However, the electric field in the annular region will introduce cross-polar components in the radiation pattern. A variation of this approach is shown in Figure 1.12(b). The antenna impedance can be transformed to a desired value by introducing electromagnetic coupling between the patch and the probe. The coupling region is increased by terminating the probe in a disk, and positioning the disk below the patch. The input impedance depends on the disk size, spacing of the disk from the patch, and the probe position. This modification is shown in Figure 1.12(c) and analyzed in [25].

1.3.2 Microstrip (Coplanar) Feeds

Excitation of the microstrip antenna by a microstrip line on the same substrate appears to be a natural choice because the patch can be considered an extension of the microstrip line, and both can be fabricated simultaneously. But this technique has some limitations. The coupling between the microstrip line and the patch could be in the form of edge/butt-in coupling as shown in Figure 1.13(a), or through a gap between them, as shown in Figure 1.13(b). The excitation of the patch by an edge-coupled microstrip line can be described in terms of the equivalent electric current density J_z associated with the magnetic field H_y of the microstrip line at the junction plane as shown in Figure 1.14.

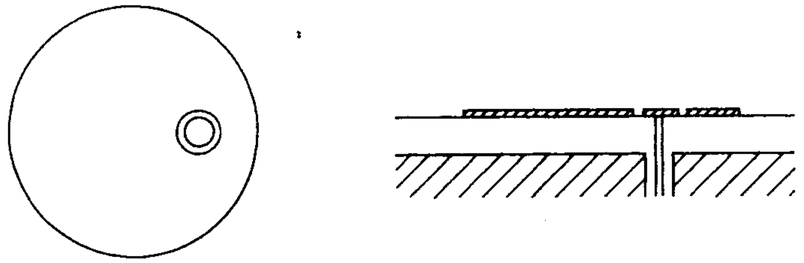

(a)

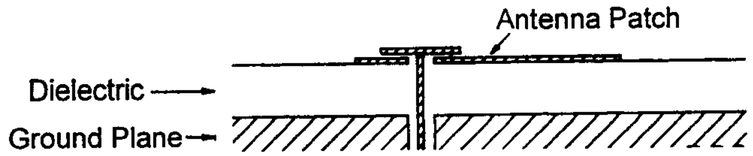

(b)

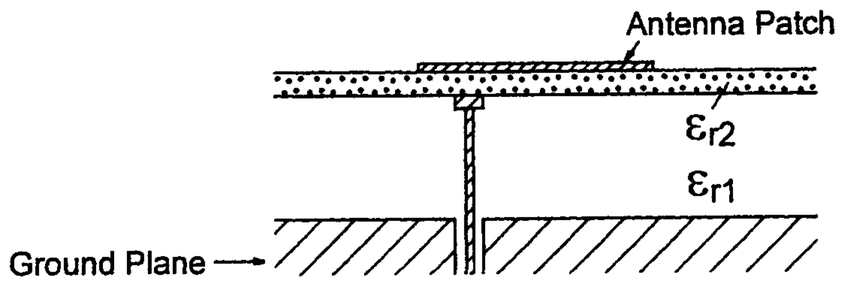

(c)

Figure 1.12 (a) Compensation of probe inductance by a series capacitor in the form of an annular slot concentric with the probe. (From [24]. © 1987 *Electronic Letters*. Reprinted with permission.) (b) Compensation of probe inductance by a series capacitor between the patch antenna and the probe disk on top of the patch. (From [7]. © 1989 Peter Peregrinus. Reprinted with permission.) (c) Transformation of the patch impedance by electromagnetic coupling between the probe and the patch. The probe is terminated in a disk for increased coupling. (From [25]. © 1994 IEEE. Reprinted with permission.)

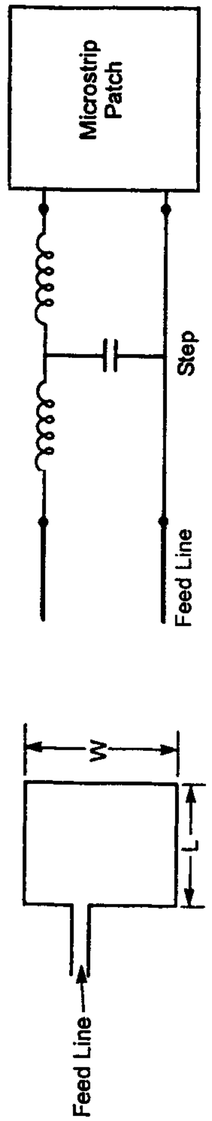

(a)

Figure 1.13 Various types of microstrip feeds and the corresponding equivalent circuits. (a) Microstrip feed at the radiating edge, (b) gap-coupled microstrip feed, (c) microstrip inset feed at the radiating edge, (d) microstrip feed at the nonradiating edge, (e) proximity coupled microstrip feed, and (f) aperture coupled microstrip feed.

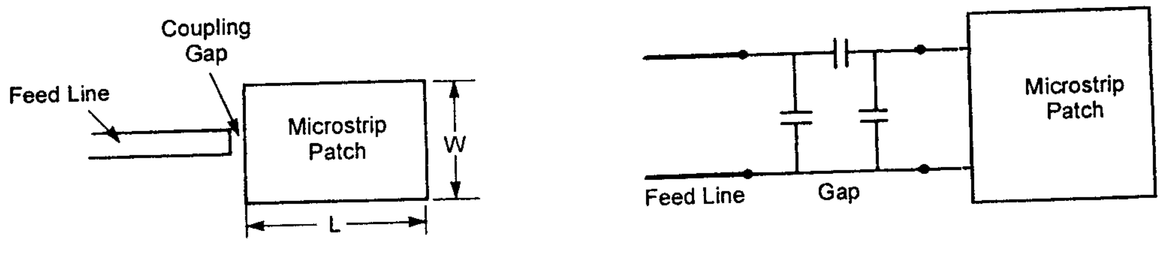

(b)

Figure 1.13 (continued).

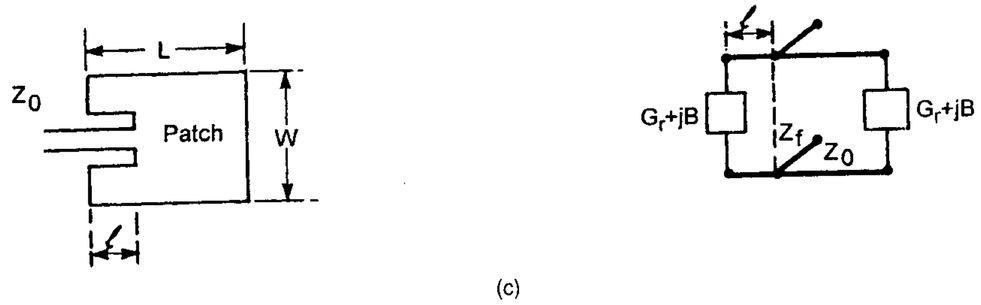

(c)

Figure 1.13 (continued).

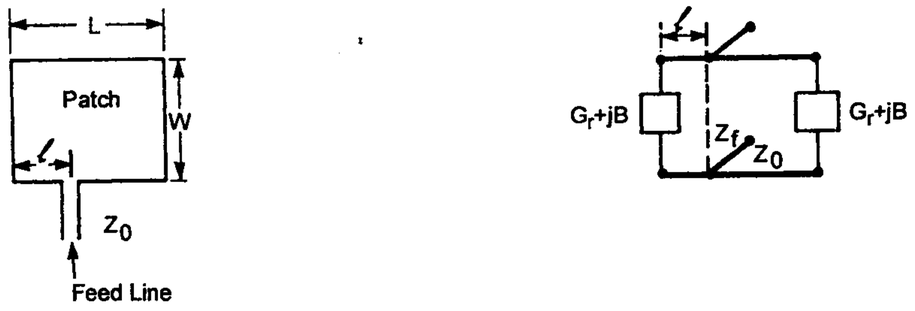

(d)

Figure 1.13 (continued).

The width of this current ribbon is taken to be the *effective width* of the microstrip line [16]. The current J_z couples with E_z of the patch antenna, and the coupling magnitude is determined using (1.5).

Modeling of Coplanar Microstrip Feed

The edge-coupled microstrip feed can be modeled by means of the step-in-width/impedance junction. The equivalent circuit for this is shown in Figure 1.13(a). Similarly, the gap-coupled microstrip feed is represented by the equivalent circuit of the gap as shown in Figure 1.13(b). The effect of direct radiation from the open end of the microstrip line can be represented by a conductance across the shunt capacitor. Equivalent circuit parameters for the discontinuities are available in [16]. A design based on edge-coupled feed is available in [7], and an analysis of the edge-coupled feed based on the FDTD approach is described in [26].

The edge-coupled feed described earlier suffers from a limitation of impedance mismatch because the input impedance of the patch at its radiating edge is very high compared to the 50Ω impedance of the feed line. Therefore, an external impedance matching circuit is used between the patch edge and the 50Ω microstrip line. The impedance matching circuit, beside giving rise to spurious radiation, cannot be accommodated in arrays, because of the nonavailability of physical space on the substrate. The microstrip line blocks radiation from the portion of the patch with which it is in contact resulting in reduced radiation. This is a serious limitation of this feed at millimeter-wave frequencies where the patch width can be comparable to the width of the microstrip line.

The gap-coupled feed requires a narrow gap width for efficient coupling of power. However, a narrow gap size will limit the power handling capability of the antenna. Moreover, the open end of the microstrip feed gives rise to spurious radiation.

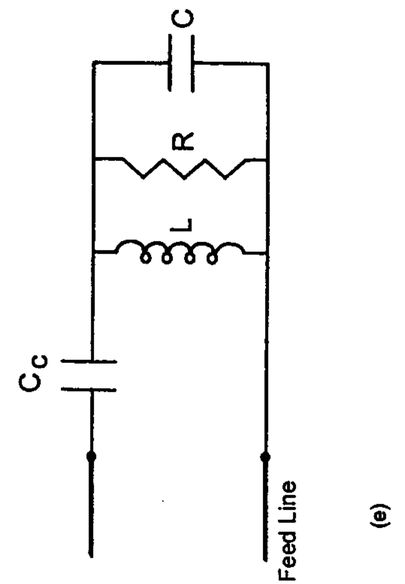

(e)

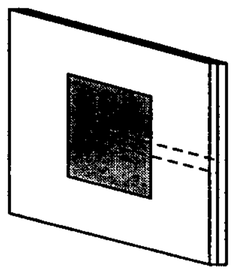

Figure 1.13 (continued).

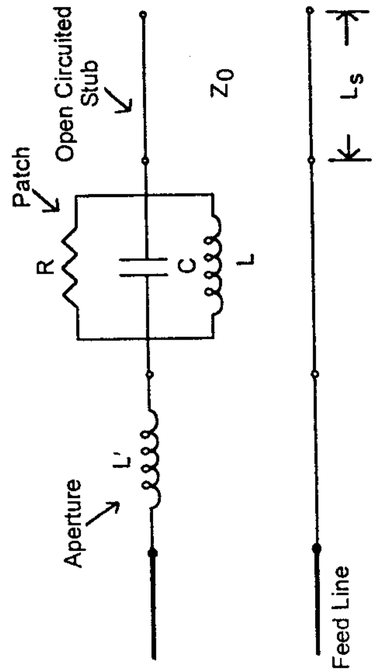

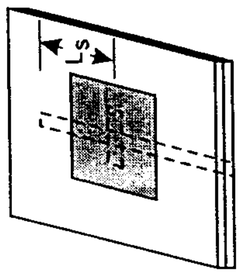

Figure 1.13 (continued).

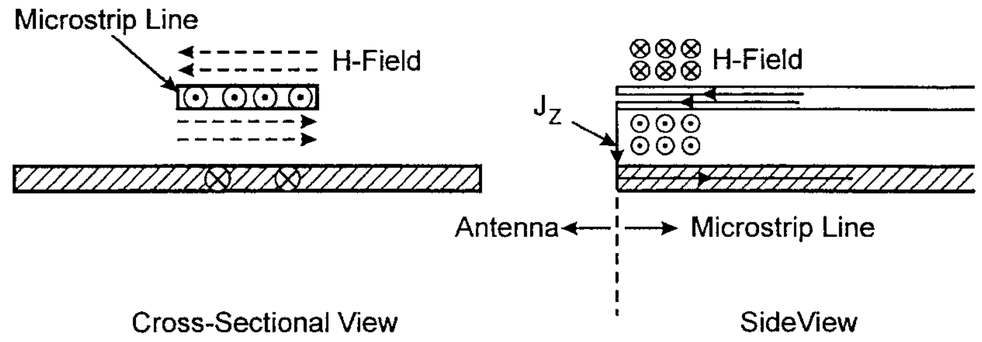

Figure 1.14 Representation of H_{tan} at the interface between the patch antenna and the feed microstrip line by an equivalent current density J_z (dotted lines signify H lines; solid lines are current lines).

An improvement of the coplanar feed that overcomes some of the shortcomings mentioned is shown in Figure 1.13(c). Here, the microstrip line is inset into the patch. The feed position is selected such that the input impedance of the antenna is 50Ω. The resulting feed point is about the same as that used for the coaxial feed. The approximate equivalent circuit for the inset microstrip feed is shown in this figure. However, the transmission line section with inset length l should be modeled as a coplanar waveguide with finite-sized ground plane and conductor backing. A parametric study of rectangular patch with various inset lengths l has been reported [27]. In another configuration for the direct microstrip feed, the feed point is selected on the nonradiating edge of the patch [28] as in Figure 1.13(d). The cross-polarized radiation is high in this case, but can be minimized by optimizing the aspect ratio W/L of the patch at about 1.5. The equivalent circuit for this feed is the same as that drawn in Figure 1.13(c). This feeding technique has been generalized for two-port coupling at the nonradiating edges for applications in series fed linear arrays [29]. Inset microstrip feed is used extensively in the integrated microstrip antennas discussed in Chapter 11.

Coplanar microstrip feeds are easy to design and fabricate. However, feed microstrip lines contribute to spurious radiation. Therefore, they have been used in applications where the demand on performance is not too stringent and the feed must be coplanar with the patch. The bandwidth achieved is 3% to 5%. Feed structure contribution to the radiation has been investigated by Wu et al. [27] for the edge fed case.

A variety of noncoplanar microstrip feeds have been developed: two-layer microstrip feed, the aperture-coupled microstrip feed, and the coplanar waveguide feed. These are inherently broadband in nature because of the number of design parameters available. These feeds are discussed next.

1.3.3 Proximity (Electromagnetically) Coupled Microstrip Feed

A configuration of this noncontacting noncoplanar microstrip feed is shown in Figure 1.13(e). It uses a two-layer substrate with the microstrip line on the lower layer and the patch antenna on the upper layer. The feed line terminates in an open end underneath the patch. This feed is better known as an "electromagnetically coupled" microstrip feed. Coupling between the patch and the microstrip is capacitive in nature. The equivalent circuit for this feed is also shown there, wherein the coupling capacitor C_c is in series with the parallel R-L-C resonant circuit representing the patch. This capacitor can be designed for impedance matching of the antenna, as well as for tuning the patch for improved bandwidth. The open end of the microstrip line can be terminated in a stub and the stub parameters can be used to improve the bandwidth. Bandwidths of the order of 13% have been achieved using this feed [30]. Analysis of this feed is available in [31, 32].

The substrate parameters of the two layers can be selected to increase the bandwidth of the patch, and to reduce spurious radiation from the open end of the microstrip. For this, the lower layer should be thin. The radiating patch being placed on the double layer gives a larger bandwidth. Fabrication of this feed is, however, slightly more difficult because of the requirement for accurate alignment between the patch and the feed line, but soldering is eliminated.

1.3.4 Aperture-Coupled Microstrip Feed

The notable features of this feed configuration [9] are wider bandwidth, and the shielding of the radiating patch from the radiation emanating from the feed structure. A configuration of this feed is shown in Figure 1.13(f). As shown there, it uses two substrates separated by a common ground plane. A microstrip feed line on the lower substrate is electromagnetically coupled to the patch through a slot aperture in the common ground plane. The slot can be of any shape or size, and these parameters can be used to improve the bandwidth. The substrate parameters for the two layers are chosen in a manner to optimize the feed and radiation functions independently. For example, the substrate for the feed line should be thin and of high dielectric constant, whereas the substrate for the patch can be thick and of lower dielectric constant. Moreover, radiation from the open end of the feed line does not interfere with the radiation pattern of the patch because of the shielding effect of the ground plane. This feature also improves the polarization purity. If the coupling slot is nonresonant, the backlobe radiation from the slot is typically 15 to 20 dB below the forward main beam.

The coupling slot is nearly centered with respect to the patch where the magnetic field of the patch is maximum. This is done purposely to enhance magnetic coupling between the magnetic field of the patch and the equivalent magnetic current near the slot. The coupling amplitude can be determined from the following expression [12]:

$$\text{Coupling} \simeq \iiint_V \overline{M} \cdot \overline{H}\, \text{dv} \simeq \sin(\pi x_0/L) \tag{1.6}$$

where x_0 is the offset of the slot from the patch edge. The equivalent circuit of the aperture-coupled microstrip patch is also shown there. In this feed configuration, the patch antenna appears in series with the feed because of slot coupling. The nonresonant slot is represented as an inductor in series with the R-L-C network of the patch. The open-circuited microstrip stub of length L_s can be replaced by a shunt capacitor C_S such that $1/\omega C_S = Z_0 \cot(\beta L_s)$, Z_0 is the characteristic impedance, and β is the propagation constant of the microstrip feed line.

In addition to the merits of the feeding technique described above, this feed can be designed to improve bandwidth by adjusting the shape and length of the coupling slot, width of the feed line, and stub length. An impedance bandwidth of about 21% has been reported for an unstacked patch [33]. Analysis of this feeding technique based on the integral equation approach and the cavity model has been carried out in [34–37]. Transmission line analysis of the aperture-coupled rectangular patch has been carried out in [38], and FDTD analysis in [23]. The transmission line and cavity models of this feeding technique are described in Section 9.4 and a mathematical model of excitation is described in Section 3.1.5.

1.3.5 Coplanar Waveguide Feed

A coplanar waveguide (CPW) is the preferred transmission line for microwave monolithic integrated circuits (MMICs) [16]. Both the CPW and microstrip antennas belong to the planar geometry. Therefore, for integrating microstrip antennas with MMICs, it is desirable to feed the microstrip antennas with a CPW [39, 40]. This type of feeding technique is shown in Figure 1.15. Here, the CPW is etched in the ground plane of the microstrip antenna. Coupling is accomplished via a slot. Three possibilities with this excitation are shown. In Figure 1.15(a) the center conductor of the CPW divides the coupling slot into two. The CPW is transformed into a slot of length L_s in Figure 1.15(b). The coupling between the patch and CPW is inductive for Figure 1.15(a),

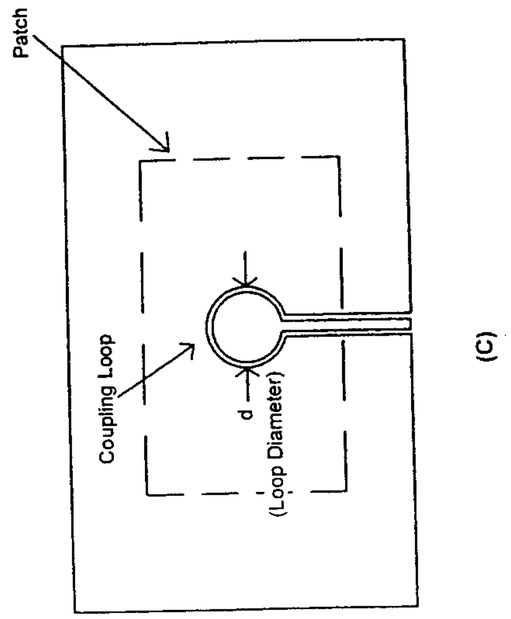

Figure 1.15 Coplanar waveguide feed of the microstrip patch antenna. (a) Inductive coupling by splitting the coupling slot into two by the CPW. (b) Capacitive coupling between the patch and the slot. (c) Coupling through an annular slot to reduce backward radiation from the slot.

and capacitive for Figure 1.15(b). This coupling arrangement is somewhat similar to the aperture coupling of Section 1.3.4; the only difference between the two is that the slot in the ground plane is fed by a microstrip line in aperture-coupled microstrip antennas. Experimental investigations of CPW excitation are reported in [39]. The 10-dB return loss bandwidth was found to be 2.8% for capacitive coupling, and 3.5% for inductive coupling at about 5 GHz on a substrate with $\epsilon_r = 2.2$ and $h = 1.58$ mm. Backward radiation from the slot was found to be about 10 dB below the main beam, which is considerable. This radiation can be reduced by converting the long linear slot into a circular loop as shown in Figure 1.15(c). The loop is centered underneath the patch [40].

An advantage of a CPW feed is that the radiation from the feed structure is negligible because the coplanar waveguide is excited in the odd mode of the coupled slot line [16]. Due to this mode, the equivalent magnetic currents on both the CPW slots radiate almost out of phase, contributing negligibly to the feed radiation. This feature of a CPW feed is useful in the design of antenna arrays since mutual coupling between adjacent lines is minimized.

A comparison of the various types of feed structures is given in Table 1.2.

1.4 Radiation Fields

We explained in Section 1.1 that the radiation field from microstrip antennas can be thought of as being due to a ribbon-like magnetic surface current at the patch periphery. In an alternative but rigorous approach, the radiation field has been determined from the surface electric current on the conducting patch of a microstrip antenna. These two approaches are shown to be equivalent [41]. However, the radiation mechanism based on the ribbon magnetic current or aperture electric field is found to be conceptually simpler. This mechanism is also the basis for a number of theoretical models for microstrip antennas. These models are described in Chapter 2.

Figure 1.6 shows that radiation from microstrip antennas can be well understood in terms of radiation from the microstrip open end. This mechanism has been very well described in the literature [42–52]. Radiation from discontinuities in microstrip was first examined by Lewin [42], whose analysis was based on the currents flowing on the conductors. The radiation pattern from the open end of a microstrip line is found to be similar to that of a Hertzian magnetic dipole. This method was also used to calculate the effect of radiation on the quality factor Q of microstrip resonators [43–45]. The analysis by Sobol [45] was based on the fields in the aperture formed by the open end of the

Table 1.2
Comparison of Various Types of Feed Structures for Microstrip Patch Antennas

				Microstrip Feed Types				
Characteristics	**Coaxial-Probe Feed**	**Radiating Edge Coupled**	**Nonradiating Edge Coupled**	**Gap Coupled**	**Inset Feed**	**Proximity Coupled**	**Aperture Coupled**	**CPW Feed**
Configuration	**Nonplanar**	**Coplanar**	**Coplanar**	**Coplanar**	**Coplanar**	**Planar**	**Planar**	**Planar**
Spurious feed radiation	More	Less	Less	More	More	More	More	Less
Polarization purity	Poor	Good	Poor	Poor	Poor	Poor	Excellent	Good
Ease of fabrication	Soldering and drilling needed	Easy	Easy	Easy	Easy	Alignment required	Alignment required	Alignment required
Reliability	Poor due to soldering	Better	Better	Better	Better	Good	Good	Good
Impedance matching	Easy	Poor	Easy	Easy	Easy	Easy	Easy	Easy
Bandwidth (achieved with impedance matching)	2–5%	9–12%	2–5%	2–5%	2–5%	13% [30]	21% [33]	3% [39, 40]

microstrip and the ground plane. Using the analysis, the effect of radiation on the overall Q factor of a microstrip resonator was described as a function of resonator dimensions, operating frequency, relative dielectric constant, and thickness of the substrate. Theoretical and experimental results showed that at high frequencies, the radiation loss is much larger than the conductor and dielectric losses. It was also confirmed that open-circuited microstrip lines radiate more power when fabricated on thick low dielectric constant substrates.

Vector potentials are used next to determine the radiation fields due to surface currents.

1.4.1 Vector Potentials and Radiation Field Formulation

First, we assume that only magnetic currents exist. The electric and magnetic fields at any point $P(r, \theta, \phi)$ outside the microstrip antenna can then be written (with $e^{j\omega t}$ time variation assumed and suppressed)

$$\overline{E}^m(r) = -\frac{1}{\epsilon}\nabla \times \overline{F} \tag{1.7}$$

$$\overline{H}^m(r) = \frac{1}{j\omega\mu\epsilon}\nabla(\nabla \cdot \overline{F}) - j\omega\overline{F} \tag{1.8}$$

where ϵ is the permittivity and μ is the permeability of the medium, the superscript m denotes the fields due to magnetic currents, and ω is the angular frequency. The vector electric potential $\overline{F}$ is defined as

$$\overline{F} = \frac{\epsilon}{4\pi}\int\int_S \overline{M}(\overline{r}')\frac{e^{-jk_0|\overline{r}-\overline{r}'|}}{|\overline{r}-\overline{r}'|}dS' \tag{1.9}$$

where k_0 is a free-space wave number and $\overline{M}(\overline{r}')$ is the surface magnetic current density at a point r' from the origin as shown in Figure 1.16(a). As in most other published literature, primed coordinates are used to denote source point location and unprimed coordinates are used to denote field point location.

Similarly, by using a vector magnetic potential, $\overline{A}$, the fields due to an electric current can be written as:

$$\overline{E}^e(r) = \frac{1}{j\omega\mu\epsilon}\nabla(\nabla \cdot \overline{A}) - j\omega\overline{A} \tag{1.10}$$

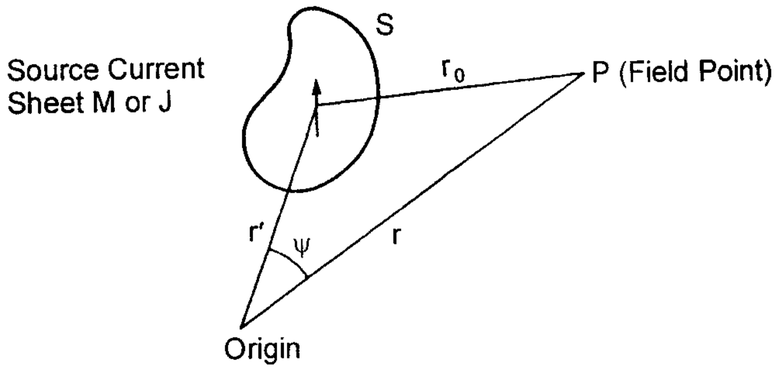

(a)

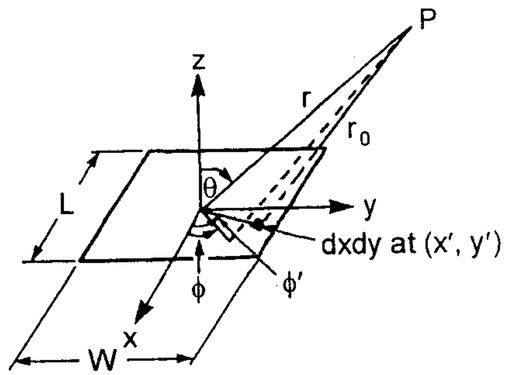

(b)

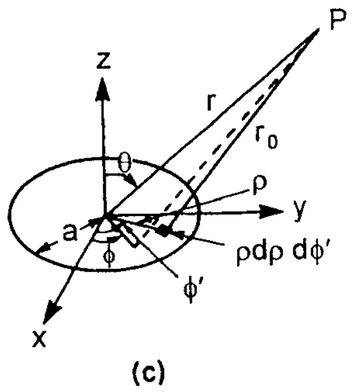

(c)

Figure 1.16 (a) An arbitrary source current sheet M or J. (b) Rectangular magnetic current sheet. (c) Circular electric current sheet.

$$\overline{H}^e(r) = \frac{1}{\mu}\nabla \times \overline{A} \tag{1.11}$$

The vector magnetic potential $\overline{A}$ is given by

$$\overline{A} = \frac{\mu}{4\pi}\int\int_S \bar{J}(\bar{r}')\frac{e^{-jk_0|\bar{r}-\bar{r}'|}}{|\bar{r}-\bar{r}'|}dS' \tag{1.12}$$

The total fields due to both the electric and magnetic current sources are:

$$\overline{E}(r) = \overline{E}^e + \overline{E}^m = \frac{1}{j\omega\mu\epsilon}\nabla(\nabla \cdot \overline{A}) - j\omega\overline{A} - \frac{1}{\epsilon}\nabla \times \overline{F} \tag{1.13}$$

$$\overline{H}(r) = \overline{H}^e + \overline{H}^m = \frac{1}{j\omega\mu\epsilon}\nabla(\nabla \cdot \overline{F}) - j\omega\overline{F} + \frac{1}{\mu}\nabla \times \overline{A} \tag{1.14}$$

The only significant field components in the far field are those transverse to the direction of propagation, that is, the θ and ϕ components. Considering only the magnetic currents, one obtains [17]

$$H_\theta = -j\omega F_\theta \text{ and } H_\phi = -j\omega F_\phi \tag{1.15}$$

and in free space

$$\overline{E} = -\eta_0\hat{r} \times \overline{H} = -\eta_0(\hat{\phi}H_\theta - \hat{\theta}H_\phi) = j\omega\eta_0(\hat{\phi}F_\theta - \hat{\theta}F_\phi) \tag{1.16}$$

where η_0 is the free-space impedance (120π ohms). Similarly, for electric currents alone,

$$E_\theta = -j\omega A_\theta \tag{1.17}$$

$$E_\phi = -j\omega A_\phi \tag{1.18}$$

and in free space

$$\overline{H} = \hat{r} \times \overline{E}/\eta_0 \tag{1.19}$$

The far fields are delineated by the condition that $r >> r'$ or $r \geq 2L^2/\lambda_0$, where L is the largest dimension of the aperture. Hence from

(1.9) with $|\bar{r} - \bar{r}'| = r - r'\cos\psi$ in the numerator and $|\bar{r} - \bar{r}'| \approx r$ in the denominator, one obtains

$$\bar{F} = \frac{\epsilon}{4\pi}\frac{e^{-jk_0 r}}{r}\int\int_S \bar{M}(r')e^{jk_0 r'\cos\psi}dS' \tag{1.20}$$

and from (1.12)

$$\bar{A} = \frac{\mu}{4\pi}\frac{e^{-jk_0 r}}{r}\int\int_S \bar{J}(r')e^{jk_0 r'\cos\psi}dS' \tag{1.21}$$

where ψ is the angle between the $\hat{r}$ and $\hat{r}'$ directions as shown in Figure 1.16(a). Now, we apply the above derivations to the far fields of rectangular and circular current distributions.

Far Fields of a Rectangular Magnetic Current Source

Consider a two-dimensional rectangular magnetic current sheet and the coordinate system shown in Figure 1.16(b). The expression for the far-zone vector potential can be expressed as (with $r\cos\psi = x\sin\theta\cos\phi + y\sin\theta\sin\phi$)

$$\bar{F} = \frac{\epsilon_0}{4\pi}\frac{e^{-jk_0 r}}{r}\int_{-L/2}^{L/2}\int_{-W/2}^{W/2}\bar{M}(x', y') \exp[jk_0(x'\sin\theta\cos\phi + y'\sin\theta\sin\phi)]dx'dy' \tag{1.22}$$

where L and W are the length and width of the current sheet. For $\bar{M}(x, y) = M_x(x, y)\hat{x} + M_y(x, y)\hat{y}$, (1.22) becomes

$$\bar{F} = \frac{\epsilon_0}{4\pi}\frac{e^{-jk_0 r}}{r}\int_{-L/2}^{L/2}\int_{-W/2}^{W/2}(M_x(x', y')\hat{x} + M_y(x', y')\hat{y}) \exp[jk_0(x'\sin\theta\cos\phi + y'\sin\theta\sin\phi)]dx'dy' \tag{1.23}$$

and the vector electric potential components are

$$F_x = \frac{\epsilon_0}{4\pi}\frac{e^{-jk_0 r}}{r}\int_{-L/2}^{L/2}\int_{-W/2}^{W/2}M_x(x', y') \exp[jk_0(x'\sin\theta\cos\phi + y'\sin\theta\sin\phi)]dx'dy' \tag{1.24a}$$

$$F_y = \frac{\epsilon_0}{4\pi}\frac{e^{-jk_0 r}}{r}\int_{-L/2}^{L/2}\int_{-W/2}^{W/2}M_y(x', y') \exp[jk_0(x'\sin\theta\cos\phi + y'\sin\theta\sin\phi)]dx'dy' \tag{1.24b}$$

$$F_z = 0 \tag{1.24c}$$

For any vector $\bar{T}$, the transformation from rectangular to spherical coordinates can be obtained from the following matrix:

$$\begin{bmatrix} T_r \\ T_\theta \\ T_\phi \end{bmatrix} = \begin{bmatrix} \sin\theta\cos\phi & \sin\theta\sin\phi & \cos\theta \\ \cos\theta\cos\phi & \cos\theta\sin\phi & -\sin\theta \\ -\sin\phi & \cos\phi & 0 \end{bmatrix}\begin{bmatrix} T_x \\ T_y \\ T_z \end{bmatrix} \tag{1.25}$$

Hence, from (1.16) and (1.25), the electric field can be obtained in terms of F_x and F_y:

$$E_\theta = j\omega\eta_0(F_x\sin\phi - F_y\cos\phi) \tag{1.26a}$$

$$E_\phi = j\omega\eta_0(F_x\cos\theta\cos\phi + F_y\cos\theta\sin\phi) \tag{1.26b}$$

Similar expressions are obtained for the magnetic field in terms of the vector magnetic potential components A_x and A_y.

Example:

Let us determine the radiation patterns of an aperture of dimensions $h \times W$ with $E_x = -V_0/h$ V/m, and $E_y = 0$. For this case $M_x = 0$ and

$$M_y = \begin{cases} V_0/h & -\frac{W}{2} \le y \le \frac{W}{2}, -\frac{h}{2} \le x \le \frac{h}{2} \\ 0 & \text{elsewhere} \end{cases} \tag{1.27}$$

Using (1.24b)

$$F_y = \frac{\epsilon_0}{4\pi} V_o W \frac{e^{-jk_0 r}}{r} \text{sinc}(k_0 h \sin\theta\cos\phi/2)\,\text{sinc}(k_0 W \sin\theta\sin\phi/2) \tag{1.28}$$

Now using (1.26), one obtains

$$E_\theta = -jk_0 V_0 W \frac{e^{-jk_0 r}}{4\pi r} \text{sinc}(k_0 h \sin\theta\cos\phi/2)\,\text{sinc}(k_0 W \sin\theta\sin\phi/2)\cos\phi \tag{1.29a}$$

$$E_\phi = jk_0 V_0 W \frac{e^{-jk_0 r}}{4\pi r} \text{sinc}(k_0 h \sin\theta\cos\phi/2)\,\text{sinc}(k_0 W \sin\theta\sin\phi/2)\cos\theta\sin\phi \tag{1.29b}$$

The above approach has been used to determine the radiation pattern of a rectangular patch by modeling it as an array of two rectangular magnetic current sources. The final expression for the radiation patterns are given in Chapter 4. Expressions (1.29a) and (1.29b) give the radiation fields of a quarter-wave rectangular patch antenna.

Far Field of a Circular Electric Current Source

The planar electric current sheet formulation for a circular patch antenna is used in the full-wave analysis described in Chapter 3. Consider a planar circular electric current sheet with a coordinate system as shown in Figure 1.16(c). The far-zone vector magnetic potential is [17]

$$\overline{A} = \frac{\mu_0}{4\pi} \frac{e^{-jk_0}}{r} \int_0^{2\pi}\int_0^a \bar{J}(\rho, \phi') \exp[jk_0 \rho \sin\theta\cos(\phi' - \phi)]\,\rho d\rho d\phi' \tag{1.30}$$

where (r, θ, ϕ) are the spherical coordinates and (ρ, ϕ', z) are the cylindrical coordinates of a point. If $\bar{J}(\rho, \phi') = J_\rho(\rho, \phi')\hat{\rho} + J_\phi(\rho, \phi')\hat{\phi}$, then

$$\overline{A} = \frac{\mu_0}{4\pi} \frac{e^{-jk_0 r}}{r} \int_0^{2\pi}\int_0^a (J_\rho(\rho, \phi')\hat{\rho} + J_\phi(\rho, \phi')\hat{\phi}) \exp[jk_0 \rho \sin\theta\cos(\phi' - \phi)]\,\rho d\rho d\phi' \tag{1.31}$$

For any vector $\overline{T}$, the transformation from cylindrical to spherical coordinates can be obtained from the following matrix:

$$\begin{bmatrix} T_r \\ T_\theta \\ T_\phi \end{bmatrix} = \begin{bmatrix} \sin\theta\cos(\phi' - \phi) & -\sin\theta\sin(\phi' - \phi) & \cos\theta \\ \cos\theta\cos(\phi' - \phi) & -\cos\theta\sin(\phi' - \phi) & -\sin\theta \\ \sin(\phi' - \phi) & \cos(\phi' - \phi) & 0 \end{bmatrix} \begin{bmatrix} T_\rho \\ T_{\phi'} \\ T_z \end{bmatrix} \tag{1.32}$$

Therefore, using (1.17), (1.18), (1.31), and (1.32), the components for the electric field can be written as:

$$A_\theta = \frac{\mu_0}{4\pi} \frac{e^{-jk_0 r}}{r} \cos\theta \int_0^{2\pi}\int_0^a (J_\rho(\rho, \phi')\cos(\phi' - \phi) - J_\phi(\rho, \phi')\sin(\phi' - \phi)) \exp[jk_0 \rho \sin\theta\cos(\phi' - \phi)]\,\rho d\rho d\phi' \tag{1.33}$$

$$A_\phi = \frac{\mu_0}{4\pi} \frac{e^{-jk_0 r}}{r} \int_0^{2\pi}\int_0^a (J_\rho(\rho, \phi')\sin(\phi' - \phi) + J_\phi(\rho, \phi')\cos(\phi' - \phi)) \exp[jk_0 \rho \sin\theta\cos(\phi' - \phi)]\,\rho d\rho d\phi' \tag{1.34}$$

Similar expressions hold for the vector electric potential components F_θ and F_ϕ, and are given here for the azimuthal component of magnetic current:

$$F_\theta = \frac{-\epsilon_0}{4\pi} \frac{e^{-jk_0 r}}{r} \cos\theta \int_0^{2\pi}\int_\rho M_\phi(\rho, \phi')\sin(\phi' - \phi) \exp[jk_0 \rho \sin\theta\cos(\phi' - \phi)]\,\rho d\rho d\phi' \tag{1.35a}$$

$$F_\phi = \frac{\epsilon_0}{4\pi} \frac{e^{-jk_0 r}}{r} \int_0^{2\pi}\int_\rho M_\phi(\rho, \phi')\cos(\phi' - \phi) \exp[jk_0 \rho \sin\theta\cos(\phi' - \phi)]\,\rho d\rho d\phi' \tag{1.35b}$$

and

$$E_\theta = -j\omega\eta_0 F_\phi \tag{1.36a}$$

$$E_\phi = j\omega\eta_0 F_\theta \tag{1.36b}$$

Therefore,

$$E_\theta = \frac{-jk_0}{4\pi}\frac{e^{-jk_0 r}}{r}\int_0^{2\pi}\int_\rho M_\phi(\rho, \phi')\cos(\phi' - \phi) \exp[jk_0\rho\sin\theta\cos(\phi' - \phi)]\rho d\rho d\phi' \tag{1.37a}$$

$$E_\phi = \frac{-jk_0}{4\pi}\frac{e^{-jk_0 r}}{r}\cos\theta\int_0^{2\pi}\int_\rho M_\phi(\rho, \phi')\sin(\phi' - \phi) \exp[jk_0\rho\sin\theta\cos(\phi' - \phi)]\rho d\rho d\phi' \tag{1.37b}$$

The approach given above assumes a free-space Green's function is employed. However, microstrip antennas employ a grounded substrate on which the antenna is printed. The effect of the substrate and the ground plane can be included in a rigorous manner by employing a suitable Green's function. However, it is possible to use an *add-on* approach in which the effects of the grounded substrate on the radiation patterns are included through suitable factors. This approach is discussed in Chapter 4.

Once the radiated fields are known, the related antenna characteristics can be obtained readily. Expressions for the radiated fields applicable to other geometries, such as triangular, pentagonal, and elliptical patches, can be derived in a similar manner to that for the rectangular or circular patches presented above.

1.4.2 Microstrip Antenna Characteristics Calculations

From the analysis presented in the preceding section, radiation patterns and hence gain and beamwidth characteristics of microstrip antennas are readily evaluated. However, for other antenna characteristics such as losses, quality factor, and efficiency, additional equations are required, as discussed next.

Radiated Power

The power radiated from an antenna can be calculated by integrating the Poynting vector over the radiating aperture:

$$P_r = \frac{1}{2}\mathrm{Re}\iint_{\text{aperture}}(\bar{E}\times\bar{H}^*)\cdot d\bar{S} \tag{1.38a}$$

For microstrip antennas, the electric field within the patch is normal to the strip conductor and the ground plane, and the magnetic field of interest is parallel to the strip edge. Alternatively, radiated power can be obtained from the radiation pattern using the following equation:

$$P_r = \frac{1}{2\eta_o}\int\int(|E_\theta|^2 + |E_\phi|^2)r^2\sin\theta d\theta d\phi \tag{1.38b}$$

Dissipated Power

The power dissipated in a microstrip antenna consists of the conductor loss P_c and the dielectric loss P_d. The former can be determined from an I^2R relationship by integrating the current density over the patch and ground plane areas:

$$P_c = 2\frac{R_s}{2}\iint_S(\bar{J}\cdot\bar{J}^*)dS \tag{1.39}$$

where R_s is the real part of the surface impedance of the metalization and S is the patch area. In (1.39) the surface current density J is obtained as the tangential component of the magnetic field.

The dielectric loss can be determined by integrating the electric field over the volume V of the microstrip cavity:

$$P_d = \frac{\omega\epsilon''}{2}\iiint_V |E|^2 dV = \frac{\omega\epsilon''}{2}h\iint_S |E|^2 dS \quad \text{for thin substrates} \tag{1.40}$$

where ω is the radian frequency, ϵ'' is the imaginary part of the complex permittivity of the substrate, and h is the substrate thickness.

Stored Energy

The total energy stored in a patch antenna is the sum of the electric and magnetic energies, and is

$$W_T = W_e + W_m = \frac{1}{4}\iiint_V(\epsilon|E|^2 + \mu|H|^2)dV \tag{1.41}$$

where μ is the permeability. The electric and magnetic energies are equal at resonance. Therefore, (1.41) can be simplified to

$$W_T = \frac{1}{2}\epsilon h \iint_S |E|^2 dS \quad \text{for thin substrates} \tag{1.42}$$

Input Impedance

Because all microstrip antennas have to be matched to the standard generator impedance or load, the input impedance calculation for antennas is particularly important. Microstrip antennas can be fed by a coaxial line or a microstrip line or a coplanar waveguide. For a coaxially fed microstrip antenna, the input power can be computed as

$$P_{\text{in}}^{c} = -\iiint_V \overline{E} \cdot \overline{J}^* dV \tag{1.43}$$

where J is the electric current density (A/m^2) on the coaxial feed source. The superscript c denotes the coaxial feed. If the coaxial current is z directed and assumed to be electrically thin, (1.43) becomes

$$P_{\text{in}}^{c} = -E(x_0, y_0) \int_0^h I^*(z')dz' \tag{1.44}$$

where (x_0, y_0) are the feed point coordinates. The input impedance can be calculated using the relationship $P_{\text{in}} = |I_{\text{in}}|^2 Z_{\text{in}}$ in (1.44) to obtain

$$Z_{\text{in}} = -\frac{E(x_0, y_0)}{|I_{\text{in}}|^2} \int_0^h I^*(z')dz' \tag{1.45}$$

When $h << \lambda_0$, E and $I(z')$ are constant so that

$$Z_{\text{in}} = V_{\text{in}}/I_{\text{in}} \tag{1.46}$$

where

$$V_{\text{in}} = -E(x_0, y_0) \int_0^h dz' = -hE(x_0, y_0) \tag{1.47}$$

The coaxial feed approach can also be used to analyze a microstrip line-fed microstrip antenna. For this, the feed current density J in (1.43) is obtained from the equivalence principle and the transverse magnetic field in the plane where the microstrip line joins the patch. This is shown in Figure 1.14. The width of the current ribbon should be taken equal to the effective width of the microstrip line (see Appendix B).

1.5 Surface Waves and Photonic Bandgap Structures

1.5.1 Surface Waves

Surface waves are excited on microstrip antennas whenever the substrate $\epsilon_r > 1$. Besides end-fire radiation, surface waves give rise to coupling between various elements of an array [13]. These undesirable features of surface waves are depicted in Figure 1.17 [10]. Surface waves are launched into the substrate at an elevation angle θ lying between $\pi/2$ and $\sin^{-1}(1/\sqrt{\epsilon_r})$. These waves are incident on the ground plane at this angle as shown, get reflected from there, then meet the dielectric-air interface, which also reflects them. Following this zigzag path, they finally reach the boundaries of the microstrip structure where they are reflected back and diffracted by the edges giving rise to end-fire radiation. On the way to the boundary, if there is any other antenna in proximity, the surface waves can become coupled to it. Because surface waves decay as $1/\sqrt{r}$, coupling also decreases away from the point of excitation.

Surface waves are TM and TE modes of the substrate. These modes are characterized by waves attenuating in the transverse direction (normal to the antenna plane) and having a real propagation constant above the cutoff

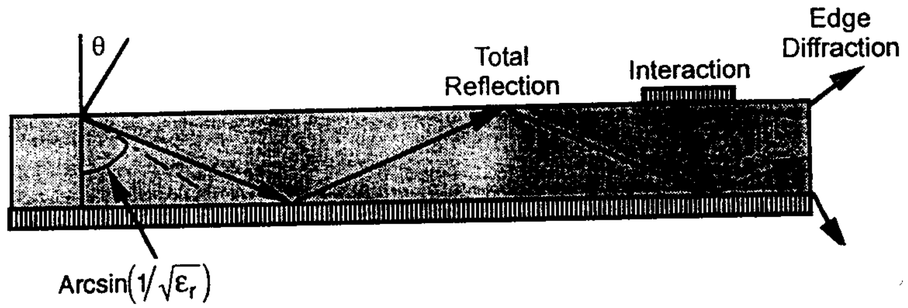

Figure 1.17 Propagation of surface waves in the substrate of a patch antenna leading to spurious coupling between different circuit or antenna elements and diffraction at the edge. (From [10]. © 1995 Artech House. Reprinted with permission.)

frequency. The phase velocity of the surface waves is strongly dependent on the substrate parameters h and ϵ_r. The solution for the propagation constant of these modes is available in [53]. The lowest order TM-type mode has no cutoff frequency. It is designated as the TM_0 mode. The cutoff frequencies for the higher order TM_n and TE_n modes are given by

$$f_c = \frac{nc}{4h\sqrt{\epsilon_r - 1}} \tag{1.48}$$

where c is the velocity of light in free space, h is the substrate thickness, and $n = 1, 3, 5, \ldots$ for TE_n modes and $n = 0, 2, 4, \ldots$ for TM_n modes. For the TE_1 mode, the calculated values of h/λ_c (where λ_c is the cutoff wavelength) are 0.217 and 0.072 for Duroid ($\epsilon_r = 2.32$) and GaAs ($\epsilon_r = 13.0$) substrates, respectively. Thus, the lowest order TE mode is excited at about 41 GHz for a 1.6-mm-thick Duroid substrate and at about 109 GHz for a 200-μm-thick GaAs substrate. Because the TM_0 mode has a zero cutoff frequency, it will always be excited at the open end of the microstrip antenna. It will even propagate on very thin substrates having low dielectric constant values at nearly the velocity of light. The field distribution of the TE_1 mode is such that it can propagate below the patch metalization, and can always be excited above the cutoff frequency.

The dispersion relations for the TM_n and TE_n modes are given below for TM_n modes, $n = 0, 2, 4, \ldots$:

$$\epsilon_r u_0 h + uh\tanh(uh) = 0 \tag{1.49}$$

and for TE_n modes, $n = 1, 3, 5, \ldots$

$$u_0 h + uh\coth(uh) = 0 \tag{1.50}$$

where

$$u_0^2 = \beta^2 - k_0^2 \tag{1.51a}$$

and

$$u^2 = \beta^2 - k_0^2\epsilon_r \tag{1.51b}$$

Graphical solutions of (1.49) and (1.50) for the propagation constant β are available in [54]. However, one needs to know the exact value of β for

the analysis of microstrip antennas. The exact value is generally obtained using a root searching algorithm. The initial value of β is still needed in a closed form for root searching. For the TM_0 mode in lossless substrates, the radial propagation constant β is real, and is bounded by $1 < \beta/k_0 < \epsilon_r$. If the substrate is electrically thin, $\beta/k_0 \approx 1$. The value of β/k_0 can then be obtained by assuming $\beta/k_0 = 1 + \delta$. Substituting this expression in (1.49) we get [55]

$$\epsilon_r\sqrt{2\delta + \delta^2} - \sum_{n=0}^{\infty}\alpha_n\delta^n = 0 \tag{1.52}$$

where the infinite sum in (1.52) is a Taylor's series for $\sqrt{\epsilon_r - z^2}\tan(k_0 h\sqrt{\epsilon_r - z^2})$ around the point $z = \beta/k_0 = 1$. In (1.52)

$$\alpha_0 = s\tan(k_0 hs)$$

$$\alpha_1 = -\frac{1}{s}\left[\tan(k_0 hs) + \frac{k_0 hs}{\cos^2(k_0 hs)}\right] \tag{1.53}$$

$$s = \sqrt{\epsilon_r - 1} \tag{1.54}$$

Retaining only the dominant term α_0 in (1.52), one can obtain [55, 56]

$$\beta/k_0 \approx 1 + \frac{1}{2}\left(\frac{\epsilon_r - 1}{\epsilon_r}k_0 h\right)^2 \tag{1.55}$$

Two-term Taylor approximation in (1.52) yields [56]

$$\frac{\beta}{k_0} = 1 + \frac{\alpha_0\alpha_1 - \epsilon_r^2 + \epsilon_r\sqrt{\epsilon_r^2 - 2\alpha_0\alpha_1 + \alpha_0^2}}{\epsilon_r^2 - \alpha_1^2} \tag{1.56}$$

This expression gives good accuracy for $sh < \lambda_0/4$. If the substrate has moderate losses defined as $\epsilon_r(1 - j\tan\delta)$, then the surface wave propagation constant will also be complex valued defined as $\beta = (\beta_r - j\beta_i)$ with $\beta_i > 0$. The approximate expression for β is found as [56]

$$\beta_r = \beta \tag{1.57a}$$

$$\beta_i \approx (\epsilon_r - 1)\tan\delta(k_0 h/\epsilon_r)^2 \tag{1.57b}$$

The value of β is defined in (1.55) or (1.56).

For a multilayered substrate consisting of N different (thin) layers, a general formula for β/k_0 for the TM_0 mode has been obtained [57]. It is a generalization of (1.55) and is given as

$$\beta/k_0 = 1 + \frac{1}{2}\left[\sum_{i=1}^{N} \frac{\epsilon_{ri} - 1}{\epsilon_{ri}} k_0 h_i\right]^2 \tag{1.58}$$

where ϵ_{ri} and h_i are the constituent parameters of the ith layer.

It is also of interest to know the value of the substrate thickness such that only the TM_0 surface wave mode propagates and all other modes are below cutoff. For the single-layer substrate one obtains from (1.48) for $n = 1$,

$$\frac{h}{\lambda_0} < \frac{1}{4\sqrt{\epsilon_r - 1}} \tag{1.59}$$

The condition for the double-layer substrate case is obtained as follows [58]:

$$\tan(k_0 h_1 \sqrt{\epsilon_{r1} - 1}) \tan(k_0 h_2 \sqrt{\epsilon_{r2} - 1}) \leq \sqrt{\frac{\epsilon_{r2} - 1}{\epsilon_{r1} - 1}} \tag{1.60}$$

Finally, it is useful to plot the surface wave mode chart. The logarithmic behavior of $\beta/k_0 - 1$ is plotted in Figure 1.18(a) for single-layer substrates with $\epsilon_r = 2.2$, 4.34, and 9.6 [55]. This plot shows the quadratic behavior of $\beta/k_0 - 1$ with $k_0 h\sqrt{\epsilon_r - 1}$ for thin substrates. The dependence of the imaginary part of β/k_0 on the loss tangent of the substrate and its thickness is plotted in Figure 1.18(b). For thin substrates β_i/k_0 is found to vary linearly with $\tan\delta$ and $k_0 h\sqrt{\epsilon_r - 1}$. Figure 1.19 shows $\beta/k_0 - 1$ for the double-layer substrate with equal thicknesses $h_2 = h_1 = h$ and $\epsilon_{r1} = 5$, $\epsilon_{r2} = 2$ and $\epsilon_{r1} = 2$, $\epsilon_{r2} = 5$ [55]. The propagation constants for the first three surface wave modes as a function of the substrate thickness h/λ_0 have been plotted in Figure 12.16 for $\epsilon_r = 2.55$.

The power carried away by the surface wave increases with increase in substrate thickness. However, for thicknesses satisfying

$$\frac{h}{\lambda_0} \leq \frac{0.3}{2\pi\sqrt{\epsilon_r}} \tag{1.61}$$

the antenna loss associated with the surface wave can be neglected [49]. The radiation efficiency of the antenna decreases due to the power carried away by

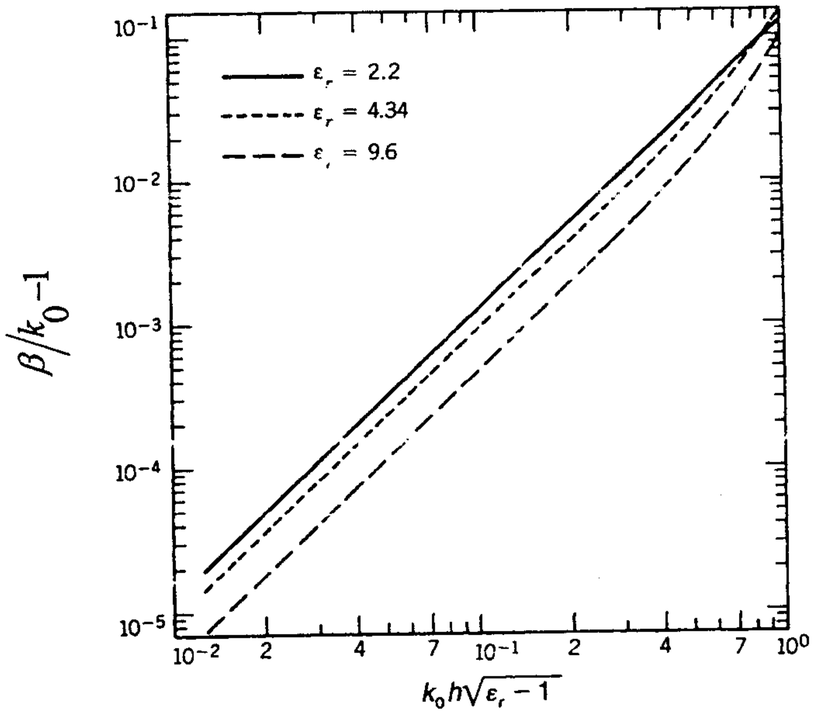

(a)

(a)

Figure 1.18 (a) Variation of β/k_0 with the normalized substrate thickness for the first TM surface wave mode on a lossless substrate. (From [55]. © 1989 John Wiley. Reprinted with permission.) (b) Variation of β_i/k_0 with the normalized substrate thickness for the first TM surface wave mode on a lossy substrate with $\epsilon_r = 4.34$. The logarithmic scale enhances linear dependence of β_i/k_0 with thickness and tan δ. (From [55]. © 1989 John Wiley. Reprinted with permission.)

the surface waves. The radiation efficiency is about 75% when $h/\lambda_0 = 0.07$ for $\epsilon_r = 2.3$, and for $h/\lambda_0 = 0.023$ for $\epsilon_r = 10$. The decrease in efficiency can be used as a criterion in deciding the value of the substrate thickness for the patch. The effect of surface waves on the radiation efficiency of patch antennas is discussed in Chapter 2.

1.5.2 Photonic Bandgap Structures

Surface wave propagation is a serious problem in microstrip antennas. Surface waves reduce antenna efficiency and gain, limit bandwidth, increase end-fire radiation, increase cross-polarization levels, and limit the applicable frequency range of microstrip antennas. Additionally, miniaturization of microstrip anten-

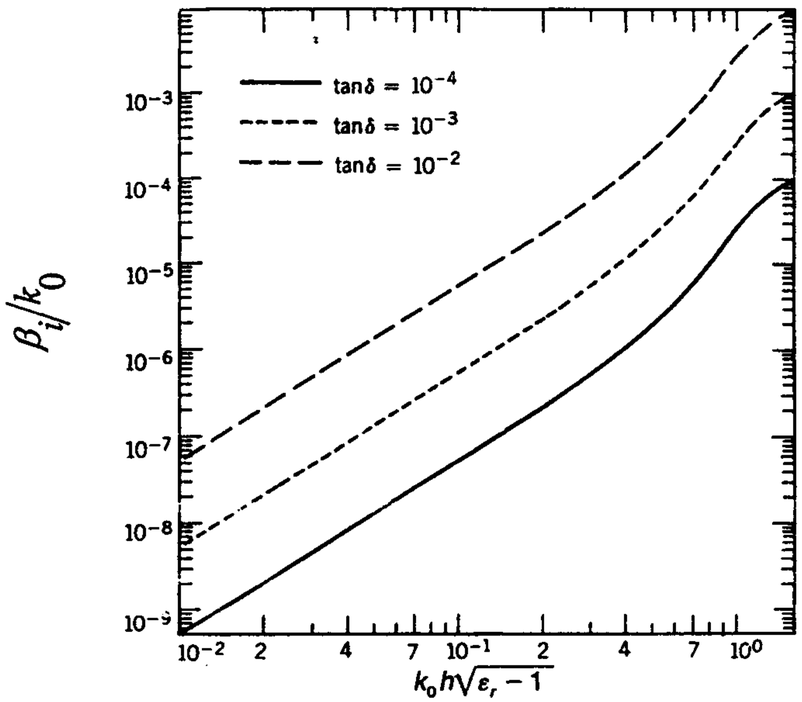

(b)

Figure 1.18 (continued).

nas and their integration with microstrip circuits is hindered because high dielectric constant substrates are required to achieve these objectives.

Two solutions to the surface wave problem are available now. One approach is based on the micromachining technology [59] in which part of the substrate beneath the radiating element is removed to realize a low effective dielectric constant environment for the antenna. In this case the power lost through surface wave excitation is reduced and coupling of power to the space wave is enhanced. The second technique relies on photonic bandgap (PBG) engineering [60, 61]. In this case, the substrate is periodically loaded so that the surface wave dispersion diagram presents a forbidden frequency range (stopband or bandgap) about the antenna's operating frequency [62]. Because the surface waves cannot propagate along the substrate, an increased amount of radiated power couples to the space wave. Also, other surface wave coupling effects like mutual coupling between array elements and interference with on-board systems are now absent.

Implementation of the latter approach is cheaper and maintains the planar nature of the microstrip antenna, which is essential for integration with microstrip circuits. A substantial amount of literature is now available on

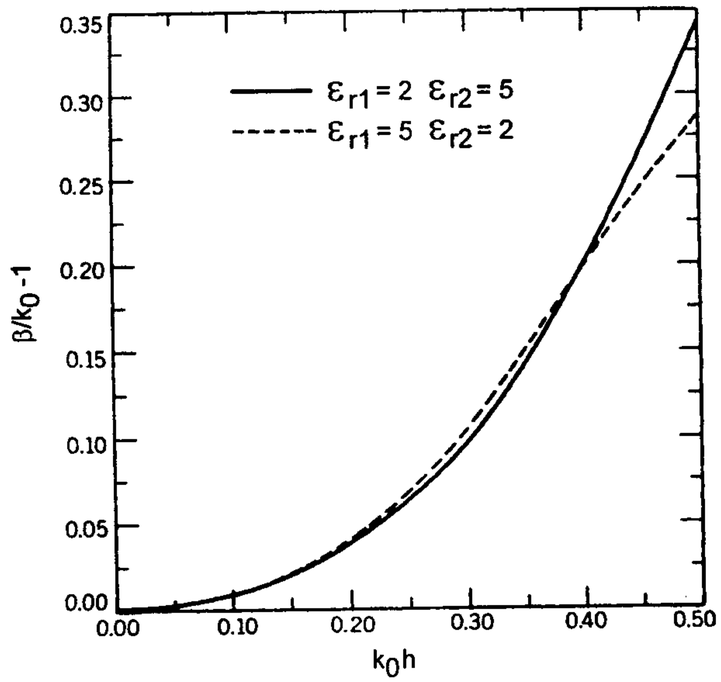

Figure 1.19 First surface wave mode on a lossless two-layer medium as a function of normalized thickness. Both layers have the same thickness $h_1 = h_2 = h$. (From [55]. © 1989 John Wiley. Reprinted with permission.)

antenna and circuit applications of photonic bandgap materials [60–73]. This technique is summarized next.

Photonic bandgap materials are a new class of periodic dielectrics, which are the photonic analogs of semiconductors. Electromagnetic waves behave in photonic substrates as electrons behave in semiconductors. Various types of periodic loading of substrates have been studied to realize the PBG nature of the substrate [60–63]. (Some of these loadings are shown later in Figure 1.27.) Early attempts involved drilling a periodic pattern of holes in the substrate [54] or etching a periodic pattern of circles in the ground plane as shown in Figure 1.20(a) [60]. Next, a periodic pattern of metallic pads was shorted to the ground plane with vias [61] as shown in Figure 1.20(b). Recently, a new loading pattern has been studied as shown in Figure 1.20(c) [62]. This type of planar or 2-D loading is simple to realize (no vias are necessary) and is compatible with standard monolithic microwave integrated circuit fabrication technology.

The transmission coefficient of a PBG substrate is characterized by a bandgap or stopband region. The transmission and reflection coefficients of a microstrip line in PBG substrate with circles etched in the ground plane are

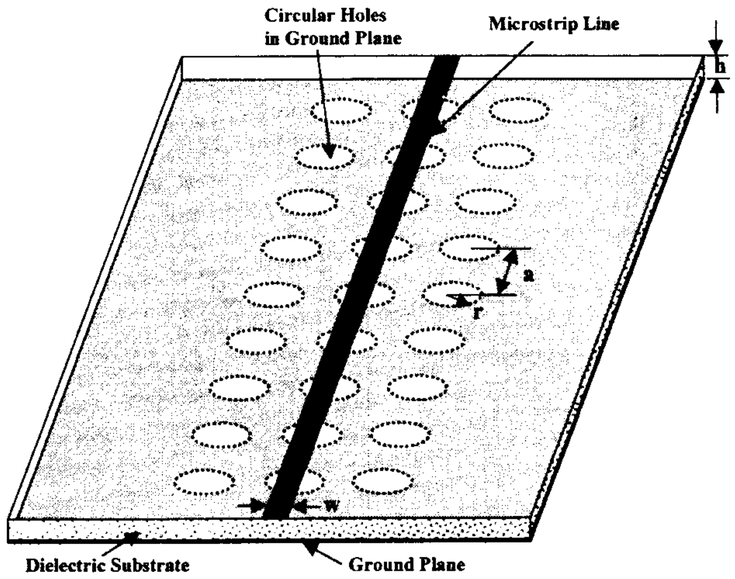

(a)

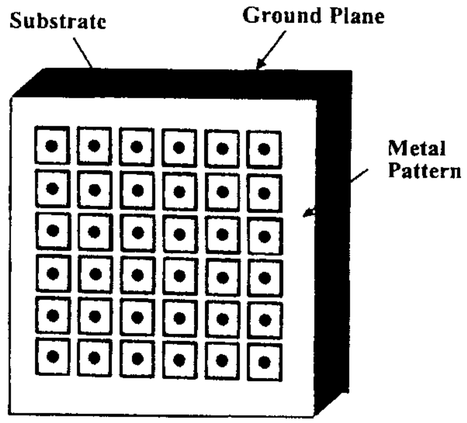

(b)

Figure 1.20 Three types of periodic loading of grounded substrate to obtain photonic bandgap characteristic: (a) Square lattice of etched circles in the ground plane. (From [60]. © 1998 IEEE. Reprinted with permission.) (b) Square lattice of small metal pads with grounding vias in the center. (From [61]. © 1999 *Microwave Journal*. Reprinted with permission.) (c) Uniplanar compact PBG substrate. (From [62]. © 1999 IEEE. Reprinted with permission.)

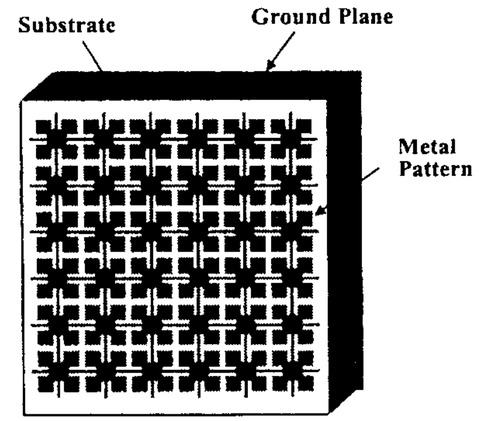

(c)

Figure 1.20 (continued).

shown in Figure 1.21 [60]. The substrate used is RT/Duroid with $\epsilon_r = 10.2$ and $h = 25$ mil. The figure shows a stopband between 9 and 13 GHz. It is also observed that the width of the stopband increases with an increase in the value of radius r. In the limiting case $r \rightarrow 0$, there is no stopband and the structure is a standard microstrip line. A similar stopband behavior was observed by Contopanagos et al. [54] when the circles in the ground plane were replaced by rectangular holes drilled in the grounded substrate.

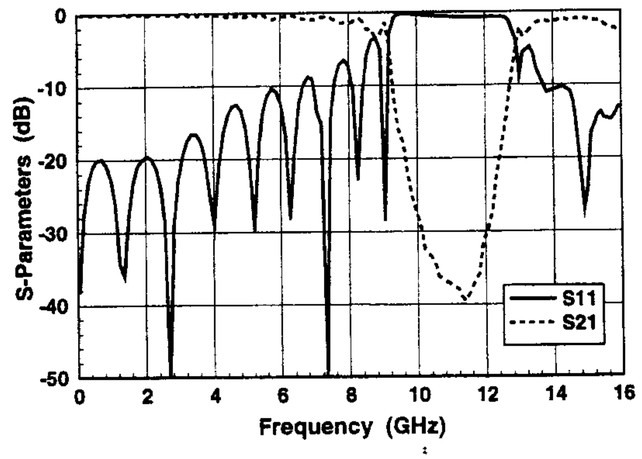

Figure 1.21 Measured S parameters for the PBG microstrip line of Figure 1.20(a), $r = 50$ mil and $a = 200$ mil. (From [60]. © 1998 IEEE. Reprinted with permission.)

A PBG substrate is characterized by a dispersion or $\omega - \beta$ diagram. A dispersion diagram for the PBG lattice of Figure 1.20(b) is shown in Figure 1.22(a) [61]. The lattice consists of square pads with 88-mil edge lengths and 8-mil gaps. The grounded via in the center of each pad has a diameter of 8 mil, and the substrate is 25-mil-thick Duroid with $\epsilon_r = 10.2$. The three sections in the graph refer to three different directions of wave propagation shown in Figure 1.22(b). This figure is the Brillouin zone of a square lattice and the irreducible zone is depicted by the shaded triangle. For each section, the propagation vector $\vec{\beta}$ in the wave vector space is varied along the sides of the triangle. The three special points Γ, X, and M in the figure correspond respectively to $\beta_x = \beta_y = 0$; $\beta_x = \pi/a$, $\beta_y = 0$; and $\beta_x = \beta_y = \pi/a$. The side Γ-X is defined by $\beta_y = 0$ and variable β_x. Similarly, $\beta_x = \pi/a$ and β_y represent the variable along side X-M. The dotted straight lines represent propagation in the air and in a homogeneous medium with a dielectric constant equal to that of the substrate, 10.2 in this case. The dash-dot line at the left of the diagram is the dispersion line of the TM_0 mode of the grounded dielectric slab without the PBG lattice. This mode is responsible for surface wave losses in patch antennas. The three continuous lines represent the three lowest order modes of the PBG substrate. It can be observed from these continuous lines that two bandgaps exist that prevent propagation regardless of the polarization and direction of wave propagation. The stopbands are in the 8.6- to 12.66-GHz and the 23.44- to 27.36-GHz ranges. The surface of the PBG lattice of Figure 1.20(b) can be characterized by a sheet impedance equal to the impedance of a parallel resonant L and C circuit. The inductance can be ascribed to the vias and capacitance to the gap between the metal pads. The impedance is very high near the resonant frequency and is responsible for the forbidden frequency region of the PBG [64].

PBG-Patch Antenna Design

Once the proper PBG lattice has been selected for surface wave suppression, the design of a PBG antenna is straightforward. The PBG antenna is basically the usual microstrip patch antenna except that the patch metalization is now surrounded by a PBG lattice. This is shown in Figure 1.23 for a 2-D PBG lattice. The patch antenna is designed in a conventional fashion because the PBG lattice does not interfere with the near field of the antenna, and it suppresses the surface wave, which is not included in the patch antenna design. However, the presence of vias near the patch may raise the resonant frequency of the patch if the PBG lattice is very close to the patch. The bandgap of the PBG should span the frequency range of operation of the antenna. A PBG substrate may also be used as a physical support for the patch. In such a

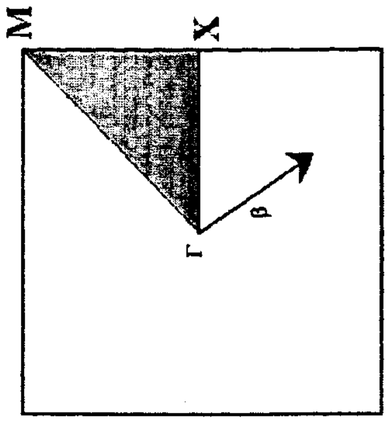

(b)

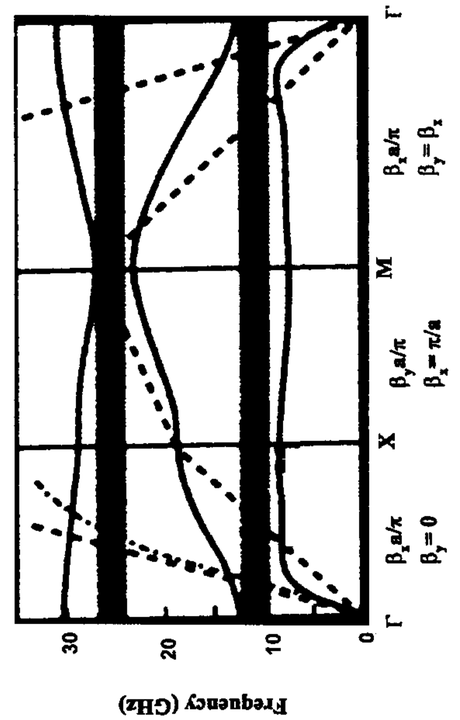

(a)

Figure 1.22 (a) Dispersion diagram of the 2-D PBG lattice of Figure 1.20(b). (From [61]. © 1999 *Microwave Journal*. Reprinted with permission.) (b) Brillouin zone of a square lattice.

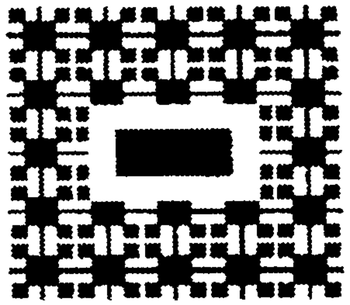

Figure 1.23 A rectangular patch antenna surrounded by a PBG substrate.

situation, the effective dielectric constant of the PBG substrate is used in antenna design.

A side view of a probe-fed circular microstrip antenna with PBG lattice is shown in Figure 1.24(a). The return loss with and without PBG lattice [64] is shown in Figure 1.24(b). In both cases, the substrate has $\epsilon_r = 10.2$, $h = 0.62$ mm, and a size of 5 cm^2. Circular patches with a radius of 1.75 mm were used for the antennas. The gap between the patch and PBG lattice was 3 mm. The lattice used was a triangular lattice with a period of 2 mm and a bandgap spanning roughly 12 to 16 GHz. The measured radiation patterns for the two antennas are compared in Figure 1.25 at 13.5 GHz where the antennas have the same return loss [64]. The patterns in both E and H planes show significant reduction in the backward radiation and ripples in the forward direction. Also, the pattern in the E plane shows significant radiation reduction along the dielectric substrate (90° from the broadside). The radiated power at the H-plane edge remains the same, and is expected because no surface wave propagates in that direction. These features clearly indicate the suppression of surface waves by the PBG. The PBG-patch combination appears to have a higher gain of about 1.5 dB.

1.6 Applications

For many applications, the advantages of microstrip antennas far outweigh their limitations. Initially, microstrip antennas found widespread applications in military systems such as missiles, rockets, aircraft, and satellites. Currently, these antennas are being increasingly used in the commercial sector due to the reduced cost of substrate material and mature fabrication technology. With continued research and development and increased usage, microstrip antennas are ultimately expected to replace conventional antennas for most applications.

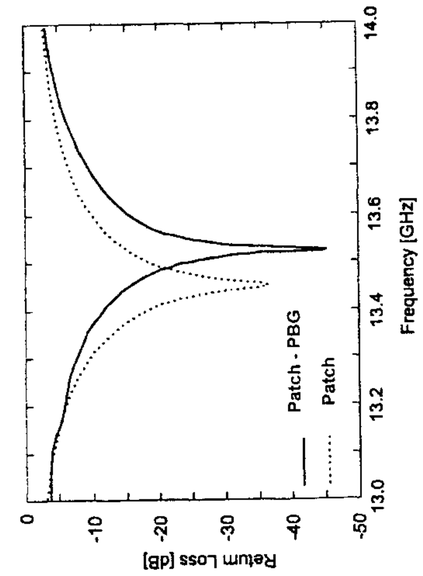

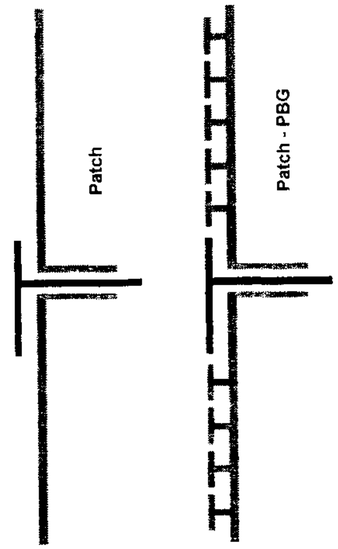

Figure 1.24 (a) A circular patch antenna and the same patch antenna embedded in a PBG substrate. (From [64]. © 1999 IEEE. Reprinted with permission.) (b) Comparison of measured return loss for the patch antenna and patch-PBG combination. (From [64]. © 1999 IEEE. Reprinted with permission.)

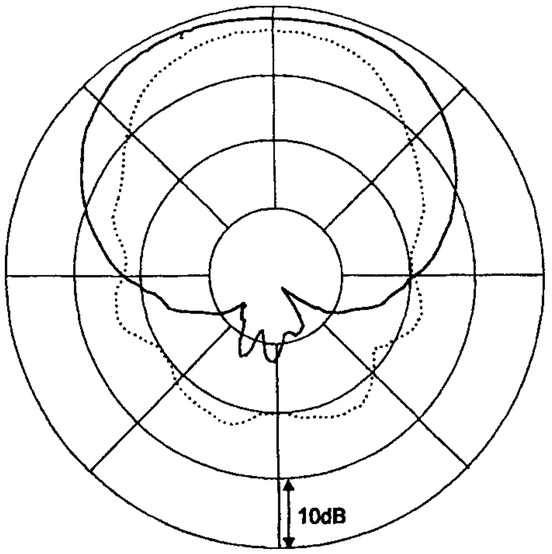

Figure 1.25 Comparison of measured radiation patterns of the antennas of Figure 1.24(a). (From [64]. © 1999 IEEE. Reprinted with permission.) (a) H-plane patterns and (b) E-plane patterns.

Some notable system applications for which microstrip antennas have been developed include:

- Satellite communication, direct broadcast services (DBS);
- Doppler and other radars;
- Radio altimeters;
- Command and control systems;
- Missiles and telemetry (stick-on sensors and weapon fusing);
- Remote sensing and environmental instrumentation;
- Feed elements in complex antennas;
- Satellite navigation receivers;
- Mobile radio (pagers, telephones, and manpack systems);
- Integrated antennas;
- Biomedical radiators and intruder alarms.

Some of these applications are elaborated on in this section.

1.6.1 Mobile and Satellite Communications Applications

Mobile communications [7, 74] often require small, lightweight, low-profile, low-cost antennas. Microstrip antennas can meet all of these requirements, and various types of microstrip antennas have been developed for use in mobile communication systems. The practical applications for mobile systems are in portable or pocket size equipment such as UHF pagers and manpack radars, and in vehicles such as cars, ships, and aircraft. Many antennas have been developed and installed on ships and aircraft. Examples include marine radar antennas, surveillance radar antennas, and synthetic aperture radar antennas for remote sensing. Small-size microstrip arrays have also been developed for automobile collision avoidance systems.

In satellite communications, circularly polarized radiation patterns are required and can be realized using either square or circular patches with one or two feed points (see Chapter 8). Beam shapes such as a sector beam, a fan beam, and a multibeam can be produced by an array of microstrip elements. A parabolic reflector antenna is generally employed for receiving direct broadcast from a satellite. This antenna requires a large area for installation, and can be replaced by a flat antenna in the form of a microstrip reflectarray.

Antennas for Satellite Systems

One of the most prominent communication systems that will utilize microstrip antennas is mobile satellite systems. For example, in a UHF cellular terrestrial

communication system, with plenty of RF power and antenna space available for its base stations, the mobile unit can perform adequately with a low-gain antenna without any concern about its system gain margin. However, in developing mobile satellite communications, because of limited power available at the satellite transponder, limited spacecraft antenna size, and the large distance between the satellite and the earth, the mobile vehicle terminal requires a medium gain antenna (of the order of 10 dB) to ensure an adequate system link margin. In addition, the antenna should cover a wide elevation angular region from 20° to 60° above the horizon with such a gain. Most antennas such as a horn, helix, monopole, and microstrip array can meet these requirements. However, a low-profile printed microstrip array not only offers an aesthetically pleasing appearance, but is also cheaper when produced in large quantities.

Current terrestrial cellular communication systems cannot provide complete coverage over a large global region. As a result, mobile-to-mobile communications would not be available in rural areas where no cellular stations exist. A satellite-based system can fulfill this need by using either a few fixed geostationary satellites or a large number of low earth-orbiting satellites such as the Iridium system, which employs 66 satellites. Two examples of geostationary satellite systems are the existing International Maritime Satellite System (INMARSAT) [75] and the developing Mobile Satellite (MSAT) system [76]. Both of these systems operate in the L-band. Earth stations for the INMARSAT generally employ reflector-type antennas. However, the standard M terminal, which is intended for land applications, uses a briefcase-size microstrip array antenna. This antenna employs six circular patches and provides 14.5 dB of gain.

The MSAT system has been studied by many countries. Because of the power limitations at the satellite end stated earlier, the associated ground terminal requires a medium gain (nearly a 10-dB gain) antenna to satisfy the communication link requirements. Microstrip antenna elements generally have a low gain of about 6.5 dB. Therefore, a microstrip array with a directive beam has to be used, and it must have a tracking capability to keep its beam pointed at the satellite while the vehicle is moving about. Two types of microstrip arrays of medium gain have been developed: electronically steered phased arrays and the mechanically steered arrays. Figure 1.26 shows two different phased arrays. Both arrays employ 19 elements and use dual-stacked circular patches to cover both the transmitting and receiving frequency bands. The size of the array is approximately 50 cm in diameter and 4 cm in height. Similar phased-array antenna systems have been installed on Boeing aircraft for commercial aeronautical satellite communications. The Jet Propulsion Laboratory (JPL) in the United States has developed a mechanically steered microstrip Yagi array [77] shown in Figure 1.27. This array also occupies a space of about 48 cm

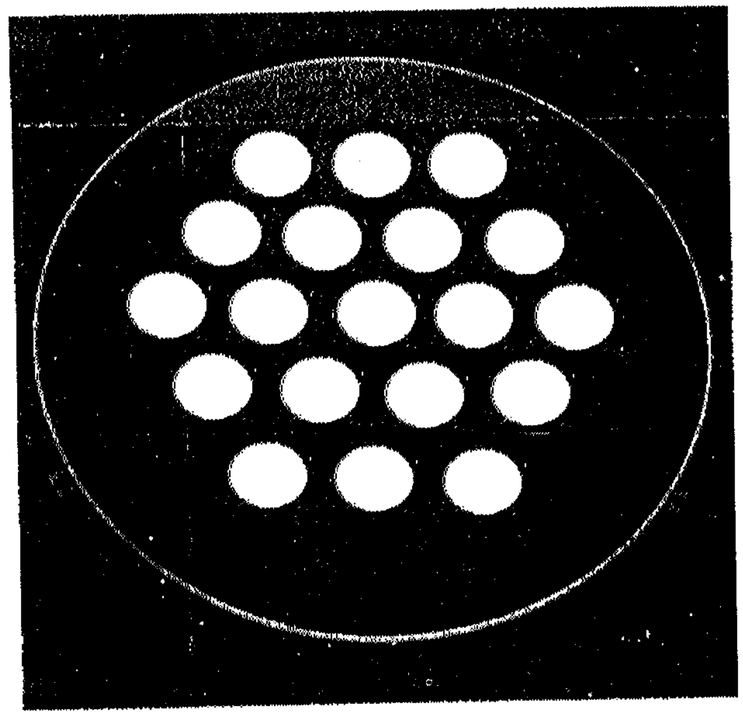

(a)

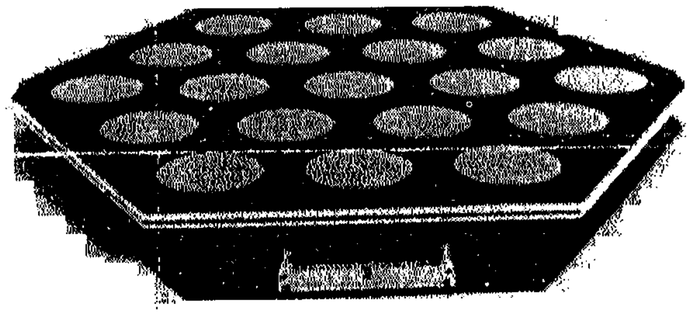

(b)

Figure 1.26 Two implementations of microstrip phased array antennas for mobile satellite communications. (From [74]. © 1995 IEEE Press. Reprinted with permission.)

in diameter and 4 cm in height. Most of the costs in either antenna system are attributed to the beam scanning and tracking components and not to the radiator portion. For example, the antenna in a mechanically steered array may cost about US$400 per unit, whereas the complete antenna system may cost about US$2,000 per unit.

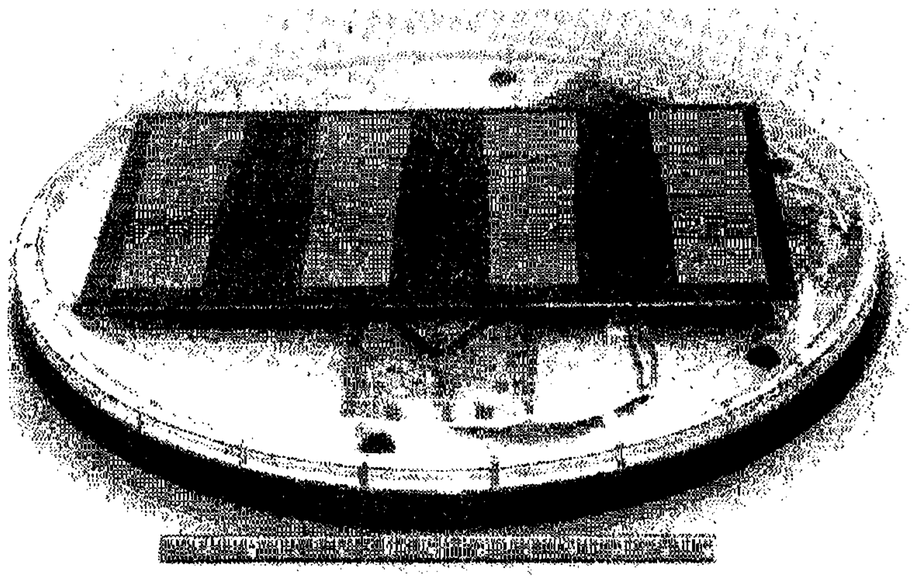

Figure 1.27 Mechanically steered microstrip Yagi array for mobile satellite communications. (From [77]. © 1991 IEEE. Reprinted with permission.)

Low earth-orbiting satellite systems, such as the L-band Iridium system [78] developed by Motorola, Inc., use multiple high-gain microstrip phased arrays on each satellite so that the low-gain omnidirectional antennas on the handheld phones on the ground can be served. Each of the satellite's phased arrays employs hundreds of microstrip patches. The phased arrays employ circularly polarized, dual probe feed, circular patches [79]. The use of patch antennas leads to lower cost, requires less volume, and contributes less mass to the satellite. For the ground terminal, if a low-gain omnidirectional antenna conformal to the vehicle's roof is required, the microstrip patch can certainly be used. A single patch excited in the fundamental mode or the higher order mode can be considered. Huang has proposed circularly polarized, higher order mode circular patch antennas for good omnidirectional coverage in the azimuthal plane and optimum sectoral coverage in the elevation plane [80]. A TM_{41} mode patch using four probe feeds with proper angular and phase arrangement is shown in Figure 1.28, and the elevation patterns for three different patch modes are shown in Figure 5.15.

Global Positioning Systems Applications

Although the satellite-based global positioning system (GPS) [74] began as a military project about 30 years ago, it is now used commercially on a large scale. It is expected that millions of GPS receivers will be used by the general

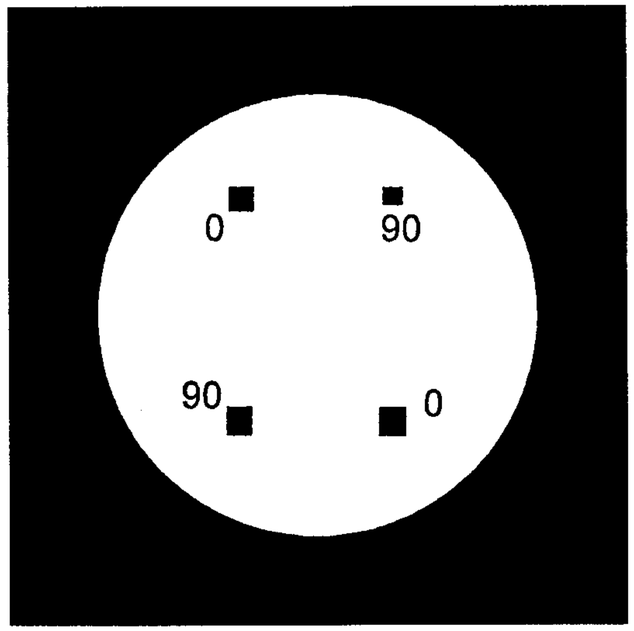

Figure 1.28 A photograph of a circular patch showing four probe feeds with proper angular and phase arrangement to excite fourth-order mode TM_{41} (From [74]. © 1995 IEEE Press. Reprinted with permission.)

population for land vehicles, aircraft, and maritime vessels to determine their position and heading accurately. The GPS consists of 24 satellites circling the earth every 12 hours at an altitude of 20,200 km. Each satellite transmits codes at two frequencies in the L-band. At any time, four of these satellites together help in determining position to an accuracy of 15m and time to an accuracy of 100 ns.

The antenna needed for the ground receiver is a circularly polarized, omnidirectional, wide-beam, low-gain antenna. Microstrip antennas are being developed for GPS receivers to minimize the antenna's size, mass, and cost at L-band. Ball Corporation has developed a ceramic loaded microstrip element in the dual-stacked configuration designed to achieve dual-frequency operation in the L-band frequencies (1573 to 1577 MHz) of the GPS system. Two feeds are used to generate circular polarization. A high dielectric constant substrate is used to reduce the size of the antenna and to increase the beamwidth. The size of the antenna developed by the Ball Corporation is 5 cm × 5 cm, has a thickness of 8 mm, and weighs 85g. Toyota Central R&D Laboratories of Japan has developed an antenna for installation on the roof of an automobile. They have used a dual-feed, stub loaded single patch to achieve circular polarization at the two frequencies of the satellite (see Chapter 8). Typical characteristics of the antenna are that it has a less than 2-dB axial ratio in the boresight

direction and a gain greater than −2 dB between 6° and 90° above the horizontal plane.

Direct Broadcast Satellite System Application

The direct broadcast satellite (DBS) [7] system has been providing television service to the general public in many countries. Its ground user antenna is expected to have a high gain of about 33 dB at 11.7 to 12.0 GHz, and a conventional parabolic reflector antenna has been the antenna of choice for many users. However, this antenna is bulky and requires separate space for installation and its performance is subject to degradation by snow and rain. As a result, several planar antennas using circularly polarized microstrip arrays have been developed for direct broadcasting reception. These antennas can be easily installed on the walls of a house or a building, their performance is less affected by wind and snow, and they are cheaper than reflector antennas. A number of these antennas are briefly discussed next.

Circular-Patch Array.

Yagi Antenna Corporation of Japan has developed an array of 1,024 elements, which has an aperture of 48 cm × 64 cm and a peak gain of about 33 dB [82]. Figure 1.29(a) shows a subarray of four elements consisting of singly fed circular patches [7]. To decrease the feeder loss, the main feeding line for four 256-element panels utilizes a rear-mounted rectangular waveguide.

Square-Patch Array.

NHK Science and Technical Research Laboratories of Japan has also developed a flat microstrip antenna array with increased bandwidth and efficiency [82]. The antenna consists of 512 square-patch elements with a size of 32 cm × 64 cm and a peak gain of 34 dB. A subarray of four patches of this antenna is shown in Figure 1.29(b) [7]. The main feeding line utilizes a rear-mounted rectangular waveguide to decrease feeder loss.

Microstrip Reflectarray.

A microstrip reflectarray [83] is the microstrip equivalent of a parabolic reflector. It consists of an illuminating feed and a thin reflecting surface as shown in Figure 1.30 [83]. On the reflecting surface there are many printed elements with no power division network. The feed antenna illuminates these elements, which are designed to reradiate the incident field with phases that are required to form a planar phase front. The reflectarray combines some of the best features of a printed array technology and the traditional parabolic reflector antenna. It provides the low-profile, beam scanning capability of a printed array and the large-aperture, low-insertion-loss characteristics of a parabolic

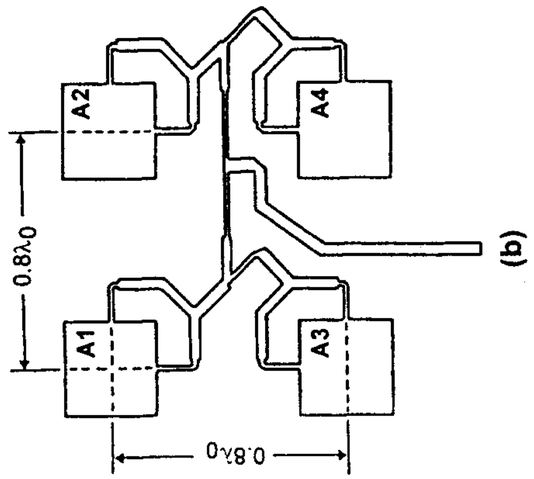

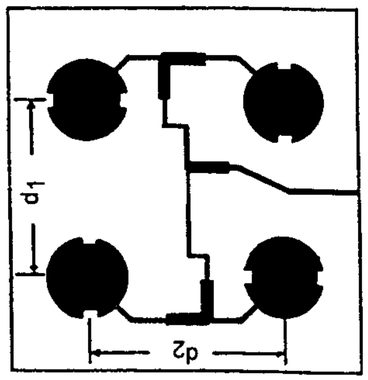

Figure 1.29 (a) Subarray of four circularly polarized circular patches. (From [7]. © 1989 Peter Peregrinus. Reprinted with permission.)
(b) Subarray of four circularly polarized square patches. (From [7]. © 1989 Peter Peregrinus. Reprinted with permission.)

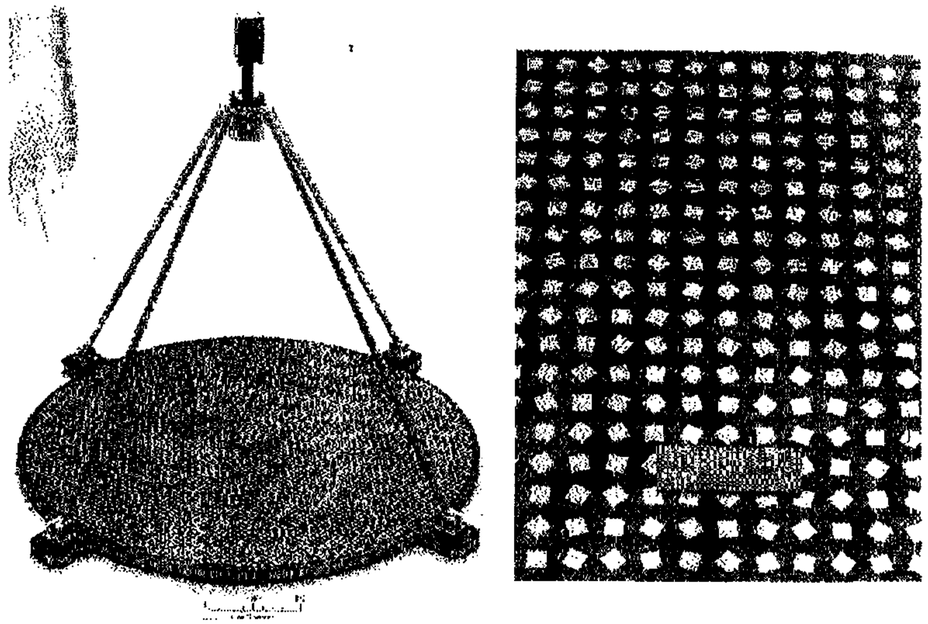

Figure 1.30 Photograph of the half-meter Ka-band microstrip reflectarray and a close-up view of the reflectarray with variably rotated but identical patch elements. (From [83]. © 1998 IEEE. Reprinted with permission.)

reflector. There are many forms of printed reflectarrays such as (1) identical microstrip patch elements with different length phase-delay lines attached [84], (2) variable-size printed dipoles [85], (3) those with variable-size microstrip patches [86], and (4) those that use variable-size circular rings [87, 88]. The reflectarray shown in Figure 1.30 demonstrates a novel means of achieving cophasal far-field radiation for a circularly polarized microstrip reflectarray with elements having variable rotation angles. Figure 1.31 shows an individual circularly polarized patch element and a rotated one with 2ψ degree relative phase shift [83]. The various patch elements in the reflectarray are not connected by any power division lines. Therefore, ohmic insertion loss is very low. Unlike the parabolic reflector, the flat reflecting surface of the reflectarray can be surface mounted onto a building or a house, and thus occupies an insignificant amount of space. Huang and Pogorzelski [83] have developed a circularly polarized reflectarray at 32 GHz. It has a diameter of 0.5m and consists of 6,924 square-patch elements on Duroid substrate with thickness 0.254 mm and $\epsilon_r = 2.2$. The reflectarray is designed for $f/D = 0.7$ with $f = 37.2$ cm and $D = 50.0$ cm. Each element has a dimension of 2.946 mm and is designed to resonate at 32 GHz. The feed horn is a circularly polarized corrugated conical horn and is designed to illuminate the reflectarray with a −9-dB edge taper.

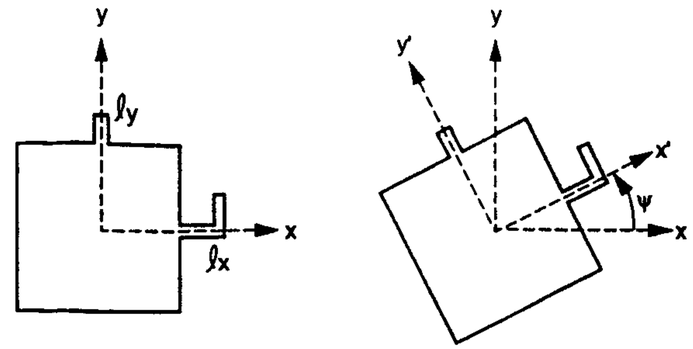

Figure 1.31 Circularly polarized patch element used in Figure 1.30. Reference element with 0° phase shift and a $\psi°$ rotated element with $2\psi°$ phase shift. (From [83]. © 1998 IEEE. Reprinted with permission.)

The antenna has a −3-dB beamwidth of 1.2° and measured gain of 41.7 dB, for an efficiency of 52% at the designed center frequency of 32 GHz. The sidelobes are mostly below −40 dB and most of the cross-polarized radiation is below −30 dB.

Mobile Systems Applications

Antennas meant for mobile systems can be divided into three principal categories according to their usage for land, maritime, and aeronautical mobile systems.

Antennas for Land Mobile Systems.

Antennas for land mobile communications can be divided into those meant for base stations and those meant for automobiles. For base stations, the antenna radiates a sector beam in the horizontal plane in the 900-MHz band. The beamwidth of the antenna could be 180°. A number of microstrip antennas have been developed for this purpose. The antenna described in [7] is composed of two or four subarrays. Each subarray consists of 2 × 4 microstrip elements with each element being a broadband microstrip element. A multibeam array has also been proposed for the base station. The array is composed of 8 × 8 broadband microstrip elements, generates eight beams within a 120° sector, and can produce vertical/horizontal polarization [7].

For automobiles, the circular patch microstrip antenna has been used as a cabin antenna. The gain of this antenna should be 1 dB more than that of a half-wave dipole, based on the assumption that the degradation in the average received power caused by installing an antenna inside the vehicle is 3 dB, and the improvement due to receiving both dominant and cross-polarization fields is 2 dB. The annular slot has been used as a roof-top antenna for vehicles because it can radiate power at low elevation angles. The radiation pattern of

this antenna can be controlled by loading it with a capacitor as discussed in Chapter 7.

Antennas for Pedestrians.

Antennas for handheld portable equipment such as pagers and portable telephones must naturally be small in size, light in weight, and compact in structure. Some of these applications require either flush-mounted or built-in antennas. It is well known that the smaller the size of the antenna, the poorer its efficiency. However, efficiency cannot be compromised very much. A number of antennas for these applications are described in Chapter 10. In these antennas, the size is reduced by loading a standard antenna with a short circuit, a dielectric cover of high ϵ_r is added to restore gain, and electromagnetic coupling of feed is used to avoid direct feed impedance mismatch problem. A planar-inverted-F-antenna (PIFA) is particularly attractive.

1.6.2 Radar Antennas

Manpack Radar

A portable manpack radar can be used for detecting moving targets such as people and vehicles. It is designed on the basis of the pulse doppler mode of operation. An X-band radar with a half-power beamwidth of about 4.5° and gain of 30 dB that weighs about 2 kg is described in [89]. It is constructed with 16 center-fed Franklin-type microstrip line standing wave antennas.

Marine Radar

Microstrip arrays have been used in low-power radars. An antenna array consisting of 48 (3×16) circular patches mounted on a rotating pedestal is described in [7]. The antenna operates in the X-band, generating a gain of about 22 dB, 6° beamwidth in azimuth, and 25° in elevation.

Secondary Surveillance Radar

For the purpose of improving the data rate, a cylindrical electronic scanning antenna, which can be turned instantaneously in any direction and aimed at any target, is believed to be more promising than a mechanically rotated antenna. A cylindrical array of one-third arc and 90° active sector is described in [7]. Its radiating elements are vertically polarized circular patches operating in the frequency range of 1030 to 1090 MHz. Ten radiating elements are arranged in elevation to produce a cosecant-squared pattern. The azimuth is composed of 32 sectors and a pencil beam is formed on the azimuth plane, which can be scanned horizontally by changing the transfer switch.

Synthetic Aperture Radar

For remote sensing applications, synthetic aperture radar (SAR) techniques have been used to determine ground soil grades, vegetation type, ocean wave speed and direction, and so on. An SAR consists of two identical microstrip arrays, separated by a prescribed distance to properly perform the interferometric function. Each array generates a fan-shaped beam in the broadside direction. These two rows are excited with opposite phases to achieve the required low cross-polarization.

1.6.3 Patch Applicators for Medicine

In the medical area [74], microwave energy has been found to be one of the most effective ways of inducing hyperthermia when treating malignant tumors. The radiator meant for this purpose should conform to the surface being treated and be lightweight, rugged, and easy to handle. Only a patch radiator can meet the first criterion. Early designs of microstrip radiators for hyperthermia applications were based on printed dipoles [90] and annular rings [91] at the S-band. A recent design involves the use of a circular microstrip disk [92] at L-band. Two coupled microstrip lines with adjustable separation have been used to measure the temperature gradient inside the human body [93]. An interesting design is the flexible patch applicator at 430 MHz. Figure 1.32 shows how this patch applicator can be applied to a curved surface for maximum efficiency [94].

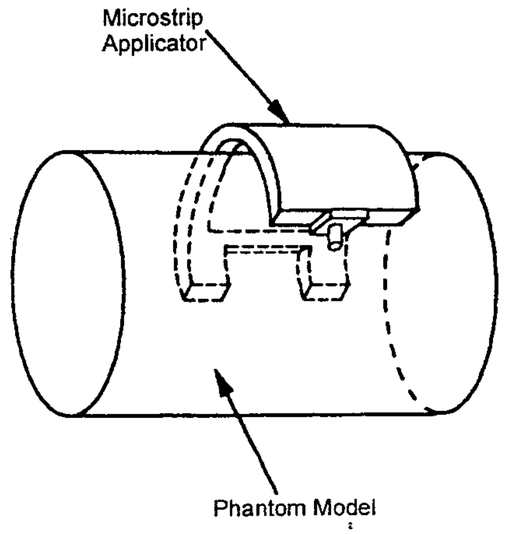

Figure 1.32 Flexible microstrip applicator for hyperthermia medical applications. (From [94]. © 1989 IEEE. Reprinted with permission.)

This list of applications is by no means exhaustive, and the number of applications will continue to grow with time.

References

[1] Deschamps, G. A., "Microstrip Microwave Antennas," *3rd USAF Symposium on Antennas*, 1953.

[2] Gutton, H., and G. Baissinot, "Flat Aerial for Ultra High Frequencies," French Patent No. 70313, 1955.

[3] Howell, J. Q., "Microstrip Antennas," *IEEE AP-S Int. Symp. Digest*, 1972, pp. 177–180.

[4] Munson, R. E., "Conformal Microstrip Antennas and Microstrip Phased Arrays," *IEEE Trans. on Antennas and Propagation*, Vol. AP-22, 1974, pp. 74–78.

[5] Bahl, I. J., and P. Bhartia, *Microstrip Antennas*, Artech House, Dedham, MA, 1980.

[6] James, J. R., P. S. Hall, and C. Wood, *Microstrip Antennas: Theory and Design*, Peter Peregrinus, London, UK, 1981.

[7] James, J. R., and P. S. Hall (Eds.), *Handbook of Microstrip Antennas*, Peter Peregrinus, London, UK, 1989.

[8] Bhartia, P., K. V. S. Rao, and R. S. Tomar, *Millimeter-Wave Microstrip and Printed Circuit Antennas*, Artech House, Norwood, MA, 1991.

[9] Pozar, D. M., and D. H. Schaubert (Eds.), *The Analysis and Design of Microstrip Antennas and Arrays*, IEEE Press, New York, 1996.

[10] Zurcher, J. F., and F. E. Gardiol, *Broadband Patch Antennas*, Artech House, Norwood, MA, 1995.

[11] Sainati, R. A., *CAD of Microstrip Antennas for Wireless Applications*, Artech House, Norwood, MA, 1996.

[12] Pozar, D. M., "Microstrip Antennas," *Proc. IEEE*, Vol. 80, 1992, pp. 79–91.

[13] January 1981 issue of *IEEE Trans. on Antennas and Propagation*, Vol. AP-29.

[14] Daniel, J. P., et al., "Research on Planar Antennas and Arrays: 'Structures Rayonnantes,' " *IEEE Antennas Propagat. Magazine*, Vol. 35, 1993, pp. 14–38.

[15] Qian, Y., et al., "A Microstrip Patch Antenna Using Novel Photonic Bandgap Structures," *Microwave J.*, Vol. 42, Jan. 1999, pp. 66–76.

[16] Gupta, K. C., et al., *Microstrip Lines and Slot Lines*, 2nd ed., Artech House, Norwood, MA, 1996.

[17] Balanis, C. A., *Antenna Theory: Analysis and Design*, 2nd ed., John Wiley, New York, 1997, Chap. 14.

[18] Dubost, G., *Flat Radiating Dipoles and Applications to Arrays*, Research Studies Press, New York, 1981.

[19] Zheng, J. X., and D. C. Chang, "End-Correction Network of a Coaxial Probe for Microstrip Patch Antennas," *IEEE Trans. on Antennas and Propagation*, Vol. AP-39, 1991, pp. 115–118.

[20] Richards, W. F., et al., "Experimental and Theoretical Investigations of the Inductances Associated With Microstrip Antenna Feed," *Electromagnetics*, Vol. 3, No. 3–4, July–Dec. 1983, pp. 327–346.

[21] Abrele, J. T., and D. M. Pozar, "Analysis of Infinite Arrays of Probe-Fed Rectangular Microstrip Antennas Using a Rigorous Feed Model," *Proc. IEE*, Pt. H, Vol. 136, 1989, pp. 110–119.

[22] Damiano, J. P., and A. Papiernik, "Survey of Analytical and Numerical Models for Probe-Fed Microstrip Antennas," *IEE Proc., Microwave Ant. Propagat.*, Vol. 141, 1994, pp. 15–22.

[23] Wu, C., et al., "Accurate Characterization of Planar Printed Antennas Using Finite-Difference Time-Domain Method," *IEEE Trans. on Antennas and Propagation*, Vol. AP-40, 1992, pp. 526–534.

[24] Hall, P. S., "Probe Compensation in Thick Microstrip Patches," *Electron. Lett.*, Vol. 23, 1987, pp. 606–607.

[25] Vandenbosch, G. A. E., and A. R. Van de Capelle, "Study of the Capacitively Fed Microstrip Antenna Element," *IEEE Trans. on Antennas and Propagation*, Vol. AP-42, 1994, pp. 1648–1652.

[26] Reinex, A., and B. Jecko, "Analysis of Microstrip Patch Antennas Using Finite Difference Time Domain Method," *IEEE Trans. on Antennas and Propagation*, Vol. AP-37, 1989, pp. 1361–1369.

[27] Wu, S.-C., N. G. Alexopoulos, and O. Fordham, "Feeding Structure Contribution to Radiation by Patch Antennas With Rectangular Boundaries," *IEEE Trans. on Antennas and Propagation*, Vol. AP-40, 1992, pp. 1245–1249.

[28] Oberhart, M. L., et al., "New Simple Feed Network for an Array Module of Four Microstrip Elements," *Electron. Lett.*, Vol. 23, 1987, pp. 436–437.

[29] Benalla, A., and K. C. Gupta, "Transmission-Line Model for Two-Port Rectangular Microstrip Patches With Ports at the Non-Radiating Edges," *Electron. Lett.*, Vol. 23, 1987, pp. 882–884.

[30] Pozar, D. M., and B. Kaufmann, "Increasing the Bandwidth of a Microstrip Antenna by Proximity Coupling," *Electron. Lett.*, Vol. 23, 1987, pp. 368–369.

[31] Oltman, H. G., and D. A. Huebner, "Electromagnetically Coupled Microstrip Dipoles," *IEEE Trans. on Antennas and Propagation*, Vol. AP-29, 1981, pp. 151–157.

[32] Katehi, P. B., and N. G. Alexopoulos, "On the Modeling of Electromagnetically Coupled Microstrip Antennas—The Printed Strip Dipole," *IEEE Trans. on Antennas and Propagation*, Vol. AP-32, 1984, pp. 1179–1186.

[33] Targonski, S. D., R. B. Waterhouse, and D. M. Pozar, "Design of Wide-Band Aperture Stacked Patch Microstrip Antennas," *IEEE Trans. on Antennas and Propagation*, Vol. AP-46, 1998, pp. 1245–1251.

[34] Pozar, D. M., "A Microstrip Antenna Aperture Coupled to a Microstrip Line," *Electron. Lett.*, Vol. 21, 1985, pp. 49–50.

[35] Gronau, G., and I. Wolff, "Aperture-Coupling of a Rectangular Microstrip Resonator," *Electron. Lett.*, Vol. 22, 1986, pp. 554–556.

[36] Sullivan, P. L., and D. H. Schaubert, "Analysis of an Aperture Coupled Microstrip Antenna," *IEEE Trans. on Antennas and Propagation*, Vol. AP-34, 1986, pp. 977–984.

[37] Himdi, M., et al., "Analysis of Aperture Coupled Microstrip Antenna Using Cavity Method," *Electron. Lett.*, Vol. 25, 1989, pp. 391–392.

[38] Himdi, M., et al., "Transmission Line Analysis of Aperture-Coupled Microstrip Antenna," *Electron. Lett.*, Vol. 25, 1989, pp. 1229–1230.

[39] Menzel, W., and W. Grabherr, "A Microstrip Patch Antenna With Coplanar Line Feed," *IEEE Microwave and Guided Wave Lett.*, Vol. 1, 1991, pp. 340–342.

[40] Smith, R., and J. T. Williams, "Coplanar Waveguide Feed for Microstrip Patch Antennas," *Electron. Lett.*, Vol. 28, 1992, pp. 2272–2274.

[41] Chuang, S. L., et al., "The Equivalence of the Electric and Magnetic Surface Current Approaches in Microstrip Antenna Studies," *IEEE Trans. on Antennas and Propagation*, Vol. AP-28, 1980, pp. 569–571.

[42] Lewin, L., "Radiation From Discontinuities in Stripline," *Proc. IEE*, Vol. 107C, 1960, pp. 163–170.

[43] Belohoubek, E., and E. Denlinger, "Loss Considerations for Microstrip Resonators," *IEEE Trans. on Microwave Theory and Techniques*, Vol. MTT-23, 1975, pp. 522–526.

[44] Easter, B., and R. J. Roberts, "Radiation From Half-Wavelength Open Circuit Microstrip Resonators," *Electron. Lett.*, Vol. 6, 1970, pp. 573–574.

[45] Sobol, H., "Radiation Conductance of Open-Circuit Microstrip," *IEEE Trans. on Microwave Theory and Techniques*, Vol. MTT-19, 1971, pp. 885–887.

[46] Van Heuven, J. H. C., "Conduction and Radiation Losses in Microstrip," *IEEE Trans. on Microwave Theory and Techniques*, Vol. MTT-22, 1974, pp. 841–844.

[47] Van der Pauw, L. J., "The Radiation of Electromagnetic Power by Microstrip Configurations," *IEEE Trans. on Microwave Theory and Techniques*, Vol. MTT-25, 1977, pp. 719–725.

[48] Lewin, L., "Spurious Radiation From Microstrip," *Proc. IEE*, Vol. 125, 1978, pp. 633–642.

[49] James, J. R., and A. Henderson, "High-Frequency Behavior of Microstrip Open-Circuit Terminations," *IEE J. Microwaves, Optics and Acoustics*, Vol. 3, 1979, pp. 205–218.

[50] Kompa, G., "Approximate Calculation of Radiation From Open-Ended Wide Microstrip Lines," *Electron. Lett.*, Vol. 12, 1976, pp. 222–224.

[51] Wood, C., P. S. Hall, and J. R. James, "Radiation Conductance of Open-Circuit Low Dielectric Constant Microstrip," *Electron. Lett.*, Vol. 14, 1978, pp. 121–123.

[52] Abouzahra, M. D., "On the Radiation From Microstrip Discontinuities," *IEEE Trans. on Microwave Theory and Techniques*, Vol. MTT-29, 1981, pp. 666–668.

[53] Harrington, R. F., *Time Harmonic Electromagnetic Fields*, McGraw-Hill, New York, 1961.

[54] Contopanagos, H., L. Zhang, and N. G. Alexopoulos, "Thin Frequency-Selective Lattices Integrated in Novel Compact MIC, MMIC, and PCA Architectures," *IEEE Trans. on Microwave Theory and Techniques*, Vol. MTT-46, 1998, pp. 1936–1948.

[55] Itoh, T. (Ed.), *Numerical Techniques for Microwave and Millimeter Wave Passive Structures*, John Wiley, New York, 1989, Chap. 3.

[56] Pozar, D. M., "Rigorous Closed-Form Expressions for the Surface Wave Loss of the Printed Antennas," *Electron. Lett.*, Vol. 26, 1990, pp. 954–956.

[57] Barlatey, L., et al., "Hybrid Integral Equation Approach for Patch Antennas in Multilayered Substrates," *IEE Proc.*, Vol. 137, Pt. H, 1990, pp. 99–107.

[58] Barlatey, L., et al., "Analysis of Stacked Microstrip Patches With a Mixed Potential Integral Equation," *IEEE Trans. on Antennas and Propagation*, Vol. AP-38, 1990, pp. 608–615.

[59] Gauthier, G. P., A. Courtay, and G. M. Rebeiz, "Microstrip Antennas on Synthesized Low Dielectric-Constant Substrates," *IEEE Trans. on Antennas and Propagation*, Vol. AP-45, 1997, pp. 1310–1314.

[60] Radisic, V., et al., "Novel 2-D Photonic Bandgap Structures for Microstrip Lines," *IEEE Microwave Guided Wave Lett.*, Vol. 8, 1998, pp. 69–71.

[61] Qian, Y., et al., "Microstrip Patch Antenna Using Novel Photonic Bandgap Structures," *Microwave J.*, Vol. 42, Jan. 1999, pp. 66–76.

[62] Coccioli, R., et al., "Aperture-Coupled Patch Antenna on UC-PBG Substrate," *IEEE Trans. on Microwave Theory and Techniques*, Vol. MTT-47, 1999, pp. 2123–2130.

[63] Brown, E. R., C. D. Parker, and E. Yablonovitch, "Radiation Properties of a Planar Antenna on a Photonic-Crystal Substrate," *J. Opt. Soc. Amer. B. Opt. Phys.*, Vol. 10, 1993, pp. 404–407.

[64] Sievenpiper, D., et al., "High-Impedance Electromagnetic Surface With a Forbidden Frequency Gap," *IEEE Trans. on Microwave Theory and Techniques*, Vol. MTT-47, 1999, pp. 2059–2074.

[65] Gonzalo, R., P. de Maagt, and M. Sorolla, "Enhanced Patch-Antenna Performance by Suppressing Surface Waves Using Photonic-Bandgap Substrates," *IEEE Trans. on Microwave Theory and Techniques*, Vol. MTT-47, 1999, pp. 2131–2138.

[66] Thevenot, M., et al., "Directive Photonic-Bandgap Antennas," *IEEE Trans. on Microwave Theory and Techniques*, Vol. MTT-47, 1999, pp. 2115–2122.

[67] Zhang, L., and N. G. Alexopoulos, "Finite-Element Based Techniques for the Modeling of PBG Materials," *Electromagnetics*, Vol. 19, 1999, pp. 225–239.

[68] Yang, F.-R., et al., "Analysis and Applications of Photonic Bandgap (PBG) Structures for Microwave Circuits," *Electromagnetics*, Vol. 19, 1999, pp. 241–254.

[69] Yang, H. Y. D., "Photonic Bandgap Materials," *Electromagnetics*, Vol. 19, 1999, pp. 255–276.

[70] Agi, K., et al., "A Two-Dimensional Photonic Crystal Substrate," *Electromagnetics*, Vol. 19, 1999, pp. 277–290.

[71] Sigalas, M. M., et al., "The Effect of Photonic Crystals on Dipole Antennas," *Electromagnetics*, Vol. 19, 1999, pp. 291–303.

[72] Leung, K. M., and Y. Qiu, "Transmission Spectra of 2-D Photonic Crystals Using a Layer-KKR Method," *Electromagnetics*, Vol. 19, 1999, pp. 305–319.

[73] Suzuki, T., and P. K. L. Yu, "Two-Dimensional Metallodielectric Photonic Crystals," *Electromagnetics*, Vol. 19, 1999, pp. 321–335.

[74] Huang, J., "Microstrip Antennas for Commercial Applications," in *Microstrip Antennas: The Analysis and Design of Microstrip Antennas and Arrays*, D. M. Pozar and D. H. Schaubert (Eds.), IEEE Press, New York, 1995, pp. 371–379.

[75] da Silva Curiel, A., "The First Generation INMARSAT System," *IEEE 3rd Int. Conf. on Satellite Systems for Mobile Commun. and Navigation*, 1983, pp. 1–7.

[76] Rafferty, W., K. Dessouky, and M. Sue, "NASA's Mobile Satellite Development Program," *Proc. of the Mobile Satellite Conf*, 1988, pp. 11–22.

[77] Huang, J., and A. C. Densmore, "Microstrip Yagi Array Antenna for Mobile Satellite Vehicle Applications," *IEEE Trans. on Antennas and Propagation*, Vol. AP-39, 1991, pp. 1024–1030.

[78] Schuss, J. J., et al., "Design of Iridium Phased Array Antennas," *IEEE AP-S Int. Symp. Digest*, 1993, pp. 218–221.

[79] Schuss, J. J., et al., "The Iridium Main Mission Antenna Concept," *IEEE Trans. on Antennas and Propagation*, Vol. AP-47, 1999, pp. 416–424.

[80] Huang, J., "Circularly Polarized Conical Patterns From Circular Microstrip Antennas," *IEEE Trans. on Antennas and Propagation*, Vol. AP-32, 1984, pp. 991–994.

[81] Haneishi, M., "A Circularly Polarized SHF Planar Array Composed of Microstrip Pairs-Element," *Int. Symp. Antennas and Propagation*, 1985, pp. 125–128.

[82] Ohmaru, K., and T. Murata, "A Planar Array Antenna for Satellite Broadcasting Reception," *Proc. Int. Microwave Symp*, 1987, pp. 115–120.

[83] Huang, J., and R. J. Pogorzelski, "A Ka-Band Microstrip Reflectarray With Elements Having Variable Rotation Angles," *IEEE Trans. on Antennas and Propagation*, Vol. AP-46, 1998, pp. 650–656.

[84] Javor, R. D., X. D. Wu, and K. Chang, "Beam Steering of a Microstrip Flat Reflectarray Antenna," *IEEE AP-S Int. Symp. Digest*, 1994, pp. 956–959.

[85] Kelkar, A., "FLAPS: Conformal Phased Reflecting Surfaces," *Proc. National Radar Conf.*, 1991, pp. 58–62.

[86] Pozar, D. M., and T. A. Metzler, "Analysis of a Reflectarray Antenna Using Microstrip Patches of Variable Size," *Electron. Lett.*, Vol. 29, 1993, pp. 657–658.

[87] Johansson, F. S., "Frequency-Scanned Reflection Gratings Consisting of Ring Patches," *Proc. IEE*, Vol. 138, Pt. H, 1991, pp. 273–276.

[88] Guo, Y. J., and S. K. Barton, "Phase Correcting Zonal Reflector Incorporating Rings," *IEEE Trans. on Antennas and Propagation*, Vol. AP-43, 1995, pp. 350–355.

[89] Nishimura, S., K. Nakano, and T. Makimoto, "Franklin-Type Microstrip Line Antenna," *IEEE AP-S Int. Symp. Digest*, 1979, pp. 134–137.

[90] Sterzer, F., et al., "Microwave Apparatus for the Treatment of Cancer," *Microwave J.*, Vol. 23, Jan. 1980, pp. 39–44.

[91] Bahl, I. J., S. S. Stuchly, and M. A. Stuchly, "A New Microstrip Radiator for Medical Applications," *IEEE Trans. on Microwave Theory and Techniques*, Vol. MTT-28, 1980, pp. 1464–1468.

[92] De Leo, R., G. Cerri, and F. Moglie, "Microstrip Patch Applicators," *IEEE AP-S Int. Symp. Digest*, 1989, pp. 524–527.

[93] Kobayashi, D., et al., "Coupled Microstrip Applicator for Hyperthermia Applications," *IEEE AP-S Int. Symp. Digest*, 1989, pp. 532–535.

[94] Kobayashi, H., et al., "Flexible Microstrip Patch Applicator for Hyperthermia," *IEEE AP-S Int. Symp. Digest*, 1989, pp. 536–539.

2

Analytical Models for Microstrip Antennas

2.1 Introduction

Various types of microstrip radiators, their applications, radiation mechanisms, models for various types of feeds, and the basic antenna characteristics were discussed in Chapter 1. Analysis of the antenna is carried out in this chapter. Antenna analysis is important for several reasons, including these:

- It can reduce the number of costly cut-and-try cycles by aiding the design process.
- Analysis can be used to ascertain the advantages as well as limitations of the antenna by carrying out parametric studies.
- Analysis can provide an understanding of the operating principles that could be useful for a new design, for modifications to an existing design, and for the development of new antenna configurations.

The objectives of antenna analysis are to predict the radiation characteristics such as radiation patterns, gain, and polarization as well as near-field characteristics such as input impedance, impedance bandwidth, mutual coupling, and antenna efficiency. The analysis of microstrip antennas is complicated by the presence of dielectric inhomogeneity, inhomogeneous boundary conditions, narrow frequency band characteristics, and a wide variety of feed, patch shape, and substrate configurations. Thus, a balance is reached between the complexity of the method and the accuracy of solution by compromising one

or more of the features listed above. The resulting model is said to be a *good* model if it has the following characteristics [1]:

- It can be used to calculate all impedance and radiation characteristics of the antenna under discussion.
- Its results are accurate enough for the intended purpose.
- It is as simple as possible, while providing the proposed accuracy for the impedance and radiation properties.
- It lends itself to interpretation in terms of known physical phenomena.

Many elaborate techniques have been proposed and used to determine microstrip antenna characteristics. The analytical techniques include the transmission line model, generalized transmission line model, cavity model, and multiport network model. These techniques maintain simplicity at the expense of accuracy. Full-wave methods have received increasing attention due to their rigor and higher accuracy. These are, in general, based on Sommerfeld-type integral equations, and the solution of Maxwell's equations in the time domain. Prominent numerical methods include integral equation analysis in the spectral domain, integral equation analysis in the space domain, and the finite-difference time-domain (FDTD) approach. The methods based on integral equation make one important assumption: The dielectric substrate and the ground plane are infinite in extent. The solutions are therefore more accurate when the substrate and ground plane are several wavelengths long. The FDTD technique is more efficient for finite-sized antennas. The effect of finite size is less severe on impedance behavior because microstrip antennas are inherently resonant structures and their impedance characteristics are primarily determined by the patch. The radiation behavior, on the other hand, is considerably influenced by the finite size of the substrate primarily due to the launching of surface waves and their diffraction at the edge of the substrate. Consequently, the theory of diffraction is occasionally used in conjunction with other methods to improve the prediction of radiation pattern.

The analytical models were the first to be developed for microstrip antennas. They use simplifying assumptions, but generally offer simple and analytical solutions, well suited for an understanding of the physical phenomena and for antenna CAD. In the analytical methods or models, the fields associated with the antenna are divided into an interior region and an exterior region [2], as shown in Figure 2.1.

The interior region is formed by the patch conductor, the portion of the ground plane under the patch, and the walls formed by the projection of the

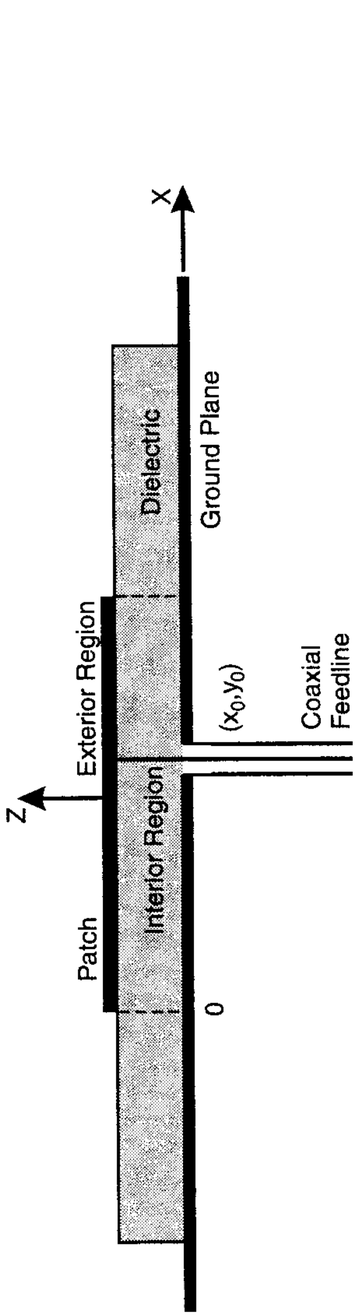

Figure 2.1 Division of fields associated with an antenna into an interior region and an exterior region. (From [2]. © 1979 New Mexico State University. Reprinted with permission.)

patch periphery onto the ground plane. The fields in this region can be modeled as a transmission line section or a cavity giving rise to the designations *transmission line model* and *cavity model.* The exterior region is the rest of the space. This includes the remainder of the ground plane, the remainder of the dielectric, and the top of the patch conducting surface. The fields in the exterior region comprise the radiation field, surface waves, and fringing field. These are characterized in the form of load admittances in some of the models. In simpler models, the effect of these fields is described in the form of increased dielectric loss tangent and equivalent dimensions of the antenna.

Aperture Model for the Fields in the Exterior Region

The mechanism of radiation from a microstrip antenna was described in Section 1.1.2, where it was shown that the radiating edges could be modeled as slots/apertures in the interface plane. The width of the slots in principle should be infinite, but the analysis shows that the electric field decays rapidly away from the edge. In support of this, computed electric and magnetic surface currents on the patch antenna are presented next. Kishk and Shafai carried out such an analysis for a circular patch antenna with finite ground plane [3]. The geometry of the patch is shown in the inset of Figure 2.2. Computed magnetic and electric surface current distributions for the TM_{11} mode are shown in Figures 2.2 and 2.3, respectively. The x axis shows the radial position on the outer boundary of the microstrip surface. Only one-half of the surface contour is shown since the geometry is rotationally symmetric. Points A to B correspond to the position on the ground plane, points B to C represent the dielectric substrate that supports both electric and magnetic surface currents, and points C to D correspond to the patch surface.

The distribution of magnetic current $\overline{M}$, that is, the tangential electric field on the substrate, is shown in Figure 2.2. The magnetic current decreases progressively from C to B, indicating a strong fringing field near C. Figure 2.3 shows that the electric current is strongest on the patch surface and is minimum on the ground plane. The contributions to the radiation field, therefore, are mainly from J_ϕ from the patch and from M_ϕ on the substrate.

Carver and Coffey have plotted dc fringing field distribution near the edge of a microstrip line [2]. They have suggested that a slot width equal to the substrate thickness h with uniform electric field therein can effectively account for the fringing field effect. The length of the apertures is taken to be slightly longer than the physical length of the edge. The increase takes into account the fringing fields at the corners of the patch. For rectangular and circular patches, the width of the aperture can be determined using well-known magnetic wall models. For a rectangular patch, the effective dimensions can be determined from the planar waveguide model of the microstrip (see Appendix

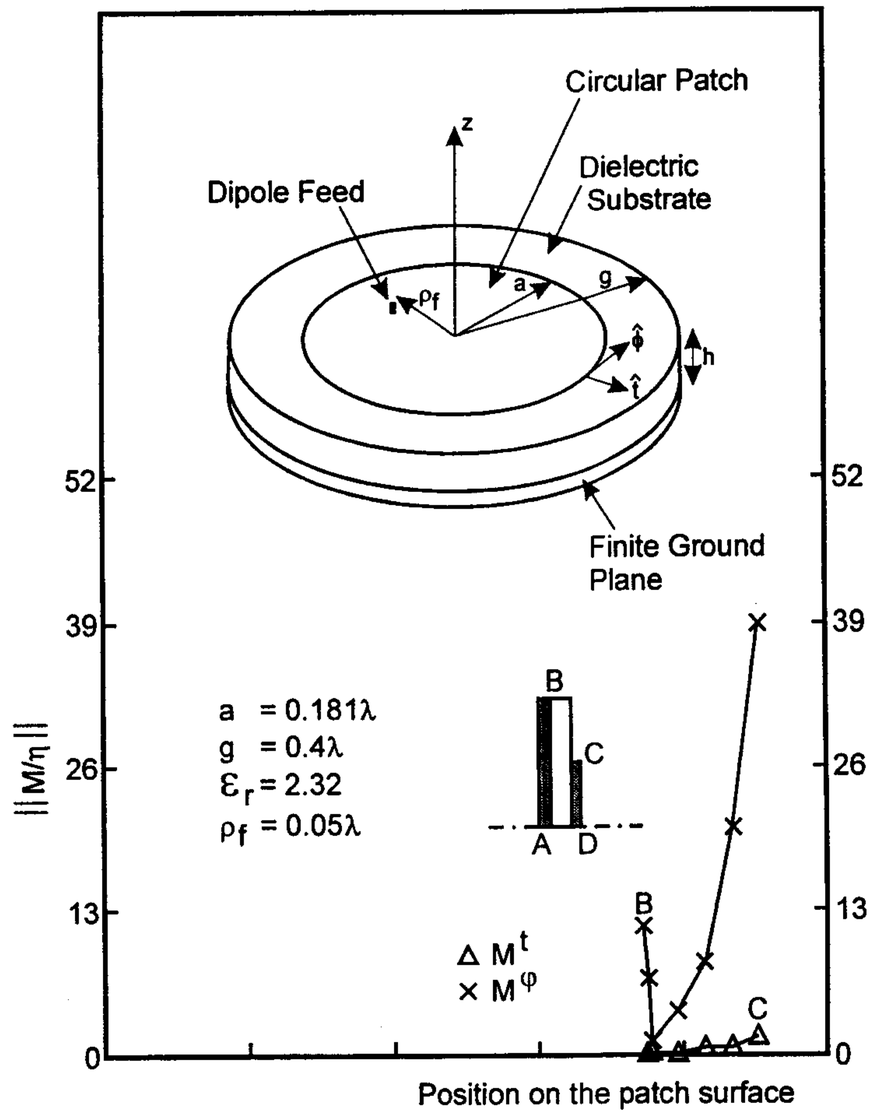

Figure 2.2 Variation of surface magnetic current for the TM_{11} mode of a circular patch. (From [3]. © 1986 IEEE. Reprinted with permission.)

B). For better accuracy, the aperture model has been extended to the nonradiating edges. Therefore, the electric field at the edges of the patch can be modeled as shown in Figure 2.4(a). Extensive calculations show that the outer corners, as modified in Figure 2.4(b), give better agreement with measured antenna characteristics [4]. For ease of implementation, however, most of the analytical models employ the aperture model of Figure 2.4(a). The aperture model is further simplified by assuming that the apertures or slots can be on the ground plane instead of at the interface plane. This approximation does not sacrifice

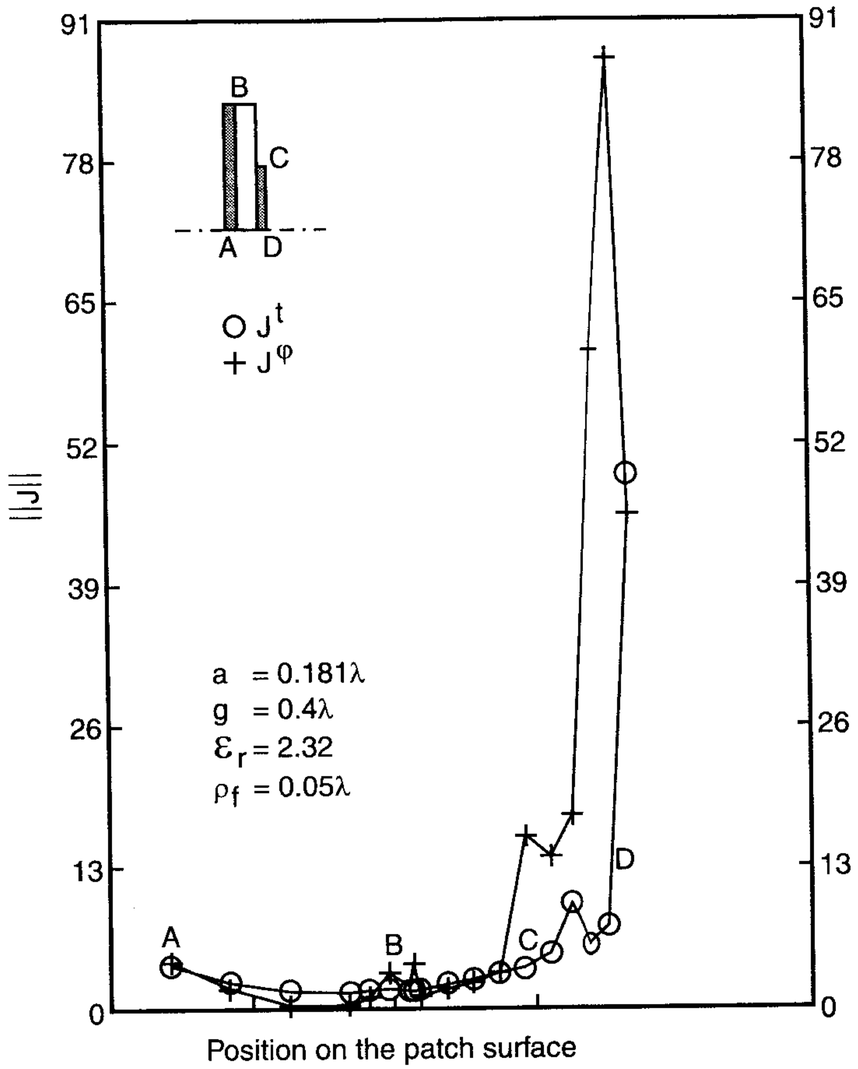

Figure 2.3 Variation of surface electric current for the TM_{11} mode of a circular patch. (From [3]. © 1986 IEEE. Reprinted with permission.)

much of the accuracy if the substrate is thin. The transmission line model based on radiation from apertures is discussed next.

2.2 Transmission Line Model

Rectangular and square patches have a physical shape derived from microstrip transmission lines. Therefore, these antennas can be modeled as sections of transmission lines. Similarly, circular patches, annular rings, and sectors of

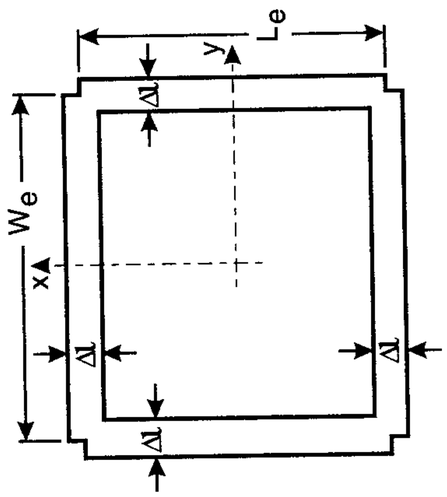

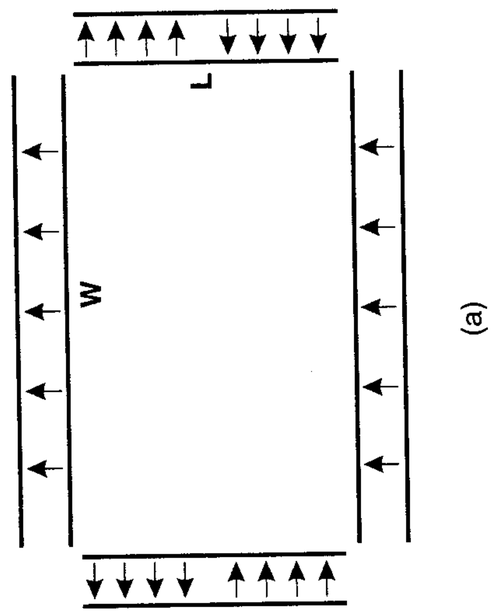

Figure 2.4 Four-slot radiation models: (a) Four-slot model. (b) Four-slot model with corners. (From [1]. © 1992 IEEE. Reprinted with permission.)

circular patches and annular rings can be modeled in terms of sections of radial transmission lines [5–7]. Therefore, the transmission line model is one of the most intuitively appealing models for a microstrip antenna.

2.2.1 Simple Transmission Line Model

This transmission line model [8–10] was the first technique employed to analyze a rectangular microstrip antenna by Munson in 1974 [8]. In this model, the interior region of the patch antenna is modeled as a section of transmission line. The characteristic impedance, Z_0, and propagation constant, β, for the line are determined by the patch size and substrate parameters. Consider a rectangular patch of dimensions $L \times W$ as shown in Figure 2.4. The periphery of this patch is described by four walls/edges at $x = 0$, L and $y = 0$, W. The four edges of the patch are classified as radiating type or nonradiating type depending on the field variation along their length. The classification is based on the observation that a radiating edge is associated with slow field variations along its length. The nonradiating edge, on the other hand, should have an integral multiple of half-wave variations along the edge, such that there is an almost complete cancellation of the radiated power from the edge. For the TM_{10} mode in the patch, the edges at $x = 0$, L are radiating types because the electric field is uniform along these edges. The walls at $y = 0$, W are nonradiating types because of half-wave variation of the field along these edges. The edges at $x = 0$, L radiate most of the power and are characterized by load admittances $Y_s = G_s + jB_s$. Here, G_s is the conductance associated with the power radiated from the edge or wall, and B_s is the susceptance due to the energy stored in the fringing field near the edge. The effect of the fringing fields at nonradiating edges at $y = 0$ and W is included in the determination of phase constant β. Based on this identification, the equivalent circuit of the rectangular patch antenna is shown in Figure 2.5(a).

The radiation patterns of the patch antenna are assumed to be the same as that of an array of two narrow slots separated by a distance equal to the length of the patch. The input admittance of the antenna at the feed port is obtained by transforming the edge admittances to the feed point. The resulting expression from the equivalent circuit of Figure 2.5(a) is obtained as

$$Y_{\text{in}} = Y_0\left(\frac{Y_0 + jY_s\tan(\beta L_1)}{Y_s + jY_0\tan(\beta L_1)} + \frac{Y_0 + jY_s\tan(\beta L_2)}{Y_s + jY_0\tan(\beta L_2)}\right) + jX_f, \qquad L_1 + L_2 = L \tag{2.1}$$

where $\gamma = j\beta$, Y_0 is the characteristic admittance of the patch fed at $x = L_1$ and X_f is the feed reactance, described in Section 2.9. Derneryd [9, 10]

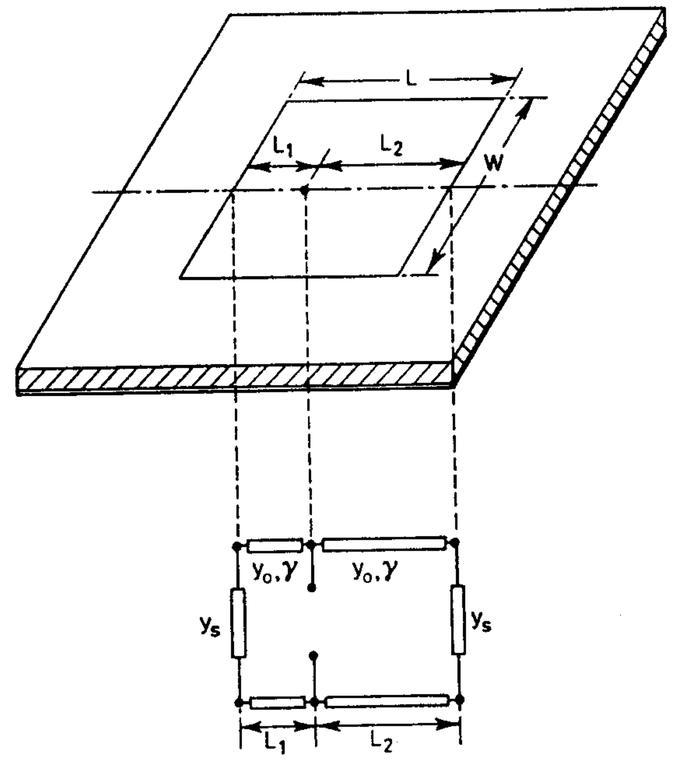

Figure 2.5 (a) Simple transmission line model and (b) transmission line model with mutual coupling.

introduced some modifications in the simple model. Mutual conductance between the radiating edges was calculated by integrating the interference component of the radiation pattern of two magnetic current sources of the patch antenna. It is given by [10]

$$G_m = \frac{1}{60\pi^2}\int_0^{\pi/2} \sin^2\left(k_0\frac{W}{2}\cos\theta\right)\tan^2\theta\sin\theta J_0(k_0 L\sin\theta)d\theta \qquad (2.2)$$

The edge admittance Y_s is now modified to include G_m, that is, $Y_s = G_s - G_m + jB_s$. This modification provided some improvement in the input impedance of the antenna.

Simplification of (2.1) for the resonant patch, $\beta(L_1 + L_2) \approx \pi$, shows that input resistance at resonance is given by [10]

$$R_{\text{in}} = \frac{1}{2G}\left\{\cos^2(\beta L_1) + \frac{G^2 + B_s^2}{Y_0^2}\sin^2(\beta L_1) - \frac{B_s}{Y_0}\sin(2\beta L_1)\right\} \qquad (2.3)$$

$$\approx \frac{1}{2G}\cos^2(\beta L_1) \quad \text{since } G,\ B_s << Y_0 \qquad (2.4)$$

where $G = G_s - G_m$. The simple model shows that input resistance varies as $\cos^2(\beta L_1)$, and can be used to select the feed position so that impedance match with the source impedance is obtained. In addition to mutual conductance, there is mutual susceptance between the radiating edges. Inclusion of mutual susceptance B_m would give rise to further improvement in input impedance, but in a rectangular patch the two sources are separated such that $\beta L \approx \pi$ and the effect of mutual susceptance on the input resistance may not be much. It is likely to affect the resonant frequency slightly.

In the model discussed above the input impedance of the antenna is not a function of feed position along the y direction. Lier has modified the model due to Derneryd by considering an additional transmission line along the y direction and represented its effect in the form of a reactance [11].

The above transmission line model is conceptually very simple. However, it is very approximate and the model is applicable for a rectangular patch only. The effects of substrate on radiation and input impedance are not considered.

2.2.2 Transmission Line Model With Mutual Coupling

In the improved transmission line model [12], mutual coupling between the radiating edges, is included through a mutual admittance Y_m connected between

the two ends of the transmission line. The feed, microstrip line, or coaxial line, can be represented by an ideal current source at the feed point along the transmission line. The resulting equivalent circuit is shown in Figure 2.5(b). This network can be solved in two different ways for determining the voltage across the feed, and therefore input impedance Z_{in}. In one of the approaches, the mutual admittance is included through voltage-dependent current sources across the self-admittances [12]. This approach requires the equivalent circuit to be a three-port network [see Figure 2.6(a)]. The admittance matrix for this equivalent circuit is obtained as

$$[Y] = \begin{bmatrix} Y_s + Y_0\coth(\gamma L_1) & -Y_m & -Y_0\operatorname{csch}(\gamma L_1) \\ -Y_m & Y_s + Y_0\coth(\gamma L_2) & -Y_0\operatorname{csch}(\gamma L_2) \\ -Y_0\operatorname{csch}(\gamma L_1) & -Y_0\operatorname{csch}(\gamma L_2) & Y_0(\coth(\gamma L_1) + \coth(\gamma L_2)) \end{bmatrix} \qquad (2.5)$$

where $\gamma = \alpha + j\beta$ is the complex propagation constant of the line, α accounting for the dielectric and conductor losses of the antenna. For the feed at port number 3 and feed current I_3, the input admittance obtained from (2.5) (with $I_1 = I_2 = 0$) is [12]

$$Y_{\text{in}} = \frac{I_3}{V_3}$$

$$= 2Y_0\left[\frac{Y_0^2 + Y_s^2 - Y_m^2 + 2Y_0Y_s\coth(\gamma L) - 2Y_0Y_m\operatorname{csch}(\gamma L)}{(Y_0^2 - Y_s^2 + Y_m^2)\operatorname{csc}(\gamma L) + (Y_0^2 - Y_s^2 + Y_m^2)\operatorname{csch}(\gamma L)\cosh(2\gamma\Delta) + 2Y_0Y_s}\right] \qquad (2.6)$$

where

$$\Delta = |L/2 - L_1| = |L_2 - L/2| \qquad (2.7)$$

and L_1 and L_2 are defined in Figure 2.5. For an edge-fed microstrip antenna one can use $I_2 = I_3 = 0$, and the input admittance is obtained as [12]

$$Y_{\text{in}} = \frac{Y_0^2 + Y_s^2 - Y_m^2 + 2Y_0Y_s\coth(\gamma L) - 2Y_0Y_m\operatorname{csch}(\gamma L)}{Y_s + Y_0\coth(\gamma L)} \qquad (2.8)$$

The effect of aperture blocking by the microstrip feed line should be included in the calculation of Y_s [12].

The above transmission line model has been used in the analysis of a microstrip-fed rectangular patch antenna [12], for the design of a matched

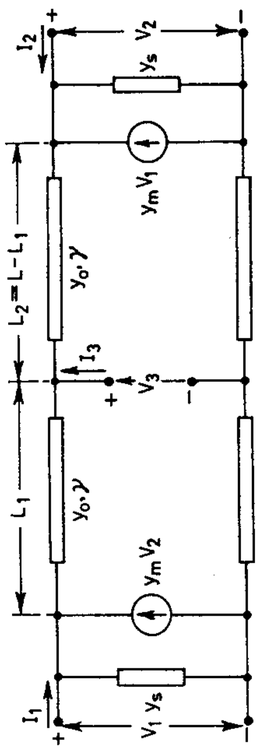

(a)

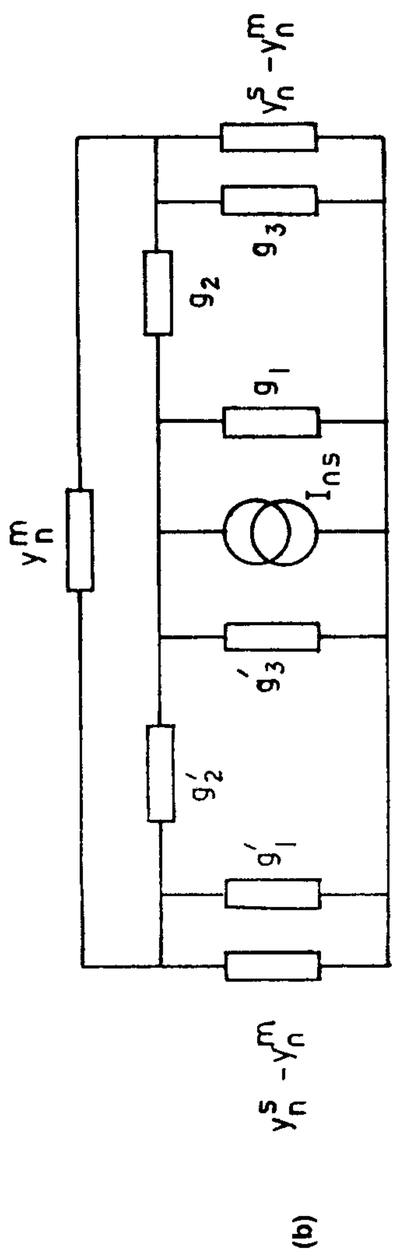

(b)

Figure 2.6 (a) Three-port equivalent network for the transmission line model of Figure 2.5(b). (From [12]. © 1984 IEE. Reprinted with permission.) (b) GTLM equivalent network for the transmission line model of Figure 2.5(b). (From [15].)

broadband rectangular patch antenna [4], for the calculation of mutual coupling between rectangular patches [13], and to predict wide-band performance [14]. For mutual coupling analysis, the effect of coupling between the various slots/edges is included by means of voltage-dependent current sources as in the case of a single patch. Because there are four radiating slots (side slots are assumed nonradiating), each slot is characterized by a self-admittance Y_s and three mutual admittances, the latter being defined in terms of voltage dependent current sources.

The equivalent circuits of Figures 2.5 and 2.6 contain the transmission line parameters Y_0 and γ, self-admittance Y_s, and mutual admittance Y_m. The line parameters are defined in Appendix B, and the self- and mutual admittances are described in Sections 2.7 and 2.8, respectively.

The improved transmission line model can be applied to rectangular and square microstrip patches only. Moreover, the variation of fields along the width of the patch is not accounted for. This model can be used for microstrip and coaxial feeds only. Proximity-coupled and aperture-coupled microstrip fed antennas cannot be analyzed. Some of these limitations are overcome in the next model.

2.2.3 Generalized Transmission Line Model

The equivalent circuit of Figure 2.5(b) has been solved differently in an approach called the generalized transmission line model (GTLM) [5, 15, 16]. In this approach, the transmission line sections, which may be nonuniform, on either side of the current source are converted into π-network equivalents. The resulting equivalent circuit is shown in Figure 2.6(b). This equivalent circuit is then simplified using the star-delta and delta-star transformations to obtain the voltage across the current source [6].

The application of GTLM is not restricted to the rectangular patch. Instead it can be applied to any separable geometry of the microstrip antenna. The majority of the practically used patches comes under this category. The patch shapes studied using this model include rectangular patch [15, 16], circular patch [5], circular ring [6], annular and circular sectors [7], and concentric array of circular rings [17] for linear polarization. Elliptical ring [18] and circular ring with a stub [19] have been studied as circularly polarized antennas.

The major difference between the transmission line model and GTLM is that a patch in GTLM is modeled in the form of transmission lines in orthogonal directions. Consequently, variation of fields along the transverse direction is included in GTLM. For application to nonrectangular geometries, the transmission lines are generally nonuniform in nature. Also, the definition

of wall admittance in GTLM is different from that employed in other models. The theoretical background of GTLM is described in detail in Appendix 2A at the end of this chapter. Next we apply this technique to a circular ring microstrip antenna.

Application of GTLM to a Circular Ring Microstrip Antenna

The geometry of a circular ring is shown in Figure 2.7. The separability criteria, (2A.6) of Appendix 2A, is satisfied for a circular geometry. The GTLM can, therefore, be employed to determine the characteristics of a circular ring microstrip antenna [6]. The other transmission line models [8–12], on the other hand, are not applicable for circular geometries. The scale factors in the cylindrical coordinate system are: $h_1 = 1, h_2 = u = \rho$; and the variables u-v are represented by ρ-ϕ. The general solutions for u dependence of E_z are

$$x_1(u) = J_n(ku) = J_n(k\rho),\ x_2(u) = Y_n(ku) = Y_n(k\rho) \tag{2.9}$$

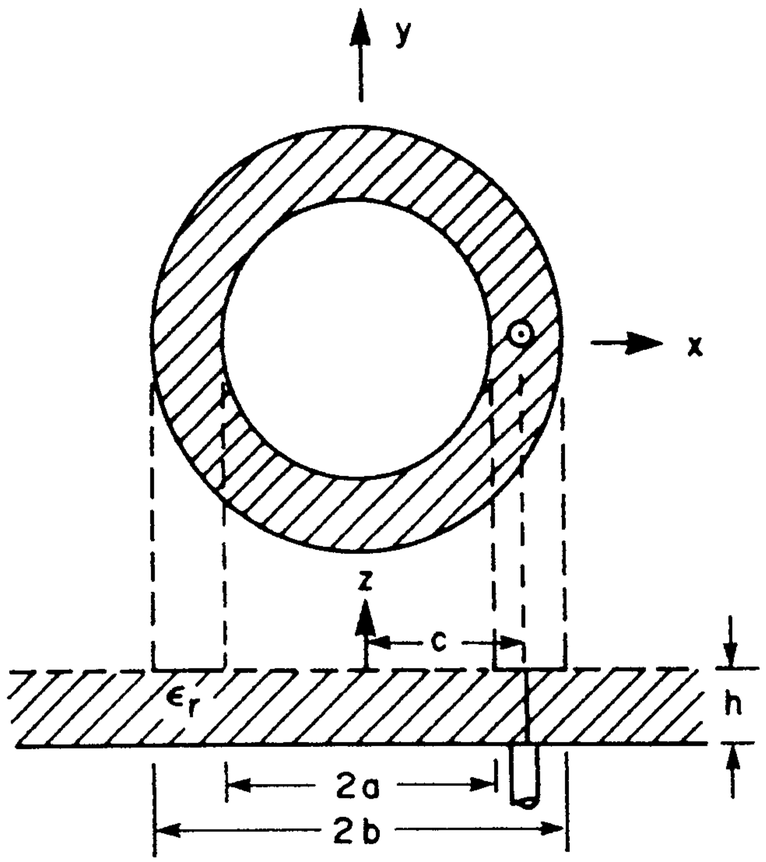

Figure 2.7 Geometry of a circular ring microstrip antenna.

where $J_n(\cdot)$ and $Y_n(\cdot)$ are the Bessel and Neumann functions, respectively, of order n, and k is the wave number in the substrate medium. The v dependence ($v = \phi$) of the field E_z is

$$f_2(v) = \cos n\phi \tag{2.10}$$

Using (2A.27), (2A.28), and (2A.29) of Appendix 2A, the lumped elements of the circuit in Figure 2.6(b) are obtained. These are given by (in the region $c < \rho < b$):

$$g_1 = Y_{11} + Y_{12} = \frac{-j}{\omega\mu\Delta(b, c)}[kb\Delta_1(b, c) + 2/\pi] \tag{2.11}$$

$$g_2 = -Y_{12} = \frac{-2j}{\pi\omega\mu\Delta(c, b)} \tag{2.12}$$

$$g_3 = Y_{22} + Y_{12} = \frac{j}{\omega\mu\Delta(c, b)}[kc\Delta_1(c, b) + 2/\pi] \tag{2.13}$$

with

$$\Delta(b, c) = J_n(kb)Y_n(kc) - Y_n(kb)J_n(kc) \tag{2.14a}$$

and

$$\Delta_1(b, c) = J_n'(kb)Y_n(kc) - Y_n'(kb)J_n(kc) \tag{2.14b}$$

where a prime indicates a derivative with respect to the argument. Expressions for the lumped elements in the region $a < \rho < c$ can be obtained by replacing c with a and b with c in (2.11), (2.12), and (2.13). The expression for mutual wall admittance is derived as [16, 20]

$$y_{12}^m = \frac{jabh}{2\pi\omega\mu}\int_0^{2\pi} \cos\alpha \frac{e^{-jk_0r}}{r^3}\Big[2(1 + jk_0r)\cos\alpha + \frac{(b\cos\alpha - a)(b - a\cos\alpha)}{r^2}(k_0^2r^2 - 3jk_0r - 3)\Big]d\alpha \tag{2.15}$$

with

$$r^2 = a^2 + b^2 - 2ab\cos\alpha$$

The self-conductance can be obtained from (2.15) by setting $b = a$ and retaining the real part. The self-susceptance should be obtained from the equivalent extension formula for the circular ring [21]. *We should point out that the definition of wall admittance in this model is different from the definitions used in other models.*

The equivalent network of Figure 2.6(b) was simplified in [6] using the delta-to-star and star-to-delta transformations and the input impedance was obtained. Computed results for the input impedance for the TM_{12} mode are plotted against frequency in Figure 2.8. Also given in this figure are the measured values. The agreement between the computed and measured results is good. In calculating the total input reactance, the reactances for the neighboring modes (TM_{02} and TM_{51}) are also added to that of the TM_{12} mode. The input resistance, however, was estimated from the TM_{12} mode alone [6]. The accuracy of GTLM can be improved by including the effect of substrate parameters on G_s and y^m_{12} [15].

The GTLM can be applied to a host of separable geometries, some of which are shown in Figure 2.9 [5]. Application of GTLM to an arbitrary patch shape is not possible. Also, some of the feeding techniques such as proximity-coupled and aperture-coupled microstrip feeds cannot be modeled. The stacked patch using GTLM has not been analyzed.

2.2.4 Lossy Transmission Line Model

Another variation of the transmission line model has been suggested by Dubost and coworkers [22–26]. A TEM mode approximation along the symmetry axis

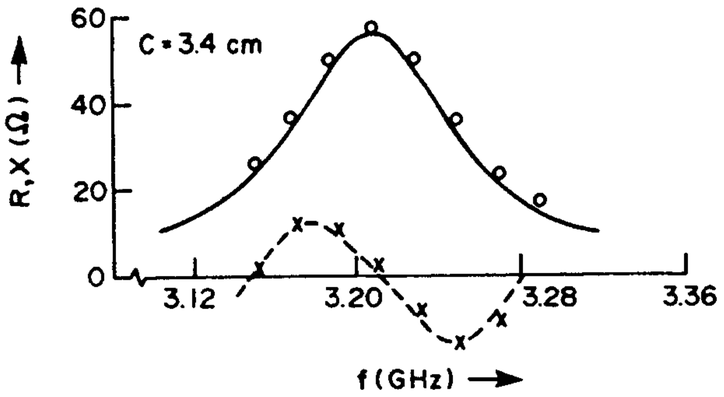

Figure 2.8 Input impedance of a circular ring microstrip antenna seen by a coaxial feed near the TM_{12} mode (a = 3 cm, b = 6 cm, c = 3.4 cm, ϵ_r = 2.2); _____, R computed; - - - -, X computed; ooo, R measured; xxx, X measured. (From [6]. © 1985 IEEE. Reprinted with permission.)

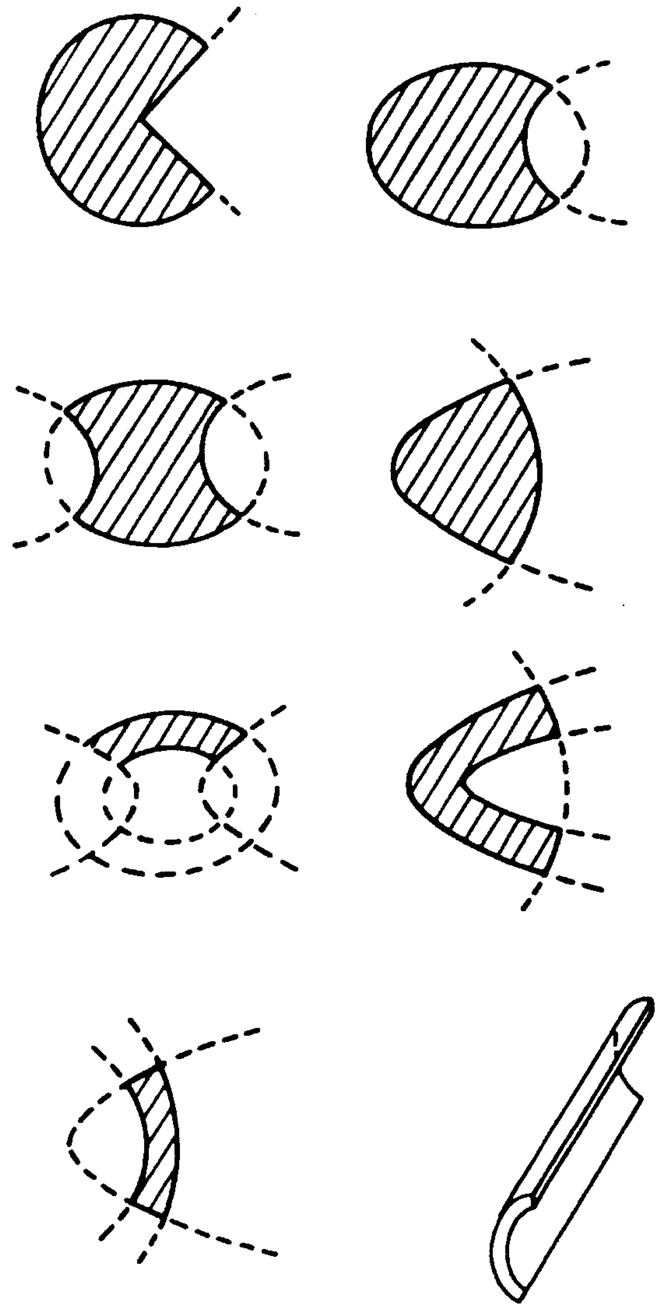

Figure 2.9 Some microstrip patch configurations that can be analyzed using GTLM. (From [5]. © 1985 IEE. Reprinted with permission.)

of the patch is assumed. In this model, various losses such as radiation loss, dielectric loss, and copper loss are combined and assumed distributed along the length of the transmission line in the form of increased dielectric loss. The transmission line section, which may be nonuniform for application to nonrectangular shapes, is divided into a number of small-sized sections. Each section with a particular strip width is characterized by the effective dielectric constant and characteristic impedance. The radiation admittance as a function of strip width is obtained from the solution of the Ricatti equation, which results from the constraint that power delivered to the lossy transmission line equals the power radiated. An analytical or numerical solution for a set of N cascaded sections is obtained to yield input admittance. This model has been applied to a number of geometries including rectangular patch, circular patch, stacked antenna geometry [23, 24], microstrip fed radiating slot, and folded dipoles [25, 26].

The accuracy of transmission line models can be improved by taking into account the effect of surface wave power loss. This may be achieved by including the surface wave conductance in the loads. The effect of multilayered substrate can be incorporated through the effective dielectric constant. Because of the *add-on* approach adopted for including the effects of radiated power, fringing field, and mutual coupling, these models suffer from limited accuracy in the resonant frequency and input impedance for substrates that are not very thin [27]. Extension of this model to large arrays may make the equivalent circuit unwieldy.

The cavity model described next is an improvement over the transmission line model in the sense that the variation of the field along the transverse direction is accounted for.

2.3 Cavity Model

Microstrip patch antennas are narrow-band resonant antennas. They can be termed *lossy cavities*. Therefore, the cavity model [28] becomes a natural choice to analyze patch antennas. A cavity model was advanced by Lo et al. [28–30]. In this model, the interior region of the patch is modeled as a cavity bounded by electric walls on the top and bottom, and a magnetic wall all along the periphery. The bases for this assumption are the following observations for thin substrates ($h \ll \lambda_0$):

- The fields in the interior region do not vary with z (that is, $\partial/\partial z \equiv 0$) because the substrate is very thin, $h \ll \lambda_0$.

- The electric field is z directed only, and the magnetic field has only the transverse components in the region bounded by the patch metalization and the ground plane. This observation provides for the electric walls at the top and bottom.
- The electric current in the patch has no component normal to the edge of the patch metalization, which implies that the tangential component of $\overline{H}$ along the edge is negligible, and a magnetic wall can be placed along the periphery. Mathematically, $\partial E_z/\partial n = 0$.

The field distribution in the patch can be divided into two regions: the interior fields and the exterior fields. The interior fields are determined next.

Consider the interior region of the cavity, as shown in Figure 2.1. Since the dielectric is thin, the field distribution in the interior region can be described by TM to z modes with $\partial/\partial z \equiv 0$. As a result, there are only three components of fields E_z, H_x, and H_y. The interior electric field $\overline{E}^i$ must satisfy the inhomogeneous wave equation

$$\nabla \times \nabla \times \overline{E}^i - k^2 \overline{E}^i = -j\omega\mu_0 \overline{J} \tag{2.16}$$

or

$$\nabla_t^2 E_z + k^2 E_z = j\omega\mu_0 \hat{z} \cdot \overline{J} \tag{2.17}$$

where $k^2 = \omega^2 \mu_0 \epsilon_0 \epsilon_r$, $\overline{J}$ is the excitation electric current density either due to the coaxial feed or the microstrip feed, $\hat{z}$ is a unit vector normal to the plane of the patch, and ∇_t is the transverse del operator with respect to the z axis.

In addition to satisfying the wave equation (2.16), the fields must also satisfy the following boundary conditions:

$$\hat{n} \times \overline{E}^i = 0 \quad \text{on the top and bottom conductors} \tag{2.18}$$

$$\left.\begin{aligned} \hat{n} \times \overline{E}^i &= \hat{n} \times \overline{E}^e \\ \hat{n} \times \overline{H}^i &= \hat{n} \times \overline{H}^e \end{aligned}\right\} \quad \text{on the walls} \tag{2.19}$$

Here $\hat{n}$ is the unit outward normal to the walls, $\overline{E}^e$ and $\overline{H}^e$ are the fields in the exterior region.

The fields on the walls, required to enforce (2.19), depend on the substrate parameters ϵ_r and h, the patch configuration and the size of the ground plane,

respectively. It is very difficult to determine these fields accurately even for the simplest patch shape. One of the assumptions that appears to work very well for almost all patch shapes is to assume a magnetic wall all around the periphery of the patch. The magnetic wall is placed at a distance Δ away from the edges of the patch (see Figure 2.10). The outward extension Δ takes into account the energy stored in the fringing fields. It is similar in nature to the effective width of a microstrip line (see Appendix B). Although for simple patch shapes Δ has been found to be a function of substrate parameters and patch shape, it is found to be approximately equal to h, the substrate thickness, for thin low dielectric constant substrates used in microstrip antennas. Equivalent dimensions for well-known antennas are given in Appendix 2B at the end of this chapter.

Under the magnetic wall assumption, (2.19) reduces to

$$\hat{n} \times \overline{H} = 0 \quad \text{on the magnetic walls} \tag{2.20}$$

It is now easy to determine the interior fields. However, these fields are correct only to the first order because the loading effect produced by the exterior fields has not been included in the determination of interior fields. The interior electric field distribution is now obtained in terms of eigenfunctions of the cavity.

The electric field in the patch cavity can be written as

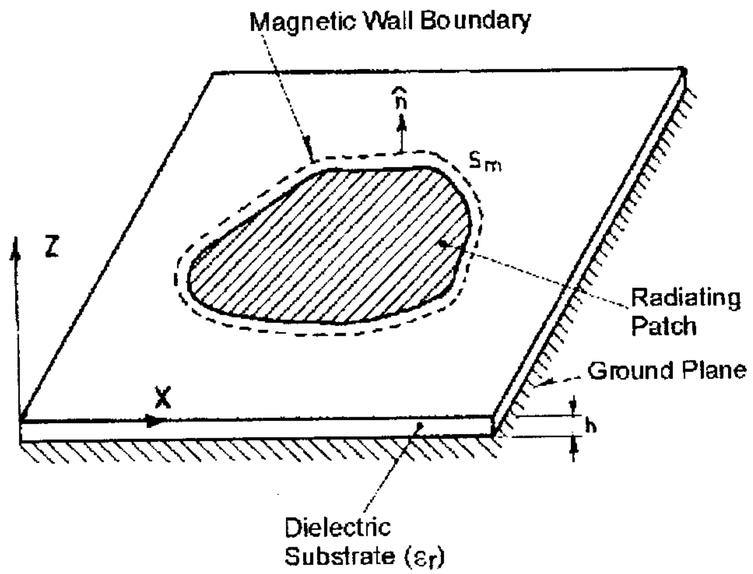

Figure 2.10 Magnetic wall model of a microstrip patch antenna.

$$E_z(x, y) = \sum_m \sum_n A_{mn} \psi_{mn}(x, y) \tag{2.21}$$

where A_{mn} are the amplitude coefficients corresponding to the electric field mode vectors or eigenfunctions ψ_{mn}. The eigenfunctions are solutions of

$$(\nabla_t^2 + k_{mn}^2)\psi_{mn} = 0 \tag{2.22}$$

with

$$\frac{\partial \psi_{mn}}{\partial n} = 0 \quad \text{on the magnetic walls} \tag{2.23}$$

Note here that the eigenfunctions depend on the shape and size of patch metalization, and not on substrate parameters.

Now substitute (2.21) for E_z in (2.17), multiply both sides by ψ_{mn}^* and integrate over the area of the patch. The amplitude coefficients are obtained as

$$A_{mn} = \frac{j\omega\mu_0}{k^2 - k_{mn}^2} \frac{\iint J_z \psi_{mn}^* ds}{\iint \psi_{mn} \psi_{mn}^* ds} \tag{2.24}$$

Therefore,

$$E_z = j\omega\mu_0 \sum_m \sum_n \frac{1}{k^2 - k_{mn}^2} \frac{\iint J_z \psi_{mn}^* ds}{\iint \psi_{mn} \psi_{mn}^* ds} \psi_{mn} \tag{2.25}$$

and

$$\overrightarrow{H} = \frac{1}{j\omega\mu_o} \hat{z} \times \nabla E_z \tag{2.26}$$

Alternatively, Green's function for the geometry can be employed to determine the electric field under the patch metalization. The solution for E_z then becomes

$$E_z = \iint G(s|s')J_z ds' \tag{2.27}$$

The interior fields are now used to determine the input impedance of the antenna. Input impedance, in the cavity model, is defined as

$$Z_{\text{in}} = \frac{V_{\text{in}}}{I_{\text{in}}} \tag{2.28}$$

where V_{in} is the RF voltage at the feed point, and is calculated as

$$V_{\text{in}} = -E_z \text{ (at the feed point)}h \tag{2.29}$$

and the feed current

$$I_{\text{in}} = \iint J_z ds \tag{2.30}$$

The preceding procedure will yield the input impedance as purely reactive because all the quantities under the summation sign in (2.25) are real. The effect of radiation and other losses on the input impedance can be included either in the form of an artificially increased substrate loss tangent [28–30] or by an impedance boundary condition at the radiating walls [2, 31]. We describe the first approach here. The other approach is used in the multiport network model described in Section 2.5.

In the cavity model, various types of losses, such as dielectric loss, conductor loss, and radiation loss, are taken into account by defining an effective loss tangent as

$$\delta_{\text{eff}} = 1/Q \tag{2.31}$$

where the Q factor of the lossy cavity is defined as

$$Q = \frac{\omega_r W_T}{P_d + P_c + P_r} \tag{2.32}$$

Therefore,

$$\delta_{\text{eff}} = \frac{P_d + P_c + P_r}{\omega_r W_T} \tag{2.33}$$

Here, P_d is the power lost in the imperfect dielectric, P_c is the power lost in the imperfect conductors, and P_r is the power radiated by the antenna. Surface wave loss can be neglected for thin substrates; otherwise, the surface power loss should also be included in (2.33). W_T is the total energy stored in the patch at resonance ω_r. The energy stored is determined by the fields under the patch, and is expressed as

$$W_T = W_e + 2W_m = \frac{\epsilon_0 \epsilon_r}{2} \iiint |E_z|^2 dV \tag{2.34}$$

The dielectric loss is calculated from the electric field under the patch,

$$P_d = \frac{\omega \epsilon_0 \epsilon_r \tan\delta}{2} \iiint |E_z|^2 dV = \omega \cdot \tan\delta \cdot W_T \tag{2.35}$$

where $\tan\delta$ is the loss tangent of the dielectric. The conductor loss P_c is calculated from the magnetic field on the patch metalization and ground plane,

$$P_c = 2\frac{R_s}{2} \iint |H_s|^2 ds \approx \frac{\omega W_T}{h\sqrt{\pi f \mu_0 \sigma}} \tag{2.36}$$

where R_s is the surface resistivity of the conductors given by $\sqrt{\pi f \mu_0 \sigma}$ and σ is the conductivity of the conductor. The power radiated from the patch P_r can be determined by integrating the radiation field over the hemisphere above the patch, that is,

$$P_r = \frac{1}{2\eta_0} \int_0^{2\pi} \int_0^{\pi/2} (|E_\theta|^2 + |E_\phi|^2) r^2 \sin\theta d\theta d\phi \tag{2.37}$$

The expressions for E_θ and E_ϕ are, in general, very complicated functions of θ and ϕ and substrate parameters. Therefore, a numerical integration is performed.

Alternatively, δ_{eff} can be described in terms of various quality factors. Defining,

$$\text{Dielectric } Q;\ Q_d = \frac{\omega_r W_T}{P_d} = 1/\tan\delta \quad \text{from (2.34) and (2.35)} \tag{2.38a}$$

Conductor Q; $Q_c = \dfrac{\omega_r W_T}{P_c}$

$= h\sqrt{\pi f \mu_0 \sigma}$ from (2.36)

$= h/\Delta$ (Δ is the skin depth for the conductor) (2.38b)

$$\text{Radiation } Q;\ Q_r = \frac{\omega_r W_T}{P_r} \tag{2.38c}$$

one obtains total Q, Q_T, as

$$\frac{1}{Q_T} = \frac{P_d + P_c + P_r}{\omega_r W_T} = \frac{1}{Q_d} + \frac{1}{Q_c} + \frac{1}{Q_r} \tag{2.39}$$

Use of (2.38) in (2.33) gives the following expression for δ_{eff}:

$$\delta_{\text{eff}} = \tan\delta + \frac{\Delta}{h} + \frac{P_r}{\omega_r W_T} \tag{2.40}$$

With the losses described in terms of δ_{eff}, the expression for k^2 in (2.25) is now modified as

$$k^2 = k_0^2 \epsilon_r (1 - j\delta_{\text{eff}}) \tag{2.41}$$

to yield the following expression for E_z:

$$E_z = j\omega\mu_0 \sum_m \sum_n \frac{1}{k_0^2 \epsilon_r (1 - j\delta_{\text{eff}}) - k_{mn}^2} \frac{\iint J_z \psi_{mn}^* ds}{\iint \psi_{mn} \psi_{mn}^* ds} \psi_{mn} \tag{2.42}$$

By varying the frequency, the input impedance is calculated at and near the resonant frequency using (2.42) and (2.28). Resonance is indicated by a real input impedance.

The cavity model, as described above, has been applied to a number of patch shapes, including rectangular patches [29, 32, 33], circular patches [28, 29, 34, 35], equilateral triangles [36], circular rings [37–39], and annular and circular sectors [39]. Circular polarization can be predicted using the cavity model [4, 29, 30; Chapter 4]. The cavity model has been modified to include the variation of fields along the substrate thickness [40]. Stacked patch antennas [41] have also been analyzed.

The mutual coupling between the apertures is included in an implicit manner in the cavity model. It is included through the power radiated, which essentially accounts for G_m only, and not mutual susceptance B_m. Moreover, the cavity model does not estimate the ratio of aperture fields correctly in microstrip antennas with more than one aperture, since the fields at the apertures are estimated from a standing wave distribution, in which all the points are in phase [7]. In fact, due to power radiation, the field inside the patch will be progressive in nature, and therefore a phase difference between the aperture fields will occur. It is confirmed by the calculations carried out for a circular ring antenna in a later chapter (see Section 5.6.3). Therefore, the cavity model as such is not suitable for array applications. However, the cavity model has been extended to determine the mutual coupling between rectangular patches [42]. For this, the electric field at the radiating edges is replaced by an equivalent magnetic current and the space wave coupling coefficient can be calculated. The cavity model has also been used to analyze an aperture-coupled patch antenna [43, 44]. In this analysis, the aperture is replaced by an equivalent magnetic current on a conductor surface.

The eigenfunctions required for the cavity model analysis of various geometries are given in Appendix 2B at the end of the chapter. The equivalent dimensions are also given there. The details of the cavity model analysis are given in Chapter 4 for the rectangular patch; in Chapter 5 for the disk, semicircular disk, and circular ring; and in Chapter 6 for the triangular patch antenna.

2.4 Generalized Cavity Model

The cavity model has also been generalized to analyze nonseparable geometries [45, 46]. For this purpose, the given geometry is first converted into an equivalent geometry with magnetic walls at the peripheries as shown in Figure 2.10. The outward extension Δ is based on an educated guess. For regular shaped geometries, the equivalent dimensions are given in Appendix 2B. For other geometries, an extension equal to the substrate thickness h appears to work well for thin, low dielectric constant substrates. Next, the geometry with the magnetic wall is segmented into regular geometries for which eigenfunctions are available. The planar circuit approach [47] is then applied to determine the electric and magnetic fields under the patch. The Q of the patch cavity is next calculated using the procedure given for the cavity model. Finally, the input impedance can be obtained from the ratio of the voltage and current at the feed point. This approach has been used to analyze a rectangular ring [48], a cross-shaped patch [49], an H-shaped patch [48], a square ring microstrip

antenna [49], and a two-port circular patch [50]. A summary of this approach is given next.

In the generalized cavity model, the electric field in the patch is determined first by segmenting the given patch shape into a number of regular shapes for which the Green's functions can be determined. The Green's functions for rectangles, circles, triangles, circular sectors, annular rings, and annular sectors are available [51]. For example, segmentation of the cross-shaped patch into three rectangular segments is shown in Figure 2.11(a). Most of the useful practical patch shapes can be decomposed into regular shapes, and the available Green's functions can be used. A completely arbitrary shape with no plane of symmetry, in general, will give higher levels of cross-polarization in the radiation patterns.

Segmentation

It is possible to determine the fields in a separable geometry by expanding the fields in various segments in terms of their natural modes, and then matching fields along the interconnection lengths. Next, the continuous interconnections between the segments are discretized by interconnections only at a finite number of points. A port is associated with each interconnection point. This is shown in Figure 2.11(a) for the cross-shaped geometry. While approximating the continuous interconnections by a finite number of ports, each port width is kept less than or equal to $\lambda/20$ to optimize the discretization error and efficiency. Here, λ denotes the intrinsic wavelength in the patch. The small size of the port width allows the assumption that the current density is uniform over the width of the port.

The individual segments are now treated as multiport planar networks, and the Z matrices for the same are evaluated using the corresponding impedance Green's function. For a rectangular segment it is defined as [51],

$$Z^s_{ij} = \frac{1}{W_i W_j} \int_{PW_i} \int_{PW_j} G^s(x_i, y_i | x_j, y_j) d_{s_i} d_{s_j} \tag{2.43}$$

where Z^s_{ij} is the ijth element of the Z matrix of the segment, W_i, W_j and PW_i, PW_j are the effective and the physical width of the ith and the jth ports, respectively. For ports entirely within the patch metalization, physical widths and effective widths are equal. The Green's function G^s is of the following form for the rectangular geometry of dimensions $a \times b$ [51]:

$$G^s(x, y | x', y') = \frac{j\omega\mu_o h}{ab} \sum_{m=-\infty}^{\infty} \sum_{n=-\infty}^{\infty} \frac{\psi^s_{mn}(x, y)\psi^{s*}_{mn}(x', y')}{k^2_{mn} - k^2} \tag{2.44}$$

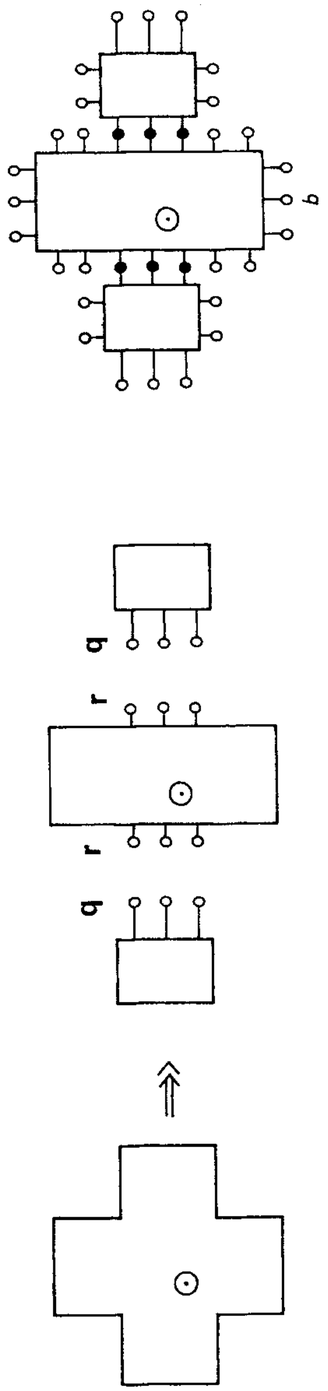

Figure 2.11 (a) Segmentation of a cross-shaped patch into three rectangular segments for the generalized cavity model. (From [49]. © 1986 IEEE. Reprinted with permission.) (b) Multiport network model of the cross-shaped patch antenna. (From [4]. © 1989 Peter Peregrinus. Reprinted with permission.)

Here $\psi^s_{mn}(x, y)$ is the eigenfunction for the mnth mode of the segment, k_{mn} is the corresponding eigenvalue, h is the substrate thickness, and $k^2 = \omega^2 \mu_0 \epsilon_0 \epsilon_r$.

Note that for calculating the impedance matrix of a segment, the local coordinate system can be oriented independent of the coordinate systems chosen for other segments. It should be oriented in such a way that the maximum number of ports lies on the coordinate axis. The integrals in (2.43) are simple and can be obtained in closed form. The input feed is also considered a port (or several ports if the width is more than $\lambda/20$) and can be treated like other port/ports of the segment in the Z-matrix evaluations. For a microstrip feed, the effective width of the feed is used for this purpose.

Multiport Connection Method

The multiport Z matrices for the various segments are now combined by using the multiport connection method [51] to obtain the overall Z matrix of the given structure. For this, the ports of the segments (to be combined) are separated into external (p) ports and connected (c) ports. The connected ports are equally divided into two groups labeled q and r ports such that q ports are the connected ports of one segment and r ports are the corresponding connected ports of the other segment, to be combined [see Figure 2.11(b)]. Based on this labeling, the Z matrix of the combination can now be written as

$$\begin{bmatrix} \vec{V}_p \\ \vec{V}_q \\ \vec{V}_r \end{bmatrix} = \begin{bmatrix} Z_{pp} & Z_{pq} & Z_{pr} \\ Z_{qp} & Z_{qq} & Z_{qr} \\ Z_{rp} & Z_{rq} & Z_{rr} \end{bmatrix} \begin{bmatrix} \vec{i}_p \\ \vec{i}_q \\ \vec{i}_r \end{bmatrix} \tag{2.45}$$

where $\vec{V}_p$, $\vec{V}_q$, $\vec{V}_r$, and $\vec{i}_p$, $\vec{i}_q$, $\vec{i}_r$, are the vectors corresponding to RF port voltages and port currents, respectively, and the Z_{pp} and so on values are the impedance submatrices. Because ports q and ports r are respective ports of two physically separate segments (that are being connected together), submatrices Z_{qr} and Z_{rq} are identically equal to zero. The boundary condition, that is, the continuity of the tangential components of the electric and magnetic fields at the boundary plane between the two combining segments, is expressed in terms of the continuity of port voltages and port currents. These are known as interconnection constraints [51] and are expressed as

$$\vec{V}_q = \vec{V}_r \text{ and } \vec{i}_q + \vec{i}_r = 0 \tag{2.46}$$

Upon substituting (2.46) in (2.45), one obtains the RF currents at the interconnecting q ports $\vec{i}_q$ and the impedance matrix of the combination as

$$\vec{i}_q = [Z_{qq} + Z_{rr}]^{-1}[Z_{rp} - Z_{qp}]\vec{i}_p \tag{2.47a}$$

$$[Z_p] = [Z_{pp}] + [Z_{pq} - Z_{pr}][Z_{qq} + Z_{rr}]^{-1}[Z_{rp} - Z_{qp}] \tag{2.47b}$$

Resonant Frequency

The input impedance evaluated from (2.47b) gives the input reactance of the lossless cavity since the radiation, conductor, dielectric, and surface wave losses have not yet been accounted for. The variation of input reactance with frequency is determined. A very large value of the input reactance indicates resonance because of the antiresonant nature of the patch antenna.

While evaluating the Z matrices of various segments using (2.43), the various combinations of m and n in the evaluation of the Green's function represent the contribution of higher order modes. Because the series is converging, the values of m and n can be limited to $m = M$ and $n = N$, as discussed next. The values of M and N depend on the dimensions of the segment, frequency of operation, and the permittivity of the substrate through k_{MN} and k. They (M and N) should be selected such that the contribution of the $[(M + 1), (N + 1)]$th mode to the Z matrix is insignificant. The values of M and N can be different for different segments depending on their shape and size.

Next, the electric field distribution in the patch is determined. This is required to determine the radiation characteristics and the input impedance.

The electric field E^s_z distribution in terms of the eigenfunctions of the segment is determined in a manner identical to that described in the cavity model (see Section 2.3). The only difference here is that the excitation current lies along the interconnection interfaces of the segment. The details can be found in [46, 51]. The calculation of the electric field in terms of the Green's function of the segment follows.

The excitation current density J_s for a segment is related to the tangential component of the magnetic field on its periphery through the relation $\vec{J}_s = \hat{n} \times \vec{H}$. In the present case, J_s can be determined from the port currents. For this, the current density along the interconnections of the segment is expanded in terms of P modes of the segment. For a rectangular segment, it is given by [46]

$$J_s(s_0) = \frac{-1}{w} \sum_{k=1}^{P} a_k \cos\left\{\frac{(k-1)\pi}{L} s_0\right\} \tag{2.48}$$

where w is the port width, L is the length of the segment along the interconnection, a_k is the expansion coefficient for the kth mode, and s_0 is the running coordinate on the interconnection. The subscript $k = 1$ corresponds to the

TEM mode and P represents the number of modes in the segment that should be taken equal to the number of ports q or r. The coefficients a_k are determined by equating the port current i_k determined in (2.47a) at the kth port to $i(s_0) = wJ_s(s_0)$ evaluated at the middle of kth port, and solving the resultant set of simultaneous equations. Equation (2.48) is repeated for all the interconnections of a segment.

The electric field E_z^s in the segment can be obtained using the definition of Green's function as

$$E_z^s = \frac{1}{h}\sum \int_{S_m} G^s(x, y/s_0) J_s(s_0) ds_0 \tag{2.49}$$

The summation is carried out over all the interconnections of a segment. Use of either eigenfunctions (2.21) or Green's functions (2.49) (both lead to the same result) gives the expression for the electric field distribution in the segment. Similarly, the electric field distribution in other segments can be evaluated. The electric field for the segmented structure is evaluated and plotted at the resonant frequency. From the nature of the variation, the mode of operation can be identified.

Input Impedance

Knowing the electric field distribution at the periphery of the antenna structure, one can calculate the radiation patterns using the magnetic current model described in Section 2.6. From the power radiated and the electric energy stored, the cavity total Q can be evaluated. This is then used to determine the input impedance of the antenna by writing $\delta_{\text{eff}} = 1/Q_T$ as in the cavity model. Then replace k^2 by $k^2{}_0\epsilon_{re}(1 - j\delta_{\text{eff}})$ in the Green's function for a segment to obtain

$$G^s(x, y|x', y') = \frac{j\omega\mu_0 h}{ab} \sum_{m=-\infty}^{\infty} \sum_{n=-\infty}^{\infty} \frac{\psi_{mn}^s(x, y)\psi_{mn}^{s*}(x', y')}{k_{mn}^2 - k_0^2\epsilon_{re}(1 - j\delta_{\text{eff}})} \tag{2.50}$$

The Z matrices for the individual segments are again evaluated using the modified Green's function (2.50) and combined as described earlier to give the input impedance of the antenna. By varying the frequency, the input impedance can be evaluated at and near the resonant frequency. It is corrected for feed reactance if a probe feed is used. Resonance is indicated by a real input impedance.

2.5 Multiport Network Model

The multiport network model (MNM) [4] can be considered an extension of the cavity model in which the impedance boundary condition at the periphery is enforced explicitly. This model also takes into account the mutual coupling between various edges. The model makes use of the planar circuit approach [47] and the edge admittances of the patch. Extensive details of MNM are available in [4, Chapter 9]. Below we give a summary of this approach.

In the MNM, the fields in the interior region and the exterior region are modeled separately. The interior region is modeled as a multiport planar circuit, with the ports located all along the periphery, as shown in Figure 2.11(b) for a cross-shaped patch antenna. The fields in the exterior region, which include the fringing fields, radiation fields, and surface wave fields, are represented by the load admittances. Unlike the transmission line model, all of the edges, radiating and nonradiating, qualify to be represented as load admittances in the MNM. Moreover, the load admittance corresponding to a given edge is equally divided into a number of ports. These loads are then connected to the corresponding ports on the planar circuit. Therefore, for a given edge, the number of ports on the multiport network and the load network are identical. The representation of a rectangular patch antenna (fed by a probe current) in the form of a multiport network model is shown in Figure 2.12.

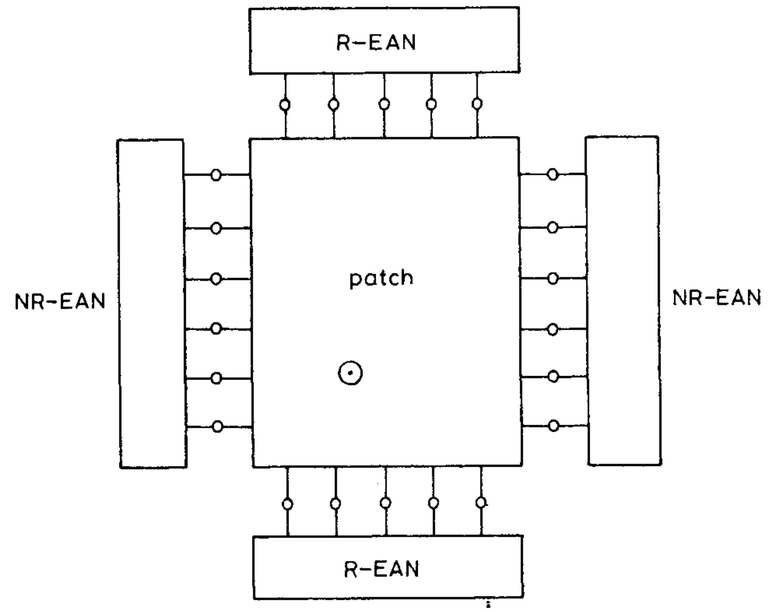

Figure 2.12 Multiport network model, without mutual coupling, of a rectangular patch antenna. (From [4]. © 1989 Peter Peregrinus. Reprinted with permission.)

In the figure, R-EAN stands for the radiating edge admittance network, and NR-EAN denotes the nonradiating edge admittance network. Next, the multiport impedance matrix $[Z^M]$ is obtained using the planar circuit approach, which makes use of the impedance Green's function available for regular/separable geometries [4, 51]. The admittance matrix for the load network $[Y^L]$ can be obtained using the known closed-form expressions for the self-admittance and mutual admittance. The matrices $[Y^M]$ and $[Y^L]$ are now combined in the network analysis [51] to obtain the input impedance of the patch. The matrices $[Z^M]$ and $[Y^L]$ are determined next.

To arrive at the multiport impedance matrix for the planar circuit of the patch, the periphery of the patch is first divided into a number of edges, each of which is then classified as radiating type or nonradiating type. The classification is based on the observation that a radiating edge is associated with slow field variation along its length. The nonradiating edge, on the other hand, should have an integral multiple of half-wave variations along the edge, such that there is almost complete cancellation of the radiated power from the edge. A simple example of this nature of field variation is found in the resonant rectangular patch operated in the TM_{mo} mode or the TM_{on} mode. The edge length is next divided into a number of equal parts, to each of which is assigned a port. The port terminals are located at the middle of the port width, with one terminal on the patch side and the other ground. For the radiating edge, the physical port width W_i is typically chosen to be about $\lambda/10$, while for the nonradiating edge, the port width is decreased to about $\lambda/20$, because of the rapid field variation. Assuming that the port voltages v_i and the port currents I_j are constant over the port widths, the impedance matrix element for $[Z^M]$ is defined as

$$Z_{ij}^M = \frac{1}{W_i W_j} \int_{W_i W_j} \int G(x_i, y_i | x_j, y_j) d_{s_i} d_{s_j} \tag{2.51}$$

where $(x_{i,j}; y_{i,j})$ the values denote the location of the two ports of widths W_i and W_j, respectively. The impedance Green's function G(•|•) for the patches of regular shapes like rectangles, circles, rings, sectors of circles and rings, and three types of triangles are available [4, 51]. These Green's functions usually employ a doubly infinite series with each term representing a particular mode of the planar resonator with magnetic walls along the periphery.

The fields in the exterior region of the patch are represented by a load admittance matrix $[Y^L]$. It is a square matrix of the same size as the multiport matrix $[Z^M]$. Each element of $[Y^L]$ is a complex number, the real part representing the power loss and the imaginary part the energy stored in the fringing

field. The port self-admittances are placed at the diagonal locations in the matrix, while the off-diagonal entries represent the mutual coupling between various ports. The matrix $[Y^L]$ is a diagonal matrix for patches with a single edge. For simplicity, the self terms for the nonradiating edges are taken to be purely imaginary, assuming that the associated power loss is negligible although the surface wave loss may be significant for thicker substrates. The load admittance values are calculated separately for each edge. Then, this edge admittance is divided equally among the various ports constituting the edge. The load at each of the ports on the radiating edge is a parallel combination of G and C, and on the nonradiating edge it is simply the fringing field capacitance C. The edge admittance networks are shown in Figure 2.13.

The MNM of a rectangular patch antenna incorporating the effect of mutual coupling between the radiating edges is shown in Figure 2.14. The patch is fed a nonradiating edge. Here, the mutual coupling effect is described by a separate block labeled MCN (mutual coupling network). Similar MCNs can be included between a nonradiating edge and a radiating edge, and between two nonradiating edges, or between the edges of different patches in an array.

Edge-Admittance Network and Mutual Coupling Network

The edge-admittance networks are shown in Figure 2.13. The values of G and C can be obtained from the closed-form expressions for radiation conductance and fringing field susceptance given in Section 2.7. These expressions can be used straightaway if the voltage distribution along the edge is uniform. However, for a nonuniform distribution of voltage, some correction is needed, as described next.

Let the edge length be W, and the power radiated from it for a uniform voltage distribution be P_r. Then using $P_r = 1/2\, V^2 G_r$, one obtains the radiation conductance per unit length as $2P_r/W$ for $V = 1$V. But when the normalized

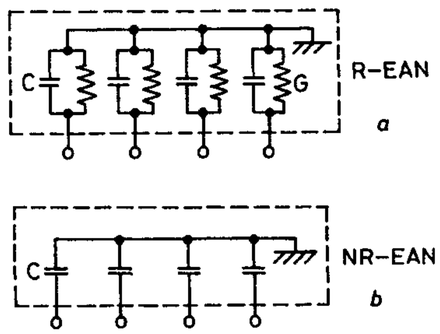

Figure 2.13 Edge admittance networks (EAN) for (a) radiating edge and (b) nonradiating edge. (From [4]. © 1989 Peter Peregrinus. Reprinted with permission.)

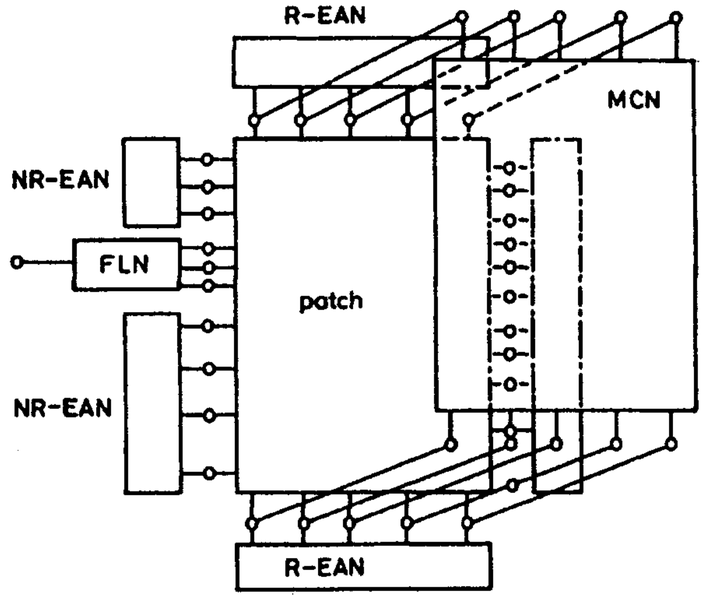

Figure 2.14 Multiport network model of a rectangular patch antenna incorporating mutual coupling between the radiating edges. (From [4]. © 1989 Peter Peregrinus. Reprinted with permission.)

voltage distribution along the edge is $V(s) = f(s)$, the radiation conductance per unit length is obtained as [4, Chapter 9]

$$G_r = \frac{2P_r}{\int_0^W f^2(s)ds} \tag{2.52}$$

where s denotes the position along the radiating edge. If we divide the edge length W into n ports of equal width W/n, the conductance shunting each of the ports is $G_r W/n$. The voltage distribution $f(s)$ for the regular shaped patches is known a priori from their eigenfunctions. However, for nonregular shaped patches and patches with discontinuities, for example, the MNM can be used to determine an accurate $f(s)$ in an iterative fashion. Similar to the radiation conductance, the surface conductance G_s can be expressed as [4, Chapter 9]

$$G_s = \frac{2P_{\text{sur}}}{\int_0^W f^2(s)ds} \tag{2.53}$$

It was pointed out in Chapter 1 that $G_s << G_r$ for thin substrates without any cover layer on the patch. The edge susceptance is also distributed uniformly over the n ports.

The multiport network model has been used to determine mutual coupling between two rectangular patches. For this, the mutual coupling between any two ports is determined by first converting the electric field on one of the ports into the equivalent magnetic current $\overline{M}_i = -\hat{n} \times \overline{E}_i h$, the unit vector $\hat{n}$ is taken normal to the ground plane, and the electric vector $\overline{E}_i$ across a slot over the ground plane. The ground plane can be removed by imaging $\overline{M}_i$ to give the current $2\overline{M}_i$ radiating in free space. Next, the magnetic field $\overline{H}_j$, radiated by the magnetic current $2\overline{M}_i$, is determined at the location of port j. The current density $\overline{J}_j = \hat{n} \times \overline{H}_j$ induced on port j is then calculated. The mutual admittance between the ports i and j is then given by [4, Chapter 9]

$$Y_{ij} = J_j W_j / M_i \tag{2.54}$$

In this way the mutual admittance matrix between two radiating edges and therefore the mutual coupling network (MCN) between two adjacent patches can be determined. The MCN between two patches is shown in Figure 2.15. Here, MCN accounts for coupling between all four radiating edges. Comparison of mutual coupling $|S_{21}|$ based on MNM with the transmission line model and experimental results is shown in Figures 2.16 and 2.17 for the E-plane and H-plane mutual coupling, respectively [52]. The agreement with the experimental values is found to be better for MNM.

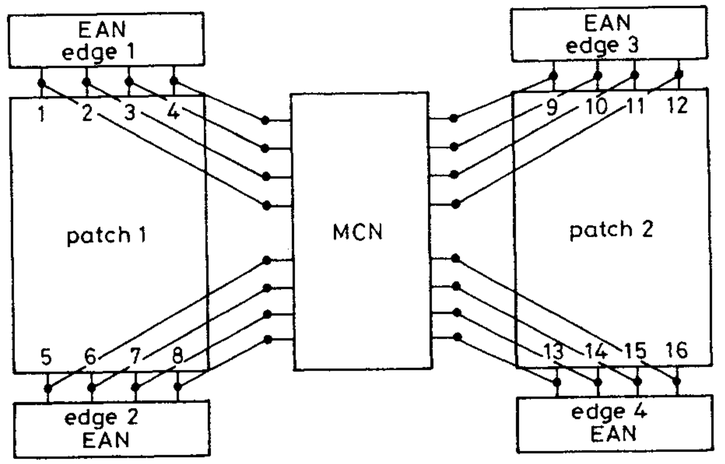

Figure 2.15 A mutual coupling network (MCN) representing the coupling between two adjacent patches in an array. (From [52]. © 1989 IEEE. Reprinted with permission.)

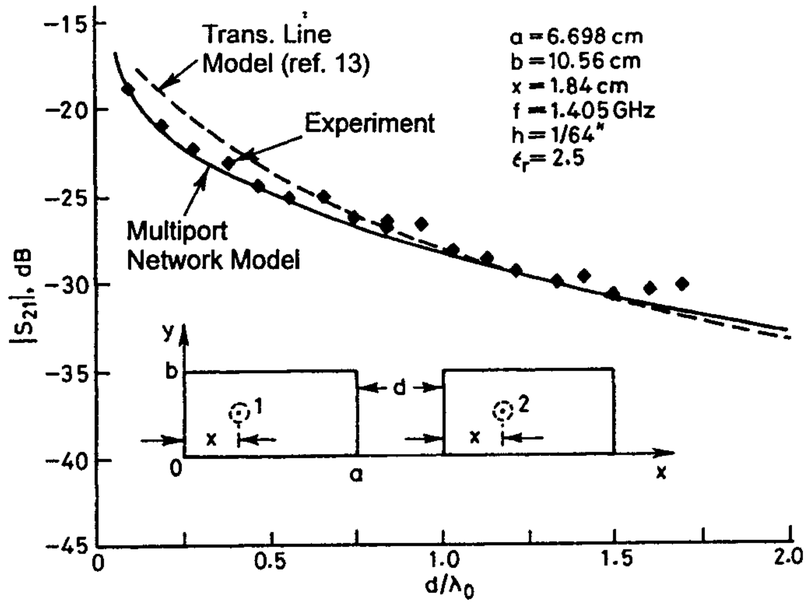

Figure 2.16 Comparison between theoretical and experimental results for E-plane mutual coupling between two rectangular microstrip patches. (From [52]. © 1989 IEEE. Reprinted with permission.)

The MNM has been applied to analyze a variety of microstrip antennas [50, 53–59], including rectangular patches, circular polarization from truncated square patches [55], square patches with diagonal slots [55], pentagonal shaped patches [54], broadband gap-coupled multiresonator rectangular patches [56, 57], direct coupled rectangular patches [58], and two-port rectangular patches [59]. Recently, MNM has been used to model proximity-coupled rectangular microstrip antennas [60]. One of the major advantages of MNM is that any discontinuity in the patch is also included in the analysis. The discontinuity effect is not calculated separately and *added* in the form of a lumped reactance.

2.6 Radiation Fields

The radiation pattern of an antenna is one of the most important characteristics and easiest to determine for patch antennas. The calculation of the radiation patterns from a patch antenna follows the same approach irrespective of the analytical models discussed earlier. It is assumed that the electric field at the perimeter of the patch is known. The equivalent source concept [61] is then used to determine the radiation fields. The equivalent magnetic current is defined as

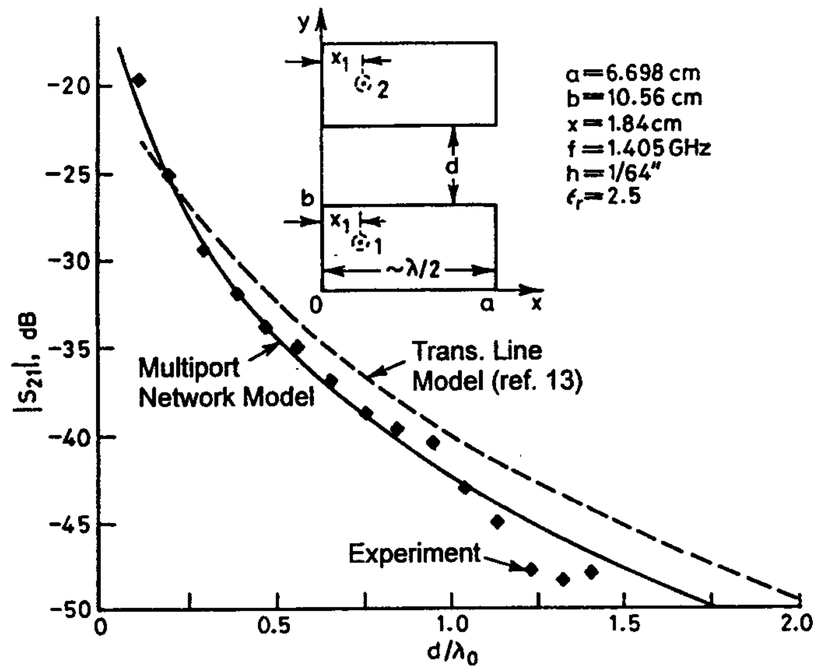

Figure 2.17 Comparison between theoretical and experimental results for H-plane mutual coupling between two rectangular microstrip patches. (From [52]. © 1989 IEEE. Reprinted with permission.)

$$\vec{M} = \vec{E} \times \hat{n} \tag{2.55}$$

If the substrate thickness h is much less than the wavelength λ_0, its effect on the radiation patterns is small and M can be assumed to radiate in free space. One can then use the vector potential approach described in Section 1.5.1 to determine the radiation patterns. Let us consider an aperture of dimensions $h \times W$ with $E_x = -V_0/h$ V/m, and $E_y = 0$. For this case, $M_x = 0$ and

$$M_y = \begin{cases} V_0/h & -\dfrac{W}{2} \le y \le \dfrac{W}{2}, -\dfrac{h}{2} \le x \le \dfrac{h}{2} \\ 0 & \text{elsewhere} \end{cases} \tag{2.56}$$

It has been derived in Chapter 1, (1.29), that

$$E_\theta = -jk_0 V_0 W \frac{e^{-jk_0 r}}{4\pi r} \operatorname{sinc}(k_0 h \sin\theta \cos\phi/2) \operatorname{sinc}(k_0 W \sin\theta \sin\phi/2) \cos\phi \tag{2.57}$$

$$E_\phi = jk_0 V_0 W \frac{e^{-jk_0 r}}{4\pi r} \sin c(k_0 h \sin\theta \cos\phi/2) \sin c(k_0 W \sin\theta \sin\phi/2) \cos\theta \sin\phi \tag{2.58}$$

The effect of the ground plane and substrate on the radiation patterns can be included in a simple manner by imaging the slot at an electrical distance kh from the ground plane, $k = k_0\sqrt{\epsilon_r}$ [31]. This approach results in an array factor $2\cos(kh\cos\theta)$ if the patch lies in the x-y plane. A better and rigorous approach is based on the reciprocity theorem applied to two infinitesimal dipoles, one located on the surface of the substrate and the other in free space at a very large distance away from it [62]. It yields the following factors for the E-plane and H-plane radiation patterns:

$$F_3(\theta) = \frac{2\cos\theta\sqrt{\epsilon_r - \sin^2\theta}}{\sqrt{\epsilon_r - \sin^2\theta} - j\epsilon_r \cos\theta \cot(k_0 h\sqrt{\epsilon_r - \sin^2\theta})} \quad \text{for E-plane pattern } (\phi = 0°) \tag{2.59a}$$

and

$$F_4(\theta) = \frac{2\cos\theta}{\cos\theta - j\sqrt{\epsilon_r - \sin^2\theta}\cot(k_0 h\sqrt{\epsilon_r - \sin^2\theta})} \quad \text{for H-plane pattern } (\phi = 90°) \tag{2.59b}$$

The radiation patterns for a substrate loaded patch are obtained by multiplying (2.58) and (2.59).

The analysis for the radiation field of a rectangular slot can be used to determine the radiation patterns of a rectangular patch antenna by multiplying the radiation fields of a slot with the array factor (see Chapter 4). Radiation patterns for other microstrip antennas can be similarly derived.

2.7 Aperture Admittance

In the (aperture) models discussed earlier, the effect of fields in the exterior region on the input impedance is represented by a load admittance. The load conductance is associated with the power radiated from the aperture, whereas the load susceptance is due to the energy stored in the near field. The load

conductance or radiation conductance G_r is defined as an ohmic conductance (distributed or lumped), which will dissipate a power equal to that radiated by the aperture. The power radiated and the energy stored can be calculated if the aperture field distribution is known exactly. It is difficult to determine the exact aperture field. However, the ideal open-circuit field behavior is found to give a fairly accurate description of the radiated power. The aperture susceptance is determined from the near-field analysis.

Radiation from an open end of a microstrip line has been determined by many investigators [63–67]. The approaches include current flowing on the conducting surface, and the aperture method. The two formulations are found to be equivalent [68] provided no approximations are made. We discuss the aperture field approach. The details of electric current formulation can be found in [63] and Chapter 3.

2.7.1 Aperture Conductance, G_s

Consider a radiating aperture or slot in the plane of the patch as shown in Figure 2.18. The aperture conductance of this slot has been calculated by a number of authors using different approximations [4, Chapter 10]. The simplest approach is to assume that the field distribution in a finite length slot of width h is similar to that in an infinitely long uniformly excited slot of width h in a ground plane. The admittance per unit length of the slot y_s is then calculated. The admittance for a slot of length W is then given by

$$Y_s = W y_s \tag{2.60}$$

To determine y_s, the slot is analyzed as a one-dimensional problem with a uniform aperture field distribution

$$\vec{E}_a = \begin{cases} \hat{y}E_0 & \text{for } |y| \le h/2 \\ 0 & \text{elsewhere} \end{cases} \tag{2.61}$$

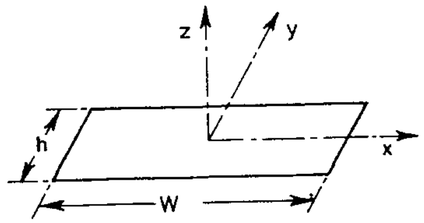

Figure 2.18 An equivalent slot radiator in an infinite, perfectly conducting plane.

The Fourier transform of the aperture field with respect to y is taken to describe the fields in the aperture in terms of plane waves. One obtains

$$\tilde{E}_y(k_y) = E_0 \int_{-h/2}^{h/2} e^{jk_y y} dy = E_0 h \frac{\sin(k_y h/2)}{k_y h/2} \tag{2.62}$$

The complex power radiated per unit slot length $(p + jq)$ is given by [61, Chapter 4]

$$p = \frac{k_o}{4\pi\eta_0} \int_{-k_0}^{+k_0} |\tilde{E}_y|^2 \frac{dk_y}{\sqrt{k_0^2 - k_y^2}} \tag{2.63a}$$

$$q = -\frac{k_0}{4\pi\eta_0} \left(\int_{-\infty}^{-k_0} + \int_{+k_0}^{+\infty} |\tilde{E}_y|^2 \frac{dk_y}{\sqrt{k_y^2 - k_0^2}} \right) \tag{2.63b}$$

where $k_0 = 2\pi/\lambda_0$ and $\eta_0 = 120\pi$. The equivalent aperture admittance corresponding to the radiated power is defined as

$$p + jq = \frac{1}{2} y_s^* |E_0 h|^2 = \frac{1}{2}(g_s - jb_s)|E_0 h|^2 \tag{2.64}$$

Comparison of (2.63) and (2.64) gives

$$g_s = \frac{k_0}{\pi\eta_0} \int_0^{+k_0} \frac{\sin^2(k_y h/2)}{(k_y h/2)^2} \frac{dk_y}{\sqrt{k_0^2 - k_y^2}} \tag{2.65a}$$

$$b_s = \frac{k_0}{\pi\eta_0} \int_{k_0}^{\infty} \frac{\sin^2(k_y h/2)}{(k_y h/2)^2} \frac{dk_y}{\sqrt{k_y^2 - k_0^2}} \tag{2.65b}$$

The integrals in (2.65) can be approximated to yield the following closed-form expressions [4, Chapter 10]:

$$g_s \approx \frac{k_0}{2\eta_0}\left(1 - \frac{s^2}{24}\right) \tag{2.66}$$

$$b_s \approx -\frac{k_0}{\pi\eta_0}\left\{\left(\ln\frac{s}{2} + \gamma - \frac{3}{2}\right)\left(1 - \frac{s^2}{24}\right) + \frac{s^2}{288}\right\} \tag{2.67}$$

where $s = k_0 h$ is the normalized slot width, and $\gamma = 0.577216$. The maximum truncation error in (2.66) and (2.67) is less than 0.1% for $s \leq 1$.

Equation (2.67) gives very approximate values for the aperture susceptance because it is found to be a sensitive function of the field distribution in the aperture, which is governed by the charge density distribution at the metal edge. Therefore, a static analysis of the open-end behavior of the microstrip edge yields more accurate values for the susceptance. We will use closed-form expressions based on the static analysis as well as full-wave analysis.

The next best approximation for the calculation of the aperture admittance is to analyze radiation from a finite length slot of width h in a ground plane as shown in Figure 2.18. Again the electric field distribution is assumed to be uniform along the length and width of the slot, that is,

$$\vec{E}_a = \begin{cases} \hat{y}E_0 & \text{for } |y| \leq h/2,\ |x| \leq W/2 \\ 0 & \text{elsewhere} \end{cases} \tag{2.68}$$

The analysis problem is now a two-dimensional one. Therefore, double Fourier transform of the aperture field is taken to give

$$\begin{aligned} \tilde{E}_y &= E_0 \int_{-h/2}^{h/2} \int_{-W/2}^{W/2} e^{jk_x x} dx dy \\ &= E_0 Wh \frac{\sin(k_x W/2)}{k_x W/2} \frac{\sin(k_y h/2)}{k_y h/2} \end{aligned} \tag{2.69}$$

The complex power radiated by the slot in Figure 2.18 is found by integrating the complex Poynting vector over the aperture area. One obtains

$$P + jQ = \frac{1}{2} \iint_{\text{aperture}} (\vec{E}_a \times \vec{H}_a^*) \cdot \hat{z}\, dx dy \tag{2.70}$$

where $\vec{H}_a$ is the aperture magnetic field. Expressed in terms of the Fourier transformed aperture field, (2.70) becomes [4, Chapter 10]

$$P + jQ = \frac{1}{8\pi^2 \eta_0 k_0} \int_{-\infty}^{+\infty} \int_{-\infty}^{+\infty} \left(k_z^2 |\tilde{E}_y|^2 + |k_y \tilde{E}_y|^2 \right) \frac{dk_x dk_y}{k_z^*} \tag{2.71}$$

where

$$k_z = \begin{cases} +\sqrt{k_0^2 - k_x^2 - k_y^2} & \text{for } k_0^2 \geq k_x^2 + k_y^2 \\ -j\sqrt{k_x^2 + k_y^2 - k_0^2} & \text{for } k_0^2 < k_x^2 + k_y^2 \end{cases} \tag{2.72}$$

The radiated power can also be written in terms of network parameters as

$$P + jQ = \frac{1}{2}(G_s - jB_s)|E_0 h|^2 \tag{2.73}$$

Comparison of (2.71) and (2.73) yields the following equation:

$$G_s = \frac{1}{\pi^2 \eta_0 k_0 |E_0 h|^2} \int_0^{k_0} \left\{ \int_0^{\sqrt{k_0^2 - k_x^2}} |\tilde{E}_y|^2 (k_0^2 - k_x^2) \frac{dk_y}{\sqrt{k_0^2 - k_x^2 - k_y^2}} \right\} dk_x \tag{2.74}$$

Use of (2.69) for $\tilde{E}_y$ in (2.74) gives

$$G_s = \frac{4}{\pi^2 \eta_0 k_0} \int_0^{k_0} \frac{k_0^2 - k_x^2}{k_x^2} \sin^2(k_x W/2) \times \left\{ \int_0^{\sqrt{k_0^2 - k_x^2}} \frac{\sin^2(k_y h/2)}{(k_y h/2)^2} \frac{dk_y}{\sqrt{k_0^2 - k_x^2 - k_y^2}} \right\} dk_x \tag{2.75}$$

The inner integral of (2.75) can be expressed as a double integral of $J_0(\cdot)$. Expanding the Bessel function in a Maclaurin's series, carrying out the integration term by term, and retaining only the first two terms of the series gives [4, Chapter 10]

$$G_s \approx \frac{1}{\pi \eta_0} \left\{ \left(wSi(w) + \frac{\sin w}{w} + \cos w - 2 \right) \left(1 - \frac{s^2}{24} \right) + \frac{s^2}{12} \left(\frac{1}{3} + \frac{\cos w}{w^2} - \frac{\sin w}{w^3} \right) \right\} \tag{2.76}$$

where $w = k_0 W$, $s = k_0 h$, and

$$Si(x) = \int_0^x \frac{\sin u}{u} du$$

In a simpler approach for radiation conductance, the radiation fields due to a slot of length W are calculated. Integration of the radiation fields yields the power radiated. Use of (2.73) then gives the value of the radiation conductance. Approximations in the integration yield the following expression [63]:

$$G_s = \begin{cases} W^2/(90\lambda_0^2) & \text{for } W \leq 0.35\lambda_0 \\ W/(120\lambda_0) - 1/(60\pi^2) & \text{for } 0.35\lambda_0 \leq W \leq 2\lambda_0 \\ W/(120\lambda_0) & \text{for } 2\lambda_0 < W \end{cases} \tag{2.77}$$

Another approach is based on the Wiener-Hopf technique [69, 70]. It is applicable to an infinitely long microstrip edge, but the effect of substrate dielectric constant is included in the analysis. A closed-form expression due to Gogoi and Gupta [69] is given:

$$G_s = W \frac{7.75 + 2.2k_0 h + 4.8(k_0 h)^2}{1000\lambda_0} \left\{ 1 + \frac{(\epsilon_r - 2.45)(k_0 h)^3}{1.3} \right\} \tag{2.78}$$

The accuracy of (2.78) is 1.1% for $0.05 \leq k_0 h \leq 0.6$ and $2.45 < \epsilon_r < 2.65$. Bhattacharyya and Garg [71] have analyzed radiation from a rectangular slot on a grounded dielectric substrate. The analysis, as before, is carried out in the spectral domain. However, a closed-form expression is not available. The effect of substrate on the radiation conductance is plotted in Figure 2.19 [15]. The length of the slot is 10.6 cm and the width is taken to be equal to the substrate thickness. It is observed from here that the radiation conductance decreases with an increase in the dielectric constant of the substrate.

The values of G_s obtained from (2.76), (2.77), and (2.78) have been compared in [4, Chapter 9]. It is found that (2.76) and (2.77) compare very

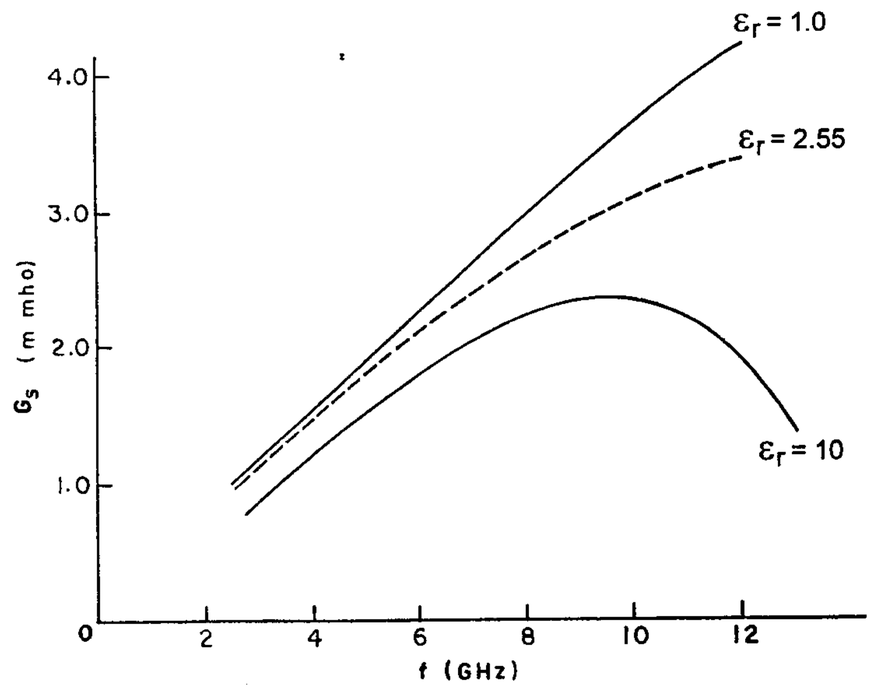

Figure 2.19 Radiation conductance G_s for a slot on a grounded substrate, $W = 10.6$ cm, $h = 0.159$ cm. (From [15]. © 1985 Indian Institute of Technology. Reprinted with permission.)

well for $W/\lambda_0 \leq 2$, whereas (2.77) and (2.78) agree for $W/\lambda_0 \geq 2$. Therefore, it is recommended that (2.77) be used for G_s for thin substrates with $h/\lambda_0 \leq 0.02$.

There is a need for improvement in the expression for G_s. This should include the effect of ϵ_r and should be valid for thicker substrates also.

2.7.2 Edge Susceptance, B_s

Full-wave analysis of the assumed aperture field does not give accurate results for the aperture susceptance. For this we invoke the idea of open-end effect to model the susceptance of a radiating edge. Both quasi-static as well as full-wave analyses have been reported.

One of the formulas for B_s is based on the concept of the edge effect in a microstrip line [72]. The rectangular patch of dimensions $L \times W$ has four edges at $x = 0$, L and $y = 0$, W. To determine the end capacitances at the $y = 0$ and $y = W$ planes, the patch is modeled as a microstrip line of width L and length W_e. The capacitance of this line can be calculated from the characteristic impedance and effective dielectric constant values for the microstrip line. It is given by

$$C = \frac{\sqrt{\epsilon_{re}(L, h, \epsilon_r)}}{cZ_0(L, h, \epsilon_r)} W_e \tag{2.79}$$

Here, W_e is the effective width of the microstrip line [see (B.13) in Appendix B]. If we now subtract the parallel plate capacitance from (2.79), we obtain the edge capacitances for the above microstrip line at the edges $y = 0$ and $y = W$. This edge capacitance for the microstrip line is the end capacitance for the patch. Thus,

$$\Delta C = \frac{1}{2}\left\{\frac{\sqrt{\epsilon_{re}(L, h, \epsilon_r)}}{cZ_0(L, h, \epsilon_r)} - \frac{\epsilon_0 \epsilon_r L}{h}\right\} W_e \tag{2.80}$$

and

$$B_s = \omega \Delta C = \pi f \left\{\frac{\sqrt{\epsilon_{re}(L, h, \epsilon_r)}}{cZ_0(L, h, \epsilon_r)} - \frac{\epsilon_0 \epsilon_r L}{h}\right\} W_e \tag{2.81}$$

The value of W_e as a function of W, h, and ϵ_r for a microstrip line can be obtained as demonstrated in Appendix B.

Wide patch approximation, based on the Wiener-Hopf approach, yields the following expression for the end susceptance [68]:

$$B_s = Y_0 \tan(\beta \Delta \ell) \tag{2.82a}$$
$$= 0.01668 \frac{\Delta \ell}{h} \frac{W_e}{\lambda_0} \epsilon_{re}$$

where

$$\frac{\Delta \ell}{h} = \frac{0.95}{1 + 0.85 k_0 h} - \frac{0.075(\epsilon_r - 2.45)}{1 + 10 k_0 h} \tag{2.82b}$$

The accuracy of (2.82b) is 2% for $0.1 < k_0 h < 0.6$ and $2.45 < \epsilon_r < 2.65$. Comparison of values obtained from (2.81) with (2.82) shows that the value of the edge susceptance is very similar in the two cases for $0.25\lambda_0 < W < 0.6\lambda_0$. However, (2.81) may be preferred because there is no restriction on the value of the patch width for this formula. More rigorous characterization of the open-edge susceptance has been reported in [73–77]. The closed-form expression reported in [76] for the open-end extension of the radiating edge is given as follows:

$$\frac{\Delta \ell}{h} = \frac{\zeta_1 \zeta_3 \zeta_5}{\zeta_4} \tag{2.83}$$

where ζ_1, ζ_3, ζ_4, ζ_5, and so on are defined in Appendix B. Equation (2.83) is very accurate and is normally used for the open-end extension and the open-end susceptance.

2.8 Mutual Admittance, Y_m

It is known from the analysis of microstrip patch antennas that mutual coupling between the edges plays an important role in the accurate determination of input impedance. This information is also needed in determining the mutual coupling between the patches for antenna array design. The mutual admittance between the radiating edges is included explicitly in the equivalent circuits for the transmission line model and the multiport network model. In the cavity model, the mutual conductance effect is included implicitly in the calculation of the effective loss tangent through the power radiated. Closed-form expressions for the mutual admittance between the apertures are very few. The expressions available in [4, Chapter 9] are given next.

2.8.1 Mutual Conductance, G_m

The mutual conductance G_m between finite length slots has been derived from a knowledge of the mutual conductance between infinite slots. Therefore, mutual conductance is defined as [4, Chapter 9]

$$G_m = G_s F_g \tag{2.84}$$

Here, G_s is the self-conductance of a finite length slot. The factor F_g accounts for mutual coupling between the slots. Its value is assigned to be the same as would exist in infinitely long slots, and is therefore defined as

$$F_g = g_m / g_s \tag{2.85}$$

where g_s and g_m are the per unit length self-conductance and mutual conductance, respectively, of two infinitely long TE excited slots in a perfectly conducting plane. The slots are shown in Figure 2.20. The expression for g_s was derived in Section 2.7.1 and is given by (2.66). The expression for g_m can also be derived in an analogous manner. For this, the mutual power between the coupled slots is determined by taking the Fourier transform of the slot fields,

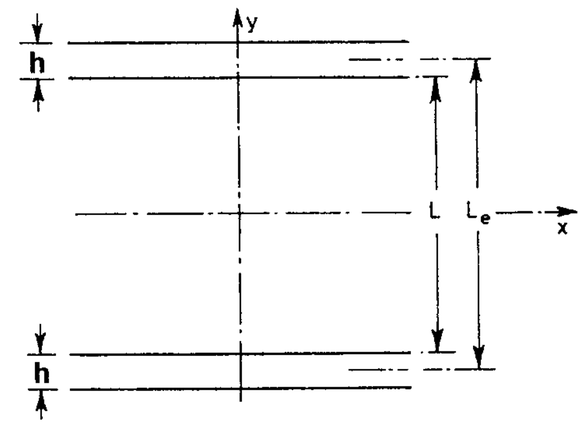

Figure 2.20 Geometry to determine mutual coupling between two infinitely long slots.

similar to (2.63a). By virtue of the separation L_e between the slots, the expression for g_m gets modified to

$$g_m = \frac{k_0}{\pi \eta_0} \int_0^{+k_0} \frac{\sin^2(k_y h/2)}{(k_y h/2)^2} \cos(k_y L_e) \frac{dk_y}{\sqrt{k_0^2 - k_y^2}} \tag{2.86}$$

where L_e is the center distance between the two slots. The integral in (2.86) is approximated to yield

$$g_m \approx \frac{k_0}{2\eta_0} \left\{ \left(1 - \frac{s^2}{24}\right) J_0(\ell) + \frac{s^2}{24} J_2(\ell) \right\} \tag{2.87}$$

where $s = k_0 h$ and $\ell = k_0 L_e$. Using (2.66) for g_s and (2.87) for g_m in (2.85), one obtains

$$F_g \approx J_0(\ell) + \frac{s^2}{24 - s^2} J_2(\ell) \tag{2.88}$$

Mutual conductance obtained from (2.84) has been compared with the mutual conductance of the four-slot arrangement, as shown in Figure 2.4(b). The agreement is found to be reasonable justifying the above model for mutual conductance.

2.8.2 Mutual Susceptance, B_m

The modeling for B_m is similar to that for G_m, except for another correction factor, that is,

$$B_m = B_s F_b K_b \tag{2.89}$$

The factor F_b is defined as

$$F_b = \frac{b_m}{b_s} = \frac{\pi}{2} \frac{Y_0(\ell) + \dfrac{s^2}{24 - s^2} Y_2(\ell)}{\ln\left(\dfrac{s}{2}\right) + \gamma - 1.5 + \dfrac{s^2/12}{24 - s^2}}, \quad s = k_0 h \quad \ell = k_0 L_e \tag{2.90}$$

where $\gamma = 0.577216$. The correction factor K_b is given by

$$K_b = 1 - \exp(-0.21 k_0 W) \tag{2.91}$$

where W is the slot width.

The expressions for mutual conductance and mutual susceptance, (2.84) and (2.89), respectively, are applicable to any pair of radiating slots belonging to the same patch or different patches.

The calculation of a mutual coupling network for use in MNM is carried out numerically. In this case, the aperture fields at the edges are first converted into equivalent magnetic currents as

$$\vec{M} = -\hat{n} \times \vec{E}_0 h$$

Now each line source of magnetic current is divided into a number of small sections, of length $d\ell$. The number of sections is equal to the number of ports. The magnetic field produced by each section of line source 1 at any section of line source 1 or 2 can be written by using the fields of a magnetic current dipole in free space. This magnetic field yields the induced current density

$$\vec{J}_j = \hat{n} \times \vec{H}_j \tag{2.92}$$

Finally, the mutual admittance between sections i and j is given by [4, Chapter 9]

$$Y_{ji} = J_j d\ell_j / M_i \tag{2.93}$$

Note that in all the expressions given above for self- and mutual admittances, the effective slot length W_e *should be used in place of physical length* W. The relationship between W_e and W for a microstrip line is given in (B.13) of Appendix B.

2.9 Model for Coaxial Probe in Microstrip Antennas

Coaxial probe feed of microstrip antennas is a convenient and useful excitation mechanism. In the full-wave techniques of antenna analysis, the excitation is treated as an integral part of the antenna and the input impedance is calculated. The probe reactance can be extracted from these data as described later in Figure 2.23. The analytical models, on the other hand, employ an ideal feed. The feed is modeled separately and its reactance calculated and added to the input impedance of the patch antenna. In the cavity model analysis of patch antennas in Section 2.3, however, the entire coaxial feeding structure is modeled as a thin strip of finite width of uniformly distributed electric current flowing vertically from the ground plane to the patch. The probe reactance in the model appears as an inductance associated with the nonresonant modes of the cavity. For a rectangular patch antenna, the probe reactance obtained from (4.19) is

$$X_p = \omega \mu_0 h \sum_{m} \sum_{n=0}^{\infty} \frac{\psi_{mn}^2(x_0, y_0)}{k_{mn}^2 - k^2} G_{mn} \tag{2.94}$$

where $m = 1$, $n = 0$ mode is excluded, and

$$G_{mn} = \text{sinc}(m\pi D_x/(2L)) \,\text{sinc}(n\pi D_y/(2W))$$

$$\psi_{mn}(x, y) = \sqrt{\frac{\epsilon_m \epsilon_n}{LW}} \cos(k_m x) \cos(k_n y)$$

Here $\epsilon_p = 1$ for $p = 0$ and $\epsilon_p = 0$ for p not equal to zero.

In this model the probe is modeled as a strip of dimensions $D_x \times D_y$ carrying a uniform current. Equation (2.94) includes the effect of feed position (x_0, y_0) substrate parameters, patch size and shape, and the probe dimensions. This model is shown to predict feed inductance that track the measured result reasonably well at all feed locations not too close to the edge of the patch. For

feed locations on or near the edge, the model is found to predict inductances that are too high due to the image produced by the magnetic wall [78].

A number of models have been advanced to model the probe reactance. In these models, a canonical problem of a probe inside a parallel plate waveguide is solved. By image theory, it is easily seen that the constant cylindrical current between two infinite parallel plates is equivalent to an infinite cylinder with a constant current density. The impedance per unit length of the infinite cylinder can be obtained in a straightforward manner [79]. This leads to the following expression for the probe impedance in the presence of two infinite plates [61]:

$$Z_p = \frac{\omega\mu_0 h}{4} H_0^{(2)}(kp) J_0(kp) \quad \text{for } k = k_0\sqrt{\epsilon_r} \tag{2.95a}$$

Here, p is the probe radius. For small kp values ($kp < 1$), this formula reduces to [80, 81]

$$Z_p = \frac{\omega\mu_0 h}{4} + j\frac{\omega\mu_0 h}{2\pi}\left[\ln\left(\frac{2}{kp}\right) - \gamma\right] \tag{2.95b}$$

where $\gamma = 0.57721$ is the Euler constant. When the substrate thickness increases, the current distribution is no longer constant. An integral equation approach leads to the following expression [82, 83]:

$$Z_p = \frac{60\pi}{\sqrt{\epsilon_r}} \frac{\tan^2(kh/2)}{kh/2} + j\frac{120}{\sqrt{\epsilon_r}} \tan(kh/2) \ln\left(\frac{1.125}{kp}\right) \tag{2.95c}$$

An actual coaxial feed produces a radial electric field in the coaxial aperture. The equivalent current in this excitation model is a ring of magnetic current on the ground plane acting in the presence of the probe [78]. The magnetic current induces current on the probe. In a more rigorous approach an incident TEM wave in the coaxial aperture is assumed [80]. This approach is described next.

Consider the geometry of a coaxial line with a truncated outer conductor flush mounted to the lower conducting plate of a parallel plate waveguide as shown in Figure 2.21(a). The inner conductor passes through the parallel plate region and is attached to the upper conducting plane. The magnetic current model of the aperture is used here. The radial transmission line mode and all higher order modes in the parallel plate region are determined from the excitation. The probe admittance is obtained by enforcing the continuity of complex

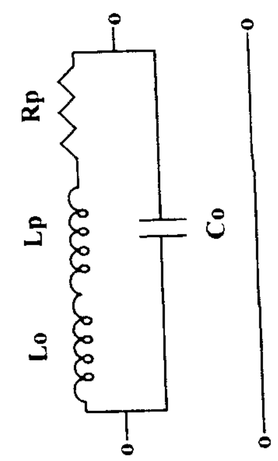

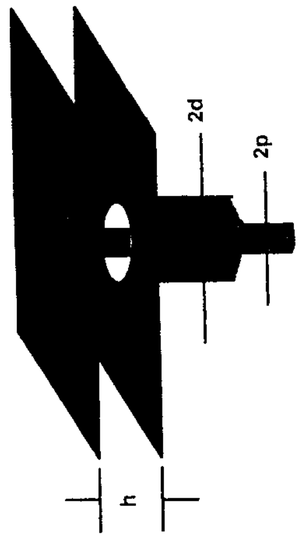

Figure 2.21 (a) Configuration of the junction between coaxial probe and parallel plates. (From [80]. © 1991 IEEE. Reprinted with permission.)
(b) Equivalent circuit for the probe impedance in part (a).

power flow at the coaxial aperture. Under the assumption of $(kh)^2 << \pi$ and $(kd)^4 << 1$, the probe admittance can be expressed as [80]

$$Y_{\text{probe}} = [R_p + j\omega(L_p + L_0)]^{-1} + j\omega C_0 \tag{2.96}$$

where

$$R_p = \omega\mu_0 h/4 \tag{2.97}$$

$$L_p = \frac{\mu_0 h}{2\pi}\left[\ln\left(\frac{2}{kp}\right) - \gamma\right] \tag{2.98}$$

$$C_0 = \frac{\epsilon_0\epsilon_r}{6hg^2}\left\{3\pi[d^2 - p^2 - 2d^2 g] + 4\pi h^2 g - \frac{12h^3}{\pi^2 d}\left(1.202 - \sum_{n=1}^{\infty} n^{-3}\exp[-2n\pi(d-p)/h]\right)\right\} \tag{2.99}$$

$$L_0 = \frac{-\mu_0 h k^2}{4\pi g}[g(d^2 + p^2) - d^2 + p^2]\left[\ln\left(\frac{kp}{2}\right) + \gamma\right] \tag{2.100}$$

$$g = \ln(d/p)$$

where d is the radius of the relief hole as shown in Figure 2.21(a). The equivalent circuit for the probe, based on the probe admittance (2.96), is shown in Figure 2.21(b). It has been suggested that this equivalent circuit can be used even when the infinite parallel plate is replaced by a finite sized patch and *the probe is not located very close to the edge of the patch*. According to (2.96), the probe impedance is not a function of probe position. Experience, however, indicates that probe reactance varies with feed location. The measured feed reactance is compared with the computed value in Figure 2.22 [78]. For unloaded patch antennas, this variation may not be a very significant design consideration because the resonant reactance often strongly dominates the feed reactance near the resonant frequency. In such cases, the feed reactance from (2.96) can be used. However, in a patch loaded with slots, shorts, or varactor diodes, the resonant frequency is different from the unloaded patch and the resonant reactance [78] may no longer dominate the feed reactance. Equation (2.96), therefore, should not be used for a loaded patch. One can use numerical techniques to calculate the antenna performance or measure the feed reactance in such a situation. A typical plot of input impedance versus frequency is

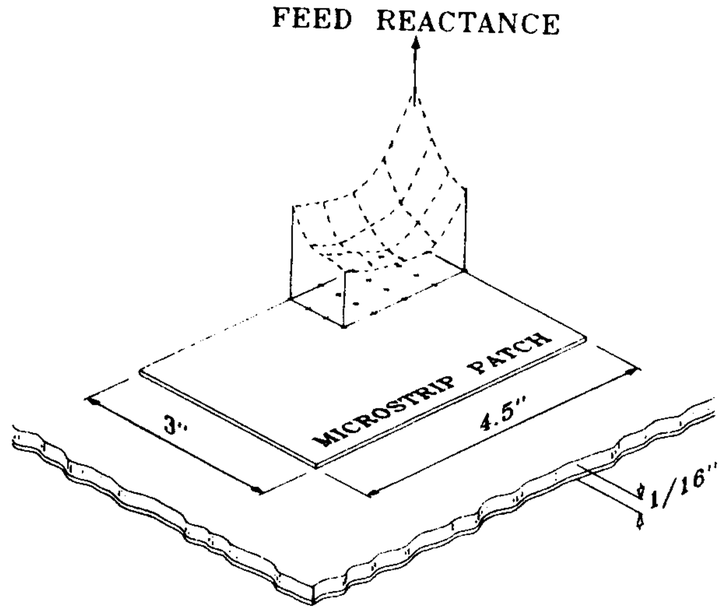

Figure 2.22 Measured feed reactance at 1400 MHz for a rectangular patch. (From [78]. © 1983 *Electromagnetics*. Reprinted with permission.)

shown in Figure 2.23 for a rectangular patch. From the $X_{\min}$ and $X_{\max}$ values, the probe reactance or feed reactance is given by

$$X_p = \frac{1}{2}(X_{\min} + X_{\max}) \tag{2.101}$$

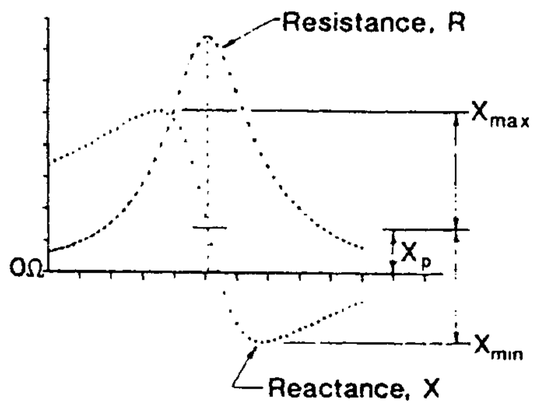

Figure 2.23 Figure illustrating the extraction of feed reactance from a typical impedance curve for a resonant microstrip antenna.

2.10 Comparison of Analytical Models

The various models discussed so far can be grouped into two categories: transmission line models and cavity models. The transmission line model (Section 2.2.1) is easy to implement and the effect of mutual coupling between radiating edges is included explicitly through loads. The effect of surface wave power loss can be included through additional load conductance. The major drawback of this model is that the fields along the width of the patch and the substrate thickness are assumed to be uniform. Therefore, this model is restricted to the rectangular patch geometry, thin substrate, single-layer, linearly polarized antennas, and to probe feed and microstrip edge feed. Array antennas of rectangular patches can be analyzed. However, GTLM (Section 2.2.3) is generalized to include variation of fields in the transverse direction also. Therefore, it can be used to analyze almost all of the useful practical microstrip antennas, circularly polarized antennas, and array antennas. However, its application is limited to thin substrate, nonstacked antennas and to probe feed and microstrip edge feed. The lossy transmission line model (Section 2.2.4) is generalized to analyze arbitrarily shaped patches, stacked geometry, and proximity coupling. The mutual coupling in this model is included implicitly. Therefore, it is not accurate for array antennas.

The cavity models of Sections 2.3 and 2.4 are basically lossy cavity models. The mutual coupling between the radiating edges is included implicitly in the form of radiated power, which accounts for the effect of mutual conductance only. The mutual susceptance is not accounted for. Surface wave power loss can also be included as a general loss term. The cavity model has been generalized to include the variation of fields along the substrate thickness, aperture coupling to microstrip line, and stacked patch configuration. Mutual coupling between rectangular patches has been determined from the magnetic current model as in the case of the transmission line model. However, application of this approach to arrays is limited because in this model, fields from various apertures are assumed to be in phase. The radiation and mutual coupling effects are incorporated explicitly through the lumped loads in the multiport network model (MNM). Variation of the fields along the width of the patch is also included as in the cavity model. Its main limitation is that the variation of fields along the substrate thickness is not included. It has not been applied to a multilayered geometry or aperture coupling. Based on this discussion, a comparison of the various analytical models appears in Table 2.1.

A major drawback of the analytical models is the limited accuracy in resonant frequency and input impedance for the substrates that are not thin. Also, they have a limited capacity to handle problems such as mutual coupling, large arrays, surface wave effects, and different substrate configurations [1].

Table 2.1
Comparison of Various Analytical Models

Application	Transmission Line Model	GTLM	Lossy Transmission Line Model	Cavity Model	Generalized Cavity Model	MNM
Patch shapes analyzed	Rectangular only	Separable geometries	Arbitrary shapes	Regular shapes	Separable geometries	Separable geometries
Substrate thickness	Thin	Thin	Thin	Thick	Thin	Thin
Feed types used	Microstrip edge feed, probe feed	Microstrip edge feed, probe feed	Possibly all types	Microstrip edge feed, probe feed, aperture coupling	Microstrip edge feed, probe feed	Microstrip edge feed, probe feed, proximity coupling
Circularly polarized antenna	No	Yes	No	Yes	Yes	Yes
Stacked antennas	No	No	Yes	Yes	No	No
Mutual coupling between edges	Explicitly included	Explicitly included	Implicitly included	Implicitly included	Implicitly included	Explicitly included
Application to arrays	Yes	Yes	No	No	No	Yes

Full-wave numerical techniques can provide analysis of the microstrip antenna in which all effects, such as space wave radiation, surface wave loss and coupling, mutual coupling between the edges, fringing fields, and so on, do not have to be modeled. These features are all integrated in the analysis technique through an accurate Green's function. These techniques are very accurate and powerful, and are discussed in the next chapter. The FDTD technique is also discussed there, and can be used to include the effect of finite substrate size and ground plane.

Appendix 2A: Theoretical Background of the Generalized Transmission Line Model

The generalized transmission line model (GTLM) [5, 14], in principle, can be applied to any microstrip antenna that has a separable geometry. A large number of practically used patches comes under this category. The theoretical background of this model is presented in this appendix.

2A.1 Introduction

Two different types of possible microstrip patch configurations with separable geometries are shown in Figure 2.24. The patch in Figure 2.24(a) has two radiating edges defined by $u = u_1$ and $u = u_2$ in the curvilinear coordinate (u-v) system. On the other hand, the patch in Figure 2.24(b) has four edges defined by $u = u_1$, $u = u_2$, $v = v_1$, and $v = v_2$. The circular ring is an example of the first kind [see Figure 2.24(a)] and a rectangular patch is an example of the second kind [see Figure 2.24(b)]. The circular patch has only one radiating edge and comes under the first kind when the inner radiating contour ($u = u_1$) has a vanishingly small area (converges to a point).

To develop the model, we start with the field configuration under the patch metalization. The longitudinal component (z component) of the electric field underneath the patch is a solution of the following wave equation (a time dependence $e^{j\omega t}$ is assumed):

$$\nabla^2 E_z + k^2 E_z = 0 \tag{2A.1}$$

where ∇^2 is the Laplacian operator and k is the wave number in the substrate on which the patch is etched. In a practical microstrip antenna, the substrate thickness h is very small compared to the wavelength in the dielectric medium (typically $h\sqrt{\epsilon_r}/\lambda_0 < 0.04$). The electric field E_z, therefore, can be regarded

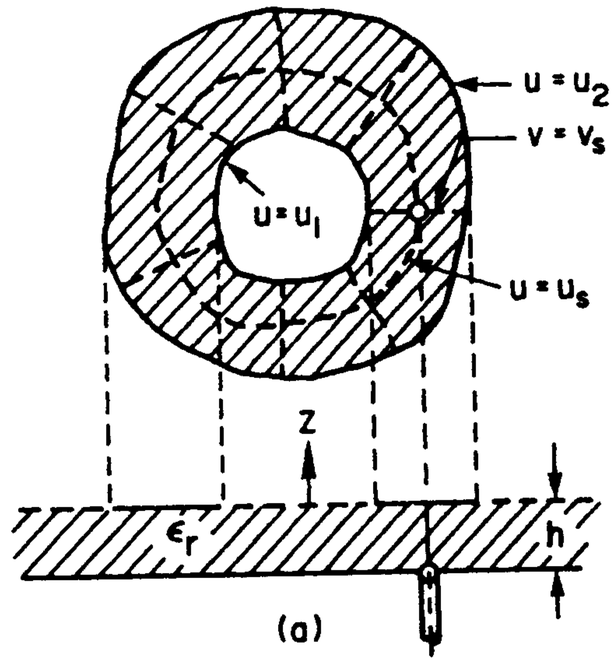

Figure 2.24 Two possible microstrip patch configurations with separable geometry. (From [5]. © 1985 IEE. Reprinted with permission.) (a) Geometry with two edges and (b) geometry with four edges.

as constant along z. Equation (2A.1) can then be written in the curvilinear coordinate system as [77]

$$\frac{1}{h_1 h_2}\left[\frac{\partial}{\partial u}\left(\frac{h_2}{h_1}\frac{\partial E_z}{\partial u}\right) + \frac{\partial}{\partial v}\left(\frac{h_1}{h_2}\frac{\partial E_z}{\partial v}\right)\right] + k^2 E_z = 0 \tag{2A.2}$$

where h_1 and h_2 are scale factors along the u and v directions, respectively, and are defined as

$$h_1 = \left|\frac{\partial \vec{r}}{\partial u}\right|, \quad h_2 = \left|\frac{\partial \vec{r}}{\partial v}\right|$$

where $\vec{r}$ is the position vector. It is assumed in this model that the patch configurations under consideration are separable, that is, the solution for E_z in (2A.2) can be expressed as

$$E_z(u, v) = f_1(u) f_2(v) \tag{2A.3}$$

Substituting (2A.3) in (2A.2) and dividing the resulting equation by $f_1(u) f_2(v)$, one obtains

$$\frac{1}{h_1 h_2}\left[\frac{1}{f_1}\frac{\partial}{\partial u}\left(\frac{h_2}{h_1}\frac{\partial f_1}{\partial u}\right) + \frac{1}{f_2}\frac{\partial}{\partial v}\left(\frac{h_1}{h_2}\frac{\partial f_2}{\partial v}\right)\right] + k^2 = 0 \tag{2A.4}$$

Let $h_2/h_1 = p(u, v)$ and $h_1 h_2 = q(u, v)$. Then (2A.4) becomes

$$\frac{p}{f_1}\frac{\partial^2 f_1}{\partial u^2} + \frac{1}{f_1}\frac{\partial p}{\partial u}\frac{\partial f_1}{\partial u} + \frac{1}{f_2 p}\frac{\partial^2 f_2}{\partial v^2} - \frac{1}{f_2}\frac{1}{p^2}\frac{\partial p}{\partial v}\frac{\partial f_2}{\partial v} + k^2 q = 0 \tag{2A.5}$$

The above bivariate equation can be separated into two single variable differential equations if either

$$p(u, v) = g(u) f(v) \text{ and } p(u, v) q(u, v) = [m_1(u) + m_2(v)] f^2(v) \tag{2A.6a}$$

or

$$p(u, v) = g(u)/f(v) \text{ and } q(u, v)/p(u, v) = [m_1(u) + m_2(v)]/g^2(u) \tag{2A.6b}$$

Apparently, (2A.6a) and (2A.6b) appear to be two distinct criteria for the separability of (2A.5). However, if one solves for either from (2A.6a) or from (2A.6b), one can see that they assume similar forms. Therefore, without loss of generality, one can consider that (2A.6a) holds. Equation (2A.5) can then be separated as

$$\frac{g^2}{f_1}\frac{\partial^2 f_1}{\partial u^2} + \frac{g}{f_1}\frac{\partial g}{\partial u}\frac{\partial f_1}{\partial u} + k^2 m_1(u) = \alpha^2 \tag{2A.7a}$$

and

$$\frac{1}{f^2}\frac{1}{f_2}\frac{\partial^2 f_2}{\partial v^2} - \frac{1}{f^3}\frac{1}{f_2}\frac{\partial f}{\partial v}\frac{\partial f_2}{\partial v} + k^2 m_2(u) = -\alpha^2 \tag{2A.7b}$$

where α is a constant, independent of u and v. Equations (2A.7a) and (2A.7b) can be rewritten as

$$\frac{\partial^2 f_1}{\partial u^2} + \frac{1}{g}\frac{\partial g}{\partial u}\frac{\partial f_1}{\partial u} + \frac{k^2 m_1 - \alpha^2}{g^2} f_1 = 0 \tag{2A.8}$$

and

$$\frac{\partial^2 f_2}{\partial v^2} - \frac{1}{f}\frac{\partial f}{\partial v}\frac{\partial f_2}{\partial v} + (k^2 m_2 + \alpha^2) f^2 f_2 = 0 \tag{2A.9}$$

Equations (2A.8) and (2A.9) are second-order nonlinear (in general) differential equations. Each of them will have two independent solutions. Let $x_1(u)$ and $x_2(u)$ be the two solutions of (2A.8). The general solution for E_z will be then

$$E_z(u, v) = \begin{Bmatrix} x_1(u) \\ x_2(u) \end{Bmatrix} f_2(v) \tag{2A.10}$$

Having determined E_z as above, the magnetic field components are obtained through the Maxwell's equation $\nabla \times \vec{E} = -j\omega\mu\vec{H}$. One obtains

$$H_u = \frac{1}{-j\omega\mu h_2}\frac{\partial E_z}{\partial v} = \frac{1}{-j\omega\mu h_2} f_1(u) f_2'(v) \tag{2A.11}$$

and

$$H_v = \frac{1}{j\omega\mu h_1}\frac{\partial E_z}{\partial u} = \frac{1}{j\omega\mu h_1} f_1'(u) f_2(v) \tag{2A.12}$$

where a prime indicates the derivative of the function with respect to the argument.

2A.2 Transmission Line Equations

We stated earlier that a patch can be modeled as a transmission line section. The transmission line voltage and the transmission line current are defined next.

In the GTLM, the transmission line is taken along the line joining two radiating apertures. The direction of the transmission line in the case of a patch with two edges, as in Figure 2.24(a), is unique (along the u direction). However, for the patch configuration shown in Figure 2.24(b), two directions may be possible for the transmission line: along the v = constant contour (joining two apertures at $u = u_1$ and $u = u_2$) and along u = constant contour (joining two apertures at $v = v_1$ and $v = v_2$). In principle, one can select any one of the above two directions. The effect of radiation from two connecting apertures will appear in the equivalent circuit through terminating loads. The effect of the other two apertures can be included by considering the transmission line to be lossy. However, to simplify the analysis, one should take the transmission line joining the two apertures that radiate a major portion of the power. From the aperture field distribution one can ascertain which of the apertures is radiating more power. The aperture on which the variation of field is slower will radiate more power.

2A.2.1 Transmission Line in u Direction

To characterize a transmission line, the transmission line voltage and the transmission line current should be defined. The definitions of these quantities should be such that they obey the transmission line equation pair (telegraphist equations). For a transmission line in the u direction, the line voltage is defined as

$$V = E_z(u, v) = f_1(u) f_2(v) \tag{2A.13}$$

and the line current is defined as

$$I = -h_2 H_v \quad \text{(along the positive } u \text{ direction)} \tag{2A.14}$$

or, using (2A.12)

$$I = \frac{-h_2}{j\omega\mu h_1} f_1'(u) f_2(v) \tag{2A.15}$$

Differentiating (2A.13) with respect to u, one gets

$$\frac{\partial V}{\partial u} = f_1'(u) f_2(v) = -j\omega\mu \frac{h_1}{h_2} I \quad \text{on using (2A.15)}$$

or, using the definition of p $(= h_2/h_1)$

$$\frac{\partial V}{\partial u} = -j\omega\mu \frac{I}{p} = \frac{-j\omega\mu}{g(u) f(v)} I \tag{2A.16}$$

Combining (2A.8) and (2A.13), we have

$$\frac{\partial^2 V}{\partial u^2} + \frac{1}{g}\frac{\partial g}{\partial u}\frac{\partial V}{\partial u} + \frac{k^2 m_1 - \alpha^2}{g^2} V = 0$$

or

$$\frac{\partial}{\partial u}\left[g \frac{\partial V}{\partial u}\right] + \frac{k^2 m_1 - \alpha^2}{g} V = 0 \tag{2A.17}$$

Substituting the expression for $\partial V/\partial u$ from (2A.16) into (2A.17) gives

$$\frac{\partial I}{\partial u} - \frac{f(v)(k^2 m_1 - \alpha^2)}{j\omega\mu g(u)} V = 0 \tag{2A.18}$$

Equations (2A.16) and (2A.18) are the transmission line equations. The transmission line parameters obtained from these equations are:

$$\text{Shunt admittance/length} = \frac{-f(v)(k^2 m_1 - \alpha^2)}{j\omega\mu g(u)} \tag{2A.19}$$

$$\text{Series impedance/length} = \frac{j\omega\mu}{g(u) f(v)} \tag{2A.20}$$

The line parameters being functions of u, the equivalent circuit of the patch is a nonuniform transmission line. Expressions for $f(v)$, $g(u)$, and $m_1(u)$ are dictated by the geometry of the separable patch. The constant α, however, depends on the *mode* of operation. The value of α is obtained from the solution of (2A.9) with appropriate boundary conditions. When the radiating contours are closed as in Figure 2.24(a), the function $f_2(v)$ must be a periodic function of v and the α values are discrete in nature. Each value of α is associated with

a mode. Therefore, a transmission line mode is designated by a single index (corresponding to the value of α). When the radiating contours are not closed [as in Figure 2.24(b)], the value of α, in general, will be complex due to leakage of power through the apertures at $v = v_1$ and $v = v_2$. The line voltage and the line current of a transmission line in the v direction are considered next.

2A.2.2 Transmission Line in *v* Direction

For the transmission line in the v direction, the line voltage is defined as

$$V = E_z(u, v) \tag{2A.21a}$$

and the line current is defined as

$$I = \frac{-h_2 H_u}{f(v)} \quad \text{(along the positive } v \text{ direction)} \tag{2A.21b}$$

Combining (2A.9), (2A.11), and (2A.21), we have

$$\frac{\partial V}{\partial v} = j\omega\mu f(v) I \tag{2A.22}$$

and

$$\frac{\partial I}{\partial v} = \frac{-f(v)}{j\omega\mu}(k^2 m_2(v) + \alpha^2) V \tag{2A.23}$$

Because the line voltage and the line current again satisfy the transmission line equations, (2A.22) and (2A.23), the line parameters of the nonuniform transmission line can be obtained from these equations.

In the preceding sections, the line voltages and the line currents for two possible transmission lines were defined. The equivalent circuit of a nonuniform transmission line section is obtained in the following section.

2A.3 Equivalent Circuit of a Nonuniform Transmission Line Section

In this section, the equivalent Π network of a transmission line section is obtained. We concentrate on the u-directed transmission line here. The equivalent Π network of a transmission line in the v direction can be obtained in a similar manner.

A transmission line section confined in the region $u_1 < u < u_2$ (nonuniform in general) and its equivalent Π network are shown in Figure 2.25. Elements of the equivalent Π network are obtained from the Y matrix of the transmission line section. The Y matrix is defined as

$$\begin{bmatrix} I_1 \\ I_2 \end{bmatrix} = \begin{bmatrix} Y_{11} & Y_{12} \\ Y_{21} & Y_{22} \end{bmatrix} \begin{bmatrix} V_1 \\ V_2 \end{bmatrix} \tag{2A.24}$$

The port currents I_1, I_2 and the port voltages V_1, V_2 are shown in Figure 2.25. The elements of the Y matrix are obtained from the following equations:

$$\begin{aligned} Y_{11} &= I_1/V_1 \quad (\text{when } V_2 = 0) \\ Y_{12} &= I_1/V_2 \quad (\text{when } V_1 = 0) \\ Y_{21} &= I_2/V_1 \quad (\text{when } V_2 = 0) \text{ and} \\ Y_{22} &= I_2/V_2 \quad (\text{when } V_1 = 0) \end{aligned}$$

Here, V is the line voltage and is given by

$$V = E_z = \{A_{x_1}(u) + B_{x_2}(u)\} f_2(v) \tag{2A.25}$$

and the line current along the u direction is given by (2A.15), that is,

$$I = \frac{-1}{j\omega\mu}\frac{h_2}{h_1}\{A_{x_1'}(u) + B_{x_2'}(u)\} f_2(v) \tag{2A.26}$$

where A and B are constants, and $x_1(u)$ and $x_2(u)$ are the independent solutions of (2A.8). Now, $V_2 = V(u = u_2) = 0$ is satisfied if

$$B/A = -x_1(u_2)/x_2(u_2)$$

The expression for Y_{11} thus becomes

$$Y_{11} = \frac{I_1}{V_1} = \frac{I(u = u_1)}{V(u = u_1)} = \frac{-h_2}{j\omega\mu h_1}\left\{\frac{x_2(u_2)x_1'(u_1) - x_1(u_2)x_2'(u_1)}{x_2(u_2)x_1(u_1) - x_1(u_2)x_2(u_1)}\right\} \tag{2A.27}$$

Similarly,

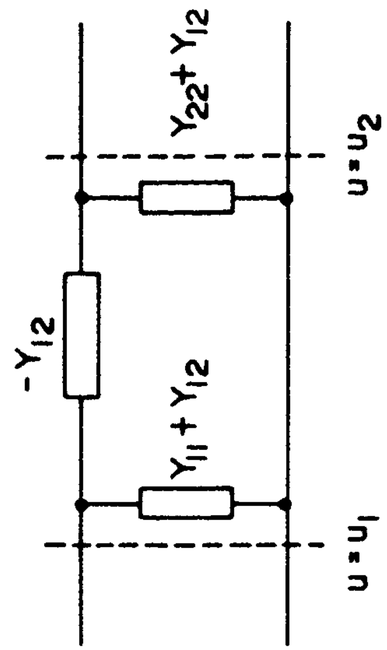

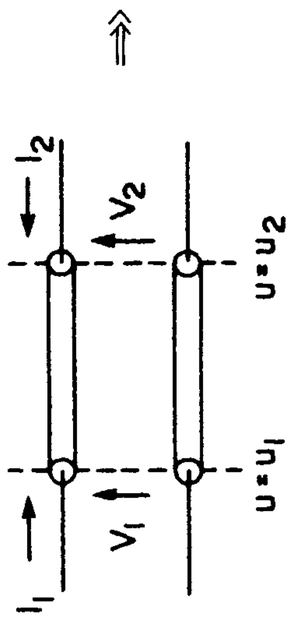

Figure 2.25 A nonuniform transmission line section and the equivalent Π network. (From [5]. © 1985 IEE. Reprinted with permission.)

$$Y_{22} = \frac{-I(u = u_2)}{V(u = u_2)} \quad \text{(when } V(u = u_1) = 0\text{)} \tag{2A.28}$$

$$= \frac{h_2}{j\omega\mu h_1}\left\{\frac{x_2(u_1)x_1'(u_2) - x_1(u_1)x_2'(u_2)}{x_2(u_1)x_1(u_2) - x_1(u_1)x_2(u_2)}\right\}$$

Note that the ratio h_2/h_1 in (2A.27) should be evaluated at $u = u_1$, whereas this ratio should be evaluated at $u = u_2$ for (2A.28). The expression for Y_{12} is given by

$$Y_{12} = \frac{1}{j\omega\mu}\frac{h_2}{h_1}\left\{\frac{x_2(u_1)x_1'(u_1) - x_1(u_1)x_2'(u_1)}{x_2(u_1)x_1(u_2) - x_1(u_1)x_2(u_2)}\right\} \tag{2A.29}$$

In a similar manner one can derive the expression for Y_{21} and can verify that

$$Y_{21} = Y_{12} \tag{2A.30}$$

The relationship just given confirms the transmission line section to be a reciprocal device, and therefore a Π-network model of the device is possible. This relationship also justifies the definition of the line voltage and line current used in (2A.13) and (2A.14), respectively. When a patch is excited by a source placed at $u = u_s$, the patch can be modeled as a combination of two transmission line sections defined by $u_1 < u < u_s$ and $u_s < u < u_2$. Each of these transmission line sections can be represented by a Π network as shown in Figure 2.25. The elements of the Y matrix for the section defined by $u_1 < u < u_s$ can be obtained by replacing u_2 by u_s in (2A.27), (2A.28), and (2A.29). Similarly, for the section defined by $u_s < u < u_2$, the matrix elements are obtained by replacing u_1 with u_s in these equations. The equivalent circuit of the patch with source is shown in Figure 2.26. This network accounts for the energy stored under the patch metalization and the dielectric loss for an imperfect dielectric substrate and the loss of power due to the leakage through the side walls at $v = v_1$ and $v = v_2$. To incorporate the effects of radiated power through the main radiating apertures, the circuit should be terminated with appropriate radiation admittances. This is considered next.

2A.4 Radiation Admittance

A radiating aperture can be characterized by an equivalent admittance, the susceptance being due to the stored energy in the fringing fields and the

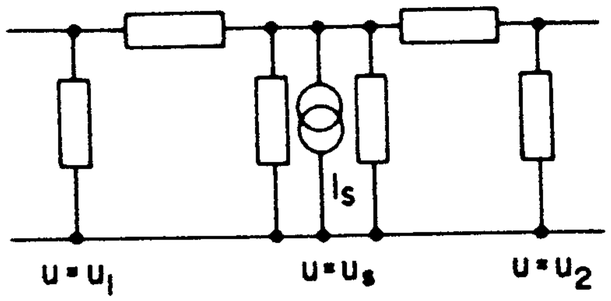

Figure 2.26 Equivalent circuit representation of the patch in terms of equivalent Π networks. (From [16]. © 1991 Elsevier Science Publishing. Reprinted with permission.)

conductance being due to the power loss from radiation. To determine the wall admittance, the magnetic current model can be used. In this model, an aperture is replaced by its equivalent magnetic current. The electromagnetic fields radiated by the equivalent magnetic current are the same as that of the aperture. Because we have two apertures, in general, there should be two equivalent magnetic current sources. The active wall admittance at $u = u_1$ is defined as

$$y_1^a = \frac{-I_t(u_1)}{V(u_1)} \tag{2A.31}$$

where $I_t(u_1)$ is the total induced line current on the aperture at $u = u_1$ due to the magnetic current sources at $u = u_1$ and $u = u_2$. According to the definition of line current in (2A.14), we have

$$I_t(u_1) = -h_2 H_{vt}(u_1)$$

where $H_{vt}(u_1)$ is the total induced magnetic field along v on the aperture at $u = u_1$. This field is the sum of the self magnetic field, $H_{vs}(u_1)$, which is generated by the source at $u = u_1$ and the coupled field, $H_{vm}(u_1, u_2)$, which is generated by the aperture source at $u = u_2$ on the aperture at $u = u_1$. Therefore,

$$H_{vt}(u_1) = H_{vs}(u_1) + H_{vm}(u_1, u_2) \tag{2A.32}$$

The active wall admittance thus becomes

$$y_1^a = \frac{h_2 H_{vs}(u_1)}{E_z(u_1)} + \frac{h_2 H_{vm}(u_1, u_2)}{E_z(u_1)} \tag{2A.33}$$

Let us define the self-admittance of the radiating wall at $u = u_1$ as

$$y_1^s = \frac{h_2 H_{vs}(u_1)}{E_z(u_1)} \tag{2A.34}$$

and the mutual admittance between the two walls as

$$y_{21}^m = \frac{-h_2 H_{vm}(u_1, u_2)}{E_z(u_2)} \tag{2A.35}$$

The negative sign in (2A.35) is taken since the equivalent magnetic currents at $u = u_1$ and $u = u_2$ are oppositely directed. One can obtain self-admittance as a special case (when u_2 approaches u_1) from this definition of mutual admittance. Using (2A.34) and (2A.35) in (2A.33), we get

$$y_1^a = y_1^s - y_{21}^m \frac{E_z(u_2)}{E_z(u_1)} = y_1^s - y_{21}^m \frac{V_2}{V_1} \tag{2A.36}$$

where V_1 and V_2 are the line voltages at ports 1 and 2, respectively. Rearranging (2A.36), we obtain

$$y_1^a = (y_1^s - y_{21}^m) + \frac{V_1 - V_2}{V_1} y_{21}^m \tag{2A.37}$$

Similarly, for the aperture at $u = u_2$ we have

$$y_2^a = (y_2^s - y_{12}^m) + \frac{V_2 - V_1}{V_2} y_{12}^m \tag{2A.38}$$

Reciprocity demands that $y_{12}^m = y_{21}^m$. Therefore, (2A.37) and (2A.38) lead to an equivalent circuit, like that shown in Figure 2.27. This circuit can be used to determine the input impedance seen by the source current I_s. It can also be used to determine the aperture voltages from which the radiation characteristics of a patch can be obtained. Note that the equivalent circuit in Figure 2.27 represents a single mode [for a given value of α in (2A.8)]. Each mode will have a circuit similar to that shown in Figure 2.27. The source current I_s is related to the feed current and the mode of operation. The input impedance seen by the feed is proportional to the impedance seen by I_s for a given mode of operation.

To determine the input impedance seen by I_s, the circuit of Figure 2.27 can be simplified using the star-delta and delta-star transformations [6]. The

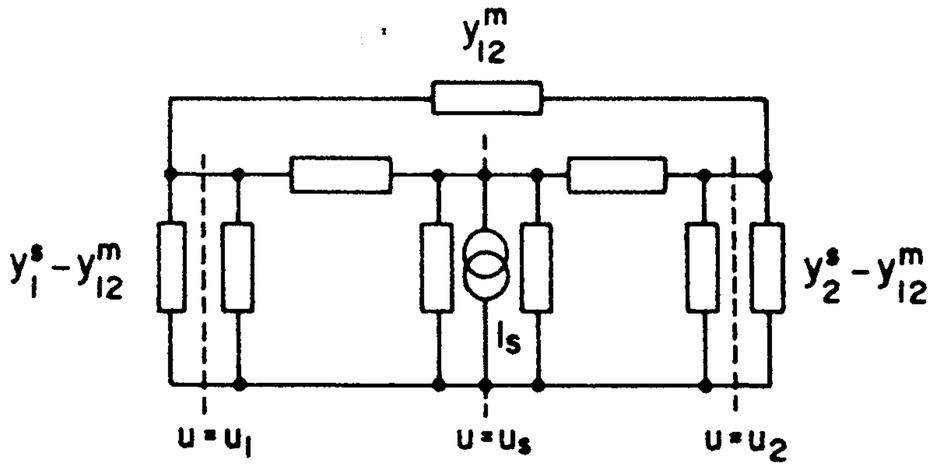

Figure 2.27 GTLM equivalent circuit of the patch antenna for a given transmission line mode. (From [5]. © 1985 IEE. Reprinted with permission.)

impedance seen by the feed current will be obtained if the relation between I_s and the feed current is known. This relationship is derived in the following section. Expressions for the input impedance will also be derived.

2A.5 Input Impedance

Suppose $\hat{z}I_0(v)$ is the feed current distribution (assumed to be a surface current lying on the fictitious surface defined by $u = u_s$). The magnetic field is discontinuous at $u = u_s$ due to the presence of feed current. For a given mode, let the magnetic fields at $u = u_s+$ and at $u = u_s-$ be

$$H_v^{(\alpha)}(u_s+) = A_\alpha^+ f_2^{(\alpha)}(v) \tag{2A.39}$$

$$H_v^{(\alpha)}(u_s-) = A_\alpha^- f_2^{(\alpha)}(v) \tag{2A.40}$$

where $f_2^{(\alpha)}(v)$ is a solution of (2A.9) for a given α. The discontinuity of the magnetic fields yields

$$\sum_\alpha [H_v^{(\alpha)}(u_s+) - H_v^{(\alpha)}(u_s-)] = I_0(v) \tag{2A.41}$$

Now, $-h_2 H_v^{(\alpha)}(u_s+)$ is the line current supplied by the source to the region $u > u_s$, and $h_2 H_v^{(\alpha)}(u_s-)$ is the line current supplied by the source to the region $u < u_s$. Therefore,

$$\begin{aligned} I_s &= -h_2 H_v^{(\alpha)}(u_s+) + h_2 H_v^{(\alpha)}(u_s-) \\ &= -h_2[A_\alpha^+ - A_\alpha^-] f_2^{(\alpha)}(v) = -h_2 B_\alpha f_2^{(\alpha)}(v) \quad \text{(say)} \end{aligned} \tag{2A.42}$$

The total current supplied for all the α values should be equal to the feed current $I_0(v)$. Therefore,

$$-\sum_\alpha B_\alpha f_2^{(\alpha)}(v) = I_0(v) \tag{2A.43}$$

It can be proved that the set of functions $f_2^{(\alpha)}(v)$ for various α form an orthogonal set and

$$\int_{v_1}^{v_2} f(v) f_2^{(\alpha)}(v) f_2^{(\alpha')}(v) dv = 0 \text{ when } \alpha \neq \alpha' \tag{2A.44}$$

Using this orthogonality property, one has from (2A.43)

$$-B_\alpha \int_{v_1}^{v_2} f(v)[f_2^{(\alpha)}(v)]^2 dv = \int_{v_1}^{v_2} f(v) f_2^{(\alpha)}(v) I_0(v) dv$$

or

$$B_\alpha = \frac{-\int_{v_1}^{v_2} f(v) f_2^{(\alpha)}(v) I_0(v) dv}{\int_{v_1}^{v_2} f(v)[f_2^{(\alpha)}(v)]^2 dv} \tag{2A.45}$$

Substituting for B_α in (2A.42), we get the relationship between the source current I_s and the feed current $I_0(v)$. In particular, when the patch is excited by a probe, the function $I_0(v)$ can be approximated as

$$I_0(v) = I_0 \delta(v - v_s)/h_2(v)$$

where (u_s, v_s) is the feed location. For this case, the expression for B_α reduces to

$$B_\alpha = \frac{-I_0 \dfrac{f(v_s)}{h_2} f_2^{(\alpha)}(v_s)}{\displaystyle\int_{v_1}^{v_2} f(v)[f_2^{(\alpha)}(v)]^2 dv}$$

and (2A.42) gives

$$I_s = \frac{f_2^{(\alpha)}(v) I_0 f(v_s) f_2^{(\alpha)}(v_s)}{\displaystyle\int_{v_1}^{v_2} f(v)[f_2^{(\alpha)}(v)]^2 dv} \tag{2A.46}$$

The input impedance seen by the feed is then given by

$$Z_{in} = \frac{-hE_z(u_s, v)}{I_0} = \frac{E_z}{I_s}\left(\frac{-hI_s}{I_0}\right) = \frac{-hI_s}{I_0} Z_s \tag{2A.47}$$

where Z_s is the impedance seen by I_s (Figure 2.27). The expression for I_s/I_0 can be substituted from (2A.46) to (2A.47) to obtain the impedance seen by the feed current I_0.

Equation (2A.47) yields the input impedance when only one transmission line mode is present. To obtain the total input impedance, individual impedances for all possible modes should be added. However, if the resonant frequencies are not very close to each other as compared to the bandwidth of the operating mode, the contribution of the off-resonant modes will be negligible near the resonance of the operating mode. On the other hand, if some other modes are very close to the operating mode, those mode impedances are to be added. A typical example of this kind is described in Section 2.4.

To determine the impedance seen by I_s in the equivalent circuit of Figure 2.27, the self- and mutual admittances should be known. General expressions for these admittances are provided in the following section.

2A.6 Self- and Mutual Wall Admittances

The magnetic current model can be used to determine the wall admittances of a patch antenna. In this model, the patch is replaced by the equivalent

magnetic current source at its periphery. The wall admittances of the patch are equivalent to the radiation admittances of the corresponding magnetic currents.

The mutual admittance between two edges at $u = u_1$ and $u = u_2$ is defined by (2A.35), that is,

$$y_{12}^m = \frac{-h_2 H_{vm}(u_1, u_2)}{E_z(u_2)} = \frac{h_2 H_{vm}(u_2, u_1)}{E_z(u_1)} \tag{2A.48}$$

where $E_z(u_1) f_2(v)$ and $E_z(u_2) f_2(v)$ are the aperture electric fields at $u = u_1$ and $u = u_2$, respectively. $H_{vm}(u_1, u_2) f_2(v)$ is the magnetic field at $u = u_1$ produced by the source at $u = u_2$. The magnetic field $H_{vm}(u_1, u_2)$ can be determined using the Green's function technique and is given by

$$\vec{H}_m(u_2, u_1) = \iint_{S_1} \vec{M}_1 \cdot \overline{\overline{G}}(r_2/r_1) dS_1 \tag{2A.49}$$

where $\vec{M}_1$ is the equivalent magnetic current on the aperture at $u = u_1$ and is equal to $E_z(u_1)(\hat{z} \times \hat{u}_1)$, $\overline{\overline{G}}$ is the dyadic Green's function that relates the magnetic current to the magnetic field, and s_1 is the surface area of the aperture at $u = u_1$. One can use the free-space Green's function in (2A.49) to determine the mutual admittance. However, to include the effect of substrate, Green's function of a stratified media should be used. For a thin substrate with low dielectric constant ($h\sqrt{\epsilon_r}/\lambda_0 < 0.02$), the effect of substrate is negligibly small and the free-space Green's function yields a good approximation to the mutual admittance.

Although mutual admittance can be calculated using (2A.48), an accurate result is provided by the stationary expression. A stationary expression for the mutual admittance is

$$y_{12}^m = \frac{\langle u_1, u_2 \rangle}{hPE_z(u_1)E_z(u_2)} \quad \text{with } P = \int_{v_1}^{v_2} [f_2(v)]^2 dv \tag{2A.50}$$

In (2A.50), h is the substrate thickness and $\langle u_1, u_2 \rangle$ is the mutual reaction between the sources at $u = u_1$ and $u = u_2$. Because $\langle u_1, u_2 \rangle = \langle u_2, u_1 \rangle$, it follows that $y_{12}^m = y_{21}^m$. If the apertures at $v = v_1$ and $v = v_2$ are considered, the stationary expression for the mutual admittance becomes

$$y_{12}^{m} = \frac{\langle v_1, v_2 \rangle}{hQE_z(v_1)E_z(v_2)} \quad \text{with } Q = \int_{u_1}^{u_2} \frac{f_1^2(u)}{g(u)}\,du \tag{2A.51}$$

where $E_z(v_1)f_1(u)$ and $E_z(v_2)f_1(u)$ are the aperture electric fields at $v = v_1$ and $v = v_2$, respectively. Equation (2A.50) should be used when the transmission line is along the u direction, and (2A.51) should be used when the transmission line is along the v direction. For the self-admittance, one should use a self-reaction in place of mutual reactions in (2A.50) and (2A.51).

Appendix 2B: Eigenfunctions, Equivalent Dimensions, and Effective Permittivities for Some Patch Shapes With Separable Geometries

The eigenfunctions required for the cavity model analysis of various geometries are given next. *We assume that the dimensions of the patch are not the physical dimensions but the equivalent dimensions, which include the effect of energy stored in the fringing fields.* The equivalent dimensions are also determined.

Rectangle

The eigenfunctions for the rectangle shown in Figure 2.28(a) are given as

$$\psi_{mn}(x, y) = \cos(k_m x)\cos(k_n y) \quad \text{for } m, n = 0, 1, 2, \ldots \tag{2B.1}$$

where

$$k_m = m\pi/L \quad \text{and} \quad k_n = n\pi/W$$

Equilateral Triangle

The eigenfunctions for the triangle shown in Figure 2.28(b) are given as

$$\begin{aligned}\psi_{m,n,\ell}(x, y) = {} & \cos\left(\frac{2\pi x'}{\sqrt{3}a}\ell\right)\sin\left(\frac{2\pi(m-n)y}{3a}\right) \\ & + \cos\left(\frac{2\pi x'}{\sqrt{3}a}m\right)\sin\left(\frac{2\pi(n-\ell)y}{3a}\right) \\ & + \cos\left(\frac{2\pi x'}{\sqrt{3}a}n\right)\sin\left(\frac{2\pi(\ell-m)y}{3a}\right)\end{aligned} \tag{2B.2}$$

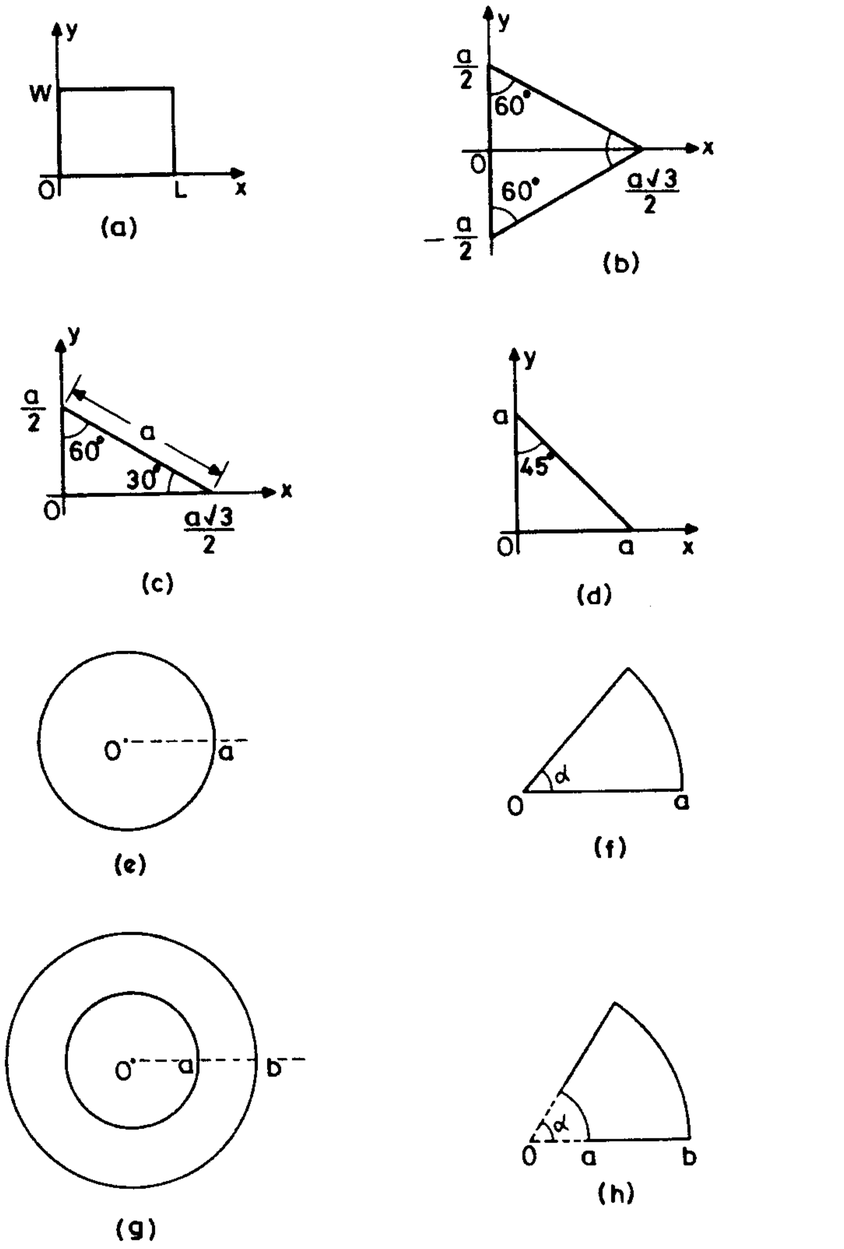

Figure 2.28 Various separable geometries for which eigenfunctions are listed: (a) rectangle, (b) equilateral triangle, (c) 30° and 60° triangles, (d) right-angle isosceles triangle, (e) disk, (f) circular sector, (g) circular ring, and (h) annular sector or circular ring segment.

where

$$x' = x + a/\sqrt{3}, \quad \ell = -(m + n)$$

Thirty- and Sixty-Degree Triangles

The triangle shown in Figure 2.28(c) can be obtained from that of Figure 2.28(b) by placing a magnetic wall at the plane of symmetry. The eigenfunctions for the triangle of Figure 2.28(c) are then obtained as

$$\begin{aligned}\psi_{m,n,\ell}(x, y) = &\cos\left(\frac{2\pi x'}{\sqrt{3}a}\ell\right)\cos\left(\frac{2\pi(m-n)y}{3a}\right) \\ &+ \cos\left(\frac{2\pi x'}{\sqrt{3}a}m\right)\cos\left(\frac{2\pi(n-\ell)y}{3a}\right) \\ &+ \cos\left(\frac{2\pi x'}{\sqrt{3}a}n\right)\cos\left(\frac{2\pi(\ell-m)y}{3a}\right)\end{aligned} \tag{2B.3}$$

where

$$x' = x + a/\sqrt{3}, \quad \ell = -(m + n)$$

Right-Angle Isosceles Triangle

The eigenfunctions for the triangle shown in Figure 2.28(d) are given as

$$\psi_{mn}(x, y) = \cos\frac{m\pi x}{a} - \cos\frac{m\pi y}{a} \tag{2B.4}$$

or

$$\psi_{mn}(x, y) = \cos\frac{m\pi x}{a} \cdot \cos\frac{m\pi y}{a}$$

Disk

The eigenfunctions for the disk shown in Figure 2.28(e) are given as

$$\psi_{mn} = J_n(k_{mn}\rho)\cos n\phi \quad n = 0, 1, 2, \ldots \quad m = 1, 2, 3, \ldots \tag{2B.5}$$

where k_{mn} are the roots of

$$J_n'(k_{mn}a) = 0$$

Circular Sector

The eigenfunctions for circular sectors are available only when the sector angle α is a submultiple of π. For the circular sector shown in Figure 2.28(f), the eigenfunctions are given as

$$\psi_{mv} = J_v(k_{mv}\rho)\cos v\phi \tag{2B.6}$$

where $v = n\pi/\alpha$, and k_{mv} satisfy

$$J_v'(k_{mv}a) = 0$$

Circular Ring

The eigenfunctions for the circular ring shown in Figure 2.28(g) are given as

$$\psi_{mn}(\rho, \phi) = [J_n(k_{mn}\rho)Y_n'(k_{mn}a) - J_n'(k_{mn}a)Y_n(k_{mn}\rho)]\cos n\phi \tag{2B.7}$$
$$n = 0, 1, 2, \ldots \quad m = 1, 2, 3, \ldots$$

where k_{mn} are solutions of

$$J_n'(k_{mn}a)Y_n'(k_{mn}b) - J_n'(k_{mn}b)Y_n'(k_{mn}a) = 0$$

Annular Sector or Circular Ring Segment

As in the case of circular sectors, the eigenfunctions for annular sectors are available only when the sector angle α is a submultiple of π. For the annular sector shown in Figure 2.28(h), the eigenfunctions are given as

$$\psi_{mv}(\rho, \phi) = [J_v(k_{mv}\rho)Y_v'(k_{mv}a) - J_v'(k_{mv}a)Y_v(k_{mv}\rho)]\cos v\phi \tag{2B.8}$$

where $v = n\pi/\alpha$, and k_{mv} are solutions of

$$J_v'(k_{mv}a)Y_v'(k_{mv}b) - J_v'(k_{mv}b)Y_v'(k_{mv}a) = 0$$

Disk With Narrow Slot

The geometry of this antenna is very similar to that of a disk [Figure 2.28(e)], but a narrow slot is cut. However, it is analyzed like a circular sector with $\alpha \approx 2\pi$ and $v = n/2$. Therefore, the eigenfunctions for a disk with a narrow slot can be written as

$$\psi_{mn} = J_{n/2}(k_{mn}\rho)\cos(n\phi/2) \tag{2B.9}$$

where k_{mn} satisfy

$$J'_{n/2}(k_{mn}a) = 0 \tag{2B.10}$$

Effective Dielectric Constant and Equivalent Dimensions

The cavity model of the antenna assumes a magnetic wall along the boundary. This involves an outward extension of the physical boundary as shown in Figure 2.10. It implies that the physical dimensions of the patch are replaced by the equivalent dimensions so that the cavity model can predict the resonant frequency accurately. For some of the geometries, the same effect is realized by replacing the permittivity of the substrate by the effective permittivity, whereas in some cases both the effective permittivity and equivalent dimensions are used. In this connection, several methods have been reported in the literature to calculate accurately the resonant frequencies of rectangular patch, circular disk, equilateral triangular patch, and elliptical disk antennas [84–91]. A generalized approach has also been reported for these microstrip antenna geometries [92]. The effective permittivity and equivalent dimensions used in this approach are given next.

Effective Permittivity

The effective relative permittivity of a patch antenna according to [92] is defined as

$$\epsilon_{re} = \frac{\epsilon_r + 1}{2} + \frac{\epsilon_r - 1}{2}F \quad \text{for } 0 < F < 1 \tag{2B.11}$$

The function F is empirically derived from the area occupied by the fringing fields and the area of the patch. It is given by

$$F = 1 - \frac{c_r\epsilon_r}{\epsilon_r - 1}\frac{\text{fringing field area}}{\text{area of the patch}} \tag{2B.12}$$

where $c_r(0)$ is a coefficient to be determined. To determine the area occupied by the fringing fields, they are assumed to extend uniformly over a distance equal to the substrate thickness h. Thus, for an elliptical disk with semi-major axis a and semi-minor axis b, the area occupied by the fringing fields is obtained as

$$\pi(a + h)(b + h) - \pi ab = \pi h(a + b + h) \tag{2B.13}$$

Therefore,

$$F = 1 - \frac{c_r\epsilon_r}{\epsilon_r - 1}\left(\frac{h}{a} + \frac{h}{b} + \frac{h^2}{ab}\right) \tag{2B.14}$$

Use of (2B.14) in (2B.11) gives

$$\epsilon_{re} = \epsilon_r - \frac{c_r\epsilon_r}{2}\left(\frac{h}{a} + \frac{h}{b} + \frac{h^2}{ab}\right) \quad \text{for an elliptical disk} \tag{2B.15}$$

$$\epsilon_{re} = \epsilon_r - \frac{c_r\epsilon_r}{2}\left(\frac{2h}{a} + \frac{h^2}{a^2}\right) \quad \text{for a circular disk or radius } a \tag{2B.16}$$

$$\epsilon_{re} = \epsilon_r - 2c_r\epsilon_r\left(\sqrt{3}\frac{h}{a} + 3\frac{h^2}{a^2}\right)$$

for an equilateral triangular patch of side length a (2B.17)

For a rectangular patch antenna one can use the well-known expression for the effective relative permittivity, (B.4) or (B.12) of Appendix B at the end of the book.

Equivalent Dimensions

The equivalent dimensions of a patch antenna are always larger than the physical dimensions. In the model discussed above for the effective permittivity, the dimensions of the patch antenna are also modified to equivalent dimensions. For a rectangular patch, the equivalent length is obtained by adding the end effect extension $\Delta\ell_x$ on either ends of the patch. An accurate expression for $\Delta\ell_x$ is given in Appendix B in (B.71). The physical width W is replaced by the effective width of the corresponding microstrip line (see Appendix B at the end of the book). For a circular disk of radius a, the equivalent radius is given by

$$a_{eq} = a\left[1 + \frac{2h}{\pi\epsilon_{re}a}\left\{\ln\frac{a}{2h} + (1.41\epsilon_{re} + 1.77) + \frac{h}{a}(0.268\epsilon_{re} + 1.65)\right\}\right]^{1/2} \tag{2B.18}$$

For an equilateral triangular patch, the expression for the equivalent side length is obtained by first converting the triangular patch into a circular disk of equal area. The equivalent radius of this disk is then used to define the effective side length of the triangle. One obtains [92]

$$a_{\text{eff}} = a\left[1 + \frac{2h}{\pi\epsilon_{re}a_{eq}}\left\{\ln\frac{a_{eq}}{2h} + (1.41\epsilon_{re} + 1.77) + \frac{h}{a_{eq}}(0.268\epsilon_{re} + 1.65)\right\}\right]^{1/2} \tag{2B.19}$$

where

$$a_{eq} = \sqrt{A/\pi}, \quad \text{where } A \text{ is the area of the triangular patch}$$

The elliptical disk can be modeled as a circular disk of equal area. For this, the area of an elliptical disk is defined as the geometric mean of the areas of two circular disks with radii a and b, that is, $\pi ab = \sqrt{\pi a^2 \cdot \pi b^2}$. Here, a is the semi-major axis and b is the semi-minor axis of the elliptical disk. The equivalent semi-major axis and semi-minor axis of this disk are obtained from the circular disk of the corresponding radius. The expression for the equivalent semi-major axis a_{eq} for the elliptic disk is therefore given by (2B.18), and the equivalent semi-minor axis b_{eq} is obtained by replacing a and a_{eq} by b and b_{eq}, respectively, in (2B.18).

The value of the constant c_r in (2B.12) is obtained by curve fitting the calculated resonant frequency from the formulas given above with the measured value and/or computed numerical value. An assigned value of 0.7 for c_r for all the patch shapes investigated gives a good match for thin substrates with $h\sqrt{\epsilon_r}/\lambda_0 \leq 0.02$ [92].

References

[1] Pozar, D. M., "Microstrip Antennas," *Proc. IEEE*, Vol. 80, 1992, pp. 79–91.

[2] Carver, K. R., and E. L. Coffey, "Theoretical Investigation of the Microstrip Antenna," Tech. Report PT-00929, Physical Science Laboratory, New Mexico State University, Las Cruces, NM, 1979.

[3] Kishk, A. A., and L. Shafai, "The Effect of Various Parameters of Circular Microstrip Antennas on Their Radiation Efficiency and the Mode Excitation," *IEEE Trans. on Antennas and Propagation*, Vol. AP-34, 1986, pp. 969–976.

[4] James, J. R., and P. S. Hall (Eds.), *Handbook of Microstrip Antennas*, Peter Peregrinus, London, UK, 1989.

[5] Bhattacharyya, A. K., and R. Garg, "Generalised Transmission Line Model for Microstrip Patches," *IEE Proc.*, Vol. 132, Pt. H, 1985, pp. 93–98.

[6] Bhattacharyya, A. K., and R. Garg, "Input Impedance of an Annular Ring Microstrip Antenna Using Circuit Theory Approach," *IEEE Trans. on Antennas and Propagation*, Vol. AP-33, 1985, pp. 217–219.

[7] Bhattacharyya, A. K., and R. Garg, "Analysis of Annular Sector and Circular Sector Microstrip Patch Antennas," *Electromagnetics*, Vol. 6, No. 3, 1986, pp. 229–242.

[8] Munson, R., "Conformal Microstrip Antennas and Microstrip Phased Arrays," *IEEE Trans. on Antennas and Propagation*, Vol. AP-22, 1974, pp. 74–78.

[9] Derneryd, A., "Linearly Polarized Microstrip Antennas," *IEEE Trans. on Antennas and Propagation*, Vol. AP-24, 1976, pp. 846–851.

[10] Derneryd, A., "A Theoretical Investigation of the Rectangular Microstrip Antenna Element," *IEEE Trans. on Antennas and Propagation*, Vol. AP-26, 1978, pp. 532–535.

[11] Lier, E., "Improved Formulas for Input Impedance of Coax-Fed Microstrip Patch Antennas," *IEE Proc.*, Vol. 129, Pt. H, 1982, pp. 161–164.

[12] Pues, H., and A. Van de Capelle, "Accurate Transmission Line Model for the Rectangular Microstrip Antenna," *IEE Proc.*, Vol. 131, Pt. H, 1984, pp. 334–340.

[13] Van Lil, E., and A. Van de Capelle, "Transmission Line Model for Mutual Coupling Between Microstrip Antennas," *IEEE Trans. on Antennas and Propagation*, Vol. AP-32, 1984, pp. 816–821.

[14] Dearnley, R. W., and A. R. F. Barel, "A Broad-Band Transmission Line Model for a Rectangular Microstrip Antenna," *IEEE Trans. on Antennas and Propagation*, Vol. AP-37, 1989, pp. 6–15.

[15] Bhattacharyya, A. K., "Generalised Transmission Line Model of Microstrip Patch Antennas and Some Applications," Ph.D. Thesis, Indian Institute of Technology, Kharagpur, India, 1985.

[16] Bhattacharyya, A. K., L. Shafai, and R. Garg, "Microstrip Antenna—A Generalised Transmission Line," *Progress in Electromagnetics Research*, Vol. 4, 1991, pp. 45–84.

[17] Bhattacharyya, A. K., and R. Garg, "A Microstrip Array of Concentric Annular Rings," *IEEE Trans. on Antennas and Propagation*, Vol. AP-33, 1985, pp. 655–659.

[18] Bhattacharyya, A. K., and L. Shafai, "Theoretical and Experimental Investigations of the Elliptical Annular Ring Antenna," *IEEE Trans. on Antennas and Propagation*, Vol. AP-36, 1988, pp. 1526–1530.

[19] Bhattacharyya, A. K., and L. Shafai, "A Wider Band Microstrip Antenna for Circular Polarization," *IEEE Trans. on Antennas and Propagation*, Vol. AP-36, 1988, pp. 157–163.

[20] Bhattacharyya, A. K., and R. Garg, "Self and Mutual Admittances Between Two Concentric, Coplanar, Circular Radiating Current Sources," *Proc. IEE*, Vol. 131, Pt. H, 1984, pp. 217–219.

[21] Bahl, I. J., and P. Bhartia, *Microstrip Antennas*, Artech House, Dedham, MA, 1980.

[22] Daniel, J. P., et al., "Research on Planar Antennas and Arrays: 'Structures Rayonnantes,' " *IEEE Antennas Propagation Magazine*, Vol. 35, Feb. 1993, pp. 14–38.

[23] Dubost, G., and A. Zerguerras, "Transmission-Line Model Analysis of Arbitrary Shape Symmetrical Patch Antenna Coupled With a Director," *Electron. Lett.*, Vol. 26, 1990, pp. 952–954.

[24] Dubost, G., et al., "Radiation of Arbitrary Shape Symmetrical Patch Antenna Coupled With a Director," *Electron. Lett.*, Vol. 26, 1990, pp. 1539–1540.

[25] Dubost, G., and A. Rabbaa, "Analysis of a Slot Microstrip Antenna," *IEEE Trans. on Antennas and Propagation*, Vol. AP-34, 1986, pp. 155–163.

[26] Dubost, G., *Flat Radiating Dipoles and Applications to Arrays*, John Wiley, New York, 1981.

[27] Schaubert, D. H., et al., "Effect of Microstrip Antenna Substrate Thickness and Permittivity: Comparison of Theories and Experiment," *IEEE Trans. on Antennas and Propagation*, Vol. AP-37, 1989, pp. 677–682.

[28] Lo, Y. T., et al., "Theory and Experiment on Microstrip Antennas," *IEEE Trans. on Antennas and Propagation*, Vol. AP-27, 1979, pp. 137–145.

[29] Richards, W. F., et al., "An Improved Theory for Microstrip Antennas and Applications," *IEEE Trans. on Antennas and Propagation*, Vol. AP-29, 1981, pp. 38–46.

[30] Lo, Y. T., and W. F. Richards, "Perturbation Approach to Design of Circularly Polarized Microstrip Antennas," *Electron. Lett.*, 1981, pp. 383–385.

[31] Carver, K. R., and J. W. Mink, "Microstrip Antenna Technology," *IEEE Trans. on Antennas and Propagation*, Vol. AP-29, 1981, pp. 2–24.

[32] Thouroude, D., et al., "CAD-Oriented Cavity Model for Rectangular Patches," *Electron. Lett., Vol. 26*, 1990, pp. 842–844.

[33] Richards, W. F., et al., "Theory and Applications for Microstrip Antennas," *Proc. Workshop Printed Circuit Antenna Tech.*, New Mexico State University, Las Cruces, NM, 1979, pp. 8/1–23.

[34] Long, S. A., et al., "Impedance of a Circular-Disc Printed-Circuit Antenna," *Electron. Lett.*, Vol. 14, 1978, pp. 684–686.

[35] Dahele, J. S., and K. F. Lee, "Effect of Substrate Thickness on the Performance of a Circular-Disc Microstrip Antenna," *IEEE Trans. on Antennas and Propagation*, Vol. AP-31, 1983, pp. 358–360.

[36] Lee, K. F., K. M. Luk, and J. S. Dahele, "Characteristics of the Equilateral Triangular Patch Antenna," *IEEE Trans. on Antennas and Propagation*, Vol. AP-36, 1988, pp. 1510–1818.

[37] Mink, J. W., "Circular Ring Microstrip Antenna Elements," *IEEE AP-S Int. Symp. Digest*, 1980, pp. 605–608.

[38] Lee, K. F., and J. S. Dahele, "Theory and Experiment on Annular-Ring Microstrip Antenna," *Ann. des Telecomm.*, Vol. 40, 1985, pp. 508–515.

[39] Richards, W. F., et al., "A Theoretical and Experimental Investigation of Annular Ring, Annular Sector and Circular Sector Microstrip Antennas," *IEEE Trans. on Antennas and Propagation*, Vol. AP-32, 1984, pp. 864–866.

[40] Lee, K. F., K. Y. Ho, and J. S. Dahele, "Circular-Disk Microstrip Antenna With an Air Gap," *IEEE Trans. on Antennas and Propagation*, Vol. AP-32, 1984, pp. 880–884.

[41] Dahele, J. S., K. F. Lee, and D. P. Wong, "Dual-Frequency Stacked Annular Ring Microstrip Antenna," *IEEE Trans. on Antennas and Propagation*, Vol. AP-35, 1987, pp. 1281–1285.

[42] Penard, E., and J. P. Daniel, "Mutual Coupling Between Microstrip Antennas," *Electron. Lett.*, Vol. 18, 1982, pp. 605–607.

[43] Himdi, M., et al., "Analysis of Aperture-Coupled Microstrip Antenna Using Cavity Method," *Electron. Lett.*, Vol. 25, 1989, 391–392.

[44] Ittipiboon, A., R. Oostlander, and Y. M. M. Antar, "Modal Expansion Method of Analysis for Slot-Coupled Microstrip Antenna," *Electron. Lett.*, Vol. 25, 1989, pp. 1338–1340.

[45] Palanisamy, V., "Generalized Cavity Model of Microstrip Patch Antennas and Some Applications," Ph.D. Thesis, Indian Institute of Technology, Kharagpur, India, 1985.

[46] Palanisamy, V., and R. Garg, "Analysis of Arbitrary Shaped Microstrip Patch Antennas Using Segmentation Technique and Cavity Model," *IEEE Trans. on Antennas and Propagation*, Vol. AP-34, 1986, pp. 1208–1213.

[47] Okoshi, T., *Planar Circuits for Microwaves and Lightwaves*, Springer Verlag, New York, 1985, Chap. 5.

[48] Palanisamy, V., and R. Garg, "Rectangular Ring and H-Shaped Microstrip Antennas—Alternatives to Rectangular Patch Antenna," *Electron. Lett.*, Vol. 21, 1985, pp. 874–876.

[49] Palanisamy, V., and R. Garg, "Analysis of Circularly Polarized Square Ring and Crossed-Strip Microstrip Antennas," *IEEE Trans. on Antennas and Propagation*, Vol. AP-34, 1986, pp. 1340–1346.

[50] Gupta, K. C., and A. Benalla, "Two-Port Transmission Characteristics of Circular Microstrip Patch Antennas," *IEEE AP-S Int. Symp. Digest*, 1986, pp. 821–824.

[51] Gupta, K. C., R. Garg, and R. Chadha, *Computer-Aided Design of Microwave Circuits*, Artech House, Dedham, MA, 1981.

[52] Benalla, A., and K. C. Gupta, "Multiport Network Approach for Modeling Mutual Coupling Effects in Microstrip Patch Antennas and Arrays," *IEEE Trans. on Antennas and Propagation*, Vol. AP-37, 1989, pp. 148–152.

[53] Gupta, K. C., "Two-Dimensional Analysis of Microstrip Circuits and Antennas," *J. Inst. Electron. Telecommun. Engrs. (India)*, Vol. 28, 1982, pp. 346–364.

[54] Gupta, K. C., and P. C. Sharma, "Segmentation and Desegmentation Techniques for the Analysis of Two-Dimensional Microstrip Antennas," *IEEE AP-S Int. Symp. Digest*, 1981, pp. 19–22.

[55] Sharma, P. C., and K. C. Gupta, "Analysis and Optimized Design of Single Feed Circularly Polarized Microstrip Antennas," *IEEE Trans. on Antennas and Propagation*, Vol. AP-31, 1983, pp. 949–955.

[56] Kumar, G., and K. C. Gupta, "Broadband Microstrip Antennas Using Additional Resonators Gap-Coupled to Radiating Edges," *IEEE Trans. on Antennas and Propagation*, Vol. AP-32, 1984, pp. 1375–1379.

[57] Kumar, G., and K. C. Gupta, "Nonradiating Edges and Four-Edges Gap-Coupled Multiple Resonator, Broadband Microstrip Antennas," *IEEE Trans. on Antennas and Propagation*, Vol. AP-33, 1985, pp. 1375–1379.

[58] Kumar, G., and K. C. Gupta, "Directly Coupled Multiple Resonator Wideband Microstrip Antennas," *IEEE Trans. on Antennas and Propagation*, Vol. AP-33, 1985, pp. 588–593.

[59] Benalla, A., and K. C. Gupta, "Multiport Network Model and Transmission Characteristics of Two-Port Rectangular Microstrip Antennas," *IEEE Trans. on Antennas and Propagation*, Vol. AP-36, 1988, pp. 1337–1342.

[60] Parrikar, R. P., and K. C. Gupta, "Multiport Network Model for CAD of Electromagnetically Coupled Patch Antennas," *IEEE Trans. on Microwave Theory and Techniques*, Vol. MTT-46, 1998, pp. 475–483.

[61] Harrington, R. F., *Time-Harmonic Electromagnetic Fields*, McGraw-Hill, New York, 1961.

[62] Jackson, D. R., and N. G. Alexopoulos, "Simple Approximate Formulas for Input Resistance, Bandwidth, and Efficiency of a Resonant Rectangular Patch," *IEEE Trans. on Antennas and Propagation*, Vol. AP-39, 1991, pp. 407–410.

[63] James, J. R., P. S. Hall, and C. Wood, *Microstrip Antenna: Theory and Design*, Peter Peregrinus, London, UK, 1981.

[64] Sobol, H., "Radiation Conductance of Open-Circuit Microstrip," *IEEE Trans. on Microwave Theory and Techniques*, Vol. MTT-19, 1971, pp. 885–887.

[65] Van der Pauw, L. J., "The Radiation of Electromagnetic Power by Microstrip Configurations," *IEEE Trans. on Microwave Theory and Techniques*, Vol. MTT-25, 1977, pp. 719–725.

[66] Lewin, L., "Spurious Radiation From Microstrip," *Proc. IEE*, Vol. 125, 1978, pp. 633–642.

[67] James, J. R., and A. Henderson, "High Frequency Behaviour of Microstrip Open-Circuit Terminations," *IEE J. Microwave Optics & Acoustics*, Vol. 3, 1979, pp. 205–218.

[68] Chuang, C. L., et al., "The Equivalence of the Electric and Magnetic Surface Current Approaches in Microstrip Antenna Studies," *IEEE Trans. on Antennas and Propagation*, Vol. AP-28, 1980, pp. 569–571.

[69] Gogoi, A., and K. C. Gupta, "Wiener-Hopf Computation of Edge-Admittances for Microstrip Patch Radiators," *Arch. Elek. Ubertragung.*, Vol. 36, 1982, pp. 247–251.

[70] Kuester, E. F., et al., "The Thin-Substrate Approximation for Reflection From the End of a Slab-Loaded Parallel Plate Waveguide With Application to Microstrip Patch Antennas," *IEEE Trans. on Antennas and Propagation*, Vol. AP-30, 1982, pp. 910–917.

[71] Bhattacharyya, A. K., and R. Garg, "Effect of Substrate on the Efficiency of an Arbitrarily Shaped Microstrip Patch Antenna," *IEEE Trans. on Antennas and Propagation*, Vol. AP-34, 1986, pp. 1181–1188.

[72] Wolff, I., and N. Knoppik, "Rectangular and Circular Microstrip Disc Capacitors and Resonators," *IEEE Trans. on Microwave Theory and Techniques*, Vol. MTT-22, 1974, pp. 857–864.

[73] Katehi, P. B., and N. G. Alexopoulos, "Frequency-Dependent Characteristics of Microstrip Discontinuities in Millimeter-Wave Integrated Circuits," *IEEE Trans. on Microwave Theory and Techniques*, Vol. MTT-33, 1985, pp. 1029–1035.

[74] Jackson, R. W., and D. M. Pozar, "Full-Wave Analysis of Microstrip Open-End and Gap Discontinuities," *IEEE Trans. on Microwave Theory and Techniques*, Vol. MTT-33, 1985, pp. 1036–1042.

[75] Jansen, R. H., and N. H. L. Koster, "Accurate Results on the End Effect of Single and Coupled Microstrip Lines for Use in Microwave Circuits Design," *AEU*, Vol. 34, 1980, pp. 453–459.

[76] Kirschning, M., et al., "Accurate Model for Open-End Effect of Microstrip Lines," *Electron. Lett.*, Vol. 17, 1981, pp. 123–125.

[77] Lewin, L., "Radiation From Discontinuities in Stripline," *Proc. IEE*, Vol. 107C, 1960, pp. 163–170.

[78] Richards, W. F., et al., "Experimental and Theoretical Investigation of the Inductance Associated With a Microstrip Antenna Feed," *Electromagnetics*, Vol. 3, 1983, pp. 327–346.

[79] Damiano, J. P., and A. Papiernik, "Survey of Analytical and Numerical Models for Probe-Fed Microstrip Antennas," *IEE Proc. Microwaves, Antennas Propagation*, Vol. 141, 1994, pp. 15–22.

[80] Zheng, J. X., and D. C. Chang, "End-Correction Network of a Coaxial Probe for Microstrip Patch Antennas," *IEEE Trans. on Antennas and Propagation*, Vol. AP-39, 1991, pp. 115–118.

[81] Tulintseff, A. N., S. M. Al, and J. A. Kong, "Input Impedance of a Probe-Fed Stacked Circular Microstrip Antenna," *IEEE Trans. on Antennas and Propagation*, Vol. AP-39, 1991, pp. 381–390.

[82] Lewin, L., "A Contribution to the Theory of Cylindrical Antennas—Radiation Between Parallel Plates," *IRE Trans.*, Vol. AP-7, 1959, pp. 162–168.

[83] Fong, K. S., H. F. Pues, and M. J. Withers, "Wideband Multilayer Coaxial-Fed Microstrip Antenna Element," *Electron. Lett.*, Vol. 21, 1985, pp. 497–499.

[84] Dearnley, R. W., and A. R. F. Barel, "A Comparison of Models to Determine the Resonant Frequencies of a Rectangular Microstrip Antenna," *IEEE Trans. on Antennas and Propagation*, Vol. AP-37, 1989, pp. 114–118.

[85] Kumprasert, N., and W. Kiranon, "Simple and Accurate Formula for the Resonant Frequency of the Circular Microstrip Disk Antenna," *IEEE Trans. on Antennas and Propagation*, Vol. AP-43, 1995, pp. 1331–1333.

[86] Kumprasert, N., and W. Kiranon, "Simple and Accurate Formula for the Resonant Frequency of the Equilateral Triangular Microstrip Patch Antenna," *IEEE Trans. on Antennas and Propagation*, Vol. AP-42, 1994, pp. 1178–1179.

[87] Damiano, J.-P., J.-M. Ribero, and R. Staraj, "Original Simple and Accurate Model for Elliptical Microstrip Antennas," *Electron. Lett.*, Vol. 31, 1995, pp. 1023–1024.

[88] Rengarajan, S. R., "Resonance Frequency of Elliptical Microstrip Antennas," *Electron. Lett.*, Vol. 29, 1993, pp. 1066–1067.

[89] Singh, R., A. De, and R. S. Yadav, "Comments on an Improved Formula for the Resonant Frequency of the Triangular Microstrip Antenna," *IEEE Trans. on Antennas and Propagation*, Vol. AP-39, 1991, pp. 1443–1444.

[90] Chew, W. C., and J. A. Kong, "Effects of Fringing Fields on the Capacitance of Circular Microstrip Ring Antenna," *IEEE Trans. on Microwave Theory and Techniques*, Vol. MTT-28, 1980, pp. 98–104.

[91] Suzuki, Y., and T. Chiba, "Computer Analysis Method for Arbitrary Shaped Microstrip Antenna With Multi-Terminals," *IEEE Trans. on Antennas and Propagation*, Vol. AP-32, 1984, pp. 585–590.

[92] Mythili, P., and A. Das, "Simple Approach to Determine Resonant Frequencies of Microstrip Antennas," *IEE Proc. Microwaves, Antennas Propagation*, Vol. 145, 1998, pp. 159–162.

3

Full-Wave Analysis of Microstrip Antennas

The approximate models of the microstrip antennas described in Chapter 2 make a number of simplifying assumptions. These assumptions (1) give rise to analytical simplicity in the form of closed-form eigenfunctions; (2) use closed-form expressions for wall admittances and are, therefore, numerically less computer intensive; and (3) use an *add-on* approach while accounting for various phenomena, such as space wave radiation, surface wave radiation, and mutual coupling. Therefore, they suffer from a number of limitations. Their principal limitations are listed below.

- The models are accurate for thin substrates ($h/\lambda_0 < 0.01$) only because of the assumption $\partial/\partial z \equiv 0$.
- These models are not accurate when applied to narrow width microstrip dipoles [1, Chapter 9].
- Some of the feed configurations such as proximity-coupled and aperture-coupled microstrip feeds are difficult to model.
- The models have not been tested for anisotropic substrates.
- Cross-polarized radiation from a patch antenna has not been predicted using the transmission line model or the multiport network model because only a single-mode analysis has been carried out.

Most of the limitations listed here can be overcome in the full-wave techniques. These techniques maintain rigor and accuracy at the expense of numerical simplicity. The principal assumption of the integral equation tech-

niques is that the substrate and ground plane are infinite in lateral dimensions. The formulation of the solution is based on rigorously enforcing the boundary conditions at the air-dielectric interface. This is done by using the exact Green's function for the composite dielectric.

The Green's function includes the effects of dielectric loss, conductor loss, surface wave modes, and space wave radiation. The boundary condition at the patch metalization leads to an integral equation. Maxwell's equations in differential form are cast in the finite-difference form and solved in the time domain using the finite-difference time-domain (FDTD) approach. This technique does not make use of Green's function, and is therefore well suited to take into account the effect of a finite-sized ground plane and substrate. Any embedded semiconductor device in the antenna can be included in the analysis at the device-field interaction level. This possibility leads to an accurate analysis of active microstrip antennas. Some of the features of the full-wave techniques include these [2]:

- *Accuracy.* Full-wave techniques generally provide the most accurate solution for the impedance and radiation characteristics.
- *Completeness.* Full-wave solutions are complete for the most part; that is, they include the effects of dielectric loss, conductor loss, space wave radiation, surface waves, and external coupling.
- *Versatility.* Full-wave techniques can be used for arbitrarily shaped microstrip elements and arrays, various types of feeding techniques, multilayer geometries, anisotropic substrates, and active antennas.
- *Computation cost.* Full-wave techniques are numerically intensive, and therefore require careful programming to reduce computation cost.

We next describe the three most popular full-wave techniques. These are called the *spectral-domain full-wave solution* [3–5], the *mixed-potential electric field integral equation approach* [1, 5, 6], and the *finite-difference time-domain* technique [7, 8].

For stratified media problems, the integral equation can be solved in two different ways:

1. The integral equation is written and solved in the spectral domain. This approach is frequently termed the *spectral-domain approach.*
2. In the other approach, the spectral domain is used for calculating the Green's function, but inverse transforms are taken at this stage and the integral equation is solved in the space domain. This approach provides more physical insight into the problem and is computationally more efficient. When the scalar potential and vector potential combination is chosen for the analysis, the technique is referred to as the mixed-potential integral equation (MPIE) technique. We shall assume only planar currents, that is, no vertical currents like vias, to keep the problem simpler. The spectral-domain analysis is described first.

3.1 Spectral-Domain Full-Wave Analysis

The spectral-domain full-wave approach [3, 4] uses the exact Green's function for the mixed dielectric nature of the microstrip antenna. The Green's function is employed in the electric field integral equation formulation to satisfy the boundary conditions at the patch metalization. The resulting integral equations are discretized into a set of linear equations by means of the moment method to yield a matrix equation. The solution of the matrix equation provides the current distribution on the patch metalization. The near-field and far-field characteristics of the antenna are then obtained from the current distribution and the Green's function. Figure 3.1 lists the major steps in the analysis. The technique is next illustrated for a rectangular microstrip antenna.

The configuration of a rectangular microstrip antenna fed by a coaxial probe is shown in Figure 3.2. It consists of a metal patch on a grounded dielectric substrate of dielectric constant ϵ_r. The microstrip antenna may employ inhomogeneous or mixed dielectric in the form of substrate ($\epsilon_r \neq 1$) below the patch metalization and free space ($\epsilon_r = 1$) above it. Because of the mixed dielectric nature, the Green's function can be obtained in a closed form only in the spectral domain. Electric field Green's functions for the x-directed and y-directed currents are derived in Appendix 3A. These expressions are given below.

For the x-directed current J_x on the air-dielectric interface at $z = h$, the electric field components in the spectral domain are (see 3A.14):

$$\tilde{E}_x(k_x, k_y, h) = \frac{-j}{\omega\epsilon_0}\left[\frac{k_x^2 k_1 k_2 \sin(k_1 h)}{\beta^2 T_m} + \frac{k_y^2 k_0^2 \sin(k_1 h)}{\beta^2 T_e}\right]\tilde{J}_x \quad (3.1a)$$

$$\tilde{E}_y(k_x, k_y, h) = \frac{-j}{\omega\epsilon_0}\left[\frac{k_x k_y k_1 k_2 \sin(k_1 h)}{\beta^2 T_m} - \frac{k_x k_y k_0^2 \sin(k_1 h)}{\beta^2 T_e}\right]\tilde{J}_x \quad (3.1b)$$

$$\tilde{E}_z(k_x, k_y, h) = \frac{-j}{\omega\epsilon_0}\left(\frac{k_1 k_x \sin(k_1 h)}{T_m}\right)\tilde{J}_x \quad (3.1c)$$

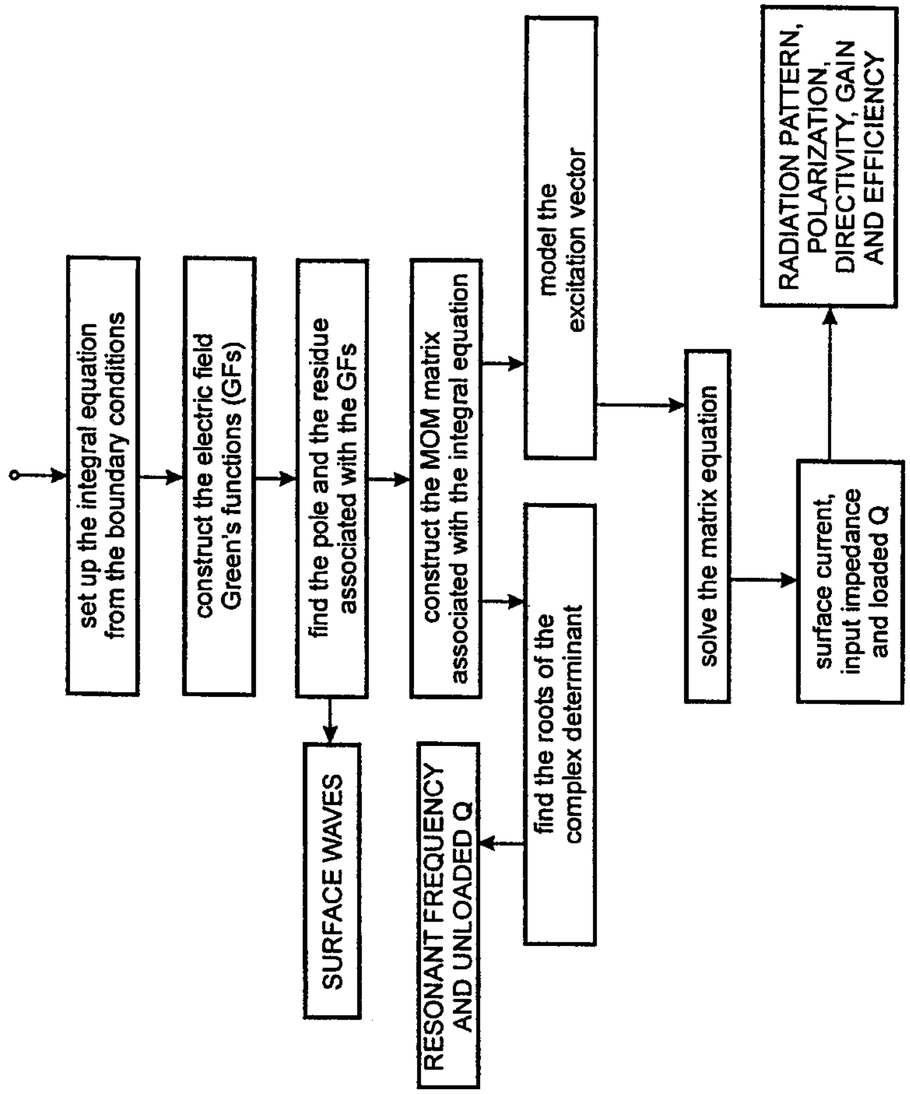

Figure 3.1 Microstrip antenna analysis steps.

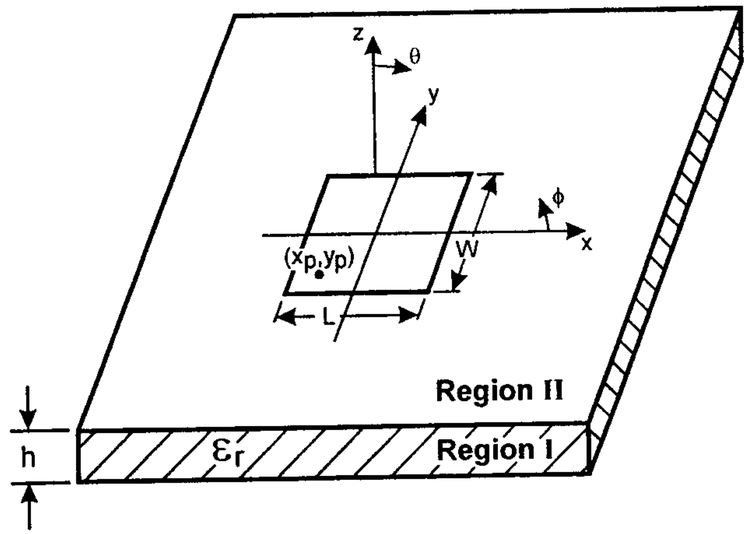

Figure 3.2 Geometry of a rectangular microstrip antenna with a probe feed. Air-dielectric interface at $z = h$.

For the y-directed current J_y on the air-dielectric interface at $z = h$, the electric field components in the spectral domain are (see 3A.15):

$$\tilde{E}_y(k_x, k_y, h) = \frac{-j}{\omega\epsilon_0}\left[\frac{k_y^2 k_1 k_2 \sin(k_1 h)}{\beta^2 T_m} + \frac{k_x^2 k_0^2 \sin(k_1 h)}{\beta^2 T_e}\right]\tilde{J}_y \quad (3.1d)$$

$$\tilde{E}_x(k_x, k_y, h) = \frac{-j}{\omega\epsilon_0}\left[\frac{k_x k_y k_1 k_2 \sin(k_1 h)}{\beta^2 T_m} - \frac{k_x k_y k_0^2 \sin(k_1 h)}{\beta^2 T_e}\right]\tilde{J}_y \quad (3.1e)$$

$$\tilde{E}_z(k_x, k_y, h) = \frac{-j}{\omega\epsilon_0}\left(\frac{k_1 k_y \sin(k_1 h)}{T_m}\right)\tilde{J}_y \quad (3.1f)$$

where

$$T_m = \epsilon_r k_2 \cos(k_1 h) + j k_1 \sin(k_1 h) \quad (3.2a)$$

$$T_e = k_1 \cos(k_1 h) + j k_2 \sin(k_1 h) \quad (3.2b)$$

$$k_1^2 = k_z^2 = \epsilon_r k_0^2 - \beta^2 \quad \text{for } 0 < z < h \text{ (region 1)} \quad \text{Im}(k_1) < 0 \quad (3.3a)$$

$$k_2^2 = k_z^2 = k_0^2 - \beta^2 \quad \text{for } z > h \text{ (region 2)} \quad \text{Im}(k_2) < 0 \quad (3.3b)$$

$$\beta^2 = k_x^2 + k_y^2 \tag{3.4}$$

and $\tilde{E}$ denotes the double Fourier transform of E, and is defined as

$$\tilde{E}(k_x, k_y, z) = \int_{-\infty}^{\infty}\int_{-\infty}^{\infty} E(x, y, z)e^{-jk_x x}e^{-jk_y y}dxdy \tag{3.5}$$

The notation k_ρ for $\sqrt{k_x^2 + k_y^2}$ clearly specifies its radial nature, but β is being retained here to help the reader with the vast amount of literature using this notation for the spectral-domain approach.

In a microstrip antenna fed by a probe current, there are two types of currents: excitation current $\bar{J}_e$ on the probe, and the surface current or patch current $\bar{J}_s$ on the patch metalization. The patch current $\bar{J}_s$ is induced by the excitation current. Both currents give rise to fields. The boundary condition that the total tangential electric fields produced by the excitation current and the induced patch current density must be zero on the patch surface gives rise to the following integral equation:

$$\hat{z} \times [\bar{\bar{E}}(\bar{J}_e) + \bar{\bar{E}}(\bar{J}_s)] = 0 \text{ for all points on the patch surface} \tag{3.6}$$

where $\bar{J}_s$ is the unknown surface current density to be determined. The second term in (3.6) is defined as

$$\bar{\bar{E}}(\bar{J}_s) = \int\int \bar{J}_s \cdot \bar{\bar{\bar{G}}}(x, y|x_0, y_0)dx_0 dy_0 \tag{3.7}$$

where $\bar{\bar{\bar{G}}}(\cdot|\cdot)$ is the dyadic Green's function. Integration in (3.7) is to be carried out on the patch surface. The use of (3.7) in (3.6) yields the integral equation

$$\hat{z} \times [\bar{\bar{E}}(\bar{J}_e) + \int\int \bar{J}_s \cdot \bar{\bar{\bar{G}}}(x, y|x_0, y_0)dx_0 dy_0] = 0 \tag{3.8}$$

which is an integral equation because the unknown $\bar{J}_s$ appears inside the integral, and is valid when the patch metalization is a perfect conductor. For a lossy conductor the effect of ohmic losses is included by introducing a surface impedance Z_s (Ω/square) equal to the ratio of the tangential electric field to the surface current density. Therefore, (3.6) should be modified to

$$\hat{z} \times [\bar{\bar{E}}(\bar{J}_e) + \bar{\bar{E}}(\bar{J}_s) = Z_s\bar{J}_s]$$

or

$$\hat{z} \times [\bar{\bar{E}}(\bar{J}_e) + \int\int \bar{J}_s \cdot \bar{\bar{\bar{G}}}(x, y|x_0, y_0)dx_0 dy_0 = Z_s\bar{J}_s] \tag{3.9}$$

The surface impedance Z_s of a metal sheet with conductivity σ is defined as [9]

$$Z_s = (1 + j)\sqrt{\frac{\pi f \mu_0}{\sigma}} \tag{3.10}$$

The dielectric loss can be accounted for by introducing a complex dielectric constant $\epsilon_r(1 - j\tan\delta)$ for the substrate.

The integral equations (3.8) or (3.9) can be solved using the method of moments [10]. In this approach, the unknown surface current $\bar{J}_s$ is expanded in a set of known basis or expansion functions with unknown coefficients. This process is sometimes also called *discretization of current*. The integral equation is then *tested* with another set of functions called *test functions*, resulting in a set of simultaneous equations. This approach, called the *method of moments*, is described in Appendix 3B. The results of the method of moments solution of (3.8) can be written succinctly in matrix form:

$$[Z]_{N\times N}[I]_{N\times 1} = [V]_{N\times 1}, \quad N = N_x + N_y \tag{3.11}$$

Here N_x and N_y are the number of x-directed and y-directed expansion currents, respectively. The impedance matrix elements are defined as follows (see 3B.7) [3]:

$$Z_{mn}^{ij} = \int_{-\infty}^{+\infty}\int F^*(J_{mi})Q_{ij}F(J_{nj})dk_x dk_y \quad m, n = 1, 2, 3, \ldots, \quad i, j = x \text{ or } y \tag{3.12}$$

The voltage vector elements are the voltage contributions produced by the patch expansion currents at the feed location. They are given by (see 3B.15)

$$V_m^i = \int_{-\infty}^{+\infty}\int F(J_{mi})Q_{zi}e^{jk_x x_p}e^{jk_y y_p}dk_x dk_y \quad i, j = x \text{ or } y \tag{3.13}$$

Here (x_p, y_p) is the feed point. The amplitudes of various expansion currents are

$$[I] = [I_{1x}, I_{2x}, \ldots, I_{N_x x}; I_{1y}, I_{2y}, \ldots, I_{N_y y}]^t \tag{3.14}$$

Also,

$$Q_{ij} = \tilde{Z}_{ij}/(4\pi^2) \quad i, j = x \text{ or } y \tag{3.15}$$

$$Q_{zi} = \tilde{Z}_{zi}/(4\pi^2) \tag{3.16}$$

and the Green's functions (see 3A.17):

$$\tilde{Z}_{xx} = \frac{-j}{\omega\epsilon_0}\left[\frac{k_x^2 k_1 k_2 \sin(k_1 h)}{\beta^2 T_m} + \frac{k_y^2 k_0^2 \sin(k_1 h)}{\beta^2 T_e}\right] \tag{3.17a}$$

$$\tilde{Z}_{xy} = \frac{-j}{\omega\epsilon_0}\left[\frac{k_x k_y k_1 k_2 \sin(k_1 h)}{\beta^2 T_m} - \frac{k_x k_y k_0^2 \sin(k_1 h)}{\beta^2 T_e}\right] \tag{3.17b}$$

$$\tilde{Z}_{yy} = \frac{-j}{\omega\epsilon_0}\left[\frac{k_y^2 k_1 k_2 \sin(k_1 h)}{\beta^2 T_m} + \frac{k_x^2 k_0^2 \sin(k_1 h)}{\beta^2 T_e}\right] \tag{3.17c}$$

$$\tilde{Z}_{yx} = \tilde{Z}_{xy} \tag{3.17d}$$

$$\tilde{Z}_{zi} = \frac{-j\eta_0}{k_0}\frac{jk_i k_2 \sin(k_1 h)}{k_1 T_m} \tag{3.18}$$

3.1.1 Input Impedance and Radiation Efficiency

Once the current vector $[I]$ has been determined from the solution of the matrix equation (3.11), the input impedance of a microstrip antenna can be obtained. The input impedance Z_{in} for a probe excited microstrip antenna is defined as

$$Z_{\text{in}} = V/I_s \tag{3.19a}$$

where V is the RF voltage across the probe and I_s is the probe current or source current. We can arbitrarily choose the source current I_s to be 1A. Then

$$Z_{\text{in}} = \text{voltage across the probe} = -\int_0^h E_z dz \tag{3.19b}$$

Here E_z is the total z-directed field generated by the patch current at the probe, and is given by

$$E_z = \sum_{nx=1}^{N_x} I_{nx} E_{znx} + \sum_{ny=1}^{N_y} I_{ny} E_{zny} \tag{3.20}$$

Use of (3.20) in (3.19b) gives

$$Z_{\text{in}} = -[I]^t[V] \tag{3.21}$$

Radiation resistance of the antenna R_r can be determined from

$$R_r = \text{Re}(Z_{\text{in}}) \tag{3.22}$$

In the above formulation the contributions of the surface wave and space wave are easily separated in the moment method impedance matrix elements. The surface wave contribution comes from the residues of the contour integral. The moment method matrix elements can be broken up as [11]

$$Z_{mn} = Z_{mn}^{\text{rad}} + Z_{mn}^{\text{sw}} \tag{3.23}$$

where Z_{mn} represents the matrix element, and Z_{mn}^{rad} and Z_{mn}^{sw} represent the space wave (direct radiation) and surface wave contributions, respectively. If I_n represents the current due to the nth expansion mode, the total input power is given by

$$P_{\text{total}} = \text{Re}\sum_n\sum_m I_n^* Z_{mn} I_m \tag{3.24}$$

The surface wave power is given by

$$P_{\text{sw}} = \sum_n\sum_m I_n^* R_{mn}^{\text{sw}} I_m \tag{3.25}$$

where $R_{mn}^{\text{sw}} = Z_{mn}^{\text{sw}}$ is the residue of the surface wave pole contribution to the matrix element. Similarly, the radiated power is given by

$$P_{\text{rad}} = \text{Re}\sum_n \sum_m I_n^* Z_{mn}^{\text{rad}} I_m \tag{3.26}$$

It is assumed here that the structure is lossless. Radiation efficiency of the antenna is defined as

$$e = \frac{P_{\text{rad}}}{P_{\text{rad}} + P_{\text{sw}}} \tag{3.27}$$

3.1.2 Radiation Patterns

The radiation patterns of the antenna can be determined from the far-zone fields in the air region ($z >> h$), which can be obtained from a stationary-phase evaluation of (3A.14) for the x-directed currents and (3A.15) for the y-directed currents. The stationary-phase point (θ, ϕ) is defined as

$$k_x = k_0 \sin\theta\cos\phi \tag{3.28a}$$

$$k_y = k_0 \sin\theta\sin\phi \tag{3.28b}$$

$$\beta = k_0 \sin\theta \tag{3.28c}$$

Transformation from (x, y) coordinates to (θ, ϕ) coordinates yields [9]

$$E_\theta(r, \theta, \phi) = j\frac{e^{-jk_0 r}}{2\pi r} k_0 [\tilde{E}_x \cos\phi + \tilde{E}_y \sin\phi] \tag{3.29}$$

$$E_\phi(r, \theta, \phi) = j\frac{e^{-jk_0 r}}{2\pi r} k_0 [\tilde{E}_y \cos\phi - \tilde{E}_x \sin\phi] \cos\theta \tag{3.30}$$

where

$$k_1^2 = k_0^2 \epsilon_r - \beta^2 = k_0^2(\epsilon_r - \sin^2\theta) \tag{3.31}$$

$$k_2 = k_0 \cos\theta \tag{3.32}$$

Radiation Patterns for the TM_{10} Mode

Let us consider the analysis of the rectangular microstrip patch (Figure 3.2) operated in the TM_{10} mode. The current density expressed in terms of a single entire domain basis function with the current in the x direction can be written as [12]

$$J_{nx} = \frac{V_0}{Z_0 W} \sin\left[\frac{n\pi}{L}(x - L/2)\right] \quad \text{for} \begin{cases} -L/2 \le x \le L/2 \\ -W/2 \le y \le W/2 \end{cases} \tag{3.33}$$

where V_0 is the voltage at $x = L/2$ and Z_0 is the characteristic impedance of the microstrip line of which the patch is a segment. The radiation patterns for the TM_{10} mode ($n = 1$) then become

$$E_\theta(r, \theta, \phi) = \frac{\eta_0}{2\pi r} e^{-jk_0 r} F(J_{1x}) \frac{k_0 k_1 \sin(k_1 h)}{T_m} \cos\theta\cos\phi \tag{3.34}$$

$$E_\phi(r, \theta, \phi) = \frac{-\eta_0}{2\pi r} e^{-jk_0 r} F(J_{1x}) \frac{k_0^2 \sin(k_1 h)}{T_e} \cos\theta\sin\phi \tag{3.35}$$

where

$$F(J_{1x}) = \frac{V_0}{Z_0} \frac{(2\pi/L)\cos(k_x L/2)}{(\pi/L)^2 - k_x^2} \text{sinc}(k_y W/2) \tag{3.36}$$

For the TM_{10} mode the patch length L is selected such that

$$L = \frac{\lambda_g}{2} = \frac{\pi}{k_0\sqrt{\epsilon_{re}}} \tag{3.37}$$

where ϵ_{re} is the effective dielectric constant of the microstrip line. Equation (3.36) then becomes

$$F(J_{1x}) = \frac{V_0}{Z_0} \frac{(2k_0\sqrt{\epsilon_{re}})\cos(\pi k_x/(2k_0\sqrt{\epsilon_{re}}))}{k_0^2 \epsilon_{re} - k_x^2} \text{sinc}(k_y W/2) \tag{3.38}$$

The principal plane power patterns are obtained from (3.34) and (3.35) and illustrated next:

For the $\phi = 0°$ plane or E-plane pattern:

$$E_\phi = 0 \tag{3.39a}$$

$$|E_\theta(\phi = 0°)|^2 = \left(\frac{\eta_0 V_0 \sqrt{\epsilon_{re}}}{2\pi r Z_0}\right)^2 \frac{\cos^2(\pi\sin\theta/(2\sqrt{\epsilon_{re}}))}{(\epsilon_{re} - \sin^2\theta)^2} \frac{(\epsilon_r - \sin^2\theta)\cos^2\theta}{(\epsilon_r - \sin^2\theta) + \epsilon_r^2 \cos^2\theta \cot^2(k_0 h\sqrt{\epsilon_r - \sin^2\theta})} \tag{3.39b}$$

For the $\phi = 90°$ plane or H-plane pattern:

$$E_\theta = 0 \tag{3.40a}$$

$$|E_\phi(\phi = 90°)|^2 = \left(\frac{\eta_0 V_0}{2\pi r Z_0}\right)^2 \cdot \frac{\cos^2\theta}{(\epsilon_r - \sin^2\theta)\cot^2(k_0 h\sqrt{\epsilon_r - \sin^2\theta}) + \cos^2\theta} \operatorname{sinc}^2(Wk_0 \sin\theta/2) \tag{3.40b}$$

Next we determine the radiation patterns for a unit strength current source. The analysis for this source current will provide the effect of substrate on the radiation patterns, and can be used to include the effect of substrate in the radiation patterns derived from the aperture current models of Chapter 2. The electric fields at (x, y, z) in the air region due to a unit strength x-directed current source at (x_0, y_0, h) is obtained from (3.1) and the Fourier transform of $\delta(x - x_0)\,\delta(y - y_0)$ [3]:

$$E_i(x, y, z) = \frac{1}{4\pi^2}\int_{-\infty}^{+\infty}\int \tilde{Z}_{ix}(k_x, k_y)\exp[jk_x(x - x_0)]\exp[jk_y(y - y_0)]\exp[-jk_z(z - h)]\,dk_x dk_y \tag{3.41}$$

where the index $i = x$, or y and the $\tilde{Z}_{ix}$ are defined in (3.17). Expressing E_i as

$$E_i(x, y, z) = \frac{1}{4\pi^2}\int_{-\infty}^{+\infty}\int P_i \exp(jk_x x)\exp(jk_y y)\exp(-jk_z z)\,dk_x dk_y \tag{3.42}$$

where

$$P_i = \tilde{Z}_{ix}\exp(jk_2 h)\exp[-j(k_x x_0 + k_y y_0)] \tag{3.43}$$

The far-zone fields obtained from the stationary-phase evaluation of (3.42) are [9]

$$E_\theta(r, \theta, \phi) = \frac{-\eta_0}{2\pi r}\exp(-jk_0 r)\exp[-j(k_x x_0 + k_y y_0)]\exp(jk_2 h)P_\theta \cos\theta\cos\phi \tag{3.44}$$

$$E_\phi(r, \theta, \phi) = \frac{-\eta_0}{2\pi r}\exp(-jk_0 r)\exp[-j(k_x x_0 + k_y y_0)]\exp(jk_2 h)P_\phi \cos\theta\sin\phi \tag{3.45}$$

and

$$P_\theta = \frac{k_0 k_1 \sin(k_1 h)}{T_m} \tag{3.46a}$$

$$P_\phi = \frac{-k_0^2 \sin(k_1 h)}{T_e} \tag{3.46b}$$

where k_x, k_y, and so on are defined by (3.28) to (3.32).

Expressions (3.44) and (3.45) give the radiation patterns due to an x-directed δ current at (x_0, y_0, h) and determine the effect of grounded substrate on the radiation patterns. Radiation patterns for the y-directed current can be obtained in a similar manner.

3.1.3 Numerical Evaluation of Matrix Elements and Voltage Vector

The evaluation of matrix elements (3.12) involves a sixfold integration. The four space-domain integrations, amounting to the Fourier transforms of J_m and J_n, can be done in closed form, leaving only two numerical integrations. The doubly infinite integrations over k_x and k_y can be reduced to a single infinite integration by converting to the polar form by means of the following transformation of variables

$$k_x = \beta\cos\alpha \tag{3.47a}$$

$$k_y = \beta\sin\alpha \tag{3.47b}$$

and therefore, $dk_x dk_y = \beta d\beta d\alpha$.

The limits of integration now become $0 \le \beta \le \infty$ and $0 \le \alpha \le 2\pi$. The matrix elements (3.12) therefore become

$$Z_{mn}^{ij} = \int_0^{2\pi}\int_0^{\infty} F^*(J_{mi})Q_{ij}F(J_{nj})\beta d\beta d\alpha \tag{3.48}$$

Numerical integrations in (3.48) are very computer intensive. The integration with respect to α does not take much computer time, but the integration over β converges very slowly.

Before the start-up of numerical integrations, the singularities of the integrand are identified and located. These are poles and branch points. Poles arise due to the zeros of T_e and T_m in the denominator of Q_{ij}. Physically, these factors represent TE and TM surface waves on the grounded dielectric slab of the patch antenna (see Section 1.6). Radial propagation constants for these modes are determined from the expressions $T_e = 0$ and $T_m = 0$. The associated poles in Q_{ij} are called *surface wave poles*. There is always at least one surface wave pole corresponding to the TM_0 mode, because it does not have any cutoff frequency. The presence of other modes is dictated by the value of h/λ_0. Exact evaluation of the propagation constant for the surface wave poles has been discussed in Section 1.6. The position of poles on the integration path is shown in Figure 3.3 [5]. For lossless substrates, it has been shown that the surface wave pole is real and is given by (1.55), that is,

$$\frac{\beta}{k_0} \approx 1 + \frac{1}{2}\left(\frac{\epsilon_r - 1}{\epsilon_r} k_0 h\right)^2 \tag{3.49}$$

If the substrate has moderate loss defined as $\epsilon_r(1 - j\tan\delta)$, then the surface wave pole is also complex valued and defined as $\beta/k_0 = (\beta_r - j\beta_i)/k_0$ with $\beta_i > 0$. The approximate expression for β/k_0 is given by (1.57):

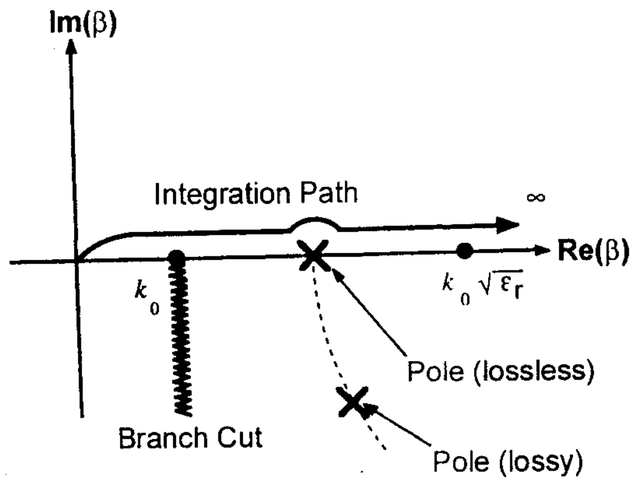

Figure 3.3 The complex plane β and the original path of integration from zero to infinity. The figure also shows the locus of the pole as the dielectric loss increases. (From [5]. © 1989 John Wiley. Reprinted with permission.)

$$\beta_r \approx \beta \tag{3.50a}$$

$$\beta_i \approx (\epsilon_r - 1)\tan\delta(k_0 h/\epsilon_r)^2 \tag{3.50b}$$

The value of β is defined in (3.49).

The branch points occur at $\beta = \pm k_0$, and correspond to the zeros of the square root function $k_2 = \sqrt{k_0^2 - \beta^2}$. The sign of radical k_1 does not affect the single-valued nature of the integral because the terms involving k_1 are even functions of k_1. Therefore, only the branch points contribution from the radical k_2 is considered. The selection of a proper branch is determined by the requirements that the radiated wave in (3.42) is propagating and attenuating away from the source. These requirements are fulfilled by the following selection:

$$\text{Im}(k_2) < 0, \text{ and } \text{Re}(k_2) > 0 \tag{3.51}$$

The infinite integration in (3.48) is performed along the real axis, and is completed in three steps: $[0, k_0]$, $[k_0, k_0\sqrt{\epsilon_r}]$, and $[k_0\sqrt{\epsilon_r}, \infty]$, that is,

$$\int_0^\infty X(\beta, \alpha)\beta d\beta = \int_0^{k_0} X(\beta, \alpha)\beta d\beta + \int_{k_0}^{k_0\sqrt{\epsilon_r}} X(\beta, \alpha)\beta d\beta + \int_{k_0\sqrt{\epsilon_r}}^\infty X(\beta, \alpha)\beta d\beta \tag{3.52}$$

where

$$X(\beta, \alpha) = F^*(J_{mi})Q_{ij}F(J_{nj}) \tag{3.53}$$

These integrations are discussed next.

Numerical integration over the interval $[0, k_0]$. Integration in this region can be carried out numerically using any efficient quadrature integration technique.

Integration over the interval $[k_0, k_0\sqrt{\epsilon_r}]$. The singularity extraction procedure is used for integration in this interval because at least one singular point is known to exist. For this, the integrand is redefined as

$$f(\beta) = [f(\beta) - f_{\text{sing}}(\beta)] + f_{\text{sing}}(\beta) \tag{3.54}$$

where

$$f_{\text{sing}}(\beta) = \frac{P}{\beta - (\beta_r - j\beta_i)} \tag{3.55}$$

Here $\beta_r - j\beta_i$ is the complex pole and P is the residue of $f(\beta)$ at the pole. The first part of (3.54) is now regular and can be integrated numerically. The singular part of (3.54) is integrated analytically and is given by [5]

$$\int_{k_0}^{k_0\sqrt{\epsilon_r}} f_{\text{sing}}(\beta)d\beta = \frac{P}{2}\ln\frac{\beta_i^2 + (k_0\sqrt{\epsilon_r} - \beta_r)^2}{\beta_i^2 + (\beta_r - k_0)^2} + jP\tan^{-1}\frac{k_0\sqrt{\epsilon_r} - \beta_r}{\beta_i} + jP\tan^{-1}\frac{\beta_r - k_0}{\beta_i} \tag{3.56}$$

For the lossless case β_i is zero and the above integral reduces to

$$\int_{k_0}^{k_0\sqrt{\epsilon_r}} f_{\text{sing}}(\beta)d\beta = P\ln\frac{k_0\sqrt{\epsilon_r} - \beta_r}{\beta_r - k_0} - j\pi P \tag{3.57}$$

The contributions of higher order surface wave modes can be obtained in a similar manner.

Numerical integration over the interval $[k_0\sqrt{\epsilon_r}, \infty]$. The integration over this interval converges very slowly and determines the efficiency of the analysis technique. This integration might consume as much as 80% of the total CPU time because of the fact that the integrand is highly oscillatory and shows slow convergence. The physical explanation for the slow convergence of the integral has been attributed to the fact that the source singularity of the Green's function in the space-domain has been eliminated but spread out in the spectral domain [2]. A number of techniques have been devised to reduce the computational effort. These range from optimizing the number of integration points to extracting the asymptotic value of the integrand [5, 13–15]. The asymptotic extraction technique has been found to be most efficient [16].

The slow convergence of the integral over this interval is due to the static part of the Green's function, and the expansion and testing functions that exist

over the infinite spectral domain. The oscillatory behavior of the integrand results from the finite separation between the expansion and test functions, which give rise to sin or cos variation in the space domain. The oscillation rate increases with the increase in separation distance between the expansion and test functions. An asymptotic extraction procedure has been suggested as the solution to the slow convergence problem. In this approach, the asymptotic part of the Green's function $Q^h(\cdot)$ is subtracted from the Green's function before integration, that is,

$$\int_0^{2\pi}\int_0^{\infty} F^*(J_{mi})Q_{ij}F(J_{nj})\beta d\beta d\alpha = \int_0^{2\pi}\int_0^{\infty} F^*(J_{mi})(Q_{ij} - Q_{ij}^h)F(J_{nj})\beta d\beta d\alpha + Z_{mn}^{hij} \tag{3.58}$$

where

$$Z_{mn}^{hij} = \int_0^{2\pi}\int_0^{\infty} F^*(J_{mi})Q_{ij}^h F(J_{nj})\beta d\beta d\alpha \tag{3.59}$$

The first integral on the RHS of (3.58) now converges faster compared to the original integral, and can be evaluated using any numerical integration scheme in the third range of β integration. The integrand in the second integral is still oscillating and slowly converging. This problem was taken up by Pan et al. [17, 18]. In [17], the integration variables are changed from polar to the Cartesian form where fewer oscillations are experienced. In [18], the authors used wavelet expansions, which have finite support in the spectral domain. Therefore, they could truncate the range of integration variable β. Park et al. have carried out analytical evaluations of Z^h based on roof-top expansion and testing functions [19, 20]. The technique used is the integral transform technique and the resulting expressions are 1-D finite integrals. However, these integrals involve a logarithmic singularity. In another approach, analytical evaluation of Z^h is carried out in the space domain [16]. The basis and testing functions used are piecewise sinusoidal (PWS) pulse functions and semi-infinite traveling-wave mode functions. This approach is applicable to those basis functions that can be fitted into an Nth-order polynomial. Some more details about numerical evaluation over the interval $(0, \infty)$ are included in Appendix 3D.

3.1.4 Basis Functions

The choice of the basis or expansion functions is of prime importance in the method of moments solution. It determines the stability, efficiency, and convergence of the solution. Basis functions suitable for the analysis of microstrip antennas can be divided into two groups: the entire domain basis functions, and the subdomain basis functions. The entire domain basis functions (EB), as the name suggests, are defined over the patch dimensions. They may have edge singularity to better represent the current density at the metal edges.

The complete set of entire domain basis functions for regular shaped geometries such as rectangles, disks, circular rings, a few triangles, and circular sectors are obtained from the eigenfunctions of the geometry. The magnetic wall cavity eigenfunctions are the most suitable and are listed in Chapter 2. The use of entire domain basis functions improves the efficiency of the solution process because only a few of these functions are sufficient to represent the actual current distribution. This is possible only when the patch geometry is unloaded or the effect of loading by the feed is neglected. The entire domain basis functions for a rectangular patch shown in Figure 3.2 are given next.

For the x-directed current

$$J_{mn}(x, y) = \sin\left(\frac{m\pi}{L}[x + L/2]\right)\cos\left(\frac{n\pi}{W}[y + W/2]\right) \tag{3.60}$$

and for the y-directed current

$$J_{mn}(x, y) = \cos\left(\frac{m\pi}{L}[x + L/2]\right)\sin\left(\frac{n\pi}{W}[y + W/2]\right) \tag{3.61}$$

Figure 3.4 illustrates the behavior of several types of basis functions for a rectangular patch. The basis functions are (1, 0), (2, 0), and (2, 1) for the x-directed current, and type (0, 3) for the y-directed current [21].

The entire domain basis functions cannot model an arbitrary current distribution. Subdomain basis functions, on the other hand, can be used in such situations. The subdomain or subsectional basis functions are valid over only a portion of the patch metalization surface, called a *cell*. Therefore, a large number of basis functions are needed to cover the entire patch surface. For smooth variations of the current, about 10 basis functions per wavelength are needed to obtain good results. However, these functions provide the flexibility to represent an arbitrary current distribution on a patch or current distribution on an arbitrarily shaped patch antenna. For example, the junction effect at the probe-patch junction [22] and the proximity effect of the microstrip feed can

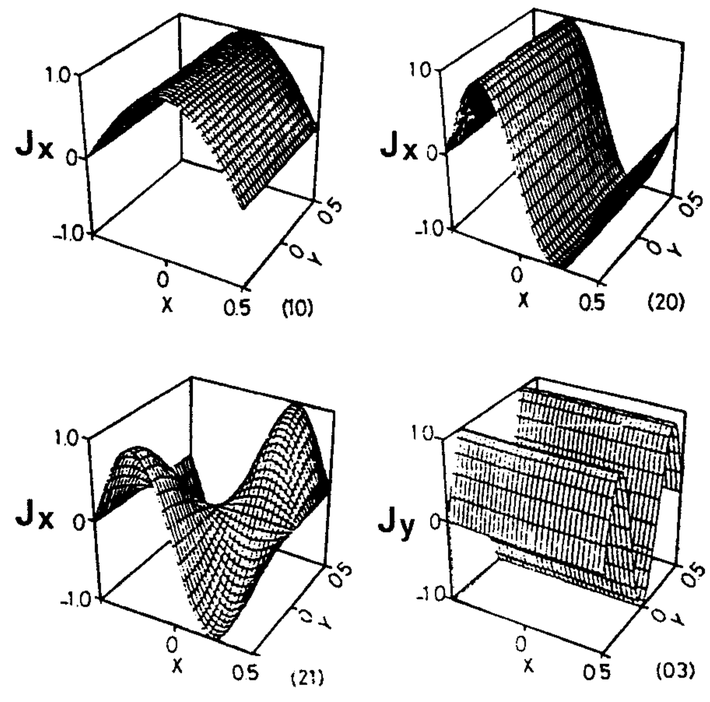

Figure 3.4 Some entire domain basis functions (without edge singularity) for the surface current on a rectangular patch. The bases shown are (1, 0), (2, 0), and (2, 1) for the x-directed current and (0, 3) for the y-directed current. (From [21]. © 1990 IEE. Reprinted with permission.)

be easily modeled [23] using subdomain basis functions. The most popular subdomain basis functions are pulse basis functions, piecewise sinusoidal basis functions (PWS), and roof-top basis functions. These basis functions are separable in nature and are characterized by uniform distribution along the direction transverse to the current.

The current density for a subdomain basis function centered at (x_m, y_n) can be expressed as

$$J_{mn}(x, y) = J_m(x)J_n(y) \tag{3.62}$$

Let the current to be modeled be x directed so that the current is uniform along the y direction, that is,

$$J_n(y) = \begin{cases} 1/h_y & \text{for } |y - y_n| < h_y/2 \\ 0 & \text{elsewhere} \end{cases} \tag{3.63}$$

and

$$J_m(x) = \begin{cases} 1/h_x & \text{for } |x - x_m| < h_x/2 \\ 0 & \text{elsewhere} \end{cases} \tag{3.64a}$$

for pulse-pulse basis functions [see Figure 3.5(a)] and

$$J_m(x) = \begin{cases} 1 - (x_m - x)/h_x & \text{for } x_m - h_x \le x \le x_m \\ 1 - (x - x_m)/h_x & \text{for } x_m \le x \le x_m + h_x \\ 0 & \text{elsewhere} \end{cases} \tag{3.64b}$$

for roof-top or piecewise linear (PWL)-pulse basis functions [see Figure 3.5(b)] and

$$J_m(x) = \begin{cases} \sin[k(x - (x_m - h_x))]/\sin(kh_x) & \text{for } x_m - h_x \le x \le x_m \\ \sin[k((x_m + h_x) - x)]/\sin(kh_x) & \text{for } x_m \le x \le x_m + h_x \\ 0 & \text{elsewhere} \end{cases} \tag{3.64c}$$

for piecewise sinusoidal (PWS)-pulse basis functions [see Figure 3.5(c)]. Here h_x and h_y are discretization lengths along x and y directions, respectively.

Figure 3.6 shows the input impedance of a probe-fed rectangular patch. The effect of entire domain and subdomain basis functions on the input impedance is studied. As shown in the figure, the two choices yield approximately the same result near the resonant frequency. However, the difference increases as one goes away from resonance. The resulting current distribution is likely to affect the cross-polar pattern. Thus, one or two entire domain basis functions may be used near resonance, but it is prudent to use subdomain basis functions when studying a single patch or an array away from resonance or when the cross-polar behavior is needed.

Input impedance of an aperture-coupled microstrip antenna has been determined using the spectral-domain approach, cavity model, and transmission line model [24]. These results are compared against measurements. The spectral-domain approach has been found to be more accurate.

Making an educated guess in deploying the basis functions helps to reduce the computation time. For example, in a rectangular patch the current distribution in the direction transverse to the resonance direction is expected to be slowly varying. Therefore, the number of basis functions in the transverse direction can be reduced without a significant penalty, resulting in large savings in computation time. Figure 3.7 [1] shows how the input impedance of a rectangular patch converges when the number of roof-top basis functions in

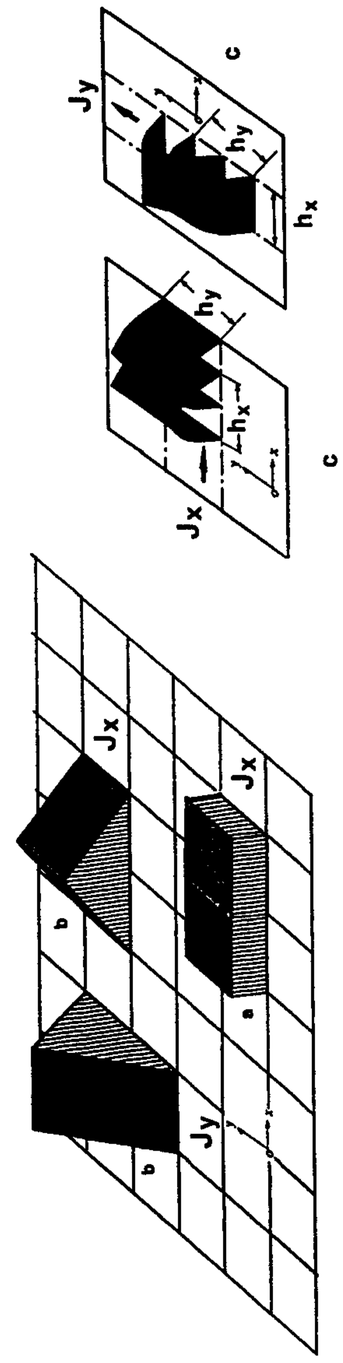

Figure 3.5 Subdomain basis functions defined over a pair of cells: (a) Pulse-pulse basis functions J_x, (b) roof-top basis functions J_x and J_y, and (c) piecewise sinusoidal-pulse basis functions J_x and J_y.

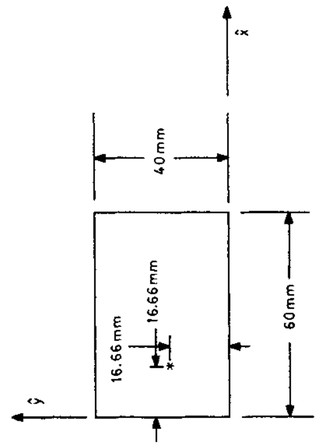

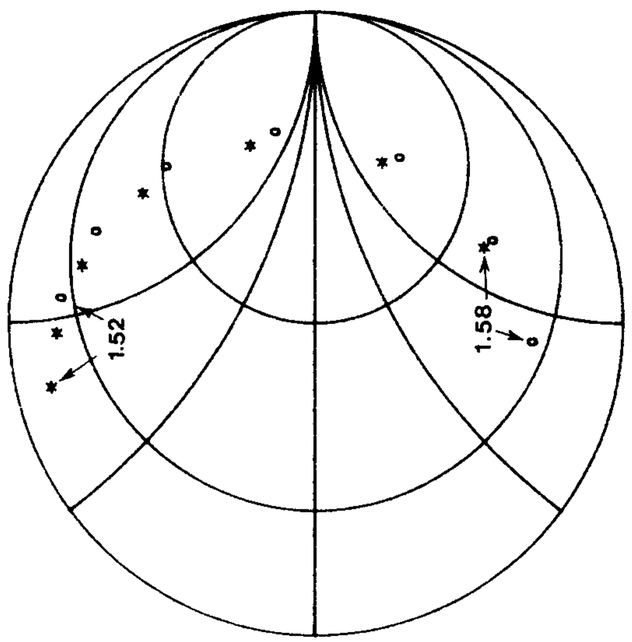

Figure 3.6 Input impedance of a rectangular patch comparing the use of entire domain and subdomain basis functions. The patch parameters are $L = 60$ mm, $W = 40$ mm, $\epsilon_r = 2.55$, $h = 1.28$ mm, and $\tan\delta = 0.002$. The probe feed is located at $x = 16.66$ mm, $y = 20$ mm. Frequency range is from 1.52 GHz increasing clockwise to 1.58 GHz with a step of 0.01 GHz. o, entire domain cosine basis functions; *, roof-top basis functions. (From [1]. © 1989 Peter Peregrinus. Reprinted with permission.)

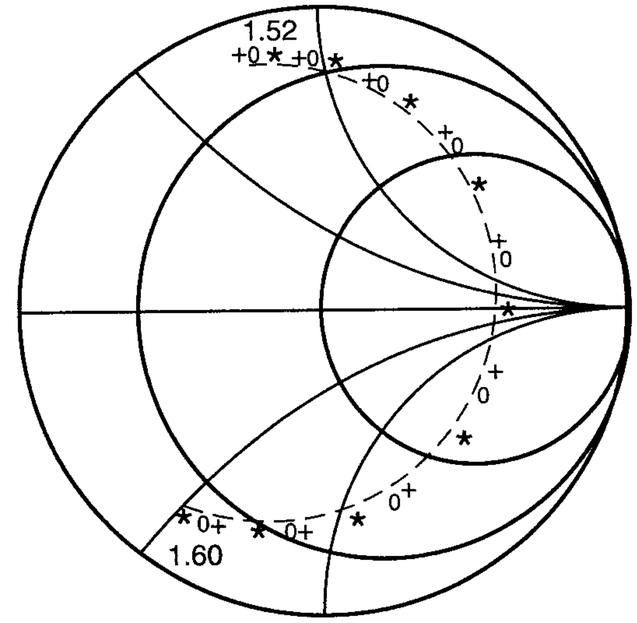

Figure 3.7 Effect of the number of basis functions (along the width) on the input impedance of a rectangular patch antenna. The patch parameters and the feed parameters are the same as in Figure 3.6. Frequency range is from 1.52 GHz increasing clockwise to 1.60 GHz with a step of 0.01 GHz. +, 9 by 7 cells; 0, 9 by 5 cells; *, 9 by 3 cells. (From [1]. © 1989 Peter Peregrinus. Reprinted with permission.)

the transverse direction is varied at frequencies near the first resonance. Note that the resonant frequency changes by only 0.3% when using three basis functions as opposed to using seven. However, the input impedance changes by approximately 20%. Thus, a rough study of the antenna's resonant frequency and radiation patterns can be performed quickly at low cost. The final analysis can then be performed using additional basis functions.

3.1.5 Mathematical Model of Excitation

To analyze the microstrip antenna, it is necessary to determine the impedance matrix as well as the voltage vector $[V]$, which represents the antenna excitation. Input impedance values depend on the model selected for the excitation. In practice, a number of excitation techniques are available, including probe excitation, coplanar microstrip feed, proximity coupling to the microstrip line underneath the patch, and aperture coupling of the microstrip line. Advantages and disadvantages of these excitation mechanisms are discussed in Chapter 1. Mathematical modeling of excitation is described next.

Probe Feed

The excitation fields are rarely known in a direct way, except in a few cases, such as excitation by a plane way or with a series voltage gap generator. Therefore, the excitation fields must usually be computed from a given distribution of currents and charges [25]. When a microstrip antenna is excited by a coaxial probe, it gives rise to a junction at the position of attachment of probe and patch. Modeling a coaxial probe feed involves two aspects: a model for the probe current and another model for the junction effect. The simplest model for probe current is a vertical filament of unit current acting at some point on the patch metalization, that is, $\bar{J}_s = \hat{z}\delta(x_0)\delta(y_0)$. A rigorous model for the probe part is a magnetic frill current at the shorted coaxial aperture. The end result of this model can be described in the form of probe reactance. An accurate expression for the probe reactance is given in Section 2.9.

It is necessary to accurately model the current distribution near the probe-patch junction because it affects the input impedance and cross-polar pattern. A survey of various models for probe-fed patches is given in [22]. An accurate model of probe excitation valid for razor testing has been developed in [26]. Hall and Mosig [27] have used a full-wave moment method based on multiple triangular basis functions on the probe, subdomain basis functions on the patch, a TEM magnetic frill current at the coaxial aperture, and a simple attachment mode at the probe-patch attachment points. A half-triangle function is used at the bottom of the coaxial feed to model the nonzero current flowing from the coaxial aperture. Similar models have been developed by others [28, 29].

Figure 3.8 shows the radiation patterns for the TM_{10} mode of a probe-fed rectangular patch antenna [1]. Subdomain roof-top functions are used to model the patch current accurately. The cross-polar pattern is due mostly to the excitation current spreading out from the coaxial probe onto the patch, and to the current in the probe. The effect of the probe position on the cross-polar pattern is also shown in Figure 3.8. Comparison of Figures 3.8(a) and (b) shows that the copolar level remains unaffected by the position of the feed. However, the cross-polar level increases as the feed is moved from the middle of the patch width y = 20 mm to y = 16.66 mm.

Microstrip Edge Feed

For the modeling of microstrip line feed as shown in Figure 3.9(a), several possibilities exist. The simplest one neglects the microstrip line in the analysis and uses a vertical filament current like that in a probe at the edge of the patch, that is, $\bar{J}_s = \hat{z}\delta(z)$. This approach shown in Figure 3.9(b) does not include the effect of step-in-impedance discontinuity at the microstrip line-patch junction. A better approach is to include a finite section of the microstrip

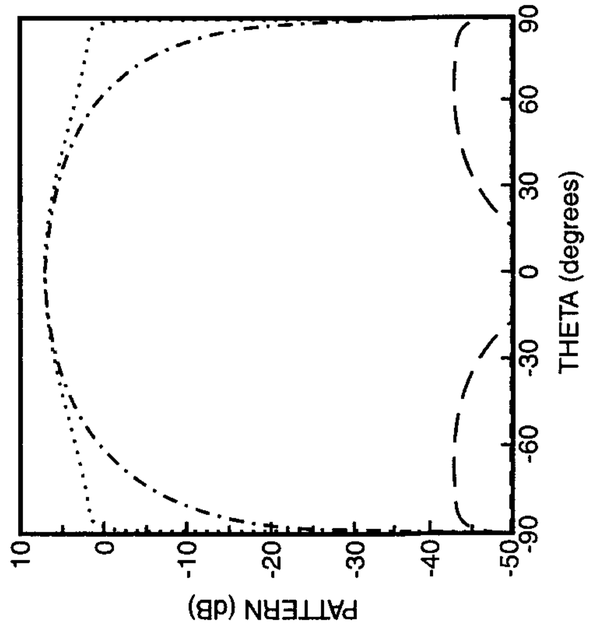

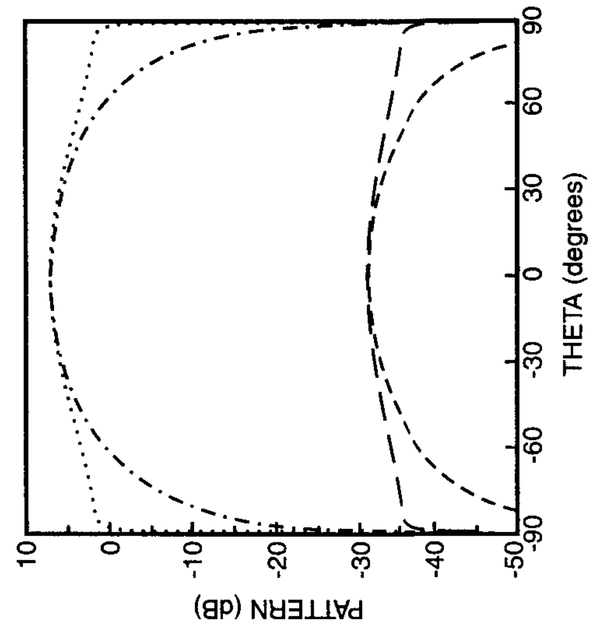

Figure 3.8 Radiation patterns for the TM_{10} mode of a rectangular patch with different feed points. The patch parameters are the same as in Figure 3.6. Frequency is 1.565 GHz. (a) Probe feed at x = 16.66 mm, y = 16.66 mm. (b) Probe feed at x = 16.66 mm, y = 20 mm. ....., E-plane copolar pattern; -----, H-plane co-polar pattern; — — —, E-plane cross-polar pattern; — — —, H-plane cross-polar pattern. (From [1]. © 1989 Peter Peregrinus. Reprinted with permission.)

feed line in the analysis, and to introduce a series current generator at the point where the feed line has been truncated [see Figure 3.9(c)] [25]. The current source can be modeled by a half roof-top function with unit current. The input impedance in these models is defined from the ratio of voltage and feed current at the point of excitation.

In a rigorous approach, the excitation is described in terms of incident TEM wave on the microstrip feed line. A reflected wave is produced at the step-in impedance discontinuity. The reflection coefficient is determined from these waves and leads to the input impedance. This approach requires special basis functions like piecewise sinusoids and $\exp(\pm jkx)$ to represent the traveling waves on the semi-infinite feed line. Proximity coupling and aperture coupling of patch antennas can also be described in terms of traveling waves on the feed. Aperture coupling is described next.

Aperture-Coupled Microstrip Feed

Microstrip antennas with aperture-coupled microstrip feed have been analyzed using the spectral-domain approach. The geometry of this antenna is shown

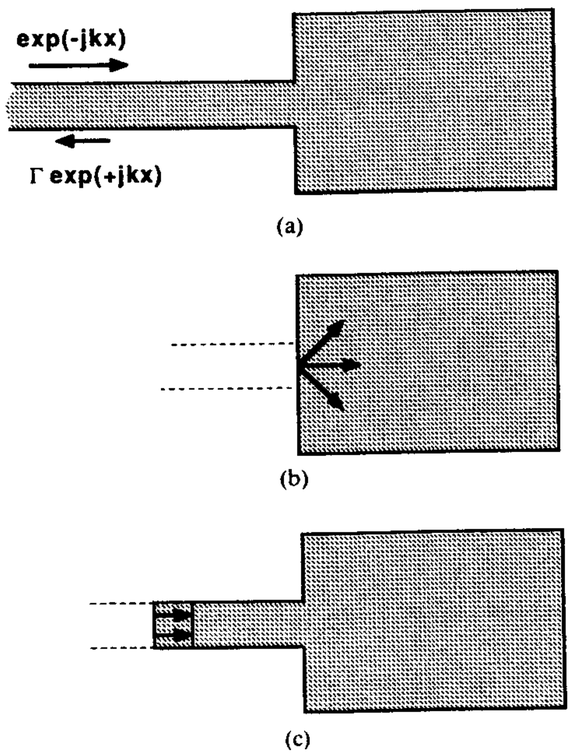

Figure 3.9 Mathematical model of coplanar microstrip feed. (a) Rigorous feed model in terms of incident and reflected traveling waves. (b) Approximate feed model totally neglecting the feed line. (c) Approximate feed model partially neglecting the feed line. (From [25]. © 1988 IEEE. Reprinted with permission.)

in Figure 3.10(a). The equivalence principle and the integral equation approach are used to formulate the full-wave analysis of this type of antenna. According to the equivalence principle, the coupling aperture in the ground plane can be replaced by an equivalent magnetic current sitting on the closed ground plane as shown in Figure 3.10(b). As a result of closing the aperture, the problem can be formulated separately in the feed region (region a) and the patch region (region b). Sources in region a are the electric surface current J_f on the feed line and the equivalent magnetic current $M_a = M_s$ on the aperture. Sources in region b are the electric surface current J_p on the patch and the equivalent magnetic current $M_b = -M_s$ on the aperture. The fields produced

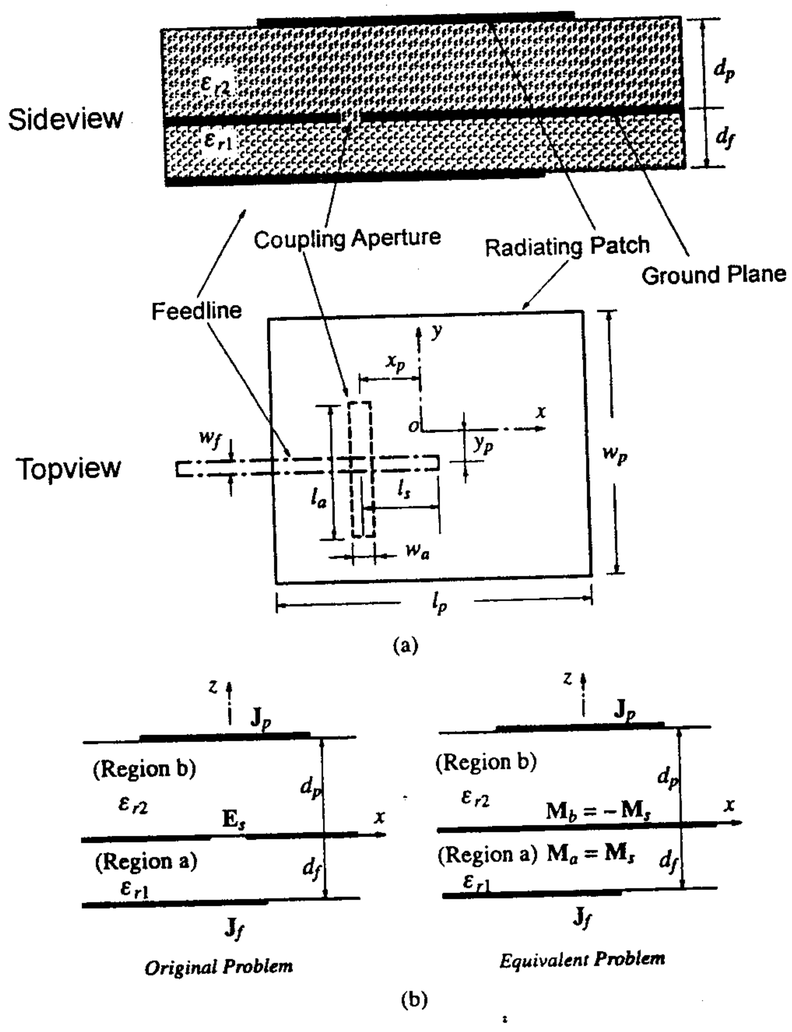

Figure 3.10 An aperture-coupled microstrip antenna. (a) Side view and top view of the antenna. (b) Use of the equivalence principle to split the given problem into two simpler problems. (From [23]. © 1995 IEEE. Reprinted with permission.)

by these sources are obtained using the spectral-domain Green's functions. The boundary conditions are

$$E_b(J_p) + E_b(M_b) = 0 \quad \text{on conducting path} \tag{3.65a}$$

$$E_a(J_f) + E_a(M_a) = 0 \quad \text{on the feed line} \tag{3.65b}$$

$$H_b(J_p) + H_b(M_b) = H_a(J_f) + H_a(M_a) \quad \text{on the aperture} \tag{3.65c}$$

These boundary conditions are enforced by selecting the testing functions and using the moments method in spectral domain. The resulting integral equations are solved for the unknown currents J_p, M_s, and J_f.

The electric current on the patch and the magnetic current in the aperture are expanded in terms of subdomain basis functions. The currents on the microstrip feed line are expanded in terms of traveling-wave modes away from the coupling aperture and subdomain basis functions near the open end. The current on the feed line should be modeled over several wavelengths. A possible deployment of basis functions on the feed line is shown in Figure 3.11. Other details for this antenna can be found in [1, 23, 30, 31]. The following expressions for $f_c(x)$, $f_s(x)$, and $f_n^f(x)$ can be used [23]:

$$f_c(x) = \cos(k_e x) \quad \text{for } -\infty < x < -\pi/2k_e \tag{3.66a}$$

$$f_s(x) = \sin(k_e x) \quad \text{for } -\infty < x < 0 \tag{3.66b}$$

$$f_n^f(x) = \frac{\sin(k_e(h_f - |x + nh_f|))}{\sin(k_e h_f)} \quad \text{for } |x + nh_f| < h_f \tag{3.66c}$$

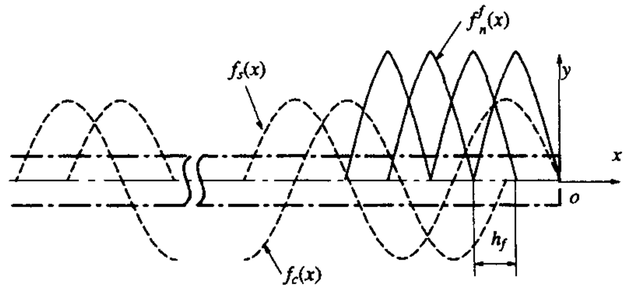

Figure 3.11 A possible deployment of traveling-wave modes and subdomain basis functions to model the electric current on the microstrip feed line of an aperture-coupled microstrip antenna. Traveling-wave mode is realized from $\cos(x)$ and $\sin(x)$ functions.

where $k_e = 2\pi\sqrt{\epsilon_{re}}/\lambda_0$ is the wave number in the feed microstrip line and h_f is the length of the piecewise sinusoidal basis function. Traveling waves are realized through $\sin(x)$ and $\cos(x)$ functions, (3.66b) and (3.66a), respectively.

It is necessary to use subdomain basis functions for modeling the patch current in this case because, as observed in [23], the current is very much disturbed about the aperture region in the patch. This is due to the proximity effect of the aperture. This current distribution cannot be modeled by entire domain basis functions alone, and is shown in Figure 3.12 [23].

3.1.6 Applications of the Spectral-Domain Technique to Microstrip Antennas

The integral equation solution in the spectral domain has been used to analyze various microstrip antenna configurations. These include various types of patch

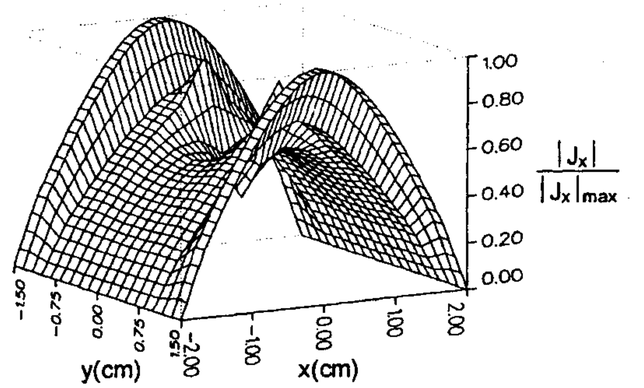

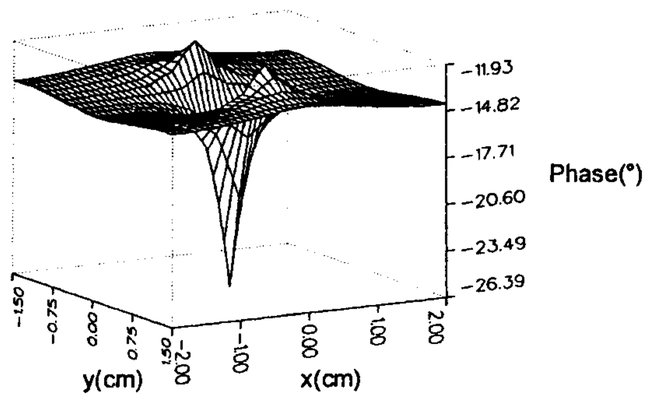

Figure 3.12 Longitudinal electric surface current distribution for TM_{10} mode of a rectangular patch at $f = 2.23$ GHz. $\epsilon_{r1} = \epsilon_{r2} = 2.54$, $d_f = d_p = 1.66$ mm, $w_f = 4.4$ mm, $x_p = y_p = 0$, $\ell_s = 1.2$ cm, $\ell_a = 1.1$ cm, $w_a = 1.6$ mm, $\ell_p = 4$ cm, and $w_p = 3$ cm. (From [23]. © 1995 IEEE. Reprinted with permission.)

shapes, feed types, stacked geometries, anisotropic substrates, and array geometries. Some of the prominent studies utilizing this technique are [3, 4, 13] for the basic technique and the analysis of a rectangular patch, [32–34] for the circular patch, [34] for the elliptic patch, [35] for a circular ring microstrip antenna, [31] for a printed slot antenna, [36] for a printed dipole, [37] for an arbitrary shaped geometry, [3] for patch on anisotropic substrate, [38] for a proximity-coupled microstrip fed antenna, [23, 31, 39, 40] for an aperture-coupled microstrip antenna, [41] for a circularly polarized microstrip antenna, [42, 43] for a stacked antenna configuration, [44, 45] for a multilayered printed antenna fed by multiple feed ports, [13] for mutual coupling between microstrip antennas, infinite array of patches [33, 46], and computation of radar cross section [37, 47].

3.2 Mixed-Potential Integral Equation Analysis

It was mentioned in the last section that the MPIE (mixed-potential integral equation) approach is computationally more efficient than the integral equation analysis described in the spectral domain. Most commercial integral equation solvers use this technique. We give here a brief description of this technique. For more details the reader is referred to [1, 5, 6, 15, 25, 26, 48].

The starting point for the MPIE is the integral equation arrived at from the boundary condition for the electric field at the patch metalization, that is,

$$\hat{z} \times [\overline{E}(\bar{J}_e) + \overline{E}(\bar{J}_s) = Z_s \bar{J}_s] \quad \text{for all points on the patch metalization} \tag{3.67}$$

where $\overline{E}(\bar{J}_e)$ is the electric field due to excitation current, $\overline{E}(\bar{J}_s)$ is the electric field due to the induced current on the patch, and Z_s is the surface impedance of the patch metalization. For a perfect conductor Z_s is zero.

Electric field Green's functions were employed in the spectral-domain approach. As the name suggests, different types of potential Green's functions are used in MPIE to set up the integral equation. Among several possible choices, Sommerfeld's choice of potentials is the most popular approach for solving stratified media problems [5]. Sommerfeld assumes $\overline{F} = 0$ in the absence of magnetic currents. Scalar and vector potentials are used in MPIE.

The vector potential $\overline{A}$ and scalar potential V are solutions of the Helmholtz wave equations. In differential form they are defined as

$$\mu \overline{H} = \nabla \times \overline{A} \tag{3.68a}$$

$$\overline{E} = -j\omega \overline{A} - \nabla V \tag{3.68b}$$

The potentials are related through the Lorentz gauge condition

$$\nabla \cdot \overline{A} + j\omega\mu\epsilon V = 0 \tag{3.69}$$

The potentials are related to the corresponding Green's functions through an integral and are defined as

$$\overline{A}(\bar{r}) = \int_S \overline{\overline{G}}_A(\bar{r}|\bar{r}') \cdot \bar{J}_s(\bar{r}')dS' \tag{3.70a}$$

$$V(\bar{r}) = \int_S G_V(\bar{r}|\bar{r}')\, q_s(\bar{r}')dS' \tag{3.70b}$$

where S refers to the patch metalization surface. Here, a dyadic is represented by a double bar above the corresponding symbol. Dyadics are used for representing Green's functions relating an elementary source (Hertz dipole) to the fields and vector potentials that it creates. The unknowns, current density J_s and charge density q_s, are not independent and are related through the continuity equation

$$\nabla \cdot \bar{J}_s + j\omega q_s = 0 \tag{3.71}$$

To set up the integral equation, we use the boundary condition (3.67) for the tangential components, field expression (3.68b), and potentials (3.70) to obtain for a perfect conductor

$$\overline{E}(\bar{J}_e) = j\omega \int\int_S \overline{\overline{G}}_A(\bar{r}|\bar{r}') \cdot \bar{J}_s(\bar{r}')dS' + \nabla \int\int_S G_V(\bar{r}|\bar{r}')\, q_s(\bar{r}')dS' \tag{3.72}$$

Equation (3.72) is the mixed-potential integral equation that will be solved for the unknowns J_s and q_s for a microstrip patch antenna.

3.2.1 Potential Green's Functions in the Spectral Domain

A horizontal electric dipole (HED) at an interface needs two components of magnetic vector potential $\overline{A}$: a component parallel to the source and A_z, where the z direction is normal to the interface. Hence, the dyadic $\overline{\overline{G}}_A$ is given in this approach by

$$\overline{\overline{G}}_A = (\hat{x}G_A^{xx} + \hat{z}G_A^{zx})\hat{x} + (\hat{y}G_A^{yy} + \hat{z}G_A^{zy})\hat{y} + \hat{z}G_A^{zz}\hat{z} \tag{3.73}$$

Here, the scalar component G_A^{pq} represents the p component of the vector potential created by a q-directed elementary dipole of unit moment.

The normal components of the fields E_z and H_z are calculated in the space domain according to [use (3.68b) in (3.69)]

$$j\omega\eta\epsilon\overline{E} = k^2\overline{A} + \nabla\nabla\cdot\overline{A} \quad k^2 = \omega^2\mu\epsilon \tag{3.74}$$

and

$$\mu\overline{H} = \nabla\times\overline{A} \tag{3.75}$$

with $\overline{A}$ obtained from

$$(\nabla^2 + k^2)\overline{A} = -\mu\overline{J} \tag{3.76}$$

The potential Green's functions are derived in Appendix 3C. For an x-directed Hertzian dipole lying on the interface of a grounded substrate of thickness h and dielectric constant ϵ_r, the Green's functions in the spectral domain are [see (3C.27)–(3C.29)] as follows:

$$\tilde{G}_A^{xx} = \frac{\mu_0}{2\pi}\frac{1}{D_{\mathrm{TE}}} = \tilde{G}_A^{yy} \tag{3.77}$$

$$\tilde{G}_A^{zx} = \frac{\mu_0}{2\pi}\frac{jk_x(\epsilon_r - 1)}{D_{\mathrm{TE}}D_{\mathrm{TM}}} \tag{3.78}$$

$$\tilde{G}_V = \frac{1}{2\pi\epsilon_0}\frac{N}{D_{\mathrm{TE}}D_{\mathrm{TM}}} \tag{3.79}$$

where

$$N = u_0 + u\tanh(uh) \tag{3.80a}$$

$$D_{\mathrm{TE}} = u_0 + u\coth(uh) = T_e/\sin(k_1 h) \tag{3.80b}$$

$$D_{\mathrm{TM}} = u_0\epsilon_r + u\tanh(uh) = jT_m/\cos(k_1 h) \tag{3.80c}$$

$$u_0^2 = -k_z^2 = k_x^2 + k_y^2 - k_0^2 = k_\rho^2 - k_0^2 \Rightarrow u_0 = jk_2 \tag{3.81a}$$

$$u^2 = -k_z^2 = k_x^2 + k_y^2 - k_0^2\epsilon_r = k_\rho^2 - k_0^2\epsilon_r \Rightarrow u = jk_1 \tag{3.81b}$$

and T_e and T_m are defined by (3.2). In (3.77)–(3.79), both the source and observer are assumed to be located on the interface. The radial spectral variable in this section is denoted by k_ρ in conformity with that in the literature, and $k_\rho = \lambda + j\nu$ where λ is the real part of k_ρ and ν the imaginary part.

3.2.2 Potential Green's Functions in the Space Domain

In MPIE the integral equation is solved in the space domain. For this, the spectral-domain potential Green's functions should be transformed to the space domain. The potential Green's functions in spectral domain are derived in Appendix 3C. These functions depend on k_x and k_y only through the radial spectral variable k_ρ. For functions exhibiting such dependence, the inverse Fourier transform becomes Bessel-Fourier or Hankel integral transform, and can be written as

$$f(\rho) = \int_0^\infty J_0(k_\rho\rho)\,\tilde{f}(k_\rho)k_\rho dk_\rho \tag{3.82}$$

where ρ is the radial distance between the source and field points, and $J_0(\cdot)$ is the zeroth-order Bessel function of the first kind. The replacement of the double Fourier transform with the Hankel transform is of great utility when performing numerical evaluation of space-domain quantities based on (3.82).

Using transformation (3.82), the Green's functions in the space domain are obtained as

$$G_A^{xx}(\overline{\rho}/\overline{\rho}') = \frac{\mu_0}{2\pi}\int_0^\infty J_0(k_\rho R)\frac{k_\rho}{D_{\mathrm{TE}}}dk_\rho \quad R = |\overline{\rho} - \overline{\rho}'|$$

or

$$G_A^{xx}(\overline{\rho}/0) = A_x(\overline{\rho}) = \frac{\mu_0}{2\pi}\int_0^\infty J_0(k_\rho\rho)\frac{k_\rho}{D_{\mathrm{TE}}}dk_\rho \tag{3.83a}$$

Similarly,

$$G_V(\overline{\rho}/0) = V(\overline{\rho}) = \frac{1}{2\pi\epsilon}\int_0^\infty J_0(k_\rho\rho)\frac{k_\rho N}{D_{\mathrm{TE}}D_{\mathrm{TM}}}dk_\rho \tag{3.83b}$$

and

$$G_A^{zx}(\bar{\rho}|0) = A_{zx}(\bar{\rho}) = j(\epsilon_r - 1)\frac{\mu_0}{2\pi}\int_0^\infty J_0(k_\rho\rho)\frac{k_x k_\rho}{D_{\mathrm{TE}} D_{\mathrm{TM}}}\,dk_\rho \quad (3.83c)$$

The integrands in (3.83) suffer from branch point and pole singularities because of D_{TE} and D_{TM}. Therefore, these singularities are separated before integration. Numerical evaluation of (3.83) is discussed in Appendix 3D.

3.2.3 Results for Potentials for a Single-Layer Microstrip Structure

Vector potential A_x for an x-directed dipole at the interface is plotted in Figure 3.13. The curves of Figures 3.13(a) and (b) give, respectively, the modulus and phase of Q as a function of normalized radial distance $k_0\rho$, and Δ as a parameter defined as $\Delta = k_0 h\sqrt{\epsilon_r - 1}$. The ratio Q is defined as

$$Q = \frac{A_x}{A_x(\epsilon_r = 1)} \quad (3.84)$$

We can observe from Figure 3.13(a) that the value of A_x differs slightly from its homogeneous counterpart, that is, A_x is almost independent of the substrate permittivity. The modulus of Q increases with distance from unity to the asymptotic limit $\tan^2\Delta/\Delta^2$. The phase of Q goes to zero in the near and far fields and reaches a maximum in the middle. The value of the maximum phase depends on the substrate thickness and permittivity. For a thin substrate with $\epsilon_r = 2.2$ and $\Delta = 0.3$, the maximum phase is only 0.23° and the $|Q|$ ranges between 1 and 1.08. Finally, it can be said that for thin substrates the vector potential can be replaced by its homogeneous value, and therefore the Sommerfeld integral may not be evaluated.

The behavior of the scalar potential V due to a point charge (3.83b) is very different than that of vector potential. The modulus and phase of normalized scalar potential $4\pi\epsilon_0\lambda_0 V$ as a function of normalized radial distance are plotted in Figures 3.14(a) and (b), respectively, for $\epsilon_r = 2.2$. The value of V is seen to change rapidly with distance. The modulus V curves of Figure 3.14(a) can be divided into three regions: (1) the near-field region in which the variation is of the type $1/\rho$, similar to the static case; (2) the far-field region with behavior $1/\sqrt{\rho}$; and (3) the transition region in between. The transition region is marked by rapid variation of phase [see Figure 3.14(b)].

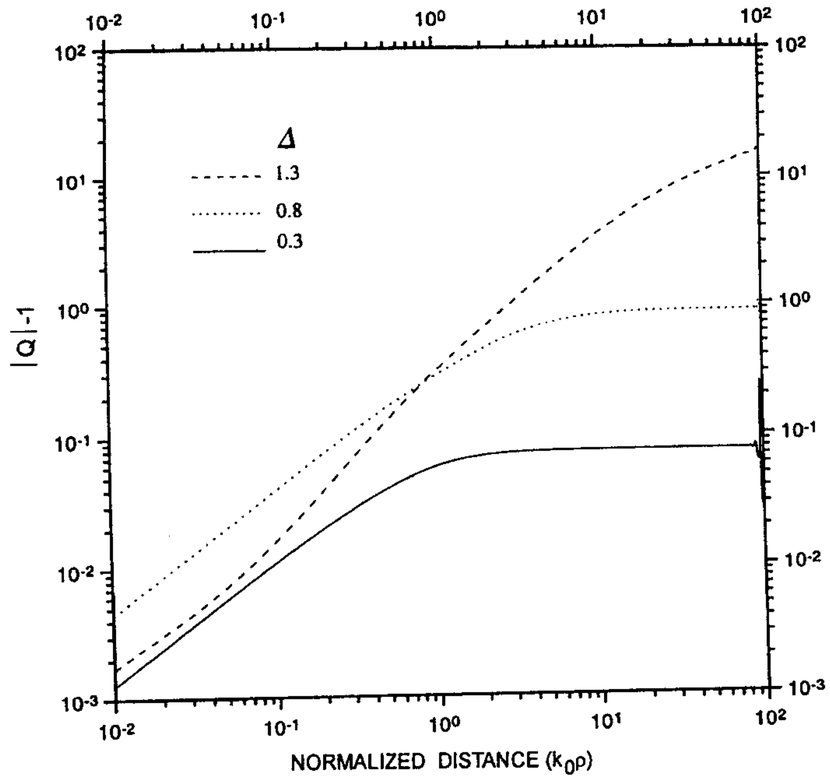

(a)

Figure 3.13 Variation of Q with normalized radial distance for a grounded substrate with $\epsilon_r = 2.2$. Q is the complex ratio $A_x(\epsilon_r)/A_x(\epsilon_r = 1)$: (a) Modulus of Q and (b) phase of Q.

3.2.4 Integral Equation Solution Using Method of Moments

The integral equation (3.72) can be solved using the method of moments [10]. This technique is discussed in detail in Section 3.1 for the spectral-domain approach. The steps specific to the space-domain approach are described next.

In addition to the basis functions for the unknown current, one needs to define the basis functions for the charge density also in MPIE. The two are related to each other through the continuity equation (3.71). For example, if the current density is described in terms of roof-top basis functions, the corresponding charge density functions are pulse doublet functions. These basis functions are shown in Figure 3.15(a) [26]. Because the current becomes zero at the ends of roof-top functions, it is necessary to have some overlap between the adjacent basis functions in order for them to properly represent the actual current distribution. The overlap is half the cell size. If the testing function is

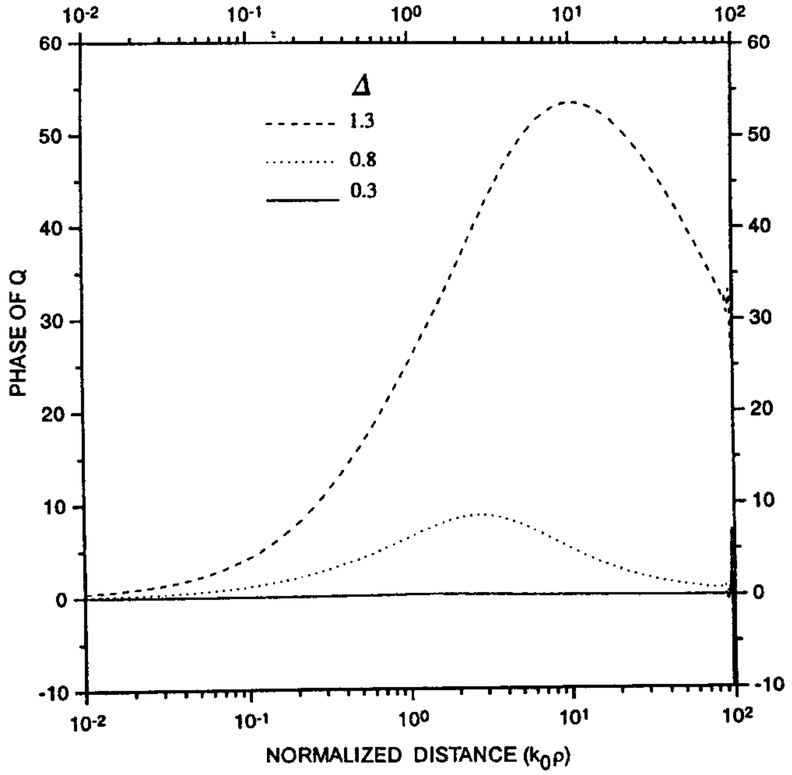

(b)

Figure 3.13 (continued).

another roof-top function, the procedure is called the *Galerkin procedure*, but the process becomes razor testing if the test function is a 1-D pulse function. Razor testing is selected here because of its efficiency. Testing is done along the line segment linking the centers of adjacent cells as shown in Figure 3.15(b). Razor testing reduces the computational effort because only a line integral is required with testing, whereas roof-top testing involves surface integration over the domain of testing function.

Let us define $\overline{T}_i$ as the vector roof-top function associated with two adjacent cells S_i^+ and S_i^- as shown in Figure 3.15(b). The union of these two cells is denoted by S_i. In general, we need to consider N_x x-directed basis functions and y-directed functions, the total number of basis functions are thus $N = N_x + N_y$, that is,

$$\overline{T}_i = \begin{cases} \hat{x}T_{ix}, & i = 1, 2, \ldots, N_x \\ \hat{y}T_{iy}, & i = N_x + 1, \ldots, N \end{cases} \tag{3.85}$$

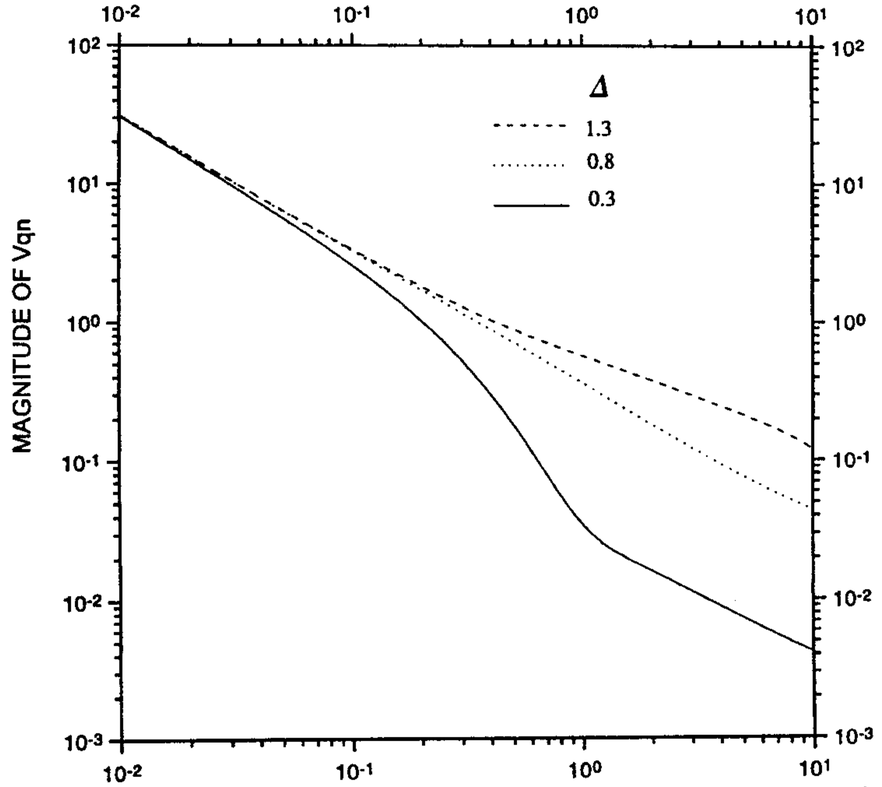

(a)

Figure 3.14 Variation of the normalized scalar potential with normalized radial distance for a grounded substrate with $\epsilon_r = 2.2$: (a) Modulus of scalar potential and (b) phase of scalar potential.

The unknown current and charge densities are expressed as

$$\overline{J}_s = \sum_{i=1}^{N} \alpha_i \overline{T}_i \tag{3.86a}$$

$$q_s = \sum_{i=1}^{N} \alpha_i \Pi_i \tag{3.86b}$$

where α_i are the unknown complex coefficients. The charge density basis functions obtained from the continuity equations (3.71) and (3.86) are

$$\Pi_i = -\nabla \cdot \overline{T}_i / j\omega \tag{3.87}$$

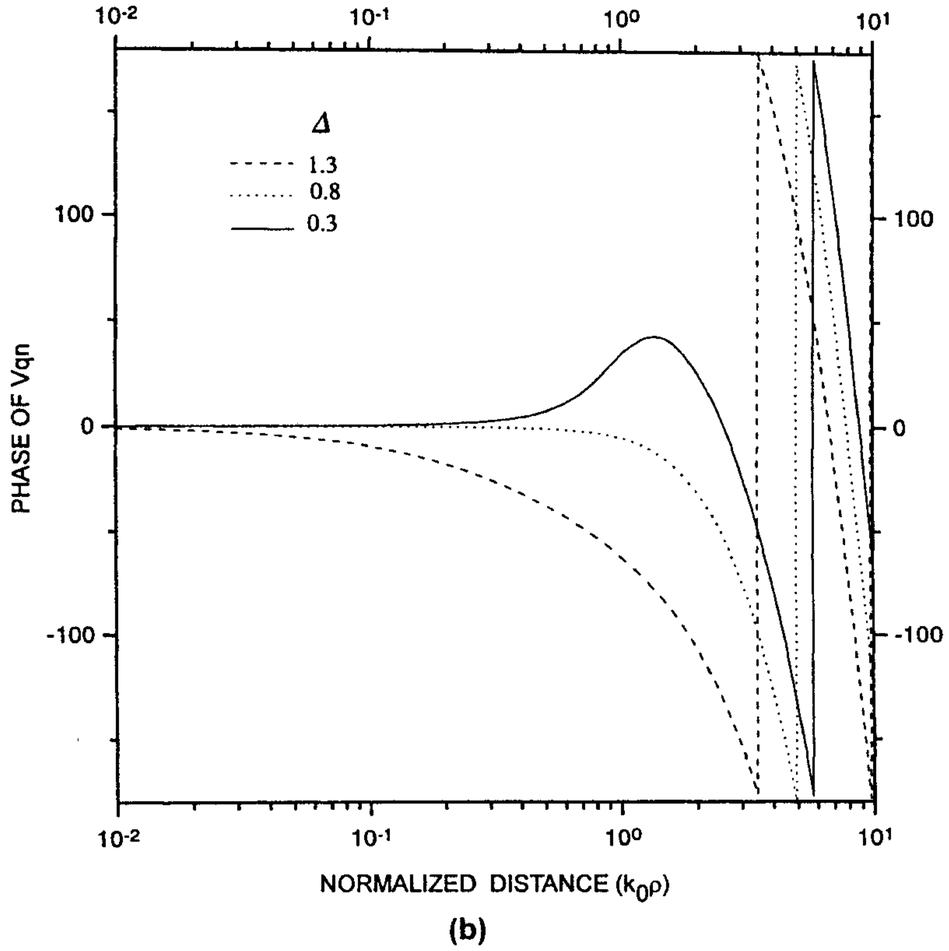

Figure 3.14 (continued).

Applying the method of moments technique yields a matrix equation [25]

$$[Z][\alpha] = [b] \tag{3.88}$$

The elements of the impedance matrix are given by

$$Z_{ij} = a_{ij} + v_{ij} \tag{3.89}$$

where a_{ij}, the contribution from $\overline{A}$ for razor testing, is

$$a_{ij} = j\omega \int_{C_i} d\bar{l} \cdot \iint_{S_j} \overline{\overline{G}}_A(\overline{\rho}|\overline{\rho}') \cdot \overline{T}_j(\overline{\rho}')dS' \tag{3.90}$$

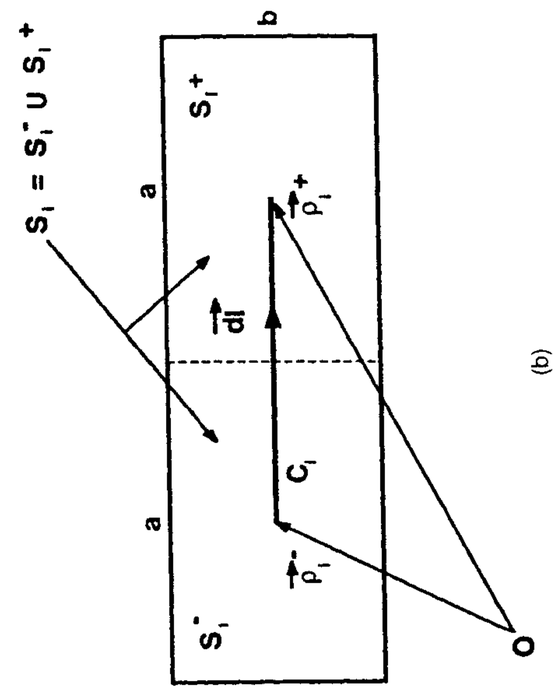

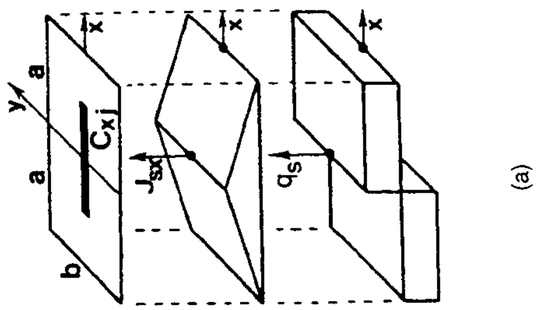

Figure 3.15 (a) Illustration of roof-top current basis function and the related charge density basis function. (From [26]. © 1985 IEE. Reprinted with permission.) (b) Razor testing segment C_i with its ends coinciding with the centers of adjacent cells S_i^- and S_i^+. (From [25]. © 1985 IEE. Reprinted with permission.)

The testing function for the scalar potential is derived from the testing function for the vector potential. Razor testing or pulse testing for the vector potential now becomes delta function sampling at ρ_i^+ and ρ_i^-, that is,

$$v_{ij} = \frac{1}{j\omega}\int\int_{S_j} [G_V(\overline{\rho}_i^+|\overline{\rho}') - G_V(\overline{\rho}_i^-|\overline{\rho}')]\Pi_j(\overline{\rho}')dS' \qquad (3.91)$$

where ρ_i^+ and ρ_i^- denote the centers of the cells and S_i^+ and S_i^-, respectively. The element b_i of the excitation vector is given by

$$b_i = \int_{C_i} \overline{E}^e(\overline{\rho}) \cdot d\overline{l} \qquad (3.92)$$

The line integral in (3.90) can be approximated by the values of the integrand at ρ_i^+ and ρ_i^- because the vector potential is slowly varying over the cell, that is,

$$a_{ij} = j\omega\int\int_{S_j} [\overline{G}_A(\overline{\rho}_i^+|\overline{\rho}') + \overline{G}_A(\overline{\rho}_i^-|\overline{\rho}')]\overline{T}_j(\overline{\rho}')dS' \qquad (3.93)$$

Roof-top testing with roof-top basis functions and point matching with pulse basis functions are also discussed in [25].

Efficient Computation of the Impedance Matrix

The evaluation of the impedance matrix of (3.89) requires a large amount of computation. For a rectangular patch divided into 10×10 cells, the size of the matrix is 180. Hence, the number of elements in the matrix is 32,400. Computation of this many elements using 4×4 Gaussian quadrature, combined with point matching, can be very time-consuming. However, the value of these integrals depends on the separation distance between the source and observer, that is, $|\rho - \rho'|$ [5, Chapter 3]. It is thus possible to tabulate these integrals for a small number (typically 50 to 200) of source-observer distances, and then interpolate between these tabulated values. The source-observer separation can range from zero to the maximum linear dimension of the patch. It is better to separate the static Green's function contribution first, that is, I^h of (3D.4), and then use interpolation on the remaining part.

The matrix equation (3.88) is solved for the current coefficient vector $[\alpha]$. These coefficients are now plugged into (3.86) to obtain the current

distribution on the patch metalization surface, which is then used to determine the antenna characteristics such as input impedance, resonant frequency, bandwidth, and radiation patterns. The procedure followed is the same as in the spectral-domain solution of integral equation (see Section 3.1). The performance of MPIE in terms of accuracy and types of problems that can be solved is very similar to that of the spectral-domain approach, provided identical basis and testing functions are used. The numerical efficiency of MPIE is obtained due to the use of look-up tables for the Green's functions and razor testing. In general, one needs to know the behavior of antennas at a number of frequencies, for example, for wide-band operation or RCS computation. Carrying out impedance matrix evaluations at each and every frequency could be very expensive, especially if subdomain basis functions are used. One can instead use an interpolation technique in such a situation. It has been found that while the input impedance of the antenna varies very fast near the resonant frequency, the matrix elements vary slowly with frequency. Therefore, matrix elements can be computed at large frequency intervals and then interpolated for other frequencies in between. Newman and Forrai have used quadratic interpolation while calculating the RCS of a rectangular patch [49].

3.2.5 Applications of the MPIE Technique to Microstrip Antennas

An integral equation solution based on MPIE has been used to analyze various types of microstrip antenna configurations. These include various types of patch shapes, feed types, stacked geometries, anisotropic substrates, and array geometries. Some of the prominent studies utilizing this technique are [1, 6, 26, 50] for the basic technique and the analysis of a rectangular patch, [28, 51, 52] for the circular patch, [51] for the triangular patch, [53, 54] for a printed slot antenna, [29, 51, 52, 55] for an arbitrary shaped geometry, [29] for the patch on anisotropic substrate, [51] for a proximity-coupled microstrip fed antenna, [55] for an aperture-coupled microstrip antenna, [55, 56, 57, 58] for a stacked antenna configuration, [50] for a multilayered printed antenna, [59] for mutual coupling between microstrip antennas, an array of patches [59, 60], computation of radar cross section [29], for a slotted rectangular patch [26], probe feed modeling [28, 29, 57, 60], crossed patch [58], pentagonal patch [52], and resistively loaded printed spiral [61].

3.3 Finite-Difference Time-Domain Analysis

In addition to the integral equation approach described earlier, the finite-difference time-domain (FDTD) technique is used extensively in the analysis

and design of microstrip antennas. The major difference between FDTD and other numerical techniques is that analytical preprocessing and modeling are almost absent in FDTD. Therefore, complex antennas can also be analyzed using FDTD. This analysis approach can be used to include the effect of finite size of the substrate and ground plane, which is very important in the design of many microstrip antennas like microstrip antennas for handheld receivers. Interaction between the device and circuits at the field level can be incorporated using FDTD. This is necessary for accurate analysis of microwave active circuits and antennas. Active microstrip antennas can be analyzed using FDTD.

The FDTD was first proposed by Yee in 1966 [62] and has been used by many investigators, because it has the following advantages over other techniques:

1. From a mathematical point of view it is a direct implementation of Maxwell's curl equations. Therefore, analytical processing of Maxwell's equations is almost negligible.
2. It is capable of predicting broadband frequency response because the analysis is carried out in the time domain.
3. It is capable of analyzing complex systems, including wave interaction with human body, or satellite, nonlinear device simulations, complex antennas, and so on.
4. It is capable of analyzing structures using different types of materials, for example, lossy dielectrics, magnetized ferrites, and anisotropic plasmas.
5. Finally, it provides a real-time animation display, which is a powerful tool for both a student and an electromagnetic designer.

To this list can be added the advantage of computational efficiency for large problems in comparison with the other techniques such as the method of moments or finite-element method, especially when predicting broadband response.

One needs a digital computer ranging in ability from a Pentium to a supercomputer, depending on the electrical size of the problem structure and the required discretization size for a given accuracy. Computer resource requirements for FDTD are large for the problems which can be analyzed using techniques based on analytical preprocessing of the problem such as integral equation, mode matching, and method of lines.

Analysis of any problem using FDTD starts with dividing the structure into various regions based on the material properties. The unbounded region, if any, is then bounded by terminating it with absorbing medium or termination such that reflections do not occur. Next, the problem's physical space is discretized in the form of a number of cuboids of size $\Delta x \Delta y \Delta z$. The time domain is also discretized with interval size Δt. The structure is then excited by an electromagnetic pulse. The wave launched by the pulse in the structure is then studied for its propagation behavior. The stabilized time-domain waveform is numerically processed to determine the time-domain and frequency-domain characteristics of the structures. A very good literature review on the FDTD technique is available in [63].

In this chapter, we first describe the essentials of FDTD, that is, discretization of Maxwell's curl equations and the associated numerical stability criteria, absorbing boundary conditions, and excitation of the structure. The computational aspect of FDTD is illustrated by analyzing propagation in a microstrip line and in a microstrip fed rectangular patch antenna.

3.3.1 Formulation of FDTD

To simulate time-varying electromagnetic fields in any linear isotropic media with constants ϵ, μ, and σ, Maxwell's curl equations are sufficient because the Maxwell's divergence equations are contained in them [8]. The curl equations are

$$\sigma\vec{E} + \epsilon\frac{\partial\vec{E}}{\partial t} = \nabla \times \vec{H} \tag{3.94}$$

$$\mu\frac{\partial\vec{H}}{\partial t} = -\nabla \times \vec{E} \tag{3.95}$$

To obtain unique solutions of (3.94) and (3.95), the following conditions may be specified:

1. The value of fields at $t = 0$ must be specified on the whole domain of interest. They are assumed to be zero except at the plane of excitation.
2. The tangential components of E and H on the boundary of the domain of interest must be given for all $t > 0$.

Partial differential equations (3.94) and (3.95) are solved subject to the conditions stated above by expressing the derivatives in terms of finite difference approximations. The central difference approximation is used for higher accuracy. It is defined as

$$\left.\frac{\partial F}{\partial u}\right|_{u_0} = \left.\frac{F\left(u_0 + \frac{\Delta u}{2}\right) - F\left(u_0 - \frac{\Delta u}{2}\right)}{\Delta u}\right|_{\Delta u \to 0} + O(\Delta u)^2 \qquad (3.96)$$

Equation (3.96) implies that the E and H fields should be known at discrete points (x_i, y_j, z_k) only, where $x_i = i\Delta x$, $y_j = j\Delta y$, and $z_k = k\Delta z$ with Δx, Δy, and Δz representing the step size. To implement the finite difference scheme in 3-D, the problem space is divided into a number of cells called *Yee cells* of dimensions mentioned above. One such cell is shown in Figure 3.16. The remarkable property of this cell is that the positions of different components of E and H satisfy the differential form of Maxwell's equation. This placement of components also obeys Maxwell's equation in the integral form. Not only

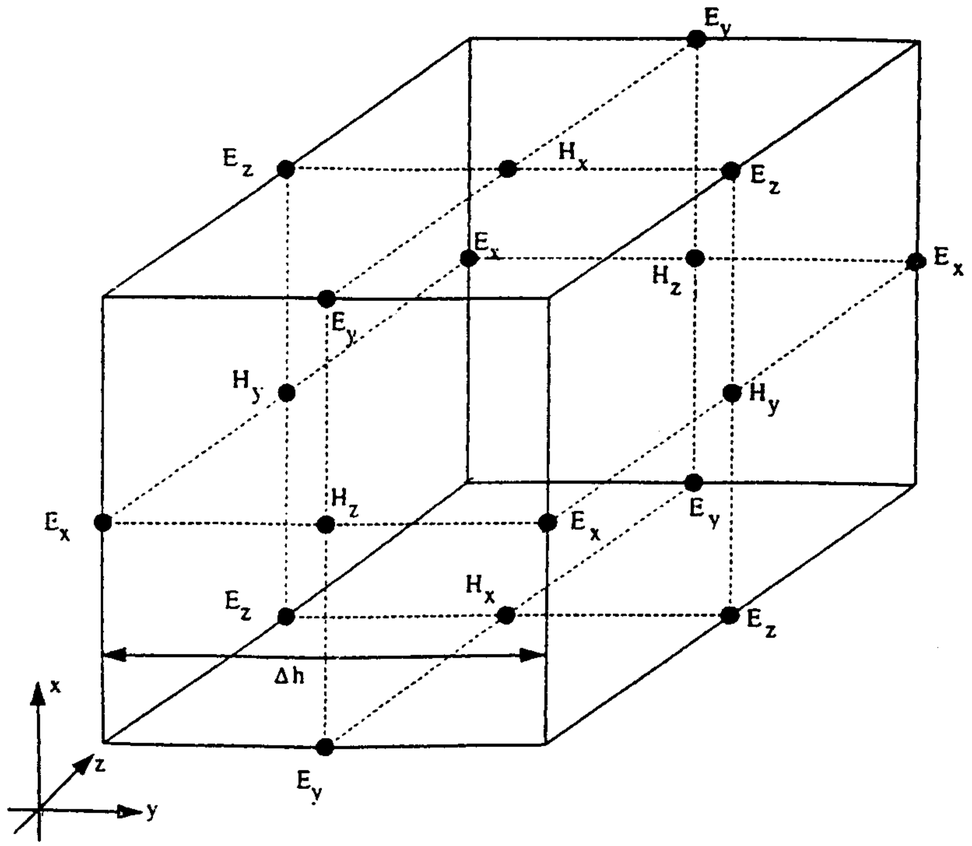

Figure 3.16 Geometry of Yee's cell used in FDTD analysis.

are the placements of the E and H nodes off in space by half a space step, but the time instants when the E and H field components are calculated are also off by half a time step. This gives rise to a *leap frog* algorithm with components of E being calculated at $n\Delta t$ and components of H being calculated at $(n + 1/2)\Delta t$, where Δt is the discretization step in time.

Equations (3.94) and (3.95) are cast in the finite difference form for use in FDTD. Use of central difference approximation (3.96) converts these equations to the following form:

$$\begin{aligned} E_x^{n+1}\left(i + \frac{1}{2}, j, k\right) &= \left(\frac{\epsilon - \sigma\Delta t/2}{\epsilon + \sigma\Delta t/2}\right) E_x^n\left(i + \frac{1}{2}, j, k\right) \\ &+ \frac{\Delta t/\Delta y}{\epsilon + \sigma\Delta t/2}\left(H_z^{n+1/2}\left(i + \frac{1}{2}, j + \frac{1}{2}, k\right)\right. \\ &\left. - H_z^{n+1/2}\left(i + \frac{1}{2}, j - \frac{1}{2}, k\right)\right) \\ &- \frac{\Delta t/\Delta z}{\epsilon + \sigma\Delta t/2}\left(H_y^{n+1/2}\left(i + \frac{1}{2}, j, k + \frac{1}{2}\right)\right. \\ &\left. - H_y^{n+1/2}\left(i + \frac{1}{2}, j, k - \frac{1}{2}\right)\right) \end{aligned} \qquad (3.97a)$$

$$\begin{aligned} E_y^{n+1}\left(i, j + \frac{1}{2}, k\right) &= \left(\frac{\epsilon - \sigma\Delta t/2}{\epsilon + \sigma\Delta t/2}\right) E_y^n\left(i, j + \frac{1}{2}, k\right) \\ &+ \frac{\Delta t/\Delta z}{\epsilon + \sigma\Delta t/2}\left(H_x^{n+1/2}\left(i, j + \frac{1}{2}, k + \frac{1}{2}\right)\right. \\ &\left. - H_x^{n+1/2}\left(i, j + \frac{1}{2}, k - \frac{1}{2}\right)\right) \\ &- \frac{\Delta t/\Delta x}{\epsilon + \sigma\Delta t/2}\left(H_z^{n+1/2}\left(i + \frac{1}{2}, j + \frac{1}{2}, k\right)\right. \\ &\left. - H_z^{n+1/2}\left(i - \frac{1}{2}, j + \frac{1}{2}, k\right)\right) \end{aligned} \qquad (3.97b)$$

$$E_z^{n+1}\left(i, j, k+\frac{1}{2}\right) = \left(\frac{\epsilon - \sigma\Delta t/2}{\epsilon + \sigma\Delta t/2}\right)E_z^n\left(i, j, k+\frac{1}{2}\right) + \frac{\Delta t/\Delta x}{\epsilon + \sigma\Delta t/2}\left(H_y^{n+1/2}\left(i+\frac{1}{2}, j, k+\frac{1}{2}\right) - H_y^{n+1/2}\left(i-\frac{1}{2}, j, k+\frac{1}{2}\right)\right) - \frac{\Delta t/\Delta y}{\epsilon + \sigma\Delta t/2}\left(H_x^{n+1/2}\left(i, j+\frac{1}{2}, k+\frac{1}{2}\right) - H_x^{n+1/2}\left(i, j-\frac{1}{2}, k+\frac{1}{2}\right)\right) \tag{3.97c}$$

$$H_x^{n+1/2}\left(i, j+\frac{1}{2}, k+\frac{1}{2}\right) = H_x^{n-1/2}\left(i, j+\frac{1}{2}, k+\frac{1}{2}\right) - \frac{\Delta t}{\mu\Delta y}\left(E_z^n\left(i, j, k+\frac{1}{2}\right) - E_z^n\left(i, j-1, k+\frac{1}{2}\right)\right) + \frac{\Delta t}{\mu\Delta z}\left(E_y^n\left(i, j+\frac{1}{2}, k\right) - E_y^n\left(i, j+\frac{1}{2}, k-1\right)\right) \tag{3.97d}$$

$$H_y^{n+1/2}\left(i+\frac{1}{2}, j, k+\frac{1}{2}\right) = H_y^{n-1/2}\left(i+\frac{1}{2}, j, k+\frac{1}{2}\right) - \frac{\Delta t}{\mu\Delta z}\left(E_x^n\left(i+\frac{1}{2}, j, k\right) - E_x^n\left(i+\frac{1}{2}, j, k-1\right)\right) + \frac{\Delta t}{\mu\Delta x}\left(E_z^n\left(i, j, k+\frac{1}{2}\right) - E_z^n\left(i-1, j, k+\frac{1}{2}\right)\right) \tag{3.97e}$$

$$H_z^{n+1/2}\left(i+\frac{1}{2}, j+\frac{1}{2}, k\right) = H_z^{n-1/2}\left(i+\frac{1}{2}, j+\frac{1}{2}, k\right) - \frac{\Delta t}{\mu\Delta x}\left(E_y^n\left(i, j+\frac{1}{2}, k\right) - E_y^n\left(i-1, j+\frac{1}{2}, k\right)\right) + \frac{\Delta t}{\mu\Delta y}\left(E_x^n\left(i+\frac{1}{2}, j, k\right) - E_x^n\left(i+\frac{1}{2}, j-1, k\right)\right) \tag{3.97f}$$

The indices i, j, and k define the positions of the field nodes, such that $x = i\Delta x$, $y = j\Delta y$, $z = k\Delta z$.

3.3.2 Stability Criteria

The numerical algorithm for the Maxwell's curl equations just derived requires the time increment Δt to have a specific *upper bound* relative to the space increments, Δx, Δy, Δz. This bound is necessary to avoid numerical instability that can cause the computed results to increase spuriously without limit as time marching continues. The cause for numerical instability is the finite-difference implementation of the derivative. The stability analysis is discussed thoroughly in [64]. The final expression for the upper bound on Δt can be written as

$$v_{\max} \cdot \Delta t \le \frac{1}{\sqrt{1/\Delta x^2 + 1/\Delta y^2 + 1/\Delta z^2}} \tag{3.98}$$

where $v_{\max}$ is the maximum phase velocity of the signal in the problem being considered. For the special case of $\Delta x = \Delta y = \Delta z = u$, the above condition becomes

$$v_{\max} \cdot \Delta t \le u/\sqrt{3} \tag{3.99}$$

The discretized wave, in this case, most closely approximates the actual wave propagation [5]. In practice, the maximum value of Δt used is about 90% of the value given by (3.98).

3.3.3 Numerical Dispersion

Dispersion is defined as the variation of the phase constant of the propagating wave with frequency. The discretization of Maxwell's equations in space and time causes dispersion of the simulated wave in an otherwise dispersion-free structure. That is, the phase velocity of the wave in an FDTD grid can differ from the analytical value. This dispersion is called *numerical dispersion* [7, 8]. The amount of dispersion depends on the wavelength, the direction of propagation in the grid, and the discretization size. Again for simplicity we present the final expressions for the numerical dispersion. The general expression, valid for a plane wave in a continuous lossless medium, is [7, 8]:

$$\left(\frac{\sin(0.5\omega\Delta t)}{c\Delta t}\right)^2 = \left(\frac{\sin(0.5k_x\Delta x)}{\Delta x}\right)^2 + \left(\frac{\sin(0.5k_y\Delta y)}{\Delta y}\right)^2 + \left(\frac{\sin(0.5k_z\Delta z)}{\Delta z}\right)^2 \tag{3.100a}$$

Equation (3.100a) can be used to determine numerical dispersion for propagation in different directions as a function of normalized frequency. For convenience, the dispersion is frequently plotted as the variation of normalized wave vector components $\chi_i (= k_i \Delta i)$, $i = x, y, z$ with normalized angular frequency Ω $(= 2\pi f \Delta t)$. For wave propagation in the (1,0,0) direction and along the x axis, we use $\chi_y = \chi_z = 0$ and (3.100a) becomes

$$\frac{\sin(0.5\omega\Delta t)}{c\Delta t} = \frac{\sin(0.5k_x\Delta x)}{\Delta x} \tag{3.100b}$$

Similarly, for wave propagation in the (1,1,0) direction and along the diagonal in the x-y plane, $\chi_x = \chi_y$, $\chi_z = 0$ and (3.100a) becomes

$$\frac{\sin(0.5\omega\Delta t)}{c\Delta t} = \sqrt{2}\frac{\sin(0.5k_x\Delta x)}{\Delta x} \tag{3.100c}$$

and

$$\frac{\sin(0.5\omega\Delta t)}{c\Delta t} = \sqrt{3}\frac{\sin(0.5k_x\Delta x)}{\Delta x} \tag{3.100d}$$

for wave propagation in (1,1,1) because $\chi_x = \chi_y = \chi_z$. For a continuous medium (Δx, Δy, Δz, and $\Delta t \to 0$), the above expressions yield the corresponding equations for the dispersion (numerical) free case. For example, (3.100a) becomes

$$\frac{\omega^2}{c^2} = k_x^2 + k_y^2 + k_z^2 \tag{3.101}$$

Dispersion based on (3.100b), (3.100c), and (3.100d), for wave propagation in free space is plotted in Figure 3.17 for $\Delta x = \Delta y = \Delta z$ and $\Delta t = 0.9\Delta t_{\max}$, where $\Delta t_{\max}$ is the upper limit in (3.99). The analytical value or linear dispersion given by (3.101) is compared with the numerical dispersion based on Yee's [62] algorithm. The dispersion diagrams help us in determining the frequency limits of applicability of the FDTD scheme for a given mode of propagation. For example, to reduce the effect of numerical dispersion on the results, we should use $\Omega \leq 0.15\pi$ for (1,0,0) propagation.

Qualitatively, (3.100a) suggests that numerical dispersion can be reduced to any degree that is desired if one uses a fine enough FDTD mesh. However, it is possible to minimize the numerical dispersion by choosing the mesh size

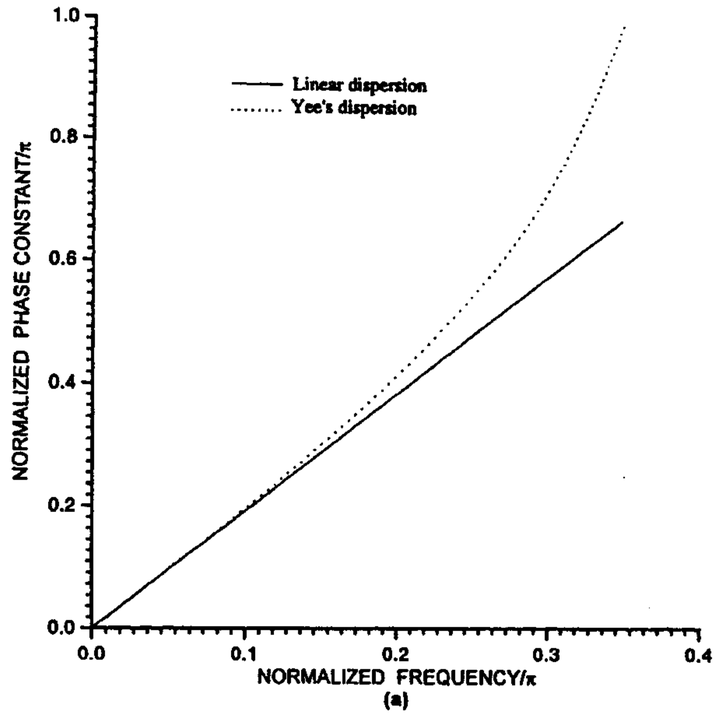

Figure 3.17 Dispersion due to discretization: (a) Dispersion along (1,0,0) propagation, (b) dispersion along (1,1,0) propagation, and (c) dispersion along (1,1,1) propagation.

in an optimal fashion. It has been found [65] that for optimal dispersion, the mesh sizes are related as $\Delta x = \Delta y = \Delta z$, and in order to be consistent with the stability criterion of (3.98), one obtains

$$\Delta x = \Delta y = \Delta z = \sqrt{3}\nu_{\max} \cdot \Delta t \tag{3.102}$$

The preceding condition, however, is not always satisfied because the physical bounds of the electromagnetic problem must match the mesh lines. However, the influence of unequal mesh size ($\Delta x \neq \Delta y \neq \Delta z$) on dispersion is relatively small, when $\Delta y/\Delta x$, $\Delta z/\Delta x$, and $\sqrt{3}\nu_{\max} \cdot \Delta t/\Delta x$ ranges from 1.0 to 1.225, where Δx represents the smallest discretization size.

3.3.4 Absorbing Boundary Conditions

A large number of electromagnetic problems have associated open space regions, where the spatial domain is unbounded in one or more directions. The solution of such a problem in this form will require an unlimited amount of computer

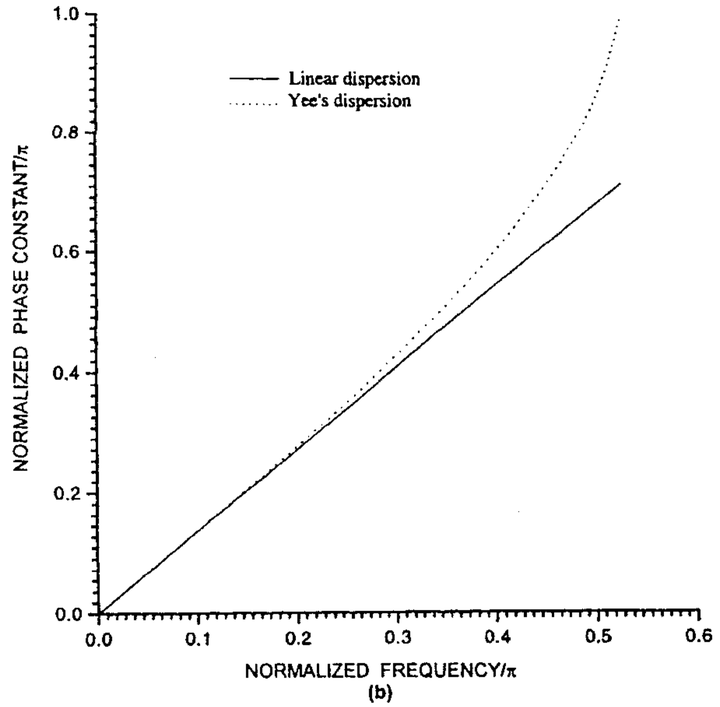

Figure 3.17 (continued).

memory and processing time, which is impossible to arrange. Therefore, the domain must be truncated such that the error involved is minimal. For this, the domain can be divided into two regions: the interior region and the exterior region as shown in Figure 3.18. The interior region must be large enough to enclose the structure of interest. The exterior region simulates the infinite space. It is a limited free space enclosing the interior region on one side and terminated on the other side by a perfect electric conductor. We apply the FDTD algorithm to the interior region. It simulates wave propagation in the forward and backward directions. However, only the outward propagation in the exterior region is desired so that infinite free-space conditions are simulated. Reflections are generated in the exterior region since it is bounded by a perfect electric conductor. These reflections must be suppressed to an acceptable level so that the FDTD solution is valid for all time steps.

Two options are available to simulate the open region surrounding the problem physical space: Terminate the interior region with equivalent currents on the surface of the interior region and use the Green's function to simulate the fields in the exterior region or to simulate the exterior region with absorbing boundary conditions to minimize reflections from the truncation of the mesh. Simulation of the open region with the help of equivalent currents yields a

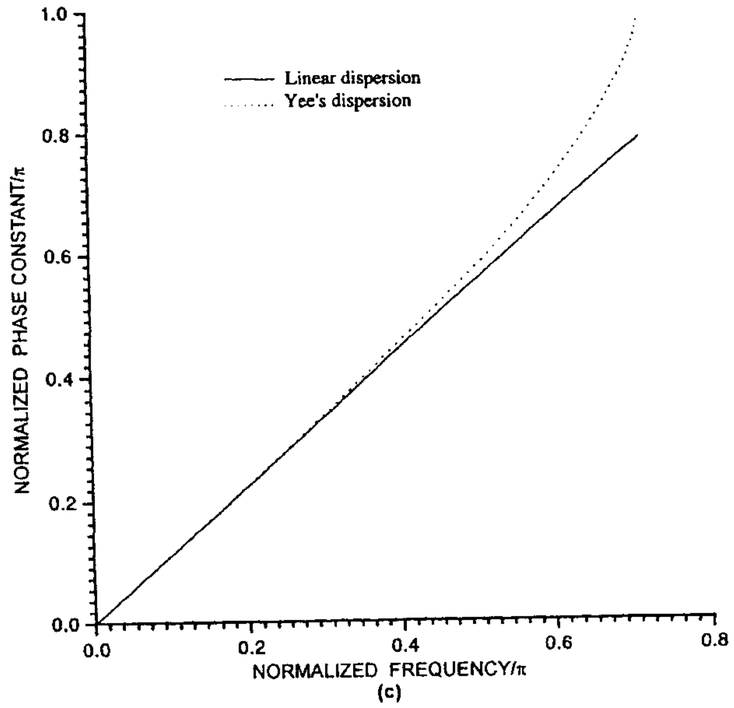

Figure 3.17 (continued).

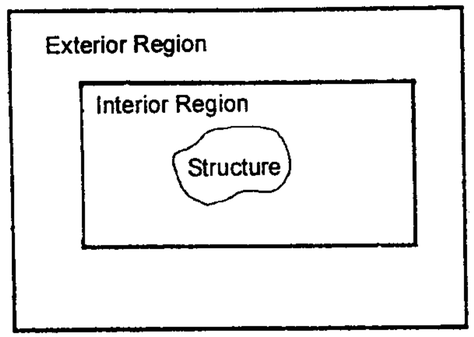

Figure 3.18 A typical truncation of the domain by the exterior region in FDTD algorithm.

solution whereby the radiation condition is satisfied exactly. But the values of fields on the surface enclosing the interior region are needed, for which solution time and storage requirement increases rapidly with the surface size. On the other hand, the absorbing boundary concept truncates the computation domain.

The absorbing boundary condition (ABC) can be simulated in a number of ways. These are classified as *analytical* (or *differential*) *ABC* and *material ABC*. The material ABC is realized from the physical absorption of the incident

signal by means of a lossy medium [66], whereas analytical ABC is simulated by approximating the wave equation on the boundary [67]. The material ABC holds great promise of truncating the computation domain. It can reach an ideal limit extending the FDTD numerical modeling capabilities to a −80- to −120-dB reflection coefficient at the boundaries. Various types of absorbing boundary conditions are analyzed next.

Analytical Absorbing Boundary Conditions

The simple and optimal analytical ABC, named *Mur's first-order absorbing boundary condition*, is selected under this section to illustrate the basic principle underlying this type of ABC.

Analysis of Mur's first-order ABC is based on the work of Enquist and Majda [67] and the optimal implementation given by Mur [68]. An arbitrary wave can be expanded in terms of a spectrum of plane waves. If a plane wave is normally incident on a planar surface, and if the surface is perfectly absorbing, there will be no reflected wave. A numerical wave traveling along the negative x direction is a solution of the following differential equation:

$$\left(\frac{\partial}{\partial x} - \frac{1}{c}\frac{\partial}{\partial t}\right)\phi(x, t) = 0 \tag{3.103}$$

If we impose the above condition on a wave normally incident on the planar surface, the wave should not be reflected. Consequently, an absorbing condition for a normally incident wave is

$$\frac{\partial \phi(x, t)}{\partial x} = \frac{1}{c}\frac{\partial \phi(x, t)}{\partial t}\bigg|_{x=\frac{\Delta x}{2}, t=\left(n+\frac{1}{2}\right)\Delta t} \tag{3.104}$$

for updating of the electric field at $x = \Delta x/2$, $t = (n + 1)\Delta t$. In finite-difference form, (3.104) can be written as follows:

$$\frac{\phi_1^{n+1/2} - \phi_0^{n+1/2}}{\Delta x} = \frac{1}{c}\frac{\phi_{1/2}^{n+1} - \phi_{1/2}^{n}}{\Delta t} \tag{3.105}$$

In this form, the finite-difference approximation is accurate to the second order in Δx and Δt. But the values at the half grid points and half time steps are not available, and can be averaged as

$$\phi_m^{n+1/2} = \frac{\phi_m^{n+1} + \phi_m^n}{2} \quad \text{and} \quad \phi_{m+1/2}^{n} = \frac{\phi_{m+1}^{n} + \phi_m^n}{2} \tag{3.106}$$

The approximation of (3.106) is also accurate to a second order if $\phi(x, t)$ is a smooth function. Use of (3.106) in (3.105) yields

$$\phi_0^{n+1} = \phi_1^n + \left(\frac{c\Delta t - \Delta x}{c\Delta t + \Delta x}\right)(\phi_1^{n+1} - \phi_0^n) \tag{3.107}$$

This equation can be used for updating the fields lying on the outer boundary of the interior region. Equation (3.107) can be shown to be unconditionally stable [68]. The boundary condition for (3.103) is exact only for a plane wave at normal incidence. Hence, the wave will still be reflected for an oblique incidence. To take care of this eventuality, one needs to use higher order absorbing boundary conditions [68, 69].

Material Absorbing Boundary Conditions

First, we discuss the fundamental material ABC known as the *absorbing sheets method*, which was the first material ABC proposed and used for FDTD computations by Hallond [66]. In this method the exterior region is replaced by a lossy medium with parameters (μ', ϵ', σ^*, σ), where σ is the electrical conductivity and σ^* is the fictitious magnetic conductivity. This medium is taken to be of finite thickness and is backed by a perfect conductor. The values of σ and σ^* are selected such that when a wave is incident normal to the interface separating the free-space interior region and this lossy medium, there should be no reflection, which is possible only if

$$Z_0 = Z_m \tag{3.108a}$$

where Z_0 is the free-space impedance (μ_0, ϵ_0, $\sigma^* = 0$, $\sigma = 0$), and Z_m is the impedance of the lossy medium (μ', ϵ', σ^*, σ). Equation (3.108a) can be expressed as

$$\sqrt{\frac{\mu_0}{\epsilon_0}} = \sqrt{\frac{\mu' + j\sigma^*}{\epsilon' + j\sigma}} \tag{3.108b}$$

For convenience if we choose $\mu' = \mu_0$ and $\epsilon' = \epsilon_0$, then the matching condition for (3.108b) yields

$$\frac{\sigma^*}{\mu_0} = \frac{\sigma}{\epsilon_0} = v \tag{3.109}$$

To reduce partial reflections (due to discretization) in the lossy medium, the ratio v, in general, is a function of position from the interface. For a lossy medium of thickness t, the attenuation is given by

$$\alpha = \exp\left(-\frac{1}{c}\int_0^t v(x) \cdot dx\right) \tag{3.110}$$

It appears from this that in the case of material ABC, one can choose a sufficiently thick lossy medium to obtain any desired amount of attenuation and associated total reflection. However, the reflection at oblique incident angles is higher, and the total reflection at the interface for the absorbing sheets method is of the same order as that obtained from analytical ABCs.

Perfectly Matched Layer ABCs

The perfectly matched layer (PML) formulation represents a generalization of the absorbing sheets method to arbitrary angles of incidence. This is achieved by splitting the electric and magnetic field components in the absorbing media, and assigning different losses in different directions. The net effect of this is to create a nonphysical absorbing medium in the exterior region such that the wave impedance in this medium is independent of the angle of incidence and frequency of the waves [70–74].

Let us assume that the E_x field is split into E_{xy} and E_{xz} components. The corresponding updating equations can be derived from the following equations [70–74]:

$$\epsilon\frac{\partial E_{xy}}{\partial t} + \sigma_y E_{xy} = \frac{\partial H_z}{\partial y} \tag{3.111a}$$

$$\epsilon\frac{\partial E_{xz}}{\partial t} + \sigma_z E_{xz} = -\frac{\partial H_y}{\partial z} \tag{3.111b}$$

$$E_x = E_{xy} + E_{xz} \tag{3.111c}$$

The other field components can also be split similarly and updated. If $\sigma_x = \sigma_y = \sigma_z = 0$ and $\sigma_x^* = \sigma_y^* = \sigma_z^* = 0$, (3.111) reduces to the corresponding Maxwell's curl equation for the lossless medium. If $\sigma_x = \sigma_y = \sigma_z$ and $\sigma_x^* = \sigma_y^* = \sigma_z^* = 0$, (3.111) reduces to those for the electrically conductive medium, and with $\sigma_x = \sigma_y = \sigma_z$ and $\sigma_x^* = \sigma_y^* = \sigma_z^*$, to those for the absorbing sheets method. The matching condition in the last case is also similar to (3.109) but should be satisfied in each principal direction, that is,

$$\frac{\sigma_i^*}{\mu_0} = \frac{\sigma_i}{\epsilon_0} \quad i = x, y, z \tag{3.112}$$

The various portions of the PML region surrounding the interior region are described by different values of σ_x, σ_y, and σ_z. These portions can be labeled as face, edge, and corner regions according to their positions on the surface of interior region as shown in Figure 3.19 [75]. For example, the z-face region is the projection of the z face of the interior region and is characterized by $\sigma_x = 0$ and $\sigma_y = 0$. Similarly, the xy-edge region surrounds the xy edge of the interior region, and is characterized by $\sigma_z = 0$. Finally, σ_x, σ_y, σ_z are used to define the corner regions surrounding the various corners of the interior region.

Theoretically, there is no reflection at the interface between the interior region and the PML region. Nevertheless, due to the finite thickness of the PML medium, reflection is generated when the outgoing waves are reflected by the terminating conductors placed on its outer boundary and they can return to the interior region. So, for a plane wave, an apparent reflection coefficient is defined, which is a function of the PML thickness t and the conductivity profile $\sigma_n(\rho)$, where ρ is the distance from the interface. Hence we use σ_n in place of σ_i for the layer normal to the ith direction, $i = x$, y, or z. The magnitude of the reflection coefficient for a wave incident at an angle ϕ with respect to the normal to the layers is [7, 70]

$$R(\phi) = [R(0)]^{\cos(\phi)} \tag{3.113}$$

with $R(0)$ the reflection coefficient for normal incidence at the interior region to PML interface defined as

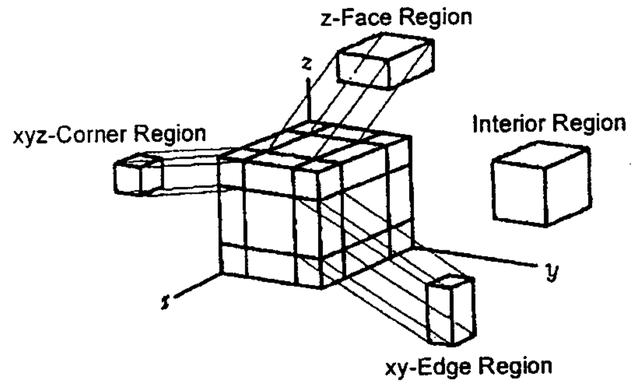

Figure 3.19 Illustration showing the face, edge, and corner regions of the PML medium surrounding the interior region. (From [75]. © 1999 *IETE Journal of Research (India)*. Reprinted with permission.)

$$R(0) = \exp\left(\frac{-2}{\epsilon_0 c}\int_0^t \sigma_n(\rho)d\rho\right) \tag{3.114}$$

In general, the profile for the PML medium can be defined as

$$\sigma_n(\rho) = \sigma_m\left(\frac{\rho}{t}\right)^n \tag{3.115}$$

and the corresponding

$$R(0) = \exp\left(\frac{-2\sigma_m t}{(n+1)\epsilon_0 c}\right) \quad n = 0, 1, 2, \ldots \tag{3.116}$$

where σ_m is the maximum value of σ of the absorbing medium.

In principle, one can obtain a reflection coefficient $R(\phi)$ as small as required by increasing the layer thickness t and/or suitably selecting the conductivity profiles. But in actual computations, a small amount of numerical reflection occurs that depends on t and n. In practice, PML layers are represented by the number of FDTD cells N, profile (L for linear or P for parabolic), and the percentage of reflection coefficient $R(0)$; that is, (N, L, or P, $R(0)$). For example, a PML with 16-cell thickness, parabolic profile of conductivity, and a desired reflection coefficient of 0.01% is specified as (16, P, 0.01).

In the above analysis for the PML, we have assumed that the medium is continuous. However, in the FDTD analysis the PML medium also is discretized into cells. The value of σ at the grid point of the cell is taken as the average value in the cell. For a cell around the location index V, the average conductivity is given by

$$\sigma_n(V) = \frac{1}{\Delta\rho}\int_{\rho(V)-\Delta\rho/2}^{\rho(V)+\Delta\rho/2} \sigma_n(u)du \quad V = 0, 1, 2, 3, \ldots \tag{3.117}$$

where V represents the index i, j, or k and $\Delta\rho$ is the cell size in that direction. The reader is reminded that σ_n is applicable to various σ_i for the FDTD grid. From (3.117) we can easily obtain an expression for the average conductivity of the cell. For the cell at the interface, half the cell occupies the interior region. Therefore,

$$\sigma_n(0) = \frac{1}{\Delta\rho}\int_0^{\Delta\rho/2} \sigma_n(u)du = \frac{\sigma_m}{(n+1)2^{n+1}N^n} \tag{3.118}$$
$$= -\frac{\epsilon_0 c \ln[R(0)]}{2^{n+2}\Delta\rho N^{n+1}} \quad \text{[using (3.115) and } t = N\Delta\rho\text{]}$$

Away from the interface,

$$\sigma_n(V>0) = \sigma_n(0)[(2V+1)^{n+1} - (2V-1)^{n+1}] \tag{3.119}$$

For an oblique incidence of waves in the PML region, one needs to split each field component and assign different conductivities as described earlier. However, it is not necessary to split the field components in the interior region. This results in different expressions for the Maxwell's curl equations in the two domains. It is possible to unify the formulations in the two domains. For this, we adopt the split field formulation in the interior region also. For example, (3.111) reduces to the following discretized form and is applicable over the entire domain

$$E_{xy}^{n+1}\left(i+\frac{1}{2}, j, k\right) = \left(\frac{\epsilon - \sigma_y\Delta t/2}{\epsilon + \sigma_y\Delta t/2}\right)E_{xy}^{n}\left(i+\frac{1}{2}, j, k\right) \tag{3.120a}$$
$$+ \frac{\Delta t/\Delta y}{\epsilon + \sigma_y\Delta t/2}\left(H_z^{n+1/2}\left(i+\frac{1}{2}, j+\frac{1}{2}, k\right) - H_z^{n+1/2}\left(i+\frac{1}{2}, j-\frac{1}{2}, k\right)\right)$$

$$E_{xz}^{n+1}\left(i+\frac{1}{2}, j, k\right) = \left(\frac{\epsilon - \sigma_z\Delta t/2}{\epsilon + \sigma_z\Delta t/2}\right)E_{xz}^{n}\left(i+\frac{1}{2}, j, k\right) \tag{3.120b}$$
$$+ \frac{-\Delta t/\Delta z}{\epsilon + \sigma_z\Delta t/2}\left(H_y^{n+1/2}\left(i+\frac{1}{2}, j, k+\frac{1}{2}\right) - H_y^{n+1/2}\left(i+\frac{1}{2}, j, k-\frac{1}{2}\right)\right)$$

$$E_x^{n+1}\left(i+\frac{1}{2}, j, k\right) = E_{xy}^{n+1}\left(i+\frac{1}{2}, j, k\right) + E_{xz}^{n+1}\left(i+\frac{1}{2}, j, k\right) \tag{3.120c}$$

In (3.120), the PML medium is characterized by σ_x, σ_y, and σ_z, whereas $\sigma_x = \sigma_y = \sigma_z$ in the interior region. The integrated approach is computationally more expensive both in computer memory and CPU time requirements, but is easier to program.

Although PML is also matched to evanescent modes, it is impossible to enhance the attenuation rate of the evanescent modes through simply adjusting the parameters specified above. The reason for this behavior is that the attenuation rate of these modes in the PML region is the same as that in free space. For the evanescent modes with low attenuation rate, sufficient thickness of the PML medium is required to get small reflections. Alternatively, PML layers should be located far from the sources and scattering objects. In either case, computer storage and run time will increase significantly. To overcome this problem, one can use an *anisotropic perfectly batched layer* (also called *perfectly matched uniaxial medium*) [74].

3.3.5 Excitation and Source Modeling

We now consider the electromagnetic wave excitation in the FDTD lattice. Pointwise linear and nonlinear circuit type sources have been introduced that are useful for 3-D FDTD modeling of the propagation, reflection, coupling, and radiation of digital pulses in multilayer circuit boards, microstrip circuit modules, microstrip antennas, and so on [75]. The sources include diodes, a transistor, and logic gates. For each source or load, a generic problem has been to realize accurately the physics of the source in as compact a manner as possible. By compact we mean using very few electric and magnetic field components localized in the space lattice to realize the source. Achieving a compact source is desirable because then the additional computer storage and running time needed to simulate the source are small compared to the resources needed for ordinary grid operations. In this manner, maximum overall algorithm efficiency is achieved.

We next discuss two types of excitation schemes that are used for eigenvalue problems and circuit modeling problems:

Excitation scheme for eigenvalue problems [76]: In eigenvalue problems, the direction of the propagation vector is usually not known and depends on the space coordinates and the eigenvalue that is to be found. A better way to start computations is to estimate the field distribution of the desired mode in the structure first and then choose the excitation field accordingly.

Excitation scheme for circuit modeling problems [77]: For many uniform guiding structures, the electromagnetic field distribution is known and this knowledge can be used to excite fields in the FDTD lattice. For many others, in particular, most planar circuits, the exact electromagnetic field distribution is not known. In such cases, the source distribution can be made to converge faster to an actual distribution by initializing with a spatial distribution that more closely resembles the actual field distribution.

Once we know the potential distribution on the source plane (see Figure 3.20), we can calculate the electric field on it, then use this electric field value as a weight of the time-varying form, that is,

$$\overline{E}_s = [E_x(x, y)\hat{x} + E_y(x, y)\hat{y} + E_z(x, y)\hat{z}]\,P(t) \tag{3.121}$$

where $P(t)$ is a time-varying source pulse such as a Gaussian or cosine pulse, modulated or unmodulated. Now we update the electric field components on the source plane as [78]

$$\overline{E} = \overline{E}_f + \overline{E}_s \tag{3.122}$$

where $\overline{E}_f$ is normal FDTD updating.

Unlike the source excitations employed in [79, 80], dc source distortions caused by the electric or magnetic wall boundary treatment are not present in this excitation scheme because the source plane is located several cells away from the front-end terminal plane. Also, the source plane is transparent to the reflections coming from the discontinuities or from the loads or from the imperfect boundary treatment.

The choice of time-varying function: The time dependence of the source $P(t)$ is chosen depending on the problem at hand. For applications where frequency-dependent data are to be generated, a pulse is used such that its frequency content covers the desired frequency range. The usable highest frequency is generally limited by the size of the Yee's cell. Usually, it is chosen to be $\lambda/20$ at the highest frequency of interest. The envelope of $P(t)$ is chosen to be Gaussian in shape because when the source is turned on or off, the pulse magnitude should increase or decrease smoothly. It is given by

$$P(t) = \exp[-(t - t_0)^2/T^2] \tag{3.123a}$$

where t_0 governs the value of the pulse amplitude at turn on or off and T governs the width of the pulse in time. At "turn off" $t = 2t_0$ and $t = 0$ at

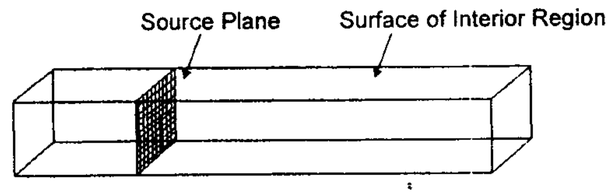

Figure 3.20 Source plane representation in FDTD grid. (From [75]. © 1999 *IETE Journal of Research (India)*. Reprinted with permission.)

"turn on." Another type of pulse commonly used is the bandpass Gaussian pulse. Basically, this is a modulated Gaussian pulse represented by

$$P(t) = \exp[-(t - t_0)^2/T^2]\cos(2\pi f_c(t - t_0)) \qquad (3.123b)$$

The spectrum of this pulse is similar to that of (3.123a) except for a shift in frequency. A bandpass Gaussian pulse is shown in Figure 3.21 [81]. The spectrum is symmetrical about f_c, the center frequency of the baseband spectrum. If T is defined as [19]

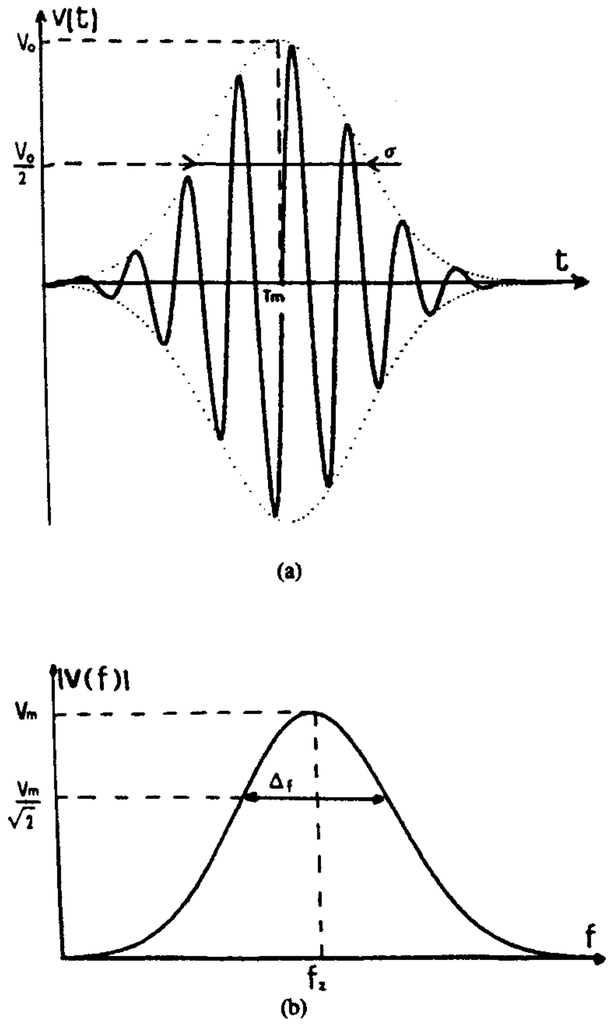

Figure 3.21 Shape of the excitation voltage: (a) Time domain $V(t)$ and (b) frequency domain $|V(f)|$. (From [81]. © 1990 IEEE. Reprinted with permission.)

$$T\frac{\sqrt{2.303A}}{\pi f_0} \qquad (3.124)$$

then the source spectrum will be $-A$ dB below the dc value at the frequency f_0. From above, we now need to choose t_0 and T so that the truncation of the source pulse does not introduce unwanted high frequencies in the spectrum, and yet does not waste computation time on determining values of the fields that are essentially zero. Normally, t_0 is selected so that when the source is turned on or off, $P(t) = e^{-16}$, that is, $t_0 = 4T$.

3.3.6 Extraction of Frequency-Domain Characteristics From Time-Domain Data

The FDTD method has been used extensively for calculating frequency-domain characteristics such as voltage or current distributions, propagation constants, S parameters, driving point impedance, and so on. When the frequency response over a broadband spectrum is of interest, a broadband pulse excitation can provide this frequency response with a single FDTD simulation. The conversion from the time domain to the frequency domain is achieved using either a discrete Fourier transform (DFT) or fast Fourier transform (FFT). For ease of implementation and the use of an arbitrary number of samples, DFT is generally preferred. Transformation from the time domain to the frequency domain, based on DFT, is described as

$$G(x, y, z, f) = \Delta t \sum_{n=0}^{N-1} g(x, y, z, n\Delta t)\exp(-j2\pi fn\Delta t) \qquad (3.125)$$

where $g(x, y, z, n\Delta t)$ is the pulse response, Δt is the sampling interval, and N is the total number of samples. Because commonly used pulse shapes do not have a uniform frequency spectrum, the final values $G(x, y, z, f)$ must be normalized by the DFT of the incident pulse to obtain frequency-domain data equivalent to data that would have been obtained if the given problem had been excited by a uniform frequency spectrum [82].

The determination of characteristics such as resonant frequency, propagation constant, impedance, and S parameters from the pulse response is described next.

Resonant Frequency

To determine the resonant frequency [76], we should select an appropriate field component in the stabilized mode pattern. Next, the positions of the

peak amplitude in the frequency spectrum are determined. These positions provide the resonant frequencies of the various modes excited in the structure under consideration. These modes can be identified if one plots the field distribution in the computation domain at these resonant frequencies.

Propagation Constant

For single-mode propagation in transmission lines [72], two z = constant planes, say, $z = z_1$ and $z = z_2$ are selected in the FDTD grid. Then the sample values for the fields, from the stabilized waveforms, at these locations are obtained. If their values are $g(z_1, t)$ and $g(z_2, t)$, their Fourier transforms at each frequency are related to each other in the following way:

$$\frac{G(z_1, f)}{G(z_2, f)} = \exp(-\gamma(f)(z_2 - z_1)) \tag{3.126}$$

Here $\gamma(f)$ is the propagation constant in the z direction. Since $\gamma(f) = \alpha(f) + j\beta(f)$, we can determine both attenuation constant and phase constant as a function of frequency. The separation $z_2 - z_1$ between the planes should be less than $\lambda/2$, otherwise one should choose the correct Riemen sheet while calculating the value of γ. For multimode propagation, additional sample values are needed to determine the excitation amplitudes and propagation constants.

Impedance Computations

In some problems, we need to determine the characteristic impedance, input impedance, wave impedance, and so on [83]. For the present case it is assumed that the fields are quasi-TEM in nature, and only a single mode propagates in the structure. To find the characteristic impedance of the transmission line, the TEM definition of voltage and current are used with the appropriate selection of paths as shown in Figure 3.22. The voltage between the ground conductor and the signal conductor is obtained as the line integral at the electric node, that is,

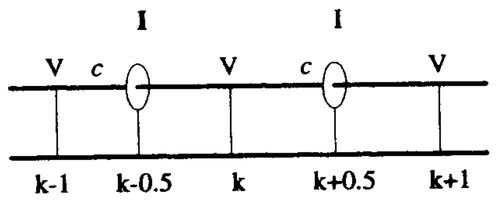

Figure 3.22 Voltage and current locations for computing impedances. (From [75]. © 1999 *IETE Journal of Research (India)*. Reprinted with permission.)

$$V_k(f) = -\int_{l_k} \bar{E} \cdot d\bar{l} \tag{3.127}$$

where l_k denotes the path of integration at node k from the ground plane to the signal conductor. The current is evaluated at $k \pm 1/2$, because of the position of the magnetic field in the Yee's cell. The current is given as

$$I_{k\pm1/2} = -\oint_{C_{k\pm1/2}} \bar{H} \cdot d\bar{l} \tag{3.128}$$

where $C_{k\pm1/2}$ represents the closed loop in the x-y plane at $k \pm 1/2$. The characteristic impedance can be determined as follows:

$$Z_1(f) = \frac{V_k(f)}{I_{k+1/2}(f)} \tag{3.129}$$

In this formula we have neglected the effect of spatial as well as temporal offsets associated with V and I evaluations. Next we compensate for the spatial offset between V and I calculations by defining

$$Z_2(f) = \frac{V_k(f)}{\sqrt{I_{k-1/2}(f) I_{k+1/2}(f)}} \tag{3.130}$$

Finally we compensate for the temporal offset $\Delta t/2$ between V and I using the following formula:

$$Z_3(f) = \frac{V_k(f) \exp(-j\pi f \Delta t)}{\sqrt{I_{k-1/2}(f) I_{k+1/2}(f)}} \tag{3.131}$$

S-Parameter Determination

In general, the frequency-dependent scattering parameters S_{ij} can be obtained as follows [7]:

$$S_{ij}(f) = \frac{V_i(f)}{V_j(f)} \sqrt{\frac{Z_{0j}(f)}{Z_{0i}(f)}} \tag{3.132}$$

where V_i and V_j are the voltages at ports i and j, respectively, and Z_{0i} and Z_{0j} are the characteristic impedances of the line connected to those ports. The voltages and characteristic impedances are determined as discussed above.

3.3.7 Propagation in a Microstrip Line

The configuration of a microstrip line to be analyzed using the FDTD technique is shown in Figure 3.23. The geometrical details and the FDTD discretization details for the analysis of this line are given in Table 3.1. A Gaussian pulse excitation is used at the $z = 0$ plane. The excitation electric fields are quasi-static fields calculated using the finite-difference approach. The propagation constant in the microstrip line is calculated as described in Section 3.3.6 and the effective dielectric constant is determined as

$$\epsilon_{re}(f) = \left(\frac{\beta(f)}{k_0}\right)^2 \tag{3.133}$$

where $\beta(f)$ is the frequency-dependent phase constant and k_0 is the free-space wave number. Two different absorbing boundary conditions are studied in order to reduce computational expenses. In one case, first-order Mur ABC

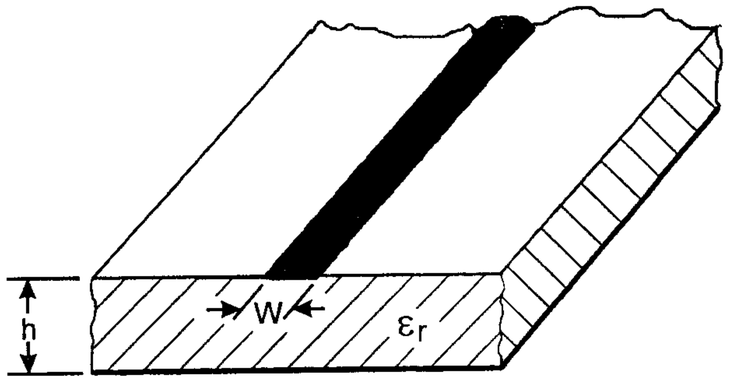

Figure 3.23 Configuration of a microstrip line.

Table 3.1
Microstrip Line Parameters and Discretization Details

Dielectric constant: $\epsilon_r = 2.2$
Width of the strip: $W = 2.394$ mm
Thickness of substrate: $h = 0.795$ mm
Cell size (mm): $\Delta x = 0.399$, $\Delta y = 0.400$, $\Delta z = 0.265$
Number of cells: $60 \times 100 \times 16$
Number of time steps: $N = 4096$
Time step: $\Delta t = 0.441$ psec.
Gaussian pulse: $T = 35\Delta t$, $t_0 = 3T$

and in the other case PML ABC (10, 2, 0.01) are used. It is observed that the value of ϵ_{re} corresponding to Mur ABC oscillates about the exact value as shown in Figure 3.24. But these oscillations are not present in the case of PML ABC. The value based on the expression given in [84] is also plotted. This example shows the accuracy provided by PML ABC over Mur ABC. However, the computational overheads increase by a factor of 2 for PML media. The computational overhead can be decreased by moving the PML lateral boundary toward the microstrip line.

Variation of the characteristic impedance with frequency is determined using various approximations from (3.129)–(3.131). This is shown in Figure 3.25 [75]. It is observed that the imaginary part of the characteristic impedance is negligible if the definition for (3.131) is used. Moreover, (3.130) and (3.131) yield almost the same value for the real part of characteristic impedance, that is, temporal offset has a negligible effect.

3.3.8 Applications of the FDTD Technique to Microstrip Antennas

The FDTD technique has been used to analyze various types of microstrip and slot antennas, including rectangular patch antennas with probe feed [85–87],

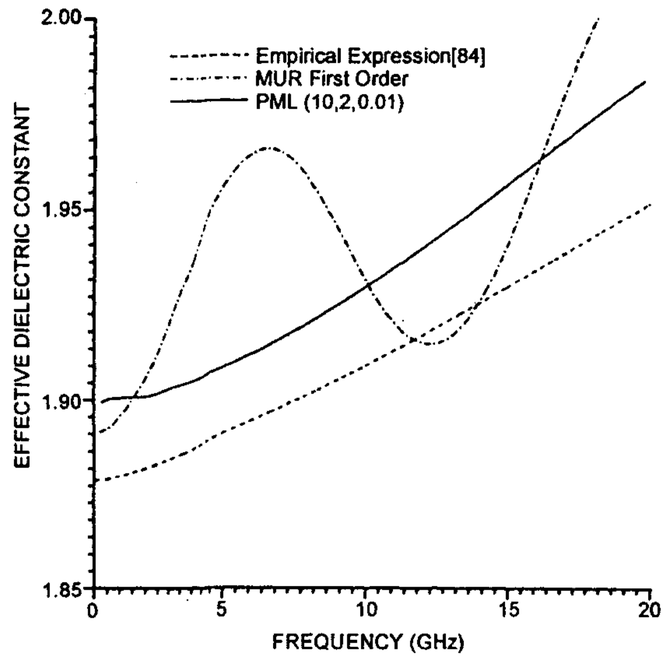

Figure 3.24 Effective dielectric constant of a microstrip line (see Table 3.1 for parameters). (From [75]. © 1999 *IETE Journal of Research (India)*. Reprinted with permission.)

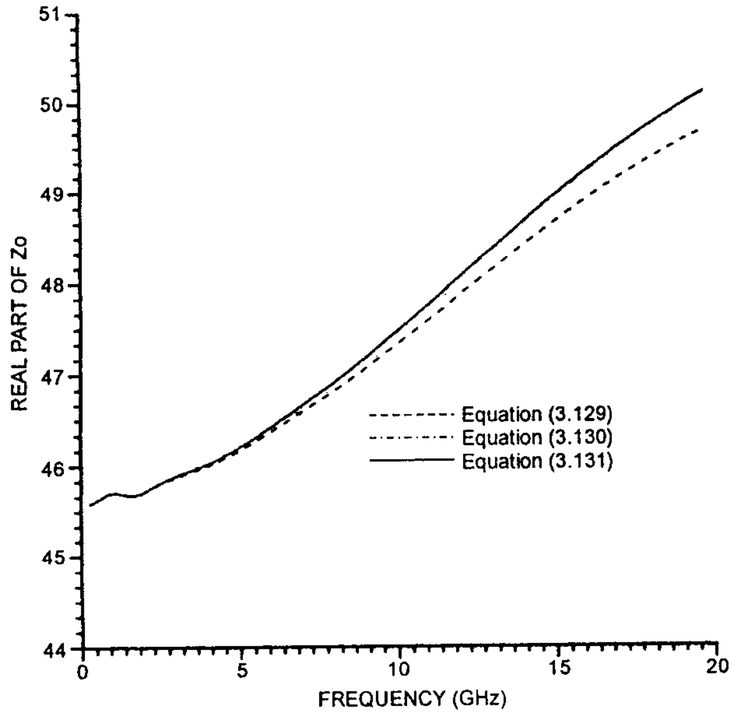

(a)

Figure 3.25 The characteristic impedance of a microstrip line (see Table 3.1 for parameters): (a) Real part of Z_0 and (b) imaginary part of Z_0. (From [75]. © 1999 *IETE Journal of Research (India)*. Reprinted with permission.)

antenna with microstrip edge feed [86, 88], microstrip line feed apertures coupled to the antenna [87], stacked microstrip antennas [85, 86, 89], circular patch antennas [90], printed dipoles [81], slot antennas [86, 91], and active microstrip antennas [92, 93]. Modeling of frequency-dependent complex permittivity is discussed in [94]. Uehara and Kagoshima analyzed mutual coupling between two microstrip antennas [95], and microstrip antennas on curved surfaces are analyzed in [96]. The FDTD technique is very useful in the analysis of handheld microstrip antennas and antennas with finite ground plane and dielectric. Details of a microstrip antenna with microstrip edge feed are given next.

The geometry of a patch antenna is shown in Figure 3.26. For the analysis of this antenna PML(10, 2, 0.01) is used. The structural parameters of the antenna are given in Table 3.2. The observed time response at the input port of the patch is a combination of incident and reflected fields. To obtain the

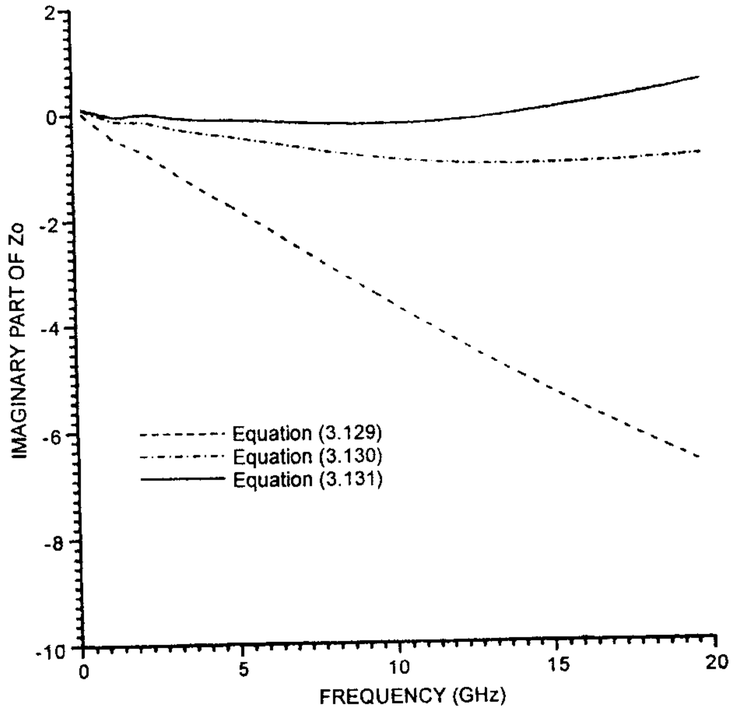

(b)

Figure 3.25 (continued).

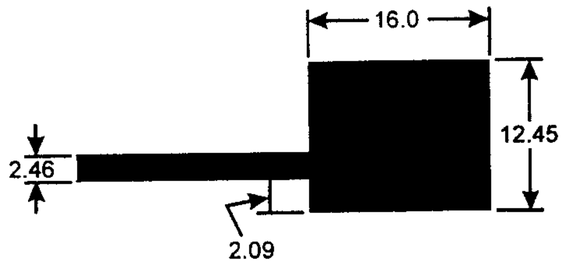

Figure 3.26 Microstrip line-fed microstrip patch antenna. (From [75]. © 1999 *IETE Journal of Research (India)*. Reprinted with permission.)

reflected fields, we need to subtract the incident field, which is obtained by replacing the patch antenna with an infinite microstrip line. The simulation results of return loss parameter $|S_{11}|$, shown in Figure 3.27 [75], compare very well with those given in [80]. The input impedance matched exactly at 7.5 and 18.0 GHz, as reported there. The time-domain response of the patch antenna at various instants of time is shown in Figure 3.28 [75]. This figure

Table 3.2
Patch Parameters and Discretization Details

Dielectric constant of the substrate: $\epsilon_r = 2.2$
Thickness of substrate: $h = 0.795$ mm
Width of the patch: $W = 16.00$ mm
Length of the patch: $L = 12.45$ mm
Cell size (mm): $\Delta x = 0.265$, $\Delta y = 0.389$, $\Delta z = 0.400$
Domain size: $60 \times 100 \times 16$
Number of time steps: $N = 8192$
Time step: $\Delta t = 0.441$ psec.
Gaussian pulse, $T = 35\Delta t$, $t_0 = 3T$

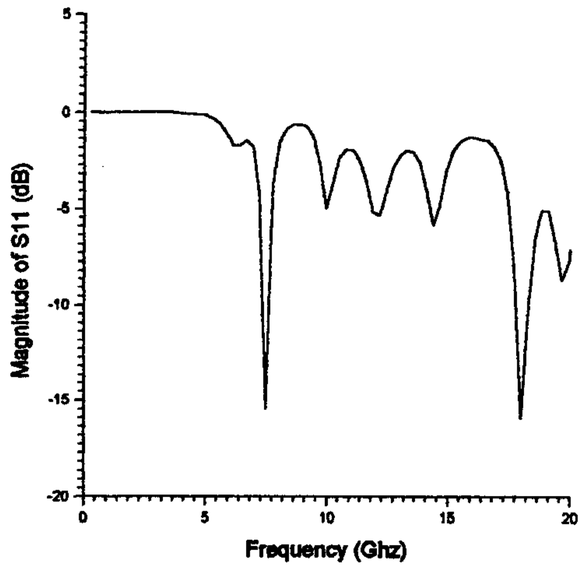

Figure 3.27 Return loss of microstrip patch antenna of Figure 3.26 (see Table 3.2 for parameters). (From [75]. © 1999 *IETE Journal of Research (India).* Reprinted with permission.)

illustrates the time marching behavior of the excitation pulse over the patch and the feed line.

Appendix 3A: Derivation of Green's Functions in the Spectral Domain

To derive the electric field Green's functions [3], let us consider a Hertzian dipole of electric current, located on the substrate surface. Equivalently, a unit

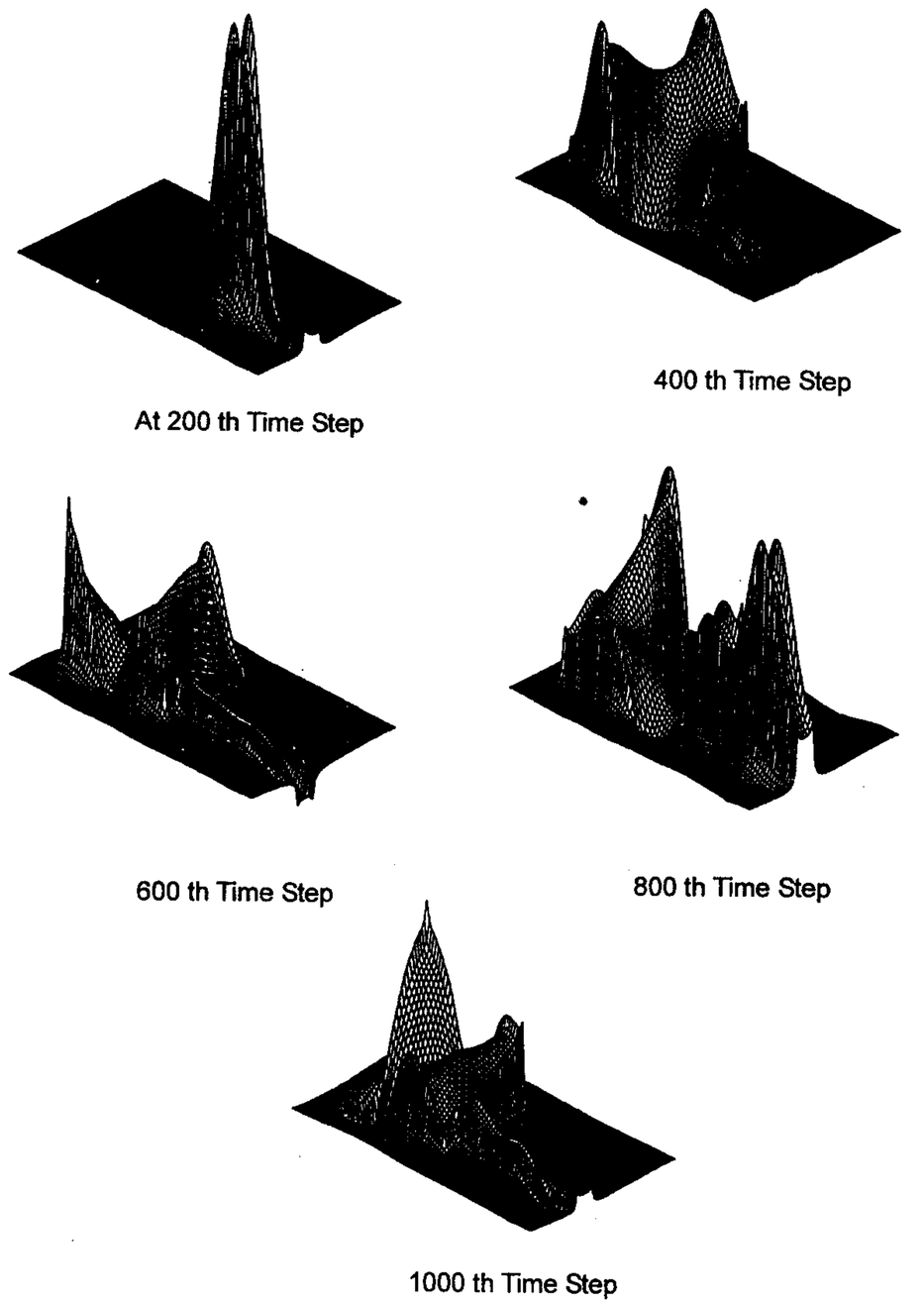

Figure 3.28 Time-domain propagation of pulse on microstrip patch antenna of Figure 3.26 (see Table 3.2 for parameters). (From [75]. © 1999 *IETE Journal of Research (India).* Reprinted with permission.)

strength infinitesimal current source in the x direction is considered first (see Figure 3.29). The substrate is assumed to be lossless and the ground plane is a perfect electric conductor. If the dipole source is located at (x_0, y_0), we can express the x-directed current as

$$J_x = \hat{x}\delta(x - x_0)\delta(y - y_0) \tag{3A.1}$$

The Green's function can be obtained through two different routes: the vector potential approach [13] and direct solution of the wave equations for E_z and H_z [3]. The latter approach involves simpler algebra and follows next. The vector potential approach is described in Appendix 3C.

The source-free Maxwell's equations, with time variation $\exp(j\omega t)$ assumed and suppressed, are

$$\nabla \times \overline{E} = -j\omega\mu_0\overline{H} \tag{3A.2a}$$

$$\nabla \times \overline{H} = +j\omega\epsilon_0\epsilon_r\overline{E} \tag{3A.2b}$$

The effect of current source J_x is included through an interface condition. Equations (3A.2a) and (3A.2b) can be solved simultaneously to give the wave equations

$$-\nabla \times \nabla \times \overline{E} + \omega^2\mu_0\epsilon_0\epsilon_r\overline{E} = 0 \tag{3A.3a}$$

$$-\nabla \times \nabla \times \overline{H} + \omega^2\mu_0\epsilon_0\epsilon_r\overline{H} = 0 \tag{3A.3b}$$

Applying the divergence condition $\nabla \cdot \overline{E} = 0$ to the z component of (3A.3a) and $\nabla \cdot \overline{H} = 0$ to the z component of (3A.3b) yields the wave equations

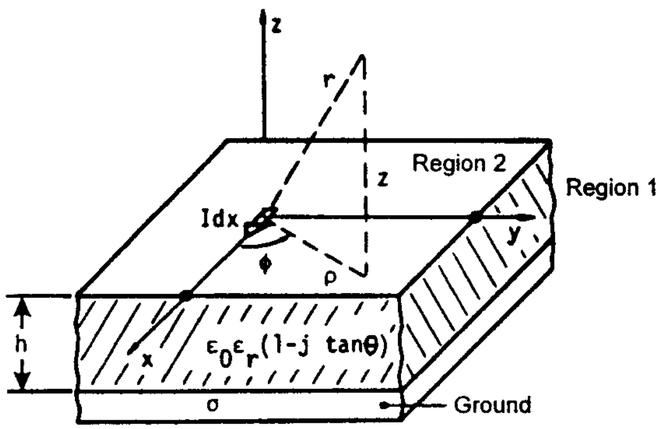

Figure 3.29 Geometry of a horizontal electric dipole (HED) on the surface of a grounded dielectric substrate.

$$\frac{\partial^2 E_z}{\partial x^2} + \frac{\partial^2 E_z}{\partial y^2} + \frac{\partial^2 E_z}{\partial z^2} + \epsilon_r k_0^2 E_z = 0 \tag{3A.4a}$$

$$\frac{\partial^2 H_z}{\partial x^2} + \frac{\partial^2 H_z}{\partial y^2} + \frac{\partial^2 H_z}{\partial z^2} + \epsilon_r k_0^2 H_z = 0 \tag{3A.4b}$$

By using the most general solutions in the form of plane waves $\exp(\pm jk_x x \pm jk_y y \pm jk_z z)$, the above wave equations yield

$$k_x^2 + k_y^2 + k_z^2 = k_0^2\epsilon_r \tag{3A.5}$$

Hence, the propagation constant k_z is given by

$$k_1^2 = k_z^2 = \epsilon_r k_0^2 - \beta^2 \quad \text{for } 0 \le z < h \text{ (region 1)} \tag{3A.6a}$$

$$k_2^2 = k_z^2 = k_0^2 - \beta^2 \quad \text{for } z > h \text{ (region 2)} \tag{3A.6b}$$

where

$$\beta^2 = k_x^2 + k_y^2 \tag{3A.7}$$

Because the analysis is carried out in the Fourier domain, we will use Fourier transformed fields, current densities, and so on. We define a Fourier transform pair as follows:

$$\psi(x, y, z) = \frac{1}{4\pi^2}\int_{-\infty}^{\infty}\int_{-\infty}^{\infty}\tilde{\psi}(k_x, k_y, z)e^{jk_x x}e^{jk_y y}dk_x dk_y \tag{3A.8a}$$

$$\tilde{\psi}(k_x, k_y, z) = \int_{-\infty}^{\infty}\int_{-\infty}^{\infty}\psi(x, y, z)e^{-jk_x x}e^{-jk_y y}dxdy \tag{3A.8b}$$

Maxwell's equations in (3A.2) can be Fourier transformed to obtain the following expressions ($\partial/\partial x \to +jk_x$, $\partial/\partial y \to +jk_y$):

$$\tilde{E}_x = \frac{jk_x}{\beta^2}\frac{\partial \tilde{E}_z}{\partial z} + \frac{\omega\mu_0 k_y}{\beta^2}\tilde{H}_z \tag{3A.9a}$$

$$\tilde{E}_y = \frac{jk_y}{\beta^2}\frac{\partial \tilde{E}_z}{\partial z} - \frac{\omega\mu_0 k_x}{\beta^2}\tilde{H}_z \tag{3A.9b}$$

$$\tilde{H}_x = \frac{jk_x}{\beta^2}\frac{\partial \tilde{H}_z}{\partial z} - \frac{\omega\epsilon_0\epsilon_r k_y}{\beta^2}\tilde{E}_z \tag{3A.9c}$$

$$\tilde{H}_y = \frac{jk_y}{\beta^2}\frac{\partial \tilde{H}_z}{\partial z} + \frac{\omega\epsilon_0\epsilon_r k_x}{\beta^2}\tilde{E}_z \tag{3A.9d}$$

The solutions for $\tilde{E}_x$ and $\tilde{E}_y$ are obtained by assuming the following general forms for $\tilde{E}_z$ and $\tilde{H}_z$ in regions 1 and 2:

$$\tilde{E}_{z2} = Ae^{-jk_2 z} \tag{3A.10a}$$

$$\tilde{H}_{z2} = Be^{-jk_2 z} \tag{3A.10b}$$

$$\tilde{E}_{z1} = C\cos(k_1 z) + D\sin(k_1 z) \tag{3A.10c}$$

$$\tilde{H}_{z1} = E\sin(k_1 z) + F\cos(k_1 z) \tag{3A.10d}$$

The constants A to F in the above equations are obtained by applying the following boundary conditions:

$$\tilde{E}_x = 0 \text{ at } z = 0 \tag{3A.11a}$$

$$\tilde{E}_y = 0 \text{ at } z = 0 \tag{3A.11b}$$

$$\text{Continuity of } \tilde{E}_x \text{ at } z = h, \text{ that is, } \tilde{E}_{x1} = \tilde{E}_{x2} \tag{3A.11c}$$

$$\text{Continuity of } \tilde{E}_y \text{ at } z = h, \text{ that is, } \tilde{E}_{y1} = \tilde{E}_{y2} \tag{3A.11d}$$

$$\text{Continuity of } \tilde{H}_x \text{ at } z = h, \text{ that is, } \tilde{H}_{x1} = \tilde{H}_{x2} \tag{3A.11e}$$

$$\text{Continuity of } \tilde{H}_y \text{ at } z = h - 0, \text{ that is, } \tilde{H}_{y1} - \tilde{H}_{y2} = \tilde{J}_x \tag{3A.11f}$$

Substitute (3A.10) for $\tilde{E}_z$ and $\tilde{H}_z$ in (3A.9) for regions 1 and 2. Now subject (3A.9) to the boundary conditions of (3A.11). After completing a considerable amount of algebraic computations, one obtains expressions for the constants A to F resulting in the following expressions for $\tilde{E}_z$ and $\tilde{H}_z$ [3]:

$$\tilde{E}_{z2} = \frac{k_x k_1 \sin(k_1 h)}{j\omega\epsilon_0 T_m} e^{-jk_2(z-h)}\tilde{J}_x \tag{3A.12a}$$

$$\tilde{H}_{z2} = \frac{-jk_y \sin(k_1 h)}{T_e} e^{-jk_2(z-h)}\tilde{J}_x \tag{3A.12b}$$

$$\tilde{E}_{z1} = \frac{k_x k_2 \cos(k_1 z)}{\omega\epsilon_0 T_m}\tilde{J}_x \tag{3A.12c}$$

$$\tilde{H}_{z1} = \frac{-jk_y \sin(k_1 z)}{T_e}\tilde{J}_x \tag{3A.12d}$$

where

$$T_m = \epsilon_r k_2 \cos(k_1 h) + jk_1 \sin(k_1 h) \tag{3A.13a}$$

$$T_e = k_1 \cos(k_1 h) + jk_2 \sin(k_1 h) \tag{3A.13b}$$

Use of (3A.12) into (3A.9a) yields at $z = h$ ($\partial/\partial z = -jk_2$),

$$\tilde{E}_x(k_x, k_y, h) = \frac{-j}{\omega\epsilon_0}\left[\frac{k_x^2 k_1 k_2 \sin(k_1 h)}{\beta^2 T_m} + \frac{k_y^2 k_0^2 \sin(k_1 h)}{\beta^2 T_e}\right]\tilde{J}_x \tag{3A.14a}$$

Similarly, $\tilde{E}_y$ at $z = h$ is

$$\tilde{E}_y(k_x, k_y, h) = \frac{-j}{\omega\epsilon_0}\left[\frac{k_x k_y k_1 k_2 \sin(k_1 h)}{\beta^2 T_m} - \frac{k_x k_y k_0^2 \sin(k_1 h)}{\beta^2 T_e}\right]\tilde{J}_x \tag{3A.14b}$$

$$\tilde{E}_z(k_x, k_y, h) = \frac{-j}{\omega\epsilon_0}\frac{k_1 k_x \sin(k_1 h)}{T_m}\tilde{J}_x \tag{3A.14c}$$

Equations (3A.14a), (3A.14b), and (3A.14c) are the electric field expressions in the spectral domain. In an analogous manner, the electric field due to a y-directed current element can be obtained. This expression can also be obtained by the interchange $x \leftrightarrow y$ in (3A.14). We obtain

$$\tilde{E}_y(k_x, k_y, h) = \frac{-j}{\omega\epsilon_0}\left[\frac{k_y^2 k_1 k_2 \sin(k_1 h)}{\beta^2 T_m} + \frac{k_x^2 k_0^2 \sin(k_1 h)}{\beta^2 T_e}\right]\tilde{J}_y \tag{3A.15a}$$

$$\tilde{E}_x(k_x, k_y, h) = \frac{-j}{\omega\epsilon_0}\left[\frac{k_x k_y k_1 k_2 \sin(k_1 h)}{\beta^2 T_m} - \frac{k_x k_y k_0^2 \sin(k_1 h)}{\beta^2 T_e}\right]\tilde{J}_y \tag{3A.15b}$$

Comparing expressions (3A.14) and (3A.15) with the matrix relationship,

$$\begin{bmatrix}\tilde{E}_x \\ \tilde{E}_y\end{bmatrix} = \begin{bmatrix}\tilde{Z}_{xx} & \tilde{Z}_{xy} \\ \tilde{Z}_{yx} & \tilde{Z}_{yy}\end{bmatrix}\begin{bmatrix}\tilde{J}_x \\ \tilde{J}_y\end{bmatrix} \tag{3A.16}$$

we obtain the following expressions for the electric field Green's functions:

$$\tilde{Z}_{xx} = \frac{-j}{\omega\epsilon_0}\left[\frac{k_x^2 k_1 k_2 \sin(k_1 h)}{\beta^2 T_m} + \frac{k_y^2 k_0^2 \sin(k_1 h)}{\beta^2 T_e}\right] \tag{3A.17a}$$

$$\tilde{Z}_{xy} = \frac{-j}{\omega\epsilon_0}\left[\frac{k_x k_y k_1 k_2 \sin(k_1 h)}{\beta^2 T_m} - \frac{k_x k_y k_0^2 \sin(k_1 h)}{\beta^2 T_e}\right] \tag{3A.17b}$$

$$\tilde{Z}_{yy} = \frac{-j}{\omega\epsilon_0}\left[\frac{k_y^2 k_1 k_2 \sin(k_1 h)}{\beta^2 T_m} + \frac{k_x^2 k_0^2 \sin(k_1 h)}{\beta^2 T_e}\right] \tag{3A.17c}$$

$$\tilde{Z}_{yx} = \tilde{Z}_{xy} \tag{3A.17d}$$

The Green's functions in the space domain can be obtained by taking the inverse transform of (3A.17). The transverse electric Green's functions at (x, y, h) due to the unit strength electric current J_j at (x_0, y_0, h) can then be expressed as

$$E_i(x, y, h) = \frac{1}{4\pi^2}\int_{-\infty}^{\infty}\int_{-\infty}^{\infty}\tilde{Z}_{ij}\exp[jk_x(x - x_0)]\exp[jk_y(y - y_0)]\,dk_x dk_y$$

$$i, j = x, y \tag{3A.18}$$

Unlike (3A.17), this Green's function is in the form of an integral.

The above procedure can also be used to determine the Green's functions for an anisotropic substrate for which the value of the dielectric constant differs in the principal directions, that is, in general, $\epsilon_{xx} \neq \epsilon_{yy} \neq \epsilon_{zz}$ [3]. Derivation

of Green's functions for a multilayered geometry involves simpler algebra if the immitance approach [97] is followed.

Appendix 3B: Moment Method Solution

As a first step in the moment method solution of (3.6), the unknown surface current density on the patch is expanded in a set of N expansion or basis modes with unknown complex coefficients I_n. That is,

$$\bar{J}_s = \hat{x}\sum_{nx=1}^{N_x} I_{nx}J_{nx}(x, y) + \hat{y}\sum_{ny=1}^{N_y} I_{ny}J_{ny}(x, y) \tag{3B.1}$$

where J_{nx} and J_{ny} are called the known expansion functions or modes, and I_{nx} and I_{ny} are the unknown complex coefficients. The Fourier transform of these functions is defined as

$$F(J_{ni}) = \int\int_s J_{ni}e^{-jk_x x}e^{-jk_y y}\,dxdy \tag{3B.2}$$

The integration in (3B.2) is carried out over the range of the nth expansion mode. The Fourier transform of the basis current density can be denoted by $\tilde{J}_{ni}$ as well.

The next step in the moment method solution procedure is to take the inner product of (3.6) with respect to the testing functions J_{ms}:

$$\int\int_s \bar{E}(\bar{J}_e)\cdot\bar{J}_{ms}ds + \int\int_s \bar{E}(\bar{J}_s)\cdot\bar{J}_{ms}ds = 0 \tag{3B.3}$$

Using Galerkin's procedure, that is, the testing function identical to the expansion function, we arrive at the matrix equation

$$[Z]_{N\times N}[I]_{N\times 1} = [V]_{N\times 1}, \quad N = N_x + N_y \tag{3B.4}$$

The impedance matrix elements of (3B.4) are defined as

$$Z_{mn} = -\int\int_s \bar{J}_m\cdot\bar{E}_n(\bar{J}_n)ds \tag{3B.5a}$$

where $\bar{E}_n$ is the electric field generated by the nth expansion mode $\bar{J}_n$. Considering the x and y components of both $\bar{E}_n$ and $\bar{J}_m$, the general form of Z_{mn} will be

$$Z_{mn}^{ij} = -\int\int_s J_{mi} E_i(J_{nj}) ds \quad i, j = x, y \tag{3B.5b}$$

where $E_i(J_{nj})$ is the i-directed electric field generated by the current J_{nj}. The electric field in the Fourier domain $\tilde{E}_i$ is given by (3A.16), that is,

$$\tilde{E}_i(J_{nj}) = \tilde{Z}_{ij}\tilde{J}_{nj} = \tilde{Z}_{ij}F(J_{nj}) \tag{3B.6}$$

Taking its inverse transform, substituting in (3B.5b), and rearranging the terms, we obtain

$$Z_{mn}^{ij} = \frac{-1}{4\pi^2}\int_{-\infty}^{+\infty}\int\left(\int\int_s J_{mi} e^{jk_x x} e^{jk_y y} ds\right)\tilde{Z}_{ij}F(J_{nj})dk_x dk_y \tag{3B.7}$$

$$= \int_{-\infty}^{+\infty}\int F^*(J_{mi})Q_{ij}F(J_{nj})dk_x dk_y$$

where

$$Q_{ij} = \frac{-1}{4\pi^2}\tilde{Z}_{ij} \tag{3B.8}$$

The impedance matrix $[Z]$ can be expressed in the form of block submatrices as

$$[Z] = \begin{bmatrix} \left[\int\int F^*(J_{mx})Q_{xx}F(J_{nx})\right] & \left[\int\int F^*(J_{mx})Q_{xy}F(J_{ny})\right] \\ \left[\int\int F^*(J_{my})Q_{yx}F(J_{nx})\right] & \left[\int\int F^*(J_{my})Q_{yy}F(J_{ny})\right] \end{bmatrix} dk_x dk_y \tag{3B.9}$$

The elements for the voltage vector $[V]$ in (3B.4) are defined as

$$V_m = \int\int_s \bar{E}_e \cdot \bar{J}_m ds \tag{3B.10a}$$

where $\bar{E}_e = \bar{E}(J_e)$ is the electric field caused by the excitation current, for example, the current on the probe. By the use of the reciprocity theorem, the excitation source and the field it produces can be interchanged and V_m can be written as

$$V_m = \int\int\int_{\text{excitation}} \bar{J}_e \cdot \bar{E}_m dxdydz \tag{3B.10b}$$

Let us consider the excitation source to be a feed probe at (x_p, y_p). Idealizing the probe current as a filament, we can write

$$\bar{J}_e = \hat{z}\delta(x - x_p)\delta(y - y_p) \tag{3B.11}$$

Because J_e is z directed, it is clear that E_m is also taken to be z directed and generated by the mth expansion mode. So the general form of V_m will be

$$V_m^i = \int\int\int_{\text{probe}} \delta(x - x_p)\delta(y - y_p)E_z(J_{mi})dxdydz \tag{3B.12}$$

Generalizing (3A.12c) for the basis currents, we have

$$\tilde{E}_z(J_{mi}) = \frac{k_i k_2 \cos(k_1 z)}{\omega\epsilon_0 T_m}\tilde{J}_{mi} \quad \text{for } 0 < z < h$$

or

$$\int_0^h \tilde{E}_z(J_{mi})dz = \frac{k_i k_2 \sin(k_1 h)}{\omega\epsilon_0 k_1 T_m}\tilde{J}_{mi} \equiv \tilde{Z}_{zi}F(J_{mi}) \tag{3B.13}$$

where

$$\tilde{Z}_{zi} = \frac{-j\eta_0}{k_0}\frac{jk_i k_2 \sin(k_1 h)}{k_1 T_m} \tag{3B.14}$$

Substituting the inverse transform of (3B.13) in (3B.12), one obtains

$$V_m^i = \frac{1}{4\pi^2}\int_{-\infty}^{+\infty}\int\left(\iint_s \delta(x-x_p)\delta(y-y_p)e^{jk_x x}e^{jk_y y}dxdy\right)\tilde{Z}_{zi}F(J_{mi})dk_x dk_y$$

or

$$V_m^i = \int_{-\infty}^{+\infty}\int F(J_{mi})Q_{zi}e^{jk_x x_p}e^{jk_y y_p}dk_x dk_y \tag{3B.15}$$

where

$$Q_{zi} = \frac{1}{4\pi^2}\tilde{Z}_{zi} \tag{3B.16}$$

The voltage vector is as follows:

$$[V] = \left[\begin{bmatrix}\iint F(J_{mx})Q_{zx}\end{bmatrix}\right]\left[\begin{bmatrix}\iint F(J_{my})Q_{zy}\end{bmatrix}\right]e^{jk_x x_p}e^{jk_y y_p}dk_x dk_y \tag{3B.17}$$

Appendix 3C: Derivation of Potential Green's Functions

We now derive the potential Green's functions [1, 6]. The scalar and vector potentials are defined in (3.68), and they are related to each other through the Lorentz gauge, (3.69). These equations are reproduced here for convenience:

$$\mu\overline{H} = \nabla\times\overline{A} \tag{3C.1a}$$

$$\overline{E} = -j\omega\overline{A} - \nabla V \tag{3C.1b}$$

$$\nabla\cdot\overline{A} + j\omega\mu\epsilon V = 0 \tag{3C.2}$$

The general solutions for potentials are obtained from the homogeneous Helmholtz equations

$$(\nabla^2 + k^2)\overline{A} = 0 \tag{3C.3a}$$

$$(\nabla^2 + k^2)V = 0 \tag{3C.3b}$$

where $k = \omega\sqrt{\mu\epsilon}$ is the wave number in the medium considered (1 or 2).

It is not possible to express the vector potential in a closed form if the medium is inhomogeneous such as for a microstrip antenna. However, (3C.3a) in the spectral domain has a closed-form solution. For this, we define the double Fourier transform as

$$\tilde{f}(k_x, k_y) = \frac{1}{2\pi}\int_{-\infty}^{+\infty}\int f(x, y)\exp(-jk_x x - jk_y y)\,dxdy \tag{3C.4a}$$

$$f(x, y) = \frac{1}{2\pi}\int_{-\infty}^{+\infty}\int \tilde{f}(k_x, k_y)\exp(jk_x x + jk_y y)\,dk_x dk_y \tag{3C.4b}$$

Note that the above form of Fourier transform employs the factor $1/2\pi$ with both the direct and inverse transforms. In this respect, it is different from the form of transforms used earlier. The Fourier transform of (3C.3a) is obtained as

$$\left(\frac{d^2}{dz^2} - u_i^2\right)\tilde{\overline{A}} = 0 \quad i = 1, 2 \tag{3C.5}$$

where

$$u_i^2 = k_x^2 + k_y^2 - k_i^2 = k_\rho^2 - k_i^2$$

Let us define

$$u_1^2 = u_0^2 = k_\rho^2 - k_0^2 \quad \text{for } z \geq h \text{ (medium 1)} \tag{3C.6a}$$

$$u_2^2 = u^2 = k_\rho^2 - \epsilon_r k_0^2 \quad \text{for } 0 \leq z \leq h \text{ (medium 2)} \tag{3C.6b}$$

Notice that the medium numbers are interchanged here with respect to those specified in Figure 3.29. The general solution of (3C.5) for a Cartesian component of vector potential is

$$\tilde{A}_s = a\exp(-u_i z) + b\exp(+u_i z) \quad s = x, y, z \quad i = 1, 2 \tag{3C.6c}$$

where the constants a, b may be functions of spectral variables.

The transformed fields are obtained by using the Fourier transformed versions of (3C.1) and (3C.2). These fields must satisfy the boundary conditions on the interface and the ground plane. Since the Fourier transform is in the x-y plane and boundary conditions are applied along the z axis, the boundary conditions in the spectral domain are obtained from the Fourier transform of the boundary conditions in the space domain, that is,

$$\hat{z} \times (\bar{\tilde{E}}_1 - \bar{\tilde{E}}_2) = 0 \quad \text{at the interface } z = h \tag{3C.7a}$$

$$\hat{z} \times (\bar{\tilde{H}}_1 - \bar{\tilde{H}}_2) = \bar{\tilde{J}}_s \quad \text{at the interface } z = h \tag{3C.7b}$$

$$\hat{z} \times (\epsilon_1 \bar{\tilde{E}}_1 - \epsilon_2 \bar{\tilde{E}}_2) = \tilde{q}_s \quad \text{at the interface } z = h \tag{3C.7c}$$

$$\hat{z} \times (\bar{\tilde{H}}_1 - \bar{\tilde{H}}_2) = 0 \quad \text{at the interface } z = h \tag{3C.7d}$$

$$\hat{z} \times \bar{\tilde{H}}_2 = 0 \quad \text{at the ground plane } z = 0 \tag{3C.7e}$$

$$\hat{z} \times \bar{\tilde{E}}_2 = 0 \quad \text{at the ground plane } z = 0 \tag{3C.7f}$$

Introducing the electric field expression (3C.1b) in (3C.7f), one obtains

$$\hat{z} \times (j\omega \bar{\tilde{A}}_2 + \hat{x} j k_x \tilde{V}_2 + \hat{y} j k_y \tilde{V}_2) = 0 \quad \text{at } z = 0 \tag{3C.8}$$

Because the potential V is defined by its gradient, an arbitrary constant can always be added to it. The value $V = 0$ can thus be assigned to it at the ground plane, and (3C.8) gives

$$\hat{z} \times \bar{\tilde{A}}_2 = 0 \quad \text{at } z = 0 \tag{3C.9a}$$

$$V_2 = 0 \quad \text{at } z = 0 \tag{3C.9b}$$

The normal component of A_2 can be obtained by applying (3C.9b) to (3C.2) to obtain

$$\frac{d\tilde{A}_{2z}}{dz} = 0 \tag{3C.10}$$

Similarly, applying the boundary conditions (3C.7) at the interface at $z = h$ yields

$$\tilde{V}_1 = \tilde{V}_2 \tag{3C.11}$$

$$\bar{\tilde{A}}_1 = \bar{\tilde{A}}_2 \tag{3C.12}$$

$$\frac{1}{\mu} \hat{z} \times \left(\frac{d\bar{\tilde{A}}_1}{dz} - \frac{d\bar{\tilde{A}}_2}{dz} \right) = -\hat{z} \times \bar{\tilde{J}}_s \tag{3C.13}$$

Applying the Lorentz gauge condition to (3C.11) gives

$$\frac{1}{\epsilon_1} \nabla \cdot \bar{\tilde{A}}_1 = \frac{1}{\epsilon_2} \nabla \cdot \bar{\tilde{A}}_2 \tag{3C.14}$$

It is also useful to have a relationship between the potentials and the sources. Introducing the electric field expression of (3C.1b) into the boundary condition of (3C.7c) yields

$$j\omega(\epsilon_1 - \epsilon_2)\tilde{A}_z + \epsilon_1 d\tilde{V}_1/dz - \epsilon_2 d\tilde{V}_2/dz = -\tilde{q}_s \tag{3C.15}$$

The two Helmholtz equations (3C.3) along with the boundary conditions (3C.9)–(3C.15) define both the potentials in the spectral domain.

Vector potential: To determine the Green's functions for the potentials, we consider an x-directed horizontal electric dipole (HED) of moment Idx equal to unity at the air-dielectric interface of grounded dielectric substrate as shown in Figure 3.29 with the medium numbers interchanged. The surface current density associated with this dipole is given by

$$\bar{J}_s = \hat{x}\delta(x)\delta(y) \tag{3C.16a}$$

or

$$\tilde{\bar{J}}_s = \hat{x}(1/2\pi) \tag{3C.16b}$$

The inhomogeneous Helmholtz equation for the HED is

$$\left(\frac{d^2}{dz^2} - u_i^2\right)\tilde{\bar{A}} = \hat{x}(1/2\pi) \tag{3C.17}$$

If the dipole is embedded in a homogeneous medium of permittivity ϵ_0, the vector potential is parallel to the dipole and exhibits a spherical symmetry, that is,

$$\bar{A} = \hat{x}\frac{\mu_0}{4\pi r}e^{-jk_0 r} \tag{3C.18a}$$

or

$$\tilde{\bar{A}} = \hat{x}\frac{\mu_0}{2\pi u_0}e^{-u_0|z|} \tag{3C.18b}$$

However, in an inhomogeneous medium such as for a microstrip antenna, two components of $\bar{A}$ are needed to satisfy the continuity of V at the interface. If we adopt the Sommerfeld's choice, then

$$\bar{A} = \hat{x}A_x + \hat{z}A_z \tag{3C.19}$$

The solutions $\tilde{A}_x$ and $\tilde{A}_z$ of (3C.6c) satisfying the boundary conditions can be expressed as

$$\tilde{A}_x = \frac{\mu_0}{2\pi}\frac{e^{-u_0(z-h)}}{D_{\mathrm{TE}}} \quad \text{for } z \geq h \tag{3C.20a}$$

$$\tilde{A}_x = \frac{\mu_0}{2\pi}\frac{\sinh(uz)}{D_{\mathrm{TE}}\sinh(uh)} \quad \text{for } 0 \leq z \leq h \tag{3C.20b}$$

$$\tilde{A}_{zx} = jk_x(\epsilon_r - 1)\frac{\mu_0}{2\pi}\frac{e^{-u_0(z-h)}}{D_{\mathrm{TE}}D_{\mathrm{TM}}} \quad \text{for } z \geq h \tag{3C.21a}$$

$$\tilde{A}_{zx} = jk_x(\epsilon_r - 1)\frac{\mu_0}{2\pi}\frac{\cosh(uz)}{D_{\mathrm{TE}}D_{\mathrm{TM}}\cosh(uh)} \quad \text{for } 0 \leq z \leq h \tag{3C.21b}$$

where A_{zx} is the z component of potential due to the x-directed current, and

$$D_{\mathrm{TE}} = u_0 + u\coth(uh) \tag{3C.22a}$$

$$D_{\mathrm{TM}} = \epsilon_r u_0 + u\tanh(uh) \tag{3C.22b}$$

It can easily be verified that if $\epsilon_r = 1$ and $h \to \infty$, the vertical component A_z vanishes and becomes the free-space potential given by (3C.18b).

Scalar potential: Associated with the dipole surface current is the surface charge density q_x, and they are related through the continuity equation

$$\nabla \cdot \bar{J}_s + j\omega q_s = 0 \tag{3C.23}$$

The continuity equation when applied to the HED results in two point charges $q = \pm I/j\omega$ at the two ends of the dipole. Because $Idx = 1$, the associated electrostatic moment becomes

$$qdx = 1/j\omega \tag{3C.24}$$

The scalar potential associated with the dipole is given by the Lorentz gauge. By introducing (3C.20) and (3C.21) in (3C.2), one obtains [1, Chapter 8]

$$\tilde{V} = \frac{-jk_x}{2\pi j\omega\epsilon_0}\frac{N}{D_{\mathrm{TE}}D_{\mathrm{TM}}}e^{-u_0(z-h)} \quad \text{for } z \geq h \tag{3C.25a}$$

$$\tilde{V} = \frac{-jk_x}{2\pi j\omega\epsilon_0}\frac{N}{D_{\mathrm{TE}}D_{\mathrm{TM}}}\frac{\sinh(uz)}{\sinh(uh)} \quad \text{for } 0 \leq z \leq h \tag{3C.25b}$$

with

$$N = u_0 + u\tanh(uh) \tag{3C.26}$$

If the point of observation is also at $z = h$, the expressions for potentials reduce to

$$\tilde{A}_x = \frac{\mu_0}{2\pi}\frac{1}{D_{\mathrm{TE}}} \tag{3C.27}$$

$$\tilde{A}_{zx} = jk_x(\epsilon_r - 1)\frac{\mu_0}{2\pi}\frac{1}{D_{\text{TE}}D_{\text{TM}}} \tag{3C.28}$$

$$\tilde{V} = \frac{-jk_x}{2\pi j\omega\epsilon_0}\frac{N}{D_{\text{TE}}D_{\text{TM}}} \tag{3C.29}$$

The scalar potential V of an electrostatic dipole of moment $1/j\omega$ is related to the scalar potential V_q of a single unit point charge by

$$V = \frac{-1}{j\omega}\frac{\partial V_q}{\partial x} \tag{3C.30}$$

or in the spectral domain ($\partial/\partial x \rightarrow jk_x$)

$$\tilde{V} = \frac{-1}{j\omega}jk_x\tilde{V}_q \tag{3C.31}$$

Comparing (3C.31) with (3C.29), we can write for a unit point charge on the air-dielectric interface of microstrip

$$\tilde{V}_q = \frac{1}{2\pi\epsilon_0}\frac{N}{D_{\text{TE}}D_{\text{TM}}} \tag{3C.32}$$

The derivation of fields in the spectral domain is now straightforward:

$$\tilde{E}_x = -j\omega\tilde{A}_x - jk_x\tilde{V} \quad \mu\tilde{H}_x = -jk_y\tilde{A}_z \tag{3C.33a}$$

$$\tilde{E}_y = -jk_y\tilde{V} \quad \mu\tilde{H}_y = (\partial\tilde{A}_x/\partial z) - jk_x\tilde{A}_z \tag{3C.33b}$$

$$\tilde{E}_z = j\omega\tilde{A}_z - (\partial\tilde{V}/\partial z) \quad \mu\tilde{H}_z = -jk_y\tilde{A}_x \tag{3C.33c}$$

The field expressions may be compared with those obtained in Appendix 3A. Green's functions for a y-directed HED on the interface can be written down by inspection.

Appendix 3D: Numerical Evaluation of Scalar and Vector Potentials

The integrands in (3.83) have a branch-point singularity at $\lambda = k_0$. In addition, there are pole singularities associated with the zeros of D_{TE} and D_{TM}. These

singularities are identical to those we have come across in the evaluation of (3.12) for the matrix elements. Therefore, numerical evaluation of (3.83) proceeds along similar lines. Here, we describe the main considerations for the integration over $[0, \infty]$ on the real axis as shown in Figure 3.3. Typical behavior of the integrand is plotted in Figure 3.30 for the scalar potential G_V [1, Chapter 8]. The parameters selected are $\epsilon_r = 2.55$, $\tan\delta = 0$, $k_0h = 0.3\pi$, and $k_0\rho = 3$. The figure depicts branch-point behavior at A ($\lambda = k_0$) and pole singularity at B due to the first zero of D_{TM}. The main difficulties in the numerical integration are the infinite derivatives at the branch point and the strong variation near the complex pole. Moreover, the function oscillates and diverges at infinity.

Like the numerical evaluation of (3.12), here also we divide the integration interval into three subintervals, $[0, k_0]$, $[k_0, k_0\sqrt{\epsilon_r}]$, and $[k_0\sqrt{\epsilon_r}, \infty]$.

1. $[0, k_0]$: In this region, the integrand has branch-point singularity at $\lambda = k_0$. This introduces a sharp peak at this point. The infinite first derivative at k_0 corresponding to this branch point is eliminated with

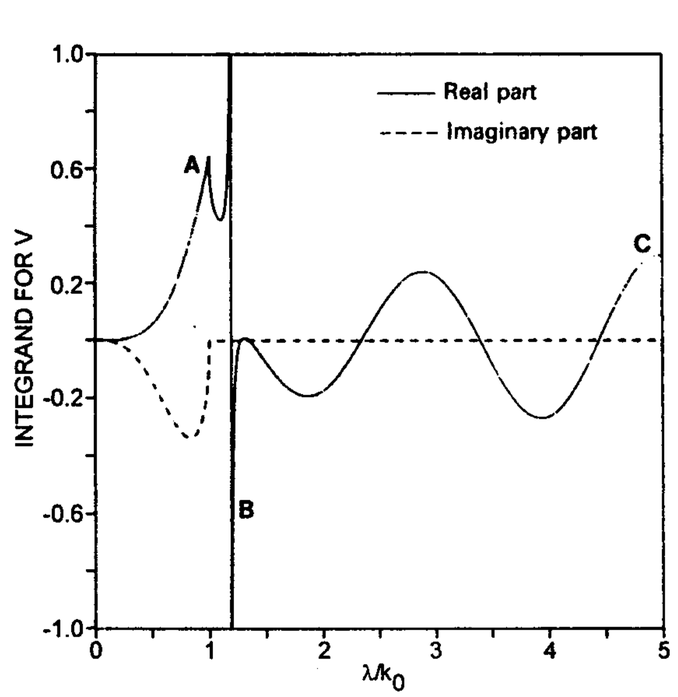

Figure 3.30 Normalized value of the integrand associated with the scalar potential. A, discontinuity due to the branch point; B, sharp peak due to the surface wave pole; C, oscillatory and divergent behavior at infinity. (From [1]. © 1989 Peter Peregrinus. Reprinted with permission.)

a change of variables $\lambda = k_0 \cosh t$. The smoother function so obtained can be integrated numerically.

2. $[k_0, k_0\sqrt{\epsilon_r}]$: The treatment of integration in this interval is similar to that carried out in Section 3.1.3. However, during the integration of the first part, one might come across a branch-point singularity. In that case, integration is carried out by first introducing the change of variables $\lambda = k_0 \cosh t$. Singularity extraction techniques can be used for evaluation near the poles. The effect of these operations is shown in Figure 3.31 [1, Chapter 8]. Here, the real part of the original integrand with singularities (solid line, A) and after the pole singularity has been extracted (dotted line, B) is plotted. Curve B still has an infinite derivative at $\lambda = k_0$. One obtains a smooth integrand after change of variables $\lambda = k_0 \cosh t$ (dashed line, C). Curve C can be integrated by Gaussian quadrature.

An alternative to choices 1 and 2 just described is to have a single interval $[0, k_0\sqrt{\epsilon_r}]$. Also, the integration in this interval is carried out along the

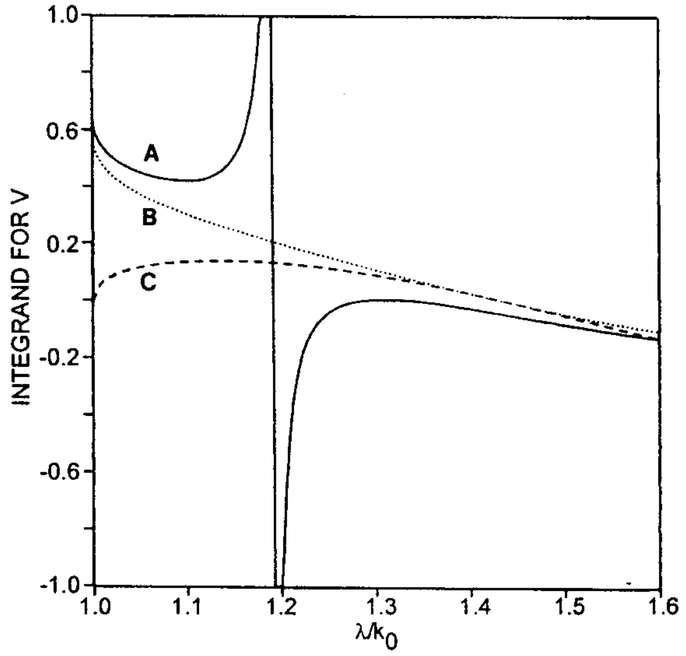

Figure 3.31 Real part of Figure 3.30 for the lossy substrate in the interval $[k_0, k_0\sqrt{\epsilon_r}]$. A, before the extraction of singularity; B, after the extraction of singularity but before the change of variable; C, after the change of variable $\lambda = k_0 \cosh t$. (From [1]. © 1989 Peter Peregrinus. Reprinted with permission.)

deformed path C_1 rather than along the real axis. The original path C and the deformed path are shown in Figure 3.32. The reasons behind the choice of deformed path follow.

While integrating along the real axis, one encounters branch-point and surface wave poles in this interval. The value of the function changes sharply as one approaches these singularities. Therefore, even if we use singularity extraction techniques, as suggested above, due to limited numerical precision in evaluating pole locations, the calculation between the original integrand and its residue terms cannot be done exactly, and results in sharp peaks around these pole locations. This problem is particularly severe for multilayered structures where one comes across a number of poles over a small spectral region. The closeness of poles also creates difficulties in finding the exact pole locations due to the limited numerical precision.

The modified contour C_1 takes an elliptical path described as [61, 49]

$$k_\rho(\theta) = B(1 + \cos\theta) + jA\sin\theta \tag{3D.1}$$

where $B = a/2$, $A \approx 0.1k_0$, and θ is the angle measured between the positive real axis with the radial point on the contour. With this change of variable, numerical integrations near the branch-point and surface wave poles are avoided. Note that A should be of the order of $0.1k_0$; otherwise, $\mathrm{Im}(k_\rho\rho)$ becomes large, and the integrand grows exponentially. If this argument is large, the integrand oscillates rapidly and severe round-off error and overflow occur.

3. $[k_0\sqrt{\epsilon_r}, \infty]$: The integrand over this interval is sketched as curve A in Figure 3.33 [1, Chapter 8]. There are oscillations and the function

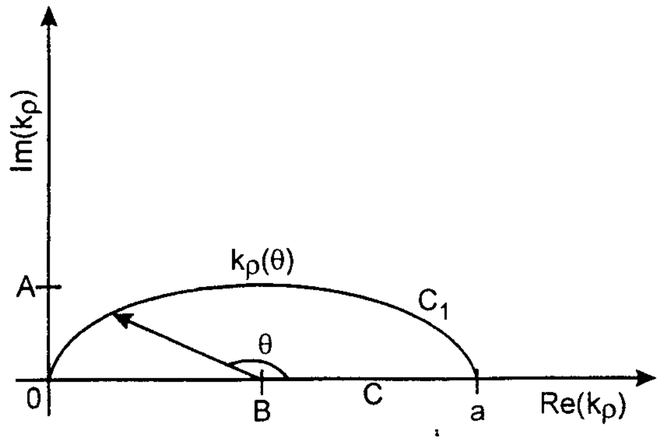

Figure 3.32 An alternative path of integration avoiding the branch point and pole singularities.

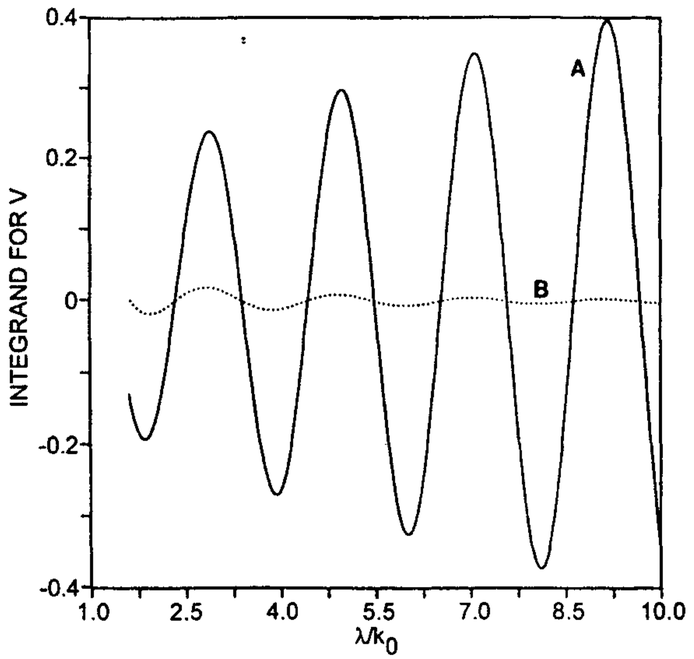

Figure 3.33 Real part of the integrand of Figure 3.30 for the lossy substrate in the interval $[k_0\sqrt{\epsilon_r}, \infty]$. A, before the extraction of static term; B, after the extraction of static term. (From [1]. © 1989 Peter Peregrinus. Reprinted with permission.)

diverges as shown in the figure. The oscillations of the integrand are due to the Bessel function. Like in Section 3.1.3, here again we use the asymptotic extraction technique to separate the dominant term. The asymptotic value ($k_\rho \to \infty$) of the integrand, which is equal to its static value ($k_0 \to 0$), is subtracted and added, that is, integral I is written as

$$I = I^d + I^h \tag{3D.2}$$

where

$$I^d = \int_0^\infty (G - C/\beta) J_0(\beta R)\, \beta d\beta \tag{3D.3}$$

and

$$I^h = \int_0^\infty C J_0(\beta R) d\beta \tag{3D.4}$$

The last integral represents the contribution from the asymptotic part of the Green's function. For the vector potential the asymptotic part is given by

$$G_s = \frac{\mu_0}{4\pi R} \tag{3D.5}$$

whereas for the scalar potential

$$G_s = \frac{1}{2\pi\epsilon_0(\epsilon_r + 1)R} \tag{3D.6}$$

The integrand of I^d is plotted as curve B in Figure 3.33 showing a slowly convergent oscillating function. This function can be integrated using a weighted-average algorithm [5, Chapter 3].

Far-field approximations for potentials: Far-field approximations are useful for calculating the coupling between distant conductors on the interface. We give below far-field approximations ($\rho \to \infty$) that can be used as a simple check of the validity of numerically integrated values. We assume a single dielectric layer with both the source and observer at the air-dielectric interface.

The asymptotic behavior of the vector potential is mainly determined by the branch point at $\lambda = k_0$ provided that no surface wave of the TE type is supported by the structure. The dominant term in the far field is [5, Chapter 3]

$$\frac{4\pi}{\mu_0} G_A^{xx} \approx \left(\frac{\tan\Delta}{\Delta}\right)^2 \frac{2j}{k_0} \frac{\exp(-jk_0\rho)}{\rho^2} \quad \Delta = k_0 h\sqrt{\epsilon_r - 1} \tag{3D.7}$$

It is of interest to check that by substituting $\epsilon_r = 1$ in (3D.7) one obtains the asymptotic expansion for the vector potential of a horizontal electric dipole over a ground plane.

The dominant TM surface wave always propagates in a microstrip structure and determines the asymptotic behavior of the scalar potential in the air-dielectric interface. For a single-layer lossless substrate, one obtains [5, Chapter 3]

$$4\pi\epsilon_0 G_V \approx -2\pi j P H_0^{(2)}(\lambda_P \rho) \tag{3D.8}$$

where P is the residue of the function $f = k_\rho N/D_{TE}D_{TM}$, $H_0^{(2)}(\cdot)$ is the Hankel function, and λ_p is the surface wave pole. Consequently, in a lossless case, the scalar potential decreases very slowly as $1/\sqrt{r}$ in the air-dielectric interface and can produce a strong coupling between various portions of a microstrip structure. Equation (3D.8) is more accurate for thick substrates and higher permittivities. Otherwise, a more precise uniform asymptotic expansion can be used [5].

References

[1] James, J. R., and P. S. Hall (Eds.), *Handbook of Microstrip Antennas*, Peter Peregrinus, London, UK, 1989.

[2] Pozar, D. M., "Microstrip Antennas," *Proc. IEEE*, Vol. 80, 1992, pp. 79–91.

[3] Pozar, D. M., "Radiation and Scattering From a Microstrip Patch on a Uniaxial Substrate," *IEEE Trans. on Antennas and Propagation*, Vol. AP-35, 1987, pp. 613–621.

[4] Deshpande, M. D., and M. C. Bailey, "Input Impedance of Microstrip Antennas," *IEEE Trans. on Antennas and Propagation*, Vol. AP-30, 1982, pp. 645–650.

[5] Itoh, T. (Ed.), *Numerical Techniques for Microwave and Millimeter-Wave Passive Structures*, John Wiley, New York, 1989.

[6] Mosig, J. R., and F. E. Gardiol, "A Dynamic Radiation Model for Microstrip Structures," *Advances in Electronics and Electron Physics*, Vol. 59, 1982, pp. 139–234.

[7] Taflove, A., *Computational Electrodynamics: The Finite Difference Time Domain Method*, Artech House, Norwood, MA, 1995.

[8] Kunz, K. S., and R. J. Lubers, *The Finite Difference Time Domain Method for Electromagnetics*, CRC Press, Boca Raton, FL, 1993.

[9] Collin, R. E., and F. J. Zucker (Eds.), *Antenna Theory, Part 1*, McGraw-Hill, New York, 1969, Chap. 3.

[10] Harrington, R. F., *Field Computation by Moment Methods*, Macmillan, New York, 1968.

[11] Pozar, D. M., "Considerations for Millimeter Wave Printed Antennas," *IEEE Trans. on Antennas and Propagation*, Vol. AP-31, 1983, pp. 740–747.

[12] Perlmutter, P., S. Shtrikman, and D. Treves, "Electric Surface Current Model for the Analysis of Microstrip Antennas With Application to Rectangular Elements," *IEEE Trans. on Antennas and Propagation*, Vol. AP-33, 1985, pp. 301–311.

[13] Pozar, D. M., "Input Impedance and Mutual Coupling of Rectangular Microstrip Antennas," *IEEE Trans. on Antennas and Propagation*, Vol. AP-30, 1982, pp. 1191–1196.

[14] Katehi, P. B., and N. G. Alexopoulos, "Real Axis Integration of Sommerfeld Integrals With Applications to Printed Circuit Antennas," *J. Math. Phys*, Vol. 24, 1983, pp. 527–533.

[15] Mosig, J. R., and F. E. Gardiol, "Analytical and Numerical Techniques in the Green's Function Treatment of Microstrip Antennas and Scatterers," *IEE Proc.*, Vol. 130, Pt. H, 1983, pp. 175–182.

[16] Reddy, V. S., and R. Garg, "An Efficient Analytical Evaluation of the Asymptotic Part of Sommerfeld Type Reaction Integrals in Microstrip/Slot Structures," *Proc. IEE*, Vol. 147, Part H, 2000, pp. 1–7.

[17] Pan, G. W. G., J. Tan, and J. D. Murphy, "Full Wave Analysis of Microstrip Floating-Line Discontinuities," *IEEE Trans.*, Vol. EC-36, 1994, pp. 49–59.

[18] Wang, G., and G. W. G. Pan, "Full Wave Analysis of Microstrip Floating Line Structures by Wavelet Expansion Method," *IEEE Trans. on Antennas and Propagation*, Vol. MTT-43, 1995, pp. 131–142.

[19] Park, S. O., and C. A. Balanis, "Analytical Technique To Evaluate the Asymptotic Part of the Input Impedance Matrix of Sommerfeld-Type Integrals," *IEEE Trans. on Microwave Theory and Techniques*, Vol. MTT-45, 1997, pp. 798–805.

[20] Park, S. O., C. A. Balanis, and C. R. Birtcher, "Analytical Evaluation of the Asymptotic Impedance Matrix of a Grounded Dielectric Slab With Roof-Top Functions," *IEEE Trans. on Antennas and Propagation*, Vol. AP-46, 1998, pp. 251–259.

[21] Damiano, J. P., J. Bennegueouche, and A. Papiernik, "Study of Multilayer Microstrip Antennas With Radiating Elements of Various Geometry," *Proc. IEE*, Pt. H, Vol. 137, 1990, pp. 163–170.

[22] Damiano, J. P., and A. Papiernik, "Survey of Analytical and Numerical Models for Probe-Fed Microstrip Antennas," *IEE Proc. Microwave Antennas Propagation*, Vol. 141, 1994, pp. 15–22.

[23] Yang, X. H., and L. Shafai, "Characteristics of Microstrip Antennas With Various Radiating Patches and Coupling Apertures," *IEEE Trans. on Antennas and Propagation*, Vol. AP-43, 1995, pp. 72–78.

[24] Himdi, M., J. P. Daniel, and C. Terret, "Transmission Line Analysis of Aperture Coupled Microstrip Antenna," *Electron. Lett.*, Vol. 25, 1989, pp. 1229–1230.

[25] Mosig, J. R., "Arbitrarily Shaped Microstrip Structures and Their Analysis With a Mixed Potential Integral Equation," *IEEE Trans. on Microwave Theory and Techniques*, Vol. MTT-36, 1988, pp. 314–323.

[26] Mosig, J. R., and F. E. Gardiol, "General Integral Equation Formulation for Microstrip Antennas and Scatterers," *Proc. IEE*, Pt. H, Vol. 132, 1985, pp. 424–432.

[27] Hall, R. C., and J. R. Mosig, "The Analysis of Dual Layer Coaxially Fed Microstrip Antennas," *JINA*, 1990, pp. 274–277.

[28] Hall, R. C., and J. R. Mosig, "Analysis of Coaxially Fed Microstrip Antennas With Electrically Thick Substrates," *Electromagnetics*, Vol. 9, 1989, pp. 367–384.

[29] Michalski, K. A., and C.-I. G. Hsu, "RCS Computation of Coax-Loaded Microstrip Patch Antennas of Arbitrary Shape," *Electromagnetics*, Vol. 14, 1994, pp. 33–62.

[30] Sullivan, P. L., and D. H. Schaubert, "Analysis of an Aperture Coupled Microstrip Antenna," *IEEE Trans. on Antennas and Propagation*, Vol. AP-34, 1986, pp. 977–984.

[31] Pozar, D. M., "A Reciprocity Method of Analysis for Printed Slot and Slot-Coupled Microstrip Antennas," *IEEE Trans. on Antennas and Propagation*, Vol. AP-34, 1986, pp. 1439–1445.

[32] Chew, W. C., and J. A. Kong, "Analysis of a Circular Microstrip Disk Antenna With a Thick Dielectric Substrate," *IEEE Trans. on Antennas and Propagation*, Vol. AP-29, 1981, pp. 68–76.

[33] Aberle, J. T., and D. M. Pozar, "Analysis of Infinite Arrays of One- and Two-Probe-Fed Circular Patches," *IEEE Trans. on Antennas and Propagation*, Vol. AP-38, 1990, pp. 421–432.

[34] Bailey, M. C., and M. D. Deshpande, "Analysis of Elliptical and Circular Microstrip Antennas Using Moment Method," *IEEE Trans. on Antennas and Propagation*, Vol. AP-33, 1985, pp. 954–959.

[35] Ali, S. M., W. C. Chew, and J. A. Kong, "Vector Hankel Transform Analysis of Annular-Ring Microstrip Antenna," *IEEE Trans. on Antennas and Propagation*, Vol. AP-30, 1982, pp. 637–644.

[36] Uzunoglu, N. K., N. G. Alexopoulos, and J. G. Fikioris, "Radiation Properties of Microstrip Dipoles," *IEEE Trans. on Antennas and Propagation*, Vol. AP-27, 1979, pp. 853–858.

[37] Shively, D. G., et al., "Scattering from Microstrip Patch Antennas Using Subdomain Basis Functions," *Electromagnetics*, Vol. 14, 1994, pp. 1–18.

[38] Pozar, D. M., and S. M. Voda, "A Rigorous Analysis of a Microstripline Fed Patch Antenna," *IEEE Trans. on Antennas and Propagation*, Vol. AP-35, 1987, pp. 1343–1350.

[39] Sullivan, P. L., and D. H. Schaubert, "Analysis of an Aperture Coupled Microstrip Antenna," *IEEE Trans. on Antennas and Propagation*, Vol. AP-34, 1986, pp. 977–984.

[40] Herscovici, N. I., and D. M. Pozar, "Analysis and Design of Multilayer Printed Antennas: A Modular Approach," *IEEE Trans. on Antennas and Propagation*, Vol. AP-41, 1993, pp. 1371–1378.

[41] Targonski, S. D., and D. M. Pozar, "Design of Wideband Circularly Polarized Aperture-Coupled Microstrip Antennas," *IEEE Trans. on Antennas and Propagation*, Vol. AP-41, 1993, pp. 214–220.

[42] Tulintseff, A. N., S. M. Ali, and J. A. Kong, "Input Impedance of a Probe-Fed Stacked Circular Microstrip Antenna," *IEEE Trans. on Antennas and Propagation*, Vol. AP-39, 1991, pp. 381–390.

[43] Hassani, H. R., and D. Mirshekar-Syahkal, "Study of Electromagnetically Coupled Stacked Rectangular Patch Antennas," *IEE Proc. Microwave Antennas Propagation*, Vol. 142, 1995, pp. 7–13.

[44] Das, N. K., and D. M. Pozar, "Multiport Scattering Analysis of General Multilayered Printed Antennas Fed by Multiple Feed Ports: Part I, Theory," *IEEE Trans. on Antennas and Propagation*, Vol. AP-40, 1992, pp. 469–481.

[45] Das, N. K., and D. M. Pozar, "Multiport Scattering Analysis of General Multilayered Printed Antennas Fed by Multiple Feed Ports: Part II, Applications," *IEEE Trans. on Antennas and Propagation*, Vol. AP-40, 1992, pp. 482–491.

[46] Pozar, D. M., "Analysis of an Infinite Array of Aperture Coupled Microstrip Patches," *IEEE Trans. on Antennas and Propagation*, Vol. AP-37, 1989, pp. 418–425.

[47] Bokhari, S. A., J. R. Mosig, and F. E. Gardiol, "Radar Cross Section Computation of Microstrip Patches," *Electromagnetics*, Vol. 14, 1994, pp. 19–31.

[48] Mosig, J. R., and T. K. Sarkar, "Comparison of Quasi-Static and Exact Electromagnetic Fields From a Horizontal Electric Dipole Above a Lossy Dielectric Backed by an Imperfect Ground Plane," *IEEE Trans. on Microwave Theory and Techniques*, Vol. MTT-34, 1986, pp. 379–387.

[49] Newman, E. H., and D. Forrai, "Scattering From a Microstrip Patch," *IEEE Trans. on Antennas and Propagation*, Vol. AP-35, 1987, pp. 245–250.

[50] Demuynck, F. J., G. A. E. Vandenbosch, and A. R. Van de Capelle, "The Expansion Wave Concept: Part I, Efficient Calculation of Spatial Green's Functions in a Stratified Dielectric Medium," *IEEE Trans. on Antennas and Propagation*, Vol. AP-46, 1998, pp. 397–406.

[51] Wu, K.-L., J. Litva, and R. Fralich, "Full Wave Analysis of Arbitrarily Shaped Line-Fed Microstrip Antennas Using Triangular Finite-Element Method," *Proc. IEE*, Pt. H, Vol. 138, 1991, pp. 421–428.

[52] Uckun, S., et al., "A Novel Technique for Analysis of Electromagnetic Scattering From Microstrip Antennas of Arbitrary Shape," *IEEE Trans. on Microwave Theory and Techniques*, Vol. MTT-45, 1997, pp. 485–491.

[53] Kahrizi, M., T. K. Sarkar, and Z. A. Maricevic, "Analysis of a Wide Radiating Slot in the Ground Plane of a Microstrip Line," *IEEE Trans. on Microwave Theory and Techniques*, Vol. MTT-41, 1993, pp. 29–37.

[54] Chen, C., and N. G. Alexopoulos, "Modeling Microstrip Line Fed Slot Antennas With Arbitrary Shape," *Electromagnetics*, Vol. 15, 1995, pp. 567–586.

[55] Hall, R. C., and J. R. Mosig, "The Analysis of Arbitrarily Shaped Aperture-Coupled Patch Antennas via a Mixed-Potential Integral Equation," *IEEE Trans. on Antennas and Propagation*, Vol. AP-44, 1996, pp. 608–614.

[56] Barlatey, L., J. R. Mosig, and T. Sphicopoulos, "Analysis of Stacked Microstrip Patches With a Mixed Potential Integral Equation," *IEEE Trans. on Antennas and Propagation*, Vol. AP-38, 1990, pp. 608–615.

[57] Vandenbosch, G. A. E., and A. R. Van de Capelle, "Mixed-Potential Integral Expression Formulation of the Electric Field in a Stratified Dielectric Medium Application to the Case of a Probe Current Source," *IEEE Trans. on Antennas and Propagation*, Vol. AP-40, 1992, pp. 806–817.

[58] Barlatey, L., J. R. Mosig, and F. E. Gardiol, "Hybrid Integral Equation Approach for Patch Antennas in Multilayered Substrates," *Proc. IEE*, Pt. H, Vol. 137, 1990, pp. 99–107.

[59] Vandenbosch, G. A. E., and F. J. Demuynck, "The Expansion Wave Concept: Part II, A New Way To Model Mutual Coupling in Microstrip Arrays," *IEEE Trans. on Antennas and Propagation*, Vol. AP-46, 1998, pp. 407–413.

[60] Michalski, K. A., and J. R. Mosig, "Discrete Complex Image Mixed-Potential Integral Equation Analysis of Microstrip Patch Antennas With Vertical Probe Feeds," *Electromagnetics*, Vol. 15, 1995, pp. 377–392.

[61] Champagne II, N. J., J. T. Williams, and D. R. Wilton, "Analysis of Resistively Loaded Printed Spiral Antennas," *Electromagnetics*, Vol. 14, 1994, pp. 363–395.

[62] Yee, K. S., "Numerical Solution of Initial Boundary Value Problems Involving Maxwell's Equations in Isotropic Media," *IEEE Trans. on Antennas and Propagation*, Vol. AP-14, 1966, pp. 302–307.

[63] Shlager, K. L., and J. B. Schneider, "A Selective Survey of the Finite Difference Time Domain Literature," *IEEE Trans.*, APM-37, No. 4, 1995, pp. 39–56.

[64] Taflove, A., and M. E. Brodwin, "Numerical Solution of Steady State Electromagnetic Scattering Problems Using the Time-Dependent Maxwell's Equations," *IEEE Trans. on Microwave Theory and Techniques*, Vol. MTT-23, 1975, pp. 623–630.

[65] Kodama, M., and M. Kunikaka, "On Precision of Solutions by Finite Difference Time Domain Method of Different Spacing," *IEICE Trans. C*, Vol. E76-B, 1993, pp. 315–317.

[66] Hallond, R., and J. W. Williams, "Total Field Versus Scattered Field Finite Difference Codes: A Comparative Assessment," *IEEE Trans.*, Vol. NS-30, 1983, pp. 4583–4588.

[67] Enquist, B., and A. Majda, "Absorbing Boundary Conditions for the Numerical Simulation of Waves," *Mathematics of Computation*, Vol. 31, 1977, pp. 629–651.

[68] Mur, G., "Absorbing Boundary Conditions for the Finite Difference Approximation of the Time Domain Electromagnetic Field Equations," *IEEE Trans.*, EMC-23, 1981, pp. 377–382.

[69] Higdon, R. L., "Numerical Absorbing Boundary Conditions for Wave Equation," *Mathematics of Computation*, Vol. 49, 1987, pp. 65–90.

[70] Berenger, J. P., "A Perfectly Matched Layer for the Absorption of Electromagnetic Waves," *J. Computational Physics*, Vol. 114, 1994, pp. 185–200.

[71] Katz, D. S., E. T. Thiele, and A. Taflove, "Validation and Extension to Three Dimensions of the Berenger PML Absorbing Boundary Condition for FDTD Meshes," *IEEE Trans.*, Vol. MGWL-4, 1994, pp. 268–270.

[72] Wu, Z., and J. Fang, "Numerical Implementation and Performance of Perfectly Matched Layer Boundary Condition for Waveguide Structures," *IEEE Trans. on Microwave Theory and Techniques*, Vol. MTT-43, 1995, pp. 2676–2683.

[73] Berenger, J. P., "Perfectly Matched Layer for the FDTD Solution of Wave Structure Interaction Problems," *IEEE Trans. on Antennas and Propagation*, Vol. AP-44, 1996, pp. 110–117.

[74] Gedney, S. D., "An Anisotropic Perfectly Matched Layer Absorbing Medium for the Truncation of FDTD Lattices," *IEEE Trans. on Antennas and Propagation*, Vol. AP-44, 1996, pp. 1630–1639.

[75] Reddy, V. S., and R. Garg, "Finite Difference Time Domain (FDTD) Analysis of Microwave Circuits—A Review With Examples," *IETE J. Research (India)*, Vol. 45, 1999, pp. 3–20.

[76] Choi, D. H., and W. J. R. Hoefer, "The Finite Difference Time Domain Method and Its Application to Eigenvalue Problems," *IEEE Trans. on Microwave Theory and Techniques*, Vol. MTT-34, 1986, pp. 1464–1470.

[77] Cherry, P. C., and M. F. Iskander, "FDTD Analysis of High Frequency Electronic Interconnection Effects," *IEEE Trans. on Microwave Theory and Techniques*, Vol. MTT-43, 1995, pp. 2445–2451.

[78] Zhao, A. P., A. V. Raisanen, and S. R. Cvetkovic, "A Fast and Efficient FDTD Algorithm for the Analysis of Planar Microstrip Discontinuities by Using Simple Source Excitation Scheme," *IEEE Trans.*, Vol. MGWL-5, 1995, pp. 341–343.

[79] Zhang, X., and K. K. Mei, "Time Domain Finite Difference Approach to the Calculation of Microstrip Discontinuities," *IEEE Trans. on Microwave Theory and Techniques*, Vol. MTT-36, 1988, pp. 1775–1787.

[80] Sheen, D. M., et al., "Application of Three Dimensional Finite Difference Time Domain Method to the Analysis of Planar Microstrip Circuits," *IEEE Trans. on Microwave Theory and Techniques*, Vol. MTT-38, 1990, pp. 849–857.

[81] Herault, J., et al., "A New Approach to Microstrip Antennas Using a Mixed Analysis: Transient Frequency," *IEEE Trans. on Antennas and Propagation*, Vol. AP-38, 1990, pp. 1166–1175.

[82] Furse, C. M., and O. P. Gandhi, "Why the DFT Is Faster Than the FFT for FDTD Time to Frequency Domain Conversions," *IEEE Trans.*, Vol. MGWL-5, 1995, pp. 326–328.

[83] Fang, J., and D. Xeu, "Numerical Errors in the Computation of Impedances by FDTD Method and Ways To Eliminate Them," *IEEE Trans.*, Vol. MGWL-5, 1995, pp. 6–8.

[84] Kirschning, M., and R. H. Jansen, "Accurate Model for Effective Dielectric Constant of Microstrip and Valid Up to Millimeter Wave Frequencies," *Electron. Lett.*, Vol. 25, 1982, pp. 272–273.

[85] Reineix, A., and B. Jecko, "Analysis of Microstrip Patch Antennas Using Finite Difference Time Domain Method," *IEEE Trans. on Antennas and Propagation*, Vol. AP-37, 1989, pp. 1361–1369.

[86] Wu, C., K.-L. Wu, Z.-Q. Bi, and J. Litva, "Accurate Characterization of Planar Printed Antennas Using Finite-Difference Time-Domain Method," *IEEE Trans. on Antennas and Propagation*, Vol. AP-40, 1992, pp. 526–534.

[87] Cheng, J.-C., N. I. Dib, and L. P. B. Katehi, "Theoretical Modeling of Cavity-Backed Patch Antennas Using a Hybrid Technique," *IEEE Trans. on Antennas and Propagation*, Vol. AP-43, 1995, pp. 1003–1013.

[88] Mittra, R., and P. H. Harms, "A New Finite-Difference Time-Domain (FDTD) Algorithm for Efficient Field Computation in Resonator Narrow-Band Structures," *IEEE Microwave Guided Wave Lett.*, Vol. 3, 1993, pp. 316–318.

[89] Chebolu, S., R. Mittra, and W. D. Becker, "The Analysis of Microwave Antennas Using the FDTD Method," *Microwave J.*, Jan. 1996, pp. 134–150.

[90] Dey, S., and R. Mittra, "A Locally Conformal Finite-Difference Time-Domain (FDTD) Algorithm for Modeling Three-Dimensional Perfectly Conducting Objects," *IEEE Microwave Guided Wave Lett.*, Vol. 7, 1997, pp. 273–275.

[91] Tsai, H.-S., and R. A. York, "FDTD Analysis of CPW-Fed Folded-Slot and Multiple-Slot Antennas on Thin Substrates," *IEEE Trans. on Antennas and Propagation*, Vol. AP-44, 1996, pp. 217–226.

[92] Toland, B., et al., "FDTD Analysis of an Active Antenna," *IEEE Microwave Guided Wave Lett.*, Vol. 3, 1993, pp. 423–425.

[93] Thomas, V. A., et al., "FDTD Analysis of an Active Antenna," *IEEE Microwave Guided Wave Lett.*, Vol. 4, 1994, pp. 296–298.

[94] Leveque, Ph., A. Reineix, and B. Jecko, "Modeling of Dielectric Losses in Microstrip Patch Antennas: Application to FDTD Method," *Electron. Lett.*, Vol. 28, 1992, pp. 539–541.

[95] Uehara, K., and K. Kagoshima, "FDTD Method Analysis of Mutual Coupling Between Microstrip Antennas," *IEICE Trans. on Commun.*, Vol. E76-B, 1993, pp. 762–764.

[96] Oonishi, T., T. Kashiwa, and I. Fukai, "Analysis of Microstrip Antennas on a Curved Surface Using the Conformal Grids FD-TD Method," *IEEE Trans. on Antennas and Propagation*, Vol. AP-42, 1994, pp. 423–427.

[97] Itoh, T., "Spectral Domain Immitance Approach for Dispersion Characteristics of Generalized Printed Transmission Lines," *IEEE Trans. on Microwave Theory and Techniques*, Vol. MTT-28, 1980, pp. 733–736.

4

Rectangular Microstrip Antennas

4.1 Introduction

A large number of microstrip patch antennas have been studied to date. An exhaustive list of these geometries along with their salient features is available [1]. The rectangular and circular patches are the basic and most commonly used microstrip antennas. These patches can be used for the simplest and the most demanding applications. For example, characteristics such as dual and circular polarizations, dual-frequency operation, frequency agility, broad bandwidth, feedline flexibility, beam scanning, omnidirectional patterning, and so on are easily obtained in these patch shapes. Because these geometries are separable in nature, their analysis is also relatively simple. This simplicity has led to their being the topic of a large number of research papers that are too numerous to list. Any new analytical or numerical technique is standardized by first applying it to these geometries.

The simplest microstrip patch configuration is undoubtedly the rectangular patch microstrip antenna. As shown in Figure 4.1, the basic antenna element is a strip conductor of dimensions L × W on a dielectric substrate of dielectric constant ϵ_r and thickness h backed by a ground plane. When the patch is excited by a feed, a charge distribution is established on the underside of the patch metalization and the ground plane. At a particular instant of time, the underside of the patch is positively charged and the ground plane is negatively charged. The attractive forces between these sets of charges tend to hold a large percentage of the charge between the two surfaces. However, the repulsive force between positive charges on the patch pushes some of these charges toward the edges, resulting in large charge density at the edges. These charges are the source of fringing fields and the associated radiation. The fringing field

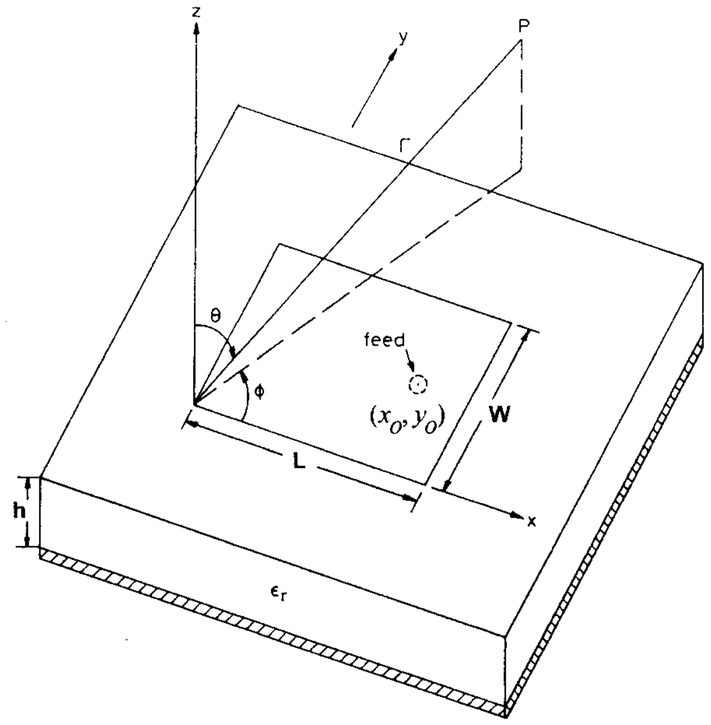

Figure 4.1 Geometry of a rectangular microstrip antenna. (From [1]. © 1989 Peter Peregrinus. Reprinted with permission.)

and the radiated power can be increased by using a thicker substrate with a lower value of dielectric constant.

Numerous attempts have been made to predict and evaluate the radiation characteristics of rectangular microstrip antennas. These have varied from elaborate mathematical formulations (Chapter 3) to simple and rigorous models (Chapter 2), which have often proven to be adequate. Nevertheless, like any other antenna, no exact solution has been possible. In this chapter, cavity model analysis is discussed in detail, and a step-by-step design procedure for rectangular microstrip antennas is presented to aid the antenna designer. The mechanical tuning of a rectangular patch is discussed. Finally, the quarter-wave rectangular patch is described. Loaded rectangular patch antennas for dual-frequency operation and mobile communications applications are discussed in Chapter 10.

4.2 Models for Rectangular Patch Antennas

The transmission line and cavity model analyses of rectangular microstrip antenna are discussed below. Details of these models are given in Chapter 2.

4.2.1 Transmission Line Model Analysis

The antenna has a physical structure derived from a microstrip transmission line. Therefore, the transmission line model is the first and obvious choice for the analysis and design of a rectangular patch. In this model, the microstrip antenna is modeled as a length of transmission line of characteristic impedance Z_0 and propagation constant $\gamma = \alpha + j\beta$. The fields vary along the length of the patch, which is usually a half-wavelength, and remain constant across the width. Radiation occurs mainly from the fringing fields at the open ends. The effect of radiation is accounted for by the radiation admittance called self-admittance Y_s attached at the open ends of the transmission line. Details of this model are given in Chapter 2. Only the salient features of this model are included here.

The simple transmission line model was proposed by Munson [2] and improved by Derneryd [3]. The probe-fed patch radiator along with the transmission line equivalent circuit is shown in Figure 4.2(a). Input impedance of the patch antenna based on this equivalent circuit is easily obtained as

$$Z_{\text{in}} = jX_L + Z_1 \tag{4.1}$$

where X_L is the probe reactance determined later in this chapter, and Z_1 ($= 1/Y_1$) is obtained from the transmission line transformation of Y_s, that is,

$$Y_1 = Y_0\left(\frac{Y_0 + jY_s\tan(\beta L_1)}{Y_s + jY_0\tan(\beta L_1)} + \frac{Y_0 + jY_s\tan(\beta L_2)}{Y_s + jY_0\tan(\beta L_2)}\right) \quad L_1 + L_2 = L \tag{4.2}$$

Here β is the phase constant in a microstrip line of width W. The simple transmission line model of Figure 4.2(a) predicts the radiation pattern of the antenna correctly, but the input impedance only approximately. This model has been improved to take into account the mutual coupling between the radiating apertures [4, 5]. In the improved transmission line model proposed by Bhattacharyya and Garg [5] [see Figure 4.2(b)], the mutual coupling effect, denoted by Y_m, is connected between the two ends of the transmission line. To solve for the voltage at the feed point, the transmission line section on either side of the feed source is converted into π-network equivalents (see Figure 2.5 in Chapter 2). The resulting equivalent circuit is then simplified using the star-delta and delta-star transformations. Pues and Van de Capelle [4] included the mutual admittance through voltage-dependent current sources across the self-admittances as shown in Figure 4.2(c). This approach requires the equivalent circuit to be a three-port network. For a microstrip antenna fed at one of the radiating edges, the input admittance is obtained as [4]

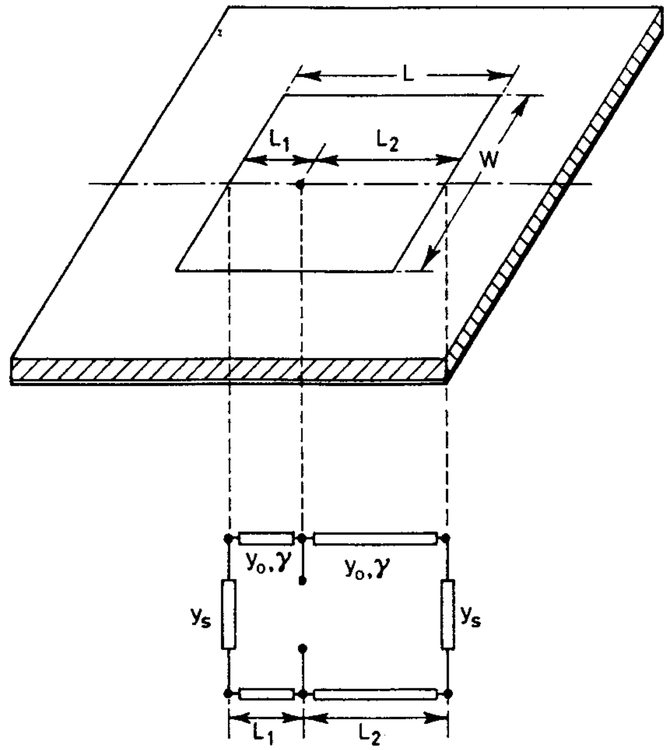

(a)

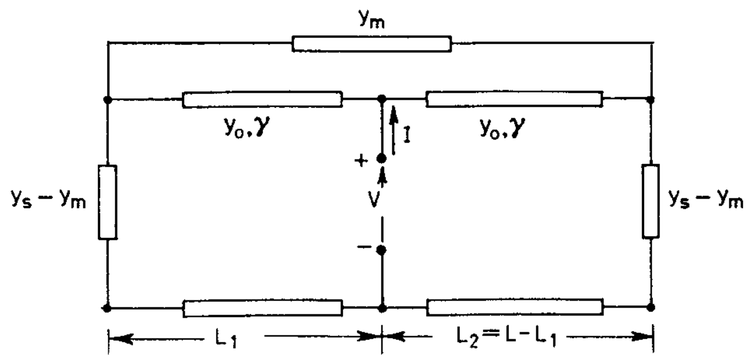

(b)

Figure 4.2 Probe-fed rectangular microstrip antenna and transmission line models: (a) Equivalent circuit based on simple transmission line model. (From [1]. © 1989 Peter Peregrinus. Reprinted with permission.) (b) Equivalent circuit including mutual coupling. (From [5]. © 1985 IEE. Reprinted with permission.) (c) Three-port alternative of part (b). (From [4]. © 1984 IEE. Reprinted with permission.)

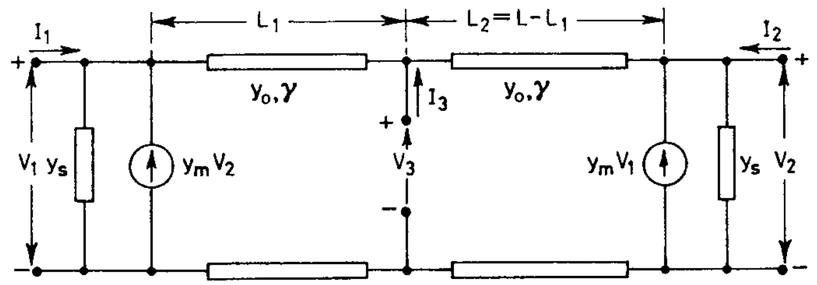

(c)

Figure 4.2 (continued).

$$Y_{in} = \frac{Y_0^2 + Y_s^2 - Y_m^2 + 2Y_0Y_s\coth(\gamma L) - 2Y_0Y_m\,\mathrm{csch}(\gamma L)}{Y_s + Y_0\coth(\gamma L)} \tag{4.3}$$

An expression for the input impedance of a probe-fed microstrip antenna is given in Chapter 2. The equivalent circuits of Figure 4.2 contain the transmission line parameters Y_0 and γ, self-admittance Y_s, and mutual admittance Y_m. The line parameters are defined in Appendix B, and the self- and mutual admittances are described in Chapter 2. The use of improved transmission line models improves the prediction of input impedance considerably as shown in [4, 5].

4.2.2 Cavity Model Analysis

The microstrip patch antennas are narrow-band resonant antennas. They are termed *lossy cavities*. Therefore, the cavity model becomes a natural choice to analyze the patch antennas. The cavity model was advanced by Richards et al. [6]. In this model, the interior region is modeled as a cavity bounded by electric walls on the top and bottom, and a magnetic wall all along the periphery. The basis for this assumption is the following observations for thin substrates ($h << \lambda_0$):

- The fields in the interior region do not vary with z (that is, $\partial/\partial z \equiv 0$) because the substrate is very thin, $h << \lambda_0$.
- The electric field is z directed only, and the magnetic field has only the transverse components H_x and H_y in the region bounded by the patch metalization and the ground plane. This observation provides for the electric walls at the top and bottom.

- The electric current in the patch normal to the edge of patch metalization is zero, which implies that the tangential component of $\overline{H}$ along the patch periphery is negligible, and a magnetic wall can be placed there. Mathematically, $\partial E_z/\partial n = 0$.

The field distribution in the patch can be divided into two regions: the interior fields and the exterior fields. The exterior fields are the fields outside the cavity region that determine the radiation characteristics of the patch antenna. The interior fields are useful in determining the input impedance of the antenna and the currents responsible for radiation. These fields are determined next.

Consider the region of the antenna between the patch metalization and ground plane. Because the dielectric is thin, the field distribution in this region can be described by TM to z modes with $\partial/\partial z \equiv 0$. As a result, there are only three components of fields E_z, H_x, and H_y. The electric field $\overline{E}$ must satisfy the wave equation

$$\nabla \times \nabla \times \overline{E} - k^2 \overline{E} = -j\omega\mu_0 \overline{J} \tag{4.4}$$

or

$$\frac{\partial^2 E_z}{\partial x^2} + \frac{\partial^2 E_z}{\partial y^2} + k^2 E_z = j\omega\mu_0 J \tag{4.5}$$

where $k^2 = \omega^2 \mu_0 \epsilon_0 \epsilon_r$ and J_z is the excitation electric current density either due to the coaxial feed or the microstrip feed.

The electric field in the patch cavity can be expressed in terms of various modes of the cavity as

$$E_z(x, y) = \sum_m \sum_n A_{mn} \psi_{mn}(x, y) \tag{4.6}$$

where A_{mn} are the amplitude coefficients corresponding to the (orthonormalized) electric field mode vectors or eigenfunctions ψ_{mn}. The electric field E_z can also be expressed as a single series [7] in place of the double series expansion of (4.6), resulting in improved computation speed. The eigenfunctions ψ_{mn} must satisfy the homogeneous wave equation, boundary conditions, and normalization conditions, that is,

$$\left.\frac{\partial \psi_{mn}}{\partial x}\right|_{x=0} = 0 = \left.\frac{\partial \psi_{mn}}{\partial x}\right|_{x=L} \tag{4.7a}$$

$$\left.\frac{\partial \psi_{mn}}{\partial y}\right|_{y=0} = 0 = \left.\frac{\partial \psi_{mn}}{\partial y}\right|_{y=W} \tag{4.7b}$$

$$\left(\frac{\partial^2}{\partial x^2} + \frac{\partial^2}{\partial y^2} + k_{mn}^2\right)\psi_{mn} = 0 \tag{4.8}$$

$$\int_x \int_y \psi_{mn} \psi_{mn}^* dx dy = 1 \tag{4.9}$$

The solutions of (4.7) to (4.9) are the orthonormalized eigenfunctions

$$\psi_{mn}(x, y) = \sqrt{\frac{\epsilon_m \epsilon_n}{LW}} \cos(k_m x) \cos(k_n y) \quad m, n = 0, 1, 2, p, \ldots \tag{4.10}$$

with

$$\epsilon_p = \begin{cases} 1 & \text{for } p = 0 \\ 2 & \text{for } p \neq 0 \end{cases}$$

$$k_m = m\pi/L,\ k_n = n\pi/W,\ k_{mn}^2 = k_m^2 + k_n^2 \tag{4.11}$$

The coefficients A_{mn} of (4.6) are determined by the excitation current. For this, substitute (4.10) into (4.5), multiply both sides of (4.5) by ψ_{mn}^*, and integrate over the area of the patch. Making use of orthonormal properties of ψ_{mn}, one obtains

$$A_{mn} = \frac{j\omega\mu_0}{k^2 - k_{mn}^2} \int_{\text{feed}} \int \psi_{mn}^* J_z dx dy \tag{4.12}$$

Let us model the coaxial feed as a rectangular current source with equivalent cross-sectional area $D_x D_y$ equal to the cross-sectional area of the probe centered at (x_0, y_0), that is,

$$J_z = \begin{cases} I_0/(D_x D_y) & x_0 - D_x/2 \le x \le x_0 + D_x/2 \quad y_0 - D_y/2 \le y \le y_0 + D_y/2 \\ 0 & \text{elsewhere} \end{cases} \tag{4.13}$$

Use of (4.13) in (4.12) gives

$$A_{mn} = \frac{1}{D_x D_y}\frac{j\omega\mu_0}{k^2 - k_{mn}^2}\iint_{\text{feed}} I_0 \psi_{mn}^* dxdy \tag{4.14}$$

$$= \frac{j\omega\mu_0 I_0}{k^2 - k_{mn}^2}\sqrt{\frac{\epsilon_m \epsilon_n}{LW}}\cos(k_m x_0)\cos(k_n y_0) G_{mn}$$

where

$$G_{mn} = \text{sinc}(n\pi D_x/(2L))\,\text{sinc}(m\pi D_y/(2W)) \tag{4.15}$$

For a microstrip line feed connected along the width of the patch, we should set $D_x = 0$ and D_y equal to the effective width of the feedline defined in Appendix B. Substituting (4.14) in (4.6) gives

$$E_z(x, y) = j\omega\mu_0 I_0 \sum_m \sum_{n=0}^{\infty} \frac{\psi_{mn}(x, y)\psi_{mn}(x_0, y_0)}{k^2 - k_{mn}^2} G_{mn} \tag{4.16}$$

The magnetic field components in the cavity region are determined from E_z and Maxwell's equations. The electric field is next used to calculate the input impedance of the antenna.

Input Impedance

Input impedance in this model is calculated as

$$Z_{\text{in}} = \frac{V_{\text{in}}}{I_0} \tag{4.17}$$

where V_{in} is the RF voltage at the feed point. It is computed from (4.16) as

$$V_{\text{in}} = -E_z(x_0, y_0)h \tag{4.18}$$

$$= -j\omega\mu_0 h I_0 \sum_m \sum_{n=0}^{\infty} \frac{\psi_{mn}^2(x_0, y_0)}{k^2 - k_{mn}^2} G_{mn}$$

Therefore, (4.17) for the input impedance becomes

$$Z_{\text{in}} = -j\omega\mu_0 h \sum_m \sum_{n=0}^{\infty} \frac{\psi_{mn}^2(x_0, y_0)}{k^2 - k_{mn}^2} G_{mn} \tag{4.19}$$

Equation (4.19) will yield the input impedance as reactive because all the quantities under the summation sign are real if the substrate is lossless. The effect of radiation and other losses on the input impedance has been included in the model in an ingenious manner. The substrate loss tangent is increased artificially to account for the power loss from the antenna [6]. The new loss tangent denoted as δ_{eff} was determined in Chapter 2. It is given by

$$\delta_{\text{eff}} = \tan\delta + \frac{\Delta}{h} + \frac{P_r}{\omega W_T} \tag{4.20}$$

Here $\tan\delta$ is the loss tangent of the substrate, Δ is the skin depth for the patch conductor, P_r is the power radiated by the patch antenna, and W_T is the time-averaged total energy stored under the patch geometry.

With the losses described in terms of δ_{eff}, the expression for k^2 in (4.19) is now modified as

$$k^2 = k_0^2\epsilon_r(1 - j\delta_{\text{eff}}) \tag{4.21}$$

to yield the following expression for Z_{in}:

$$Z_{\text{in}} = -j\omega\mu_0 h \sum_m \sum_{n=0}^{\infty} \frac{\psi_{mn}^2(x_0, y_0)}{k_0^2\epsilon_r(1 - j\delta_{\text{eff}}) - k_{mn}^2} G_{mn} \tag{4.22}$$

with

$$\psi_{mn}(x_0, y_0) = \sqrt{\frac{\epsilon_m \epsilon_n}{LW}}\cos(k_m x_0)\cos(k_n y_0)$$

The various terms in (4.22) can be identified as the contribution of various modes of the patch cavity. Based on this identification, an equivalent network for the patch can be drawn as in Figure 4.3(a) [6]. The (0, 0) term with $k_{00} = 0$ is the static capacitance of the patch, with a shunt resistance R_{00} accounting for the lossy substrate with loss tangent δ. The next term (1, 0) represents the resonant mode of the patch. It is identical to the transmission line mode discussed in Section 4.2.1. The impedance behavior for this mode can be expressed in the form of a parallel R-L-C network, where R_{10} represents the radiation, conductor, and dielectric losses. The (0, 1) mode can be represented by a similar R-L-C network. All the higher order modes have negligible losses (corresponding higher R), and their reactances can be clubbed in a single inductor L. The network of Figure 4.3(a) can be simplified to that of

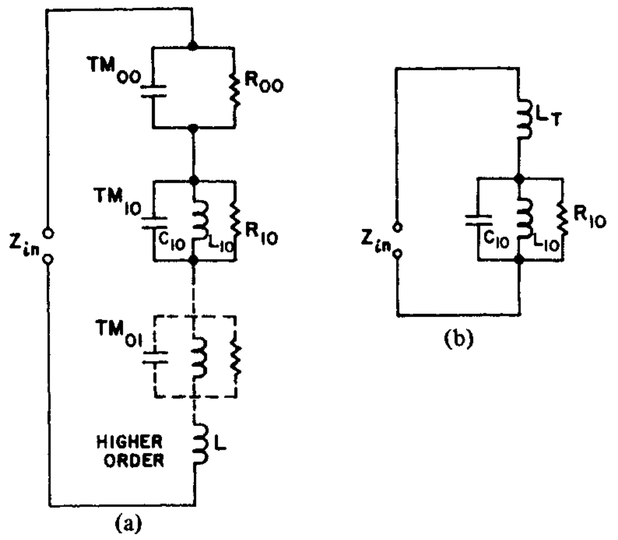

Figure 4.3 (a) General network model for microstrip antenna. (From [6]. © 1981 IEEE. Reprinted with permission.) (b) Simplified model of part (a) about the TM_{10} mode resonant frequency. (From [6]. © 1981 IEEE. Reprinted with permission.)

Figure 4.3(b) over the narrow band of frequencies about the resonant frequency of the TM_{10} mode. Here, the capacitance C_{00} and the inductance L have been combined to give the series inductance L_T. Expressions for the lumped elements C_{10} and L_{10} can be obtained from the (1, 0) term of (4.22) and are given below:

$$C_{10} = \lim_{\omega \to \infty} \frac{1}{j\omega X_{10}}$$

$$= \frac{\epsilon_0 \epsilon_r LW}{2h} \cos^{-2} \frac{\pi x_0}{L} \tag{4.23a}$$

$$L_{10} = \lim_{\omega \to 0} \frac{X_{10}}{j\omega} = \frac{1}{C_{10}\omega_r^2} \tag{4.23b}$$

Evaluation of Z_{in} for the (1, 0) mode at $k_{10}^2 = k_0^2 \epsilon_r$ gives

$$R_{10} = \frac{\omega \mu_0 h}{k_0^2 \epsilon_r \delta_{eff}} \frac{2}{LW} \cos^2\left(\frac{\pi x_0}{L}\right) \tag{4.23c}$$

$$= \frac{Q_T}{\omega_r C_{10}}$$

In deriving the above expressions we have used $\omega_r = k_0 c$ and $Q_T = 1/\delta_{eff}$. The reactance X_{10} is the input reactance for the $m = 1$, $n = 0$ mode. Alternatively, the lumped element values can be obtained from the measured impedance curve or the computed curve. If f_r is the resonant frequency of the patch antenna, R is the resonant resistance and Q_T is the total quality factor of the resonator, all obtained from the impedance curve, then

$$f_r = \frac{1}{2\pi\sqrt{LC}} \quad \text{and} \quad Q_T = R\sqrt{C/L}$$

The values of L and C are given by

$$L = \frac{R}{2\pi f_r Q_T}$$

$$C = \frac{Q_T}{2\pi f_r R}$$

and the input impedance for a R-L-C parallel resonant circuit is found to be

$$Z_{in} = R_{in} + jX_{in} = \frac{1}{\frac{1}{R} + j\omega C + \frac{1}{j\omega L}}$$

This simple model can be used to obtain an approximate value of input impedance as a function of frequency. We should point out that the feed reactance should be subtracted from the input reactance value before the resonant frequency is extracted, or the peak input resistance can be used to define the resonant frequency.

The input impedance of a probe-fed rectangular patch antenna is plotted in Figure 4.4 for three different feed locations [6]. The agreement between the computed values based on the cavity model and measured input impedance values appears to be very good. The resonant frequency for the given feed locations corresponds to the smaller dimension of 7.62 cm. It is observed from this figure that the impedance locus shrinks in size as the feed is shifted away from the radiating edge. The feed inductance can be determined from the impedance locus. For the moment let us consider the R-L-C network for the TM_{10} mode of Figure 4.3(b). The impedance locus of this network will be a circle symmetric about the $x = 0$ axis in the Smith chart. The asymmetry of the impedance locus in Figure 4.4 is due to the inductance L_T, also called

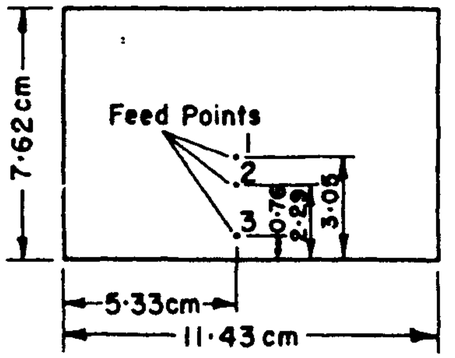

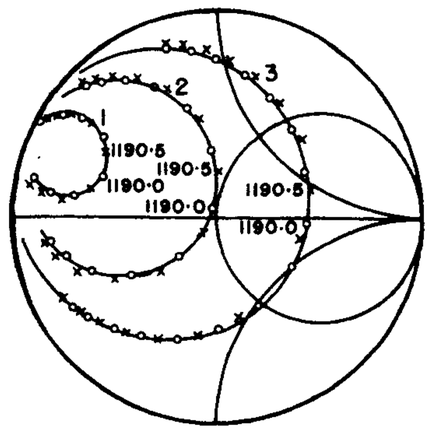

Figure 4.4 Comparison of computed and measured input impedance for a rectangular microstrip antenna for three different feed locations. Parameters: h = 1.59 mm, ϵ_r = 2.62, $\tan\delta$ = 0.001. (From [6]. © 1981 IEEE. Reprinted with permission.)

the feed inductance. The value of the feed reactance can be determined from Figure 4.4 by marking the center of the impedance circle. The reactance value for this point read from the Smith chart is the feed reactance.

Various other models have been used to predict the performance of the rectangular patch antenna. These include the modal expansion model, wire grid model, cavity with impedance walls, and multiport network model. The multiport network model was discussed in Chapter 2. Other models are discussed in [8]. Most of these models are viable, but all have their drawbacks. From the designer's point of view, the cavity model is simple and can provide closed-form design equations. Therefore, in the following section a design procedure is developed based largely on this model. The accuracy of the design information is improved by borrowing from full-wave analysis.

4.3 Design Considerations for Rectangular Patch Antennas

A microstrip antenna element can be used alone or in combination with other like elements as part of an array. In either case, the designer should have a step-by-step element design procedure. Feeding techniques have been discussed in Chapter 1 and will not be discussed further here.

Usually, the overall goal of a design is to achieve specific performance characteristics at a stipulated operating frequency. If a microstrip antenna configuration can achieve these overall goals, then the first decision is to select a suitable antenna geometry. A rectangular patch antenna can be designed using the procedure described in the next subsection.

4.3.1 Substrate Selection

The first design step is to choose a suitable dielectric substrate of appropriate thickness h and loss tangent. A thicker substrate, besides being mechanically strong, will increase the radiated power, reduce conductor loss, and improve impedance bandwidth. However, it will also increase the weight, dielectric loss, surface wave loss, and extraneous radiations from the probe feed. A rectangular patch antenna stops resonating for substrate thicknesses greater than $0.11\lambda_0$ (ϵ_r = 2.55) due to inductive reactance of the probe feed [9]. The substrate dielectric constant ϵ_r plays a role similar to that of substrate thickness. A low value of ϵ_r for the substrate will increase the fringing field at the patch periphery, and thus the radiated power. Therefore, substrates with $\epsilon_r \leq 2.5$ are preferred unless a smaller patch size is desired. An increase in the substrate thickness has a similar effect on antenna characteristics as a decrease in the value of ϵ_r. A high loss tangent increases dielectric loss and therefore reduces antenna efficiency. The other constraints and factors to be considered in making the choice of the substrate are detailed in Appendix A. The four most commonly used substrate materials are honeycomb (ϵ_r = 1.07), Duroid (ϵ_r = 2.32), quartz (ϵ_r = 3.8), and alumina (ϵ_r = 10).

4.3.2 Element Width and Length

Patch width has a minor effect on the resonant frequency and radiation pattern of the antenna. It affects the input resistance and bandwidth to a larger extent. A larger patch width increases the power radiated and thus gives decreased resonant resistance, increased bandwidth, and increased radiation efficiency. With proper excitation one may choose a patch width W greater than the patch length L without exciting undesired modes. A constraint against a larger patch width is the generation of grating lobes in antenna arrays, and a small

patch size might be preferred to reduce the real estate requirements. The patch width also affects cross-polarization characteristics. The patch width should be selected to obtain good radiation efficiency if real estate requirements or a grating lobe are not overriding factors. It has been suggested that $1 < W/L < 2$ [6, 7].

The patch length determines the resonant frequency, and is a critical parameter in design because of the inherent narrow bandwidth of the patch. To a zeroth-order approximation, the patch length L for the TM_{10} mode is given by

$$L = \frac{c}{2f_r\sqrt{\epsilon_r}} \tag{4.24}$$

The factor $\sqrt{\epsilon_r}$ in (4.24) is due to the loading by the substrate and is strictly valid for a very wide patch. In practice, the fields are not confined to the patch. A fraction of the fields lie outside the physical dimensions $L \times W$ of the patch. This is called the *fringing field*. The effect of the fringing field along the edges $y = 0$ and $y = W$ can be included through the effective dielectric constant ϵ_{re} for a microstrip line of width W on the given substrate. With the replacement of ϵ_r by ϵ_{re}, (4.24) becomes

$$L = \frac{c}{2f_r\sqrt{\epsilon_{re}}} \tag{4.25}$$

An expression for ϵ_{re} is given in Appendix B. The next improvement over (4.25) is obtained by including the effect of fringing fields at the other ends of the patch, that is, along the edges $x = 0$ and $x = L$. This effect can be described in terms of an additional line length ΔL on either ends of the patch length. Consequently, the effective patch length L_e becomes $L + 2\Delta L$, with [10]

$$\frac{\Delta L}{h} = \frac{\zeta_1\zeta_3\zeta_5}{\zeta_4} \tag{4.26}$$

The expressions for ζ_1, ζ_3, ζ_4, and ζ_5 are given in Appendix B. Based on this approach, one obtains the following design value for L:

$$L = \frac{c}{2f_r\sqrt{\epsilon_{re}}} - 2\Delta L \tag{4.27}$$

or

$$f_r = \frac{c}{2(L + 2\Delta L)\sqrt{\epsilon_{re}}} \tag{4.28}$$

Another way to include the effect of fringing fields at all edges of the patch is to describe these in terms of the effective dielectric constants for the width and length separately. Let $\epsilon_{re}(W)$ and $\epsilon_{re}(L)$ be the effective dielectric

$$\epsilon_{re}(W) = \frac{\epsilon_r + 1}{2} + \frac{\epsilon_r - 1}{2}F(W/h) \tag{4.29}$$

$$\epsilon_{re}(L) = \frac{\epsilon_r + 1}{2} + \frac{\epsilon_r - 1}{2}F(L/h) \tag{4.30}$$

where

$$F\left(\frac{a}{h}\right) = \begin{cases} (1 + 12h/a)^{-1/2} + 0.04(1 - a/h)^2 & a/h \le 1 \\ (1 + 12h/a)^{-1/2} & a/h \ge 1 \end{cases}$$

James et al. [11] have used this approach to determine the resonance frequency for the dominant TM_{10} mode of the rectangular patch antenna. It is given by

$$f_{10} = \frac{c}{2L}\frac{1}{1 + \Delta}\frac{\epsilon_r}{\sqrt{\epsilon_{re}(L)\,\epsilon_{re}(W)}} \tag{4.31}$$

Here Δ is an empirical correction factor obtained as

$$\Delta = \frac{h}{L}\left[0.882 + \frac{0.164(\epsilon_r - 1)}{\epsilon_r^2} + \frac{\epsilon_r + 1}{\pi\epsilon_r}\left\{0.758 + \ln\left(\frac{L}{h} + 1.88\right)\right\}\right] \tag{4.32}$$

Equation (4.31) is found to yield resonant frequency within 3% of the experimental value. The design based on (4.28) is more popular because of its better accuracy. The above design for the patch dimensions for the TM_{10} mode can be easily generalized to other resonant modes.

Kara has carried out a number of experimental investigations on the resonant frequency for the TM_{10} mode of a rectangular patch antenna [12,

13]. The substrates used were Duroid with $\tan\delta = 0.001$ and $\epsilon_r = 2.22$, $h = 0.17$ mm; $\epsilon_r = 2.33$, $h = 0.79$ and 1.57 mm; $\epsilon_r = 10.2$, $h = 1.27$ mm; and PTFE substrates with $\tan\delta = 0.002$, $\epsilon_r = 2.50$, $h = 1.50$ mm; and $\epsilon_r = 2.55$, $h = 1.63$ and 4.76 mm. The resonant frequency ranged from 3.97 to 8.45 GHz, and the substrate electrical thickness covered the range $0.0065 \leq h/\lambda_d \leq 0.1292$, $\lambda_d = \lambda_0/\sqrt{\epsilon_r}$. His studies show that ΔL calculated from [14]

$$\Delta L = 0.412h \frac{\epsilon_{re} + 0.300}{\epsilon_{re} - 0.258} \frac{W/h + 0.264}{W/h + 0.813} \tag{4.33a}$$

fits the measured resonant frequency within ±1.6% [12]. The value of ΔL given by (4.26) was not tested by him. It is expected that the use of (4.26) should result in a better fit. The value of the patch width W, necessary to obtain 50Ω input impedance, was found to be given by [13]

$$W = \sqrt{h\lambda_d}\,[\ln(\lambda_d/h) - 1] \tag{4.33b}$$

Multilayered Dielectric Microstrip Antenna

For certain feed designs like aperture coupling and proximity coupling, it is convenient to fabricate the antenna using two dielectric layers. In such instances, it is necessary to include the effect of these layers to determine the resonant frequency. Zhong et al. [15] have developed a closed-form expression for the resonant frequency of the TM_{10} mode. Conformal transformation is used to determine the effective dielectric constant of the multilayered microstrip line of which the rectangular patch is a section. End effect and dispersion effects from well-known sources are used to arrive at an accurate expression. The geometry of the rectangular microstrip antenna employing multilayered dielectric is shown in Figure 4.5. Substrate parameters are also defined in this figure. The resonant frequency of this antenna is given by (4.28) with the expression for ϵ_{re} for the multilayered microstrip line given in Appendix B, (B.27c). The open-end extension ΔL is obtained from (4.26) with quantities ϵ_r and W/h replaced by ϵ_r' and W_e/h_{12}, respectively. The expression for the equivalent relative permittivity ϵ_r' is given by [15]

$$\epsilon_r' = \frac{2\epsilon_{re} - 1 + A}{1 + A} \tag{4.34a}$$

$$A = \left(1 + \frac{12h_{12}}{W}\right)^{-1/2} \tag{4.34b}$$

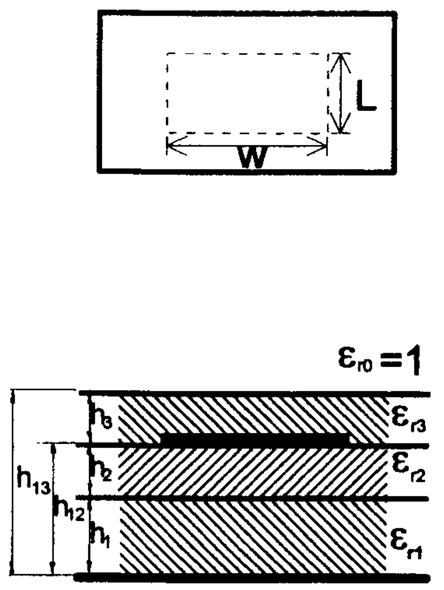

Figure 4.5 A rectangular microstrip antenna with multilayered dielectric substrate. (From [15]. © 1994 IEEE. Reprinted with permission.)

The effect of dispersion on effective permittivity is included through (B.27d). The resonant frequency obtained from the above closed-form expressions is reported to be accurate to within 2% provided that the total dielectric thickness satisfies

$$h_1/\lambda_{d1} + h_2/\lambda_{d2} + h_3/\lambda_{d3} \leq 0.1$$

where λ_{di} is the wavelength in the ith dielectric layer.

4.3.3 Radiation Patterns and Radiation Resistance

The radiation patterns of an antenna are of prime importance in determining most of its radiation characteristics, which include beamwidth, beam shape, sidelobe level, directivity, polarization, and radiated power. The radiation patterns are calculated from the potential functions derived in Chapter 1. The radiation from the patch can be derived either from the E_z field across the aperture between the patch and the ground plane (using vector electric potential) or from the currents on the surface of the patch conductor (employing vector magnetic potentials). The transmission line model and cavity model employ the aperture field approach. In the transmission line model, two slots at the radiating edges are considered. The cavity model employs four slots along the

periphery of the patch. However, the contribution of the nonradiating slots to the radiation pattern can be neglected for approximate calculations.

The equivalent magnetic current source on the perimeter of the rectangular patch antenna is derived from the electric field distribution under the patch metalization. It is given by

$$\vec{M}(x, y) = -\hat{n} \times \hat{z}E_z \tag{4.35}$$

The electric field and the corresponding magnetic currents are shown in Figure 4.6 for various modes.

Radiation Pattern Based on a Two-Slot Model

In this model, the radiation patterns for the TM_{10} mode are calculated by modeling the antenna as a combination of two parallel slots of length W, width h, and spaced a distance L apart, as suggested in Figure 4.7. The radiation from the patch is linearly polarized with the electric field directed along the patch length. If the voltage across either radiating slot is taken as V_0, the radiation fields are obtained by multiplying the radiation pattern of one slot, (1.29), with the array factor $2\cos(k_0 L \sin\theta \cos\phi/2)$. One obtains

$$E_\theta = -jk_0 V_0 W \frac{e^{-jk_0 r}}{4\pi r} \cos\phi F_1 F_2 \tag{4.36a}$$

$$E_\phi = jk_0 V_0 W \frac{e^{-jk_0 r}}{4\pi r} \cos\theta \sin\phi F_1 F_2 \tag{4.36b}$$

where

$$F_1 = \text{sinc}(k_0 h \sin\theta \cos\phi/2)\,\text{sinc}(k_0 W \sin\theta \sin\phi/2)$$

$$F_2 = 2\cos(k_0 L \sin\theta \cos\phi/2)$$

Equations (4.36a) and (4.36b) yield the following expressions for the radiation field in the principal planes of a rectangular microstrip antenna operated in the TM_{10} mode.

For the $\phi = 0°$ plane or E plane:

$$E_\phi(\theta) = 0 \tag{4.37}$$

$$E_\theta(\theta) = -jk_0 V_0 W \frac{e^{-jk_0 r}}{2\pi r} F_E(\theta) \tag{4.38a}$$

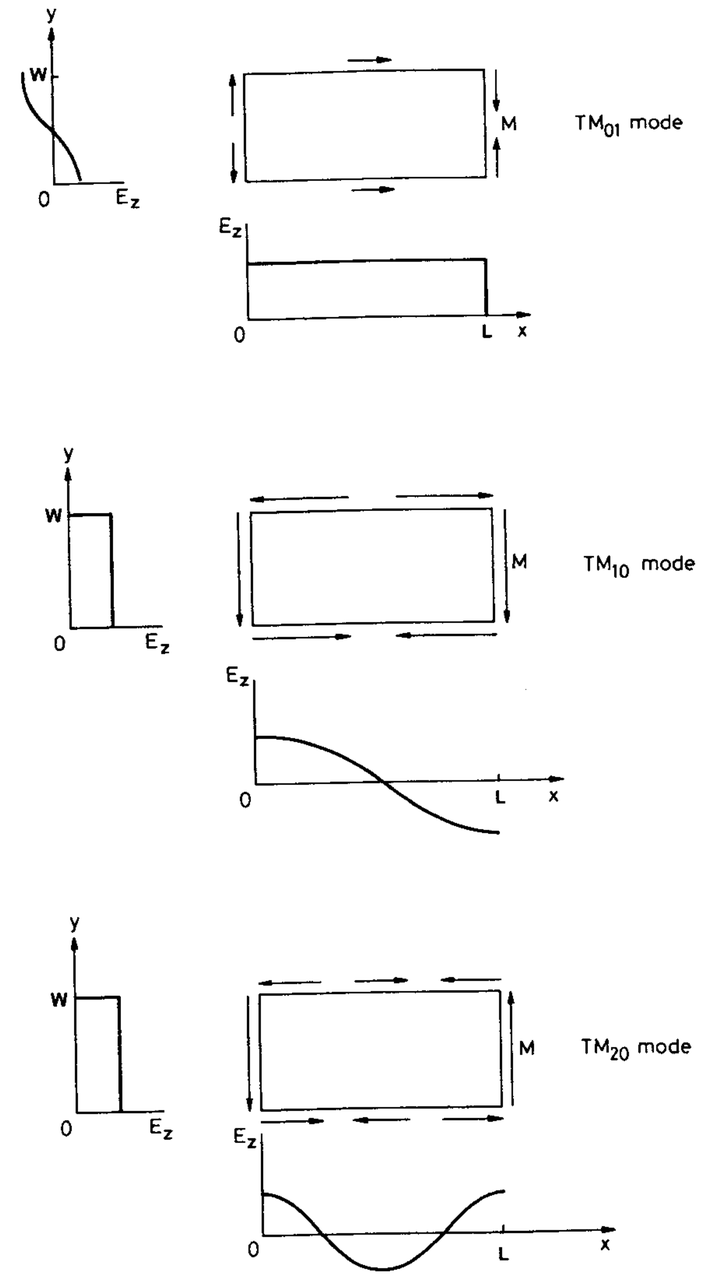

Figure 4.6 Electric field and magnetic surface current distributions along the periphery for various modes of a rectangular microstrip antenna.

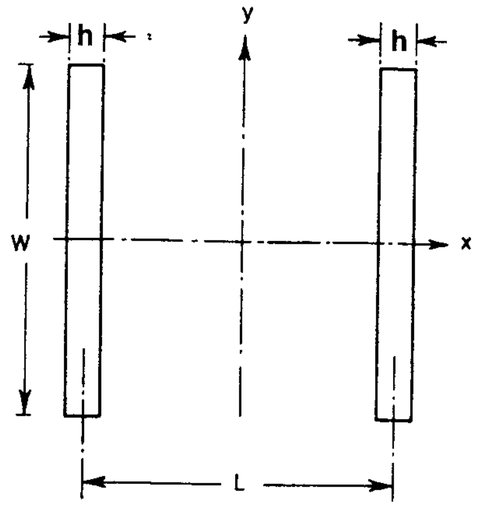

Figure 4.7 Two-slot model of a rectangular patch antenna for determining the radiation patterns.

where

$$F_E = \text{sinc}(k_0 h \sin\theta/2)\cos(k_0 L \sin\theta/2) \tag{4.38b}$$

For the $\phi = 90°$ plane or H plane:

$$E_\theta(\theta) = 0 \tag{4.39}$$

$$E_\phi(\theta) = jk_0 V_0 W \frac{e^{-jk_0 r}}{2\pi r} F_H(\theta) \tag{4.40a}$$

where

$$F_H = \text{sinc}(k_0 W \sin\theta/2)\cos\theta \tag{4.40b}$$

The above expressions for radiation fields assume that the radiating slots are in free space. The effect of the ground plane and substrate of the antenna on the radiation patterns can be included by means of factors $F_3(\theta)$ and $F_4(\theta)$; see (2.59) in Chapter 2. These factors follow.

For the E-plane pattern:

$$F_3(\theta) = \frac{2\cos\theta\sqrt{\epsilon_r - \sin^2\theta}}{\sqrt{\epsilon_r - \sin^2\theta} - j\epsilon_r \cos\theta \cot(k_0 h\sqrt{\epsilon_r - \sin^2\theta})} \tag{4.41}$$

and for the H-plane pattern:

$$F_4(\theta) = \frac{2\cos\theta}{\cos\theta - j\sqrt{\epsilon_r - \sin^2\theta}\cot(k_0 h\sqrt{\epsilon_r - \sin^2\theta})} \tag{4.42}$$

The final radiation patterns are then, for the E-plane pattern,

$$E_\theta(\theta) = -jk_0 V_0 W \frac{e^{-jk_0 r}}{2\pi r} F_E(\theta) F_3(\theta) \tag{4.43a}$$

and for the H-plane pattern,

$$E_\phi(\theta) = jk_0 V_0 W \frac{e^{-jk_0 r}}{2\pi r} F_H(\theta) F_4(\theta) \tag{4.43b}$$

Radiation Pattern Based on the Electric Surface Current Model

This mechanism of radiation is employed in the full-wave analysis techniques for microstrip antennas (Chapter 3). In this model the patch metalization is replaced by the surface current distribution, and the fields are solved for, taking into account the grounded substrate through an exact Green's function. The radiation patterns are found to be [16, 17]

$$E_\phi(\theta, \phi) = \sin\phi\left(\frac{j\omega\mu_0}{4\pi r}\right) e^{-jk_0 r} \tilde{J}(\theta, \phi) F_4(\theta) \tag{4.44a}$$

$$E_\theta(\theta, \phi) = -\cos\phi\left(\frac{j\omega\mu_0}{4\pi r}\right) e^{-jk_0 r} \tilde{J}(\theta, \phi) F_3(\theta) \tag{4.44b}$$

where $\tilde{J}(\theta, \phi)$ is the Fourier transform of the patch current. For the TM_{10} mode with [17]

$$\vec{J}(x, y) = \hat{x}\frac{V_0}{Z_0 W}\sin(\beta x) \qquad \text{for } 0 < x < L, \quad 0 < y < W \tag{4.45}$$

the expression for $\tilde{J}(\theta, \phi)$ is obtained as [17]

$$\tilde{J}(\theta, \phi) = \frac{V_0}{Z_0} \frac{2\sqrt{\epsilon_{re}}\cos(\pi \sin\theta\cos\phi/(2\sqrt{\epsilon_{re}}))}{k_0(\sin^2\theta\cos^2\phi - \epsilon_{re})} \text{sinc}(0.5k_0 W \sin\theta\sin\phi) \tag{4.46}$$

where $\sqrt{\epsilon_{re}} = \beta/k_0$ is the effective dielectric constant of the microstrip line of which the patch is a segment and Z_0 is the characteristic impedance corresponding to width W. For the TM_{10} mode the patch length L is selected such that

$$L = \lambda_g/2 \Rightarrow k_0 L = \pi/\sqrt{\epsilon_{re}}$$

The principal plane power patterns are then obtained as follows [17]. For the $\phi = 0°$ plane or E-plane pattern:

$$E_\phi = 0 \tag{4.47}$$

$$|E_\theta(\theta)|^2 = \epsilon_{re}[1 + \epsilon_r \cot^2(k_0 h\sqrt{\epsilon_r})] \frac{\cos^2(k_0 L \sin\theta/2)}{(\epsilon_{re} - \sin^2\theta)^2} \tag{4.48}$$

$$\frac{(\epsilon_r - \sin^2\theta)\cos^2\theta}{(\epsilon_{re} - \sin^2\theta) + \epsilon_r^2 \cos^2\theta \cot^2(k_0 h\sqrt{\epsilon_r - \sin^2\theta})}$$

and for the $\phi = 90°$ plane or H-plane pattern:

$$E_\theta = 0 \tag{4.49}$$

$$|E_\phi(\theta)|^2 = [1 + \epsilon_r \cot^2(k_0 h\sqrt{\epsilon_r})] \tag{4.50}$$

$$\frac{\cos^2\theta}{(\epsilon_r - \sin^2\theta)\cot^2(k_0 h\sqrt{\epsilon_r - \sin^2\theta}) + \cos^2\theta} \operatorname{sinc}^2(k_0 W \sin\theta/2)$$

The radiation patterns based on the two different radiation mechanisms described above are similar. They have been compared with measured radiation patterns for various values of substrate thickness with $\epsilon_r = 2.5$ [18]. The aperture model, without the factors $F_3(\theta)$ and $F_4(\theta)$, is found to give radiation patterns that compare well with measurements. Typical radiation patterns based on (4.48) and (4.50) are plotted in Figure 4.8 [17]. It is observed from here that both the E-plane and H-plane radiation patterns are broad with no sidelobes. The radiation field approaches zero at $\theta = \pi/2$. This is due to the image of the patch in the ground plane. The narrow patch, that is, patch with smaller value of W, broadens the H-plane pattern while thinner substrate broadens the E-plane pattern.

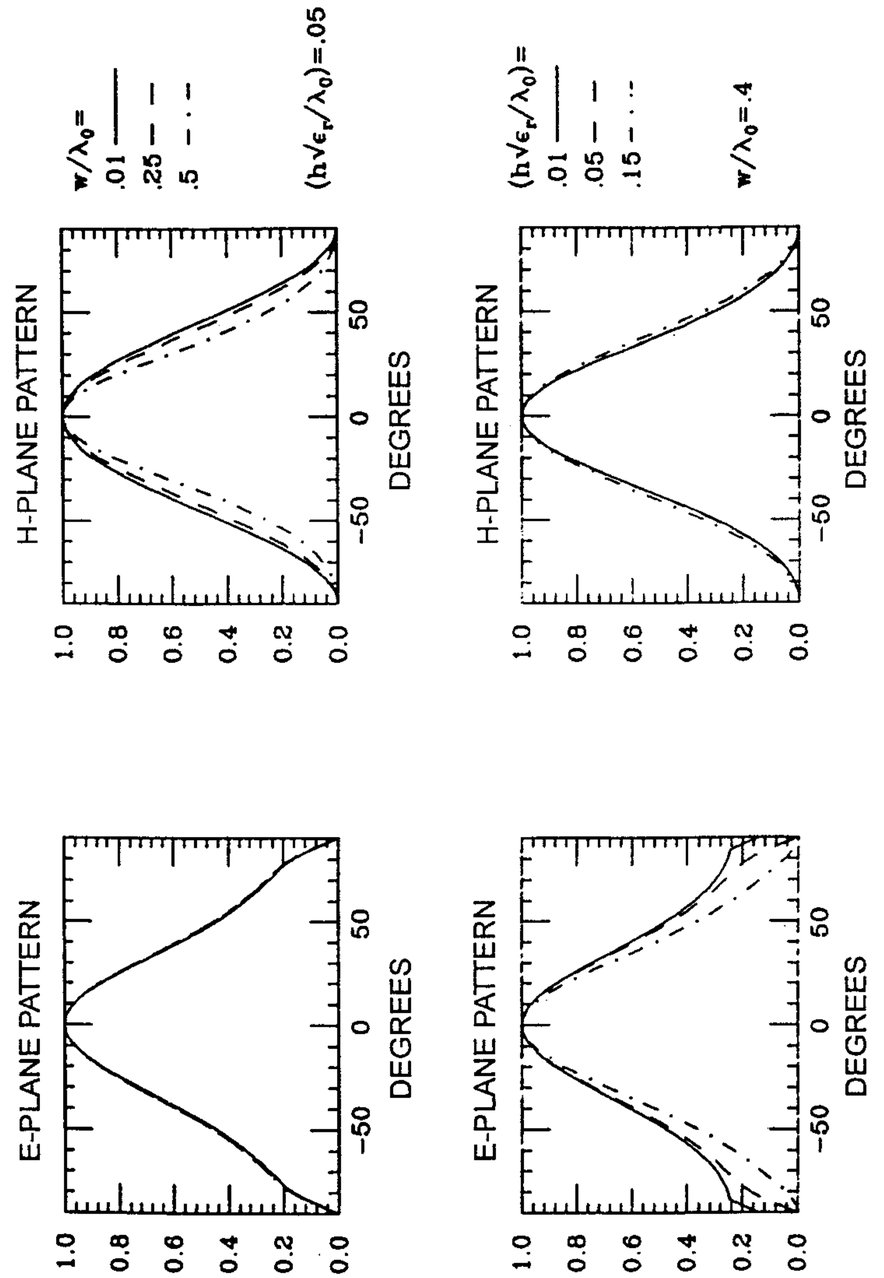

Figure 4.8 Dependence of E- and H-plane power patterns of a resonant rectangular element on W and h for $\epsilon_r = 2.2$. (From [17]. © 1985 IEEE. Reprinted with permission.)

Beamwidth

The half power beamwidth of an antenna is equal to the angular width between directions where the radiated field reduces to $1/\sqrt{2}$ of the maximum value. After some approximations and algebra, one can obtain the following relationships from (4.38b) and (4.40b):

$$\theta_H = 2\sin^{-1}\left\{\frac{1}{2 + k_0 W}\right\}^{1/2} \tag{4.51a}$$

$$\theta_E = 2\sin^{-1}\left\{\frac{7.03}{3k_0^2 L^2 + k_0^2 h^2}\right\}^{1/2} \tag{4.51b}$$

where θ_H and θ_E are the half-power beamwidths in the H and E planes, respectively. The beamwidth of a microstrip element can be increased by choosing a smaller element, thus reducing W and L. For a given resonant frequency, these dimensions can be reduced by selecting a substrate having a higher relative permittivity. In many applications, a decrease in physical size is desirable. As beamwidth increases, antenna gain and directivity decrease.

Directivity and Gain

The directivity is a measure of the directional properties of an antenna compared to those of an isotropic antenna. The directivity is always greater than 1 since an isotropic radiator is not directional. The directivity is defined as the ratio of the maximum power density in the main beam direction to the average radiated power density. The directivity of the patch antenna is expressed as

$$D = \frac{\frac{1}{2}\mathrm{Re}(E_\theta H_\phi^* - E_\phi H_\theta^*)|_{\theta=0}}{P_r/4\pi r^2} = \frac{\frac{r^2}{2\eta_0}(|E_\theta|^2 + |E_\phi|^2)|_{\theta=0}}{P_r/4\pi} \tag{4.52}$$

where P_r is the radiated power, $\eta_0 = 120\pi\Omega$, and radiation fields E_θ and E_ϕ were defined earlier. A simple approximate expression for the directivity D of a rectangular patch is given as [1, p. 554]

$$D \approx \frac{4(k_0 W)^2}{\pi\eta_0 G_r} \tag{4.53}$$

where G_r is the radiation conductance of the patch, defined later. The directive gain G of an antenna is defined as

$$G = e_r D \tag{4.54}$$

where e_r is the radiation efficiency of the antenna. Gain is always less than directivity because e_r lies in the range $0 < e_r < 1$. The directivity of a rectangular patch determined from the radiation pattern is plotted in Figure 4.9 as a function of normalized substrate thickness and W/λ_0 as a parameter [17]. It is observed from this figure that directivity increases with increase in substrate thickness and patch width. Conversely, the beamwidth is expected to decrease for higher values of h and W.

Radiated Power and Radiation Resistance

The power radiated by an antenna can be obtained by integrating the real part of the Poynting vector over the hemisphere above the patch, that is,

$$P_r = \frac{1}{2\eta_0}\int_0^{2\pi}\int_0^{\pi/2}(|E_\theta|^2 + |E_\phi|^2) r^2 \sin\theta d\theta d\phi \tag{4.55a}$$

If (4.44) is used for E_θ and E_ϕ, one obtains [17]

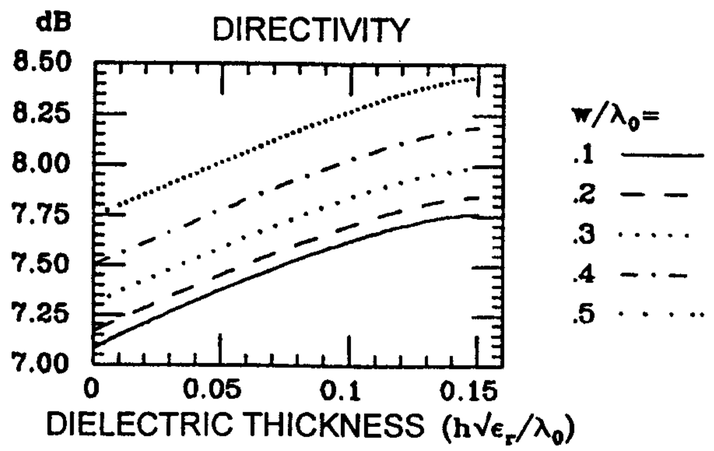

Figure 4.9 Directivity of a resonant rectangular patch antenna as a function of dielectric thickness for different values of W/λ_0 and $\epsilon_r = 2.2$. (From [17]. © 1985 IEEE. Reprinted with permission.)

$$P_r = \frac{V_0^2}{Z_0^2}\frac{60\epsilon_{re}}{\pi}\int_0^{2\pi}\int_0^{\pi/2}\frac{\cos^2(\pi\sin\theta\cos\phi/(2\sqrt{\epsilon_{re}}))}{(\sin^2\theta\cos^2\phi-\epsilon_{re})^2}$$
$$\cdot \sin c^2(k_0 W\sin\theta\sin\phi/2)\sin\theta d\theta d\phi$$
$$\times\left[\frac{\cos^2\theta\sin^2\phi}{(\epsilon_r-\sin^2\theta)\cot^2(k_0h\sqrt{\epsilon_r-\sin^2\theta})+\cos^2\theta}\right.$$
$$\left.+\frac{(\epsilon_r-\sin^2\theta)\cos^2\theta\cos^2\phi}{(\epsilon_r-\sin^2\theta)+\epsilon_r^2\cos^2\theta\cot^2(k_0h\sqrt{\epsilon_r-\sin^2\theta})}\right] \quad (4.55b)$$

This expression is a very complicated function of θ and ϕ and substrate parameters. Therefore, a numerical integration is performed to obtain P_r. However, if the effect of the substrate is neglected, an approximate closed-form expression can be obtained for P_r. Thouroude et al. [19] have obtained such an expression having an accuracy of 2.5% for $L/\lambda_0 = 0.3(\epsilon_r = 2.5)$ and $W/\lambda_0 \le 0.6$; and 4% for $L/\lambda_0 = 0.15(\epsilon_r \approx 12)$ and $W/\lambda_0 \le 0.3$. This expression is given next:

$$P_r = \frac{(E_0h)^2A\pi^4}{23040}\left[(1-B)\left(1-\frac{A}{15}+\frac{A^2}{420}\right)+\frac{B^2}{5}\left(2-\frac{A}{7}+\frac{A^2}{189}\right)\right] \quad (4.56)$$

where $A = (\pi W/\lambda_0)^2$, and the normalized resonant length $B = (2L/\lambda_0)^2$. Equation (4.56) highlights the fact that the radiated power is directly proportional to $(k_0W)^2$ and $(k_0h)^2$ and (4.56) does not include the effect of substrate parameters. Gera has derived a closed-form approximate expression for P_r by integrating (4.55b) analytically [20]. This required making some assumptions. The most serious approximation was $\cot(k_0h\sqrt{\epsilon_r-\sin^2\theta}) \approx 1/(k_0h\sqrt{\epsilon_r-\sin^2\theta})$, which restricts the accuracy of resulting expressions. The radiated power was determined in a closed form.

The resonant radiation conductance G_r for a patch fed at an edge can be determined from power radiated P_r as follows:

$$P_r = \frac{1}{2}G_r(E_0h)^2 = \frac{1}{2}G_rV_0^2 \quad (4.57a)$$

$$R_r = 1/G_r \quad (4.57b)$$

The expressions for R_r with an estimated accuracy of 10% average for $h \le 0.03\lambda_0$ and $\epsilon_r \le 10$ are given below [20]:

$$R_r = \frac{V_0^2}{2P_r} = \epsilon_{re}\frac{Z_0^2}{120I_2} \quad (4.58)$$

where Z_0 is the characteristic impedance of the microstrip line of which the patch is a segment, and for $\epsilon_r \le 5$,

$$I_2 = (k_0h)^2[0.53 - 0.03795(k_0W/2)^2 - 0.03553/\epsilon_{re}] \quad (4.59)$$

whereas for $5 \le \epsilon_r < 10$

$$I_2 = I_L/I_1 \quad (4.60)$$

$$I_1 = (\epsilon_r - 1)(1.29 - 3.57h\sqrt{\epsilon_r}/\lambda_0)/9 \quad (4.61)$$

$$I_L = (k_0h)^2\{1.3 - 4/(3\epsilon_r) + 0.53/\epsilon_r^2$$
$$- (k_0W/2)^2[0.08856 - 0.08856/\epsilon_r + 0.03795/\epsilon_r^2]$$
$$- [0.248714 - 0.373071/\epsilon_r + 0.159887/\epsilon_r^2]/\epsilon_r\} \quad (4.62)$$

Comparison with the numerical results for R_r show that (4.59) and (4.60) have better accuracy for thin substrates with lower ϵ_r. An approximate expression has been derived in [16] also.

The numerically computed radiation resistance is plotted in Figure 4.10. The radiation resistance is found to decrease with increase in substrate thickness and patch width because power radiated increases. If the patch is fed at a distance x_f from one of the radiating edges, the input resistance is obtained as

$$R_{in} = R_r\cos^2(\pi x_f/L) \quad (4.63)$$

The factor $\cos(\pi x_f/L)$ arises due to electric field variations for the dominant mode.

4.3.4. Losses and *Q* Factor

The quality factor of a patch antenna needs to be determined to implement the cavity model. It is also useful in determining the VSWR bandwidth of the

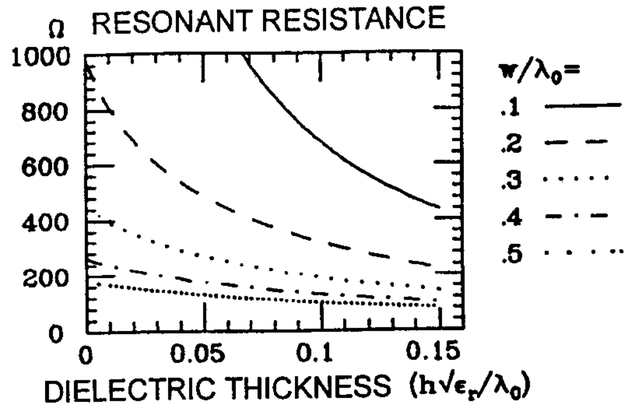

Figure 4.10 Radiation resistance of a resonant rectangular patch antenna as a function of dielectric thickness for different values of W/λ_0 and $\epsilon_r = 2.2$. (From [17]. © 1985 IEEE. Reprinted with permission.)

antenna. The total quality factor of the patch Q_T can be defined in terms of the quality factors associated with various type of losses in the patch antenna. One can write

$$\frac{1}{Q_T} = \frac{1}{Q_d} + \frac{1}{Q_c} + \frac{1}{Q_r} + \frac{1}{Q_{\text{sur}}} \tag{4.64}$$

where Q representing any of the quality factors on the right-hand side of (4.64) is defined as

$$Q = \frac{\omega_r W_T}{\text{Associated power loss}} \tag{4.65}$$

The energy stored at resonance W_T is the same, independent of the mechanism of power loss. Therefore, (4.64) can be expressed as

$$\frac{1}{Q_T} = \frac{P_d + P_c + P_r + P_{\text{sur}}}{\omega_T W_T} \tag{4.66}$$

Here, P_d is the power lost in the lossy dielectric of the substrate, P_c is the power lost due to the finite conductivity of metalization (also called copper loss), P_r is the power radiated in the form of space wave (4.55), and P_{sur} is the power lost in the form of power carried away by the surface waves. The power losses P_r, P_c, and P_d are plotted in Figure 4.11 for two types of substrates [1]. Here, $P_T = P_r + P_c + P_d$. Note that the substrate material can be chosen

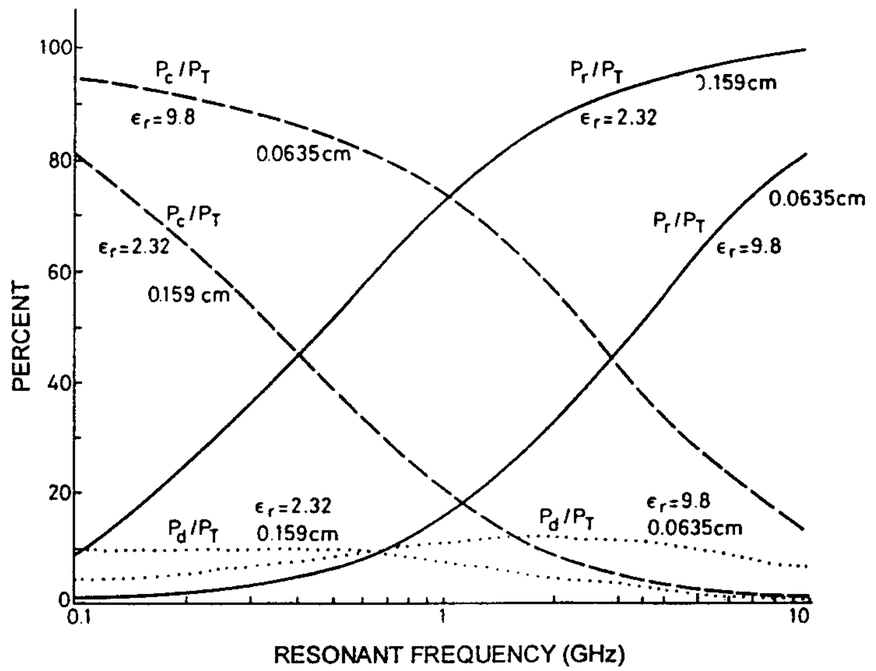

Figure 4.11 Variation of radiated power (P_r), conductor loss (P_c), and dielectric loss (P_d) as a function of resonant frequency for the TM_{10} mode. $L = 1.5W$, $h = 1.59$ mm, $\epsilon_r = 2.32$; and $L = 1.5W$, $h = 0.635$ mm, $\epsilon_r = 9.8$. (From [1]. © 1989 Peter Peregrinus. Reprinted with permission.)

such that at the desired resonant frequency $P_r > P_c > P_d$ for a reasonably good radiation efficiency. Expressions for P_d, P_c, P_r, W_T, Q_d, Q_c, and Q_r were derived in Section 2.3. Some of these expressions are given next:

$$Q_d = 1/\tan\delta \qquad \tan\delta\text{: loss tangent of the substrate material} \tag{4.67a}$$

$$Q_c = h\sqrt{\pi f \mu_0 \sigma} \qquad \sigma\text{: conductivity of patch metalization} \tag{4.67b}$$

$$Q_r = \omega_T W_T / P_r \tag{4.67c}$$

$$W_T = \frac{1}{4}\epsilon_0 \epsilon_r h L W \tag{4.67d}$$

The surface wave power is given by [16]

$$P_{\text{sur}} = -\frac{1}{2}\text{Re}\int_0^\infty \int_0^{2\pi} E_z H_\phi^* \rho d\phi dz \tag{4.68}$$

where E_z and H_ϕ are the fields of the dominant TM_0 surface wave mode. The power lost to the surface waves can be neglected for thin and low dielectric constant substrates. However, for accurate analysis one can use the following expression [17]:

$$P_{\text{sur}} = 60\epsilon_{re}A_s \int_0^{2\pi} \frac{\cos^2(\pi x_0 \cos\phi/(2\sqrt{\epsilon_{re}}))}{(x_0^2\cos^2\phi - \epsilon_{re})^2} \operatorname{sinc}^2(Wk_0x_0\sin\phi/2)\cos^2\phi\, d\phi \tag{4.69}$$

where

$$A_s = \frac{\epsilon_r(x_0^2-1)x_0}{\epsilon_r x_0\left[\dfrac{1}{\sqrt{x_0^2-1}} + \dfrac{\sqrt{x_0^2-1}}{\epsilon_r - x_0^2}\right] + x_0k_0h\left[1 + \dfrac{\epsilon_r^2(x_0^2-1)}{\epsilon_r - x_0^2}\right]}$$

and $x_0 = \beta/k_0$ is the normalized phase constant for the TM_0 surface wave, for which the expression is available in Section 1.5. The surface wave power increases with h and ϵ_r.

To get an idea of the variation of Q_T with h and ϵ_r, let us approximate

$$Q_T \approx \frac{\omega_r W_T}{P_r}$$

Also,

$$W_T \propto h\epsilon_r \quad \text{and} \quad P_r \propto h^2 \quad \Rightarrow Q_T \propto \epsilon_r/h \tag{4.70}$$

Similarly, it can be shown from (4.56) and (4.67d) that

$$Q_T \propto 1/W$$

Figure 4.12 shows that the total quality factor follows this type of behavior [1].

4.3.5 Bandwidth

For an antenna, the bandwidth can be defined in a number of ways depending on the characteristics selected. For example, for circularly polarized antennas

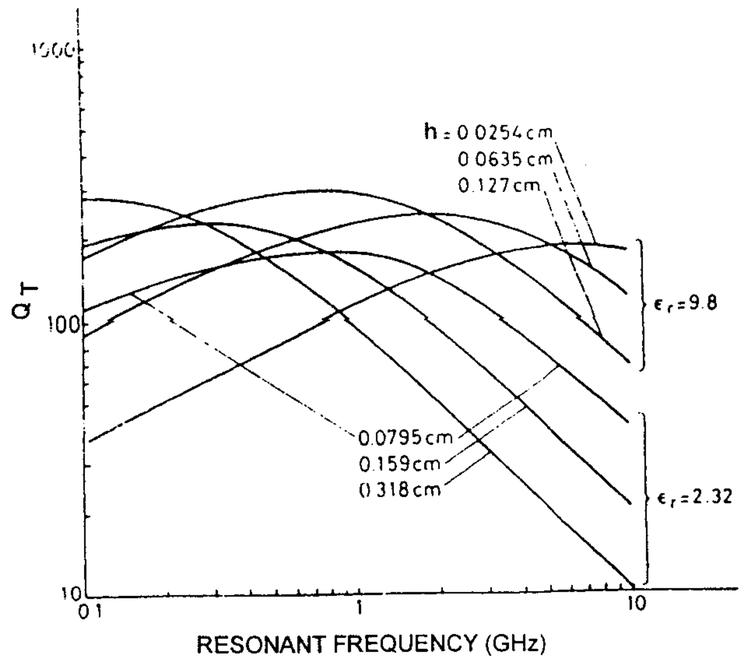

Figure 4.12 Variation of total Q with resonant frequency for the TM_{10} mode of a rectangular patch with $L = 1.5W$. (From [1]. © 1989 Peter Peregrinus. Reprinted with permission.)

the axial ratio bandwidth can be given precedence over other characteristics. Similarly, gain and pattern bandwidth are more important for arrays. In the absence of any such stated preference, the impedance bandwidth or VSWR bandwidth for microstrip antennas is specified. The bandwidth for a feed line VSWR < S can be shown to be [8]

$$\text{BW} = \frac{S-1}{Q_T\sqrt{S}} \tag{4.71}$$

Expression (4.66) for Q_T can be used to determine the bandwidth of the patch antenna. Figure 4.13 shows the bandwidth as a function of resonant frequency [1]. Note from this figure that the bandwidth increases with increase in substrate thickness and decrease in dielectric constant. Since $Q_T \propto (k_0W)^{-1}$, the bandwidth is expected to increase with the aspect ratio W/L of the patch. Variation of bandwidth with h, ϵ_r, W, and L is clearly brought out by the approximate expression given below [16]:

$$\text{BW} = \frac{16}{3\sqrt{2}}\frac{p}{e_r}\frac{1}{\epsilon_r}\frac{h}{\lambda_0}\frac{W}{L}q \tag{4.72a}$$

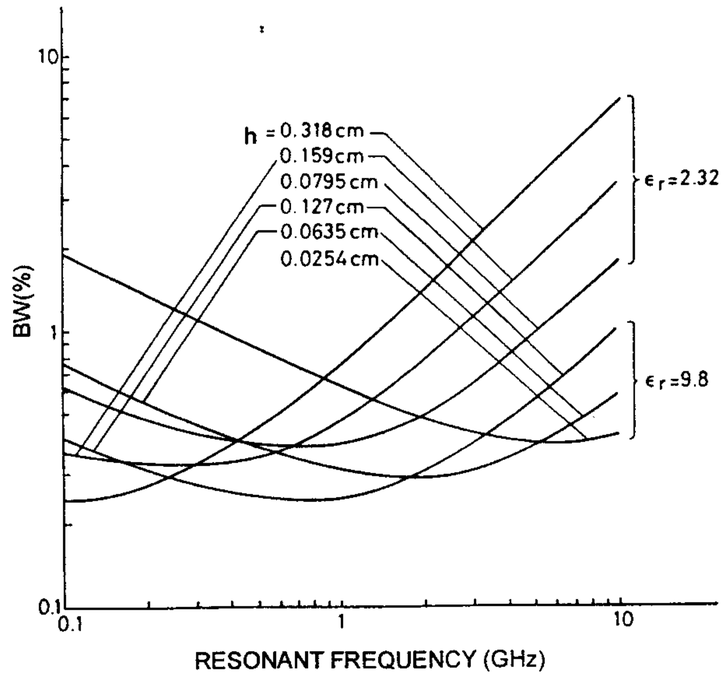

Figure 4.13 Variation of impedance bandwidth with resonant frequency for the TM_{10} mode of a rectangular patch with $L = 1.5W$. (From [1]. © 1989 Peter Peregrinus. Reprinted with permission.)

where

$$p = 1 - \frac{0.16605}{20}(k_0 W)^2 + \frac{0.02283}{560}(k_0 W)^4 - 0.009142(k_0 L)^2 \tag{4.72b}$$

$$q = 1 - \frac{1}{\epsilon_r} + \frac{2}{5\epsilon_r^2} \tag{4.72c}$$

and e_r is the radiation efficiency defined in the next subsection. Comparison with numerical results show that (4.72a) has better accuracy for low values of ϵ_r. For $\epsilon_r = 2.2$, (4.72a) gives very good accuracy for $h/\lambda_0 \leq 0.05$. Comparison of the bandwidth value calculated using the cavity model and the full-wave approach shows that cavity model predicts a lower value of bandwidth [9].

The bandwidth of the patch antenna can also be increased by increasing the inductance of the radiators by cutting holes or slots in it or by adding reactive components to improve the match of the radiator to the feed line or

by parasitic loading of the radiator. This topic is discussed in more detail in Chapter 9.

4.3.6 Radiation Efficiency, e_r

The radiation efficiency is defined as the ratio of the radiated power P_r to the input power P_i, that is,

$$e_r = \frac{P_r}{P_i} \tag{4.73}$$

The input power gets distributed in the form of radiated power, surface wave power, and dissipation in the conductors and dielectric. Therefore, (4.73) can be expressed as

$$e_r = \frac{P_r}{P_r + P_c + P_d + P_{\text{sur}}} \tag{4.74}$$

The dissipated power is generally small for low-loss substrates at microwave frequencies, and one can write

$$e_r = \frac{P_r}{P_r + P_{\text{sur}}} \tag{4.75}$$

It is not necessary to evaluate (4.55) and (4.69) to determine the radiation efficiency of a rectangular microstrip antenna. Instead, it has been observed that radiation efficiency depends primarily on the substrate thickness and permittivity, and is not affected very much either by the patch shape or the feed [21]. Numerical results indicate that radiation efficiency is almost independent of aspect ratio W/L of the rectangular patch [17]. It means that e_r can be determined from any assumed current distribution. Pozar has used an infinitesimal current source on the substrate and obtained the following closed-form expressions for P_r and P_{sur} [21]:

$$P_r = 40k_0^2(k_0 h)^2\left(1 - \frac{1}{\epsilon_r} + \frac{2}{5\epsilon_r^2}\right) \tag{4.76a}$$

$$P_{\text{sur}} = 30\pi k_0^2 \frac{\epsilon_r(x_0^2 - 1)}{\epsilon_r\left[\dfrac{1}{\sqrt{x_0^2 - 1}} + \dfrac{\sqrt{x_0^2 - 1}}{\epsilon_r - x_0^2}\right] + k_0 h\left[1 + \dfrac{\epsilon_r^2(x_0^2 - 1)}{\epsilon_r - x_0^2}\right]} \tag{4.76b}$$

where x_0 is the normalized phase constant for the TM_0 surface wave. The radiation efficiency obtained using (4.76) is found to be accurate to at least 5% for $h\sqrt{\epsilon_r} < \lambda_0/8$ [21]. Closed-form expressions reported in [16] are similar to (4.76).

The radiation efficiency as a function of resonant frequency is plotted in Figure 4.14 [1]. Note that efficiency decreases as the substrate thickness or substrate dielectric constant increases. This is due to the fact that surface wave power increases with h and ϵ_r.

The power terms in (4.75) can also be expressed in terms of corresponding conductances, similar to (4.57) for P_r. Therefore, one can write

$$e_r = \frac{G_r}{G_r + G_{\text{sur}}}$$

As stated earlier, radiation efficiency affects the directive gain of the antenna through $G = e_r D$. The gain is plotted in Figure 4.15 [1]. The gain variation with frequency is almost identical to that of radiation efficiency because directivity is constant with resonant frequency for a given substrate ϵ_r.

The effect of substrate dielectric constant on bandwidth, resonant resistance, directivity, and radiation efficiency is plotted in Figure 4.16 [17]. It is observed from here that bandwidth, directivity, and radiation efficiency decrease

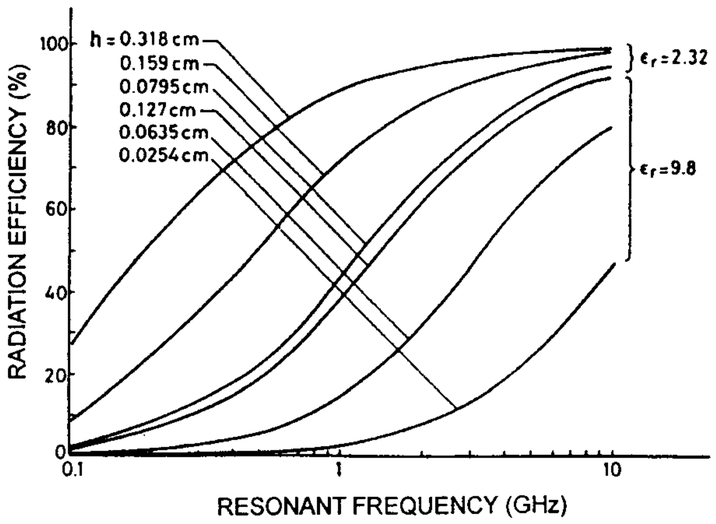

Figure 4.14 Variation of radiation efficiency with resonant frequency for the TM_{10} mode of a rectangular patch with $L = 1.5W$, $\sigma = 5.8 \times 10^7$ S/m, $\delta = 0.0005$. (From [1]. © 1989 Peter Peregrinus. Reprinted with permission.)

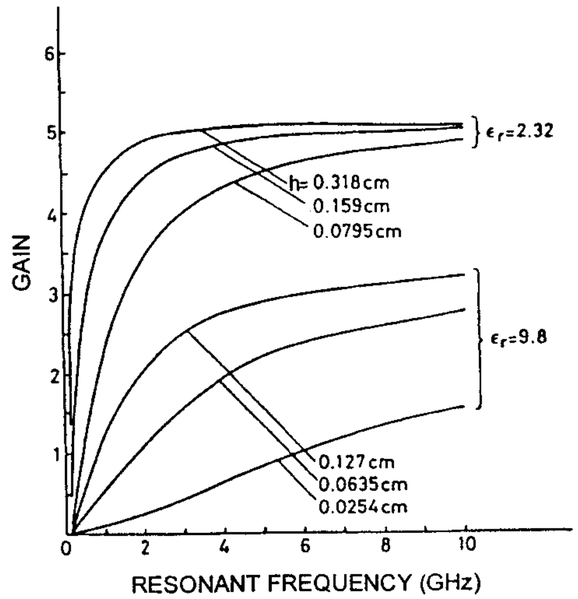

Figure 4.15 Variation of directive gain with resonant frequency for the TM_{10} mode of a rectangular patch with $L = 1.5W$, $\sigma = 5.8 \times 10^7$ S/m, $\delta = 0.0005$. (From [1]. © 1989 Peter Peregrinus. Reprinted with permission.)

with increases in ϵ_r, while radiation resistance increases. This behavior is due to the reduction in fringing field and patch length with increase in ϵ_r.

4.3.7 Feed Point Location

After selecting the patch dimensions L and W for a given substrate, the next task is to determine the feed point (x_0, y_0) so as to obtain a good impedance match between the generator impedance and the input impedance of the patch element. It is observed from (4.22) that the change in feed location gives rise to a change in the input impedance and hence provides a simple method for impedance matching. From (4.22) we see that if the feed is located at $x_0 = x_f$ and $0 \le y_f \le W$, the input resistance at resonance for the dominant TM_{10} mode can be expressed as

$$R_{\text{in}} = R_r \cos^2(\pi x_f/L) \qquad R_r \ge R_{\text{in}} \tag{4.77}$$

where x_f is the inset distance from the radiating edge, and R_r is the radiation resistance at resonance when the patch is fed at a radiating edge. The radiation resistance R_r has been determined in Section 4.3.3. The inset distance x_f is selected such that R_{in} is equal to the feed line impedance, usually taken to be

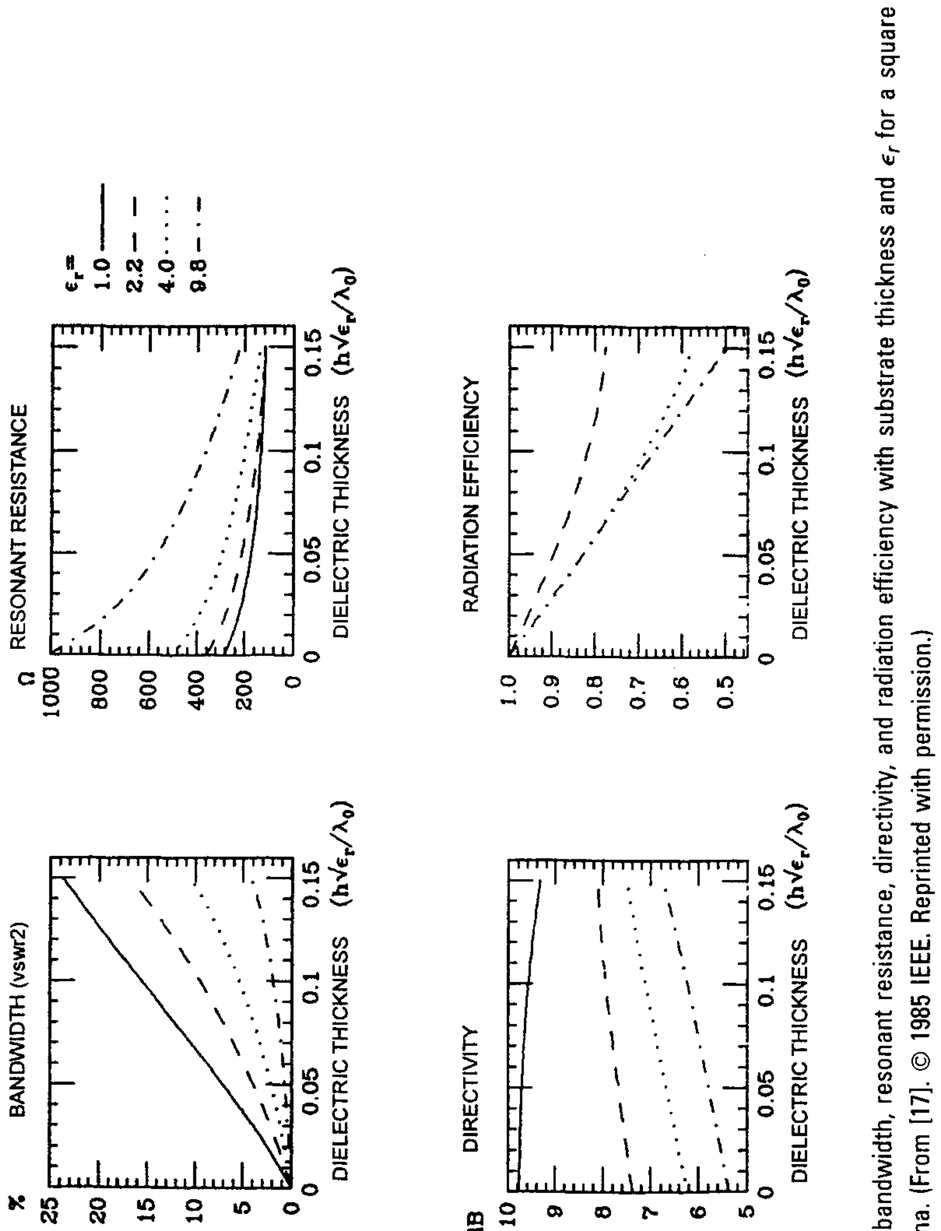

Figure 4.16 Variation of bandwidth, resonant resistance, directivity, and radiation efficiency with substrate thickness and ϵ_r for a square patch antenna. (From [17]. © 1985 IEEE. Reprinted with permission.)

50Ω. Although the feed point can be selected anywhere along the patch width, it is better to choose $y_f = W/2$ if $W \geq L$ so that TM_{0n} (n odd) modes are not excited along with the TM_{10} mode. Determination of the exact feed point requires an iterative solution for (4.22). Equation (4.77) provides a useful guideline for the purpose. Kara has suggested an expression for x_f that does not need calculation of radiation resistance. It is approximately given by [13]

$$x_f = \frac{L}{2\sqrt{\epsilon_{re}(L)}} \tag{4.78}$$

where $\epsilon_{re}(L)$ is defined by (4.30).

4.3.8 Polarization

The polarization of a rectangular patch antenna is linear and directed along the resonating dimension, when operated in the dominant mode. Large bandwidth patch antennas may operate in the higher order mode also. The radiation pattern and polarization for these modes can be different from the dominant mode. Another source for cross-polarization is the fringing field along the nonradiating edges. These fields are oriented 90° with respect to the field at the radiating edges. Their contribution to the radiation fields in the E and H planes is zero. However, in the intercardinal planes, even the ideal, single-mode patch will radiate cross-polarized fields. The cross-polarization level increases with substrate thickness. Circular polarization can be obtained from a nearly square patch by suitably locating the feed point [22]. Polarization of the antenna can be changed mechanically or electronically. For electronic tuning, PIN diodes or varactor diodes can be used. Polarization diversity, used in mobile communications to account for the decrease in signal strength due to fading, is discussed in Chapter 10.

For the dominant (1, 0) mode excitation and linear polarization, the mode (0, 2) contributes maximum to the cross-polarization. To clarify this point, the electric fields at the edges of the patch for the (1, 0) and (0, 2) modes are plotted in Figure 4.17 (see inset). The vertical arrows in the (1, 0) mode indicate the copolar edge field, and the horizontal arrows in the (0, 2) mode indicate the cross-polar edge field. Notice that the cross-polar arrows for the (0, 2) mode are pointed in opposite directions and give rise to zero cross-polar field in the broadside direction [23]. The cross-polarized component of a rectangular patch can be minimized by a suitable choice of patch width W. It has been shown using the cavity model and simple arguments that [24]

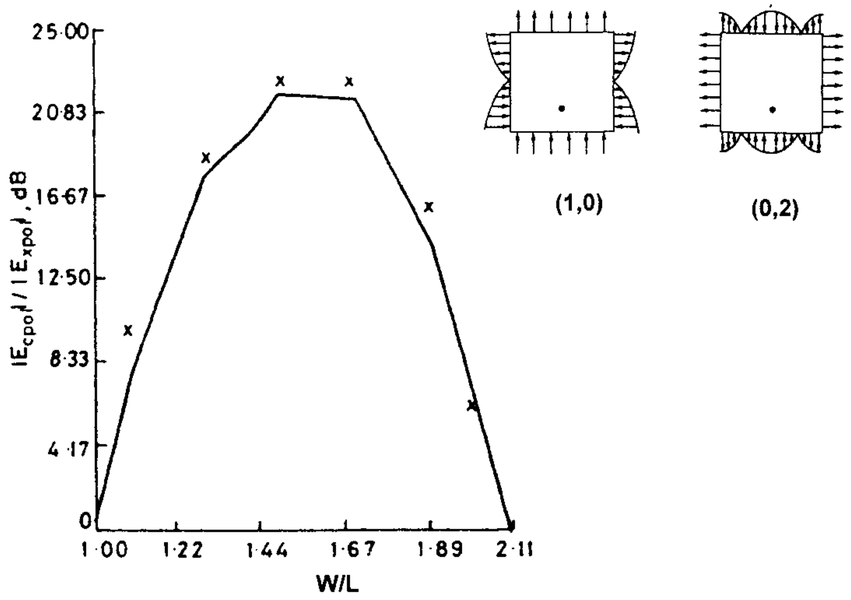

Figure 4.17 Variation of cross-polar component with aspect ratio W/L for a rectangular patch with direct coupled microstrip feed. Parameters: $y_0 = 0$, $x_0 = 0.31L$, $f = 3.8$ GHz, and $h = 0.032\lambda_g$; x, measured. (From [24]. © 1987 *Electronics Letters*. Reprinted with permission.)

$$\frac{E_{\text{cpol}}}{E_{\text{xpol}}} = \frac{E_{10}}{E_{0n}} \tag{4.79}$$

$$= \frac{\cos(\pi x_0/L)}{\cos(n\pi y_0/W)}\left[\frac{j}{\delta_{\text{eff}}}\left(1 - \left(\frac{nL}{W}\right)^2\right) + 1\right]\frac{1}{\text{sinc}(n\pi h/2W)}\frac{|A_{10}(\theta, \phi)|_{\max}}{|A_{0n}(\theta, \phi)|_{\max}}$$

where A_{10} and A_{0n} are excitation amplitudes.

The variation of $|E_{\text{cpol}}|/|E_{\text{xpol}}|$ with aspect ratio W/L is plotted in Figure 4.17 for a direct coupled microstrip feed. The other parameters are $y_0 = 0$, $x_0 = 0.31L$, $f = 3.8$ GHz, and $h = 0.032\lambda_g$. The ratio $|E_{\text{cpol}}|/|E_{\text{xpol}}|$ is one when $W/L = 1.0$ and 2.0, and it is maximum for $W/L \cong 1.5$. Huynh et al. have carried out a similar analysis for the probe-fed rectangular patch. Their results show that copolarization radiation is not affected by resonant frequency and substrate thickness, but the cross-polarization level increases with resonant frequency and/or substrate thickness [25].

4.3.9 RCS of a Rectangular Patch

The scattering behavior of a patch antenna is described in terms of its radar cross section, RCS. It is defined as

$$\sigma_{\theta\theta} = 4\pi r^2 |E_\theta^s|^2 \tag{4.80}$$

where E_θ^s is the θ-polarized scattered field from the patch. A similar definition holds for the ϕ-polarized field. The RCS analysis is based on the incident field and the scattered field satisfying the various boundary conditions and interface condition. Analysis based on the integral equation approach shows that like any other scatterer, a patch antenna has a peak value of RCS at the resonant frequencies of the patch [26]. This is shown in Figure 4.18. At these frequencies, the RCS value is more than the cross-sectional area of the patch, $LW\cos\theta$ (θ is the angle of the ray incident on it) [26]. Variation of RCS with θ and ϕ is similar to that of the radiation pattern of the patch antenna.

4.3.10 Effects of a Dielectric Cover

A microstrip antenna can be subjected to icing or be coated with paint or dielectric material for protection from the environment. This cover affects

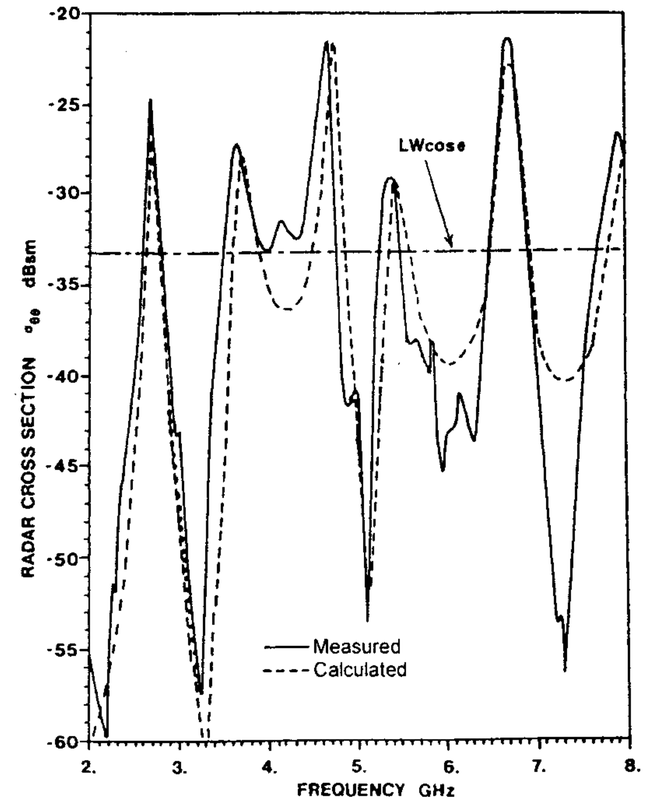

Figure 4.18 Variation of RCS with frequency of a rectangular microstrip antenna ($L = 3.66$ cm, $W = 2.60$ cm, $\epsilon_r = 2.17$, $h = 0.158$ cm, $\theta = 60°$, $\phi = 45°$). (From [26]. © 1987 IEEE. Reprinted with permission.)

performance to an extent that should be known. In particular, the resonant frequency is lowered, causing tuning problems and severely degrading performance, which can be serious, because the bandwidth of these antennas is inherently low.

When a microstrip patch is covered by a dielectric sheet (called a superstrate), its properties, like effective dielectric constant, losses, Q factor, and directive gain, change. The change in effective dielectric constant is more than other characteristics. The amount of change is dependent on the thickness and relative permittivity of the superstrate. The properties of the configuration (see Figure 4.5) have been studied using various approaches [15, 27, 28]. Zhong et al. [15] have determined the effect of superstrate on the effective dielectric constant, end-effect extension, and dispersion of a microstrip line. Expressions for ϵ_{re} and dispersion are given in Appendix B, (B.27c) and (B.27d), respectively. An expression for the open-end extension ΔL is given in Section 4.3.2. The resonant frequency of a microstrip antenna with a superstrate layer is plotted in Figure 4.19 as a function of the dielectric constant of the superstrate [15]. The resonant frequency is found to decrease with ϵ_{r3} but slowly.

The presence of the cover layer produces changes in the radiation pattern also. These effects have been determined [29, 30]. The final expressions for the radiation fields are given by (4.44), except that the factors $F_3(\theta)$ and $F_4(\theta)$ now include the effect of the cover layer. The new expressions for a single layer substrate of thickness h and superstrate thickness d are [29]

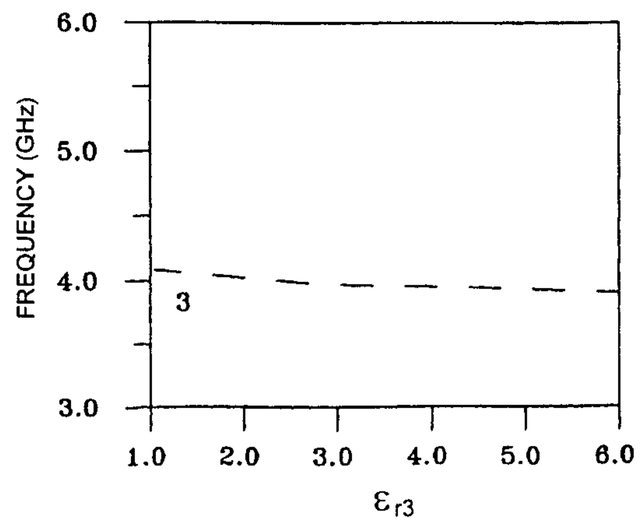

Figure 4.19 Resonant frequency of a rectangular microstrip antenna with a superstrate. Parameters: L = 22.9 mm, W = 19 mm, h_1 = 1 mm, ϵ_{r1} = 2.32; h_2 = 0.59 mm, ϵ_{r2} = 2.32; h_3 = 1.59 mm. (From [15]. © 1994 IEEE. Reprinted with permission.)

$$F_3(\theta) = 2\cos\theta\tan(\beta_1 h)\sec(\beta_2 d)\left\{\tan(\beta_1 h) + \frac{\epsilon_{r1} n_2(\theta)}{\epsilon_{r2} n_1(\theta)}\tan(\beta_2 d) - j\left[\frac{\epsilon_{r1}}{n_1(\theta)}\cos\theta\left(1 - \frac{\epsilon_{r2} n_1(\theta)}{\epsilon_{r1} n_2(\theta)}\tan(\beta_1 h)\tan(\beta_2 d)\right)\right]\right\}^{-1} \quad (4.81)$$

$$F_4(\theta) = 2\tan(\beta_1 h)\sec(\beta_2 d)\left\{\tan(\beta_1 h) + \frac{n_1(\theta)}{n_2(\theta)}\tan(\beta_2 d) - j\left[n_1(\theta)\sec\theta\left(1 - \frac{n_2(\theta)}{n_1(\theta)}\tan(\beta_1 h)\tan(\beta_2 d)\right)\right]\right\}^{-1} \quad (4.82)$$

with

$$\beta_1 = k_0 n_1(\theta) \qquad \beta_2 = k_0 n_2(\theta)$$

and

$$n_1(\theta) = \sqrt{\epsilon_{r1} - \sin^2\theta} \qquad n_2(\theta) = \sqrt{\epsilon_{r2} - \sin^2\theta}$$

Radiation patterns of a microstrip patch antenna with a cover layer are plotted in Figure 4.20 [31]. The parameters used are ϵ_{r1} = 2.32, h = 0.159 cm, $\tan\delta$ = 0.001, ϵ_{r2} = 2.60, d = 0.3175 cm, L = 2.318 cm, and W = 1.9 cm. The H-plane pattern is found to become narrow due to the presence of the cover layer. The associated increase in gain is a useful feature of the microstrip antenna with a superstrate [29]. Superstrates with large ϵ_r have been used to improve the gain of small antennas useful for handset receivers. Huang et al. were able to enhance the gain by 10.8 dB using a superstrate with ϵ_{r2} = 79 and d = 3.05 mm [32]. Some more examples are included in Chapter 10. The studies on superstrate effects are also useful in biomedical applications of such antennas.

4.3.11 Effects of Finite Size Ground Plane

It has been assumed in the analysis and design of microstrip antennas that the size of ground plane is infinite. In actual usage only a finite size ground plane can be implemented. In some applications, for instance, in handheld receivers, space is at a premium. Also, for the use of a microstrip antenna as a reflector feed, the ground plane size should be limited. The goal is to reduce the antenna size and the ground plane extension beyond the patch dimensions to

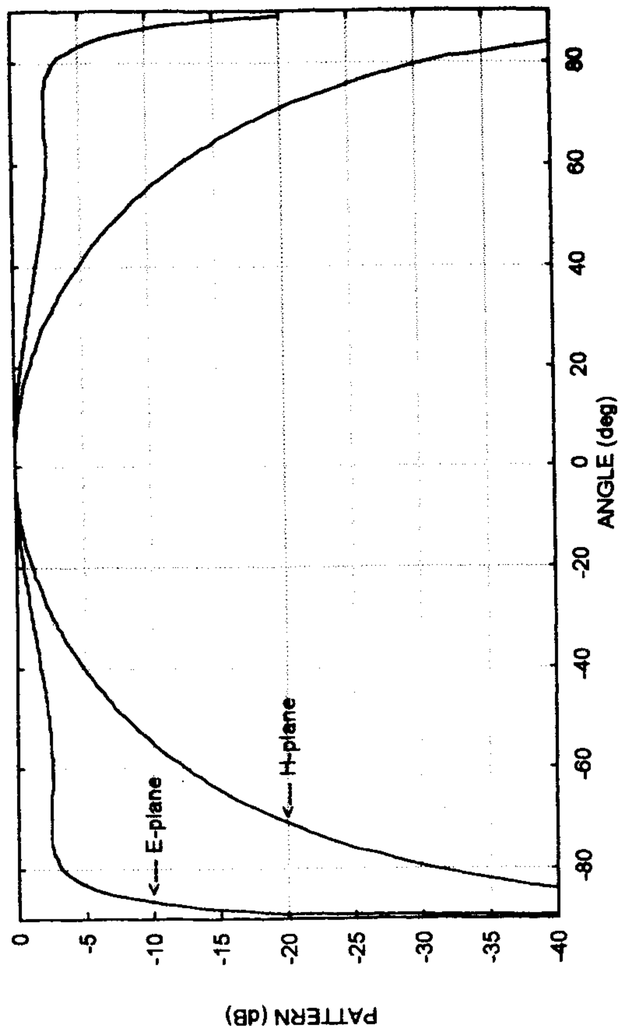

Figure 4.20 Radiation patterns of a microstrip antenna with a superstrate. Parameters: h = 1.59 mm, ϵ_{r1} = 2.32, $\tan\delta$ = 0.001; ϵ_{r2} = 2.6, d = 3.175 mm, $\tan\delta$ = 0.001, f = 3.874 GHz. (From [31]. © 1996 Artech House. Reprinted with permission.)

a minimum. Numerical and analytical techniques have been used to analyze such antennas [23, 33–36]. Finite ground plane gives rise to diffraction of radiation from the edges of the ground plane resulting in changes in radiation pattern, radiation conductance, and resonant frequency. Kuboyama et al. have reported the results of experimental investigations on the resonant frequency, radiation pattern, and gain of a rectangular patch as a function of ground plane size [36]. It was found that for a patch antenna with the ground plane size equal to the patch metalization, the resonant frequency is higher compared to that of an infinitely sized ground plane antenna. Denoting the ground plane extension by d (see Figure 4.21), the fractional change in resonant frequency is given by [33]

$$\lim_{k_0 d \to 0} \frac{\Delta f}{f_r} \approx \frac{1}{\pi} \frac{\epsilon_r + 1}{\sqrt{\epsilon_r}} \frac{h}{\lambda_0} \ln(W/h) \qquad \text{for } W/h >> 1 \tag{4.83a}$$

For other values of d not satisfying the limit, one can use [33]

$$\frac{\Delta f}{f_r} = -\frac{240}{\sqrt{\epsilon_{re}}} \frac{h}{W} B_d \tag{4.83b}$$

with

$$B_d = \frac{k_0 W}{8\eta_0} [J_0^2(k_0 d) - Y_0^2(k_0 d)] \tag{4.84}$$

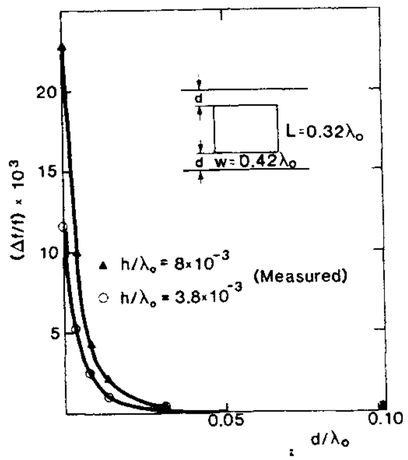

Figure 4.21 Measured change in the resonant frequency with ground plane size (ϵ_r = 2.32, f = 1.58 GHz). (From [33]. © 1983 IEEE. Reprinted with permission.)

The effect of ground plane size on the resonant frequency is plotted in Figure 4.21 [33]. It shows that as the size of the ground plane is increased, the resonant frequency decreases and approaches that of the infinite sized ground plane case when the increase in size is about $\lambda_0/20$ on all sides.

The effect of a finite ground plane on radiation fields has been studied by Huang using the aperture model for radiation and uniform geometrical theory of diffraction (GTD). The effect of the substrate in the edge diffraction calculations is not included. The E-plane radiation pattern is affected more than the H-plane pattern by the finite sized ground plane. Figure 4.22 illustrates the difference between the E-plane patterns for a two-wavelength ground plane and an infinite ground plane [23]. For very small ground planes ($< \lambda_0$), ripples are introduced into the pattern over a wide range of angles. As the size of the ground plane is increased, the ripples in the main pattern diminish. Also, a finite ground plane gives rise to scattered radiation in the backward direction.

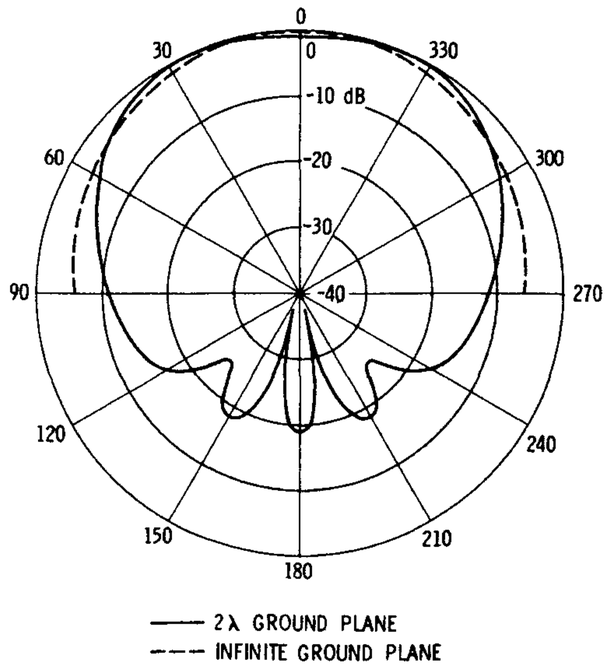

Figure 4.22 Comparison of the E-plane computed patterns when the rectangular patch is on a two-wavelength ground plane and an infinite ground plane. Parameters: L = 1.488 in, W = 2.126 in, ϵ_r = 2.55, h = 0.125 in, f_r = 2.295 GHz. Ground plane dimensions: $2\lambda_0 \times 2.7\lambda_0$. (From [23]. © 1983 IEEE. Reprinted with permission.)

4.3.12 Computer-Aided Design

The design information presented earlier can be included in a CAD package. To clarify the various steps in the design process, let us consider the design of a microstrip antenna for which the substrate dielectric constant has already been selected. The considerations for the selection of substrate are given in Section 4.3.1 and Appendix A. The patch dimensions L and W and substrate thickness h are to be determined for a desired resonant frequency f_r and bandwidth B. Further, the feed location (x_f, y_f) is to be determined for a 50Ω input impedance.

The design starts with the determination of substrate thickness h because this parameter along with ϵ_r influences the bandwidth considerably. Equation (4.72) is used to calculate the value of h. To implement (4.72), a suitable value of aspect ratio W/L and radiation efficiency e_r needs to be selected. One should select W/L such that radiation resistance R_r for the given ϵ_r is greater than the feed line impedance. For this, one can use a design graph between R_r and W/L for a number of values of h. These parameters and an assigned value of $e_r = 1$ can be used in (4.72) to determine the value of h. This value of h is now used in (4.75) to calculate the actual e_r. The value of h can be corrected in a similar manner. These considerations determine the values of h, ϵ_r, and W/L. The patch length L is determined next from the resonance condition, (4.28). The next step is to determine the feed location. The value of x_f is governed by (4.77). For this, the radiation resistance R_r is determined through (4.57) after P_r is known. For better accuracy, (4.55b) is integrated numerically to calculate P_r. The feed point is taken as $y_f = W/2$ and x_f calculated from (4.77). The preliminary design of the patch antenna is now complete.

The design should now be tested for the resonant frequency, input impedance, and bandwidth. For this, we should calculate the input impedance as a function of frequency. Let us use the cavity model. The value of equivalent loss tangent δ_{eff} should be known to evaluate the input impedance expression (4.22). We know that $\delta_{\text{eff}} = 1/Q_T$. Next, Q_T is determined. Although the value of Q_T can be determined from the desired VSWR bandwidth and (4.71), the suggestion is that (4.66), (4.67), and P_r, as determined earlier, be used instead for better accuracy in Q_T. Input impedance is now computed as a function of frequency near the design frequency. Ten values each of m and n in (4.22) should be sufficient to compute Z_{in}. The computed values of resonant frequency, input resistance, and bandwidth are determined from these data. It is very likely that the computed values are slightly different from the design values due to the approximate nature of the design equations, and the effect

of feed reactance on resonant frequency not being included in the design. Feed reactance can be calculated from (2.96) and added to the calculated input impedance value. The patch length L and feed location x_f are now varied iteratively to arrive at an accurate design. For this, the Newton-Raphson procedure can be used.

To correct for the change in resonant frequency from the design value, the patch length should be adjusted. For this, it can be assumed that the input reactance curve is linear about the resonant length, that is,

$$X_{\text{in}} = X_{\text{in}}(0) + \frac{\partial X_{\text{in}}}{\partial L}\delta L \tag{4.85a}$$

Here, X_{in} is the desired input reactance at the resonant frequency, and $X_{\text{in}}(0)$ is the actual reactance obtained at the design frequency. Because X_{in} should be zero at the resonant frequency, one obtains from (4.85a)

$$\partial L = -\frac{X_{\text{in}}(0)}{\partial X_{\text{in}}/\partial L} \tag{4.85b}$$

The slope $\partial X_{\text{in}}/\partial L$ is determined numerically from two different values of L. The new patch length is $(L + \delta L)$. Input impedance is calculated again with this patch length. This process is repeated until the desired tolerance in resonant frequency is attained. Usually three to four iterations are needed. With this corrected length, a slight change in input resistance is observed. Therefore, the feed position is now adjusted to obtain a 50Ω input resistance. For this, we can write

$$R'_{\text{in}} = KR_r\cos^2(\pi x'_f/L) \tag{4.86a}$$

where R'_{in} is the input resistance (which is different from the desired value R_{in}) obtained at the feed point x'_f, and K is an arbitrary constant. Let the correct feed position be x_f, then

$$R_{\text{in}} = KR_r\cos^2(\pi x_f/L) \tag{4.86b}$$

From (4.86), one obtains the corrected feed location as

$$x_f = \frac{L}{\pi}\cos^{-1}\left\{\sqrt{\frac{R_{\text{in}}}{R'_{\text{in}}}}\cos\left(\frac{\pi x'_f}{L}\right)\right\} \tag{4.87}$$

A similar adjustment in substrate thickness h can be required to obtain the required bandwidth. The designed patch may now be investigated for its other characteristics such as radiation pattern, beamwidth, gain, radiation efficiency, and directivity. These characteristics can be determined by computing the expressions given earlier.

The CAD approach presented above does not have the accuracy of a full-wave analysis, but is useful for parametric studies of the characteristics of a rectangular microstrip antenna. It can also be used for instructional purposes. A similar software is available in [31].

4.4 Tolerance Analysis of Rectangular Microstrip Antennas

Deviations in the effective electrical dimensions of the patch antenna from the designed values can lead to discrepancies between the designed and actual resonant frequencies. These deviations may include the variations in the relative permittivity of the substrate material, or nonuniformity in the substrate thickness, or slight variations in finished antenna length and width. The discrepancy in the resonant frequency is especially significant because of the narrow bandwidth of such antennas. In this section, the effect of fabrication inaccuracies and substrate tolerances on the resonant frequency is considered.

Manufacturing tolerances that can alter the resonant frequency are the substrate thickness Δh and dielectric constant $\Delta\epsilon_r$. Low dielectric constant substrates ($2.1 < \epsilon_r < 2.6$), such as polyolefin, polystyrene, and rexolite, typically have tolerances of ±1% in dielectric constant and ±3% in substrate thickness. Higher dielectric constant substrates, such as alumina, have tolerances of ±2% in dielectric constant and ±4% in substrate thickness.

Most fabrication errors arise as a result of inaccuracies in etching. Etching accuracy depends on both the process and the chemicals used in the photoetching process. Substrate properties such as surface finish and metalization thickness also determine the etching accuracy. It is well known that without special precautions, etching accuracy is equal to the metalization thickness, t. Because the bandwidth of microstrip antennas is narrow, it is important and interesting to study the variations in resonant frequency due to the above factors. The effect of these factors on other characteristics of the patch antenna is expected to be negligible.

For rectangular (or square) geometry antennas, the lowest order resonant frequency f_r can be accurately predicted from:

$$f_r = \frac{c}{2(L + 2\Delta L)\sqrt{\epsilon_{re}}} \tag{4.88}$$

where ΔL is the end-effect extension and is defined in (4.26). A first-order change in the resonant frequency can be obtained by using tolerance analysis [37] resulting in

$$|\Delta f_r| = \left[\left(\frac{\partial f_r}{\partial L}\Delta L'\right)^2 + \left(\frac{\partial f_r}{\partial \epsilon_{re}}\Delta\epsilon_{re}\right)^2\right]^{1/2} \tag{4.89}$$

where $\Delta\epsilon_{re}$ is the change in the effective relative permittivity due to inaccuracy in the fabrication of the patch and tolerances in substrate parameters, and is given by

$$\Delta\epsilon_{re} = \left[\left(\frac{\partial\epsilon_{re}}{\partial W}\Delta W\right)^2 + \left(\frac{\partial\epsilon_{re}}{\partial h}\Delta h\right)^2 + \left(\frac{\partial\epsilon_{re}}{\partial\epsilon_r}\Delta\epsilon_r\right)^2 + \left(\frac{\partial\epsilon_{re}}{\partial t}\Delta t\right)^2\right]^{1/2} \tag{4.90}$$

where ΔW, Δh, Δt, $\Delta\epsilon_r$, and $\Delta L'$ are the tolerances in patch parameters. From (4.88) to (4.90) we obtain

$$\frac{|\Delta f_r|}{f_r} = \left[\left(\frac{\Delta L'}{L}\right)^2 + \left(\frac{0.5}{\epsilon_{re}}\right)^2\left\{\left(\frac{\partial\epsilon_{re}}{\partial W}\Delta W\right)^2 + \left(\frac{\partial\epsilon_{re}}{\partial h}\Delta h\right)^2 + \left(\frac{\partial\epsilon_{re}}{\partial\epsilon_r}\Delta\epsilon_r\right)^2 + \left(\frac{\partial\epsilon_{re}}{\partial t}\Delta t\right)^2\right\}\right]^{1/2} \tag{4.91}$$

For microstrip antennas, $W/h >> 1$ and the inaccuracy in W is of the order of metalization thickness t, thus the $(\partial\epsilon_{re}/\partial W)\Delta W$ term will be negligible. Also, the effect of strip thickness on ϵ_{re} is very small; hence, (4.91) becomes

$$\frac{|\Delta f_r|}{f_r} = \left[\left(\frac{\Delta L'}{L}\right)^2 + \left(\frac{0.5}{\epsilon_{re}}\right)^2\left\{\left(\frac{\partial\epsilon_{re}}{\partial h}\Delta h\right)^2 + \left(\frac{\partial\epsilon_{re}}{\partial\epsilon_r}\Delta\epsilon_r\right)^2\right\}\right]^{1/2} \tag{4.92}$$

As the uncertainties due to the manufacturing tolerance are known a priori, the effect of tolerances on the resonant frequency can be determined using (4.92).

Using (B.4) for the variation of ϵ_{re} with h and ϵ_r, one obtains

$$\frac{\partial\epsilon_{re}}{\partial\epsilon_r} = 0.5\left[1 + \left(1 + \frac{10h}{W}\right)^{-ab}\right] \tag{4.93}$$

and

$$\frac{\partial\epsilon_{re}}{\partial h} = -(\epsilon_r - 1)\left[\frac{5ab}{W}\left(1 + \frac{10h}{W}\right)^{-ab-1}\right] \tag{4.94}$$

Using the above equations, the fractional change in the resonant frequency of a typical microstrip antenna, of dimensions shown, is plotted as a function of the resonant frequency in Figures 4.23 and 4.24 [8]. In Figure 4.23 note that the change in resonant frequency due to given tolerances is less than 0.5% up to a resonant frequency of 2.5 GHz. For frequencies above 2.5 GHz, the change in resonant frequency is essentially independent of the effect of Δh or $\Delta\epsilon_r$. The major effect on the change in resonant frequency is due to the fabrication tolerance in L.

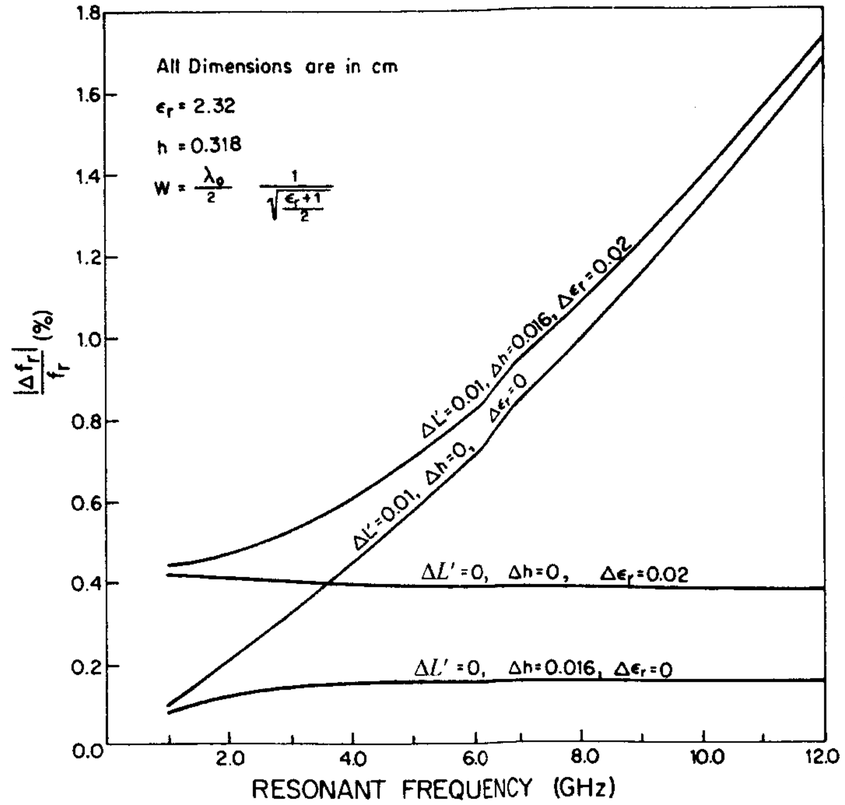

Figure 4.23 The fractional change in the resonant frequency for the TM_{10} mode of a rectangular microstrip antenna with given tolerances and $\epsilon_r = 2.32$. (From [8]. © 1980 Artech House. Reprinted with permission.)

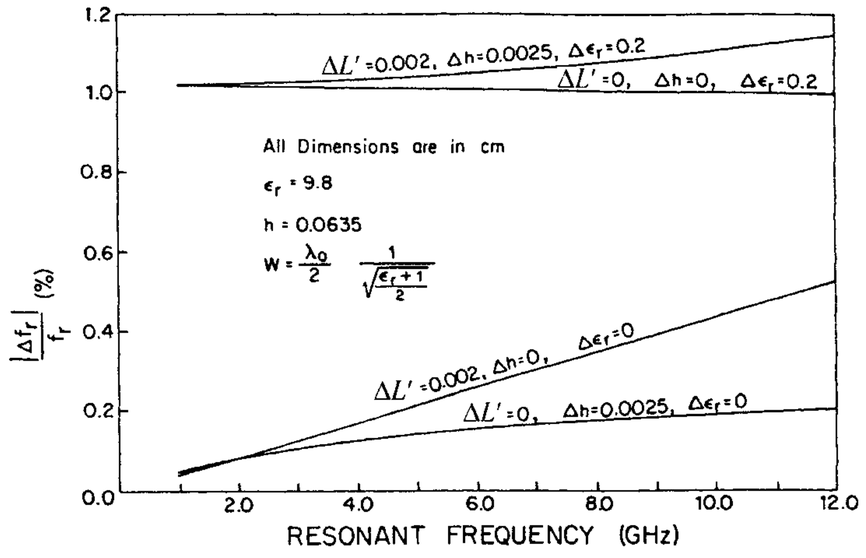

Figure 4.24 The fractional change in the resonant frequency for TM_{10} mode of a rectangular microstrip antenna with given tolerances and $\epsilon_r = 9.8$. (From [8]. © 1980 Artech House. Reprinted with permission.)

The change in the resonant frequency of a microstrip antenna fabricated on an alumina substrate is shown in Figure 4.24. In this case, it can be seen that the error in the resonant frequency is mainly caused by tolerances in ϵ_r, and that a tolerance of 2% in the dielectric constant is not acceptable. To obtain better results, substrate tolerance should be ±1% or less.

We conclude that for microstrip antennas fabricated on low dielectric constant substrates, the critical parameter affecting the resonant frequency is the fabrication error $\Delta L'$ in antenna length, and hence considerable care should be exercised when etching. For substrates of high permittivity, such as alumina or GaAs, the dielectric constant ϵ_r is the critical parameter, and hence it is essential to specify lower tolerance limits in procuring the material to be used. Here it is assumed that $\Delta L' = 0.002$ cm.

The percent change in resonant frequency values due to tolerances are significant in comparisons of theoretically predicted and measured results and may well account for the differences observed in many cases.

4.5 Mechanical Tuning of Patch Antennas

Microstrip antennas are in general narrow-band antennas. Due to fabrication inaccuracies, substrate parameter tolerances, and modeling inaccuracies, the

actual frequency of the antenna can be different from the design value. Also, wide-band operation of the antenna can be a requirement for certain applications. Therefore, tuning of a patch antenna to a desired frequency is very useful.

The resonant frequency of a microstrip antenna can be changed in a number of ways. These include mechanical tuning and electronic tuning. In principle, any reactive loading of the patch antenna will give rise to a change in the resonant frequency. Some of the techniques that have been used are shorting pins or posts, stubs, variable dielectric layer thickness, varactor diodes, and optical control. Pins, posts, stubs, and so on give rise to mechanical tuning, whereas varactor diodes embedded in the patch and optical control of PIN diode impedance can be used for electronic tuning or frequency agility of the patch antenna. Electronic tuning is discussed in Chapter 10. A number of arrangements have been reported for mechanical tuning of patch antennas. Some of these configurations are shown in Figure 4.25 and described next.

4.5.1 Mechanical Tuning Using Stubs

Frequency tuning can be accomplished by varying the length of a printed or coaxial transmission line stub attached to the antenna. Two tuning stubs positioned on the opposite radiating edges of the patch are used in Figure 4.25(a). The patch is then tuned in an iterative manner by systematic trimming of either of the stubs. Narrow stubs allow fine tuning, whereas wide stubs are useful for larger tuning ranges. In this technique, tuning is only possible from a lower frequency to a higher frequency owing to the destructive nature of trimming. A tuning range of about 14% can be achieved by using a single stub. Simultaneous tuning of reflection coefficient and resonant frequency is also possible by using two stubs [38]. This is because the length of the antenna determines the resonant frequency and the feed position determines the input impedance, and the effective position of the feed point will be shifted toward the shortened stub. It has been demonstrated that the two-stub approach allows the adjustment of the input reflection coefficient of a patch to less than −60 dB, at a frequency that is within 0.005% of specifications [38]. Coaxial stub tuning was studied by Richards et al. [39].

4.5.2 Mechanical Tuning Based on Shorting Posts or Pins

Reactive loading in a patch antenna can also be introduced by means of metallic posts or pins between the patch metalization and ground plane. These shorting posts present an inductance. Therefore, this type of tuning increases the resonant frequency of the patch. This technique was first introduced by Schaubert et al.

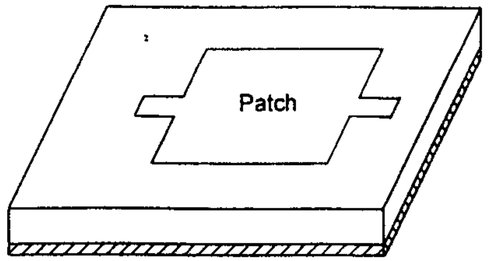

(a)

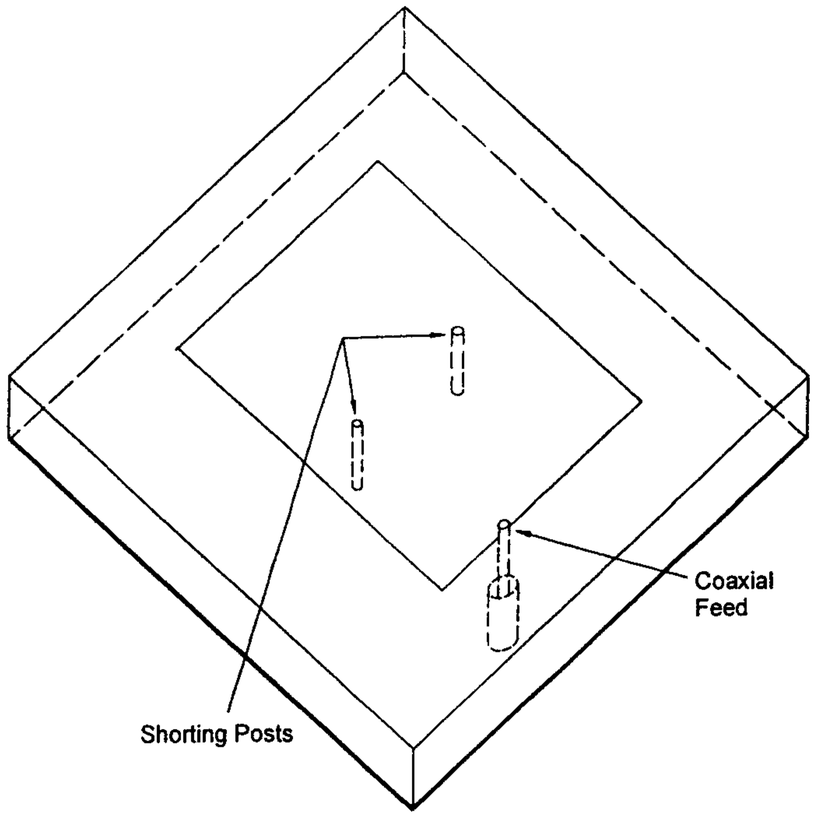

(b)

Figure 4.25 Various schemes for the mechanical tuning of microstrip antennas: (a) Tuning using stubs. (b) Tuning using shorting pins. (From [40]. © 1981 IEEE. Reprinted with permission.) (c) Tuning based on an adjustable air gap.

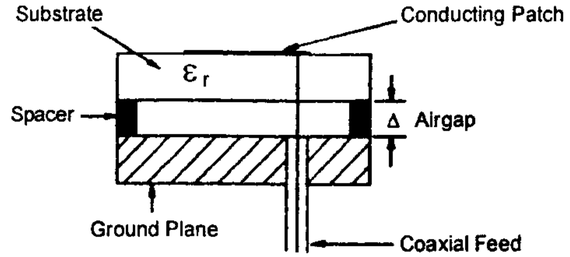

(c)

Figure 4.25 (continued).

in 1981 and is illustrated in Figure 4.25(b) [40]. The posts are located along the length L of the patch at the centerline $y = W/2$. With two posts located symmetrically about the plane $x = L/2$, a tuning range of 18% is obtained as the separation s between the posts varies between 0 and L (see Figure 4.26) [40]. The radiation pattern remained well behaved over the tuning range [41]. A simplified transmission line model without mutual coupling between the radiating ends was used by Schaubert to explain the tuning of the patch [40].

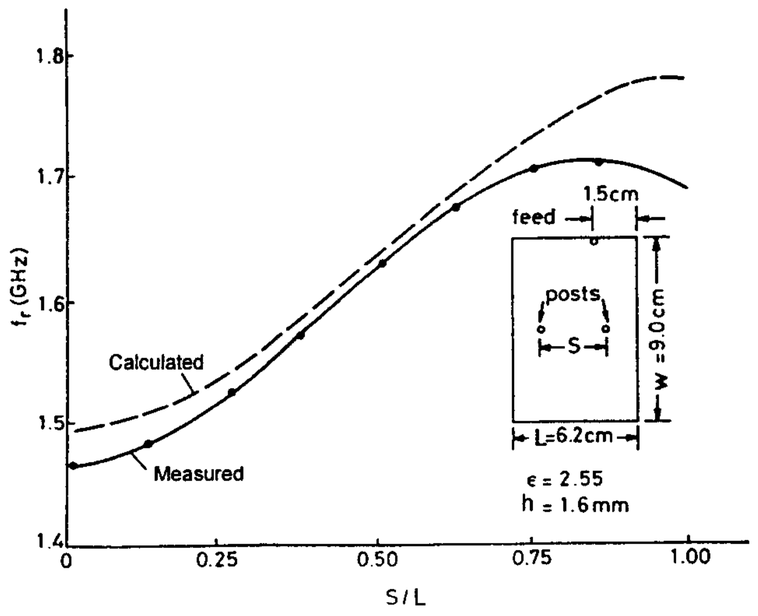

Figure 4.26 Resonant frequency versus separation of posts for a rectangular microstrip antenna. (From [40]. © 1981 IEEE. Reprinted with permission.)

A tuning range in excess of 50% was reportedly achieved by adding more posts. The model was refined by Sengupta to better explain the change in resonant frequency [42].

4.5.3 Mechanical Tuning Using an Adjustable Air Gap

Figure 4.25(c) shows an arrangement in which an air gap is introduced between the substrate and the ground plane [1]. Tuning is achieved in this case by adjusting the thickness of the air layer. The principle employed is very simple to follow. The effective dielectric constant ϵ_{re} for this patch antenna is a function of air layer thickness Δ in addition to other patch parameters. When the value of Δ is changed mechanically, the value of ϵ_{re} also changes, resulting in a new resonant frequency. As a by-product, the bandwidth of this antenna is more because of the lower value of ϵ_{re} and the increased thickness due to the additional air layer. This idea was proposed by Dahele and Lee [43]. They carried out experiments on circular patches and annular rings. The analysis of the cavity model was extended to this multilayer configuration with good agreement between theory and measured impedance values [43]. It was found that for the TM_{11} mode in a circular patch, a tuning range of about 20% in frequency and a more than twofold increase in bandwidth could be achieved with the help of a 1-mm-thick air layer. The above tuning approach is also applicable to rectangular patch shapes.

The bandwidth of a rectangular patch can be increased by using various approaches such as increase in substrate thickness, decrease in permittivity of substrate, excitation of more than one mode, parasitic loading, impedance matching, and so on. These techniques are discussed in Chapter 9. Bandwidths of more than 50% are now possible. Loading of a microstrip antenna to reduce size and electronic tuning is discussed in Chapter 10.

4.6 Quarter-Wave Rectangular Patch Antennas

The rectangular patch antenna discussed so far is a half-wave rectangular patch. The electric field distribution under the patch is given by $E_0 \cos(\pi x/L)$, with a maximum electric field at one of the radiating edges, zero in the middle (i.e., at $x = L/2$), becoming maximum again at the other radiating edge with 180° phase reversal. Since the electric field is zero at the plane $x = L/2$, an electric wall can be erected there without disturbing the field distribution under the patch. One-half of this patch can now be discarded. The patch will still be resonant at the design frequency of a half-wave rectangular patch. A rectangular patch geometry of this type (see Figure 4.27) is called a *quarter-wave patch*

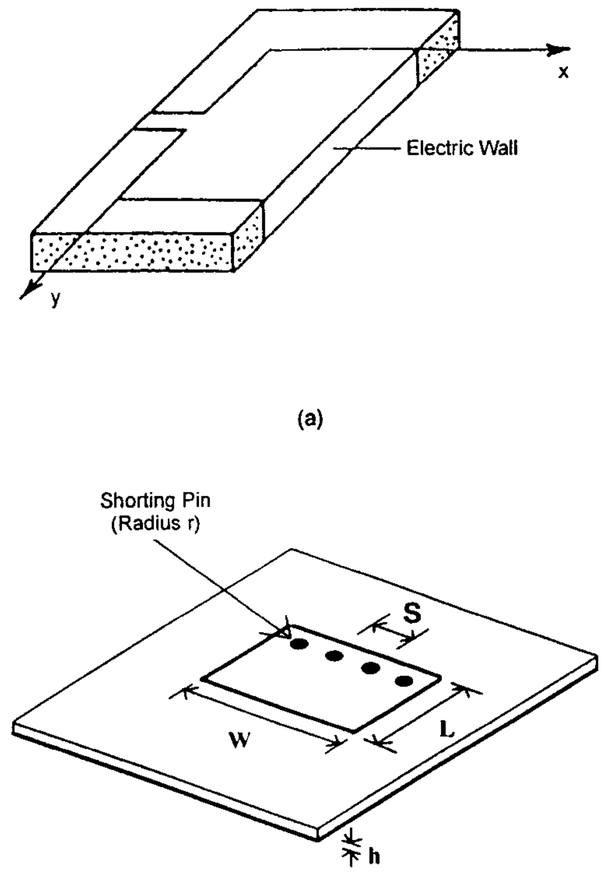

Figure 4.27 A quarter-wave rectangular microstrip antenna: (a) Quarter-wave patch with a continuous sheet as a short. (From [1]. © 1989 Peter Peregrinus. Reprinted with permission.) (b) Quarter-wave patch with shorting pins. (From [31]. © 1996 Artech House. Reprinted with permission.)

because the separation between the radiating edge and the electric wall is about $\lambda_g/4$. Because this patch geometry is a derivative of the half-wave patch, its characteristics can be easily derived from those of the half-wave patch. A quarter-wave patch can be used in those applications where small-sized antennas are needed, and a deterioration in cross-polarization characteristics can be tolerated.

The major difference between the half-wave patch and the quarter-wave patch is that the quarter-wave patch has one radiating edge compared to two for the half-wave patch. This physical difference is responsible for all the differences in antenna characteristics:

1. The E-plane pattern of the quarter-wave patch becomes broader because the array effect of two radiating edges for a half-wave patch is absent here. Also, the half-length nature of the patch gives rise to a cross-polarized E_θ component in the H plane.
2. The radiation conductance G_r of a quarter-wave patch is due to radiation from a single edge. Its value is given by (2.77), and is lower by a factor of about 2 compared to that obtained from (4.57) for a half-wave patch. Therefore, the radiation resistance at resonance will be about two times. Numerical calculations show that this is true for $\epsilon_r \neq 1$.
3. The stored energy in a quarter-wave patch is exactly one-half that of the half-wave patch because of identical field distribution over half the area.
4. Use of (4.66) for the Q factor calculation shows that the bandwidth of the quarter-wave patch is about the same as that of the half-wave patch. Again this reasoning has been found to be approximately true for $\epsilon_r \neq 1$.

Resonant resistances and Q factors of a quarter-wave and a half-wave patch are compared in Figures 4.28 and 4.29, respectively [1]. It is seen that the radiation resistances for the two patches are almost the same for $\epsilon_r = 1$, but a quarter-wave patch has almost twice the resistance compared to that of a half-wave patch for $\epsilon_r = 2.1$. The Q factor of a quarter-wave patch for $\epsilon_r = 1$ is lower than that of the half-wave patch resulting in larger bandwidth. For $\epsilon_r = 2.1$, the two patches have almost the same Q factor and therefore the same bandwidth. These comparisons show that a quarter-wave patch with $\epsilon_r = 1$ is a better antenna compared to that with $\epsilon_r > 1$.

4.6.1 Quarter-Wave Patch With Shorting Pins

The geometry of a quarter-wave patch with a continuous sheet as a short is shown in Figure 4.27(a) [1]. Mechanical implementation of this type of short circuit may require a long slot to be cut in the substrate material requiring a machining operation. RF characteristics of a short can be realized by using a number of pins or plated through via holes connected between the patch metalization and the ground plane, as shown in Figure 4.27(b) [31]. However, this approach gives rise to a residual inductance at the shorting edge. As a result, the patch length must be adjusted to account for the postinductance. The normalized inductance associated with an array of shorting pins is given by [11, p. 104]

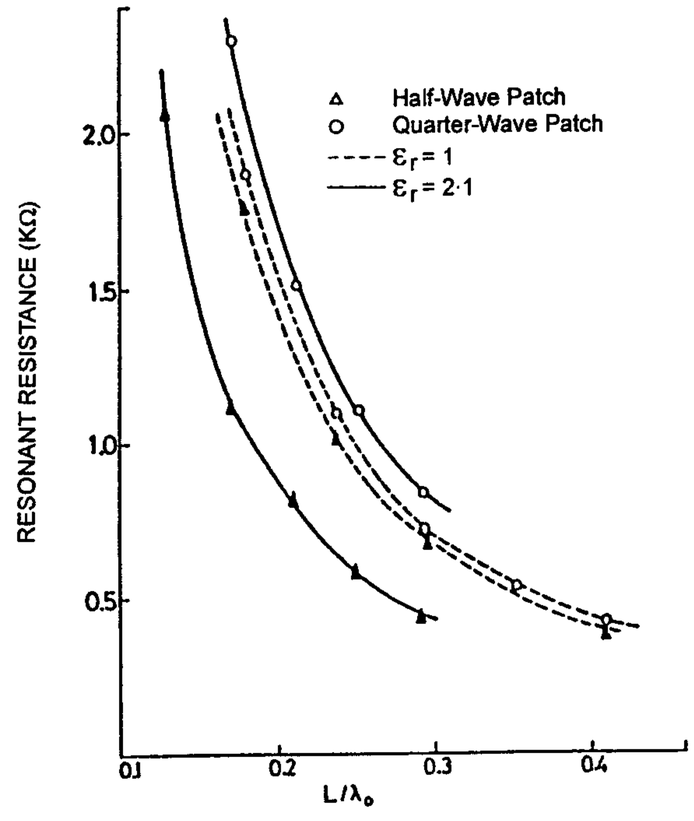

Figure 4.28 Comparison of resonant resistances of quarter-wave and half-wave rectangular patch antennas at the same resonant frequency for the TM_{10} mode. (From [1]. © 1989 Peter Peregrinus. Reprinted with permission.)

$$\frac{X}{Z_0} = \frac{S}{\lambda_d}\left[\ln\left(\frac{S}{2\pi r}\right) + 0.601\left(\frac{S}{\lambda_d}\right)^2 - \left(\frac{2\pi r}{S}\right)^2\right] \tag{4.95}$$

where S is the separation between the pins of diameter $2r$, and λ_d is the wavelength in the dielectric medium. The effective position of the short circuit is then located outward at a distance Δl from the actual position, and is given by

$$\Delta l = \frac{\lambda_d}{2\pi}\frac{X}{Z_0} \tag{4.96}$$

Use of (4.95) in (4.96) gives

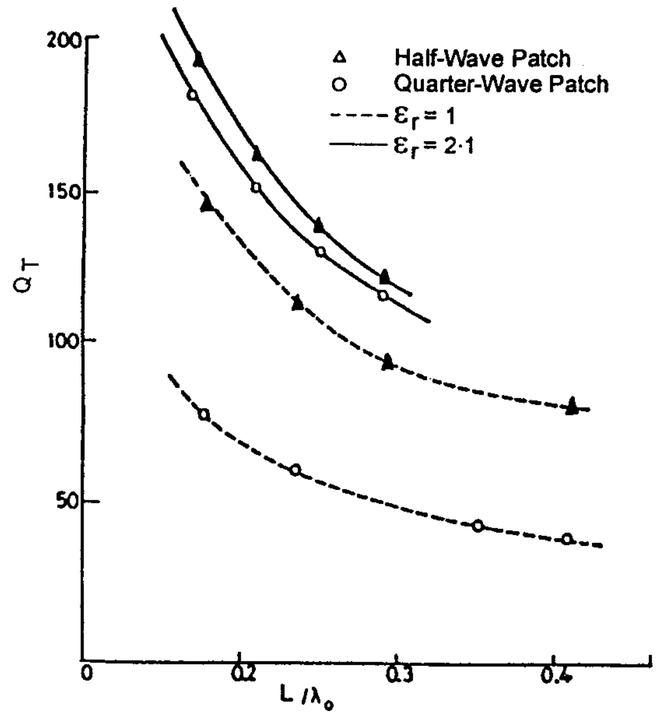

Figure 4.29 Comparison of Q factors of quarter-wave and half-wave rectangular patch antennas at the same resonant frequency for the TM_{10} mode. (From [1]. © 1989 Peter Peregrinus. Reprinted with permission.)

$$\frac{\Delta l}{S} = \frac{1}{2\pi}\left[\ln\left(\frac{S}{2\pi r}\right) + 0.601\left(\frac{S}{\lambda_d}\right)^2 - \left(\frac{2\pi r}{S}\right)^2\right] \tag{4.97}$$

The effective patch length of the antenna shown in Figure 4.27(b) is

$$L_{\text{eff}} = L + \Delta L + \Delta l \tag{4.98}$$

where ΔL has been defined in (4.26).

The radiation patterns of the quarter-wave patch are obtained as follows.

For E-plane patterns, the E_θ pattern for the quarter-wave patch can be obtained from that of the half-wave patch by eliminating the array factor from (4.38b) or from (1.29a) for an aperture. It gives

$$E_\theta(\theta) = -jk_0 V_0 W \frac{e^{-jk_0 r}}{2\pi r}\,\text{sinc}(k_0 h \sin\theta/2) \qquad \phi = 0° \tag{4.99}$$

This pattern is nearly omnidirectional in nature because of a single line source with constant magnetic current. The E_ϕ component in the radiation pattern is theoretically zero because of the equal but oppositely directed fringing field along the two edges laid out along the length of the patch.

For H-plane patterns, the E_ϕ polarization pattern is the same as that given by (4.40) for the half-wave case or by (1.29b) for an aperture. But the cross-polarized E_θ component is not zero. This component arises from the fringing electric field along the length of the patch, and is given by

$$E_\theta(\theta) = -jV_0 \frac{k_0 L}{\pi} \frac{e^{-jk_0 r}}{2\pi r} F_h(\theta) \qquad \phi = 90° \tag{4.100a}$$

where

$$F_h = \text{sinc}(k_0 W \sin\theta/2)$$

Also, from (4.40)

$$E_\phi(\theta) = jk_0 V_0 W \frac{e^{-jk_0 r}}{2\pi r} F_H(\theta) \qquad \phi = 90° \tag{4.100b}$$

where

$$F_H = \text{sinc}(k_0 W \sin\theta/2)\cos\theta$$

The computed radiation patterns for the TM_{10} mode for quarter-wave patch are compared with measurements in Figure 4.30 [1]. The agreement is seen to be good.

4.6.2 Stacked Quarter-Wave Antennas

Dual-frequency and broadband antennas have been developed by stacking two quarter-wave elements [44]. Coupling between the antennas gives rise to two modes of operation and hence dual-frequency behavior. This antenna is realized by positioning the short circuits along diametrically opposite planes in the form of the letter S, as shown in Figure 4.31(a). The ratio between the two frequencies can be controlled within the range of 1.3 to 2.

A distinguishing feature of this configuration is that the radiation patterns in the two bands are different. At the lower frequency the radiation pattern is like a difference pattern with a null in the broadside, due to oppositely

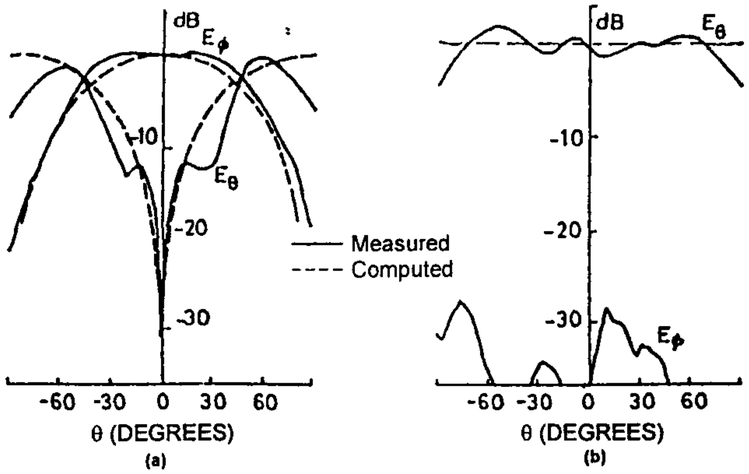

Figure 4.30 Comparison of computed and measured radiation patterns of a quarter-wave microstrip antenna. Parameters: $W = 6.0$ cm, $L = 4.0$ cm, $\epsilon_r = 2.56$, $h = 0.146$ cm, $\tan\delta = 0.001$): (a) H-plane pattern ($\phi = 90°$) and (b) E-plane pattern ($\phi = 0°$). (From [1]. © 1989 Peter Peregrinus. Reprinted with permission.)

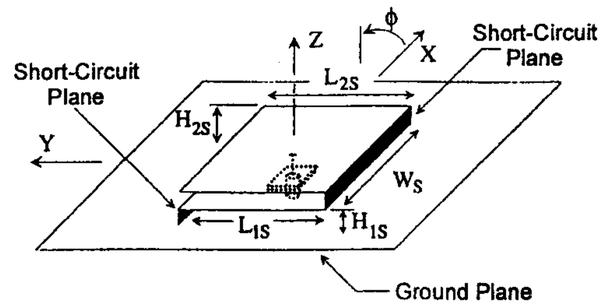

Figure 4.31 Geometry of stacked quarter-wave patches with probe feed: (a) S antenna and (b) E antenna. (From [44]. © 1999 IEEE. Reprinted with permission.)

directed currents on the two halves of the antenna. This radiation pattern is shown in Figure 4.32(a). However, at the upper frequency, the radiation from the two halves adds up to give rise to a sum pattern as shown in Figure 4.32(b). It is possible to achieve impedance match at both the frequencies using a probe feed.

Stacked quarter-wave patches with short circuits along the same plane are found to be useful as a broadband antenna. This configuration, called an

(a)

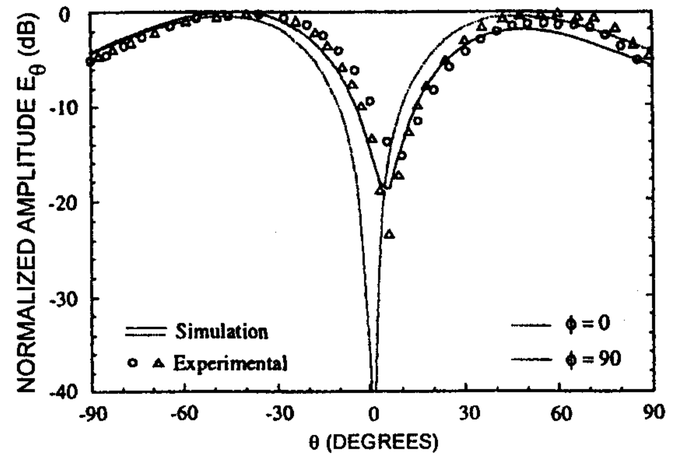

S-antenna: Measured and simulated radiation patterns at $F_{1S} = 1.55$ GHz.

(b)

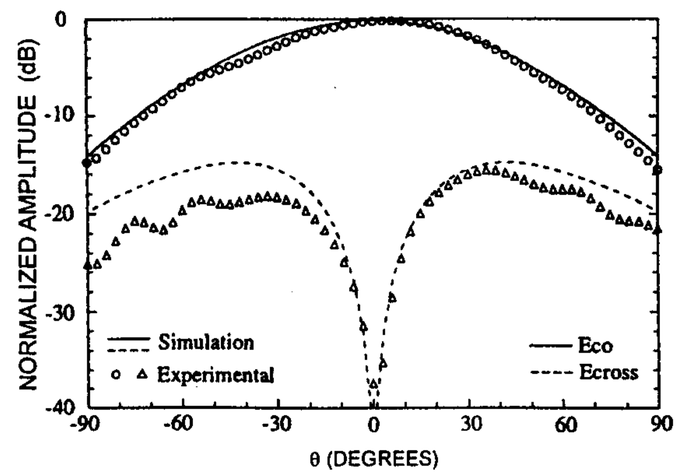

Figure 4.32 Radiation patterns of S antenna of Figure 4.31 where $L_{1S} = L_{2S} = W_S = 35$ mm, $H_{1S} = 8$ mm, $H_{2S} = 13.5$ mm, $W_E = 35$ mm, $L_{1E} = 35$ mm, $L_{2E} = 25$ mm, $H_{1E} = 6.8$ mm, $H_{2E} = 11.6$ mm. (From [44]. © 1999 IEEE. Reprinted with permission.) (a) Measured and simulated radiation patterns at 1.55 GHz. (b) Radiation patterns in the $\phi = 0°$ plane at 2.2 GHz.

E antenna, is shown in Figure 4.31(b). Impedance bandwidths of 30% but with high levels of cross-polarization have been realized.

References

[1] James, J., and P. S. Hall (Eds.), *Handbook of Microstrip Antennas*, Peter Peregrinus, London, UK, 1989.

[2] Munson, R. E., "Conformal Microstrip Antennas and Microstrip Phased Arrays," *IEEE Trans. on Antennas and Propagation*, Vol. AP-22, 1974, pp. 74–78.

[3] Derneryd, A. G., "Linearly Polarized Microstrip Antennas," *IEEE Trans. on Antennas and Propagation*, Vol. AP-24, 1976, pp. 846–851.

[4] Pues, H., and A. Van de Capelle, "Accurate Transmission-Line Model for the Rectangular Microstrip Antenna," *IEE Proc.*, Vol. 131, Pt. H, 1984, pp. 334–340.

[5] Bhattacharyya, A. K., and R. Garg, "Generalised Transmission Line Model for Microstrip Patches," *IEE Proc.*, Vol. 132, Pt. H, 1985, pp. 93–98.

[6] Richards, W. F., Y. T. Lo, and D. D. Harrison, "An Improved Theory for Microstrip Antennas and Applications," *IEEE Trans. on Antennas and Propagation*, Vol. AP-29, 1981, pp. 38–46.

[7] Lo, Y. T., D. Solomon, and W. F. Richards, "Theory and Experiment on Microstrip Antennas," *IEEE Trans. on Antennas and Propagation*, Vol. AP-27, 1979, pp. 137–145.

[8] Bahl, I. J., and P. Bhartia, *Microstrip Antennas*, Artech House, Dedham, MA, 1980, Chap. 2.

[9] Pozar, D. M., "Considerations for Millimeter Wave Printed Antennas," *IEEE Trans. on Antennas and Propagation*, Vol. AP-31, 1983, pp. 740–747.

[10] Kirschning, M., R. Jansen, and N. Koster, "Accurate Model for Open-End Effect of Microstrip Lines," *Electron. Lett.*, Vol. 17, 1981, pp. 123–125.

[11] James, J. R., P. S. Hall, and C. Wood, *Microstrip Antenna: Theory and Design*, Peter Peregrinus, London, UK, 1981.

[12] Kara, M., "The Resonant Frequency of Rectangular Microstrip Antenna Elements With Various Substrate Thicknesses," *Microwave and Opt. Technol. Lett.*, Vol. 11, 1996, pp. 55–59.

[13] Kara, M., "Formulas for the Computation of the Physical Properties of Rectangular Microstrip Antenna Elements With Various Substrate Thicknesses," *Microwave and Opt. Technol. Lett.*, Vol. 12, 1996, pp. 234–239.

[14] Hammerstad, E. O., "Equations for Microstrip Circuit Design," *5th European Microwave Conf.*, 1975, pp. 268–272.

[15] Zhong, S.-S., G. Liu, and G. Qasim, "Closed-Form Expressions for Resonant Frequency of Rectangular Patch Antennas With Multidielectric Layers," *IEEE Trans. on Antennas and Propagation*, Vol. AP-42, 1994, pp. 1360–1363.

[16] Jackson, D. R., and N. G. Alexopoulos, "Simple Approximate Formulas for Input Resistance, Bandwidth, and Efficiency of a Resonant Rectangular Patch," *IEEE Trans. on Antennas and Propagation*, Vol. AP-39, 1991, pp. 407–410.

[17] Perlmutter, P., S. Shritkman, and D. Treves, "Electric Surface Current Model for the Analysis of Microstrip Antennas With Application to Rectangular Elements," *IEEE Trans. on Antennas and Propagation*, Vol. AP-33, 1985, pp. 301–311.

[18] Kara, M., "Calculation of the Radiation Patterns of Rectangular Microstrip Antenna Elements With Various Substrate Thicknesses," *Microwave and Opt. Technol. Lett.*, Vol. 13, 1996, pp. 221–226.

[19] Thouroude, D., et al., "CAD-Oriented Cavity Model for Rectangular Patches," *Electron. Lett.*, Vol. 26, 1990, pp. 842–844.

[20] Gera, A. E., "The Radiation Resistance of a Microstrip Element," *IEEE Trans. on Antennas and Propagation*, Vol. AP-38, 1990, pp. 568–570.

[21] Pozar, D. M., "Rigorous Closed-Form Expressions for the Surface Wave Loss of Printed Antennas," *Electron. Lett.*, Vol. 26, 1990, pp. 954–956.

[22] Deshpande, M. D., and N. K. Das, "Rectangular Microstrip Antenna for Circular Polarization," *IEEE Trans. on Antennas and Propagation*, Vol. AP-34, 1986, pp. 745–746.

[23] Huang, J., "The Finite Ground Plane Effect on the Microstrip Antenna Radiation Pattern," *IEEE Trans. on Antennas and Propagation*, Vol. AP-31, 1983, pp. 649–653.

[24] Oberhart, M. L., Y. T. Lo, and R. Q. H. Lee, "New Simple Feed Network for an Array Module of Four Microstrip Elements," *Electron. Lett.*, Vol. 23, 1987, pp. 436–437.

[25] Huynh, T., K. F. Lee, and R. Q. Lee, "Crosspolarisation Characteristics of Rectangular Patch Antennas," *Electron. Lett.*, Vol. 24, 1988, pp. 463–464.

[26] Pozar, D. M., "Radiation and Scattering From a Microstrip Patch on Uniaxial Substrate," *IEEE Trans. on Antennas and Propagation*, Vol. AP-35, 1987, pp. 613–621.

[27] Bahl, I. J., and S. S. Stuchly, "Analysis of a Microstrip Covered With a Lossy Dielectric," *IEEE Trans. on Microwave Theory and Techniques*, Vol. MTT-28, 1980, pp. 104–109.

[28] Alexopoulos, N. G., and D. R. Jackson, "Fundamental Superstrate (Cover) Effects on Printed Circuit Antennas," *IEEE Trans. on Antennas and Propagation*, Vol. AP-32, 1984, pp. 807–816.

[29] Jackson, D. R., and N. G. Alexopoulos, "Gain Enhancement Methods for Printed Circuit Antennas," *IEEE Trans. on Antennas and Propagation*, Vol. AP-33, 1985, pp. 976–987.

[30] Yang, H. Y., and N. G. Alexopoulos, "Gain Enhancement Methods for Printed Circuit Antennas Through Multiple Superstrates," *IEEE Trans. on Antennas and Propagation*, Vol. AP-35, 1987, pp. 860–863.

[31] Sainati, R. A., *CAD of Microstrip Antennas for Wireless Applications*, Artech House, Norwood, MA, 1996.

[32] Huang, C.-Y., et al., "Gain-Enhanced Compact Broadband Microstrip Antenna," *Electron. Lett.*, Vol. 34, 1998, pp. 138–139.

[33] Lier, E., and K. R. Jacobson, "Rectangular Microstrip Patch Antennas With Infinite and Finite Ground Plane Dimensions," *IEEE Trans. on Antennas and Propagation*, Vol. AP-31, 1983, pp. 978–984.

[34] Vaudon, P., et al., "Asymptotic Method in Prediction of E-Plane Radiation Pattern of Rectangular Microstrip Patch Antennas on Finite Ground," *Electron. Lett.*, Vol. 26, 1990, pp. 956–957.

[35] Bokhari, S. A., J. R. Mosig, and F. E. Gardiol, "Radiation Pattern Computation of Microstrip Antennas on Finite Size Ground Plane," *Proc. IEE*, Vol. 139, Pt. H, 1992, pp. 278–286.

[36] Kuboyama, H., et al., "Post Loaded Microstrip Antenna for Pocket Size Equipment at UHF," *Proc. ISAP*, 1985, pp. 433–436.

[37] Garg, R., "Effect of Tolerances on Microstrip Line and Slotline Performances," *IEEE Trans. on Microwave Theory and Techniques*, Vol. MTT-26, 1978, pp. 16–19.

[38] Piessis, M. du, and J. H. Cloete, "Tuning Stubs for Microstrip-Patch Antennas," *IEEE Antennas and Propagation Society Magazine*, Vol. 36, No. 6, 1994, pp. 52–55.

[39] Richards, W. F., S. E. Davidson, and S. A. Long, "Dual-Band Reactively Loaded Microstrip Antenna," *IEEE Trans. on Antennas and Propagation*, Vol. AP-33, 1985, pp. 556–560.

[40] Schaubert, D. H., et al., "Microstrip Antennas With Frequency Agility and Polarization Diversity," *IEEE Trans. on Antennas and Propagation*, Vol. AP-29, 1981, pp. 118–121.

[41] Schaubert, D. H., "A Review of Some Microstrip Antenna Characteristics," in *Microstrip Antennas: The Analysis and Design of Microstrip Antennas and Arrays*, D. M. Pozar and D. H. Schaubert (Eds.), IEEE Press, New York, 1995, pp. 59–67.

[42] Sengupta, D. L., "Resonant Frequency of a Tunable Rectangular Patch Antennas," *Electron. Lett.*, Vol. 20, 1984, pp. 614–615.

[43] Dahele, J. S., and K. F. Lee, "Theory and Experiment on Microstrip Antennas With Airgaps," *IEE Proc.*, Vol. 132, Pt. H, 1985, pp. 455–460.

[44] Zaid, L., et al., "Dual-Frequency and Broad-Band Antennas With Stacked Quarter Wavelength Elements," *IEEE Trans. on Antennas and Propagation*, Vol. AP-47, 1999, pp. 654–660.

5

Circular Disk and Ring Antennas

5.1 Introduction

Circular disk antennas offer performance similar to that of the rectangular geometries discussed in Chapter 4. The circular disk tends to be slightly smaller than the rectangular disk. In some applications, such as arrays, circular geometries offer certain advantages over other configurations. The circular disk can be easily modified to produce a range of impedance values, radiation patterns, and frequencies of operation. Various aspects of circular disk antennas are presented in this chapter. These include model-based analyses, design, and effects of various antenna parameters on input impedance, radiation pattern, radiation efficiency, polarization, and dielectric covers.

The circular disk antenna for circular polarization is analyzed in Chapter 8. Loaded disks for smaller size antennas are described in Chapter 10. Examples of the use of a circular disk for dual frequency and dual polarization are included in Chapter 10. The annular ring antenna, which is a variation of the circular disk antenna, is discussed in detail. Square ring antennas are described in Section 5.8. Circular sector and annular sectors are also discussed.

5.2 Analysis of a Circular Disk Microstrip Antenna

The circular microstrip disk antenna has been studied extensively [1–16]. Various methods of analysis have been applied to the circular disk antenna, including the cavity model [5, 6], mode matching with edge admittance [7–9], the generalized transmission line model [10–12], an integral equation approach [13–15], and FDTD [16]. The cavity model, mode matching with edge admit-

tance, and generalized transmission line model are discussed next. These models are applicable to thin substrates only because the variation of the field along the substrate thickness is assumed to be negligible. A very good review of models vis-à-vis numerical techniques with reference to a circular disk has been reported [17].

5.2.1 Cavity Model

The basic disk antenna geometry shown in Figure 5.1 comprises a thin, conducting circular disk on a dielectric substrate backed by a ground plane. Because $h << \lambda_0$, the fields do not vary along the z direction. Therefore, the electric field within the substrate has only a z component, and the magnetic field essentially has only ρ and ϕ components. The component of the current normal to the edge of the microstrip disk approaches zero at the edge. This implies that the tangential component of the magnetic field at the edge of the disk is vanishingly small. With these assumptions, the microstrip disk can be modeled as a cylindrical cavity, bounded at its top and bottom by electric walls and on its edge by a magnetic wall. Thus the fields within the dielectric region of the microstrip cavity, corresponding to TM_{nm} modes, can be determined by solving the wave equation for a cavity.

Fields and Currents

With no excitation current the wave equation for the electric field can be written as:

$$(\nabla^2 + k^2)\vec{E} = 0 \qquad k = 2\pi\sqrt{\epsilon_r}/\lambda_0 \tag{5.1}$$

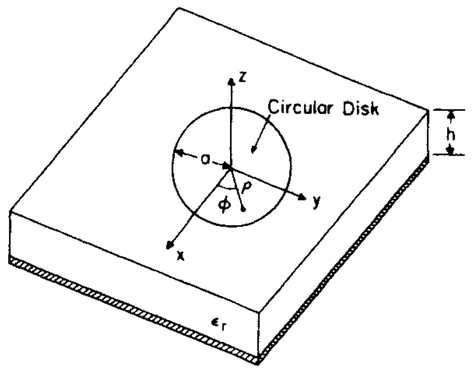

Figure 5.1 Configuration of a circular disk microstrip antenna.

The electric field in the cavity must satisfy the above wave equation and the magnetic wall boundary condition. The solution of the wave equation in cylindrical coordinates is

$$E_z = E_0 J_n(k\rho)\cos n\phi \tag{5.2}$$

where $J_n(k\rho)$ are Bessel functions of order n. Because $\vec{E}$ has only a z component and $\partial/\partial z = 0$, the magnetic field components become

$$H_\rho = \frac{j}{\omega\mu\rho}\frac{\partial E_z}{\partial \phi} = -\frac{jn}{\omega\mu\rho}E_0 J_n(k\rho)\sin n\phi \tag{5.3}$$

$$H_\phi = -\frac{j}{\omega\mu}\frac{\partial E_z}{\partial \rho} = -\frac{jk}{\omega\mu}E_0 J_n'(k\rho)\cos n\phi \tag{5.4}$$

where the prime sign denotes differentiation with respect to $k\rho$, the argument. The other field components are zero inside the cavity, that is,

$$E_\rho = E_\phi = H_z = 0 \tag{5.5}$$

The magnetic field boundary condition at the wall is defined as

$$H_\phi(\rho = a) = 0 \tag{5.6}$$

An alternative way of expressing the magnetic wall boundary condition is in terms of the electric surface current at the edge of the disk. The magnetic field inside the cavity gives rise to the induced electric current, and the currents on the inner surface of the circular disk can be calculated from

$$\vec{J} = -\hat{z} \times \vec{H} = \hat{\rho}H_\phi - \hat{\phi}H_\rho \tag{5.7}$$

where $\hat{\rho}$ and $\hat{\phi}$ are unit vectors in the ρ and ϕ directions, respectively. At the edge of the disk, the surface current J_ρ must vanish, that is,

$$J_\rho(\rho = a) = H_\phi(\rho = a) = 0 \tag{5.8}$$

where a is the radius of the disk. Therefore,

$$J_n'(ka) = 0 \tag{5.9}$$

Thus, for each mode configuration, a radius can be found that results in a resonance corresponding to the zeros of the derivative of the Bessel function.

For example, if χ_{nm} is the mth zero of $J_n'(ka)$, the resonance occurs when $ka = \chi_{nm}$, $n = 0, 1, 2, \ldots$, $m = 1, 2, 3, \ldots$. This relationship can be used to determine the radius of the disk for a given resonance frequency. Alternatively, for a fixed value of radius it will give the resonance frequency. A few of the lower order modes are listed in Table 5.1 in ascending order of χ_{nm} values. From the value of χ_{nm} for the various modes (see Table 5.1), one infers that the mode corresponding to $n = m = 1$ has the minimum radius or resonance frequency, and is known as the dominant mode. The field and surface current components for this mode can be found from (5.2)–(5.7). These are

$$E_z = E_0 J_1(k\rho)\cos\phi \tag{5.10}$$

$$H_\rho = -J_\phi = -\frac{j}{\omega\mu\rho} E_0 J_1(k\rho)\sin\phi \tag{5.11}$$

$$H_\phi = J_\rho = -\frac{jk}{\omega\mu} E_0 J_1'(k\rho)\cos\phi \tag{5.12}$$

The fields and surface currents for the various modes are shown in Figure 5.2 at resonance [18].

Radiation Fields

The radiation fields of a disk antenna can be derived either from the E_z field across the aperture between the disk and the ground plane at $\rho = a$ (using vector electric potential) or from the electric current on the surface of the disk conductor (employing vector magnetic potential). The electric surface current approach is described in Chapter 1. We use the aperture field approach here because of its simplicity. The magnetic current equivalent of the aperture electric field is given by

$$\vec{M} = \vec{E} \times \hat{\rho} = E_z\hat{\phi} = \hat{\phi}\sum_{n=0}^{\infty} E_n J_n(k\rho)\cos n\phi \qquad a \le \rho \le a + h \tag{5.13}$$

Table 5.1
Roots of $J_n'(ka) = 0$

Mode (n,m)	0,1	1,1	2,1	0,2	3,1	4,1	1,2
Root χ_{nm} or $k_{nm}a$	0	1.84118	3.05424	3.83171	4.20119	5.317	5.331

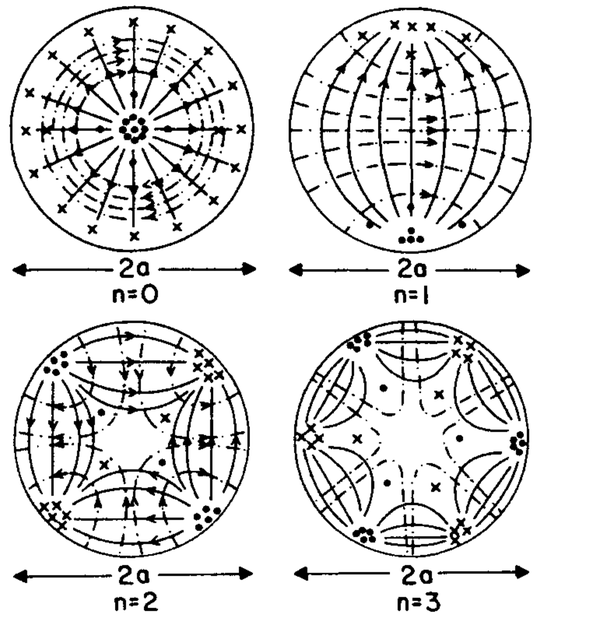

Figure 5.2 Fields and surface current patterns for various modes at resonance ($m = 1$). (From [1]. © 1969 *Electronics Letters*. Reprinted with permission.)

The useful radial extent of the magnetic current is assumed to be equal to the substrate thickness h because of the exponential decay of the electric field for $\rho > a$; see Section 2.1. The magnetic current distribution around the edge is illustrated in Figure 5.3 for some of the modes.

The vector electric potential can be calculated by integrating the equivalent magnetic current over the aperture, and the far field in spherical coordinates can then be found from this potential (see Section 1.5). From (1.37) in Chapter 1 we have

$$E_\theta = \frac{-jk_0}{4\pi}\frac{e^{-jk_0 r}}{r}\int_0^{2\pi}\int_\rho M_\phi(\rho, \phi')\cos(\phi' - \phi) \exp[jk_0\rho\sin\theta\cos(\phi' - \phi)]\,\rho\,d\rho\,d\phi' \tag{5.14a}$$

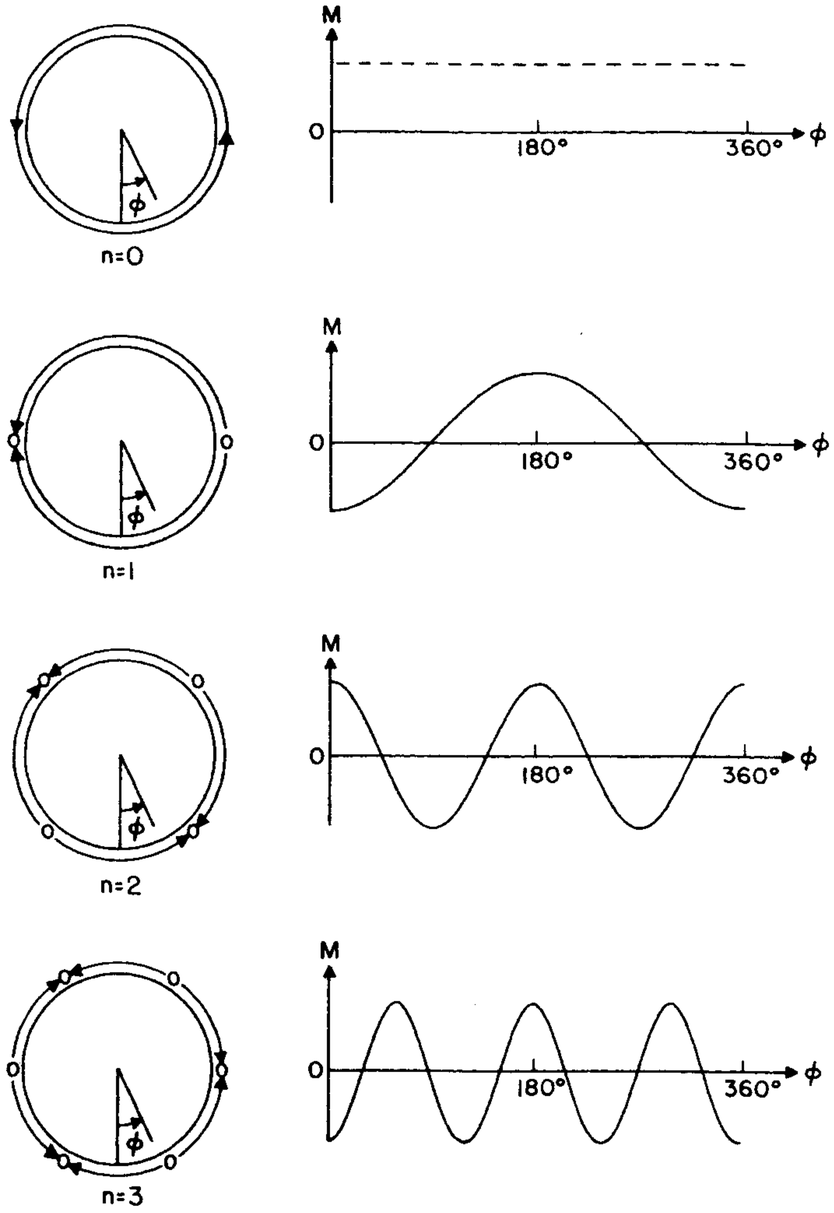

Figure 5.3 Magnetic current distribution around the edge of the disk for the nth mode. (From [18]. © 1980 Artech House. Reprinted with permission.)

$$E_\phi = \frac{-jk_0}{4\pi}\frac{e^{-jk_0 r}}{r}\cos\theta \int_0^{2\pi}\int_\rho M_\phi(\rho, \phi')\sin(\phi' - \phi)$$
$$\exp[jk_0\rho\sin\theta\cos(\phi' - \phi)]\,\rho d\rho d\phi' \tag{5.14b}$$

Using the resonance approximation in which only one mode contributes in general at a given frequency, we obtain the following expression for the radiation fields

$$E_\theta = \frac{-jk_0}{4\pi}\frac{e^{-jk_0 r}}{r}E_n \int_0^{2\pi}\int_a^{a+h} J_n(\chi_{nm}\rho/a)\cos n\phi'\cos(\phi' - \phi)$$
$$\exp[jk_0\rho\sin\theta\cos(\phi' - \phi)]\,\rho d\rho d\phi' \tag{5.15}$$

A similar expression for the E_ϕ component can be determined.

The exact behavior of E_z across the substrate thickness is not known, but for $h/\lambda_0 << 1$, it can be considered constant to a first-order approximation. The corresponding magnetic current is also constant along the radial direction. The integration over ρ in (5.15) is simple and results in

$$E_\theta = \frac{-jk_0}{4\pi}\frac{e^{-jk_0 r}}{r}ahE_nJ_n(\chi_{nm})\int_0^{2\pi}\cos n\phi'\cos(\phi' - \phi)$$
$$\exp[jk_0 a\sin\theta\cos(\phi' - \phi)]\,d\phi' \tag{5.16}$$

Using the following standard integration

$$\int_0^{2\pi}\cos n\phi'\cos(\phi - \phi')\exp[jk_0 a\sin\theta\cos(\phi - \phi')]\,d\phi'$$
$$= -2\pi(j)^{n+1}\cos n\phi J_n'(k_0 a\sin\theta)$$

we obtain

$$E_\theta = -j^n\frac{Vak_0}{2}\frac{e^{-jk_0 r}}{r}\cos n\phi J_n'(k_0 a\sin\theta) \tag{5.17}$$

where $V = hE_nJ_n(\chi_{nm})$ and is known as the edge voltage at $\phi = 0$. Similarly, the integration over ϕ' for E_ϕ requires the following standard integration

$$\int_0^{2\pi} \cos n\phi' \sin(\phi - \phi') \exp[jk_0 a \sin\theta \cos(\phi - \phi')]\, d\phi'$$

$$= 2\pi n (j)^{n+1} \sin n\phi \frac{J_n(k_0 a \sin\theta)}{k_0 a \sin\theta}$$

One obtains

$$E_\phi = nj^n \frac{Vak_0}{2} \frac{e^{-jk_0 r}}{r} \sin n\phi \frac{J_n(k_0 a \sin\theta)}{k_0 a \sin\theta} \cos\theta \tag{5.18}$$

The above radiation field expressions do not include the effect of substrate and the ground plane. Suitable correction factors are included to account for these effects. As discussed in Section 4.3, the E-plane radiation fields should be multiplied by $F_3(\theta)$, and the H-plane fields by $F_4(\theta)$, that is,

$$E_\theta = -j^n \frac{Vak_0}{2} \frac{e^{-jk_0 r}}{r} \cos n\phi J_n'(k_0 a \sin\theta) \cdot F_3(\theta) \tag{5.19}$$

$$E_\phi = nj^n \frac{Vak_0}{2} \frac{e^{-jk_0 r}}{r} \sin n\phi \frac{J_n(k_0 a \sin\theta)}{k_0 a \sin\theta} \cos\theta \cdot F_4(\theta) \tag{5.20}$$

The simplest approximation to $F_3(\theta)$ and $F_4(\theta)$ is a multiplication factor of 2.

Resonant Frequency

The resonant frequency of a disk antenna for the TM_{nm} mode can be evaluated from the basic relation $\chi_{nm} = ka$ and k defined in (5.1). Thus,

$$f_{nm} = \frac{\chi_{nm} c}{2\pi a_e \sqrt{\epsilon_r}} \tag{5.21}$$

where χ_{nm} is the mth zero of $J_n'(ka)$ and c is the velocity of light in free space. An effective radius a_e has been introduced in (5.21) to account for the fringe fields along the edge of the resonator. For the TM_{11} mode of the disk, it has been suggested that [2, 6]

$$a_e = a\left\{1 + \frac{2h}{\pi a \epsilon_r}\left(\ln\frac{\pi a}{2h} + 1.7726\right)\right\}^{1/2} \tag{5.22}$$

This expression predicts the radius with an error of less than 2.5% for $a/h >> 1$. Equation (5.22) is used as a design guide for determining the radius of the disk. A number of modifications of (5.22) have been suggested. For thick substrates, one may use (5.71).

Fields Excited by the Feed Source

Consider a circular disk of radius a being excited by a coaxial feed located at (ρ_0, π). As shown in Figure 5.4, such a feed can be modeled by a uniform current ribbon of effective angular width 2Δ centered about the feed axis at $\phi_0 = \pi$, that is,

$$\vec{J} = \hat{z} J_z(\phi_0) \frac{\delta(\rho - \rho_0)}{\rho_0} \tag{5.23}$$

where

$$J_z(\phi_0) = \begin{cases} I & \pi - \Delta < \phi_0 < \pi + \Delta \\ 0 & \text{elsewhere} \end{cases} \tag{5.24}$$

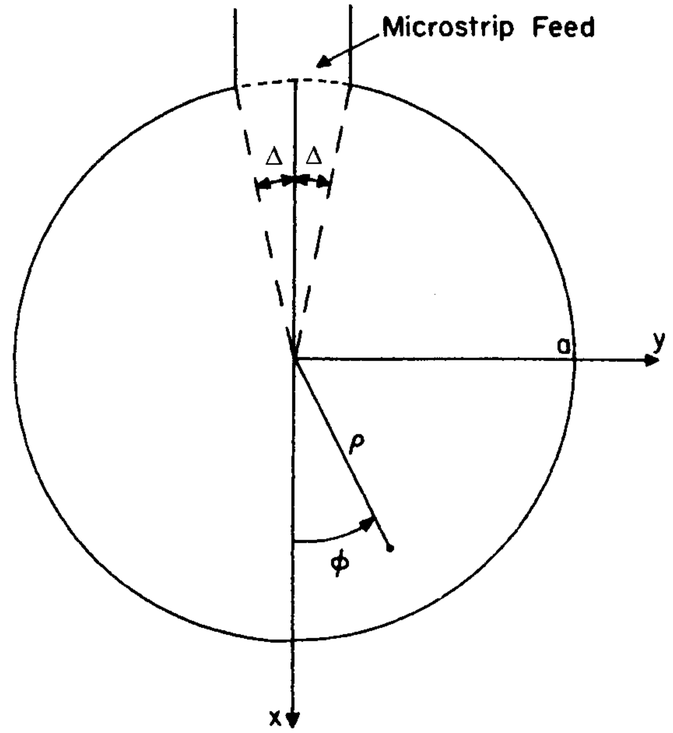

Figure 5.4 Configuration of a microstrip disk antenna with a feed at $\phi = \pi$. (From [18]. © 1980 Artech House. Reprinted with permission.)

The wave equation in the presence of a current source $\vec{J}$ is

$$\nabla^2\vec{E} + k^2\vec{E} = j\omega\mu_0\vec{J} - \frac{\nabla(\nabla\cdot\vec{J})}{j\omega\epsilon}, \quad \epsilon = \epsilon_0\epsilon_r \tag{5.25}$$

As before, $\vec{J}$ and $\vec{E}$ are assumed to have z components only and no z variation. This implies that

$$\nabla\cdot\vec{J} = \frac{\partial J_z}{\partial z} = 0 \tag{5.26}$$

Thus, (5.25) becomes

$$\nabla^2 E_z + k^2 E_z = j\omega\mu_0\vec{J}\cdot\hat{z} = j\omega\mu_0 J_z \tag{5.27}$$

To solve the above equation, we expand E_z in terms of the eigenfunctions of the cavity, that is,

$$E_z = \sum_n\sum_m A_{nm}\psi_{nm}(\rho, \phi) \tag{5.28}$$

where ψ_{nm} satisfy the wave equation and boundary condition

$$(\nabla^2 + k_{nm}^2)\psi_{nm} = 0 \tag{5.29}$$

$$\left.\frac{\partial\psi_{nm}}{\partial\rho}\right|_{\rho=a} = 0 \tag{5.30}$$

The solutions are

$$\psi_{nm} = J_n(k_{nm}\rho)\cos n\phi \quad n = 0, 1, 2, \ldots, \quad m = 1, 2, 3, \ldots \tag{5.31}$$

The mode coefficients A_{nm} of (5.28) are determined by substituting (5.28) into (5.27) and making use of the orthogonality properties of ψ_{nm}. One obtains

$$A_{nm} = \frac{\iint\psi_{nm}^*(j\omega\mu_0 J_z)ds}{(k^2 - k_{nm}^2)\iint\psi_{nm}^*\psi_{nm}ds} \tag{5.32}$$

where the integration is carried over the area enclosed by the magnetic wall of the cavity. One obtains

$$A_{01} = j\omega\mu_0 I\frac{2\Delta}{\pi a^2 k^2} \quad n = 0, \quad m = 1 \tag{5.33a}$$

$$A_{0m} = j\omega\mu_0 I\frac{2\Delta J_0(k_{0m}\rho_0)}{\pi a^2 J_0^2(k_{0m}a)(k^2 - k_{0m}^2)} \quad m \geq 2, \quad n = 0 \tag{5.33b}$$

$$A_{nm} = j\omega\mu_0 I\frac{(-1)^n 4\sin(n\Delta)J_n(k_{nm}\rho_0)k_{nm}^2}{n\pi(k^2 - k_{nm}^2)(k_{nm}^2 a^2 - n^2)J_n^2(k_{nm}a)} \quad n \geq 1 \tag{5.33c}$$

where $k_{nm}a$ is listed in Table 5.1. From (5.28) and (5.33) the expression for the electric field can be written as

$$E_z = j\omega\mu_0 I\left\{\frac{2\Delta}{\pi a^2 k^2} + \sum_{m=2}^{\infty}\frac{2\Delta J_0(k_{0m}\rho_0)J_0(k_{0m}\rho)}{\pi a^2 J_0^2(k_{0m}a)(k^2 - k_{0m}^2)} + \sum_{n=1}^{\infty}\sum_{m=1}^{\infty}\frac{(-1)^n 4\sin(n\Delta)J_n(k_{nm}\rho_0)J_n(k_{nm}\rho)k_{nm}^2\cos n\phi}{n\pi(k^2 - k_{nm}^2)(k_{nm}^2 a^2 - n^2)J_n^2(k_{nm}a)}\right\} \tag{5.34}$$

Input Impedance

Input impedance of the disk antenna can be defined as

$$Z_{\text{in}} = V_{\text{in}}/I_0 \tag{5.35}$$

where V_{in} is the RF voltage at the feed point, and is calculated from the average electric field, that is,

$$V_{\text{in}} = -E_{\text{av}}h \tag{5.36}$$

$$E_{\text{av}} = \frac{1}{2\Delta}\int_{\pi-\Delta}^{\pi+\Delta} E_z(\rho_0, \phi)d\phi \tag{5.37}$$

$$E_{\text{av}} = \frac{1}{2\Delta}\sum_n\sum_m A_{nm}J_{nm}(k_{nm}\rho_0)\int_{\pi-\Delta}^{\pi+\Delta}\cos n\phi\, d\phi \tag{5.38}$$

or

$$V_{\text{in}} = (-1)^{n+1} h \frac{\sin n\Delta}{n\Delta} \sum_n \sum_m A_{nm} J_{nm}(k_{nm}\rho_0) \tag{5.39}$$

The feed current is

$$I_0 = 2I\Delta \tag{5.40}$$

The input impedance, therefore, becomes

$$Z_{\text{in}} = \sum_n^0 \sum_m^1 A_{nm} J_{nm}(k_{nm}\rho_0)(-1)^{n+1} \frac{\sin n\Delta}{n\Delta} \frac{h}{2I\Delta} \tag{5.41}$$

or

$$Z_{\text{in}} = -j\omega\mu_0 h \left\{ \frac{1}{\pi a^2 k^2} + \sum_{m=2}^{\infty} \frac{J_0^2(k_{0m}\rho_0)}{\pi a^2 J_0^2(k_{0m}a)(k^2 - k_{0m}^2)} \right. \tag{5.42}$$

$$\left. + \frac{2}{\pi} \sum_{n=1}^{\infty} \sum_{m=1}^{\infty} \left(\frac{\sin n\Delta}{n\Delta} \right)^2 \frac{J_n^2(k_{nm}\rho_0)}{J_n^2(k_{nm}a)} \frac{k_{nm}^2}{(k^2 - k_{nm}^2)(k_{nm}^2 a^2 - n^2)} \right\}$$

The value of Z_{in}, as calculated from (5.42), will be purely reactive if the structure is lossless. In the cavity model, the effect of various losses in the form of dielectric loss, conductor loss, and radiation loss is included by lumping all of these losses in the loss tangent of the dielectric. For this an effective loss tangent is defined as

$$\delta_{\text{eff}} = 1/Q_T \tag{5.43}$$

As a result of this modeling, the term k^2 in (5.42) for $n \geq 1$ terms is replaced by $k^2(1 - j\delta_{\text{eff}})$, and k^2 for $n = 0$ terms is replaced by $k^2(1 - j\delta)$, where δ is the loss tangent of the substrate used. The differentiation between the $n = 0$ and $n \geq 1$ modes arises because $n \geq 1$ modes are normally used for radiation. Therefore, (5.42) is modified to

$$Z_{\text{in}} = -j\omega\mu_0 h \left\{ \frac{1}{\pi a^2 k^2 (1 - j\delta)} + \sum_{m=2}^{\infty} \frac{J_0^2(k_{0m}\rho_0)}{\pi a^2 J_0^2(k_{0m}a)\{k^2(1 - j\delta) - k_{0m}^2\}} \right.$$

$$\left. + \frac{2}{\pi} \sum_{n=1}^{\infty} \sum_{m=1}^{\infty} \left(\frac{\sin n\Delta}{n\Delta} \right)^2 \frac{J_n^2(k_{nm}\rho_0)}{J_n^2(k_{nm}a)} \frac{k_{nm}^2}{\{k^2(1 - j\delta_{\text{eff}}) - k_{nm}^2\}(k_{nm}^2 a^2 - n^2)} \right\} \tag{5.44a}$$

An expression for δ_{eff} was obtained in Chapter 2, (2.31). Equation (5.44a) is identical to that obtained in [19]. The above analysis can be generalized for an arbitrary feed point (ρ_0, ϕ_0) as well as for a microstrip feed. For a probe feed located at (ρ_0, ϕ_0), (5.44a) becomes

$$Z_{\text{in}} = -j\omega\mu_0 h \left\{ \frac{1}{\pi a^2 k^2 (1 - j\delta)} + \sum_{m=2}^{\infty} \frac{J_0^2(k_{0m}\rho_0)}{\pi a^2 J_0^2(k_{0m}a)\{k^2(1 - j\delta) - k_{0m}^2\}} \right.$$

$$\left. + \frac{2}{\pi} \sum_{n=1}^{\infty} \sum_{m=1}^{\infty} \left(\frac{\sin n\Delta}{n\Delta} \right)^2 \frac{J_n^2(k_{nm}\rho_0)}{J_n^2(k_{nm}a)} \frac{k_{nm}^2 \cos^2 n\phi_0}{\{k^2(1 - j\delta_{\text{eff}}) - k_{nm}^2\}(k_{nm}^2 a^2 - n^2)} \right\} \tag{5.44b}$$

However, when measurements are carried out for the input impedance on a circular disk antenna, the measured value corresponds to $\phi_0 = 0$ because there is no preferred axis in the circular geometry, in comparison to the rectangular geometry. Therefore, the measured input resistance is always maximum for an edge-fed antenna unless designed otherwise (see Section 5.3.5).

The input impedance behavior of a circular microstrip disk antenna has been studied by a number of authors. Comparison between the computed and measured input impedance of a coaxially fed circular disk as a function of frequency for three different radial feed locations is shown in Figure 5.5 for the TM_{11} mode [20]. The VSWR = 2 circle is also shown in this figure. The agreement is found to be good. It is seen that the locus of input impedance with frequency traces a circle on the Smith chart. The center of this circle lies in the upper half of the chart. However, the impedance locus for a resonant circuit should be a symmetrical circle about the $X = 0$ axis. The shift of the center of the circle is due to the series feed inductance, which can be read from the Smith chart. Further, the impedance circles for different feed locations are seen to have different shifts from the $X = 0$ axis, meaning that the feed inductance is a function of the feed location. It is also observed from this figure that the input resistance at resonance increases when fed nearer to the edge of the disk. It means that it is possible to achieve a 50Ω resistance by selecting a proper feed location. To determine this position accurately, the variation of input resistance is plotted as a function of radial feed location. This is shown in Figure 5.6 [20]. The effect of substrate thickness on the input impedance is shown in Figure 5.7 [21].

5.2.2 Mode Matching With Edge Admittance

The geometry of a circular microstrip disk fed by a probe at $\rho = \rho_0$ is shown in Figure 5.8. In the mode matching with edge admittance approach [7], the

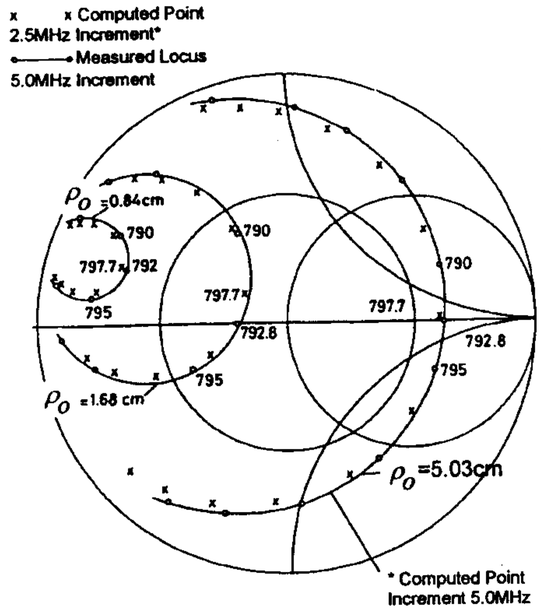

Figure 5.5 Computed and measured input impedance for the TM_{11} mode of a circular disk antenna (a = 6.7 cm, h = 0.159 cm, ϵ_r = 2.62). (From [20]. © 1981 IEEE. Reprinted with permission.)

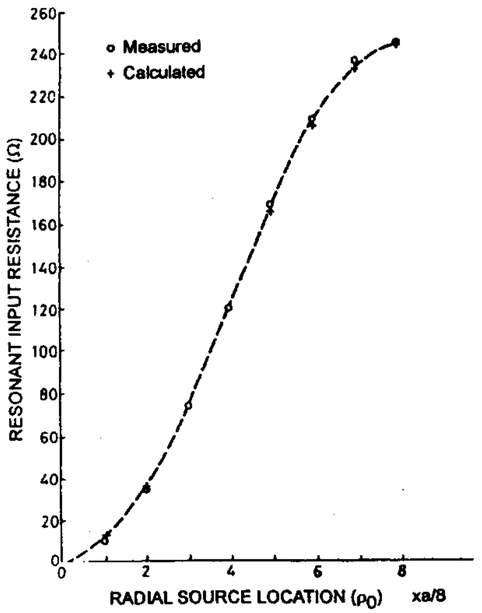

Figure 5.6 Variation of input resistance R_{in} with feed location for the TM_{11} mode of a circular disk antenna (a = 6.7 cm, h = 0.159 cm, ϵ_r = 2.62). (From [20]. © 1981 IEEE. Reprinted with permission.)

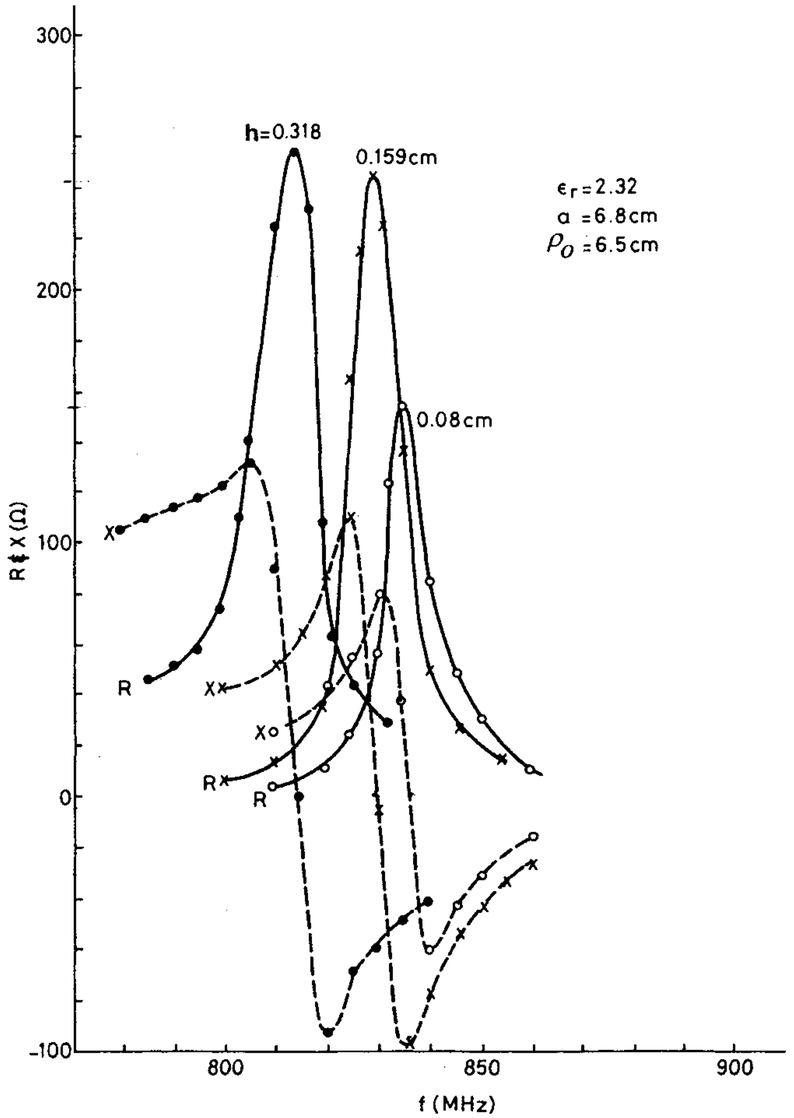

Figure 5.7 Measured input impedance as a function of frequency for the TM_{11} mode of a circular disk antenna (a = 6.8 cm, ρ_0 = 6.5 cm, ϵ_r = 2.32). (From [21]. © 1983 IEEE. Reprinted with permission.)

disk is divided into two regions about the probe position. The total fields due to the constant probe current I_p follow (with time variation as $e^{j\omega t}$). In region I ($\rho < \rho_0$),

$$E_z = \sum_{n=0}^{\infty} A_n J_n(k\rho)\cos n\phi \tag{5.45a}$$

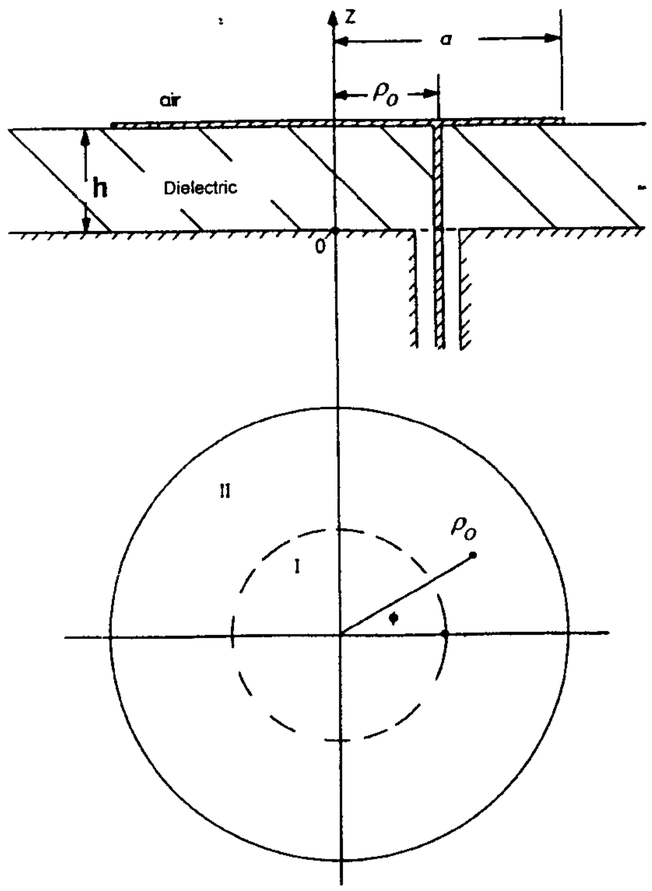

Figure 5.8 Circular disk microstrip antenna with coaxial feed at $\rho = \rho_0$. (From [7]. © 1979 IEE. Reprinted with permission.)

$$H_\rho = \frac{1}{j\omega\mu_0\rho}\sum_{n=0}^{\infty} nA_nJ_n(k\rho)\sin n\phi \tag{5.45b}$$

$$H_\phi = \frac{k}{j\omega\mu_0}\sum_{n=0}^{\infty} A_nJ_n'(k\rho)\cos n\phi \tag{5.45c}$$

and, in region II ($\rho > \rho_0$),

$$E_z = \sum_{n=0}^{\infty}[B_nJ_n(k\rho) + C_nY_n(k\rho)]\cos n\phi \tag{5.46a}$$

$$H_\rho = \frac{1}{j\omega\mu_0\rho}\sum_{n=0}^{\infty} n[B_nJ_n(k\rho) + C_nY_n(k\rho)]\sin n\phi \tag{5.46b}$$

$$H_\phi = \frac{k}{j\omega\mu_0}\sum_{n=0}^{\infty}[B_nJ_n'(k\rho) + C_nY_n'(k\rho)]\cos n\phi \tag{5.46c}$$

The constants A_n, B_n, and C_n are determined from mode-matching conditions at $\rho = \rho_0$ as follows:

(a) E_z and H_ρ are continuous at $\rho = \rho_0$, that is,

$$A_nJ_n(k\rho_0) = B_nJ_n(k\rho_0) + C_nY_n(k\rho_0) \tag{5.47}$$

(b) H_ϕ is discontinuous at $\rho = \rho_0$ due to the excitation current, that is,

$$\frac{k}{j\omega\mu_0}\sum_{n=0}^{\infty}[B_nJ_n'(k\rho_0) + C_nY_n'(k\rho_0) - A_nJ_n'(k\rho_0)]\cos n\phi = I_s \tag{5.48}$$

where I_s is the z-directed feed current at $\rho = \rho_0$. For a thin probe with constant current I_p and located at (ρ_0, ϕ), the expression for I_s is

$$I_s = I_p\delta(\phi)/\rho_0 \tag{5.49}$$

Substituting (5.49) in (5.48), we obtain

$$\frac{k}{j\omega\mu_0}\sum_{n=0}^{\infty}[B_nJ_n'(k\rho_0) + C_nY_n'(k\rho_0) - A_nJ_n'(k\rho_0)]\cos n\phi = I_p\delta(\phi)/\rho_0 \tag{5.50}$$

We now expand the right-hand side of (5.50) in a Fourier cosine series. This yields

$$\frac{k}{j\omega\mu_0}[B_nJ_n'(k\rho_0) + C_nY_n'(k\rho_0) - A_nJ_n'(k\rho_0)](1 + \epsilon_n)\pi = I_p/\rho_0 \tag{5.51}$$

where $\epsilon_0 = 1$, and $\epsilon_n = 0$ for $n > 0$.

(c) The admittance boundary condition at $\rho = a$ is satisfied through

$$H_{\phi n}(a, \phi) = -y_{sn}E_{zn}(a, \phi)$$

or

$$\frac{k}{j\omega\mu_0}[B_nJ_n'(ka) + C_nY_n'(ka)] = -y_{sn}[B_nJ_n(ka) + C_nY_n(ka)] \tag{5.52}$$

Here y_{sn} is the boundary admittance and the negative sign on the right-hand side is used to make the real part of y_{sn} positive [7].

Constants A_n, B_n, and C_n of (5.45) and (5.46) are obtained by solving (5.47), (5.51), and (5.52). One obtains

$$A_n = \frac{-j\omega\mu_0 I_p}{2(1+\epsilon_n)}\frac{1}{D_n}\{J_n(k\rho_0)[Y_n'(ka) + j\eta_1 y_{sn}Y_n(ka)] - D_nY_n(k\rho_0)\} \tag{5.53a}$$

$$B_n = \frac{-j\omega\mu_0 I_p}{2(1+\epsilon_n)}\frac{1}{D_n}\{J_n(k\rho_0)[Y_n'(ka) + j\eta_1 y_{sn}Y_n(ka)]\} \tag{5.53b}$$

$$C_n = \frac{j\omega\mu_0 I_p}{2(1+\epsilon_n)}J_n(k\rho_0) \tag{5.53c}$$

where

$$D_n = J_n'(ka) + j\eta_1 y_{sn}J_n(ka) \quad \eta_1 = 120\pi/\sqrt{\epsilon_r}$$

Boundary Admittance

The boundary admittance $y_{sn} = g_{sn} + jb_{sn}$ for the nth mode is related to the power flow through the cylindrical surface of the disk at $\rho = a$. It is given by [8]

$$\frac{1}{2}\int_0^{2\pi}\int_0^h y_{sn}|E_{zn}|^2 dz\,ad\phi = P_r - 2j\omega W_f \tag{5.54a}$$

or

$$\frac{1}{2}\int_0^{2\pi}\int_0^h g_{sn}|E_{zn}|^2 dz\,ad\phi = P_r \tag{5.54b}$$

where P_r is the power radiated, and W_f is the energy stored in the fringing field. P_r is obtained by integrating the Poynting vector over a large hemisphere. From (5.19) and (5.20), the following relation is obtained [8]:

$$g_{sn} = \begin{cases} \dfrac{1}{k_0ak_0h\eta_0}\displaystyle\int_0^{\pi/2}(I_1^2 + I_2^2)\sin\theta d\theta & \text{for } n = 1 \\ 0 & \text{for } n \neq 1 \end{cases} \tag{5.55}$$

where

$$I_1 = \frac{k_0a\sin(k_0h\cos\theta)}{\cos\theta}J_1'(k_0a\sin\theta)$$

$$I_2 = \frac{\sin(k_0h\cos\theta)}{\sin\theta}J_1(k_0a\sin\theta)$$

The quantity W_f is difficult to determine accurately. However, the susceptance b_{sn} can be obtained from the effective radius of the disk. It is given by [7]

$$b_{sn} = \sqrt{\epsilon_r}\frac{J_n'(w)}{\eta_0 J_n(w)} \tag{5.56}$$

where $w = ka_e$ and $\eta_0 = 120\pi\Omega$.

Input Impedance

The input impedance for the disk antenna may be defined as follows:

$$Z_{\text{in}} = \frac{\frac{1}{2}VV^*}{P_T + 2j\omega(W_e - W_m)} \tag{5.57}$$

where

$$V = -\int_0^h E_z dz$$

and $P_T = P_r + P_c + P_d$. Each of these quantities has been defined in Chapter 2. Assuming that the $n = 1$ mode is dominant, the above quantities can be obtained in closed forms as

$$V = -A_1hJ_1(k\rho_0) \tag{5.58}$$

From (5.54b),

$$P_r = \frac{1}{2}\pi ah|B_1J_1(ka) + C_1Y_1(ka)|^2 g_{s1}$$

The conductor loss and the time-averaged stored magnetic energy are related by (2.36)

$$P_c = \frac{2\omega W_m}{h\sqrt{\pi f\mu_0\sigma}} \tag{5.59}$$

The dielectric loss and time-averaged stored electric energy are related by (2.35)

$$P_d = 2\omega W_e \tan\delta \tag{5.60}$$

where

$$W_e = \frac{\pi\epsilon_0\epsilon_r h}{8k^2}\{|A_1|^2[x^2(J_1^2 - J_0J_2)]_0^k\rho_0 + |B_1|^2[x^2(J_1^2 - J_0J_2)]_k^{ka}\rho_0$$
$$+ |C_1|^2[x^2(Y_1^2 - Y_0Y_2)]_k^{ka}\rho_0$$
$$+ \frac{1}{2}(B_1C_1^* + B_1^*C_1)[x^2(2J_1Y_1 - J_0Y_2 - J_2Y_0)]_k^{ka}\rho_0\}$$

$$W_m = \frac{\pi\epsilon_0\epsilon_r h}{8k^2}\{|A_1|^2[x^2(J_0^2 + J_1^2) - 2J_1^2]_0^k\rho_0 + |B_1|^2[x^2(J_0^2 + J_1^2) - 2J_1^2]_k^{ka}\rho_0$$
$$+ |C_1|^2[x^2(Y_0^2 + Y_1^2) - 2Y_1^2]_k^{ka}\rho_0$$
$$+ \frac{1}{2}(B_1C_1^* + B_1^*C_1)[x^2(J_0Y_0 + J_1Y_1 + J_2Y_2 - \frac{1}{2}J_1Y_3 - \frac{1}{2}J_3Y_1)]_k^{ka}\rho_0\}$$

in which $[f]_B^A$ means $f(A) - f(B)$, σ is the conductivity of the disk metalization, and $\tan\delta$ is the loss tangent of the substrate.

Shen [7] has compared theoretical results with the measurements for the input impedance. The agreement is found to be good except that the theoretical values of input resistance are lower than the measured values. This is due to the use of radiation conductance only and does not include the effect of substrate loss. Usefulness of this approach has been improved by Bhattacharyya

[9] by including the effect of substrate parameters and the contribution of equivalent electric current in the aperture surface.

5.2.3 Generalized Transmission Line Model for a Circular Disk

The generalized transmission line model has been used to analyze a circular disk antenna [10–12]. The details of the analysis are similar to those given in [11] for the annular ring antenna and are included in Appendix 2A. In this model, the interior region of the disk is modeled in the form of two sections of (nonuniform) radial transmission line. The transmission line equivalent circuit of the disk is shown in Figure 5.9(a). In this figure the region $\rho > \rho_0$ is represented by a section of radial line. The end $\rho = a$ of this line is loaded by an admittance due to the circularly cylindrical radiating aperture of radius a. The other end is connected to the excitation source. The region $\rho < \rho_0$ of the disk is described by another section of radial line. The end at $\rho = 0$ is shorted because the electric field is zero here.

The analysis of the disk is carried out for the TM_n mode, the transmission line mode with single index. Here n stands for the angular eigenvalue. In the cavity model of the disk antenna, the field is described by double index TM_{nm} modes, the index m being associated with the eigenvalue of the radial function. The single index transmission line mode is equivalent to the sum of double index cavity modes, summed over the second index, that is, $TM_n = \sum_m TM_{nm}$. Thus, the analysis for the TM_n mode takes into account the effect of all cavity modes TM_{nm} with $m = 1, 2, 3, \ldots$. The characteristics of the antenna for a particular cavity mode can be obtained by evaluating the characteristics of the transmission line mode in the neighborhood of the cavity mode's resonant frequency.

The transmission line being in the ρ direction, the modal voltage and current for the TM_n mode defined in Appendix 2A are given as

$$V = E_{zn}(\rho, \phi) \tag{5.61}$$

$$I_n = \begin{cases} +\rho H_{\phi n} & \text{for } \rho < \rho_0 \\ -\rho H_{\phi n} & \text{for } \rho > \rho_0 \end{cases} \tag{5.62}$$

The fields in the two regions $\rho < \rho_0$ and $\rho > \rho_0$ are expressed as in (5.45) and (5.46). The boundary conditions at $\rho = \rho_0$ are also the same, (5.47) and (5.51). However, by virtue of the definitions of modal voltage and modal current given above, the boundary condition at $\rho = a$, in this model, is defined as

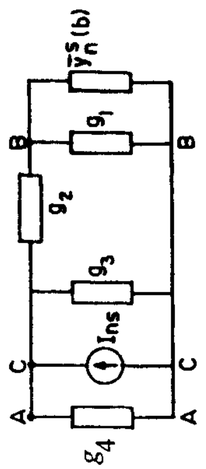

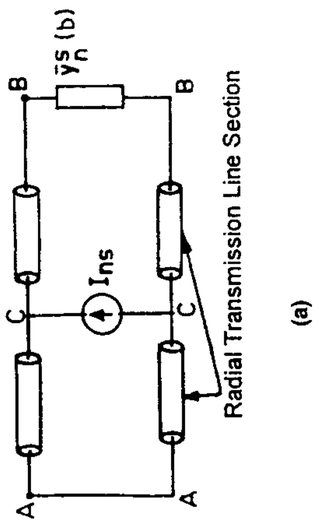

Figure 5.9 (a) Transmission line equivalent circuit of the circular disk antenna. (b) Equivalent circuit of part (a) when transmission line sections are replaced by their π-section equivalents.

$$aH_{\phi n}(a, \phi) = -y_{sn}E_{zn}(a, \phi) \tag{5.63}$$

The expression for y_{sn} is the same as described earlier in Section 5.2.2.

Next, the transmission line sections representing the two regions are replaced by their equivalent π networks, the transmission lines being nonuniform. The equivalent circuit for the transmission line model then becomes as shown in Figure 5.9(b). Network theory is now used to determine g_1, g_2, g_3, and g_4 in terms of the field quantities. For example,

$$g_2 = -Y_{12} = \left.\frac{-aH_{\phi n}(a, \phi)}{E_{zn}(\rho_0, \phi)}\right|_{E_{zn}(a,\phi)=0} = \frac{2}{\pi}\frac{1}{j\omega\mu_0\{J_n(k\rho_0)Y_n(ka) - Y_n(k\rho_0)J_n(ka)\}} \tag{5.64}$$

$$g_4 = \frac{\rho_0 H_{\phi n}(\rho_0, \phi)}{E_{zn}(\rho_0, \phi)} = \frac{k\rho_0}{j\omega\mu_0}\frac{J_n'(k\rho_0)}{J_n(k\rho_0)} \tag{5.65}$$

The input impedance of the disk antenna is defined in Appendix 2A and is given as

$$Z_{\text{in}} = -\sum_{n=0}^{\infty}\frac{hE_{zn}(\rho_0, 0)}{I_p} = \sum_{n=0}^{\infty}\frac{hE_{zn}(\rho_0, 0)}{\pi(1 + \epsilon_n)I_{ns}} \tag{5.66}$$

with

$$\frac{E_{zn}}{I_{ns}} = \left\{\frac{(y_{sn} + g_1)g_2}{y_{sn} + g_1 + g_2} + g_3 + g_4\right\}^{-1} \tag{5.67}$$

where $\epsilon_0 = 1$ and $\epsilon_n = 1$ for $n > 0$.

Input impedance plot of a circular disk antenna is given in [9, 12].

5.3 Design Considerations for Circular Disk Antennas

5.3.1 Substrate Selection and Disk Radius

The considerations for the choice of substrate for the circular disk antenna are the same as those for the rectangular disk discussed in Section 4.3.1. The

substrate used should have low dielectric constant for higher radiation efficiency, and a thicker substrate increases the impedance bandwidth.

The disk metalization radius a is determined by the resonance condition (5.9), that is, $J_n'(k_0 a\sqrt{\epsilon_r}) = 0$. For the lowest order mode, $n = 1$ and the first root of $J_1'(\cdot)$ occurs at 1.841. Thus,

$$k_0 a\sqrt{\epsilon_r} = 1.841 \tag{5.68a}$$

or

$$a = \frac{1.841}{k_0\sqrt{\epsilon_r}} \tag{5.68b}$$

Due to the fringing fields at the periphery of the disk conductor, a disk with physical radius a has an effective radius a_e such that $a_e > a$. Therefore, (5.68b) should be modified as

$$a_e = \frac{1.841}{k_0\sqrt{\epsilon_r}} \tag{5.69}$$

The semiempirical relationship between a_e and a is given by (5.22). The effective radius can also be estimated from the disk capacitance given by [22]

$$C = \frac{\pi a^2 \epsilon_0 \epsilon_r}{h}\left[1 + \frac{2h}{\pi a \epsilon_r}\left\{\ln\left(\frac{a}{2h}\right) + (1.41\epsilon_r + 1.77) + \frac{h}{a}(0.268\epsilon_r + 1.65)\right\}\right] \tag{5.70}$$

This formula gives

$$a_e = a\left[1 + \frac{2h}{\pi a \epsilon_r}\left\{\ln\left(\frac{a}{2h}\right) + (1.41\epsilon_r + 1.77) + \frac{h}{a}(0.268\epsilon_r + 1.65)\right\}\right]^{1/2} \tag{5.71}$$

For the design of the antenna, the desired value of a_e at the operating frequency f_r is first obtained from (5.69), that is,

$$a_e = \frac{1.841}{k_0\sqrt{\epsilon_r}} = \frac{8.794}{f_r\sqrt{\epsilon_r}}\text{cm} \qquad (f_r \text{ in GHz}) \tag{5.72}$$

The relationship of (5.71) between a and a_e is now used to obtain the required value of a for a given h, ϵ_r, and f_r. This calculation needs a few iterations. The starting value for the iteration can be chosen as that given by (5.72). The disk radius a as a function of resonant frequency for two values of ϵ_r and three different values of h is plotted in Figure 5.10 [18]. Note that the effect of substrate thickness is insignificant for frequencies of less than 2 GHz. The disk size for the higher order modes can be determined in a similar manner.

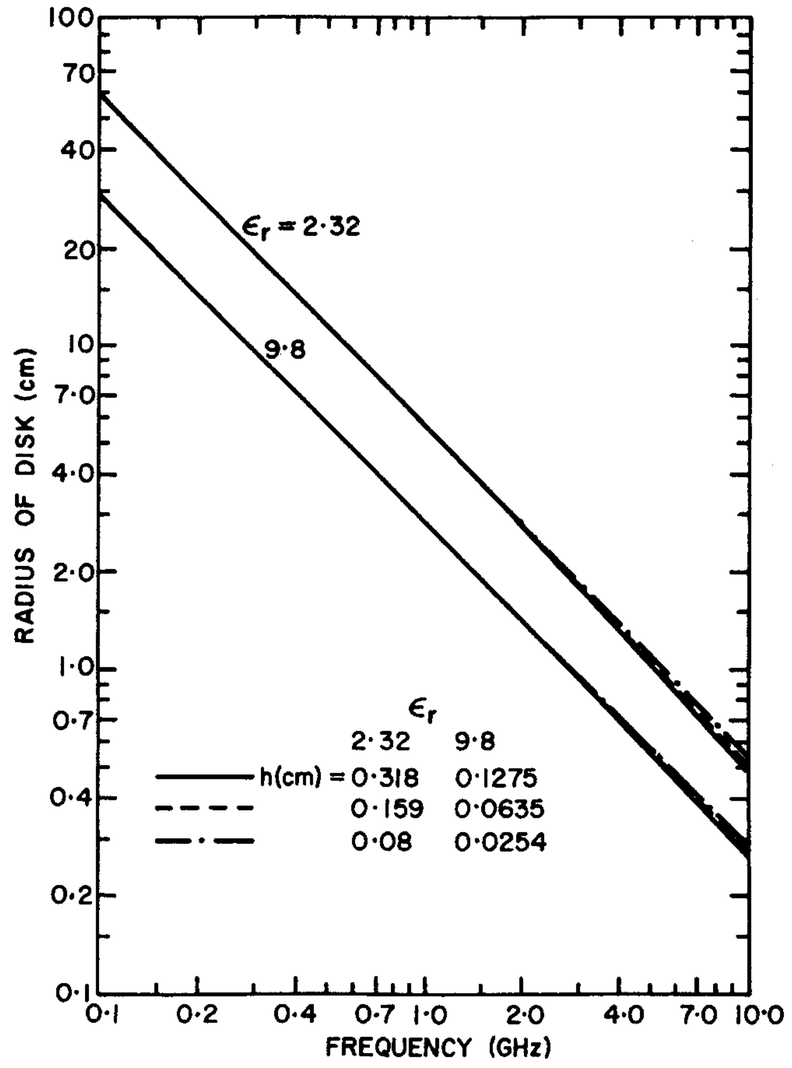

Figure 5.10 Radius of disk antenna as a function of frequency for two different dielectric substrates. (From [18]. © 1980 Artech House. Reprinted with permission.)

5.3.2 Radiation Patterns

Various mathematical models have been suggested for predicting the radiation characteristics of a circular disk microstrip radiator. The far-field expressions obtained from the cavity model are simple and adequate for practical purposes. The radiation patterns can be plotted by using (5.17) and (5.18). For the dominant TM_{11} mode, these expressions reduce to

$$E_\theta = -jV\frac{ak_0}{2}\frac{e^{-jk_0r}}{r}\cos\phi J_1'(k_0a\sin\theta) \tag{5.73}$$

$$E_\phi = jV\frac{ak_0}{2}\frac{e^{-jk_0r}}{r}\frac{J_1(k_0a\sin\theta)}{k_0a\sin\theta}\cos\theta\sin\phi \tag{5.74}$$

The E- and H-plane radiation patterns for circular disk elements at 2 GHz and $\epsilon_r = 2.32$ and $\epsilon_r = 9.8$ are plotted in Figures 5.11(a) and (b), respectively [18]. The E-plane pattern for a disk on a high dielectric constant material such as alumina is almost constant with θ.

Beamwidth

Beamwidths for the radiated field components can be measured from the radiation patterns. The 3-dB beamwidths versus substrate thickness are plotted in Figure 5.12 for three values of substrate dielectric constant [14]. It is interesting to note that the beamwidth for E_θ decreases for $\epsilon_r > 1$, whereas it increases for $\epsilon_r = 1$ as h/a is increased. This phenomenon might be a result of the increasing role played by the surface waves for $\epsilon_r > 1$.

Radiated Power and Radiation Resistance

The power radiated by an antenna can be obtained by integrating the real part of the Poynting vector over the hemisphere above the disk, that is,

$$P_r = \frac{1}{2\eta_0}\int_0^{2\pi}\int_0^{\pi/2}(|E_\theta|^2 + |E_\phi|^2)r^2\sin\theta d\theta d\phi \tag{5.75}$$

The expressions (5.73) and (5.74) for E_θ and E_ϕ, respectively, are used in (5.75). These expressions are very complicated functions of θ and ϕ. Therefore, a numerical integration is performed. However, if the effect of substrate thickness is neglected, an approximate closed form can be obtained for P_r. By using the series expansion of the product of Bessel's functions, one obtains for the $n = 1$ mode [23, p. 86]

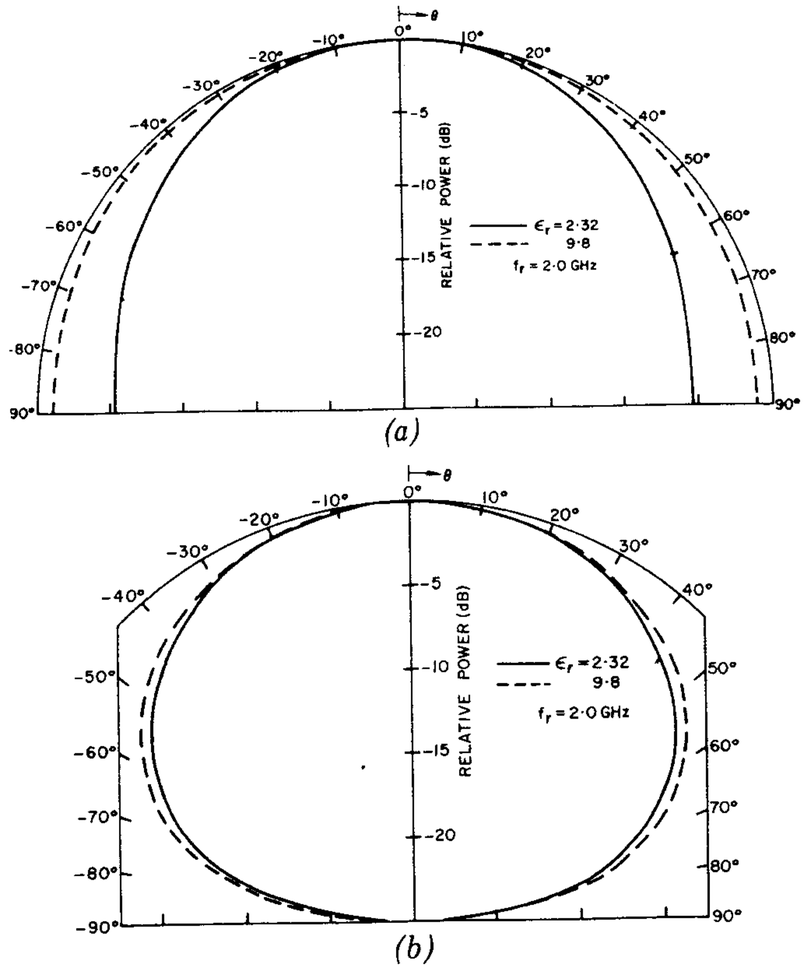

Figure 5.11 Radiation patterns of the microstrip disk antenna for the TM_{11} mode. (a) E_θ pattern in $\phi = 0°$ or E plane and (b) E_ϕ pattern in $\phi = 90°$ or H plane. (From [18]. © 1980 Artech House. Reprinted with permission.)

$$P_r = \frac{(E_0h)^2\pi^3a^2}{2\lambda_0^2\eta_0}\left[\frac{4}{3} - \frac{8}{15}(k_0a)^2 + \frac{11}{105}(k_0a)^4 - \ldots\right] \tag{5.76}$$

The resonant radiation conductance G_r for a disk fed at an edge can be determined from the power radiated P_r as follows:

$$P_r = \frac{1}{2}G_r(E_0h)^2 = \frac{1}{2}G_rV_0^2 \tag{5.77}$$

$$R_r = 1/G_r \tag{5.78}$$

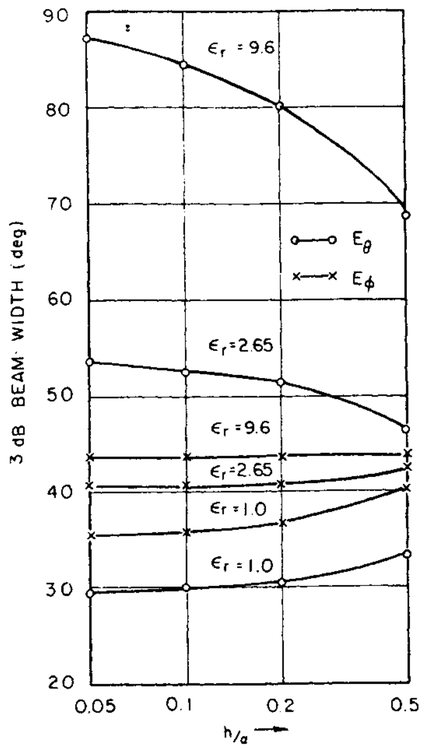

Beamwidth of circular printed antenna.

Figure 5.12 Beamwidth versus substrate thickness for the TM_{11} mode of circular disk antenna. (From [14]. © 1981 IEEE. Reprinted with permission.)

Variation of radiation resistance with resonant frequency is plotted in Figure 5.13 [18]. It is seen to vary very slowly with frequency, but the substrate dielectric constant has a large effect.

Directivity and Gain

The directivity is a measure of the directional properties of an antenna compared to those of an isotropic antenna. The directivity is always greater than 1 since an isotropic radiator is not directional. The directivity is defined as the ratio of the maximum power density in the main beam direction to the average radiated power density and can be expressed as

$$D = \frac{\frac{1}{2}\mathrm{Re}(E_\theta H_\phi^* - E_\phi H_\theta^*)|_{\theta=0}}{P_r/4\pi r^2} = \frac{\frac{r}{2\eta_0}(|E_\theta|^2 + |E_\phi|^2)|_{\theta=0}}{P_r/4\pi} \tag{5.79}$$

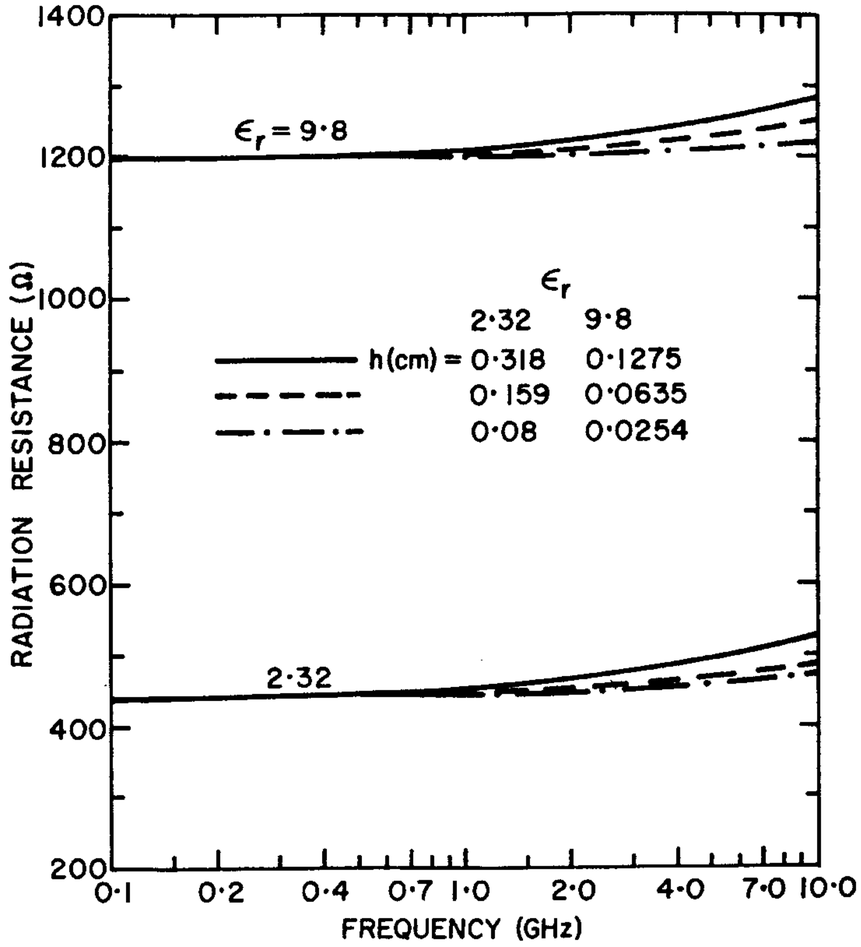

Figure 5.13 Variation of radiation resistance as a function of resonant frequency for two dielectric substrates. (From [18]. © 1980 Artech House. Reprinted with permission.)

where P_r is the radiated power, $\eta_0 = 120\pi$, and the radiation fields were determined earlier in Section 5.3.2. The directivity versus resonant frequency is plotted in Figure 5.14 [18]. A circular disk antenna on alumina substrate has a directivity of about 3.5, which is almost independent of substrate thickness for $h \leq 0.1275$ cm and resonant frequency. On a substrate with $\epsilon_r = 2.32$, the circular disk antenna has a maximum directivity of about 5.3, which decreases with increasing resonant frequency and dielectric thickness. The gain G of an antenna is defined as

$$G = e_r D \tag{5.80}$$

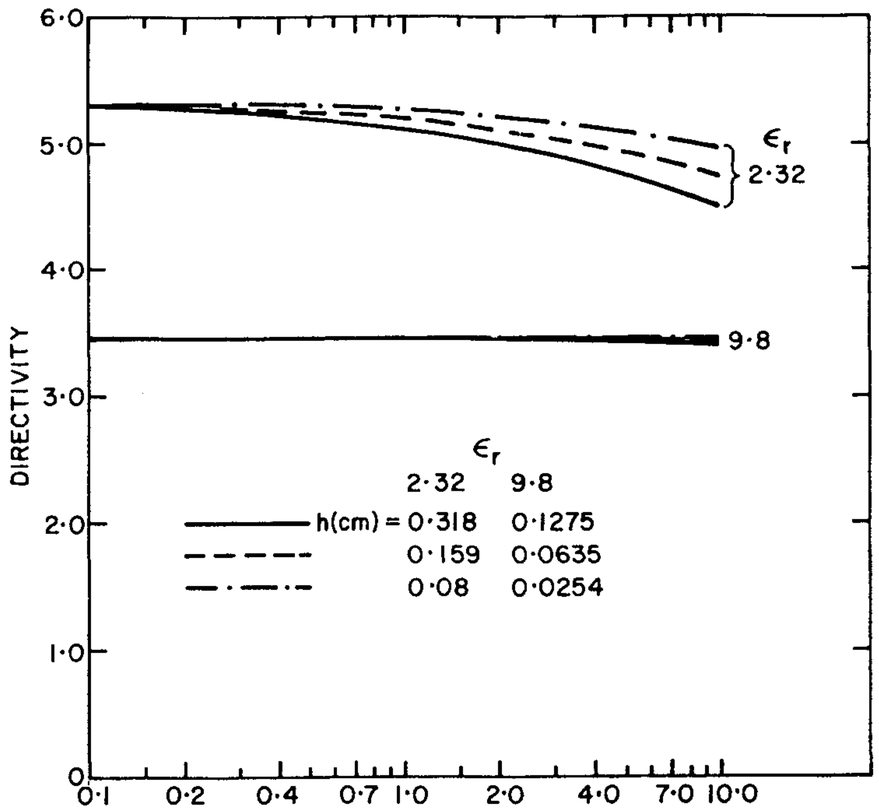

Figure 5.14 Directivity versus resonant frequency for the TM_{11} mode of a circular disk antenna. (From [18]. © 1980 Artech House. Reprinted with permission.)

where e_r is the radiation efficiency of the antenna. Gain is always less than directivity because e_r lies in the range $0 < e_r < 1$.

Higher Order Mode Radiation Patterns

The fundamental mode of the circular microstrip antenna generates a broadside radiation pattern. The second and higher order modes in the disk have also been studied [6, 24, 25] for linear polarization. A conical pattern with null at broadside is formed. Huang has used the higher order modes in a circular disk for generating circularly polarized conical patterns [26]. These patterns provide good omnidirectional coverage in the azimuthal plane and optimum sectoral coverage in the elevation plane. Therefore, a circular microstrip antenna can meet the requirement of low-gain omnidirectional antenna on the ground terminals of the low Earth-orbiting satellite systems, such as the Iridium system.

The conical pattern shape of the circular microstrip antenna can be adjusted by exciting different order modes in the antenna and/or by using

different dielectric materials. Calculated radiation patterns for the TM_{21}, TM_{31}, and TM_{41} modes are plotted in Figure 5.15 [26]. This plot shows that the peak of the conical pattern can be changed over a wide angular range from 35° to 69° from the broadside.

Effects of Finite Substrate and Ground Plane Size

The antenna characteristics presented so far assume an infinite size for the ground plane and substrate. In practice both are finite in size and may influence the characteristics considerably for thick substrates. The geometry of a circular disk with finite sized ground plane and substrate is shown in Figure 5.16(a). The finite size is defined as g. Kishk and Shafai [27] have studied the effect of finite size on the radiation fields and the excitation amplitude of various modes. Bhattacharyya has determined the effect of finite size on the input impedance, radiation pattern, efficiency, and directive gain [28–30].

The radiation near the broadside direction is determined primarily by the disk. The finite size of the substrate or ground plane influences the radiation near the end-fire direction, and particularly behind the antenna. It is found that the radiation pattern of various modes can easily be controlled by the ground plane size g. Figure 5.16(b) shows the computed patterns for the dominant TM_{11} mode for a substrate and ground plane size of $0.4\lambda_0$. It can be observed that the radiation peak is in the broadside with a significant

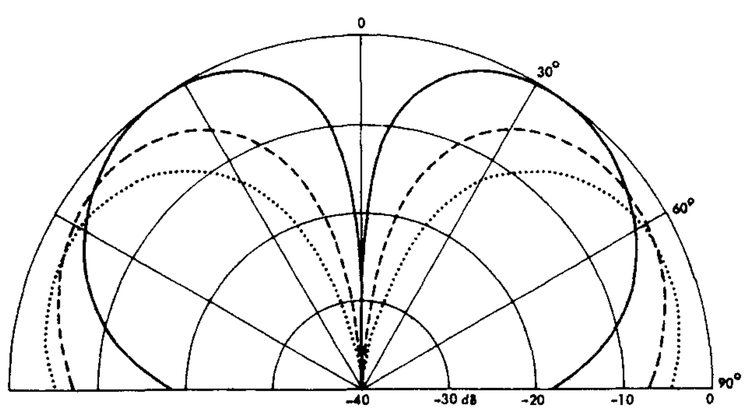

	MODE	RELATIVE DIELECTRIC CONSTANT	PEAK DIRECTIVITY	PEAK DIRECTION FROM ZENITH	RADIATOR DIAMETER
———	TM_{21}	1.25	6.9 dBi	35°	$0.9\lambda_0$
- - - - - -	TM_{31}	2.2	4.6	54°	$0.93\lambda_0$
.....	TM_{41}	4.2	4.0	69°	$0.88\lambda_0$

Figure 5.15 Computed radiation patterns in elevation plane for TM_{21}, TM_{31}, and TM_{41} modes of circular disk antenna. (From [26]. © 1984 IEEE. Reprinted with permission.)

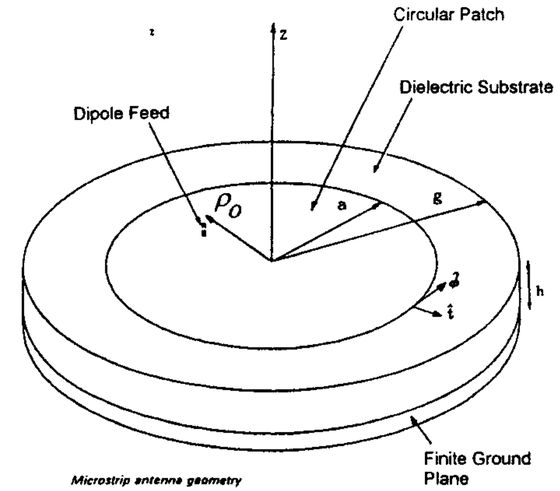

(a)

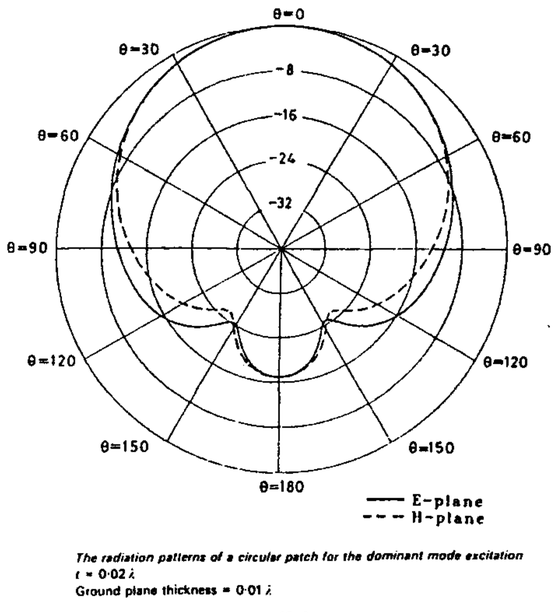

(b)

Figure 5.16 (a) Circular disk antenna with finite sized ground plane and substrate. (From [27]. © 1986 IEEE. Reprinted with permission.) (b) TM_{11} mode radiation patterns of a circular disk antenna with finite sized ground plane and substrate ($a = 0.181\lambda_0$, $g = 0.4\lambda_0$, $\rho_0 = 0.05\lambda_0$, $h = 0.02\lambda_0$, $\epsilon_r = 2.32$). (From [25]. © 1989 Peter Peregrinus. Reprinted with permission.)

radiation level behind the ground plane, owing to its finite size. The size of the ground plane also affects the excitation amplitude of the nearby nonresonant modes. It was observed that the peak amplitudes of nonresonant TM_{01} and TM_{21} modes increased from −30 to −17 dB when the ground plane size was increased from $0.3\lambda_0$ to $0.4\lambda_0$ [25]. The generated cross-polarization increased from −25 to −20 dB. These studies are useful in the design of small sized antennas, and particularly for the circular disk antenna as a feed for the reflector antenna.

5.3.3 Quality Factor and Impedance Bandwidth

The frequency selectivity of a microstrip antenna is determined by its quality factor Q_T. It also determines the impedance bandwidth of the antenna through the relation (4.71). The quality factor of a circular disk is calculated by following the procedure given in Section 4.3.4 for the rectangular patch. The expressions for Q_d and Q_c given there are independent of patch shape, and therefore

$$Q_d = 1/\tan\delta \tag{5.81}$$

$$Q_c = h\sqrt{\pi f \mu_0 \sigma} \tag{5.82}$$

$$W_T = \frac{\epsilon_0 \epsilon_r}{2} \int\int\int_V |E|^2 dv = \frac{h\epsilon_0 \epsilon_r \pi E_0^2}{2} \int_0^a J_n^2(k\rho)\, \rho d\rho$$

Since

$$\int_0^a J_n^2(k\rho)\, \rho d\rho = \frac{a^2}{2} J_n^2(ka)\left(1 - \frac{n^2}{k^2 a^2}\right)$$

$$W_T = \frac{hE_0^2}{8\omega f \mu_0} J_n^2(ka)\left((ka)^2 - n^2\right) \tag{5.83}$$

$$P_r = \frac{1}{2\eta_0} \int_0^{2\pi} \int_0^{\pi/2} (|E_\theta|^2 + |E_\phi|^2) r^2 \sin\theta d\theta d\phi$$

Using (5.17) and (5.18) for the radiation fields and factoring 2 for the ground plane effect, one obtains

$$P_r = \frac{(Vak_0)^2}{2\eta_0} \int_0^{2\pi} \int_0^{\pi/2} [\cos^2 n\phi J_n'^2(k_0 a \sin\theta) + \cos^2\theta \sin^2 n\phi J_n^2(k_0 a \sin\theta)/(k_0 a \sin\theta)^2] \sin\theta d\theta d\phi \tag{5.84}$$

which becomes

$$P_r = \frac{(hE_0 J_n(ka) ak_0)^2}{240} I_1 \qquad \text{for } n \geq 1 \tag{5.85}$$

where

$$I_1 = \int_0^{\pi/2} [J_n'^2(k_0 a \sin\theta) + \cos^2\theta J_n^2(k_0 a \sin\theta)/(k_0 a \sin\theta)^2] \sin\theta d\theta \tag{5.86}$$

Also,

$$Q_r = \frac{\omega W_T}{P_r} \tag{5.87}$$

Using (5.83) and (5.85) in (5.87) gives

$$Q_r = \frac{30[(ka)^2 - n^2]}{hf\mu_0 (k_0 a)^2 I_1} \tag{5.88}$$

From equations (5.81), (5.82), and (5.88), one obtains [18]

$$Q_T = \left[\tan\delta + \frac{1}{h\sqrt{\pi f \mu_0 \sigma}} + \frac{hf\mu_0 (k_0 a)^2 I_1}{30[(ka)^2 - n^2]} \right]^{-1} \tag{5.89}$$

It has been assumed in the derivation of (5.89) that surface wave loss is negligible, otherwise (4.56) and (5.83) can be used to calculate Q_{sur} and (5.89) modified. The Q factor is plotted in Figure 5.17 for a typical [18] set of parameters. For $\epsilon_r = 2.32$ and $f \geq 500$ MHz, the quality factor decreases with an increase in resonant frequency and substrate thickness.

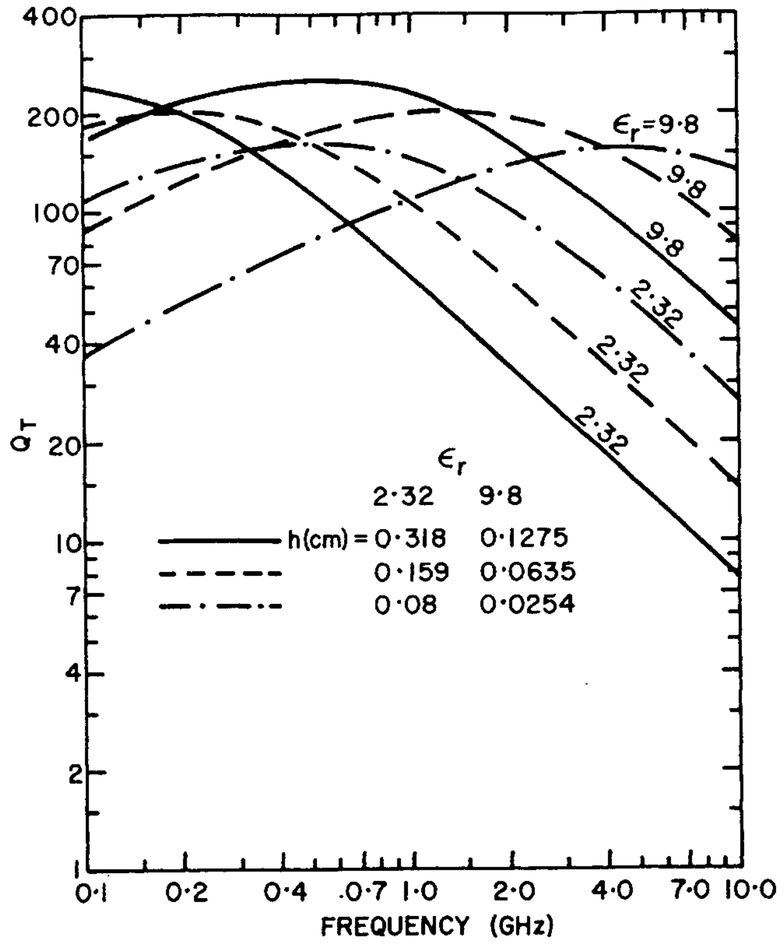

Figure 5.17 Variation of Q with resonant frequency for various microstrip disk antennas. (From [18]. © 1980 Artech House. Reprinted with permission.)

The Q-factor data are used along with the relation (4.57) to calculate the VSWR = 2 bandwidth. This is plotted in Figure 5.18 [18]. This figure shows that at a particular resonant frequency a larger bandwidth is possible by choosing a thicker substrate of lower dielectric constant material. This variation is similar to that for a rectangular patch.

5.3.4 Radiation Efficiency

Radiation efficiency is defined as the ratio of the radiated power to the input power, that is,

$$e_r = \frac{P_r}{P_i} = \frac{P_r}{P_r + P_c + P_d + P_{sur}} \tag{5.90}$$

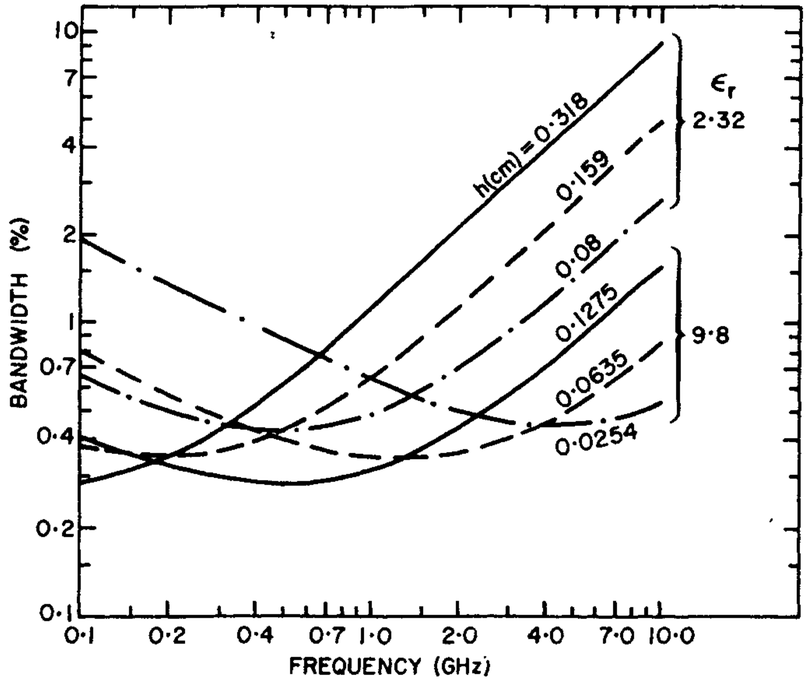

Figure 5.18 Variation of VSWR = 2 bandwidth with resonant frequency for the TM_{11} mode. (From [18]. © 1980 Artech House. Reprinted with permission.)

Radiation efficiency is calculated using this definition and plotted in Figure 5.19 for the TM_{11} mode [25]. Similar to that of a rectangular patch, the efficiency of a circular disk increases with increasing substrate thickness and decreasing dielectric constant.

5.3.5 Feed Point Location

After selecting the disk radius for a given substrate the next task is to determine the feed point (ρ_0, ϕ_0) such that there is a good match between the input impedance of the disk and the generator impedance. Because there is no preferred axis for a circular disk, the axis passing through the feed point can be labeled as $\phi_0 = 0$. Now, the value of ρ_0 can be selected to vary the input impedance of the antenna.

Note from (5.44a) that the variation of the input impedance with feed location is governed by $J_n^2(k_{nm}\rho_0)$ for $n \geq 1$. Variation of R_{in} with radial feed location is plotted in Figure 5.6 for the TM_{11} mode, and this variation is consistent with the variation of $J_1^2(k_{11}\rho_0)$. Based on these observations, the input resistance for the TM_{11} mode can be expressed as

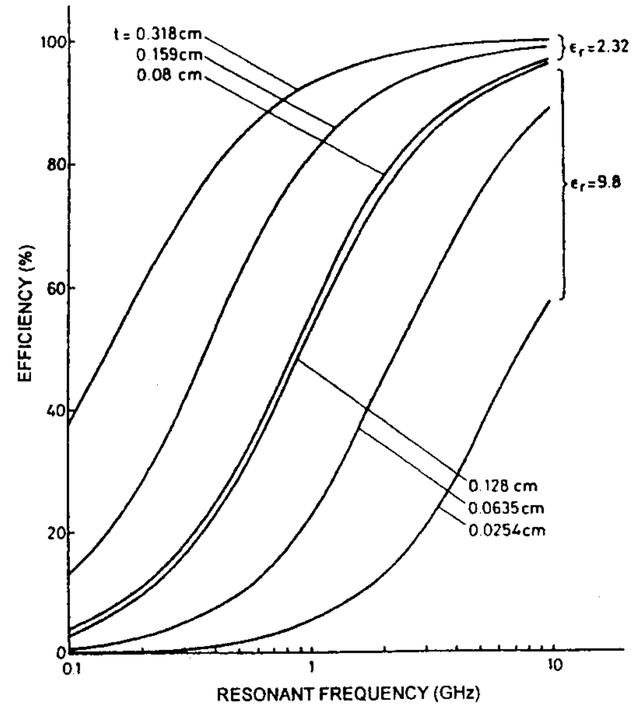

Figure 5.19 Radiation efficiency versus resonant frequency for the TM_{11} mode of the circular disk with $\tan\delta = 0.0005$, $\sigma = 5.8 \times 10^7$ S/m, and (i) $\epsilon_r = 2.32$, $h = 0.079$ cm, 0.159 cm, 0.318 cm, and (ii) $\epsilon_r = 9.8$, $h = 0.0254$ cm, 0.0635 cm, 0.127 cm. (From [25]. © 1989 Peter Peregrinus. Reprinted with permission.)

$$R_{\text{in}} = R_r \frac{J_1^2(k_{11}\rho_0)}{J_1^2(k_{11}a)} \qquad k_{11}a = 1.84118 \tag{5.91}$$

The radiation resistance R_r is defined in (5.78). Equation (5.91) is used to determine the feed location for a desirable input resistance value. Determination of the exact feed location requires an iterative solution for (5.44a). Equation (5.91) provides a useful guideline for this purpose. This approach is useful for a probe feed, which can be located inside the disk. Microstrip feed, however, can be located at the periphery only. A slot should be cut in the disk, for an inset feed.

It is possible to have a microstrip edge feed with a 50Ω input impedance. For this purpose, let us consider (5.44b). According to this expression, the input impedance can be varied by varying ϕ_0 also. We can define a reference plane for ϕ_0 by introducing a short at any point on the periphery of the circular disk. Since the electric field E_z is zero at the location of short, the corresponding value of ϕ is 90° as per (5.10). Now that the reference axis for

ϕ has been defined, we can determine the value of the feed location (ϕ_0, a) which will give rise to 50Ω input resistance according to (5.44b). The procedure for calculating ϕ_0 is exactly similar to that used for finding ρ_0 [see (5.91)]. An alternative approach has been followed in [31, 32]. In [31], a slot is cut in the disk. A part of the slot is then loaded by a thin strip. These modifications destroy the circular symmetry of the disk and clearly establish a preferred axis. The modified geometry of the circular disk is shown in Figure 5.20. The impedance bandwidth and radiation characteristics are found to be unaffected by the structural modifications. Impedance at the edge of the disk can be lowered by resistively loading the disk. This approach is followed in [33].

5.3.6 Polarization

The polarization of a circular disk element is linear, as in the case for a rectangular patch antenna. Large bandwidth disk antennas may also operate in a higher order mode. The radiation pattern and polarization for these modes may be different from the dominant mode. Another source of cross-polarization could be the finite size of the dielectric and ground plane. It has been pointed out that the amplitude of excitation of nonresonant higher order modes can be influenced by the finite size [27]. For example, for $a = 0.1806\lambda_0$,

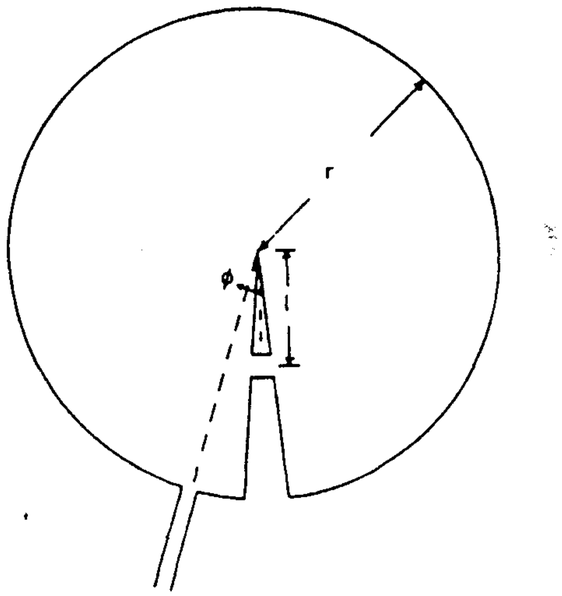

Figure 5.20 Schematic diagram of a modified circular disk antenna for microstrip feed. (From [31]. © 1993 *Electronics Letters*. Reprinted with permission.)

$h = 0.02\lambda_0$, $\epsilon_r = 2.32$, $\rho_0 = 0.05\lambda_0$ and a ground plane size of $0.4\lambda_0$, the cross-polarization level due to nonresonant higher order modes was more than −20 dB [27]. For the dominant mode, the cross-polarization level depends on the feed position, substrate thickness, substrate permittivity, resonant frequency, and the plane ϕ [34]. The cross-polar component E_ϕ is zero in the E plane ($\phi = 0°$). In the H plane ($\phi = 90°$), the cross-polar component is minimum in the broadside direction and maximum in the end-fire direction. A variation of the cross-polarization level in the H plane with resonance frequency and feed location as a parameter is shown in Figure 5.21(a). Note that the cross-polarization level increases as the feed point nears the center of the patch. Also, the cross-polarization level is higher for higher frequencies. A variation of the

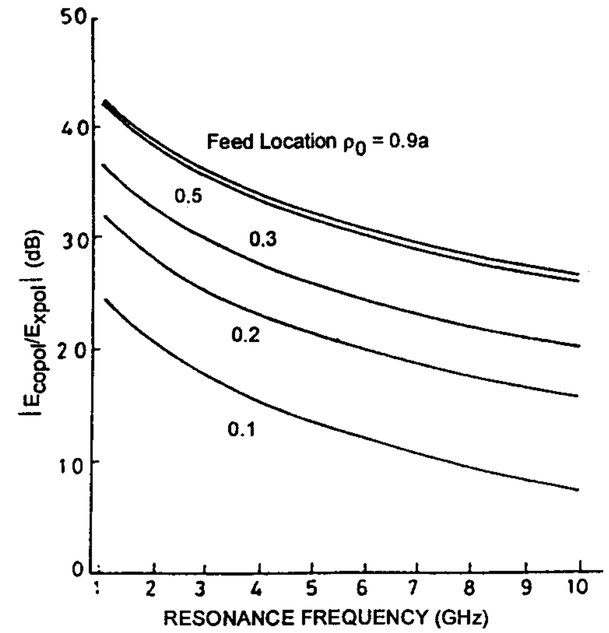

$|E_{copol}/E_{xpol}|$ as function of resonance frequency for different feed positions

$\epsilon_r = 2{\cdot}32$, $h = 1{\cdot}9$ mm, $\phi = 90°$

(a)

Figure 5.21 (a) Variation of $|E_{\text{copol}}|/|E_{\text{xpol}}|$ as a function of resonant frequency for different feed positions [34] where $h = 1.9$ mm, $\epsilon_r = 2.32$, $\phi = 90°$. (b) Variation of $|E_{\text{copol}}|/|E_{\text{xpol}}|$ as a function of resonant frequency for different substrate thicknesses $\rho_0/a = 0.2$, $\epsilon_r = 2.32$, $\phi = 90°$. (From [34]. © 1992 *Electronics Letters*. Reprinted with permission.)

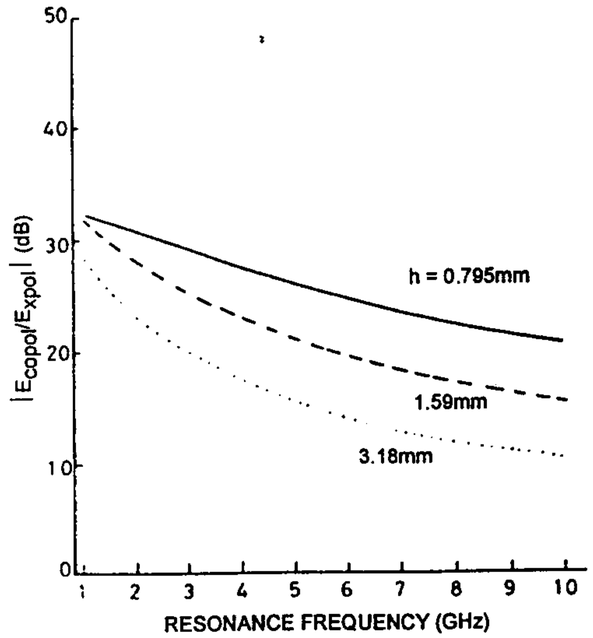

$|E_{copol}/E_{xpol}|$ as function of resonance frequency for different substrate thickness: $\epsilon_r = 2.32$, $\rho_0/a = 0.2$, $\phi = 90°$

——— $h = 0.795$ mm
– – – $h = 1.59$ mm
····· $h = 3.18$ mm

(b)

Figure 5.21 (continued).

cross-polarization level with substrate thickness is plotted in Figure 5.21(b) for $\epsilon_r = 2.32$ [34]. Thicker substrates give rise to higher cross-polarization. Also, higher values of ϵ_r give rise to higher levels of cross-polarization [34].

Circular polarization from a circular disk can be obtained by exciting degenerate orthogonal modes with signals of equal amplitude but 90° phase difference. A hybrid can be used to obtain the proper amplitude and phase relationship between the two signals. This topic is discussed in detail in Chapter 8.

5.3.7 Circular Disk Antenna With an Air Gap

The cross section of a circular microstrip antenna with an air gap is shown in Figure 5.22. This antenna employs an air layer of thickness Δ between the dielectric substrate and ground plane. The air gap has the effect of lowering the effective permittivity of the disk antenna, resulting in an upward shift in

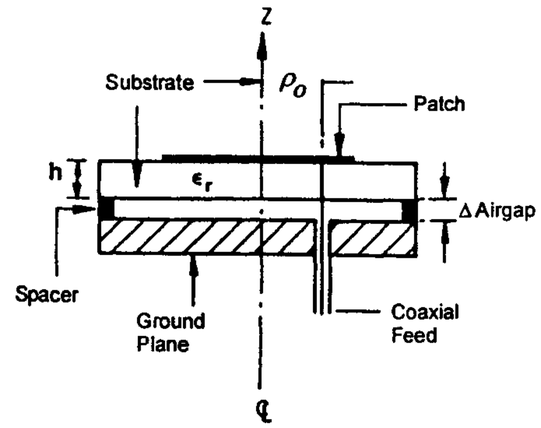

Figure 5.22 Cross section of a circular disk antenna with an air gap. (From [35]. © 1984 IEEE. Reprinted with permission.)

the resonant frequency and the increase in bandwidth. The resonant frequency can therefore be tuned by adjusting the air gap thickness, and is given by [35]

$$f_{nm} = \frac{\chi_{nm} c}{2\pi a_e \sqrt{\epsilon_{re}}} \tag{5.92}$$

where ϵ_{re} is the effective relative permittivity of the two-layered cavity given by

$$\epsilon_{re} = \frac{\epsilon_r (h + \Delta)}{h + \epsilon_1 \Delta} \tag{5.93}$$

and

$$a_e = a\left\{1 + \frac{2h}{\pi a \epsilon_{re}}\left(\ln\frac{\pi a}{2h} + 1.7726\right)\right\}^{1/2} \tag{5.94}$$

Note that the effective permittivity has been used in (5.94). Analysis of the antenna with an air gap has been carried out using the cavity model and the results for input impedance compared with measurements [35].

5.3.8 Effects of a Dielectric Cover or Superstrate

A microstrip antenna can be subjected to icing or be coated with paint or dielectric material for environment protection. This cover affects performance

to an extent that should be known. In particular, the resonant frequency is lowered, causing tuning problems and severely degrading performance, which can be serious, because the bandwidth of these antennas is inherently low. Antenna gain increases if a superstrate with sufficient thickness is used, and this is discussed in Chapter 4.

When a microstrip disk is covered by a dielectric sheet (called a superstrate), its properties, such as effective dielectric constant, losses, and Q factor, change. The effective dielectric constant changes more than other characteristics. The amount of change is dependent on the thickness and relative permittivity of the superstrate. The properties of this configuration have been studied using the mode-matching technique [9]. Numerical results show that the radiated power and surface wave power decrease due to the presence of a thin dielectric cover [9]. However, by properly choosing the superstrate parameters, a significant increase in gain, radiation resistance, and efficiency can be achieved, enabling the cover to act as a desirable part of the antenna as well as a protective layer [36].

5.3.9 RCS of a Circular Disk Antenna

The radar cross section (RCS) of a microstrip antenna can assume values much larger than its physical area. In applications where RCS control is desirable, efficient theoretical methods for its prediction are necessary because the RCS values will be required over a wide frequency range with high resolution. This subject has received much attention in recent times. A special issue of *Electromagnetics* has been devoted to this aspect [37].

The scattering behavior of a disk antenna is described in terms of RCS as follows:

$$\sigma_{\theta\theta} = 4\pi r^2 |E_\theta^s|^2 \tag{5.95}$$

where E_θ^s is the θ-polarized scattered field from the disk. A similar definition holds for the ϕ-polarized field. The analysis for RCS is based on the incident field and the scattered field satisfying the various boundary conditions and interface condition. RCS analysis of a circular disk antenna has been reported by many investigators [38–41]. These analyses are based on an integral equation approach along with a moment method solution. Calculated and measured RCSs for a circular disk are shown in Figure 5.23 [40]. It is observed from here that RCS approaches a peak value at the resonant frequency.

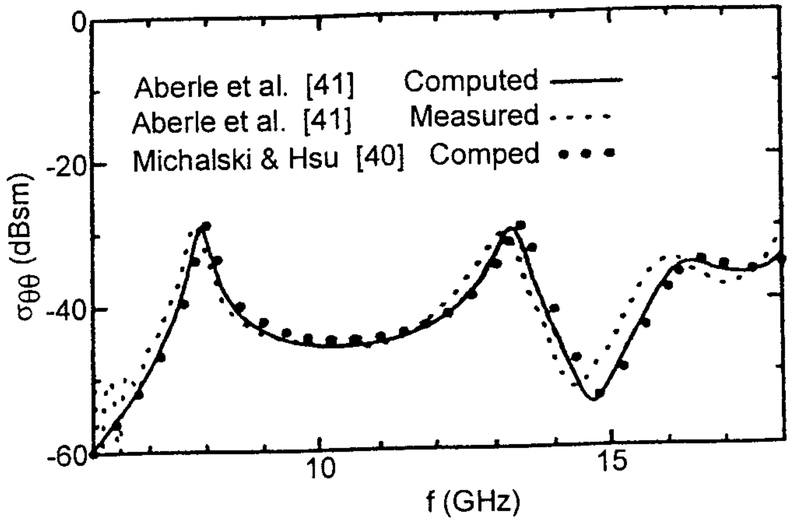

Figure 5.23 Comparison of computed and measured RCS of a circular disk antenna. (a = 7.1 mm, h = 0.787 mm, ϵ_r = 2.2, $\tan\delta$ = 0.0009, ϕ_i = 0°, θ_i = 63°). (From [40]. © 1994 *Electromagnetics*. Reprinted with permission.)

5.3.10 Computer-Aided Design

The design information presented earlier can be included in a CAD package. To clarify the various steps in the design process, let us consider the design of a circular microstrip antenna for which the substrate dielectric constant has already been selected. The considerations for the selection of substrate are given in Section 4.3.1 and Appendix A. The patch radius a and substrate thickness h are to be determined for a desired resonant frequency f_r and bandwidth B. Further, the feed location ρ_0 is to be determined for a 50Ω input impedance.

The design starts with the determination of substrate thickness h, because this parameter along with ϵ_r influences the bandwidth considerably. Equations (5.88) and (4.71) are used to calculate the value of h. To implement (5.88), a suitable value of patch radius a needs to be selected. One can use (5.68b) for this purpose because the substrate thickness has a minor effect on the patch radius. The patch radius a is determined next from (5.71) using the calculated value of h. The next step is to determine the feed location ρ_0. The value of ρ_0 is governed by (5.91). The radiation resistance R_r can be determined from (5.76) to (5.78). However, these equations are valid for ϵ_r = 1. For better accuracy, (5.19) and (5.20) are used in (5.75) and integrated numerically to calculate P_r. Knowing the value of R_r, the feed point is calculated from (5.91), that is,

$$J_1(k_{11}\rho_0) = \sqrt{\frac{R_{\text{in}}}{R_r}}\, J_1(k_{11}a) = \sqrt{\frac{R_{\text{in}}}{R_r}}\, J_1(1.84118) = 0.5819\sqrt{\frac{R_{\text{in}}}{R_r}}$$

The above equation cannot be inverted to determine ρ_0. For this, one can use the Newton-Raphson approach. An initial guess for $J_1(x)$ can be taken as $0.5x$, and

$$x_n = x_{n-1} - J_1(x)/J_1'(x)$$

The preliminary design of the patch antenna is now complete. The design should now be tested for the resonant frequency, input impedance, and bandwidth. For this, we should calculate the input impedance as a function of frequency. To do so, we use the cavity model. The value of the equivalent loss tangent δ_{eff} is needed to evaluate the input impedance of (5.44a). We know that $\delta_{\text{eff}} = 1/Q_T$. Next, Q_T is determined. Although the value of Q_T can be determined from the desired VSWR bandwidth and (4.71), it is suggested that (4.66), (5.81), (5.82), (5.83), (5.87), and P_r, determined earlier, be used for better accuracy in Q_T. The input impedance is now computed as a function of frequency near the design frequency. Four values of m and n each should be sufficient to compute Z_{in}. The computed values of resonant frequency, input resistance, and bandwidth are determined from these data. It is very likely that the computed values are slightly different from the design values. This is due to the approximate nature of the design equations, and because the effect of feed reactance on resonant frequency is not included in the design. Probe/feed reactance can be calculated from (2.96) and added to the calculated input impedance value. The patch radius a and feed location ρ_0 are now varied iteratively to arrive at an accurate design. For this, the Newton-Raphson procedure can be used. Details of this procedure for the rectangular patch were given in Section 4.3.12. This procedure can be easily adapted for the circular disk.

The CAD approach presented above does not have the accuracy of a full-wave analysis, but is useful for parametric studies of the characteristics of a circular microstrip antenna. It can also be used for instructional purposes. A similar software package is available in [42].

5.4 Semicircular Disk and Circular Sector Microstrip Antennas

It can be advantageous in some applications where space is at a premium to deploy a circular sector disk antenna. With this in mind, a brief description of these antennas is included here.

The metalization for a semicircular disk antenna is shown in Figure 5.24. The cavity model analysis of the disk antenna can be easily adapted for the

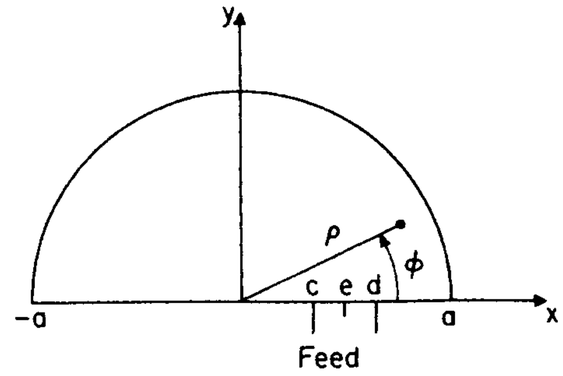

Figure 5.24 Geometry of a semicircular disk antenna.

semicircular disk case. For this purpose only one observation is enough, that is, the field distribution in a disk antenna of Figure 5.1 remains unchanged if a magnetic wall is inserted along the x axis. Therefore, the modes in a semicircular disk antenna with a magnetic wall at $y = 0$ in Figure 5.24 will be identical to that of a disk antenna.

Lo et al. [5, 43] have analyzed the semicircular disk antenna using the cavity model. The cavity is bounded above and below by electric walls, surrounded along the periphery by a magnetic wall, and excited by a source along the x axis. The excitation current is defined as

$$\vec{J} = \hat{z} J_z(\rho)\delta(\phi)/\rho \tag{5.96}$$

where

$$J_z(\rho) = \begin{cases} I & \text{if } c < \rho < d \\ 0 & \text{elsewhere} \end{cases} \tag{5.97}$$

Because the field distribution in the semicircular disk is derived from the corresponding circular disk, the eigenfunctions, the eigenvalues, and hence the resonant frequency for various TM_{nm} modes in the semicircular disk are the same as that for the corresponding modes in circular disk. However, because of different excitation, the excitation amplitudes will be different. The electric field in this case can be written as [18, 43]:

$$E_z = j\omega\mu_0 I\left\{\frac{2(d-c)}{\pi a^2 k^2} + \sum_{m=2}^{\infty} \frac{2(d-c)J_0(k_{0m}\rho_0)J_0(k_{0m}\rho)}{\pi a^2 J_0^2(k_{0m}a)(k^2 - k_{0m}^2)} + \sum_{n=1}^{\infty}\sum_{m=1}^{\infty} \frac{2(d-c)J_n(k_{nm}\rho_0)J_n(k_{nm}\rho)k_{nm}^2 \cos n\phi}{\pi(k^2 - k_{nm}^2)(k_{nm}^2 a^2 - n^2)J_n^2(k_{nm}a)}\right\} \tag{5.98}$$

where $\rho_0 = (d + c)/2$. The magnetic current distribution around the periphery of the antenna is determined as follows for $\phi = 0$ and $0 \le \rho \le a$:

$$\vec{M}(\rho, 0) = \hat{x}2j\omega\mu_0 I\left\{\frac{2(d-c)}{\pi a^2 k^2} + \sum_{m=2}^{\infty} \frac{2(d-c)J_0(k_{0m}\rho_0)J_0(k_{0m}\rho)}{\pi a^2 J_0^2(k_{0m}a)(k^2 - k_{0m}^2)} + \sum_{n=1}^{\infty}\sum_{m=1}^{\infty} \frac{F_{nm}J_n(k_{nm}\rho)}{(k^2 - k_{nm}^2)D_{nm}}\right\} \tag{5.99a}$$

for $\phi = \pi$ and $0 \le \rho \le a$:

$$\vec{M}(\rho, \pi) = (-1)^n \vec{M}(\rho, 0) \tag{5.99b}$$

and for $\rho = a$ and $0 < \phi < \pi$

$$\vec{M}(a, \phi) = \hat{\phi}2j\omega\mu_0 I\left\{\frac{2(d-c)}{\pi a^2 k^2} + \sum_{m=2}^{\infty} \frac{2(d-c)J_0(k_{0m}\rho_0)J_0(k_{0m}a)}{\pi a^2 J_0^2(k_{0m}a)(k^2 - k_{0m}^2)} + \sum_{n=1}^{\infty}\sum_{m=1}^{\infty} \frac{F_{nm}J_n(k_{nm}\rho)\cos n\phi}{(k^2 - k_{nm}^2)D_{nm}}\right\} \tag{5.99c}$$

where

$$F_{nm} = 2(d-c)J_n(k_{nm}\rho_0)k_{nm}^2$$
$$D_{nm} = \pi(a^2 k_{nm}^2 - n^2)J_n^2(k_{nm}a)$$
$$k_{nm} = \chi_{nm}/a$$

The magnetic current distribution for several modes is sketched in Figure 5.25. These current distributions can also be obtained from the corresponding modes in Figure 5.3. Radiation patterns for the semicircular disk with radius $a = 6.75$ cm on a substrate with $\epsilon_r = 2.62$, $\tan\delta = 0.001$, and $h = 1/16$-in. are plotted in Figure 5.26 for the TM_{11} and TM_{21} modes [5]. Comparison with the radiation patterns for the corresponding mode in the circular disk shows that the two patterns are identical for the dominant mode. However, there is a considerable difference for the TM_{21} mode. Perhaps it is due to the extra current on the x axis of the semicircular disk. Input impedance variation for this antenna is shown in Figure 5.27.

Analysis of a circular sector of sector angle α can be carried out in the same manner [44]. However, such an antenna may not offer any advantages.

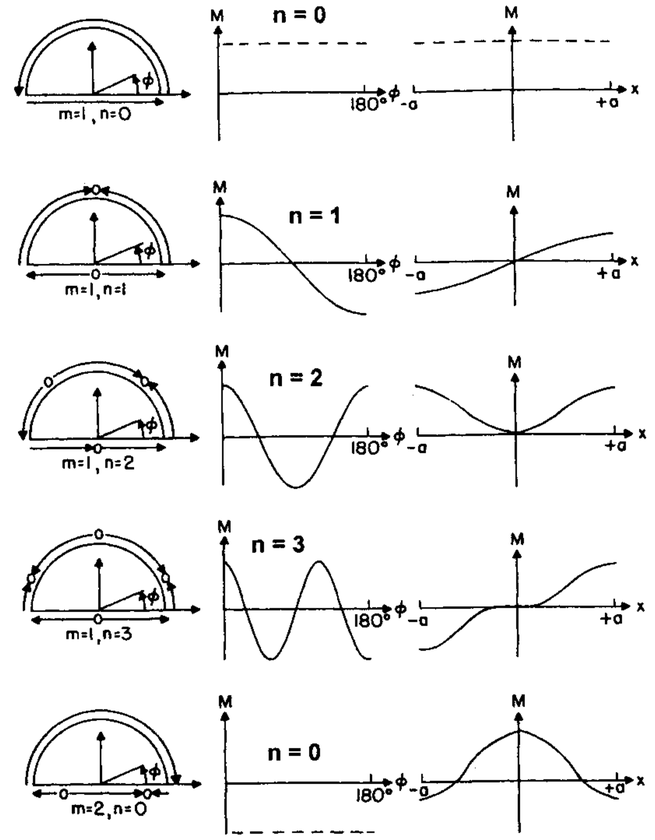

Figure 5.25 Magnetic current distribution for the various modes of a semicircular disk antenna. (From [18]. © 1980 Artech House. Reprinted with permission.)

The eigenfunctions for a circular sector microstrip antenna are given as [5, 44]

$$\psi_{mv} = J_v(k_{mv}\rho)\cos v\phi, \qquad v = n\pi/\alpha \tag{5.100a}$$

with

$$J_v'(k_{mv}a) = 0 \tag{5.100b}$$

The generalized transmission line model has also been used for the analysis of a circular sector microstrip antenna [45]. This analysis is more rigorous and estimates the phase of the aperture fields correctly, which is important in array design.

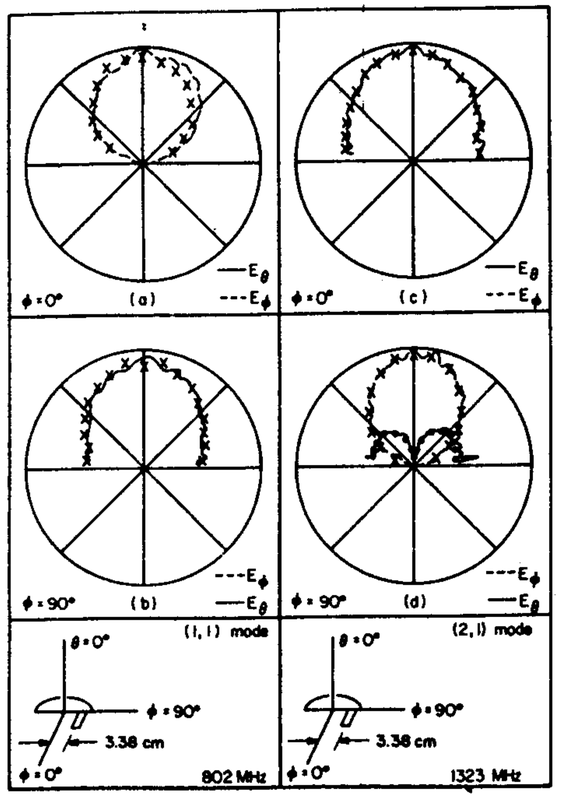

Figure 5.26 Radiation patterns for TM_{11} and TM_{21} modes of a semicircular disk antenna: (a) TM_{11} mode, $\phi = 0°$ plane; (b) TM_{11} mode, $\phi = 90°$ plane; (c) TM_{21} mode, $\phi = 0°$ plane; and (d) TM_{21} mode, $\phi = 90°$ plane. (From [5]. © 1979 IEEE. Reprinted with permission.)

5.5 Comparison of Rectangular and Circular Disk Microstrip Antennas

The design of rectangular and circular disk antennas has been discussed in Chapters 4 and 5, respectively. It is instructive to compare the performance of these antennas through an example.

Assume an operating frequency of 2 GHz and the substrate parameters as $h = 0.159$ cm, $\epsilon_r = 2.32$. The physical dimensions of the rectangular geometry are evaluated to be $W = 5.82$ cm, $L = 4.85$ cm, and for the circular disk $a = 2.78$ cm. Table 5.2 summarizes various characteristics for the two antennas [18].

As can be seen from Table 5.2, the circular disk antenna has a smaller beamwidth in both planes than does the rectangular antenna. The directivity and efficiency are the same for both antennas. The bandwidth characteristic

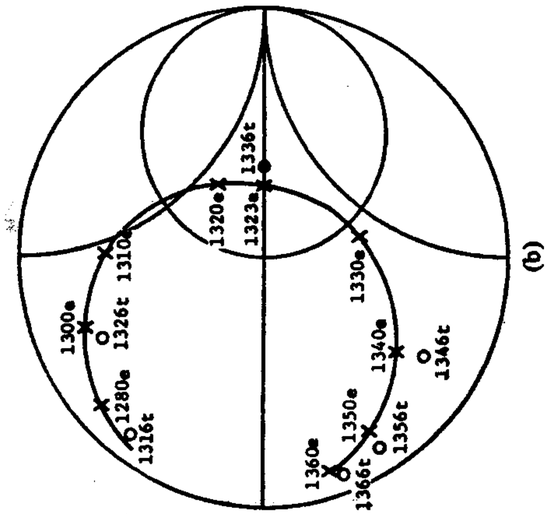

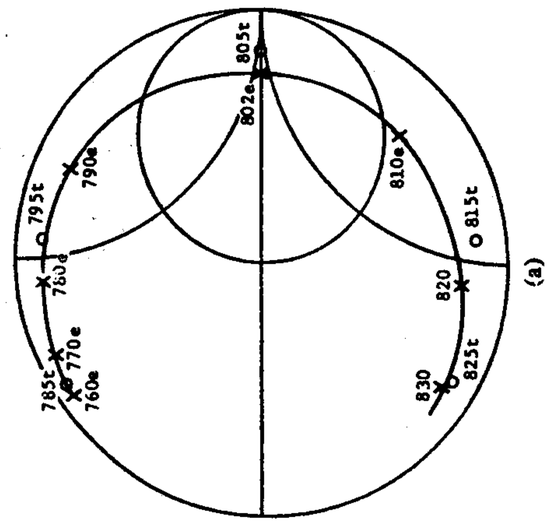

Figure 5.27 Input impedance loci for a semicircular disk antenna: (a) TM_{11} mode and (b) TM_{21} mode. (From [5]. © 1979 IEEE. Reprinted with permission.)

Table 5.2
Comparison of the Characteristics of Rectangular and Circular Disk Microstrip Antennas

Characteristics	Configuration	
	Rectangular	Circular
Beam position	Broadside	Broadside
3-dB beamwidth,		
E Plane	111°	100°
H Plane	123°	80°
Directivity	7.08 dB	7.1 dB
Efficiency	91.2%	91%
Bandwidth (VSWR = 2)	2%	1.149%
Physical area of the patch	28.2 cm^2	24.3 cm^2

is better for the rectangular geometry. The physical area of the rectangular configuration is 16% more than that of the circular disk.

5.6 Circular Ring or Annular Ring Microstrip Antennas

Ring microstrip antennas of various shapes, such as circular, rectangular, square, and triangular, have been studied as alternatives to standard rectangular and circular disks. These antennas are geometrically and electrically an intermediate configuration between a printed loop and a patch [46]. Several interesting properties are associated with ring antennas. The geometries of a printed square loop, square ring, and square microstrip patch are shown in Figure 5.28. The size of the resonant ring is substantially smaller than that of the corresponding patch and depends on the width of the microstrip used. In general, the mean circumference of a ring equals the guide wavelength of the microstrip used. Input impedance of a ring operated in the TM_{11} mode is considerably higher, whereas its impedance bandwidth is smaller, in comparison with the patch. As the strip width is increased, the characteristics of a ring approach that of the patch. The circular ring antenna has been studied and used most frequently. The details of the design of this antenna are given next.

The circular ring antenna has a number of useful features. The separation of resonant modes can be controlled by the ratio of outer to inner radii. The impedance bandwidth of this antenna, when operated in the TM_{12} mode, is found to be several times larger than is achievable with other patches, although at the cost of larger size. It is possible to combine the circular ring with a concentric circular disk to form a compact dual-band antenna [47]. The microstrip ring structure has been used to measure the dielectric constant of the

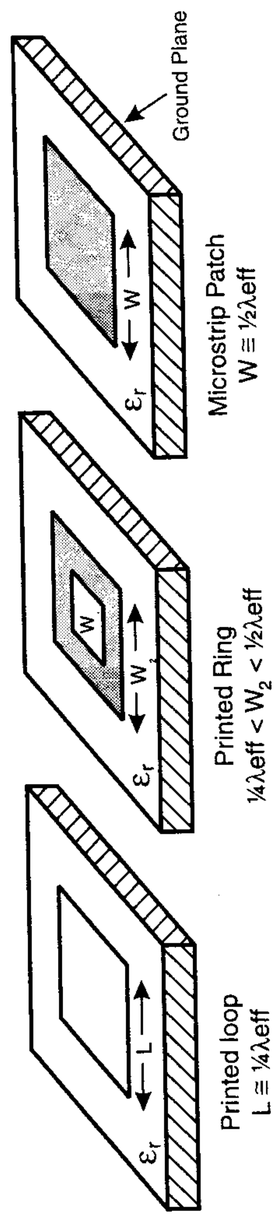

Figure 5.28 Geometry of a printed square loop, square ring, and square patch microstrip antenna. (From [46]. © 1996. Reprinted with permission.)

substrate material [48], and proposed as a radiator for medical applications [49]. It has been shown that the structure is a good resonator (with very little radiation) for TM_{1m} modes (m odd), and a good radiator for TM_{1m} modes (m even) [50, 51].

The circular ring has been analyzed extensively using the cavity model [18, 25, 47, 52], generalized transmission line model [11], analysis in the Fourier-Hankel transform domain [53], and the method of matched asymptotic expansion [50]. The cavity model analysis, which is found to be simple and useful in the design for the structure, is presented next [18, 25, 52, 54].

5.6.1 Fields and Currents

Consider a circular ring microstrip antenna with the coordinate system as shown in Figure 5.29. It comprises a ring-shaped conductor on one side of a dielectric substrate with a ground plane on the other side. The cavity model of the ring is obtained by replacing its peripheries with magnetic walls. Because there is no variation of the fields along the z direction for thin substrates, the modes are designated as TM_{nm} modes.

Following the procedure given in Section 5.2.1 for a circular disk antenna, the general solution for the wave equation (5.1) in cylindrical coordinates is given as [18, 48, 55]

$$E_z = E_0[J_n(k\rho)Y_n'(ka) - J_n'(ka)Y_n(k\rho)]\cos n\phi \qquad (5.101)$$

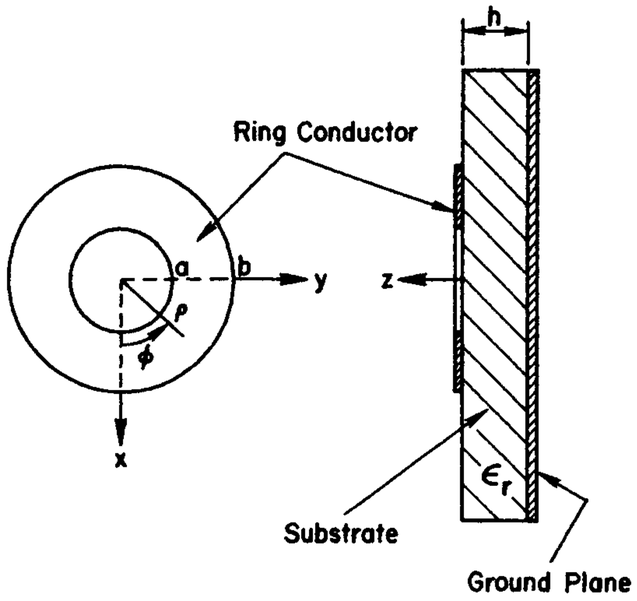

Figure 5.29 Geometry of a circular ring microstrip antenna.

$$H_\rho = \frac{j}{\omega\mu\rho}\frac{\partial E_z}{\partial\phi}, \qquad H_\phi = -\frac{j}{\omega\mu}\frac{\partial E_z}{\partial\rho} \qquad (5.102)$$

where $J_n(\cdot)$ and $Y_n(\cdot)$ are the Bessel functions of the first and second kind, and of order n, respectively. The other field components are zero inside the cavity. The surface current on the lower surface of ring metalization is given by

$$\vec{J}_S = -\hat{z}\times\vec{H} = -\hat{\phi}H_\rho + \hat{\rho}H_\phi \qquad (5.103)$$

or

$$J_\phi = \frac{jnE_0}{\omega\mu\rho}[J_n(k\rho)Y_n'(ka) - J_n'(ka)Y_n(k\rho)]\sin n\phi \qquad (5.104a)$$

$$J_\rho = \frac{-jkE_0}{\omega\mu}[J_n'(k\rho)Y_n'(ka) - J_n'(ka)Y_n'(k\rho)]\cos n\phi \qquad (5.104b)$$

The radial component of the surface current must vanish along the edges at $\rho = a$ and $\rho = b$ to satisfy the magnetic wall boundary conditions. This leads to

$$J_\rho(\rho = b) = H_\phi(\rho = b) = 0 \qquad (5.105)$$

Application of this boundary condition leads to the well-known characteristic equation for the resonant modes:

$$J_n'(kb)Y_n'(ka) - J_n'(ka)Y_n'(kb) = 0 \qquad (5.106)$$

For the given values of a, b, ϵ_r, and n, the frequency is varied and the roots of (5.106) are determined. Let us denote these roots by k_{nm} for the resonant TM_{nm} modes and form χ_{nm} such that $\chi_{nm} = k_{nm}a$. The integer n denotes the azimuthal variation as per $\cos n\phi$, while the integer m represents the mth zero of (5.106) and denotes the variation of fields across the width of the ring. The mode field patterns and current distributions for some of the modes on the microstrip ring are shown in Figure 5.30 [51]. For $m = 1$, the field across the strip width is constant. For any given frequency, the mode corresponding to $n = m = 1$ (TM_{11} mode) has the minimum mean radius of the ring, and is known as the dominant mode. This mode is also sustained when a linear full-wave microstrip resonator is bent to form a circular resonator.

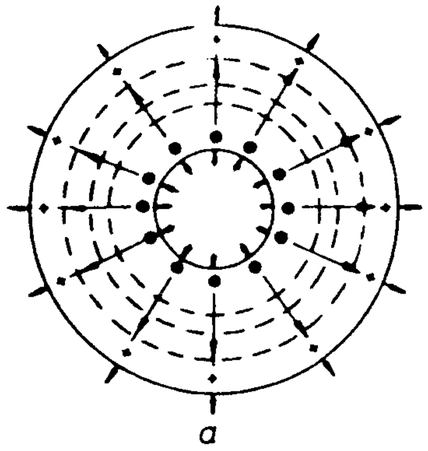

Figure 5.30 Field patterns and current distributions for some of the resonant modes of microstrip ring. (From [51]. © 1984 IEE. Reprinted with permission.)

The TM_{0m} modes (m even) would have no field variation in the ϕ direction, but would vary across the width of the strip. The TM_{02} mode is the lowest mode of this nature.

An approximate value of $k_{n1}a$ can also be obtained using:

$$k_{n1}a = 2an/(a + b)$$

This expression gives a reasonably accurate value of k_{n1} for $n \leq 5$ and $(b - a)/(b + a) < 0.35$ [18]. For more accurate calculations the roots, χ_{nm}, of the characteristic equation are given in Table 5.3 for $b/a = 2$.

For the general case, the solutions of (5.106) are presented in [55] in the form of a mode chart. It can be pointed out that for the microstrip ring antenna, (5.106) should be solved after replacing the radii a and b with their effective values. Calculations of the effective radii in terms of physical dimensions are discussed next.

5.6.2 Resonant Frequency

Several numerical techniques have been used for calculating the resonant frequencies of the circular ring [55, 56]. Approximate value of the resonant frequency can be obtained by following the approaches used for other patch antennas. To the zeroth-order approximation, the resonant frequency is obtained by setting

$$k = \chi_{nm}/a \tag{5.107}$$

or

Table 5.3
Roots χ_{nm} of the Characteristics Equation $J_n'(2\chi_{nm})Y_n'(\chi_{nm}) - J_n'(\chi_{nm})Y_n'(2\chi_{nm}) = 0$ [25]

m→ n↓	1	2	3	4	5
0	—	3.1966	5.6123	9.4445	12.5812
1	0.6773	3.2825	5.6532	9.4713	12.6012
2	1.3406	3.5313	6.4747	9.5516	12.6612
3	1.9789	3.9201	6.6738	9.6842	12.7607
4	2.5876	4.4182	6.9461	9.8677	12.8989
5	3.1694	4.9929	7.2868	10.1000	13.0750

$$f_{nm} = \frac{\chi_{nm} c}{2\pi a \sqrt{\epsilon_r}} \tag{5.108}$$

where c is the velocity of light in free space. So far the effect of fringing fields has not been accounted for. As a result, the frequency calculated using (5.108) is lower than the measured value. The accuracy can be improved if the effective dielectric constant ϵ_{re} is used in place of ϵ_r in (5.108), that is,

$$f_{nm} = \frac{\chi_{nm} c}{2\pi a \sqrt{\epsilon_{re}}} \tag{5.109}$$

To determine the value of ϵ_{re}, the ring resonator is modeled as a microstrip line bent in a circular shape. The effect of curvature on the resonant frequency is expected to be small provided the radius of curvature is large compared with the width of the strip conductor. In such a situation, the value of ϵ_{re} for the ring can be taken to be the same as that of an equivalent microstrip line with strip width equal to $W = b - a$. An approximate but quite accurate (within 1%) expression for ϵ_{re} of a microstrip line is given in Appendix B. Using this approach, the difference between the theoretical and measured values of the resonant frequency is found to be approximately 3% [55]. The accuracy of prediction can be further improved by using the parallel plate waveguide model of a microstrip line (Appendix B).

A parallel plate model of circular ring is shown in Figure 5.31. In this model, the microstrip line is replaced by an equivalent parallel plate waveguide with identical ϵ_{re} and Z_0. The parallel plate ring resonator is assumed to have the same arithmetic mean radius as the microstrip ring. The modified values of the inner and outer radii are given by

$$a_e = a - (W_e - W)/2 \tag{5.110a}$$

$$b_e = b + (W_e - W)/2 \tag{5.110b}$$

where W_e is the effective width of the ring conductor, and is given by (B.13). A pair of empirical formulas for the modified radii is given below [55]

$$a_e = a - 3h/4 \tag{5.111a}$$

$$b_e = b + 3h/4 \tag{5.111b}$$

For the given values of a and b, a_e and b_e are calculated using (5.110). Then (5.106) is solved by replacing a and b with a_e and b_e, respectively. After

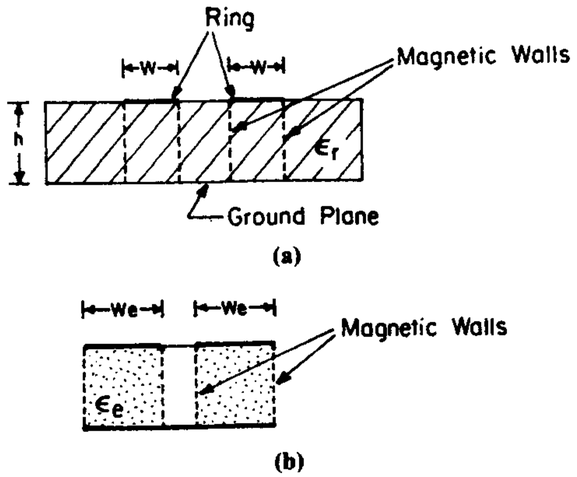

Figure 5.31 Parallel plate model of a microstrip ring: (a) Cross-sectional view of microstrip ring and (b) parallel plate model of part (a). (From [54]. © 1992 *International Journal of Microwave and Millimeter-Wave Computer-Aided Engineering.* Reprinted with permission.)

solving for χ_{nm}, the resonant frequency is determined from (5.109). It has been pointed out that this model gives reasonably accurate results as long as W_e is less than the mean diameter of the ring, $(a + b)$ [57]. Comparison of the calculated resonant frequencies based on the parallel plate waveguide model and the reaction method of [56] is shown in Table 5.4 [54] for TM_{11} and TM_{31} modes. The agreement between the two sets is very good. A curve-fitted expression for the resonant wave number k_{12} is given next [52]:

$$k_{12} = \frac{51.975 a_{es}}{(b_{es} - a_{es})(17.8 a_{es} - b_{es})} \tag{5.112a}$$

where

$$b_{es} = b\left(1 + \frac{2hX_b}{b\pi\epsilon_r}\right) \tag{5.112b}$$

$$a_{es} = a\left(1 - \frac{2hX_a}{a\pi\epsilon_r}\right) \tag{5.112c}$$

with

$$X_b = \ln\left(\frac{b}{2h}\right) + 1.41\epsilon_r + 1.77 + \frac{h}{b}(0.268\epsilon_r + 1.65) \tag{5.112d}$$

Table 5.4
Resonant Frequencies of Microstrip Ring Structures (ϵ_r = 9.85, h = 0.635 mm) [54]

W (cm)	R (cm)	Mode	f_{nm} (GHz) Reaction Method [56]	Parallel Plate Model
0.058	0.3	TM_{11}	6.17	6.211
	0.5	-do-	3.68	3.692
	1.0	-do-	1.829	1.832
	2.0	-do-	0.902	0.907
0.3175	0.3	TM_{11}	5.60	5.623
	0.5	-do-	3.43	3.441
	1.0	-do-	1.69	1.708
	2.0	-do-	0.82	0.823
0.058	0.5	TM_{31}	10.85	10.854
	1.0	-do-	5.47	5.532
	1.5	-do-	3.68	3.688
	2.0	-do-	2.74	2.770
0.3175	1.0	TM_{31}	5.00	5.065
	1.5	-do-	3.36	3.396
	2.0	-do-	2.45	2.553

The expression for X_a is obtained by replacing the radius b with a in (5.112d). Equation (5.112a) is valid for $k_{12}a_{es} > 0.73$. When compared with numerical results, the error in k_{12} is less than 0.12% over the range $1.3 \leq b_{es}/a_{es} \leq 3.0$. Further, it can be seen that in the asymptotic limit $b \rightarrow a$, (5.112) gives the ring width $W = b_{es} - a_{es} \cong \lambda_g/2$, which compares with the numerical solution of (5.106).

Figure 5.32 depicts the variations of the calculated resonant frequency as a function of the mean radius $R = (a + b)/2$, for various microstrip ring resonators on a Duroid substrate (ϵ_r = 2.32 and h = 0.159 cm) [54]. For TM_{n1} modes, the resonant frequency decreases with increasing R and W, and becomes independent of W for large values of R. However, for the TM_{02} mode the resonant frequency is almost constant with R, but decreases with increases in W.

5.6.3 Radiation Fields

The radiation fields of a circular ring antenna can be obtained either from the magnetic current approach or the electric current distribution on the surface

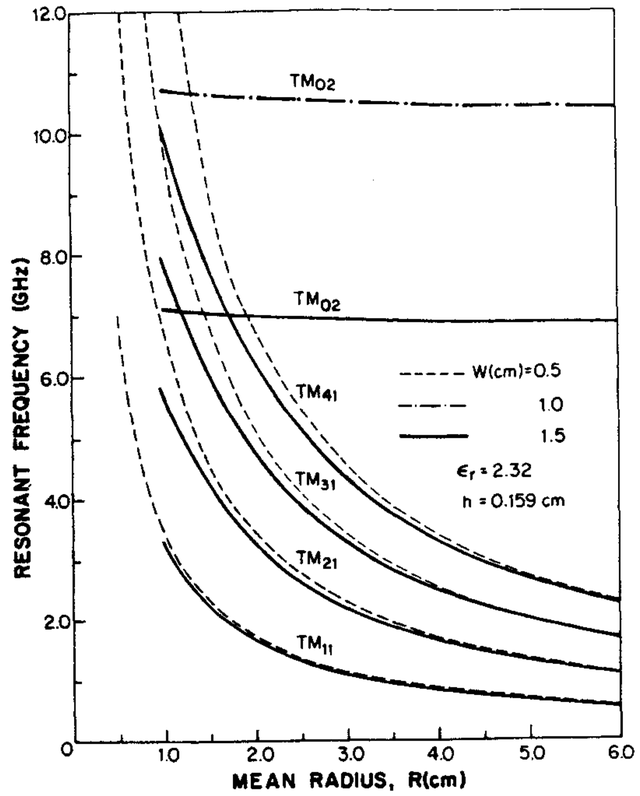

Figure 5.32 Resonant frequency versus mean radius R of the ring. (From [54]. © 1992 *International Journal of Microwave and Millimeter-Wave Computer-Aided Engineering.* Reprinted with permission.)

of the ring. We shall use the equivalent magnetic current formulation because of its simplicity. Calculations for the radiation fields of the ring are a straight forward extension of the approach used for the circular disk antenna. The only difference between the two cases is that in a circular ring there are two magnetic current sources compared to one for the circular disk. Radiation fields from the magnetic currents at $\rho = a$ and $\rho = b$ are calculated independently and added vectorially to obtain the radiation patterns for the ring antenna. The radiation fields due to the magnetic ring source at $\rho = a$ are obtained as [(5.17) and (5.18)]

$$E_\theta^a = j^n \frac{e^{-jk_0 r}}{r} ak_0 hE_{zn}(a) J_n'(k_0 a \sin\theta) \cos n\phi \tag{5.113}$$

and

$$E_\phi^a = -nj^n \frac{e^{-jk_0 r}}{r} \pi a k_0 h E_{zn}(a) \frac{J_n(k_0 a \sin\theta)}{k_0 a \sin\theta} \sin n\phi \cos\theta \qquad (5.114)$$

where for the TM_{nm} mode, (5.101) gives

$$E_{zn}(a) = E_0[J_n(k_{nm}a)Y_n'(k_{nm}a) - J_n'(k_{nm}a)Y_n(k_{nm}a)] \qquad (5.115)$$

$$= \frac{2E_0}{\pi k_{nm} a} \quad \text{(using the Wronskian for the Bessel equation)} \qquad (5.116)$$

The effect of ground plane is included in the derivations of (5.113) and (5.114), but it has been assumed that the magnetic current is constant along the radial direction. The radiation field due to the current source at $\rho = b$ is obtained by replacing a with b in (5.113) and (5.114), and $E_{zn}(a)$ with $-E_{zn}(b)$. The radiation patterns for the ring antenna are then given by

$$E_\theta = j^n \frac{e^{-jk_0 r}}{r} k_0 h [aE_{zn}(a)J_n'(k_0 a \sin\theta) - bE_{zn}(b)J_n'(k_0 b \sin\theta)] \cos n\phi \qquad (5.117a)$$

$$E_\phi = -nj^n \frac{e^{-jk_0 r}}{r} k_0 h \left[aE_{zn}(a) \frac{J_n(k_0 a \sin\theta)}{k_0 a \sin\theta} - bE_{zn}(b) \frac{J_n(k_0 b \sin\theta)}{k_0 b \sin\theta} \right] \sin n\phi \cos\theta \qquad (5.117b)$$

where

$$E_{zn}(b) = E_0[J_n(k_{nm}b)Y_n'(k_{nm}a) - J_n'(k_{nm}a)Y_n(k_{nm}b)] \qquad (5.118)$$

Use of the characteristic equation and the property of the Wronskian simplifies $E_{zn}(b)$ to

$$E_{zn}(b) = \frac{a}{b} \frac{2E_0}{\pi k_{nm} a} \frac{J_n'(k_{nm}a)}{J_n'(k_{nm}b)} \qquad (5.119)$$

Substituting for $E_{zn}(a)$ and $E_{zn}(b)$ in (5.117) gives [55]

$$E_\theta = j^n \frac{2E_0}{\pi k_{nm}} \frac{e^{-jk_0 r}}{r} k_0 h \left[J_n'(k_0 a \sin\theta) - \frac{J_n'(k_{nm}a)}{J_n'(k_{nm}b)} J_n'(k_0 b \sin\theta) \right] \cos n\phi \qquad (5.120a)$$

$$E_\phi = -nj^n \frac{2E_0}{\pi k_{nm}} \frac{e^{-jk_0 r}}{r} k_0 h \left[\frac{J_n(k_0 a \sin\theta)}{k_0 a \sin\theta} - \frac{J_n'(k_{nm}a)}{J_n'(k_{nm}b)} \frac{J_n(k_0 b \sin\theta)}{k_0 b \sin\theta} \right] \sin n\phi \cos\theta \qquad (5.120b)$$

where

$$k_{nm}a = \chi_{nm}$$

These expressions are identical to those given in [25]. The effect of radial variation of magnetic current on the radiation fields is discussed in [51]. The effect of the substrate can be accounted for through the correction factor $F_3(\theta)/2$ for the E-plane pattern, and $F_4(\theta)/2$ for the H-plane pattern. The factors $F_3(\theta)$ and $F_4(\theta)$ are defined in Section 4.3.3. Radiation patterns for the TM_{11}, TM_{12}, and TM_{13} modes are plotted in Figure 5.33 [51]. For the TM_{1m} modes (m odd), the fringing fields at the inner and outer apertures are of opposite polarity, giving rise to less radiation due to destructive interference. These modes, therefore, have narrow bandwidth. The aperture fields for the TM_{1m} modes (m even), are of the same polarity, making these modes good radiation modes. As the ratio b/a increases, the directivity of the antenna increases and the sidelobe level also increases. This is because for higher b/a ratios the two apertures are electrically far apart, giving rise to higher sidelobe levels. Thus, for higher order modes, the beamwidth of the radiation pattern decreases and sidelobe level increases as seen from Figure 5.33. It has been observed that TM_{nm} modes (n even) possess nulls in the broadside direction. Directivity of the circular ring for the TM_{11} and TM_{12} modes are plotted in Figure 5.34 for two values of ϵ_r and $b = 2a$ [25]. It is seen that the directivity is higher for the higher order mode and lower dielectric constant substrate.

Note that the cavity model predicts the resonant frequency and the input impedance of the antenna elements fairly accurately. However, the cavity model does not estimate the ratio of the aperture fields correctly, since the fields at the apertures are estimated from a standing wave distribution, in which all the points are in phase [45]. In fact, due to power radiation, the field inside the patch will be progressive in nature, and therefore a phase difference between the aperture fields will occur. An incorrect estimate of phase difference gives rise to a consequent error in beam position and the sidelobe level. The difference in phase is confirmed by the calculations carried out for an annular ring antenna.

The ratio of the electric field at the apertures is compared in Table 5.5. The calculations in the last column are based on the generalized transmission

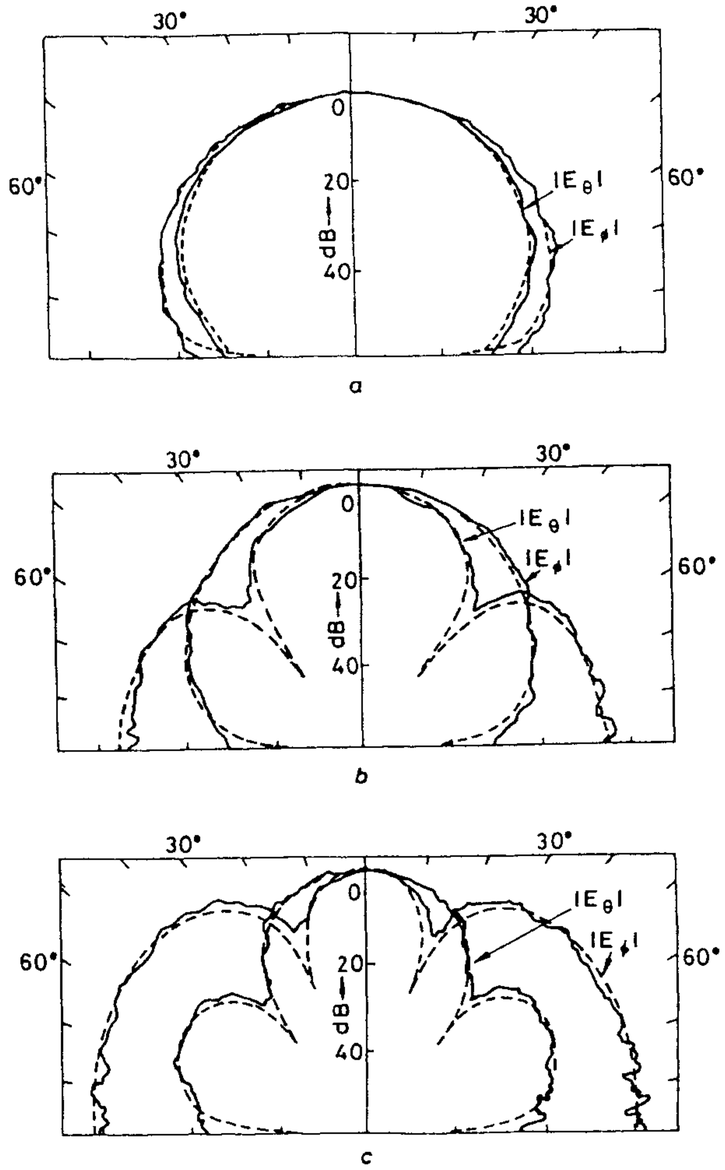

Figure 5.33 Radiation patterns for the TM_{11}, TM_{12}, and TM_{13} modes of a microstrip ring. (From [51]. © 1984 IEE. Reprinted with permission.)

line model (GTLM). Also shown in Table 5.5 is the effect of feed location on the ratio of aperture fields. This effect cannot be determined in the cavity model, because in this model the distribution of fields under the metalization remains unaltered with the feed location and only the amplitude of excitation changes. The phase error in the aperture fields may not affect the radiation pattern of an element considerably, but it can be intolerable in an array design.

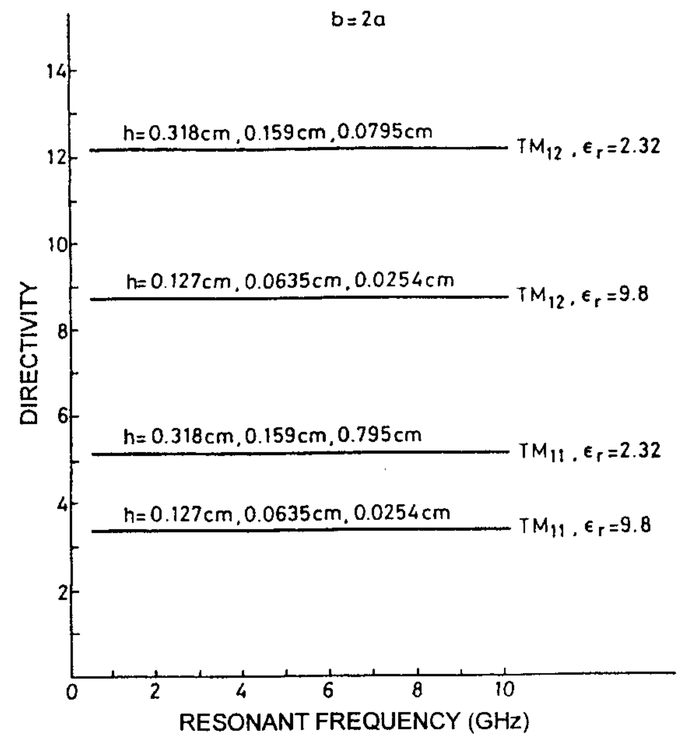

Figure 5.34 Directivity of the circular ring for TM_{11} and TM_{12} modes. (From [25]. © 1989 Peter Peregrinus. Reprinted with permission.)

Table 5.5
Ratio of the Aperture Fields $E_z(\rho = b)/E_z(\rho = a)$ for a Circular Ring Antenna Operating in the TM_{12} Mode (a = 2.2 cm, b = 4.4 cm, and ϵ_r = 2.2) [45]

Feed Location ρ_0 (cm)	Dielectric Thickness h (cm)	Ratio $E_z(\rho = b)/E_z(\rho = a)$ Cavity Model	GTLM
2.3	0.159	$-0.72\angle 0°$	$-0.6802\angle 1.33°$
3.2	0.159	$-0.72\angle 0°$	$-0.674\angle -25.2°$
3.6	0.320	$-0.71\angle 0°$	$-0.850\angle -50.2°$
3.6	0.480	$-0.70\angle 0°$	$-0.8523\angle -67.9°$
3.9	0.480	$-0.70\angle 0°$	$-0.726\angle -22.7°$

5.6.4 Losses, *Q*, and Resonant Resistance

Following the procedure given in Chapter 2, the dielectric loss, copper loss, radiated power, and total energy stored at resonance are given by the following expressions [25] and [58]:

$$P_d = \frac{\omega\epsilon\tan\delta}{2}\int\int\int_V \vec{E}\cdot\vec{E}\,dv$$

or

$$P_d = \frac{\omega\epsilon\tan\delta E_0^2\pi h}{2}\int_{a_e}^{b_e}[J_n(k_{nm}\rho)Y_n'(k_{nm}a_e) - J_n'(k_{nm}a_e)Y_n(k_{nm}\rho)]^2\rho d\rho$$

or

$$P_d = \frac{\omega\epsilon h\tan\delta}{\pi}\left(\frac{E_0}{k_{nm}}\right)^2\left[\left(\frac{J_n'(k_{nm}a_e)}{J_n'(k_{nm}b_e)}\right)^2\left(1-\frac{n^2}{k_{nm}^2b_e^2}\right)-\left(1-\frac{n^2}{k_{nm}^2a_e^2}\right)\right] \tag{5.121}$$

$$P_c = 2\frac{R_S}{2}\int_a^b\int_0^{2\pi}(|J_\phi|^2+|J_\rho|^2)\rho d\phi d\rho$$

or

$$P_c = \frac{2R_S}{\pi}\left(\frac{E_0}{\omega\mu_0}\right)^2\left[\left(\frac{J_n'(k_{nm}a)}{J_n'(k_{nm}b)}\right)^2\left(1-\frac{n^2}{k_{nm}^2b^2}\right)-\left(1-\frac{n^2}{k_{nm}^2a^2}\right)\right] \tag{5.122}$$

$$P_r = \frac{2\omega h}{\eta_0}\left(\frac{E_0k_0}{k_{nm}}\right)^2 I_1 \tag{5.123}$$

$$W_T = \frac{\epsilon}{2}\int\int\int_V \vec{E}\cdot\vec{E}\,dv = \frac{P_d}{\omega\tan\delta} \tag{5.124}$$

where the quantity I_1 is the integral

$$I_1 = \int_0^{\pi/2}\left[\frac{n^2\cos^2\theta}{k_0^2\sin\theta}\left(\frac{J_n(k_0a\sin\theta)}{a}-\frac{J_n'(k_{nm}a)}{J_n'(k_{nm}b)}\frac{J_n(k_0b\sin\theta)}{b}\right)^2\right. \tag{5.125}$$
$$\left.+\sin\theta\left(J_n'(k_0a\sin\theta)-\frac{J_n'(k_{nm}a)}{J_n'(k_{nm}b)}J_n'(k_0b\sin\theta)\right)^2\right]d\theta$$

The effective loss tangent is then given by

$$\delta_{\text{eff}} = \tan\delta + \frac{1}{h\sqrt{\sigma\mu_0\pi f}} + \frac{2\omega\mu_0 h}{\eta_0\epsilon_r}I_1 \tag{5.126}$$

$$Q_T = 1/\delta_{\text{eff}} \tag{5.127}$$

The radiation resistance at resonance can be calculated as

$$R_r = \frac{V_0^2}{2P_T}, \qquad P_T = P_r + P_c + P_d \tag{5.128}$$

where V_0 is the voltage at $\rho = b$, $\phi = 0$.

5.6.5 Input Impedance

Input impedance of a ring antenna can be determined by extending the techniques used for the circular disk (see Section 5.2). Here we use the cavity model approach of Section 5.2.1. Consider a circular ring microstrip antenna fed by a coaxial probe at $\rho = \rho_0$ from the center. The effect of the finite diameter of the probe is included by modeling it as a uniform current ribbon of angular width $2w_f$. The electric field in the ring cavity due to this excitation is obtained by the superposition of all the cavity modes with appropriate excitation coefficients, and is given by [52, 58]

$$E_z = j\omega\mu_0 I\left\{\sum_{n=0}^{\infty}\sum_{m=1}^{\infty}A_{nm}[J_n(k_{nm}\rho)Y_n'(k_{nm}a_e) - J_n'(k_{nm}a_e)Y_n(k_{nm}\rho)]\right\}\cos n\phi \tag{5.129a}$$

where

$$A_{nm} = \frac{k_{nm}^2 \pi \sin(2nw_f) \cos n\pi [J_n(k_{nm}\rho_0) Y_n'(k_{nm}a_e) - J_n'(k_{nm}a_e) Y_n(k_{nm}\rho_0)]}{\epsilon_{0n} n (k^2 - k_{nm}^2) \left[\frac{J_n'^2(k_{nm}a_e)}{J_n'^2(k_{nm}b_e)} \left(1 - \frac{n^2}{k_{nm}^2 b_e^2}\right) - \left(1 - \frac{n^2}{k_{nm}^2 a_e^2}\right) \right]} \tag{5.129b}$$

and

$$\epsilon_{0n} = \begin{cases} 1 & \text{for } n \neq 0 \\ 2 & \text{for } n = 0 \end{cases} \tag{5.129c}$$

The input impedance is now calculated by averaging over the feed angular width $2w_f$ and using the approach of (5.35) to (5.40). One obtains

$$Z_{\text{in}} = j\omega\mu_0 h \left\{ \sum_{n=0}^{\infty} \sum_{m=1}^{\infty} \frac{\pi k_{nm}^2 \left(\frac{\sin 2nw_f}{2nw_f}\right)^2 [J_n(k_{nm}\rho_0) Y_n'(k_{nm}a_e) - Y_n(k_{nm}\rho_0) J_n'(k_{nm}a_e)]^2}{2\epsilon_{0n} n (k_{\text{eff}}^2 - k_{nm}^2) \left[\frac{J_n'^2(k_{nm}a_e)}{J_n'^2(k_{nm}b_e)} \left(1 - \frac{n^2}{k_{nm}^2 b_e^2}\right) - \left(1 - \frac{n^2}{k_{nm}^2 a^2}\right) \right]} \right\} \cos^2 n\phi_0 \tag{5.130}$$

where a_e and b_e are the effective radii defined by (5.110) and

$$k_{\text{eff}} = k_0 \sqrt{\epsilon_{re}(1 - j\delta_{\text{eff}})} \tag{5.131}$$

A slightly different approach has been followed in [52] to determine the input impedance. In this approach equivalent circuit parameters L, C, and G for the parallel resonant circuit for the excited mode are determined. The input impedance is then given by

$$Z_{\text{in}} = \frac{1}{G + j\omega C + 1/(j\omega L)} \tag{5.132}$$

The calculated input impedance based on (5.130) and the measured values are compared in Figure 5.35 for the TM_{11} mode [58]. The agreement

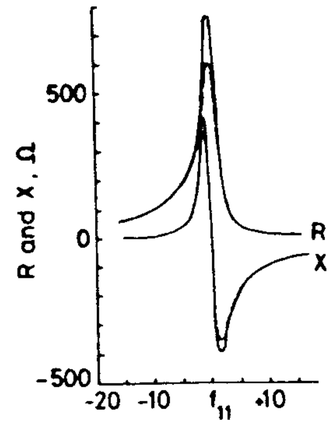

Figure 5.35 Comparison of computed and measured input impedance of a circular ring for the TM_{11} mode (a = 3.5 cm, b = 7.0 cm, h = 0.159 cm, ϵ_r = 2.32; ____, theory; ----, measurement). (From [58]. © 1985 IEE. Reprinted with permission.)

is found to be very good. The impedance bandwidth for this mode is 0.6% with calculated f_{11} = 622 MHz, measured f_{11} = 626 MHz, and δ_{eff} = 0.004. The effective feed width was chosen such that the calculated results provide the best fit with experiment. The value of w_f used was $\pi/10$. The input resistance for this mode is found to be insensitive to the feed position because for the m = 1 mode, the field across the strip width is constant (see Figure 5.30). The input resistance for the TM_{11} mode is high. Therefore, a direct feed like a probe feed or a microstrip feed will result in a high VSWR value. Electromagnetic coupling has been suggested in [59] to reduce the input VSWR.

The most promising feature of the circular ring microstrip antenna is its wider bandwidth for the TM_{12} mode, though the antenna size is also larger. The large bandwidth occurs because the radial variation of the electric field is such that it undergoes a phase reversal across the strip width as shown in Figure 5.30. It is observed that an accurate value of the input resistance is obtained only when the effect of substrate is included. For one set of parameters with ϵ_r = 2.2 and h = 0.159 cm, the input resistance was found to be higher by about 8% when the free-space Green's function was used [12]. In an analysis suitable for magnetic current modeling of microstrip antennas, the effect of substrate on wall admittance has been carried out rigorously [60, 61]. Figure 5.36 shows the comparison between measured and calculated values of input impedance with feed position as a parameter [11]. The generalized transmission line model was used for calculations. It was found that the larger bandwidth (about 5%) for ρ_0 = 3.1 cm is partly due to the excitation of higher order

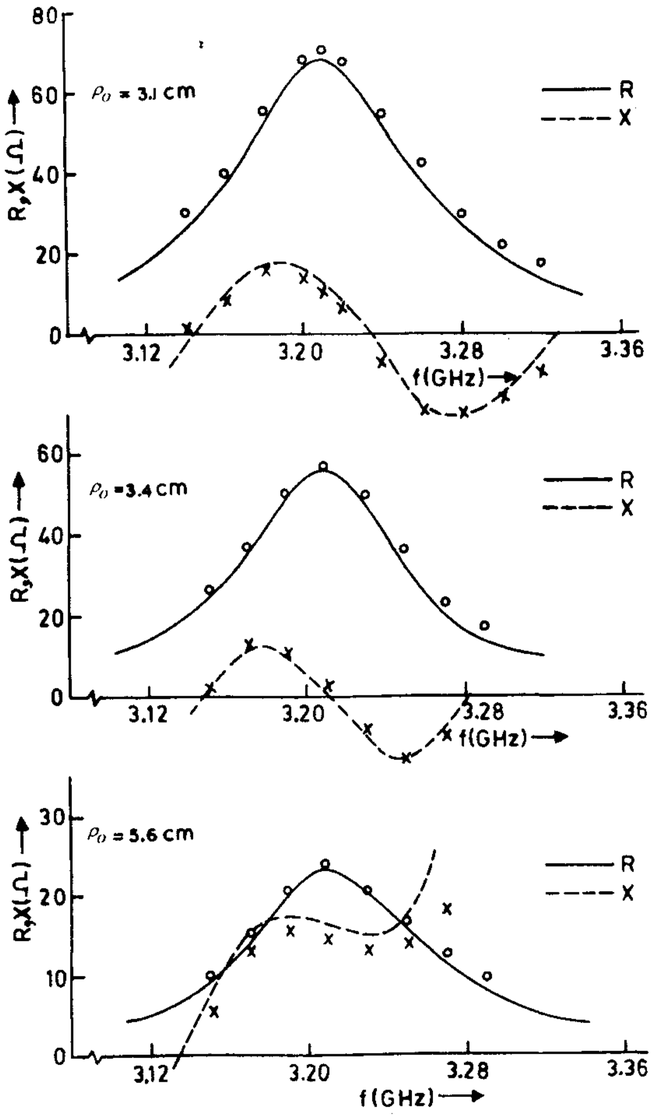

Figure 5.36 Comparison of computed and measured input impedance of a circular ring for the TM_{12} mode with feed position as a parameter (a = 3 cm, b = 6 cm, h = 0.159 cm, ϵ_r = 2.2; o, measured R; x, measured X. (From [11]. © 1985 IEEE. Reprinted with permission.)

modes in the vicinity. Comparison of computed and measured input impedance for the TM_{12} mode has also been carried out in [52]. It has been found that the calculated input resistance is slightly lower than the measured value due to the use of free-space Green's function.

Figure 5.37 shows the variation of input resistance at resonance with feed location for the TM_{12} mode [11]. As shown there, the input resistance first decreases, goes through a minimum, and then increases with increase in

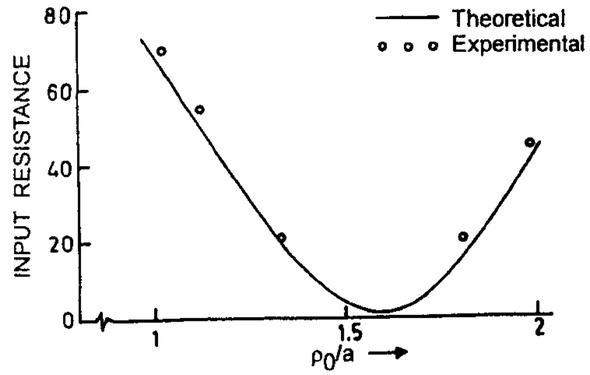

Figure 5.37 Variation of input resistance with feed location for the TM_{12} mode. Antenna parameters are the same as in Figure 5.36. (From [11]. © 1985 IEEE. Reprinted with permission.)

the value of ρ_0/a. This curve can be used for selecting the feed location. The behavior of the input resistance curve is consistent with the radial variation of the electric field shown in Figure 5.30 for this mode. The impedance bandwidth of the antenna as a function of b/a ratio is plotted in Figure 5.38 for the mode [11]. It is seen that the bandwidth decreases with the increase in b/a. This behavior can be explained on the basis of increase in Q due to the increase in stored energy as the ratio b/a increases.

5.6.6 Circular Microstrip Ring Antenna With a Dielectric Cover or Superstrate

In many applications, a dielectric cover is required over the microstrip antennas for protection against heat, physical damage, and the environment. Because

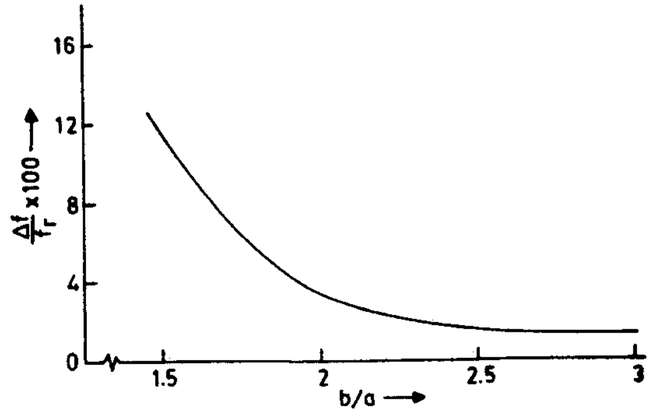

Figure 5.38 Impedance bandwidth (VSWR = 2) as a function of b/a for the TM_{12} mode (a = 3.2 cm, h = 0.159 cm, ϵ_r = 2.5). (From [11]. © 1985, IEEE. Reprinted with permission.)

the ring antenna can be modeled as a transmission line bent in a circular shape, the resonant frequency of the ring covered with a dielectric layer can be calculated using (5.109) and the new value of ϵ_{re} [62]. An equation for the effective dielectric constant of a microstrip line with a dielectric cover is given in Appendix B. For a matched antenna, the fractional change in resonant frequency with respect to the antenna without dielectric cover is defined as

$$\frac{\Delta f_r}{f_r} = \frac{f_r(d = 0) - f_r(d)}{f_r(d = 0)} \tag{5.133}$$

where d is the thickness of the dielectric cover over the ring antenna. Figure 5.39 depicts the fractional change in the resonant frequency as a function of the dielectric cover thickness [54]. The mode considered in the calculations is the dominant TM_{11} mode. The decrease in the resonant frequency for thin dielectric layers ($d < 10$ mm) and $W > 20$ mm is less than 1% and is independent of the resonant frequency.

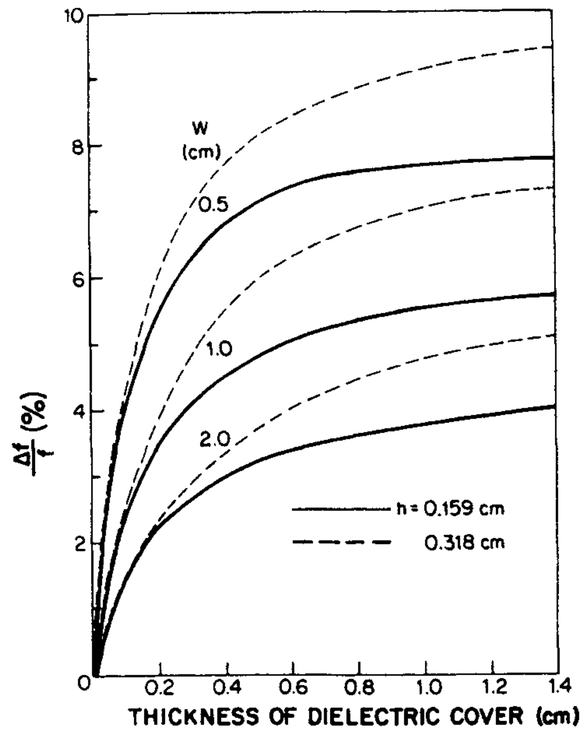

Figure 5.39 Fractional change in resonant frequency for the TM_{11} mode of a circular ring antenna with a dielectric cover. $\epsilon_r = 2.32$ for both the substrate and the superstrate. (From [54]. © 1992 *International Journal of Microwave and Millimeter-Wave Computer-Aided Engineering*. Reprinted with permission.)

5.6.7 Circular Microstrip Ring Antenna With an Air Gap

The geometry of a circular ring microstrip antenna with an air gap between the ground plane and the substrate is shown in Figure 5.40. The air-gap thickness is denoted by Δ and the dielectric substrate thickness by h. The presence of an air gap reduces the effective dielectric constant for the antenna, giving rise to an increase in resonant frequency and the impedance bandwidth. The adjustable air-gap thickness can be used to reduce the effective loss of a lossy substrate and to tune the antenna frequency. The new resonant frequency for the TM_{nm} mode is given by [25]

$$f_{nm}(\Delta) = f_{nm}(0)\sqrt{\epsilon_r/\epsilon_{reff}} \tag{5.134}$$

where $f_{nm}(0)$ is the resonant frequency when there is no air gap, and ϵ_{reff} is the effective permittivity of the two-layered medium:

$$\epsilon_{reff} = \frac{\epsilon_r(h + \Delta)}{(h + \Delta\epsilon_r)} \tag{5.135}$$

The new values of effective loss tangent and input impedance are given in [58]. The measured values of resonant frequency and the impedance bandwidth for three values of air-gap thicknesses are listed in Table 5.6 for the TM_{11} and TM_{12} modes.

5.7 Circular Sector Microstrip Ring Antennas

It can be advantageous in many applications to use shapes that are sectors of a circular ring. The geometry of a circular sector ring is shown in Figure 5.41. It consists of a curved microstrip line of sector angle α. The circular sector

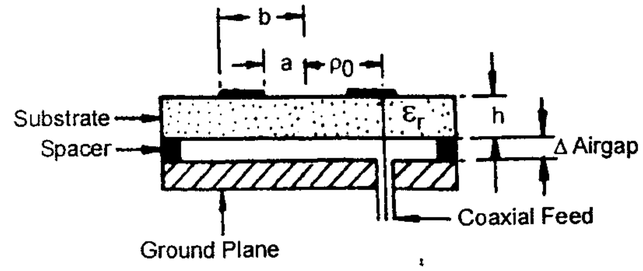

Figure 5.40 Cross section of a microstrip circular ring with an air gap. (From [58]. © 1985 IEE. Reprinted with permission.)

Table 5.6
Measured Resonant Frequencies and Impedance Bandwidths for a Circular Ring Antenna With an Air Gap of Thickness Δ (a = 3.5 cm, b = 7.0 cm, h = 0.159 cm, ρ_0/a = 1.05, and ϵ_r = 2.32) [58]

	Δ = 0		Δ = 0.5 mm		Δ = 1.0 mm	
Mode	f_{nm}	**% BW**	f_{nm}	**% BW**	f_{nm}	**% BW**
TM_{11}	626 MHz	0.6	720 MHz	0.7	778 MHz	0.8
TM_{12}	2757 MHz	4.0	3040 MHz	8.0	3240 MHz	8.6

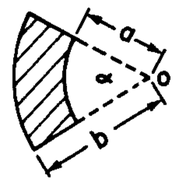

Figure 5.41 Geometry of a circular ring sector.

microstrip ring antenna has been analyzed using the cavity model [44] and generalized transmission line model [45]. The cavity model is easy to implement. The eigenfunctions for the TM_{mv} modes are

$$\psi_{mv} = [J_v(k_{mv}\rho)Y_v'(k_{mv}a) - J_v'(k_{mv}a)Y_v(k_{mv}\rho)]\cos v\phi \quad (5.136)$$

where $v = n\pi/\alpha$.

The analysis of the circular sector based on generalized transmission line is more rigorous. It also takes into account the radiation from the edges at $\phi = 0$ and $\phi = \alpha$. Impedance bandwidth of the circular sector ring antenna increases with the increase in the value of α, with the maximum occurring for $\alpha = \pi$. Circular sector microstrip ring antennas have been compared with rectangular patch antennas of almost the same size [12]. It has been observed that there is no particular advantage gained by using a circular sector ring antenna where a rectangular patch can be deployed.

5.8 Microstrip Ring Antennas With Noncircular Shapes

Ring microstrip antennas that have noncircular shapes have also been studied. These shapes include rectangular, square, triangular, and other polygonal shapes [46, 63–69]. The properties of rectangular-, square-, and triangular-shaped

rings are similar to that of a circular ring, that is, resonance frequency and bandwidth decrease with the decrease in the width of the strip. The input resistance, however, increases with the decrease in the strip width because the power radiated also decreases.

The effect of finite ground plane size on the directivity of a square ring microstrip antenna has been studied by Moosavi and Shafai [66]. A set of computed results is plotted in Figure 5.42. It is seen that when the ground plane size is about the ring size, the directivity is at a minimum. It increases initially on increasing the ground plane size, and exceeds well beyond infinite ground plane directivity. It reaches a maximum when the size is $1.1\lambda_0$, starts decreasing, and thereafter oscillates about the infinite ground plane value. The gain enhancement for this case was about 1.5 dB over the directivity for the infinite ground plane case.

A polygonal ring antenna with interesting properties has been developed by Cai and Ito [68, 69]. The geometry of the polygonal rings, end-driven type and center-driven type, are shown in Figure 5.43 [68]. The dimensions shown there are in millimeters and the frequency is 3.3 GHz. The inner perimeter of the end-driven type is about $3/4\lambda_0$. The center-driven type ring can be formed by connecting two end-driven type rings symmetrically at their feed points. Therefore, the inner perimeter is about $3/2\lambda_0$. This antenna has the following features [68]:

1. The center slot formed by the inner edge of the polygonal ring acts as a slot antenna.
2. The radiation pattern of the antenna is mainly determined by the radiation from the center slot.
3. The width of the ring strip can be tailored to obtain the desired input impedance. In this way, the radiation and impedance characteristics can be almost independently controlled.

The antenna was analyzed using the integral equation in the spectral domain. The ring metalization was divided into a number of small cells, and roof-top type basis functions were used. Radiation patterns for an end-driven type ring antenna are shown in Figure 5.44 [68]. It is seen that the cross-polarized component in this antenna is only about −10 dB. Radiation patterns of the center-driven type ring are plotted in Figure 5.45. In this case, the cross-polar component is much lower due to the symmetry of the structure. The gain of this antenna is 9.5 dB and the impedance bandwidth is about 20% for a reference impedance of 150 ohm.

A circularly polarized antenna with omnidirectional pattern in the plane of the ring and conical beam in the vertical plane has been configured by using

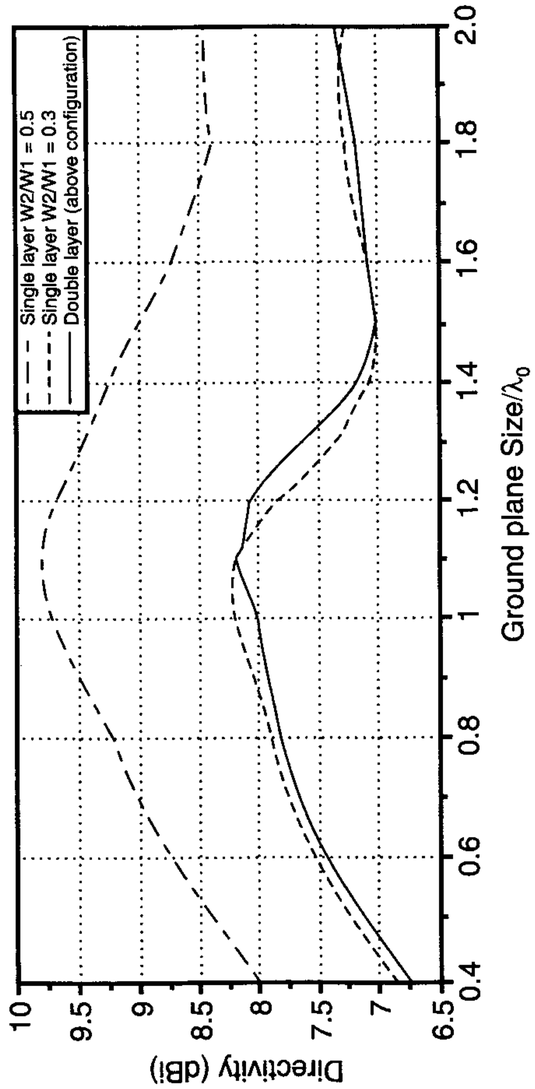

Figure 5.42 Directivity variation for a microstrip square ring antenna with the finite ground plane size (W_1 = 30 mm, h = 3.2 mm, ϵ_r = 2.5). (From [66]. © 1998 IEEE. Reprinted with permission.)

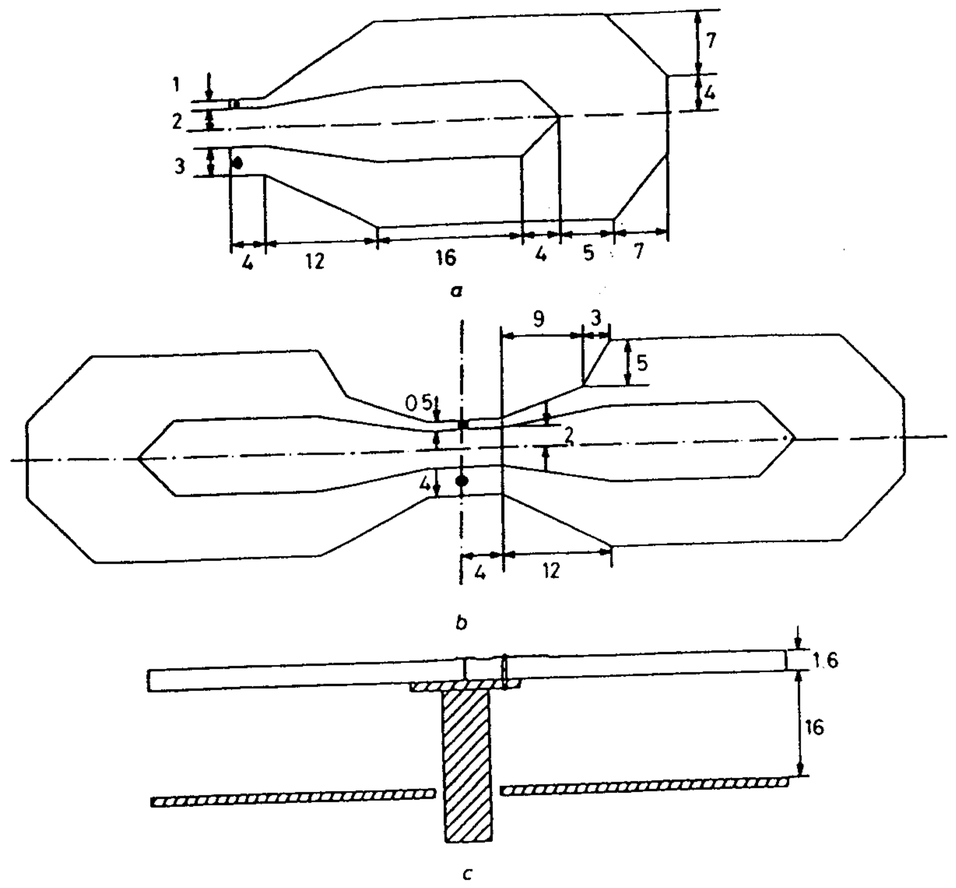

Figure 5.43 Geometry of a microstrip polygonal ring antenna. All dimensions are in millimeters. (a) End-driven type, (b) center-driven type, and (c) side view for part (b). (From [68]. © 1991 IEE. Reprinted with permission.)

four rings. This geometry is shown in Figure 5.46 [68]. The diameter of this antenna is about one wavelength at the operating frequency. A circularly polarized antenna with a broadside beam can be obtained easily [68] by changing the connections at the feed point in Figure 5.46.

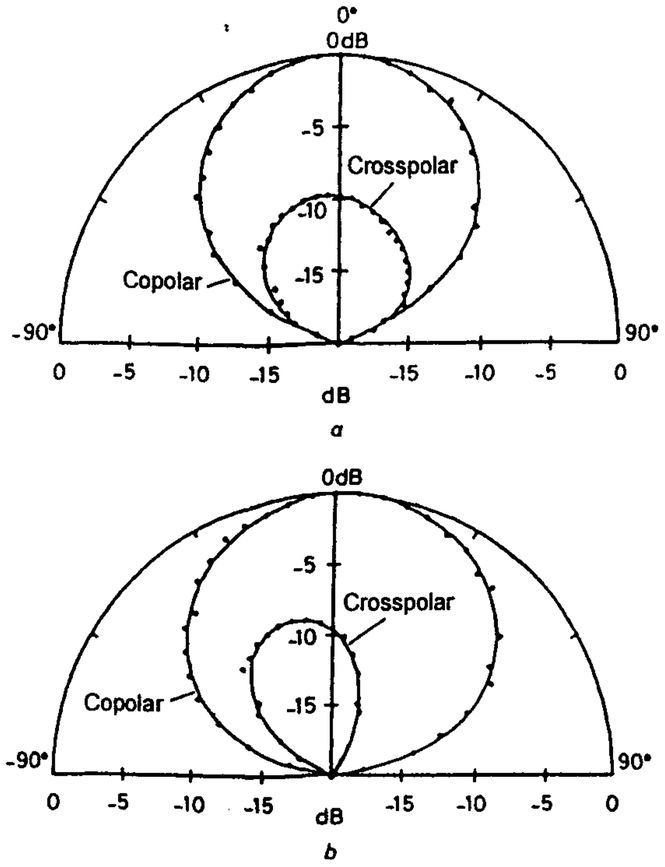

Figure 5.44 Radiation patterns of an end-driven polygonal ring microstrip antenna (___, computed; ...., experimental). (a) Radiation pattern in *y-z* plane and (b) radiation pattern in *x-z* plane. (From [68]. © 1991 IEE. Reprinted with permission.)

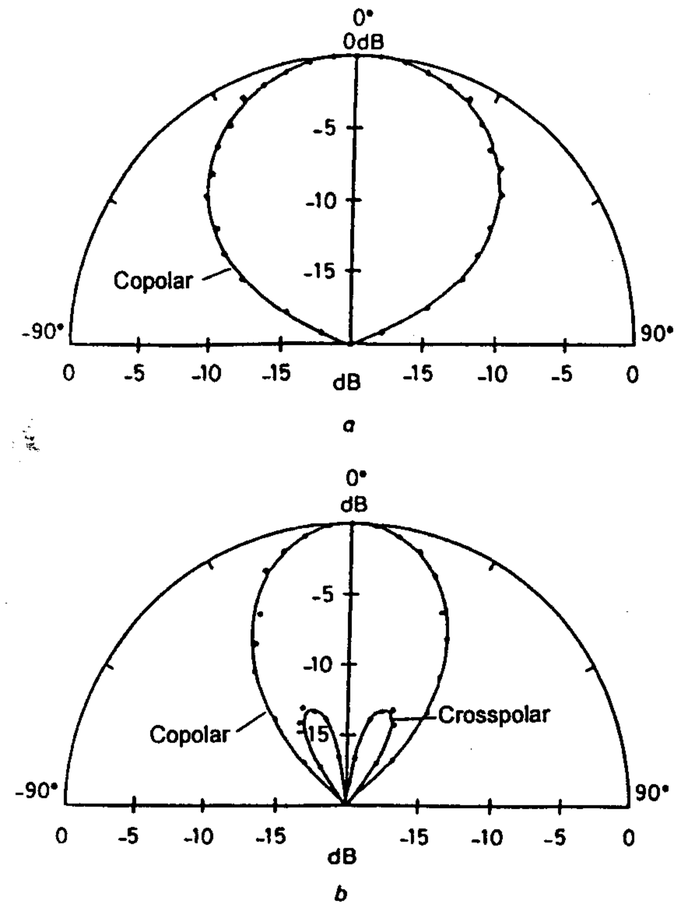

Figure 5.45 Radiation patterns of a center-driven polygonal ring microstrip antenna (___, computed; ...., experimental). (a) Radiation pattern in *y-z* plane and (b) radiation pattern in *x-z* plane. (From [68]. © 1991 IEE. Reprinted with permission.)

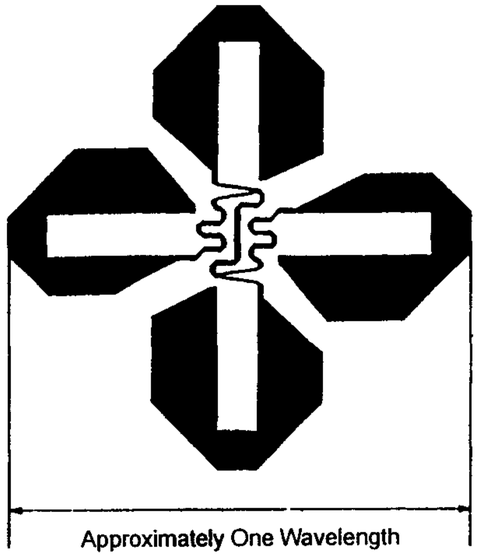

Figure 5.46 Arrangement of four polygonal ring microstrip antennas to produce a circularly polarized, omnidirectional conical beam. (From [68]. © 1991 IEE. Reprinted with permission.)

References

[1] Watkins, J., "Circular Resonant Structures in Microstrip," *Electron. Lett.*, Vol. 5, 1969, pp. 524–525.

[2] Shen, L. C., et al., "Resonant Frequency of a Circular Disk Printed-Circuit Antenna," *IEEE Trans. on Antennas and Propagation*, Vol. AP-25, 1977, pp. 595–596.

[3] Long, S. A., L. C. Shen, and P. B. Morel, "Theory of the Circular Disk Printed-Circuit Antenna," *Proc. IEE*, Vol. 125, 1978, pp. 925–928.

[4] Long, S. A., et al., "Impedance of a Circular Disk Printed-Circuit Antenna," *Electron. Lett.*, Vol. 14, 1978, pp. 684–686.

[5] Lo, Y. T., D. Solomon, and W. F. Richards, "Theory and Experiment on Microstrip Antennas," *IEEE Trans. on Antennas and Propagation*, Vol. AP-27, 1979, pp. 137–145.

[6] Derneryd, A. G., "Analysis of the Microstrip Disk Antenna Element," *IEEE Trans. on Antennas and Propagation*, Vol. AP-27, 1979, pp. 660–664.

[7] Shen, L. C., "Analysis of a Circular-Disk Printed-Circuit Antenna," *Proc. IEE*, Vol. 126, 1979, pp. 1220–1222.

[8] Yano, S., and A. Ishimaru, "A Theoretical Study of the Input Impedance of a Circular Microstrip Disk Antenna," *IEEE Trans. on Antennas and Propagation*, Vol. AP-29, 1981, pp. 77–83.

[9] Bhattacharyya, A. K., "Characteristics of Circular Patch on Thick Substrate and Superstrate," *IEEE Trans.*, Vol. 39, 1991, pp. 1038–1041.

[10] Bhattacharyya, A. K., and R. Garg, "Generalised Transmission Line Model for Microstrip Patches," *IEE Proc.*, Vol. 132, Pt. H, 1985, pp. 93–98.

[11] Bhattacharyya, A. K., and R. Garg., "Input Impedance of Annular Ring Microstrip Antenna Using Circuit Theory Approach," *IEEE Trans. on Antennas and Propagation*, Vol. AP-33, 1985, pp. 369–374.

[12] Bhattacharyya, A. K, "Generalized Transmission Line Model of Microstrip Patch Antennas and Some Applications," Ph.D. Thesis, Indian Institute of Technology, Kharagpur, India, 1985.

[13] Chew, W. C., and J. A. Kong, "Analysis of a Circular Microstrip Disk Antenna With a Thick Dielectric Substrate," *IEEE Trans. on Antennas and Propagation*, Vol. AP-29, 1981, pp. 68–76.

[14] Araki, K., and T. Itoh, "Hankel Transform Domain Analysis of Open Circular Microstrip Radiating Structures," *IEEE Trans. on Antennas and Propagation*, Vol. AP-29, 1981, pp. 84–89.

[15] Wu, K.-L., et al., "Full Wave Analysis of Arbitrarily Shaped Line-Fed Microstrip Antennas Using Triangular Finite-Element Method," *IEE Proc.*, Vol. 138, Pt. H, 1991, pp. 421–428.

[16] Turner, G. M., and C. G. Christodoulu, "Finite Difference Time Domain Analysis of Circular Microstrip Antennas," *IEEE AP-S Int. Symp. Digest*, 1996, pp. 1292–1295.

[17] Griffin, J. M., and P. R. Cowles, "Modelling of Microstrip Disk Antennas," *Fourth Int. Conf. on Antennas and Propagation, ICAP 85*, Pub. No. 248, 1985.

[18] Bahl, I. J., and P. Bhartia, *Microstrip Antennas*, Artech House, Dedham, MA, 1980, Chap. 3.

[19] Chew, W. C., J. A. Kong, and L. C. Shen, "Radiation Characteristics of a Circular Microstrip Antenna," *J. Appl. Phys.*, Vol. 51, 1980, pp. 3907–3915.

[20] Richards, W. F., Y. T. Lo., and D. D. Harrison, "An Improved Theory for Microstrip Antennas and Applications," *IEEE Trans. on Antennas and Propagation*, AP-29, 1981, pp. 38–46.

[21] Dahele, J. S., and K. F. Lee, "Effect of Substrate Thickness on the Performance of a Circular-Disk Microstrip Antenna," *IEEE Trans. on Antennas and Propagation*, Vol. AP-31, 1983, pp. 358–360.

[22] Chew, W. C., and J. A. Kong, "Effect of Fringing Fields on the Capacitance of Circular Microstrip Disc," *IEEE Trans. on Microwave Theory and Techniques*, Vol. MTT-28, 1980, pp. 98–104.

[23] James, J. R., P. S. Hall, and C. Wood, *Microstrip Antennas: Theory and Design*, Peter Peregrinus, London, UK, 1981.

[24] Hall, P. S., "Probe Compensation in Thick Microstrip Patches," *Electron. Lett.*, Vol. 23, 1987, pp. 606–607.

[25] James, J. R., and P. S. Hall (Eds.), *Handbook of Microstrip Antennas*, Peter Peregrinus, London, UK, 1989.

[26] Huang, J., "Circularly Polarized Conical Patterns From Circular Microstrip Antennas," *IEEE Trans. on Antennas and Propagation*, Vol. AP-32, 1984, pp. 991–994.

[27] Kishk, A. A., and L. Shafai, "The Effect of Various Parameters of Circular Microstrip Antennas on Their Radiation Efficiency and the Mode Excitation," *IEEE Trans. on Antennas and Propagation*, Vol. AP-34, 1986, pp. 969–977.

[28] Bhattacharyya, A. K., "Effects of Finite Ground Plane on the Radiation Characteristics of a Circular Patch Antenna," *IEEE Trans*, Vol. AP-38, 1990, pp. 152–159.

[29] Bhattacharyya, A. K., "Effects of Ground Plane and Dielectric Truncations on the Efficiency on the Efficiency of a Printed Structure," *IEEE Trans. on Antennas and Propagation*, Vol. AP-39, 1991, pp. 303–308.

[30] Bhattacharyya, A. K., "Effects of Ground Plane Truncation on the Impedance of a Patch Antenna," *IEE Proc.*, Vol. 138, Pt. H, 1991, pp. 560–564.

[31] Dey, S., et al., "Modified Circular Patch Antenna," *Electron. Lett.*, Vol. 29, 1993, pp. 1126–1127.

[32] Kumar, M. D., et al., "A Peripherally Fed Broadband Modified Circular Microstrip Antenna," *IEEE AP-S Int. Symp. Digest*, 1996, pp. 37–40.

[33] Wong, K. L., and Y.-F. Lin, "Microstrip Line Fed Compact Microstrip Antenna With Broadband Operation," *IEEE AP-S Int. Symp. Digest*, 1998, pp. 1120–1123.

[34] Lee, K. F., K. M. Luk, and P. Y. Tam, "Crosspolarisation Characteristics of Circular Patch Antennas," *Electron. Lett.*, Vol. 28, 1992, pp. 587–589.

[35] Lee, K.-F., K. Y. Ho, and J. S. Dahele, "Circular-Disk Microstrip Antenna With an Air Gap," *IEEE Trans. on Antennas and Propagation*, Vol. AP-32, 1984, pp. 880–884.

[36] Alexopoulos, N. G., and D. R. Jackson, "Fundamental Superstrate (Cover) Effects on Printed Circuit Antennas," *IEEE Trans. on Antennas and Propagation*, Vol. AP-32, 1984, pp. 807–816.

[37] *Electromagnetics*, Vol. 14, No. 1, 1994.

[38] Shively, D. G., et al., "Scattering From Microstrip Patch Antennas Using Sub-Domain Basis Functions," *Electromagnetics*, Vol. 14, 1994, pp. 1–18.

[39] Bokhari, S. A., J. R. Mosig, and F. E. Gardiol, "Radar Cross Section Computation of Microstrip Patches," *Electromagnetics*, Vol. 14, 1994, pp. 19–31.

[40] Michalski, K., and C.-I. G. Hsu, "RCS Computation of Coax-Loaded Microstrip Patch Antennas of Arbitrary Shape," *Electromagnetics*, Vol. 14, 1994, pp. 32–62.

[41] Aberle, J. T., D. M. Pozar, and C. R. Birtcher, "Evaluation of Input Impedance and Radar Cross Section of Probe-Fed Microstrip Patch Elements Using an Accurate Feed Model," *IEEE Trans. on Antennas and Propagation*, Vol. AP-39, 1991, pp. 1691–1696.

[42] Sainati, R. A., *CAD of Microstrip Antennas for Wireless Applications*, Artech House, Norwood, MA, 1996.

[43] Lo, Y. T., et al., "Study of Microstrip Antennas, Microstrip Phased Arrays, and Microstrip Feed Networks," Technical Report RADC-TR-77-406, Electromagnetics Lab., University of Illinois at Urbana–Champaign, Oct. 1977.

[44] Richards, W. F., J. D. Ou, and S. A. Long, "A Theoretical and Experimental Investigation of Annular, Annular Sector, and Circular Sector Microstrip Antennas," *IEEE Trans. on Antennas and Propagation*, Vol. AP-32, 1984, pp. 864–867.

[45] Bhattacharyya, A. K., and R. Garg, "Analysis of Annular Sector and Circular Sector Microstrip Patch Antennas," *Electromagnetics*, Vol. 6, 1986, pp. 229–242.

[46] Shafai, L., "Characteristics of Printed Ring Microstrip Antennas," *ANTEM'96*, pp. 379–382.

[47] Mink, J. W., "Circular Ring Microstrip Antenna Elements," *IEEE AP-S Int. Symp. Digest*, 1980, pp. 605–608.

[48] Wolf, I., and N. Knoppik, "Microstrip Ring Resonator and Dispersion Measurement on Microstrip Lines," *Electron. Lett.*, Vol. 7, 1971, pp. 779–781.

[49] Bahl, I. J., S. S. Stuchly, and M. A. Stuchly, "A New Microstrip Radiator for Medical Applications," *IEEE Trans. on Microwave Theory and Techniques*, Vol. MTT-28, 1980, pp. 1464–1468.

[50] Chew, W. C., "A Broad-Band Annular-Ring Microstrip Antenna," *IEEE Trans. on Antennas and Propagation*, Vol. AP-30, 1982, pp. 918–922.

[51] Das, A., S. K. Das, and S. P. Mathur, "Radiation Characteristics of Higher Order Modes in Microstrip Ring Antenna," *IEE Proc.*, Vol. 131, Pt. H, 1984, pp. 102–106.

[52] Bhattacharyya, A., and R. Garg, "Analysis of Annular Ring Microstrip Antenna Using Cavity Model," *Arch. Elek. Ubertragung.*, Vol. 39, 1985, pp. 185–189.

[53] Ali, S. M., W. C. Chew., and J. A. Kong., "Vector Hankel Transform Analysis of Annular-Ring Microstrip Antenna," *IEEE Trans. on Antennas and Propagation*, Vol. AP-30, 1982, pp. 637–644.

[54] Bahl, I. J., and S. S. Stuchly, "Closed-Form Expressions for Computer-Aided Design of Microstrip Ring Antennas," *Int. J. of Microwave and Millimeter-Wave Computer-Aided Engineering*, Vol. 2, 1992, pp. 144–154.

[55] Wu, Y. S., and F. J. Rosenbaum, "Mode Chart for Microstrip Ring Resonators," *IEEE Trans. on Microwave Theory and Techniques*, Vol. MTT-21, 1973, pp. 487–489.

[56] Pintzos, S. G., and R. Pregla, "A Simple Method for Calculating the Resonant Frequencies of Microstrip Ring Resonators," *IEEE Trans. on Microwave Theory and Techniques*, Vol. MTT-26, 1978, pp. 809–813.

[57] Kompa, G., and R. Mehran, "Planar-Waveguide Model for Calculating Microstrip Components," *Electron. Lett.*, Vol. 11, 1975, pp. 459–460.

[58] Dahele, J. S., and K. F. Lee, "Theory and Experiment on Microstrip Antennas With Airgaps," *IEE Proc.*, Vol. 132, Pt. H, 1985, pp. 455–460.

[59] Tsai, M.-J., and N. G. Alexopoulos, "Electromagnetically Coupled Microstrip Ring-Type Antennas of Arbitrary Shape," *IEEE AP-S Int. Symp. Digest*, 1995, pp. 684–687.

[60] Bhattacharyya, A. K., and R. Garg, "Spectral Domain Analysis of Wall Admittances for Circular and Annular Microstrip Patches and the Effect of Surface Waves," *IEEE Trans. on Antennas and Propagation*, Vol. AP-33, 1985, pp. 1067–1073.

[61] Bhattacharyya, A. K., *Electromagnetic Fields in Multilayered Structures: Theory and Applications*, Artech House, Norwood, MA, 1994.

[62] Bahl, I. J., P. Bhartia, and S. S. Stuchly, "Design of Microstrip Antennas Covered With a Dielectric Layer," *IEEE Trans. on Antennas and Propagation*, Vol. AP-30, 1982, pp. 314–318.

[63] Palanisamy, V., and R. Garg, "Rectangular Ring and H-Shaped Microstrip Antennas: Alternatives to Rectangular Patch Antenna," *Electron. Lett.*, Vol. 21, 1985, pp. 874–876.

[64] Palanisamy, V., and R. Garg, "Analysis of Circularly Polarized Ring and Crossed Strip Microstrip Antennas," *IEEE Trans. on Antennas and Propagation*, Vol. AP-34, 1986, pp. 1340–1346.

[65] Moosavi, P., and L. Shafai, "Characteristics and Design of Microstrip Square Ring Antennas," *Fifth Iranian Conf. on Electrical Engineering, ICEE97*, Tehran, 1997.

[66] Moosavi, P., and L. Shafai, "Directivity of Microstrip Ring Antennas and Effects of Finite Ground Plane on the Radiation Parameters," *IEEE AP-S Int. Symp. Digest*, 1998, pp. 672–675.

[67] Misra, I. S., and S. K. Chowdhury, "Study of Impedance and Radiation Properties of a Concentric Microstrip Triangular-Ring Antenna and Its Modeling Techniques Using FDTD Method," *IEEE Trans.*, Vol. 46, 1998, pp. 531–537.

[68] Cai, M., and M. Ito, "New Type of Printed Polygonal Loop Antenna," *IEE Proc.-H*, Vol. 138, 1991, pp. 389–396.

[69] Cai, M., and M. Ito, "Combined Polygonal Loop Antenna With Circularly Polarized Conical Pattern," *Electron. Lett.*, Vol. 17, 1989, pp. 1141–1142.

6

Dipoles and Triangular Patch Antennas

Dipole antennas are perhaps the oldest of all types of antennas. The printed dipole, on the other hand, came into being only after successful demonstration of the operation of the rectangular patch antenna. However, printed dipoles have found widespread usage in array antennas because they occupy less area compared to other microstrip antennas. Various types of printed dipoles are studied in this chapter. The bow-tie dipole can achieve 40% impedance bandwidth. The printed dipole is treated as a narrow rectangular patch to arrive at the design principles. Its characteristics are studied with an emphasis on design. Equilateral triangular patch antennas are discussed in the second half of the chapter. Cavity model analysis of this antenna is described in detail. Characteristics of a triangular patch are similar to those of rectangular and circular patch antennas.

6.1 Microstrip Dipole and Center-Fed Dipoles

Rectangular microstrip antennas can be classified into two main categories depending on their length-to-width ratio. An antenna with a narrow rectangular strip (typically strip width less than $0.05\lambda_0$) is called a *microstrip dipole*, whereas a broad rectangular antenna is called a *microstrip patch*. In addition to the microstrip dipole, another popular configuration is the *center-fed dipole*. This geometry is a printed version of the free-space cylindrical dipole and will be called a *printed dipole*. The basic dipole geometries are shown in Figure 6.1. Figure 6.1(a) shows a typical center-fed printed dipole with a feed line. Figure 6.1(b) shows the dipole configuration of part (a) with rectangular dipole strips replaced by triangular strips. In Figure 6.1(c) the coplanar strip conductors of

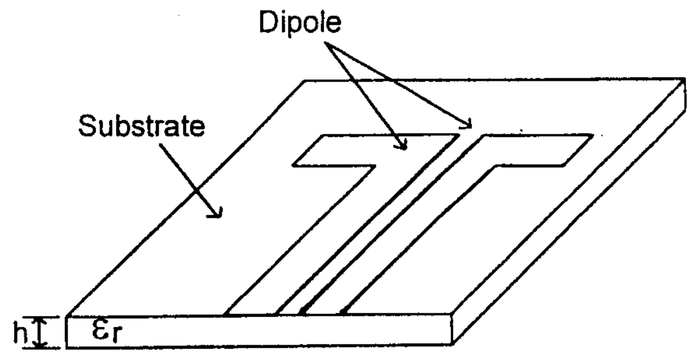

(a)

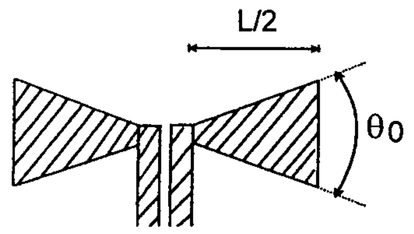

(b)

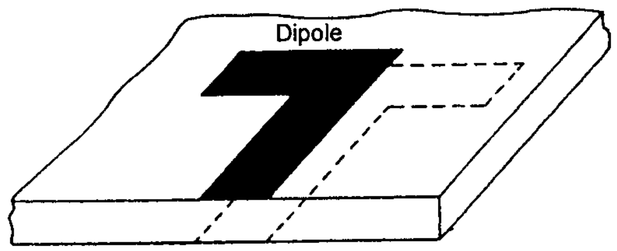

(c)

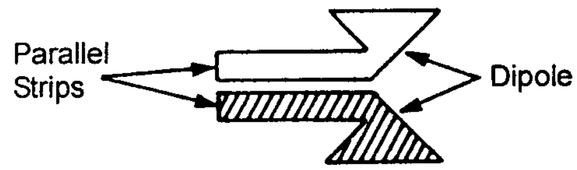

(d)

Figure 6.1 Basic printed dipole and microstrip dipole geometries: (a) Center-fed coplanar strips dipole. (b) Dipole geometry of part (a) with rectangular strips replaced by triangular strips; also called uniplanar bow-tie antenna. (c) Double-sided printed dipole. (d) Dipole geometry of part (c) with rectangular strips replaced by triangular strips; also called bow-tie antenna. The dipole strips are shown separated for clarity. (e) Microstrip dipole.

Figure 6.1 (continued).

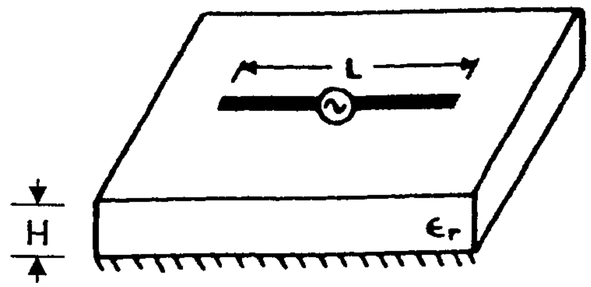

(e)

Figure 6.1 (continued).

part (a) are printed on the opposite surfaces of a dielectric sheet to simplify the feed arrangement. The strip conductors have been changed from the rectangular shape to a triangular shape in Figure 6.1(d) to improve the bandwidth of the dipole antenna. The microstrip dipole, with no feed gap, is shown in Figure 6.1(e). The center-fed dipole antenna is generally suspended in front of a metal reflector to produce unidirectional radiation. The dipole to reflector spacing H is typically $0.01 < H/\lambda_0 < 0.1$.

The geometries of Figures 6.1(b) and (d) are sometimes called *bow-tie antennas*. The linear taper in these geometries is described by the opening angle θ_0, and gives rise to gradual impedance transformation resulting in a wider bandwidth. It has been found that there is an optimum angle for which the bandwidth is maximum. The length of the dipole is denoted by L. A uniplanar bow-tie antenna [Figure 6.1(b)] with a coplanar waveguide (CPW) feed has been reported [1]. This antenna utilizes a CPW-to-CPS transition, an optimum angle $\theta_0 = 90°$, $L/2 = 0.965$ in, and is fabricated on an FR-4 substrate ($\epsilon_r = 4.8$) of thickness 63 mil. The measured VSWR = 2 bandwidth is 36% at the 2.44-GHz band. The authors of the uniplanar bow-tie antenna have also studied a double-sided bow-tie antenna of the type shown in Figure 6.1(d). The antenna was fed by a microstrip line with a balun between the microstrip and the parallel strips feed. Using the same substrate (FR-4) of thickness 63 mil and an angle of 90°, the VSWR = 2 bandwidth achieved was 40% [2]. For comparison, the dipole with rectangular strips ($\theta_0 = 0°$) yielded a bandwidth of only 20% [2]. This establishes the bandwidth enhancing feature of the triangular strips. The double-sided bow-tie antenna element has been used to develop a monopulse dipole array [3] and a printed circuit cylindrical array antenna [4]. The cylindrical array provides 360° azimuth coverage over an operating bandwidth of 1 GHz (16.0 to 17.0 GHz) with 20-dB sidelobes. The array consists of 16 facets of 2 × 4 dipole array modules.

Microstrip Dipole Versus Microstrip Patch

The geometries of the dipole and the rectangular patch being similar, their radiation characteristics are also expected to be similar except for those features that depend on the width-to-length ratio. The gap size in the dipole does not affect the characteristics as long as it is smaller than a wavelength. The longitudinal current distributions for the fundamental mode are similar on both structures. Therefore, their radiation patterns and gains are also similar. The resonant lengths are slightly different because of the dependence of effective dielectric constant on the strip width. However, the input impedance, bandwidth, and cross-polar radiation can differ widely. Advantages of the dipole are that it occupies less substrate area compared to the patch, and the cross-polar component is also lower because the transverse current component on the strip decreases as the width-to-length ratio decreases. The dipoles are well suited for millimeter-wave frequencies in particular, where the substrate can be electrically thick, and therefore the bandwidth of the dipoles can be significant [5, Chapter 5]. The microstrip dipole has been compared rigorously with the microstrip patch in terms of resonant length, resonant resistance, bandwidth, surface wave loss, dielectric loss, and mutual coupling [6].

6.1.1 Feed Design Considerations

Feed design is an important part of dipole antenna design. Like the patch antenna, the dipole can be fed by various types of printed lines.

Feed for the Printed Dipole

As in the free-space cylindrical dipole case, the electric field between the gap in the strip conductors of a printed dipole is along the length of the dipole. This distribution is different from that in a patch antenna in which the dominant electric field component is normal to the substrate. Therefore, a printed dipole cannot be fed *directly* with a microstrip line where again the major electric field component is normal to the substrate. One possible feed structure is a coplanar strips (CPS) geometry, which is compatible, physically and electrically, with the coplanar strips printed dipole. A cross section of this printed line is shown in Figure 6.2(a). Design equations for CPS are given in Appendix B. To feed a printed dipole by any other transmission line such as microstrip line, coplanar waveguide, or coaxial probe, suitable transitions to CPS are needed. These are discussed in [7, Chapter 7]. Sometimes, the dipole is suspended in front of a metal reflector for unidirectional radiation. In such cases, the center-fed dipole along with the metal plane can be modeled as a coupled microstrip line. The useful mode of propagation in coupled lines is the odd-mode. Design equations for the coupled microstrip line are given in Appendix B.

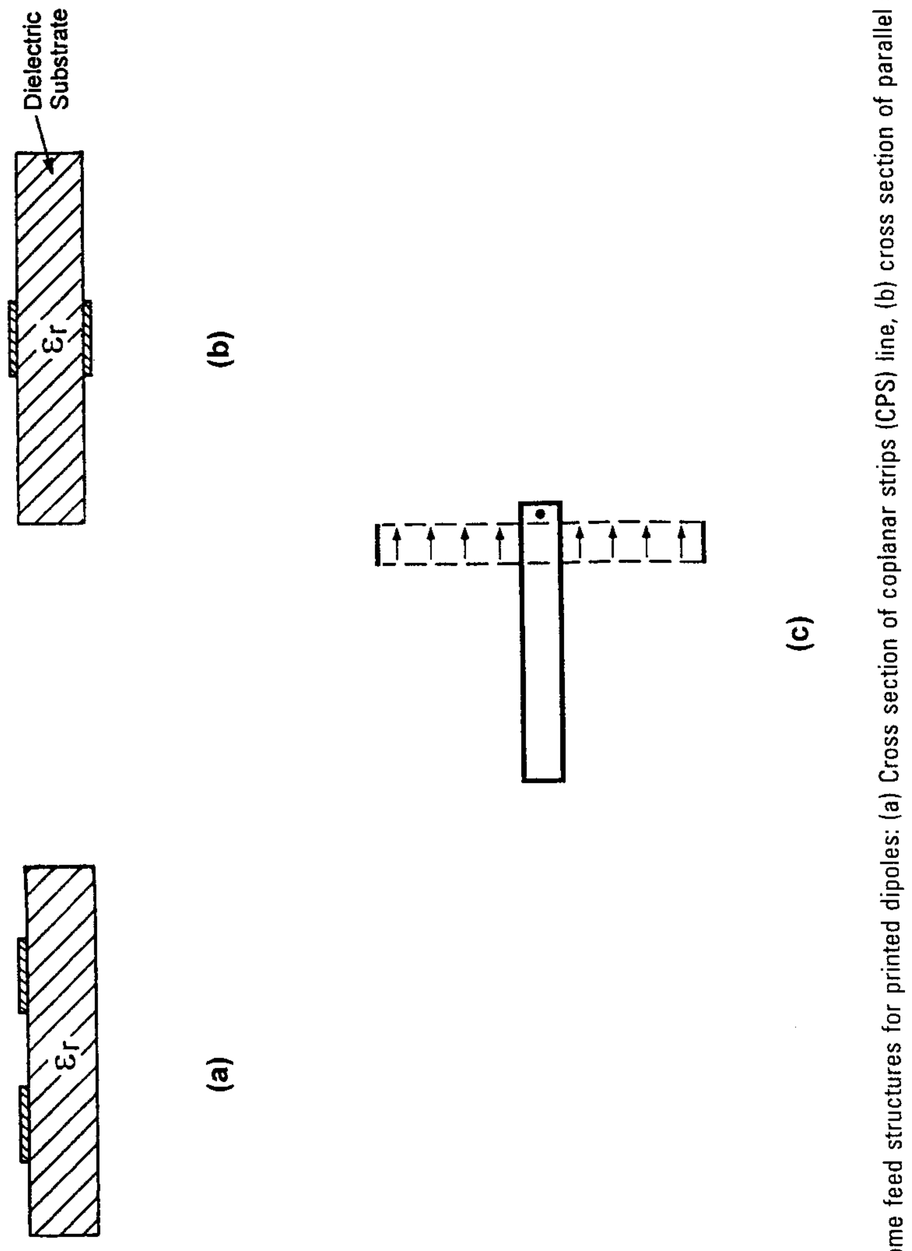

Figure 6.2 Some feed structures for printed dipoles: (a) Cross section of coplanar strips (CPS) line, (b) cross section of parallel strips line, and (c) microstrip to slot line cross-junction transition.

When the strips of the dipole are printed on the opposite surfaces of a dielectric sheet as in Figures 6.1(c) and (d), the compatible feed structure is the printed version of a parallel two-wire line, called a *parallel strip line*. This feed line is shown in Figure 6.2(b), and analyzed by Wheeler [8]. The design of parallel strip lines is simply related to the design of a microstrip line and is discussed in Appendix B.

The feed structures of Figures 6.2(a) and (b) are balanced with respect to the ground plane, which can be a serious disadvantage in some applications [6, 9]. The use of a microstrip feed line can alleviate this difficulty. Two such schemes for feeding a center-fed dipole and a microstrip dipole are described next.

In an ingenious feed arrangement, the gap between the dipole arms is treated as a slot, and this slot is fed by a microstrip line employing the microstrip slot line cross-junction transition [9]. However, the dipole is sometimes first converted into a folded dipole to increase its input resistance so that it is comparable to the characteristic impedance of the feed line. The microstrip-to-slot line transition is shown in Figure 6.2(c), and details of this transition are given in Section 7.2. The feed arrangement along with the folded dipole is shown in Figure 6.3. In this feed design, the microstrip line and the dipole are located on opposite surfaces of the substrate, and the dipole metalization is used as the ground plane for the microstrip line. Therefore, the minimum width of the dipole is taken to be about three times the width of the microstrip line so that the standard design equations for microstrip lines can be used. The dipole antenna is suspended in front of a metal reflector as shown in the figure. Impedance matching networks have been integrated with this feed

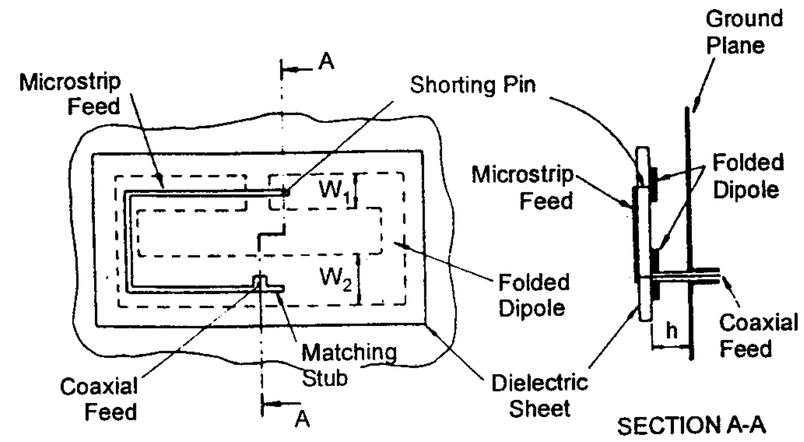

Figure 6.3 Folded printed dipole antenna with the feed structure. (From [9]. © 1981 Peter Peregrinus. Reprinted with permission.)

design to increase the bandwidth of the antenna. Dubost [10] has reported a measured directivity of more than 8 dB, and VSWR = 2 bandwidth between 500 and 850 MHz for H = 10 cm and ϵ_r = 1 [10]. Sidford [11] was able to match the dipole over a 10% bandwidth (VSWR = 2) at 1.55 GHz for $H/\lambda_0 = 0.08$.

Cross-polarized radiation is higher for this asymmetric structure [10]. This deficiency can be overcome by using a symmetric folded dipole structure. This multiresonant broadband structure is discussed in Chapter 9. A feed arrangement similar to that described above has been used in the printed half-wave dipole reported in [12] and shown in Figure 6.4. The length of the dipole is $0.4\lambda_0$ and width $0.05\lambda_0$. It is printed on a 0.64-mm fused silica substrate (ϵ_r = 3.8) and is mounted on a quarter-wavelength above a 10.16-cm^2 ground plane. By proper design of the impedance matching network, the dipole yielded a VSWR = 2 bandwidth of more than 40% [12]. Analysis of an infinite array of this dipole configuration has been carried out by Bayard [13].

Feed for the Microstrip Dipole

The feed for the microstrip dipole is shown in Figure 6.5. In this arrangement the dipole is proximity coupled to the microstrip line. The proximity coupling of a patch antenna was described in Section 1.3. Coupling can be varied in amplitude and phase by offsetting the dipole either transversely or longitudinally relative to the microstrip, by changing the length of the dipole, and the dielectric thickness t between the dipole and the microstrip line.

Of all the possible parameters that affect the coupling, the most critical is the distance t between the dipole and the microstrip line. Coupling between

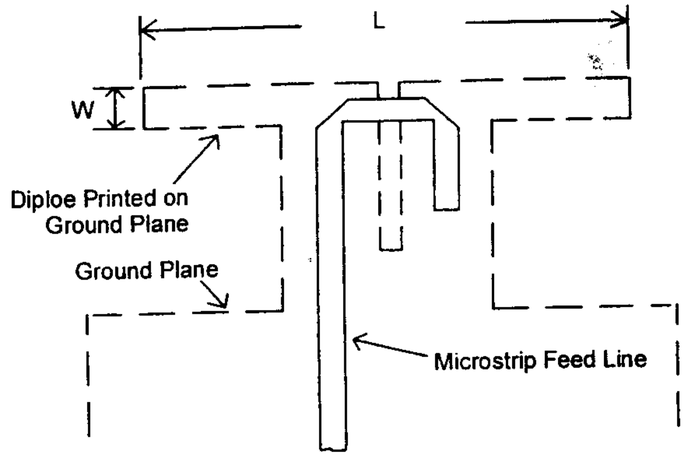

Figure 6.4 A printed dipole with the microstrip feed and balun. (From [12]. © 1987 *Microwave Journal*. Reprinted with permission.)

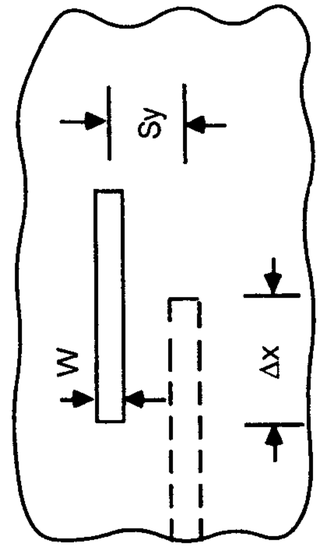

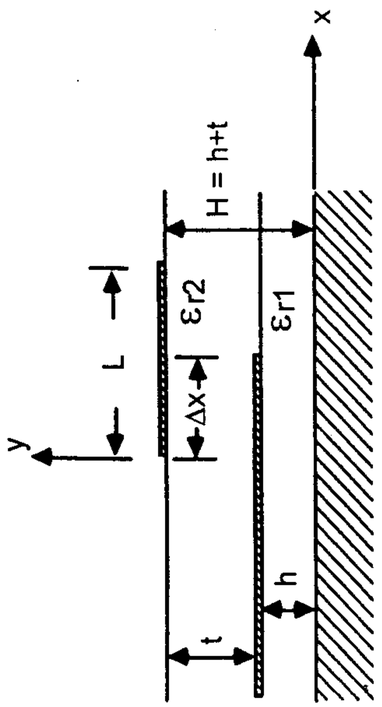

Figure 6.5 Microstrip dipole proximity coupled to a microstrip line. (From [5]. © 1989 Peter Peregrinus. Reprinted with permission.)

the dipole and microstrip line involves both electric and magnetic fields. Therefore, a perfect impedance match between the two is described by a near ellipsoidal surface centered over the end of the microstrip line. This is shown in Figure 6.6 [14].

For a given spacing t, perfect matching occurs when the locus of points for the center of the dipole lies on an ellipse centered at a height t over the end of the microstrip line. The size of this ellipse decreases as the value of t increases. The ellipse reduces to a point for $t = t_{max}$, and the dipole is said to be critically coupled. Coupling beyond this height is weak, and the dipole is said to be undercoupled. For a given value of substrate thickness h for the microstrip line, the value of t_{max} is fixed. It is always possible to match the dipole to the feed line provided $t < t_{max}$. In this situation the dipole is said to be overcoupled. When the dipole is positioned at t_{max}, the overlap between the dipole and microstrip is half the dipole length.

The dipole and the proximity coupling have been analyzed thoroughly using the integral equation approach [15–17]. The results of one of these studies are presented in Figures 6.7 and 6.8. These figures show how an input match can be achieved for the $t < t_{max}$ case by varying either the longitudinal offset Δx (see Figure 6.7) or the transverse offset S_y (see Figure 6.8) for $\epsilon_r = \epsilon_{r1} = \epsilon_{r2} = 2.35$ [16]. The effect of superstrate on the antenna characteristics has also been studied [18–20]. The superstrate can be used to eliminate surface wave excitation [18], to produce nearly omnidirectional patterns [19], or to produce a narrow beam at any desired angle in space by exciting leaky waves on the structure [20].

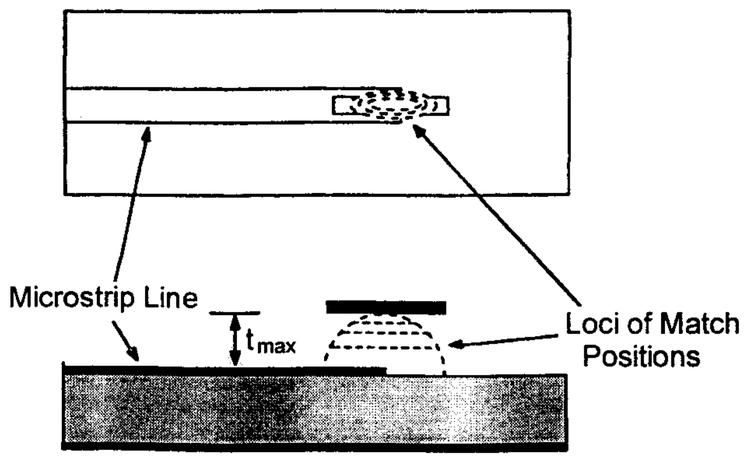

Figure 6.6 Loci of dipole center positions for which the dipole is matched to the microstrip feed line. (From [14]. © 1981 IEEE. Reprinted with permission.)

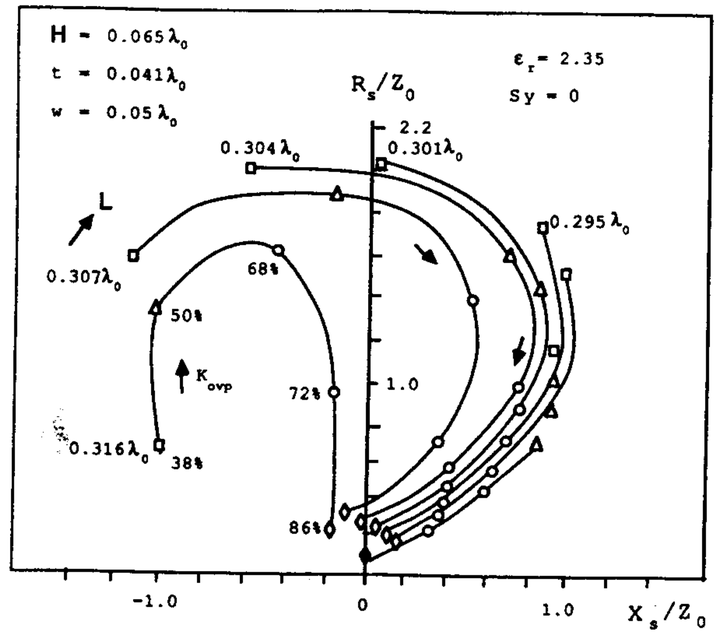

Figure 6.7 Input impedance as a function of dipole length L and longitudinal offset Δx, $\epsilon_r = \epsilon_{r1} = \epsilon_{r2}$. The offset is defined as percent overlap $K_{ovp} = (\Delta x/L) \times 100$. Transverse offset is zero. The impedance reference plane is at the position of a current maximum on the feed line. (From [16]. © 1984 IEEE. Reprinted with permission.)

It has been found that the bandwidth of a proximity-coupled dipole is almost identical to that of a center-fed dipole on the same substrate, provided the proximity-coupled dipole is matched [5, 9].

6.1.2 Input Impedance of a Dipole

The radiation resistance of a rectangular microstrip patch antenna refers to the resistance at the radiating edge of the patch. The input resistance decreases as $\cos^2(\pi x/L)$ as the feed point is located inside the patch. The x value is measured from the radiating edge and L is the resonating length. The input resistance of a strip dipole also is expected to show this variation with feed point shift. When the dipole is fed at the center, the input impedance behavior is better described by transforming the equivalent circuit of an end-fed case by a quarter-wave section, which represents the half-length of the dipole. Because the equivalent circuit for the end-fed case is a parallel resonant circuit, the impedance behavior of a center-fed dipole is described by a series resonant circuit, because a quarter-wave section behaves as an impedance inverter [21]. This transforma-

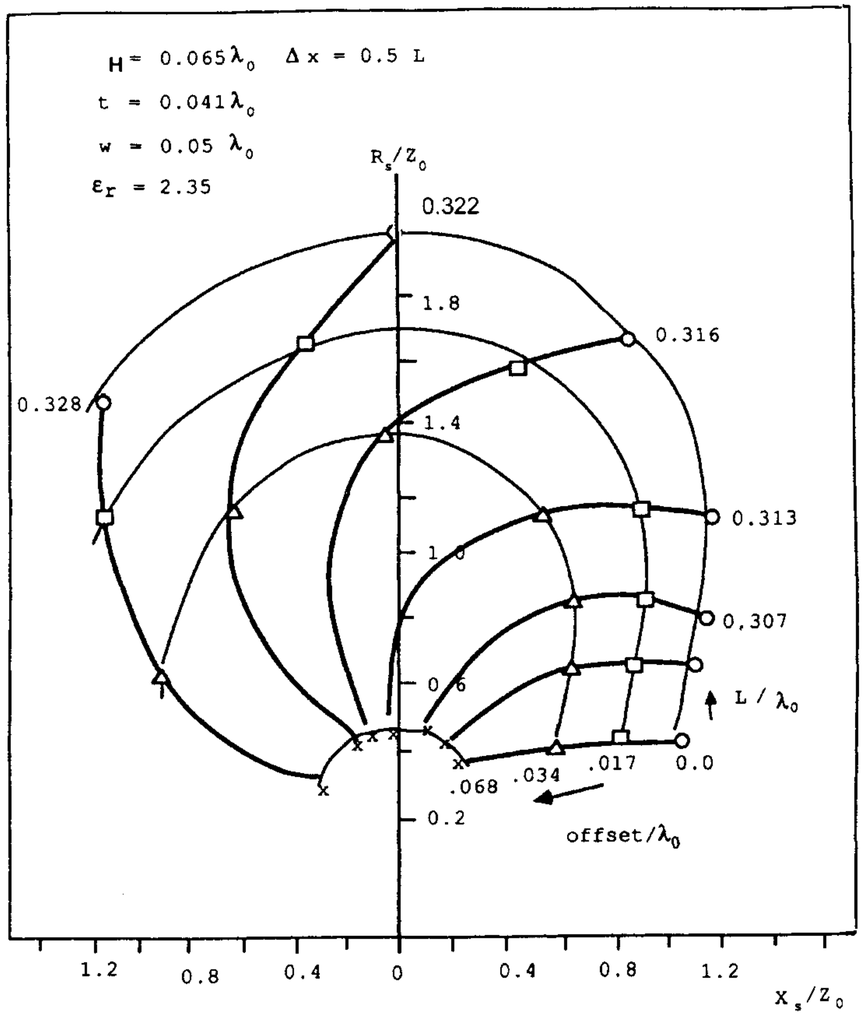

Figure 6.8 Input impedance as a function of dipole length L and transverse offset S_y/λ_0, $\epsilon_r = \epsilon_{r1} = \epsilon_{r2}$. The longitudinal offset is 50% of the dipole length. The transverse offset is specified as offset/λ_0. The impedance reference plane is at the position of a current maximum on the feed line. (From [16]. © 1984 IEEE. Reprinted with permission.)

tion is shown in Figure 6.9. The relationship between the radiation resistances in the two cases is

$$R_S(\text{center-fed dipole}) \times R_p(\text{end-fed dipole}) = Z_0^2 \qquad (6.1)$$

where Z_0 is the characteristic impedance of the transmission line of which the dipole is a segment. The radiation resistance of an end-fed strip dipole with

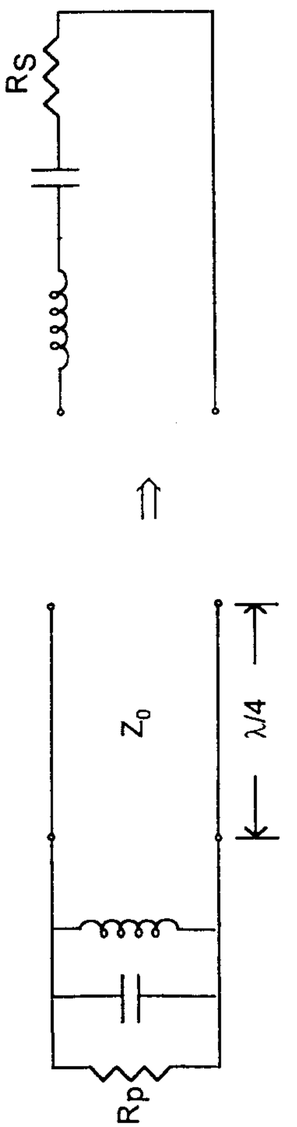

Figure 6.9 Impedance transformation of an end-fed dipole by a quarter-wave section to yield the impedance of a center-fed dipole.

a small value of width-to-length ratio is high because the radiated power decreases with the decrease in strip width and the radiation resistance is inversely proportional to the power radiated. The impedance transformation of (6.1) coupled with the high radiation resistance of the end-fed dipole will give rise to a low value of input resistance for the center-fed dipole. In typical cases it can be as low as a few ohms. This value is expected to increase as the radiated power increases with increase in substrate thickness or the strip width of the dipole.

An approximate expression for the input impedance of a center-fed dipole has been obtained by Levine et al. [22]. The admittance of an end-fed rectangular microstrip patch is obtained first. This is then transformed through a quarter-wave section to obtain the impedance for a center-fed dipole. As described in Section 4.3, the resonant radiation resistance of an end-fed microstrip patch is given by

$$R_p = \frac{V_0^2}{2P_r} = \frac{Z_0^2}{2P_r} \tag{6.2}$$

where P_r is the radiated power corresponding to 1A feed current and $I_0 = V_0/Z_0$. The admittance of the antenna is obtained by adding the end susceptance to the conductance of the antenna. The susceptance B is calculated by modeling the antenna as an open-circuited transmission line of length L, phase constant β and characteristic impedance Z_0. The expression for B is obtained as

$$B = \tan(\beta L)/Z_0 \tag{6.3}$$

The input admittance is, therefore,

$$Y_{\text{in}} = G_r + jB \tag{6.4}$$

$$G_r = 1/R_p \tag{6.5}$$

The input resistance of a center-fed dipole is obtained by using the values of R_p and Z_0 in (6.1).

The bandwidths of the end-fed and center-fed dipoles are the same because the quality factor that depends on the power radiated and energy stored is also the same for the two cases. A closed-form expression for the VSWR = 2 bandwidth is also available [23]. It is given by

$$\text{BW} = \frac{1}{\sqrt{2}} \frac{W}{\lambda_0} \frac{H}{\lambda_0} \frac{4\pi^2}{5\sqrt{\epsilon_{re}}} \tag{6.6}$$

Using (6.6) one finds that for a strip width of $W/\lambda_0 = 0.15$ and H/λ_0 between 0.1 to 0.2, the bandwidth ranges between 8% and 17%. Computed results by Levine et al. for the radiation resistance of a center-fed dipole are shown in Figure 6.10 as a function of separation distance between the dipole and reflector plane, H/λ_0 [22, 24]. The effective dielectric constant of the substrate is assumed to be 1.1. The radiation resistance of the end-fed dipole is also plotted for comparison. Note that the radiation resistance of a center-fed dipole is independent of the strip width. The radiation resistance of the end-fed dipole, on the other hand, is a strong function of strip width and a weak function of H.

Alternative Approach for Input Impedance

Closed-form expressions for the input impedance and Q of a symmetrical cylindrical dipole in air and at a height H from a reflector plane have been obtained by Dubost [10]. These expressions with simple modifications can be applied to printed and microstrip dipoles also.

Consider a symmetrical cylindrical dipole of length L and radius a as shown in Figure 6.11 [10]. Its input impedance $Z_{\text{in}} = R_{\text{in}} + jX_{\text{in}}$ is given by the following expression [10, p. 9]:

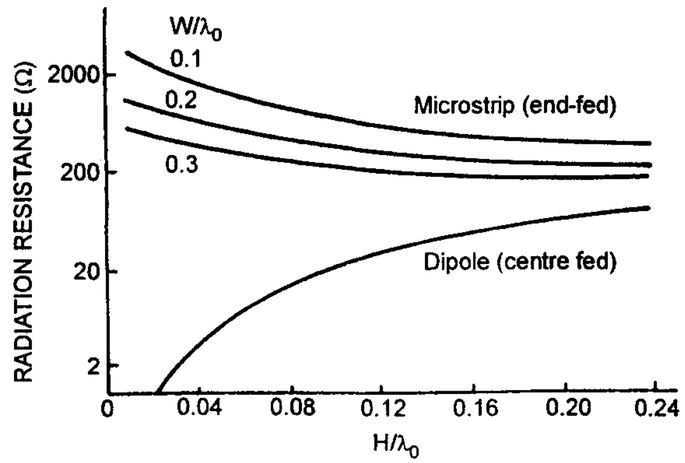

Figure 6.10 Variation of radiation resistance of a center-fed dipole and an end-fed dipole as a function of separation distance $H/\lambda_0 \cdot \epsilon_{re} = 1.1$. (From [22]. © 1988 IEE. Reprinted with permission.)

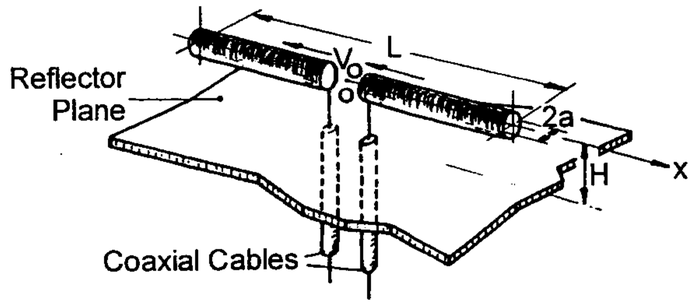

Figure 6.11 A cylindrical dipole parallel to a reflector plane. (From [10]. © 1981 Research Studies Press. Reprinted with permission.)

$$R_{\text{in}} = R_i\left\{1 - \frac{3}{2}\left[\frac{\sin(2kH)}{2kH} + \frac{\cos(2kH)}{(2kH)^2} - \frac{\sin(2kH)}{(2kH)^3}\right]\right\} \tag{6.7a}$$

$$X_{\text{in}} = -2Z_0\cot(kL/2) \tag{6.7b}$$

where R_i is the radiation resistance of the dipole in the absence of the reflector, Z_0 is the characteristic impedance of the transmission line of which the dipole is a segment, k is the wave number in free space ($k = 2\pi/\lambda_0$), and λ_0 is the wavelength in free space. The expressions for R_i and Z_0 are [10]

$$R_i = 60(kL/2)^2\frac{1 - \sin(kL)/(kL)}{1 - \cos(kL)} \tag{6.8}$$

$$Z_0 = 60\ln(2H/a) \tag{6.9}$$

For $H/\lambda_0 \leq 0.1$, (6.7a) can be simplified to obtain [10]

$$R_{\text{in}} = 24(kH)^2\frac{kL}{2}\frac{kL - \sin(kL)}{1 - \cos(kL)} \tag{6.10}$$

and the Q factor as

$$Q = \frac{Z_0}{120\pi}\frac{10\pi}{(kH)^2}\frac{1}{kL - \sin(kL)} \tag{6.11}$$

where the conductor and dielectric losses have been neglected. At resonance, $L = \lambda_0/2$ and $X_{\text{in}} = 0$. For a resonant dipole (6.10) gives

$$R_r = R_{\text{in}} = 24\pi^4(H/\lambda_0)^2 \tag{6.12}$$

This expression shows that the resonant resistance of a center-fed dipole is independent of the characteristic impedance Z_0 or stripwidth W. For a resonant dipole, (6.11) reduces to

$$Q = \frac{Z_0}{48\pi^3}(\lambda_0/H)^2 \tag{6.13}$$

and VSWR = 2 bandwidth

$$\text{BW} = \frac{1}{\sqrt{2}Q} = \frac{48\pi^3}{\sqrt{2}Z_0}\left(\frac{H}{\lambda_0}\right)^2 \tag{6.14}$$

The above results for a cylindrical dipole can be applied to a printed or microstrip dipole also with the following definitions:

1. An equivalent radius r_e can be defined for a strip dipole of width W and metal thickness T. For zero strip thickness the expression for r_e is [25]

$$r_e = W/4 \tag{6.15}$$

2. The effect of dielectric loading in the case of printed and microstrip dipoles can be included by defining an effective dielectric constant ϵ_{re}. The microstrip dipole resembles a finite length microstrip line and the expressions for ϵ_{re} and Z_0 given in Appendix B are applicable. The printed dipole, on the other hand, resembles a suspended microstrip line. The expressions for Z_0 and ϵ_{re} for a suspended microstrip line are also given in Appendix B. The variable k now represents the wave number in the double-dielectric medium of the printed dipole, and is defined as $k = 2\pi/\lambda$, with $\lambda = \lambda_0/\sqrt{\epsilon_{re}}$.

3. For accurate resonant length determination, the physical length L of the dipole should be replaced by an effective length L_e by including the open-end effect. One obtains

$$L_e = L + 2\Delta l_{oc} \tag{6.16}$$

where Δl_{oc} is again given in Appendix B for the microstrip line. This expression can be used for suspended microstrip lines also.

Moment Method Approach for Input Impedance

The integral equation along with the moment method has been used to obtain an accurate value for input impedance and resonance length of the microstrip dipole [5, Chapter 5; 15]. Figure 6.12 shows the input impedance of a strip dipole as a function of dipole length with strip width as a parameter. The first resonance is obtained when $L/\lambda_0 \approx 0.33$, and this value is relatively insensitive to the width of the dipole [see Figure 6.12(a)]. The resonant input resistance is almost constant independent of the width of the dipole [see Figure 6.12(b)]. The slopes dX_{in}/dL and $dX_{in}/d\omega$ at the resonance are lower for wider dipoles, indicating an increase in bandwidth with increase in width [see (6.18)]. The effect of gap size on the input impedance is found to be negligible, provided the gap width is less than $0.1\lambda_0$.

6.1.3 Radiation Patterns

The far-zone electromagnetic fields produced by a dipole can be obtained from the current distribution on the dipole and the Green's function. The surface current model has been used to obtain the radiation patterns of a microstrip dipole [15, 26, 27]. This model was employed in Section 4.3 for the rectangular patch antenna. Therefore, (4.43) for the radiation fields can be used for the microstrip dipole also. The resulting radiation patterns will be broad in the E plane and H plane. The effect of substrate thickness and the dielectric constant on the radiation pattern has been discussed in [27]. The number of lobes in the radiation patterns can be increased by increasing either h or ϵ_r. These radiation patterns are applicable to the coplanar strips dipole of Figure 6.1(a), also [28]. However, bow-tie antennas have a different radiation pattern in the E plane. In this case, there is a null in the broadside direction. Radiation patterns of the coplanar bow-tie antenna of Figure 6.1(b) are plotted in Figure 6.13 [1], where we observe that the H-plane radiation pattern is a typical omnidirectional pattern. In the E-plane pattern, there is a null in the broadside and the radiation level is about 2 dB higher in the substrate than on the air side. The cross-polarization level is poor in both the planes. Similar radiation patterns were observed for the double sided bow-tie antenna of Figure 6.1(d) [2].

6.1.4 Design of a Printed Dipole and a Microstrip Dipole

Resonant Length

The first consideration in the design of a dipole antenna is the length L of the element required for resonance. For calculating this, the dipole can be

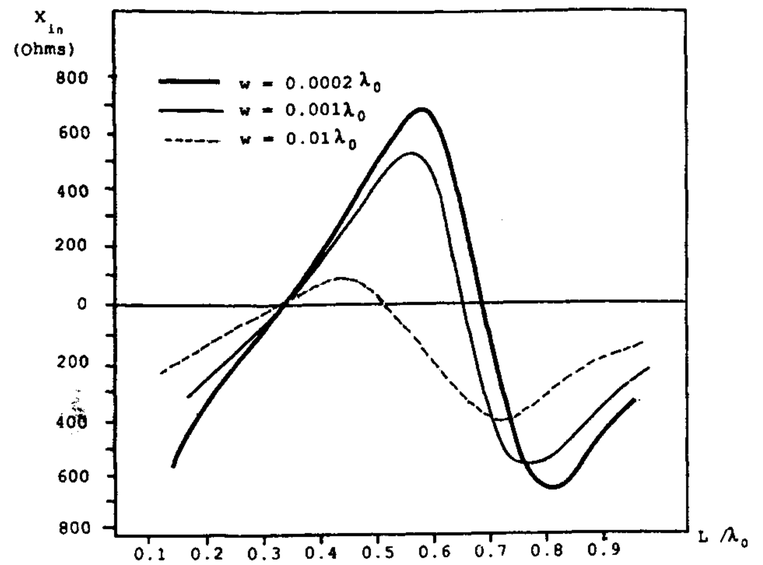

(a)

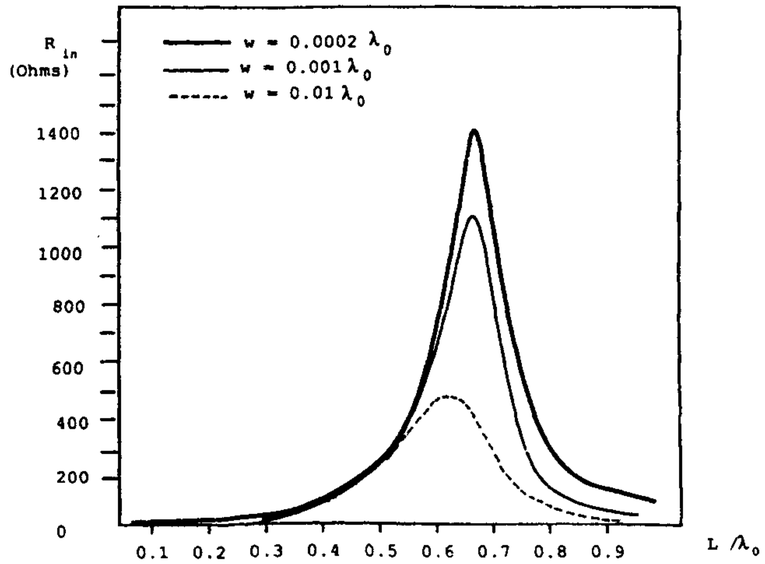

(b)

Figure 6.12 Input impedance of a center-fed microstrip dipole as a function of length L with strip width as a parameter ($\epsilon_r = 2.45$, $h = 0.2\lambda_0$): (a) Input reactance and (b) input resistance. (From [5]. © 1989 Peter Peregrinus. Reprinted with permission.)

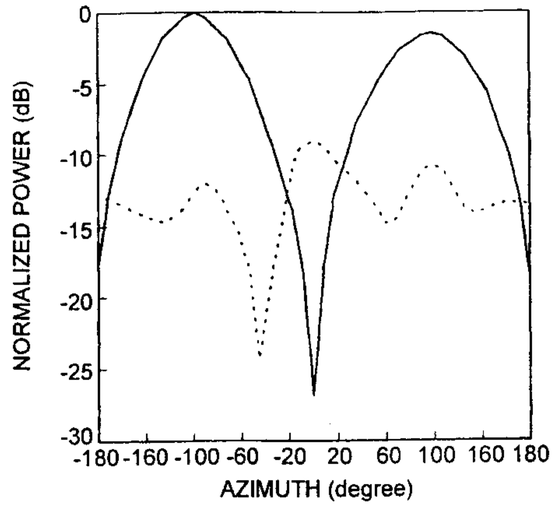

Figure 6.13 Radiation patterns of a uniplanar bow-tie antenna: (a) E-plane pattern and (b) H-plane pattern. (From [1]. © 1997 IEEE. Reprinted with permission.)

treated like a rectangular patch antenna, and according to the design presented in Section 4.3 the length L is given by

$$L = \frac{c}{2f_r\sqrt{\epsilon_{re}}} - 2\Delta l_{oc} \tag{6.17}$$

where ϵ_{re} is the effective dielectric constant of the microstrip line for the microstrip dipole, and that of a suspended microstrip line for the printed dipole. The length L is a function of the strip width W, substrate parameters h and ϵ_r, and thickness of the air dielectric. For a wire dipole of radius $0.0001\lambda_0$ located on a substrate with $\epsilon_r = 3.25$ and $h = 0.1016\lambda_0$, the resonant length of the microstrip dipole has been found to be $0.317\lambda_0$ [15]. The resonant length decreases to $0.315\lambda_0$ when the substrate thickness is increased to $0.127\lambda_0$. This decrease is due to the increase in the end-effect capacitance.

Bandwidth

A center-fed dipole behaves as a series resonant circuit. The half-power bandwidth from the impedance response of this resonant circuit is obtained as

$$\text{BW} = \frac{2R}{\omega_0 \left.\dfrac{dX}{d\omega}\right|_{\omega_0}} \tag{6.18}$$

where $Z = R + jX$ is the input impedance at the resonant frequency ω_0. This definition of bandwidth corresponds to a VSWR ratio of 2.4 when fed by a transmission line of characteristic impedance R.

We pointed out earlier that the bandwidth of an end-fed dipole, a center-fed dipole, and a proximity-coupled microstrip dipole are the same for the same set of geometrical and substrate parameters. Therefore, the bandwidth of a dipole can be obtained using the design equations for a rectangular patch (Section 4.3). Equation (6.6), derived for a strip dipole, can also be used for the design. A plot of this equation in Figure 6.14 shows that the bandwidth increases rapidly with substrate thickness so that bandwidths of 10% to 20% can be easily obtained for substrate thicknesses in the range of $0.1\lambda_0$ to $0.2\lambda_0$.

Dipoles in the stacked configuration can be used to increase the bandwidth. This study has been carried out for microstrip dipoles [29]. In the stacked configuration the lower dipole is proximity coupled to the microstrip line and the upper dipole is parasitically coupled to the fed dipole. The bandwidth critically depends on the separation distance between the dipoles. A bandwidth of 12% has been reported for an antenna thickness of 4.5 mm with $\epsilon_r = 2.35$ [5, Chapter 5].

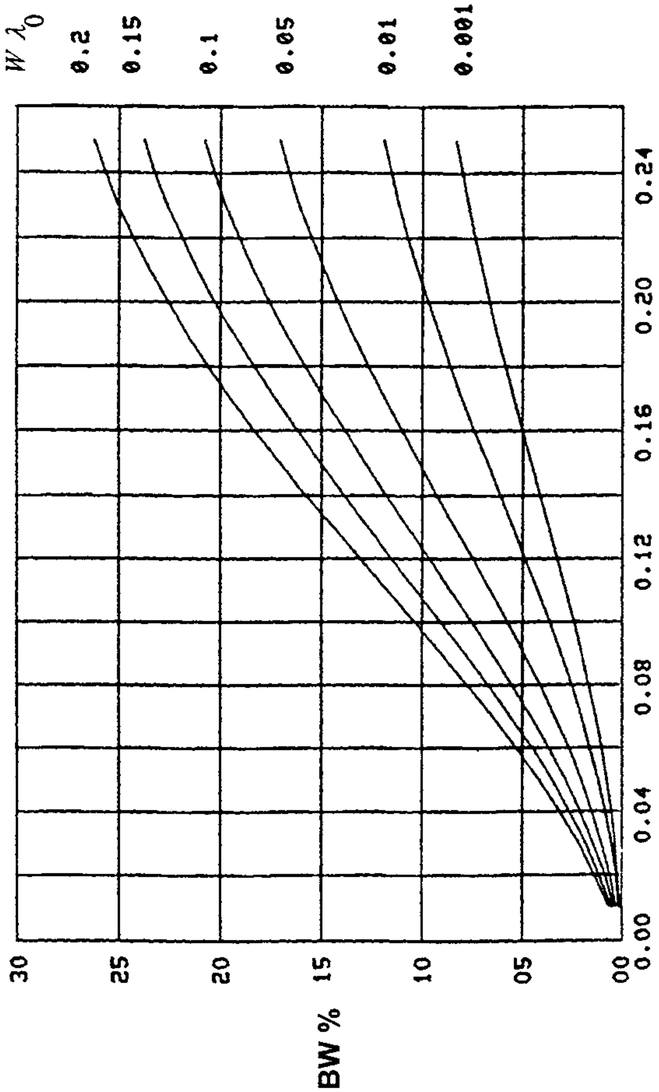

Figure 6.14 Variation of VSWR = 2 bandwidth of a center-fed dipole as a function of separation distance $H/\lambda_0 \cdot \epsilon_{re} = 1.1$. (From [22]. © 1988 IEE. Reprinted with permission.)

Resonant Resistance

The value of resonant resistance of a dipole is needed to match the dipole to the characteristic impedance of the feed line. Equation (6.12) and Figure 6.10 show that the resonant resistance is independent of the strip width. For the design, one can use (6.12) or the data generated for very thin center-fed dipoles. Figure 6.15 shows the dependence of the resonant resistance of a center-fed microstrip dipole on h and ϵ_r [6]. The resonant resistance is very small for thinner substrates, because the resonance is of series type and the power radiated is also small.

Radiation Efficiency, η

Radiation efficiency is defined as

$$\eta = \frac{P_{\text{rad}}}{P_{\text{rad}} + P_{\text{sw}}} = \frac{R_r}{R_r + R_{\text{sw}}} \tag{6.19}$$

where the conductor and dielectric losses have been neglected. The values of R_r and R_{sw} are independent of strip width. Therefore, data generated for very thin dipoles can be used in the design of strip dipoles also. The effect of substrate thickness on radiation efficiency η of a microstrip dipole is plotted in Figure 6.16 for $\epsilon_r = 2.55$ [6]. As is evident from this figure, there is an optimum value of h for which η is maximum. This optimum h has been shown to be near the cutoff thickness of the TE_1 surface wave mode [6]. The dependence of h_{opt} on ϵ_r is shown in Figure 6.17, along with the corresponding η_{max} obtained [30]. This figure indicates that if a maximum radiation efficiency

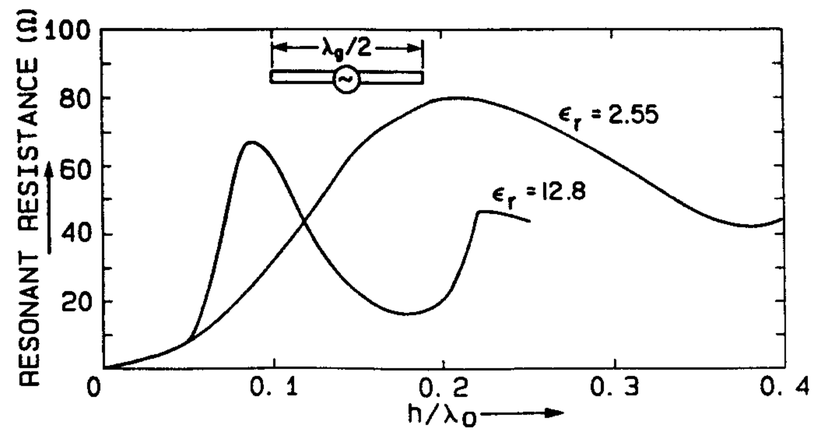

Figure 6.15 Resonant resistance of a microstrip dipole versus substrate thickness. (From [6]. © 1983 IEEE. Reprinted with permission.)

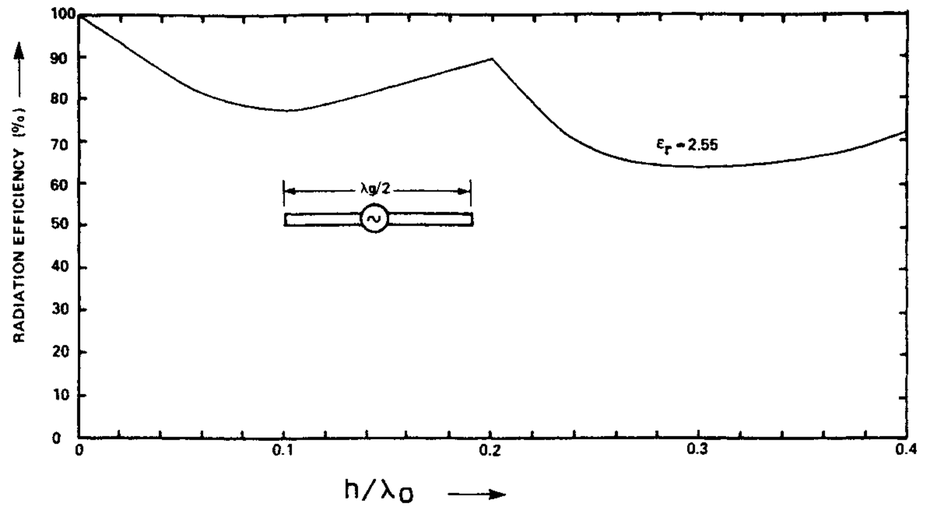

Figure 6.16 Radiation efficiency of a microstrip dipole versus substrate thickness. (From [6]. © 1983 IEEE. Reprinted with permission.)

of more than 50% is desired, the substrate permittivity should be $\epsilon_r < 4.5$ with a resulting substrate thickness greater than $0.15\lambda_0$.

6.1.5 Mutual Coupling Between Dipoles

The dipoles are generally placed in an array configuration to achieve the desired radiation characteristics such as narrow beamwidth, low sidelobe levels, beam shape, beam scanning, and so on. The large mutual coupling levels between the elements of an array can degrade these characteristics. Inclusion of these coupling effects into the array design can minimize the degradation. The calculation of mutual coupling has been carried out by a number of researchers using the integral equation approach [6, 31, 32]. The mutual coupling calculation is carried out for two configurations: parallel (or broadside) and colinear (or end-fire). These arrangements are shown in the inset of Figure 6.18. Mutual coupling is determined by the fields that exist along the air-dielectric interface. The fields excited by a microstrip dipole along the interface can be decomposed as a space wave or direct wave ($1/r$ dependence), a higher order wave ($1/r^2$ dependence), a surface wave ($1/\sqrt{r}$ dependence), and leaky waves ($\exp(-\lambda r)/\sqrt{r}$ dependence) [31].

Mutual coupling between center-fed half-wave resonant thin wire dipoles is plotted in Figure 6.18 as a function of separation S/λ_0 between them [31]. Figure 6.18(a) shows the mutual coupling in the broadside direction. The lowest order surface wave mode has a launching pattern shape of $\cos\phi$. This means that in the broadside configuration, $\phi = 90°$, the surface wave contribu-

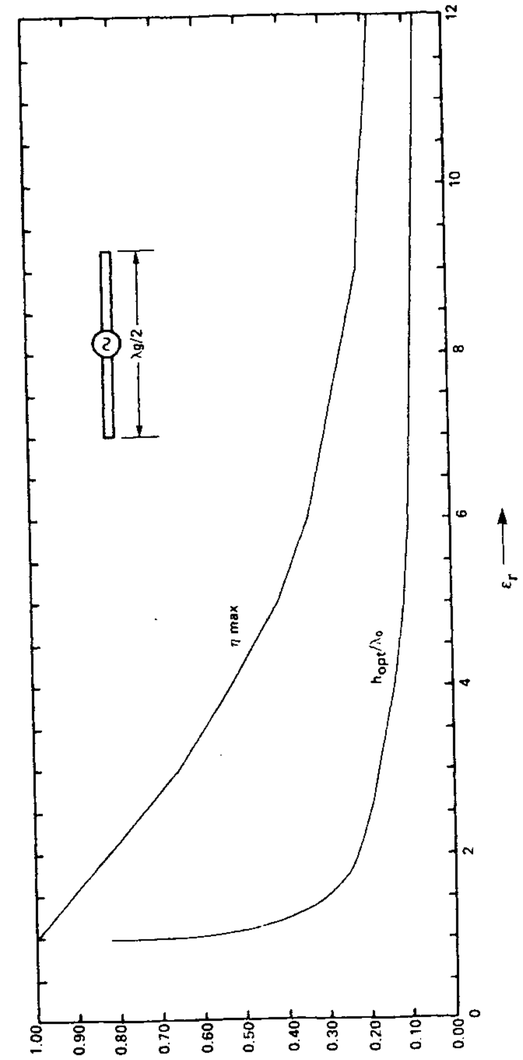

Figure 6.17 Optimum substrate thickness and the corresponding maximum radiation efficiency for a microstrip dipole. (From [30]. © 1983 IEEE. Reprinted with permission.)

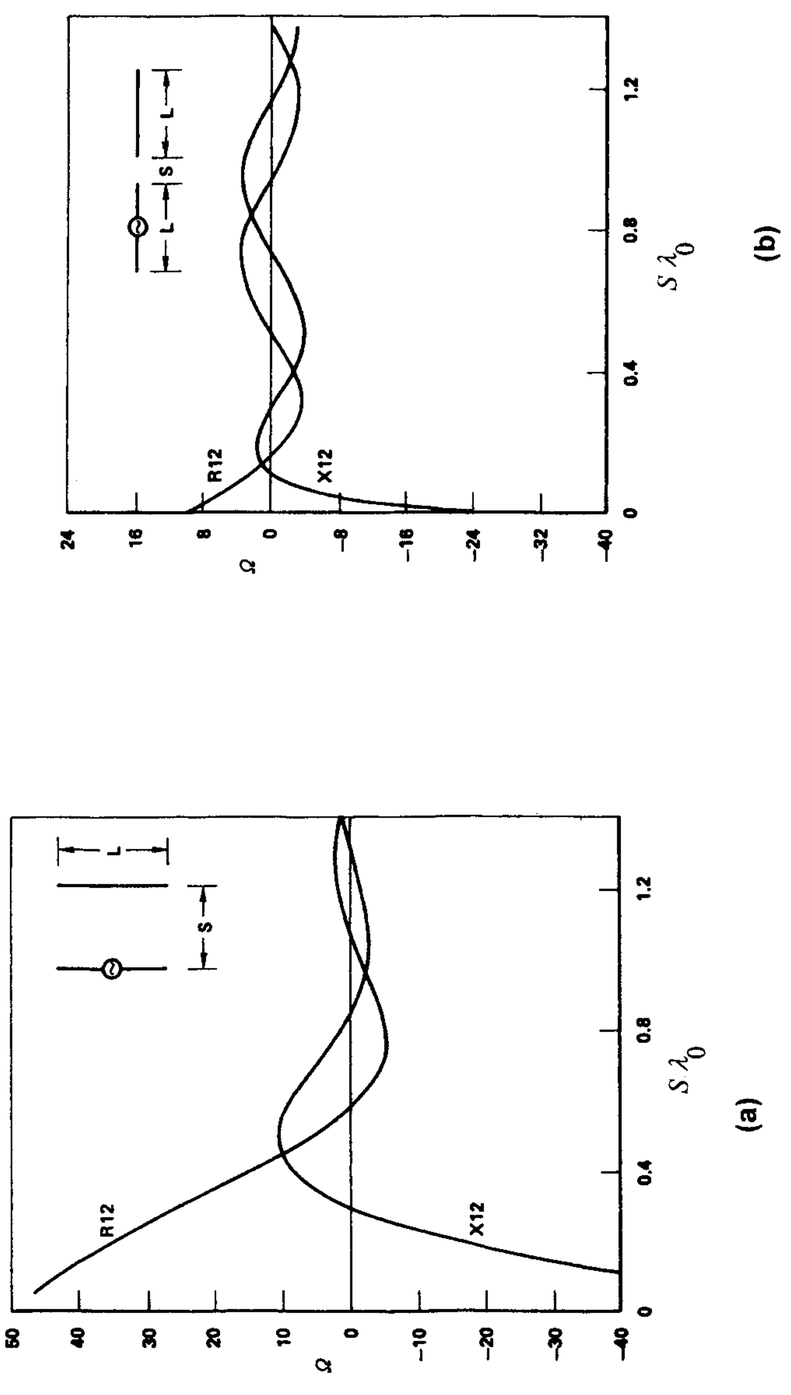

Figure 6.18 Mutual impedance between wire dipoles on a grounded substrate. (a) Mutual impedance between two broadside dipoles versus separation between them s/λ_0 ($h = 0.1016\lambda_0$, $\epsilon_r = 3.25$, $L = 0.25\lambda_0$, wire diameter = $0.00001\lambda_0$). (b) Mutual impedance between two colinear dipoles versus separation between them s/λ_0 ($h = 0.1016\lambda_0$, $\epsilon_r = 3.25$, $L = 0.25\lambda_0$, wire diameter = $0.00001\lambda_0$). (From [31]. © 1981 IEEE. Reprinted with permission.)

tion to the mutual coupling will be minimum. The coupling is mainly due to direct, higher order, and leaky waves excited by the dipole. The rapid fall in the mutual coupling for small separation ($S < 0.4\lambda_0$) confirms that the coupling is mainly due to the higher order modes. For $S > 0.8\lambda_0$, the space wave coupling dominates. In the intermediate zone $0.4\lambda_0 < S < 0.8\lambda_0$, the leaky modes are dominant [31]. For colinear dipoles, coupling takes place due to surface waves which are launched in the end-fire direction. Because surface waves decay as $1/\sqrt{r}$, the mutual coupling should decay slowly in this configuration, as shown in Figure 6.18(b). The period of oscillation of the mutual impedance from this figure is $0.88\lambda_0$, while the wavelength of the excited surface wave is $0.8811\lambda_0$. This agreement is excellent and confirms that in the colinear configuration the mutual coupling is due to the TM surface wave alone [31]. Coupling between the electromagnetically excited (or proximity-coupled) microstrip dipoles has also been studied [33–35].

6.2 Triangular Microstrip Patch Antennas

Triangular patches have been studied, both theoretically and experimentally. They are found to provide radiation characteristics similar to those of rectangular patches, but with a smaller size. The size of the antenna can be further reduced by loading it with a short and/or slot and is discussed in Chapter 10. The geometry of an equilateral triangle and the coordinate system are shown in Figure 6.19. The simplest of the triangular shapes, it comprises an equilateral triangular conductor on a grounded dielectric substrate. A nearly equilateral triangular patch has been found to sustain circular polarization similar to that in a nearly square patch antenna [36]. The equilateral triangle can be loaded with a slit or a slot to produce a compact circularly polarized antenna, and is discussed in Chapter 10 [37, 38].

6.2.1 Field Representation

The field distribution in a triangular patch can be found using the cavity model, in which the triangle is surrounded by a magnetic wall along the periphery (see Figure 6.20) as was done for the rectangular and circular configurations.

Consider a triangular resonator with magnetic side walls filled with a dielectric material of relative permittivity ϵ_r and thickness h. Since $h << \lambda_0$, there is no variation of the fields along the z direction; therefore, the structure supports TM to z modes. The solutions for the TE fields in an equilateral triangular waveguide with an electric boundary have been described by Schelku-

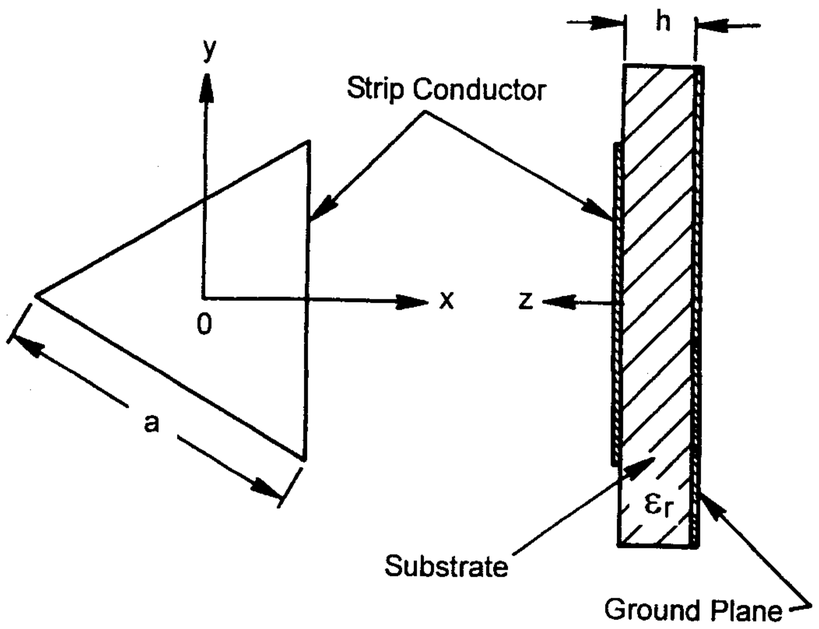

Figure 6.19 Configuration of an equilateral triangle microstrip antenna.

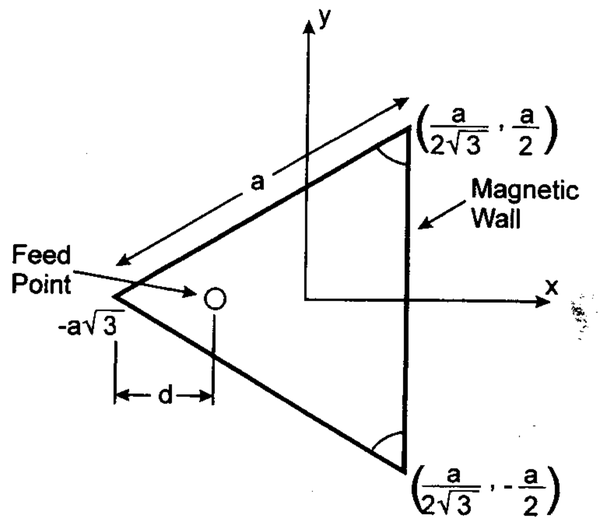

Figure 6.20 Triangular geometry with the coordinate system and the probe feed.

noff [39] and Akaiwa [40]. By the duality principle, the TM field patterns with magnetic boundary conditions are the same as those for the TE modes with electric boundary conditions. The electric and magnetic field distributions for the TM_{mn} modes can be found as follows [39–44]:

$$E_z^{mn} = A_{m,n,l}\psi_{m,n,l}(x, y) \tag{6.20}$$

$$H_x^{mn} = \frac{j}{\omega\mu}\frac{\partial E_z^{mn}}{\partial y} \tag{6.21}$$

$$H_y^{mn} = \frac{-j}{\omega\mu}\frac{\partial E_z^{mn}}{\partial x} \tag{6.22}$$

$$H_z = E_x = E_y = 0 \tag{6.23}$$

where $\psi_{m,n,l}(x, y)$ are the eigenfunctions defined as

$$\begin{aligned}\psi_{m,n,l}(x, y) = {} & \cos\left(\frac{2\pi x'}{\sqrt{3}a}l\right)\cos\left(\frac{2\pi(m-n)y}{3a}\right) \\ & + \cos\left(\frac{2\pi x'}{\sqrt{3}a}m\right)\cos\left(\frac{2\pi(n-l)y}{3a}\right) \\ & + \cos\left(\frac{2\pi x'}{\sqrt{3}a}n\right)\cos\left(\frac{2\pi(l-m)y}{3a}\right)\end{aligned} \tag{6.24}$$

and

$$x' = x + a/\sqrt{3}$$

Expression (6.24) assumes that the origin of the coordinate system coincides with the centroid of the triangle, $A_{m,n,l}$ is an amplitude constant determined by excitation, a is the length of a side of the triangle, and m, n, l are integers which are not zero simultaneously, and satisfy the condition

$$m + n + l = 0 \tag{6.25}$$

The modal fields satisfy the wave equation

$$\left(\frac{\partial^2}{\partial x^2} + \frac{\partial^2}{\partial y^2} + k_{mn}^2\right)E_z^{mn} = 0 \tag{6.26}$$

where

$$k_{mn} = \frac{4\pi}{3a}\sqrt{m^2 + mn + n^2} \tag{6.27}$$

It is seen from (6.27) that interchanging the three digits m, n, l leaves the wave number k_{mn} and the corresponding resonant frequency unchanged. The field patterns for the first two modes TM_{10} and TM_{11} are shown in Figure 6.21 [44]. The fields for the TM_{10} mode are symmetrical about the bisector line.

The above expressions for the fields are general. The particular case, $m = 1$, $n = 0$, and $l = -1$, corresponds to the dominant mode, for which the field expressions are:

$$E_z^{10} = A_{1,0,-1}\left[2\cos\frac{2\pi x'}{\sqrt{3}a}\cos\frac{2\pi y}{3a} + \cos\frac{4\pi y}{3a}\right] \tag{6.28a}$$

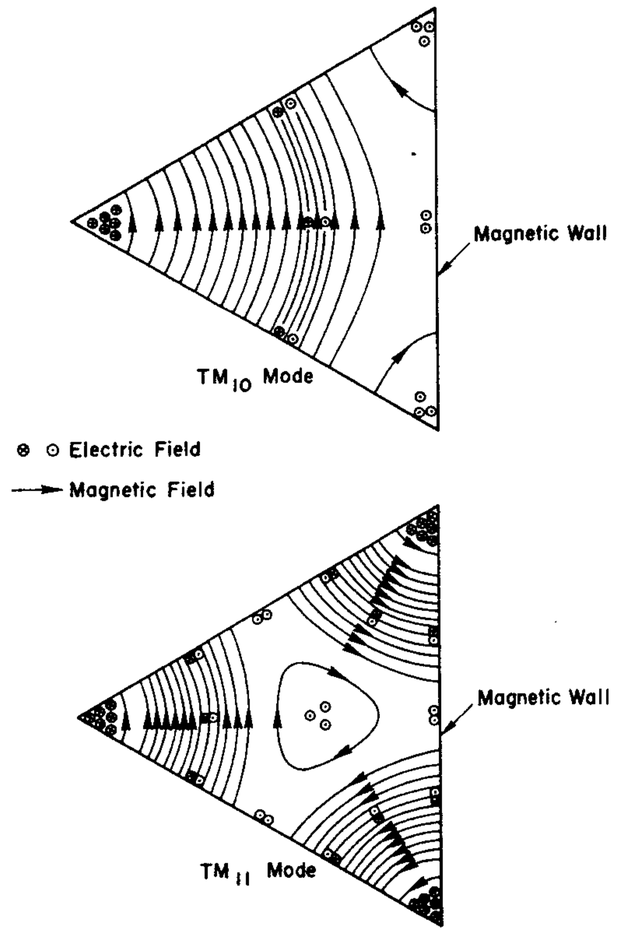

Figure 6.21 Field patterns in an equilateral triangular resonator with magnetic walls in TM_{10} mode and TM_{11} mode. (From [42]. © 1978 IEEE. Reprinted with permission.)

$$H_x^{10} = -jA_{1,0,-1}\xi_0\left[\cos\frac{2\pi x'}{\sqrt{3}a}\sin\frac{2\pi y}{3a} + \sin\frac{4\pi y}{3a}\right] \tag{6.28b}$$

$$H_y^{10} = j\sqrt{3}A_{1,0,-1}\xi_0\left[\sin\frac{2\pi x'}{\sqrt{3}a}\cos\frac{2\pi y}{3a}\right] \tag{6.28c}$$

where

$$\xi_0 = \frac{4\pi}{3a}\frac{1}{\omega\mu}\left(= \frac{1}{120\pi} \text{ at } \omega = \omega_{1,0,-1}\right) \tag{6.29}$$

6.2.2 Resonant Frequency

The resonant frequency corresponding to the various modes described by k_{mn} is:

$$f_r = \frac{ck_{mn}}{2\pi\sqrt{\epsilon_r}} = \frac{2c}{3a\sqrt{\epsilon_r}}\sqrt{m^2 + mn + n^2} \tag{6.30}$$

where c is the velocity of light in free space. The above expression is valid when the triangular resonator is surrounded by a perfect magnetic wall. The effect of a nonperfect magnetic wall on the resonant frequency can be included in an empirical fashion for easy calculation.

A number of suggestions have been made with regard to how to modify (6.30) to yield an accurate expression for a triangular microstrip patch antenna that is not enclosed by a perfect magnetic wall. Most of the suggestions are about replacing the side length a by an effective value a_e and leaving the substrate dielectric constant unchanged [44–53]. The other set of suggestions proposes replacing both a and ϵ_r with their effective values [54–56]; see Appendix B. An expression for a_e has been arrived at by curve fitting the experimental and theoretical results for the resonant frequency for TM_{10} mode [51]. It is given by

$$f_{10} = \frac{2c}{3a_e\sqrt{\epsilon_r}} \tag{6.31}$$

with

$$a_e = a\left[1 + 2.199\frac{h}{a} - 12.853\frac{h}{a\sqrt{\epsilon_r}} + 16.436\frac{h}{a\epsilon_r} + 6.182\left(\frac{h}{a}\right)^2 - 9.802\frac{1}{\sqrt{\epsilon_r}}\left(\frac{h}{a}\right)^2\right] \quad (6.32)$$

Accuracy of this empirical expression is claimed to be within 1% when compared with the value obtained from the moment method analysis [51]. The comparisons were carried out for $\epsilon_r = 2.32$, $0.002 \le h/\lambda_0 \le 0.125$; and $\epsilon_r = 10.0$, $0.008 \le h/\lambda_0 \le 0.032$. Knowing f_{10} from above, the resonant frequency for higher order modes is calculated from (6.30), that is,

$$f_{mn} = f_{10}\sqrt{m^2 + mn + n^2} \quad (6.33)$$

Accuracy of (6.33) is stated to be 0.5% [51]. The entire domain basis functions used in the analysis are given below.

$$f_x(m, n) = \sqrt{3}\left[l\sin\left(\frac{2\pi lx}{\sqrt{3}a}\right)\cos\left(\frac{2\pi(m-n)y}{3a}\right) + m\sin\left(\frac{2\pi mx}{\sqrt{3}a}\right)\cos\left(\frac{2\pi(n-l)y}{3a}\right) + n\sin\left(\frac{2\pi nx}{\sqrt{3}a}\right)\cos\left(\frac{2\pi(l-m)y}{3a}\right)\right] \quad (6.34a)$$

$$f_y(m, n) = (m-n)\cos\left(\frac{2\pi lx}{\sqrt{3}a}\right)\sin\left(\frac{2\pi(m-n)y}{3a}\right) + (n-l)\cos\left(\frac{2\pi mx}{\sqrt{3}a}\right)\sin\left(\frac{2\pi(n-l)y}{3a}\right) + (l-m)\cos\left(\frac{2\pi nx}{\sqrt{3}a}\right)\sin\left(\frac{2\pi(l-m)y}{3a}\right) \quad (6.34b)$$

These basis functions may also be used for calculating the input impedance of the patch using the surface integral equation approach.

6.2.3 Input Impedance

The input impedance of an equilateral triangular patch antenna has been determined using the cavity model [5, Chapter 3; 52, 55] and integral equation

approach [57–59]. Probe-fed, microstrip edge-fed, and aperture-coupled patches have been analyzed. Cavity model analysis of the triangular patch geometry can be carried out by following the detailed procedure given in Section 4.2.2 for the rectangular patch geometry, and the cavity mode eigenfunctions (6.24). Below we summarize this for the triangular patch antenna fed by a coaxial probe [5, Chapter 3].

Let the coaxial probe be located on the bisector line at a distance d from the tip of the triangle as shown in Figure 6.20. The coordinates of the feed are $(-a/\sqrt{3} + d, 0, h)$. The feed is modeled here as a current ribbon of effective width $2w$ laid out along the x axis, that is,

$$\vec{J} = \hat{z}J(x)\delta(y) \quad (6.35)$$

where

$$J(x) = \begin{cases} 1 & -a/\sqrt{3} + d - w < x < -a/\sqrt{3} + d + w \\ 0 & \text{elsewhere} \end{cases} \quad (6.36)$$

Using the cavity model procedure of Section 4.2.2 and the eigenfunctions (6.24), one can arrive at the following expressions for the electric field under the patch metalization and the input impedance [52]:

$$E_z(x, y) = j\omega\mu\sum_{n=0}^{\infty}\sum_{m\ge n}^{\infty} C_{mn}\left[\cos\frac{2\pi lx'}{\sqrt{3}a}\cos\frac{2\pi(m-n)y}{3a} + \cos\frac{2\pi mx'}{\sqrt{3}a}\cos\frac{2\pi(n-l)y}{3a} + \cos\frac{2\pi nx'}{\sqrt{3}a}\cos\frac{2\pi(l-m)y}{3a}\right] \quad (6.37)$$

where

$$C_{mn} = C'_{mn}\frac{4\sqrt{3}}{27a^2(k^2 - k_{mn}^2)}\left\{(d+w)\left[\operatorname{sinc}\left(\frac{2\pi l}{\sqrt{3}a}(d+w)\right) + \operatorname{sinc}\left(\frac{2\pi m}{\sqrt{3}a}(d+w)\right) + \operatorname{sinc}\left(\frac{2\pi n}{\sqrt{3}a}(d+w)\right)\right] - (d-w)\left[\operatorname{sinc}\left(\frac{2\pi l}{\sqrt{3}a}(d-w)\right) + \operatorname{sinc}\left(\frac{2\pi m}{\sqrt{3}a}(d-w)\right) + \operatorname{sinc}\left(\frac{2\pi n}{\sqrt{3}a}(d-w)\right)\right]\right\} \quad (6.38)$$

$$C'_{mn} = \begin{cases} 1 & \text{if, } m = n = 0 \\ 6 & \text{if } (m = n \neq 0) \text{ or } (m = 0 \text{ and } n \neq 0) \\ & \text{or } (n = 0 \text{ and } m \neq 0) \\ 12 & \text{otherwise} \end{cases} \tag{6.39}$$

$$Z_{\text{in}} = R + jX = -j\omega\mu \sum_{n=0}^{\infty} \sum_{m \geq n}^{\infty} \frac{4\sqrt{3}hC'_{mn}}{27a^2} \left[\cos\left(\frac{2\pi ld}{\sqrt{3}a}\right) \text{sinc}\left(\frac{\pi l 2w}{\sqrt{3}a}\right) + \cos\left(\frac{2\pi md}{\sqrt{3}a}\right) \text{sinc}\left(\frac{\pi m 2w}{\sqrt{3}a}\right) + \cos\left(\frac{2\pi nd}{\sqrt{3}a}\right) \text{sinc}\left(\frac{\pi n 2w}{\sqrt{3}a}\right) \right]^2 \frac{1}{(\omega^2 - \omega_{mn}^2)\mu\epsilon - j\delta_{\text{eff}}k^2} \tag{6.40}$$

where δ_{eff} is the effective loss tangent, determined in the same manner as for the rectangular patch in Chapter 4. The input impedance of an equilateral triangular patch for the TM_{10} mode, as a function of frequency, is shown in Figure 6.22. The value used for $2w$ is 6 mm. The input impedance is seen to vary sharply with frequency, indicating a high value of resonator Q. The resonant frequency is 1.3 GHz and the total Q for the antenna is 127. The variation of input resistance (at resonance) as a function of feed position d is plotted in Figure 6.23. It is seen from this figure that the input resistance decreases with increase in d only up to a certain value of d. After this value of d it starts increasing again. This graph can be used to select the feed location such that the input resistance is comparable to the feed characteristic impedance to achieve a low VSWR value.

6.2.4 Radiation Patterns

The far-zone electric field at a point $P(r, \theta, \phi)$ is given by [52]

$$E_\theta = -j\omega\eta_0(F_x \cos\theta\cos\phi + F_y \cos\theta \sin\phi) \tag{6.41a}$$

$$E_\phi = -j\omega\eta_0(-F_x \sin\phi + F_y \cos\phi) \tag{6.41b}$$

where $\eta_0 = 120\pi$ is the free space impedance and F_x and F_y are the electric potential components. The expressions for potential functions are very lengthy and are available in [5, Chapter 3] and [52]. The radiation patterns for the TM_{10} mode for $\epsilon_r = 2.32$, $h = 0.159$ cm and $\epsilon_r = 9.8$, $h = 0.635$ mm are shown in Figure 6.24 [5, Chapter 3]. Notice that in the $\phi = 0°$ plane, only

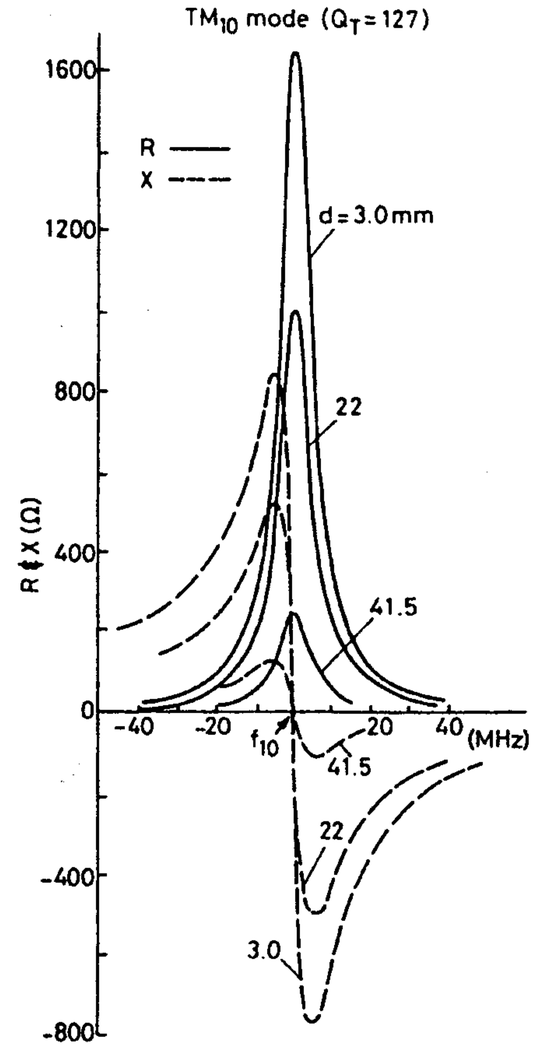

Figure 6.22 Input impedance as a function of frequency and feed position for the TM_{10} mode of an equilateral triangular patch with $a = 10$ cm, $h = 0.159$ cm, and $\epsilon_r = 2.32$. (From [52]. © 1988 IEEE. Reprinted with permission.)

the E_θ component is present. In the $\phi = 90°$ plane, however, both the E_θ and E_ϕ components are nonzero, except in the broadside direction, $\theta = 0°$. This feature is different from the rectangular and circular patches, for which the principal planes contain only one component of the radiation field.

6.2.5 Design of an Equilateral Triangular Patch Antenna

The design starts with the selection of the substrate. The main considerations governing the choice of the substrate are discussed in Appendix A. Side length

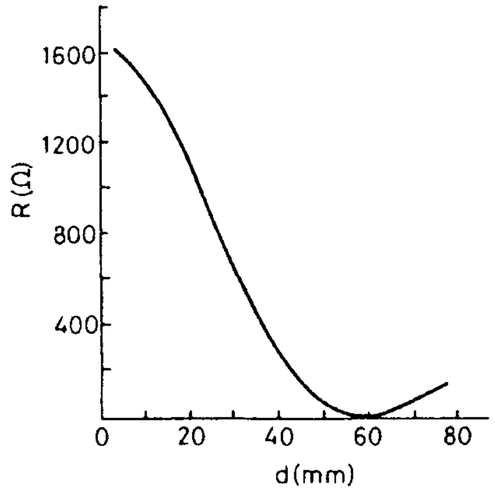

Figure 6.23 Input resistance as a function of feed position d for the TM_{10} mode of an equilateral triangular patch with a = 10 cm, h = 0.159 cm, and ϵ_r = 2.32. (From [52]. © 1988 IEEE. Reprinted with permission.)

of patch a is determined next. This is governed by the resonant frequency and the mode. Expressions (6.31)–(6.33) are used for this purpose. For a more accurate design of a, one can use a full-wave analysis such as the moment method.

Next, the feed location d is calculated such that the input resistance of the antenna matches the characteristic impedance of the feed line. For this purpose, the input resistance curve, similar to that of Figure 6.23, is developed from the input impedance expression, (6.40). In this respect, one needs to calculate the total quality factor Q_T for the antenna, since $\delta_{\text{eff}} = 1/Q_T$. The value of the total quality factor can be calculated by following the approach given in Chapter 4 for the rectangular patch. Alternatively, one can use the available graphs. One such graph is shown in Figure 6.25 for ϵ_r = 2.32 and 9.8 [5, Chapter 3].

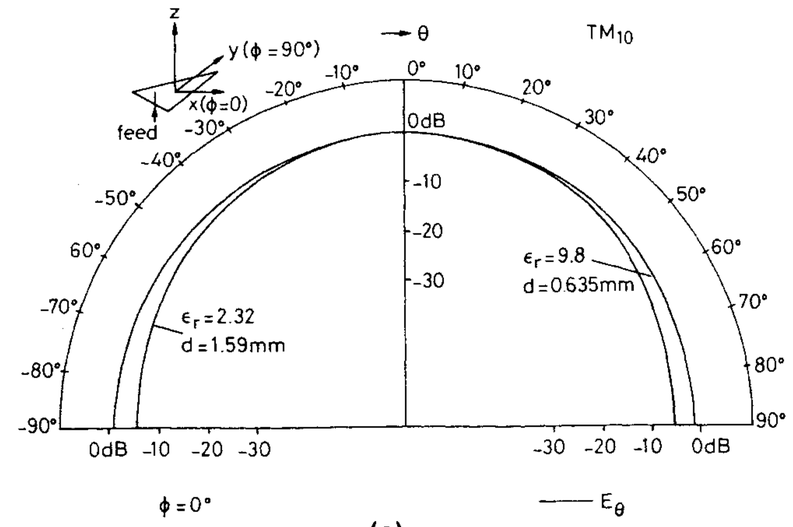

(a)

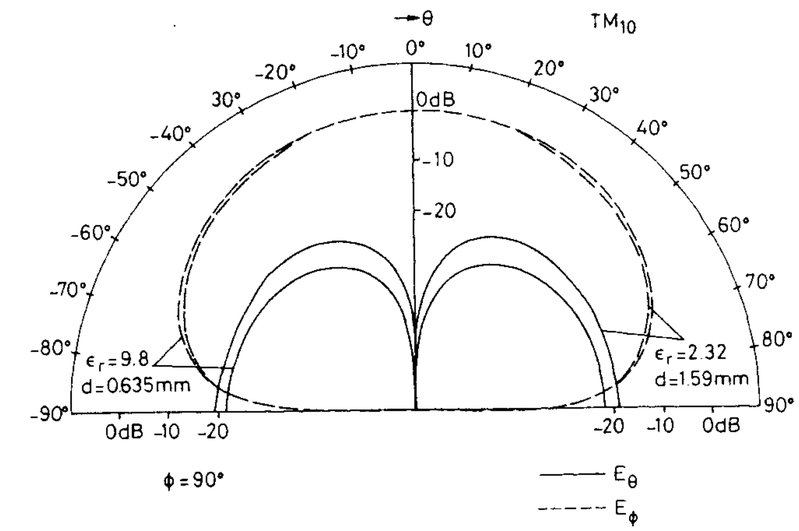

(b)

Figure 6.24 Radiation patterns for the TM_{10} mode in an equilateral triangular patch at f_{10} = 1 GHz: (a) ϕ = 0° and (b) ϕ = 90°. (From [5]. © 1989 Peter Peregrinus. Reprinted with permission.)

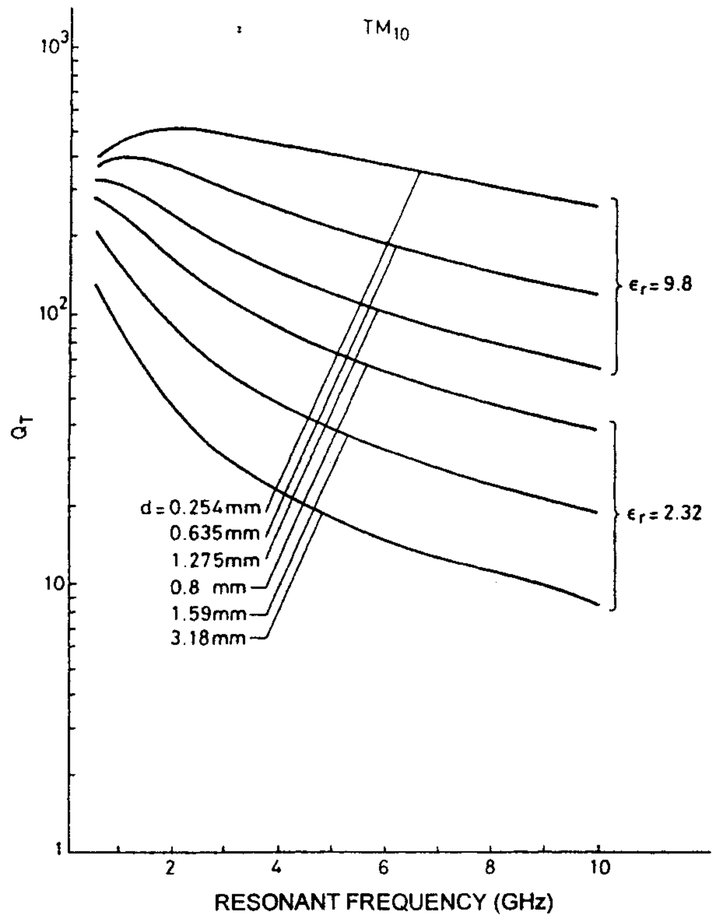

Figure 6.25 Total Q factor versus resonant frequency for the TM_{10} mode in an equilateral triangular patch with $\sigma = 5.8 \times 10^7$ S/m, $\delta = 0.0005$ and (i) $\epsilon_r = 2.32$, $d = 0.318$, 0.159, 0.0795 cm; (ii) $\epsilon_r = 9.8$, $d = 0.127$, 0.0635, 0.0254 cm. (From [5]. © 1989 Peter Peregrinus. Reprinted with permission.)

References

[1] Lin, Y.-D., and S.-N. Tsai, "Coplanar Waveguide-Fed Uniplanar Bow-Tie Antenna," *IEEE Trans. on Antennas and Propagation*, Vol. AP-45, 1997, pp. 305–306.

[2] Lin, Y.-D., and S.-N. Tsai, "Analysis and Design of Broadside-Coupled Striplines-Fed Bow-Tie Antennas," *IEEE Trans. on Antennas and Propagation*, Vol. AP-46, 1998, pp. 459–460.

[3] Agrawal, A. K., and W. E. Powell, "Monopulse Printed Circuit Dipole Array," *IEEE Trans. on Antennas and Propagation*, Vol. AP-33, 1985, pp. 1280–1283.

[4] Agrawal, A. K., and W. E. Powell, "A Printed Circuit Cylindrical Array Antenna," *IEEE Trans. on Antennas and Propagation*, Vol. AP-34, 1986, pp. 1288–1293.

[5] James, J. R., and P. S. Hall (Eds.), *Handbook of Microstrip Antennas*, Peter Peregrinus, London, UK, 1989.

[6] Pozar, D. M., "Considerations for Millimeter Wave Printed Antennas," *IEEE Trans. on Antennas and Propagation*, Vol. AP-31, 1983, pp. 740–747.

[7] Gupta, K. C., et al., *Microstrip Lines and Slotlines, 2nd Edition*, Artech House, Norwood, MA, 1996.

[8] Wheeler, H. A., "Transmission Line Properties of Parallel Strips Separated by a Dielectric Sheet," *IEEE Trans. on Microwave Theory and Techniques*, Vol. MTT-13, 1965, pp. 172–185.

[9] James, J. R., P. S. Hall, and C. Wood, *Microstrip Antenna: Theory and Design*, Peter Peregrinus, London, UK, 1981, Chap. 10.

[10] Dubost, G., *Flat Radiating Dipoles and Applications to Arrays*, Research Studies Press, Chichester, England, 1981.

[11] Sidford, M. J., "A Radiating Element Giving Circularly Polarised Radiation Over a Large Solid Angle," *IEE Conf. Publ. 95*, 1973, pp. 18–25.

[12] Edward, B., and D. Rees, "A Broadband Printed Dipole With Integrated Balun," *Microwave J.*, 1987, pp. 339–344.

[13] Bayard, J.-P. R., "Analysis of Infinite Arrays of Microstrip-Fed Dipoles Printed on Protruding Dielectric Substrates and Covered With a Dielectric Radome," *IEEE Trans. on Antennas and Propagation*, Vol. AP-42, 1994, pp. 82–89.

[14] Oltman, H. G., and Huebner, D. A., "Electromagnetically Coupled Microstrip Dipoles," *IEEE Trans. on Antennas and Propagation*, Vol. AP-29, 1981, pp. 151–157.

[15] Rana, I. E., and N. G. Alexopoulos, "Current Distribution and Input Impedance of Printed Dipoles," *IEEE Trans. on Antennas and Propagation*, Vol. AP-29, 1981, pp. 106–111.

[16] Katehi, P. B., and N. G. Alexopoulos, "On the Modeling of Electromagnetically Coupled Microstrip Antennas—The Printed Strip Dipole," *IEEE Trans. on Antennas and Propagation*, Vol. AP-32, 1984, pp. 1179–1186.

[17] Zhang, Q., Y. Fukuoka, and T. Itoh, "Analysis of a Suspended Patch Antenna Excited by an Electromagnetically Coupled Inverted Microstrip Feed," *IEEE Trans. on Antennas and Propagation*, Vol. AP-33, 1985, pp. 895–899.

[18] Alexopoulos, N. G., and D. R. Jackson, "Fundamental Superstrate (Cover) Effects on Printed Circuit Antennas," *IEEE Trans. on Antennas and Propagation*, Vol. AP-32, 1984, pp. 807–816.

[19] Alexopoulos, N. G., D. R. Jackson, and P. B. Katehi, "Criteria for Nearly Omnidirectional Radiation Patterns for Printed Antennas," *IEEE Trans. on Antennas and Propagation*, Vol. AP-33, 1985, pp. 195–205.

[20] Jackson, D. R., and A. A. Oliner, "A Leaky-Wave Analysis of the High Gain Printed Antenna Configuration," *IEEE Trans. on Antennas and Propagation*, Vol. AP-36, 1988, pp. 905–910.

[21] Matthaei, G., L. Young, and E. M. T. Jones, *Microwave Filters, Impedance-Matching Networks and Coupling Structures*, Artech House, Dedham, MA, 1980, Chap. 8.

[22] Levine, E., S. Shtrikman, and D. Treves, "Double-Sided Printed Arrays With Large Bandwidth," *IEE Proc.*, Vol. 135, Pt. H, 1988, pp. 54–59.

[23] Dubost, G., "Transmission Line Model Analysis of a Lossy Rectangular Patch," *Electron. Lett.*, Vol. 18, 1982, pp. 281–282.

[24] Levine, E., P. Perlmutter, and D. Treves, "Double-Sided Printed Dipole Arrays," *14th Conv. of Electrical and Electronics Engineers in Israel*, Tel Aviv, 1985, Paper No. 2.3.10.

[25] Butler, C. M., "The Equivalent Radius of a Narrow Conducting Strip," *IEEE Trans. on Antennas and Propagation*, Vol. AP-30, 1982, pp. 755–758.

[26] Uzunoglu, N. K., N. G. Alexopoulos, and J. G. Fikioris, "Radiation Properties of Microstrip Dipoles," *IEEE Trans. on Antennas and Propagation*, Vol. AP-27, 1979, pp. 853–858.

[27] Katehi, P. B., and N. G. Alexopoulos, "On the Effect of Substrate Thickness and Permittivity on Printed Circuit Dipole Properties," *IEEE Trans. on Antennas and Propagation*, Vol. AP-31, 1983, pp. 34–38.

[28] Tilley, K., X.-D. Wu, and K. Chiang, "Coplanar Waveguide Fed Coplanar Strip Dipole Antenna," *Electron. Lett.*, Vol. 30, 1994, pp. 176–177.

[29] Katehi, P. B., N. G. Alexopoulos, and I. Y. Hsia, "A Bandwidth Enhancement Method for Microstrip Antennas," *IEEE Trans. on Antennas and Propagation*, Vol. AP-35, 1987, pp. 5–12.

[30] Alexopoulos, N. G., P. B. Katehi, and D. B. Rutledge, "Substrate Optimization for Integrated Circuit Antennas," *IEEE Trans. on Microwave Theory and Techniques*, Vol. MTT-31, 1983, pp. 550–557.

[31] Alexopoulos, N. G., and I. E. Rana, "Mutual Impedance Computation Between Printed Dipoles," *IEEE Trans. on Antennas and Propagation*, Vol. AP-29, 1981, pp. 106–111.

[32] Katehi, P. B., "A Generalized Method for the Evaluation of Mutual Coupling in Microstrip Arrays," *IEEE Trans. on Antennas and Propagation*, Vol. AP-35, 1987, pp. 125–133.

[33] Elliot, R. S., and G. J. Stern, "The Design of Microstrip Dipole Arrays Including Mutual Coupling Part I: Theory," *IEEE Trans. on Antennas and Propagation*, Vol. AP-29, 1981, pp. 757–760.

[34] Stern, G. J., and R. S. Elliot, "The Design of Microstrip Dipole Arrays Including Mutual Coupling Part I: Experiment," *IEEE Trans. on Antennas and Propagation*, Vol. AP-29, 1981, pp. 761–765.

[35] Pozar, D. M., and D. H. Schaubert, "Scan Blindness in Infinite Phased Arrays of Printed Dipoles," *IEEE Trans. on Antennas and Propagation*, Vol. AP-32, 1984, pp. 602–610.

[36] Suzuki, Y., N. Miyano, and T. Chiba, "Circularly Polarised Radiation from Singly Fed Equilateral-Triangular Microstrip Antenna," *Proc. IEE*, Vol. 134, Pt. H, 1987, pp. 194–198.

[37] Lu, J.-H., C.-L. Tang, and K.-L., Wong, "Circular Polarisation Design of a Single-Feed Equilateral-Triangular Microstrip Antenna," *Electron. Lett.* Vol. 34, 1998, pp. 319–321.

[38] Lu, J.-H., C.-L. Tang, and K.-L. Wong, "Single-Feed Slotted Equilateral-Triangular Microstrip Antenna for Circular Polarization," *IEEE Trans. on Antennas and Propagation*, Vol. AP-47, 1999, pp. 1174–1178.

[39] Schelkunoff, S. A., *Electromagnetic Waves*, Van Nostrand, New York, 1943, Chap. 10.

[40] Akaiwa, Y., "Operation Modes of a Waveguide Y-Circulator," *IEEE Trans. on Microwave Theory and Techniques*, Vol. MTT-22, 1974, pp. 954–959.

[41] Cuhaci, M., and D. S. James, "Radiation From Triangular and Circular Resonators in Microstrip," *IEEE MTT-S Int. Microwave Symp. Digest*, 1977, pp. 438–441.

[42] Helszajn, J., and D. S. James, "Planar Triangular Resonators With Magnetic Walls," *IEEE Trans. on Microwave Theory and Techniques*, Vol. MTT-26, 1978, pp. 95–100.

[43] Helszajn, J., D. S. James, and W. T. Nisbet, "Circulators Using Planar Triangular Resonators," *IEEE Trans. on Microwave Theory and Techniques*, Vol. MTT-27, 1979, pp. 188–193.

[44] Bahl, I. J., and P. Bhartia, *Microstrip Antennas*, Artech House, Dedham, MA, 1980.

[45] Helszajn, J., and D. S. James, "Planar Triangular Resonators With Magnetic Walls," *IEEE Trans. on Microwave Theory and Techniques*, Vol. MTT-26, 1978, pp. 95–100.

[46] Suzuki, Y., and T. Chiba, "Computer Analysis Method for Arbitrarily Shaped Microstrip Antenna With Multiterminals," *IEEE Trans. on Antennas and Propagation*, Vol. AP-32, 1984, pp. 585–590.

[47] Dahele, J. S., and K. F. Lee, "On the Resonant Frequencies of the Triangular Patch Antenna," *IEEE Trans. on Antennas and Propagation*, Vol. AP-35, 1987, pp. 100–101.

[48] Garg, R., and S. A. Long, "An Improved Formula for the Resonant Frequency of the Triangular Microstrip Patch Antenna," *IEEE Trans. on Antennas and Propagation*, Vol. AP-36, 1988, p. 570.

[49] Singh, R., A. De, and R. S. Yadav, "Comments on an Improved Formula for the Resonant Frequency of the Triangular Microstrip Patch Antenna," *IEEE Trans. on Antennas and Propagation*, Vol. AP-39, 1991, pp. 1443–1445.

[50] Gang, X., "On the Resonant Frequencies of Microstrip Antennas," *IEEE Trans. on Antennas and Propagation*, Vol. AP-37, 1989, pp. 245–247.

[51] Chen, W., K. F. Lee, and J. S. Dahele, "Theoretical and Experimental Studies of the Resonant Frequencies of the Equilateral Triangular Microstrip Antenna," *IEEE Trans. on Antennas and Propagation*, Vol. AP-40, 1992, pp. 1253–1256.

[52] Lee, K.-F., K.-M. Luk, and J. S. Dahele, "Characteristics of the Equilateral Triangular Patch Antenna," *IEEE Trans. on Antennas and Propagation*, Vol. AP-36, 1988, pp. 1510–1518.

[53] Kumprasert, N., and W. Kiranon, "Simple and Accurate Formula for the Resonant Frequency of an Equilateral Triangular Microstrip Patch Antenna," *IEEE Trans. on Antennas and Propagation*, Vol. AP-42, 1994, pp. 1178–1179.

[54] Guney, K., "Resonant Frequency of a Triangular Microstrip Antenna," *Microwave and Optical Technology Lett.*, Vol. 6, 1993, pp. 555–557.

[55] Guney, K., "Input Impedance of an Equilateral Triangular Microstrip Antenna," *Proc. Electrotechnical Conf.*, 1994, pp. 414–417.

[56] Mythili, P., and A. Das, "Simple Approach to Determine Resonant Frequencies of Microstrip Antennas," *IEE Proc. Microwaves, Antennas and Propagation*, Vol. 145, 1998, pp. 159–162.

[57] Wu, K.-L., et al., "Full Wave Analysis of Arbitrarily Shaped Line-Fed Microstrip Antennas Using Triangular Finite-Element Method," *IEE Proc.*, Vol. 138, Pt. H, 1991, pp. 421–428.

[58] Yang, X. H., and L. Shafai, "Nodal-Based Basis Function for Full Wave Analysis of Microstrip Antennas With Arbitrary Geometries," *Electron. Lett.*, Vol. 30, 1994, pp. 830–831.

[59] Hassani, H. R., and D. Mirshekar-Syahkal, "Analysis of Triangular Patch Antennas Including Radome Effects," *IEE Proc.*, Vol. 139, Pt. H, 1992, pp. 251–256.

7

Microstrip Slot Antennas

7.1 Introduction

The concept of microstrip slot antennas has evolved from slot antennas excited by a strip line. These types of slot antennas have been extensively discussed in the literature [1–9]. They have numerous promising features, but they suffer from undesired modes such as the parallel plate mode excited between the ground planes of the strip line.

Microstrip slot antennas (MSAs) have the advantage of being able to produce bidirectional and unidirectional radiation patterns with larger bandwidth. Strip and slot combinations offer an additional degree of freedom in the design of microstrip antennas. A combination of strip conductors and slots arranged along the sides of a microstrip feed can produce circularly polarized radiation [10, 11]. Antennas with desired polarization can be produced, and they are less sensitive to manufacturing tolerances than are microstrip patch antennas. Annular slot antennas can be used as vehicular antennas for mobile communications. Tapered slot antennas produce end-fire radiation and find a number of applications at millimeter-wave frequencies. This chapter presents various aspects of rectangular slot, annular slot, and tapered slot antennas. Microstrip-fed rectangular slot antennas are analyzed in greater detail.

7.2 Microstrip-Fed Rectangular Slot Antennas

A microstrip slot antenna comprises a slot cut in the ground plane of the microstrip line such that the slot is perpendicular to the strip conductor of the microstrip line. The fields of the microstrip line excite the slot. For efficient

excitation of the slot, the strip conductor is either short-circuited through the dielectric substrate to the edge of the slot as shown in Figure 7.1(a), or the strip conductor is terminated in an open-circuited stub beyond the edge of the slot as shown in Figure 7.1(b) [12]. The length L_m of the open-circuited microstrip stub is approximately a quarter-wave long so that an *effective* short circuit is realized at the outer edge of the slot as shown in Figure 7.1(a). A center-fed slot antenna has a very high radiation resistance, and a matching network may be needed to match the antenna to the characteristic impedance of the microstrip line.

For a given slot size, the resistance seen by the feed line can be reduced in three possible ways [13]. The first is off-center feeding as suggested by Yoshimura [12] and shown in Figure 7.2(a). The second technique is stub-tuning of the slot antenna as suggested by Pozar [14]. This technique is very similar to that of Figure 7.1(b) except that the length L_m of the microstrip stub is longer than a quarter-wave. The stub-tuning introduces reactive loading of the antenna, thereby changing the resonant frequency. The stub is designed so that the input resistance compares with the feed line impedance at the new resonant frequency. The third feeding possibility is that the slot is center fed but is inclined as shown in Figure 7.2(b). The last approach is similar to that used in waveguide slot antennas.

The microstrip-fed slot antenna has the advantage of very low cross-polarization (typically −35 dB) as compared to microstrip patch antennas [15]. Its drawback is the inherently bidirectional radiation, which can be corrected by using a metallic cavity or a metallic reflector on one side.

The microstrip excited rectangular slot antenna has been studied theoretically and experimentally by many researchers [12–20]. The full-wave rigorous analyses are the most accurate so far [14, 17, 18]. These techniques are computationally very intensive and are based on the use of the reciprocity theorem and the integral equation in a manner similar to the waveguide excited slot. The analysis is carried out in the spectral domain in [14, 17], but the mixed-potential integral equation (MPIE) is used in [18] in the space domain.

Some approximate network models have been proposed to design the antenna efficiently. Axelrod et al. [15] modeled the microstrip-slot junction by employing an ideal transformer, and the power radiated by the slot was expressed in the form of an equivalent radiation resistance and located at the center of the slot. Himdi and Daniel [19] used a lossy transmission line model and the power radiated to determine the attenuation constant, radiation conductance and the power radiated of the slot. Akhavan and Mirshekar-Syahkal [20] have developed an approximate model by using a standard expression for the radiation conductance of a resonant slot without substrate and approximately determined the self- and mutual inductances of the transformer. Kim

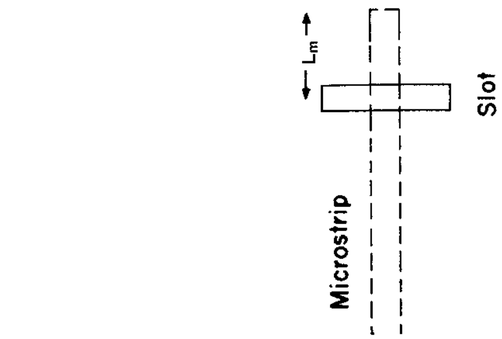

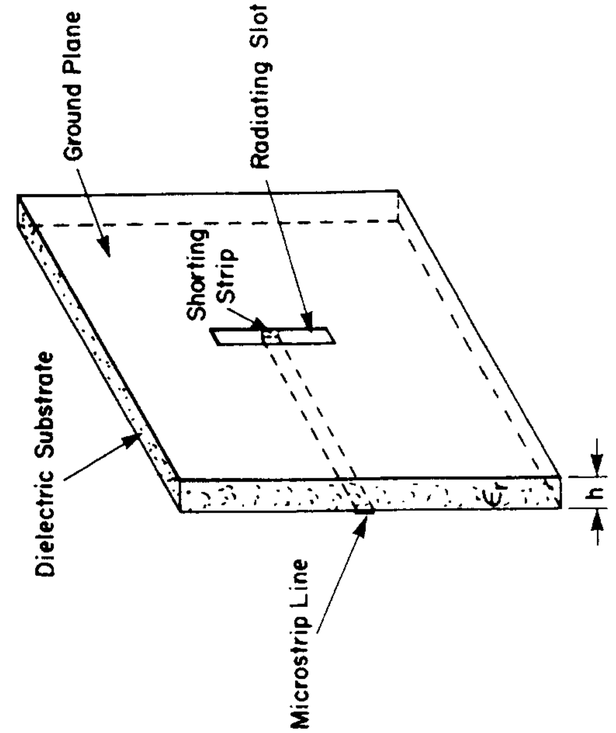

Figure 7.1 Center-fed microstrip slot antenna configurations: (a) Microstrip terminated in a short circuit and (b) microstrip terminated in an open-circuited stub.

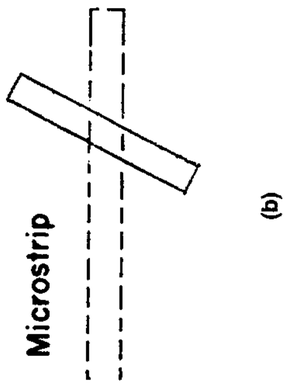

Figure 7.2 Two possible ways of reducing the high input impedance of a slot antenna: (a) Offset microstrip feed and (b) center-fed but inclined microstrip feed.

and Park [13] have developed an accurate network model of an inclined and off-centered microstrip-fed slot antenna. Values of some of the components of the network model are derived from the full-wave approach of [14], which has been recast to include the effect of inclination angle of the slot with respect to the microstrip line. We describe below the network model proposed in [13] for the off-center microstrip-fed slot antenna. The feed and the slot are taken to be at right angles to each other. Note that this model is not directly applicable to a wide slot antenna.

Figure 7.3 shows the off-center fed slot antenna and its equivalent circuits [13]. In Figure 7.3(a) L_S and W_S denote the length and width of the radiating slot, d is the off-set distance from the center of the slot, the width of the microstrip line is W_m, and h and ϵ_r are the substrate parameters. The slot

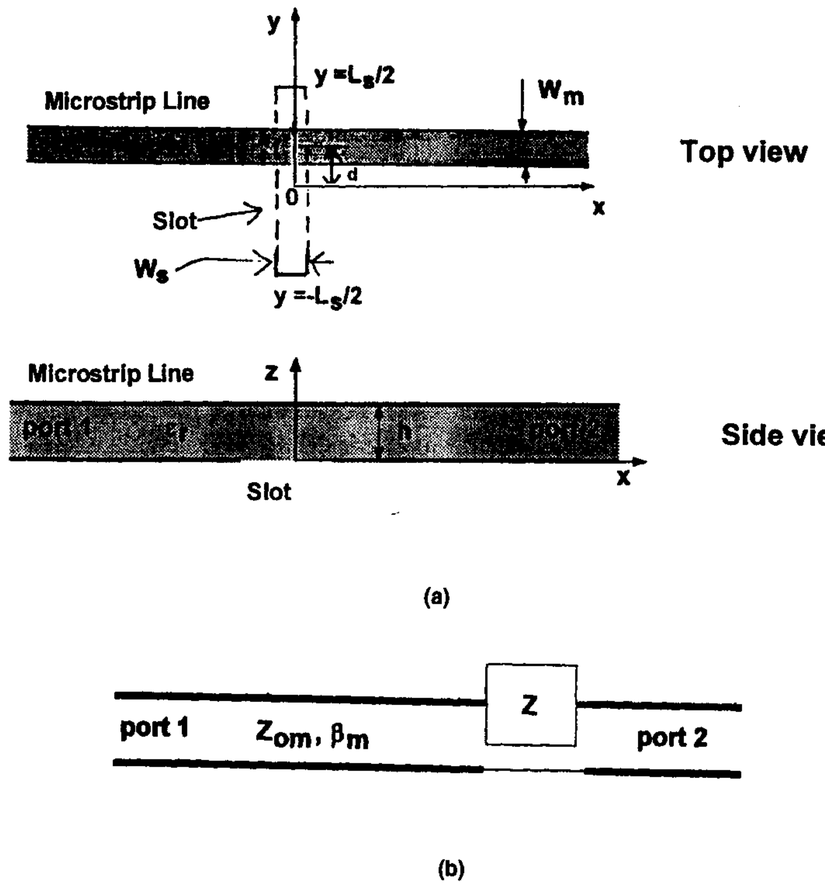

Figure 7.3 (a) Top and side views of an offset microstrip fed slot antenna. (After [13].) (b) Equivalent circuit for the microstrip fed slot antenna. (c) Equivalent network model of a microstrip-fed slot antenna of part (a). (From [13]. © 1998 IEEE. Reprinted with permission.)

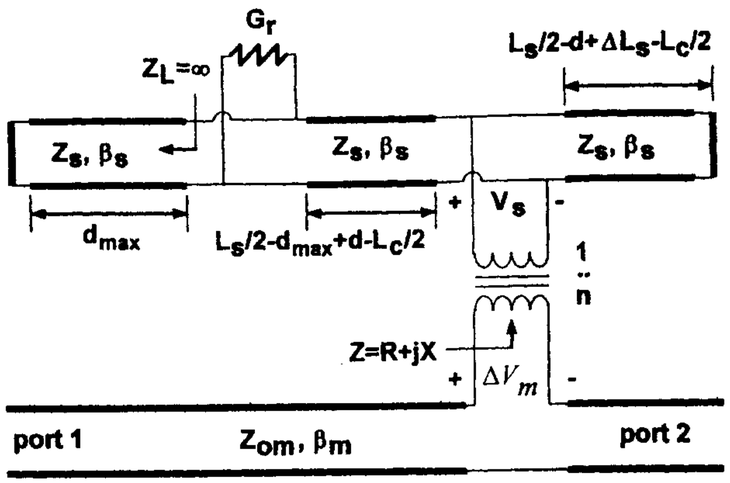

(c)

Figure 7.3 (continued).

antenna can be modeled as a series load impedance Z in the microstrip line as explained in [21]. This equivalent circuit is shown in Figure 7.3(b). The details of the model for impedance Z are described next.

7.2.1 Equivalent Circuit

The microstrip-fed slot antenna can be viewed as a microstrip line discontinuity and represented by an equivalent circuit [13] as shown in Figure 7.3(b). It consists of an ideal transformer, a radiation conductance, and a slot line terminated by short circuits at the two ends. Further, the slot appears as two parallelly connected sections of slot line with characteristic impedance Z_S and phase constant β_S. The power radiated from the slot is accounted for by the radiation conductance G_r. The effective length of the slot is taken as $L_S + \Delta L_S - L_C$, where L_S is the physical length of the slot and ΔL_S is the equivalent length associated with the nonzero inductance at the two shorted ends of the slot (similar to the open end extension of the microstrip patch antenna). A compensation length L_C is introduced to take into account the proximity effect of the microstrip line on the slot without using a complicated expression for the slot voltage. This length describes the variation in the observed resonant frequency with microstrip width, substrate parameters, offset distance d, β_S, and turns ratio n of the transformer. The ideal transformer represents the coupling between the slot and the microstrip line, and determines the

amount of slot voltage coupled in series to the microstrip. This voltage is also called the *discontinuity voltage*. The turns ratio n of the transformer is defined as $n = \Delta V_m / V_S$, where ΔV_m is the voltage discontinuity on the microstrip line and V_S is the voltage across the slot at the feed point.

7.2.2 Determination of Network Quantities

To determine the equivalent circuit parameters efficiently, a number of simplifying assumptions are made. These include the voltage distribution along the slot, and surrounding the microstrip line by fictitious boundary walls. These assumptions reduce the computer time considerably compared to the comprehensive rigorous solution given in [14].

For a *narrow slot* the induced electric field $\vec{E}_S$ for a voltage V_S across the slot at the feed point can be represented as

$$\vec{E}_S = -\hat{x} V_S e_s \tag{7.1}$$

with

$$e_s = \frac{1}{\pi\sqrt{(W_S/2)^2 - x^2}} g(y) \tag{7.2}$$

and

$$g(y) = \begin{cases} \dfrac{\sin\beta_s(y + L_s/2)}{\sin\beta_s(d + L_s/2)} & -L_s/2 \le y \le d \\ \dfrac{\sin\beta_s(y - L_s/2)}{\sin\beta_s(d - L_s/2)} & d \le y \le L_s/2 \end{cases} \tag{7.3}$$

The variation of slot voltage $g(y)V_S$ along the slot axis is plotted in Figure 7.4. At the feed point $y = d$, the slot voltage is V_S.

Radiation Conductance G_r

As in the case of a microstrip patch antenna, the radiation conductance is defined as

$$G_r = \frac{P_{rd} + P_{ra} + P_{\text{sur}}}{2V_{\text{ref}}^2} \tag{7.4}$$

where the reference voltage in the slot is defined as V_{ref} given by

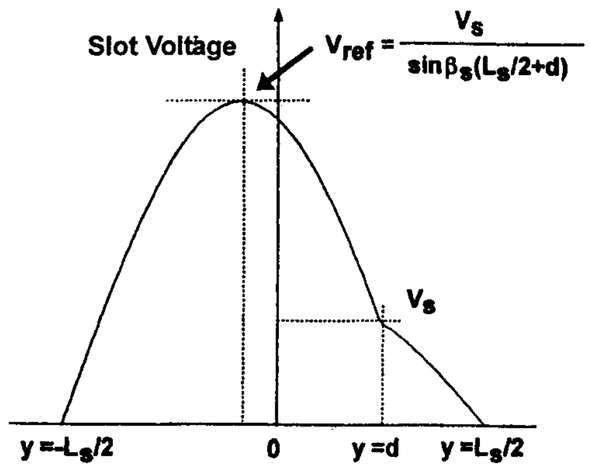

Figure 7.4 Assumed slot voltage distribution along the slot axis for determining the network quantities of Figure 7.3(b). (From [13]. © 1998 IEEE. Reprinted with permission.)

$$V_{\text{ref}} = \frac{V_s}{\sin\beta_s(L_s/2 + d)} \tag{7.5}$$

In (7.4) P_{rd} and P_{ra} are the radiated powers (in the form of space waves) from the slot into the substrate and air sides, respectively, and P_{sur} is the power carried by the surface wave and can be neglected for thin, low dielectric constant substrates. With the help of the reaction theorem and Parseval's theorem [22], P_{rd} can be expressed as

$$P_{rd} = \text{Re}\int_{k_y}\int_{k_x} \frac{k_x^2\tilde{Y}_{\text{TE}} + k_y^2\tilde{Y}_{\text{TM}}}{8\pi^2(k_x^2 + k_y^2)}|\tilde{M}|^2 dk_x dk_y \tag{7.6}$$

where the values of k_x and k_y are limited to the visible region $k_x^2 + k_y^2 \le k_0^2$.

The admittance parameter $\tilde{Y}_{\text{TE}}$ for the TE_z mode for the substrate side is given as [23]

$$\tilde{Y}_{\text{TE}} = Y_{0d}^{\text{TE}} \frac{Y_{00}^{\text{TE}} + Y_{0d}^{\text{TE}}\tanh(\gamma_{dz}h)}{Y_{0d}^{\text{TE}} + Y_{00}^{\text{TE}}\tanh(\gamma_{dz}h)} \tag{7.7}$$

where

$$Y_{00}^{\text{TE}} = \gamma_{0z}/j\omega\mu_0 \qquad Y_{0d}^{\text{TE}} = \gamma_{dz}/j\omega\mu_0$$

$$\gamma_{0z} = \sqrt{k_x^2 + k_y^2 - k_0^2} \qquad \gamma_{dz} = \sqrt{k_x^2 + k_y^2 - k_0^2\epsilon_r}$$

The expression for $\tilde{Y}_{\text{TM}}$ in (7.6) is similar to that for $\tilde{Y}_{\text{TE}}$ with the related parameters for the TM modes given as

$$Y_{00}^{\text{TM}} = j\omega\epsilon_0/\gamma_{0z} \qquad Y_{0d}^{\text{TM}} = j\omega\epsilon_0\epsilon_r/\gamma_{dz}$$

The quantity $\tilde{M}$ in (7.6) is the Fourier transform of the slot magnetic current. It is well behaved in the integration range and can be evaluated numerically without any difficulty. The P_{ra} term can be evaluated in a similar way for the air side by using $\epsilon_r = 1$ in (7.6). The P_{sur} term can also be determined from (7.6) but the integration is carried out in the neighborhood of singular points associated with the surface wave modes. This integration was discussed in Chapter 3.

In the equivalent circuit of Figure 7.3(b), the position of the radiation conductance in the slot line is set at $y = -L_S/2 + d_{\max}$ instead of the feed position $y = d$. Here $d_{\max}$ denotes the distance from the slot end to the first maximum of the electric field of a semi-infinite slot line, and $d_{\max}$ is nearly equal to $\lambda_s/4 - \Delta L_S/2$. The use of $d_{\max}$ enables one to neglect the effect of the slot line between G_r and the shorted end, and prevents the slot admittance from being infinite even for a zero electric field at the feed point [13].

Discontinuity Voltage ΔV_m

The discontinuity voltage ΔV_m on the microstrip line arises because of coupling to the slot. It is defined as

$$\Delta V_m = (\Gamma_1 - \Gamma_2)V_m \tag{7.8}$$

where Γ_1 and Γ_2 are the scattering coefficients at the two ends of the discontinuity, and V_m is the line voltage in the microstrip and equals $\sqrt{Z_{0m}}$ for unit power flow.

To determine Γ_1 and Γ_2, let us consider that an incident field is launched from $x = -\infty$ into port 1 and propagates to port 2 with the slot absent. The scattered field generated by the slot exists on both port 1 and port 2. If Γ_1 and Γ_2 are the scattering coefficients then the total magnetic field $\vec{H}$ on the microstrip is expressed as

$$\vec{H} = \begin{cases} \vec{h}^{+}\exp(-j\beta_m x) + \Gamma_1 \vec{h}^{-}\exp(j\beta_m x) & \text{for } x \le 0 \\ (1 + \Gamma_2)\vec{h}^{+}\exp(-j\beta_m x) & \text{for } x \ge 0 \end{cases} \tag{7.9}$$

where β_m is the phase constant for the dominant mode of the microstrip line. The total electric field is similarly obtained when $\vec{h}$ is replaced by $\vec{e}$ in (7.9). For the discontinuity centered at $x = 0$, the voltage at the two ends of the discontinuity are $(1 + \Gamma_1)V_m$ and $(1 + \Gamma_2)V_m$. Therefore, the discontinuity voltage is given by (7.8).

The field eigenvectors of the microstrip line, $\vec{e}^{+}$ and $\vec{h}^{+}$, are normalized for unit power flow, that is,

$$\iint_{S_m} (\vec{e}^{+} \times \vec{h}^{+}) \cdot \hat{x}\, dy\, dz = 1 \tag{7.10}$$

where S_m is the cross section of the microstrip line ($-\infty \le y \le \infty$, $0 \le z \le \infty$). The eigenvectors $\vec{e}^{-}$ and $\vec{h}^{-}$ are similarly normalized.

Invoking the reciprocity relationship between the microstrip and slot fields, one obtains after some algebraic manipulations [13]

$$\frac{\Gamma_i}{V_S} = \frac{-1}{2} \iint_{\text{slot}} (-\hat{x}e_s \times \vec{h}_i) \cdot \hat{z}\, ds \qquad (i = 1, 2) \tag{7.11}$$

with

$$\vec{h}_1 = \vec{h}^{+}\exp(-j\beta_m x)$$

$$\vec{h}_2 = \vec{h}^{-}\exp(+j\beta_m x)$$

Turns ratio *n*

The transformer turns ratio n is defined as $\Delta V_m / V_S$, that is,

$$n = (\Gamma_1 - \Gamma_2)V_m / V_S \tag{7.12}$$

and use of (7.11) and $V_m = \sqrt{Z_{0m}}$ gives

$$n = \sqrt{Z_{0m}}(n_{y1} - n_{y2})/2 \tag{7.13}$$

with

$$n_{y1} = \iint_{\text{slot}} e_s h_y \exp(-j\beta_m x)\, ds \tag{7.14a}$$

$$n_{y2} = \iint_{\text{slot}} e_s h_y \exp(j\beta_m x)\, ds \tag{7.14b}$$

where h_y denotes the y component of the magnetic field eigenvector $\vec{h}^{+}$. To evaluate (7.14), we need to determine h_y. The source of $\vec{h}^{+}$ is the forward traveling current on the microstrip line whose magnitude equals $1/\sqrt{Z_{0m}}$ and is evaluated as the convolution of the microstrip electric current distribution and the Green's function. To reduce the number of computations, the microstrip line is surrounded by fictitious boundary walls at a large distance $y = \pm L$ so that the walls do not disturb the electromagnetic field distribution. This assumption enables one to use the finite Fourier transform in place of the infinite Fourier integral for the y direction as

$$\tilde{h}_y(k_{ym}, z) = \int_{-L}^{L} h_y(y, z)\exp(jk_{ym}y)\, dy \tag{7.15a}$$

or

$$h_y(y, z) = \frac{1}{4L} \sum_{m=-\infty}^{\infty} \tilde{h}_y(k_{ym}, z)\exp(-jk_{ym}y) \tag{7.15b}$$

with

$$k_{ym} = m\pi/(2L) \quad \text{and} \quad m = 0, \pm 1, \pm 2, \ldots$$

For a narrow strip, the surface current density on the microstrip can be approximated by J_x alone and can be written as

$$J_x(y) = \frac{1}{\sqrt{Z_{0m}}} \frac{1}{\pi\sqrt{(W_m/2)^2 - y^2}} \tag{7.16a}$$

$$\tilde{J}_x(k_{ym}) = \frac{1}{\sqrt{Z_{0m}}} J_0\left(\frac{W_m}{2}|k_{ym}|\right) \tag{7.16b}$$

where $J_0(x)$ is the zeroth-order Bessel function. Using the spectral-domain immittance approach, $\tilde{h}_y$ on the ground plane at $z = 0$ can be derived as [23]

$$\tilde{h}_y(k_{ym}, 0) = \frac{1}{\cosh(\gamma_{dzm}h)} \frac{\tilde{J}_x(k_{ym})}{\beta_m^2 + k_{ym}^2} \left[\frac{\beta_m^2 Y_{\text{TM}}^-}{Y_{\text{TM}}^- + Y_{\text{TM}}^+} + \frac{k_{ym}^2 Y_{\text{TE}}^-}{Y_{\text{TE}}^- + Y_{\text{TE}}^+} \right] \tag{7.17}$$

with

$$Y_{\text{TM}}^+ = \frac{j\omega\epsilon_0}{\gamma_{0zm}} \qquad Y_{\text{TM}}^- = \frac{j\omega\epsilon_0\epsilon_r}{\gamma_{dzm}} \coth(\gamma_{dzm}h)$$

$$Y_{\text{TE}}^+ = \frac{\gamma_{0zm}}{j\omega\mu_0} \qquad Y_{\text{TE}}^- = \frac{\gamma_{dzm}}{j\omega\mu_0} \coth(\gamma_{dzm}h)$$

$$\gamma_{0zm} = \sqrt{\beta_m^2 + k_{ym}^2 - k_0^2} \qquad \gamma_{dzm} = \sqrt{\beta_m^2 + k_{ym}^2 - k_0^2\epsilon_r}$$

When we substitute (7.2) and (7.15b) into (7.14), we obtain

$$\begin{aligned} n_{y1} &= \frac{1}{4L} \sum_{m=-\infty}^{\infty} \int_{-L_S/2}^{L_S/2} \int_{-W_S/2}^{W_S/2} \\ &\quad \frac{1}{\pi\sqrt{(W_S/2)^2 - x^2}} g(y) \tilde{h}_y(k_{ym}, 0) \exp(-jk_{ym}(y - d)) \exp(-j\beta_m x)\, dx dy \\ &= \frac{1}{4L} I_{x1}(\beta_m) \sum_{m=-\infty}^{\infty} \tilde{h}_y(k_{ym}, 0) I_{y1}(k_{ym}) \end{aligned} \tag{7.18}$$

where

$$I_{y1}(k_{ym}) = \int_{-L_S/2}^{L_S/2} g(y) \exp(-jk_{ym}(y - d))\, dy \tag{7.19}$$

$$I_{x1}(\beta_m) = \int_{-W_S/2}^{W_S/2} \frac{1}{\pi\sqrt{(W_S/2)^2 - x^2}} \exp(-j\beta_m x)\, dx = J_0\left(\frac{W_S}{2}\beta_m\right) \tag{7.20}$$

We obtain an integral similar to (7.18) for n_{y2}, except that the exponents of e are positive.

Expressions for L_c, Z_S, β_S, and ΔL_S, etc.

An empirical expression for the compensation length L_c has been reported in [13]. It is

$$L_c = 2 \times 10^{-2} \frac{W_m}{h\sqrt{\epsilon_r}/\lambda_0} n^2 \sin\beta_S(L_S/2 + d) \tag{7.21}$$

The slot line parameters Z_S, β_S, and ΔL_S can be calculated using various analysis methods [21]. Closed-form expressions for Z_S and β_S are available in Appendix B.

Results

The results for the microstrip-fed slot antenna available in [13] are reproduced below. First we consider an antenna with the centered slot ($d = 0$). The structural parameters considered are $W_m = 5$ mm, $h = 1.6$ mm, $\epsilon_r = 2.20$, $L_S = 40.2$ mm, and $W_S = 0.7$ mm. The calculated slot line parameters λ_S/λ_0 and Z_S, the turns ratio n, the short-circuit end-effect ΔL_S, and the radiation conductance are plotted in Figure 7.5 over the frequency range of 2 to 4 GHz. At $f = 3$ GHz, the value of ΔL_S is about 2 mm, n is approximately 0.9, G_r is about 1 mmho, d_{max} is calculated to be 19.77 mm, and the radiation efficiency is 0.94. It is reported that if $L = 4W_m$ and m of (7.18) is restricted to $-7 \le m \le 7$ then the error in n is less than 0.5%. The computed results for the antenna series impedance are plotted in Figure 7.6 and compared with the measured results of Himdi and Daniel [19], and the rigorous integral equation solution. The comparison is seen to be good. It may also be determined from Figures 7.5 and 7.6 that the resonant length of the slot antenna can be expressed as $L_r = \lambda_S/2 - \Delta L_S$.

The effect of off-centering the slot on the reduction in antenna impedance is shown in Figure 7.7. Note that the peak series resistance decreases with the increase in the value of d and it is possible to obtain a value comparable to the microstrip characteristic impedance.

7.2.3 Inclined Slot

It was pointed out earlier that one way to reduce antenna impedance seen by the feed is to rotate the slot with respect to the microstrip feed line. The geometry of an inclined slot is shown in Figure 7.8. The equivalent circuit for this geometry remains the same [see Figure 7.3(b)]. Also, the value of G_r does

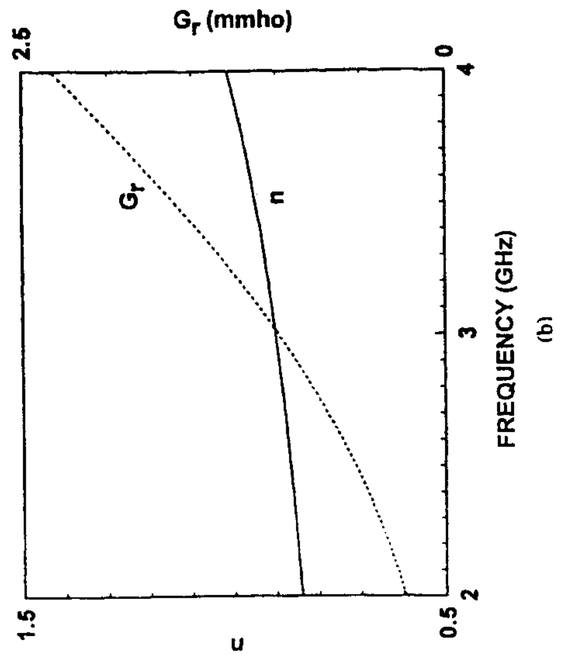

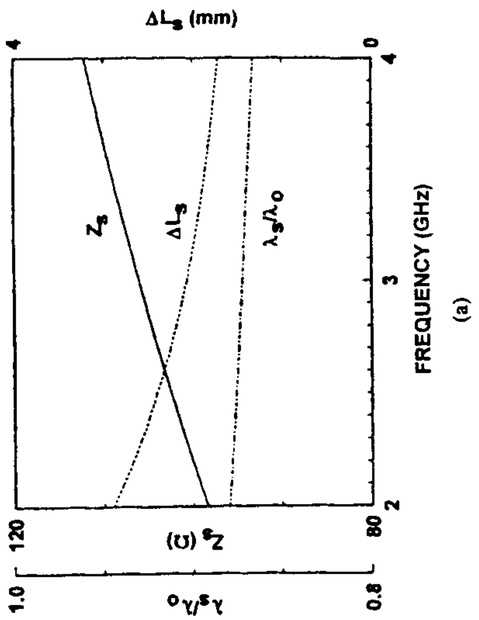

Figure 7.5 Frequency variation of lumped equivalent circuit parameters of Figure 7.3(c) (W_m = 5 mm, h = 1.6 mm, ϵ_r = 2.2, L_S = 40.2 mm, W_S = 0.7 mm, d = 0 mm, θ_S = 0°). (a) Characteristic impedance Z_S, normalized guide wavelength λ_S/λ_0, and short-circuit end-effect ΔL_S. (b) Turns ratio n and radiation conductance G_r. (From [13]. © 1998 IEEE. Reprinted with permission.)

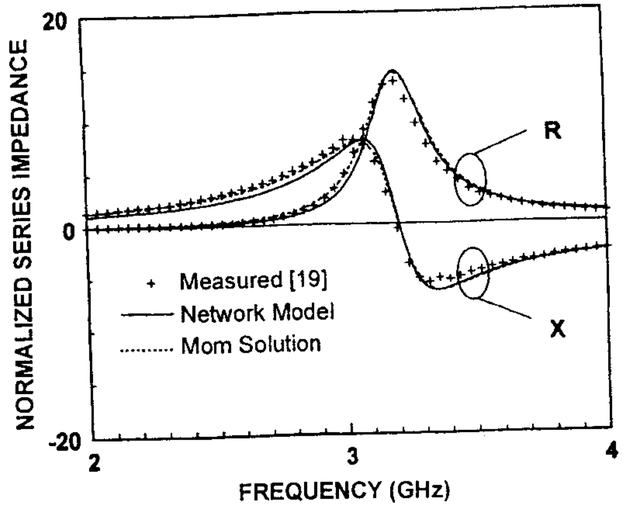

Figure 7.6 Normalized series impedance of a microstrip-fed slot antenna (parameters of Figure 7.5 apply). (From [13]. © 1998 IEEE. Reprinted with permission.)

not change due to the inclination. The values of n and L_c change with the inclination angle θ_S. The effect of slot inclination on the impedance seen by the feed line has been studied by many authors [13, 17, 18]. Figure 7.9 shows the effect of θ_S on n. It shows that n decreases with the increase in the value of θ_S. As a result the antenna impedance decreases. The antenna impedance is plotted in Figure 7.10. The structure dimensions and the parameters are the same as discussed above. Axelrod et al. [15] have described the broadbanding of an off-center fed slot antenna using an external matching network. The VSWR = 3 bandwidth has been reported to be about 47%.

A cavity-backed broadband slot radiator has also been described there. It may be observed from Figures 7.7 and 7.10 that the series reactance is nonzero at the frequency at which the normalized series resistance is unity. The series reactance of the antenna can be cancelled by the use of a suitable length of the microstrip open stub on the feed line [14].

7.2.4 Design of Microstrip-Fed Slot Antenna

The first step in the design of a slot antenna is to determine the physical length of the resonant slot. It has been found that for a slot resonant in its dominant mode, the resonant length L_r is given approximately by $L_r = \lambda_S/2 - \Delta L_S$, where ΔL_S is the equivalent length associated with the nonzero inductance at the shorted ends. The next step is to design the feed such that the series resistance of the slot antenna matches the feed impedance. For this, one can use an off-centered microstrip feed or the slot can be inclined with respect to

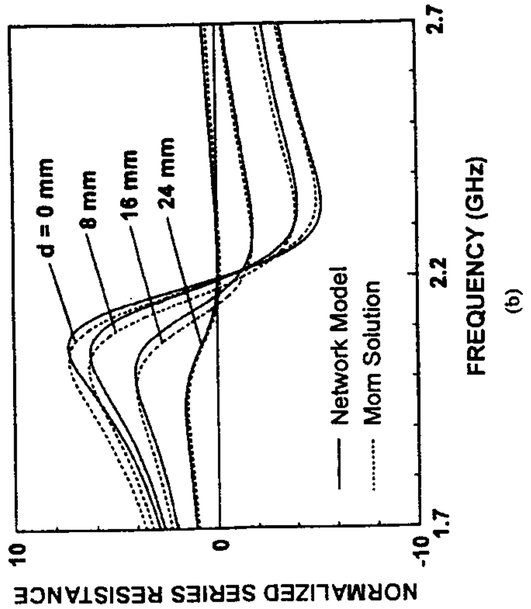

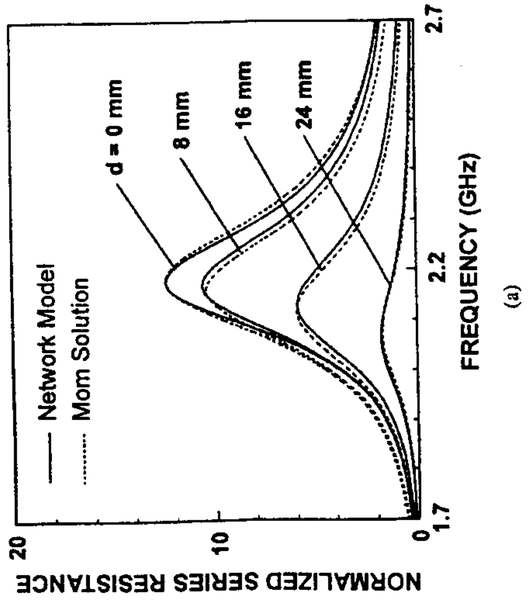

Figure 7.7 Effect of the offset distance d of a slot on the normalized series impedance of a microstrip-fed slot antenna (W_m = 5 mm, h = 1.6 mm, ϵ_r = 2.2, L_S = 60 mm, W_S = 2 mm, θ_S = 0°). (a) Normalized series resistance and (b) normalized series reactance. (From [13]. © 1998 IEEE. Reprinted with permission.)

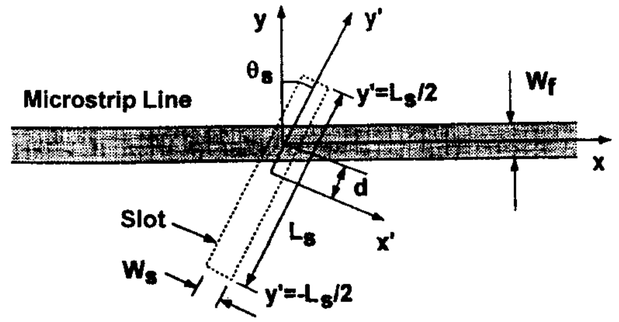

Figure 7.8 Top view of a microstrip-fed slot antenna with an offset and inclined slot. (From [13]. © 1998 IEEE. Reprinted with permission.)

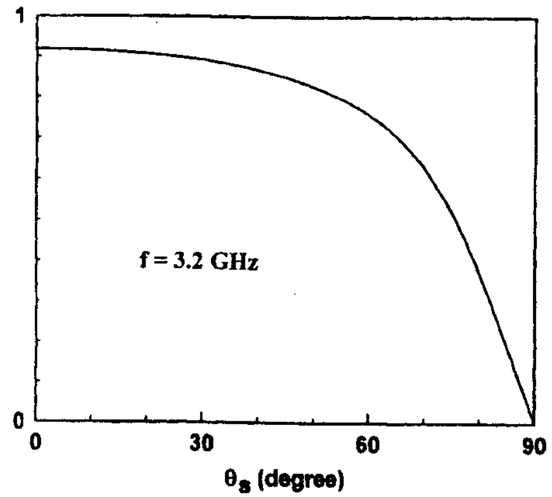

Figure 7.9 Decrease in the turns ratio n due to the inclination angle θ_S (parameters of Figure 7.7 apply, f = 3.2 GHz). (From [13]. © 1998 IEEE. Reprinted with permission.)

the feed to obtain 50Ω antenna impedance. The design curves, similar to those in Figures 7.7. and 7.10, need to be generated as a function of offset distance d or the inclination angle θ_S. These curves are then used to determine the feed position. Return loss curves based on inclined slot and offset feed approaches are plotted in Figure 7.11 [13]. Figure 7.11(a) corresponds to the case when d = 0 mm and θ_S = 60°; and d = 20 mm and θ_S = 0° for Figure 7.11(b).

7.2.5 Radiation Patterns

The radiation fields of a slot antenna can be evaluated by using the vector electric potential method and the electric field distribution in the slot. The

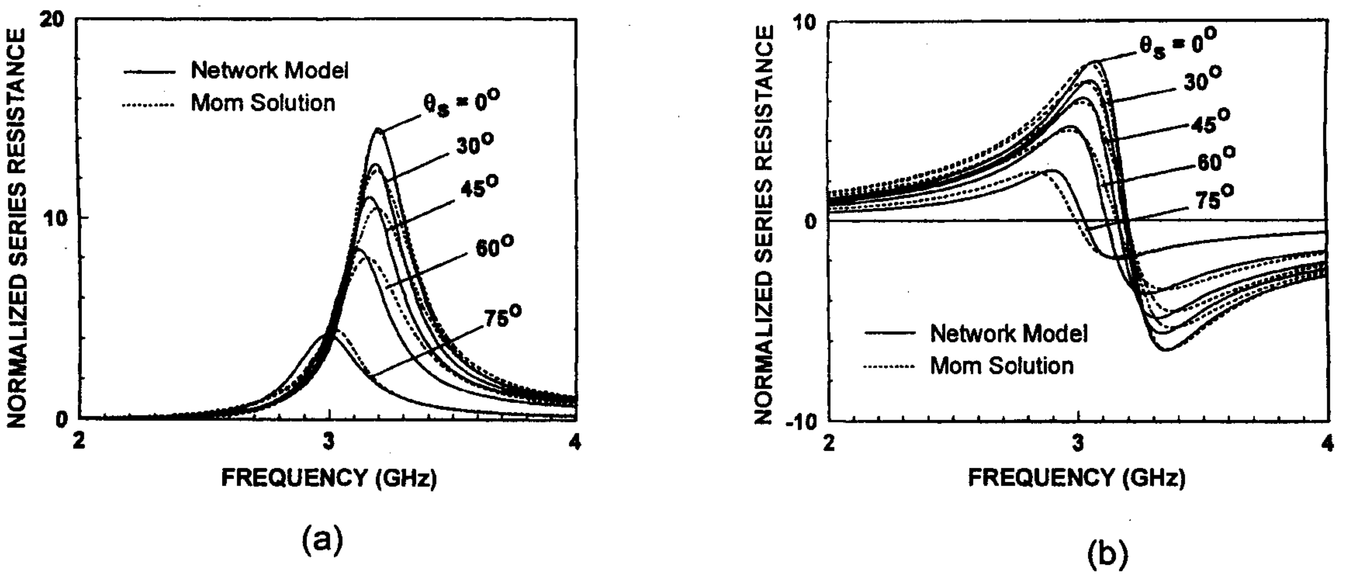

Figure 7.10 Effect of the inclination angle θ_S of a center-fed slot on the normalized series impedance of a microstrip-fed slot antenna (parameters of Figure 7.5 apply). (a) Normalized series resistance and (b) normalized series reactance. (From [13]. © 1998 IEEE. Reprinted with permission.)

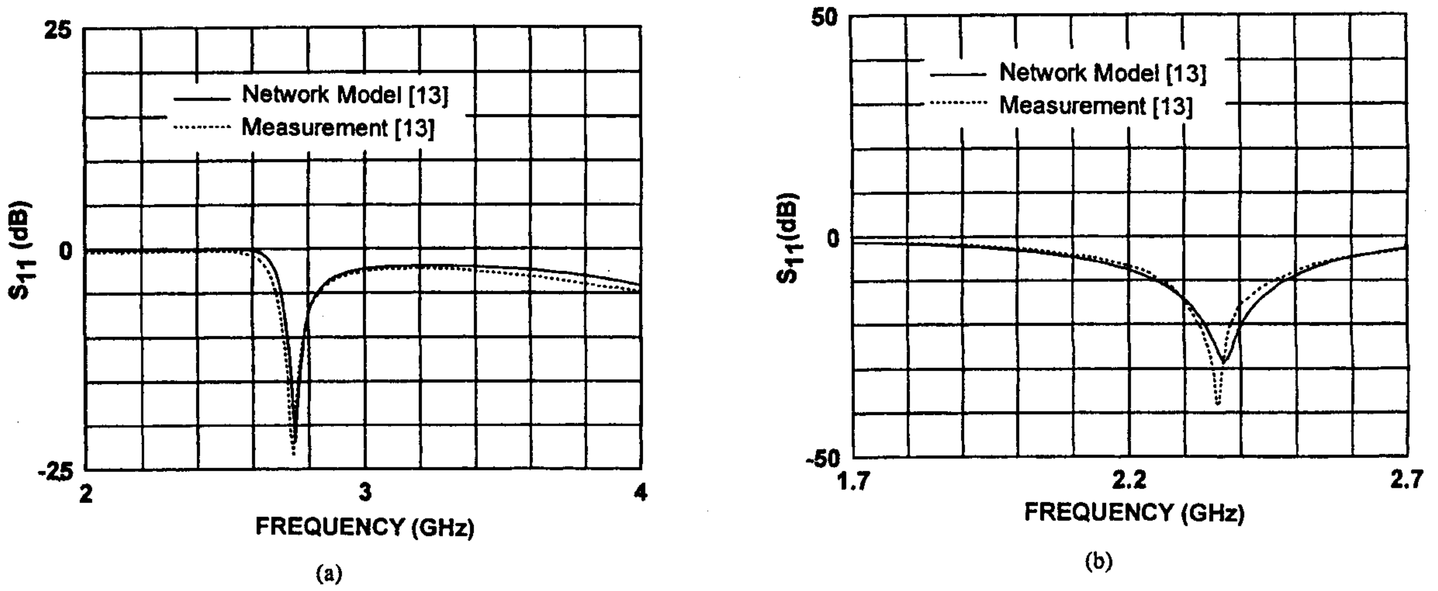

Figure 7.11 Return loss for the microstrip-fed slot antenna (a) with an inclined, centered slot (parameters of Figure 7.5 apply, and $\theta_S = 60°$, microstrip stub length $L_m = 42.6$ mm) and (b) with an off-centered noninclined slot (parameters of Figure 7.7 apply, and $d = 20$ mm, $L_m = 29.2$ mm). (From [13]. © 1998 IEEE. Reprinted with permission.)

far-field components for a center-fed slot can be written as (assuming the effect of substrate to be negligible)

$$E_\theta = \frac{-jk_0}{4\pi}\frac{e^{-jk_0 r}}{r} \int_{-W_S/2}^{W_S/2}\int_{-L_S/2}^{L_S/2} [-M_x \sin\phi + M_y \cos\phi] \exp[jk_0(x\sin\theta\cos\phi + y\sin\theta\sin\phi)]\,dxdy \tag{7.22a}$$

$$E_\phi = \frac{jk_0}{4\pi}\frac{e^{-jk_0 r}}{r}\cos\theta \int_{-W_S/2}^{W_S/2}\int_{-L_S/2}^{L_S/2} [M_x \cos\phi + M_y \sin\phi] \exp[jk_0(x\sin\theta\cos\phi + y\sin\theta\sin\phi)]\,dxdy \tag{7.22b}$$

where $\vec{M}(x, y) = M_x\hat{x} + M_y\hat{y}$ is the magnetic surface current and can be expressed in terms of the slot electric field $\vec{E}(x, y)$ as

$$\vec{M}(x, y) = \vec{E}(x, y) \times \hat{z} = E_y\hat{x} - E_x\hat{y} \tag{7.23}$$

When the slot is narrow compared to the free-space wavelength, that is, $W_S << \lambda_0$, to a first-order approximation, the electric field across the slot can be assumed to be constant. If $E_x = 0$ and $E_y = E_0\cos(\pi x/L_S)$, after integration (7.22) reduces to (assuming $k_0 W_S \to 0$).

$$E_\theta = \frac{-jk_0 E_0 L_S W_S}{2\pi^2}\frac{e^{-jk_0 r}}{r}\frac{\cos X}{(2X/\pi)^2 - 1}\sin\phi \tag{7.24a}$$

$$E_\phi = \frac{jk_0 E_0 L_S W_S}{2\pi^2}\frac{e^{-jk_0 r}}{r}\frac{\cos X}{(2X/\pi)^2 - 1}\cos\phi\cos\theta \tag{7.24b}$$

where

$$X = \frac{k_0 L_S}{2}\sin\theta\cos\phi$$

The radiation patterns in the E plane ($\phi = \pi/2$) are obtained as follows:

$$E_\phi = 0 \quad \text{and} \quad E_\theta = \frac{jk_0}{2\pi^2}\frac{e^{-jk_0 r}}{r}E_0 W_S L_S \tag{7.25a}$$

and for the H plane ($\phi = 0$) as follows:

$$E_\theta = 0 \quad \text{and} \quad E_\phi = \frac{jk_0}{2\pi^2}\frac{e^{-jk_0 r}}{r}E_0 W_S L_S \cos\theta \frac{\cos(k_0 L_S \sin\theta/2)}{(k_0 L_S \sin\theta/\pi)^2 - 1} \tag{7.25b}$$

In deriving the preceding equations, the ground plane of the slot antenna is assumed to be infinite, and the electric field is assumed to be entirely across the width of the slot with no field component along the length of the slot. The effect of the substrate is also neglected.

The measured and computed radiation patterns of a matched offset-fed resonant slot are shown in Figure 7.12. The H-plane radiation pattern is similar to the E-plane pattern of a dipole antenna. The measured beamwidth in the

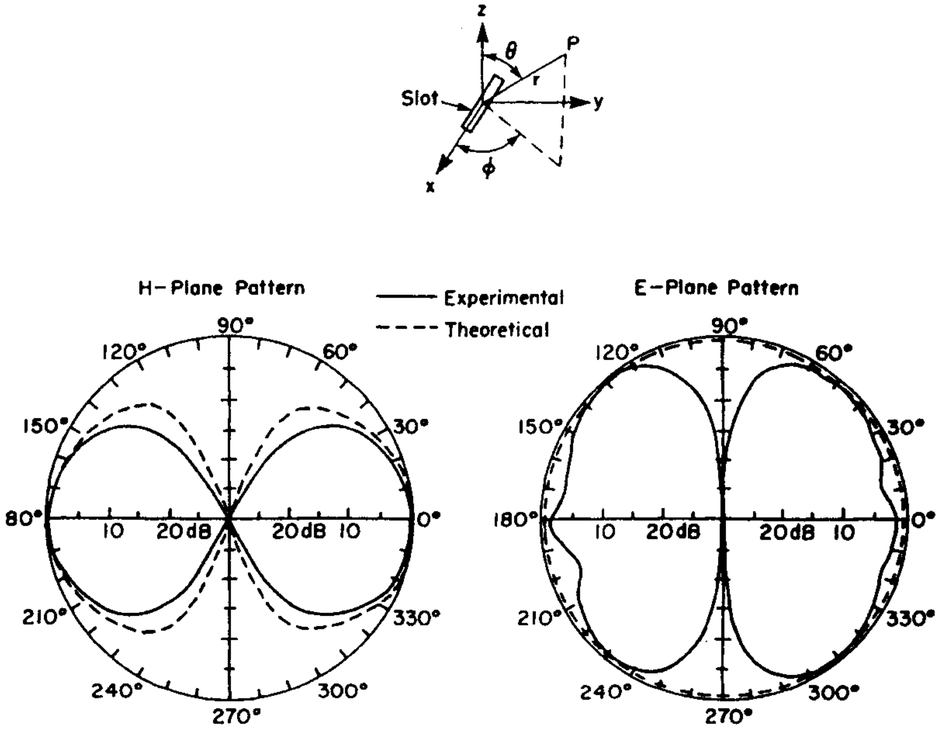

Figure 7.12 Radiation patterns of a matched offset-fed slot. (From [12]. © 1972 IEEE. Reprinted with permission.)

H plane is about 68° for the offset-fed case. The distortions of the measured E-plane radiation pattern are due to the finite size of the ground plane [12], whereas the nulls are due to the finite width of the slot. The use of an exact Green's function in the determination of radiation pattern, however, shows that nulls appear in the end-fire direction in both planes [14]. The slot antennas can be regarded as being complementary to dipoles. As long as $h << \lambda_0$, the dielectric substrate has only a negligible effect on the far field. Furthermore, since the width of the microstrip conductor for a characteristic impedance of 50Ω is much smaller than the length of the slot, the field disturbances caused by the proximity of the strip conductor produce only negligible far-field distortions.

The radiation patterns of microstrip-fed slot antennas are bidirectional. Unidirectional radiation can be obtained by placing a plane reflector at one side of the strip conductor, parallel to the substrate surface (see Figure 7.13). The dependence of the input impedance and radiation characteristics on the slot-to-reflector spacing has been discussed by Yoshimura [12]. From the H-plane pattern measurements for various slot-to-reflector spacings, the optimum spacing between the slot and the reflector is approximately $\lambda_0/4$ for minimum sidelobe level, and maximum front-to-back ratio. The final impedance match for a radiator with a reflector is obtained by changing the size of the slot.

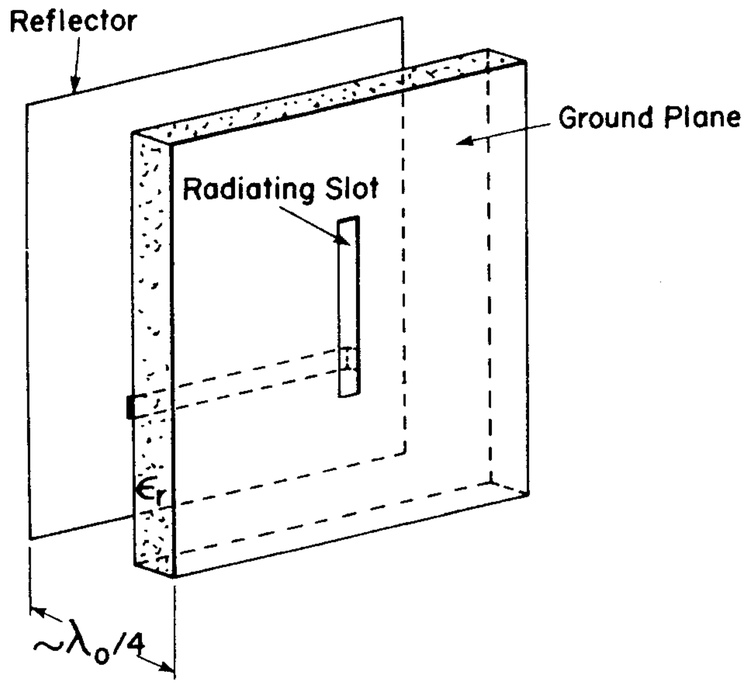

Figure 7.13 Offset-fed microstrip slot geometry with a plane reflector for unidirectional radiation.

Microstrip-Fed Cylindrical Slot Antenna

The reciprocity approach has been used to analyze a slot in the ground plane of a cylindrical microstrip line [24]. It has been found that the back radiation decreases when the size of the cylinder is increased. Design and experimental results of a microstrip slot radiator operating at 2.45 GHz for local hypothermia applications have been reported by Bahl et al.[†]

7.3 CPW-Fed Slot Antennas

The microstrip feed for slot antennas suffers from the need for careful alignment of the etchings on the two sides of the board. Also, the use of a microstrip line is not compatible with monolithic fabrication and therefore easier integration with active solid-state devices is not possible. These problems have been solved by the introduction of the coplanar waveguide (CPW) feed.

CPW-fed aperture antennas have been studied extensively [25–36]. Rigorous analysis of these antennas is based on the integral equations solution in the spectral domain [25], integral equation solution in space domain [33, 36], and FDTD analysis [35]. Experimental results for loop antennas with a CPW feed [26] and approximate transformation analysis for electrically narrow slots [27] have been published. Loop antennas [28, 29] and slot antennas [30, 33–36] fed by a CPW have also been reported. Nesic has used CPW-fed slots as primary radiators in a phase scanned antenna [31, 32]. A folded slot configuration can be used to scale down the antenna impedance [35]. CPW line inductively coupled to the slot antenna can be used for series-fed arrays [36]. A bow-tie slot antenna [37] is the slot configuration equivalent of the bow-tie printed dipole studied in Chapter 6.

One of the main issues with CPW-fed slot antennas is the need for a suitable transition. Many types of CPW slot line transitions have been proposed for antenna applications. Some of these are one-wavelength long center-fed slot antenna [31] shown in Figure 7.14(a), the one-wavelength long offset-fed slot antenna [34] of Figure 7.14(b), the half-wave long capacitively fed slot antenna of Figure 7.14(c), and the inductively coupled slot antenna [36] of Figure 7.14(d). The coplanar waveguide is excited in the odd mode of the coupled slot line, also called the CPW mode. In this mode, the equivalent magnetic currents on both CPW slots radiate almost out of phase, contributing negligibly to the cross-polar component of the radiation pattern. This feature

[†] Bahl, I. J., S. S. Stuchly, and M. A. Stuchly, "New Microstrip Slot Radiator for Medical Applications," *Electron. Lett.*, Vol. 16, 1980, pp. 731–732.

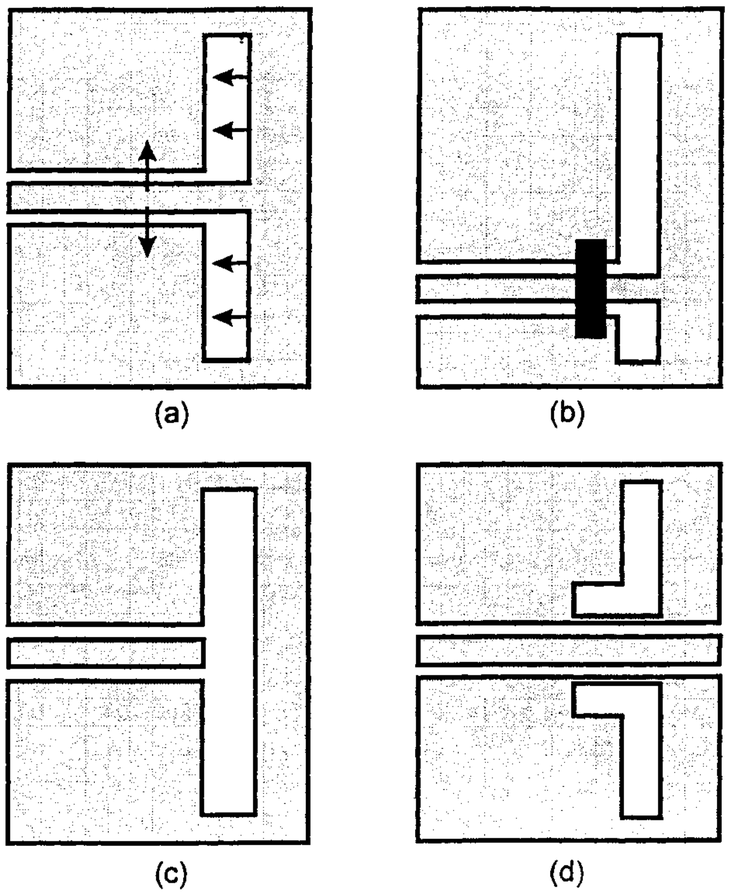

Figure 7.14 CPW-fed slot antennas: (a) Center-fed slot antenna, (b) offset-fed slot antenna, (c) capacitively coupled slot antenna, and (d) inductively coupled slot antenna.

of CPW feed is useful in the design of antenna arrays, since the mutual coupling between adjacent lines is minimized.

The excitation mechanism in Figure 7.14(a) is easy to understand. In this case, the electric field lines in the two CPW apertures excite the respective slots of the antenna. The radiated field of the antenna is linearly polarized along the slot width. Active slot antennas of this type on $\epsilon_r = 1$ and $\epsilon_r = 12$ substrates have been developed [33]. An offset feed in Figure 7.14(b) is used for proper impedance matching of the slot antenna to the characteristic impedance of the CPW. The excitation of the inductively coupled slot antenna of Figure 7.14(d) is explained from the magnetic field coupling between the CPW and the slot antenna. This coupling is shown in Figure 7.15. The magnetic field induces the electric field in the coupled slots as shown. Since

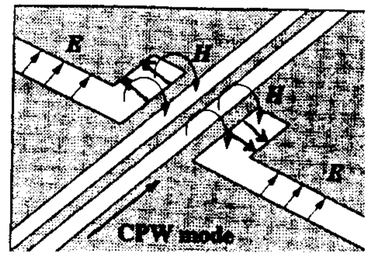

Figure 7.15 Electric and magnetic fields in the coupling region of the inductively coupled CPW-slot antenna. (After [36]. © 1999 IEEE. Reprinted with permission.)

the electric fields in the horizontal portions of the slots are oppositely directed, they do not contribute to the radiation, but are used to increase coupling between the CPW and slot antenna, and are responsible for cross-polarization in the radiation patterns. The vertical arms of the slots are responsible for radiation because of the similarly directed aperture fields. The antenna appears as a series load in the CPW feed line and the equivalent circuit of Figure 7.3(b) applies. The inductively coupled CPW feed introduces extra variables such as the length of the horizontal arm of the slot and spacing between the CPW and the horizontal arm. The extra variables can be used to tune the antenna characteristics. The inductive feed is particularly suitable for a series-fed array configuration. The layout of a three-element log-periodic slot array is shown in Figure 7.16 [36].

Folded-Slot Antenna

The radiation resistance of a single slot antenna in free space is nearly 500Ω. The use of additional slots allows the radiation resistance to be scaled down over a wide range according to [35]

$$Z_{\text{in},N} = \frac{Z_{\text{slot}}}{N^2} \tag{7.26}$$

where $Z_{\text{in},N}$ is the impedance of an N-element slot antenna. Equation (7.26) can be used for up to a value of 5 [35]. The feed arrangement of Figure 7.14(a) can be used to develop a multiple-slot antenna. The inset of Figure 7.17 shows a number of multiple-slot or folded-slot antennas. A folded-slot antenna corresponds to $N = 2$. Variation of the input impedance with frequency for a number of folded-slot antennas is shown in Figure 7.17 [35]. The impedance scales in close agreement with (7.26) as the number of slots increase. The resonant frequencies of all of these antennas are about the same, near 10.5 GHz. In another study, a double-folded/triple-slot antenna on $\epsilon_r = 2.2$

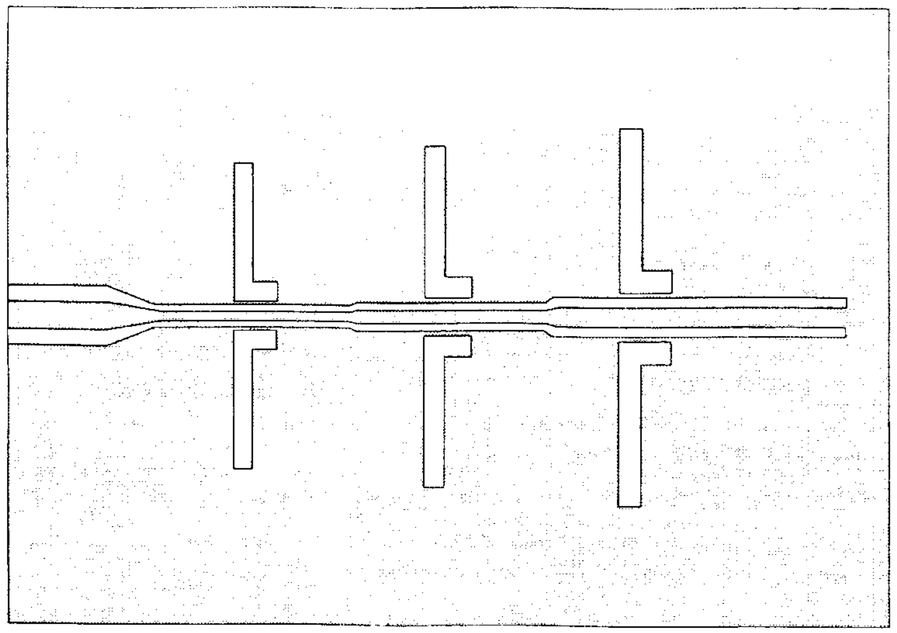

Figure 7.16 Layout of three-element log-periodic slot array fed by a CPW. (From [36]. © 1999 IEEE. Reprinted with permission.)

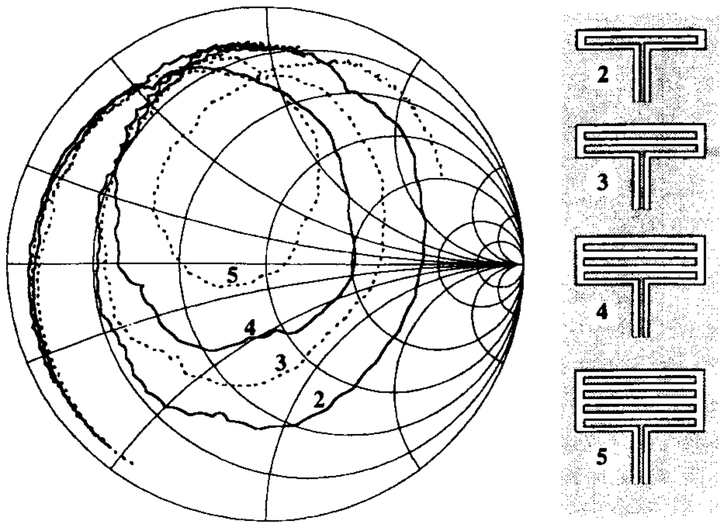

Figure 7.17 Variation of input impedance with frequency for a number of multiple-slot antennas. The input impedance at resonance scales according to (7.26). (From [35]. © 1995 IEEE. Reprinted with permission.)

substrate with h = 0.813 mm provided a −10-dB return loss bandwidth of about 30%. The measured input impedance of this antenna was 60Ω at 1.66 GHz [35].

Unidirectional Slot Antennas

The radiation from the slot antennas described earlier is bidirectional in nature. Liu et al. have used grounded substrates to obtain unidirectional radiation from rectangular slot and (slot) loop antennas [25]. They have used dielectric layers with different dielectric constants to avoid parallel plate TEM modes between the two parallel conductor planes. A configuration of these antennas is shown in Figure 7.18 [25]. Theoretical studies indicate that VSWR ≤ 2 bandwidth is about 26.7% for the loop antenna centered at 14.6 GHz, and is about 25.4% for the slot antenna for resonance at 10.6 GHz [25]. The composite substrate used was 0:787-mm-thick Duroid RT/5880 with ϵ_r = 2.2, and an air dielectric of thickness 0.635 mm was placed between the upper substrate and the back conductor.

CPW-fed aperture antennas analyzed in [25] employ relatively wide slots. Therefore, both components of the electric field in the aperture are modeled. It is possible to obtain a match between the feed line and these antennas by adjusting the slot antenna width and/or the thickness of the substrate. The resonant frequency can be adjusted by adjusting the length of the loop and slot, since the resonant length of a loop is approximately equal to one guide

Figure 7.18 Configurations of a loop antenna and a slot antenna with a CPW feed: (a) Loop antenna and (b) slot antenna. (From [25]. © 1995 IEEE. Reprinted with permission.)

wavelength and the resonant length of a slot is approximately half a guide wavelength.

The radiation efficiency of the loop antenna is found to be maximum 54% at resonance, and that of the slot antenna is about 36% for the composite substrate parameters given earlier [25]. For experimental verification of the theoretical results, the composite substrate had 31-mil-thick RT/5880 with ϵ_r = 2.2 and 1-in.-thick honeycomb substrate (ϵ_r = 1.08). The input impedance of a wide slot antenna is plotted in Figure 7.19(a). Good agreement is observed between the computed and measured input impedance from 6 to 9.5 GHz. The far-field patterns of this slot antenna in the ϕ = 90° plane are plotted in Figure 7.19(b) at 9.5 GHz. The nulls near ±60° are due to the array factor introduced by the wide separation of the two slots. The far-field radiation patterns of the loop antenna in the ϕ = 90° plane at 8.65 GHz are plotted in Figure 7.20. The agreement between the measured and calculated patterns appears to be good except near end fire. This difference is due to the use of absorbing material at the edge of the board to reduce edge diffraction.

CPW-fed slot antennas have also been used for power combining at millimeter-wave frequencies. The substrate used is normally thick with thicknesses selected in odd multiples of a quarter-dielectric wavelength, λ_d. The power lost in the substrate due to the surface waves could be considerable when a single slot is used [38]. The loss decreased to half when a four slot-array antenna with two parasitics is used, and the power gain improved by 5 dB [38]. Figure 7.21 shows two configurations of the CPW-fed slot array antennas. The antenna in Figure 7.21(a) consists of two resonant slots fed by CPW and there are a number of parasitic slots. The separation d_k of a pair of parasitic slots is given by $d_k = (k - 0.4)\lambda_d$. Figure 7.21(b) shows an array of slots in which the length of CPW between each pair of slots is 1 λ_m so that all the slots are excited in phase. It was found that the power gain of the slot antenna array of the type shown in Figure 7.21(b) at 94 GHz could be increased by 11 dB over a single-slot antenna by using a two-dimensional 8 × 3 slot array fed by a CPW [38].

CPW-Fed Bow-Tie Slot Antennas

A bow-tie slot antenna fed by CPW has been introduced by Soliman et al. [37]. This antenna is the equivalent of a printed dipole antenna in the slot configuration. The geometry and the various dimensions of the antenna are shown in Figure 7.22. Antennas with two different flare angles, 60° and 90°, have been studied. It was found that the bow-tie slot antenna has a dipole-like radiation pattern with measured cross-polarization level less than −20 dB in the E plane and less than −18 dB around the boresight direction. The measured gain of the antenna is nearly 5.5 dB. A bow-tie antenna with 90°

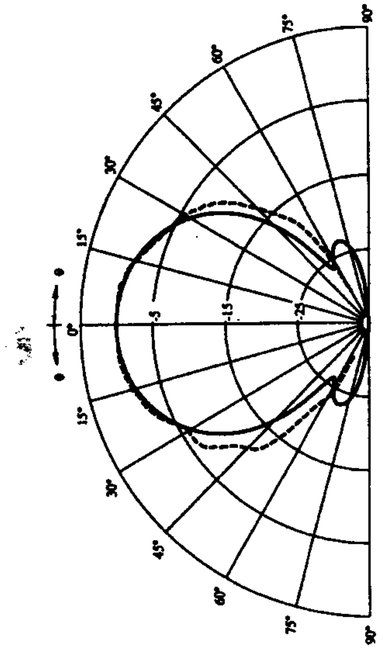

(b)

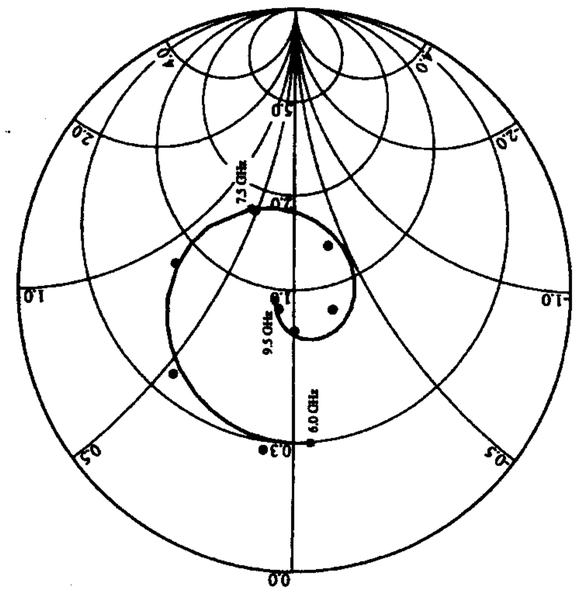

(a)

Figure 7.19 Input impedance and radiation pattern of a slot antenna (slot length = 11.6 mm, slot width = 3.3 mm, feed line slot width = 1.651 mm, center strip width = 5.5 mm, composite substrate: 31 mil thick with ϵ_r = 2.2 and 1 in. thick with ϵ_r = 1.08). (a) Input impedance (____, experiment; • • •, analysis). (b) Far-field pattern in ϕ = 90-degree plane (f = 9.5 GHz; ____ analysis; ----, measurement). (From [25]. © 1995, IEEE. Reprinted with permission.)

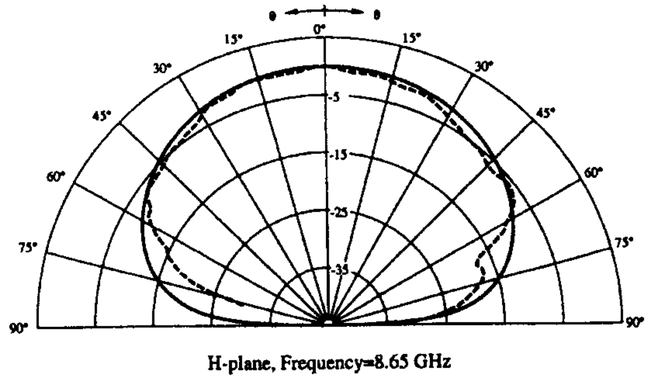

Figure 7.20 Far-field pattern of a loop antenna in the ϕ = 90-degree plane (f = 8.65 GHz, loop length = 17.1 mm, loop width = 8.26 mm, feed line slot width = 1.651 mm, center strip width = 4.95 mm, composite substrate: 31 mil thick with ϵ_r = 2.2 and 1 in. thick with ϵ_r = 1.08; ____, analysis; ----, measurement). (From [25]. © 1995 IEEE. Reprinted with permission.)

flare angle is found to be better because it provides a larger bandwidth of about 34.6% compared to 32% for the 60° flare angle. The cross-polarization level is also lower for the antenna with 90° flare angle.

7.4 Annular Slot Antennas

The rectangular (slot) loop antenna was described in the last section. A variation of this is a circular loop antenna called an *annular slot antenna*. This antenna is very versatile and is discussed next.

An annular slot antenna comprises a circular slot in the ground plane of a dielectric substrate, fed by a microstrip conductor as shown in Figure 7.23. This geometry is of interest because of its possible application as a vehicular antenna for mobile communications, since it can radiate power at low elevation angles [39]. In urban mobile communications, incident waves to mobile stations come mostly from directions having low elevation angles, about 30° up from the horizontal plane. Radiation pattern analysis of an annular slot antenna is presented next.

Consider the geometry of an annular slot in the coordinate system of Figure 7.24. An annular slot in a conducting plane of infinite extent can be viewed as an annular distribution of the magnetic surface current given by

$$\vec{M}(\rho, \phi') = \vec{E}_a(\rho, \phi') \times \hat{n}$$

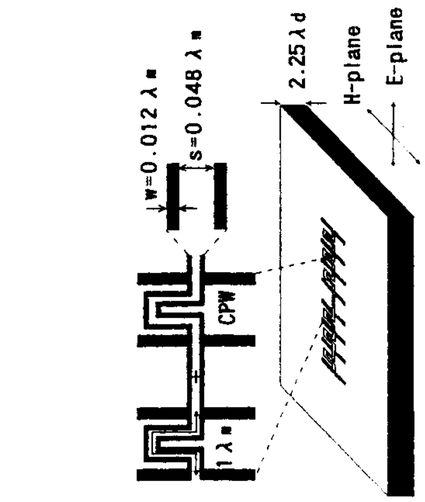

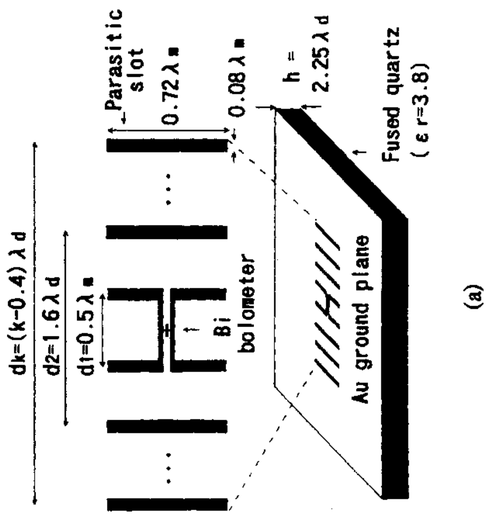

Figure 7.21 Two configurations of the slot-array antennas fed by CPW for power combining applications at millimeter-wave frequencies. (a) Slot-array antenna with two CPW-fed slots and a number of parasitic slots. (b) Slot-array antenna with meandering CPW feed. (From [38]. © 1998 IEEE. Reprinted with permission.)

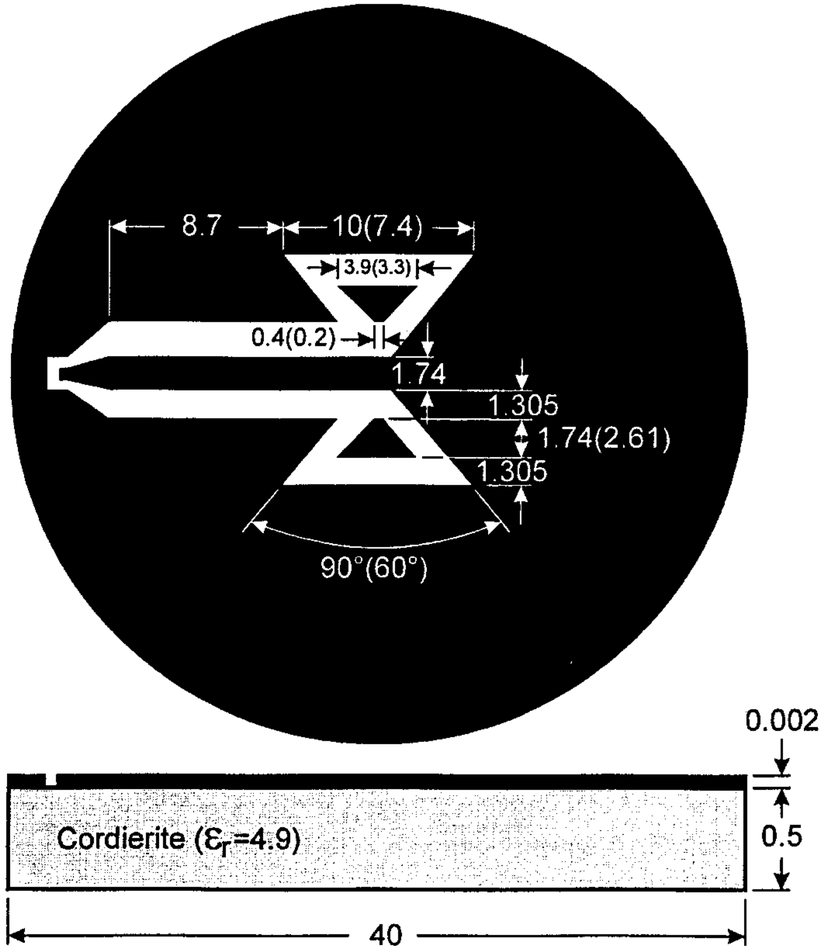

Figure 7.22 Bow-tie antenna in slot configuration fed by a CPW. All dimensions are in mm, and dimensions in parentheses correspond to the case of 60° flare angle. (From [37]. © 1999 *Electronic Letters.* Reprinted with permission.)

where $\vec{E}_a$ is the aperture electric field and $\hat{n}$ is the unit vector normal to the aperture.

The far-field radiation patterns of an annular slot antenna can be evaluated by using the vector electric potential method as discussed in Chapter 1. From the vector electric potential components, the far-electric field components E_θ and E_ϕ can be written as

$$E_\theta = \frac{-jk_0}{4\pi}\frac{e^{-jk_0 r}}{r}\int_0^{2\pi}\int_a^{a+W_S}\{M(\rho)\sin(\phi'-\phi)+M(\phi')\cos(\phi'-\phi)\}$$
$$\times \exp(j\rho k_0 \sin\theta\cos(\phi'-\phi))\,\rho\,d\rho\,d\phi' \qquad (7.27a)$$

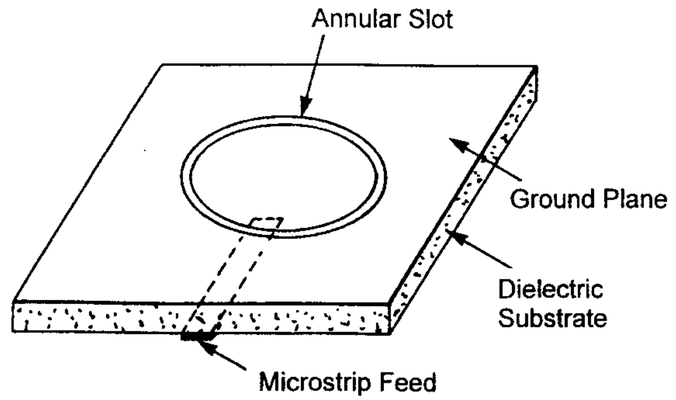

Figure 7.23 An annular slot with microstrip feed.

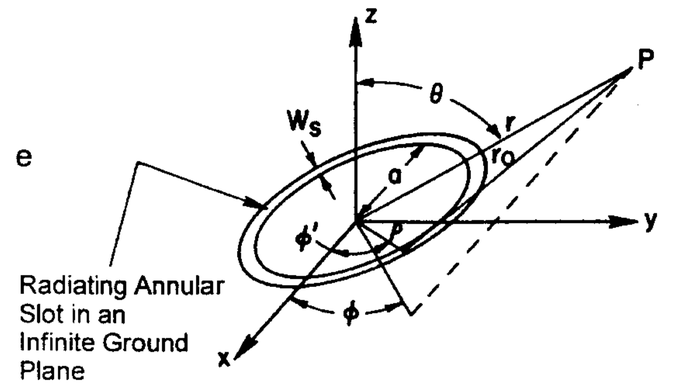

Figure 7.24 An annular slot with the coordinate system.

$$E_\phi = \frac{jk_0}{4\pi}\frac{e^{-jk_0 r}}{r}\cos\theta\int_0^{2\pi}\int_a^{a+W_S}\{M(\rho)\cos(\phi'-\phi)-M(\phi')\sin(\phi'-\phi)\}$$
$$\times \exp(j\rho k_0 \sin\theta\cos(\phi'-\phi))\,\rho\,d\rho\,d\phi' \qquad (7.27b)$$

where a is the inner radius of the slot, W_S is the slot width, and

$$\vec{M}(\rho,\phi') = M(\rho)\hat{\rho} + M(\phi')\hat{\phi} = -E_\phi\hat{\rho} + E_\rho\hat{\phi} \qquad (7.28)$$

E_ρ and E_ϕ are the slot electric field components in the ρ and ϕ directions, respectively. Determining these components accurately requires a rigorous approach, such as that used for the analysis of an annular ring microstrip antenna. We give below the radiation pattern calculations for a narrow slot, $W_S << \lambda_0$, for which one can assume $E_\phi = 0$.

Case I: E_ρ is constant and equal to E_0. For this case (7.27) reduces to

$$E_\theta = \frac{-jk_0W_S}{4\pi}\frac{E_0ae^{-jk_0r}}{r}\int_0^{2\pi}\cos(\phi'-\phi)\exp(jak_0\sin\theta\cos(\phi'-\phi))\,d\phi' \tag{7.29a}$$

$$E_\phi = \frac{-jk_0W_S}{4\pi}\frac{E_0ae^{-jk_0r}}{r}\cos\theta\int_0^{2\pi}\sin(\phi'-\phi)\exp(jak_0\sin\theta\cos(\phi'-\phi))\,d\phi' \tag{7.29b}$$

Integration with respect to ϕ' gives

$$\int_0^{2\pi}\cos(\phi'-\phi)\exp(jak_0\sin\theta\cos(\phi'-\phi))\,d\phi' = 2\pi jJ_1(ak_0\sin\theta) \tag{7.30a}$$

$$\int_0^{2\pi}\sin(\phi'-\phi)\exp(jak_0\sin\theta\cos(\phi'-\phi))\,d\phi' = 0 \tag{7.30b}$$

Thus

$$E_\theta = E_0a\frac{k_0W_S}{2}\frac{e^{-jk_0r}}{r}J_1(ak_0\sin\theta) \tag{7.31a}$$

$$E_\phi = 0 \tag{7.31b}$$

Case II: $E_\rho = E_0\cos n\phi'$. For this case (7.27) reduces to

$$E_\theta = \frac{-jk_0W_S}{4\pi}\frac{E_0ae^{-jk_0r}}{r}\int_0^{2\pi}\cos(\phi'-\phi)\cos n\phi'\exp[jak_0\sin\theta\cos(\phi'-\phi)]\,d\phi' \tag{7.32a}$$

$$E_\phi = \frac{-jk_0W_S}{4\pi}\frac{E_0ae^{-jk_0r}}{r}\cos\theta\int_0^{2\pi}\sin(\phi'-\phi)\cos n\phi'\exp[jak_0\sin\theta\cos(\phi'-\phi)]\,d\phi' \tag{7.32b}$$

Again, integration with respect to ϕ' gives

$$E_\theta = -j^nE_0a\frac{k_0W_S}{2}\frac{e^{-jk_0r}}{r}\cos n\phi J_n'(ak_0\sin\theta) \tag{7.33a}$$

$$E_\phi = j^nnE_0\frac{W_S}{2}\frac{e^{-jk_0r}}{r}\sin n\phi\cot\theta J_n(ak_0\sin\theta) \tag{7.33b}$$

The radiation power patterns $R(\theta) = |E_\theta|^2 + |E_\phi|^2$ for $n = 0$, 1, and $ak_0 = 1$, 2 are shown in Figures 7.25, 7.26, and 7.27 [40]. Figure 7.25 shows the radiation patterns for $n = 0$, that is, constant electric field in the annular slot. In this case, the radiation patterns in the E and H planes are the same, and the maximum radiation is along the end-fire direction. We can see from Figure 7.26 that for $n = 1$ the radiation patterns depend on the radius of the slot. The E-plane pattern for $n = 1$ and $ak_0 = 1$ is essentially constant with angle θ, whereas for $ak_0 = 2$, the pattern has the main lobe in the broadside direction and a sidelobe along the end-fire direction. The level of the sidelobe is −18 dB with respect to the main lobe level. The H-plane patterns for

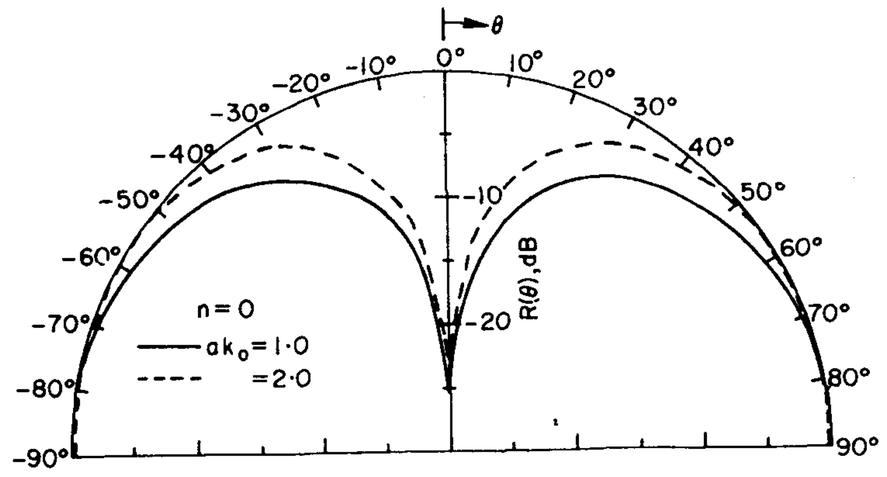

Figure 7.25 Radiation patterns of annular slots when $n = 0$ and $W_S << \lambda_0$.

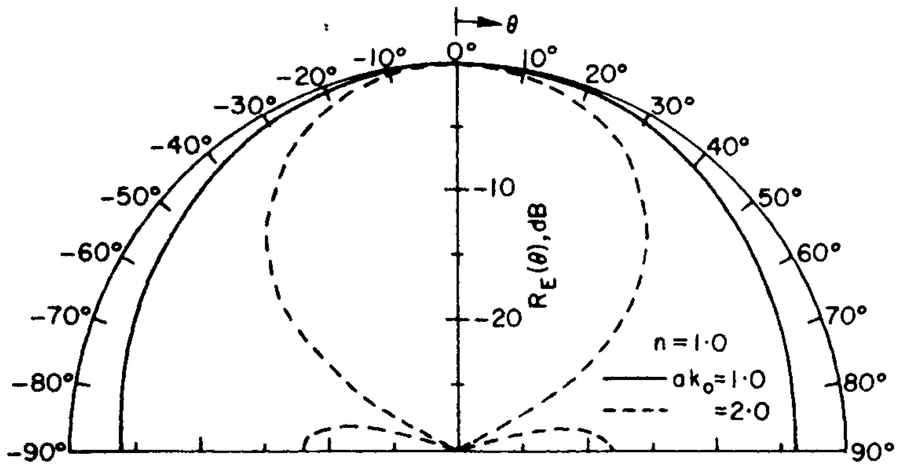

Figure 7.26 E-plane radiation patterns of annular slots when $n = 1$ and $W_S << \lambda_0$.

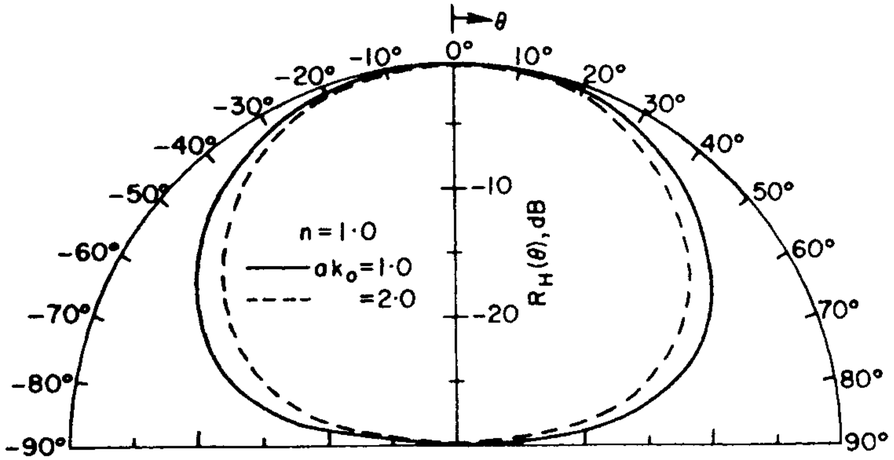

Figure 7.27 H-plane radiation patterns of annular slots when $n = 1$ and $W_S << \lambda_0$.

$n = 1$, shown in Figure 7.27, are the same for both the values of ak_0; that is, $ak_0 = 1$ and 2.

Circular polarization from the annular slot can be realized by feeding it such that two modes with orthogonal polarizations, equal amplitude, and 90° phase difference are excited. For this purpose one can choose between a single-feed design and a dual-feed design. The dual-feed design can be based on a power splitter or a typical hybrid coupler. A hybrid coupler might be preferred over a power splitter because of the built-in isolation between the feed ports.

Effect of Loading on an Annular Slot

The effect of loading on an annular slot has been studied analytically and experimentally by Morishita et al. [39]. The antenna considered is a cavity-

backed annular slot antenna and the load is a short. The antenna characteristics such as input impedance, resonance frequency, bandwidth, radiation pattern, and polarization have been studied as a function of position of a short in the slot aperture. It has been observed that the resonant frequency can be varied by changing the shorting position. Wideband impedance characteristics are achieved by selecting the short position properly. The polarization can be changed from linear to circular polarization, and the radiation patterns can be varied.

The geometry of a cavity-backed annular slot is shown in Figure 7.28. The inner radius of the annular slot is ρ_0 and the slot width is b. The short is located at an angle α from the x axis. The radius of the cylindrical cavity is denoted by a and the height of the cavity is d. The measured resonant frequency f_r and the VSWR ≤ 2 bandwidth are plotted in Figure 7.29 as a function of short position α. The resonant frequency is defined as that frequency at which the VSWR becomes minimum. It is observed that two resonant frequencies exist, except for $\alpha = 0°$ (no short) and 105°. The two resonances are due to the separation of degenerate modes of the annular slot under the loading effect of the short. As α is increased from 0° to 105°, the two resonant frequencies approach each other and merge at $\alpha = 105°$. As α is increased further, the two frequencies move apart from each other. By varying α, the separation of the two frequencies can be controlled.

Figure 7.29 also shows that the bandwidth can be increased by selecting the short position. The maximum bandwidth for the given set of antenna

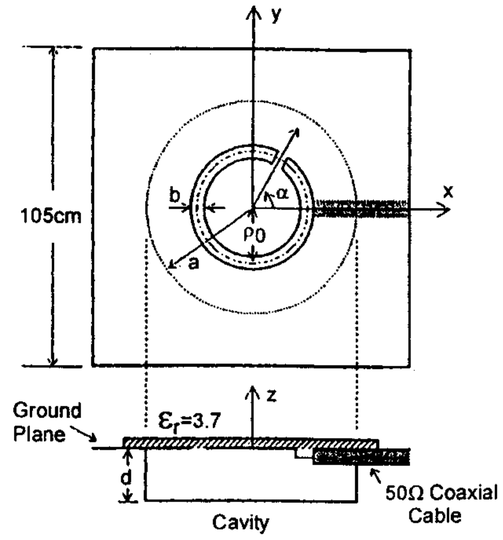

Figure 7.28 A cavity-backed annular slot antenna. (From [39]. © 1991 IEEE. Reprinted with permission.)

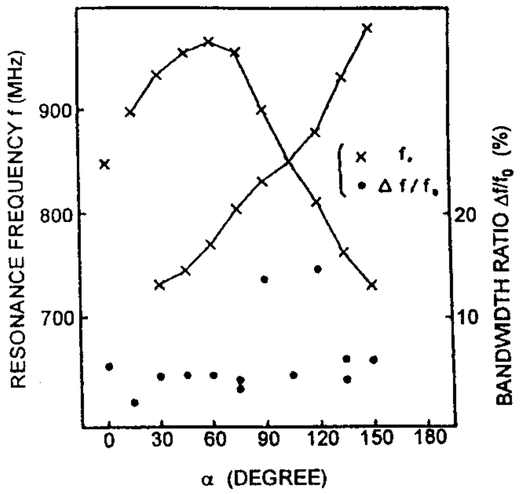

Figure 7.29 Measured resonance frequency and bandwidth for the loaded annular slot of Figure 7.28 (a = 12.35 cm, d = 3.0 cm, b = 0.75 cm, ρ_0 = 7.7 cm, ϵ_r = 3.7, substrate thickness = 1.5 mm, width of the short = 3 mm). (From [39]. © 1991 IEEE. Reprinted with permission.)

parameters is more than 10% when α is near 90° and 120°. The circular polarization behavior of the shorted annular slot can again be explained by the presence of nearly degenerate modes (see Chapter 8 on circular polarization). Although the antenna characteristics to be presented next are meant for a cavity-backed annular slot, the main features should also be true without cavity backing.

The radiation patterns of the annular slot can be controlled electronically by loading the slot with a tunable capacitor as shown in Figure 7.30. One application of this loading is to make the radiation patterns asymmetric and useful for applications in communications. An almost one-sided radiation pattern is obtainable, and a typical example is shown in Figure 7.31. In Figure

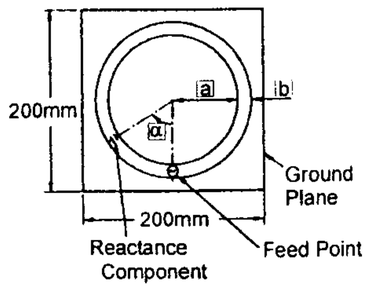

Figure 7.30 Geometry of an annular slot with reactive loading. (From [41]. © 1989 Peter Peregrinus. Reprinted with permission.)

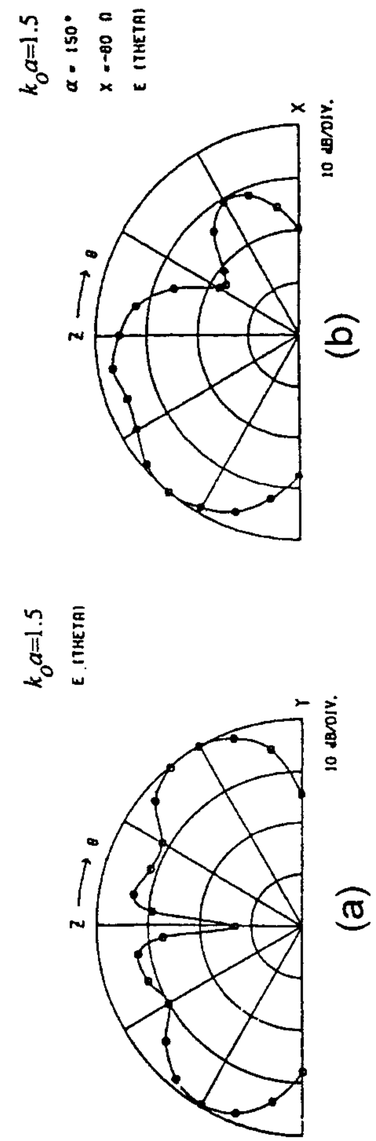

Figure 7.31 Measured E_θ patterns of an annular slot with $k_0 a$ = 1.5 (a) without load and (b) with a capacitive load of $-j80\Omega$ at 1.5 GHz and α = 150°. (From [41]. © 1989 Peter Peregrinus. Reprinted with permission.)

7.31(a) the radiation pattern for $ak_0 = 1.5$ *without load* is symmetric. When this antenna is loaded with $-j80$ ohm at an operating frequency of 1.5 GHz, the radiation pattern becomes asymmetric as shown in Figure 7.31(b) [41]. The radiation patterns can also be rotated electronically by varying the capacitive load on the annular slot by the bias supply. This facility can be made use of to reduce the multipath fading in urban mobile communications when the antenna is mounted on a vehicle.

7.5 Tapered Slot Antennas

The tapered slot antenna (TSA) was invented by Prasad and Mahapatra [42] and Gibson [43] at about the same time. Unlike other antennas discussed so far, this antenna is an end-fire radiator, and is used at millimeter-wave frequencies due to its larger length. A typical TSA consists of a tapered slot that has been etched in the metalization on a dielectric substrate. Figure 7.32 shows three types of TSA elements with different taper shapes: the Vivaldi (exponential taper) antenna, the LTSA (linear taper), and the CWSA (constant width, no taper). The length of the antenna is denoted by L, the width of the antenna $2H$, opening angle or aperture angle 2γ, and substrate parameters h and ϵ_r. Some of the advantages of TSA elements over conventional elements are as follows:

- Narrow 3-dB beamwidths of the order of 15° and the resulting higher gain up to about 16 dB for longer elements;
- Simple and convenient integration of the element with the feed transition;
- Comparatively larger pattern bandwidth of the order of even two octaves;
- Constant input impedance over a 3:1 frequency range.

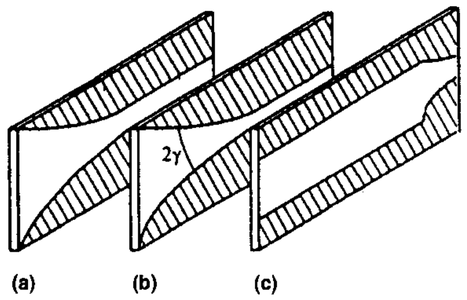

Figure 7.32 Various forms of tapered slot antenna configurations: (a) Vivaldi, (b) LTSA, and (c) CWSA.

Let's take a look at the characteristics of the TSA element. The basic properties of the TSA that need to be studied are the beamwidth, directivity, and gain of the antenna. The input impedance of the antenna does not vary much with frequency [44] and, therefore, is not emphasized. TSA is basically a surface-wave type of traveling-wave antenna. In this antenna, the structure supports a surface wave that propagates until the end of the structure and radiates at the termination. The phase velocity of the surface wave v_{ph} is generally less than the velocity of light, c. Hence a TSA is a slow-wave structure. This antenna can produce symmetric radiation patterns in the planes parallel to the substrate (the E plane), and perpendicular to the substrate (the H plane) despite its planar geometry. The physics, mechanism of radiation, and the design of surface wave antennas is very well described in the books [45, 46]. These guidelines are also applicable to TSA. The directivity of a TSA increases and beamwidth decreases as the length L of the antenna is increased. For a traveling-wave antenna with a constant phase velocity along the length, there is an optimum phase velocity ratio $p = c/v_{ph}$ that results in maximum directivity and higher gain. It is called Zucker's *high gain* case here. In the LTSA and Vivaldi antennas, however, the phase velocity is not constant, due to tapering of the slot. This variation in phase velocity with distance along the antenna leads to lowering of directivity and associated decrease in sidelobe level, called by Zucker the *low-sidelobe* case. The case of air dielectric, $p = 1$ results in a wider beamwidth but nevertheless useful antenna. For TSAs the beamwidths are expected to fall between standard cases of Zucker's high gain and low sidelobe. Another general constraint for the TSAs is that the slot width at the termination $2H$ should reach at least one-half wavelength for effective radiation to occur. Typical LTSAs have opening angles (2γ) in the range of 5° to 12°. The polarization of the radiated fields is linear and along the width of the antenna.

7.5.1 Beamwidth

The analysis of TSAs has not yet fully matured. Three different approaches have been used to predict the radiation patterns of TSAs. These techniques have been worked out by Janaswamy and Schaubert [47–49]. For a TSA with air dielectric, all three approaches give accurate results for the radiation pattern. In the first approach, conformal mapping is used to predict the radiation patterns for an air dielectric TSA [47]. The other approaches are also applicable to the dielectric-loaded TSA [48, 49]. These methods predict accurate radiation patterns for the thin and low ϵ_r substrates only.

One of these methods is based on a determination of the aperture electric field [48]. In this method the aperture field is obtained by modeling the tapered

geometry in terms of a stepped approximation and utilizing the uniform slot line data. A half-plane Green's function is used along with the aperture field to calculate the radiation pattern. This model is ideally valid for infinite width of the antenna. Good results are, however, obtained when the width of the antenna is at least $3\lambda_0$. In the third approach, the moment method has been used to determine the current distribution on the TSA metalization [49]. The effect of dielectric loading is included via the impedance boundary condition. This model has been used with finite antenna width, and is accurate for substrates satisfying the condition, $(\epsilon_r - 1)h/\lambda_0 \leq 0.1$, where h is the substrate thickness. Comparison between the measured and computed radiation pattern based on the moment method approach is shown in Figure 7.33 for an antenna with $h = 0.71$ mm, $\epsilon_r = 2.33$, $L = 10$ cm, $\gamma = 6°$, and $f = 9$ GHz [49]. We can see from this figure that the computed radiation pattern agrees favorably with the measured patterns, except for some regions in the backlobe.

In the absence of accurate analysis and design techniques for TSA, we give below the design information based on the works of Yngvesson and his team [44, 50]. It has been observed by them, through a study of numerous experimental data, that some consistent empirical design rules can be formulated that result in antennas with beamwidths that agree with the *standard data* for traveling-wave antennas given by Zucker [45]. Based on numerous measurements, it has been found that for LTSA Zucker's curve applies if the effective dielectric thickness of the substrate defined as

$$h_{\text{eff}}/\lambda_0 = (\sqrt{\epsilon_r} - 1)h/\lambda_0 \tag{7.34}$$

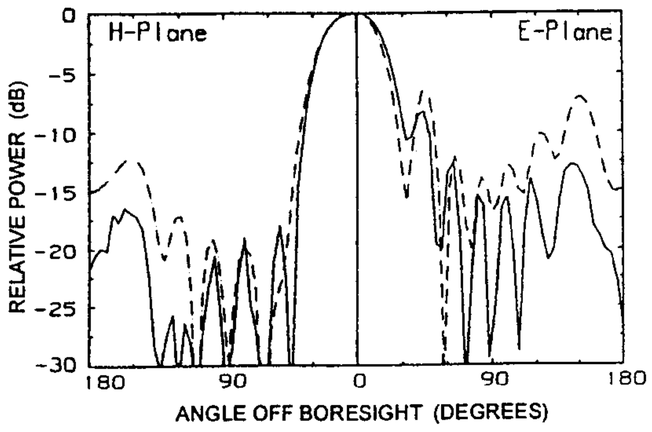

Figure 7.33 Comparison of measured and computed radiation patterns for a dielectric supported LTSA. ($L = 3\lambda_0$, $H = 0.9\lambda_0$, $\gamma = 6°$, $\epsilon_r = 2.33$, and $h = 0.021\lambda_0$; ——, measured, ----, theory). (From [49]. © 1989 IEEE. Reprinted with permission.)

lies between 0.005 and 0.01 for antenna lengths of the order of 4 to $10\lambda_0$ [50]. Increasing the dielectric thickness beyond that given by (7.34) first results in increased gain, with higher sidelobes, and then in marked disagreement with the Zucker's curves. These standard curves are plotted in Figure 7.34 for gain and beamwidth of an end-fire antenna as a function of antenna length L/λ_0 for the optimum gain case and low sidelobe case [45]. The 3-dB beamwidth data for LTSA with Kapton ($\epsilon_r = 3.5$) taken at 94 GHz with substrates of thickness 0.025, 0.05, and 0.076 mm are plotted in Figure 7.35 [50]. These data show agreement with Zucker's curves. There is a clear progression from low sidelobe traveling-wave performance at 0.025 mm to increased gain at 0.05 mm, and finally to unequal beamwidths in the E and H planes at 0.076 mm. Also, as expected, the beamwidth decreases and directivity increases as the antenna length increases.

7.5.2 Input Impedance

The input impedance of a LTSA with air as dielectric has been determined by Yngvesson et al. [50] based on the conformal mapping method first proposed

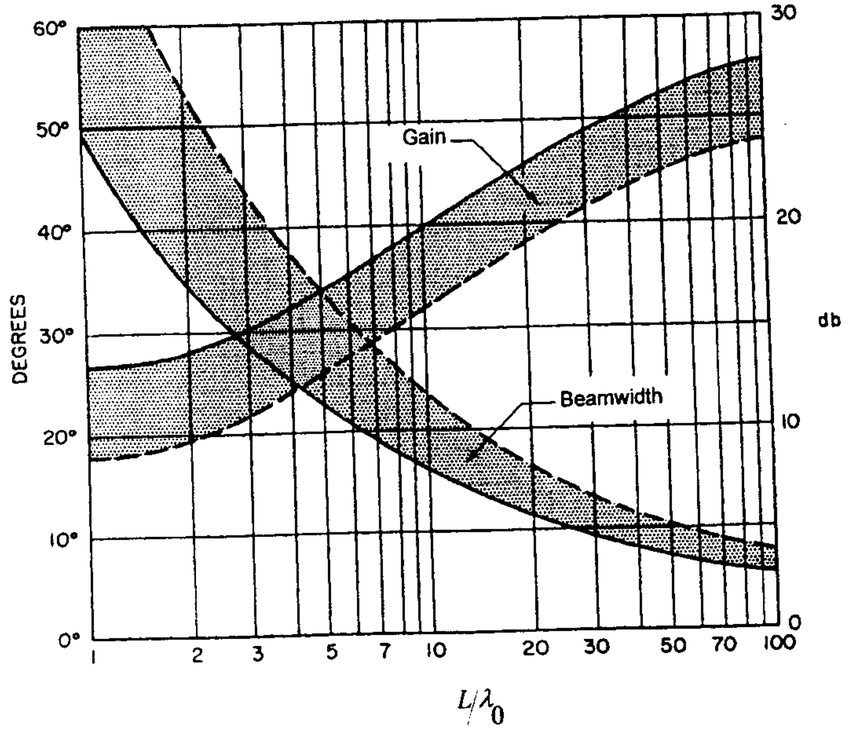

Figure 7.34 Gain and beamwidth of a surface wave antenna as a function of relative length L/λ_0. Solid lines are optimum values; dashed lines are for low sidelobe and broadband design. (From [45]. © 1984 McGraw-Hill. Reprinted with permission.)

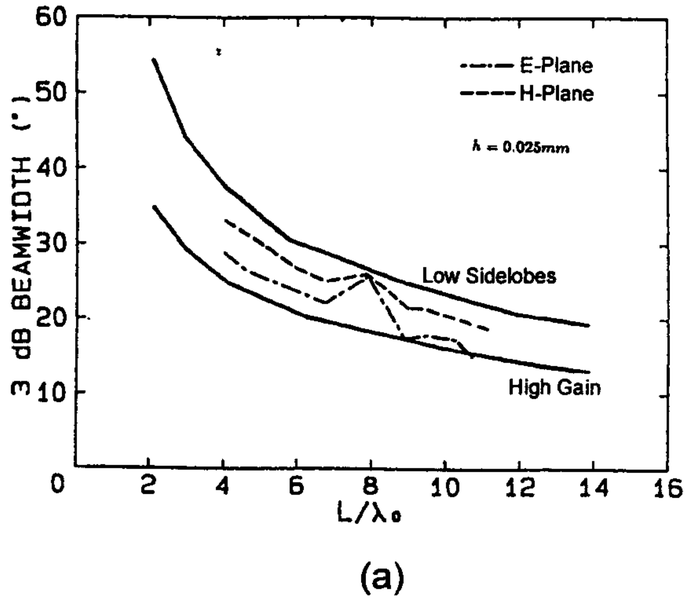

Figure 7.35 Variation of half-power beamwidth as a function of length L/λ_0 of LTSA over Kapton substrate ($\epsilon_r = 3.5$) at 94 GHz with $2\gamma = 11.2°$: (a) $h = 0.025$ mm, (b) $h = 0.050$ mm, and (c) $h = 0.075$ mm. (From [50]. © 1985 IEEE. Reprinted with permission.)

by Carrel for the fin-line structure [51]. The input impedance of a fin-line with $\epsilon_r = 1$ is given by the following equation:

$$Z_0 = 120\pi \frac{K(k)}{K'(k)} \tag{7.35}$$

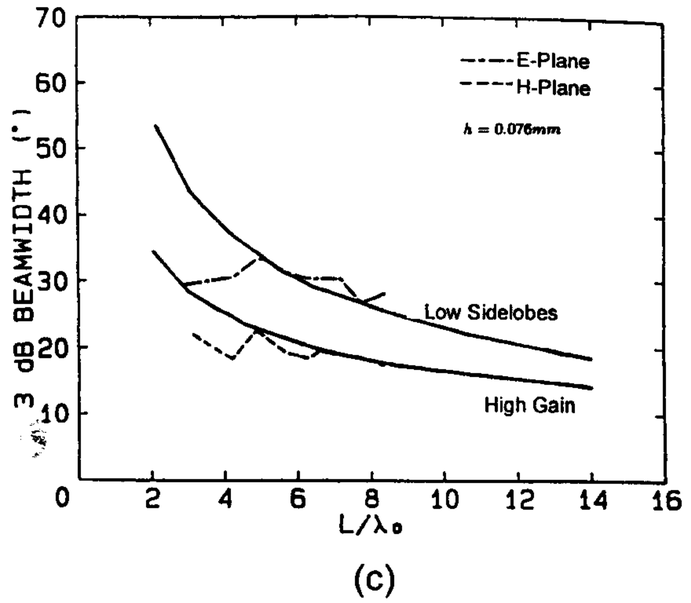

Figure 7.35 (continued).

with

$$k = \sqrt{1 - k'^2} = \frac{1 - \cos\gamma}{1 + \cos\gamma} \tag{7.36}$$

where $K(\cdot)$ and $K'(\cdot)$ are the complete elliptic and complementary integrals, respectively, with modulus k, and 2γ is the aperture angle of the LTSA. The above expression for the input impedance has also been found suitable for a thin dielectric substrate. The measured results on such a thin LTSA agreed quite well with Carrel's findings. These results are shown in Figure 7.36 [50].

The single-element TSA can be used in the following applications [44]:

1. In broadband detectors and receivers, a constant 3-dB beamwidth of 30–40° can be obtained from a Vivaldi element up to a frequency of 40 GHz.
2. A CWSA element can be integrated with different kinds of SIS mixer receivers. These integrated systems can be used at frequencies as high as 700 GHz. Receiver modules of this kind can be used in focal plane arrays.

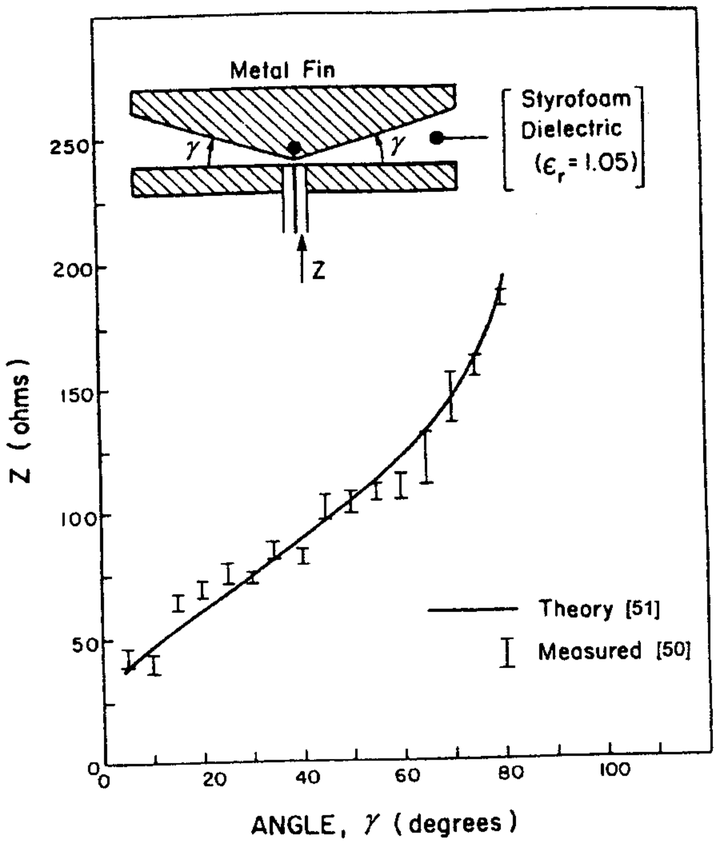

Figure 7.36 Comparison of measured and computed results on input impedance of LTSA. (From [50]. © 1985 IEEE. Reprinted with permission.)

3. Single-element TSAs can be used as feeds for reflector or lens antennas.
4. Single-element TSAs provide high gain (up to 17 dB) compared to other antennas, and can be used as a low-cost antenna element in high-gain receivers.
5. Arrays of TSAs have been used for high-resolution millimeter-wave imaging, multibeam satellite communication systems, power combining, and phased arrays.

7.5.3 Excitation of TSA

The tapered slot line antenna can be fed by means of a coaxial-line or microstrip or coplanar waveguide or rectangular waveguide. TSA with microstrip feed is shown in Figure 7.37. Here, both the microstrip and slot line stubs at the junction are a quarter-wave long. Transitions from coaxial-to-slot line and from microstrip-to-slot line are described in detail in [21]. A transition between

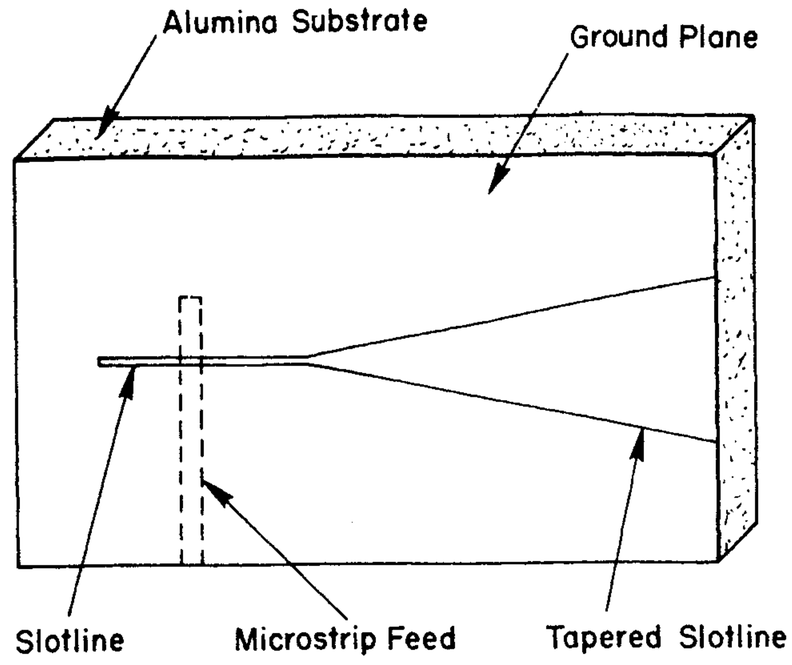

Figure 7.37 Excitation of a tapered slot line antenna by a microstrip feed.

slot line and coplanar waveguide has been described in [52], and that between rectangular waveguide and slot line in [53]. The transition between a microstrip line and a slot line with an intermediate step of coupled microstrips is described in [54].

7.6 Comparison of Slot Antennas With Microstrip Antennas

Various types of microstrip patch and slot antennas have been discussed in Chapters 1 through 7. A qualitative comparison of these classes of antennas is given in Table 7.1. It can be seen from this table that both types have advantages and disadvantages. Microstrip antennas are easy to design and fabricate, and can have different shapes: rectangular, circular, triangular, and so on. Linear or circular polarization can be achieved by nearly changing the feed position. Loading of the patch can be used to obtain dual-frequency operation, circular polarization, change in the radiation pattern, and increase in bandwidth. On the other hand, slot antennas can produce unidirectional or bidirectional radiation. An interesting feature of slot antennas is their greater bandwidth because of bidirectional radiation. Slot antennas are less sensitive to manufacturing tolerances compared with patch antennas.

Table 7.1
Qualitative Comparison of Microstrip Patch and Slot Antennas

Characteristic	Patch	Slot
Analysis and design	Easy	Easy
Fabrication	Very easy	Very easy
Tolerance in fabrication	Critical	Not very critical
Profile	Thin	Thin
Shape flexibility	Any shape	Limited
Radiation fields	Unidirectional	Unidirectional and bidirectional
Polarization	Linear and circular	Linear and circular
Bandwidth	Narrow	Wide
Dual frequency operation	Possible	Possible
Spurious radiation	Moderate	Low
Isolation between radiating elements	Fair	Good
Frequency scanning	Easily possible	Possible
Cross-polarization level	Low	Very low
End-fire antenna	Not possible	Possible

References

[1] Oliner, A. A., "The Radiation Conductance of a Series Slot in Strip Transmission Line," *IRE National Conv. Rec.*, Vol. 2, Part 8, 1954, pp. 89–90.

[2] Sommers, D. J., "Slot Array Employing Photo-Etched Triplate Transmission Line," *IRE Trans.*, Vol. MTT-3, Mar. 1955, pp. 157–162.

[3] Fubini, E. G., J. A. McDonough, and R. Malech, "Strip Line Radiators," *IRE Trans.*, Vol. MTT-3, Mar. 1955, pp. 51–55.

[4] Breithaupt, R. W., "Conductance Data for Offset Series Slots in Strip Line," *IEEE Trans. on Microwave Theory and Techniques*, Vol. MTT-16, 1968, pp. 969–970.

[5] Waterman, A., et al., "Strip Line Strap-On Antenna Array," *Proc. Array Antenna Conf.*, Naval Electronics Laboratory Center, San Diego, CA, Feb. 1972, Paper 10.

[6] Proctor, D., "Some Aspects of TEM Slot Design in Strip Line," *Proc. Array Antenna Conf.*, Naval Electronics Laboratory Center, San Diego, CA, Feb. 1972, Paper 35.

[7] Josefsson, L., L. Moeshlin, and I. Svensson, "A Strip Line Flat Plate Antenna With Sidelobes," *IEEE AP-S Int. Symp. Digest*, 1974, pp. 282–285.

[8] Fritz, W. A., and P. E. Mayes, "A Frequency-Scanning Strip Line-Fed Periodic Slot Array," *IEEE AP-S Int. Symp. Digest*, 1974, pp. 278–281.

[9] Rao, J. S., and B. N. Das, "Impedance of Off-Centered Strip Line Fed Series Slot," *IEEE Trans. on Antennas and Propagation*, Vol. AP-26, 1978, pp. 893–895.

[10] Ito, K., N. Aizawa, and N. Goto, "Circularly Polarized Printed Array Antennas Composed of Strips and Slots," *Electron. Lett.*, Vol. 15, 1979, pp. 811–812.

[11] Ito, K., N. Aizawa, and N. Goto, "Increasing the Bandwidth of Circularly Polarized Printed Array Antennas Composed of Strips and Slots," *IEEE AP-S Int. Symp. Digest*, 1980, pp. 597–600.

[12] Yoshimura, Y., "A Microstrip Line Slot Antenna," *IEEE Trans. on Microwave Theory and Techniques*, Vol. MTT-20, 1972, pp. 760–762.

[13] Kim, J. P., and W. S. Park, "Network Modeling of an Inclined and Off-Center Microstrip-Fed Slot Antenna," *IEEE Trans. on Antennas and Propagation*, Vol. AP-46, 1998, pp. 1182–1188.

[14] Pozar, D. M., "Reciprocity Method of Analysis for Printed Slot and Slot-Coupled Microstrip Antennas," *IEEE Trans. on Antennas and Propagation*, Vol. AP-34, 1986, pp. 1439–1446.

[15] Axelrod, A., M. Kisliuk, and J. Maoz, "Broadband Microstrip-Fed Slot Radiator," *Microwave J.*, June 1989, pp. 81–94.

[16] Das, B. N., and K. K. Joshi, "Impedance of a Radiating Slot in the Ground Plane of a Microstrip Line," *IEEE Trans. on Antennas and Propagation*, Vol. AP-30, 1982, pp. 922–926.

[17] Bhattacharyya, A. K., Y. M. M. Antar, and A. Ittipiboon, "Full Wave Analysis for the Equivalent Circuit of an Inclined Slot on a Microstrip Ground Plane," *Proc. IEE*, Vol. 139, Pt. H, 1992, pp. 245–250.

[18] Chen, C., and N. G. Alexopoulos, "Modeling Microstrip Line Fed Slot Antennas With Arbitrary Shape," *Electromagnetics*, Vol. 15, 1995, pp. 567–586.

[19] Himdi, M., and J. P. Daniel, "Analysis of Printed Linear Slot Antenna Using Lossy Transmission Line Model," *Electron. Lett.*, Vol. 28, 1992, pp. 598–601.

[20] Akhavan, H. G., and D. Mirshekar-Syahkal, "Approximate Model for Microstrip Fed Slot Antennas," *Electron. Lett.*, Vol. 30, 1994, pp. 1902–1903.

[21] Gupta, K. C., et al., *Microstrip Lines and Slotlines*, 2nd ed., Artech House, Norwood, MA, 1996, Chap. 5.

[22] Rhodes, D. R., "On a Fundamental Principle in the Theory of Planar Antennas," *Proc. IEEE*, Vol. 52, 1964, 1013-1021.

[23] Itoh, T., "Spectral Domain Immittance Approach for Dispersion Characteristics of Generalized Printed Transmission Lines," *IEEE Trans. on Microwave Theory and Techniques*, Vol. MTT-28, 1980, pp. 733–736.

[24] Tam, W. Y., "Microstripline-Fed Cylindrical Slot Antenna," *IEEE Trans. on Antennas and Propagation*, Vol. AP-46, 1998, pp. 1587–1589.

[25] Liu, H. C., T. S. Horng, and N. G. Alexopoulos, "Radiation of Printed Antennas With a Coplanar Waveguide Feed," *IEEE Trans. on Antennas and Propagation*, Vol. AP-43, 1995, pp. 1143–1148.

[26] Greiser, J. W., "Coplanar Strip Line Antenna," *Microwave J.*, Oct. 1976, pp. 47–49.

[27] Nesic, A., "Bandwidth and Radiation Characteristics of the Printed Slot Excited by a Coplanar Waveguide," *Proc. Third Int. Conf. Antennas Propagat., ICAP 83*, 1983, pp. 404–406.

[28] Cai, M., P. S. Kooi, and M. S. Leong, "Compact Slot Loop Antenna," *Microwave Opt. Tech. Lett.*, Vol. 6, 1993, pp. 292–294.

[29] Rexberg, L., N. Dib, and L. P. Katehi, "A Microshield Line Loop Antenna for Sub-Millimeter-Wave Wavelength Applications," *IEEE AP-S Int. Symp. Digest*, 1992, pp. 1890–1893.

[30] Laheurte, J., L. P. Katehi, and G. M. Rebeiz, "CPW-Fed Active Twin-Slots Antennas Radiating Through Layered Substrates," *1993 URSI Conf.*, p. 14.

[31] Nesic, A., "Slotted Antenna Array Excited by a Coplanar Waveguide," *Electron. Lett.*, Vol. 18, 1982, pp. 275–276.

[32] Nesic, A., "A Printed Antenna Array With Slots as Primary Radiators for Phase Scanned Antenna," *Journ. Inter. de Nice sur les Antennes*, Nice, France, 1986, pp. 281–283.

[33] Kormanyos, B. K., et al., "CPW-Fed Active Slot Antennas," *IEEE Trans. on Microwave Theory and Techniques*, Vol. MTT-42, 1994, pp. 541–545.

[34] Schoenberg, J., et al., "Quasi-Optical Antenna Array Amplifiers," *Int. Microwave Symp. Digest*, 1995, pp. 605–608.

[35] Tsai, H., and R. York, "Multi-Slot Antennas for Quasi-Optical Circuits," *IEEE Microwave Guided Wave Lett.*, Vol. 5, 1995, pp. 180–182.

[36] Sierra-Garcia, S., and J.-J. Laurin, "Study of a CPW Inductively Coupled Slot Antenna," *IEEE Trans. on Antennas and Propagation*, Vol. AP-47, 1999, pp. 58–64.

[37] Soliman, E. A., et al., "Bow-Tie Slot Antenna Fed by CPW," *Electron. Lett.*, Vol. 35, 1999, pp. 514–515.

[38] Kobayashi, H., and Y. Yasuoka, "Slot Array Antennas Fed by Coplanar Waveguide for Millimeter-Wave Radiation," *IEEE Trans. on Microwave Theory and Techniques*, Vol. MTT-46, 1998, pp. 800–805.

[39] Morishita, H., K. Hirasawa, and K. Fujimoto, "Analysis of a Cavity-Backed Annular Slot Antenna With One Point Shorted," *IEEE Trans. on Antennas and Propagation*, Vol. AP-39, 1991, pp. 1472–1478.

[40] Bahl, I. J., and P. Bhartia, *Microstrip Antennas*, Artech House, Dedham, MA, 1980, Chap. 6.

[41] James, J. R., and P. S. Hall (Eds.), *Handbook of Microstrip Antennas*, Peter Peregrinus, London, UK, 1989, Chap. 19.

[42] Prasad, S. N., and S. Mahapatra, "A Novel MIC Slot Line Aerial," *Proc. 9th European Microwave Conf.*, 1979, pp. 120–124.

[43] Gibson, P. J., "The Vivaldi Aerial," *Proc. 9th European Microwave Conf.*, 1979, pp. 101–105.

[44] Yngvesson, K. S., et al., "The Tapered Slot Antenna—A New Integrated Element for Millimeter-Wave Applications," *IEEE Trans. on Microwave Theory and Techniques*, Vol. MTT-37, 1989, pp. 365–374.

[45] Zucker, F. J., "Surface-Wave Antennas and Surface-Wave Excited Arrays," in *Antenna Engineering Handbook*, 2nd ed., R. C. Johnson and H. Jasik (Eds.), McGraw-Hill, New York, 1984, Chap. 12.

[46] Walter, C. H., *Traveling-Wave Antennas*, McGraw-Hill, New York, 1965.

[47] Janaswamy, R., D. H. Schaubert, and D. M. Pozar, "Analysis of the Transverse Electromagnetic Mode Linearly Tapered Slot Antenna," *Radio Sci.*, Vol. 21, 1986, pp. 797–804.

[48] Janaswamy, R., and D. H. Schaubert, "Analysis of the Tapered Slot Antenna," *IEEE Trans. on Antennas and Propagation*, Vol. AP-35, 1987, pp. 1058–1065.

[49] Janaswamy, R., "An Accurate Moment Method Model for the Tapered Slot Antenna," *IEEE Trans. on Antennas and Propagation*, Vol. AP-37, 1989, pp. 1523–1528.

[50] Yngvesson, K. S., et al., "End-Fire Tapered Slot Antennas on Dielectric Substrates," *IEEE Trans. on Antennas and Propagation*, Vol. AP-33, 1985, pp. 1392–1400.

[51] Carrel, R., "The Characteristic Impedance of Two Infinite Cones of Arbitrary Cross-Section," *IRE Trans.*, Vol. AP-6, 1958, pp. 197–201.

[52] Hirota, T., Y. Tarusawa, and H. Ogawa, "Uniplanar MMIC Hybrids—A Proposed New MMIC Structure," *IEEE Trans. on Microwave Theory and Techniques*, Vol. MTT-35, 1987, pp. 576–581.

[53] Bhat, B., and S. K. Koul, *Analysis, Design, and Applications of Fine Lines*, Artech House, Norwood, MA, 1987, Chap. 9.

[54] Simons, R. N., et al., "Integrated Uniplanar Transition," *IEEE Trans. on Antennas and Propagation*, Vol. AP-43, 1995, pp. 998–1002.

8

Circularly Polarized Microstrip Antennas and Techniques

8.1 Introduction

The theoretical aspects and design procedures for various types of microstrip antennas have been discussed in previous chapters. However, there are other aspects that are equally important and should be considered in a complete design. These include the design of feeds, polarization of the radiated fields, and frequency diversity of operation. In this chapter, the design considerations for circularly polarized microstrip antennas are presented. Our treatment is confined to two types of circularly polarized microstrip antennas: the resonator and the traveling-wave types. Various techniques for circularly polarized radiation generation and bandwidth enhancement are also discussed.

8.2 Various Types of Circularly Polarized Printed Antennas

In general, an antenna will radiate an elliptical polarization, which is defined by three parameters: axial ratio, tilt angle, and sense of rotation [1, 2]. When an axial ratio is infinite or zero, the polarization becomes linear with the tilt angle defining the orientation. Sense is not applicable in this case. The quality of a linear polarization is usually indicated by the level of the cross polarization. For a unity axial ratio, a perfect circular polarization (CP) results and the tilt angle is not applicable. The axial ratio is generally used to specify the quality of the circularly polarized waves [3].

Antennas produce circularly polarized waves when two orthogonal field components with equal amplitude but in phase quadrature are radiated. Various

printed antennas are capable of satisfying these requirements. They can be classified as resonator and traveling-wave types. A resonator-type antenna consists of a single patch antenna that is capable of simultaneously supporting two orthogonal modes in phase quadrature or an array of linearly polarized resonating patches with proper orientations and phasings. A traveling-wave type of antenna is usually constructed from a microstrip transmission line. It generates circular polarization by radiating orthogonal field components with appropriate phasings along discontinuities in the traveling-wave line. These printed antennas are discussed in this section.

8.2.1 Microstrip Patch Antennas

A microstrip antenna is a resonator-type antenna. It is usually designed for single-mode operation that radiates mainly linear polarization. For a circular polarized radiation, a patch must support orthogonal fields of equal amplitude but in-phase quadrature. This requirement can be accomplished by a single patch with proper excitations or by an array of patches with an appropriate arrangement and phasing.

Circularly Polarized Patch

A microstrip patch is one of the most widely used radiators for circular polarization generation. Various shapes for microstrip antennas capable of circular polarization operation have been reported in literature. Figure 8.1 shows some of these patches, including square, circular, pentagonal [4], equilateral triangular [5], ring [6], and elliptical shapes [7, 8]. However, square and circular patches are widely utilized in practice.

A single patch antenna can be made to radiate circular polarization if two orthogonal patch modes are simultaneously excited with equal amplitude and ±90° out of phase with the sign determining the sense of rotation. Two types of feeding schemes can accomplish the task as illustrated in Figure 8.2. The first type is a dual-orthogonal feed, which employs an external power divider network. The other is a single-point feed for which an external power divider is not required.

Dual-Orthogonal Fed Circularly Polarized Patch

The fundamental configurations of a dual-orthogonal fed circularly polarized patch using an external power divider are shown in Figure 8.3. The patch is usually square or circular. The dual-orthogonal feeds excite two orthogonal modes with equal amplitude but in-phase quadrature. Several power divider circuits that have been successfully employed for CP generation include the quadrature hybrid, the ring hybrid, the Wilkinson power divider, and the

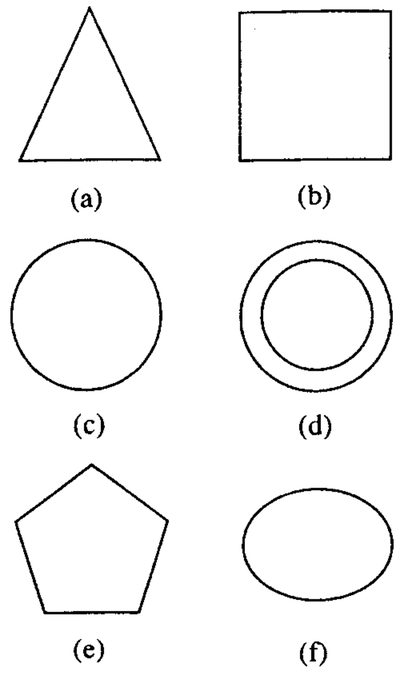

Figure 8.1 Various types of circularly polarized microstrip patch antennas: (a) triangular patch, (b) square patch, (c) circular patch, (d) ring, (e) pentagonal patch, and (f) elliptical patch.

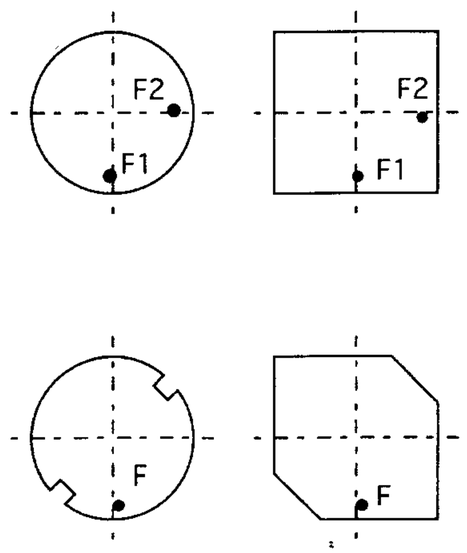

Figure 8.2 Two types of excitations for circularly polarized microstrip antennas: (a) dual-fed patch and (b) singly fed patch.

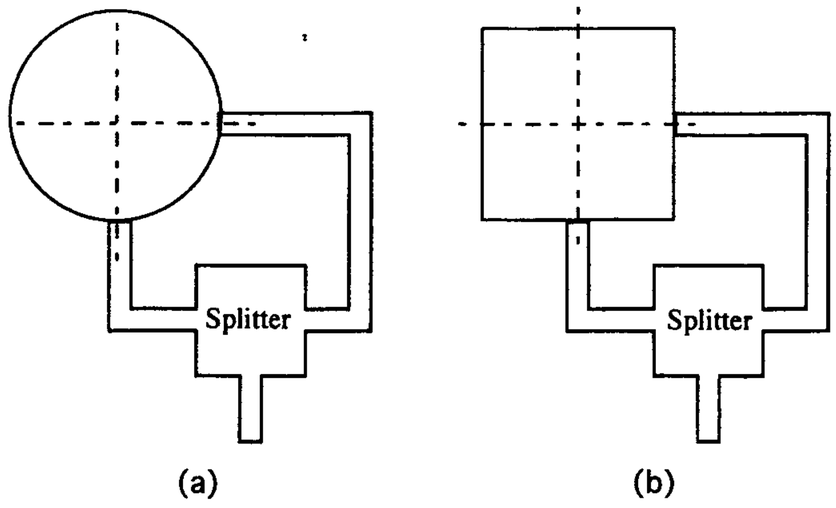

Figure 8.3 Typical configurations of dual-fed circularly polarized microstrip antennas: (a) circular patch and (b) square patch.

T-junction power splitter [9]. The quadrature hybrid splits the input into two outputs with equal amplitude but 90° out of phase. Other types of dividers, however, need a quarter-wavelength line in one of the output arms to produce a 90° phase shift at the two feeds. Consequently, the quadrature hybrid provides a broader axial ratio bandwidth. These splitters can be easily constructed from various planar transmission lines. More discussion on these splitters is given in Section 8.4.

Singly Fed Circularly Polarized Patch

Typical configurations for singly fed CP microstrip antennas are shown in Figure 8.4. A single-point feed patch capable of producing CP radiation is very desirable in situations where it is difficult to accommodate dual-orthogonal

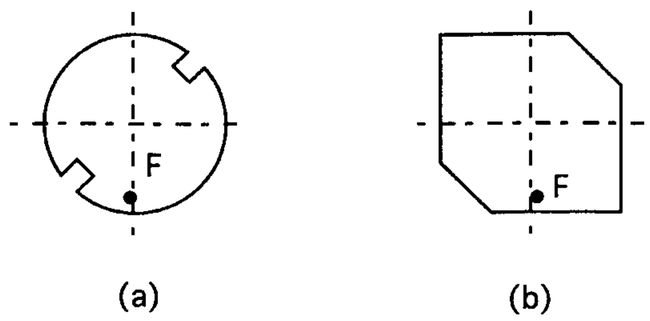

Figure 8.4 Typical configurations of singly fed circularly polarized microstrip antennas: (a) circular patch and (b) square patch.

feeds with a power divider network. Because a patch with a single-point feed generally radiates linear polarization, in order to radiate CP, it is necessary for two orthogonal patch modes with equal amplitude and in-phase quadrature to be induced. This can be accomplished by slightly perturbing a patch at appropriate locations with respect to the feed.

Although various perturbation configurations for generating CP have been reported [10], they operate on the same principle of detuning degenerate modes of a symmetrical patch by perturbation segments as illustrated in Figure 8.5. The fields of a singly fed patch can be resolved into two orthogonal degenerate modes, 1 and 2. Proper perturbation segments will detune the frequency response of mode 2 such that, at the operating frequency f_0, it is of the same amplitude but 90° out of phase with respect to mode 1. Hence, the two modes satisfy the required condition for CP radiation. As the frequency moves away from f_0, the axial ratio rapidly degrades while the input match usually remains acceptable. The actual detuning occurs either for one or both modes depending on the placement of perturbation segments.

A circular polarization can also be obtained from a single-point-fed square or circular patch on a normally biased ferrite substrate, as depicted in Figure

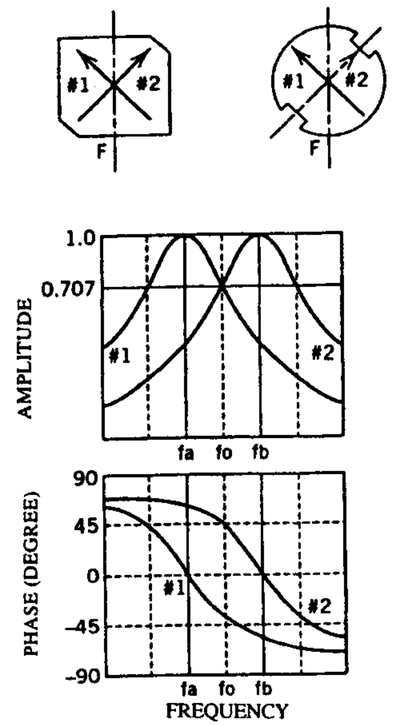

Figure 8.5 Amplitude and phase of orthogonal modes for singly fed circularly polarized microstrip antennas. (From [4]. © 1989 Peter Peregrinus. Reprinted with permission.)

8.6. Pozar demonstrated that a singly fed square patch radiates both left-hand circularly polarized (LHCP) and right-hand circularly polarized (RHCP) at the same level and polarity of bias magnetic field; however, LHCP and RHCP have different resonant frequencies [11]. At the same operating frequency, the sense of polarization can be reversed by reversing the polarity of the bias field. The axial ratio bandwidth is found to be larger than the impedance bandwidth. The radiation efficiency is on the order of 70%.

Dual circular polarizations have also been achieved using a singly fed triangular or pentagonal microstrip antenna [4, 5]. A schematic diagram of an isosceles triangular patch and its feed loci is shown in Figure 8.7. A triangular patch radiates circular polarization at dual frequencies, f_1 and f_2, with the separation depending on the aspect ratio b/a. As indicated in Figure 8.7, RHCP can be changed to LHCP at each frequency by moving the feed location from Γ_1 to Γ_2 or from Γ_4 to Γ_3. The aspect ratio b/a is generally very close to unity; hence, a triangular patch is almost equilateral. A pentagonal patch in Figure 8.8, with the aspect ratio c/a as a design parameter, also behaves in a similar manner [4]. It radiates RHCP when the feed point is on Γ_2 or Γ_3 and LHCP for the feed on Γ_1 or Γ_4.

Arrays of Linearly Polarized Patches for Circularly Polarized Radiation

Two linear LP patch antennas can be orthogonally arranged as shown in Figure 8.9 with one of the patches being fed 90° out of phase [12]. The disadvantages of this configuration are larger space requirements and rapid degradation of CP with angle off the boresight as a result of spatial phase delay due to different path lengths from the phase centers of the two radiating elements. An alternative

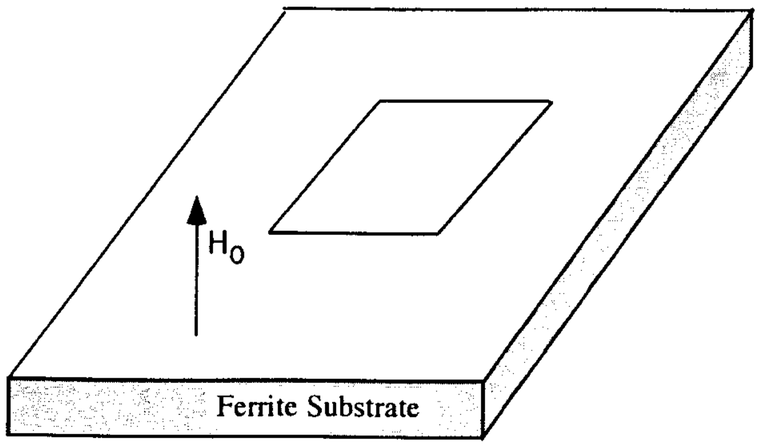

Figure 8.6 Geometry of a rectangular microstrip patch antenna on a normally biased ferrite substrate. (From [11]. © 1992 IEEE. Reprinted with permission.)

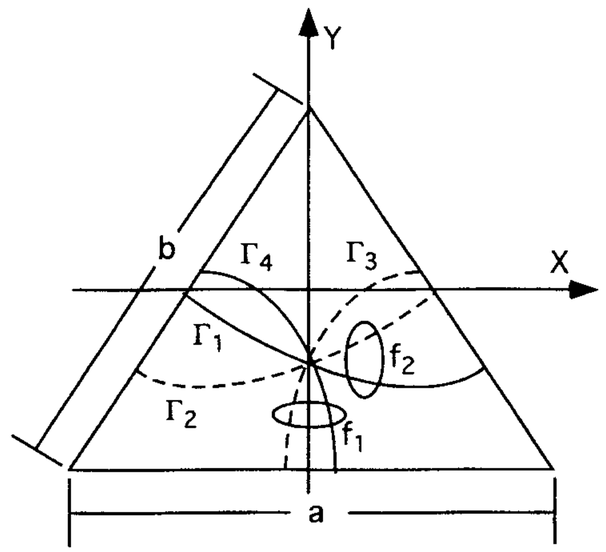

Figure 8.7 Schematic diagram of an isosceles triangular patch and the feed loci for circular polarization radiations: Γ_1 and Γ_4 for RHCP; Γ_2 and Γ_3 for LHCP. (From [4]. © 1989 Peter Peregrinus. Reprinted with permission.)

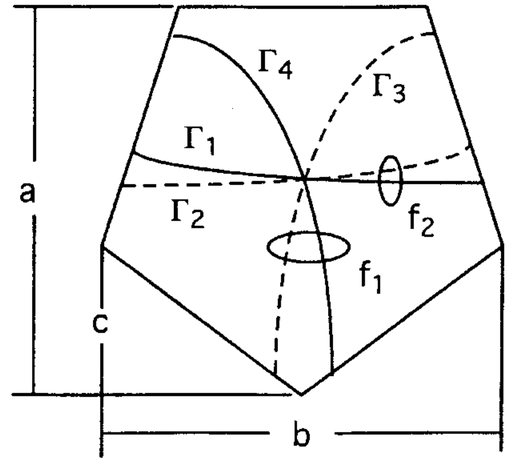

Figure 8.8 Schematic diagram of a pentagonal microstrip patch and the feed loci for circular polarization radiations: Γ_1 and Γ_4 for LHCP; Γ_2 and Γ_3 for RHCP. (From [4]. © 1989 Peter Peregrinus. Reprinted with permission.)

arrangement in Figure 8.10 by Huang [13] significantly improves the CP quality. The axial ratio bandwidth of the array substantially increases. The cross-polar levels are significantly suppressed on the two principal planes, the x-z and the y-z planes, but this is not true on the two diagonal planes.

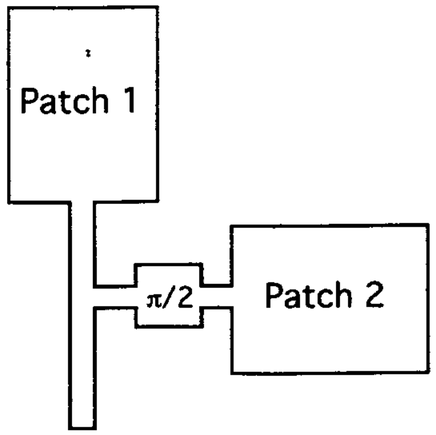

Figure 8.9 Possible arrangement of two linearly polarized patches for circular polarization radiation. (From [12]. © 1981 Peter Peregrinus. Reprinted with permission.)

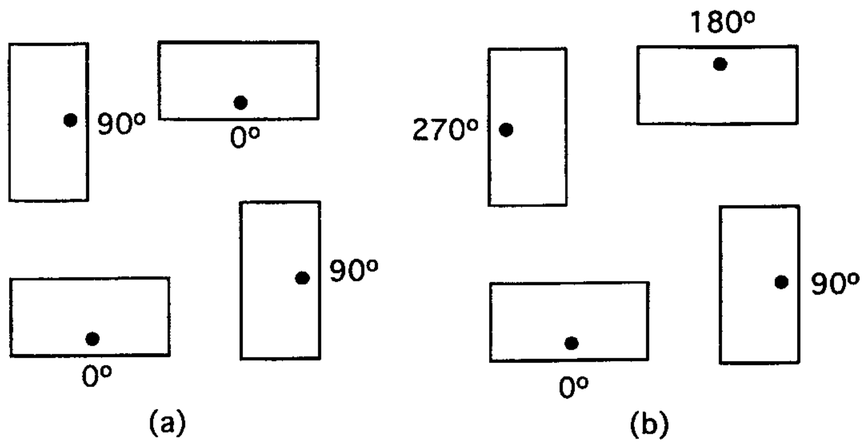

Figure 8.10 2 × 2 microstrip arrays with LP elements for CP generation: (a) narrow-band arrangement and (b) wide-band arrangement. (From [13]. © 1986 IEEE. Reprinted with permission.)

8.2.2 Other Types of Circularly Polarized Antennas

Other types of printed CP antennas are compact in their feed requirements and radiating element configurations. These types of CP printed antennas, which can be easily constructed from microstrip lines, are described next.

Microstrip Spiral Antennas

To obtain a wide bandwidth, the concept of conventional spiral antennas has been applied to microstrip spiral design. A conventional spiral radiates good CP because small residual current remains after the active zone, which corresponds to a spiral arm with a wavelength circumference. However, Wood found that this was not true for the case of microstrip spirals [14]. The decaying of a current in microstrip spirals in the active region was not large enough to prevent significant interference radiation from successive turns in the spiral that adversely affected CP performance. Hence, Wood's design took on the form of a sector of a circular transmission line and one turn of a loosely wound spiral with a feed at one end and a matched termination at the other, as shown in Figure 8.11. The antennas achieve the bandwidth of 40% with axial ratio of less than 3 dB at the cost of reducing the average radiation efficiency to 50% [15]. Wang and Tripp experimented with microstrip spirals using microwave absorbing material placed half inside the truncated spiral and half outside to dissipate the residual energy. They were able to achieve a bandwidth of 6:1 for patterns [16].

Arrays of Composite Elements

A circular polarization can be produced from an array of composite electric and magnetic radiating elements that radiate mutually orthogonal fields with 90° phase difference. One such array consists of standing-wave fed slots and strip dipoles as shown in Figure 8.12 [17]. It is composed of strips on a thin substrate, slots in the ground plane, and a microstrip feed line terminating in a short circuit. The strips and the slots are a half-wavelength long and are spaced at a quarter-guide wavelength apart along the feed line to provide the 90° phase difference requirement. When the strips and the slots are located at the maximum points of voltage and current standing waves, the array can efficiently produce CP in the broadside direction.

Traveling-Wave Arrays

Alternative design of CP printed antennas is in the form of a linear traveling-wave array consisting of microstrip transmission line excitation of microstrip

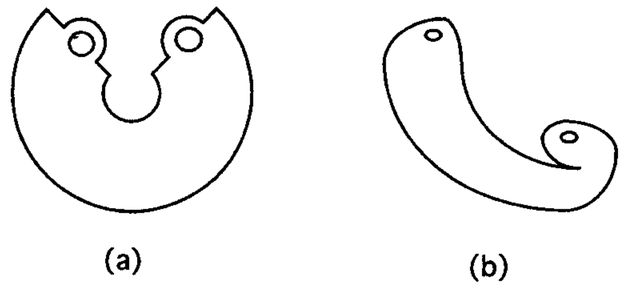

Figure 8.11 Circular polarized curved microstrip line antennas: (a) sector of circular microstrip transmission line and (b) spiral microstrip line antenna. (From [14]. © 1988 Artech House. Reprinted with permission.)

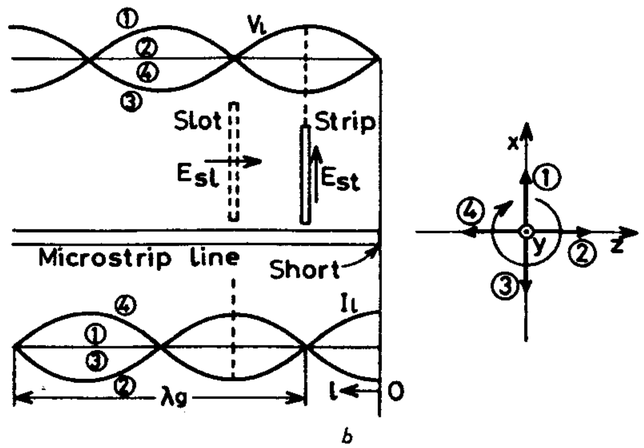

Figure 8.12 Array of composite elements for circular polarization. (From [17]. © 1989 Peter Peregrinus. Reprinted with permission.)

CP radiating elements. The residual power at the end of the microstrip feed line is dissipated in a matched termination to prevent reflection that otherwise can adversely degrade CP quality. The element spacing is generally greater than $\lambda_0/2$; thus, it is possible to use previously described resonator-type CP elements in the design. However, CP radiating elements can also be constructed from an orthogonal arrangement of linearly polarized (LP) radiators as depicted in Figure 8.13, which shows traveling-wave printed dipole and slot arrays [17].

In the dipole array, each unit cell consists of inclined half-wavelength printed dipoles arranged along both sides of a microstrip feed line. The spacing D_S between adjacent dipoles in each unit cell is a quarter-guide wavelength. The spacing D_P between unit cell and the inclined angle α are determined from the desired main beam direction. Slot array arrangements can be determined in a similar manner. However, the operation of the slot array requires a reflector under the substrate for back radiation suppression.

Other designs of traveling-wave arrays utilize a radiating property at discontinuities that are periodically introduced in traveling-wave transmission lines. In these designs, a CP radiating element in each unit cell of the arrays is constructed from bending a microstrip feed line into an appropriate meander. Different design configurations reported in literature include rampart line antennas [15, 17, 18], chain antennas [17, 19], square-loop-type microstrip line antennas [17], and crank-type microstrip line antennas [17, 20]. These configurations are shown in Figure 8.14.

The rampart line antenna consists of four rectangular bends in each unit cell. The crank-type microstrip line antenna is simply two parallel rampart lines of the same dimensions with one line shifted by half a period. This

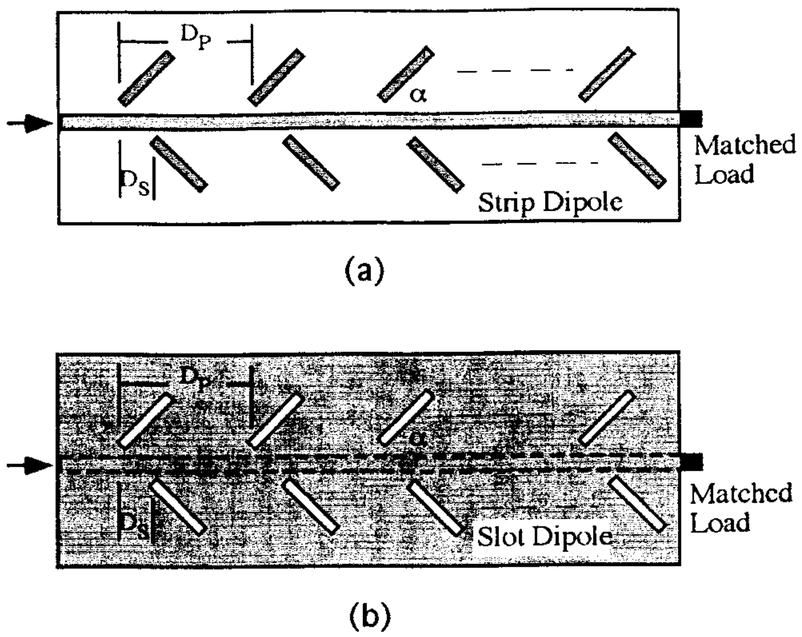

Figure 8.13 Traveling-wave printed arrays for circular polarization: (a) dipole array and (b) slot array.

arrangement results in better frequency characteristics for the axial ratio and radiation pattern. For the chain antenna, its fundamental element is built from a V-shape circularly polarized radiating element and a U-shape phase shifter while each unit cell of the square-loop-type microstrip antenna is made of a CP radiating square loop. In the design, the period of the unit cell is less than λ_0 to avoid grating lobes, and the electrical line length in each unit cell should not be equal to a multiple of a guide wavelength to eliminate the situation in which small reflections can be combined in phase to produce a high return loss. These antennas radiate RHCP when they are fed from the left. The sense of the polarization is reversed when they are fed from the right.

8.3 Singly Fed Circularly Polarized Microstrip Antennas

In this section, a method for designing a circularly polarized microstrip antenna with one point feed is given. The derivation is based on a variational method for the resonant frequency of a perturbed cavity as derived by Haneishi et al. [4, 10]. The derivation is first given for a rectangular patch and then for a cylindrical patch.

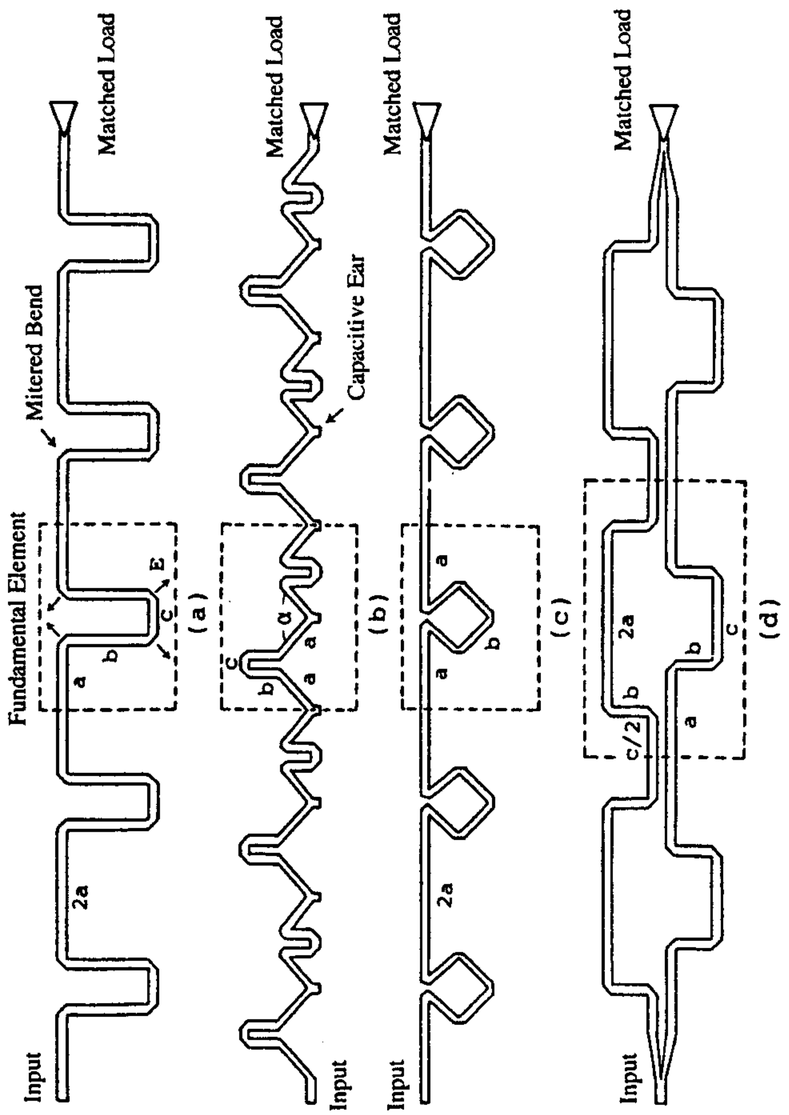

Figure 8.14 Circularly polarized microstrip line antennas: (a) rampart line antenna, (b) chain antenna, (c) square-loop microstrip line antenna, and (d) crank-type microstrip line antenna. (From [17]. © 1989 Peter Peregrinus. Reprinted with permission.)

8.3.1 Rectangular-Type Circularly Polarized Microstrip Antennas

The following derivation is applicable for different types of perturbations, some of which are shown in Figure 8.15 [10]. They have been classified into type A and type B depending on the feed location. Referring to Figure 8.15, it is type A when the feed location is either on the x or the y axis, whereas in type B, the feed is placed on the diagonal axis of a patch. Note that the feed is always located diagonal to perturbation segments that are appropriately selected to produce two orthogonally degenerate modes in the patch for CP radiation.

The fundamental configuration of the patch and its coordinate system are shown in Figure 8.16. The square patch is considered to be an electrically thin cavity with perfect magnetic walls at the boundaries, $x = \pm\frac{a}{2}$ and $y = \pm\frac{a}{2}$. In the figure, F is the feed point and ΔS represents the total sum of perturbation segments and may consist of a single or multiple segments. The introduction of perturbation segments will affect the cavity modal field and its eigenvalue, which can be determined from a stationary formula given by [21]:

$$k'^2 = \frac{\int_{S+\Delta S} \nabla\phi' \cdot \nabla\phi' dS}{\int_{S+\Delta S} \phi'^2 dS} \tag{8.1}$$

where ϕ' and k' are the new modal field and the new eigenvalue. Following the derivation by Haneishi et al. [10], ϕ' can be expanded as

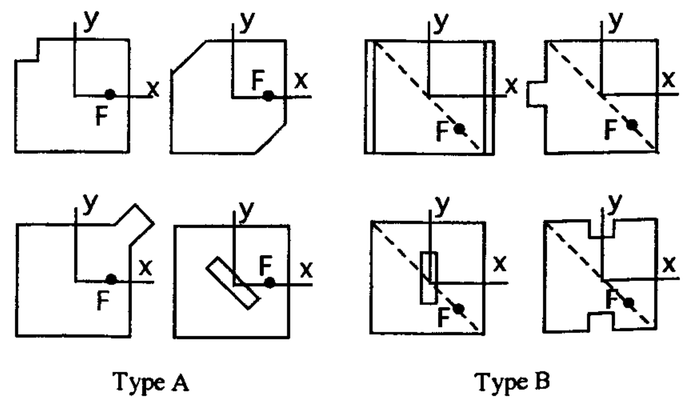

Figure 8.15 Various types of microstrip antenna perturbations for circular polarization generation.

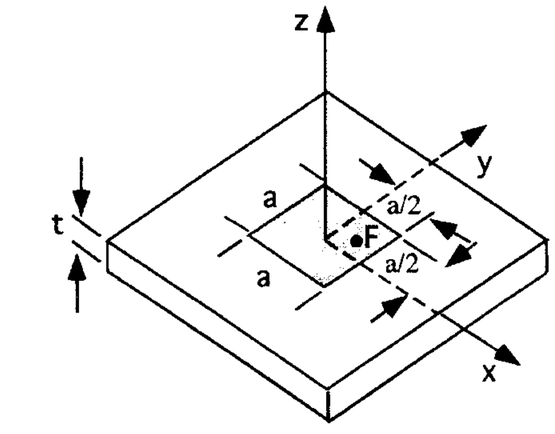

(a)

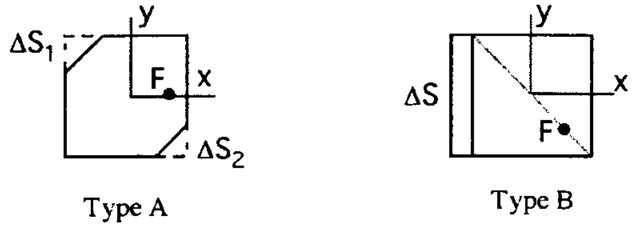

(b)

Figure 8.16 Configurations of singly fed microstrip patch antennas: (a) patch diagram and (b) type A and type B microstrip patch perturbations.

$$\phi' = P\phi_a + Q\phi_b \tag{8.2}$$

where P and Q are unknown expansion coefficients that have to be determined to make (8.1) stationary. Substituting (8.2) in (8.1) gives

$$k'^2 = \frac{\displaystyle\int_{S+\Delta S} (P\nabla\phi_a + Q\nabla\phi_b)\cdot(P\nabla\phi_a + Q\nabla\phi_b)\,dS}{\displaystyle\int_{S+\Delta S} (P\phi_a + Q\phi_b)^2\,dS} = \frac{U(P, Q)}{V(P, Q)} \tag{8.3}$$

Following the Ritz-Galerkin method, P and Q can be determined from [22]

$$\frac{\partial U(P, Q)}{\partial P} - k'^2\frac{\partial V(P, Q)}{\partial P} = 0$$
$$\frac{\partial U(P, Q)}{\partial Q} - k'^2\frac{\partial V(P, Q)}{\partial Q} = 0 \tag{8.4}$$

Equation (8.4) will result in a set of homogeneous equations that have nontrivial solutions only if the determinant vanishes. Exact parameters of the determinant depend on the type of feed and perturbation placements. It can generally be written in the form [4, 10]

$$\det\begin{vmatrix} k^2 + q_1 - k'^2(1 + p_1) & q_{12} - k'^2 p_{12} \\ q_{12} - k'^2 p_{12} & k^2 + q_2 - k'^2(1 + p_1) \end{vmatrix} = 0 \tag{8.5}$$

Type A Patch

For the type A-fed patch, ϕ_a and ϕ_b are the two normalized degenerates modes, TM_{100} and TM_{010}, of a thin patch which can be written as

$$\phi_a = V_0 \sin(kx)$$
$$\phi_b = V_0 \sin(ky) \tag{8.6}$$

where $V_0 = \sqrt{2}/a$, $k = \pi/a$, and a is the patch size. Using (8.6) in (8.2), all other parameters in (8.5) can be obtained from (8.4) as

$$q_1 = q_2 = q_{12} = 0$$
$$p_1 = p_2 = 2\left(\frac{\Delta S}{S}\right)$$
$$p_{12} = -2\left(\frac{\Delta S}{S}\right) \tag{8.7}$$

Substituting (8.7) into (8.5), the new eigenvalues k_a' and k_b' for the modal fields ϕ_a and ϕ_b can be found from (8.5) as

$$k'^2_a = k^2\left(1 + 4\frac{\Delta S}{S}\right)^{-1}$$
$$k'^2_b = k^2 \tag{8.8}$$

from which the new resonant frequencies of ϕ_a' and ϕ_b' modes are obtained:

$$f_a = f_{0r} + \Delta f_a' = f_{0r}\left(1 - 2\frac{\Delta S}{S}\right) \tag{8.9}$$

$$f_b = f_{0r} + \Delta f_b' = f_{0r}$$

where f_{0r} is the resonant frequency of the square patch before perturbation, and $\Delta f_a'$ and $\Delta f_b'$ are the shifts in resonant frequencies for ϕ_a' and ϕ_b' modes after perturbation. Once the new eigenvalues k_a' and k_b' are determined, expansion coefficients P and Q can be found from the original set of the homogeneous equations and are given by

$$P_a = -Q_a = \frac{1}{\sqrt{2}} \tag{8.10}$$

$$P_b = Q_b = \frac{1}{\sqrt{2}}$$

for the normalized ϕ_a' and ϕ_b', which can be written in closed forms, using the first-order approximation of $k_a' \approx k_b' \approx k$, as

$$\phi_a' \approx \frac{V_0}{\sqrt{2}}(\sin(kx) - \sin(ky)) \tag{8.11}$$

$$\phi_b' \approx \frac{V_0}{\sqrt{2}}(\sin(kx) + \sin(ky))$$

The energy distribution ratios for both ϕ_a' and ϕ_b' modes after perturbation are defined as turn ratios N_a' and N_b', which are given by

$$N_a' = \frac{\sqrt{S}}{a}(\sin(kx) - \sin(ky)) \tag{8.12}$$

$$N_b' = \frac{\sqrt{S}}{a}(\sin(kx) + \sin(ky))$$

Using (8.6)–(8.12), the equivalent circuit after perturbation can be derived as shown in Figure 8.17 [10]. T_A' and T_B' represent ideal transformers with turn ratios N_a' and N_b', respectively, whereas $\dot{V}_f$ is input voltage applied to the $1-1'$ terminal. $\dot{Y}_a$ and $\dot{Y}_b$ are the patch input admittances corresponding to the orthogonally polarized ϕ_a' and ϕ_b' modes. The equivalent conductances G_a' and G_b' generally include radiation, dielectric, and copper losses. However,

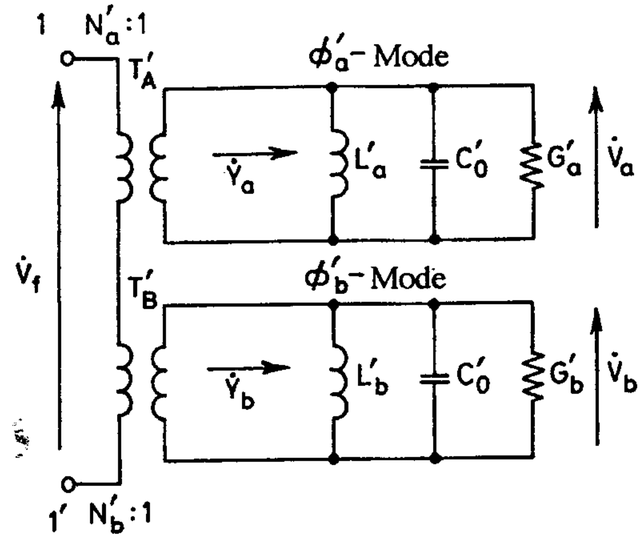

Figure 8.17 Equivalent circuit of a microstrip patch antenna with perturbation. (From [10]. © 1988 Artech House. Reprinted with permission.)

the radiation will be the main contribution to the conductances if it is dominant as compared with the other losses.

Type B Patch

A similar procedure employed for type A can be applied to obtain different parameters for type B patch antennas, using the normalized modes ϕ_a and ϕ_b given by

$$\phi_a = V_{00}(\sin(kx) + \sin(ky)) \tag{8.13}$$

$$\phi_b = V_{00}(-\sin(kx) + \sin(ky))$$

where $V_{00} = 1/a$ and $k = \pi/a$. Other parameters are as follows [4, 10]:

$$p_1 = p_2 = \left(\frac{3}{2}\right)\left(\frac{\Delta S}{S}\right)$$

$$p_{12} = \left(-\frac{1}{2}\right)\left(\frac{\Delta S}{S}\right)$$

$$q_1 = q_2 = q_{12} = \left(\frac{1}{2}\right)\left(\frac{\Delta S}{S}\right)k^2$$

$$k_a'^2 = k^2\left(1 + 2\frac{\Delta S}{S}\right)^{-1}$$

$$k_b'^2 = k^2$$

$$f_a = f_{0r} + \Delta f_a' = f_{0r}\left(1 - \frac{\Delta S}{S}\right)$$

$$f_b = f_{0r} + \Delta f_b' = f_{0r}$$

$$\phi_a' = \left(\frac{\sqrt{2}}{a}\right)\left(1 - \frac{\Delta S}{S}\right)\sin(kx)$$

$$\phi_b' = \left(\frac{\sqrt{2}}{a}\right)\left(1 - \frac{\Delta S}{2S}\right)\sin(ky)$$

$$N_a' = \sqrt{S}\phi_a' \approx \sqrt{2}\sin(kx)$$

$$N_b' = \sqrt{S}\phi_b' \approx \sqrt{2}\sin(ky) \tag{8.14}$$

The equivalent circuit as shown in Figure 8.17 is also applicable for type B antennas after perturbation [4]. It can be derived in the same manner as for type A.

Circular Polarization Radiation Condition

Referring to the equivalent circuit in Figure 8.17, the complex amplitude ratio $\dot{V}_a/\dot{V}_b$ in the two orthogonal modes is given by

$$\left(\frac{\dot{V}_b}{\dot{V}_a}\right) = \left(\frac{N_b'}{N_a'}\right)\left(\frac{Y_a'}{Y_b'}\right) = \left(\frac{N_b'}{N_a'}\right)\frac{\left\{\frac{f_a}{Q_0} + j\left(f - \frac{f_a^2}{f}\right)\right\}}{\left\{\frac{f_b}{Q_0} + j\left(f - \frac{f_b^2}{f}\right)\right\}} \tag{8.15}$$

It is assumed in (8.15), to the first-order approximation, that the unloaded Q factors Q_{0a} and Q_{0b} of the two orthogonal modes ϕ_a' and ϕ_b' are equal to Q_0. For the patch to radiate CP, it is required that

$$\left(\frac{\dot{V}_b}{\dot{V}_a}\right) = \pm j \tag{8.16}$$

If the turn ratios N_a' and N_b' are selected such that

$$\left(\frac{N_b'}{N_a'}\right) = \pm 1 \tag{8.17}$$

then (8.15) is reduced to

$$\left(\frac{\dot{V}_b}{\dot{V}_a}\right) = \pm\frac{\left\{\frac{f_a}{Q_0} + j\left(f - \frac{f_a^2}{f}\right)\right\}}{\left\{\frac{f_b}{Q_0} + j\left(f - \frac{f_b^2}{f}\right)\right\}} \tag{8.18}$$

From (8.18), the frequency f and the perturbation segment $\Delta S/S$ can be determined in terms of Q_0 such that the CP radiation condition (8.16) is satisfied. This leads to the relation between $\Delta S/S$ and Q_0, which can be expressed as [4, 10]

$$\frac{(Q_0^2 - 1)Q_0^2}{(2Q_0^2 - 1)}(M^2 + N^2) = MN\left\{1 + \frac{(2Q_0^2 - 1)MN}{(M^2 + N^2)}\right\} \tag{8.19}$$

where $M = (1 + m\Delta S/S)$, $N = (1 + n\Delta S/S)$, and m and n are the constants in $f_a = f_{0r}(1 + m\Delta S/S)$ and $f_b = f_{0r}(1 + n\Delta S/S)$, which are determined from the stationary formula as previously described.

In case of the type A patch, $(N_b'/N_a') = 1$ when the feed point F is on the x axis, and it is equal to -1 when the feed F is shifted to the y axis. Hence, (8.17) is satisfied by placing the feed F either on the x or the y axis. From the expressions of f_a and f_b given in (8.9), the constants $m = -2$ and $n = 0$ are substituted into (8.19), for which, after some simplifications, the following useful design equation is obtained:

$$\left|\frac{\Delta S}{S}\right| = \frac{1}{2Q_0} \tag{8.20}$$

It is also interesting to note that from the resonating curves of the input admittances Y_a' and Y_b', the phase quadrature relation can be achieved when

their amplitude has dropped to $1/\sqrt{2}$ of the maximum values, which occurs at $\Delta f_1 = f_{0r}/(2Q_0)$ [23]. From (8.9), this is approximately half of the frequency shift between f_a' and f_b', which is $|\Delta S/S| f_{0r}$. Hence, equating Δf_1 to $|\Delta S/S| f_{0r}$, leads to the same expression as in (8.20).

Following the same procedure as for the type A antenna, the design equation for the type B microstrip antenna can be derived and is given by

$$\left|\frac{\Delta S}{S}\right| = \frac{1}{Q_0} \tag{8.21}$$

Because the feed of the type B antenna is on either diagonal axis, (8.17) will always be satisfied. The sense of CP can be reversed by moving the feed from one of the diagonal axes to the other. Figure 8.18 shows the plots of $|\Delta S/S|$ versus Q_0.

Design Procedure for CP Patch With a Single-Point Feed

The general design procedure can be summarized as follows:

1. Determine the unloaded Q_0 of the patch, which depends on dimensions a, substrate thickness t, and the substrate dielectric constant ϵ_r. For better accuracy Q_0 should be selected to ensure the patch radiation efficiency $\eta > 90\%$.

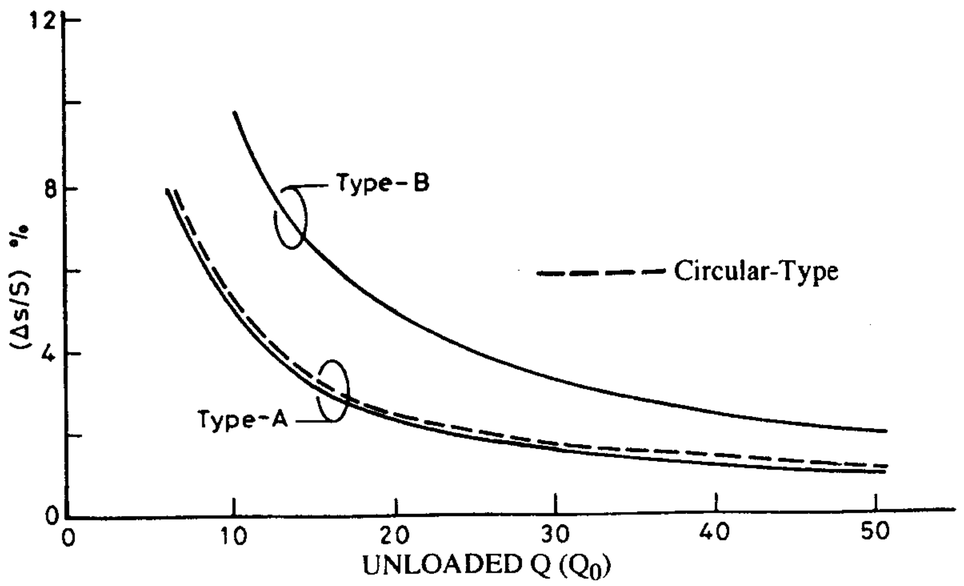

Figure 8.18 Variation of perturbation segments ($\Delta S/S$) versus patch unloaded Q. (From [4]. © 1989 Peter Peregrinus. Reprinted with permission.)

2. Determine the amount of perturbation ($\Delta S/S$) from (8.20) for the type A patch or from (8.21) when the patch is of type B.
3. The location of the feed on the axis can be selected to provide a good match; alternatively a quarter-wavelength transformer can be used for matching purpose.
4. Depending on whether each type of the antenna is type A or type B, the sense of CP can be changed by switching the feed axis.

As a design sample, a singly fed patch with dimension $a = 9.14$ mm on the substrate with thickness $t = 1.18$ mm and $\epsilon_r = 2.55$ is demonstrated for both type A and B perturbations. First, the unloaded Q_0 and the radiation efficiency η versus substrate thickness t are plotted in Figure 8.19 [10]. The value of Q_0 at $t = 1.18$ mm is found from the graph to be 28, which corresponds to the efficiency η exceeding 90%. At $Q_0 = 28$, the percentage of the perturbation segment ($\Delta S/S$) can be found from Figure 8.18. For type A, ($\Delta S/S$) is 2.9%, and it is 6.5% for type B. The axial ratios versus frequency are shown in Figure 8.20 [10].

8.3.2 Circularly Polarized Circular Microstrip Antennas

The configuration of a circular patch antenna and its feed system is shown in Figure 8.21. The feed is always located at a diagonal with respect to the perturbation segments. Similar to the case of square patches, the dominant

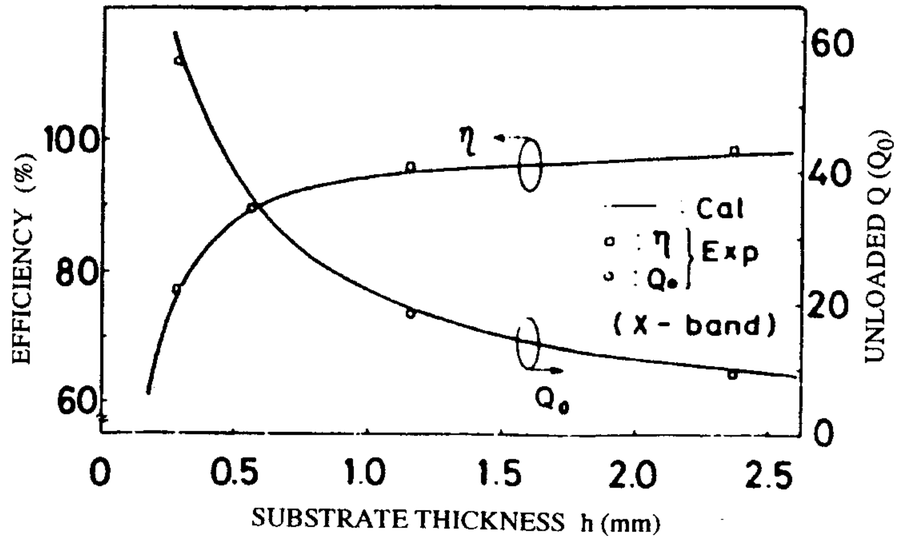

Figure 8.19 Variation of radiation efficiency η versus substrate thickness. (From [10]. © 1988 Artech House. Reprinted with permission.)

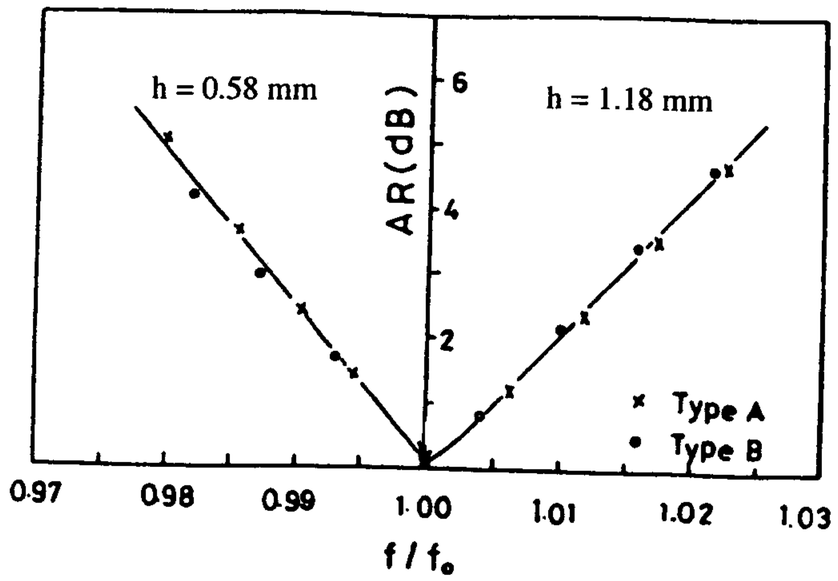

Figure 8.20 Variation of axial ratio versus f/f_0. (From [10]. © 1988 Artech House. Reprinted with permission.)

mode TM_{110} will be separated into two orthogonal degenerated modes by perturbation segments. The analysis follows the same procedure as described in the previous section for a square patch.

The equivalent circuit for circular singly fed CP patch antenna is similar to that of a singly fed rectangular patch as illustrated in Figure 8.17. The following parameters are obtained [4, 24]:

$$f_a = f_{0r}\left(1 + 0.4185\frac{\Delta S}{S}\right)$$

$$f_b = f_{0r}\left(1 - 1.4185\frac{\Delta S}{S}\right)$$

$$N_a' = K\cos(\phi_F + 45°)$$

$$N_b' = K\sin(\phi_F + 45°)$$

$$K = \sqrt{2}\sqrt{\frac{\chi_{11}^2}{\chi_{11}^2 - 1}}\left(\frac{J_1\left(\frac{\chi_{11}\rho_0}{a}\right)}{J_1(\chi_{11})}\right) \tag{8.22}$$

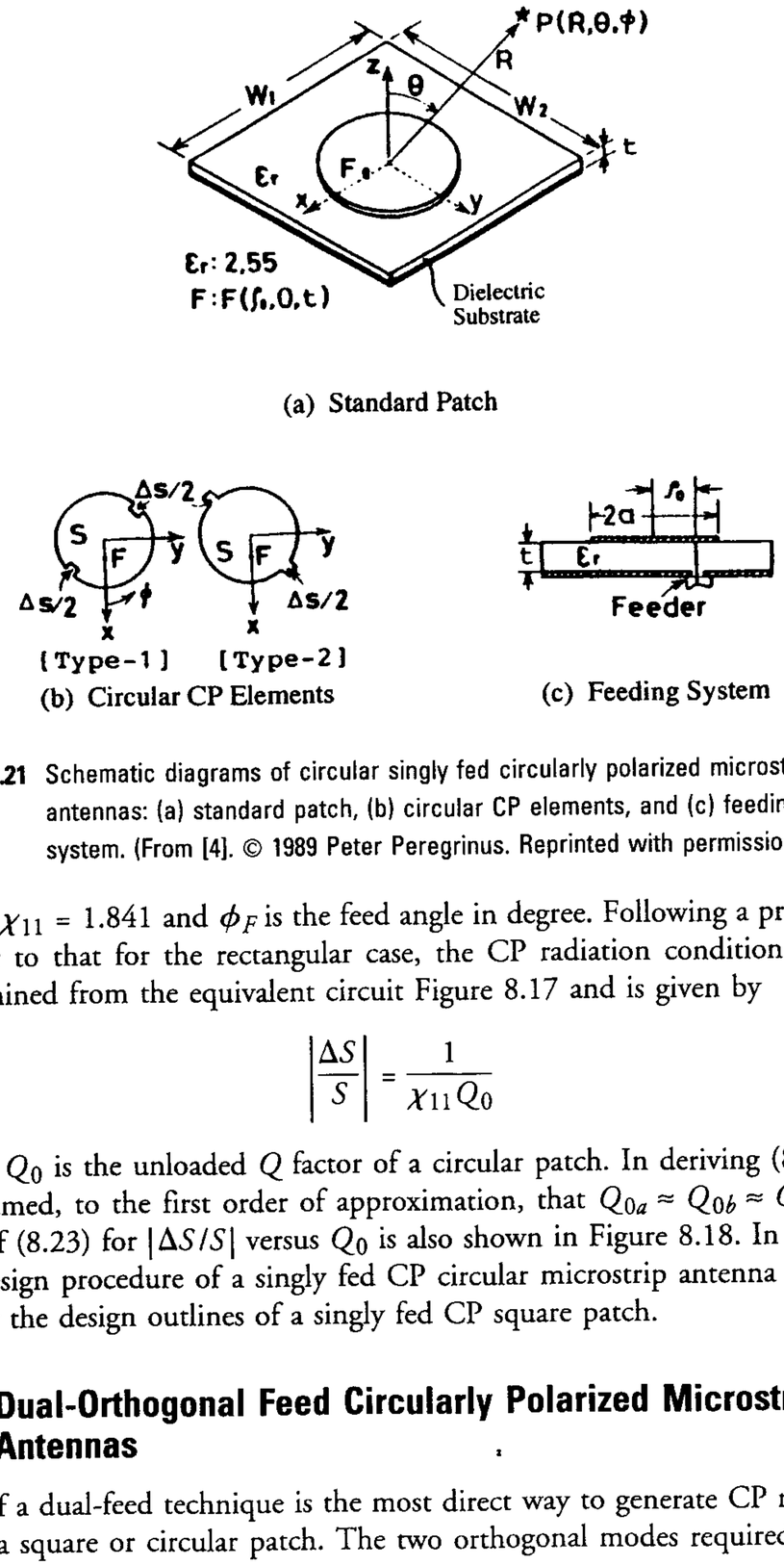

Figure 8.21 Schematic diagrams of circular singly fed circularly polarized microstrip antennas: (a) standard patch, (b) circular CP elements, and (c) feeding system. (From [4]. © 1989 Peter Peregrinus. Reprinted with permission.)

where $\chi_{11} = 1.841$ and ϕ_F is the feed angle in degree. Following a procedure similar to that for the rectangular case, the CP radiation condition can be determined from the equivalent circuit Figure 8.17 and is given by

$$\left|\frac{\Delta S}{S}\right| = \frac{1}{\chi_{11} Q_0} \tag{8.23}$$

where Q_0 is the unloaded Q factor of a circular patch. In deriving (8.23), it is assumed, to the first order of approximation, that $Q_{0a} \approx Q_{0b} \approx Q_0$. The plot of (8.23) for $|\Delta S/S|$ versus Q_0 is also shown in Figure 8.18. In general, the design procedure of a singly fed CP circular microstrip antenna can still follow the design outlines of a singly fed CP square patch.

8.4 Dual-Orthogonal Feed Circularly Polarized Microstrip Antennas

Use of a dual-feed technique is the most direct way to generate CP radiation from a square or circular patch. The two orthogonal modes required for the

generation of CP can be simultaneously excited using dual-orthogonal feeds. In designing, a patch is first matched to the feed lines by either appropriately selecting the feed locations or through the use of impedance transformers. The two feeds are then connected to the output ports of a power divider circuit, which provides the required amplitude and phase excitations. Various types of power divider circuits that have been successfully employed in a feed network of a CP patch are discussed in this section.

8.4.1 The Quadrature Hybrid

Referring to Figure 8.22(a), the quadrature hybrid is a four-port network. Typically, the input is at port 1 and the output at ports 2 and 3, while port 4 is terminated in a match load. Alternately, port 4 can be the input and port 1 match-terminated while the output remains at ports 2 and 3. With a high degree of symmetry, the operation of the hybrid is not affected when ports 1 and 4 are interchanged with ports 2 and 3. The basic properties of a quadrature hybrid can be deduced directly from the scattering matrix, which is given by [9]:

$$[S] = \frac{-1}{\sqrt{2}}\begin{bmatrix} 0 & j & 1 & 0 \\ j & 0 & 0 & 1 \\ 1 & 0 & 0 & j \\ 0 & 1 & j & 0 \end{bmatrix} \tag{8.24}$$

As a power divider in a CP patch feed network, the input is connected to port 1 and port 4 is match-terminated or vice versa, depending on the required sense of CP rotation. The output from ports 2 and 3 is then fed to the patch. The signal is evenly divided in amplitude but in phase quadrature at ports 2 and 3. Mismatch at the patch will return to the absorbing load at port 4, thus a good match is maintained. Because ports 2 and 3 are uncoupled, good isolation, generally exceeding 20 dB, also exists between the outputs. Consequently, the axial ratio is not degraded.

A 3-dB quadrature hybrid can be designed using the expressions of a four-port direct-coupled power divider [25]. The characteristic impedances Z_a and Z_b of a quarter-guide wavelength shunt and series arms are obtained as

$$Z_b = \frac{Z_0}{\sqrt{2}} \tag{8.25}$$

$$Z_a = Z_0$$

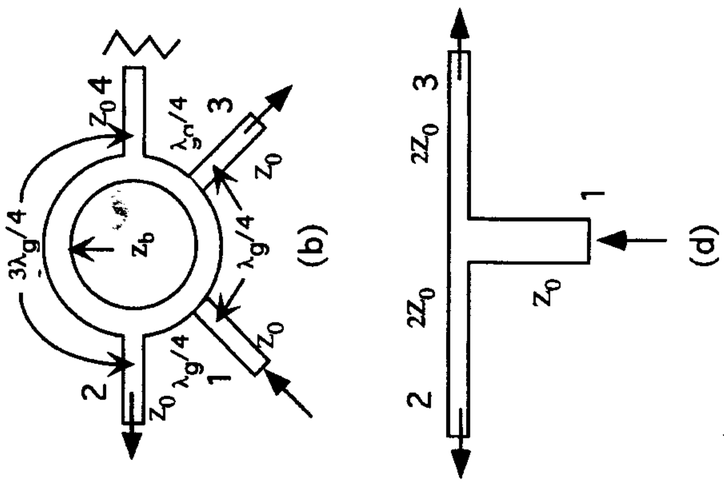

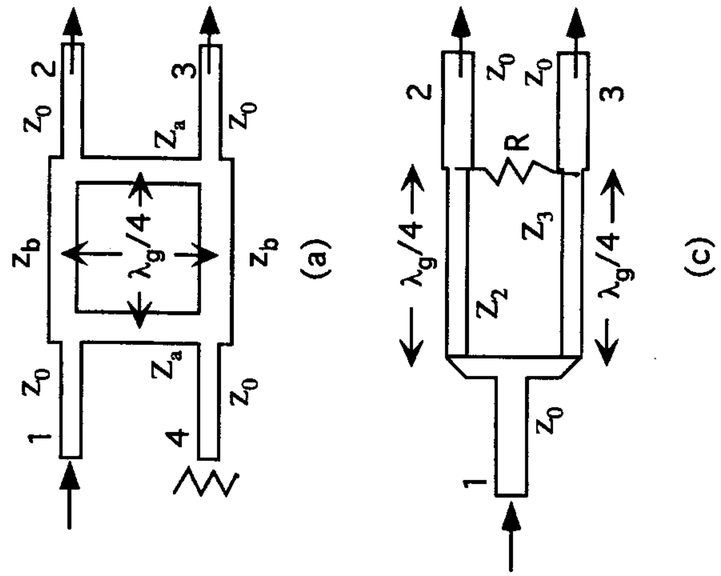

Figure 8.22 Schematic diagrams of power dividers: (a) quadrature hybrid, (b) ring hybrid, (c) Wilkinson power divider, and (d) T-junction power divider.

8.4.2 The 180-Degree Hybrid

The ring hybrid, or a rat-race, is a 180-degree hybrid junction, as shown in Figure 8.22(b). It is a four-port network with the scattering matrix for the ideal 3-dB case given by [9]

$$[S] = \frac{-j}{\sqrt{2}}\begin{bmatrix} 0 & 1 & 1 & 0 \\ 1 & 0 & 0 & -1 \\ 1 & 0 & 0 & 1 \\ 0 & -1 & 1 & 0 \end{bmatrix} \tag{8.26}$$

The input at port 1 is equally split in amplitude and phase at the output ports 2 and 3, which are connected to the patch dual-orthogonal feeds. A quadrature phase difference between the two orthogonal excitations can be achieved by a quarter-wavelength differential line length between the two output lines. Because of the 90° phase shift between the output arms, any reflections from the patch tend to cancel at the input port 1 so that the match remains acceptable. However, the combined mismatch at port 4 should be absorbed by a matched load to prevent potential power division degradation of the hybrid which, otherwise, can affect axial ratio performance. Because ports 2 and 3 are uncoupled, the isolation between the outputs is good. It is usually better than 20 dB. When port 4 becomes the input and port 1 is match-terminated while keeping everything else the same, the sense of CP rotation is changed.

The line parameters can be obtained from the general design equations of a hybrid-ring coupler [25]. The characteristic impedance of the ring Z_b is found to be $\sqrt{2}Z_0$ for a 3-dB split.

8.4.3 The Wilkinson Power Divider

The Wilkinson power divider is generally an N-way hybrid splitter with arbitrary power division. In a CP feed network application, a Wilkinson will be considered to be a three-port device with the scattering matrix for the ideal case given by [9]

$$[S] = \frac{-j}{\sqrt{2}}\begin{bmatrix} 0 & 1 & 1 \\ 1 & 0 & 0 \\ 1 & 0 & 0 \end{bmatrix} \tag{8.27}$$

As depicted in Figure 8.22(c), the input at port 1 is evenly divided in amplitude and phase at output ports 2 and 3. Similar to the ring hybrid

previously described, a 90° phase difference at the dual feeds can be realized by a quarter-wavelength differential line length between the output arms of ports 2 and 3. As a result of a 90° phase shift between the two output arms, any reflection at the patch appears as odd mode excitation, which is dissipated in the isolation resistor. Hence, a good match is maintained, but the antenna efficiency may decrease. Good isolation between output ports 2 and 3 also prevents axial ratio degradation by the patch mismatch.

The line parameters for an equal-split Wilkinson power divider can be determined from design equations of the split-T power divider [9, 25, 26]. They are given by

$$Z_2 = Z_3 = \sqrt{2}Z_0 \tag{8.28}$$
$$R = 2Z_0$$

8.4.4 The T-Junction Power Divider

The T-junction power divider as illustrated in Figure 8.22(d) behaves similarly to a three-port Wilkinson except there is no isolation between output ports 2 and 3 [9, 25]. Hence, the axial ratio is adversely affected by reflections at the patch. VSWR, however, remains acceptable because the reflections tend to cancel each other at the input due to a quarter-wavelength difference between the two output arms. For equal split, the characteristic impedances in the T arms are given by $Z_2 = Z_3 = 2Z_0$.

General characteristics of these hybrids are summarized in Table 8.1.

Table 8.1
General Characteristics of Power Divider Networks

	90° Phase Shift	Output Port Isolation	Input Match	Change of CP
T-junction divider	No*	No	Yes†	No
Wilkinson divider	No*	Yes	Yes†	No
Quadrature hybrid	Yes	Yes	Yes	Yes, by switching input and isolate ports
Ring hybrid	No*	Yes	Yes†	Yes,† by switching input and isolate ports

*Requires a quarter-wavelength of line extension in one output arm to generate phase shift.
†With a quarter-wavelength of line extension in one output arm in place.

Because a 3-dB quadrature hybrid produces fields with equal amplitudes and 90° out of phase without the need for a quarter-wavelength line extension in one of the feed arms, this results in a broader VSWR and axial ratio bandwidth as compared to other types of splitters.

8.4.5 Design Procedure

The design procedure for dual-orthogonal feed CP patch antenna can be summarized as follows:

1. Design a patch using two orthogonal feeds. Depending on applications, various types of feeding techniques can be employed, including direct contact methods such as probe or microstrip line feed and noncontacting feeds of proximity and slot couplings. Matching can be achieved by appropriately choosing the feed location and dimensions or by using impedance transformers.
2. A power divider network is selected and designed. The output ports are connected to antenna feeds. The output port line impedances should be matched to the antenna feeds. Impedance transformers can be used if necessary.

In the design, it is preferable to minimize the coupling between the two feeds for a better axial ratio performance. If the coupling between the two feeds remains strong, a splitter with good isolation such as the quadrature hybrid or the Wilkinson divider is required for good CP quality.

More design examples of single-feed and dual-fed circularly polarized patch antennas are given in Chapter 10.

8.5 Circularly Polarized Traveling-Wave Microstrip Line Arrays

CP traveling-wave microstrip line arrays utilize a radiating property at discontinuities of a microstrip line by periodically bending the line into an appropriate meander. Each fundamental element of a periodic array radiates circularly polarized waves in $\theta = \theta_m$, $\phi = 0$ if the following condition is satisfied [17]:

$$E_\phi = \pm jE_\theta \tag{8.29}$$

where E_ϕ and E_θ are the radiation field components of the fundamental element. They can be determined from the strip electric current and its image formed

by the ground plane. A linear array constructed from these fundamental elements will have a beam peak at θ_m when

$$k_0 L\cos(\theta_m) - \beta' l = 2n\pi \tag{8.30}$$

where $k_0 = 2\pi/\lambda_0$, λ_0 is the free-space wavelength, β' is the propagation constant along a meander line, l is the fundamental element line length, and L is the element spacing of the array. The conditions for circular polarization in θ_m direction for a rampart line antenna, a chain antenna, a square-loop-type microstrip line antenna, and a crank-type microstrip line antenna can be determined from (8.29) and (8.30).

In the calculation of (8.29), it is assumed that the amplitude of the current distribution along the strip conductor length of the fundamental element is uniform and all reflections at bends are negligible. The term β' is also approximately taken to be the same as β, the propagation constant of the microstrip line, but l is replaced by l', the electrical line length of the fundamental element to account for the bends in terms of δ parameter. The results for these traveling-wave arrays are given next [17].

8.5.1 Rampart Line Antenna and Crank-Type Microstrip Line Antenna

Referring to Figures 8.23(a) and (d), the following design equations are obtained:

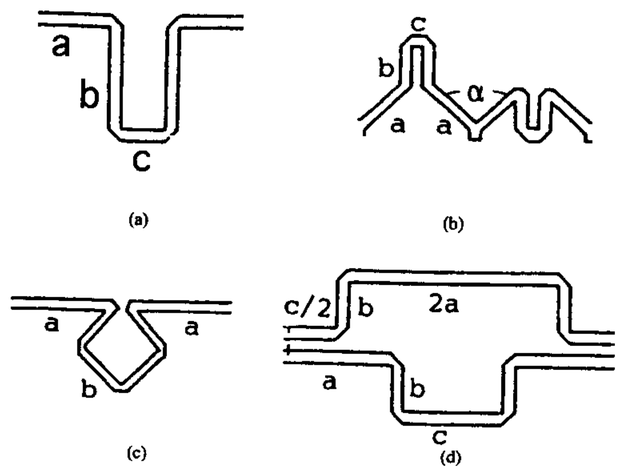

Figure 8.23 The fundamental element of microstrip line antennas: (a) rampart line antenna, (b) chain antenna, (c) square-loop microstrip line antenna, and (d) crank-type microstrip line antenna. (From [17]. © 1989 Peter Peregrinus. Reprinted with permission.)

$$L = 2a + c$$

$$l = 2a + 2b + c$$

$$l' = l - 4\delta$$

$$a = \frac{1}{2U}\left\{\left(1 \mp \frac{1}{\pi}\tan^{-1}\Theta\right)\lambda_g - b + 2\delta\right\}$$

$$b = \frac{1}{U}\left\{\left(1 \pm \frac{1}{\pi}\tan^{-1}\Theta\right)\lambda_g - b + 2\delta\right\} \tag{8.31}$$

$$\Theta = \frac{(W-\delta)\sin\theta_m}{WU-\delta}\,\frac{\sin\frac{\beta}{2}(b-\delta) - \frac{\delta}{WU}\sin\frac{\beta}{2}(b + WU - 2\delta)}{\sin\frac{\beta}{2}(b-\delta) - \frac{\delta}{W}\sin\frac{\beta}{2}(b-W)}$$

$$U = 1 - \frac{\lambda_g}{\lambda_0}\cos\theta_m$$

where W is the width of the line and θ_m is the direction of the main beam. The optimum value of b is approximately $\lambda_g/2$ and a and c can be found from (8.31).

8.5.2 Chain Antenna

The fundamental element is illustrated in Figure 8.23(b) and these are the design equations:

$$L = 2\left(2a\sin\frac{\alpha}{2} + c\right)$$

$$l = 2(2a + 2b + c)$$

$$l' = 1 - 10\delta$$

$$\tan\frac{\alpha}{2}\sin\theta_m = \tan\left(\frac{k_0(a-\delta)T}{2}\right) \tag{8.32}$$

$$T = \frac{\beta}{k_0} - \cos\theta_m\sin\frac{\alpha}{2}$$

$$\cos\theta_m = \frac{1}{L}\left(\frac{\beta l'}{k_0} - 2\lambda_0\right)$$

8.5.3 Square-Loop-Type Microstrip Line Antenna

The fundamental element is given in Figure 8.23(c) and these are the design equations:

$$L = 2a + c$$

$$l = 2a + 4b$$

$$l' = 1 - 5\delta$$

$$\theta_m = 90° \tag{8.33}$$

$$a = \frac{1}{2}(\lambda_g - \delta)$$

$$b = \frac{\lambda_g}{4} + \delta$$

In designing these microstrip line antennas, the length of the fundamental element L (i.e., the element spacing) should be selected to prevent grating lobes from simultaneously appearing in the visible region. This requirement is satisfied if

$$\frac{L}{\lambda_0} < \frac{\nu}{1 + \cos\theta_m} \tag{8.34}$$

where

$\nu = 1$ for rampart and square-loop antennas

$\nu = 2$ for chain and crank-type antennas

Also δ has to be known and it can be determined by the following method [17]:

1. Construct an experimental model of the antenna using the values a, b, and c as determined by setting $\theta_m = 90°$ and $\delta = 0$. The frequency f_m, where $\theta_m = 90°$, is then measured.
2. From the measured frequency f_m and the design frequency f_d, δ is obtained from

$$\delta = \frac{c_0}{2}\frac{\lambda_g}{\lambda_0}\left(\frac{1}{f_d} - \frac{1}{f_m}\right) \tag{8.35}$$

where c_0 is the velocity of light.

Because a traveling-wave microstrip line antenna is periodically bent, $l' = m\lambda_g/2$ (where m is an integer) must be avoided to prevent high return loss as a result of in-phase combining of reflected waves from every fundamental element. However, when $\theta_m = 90°$, $l' = 2\lambda_g$, bends must be carefully arranged to minimize the total reflections at each fundamental element.

8.6 Bandwidth Enhancement Techniques

Traditionally, a microstrip antenna has a narrow impedance bandwidth of the order of a few percent as a result of the fundamental limitation set by the small electrical volume occupied by the element. This is the most serious disadvantage preventing it from being used in many microwave applications. When a narrow-bandwidth microstrip antenna is used in circular polarization applications, its axial ratio characteristic rapidly degrades off resonance, especially for a singly fed patch or a dual-orthogonal fed patch with a nonisolated splitter. However, several techniques have been successfully employed for achieving wide-band circular polarization, including (1) utilization of a wide-band microstrip element and (2) sequentially rotated array configurations, both of which are discussed next.

8.6.1 Utilization of Wide-Band Microstrip Antennas

In a circularly polarized microstrip antenna, the narrow bandwidth arises mainly from the difficulty in maintaining the proper excitation conditions for polarization purity, which results in the rapid axial ratio degradation off resonance. The problem can be alleviated by employing a wide impedance bandwidth patch using a thick, low dielectric constant substrate. If conventional unbalanced dual-orthogonal feeds are used, this method frequently leads to higher order mode generation and unacceptable spurious feed radiation, which adversely affect the axial ratio performance. By employing four sequentially rotated feeds, the higher order modes and spurious feed radiation can be suppressed.

An example of a square patch with sequentially rotated feeds [27] is shown in Figure 8.24 where four mutually orthogonal feeds with 0°, 90°, 180°, and 270° phase differentials are used to excite the dominant TM_{010} and TM_{100} modes. Because each pair of feeds on the same axis is 180° out of phase, the undesired TM_{020} and TM_{200} modes and feed radiation are suppressed

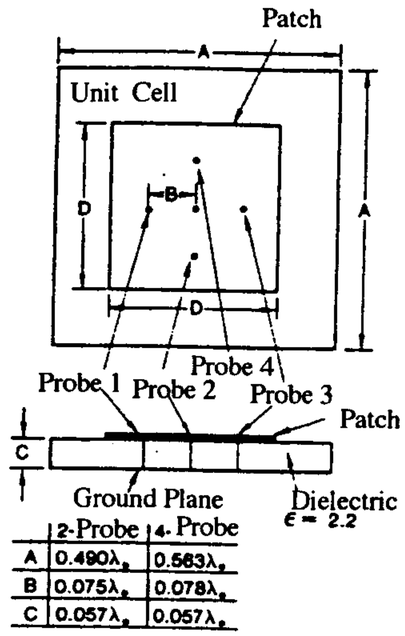

	2-Probe	4-Probe
A	0.490λ₀	0.563λ₀
B	0.075λ₀	0.078λ₀
C	0.057λ₀	0.057λ₀

Figure 8.24 Configuration of a square patch with sequentially rotated feeds. (From [27]. © 1987 IEEE. Reprinted with permission.)

by this excitation arrangement. The comparison of the boresight axial ratio performance using the unbalanced two feeds and the balanced four feeds is shown in Figure 8.25.

8.6.2 Sequentially Rotated Arrays

Sequentially rotating each patch element together with an appropriate offset in the feed excitation phase has been demonstrated to significantly enhance the bandwidth and the polarization purity [28, 29] of an array of CP patches.

Basic Operation

The technique [28] of sequentially rotated microstrip patch feeding requires that the mth patch have both a physical rotation ϕ_{pm} and a feeding phase shift ϕ_{em} as shown in Figure 8.26. If the radiation characteristic of each element has an angular periodicity of $2\pi/n$ in the ϕ direction of the spherical coordinate, then

$$\phi_{em} = (m-1)\frac{p\pi}{M}$$
$$\phi_{pm} = (m-1)\frac{p\pi}{nM} \tag{8.36}$$

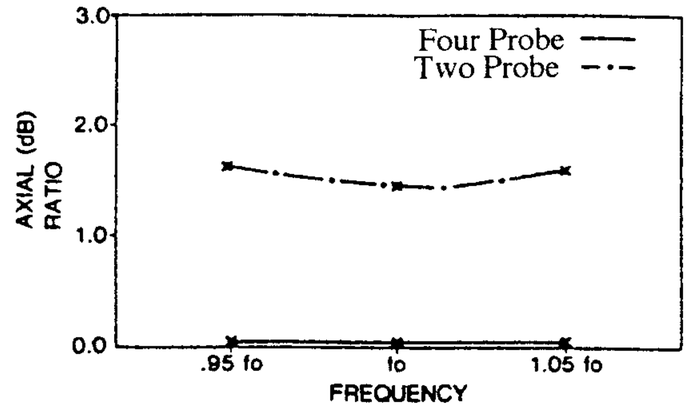

Figure 8.25 Axial ratio at boresight of the two and four probe-fed patches versus frequency. (From [27]. © 1987 IEEE. Reprinted with permission.)

where p is an integer, $1 \leq m \leq M$, and M is the total number of radiating elements. For a microstrip antenna, n represents the mode number, which is equal to 1 for the fundamental mode. Figures 8.26(c) and (d) are examples of typical arrays with sequential rotation. In Figure 8.26(c), one pair of patches rotates 90° with respect to the other pair, hence, $M = 2$ and $p = 1$. In another example, shown in Figure 8.26(d), $M = 4$ and $p = 2$ since rotation is applied to all four elements. Examples of a feeding arrangement in sequential rotation are given in Figure 8.26(e) for $M = 2$ and $p = 1$, in Figure 8.26(f) for $M = 3$ and $p = 2$, and in Figure 8.26(g) for $M = 4$ and $p = 2$.

The total radiated fields of a sequentially rotated array can be written as

$$\mathbf{E}_t(\theta, \phi) = \sum_{m=1}^{M} \mathbf{E}_m(\theta, \phi) \tag{8.37}$$

where $\mathbf{E}_m$ is the radiated field of the mth element. For a linear array shown in Figure 8.27 in the $\phi = 0$ plane, the total field $\mathbf{E}_t(\theta, 0)$ is given by

$$\begin{aligned}\mathbf{E}_t(\theta, 0) &= \sum_{m=1}^{M} \mathbf{E}_m(\theta, 0) \\ &= \sum_{m=1}^{M} \{[a(\theta, 0)\cos n\phi_{pm} - jb(\theta, 0)\sin n\phi_{pm}]\hat{\theta} \\ &\quad + [a(\theta, 0)\sin n\phi_{pm} + jb(\theta, 0)\cos n\phi_{pm}]\hat{\phi}\}e^{j(\phi_{em}-\psi_m)}\end{aligned} \tag{8.38}$$

where $\psi_m = (m-1)k_0 d\sin\theta$. In (8.38), it is assumed that the radiated field from the first element is elliptically polarized and expressed by

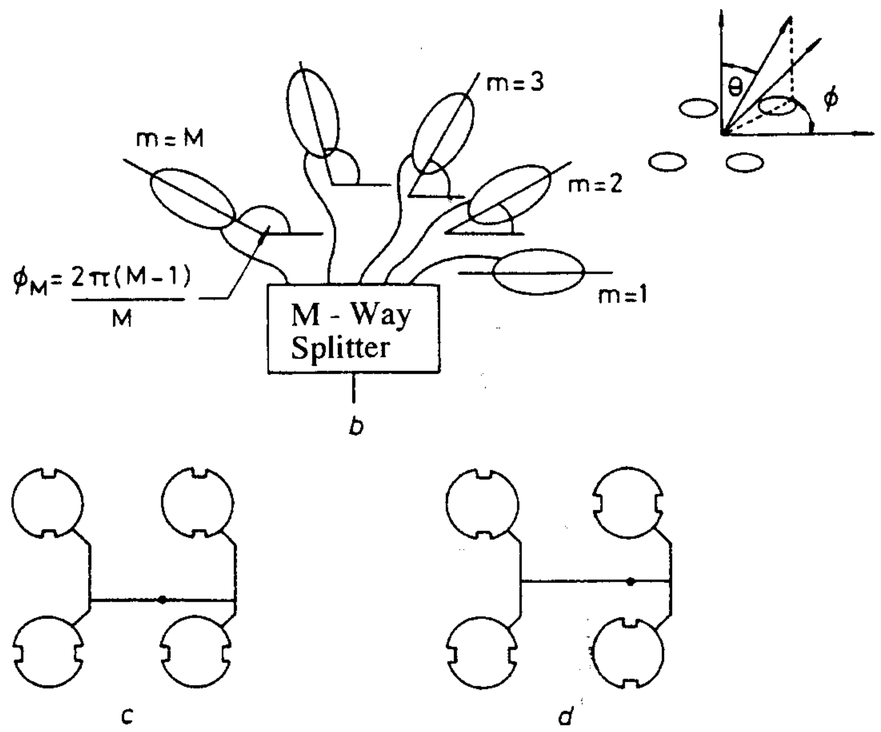

Figure 8.26 Configurations of sequentially rotated microstrip patch feeding. (From [28]. © 1989 IEE. Reprinted with permission.)

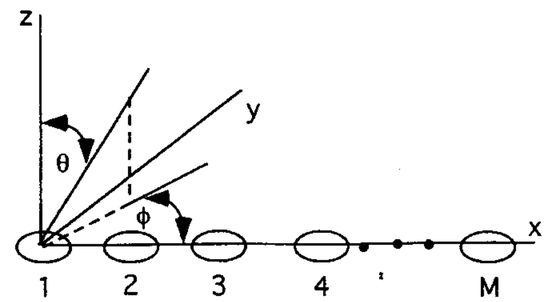

Figure 8.27 Configuration of a linear array with sequential feeding.

$$\mathbf{E}_1(\theta, 0) = a(\theta, 0)\hat{\theta} + jb(\theta, 0)\hat{\phi} \tag{8.39}$$

On the boresight ($\phi = 0$), (8.38) reduces to

$$\mathbf{E}_t(0, 0) \tag{8.40}$$
$$= \frac{M}{2}(a + b)(\hat{\theta} + j\hat{\phi}) + \frac{1}{2}(a - b)(\hat{\theta} - j\hat{\phi})\frac{\sin p\pi}{\sin\dfrac{p\pi}{M}}\exp\left[j\left(\frac{(M-1)p\pi}{M}\right)\right]$$

where $a = a(0, 0)$, $b = b(0, 0)$. It is noted that $\mathbf{E}_t(0, 0)$ is independent of n and the element position. When p is chosen to be smaller than M such that $0 < p < M$, (8.40) reduces to

$$\mathbf{E}_t(0, 0) = \frac{M}{2}(a + b)(\hat{\theta} + j\hat{\phi}) \tag{8.41}$$

which shows that the array radiates a perfect circularly polarized wave in the boresight direction regardless of the polarization of the element. If a feeding phase shift ϕ_{em} in (8.36) is replaced by $\phi_{em} = -(m - 1)p\pi/M$ in (8.38), in this case (8.40) becomes

$$\mathbf{E}_t(0, 0) \tag{8.42}$$
$$= \frac{M}{2}(a - b)(\hat{\theta} - j\hat{\phi}) + \frac{1}{2}(a + b)(\hat{\theta} + j\hat{\phi})\frac{\sin p\pi}{\sin\dfrac{p\pi}{M}}\exp\left[-j\left(\frac{(M-1)p\pi}{M}\right)\right]$$

which shows that the array radiates a perfect CP of the opposite sense for $0 < p < M$.

A square array can be constructed by combining linear sequential arrays in a recurrent arrangement as illustrated in Figure 8.28. However, a more generalized configuration exists for a rectangular array as shown in Figure 8.29 whereby the orientation angle and the differential phase shift for the (m, n)th element is defined by

$$\phi_{mn} = {}_M\phi_m + {}_N\phi_n \tag{8.43}$$

where

$$\begin{aligned} {}_M\phi_n &= (m - 1)\pi/M \\ {}_N\phi_n &= (n - 1)\pi/N \end{aligned} \tag{8.44}$$

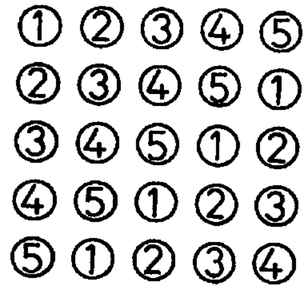

Figure 8.28 Square array using recurrent arrangement of linear sequential arrays. (From [17]. © 1989 Peter Peregrinus. Reprinted with permission.)

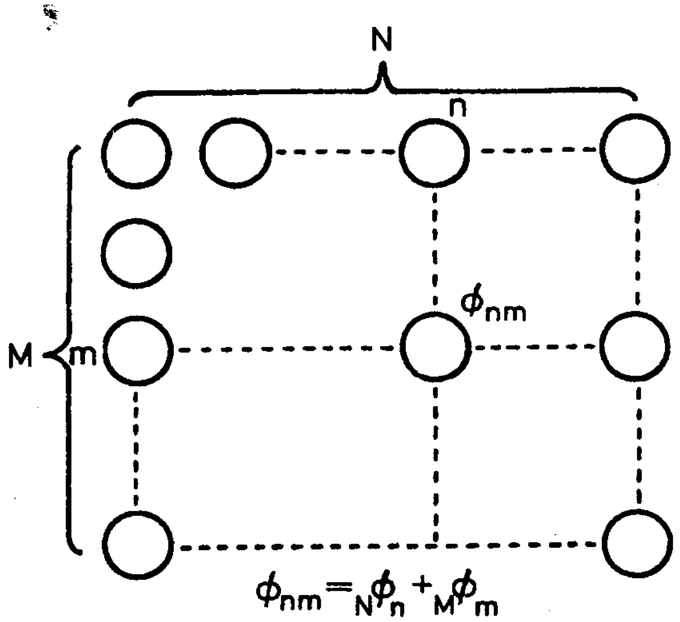

Figure 8.29 Generalized configuration of rectangular sequential array. (From [17]. © 1989 Peter Peregrinus. Reprinted with permission.)

Note that substantial performance improvement of a single patch can also be achieved by the use of multiple feeds arranged sequentially, provided the feeders are isolated from one another. Estimated performance of a patch with sequentially rotated feeds is summarized in Table 8.2 [3].

Table 8.2
Estimated Performance of Sequentially Fed Disk Antennas

Sequential Rotation Arrangement		Feeding Configuration	Cross-Polar Due to Multiple Reflections	Cross-Polar Due to Feed Phase Errors	Cross-Polar Due to Higher Order Modes
M	*p*				
2	1		Moderate	Moderate	High
3	1		Zero	Low	High
3	2		Zero	High	Low
4	1		Zero	Very low	Very high
4	2		High	Moderate	Very low

References

[1] Balanis, C. A., *Antenna Theory Analysis and Design*, John Wiley & Sons, New York, 1997.

[2] Stutzman, W. L., and G. A. Thiele, *Antenna Theory and Design*, John Wiley & Sons, New York, 1981.

[3] Hall, P. S., and J. S. Dahele, "Dual and Circularly Polarized Microstrip Antennas," in *Advances in Microstrip and Printed Antennas*, K. F. Lee and W. Chen (Eds.), John Wiley & Sons, New York, 1997.

[4] Haneishi, M., and Y. Suzuki, "Circular Polarization and Bandwidth," in *Handbook of Microstrip Antennas*, Vol. 1, J. R. James and P. S. Hall (Eds.), Peter Peregrinus, London, UK, 1989.

[5] Suzuki, Y., N. Miyano, and T. Chiba, "Circularly Polarized Radiation From Singly Fed Equilateral-Triangular Microstrip Antenna," in *Microstrip Antenna Design*, K. C. Gupta and A. Benalla (Eds.), Artech House, Norwood, MA, 1988, pp. 338–342.

[6] Tsang, K. K., and R. J. Langley, "Design of Circular Patch Antennas on Ferrite Substrates," *IEE Proc. Microwave Antennas Propagation*, Vol. 145, No. 1, 1998, pp. 49–55.

[7] Shen, L. C., "The Elliptical Microstrip Antenna With Circular Polarization," *IEEE Trans. Antennas and Propagation*, Vol. AP-29, 1981, pp. 90–94.

[8] Long, S. A., et al., "An Experimental Study of the Circular-Polarized Elliptical Printed-Circuit Antenna," *IEEE Trans. Antennas and Propagation*, Vol. AP-29, 1981, pp. 95–99.

[9] Pozar, D. M., *Microwave Engineering*, John Wiley & Sons, New York, 1998.

[10] Haneishi, M., and S. Yoshida, "A Design Method of Circularly Polarized Rectangular Microstrip Antenna by One-Point Feed," in *Microstrip Antenna Design*, K. C. Gupta and A. Benalla (Eds.), Artech House, Norwood, MA, 1988, pp. 313–321.

[11] Pozar, D. M., "Radiation and Scattering Characteristics of Microstrip Antennas on Normally Biased Ferrite Substrates," *IEEE Trans. Antennas and Propagation*, Vol. AP-40, 1992, pp. 1084–1092.

[12] James, J. R., P. S. Hall, and C. Wood, *Microstrip Antenna: Theory and Design*, Peter Peregrinus, London, UK, 1981.

[13] Huang, J., "A Technique for an Array To Generate Circular Polarization With Linearly Polarized Elements," *IEEE Trans. Antennas and Propagation*, Vol. AP-34, 1986, pp. 1113–1124.

[14] Wood, C., "Curved Microstrip Lines as Compact Wideband Circularly Polarised Antennas," in *Microstrip Antenna Design*, K. C. Gupta and A. Benalla (Eds.), Artech House, Norwood, MA, 1988, pp. 304–312.

[15] Wood, C., P. S. Hall, and J. R. James, "Design of Wideband Circularly Polarised Microstrip Antennas and Arrays," *Int. Conf. on Antennas and Propagation*, 1978, pp. 312–316.

[16] Wang, J. J. H., and V. K. Tripp, "Design of Multioctave Spiral-Mode Microstrip Antennas," *IEEE Trans. Antennas and Propagation*, Vol. AP-39, 1991, pp. 332–335.

[17] Ito, K., T. Teshirogi, and S. Nishimura, "Circularly Polarised Antenna Arrays," in *Handbook of Microstrip Antennas*, Vol. 1, J. R. James and P. S. Hall (Eds.), Peter Peregrinus, London, UK, 1989.

[18] Hall, P. S., "Microstrip Linear Array With Polarisation Control," *IEE Proc.*, Vol. 130, Pt. H, 1983, pp. 215–224.

[19] Henriksson, J., K. Markus, and M. Tiuri, "A Circularly Polarised Traveling-Wave Chain Antenna," *Proc. 9th European Microwave Conf.*, Microwave Exhibitions and Publishers, England, 1979, pp. 174–178.

[20] Nishimura, S., Y. Sugio, and T. Makimoto, "Crank-Type Circularly Polarized Microstrip Line Antenna," *IEEE AP-S Int. Symp. Antennas Propagation*, 1983, pp. 162–165.

[21] Cairo, L., and T. Kahan, *Variational Techniques in Electromagnetism*, Blackie and Son, London, UK, 1965.

[22] Argence, E., and T. Kahan, *Theory of Waveguides and Cavity Resonator*, Hart Publishing Company, New York, 1968.

[23] Collin, R. E., *Foundations for Microwave Engineering*, McGraw-Hill, New York, 1966.

[24] Haneishi, M., T. Nambara, and S. Yoshida, "Study on Ellipticity Properties of Single-Feed-Type Circularly Polarized Microstrip Antennas," *Electron. Lett.*, Vol. 18, No. 5, 1982, pp. 191–193.

[25] Owens, R. P., "Microstrip Antenna Feeds," in *Handbook of Microstrip Antennas*, Vol. 2, J. R. James and P. S. Hall (Eds.), Peter Peregrinus, London, UK, 1989.

[26] Parad, L. I., and R. L. Moynihan, "Split-Tee Power Divider," *IEEE Trans. on Microwave Theory and Techniques*, Vol. MTT-13, 1965, pp. 91–95.

[27] Bauer, R. L., and J. J. Schuss, "Axial Ratio of Balanced and Unbalanced Fed Circularly Polarized Patch Radiator Arrays," *IEEE AP-S Int. Symp. Antennas Propagation*, 1987, pp. 286–289.

[28] Hall, P. S., J. S. Dahele, and J. R. James, "Design Principles of Sequentially Fed, Wide Bandwidth, Circularly Polarised Microstrip Antennas," *IEE Proc.*, Vol. 136, Pt. H, 1989, pp. 381–389.

[29] Hall, P. S., "Applications of Sequentially Feeding to Wide Bandwidth, Circularly Polarised Microstrip Patch Arrays," *IEE Proc.*, Vol. 136, Pt. H, 1989, pp. 390–398.

9

Broadbanding of Microstrip Antennas

9.1 Introduction

Microstrip antennas have a number of useful properties, but one of the serious limitations of these antennas has been their narrow bandwidth characteristic. The impedance bandwidth of a typical microstrip patch antenna is less than 1% to several percent for thin substrates satisfying the criteria $h/\lambda_0 < 0.023$ for $\epsilon_r \approx 10$ to $h/\lambda_0 < 0.07$ for $\epsilon_r \approx 2.3$. This is in contrast to 15% to 50% bandwidth of commonly used antenna elements such as dipoles, slots, and waveguide horns. Researchers have been engaged in removing this limitation for the past 20 years, and have been successful in achieving an impedance bandwidth of up to 90% and gain bandwidth up to 70% in separate antennas. Most of these innovations utilize more than one mode, give rise to increase in size, height, or volume, and are accompanied by degradation of the other characteristics of the antenna. Increase in bandwidth can also be achieved by a suitable choice of feeding technique and impedance matching network.

A considerable amount of literature has appeared on the broadbanding aspect of microstrip antennas. Two excellent review articles [1, 2] and a book [3] have been published, in addition to numerous publications on this topic. Only some of these papers are cited here due to the limitation of space.

We begin by defining bandwidth. An antenna has a number of associated characteristics, such as input VSWR, beamwidth, sidelobe level, gain, polarization, and power handling capability. Each of these characteristics in turn can vary with frequency. If we specify a maximum or a minimum level for any of these, we end up with various definitions of bandwidth. For a microstrip patch antenna the radiation pattern is similar to that of a dipole. Therefore, pattern bandwidth, beamwidth, sidelobe level, and gain do not vary appreciably with

frequency, and are thus comparable to other types of antenna elements. The polarization bandwidth of a patch can be described either by specifying a maximum cross-polarization level for a linearly polarized element or by the maximum axial ratio level for a circularly polarized antenna element.

The input impedance of a patch antenna is found to vary faster with frequency, thus limiting the frequency range over which the element can be matched to its feed line. We will use the impedance bandwidth in the rest of the chapter to define the bandwidth of the patch antenna (although axial ratio bandwidth could still be lower for circularly polarized elements). The impedance bandwidth of a microstrip resonant antenna can be determined from the frequency response of its equivalent circuit. For a parallel-type resonance the half-power bandwidth (BW) is given as [4]

$$\text{BW} = \frac{2G}{\omega_0 \left.\dfrac{dB}{d\omega}\right|_{\omega_0}} \tag{9.1}$$

where $Y = G + jB$ is the input admittance at the resonant frequency ω_0. For a series-type resonance, as in a printed dipole, G is replaced by R and B is replaced by X in (9.1), where $Z = R + jX$ is the input impedance at resonance. Some researchers define impedance bandwidth in terms of VSWR = 2 bandwidth. The half-power bandwidth of (9.1) is equivalent to VSWR $\approx$ 2.4 bandwidth when the antenna is fed by a transmission line of characteristic impedance R [2]. Conversion of bandwidth from one value of VSWR to another can be done through the relation

$$\text{BW} = \frac{\text{VSWR} - 1}{Q\sqrt{\text{VSWR}}} \tag{9.2}$$

where Q is the quality factor of the patch antenna. Use of (9.2) shows that VSWR $\leq$ 2 bandwidth is about 78% of its half-power bandwidth. We should emphasize that the obtained impedance bandwidth does not necessarily mean that the bandwidth criterion for the other characteristics of the antenna is also satisfied. Recent studies show that cross-polarization is a major factor limiting the bandwidth of broadband microstrip antennas.

9.2 Effects of Substrate Parameters on Bandwidth

Impedance bandwidth of a patch antenna varies inversely as Q of the patch antenna [see (9.2)]. Therefore, substrate parameters such as dielectric constant

ϵ_r and thickness h can be varied to obtain different Q, and ultimately the increase in impedance bandwidth. Q of a resonator is defined as

$$Q = \frac{\text{Energy stored}}{\text{Power lost}} \tag{9.3}$$

Figure 9.1 shows the effect of substrate thickness on impedance bandwidth and efficiency for two values of dielectric constants [5]. Note that the bandwidth increases monotonically with thickness. Also, a decrease in the ϵ_r value increases the bandwidth. This behavior can be explained from the change in Q value.

Radiation Q of a rectangular patch antenna as a function of ϵ_r and h is plotted in Figures 9.2 and 9.3, respectively. Figure 9.2 shows that Q increases almost linearly with increase in ϵ_r. Modeling the rectangular patch as a lossy capacitor, the increase in Q is explained by the fact that the energy stored increases and the power radiated decreases with increase in ϵ_r. Similarly, when the substrate thickness is increased, the decrease in stored energy decreases the Q factor as shown in Figure 9.3. Physically, this behavior occurs because the fringing field increases with the increase in h and decrease in ϵ_r.

In conclusion, we can say that the increase in h and decrease in ϵ_r can be used to increase the impedance bandwidth of the antenna. However, this approach is useful up to $h < 0.02\lambda$ only. The disadvantages of using thick and high dielectric constant substrates are many, including these:

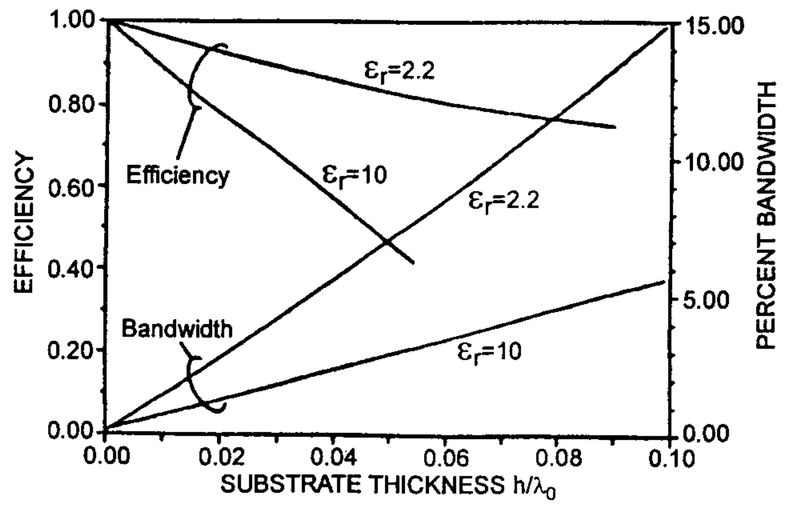

Figure 9.1 Effect of substrate thickness and dielectric constant on the impedance bandwidth (VSWR < 2) and radiation efficiency. (From [5]. © 1992 IEEE. Reprinted with permission.)

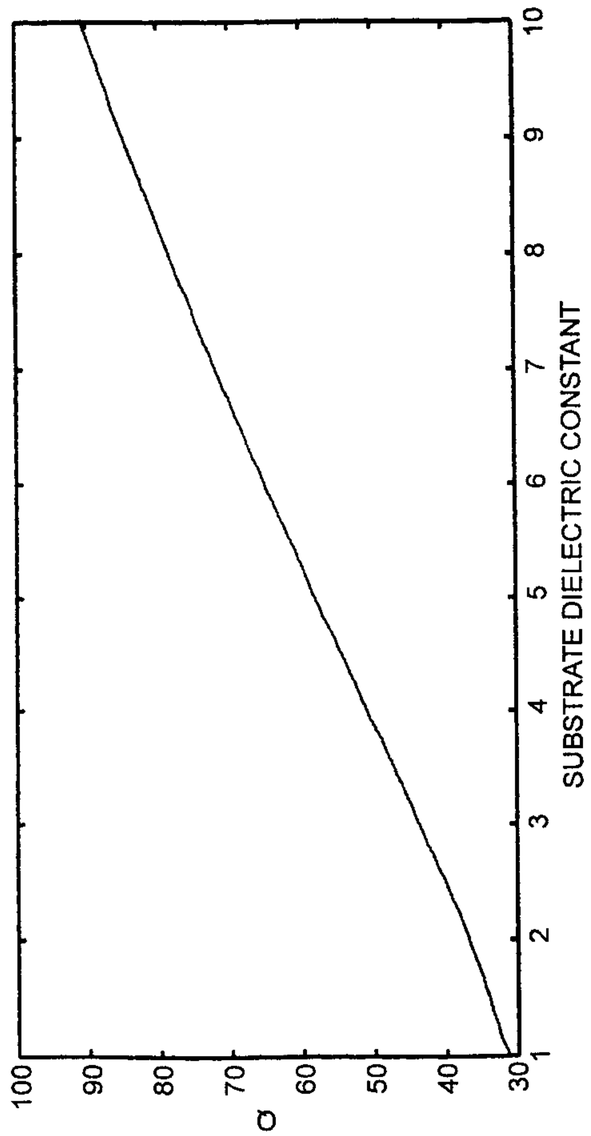

Figure 9.2 Variation of radiation Q for a rectangular patch antenna as a function of substrate dielectric constant; $h = 1.59$ mm, $W = 0.9L$, $f = 3$ GHz.

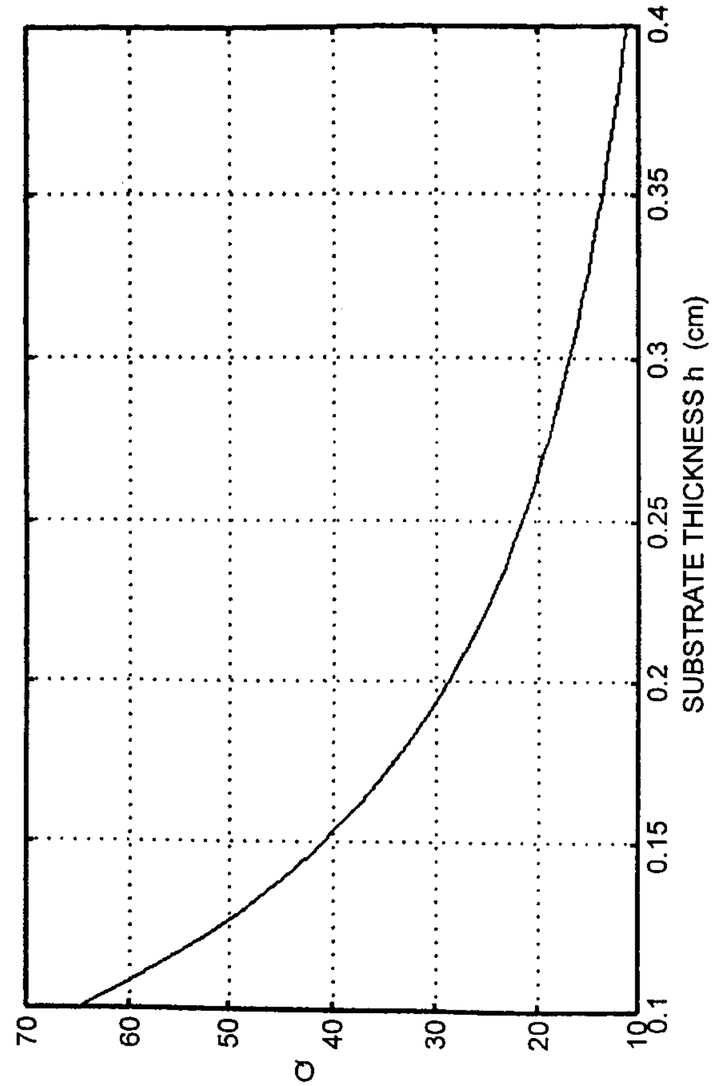

Figure 9.3 Variation of radiation Q for a rectangular patch antenna as a function of substrate thickness; $\epsilon_r = 2.2$, $W = 0.9L$, $f = 3$ GHz.

- Surface wave power increases, resulting in poor radiation efficiency (see Figure 9.1). The radiation from surface waves may lead to pattern degradation near end-fire.
- Thick substrates with microstrip edge feed will give rise to increased spurious radiation from the microstrip step-in-width and other discontinuities. Radiation from the probe feed will also increase.
- Substrates thicker than $0.11\lambda_0$ for $\epsilon_r = 2.2$ make the impedance locus of the probe-fed patch antenna increasingly inductive in nature, resulting in impedance matching problems [6].
- Higher order modes along the thickness may develop, giving rise to distortions in the radiation patterns and impedance characteristics. This is a limiting factor in achieving an octave bandwidth.

Most of the problems just listed are not experienced if thick air dielectric and aperture coupling of the antenna to the feed are used. Surface wave effects can be controlled by the use of photonic bandgap structures.

9.3 Selection of Suitable Patch Shape

It has been found that some of the patch shapes have inherently lower Q compared to others. Correspondingly, their bandwidth is higher. These patch shapes include annular ring, rectangular/square ring, quarter-wave (shorted) patch, and other geometries. A circular ring antenna with $b = 2a$ when operated in the TM_{12} mode is found to have more than five times the bandwidth of a rectangular patch antenna with $L = 1.5W$. Similarly, a rectangular/square ring antenna with an average circumference of one λ_g can be used.

Bandwidths of annular ring and shorted quarter-wave patch are compared with rectangular and circular patch geometries in Table 9.1. We can see from this table that the bandwidth of a rectangular patch increases with an increase in the patch width.

9.4 Selection of Suitable Feeding Technique

Of the various feeding techniques available (namely, probe feeding, edge feeding, proximity coupling to a microstrip line, and aperture coupling to a microstrip feed line), the aperture coupling method has been used in broadband antennas employing thick substrates. This is due to the fact that this feeding technique has a large number of adjustable parameters in the form of aperture

Table 9.1
Comparison of VSWR = 2 Bandwidth

Element Shape	Element Size	Bandwidth (%)
Narrow rectangular patch	$L = 4.924$ cm, $W = 2.0$ cm	0.7
Wide rectangular patch	$L = 4.79$ cm, $W = 7.2$ cm	1.6
Square patch	$L = W = 4.82$ cm	1.3
Circular disk	$a = 2.78$ cm	1.3
Annular ring	$b = 8.9$ cm, $a = 4.45$ cm	3.8
Quarter-wave patch	$L = 2.462$ cm, $W = 2.0$ cm	1.05

$\epsilon_r = 2.32$, $h = 1.59$ mm, $f = 2$ GHz. After [1, 7].

length, width, and shape, and stub parameters. The coupling aperture when used judiciously can give rise to a considerable increase in bandwidth. About 70% bandwidth has been realized using this feeding technique. The design of aperture-coupled antennas is discussed next.

9.4.1 Aperture-Coupled Microstrip Antennas

An exploded view of an aperture-coupled microstrip antenna is shown in Figure 9.4. It consists of a rectangular patch of dimensions $a \times b$ printed on a substrate of thickness h and dielectric constant ϵ_{ra}. The microstrip patch is fed by a microstrip line through an aperture or slot in the common ground plane of patch and microstrip feed as shown in the figure. The aperture is of dimensions $L_a \times W_a$ and centered at (x_0, y_0). The width of the microstrip line is W and is printed on a substrate described by t and ϵ_{rf}. The characteristic impedance of the microstrip line is denoted by Z_{0m} and that of the slot line by Z_{0s}. Coupling of the slot to the dominant mode of the patch and the microstrip line occurs because the slot interrupts the longitudinal current flow in them. The analysis of aperture-coupled microstrip antennas, for the most part, is similar to that of a microstrip fed slot antenna (see Section 7.2).

The aperture coupling feed was proposed by Pozar [8] and has many advantages over other types of feeds. These include shielding of antenna from spurious feed radiation, use of suitable substrates for feed structure and antenna, and use of thick substrate for increasing the antenna bandwidth. The antenna of Figure 9.4 has been analyzed using various techniques, including the integral equation approach [9–12], cavity model [13–15], transmission line model [16, 17], modal expansion method [18], and a hybrid approach [19]. The integral equation approach is the most accurate and was described in Chapter 3. Here we discuss the transmission line model and the modal expansion method because of their utility in arriving at a simpler design.

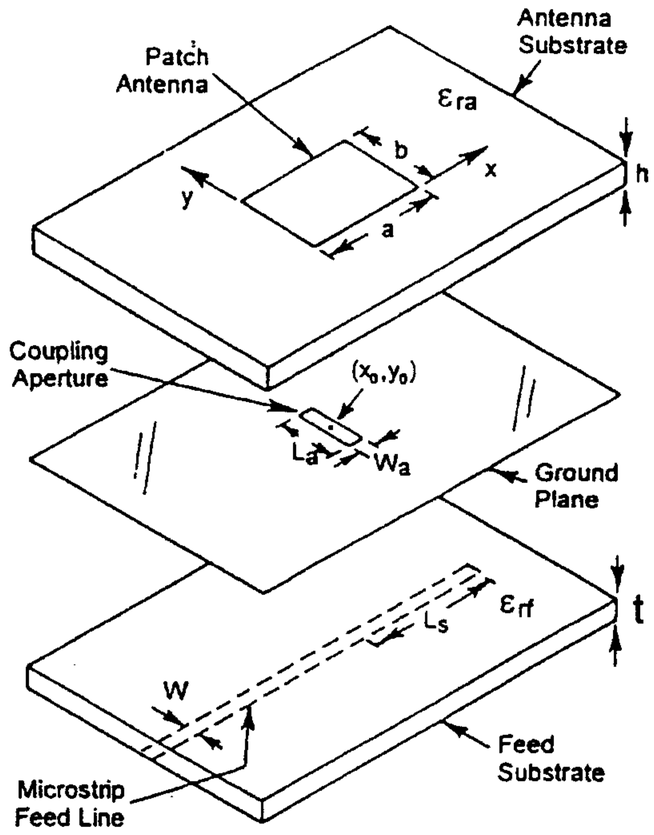

Figure 9.4 Exploded view of an aperture-coupled microstrip antenna.

9.4.2 Transmission Line Model of Aperture Coupling

A simplified equivalent circuit of an aperture-coupled microstrip antenna is shown in Figure 9.5 [16]. In this equivalent circuit, the patch is characterized by admittance Y_{patch} and the aperture by an admittance Y_{ap}.

The coupling of the patch to the aperture is described by an impedance transformer of turns ratio n_1 roughly equal to the fraction of patch current intercepted by the slot to the total patch current, that is, $n_1 = L_a/b$. The patch admittance is determined at the center of the slot and its value can be obtained from the simple transmission line model of Section 2.2. If Z_1 and Z_2 are the impedances looking toward the left and right of the aperture as shown in Figure 9.6, then

$$Z_{\text{patch}} = Z_1 + Z_2 = 1/Y_1 + 1/Y_2 \tag{9.4}$$

$$Y_1 = Y_0 \frac{(G_r + jB_{\text{open}}) + jY_0 \tan(\beta L_1)}{Y_0 + j(G_r + jB_{\text{open}}) \tan(\beta L_1)} \qquad L_1 = x_0 \tag{9.5}$$

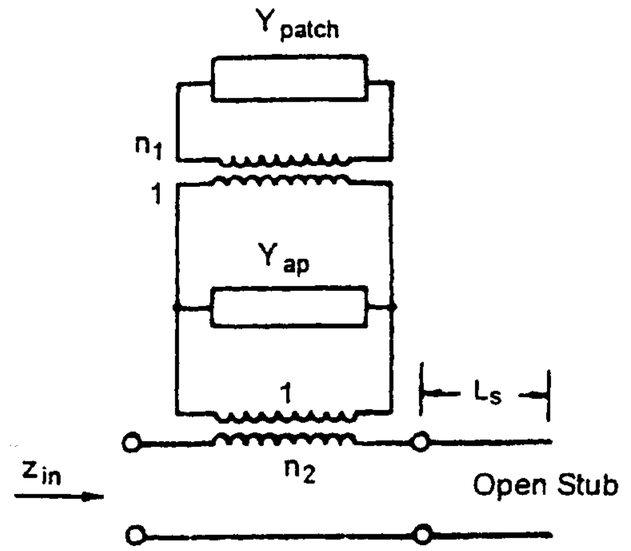

Figure 9.5 A simplified equivalent circuit of an aperture-coupled microstrip antenna. (From [16]. © 1989 *Electronics Letters*. Reprinted with permission.)

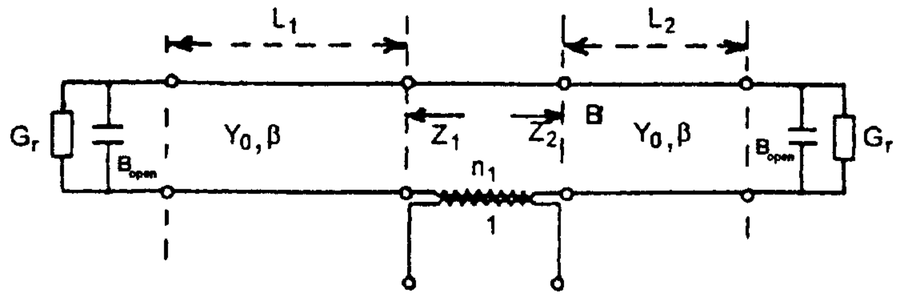

Figure 9.6 Transmission line equivalent circuit of a rectangular patch fed by a slot in the ground plane. (From [16]. © 1989 *Electronics Letters*. Reprinted with permission.)

$$Y_2 = Y_0 \frac{(G_r + jB_{\text{open}}) + jY_0 \tan(\beta L_2)}{Y_0 + j(G_r + jB_{\text{open}}) \tan(\beta L_2)} \qquad L_2 = a - L_1 \tag{9.6}$$

Here, (Y_0, β) characterizes the rectangular patch antenna as a microstrip line of width b, and $(G_r + jB_{\text{open}})$ is the edge admittance of the patch. The aperture susceptance Y_{ap} describes the energy stored near the slot. It is inductive in nature because the slot is electrically small. The value of Y_{ap} can again be obtained from the transmission line model of a shorted slot and is given by (neglecting the end effect)

$$Y_{\text{op}} = -j2Y_{0s} \cot(\beta_s L_a/2) \tag{9.7}$$

A transformer is used to describe the coupling of the patch to the microstrip feed line. The turns ratio n_2 of this transformer is calculated from the discontinuity ΔV in modal voltage of the feed microstrip line, that is, $n_2 = \Delta V / V_0$, where V_0 is the slot voltage. The expression for n_2 for finite and infinite slots is reported in [20]. For an infinite slot n_2 is given by

$$n_2 = \frac{J_0(\beta_s W/2) J_0(\beta_m W_a/2)}{\beta_s^2 + \beta_m^2} \left[\frac{\beta_m^2 k_2 \epsilon_{\text{rf}}}{k_2 \epsilon_{\text{rf}} \cos k_1 h - k_1 \sin k_1 h} + \frac{\beta_s^2 k_1}{k_1 \cos k_1 h + k_2 \sin k_1 h} \right] \tag{9.8}$$

where $J_0(\cdot)$ is the zeroth-order Bessel function and

$$k_1 = k_0 \sqrt{|\epsilon_{\text{rf}} - \epsilon_{\text{res}} - \epsilon_{\text{rem}}|} \tag{9.9}$$

$$k_2 = k_0 \sqrt{|\epsilon_{\text{res}} + \epsilon_{\text{rem}} - 1|} \tag{9.10}$$

$$\beta_s = k_0 \sqrt{\epsilon_{\text{res}}} \qquad \beta_m = k_0 \sqrt{\epsilon_{\text{rem}}} \tag{9.11}$$

Here, $(W, \epsilon_{\text{rem}}, \beta_m, Z_{0m})$ are the microstrip line parameters, and $(W_a, \epsilon_{\text{res}}, \beta_s, Y_{0s})$ are the slot line parameters. Taking into account the impedance of the microstrip open-circuited stub of length L_s, the input impedance of the antenna at the center of the slot is given by

$$Z_{\text{in}} = \frac{n_2^2}{n_1^2 Y_{\text{patch}} + Y_{\text{ap}}} - jZ_{0m} \cot(\beta_m L_s) \tag{9.12}$$

Setting $n_1^2 B_{\text{patch}} + B_{\text{ap}} = 0$ yields the following condition for resonance:

$$B_{\text{patch}} = \frac{-B_{\text{ap}}}{n_1^2} \approx \frac{4b^2}{Z_{0s} \beta_s L_a^3} \tag{9.13}$$

That is, increasing L_a requires a decrease in B_{patch} and the resonant frequency decreases.

The input impedance based on this simple transmission line model is compared in Figure 9.7 [16] with that of the cavity model [13] and the integral equation approach [9, 10]. The agreement has been found to be good except for a very small shift in resonant frequency. The variation of input impedance

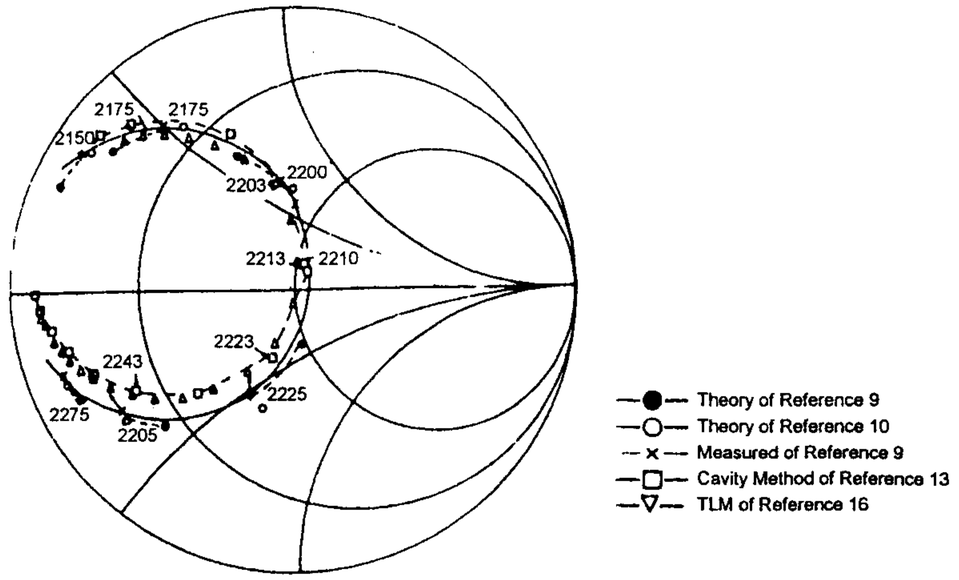

Figure 9.7 Input impedance of an aperture-coupled rectangular patch antenna as a function of frequency; a = 4.0 cm, b = 3.0 cm, ϵ_{ra} = 2.54, h = 0.16 cm, W_a = 0.155 cm, L_a = 1.12 cm, $x_0 = a/2$, $y_0 = b/2$, t = 0.16 cm, ϵ_{rf} = 2.54, W = 0.442 cm, L_s = 2.0 cm. (From [16]. © 1989 *Electronics Letters*. Reprinted with permission.)

with slot length is shown in Figure 9.8 [16]. Four different values of slot length have been used. This figure shows that when the slot length is small, the patch is undercoupled and the resonant resistance is less than the characteristic impedance of the feed line. As the slot length increases, the coupling, the resonant resistance, and the size of the loop increase. A similar behavior is observed when the antenna substrate thickness is decreased. Thus, a wide range of resistance and reactance values can be obtained by adjusting the aperture length. The antenna input reactance can also be adjusted by changing the stub length according to $-jZ_{0m} \cot(\beta_m L_s)$.

The transmission line model has been extended to include different shapes of coupling aperture [17]. Some of the aperture shapes shown in Figure 9.9 can be modeled easily by the transmission line model. In these apertures/slots only the transverse portion of the slot couples to the patch and line. The longitudinal portion of the slot is used to obtain nearly uniform field distribution in the transverse portion. The uniformity of the field increases coupling without an increase in back radiation. Other aperture shapes that give rise to improved coupling are also shown in Figure 9.9. These are dog-bone-shaped and hourglass-shaped apertures that simulate open end and thus maximum electric field at the ends of the aperture [21, Chapter 5].

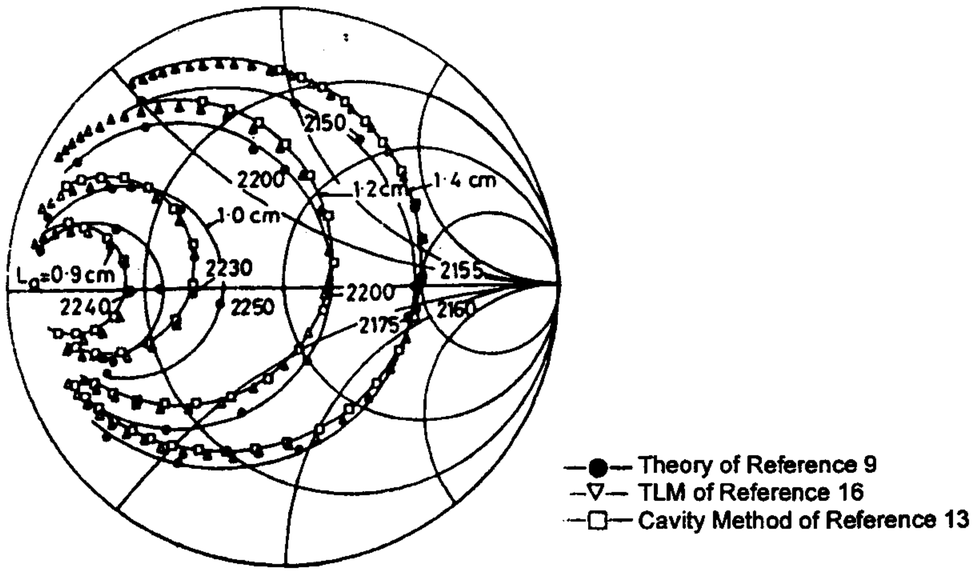

Figure 9.8 Variation of input impedance of an aperture-coupled microstrip antenna with slot length; a = 4.0 cm, b = 3.0 cm, ϵ_{ra} = 2.54, h = 0.16 cm, W_a = 0.155 cm, $x_0 = a/2$, $y_0 = b/2$, t = 0.16 cm, ϵ_{rf} = 2.54, W = 0.495 cm, L_s = 2.0 cm. (From [16]. © 1989 *Electronics Letters*. Reprinted with permission.)

The aperture admittance for different shapes can again be obtained from transmission line theory. For example, for the H-shaped aperture of Figure 9.9 one obtains [17]

$$Y_{ap} = j2Y_{0s}\frac{-\frac{Y_{0s}}{2}\cot(\beta_s L_h/2) + Y_{0s}\tan(\beta_s L_a/2)}{Y_{0s} + \frac{Y_{0s}}{2}\cot(\beta_s L_h/2)\tan(\beta_s L_a/2)} \tag{9.14}$$

Here, L_h and L_a are the lengths of the longitudinal and transverse portions of the H-shaped slot.

The transmission line model is useful when only the dominant mode contribution of the patch is sufficient, which is true for thin substrates. For thick substrates, the effect of higher order modes in the patch and the aperture must be included for improved accuracy. The modal expansion model discussed next considers higher order modes also.

9.4.3 Modal Expansion Model of Aperture Coupling

In the modal expansion model [18] of aperture coupling, the patch is modeled as a cavity, the microstrip line as a planar waveguide, and the coupling between

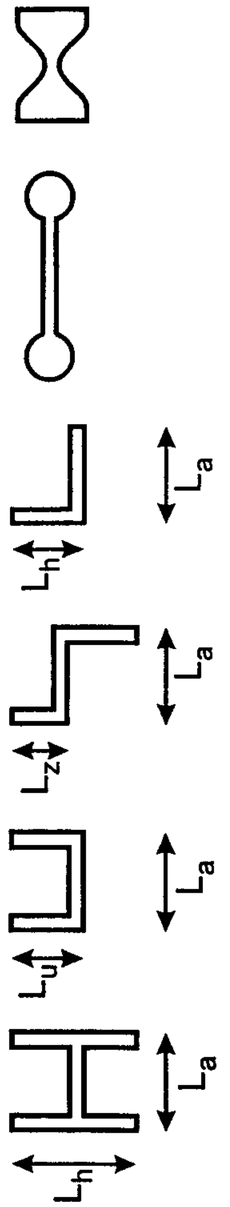

Figure 9.9 Various aperture shapes used in aperture-coupled microstrip antennas.

them is via a magnetic current on the aperture. This model is useful in arriving at an improved equivalent circuit of the structure and the design charts. The cavity model is discussed in Chapter 2 and the planar waveguide model is discussed in Appendix B.

The equivalent circuit of the aperture-coupled microstrip antenna based on this model is shown in Figure 9.10 [18]. It consists of two admittances (referred to the slot center) representing various radiation mechanisms and a transformer representing the coupling between the feed line and the aperture. The turns ratio n of the transformer determines the amount of antenna impedance coupled in series to the microstrip line. Here, Z_L is the open-circuited stub impedance at the slot center, Y_a is the antenna admittance, and Y_e is the admittance of the coupling slot.

The microstrip antenna is modeled as a series load Z_s in the feed line. From the equivalent circuit of Figure 9.10 one obtains

$$Z_{\text{in}} = Z_L + Z_s \tag{9.15}$$

where

$$Y_s = Y_e + Y_a/n^2 \tag{9.16}$$

The turns ratio n is given by n_2 of (9.8), that is,

$$n = n_2 \tag{9.17}$$

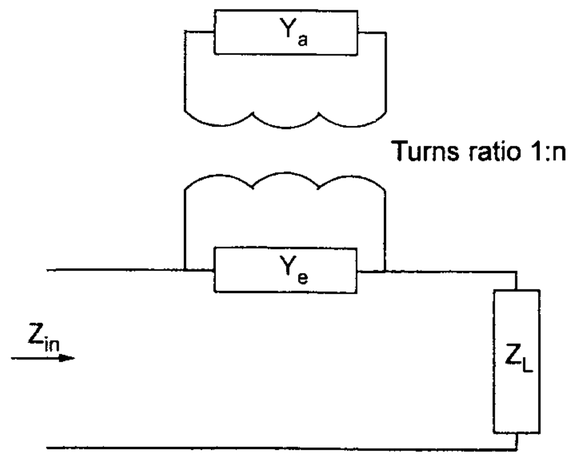

Figure 9.10 An improved equivalent circuit for the aperture-coupled microstrip antenna. (From [18]. © 1991 IEEE. Reprinted with permission.)

and

$$Z_L = -jZ_{0m}\cot\beta_m(L_s + \Delta) + R_r, \quad \beta_m = 2\pi\sqrt{\epsilon_{rfe}}/\lambda_0 \tag{9.18}$$

where L_s is the stub length, Δ is the open-end extension, and R_r is the radiation resistance of the open end. The value of Δ is defined in (B.71) and $R_r = 1/G$ is obtained from (2.77). Z_{0m}, β_m, and ϵ_{rfe} characterize the microstrip line of the stub. The antenna or patch admittance is obtained as [18]

$$Y_a = \frac{1}{j\omega\mu}\frac{2W_a^2}{a_e b_e}\left[\frac{\omega^2\alpha_0^2}{2h}\sin^2\left(\frac{\pi x_0}{a_e}\right)\left\{\frac{1}{\omega_{01}'(\omega-\omega_{01}')} - \frac{1}{2\omega_{01}'^2}\right\}\right.$$
$$\left. + \sum_{m,n}{}' \frac{k_0^2\epsilon_{rae} - (m\pi/b_e)^2}{\delta_m}\sin^2\left(\frac{n\pi x_0}{a_e}\right)\frac{\alpha_m^2\cos(k_z h)}{k_z\sin(k_z h)}\right] \tag{9.19}$$
$$m = 0, 1, 2, \ldots \quad n = 1, 2, 3, \ldots$$

$$\omega_{01}' = \omega_{01}\left(1 + \frac{j}{2Q}\right) \tag{9.20}$$

$$\omega_{01} = \frac{c\pi}{a_e\sqrt{\epsilon_{rae}}}, \quad c = 3\times 10^8 \text{ m/s} \tag{9.21}$$

Σ' denotes that the $m = 0$, $n = 1$ term is excluded. The effective dimensions of the rectangular patch are denoted by a_e and b_e (see Chapter 4), and ϵ_{rae} is the effective dielectric constant of the antenna substrate (see Appendix B). Q is the total quality factor of the patch antenna. Also,

$$k_z^2 = k_0^2\epsilon_{rae} - (m\pi/b_e)^2 - (n\pi/a_e)^2 \tag{9.22}$$

$$\delta_m = \begin{cases} 1 & \text{for } m = 0 \\ \dfrac{1}{2} & \text{for } m \geq 1 \end{cases} \tag{9.23}$$

In this antenna, magnetic current of the aperture is assumed to couple to the magnetic field of the patch and the coupling coefficient is given by

$$\alpha_m = \int_0^{b_e} f(y)\cos(m\pi y/b_e)\,dy \tag{9.24}$$

$$f(y) = \begin{cases} \dfrac{1}{W_a} & \text{for } y_0 - \dfrac{W_e}{2} \le y \le y_0 + \dfrac{W_e}{2} \\ \dfrac{1}{W_a}\dfrac{\sin[k_s(L_a/2 - |y - y_0|)]}{\sin[k_s(L_a - W_e)/2]} & \text{for } \dfrac{W_e}{2} \le |y - y_0| \le \dfrac{L_a}{2} \end{cases} \tag{9.25}$$

$$k_s = k_0\sqrt{\frac{\epsilon_{ra} + \epsilon_{rf}}{2}} \tag{9.26}$$

The aperture admittance Y_e, as seen by the feed, is obtained as

$$Y_e = \frac{1}{2}\sum_{p,n}{}' Y_{pn}\frac{\left[\displaystyle\int_{S_a} f(y)\psi_{pn}\,dx\,dy\right]^2}{\displaystyle\int_S \psi_{pn}^2\,dy\,dz} \qquad p = 0 \quad n = 0 \text{ term excluded} \tag{9.27}$$

where s is the cross-sectional area of the planar waveguide model of the microstrip line ($W_e \times h$) and S_a represents the aperture ($L_a \times W_a$). Also, with reference to the coordinate system of Figure 9.4, the field distribution in the planar waveguide model of the microstrip line is described as

$$\psi_{pn} = \cos\left[\frac{p\pi}{t}(z + h + t)\right]\cos\left[\frac{n\pi}{W_e}(y - y_0 + W_e/2)\right] \tag{9.28}$$

$$Y_{pn} = j\frac{k_0^2\epsilon_{rfe} - (n\pi/W_e)^2}{\omega\mu\alpha_{pn}} \tag{9.29}$$

$$\alpha_{pn}^2 = (p\pi/t)^2 + (n\pi/W_e)^2 - k_0^2\epsilon_{rfe} \tag{9.30}$$

where ϵ_{rfe} is the effective permittivity of the microstrip line. The input impedance of an aperture-coupled rectangular patch antenna is shown in Figure 9.11 [18]. The results based on the modal expansion model show good agreement with those obtained from the integral equation approach of [9]. A small shift in the resonant frequency of about 0.9% is observed [18]. The measured front-to-back ratio was −15 dB maximum in the E-plane and −20 dB in the H-plane patterns.

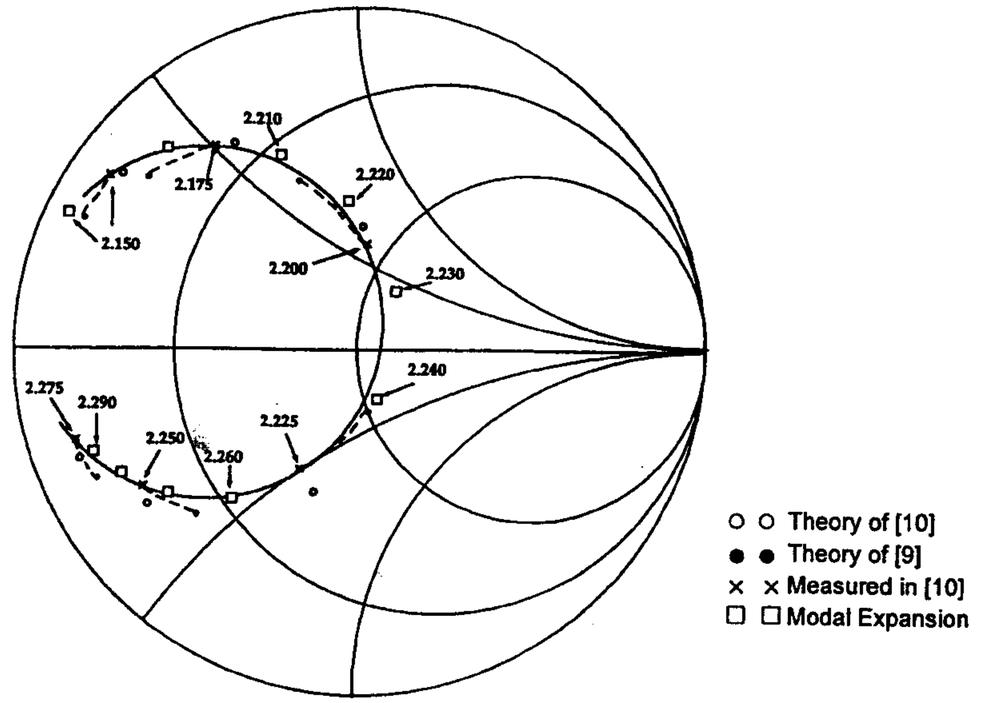

Figure 9.11 Input impedance of an aperture-coupled rectangular patch antenna as a function of frequency. The antenna parameters are the same as in Figure 9.7. (From [18]. © 1991 IEEE. Reprinted with permission.)

Of all the parameters, the effect of aperture length has been studied most carefully. Design curves for the resonant frequency and resonant resistance as a function of slot length are plotted in Figures 9.12 and 9.13 for the resonant frequencies in the vicinity of 5 and 10 GHz, respectively [18]. Antenna substrate thickness h and patch width b are used as parameters in these figures. Note that resonant resistance always increases with the increase in slot length and decrease in antenna substrate thickness, implying that coupling of the patch to the feed line increases. This trend is similar to that observed in Figure 9.8. The resonant frequency, on the other hand, decreases with the increase in coupling because of the loading effect produced by the aperture. Also, a decrease in resonant resistance can always be obtained by increasing the patch width.

Aperture-coupled patch elements retain many of the desirable features of conventional patch elements but with greatly increased bandwidth [22]. The impedance locus of this antenna is that of a parallel R-L-C circuit resonance with a single loop. However, when the slot length reaches resonance, the impedance locus changes to that of a series type resonance. The series resonance behavior is shown in Figure 9.14 for four different slot locations [23]. This behavior is explained in [24] and is similar to that of a center-fed dipole

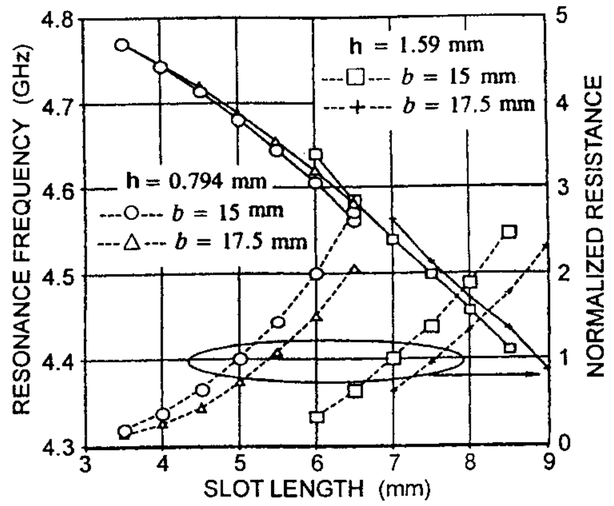

Figure 9.12 Resonant frequency and normalized resonant resistance as a function of slot length; a = 2.0 cm, ϵ_{ra} = 2.33, W_a = 1.16 mm, $x_0 = a/2$, $y_0 = b/2$, t = 0.635 mm, ϵ_{rf} = 9.8, L_s = 5.63 mm. (From [18]. © 1991 IEEE. Reprinted with permission.)

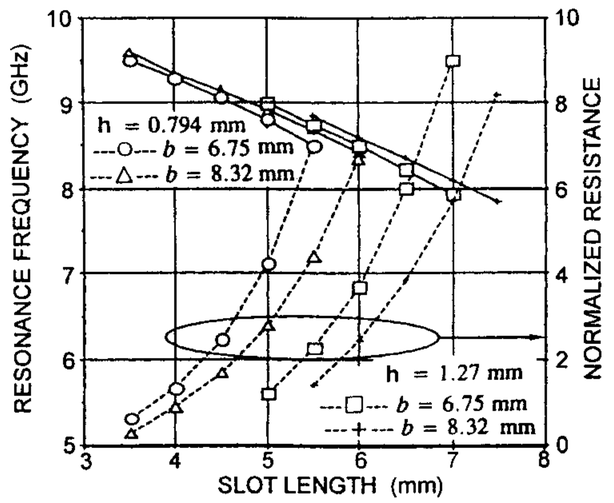

Figure 9.13 Resonant frequency and normalized resonant resistance as a function of slot length; a = 9.5 mm, ϵ_{ra} = 2.33, W_a = 0.58 mm, $x_0 = a/2$, $y_0 = b/2$, t = 0.635 mm, ϵ_{rf} = 9.8, L_s = 2.72 mm. (From [18]. © 1991 IEEE. Reprinted with permission.)

discussed in Chapter 6. If properly designed, the patch and slot resonances can be coupled to produce mutual resonance and a wide bandwidth as shown in Figure 9.15 [25]. In this case, the overcoupled resonance (at the higher frequency) is that of the aperture and the low-Q resonance (at the lower frequency) is that of the patch. An optimized bandwidth of 22% (VSWR < 1.5) has been

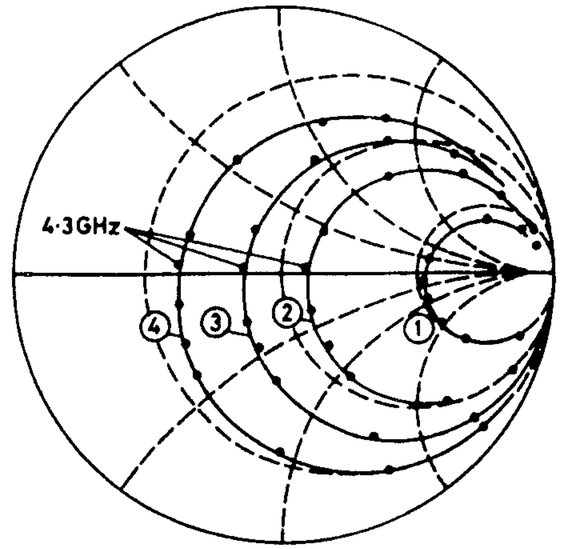

Figure 9.14 Computed input impedance of an aperture-coupled microstrip antenna as a function of frequency. The aperture is near resonant; a = 28 mm, b = 30 mm, h = 3.15 mm, ϵ_{ra} = 1, W_a = 1 mm, L_a = 26.5 mm, y_0 = 15 mm, t = 0.635 mm, ϵ_{rf} = 6, Z_0 = 50Ω, L_s = 8 mm; radome parameters: ϵ_r = 2.2, thickness = 1.575 mm; 1: x_0 = 0 mm, 2: x_0 = 3 mm, 3: x_0 = 5 mm, 4: x_0 = 8 mm. (From [23]. © 1986 *Electronics Letters*. Reprinted with permission.)

reported. The maximum cross-polar radiation in the diagonal planes for this antenna is found to be −15 dB and the maximum front-to-back ratio is −14 dB in the E plane. The poor front-to-back ratio of this antenna is because of back radiation from the large aperture used. This ratio can be improved if a stripline-like feed is used [26]. Alternatively, a grounded coplanar waveguide (CPW) can be employed. It has been reported that a channelized CPW when aperture coupled to a patch antenna can improve the bandwidth as well as the front-to-back ratio [27].

A higher bandwidth, with low back radiation, can also be achieved by using stacked patches and a nonresonant aperture. The stacked patch antenna is described next.

9.5 Multimoding Techniques

The use of a number of resonant modes is a very successful approach in the design of broadband microstrip antennas. The basic idea underlying this approach has been borrowed from the coupled resonators in which two or more resonators are stagger-tuned to cover the frequency range of interest.

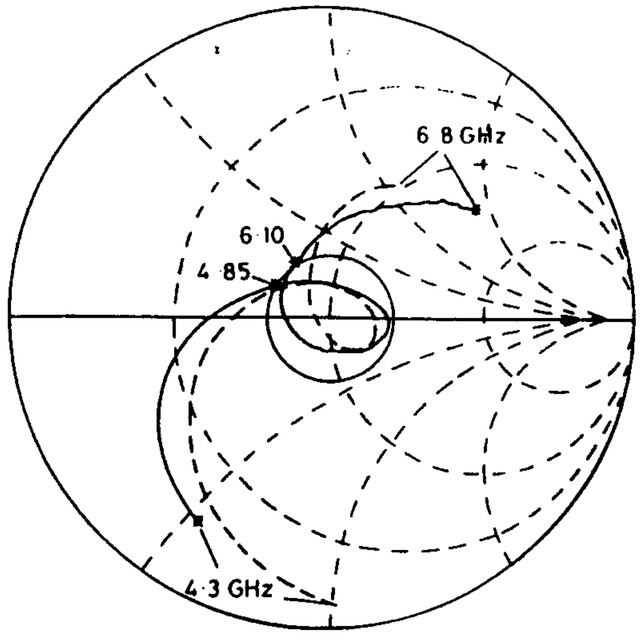

Figure 9.15 Comparison of computed and measured input impedance of an aperture-coupled microstrip antenna as a function of frequency. The aperture is near resonant; $a = b = 17$ mm, $h = 5.5$ mm, $\epsilon_{ra} = 1.01$, $W_a = 0.8$ mm, $L_a = 15.4$ mm, $t = 0.762$ mm, $\epsilon_{rf} = 2.2$, $\tan\delta = 0.001$, $W = 2.32$ mm, $L_s = 2.85$ mm; radome parameters: $\epsilon_r = 2.2$, thickness = 1.6 mm, $\tan\delta = 0.001$; ----, computed; ____, measured. (From [25]. © 1990 *Electronics Letters*. Reprinted with permission.)

This approach has been applied to various shapes of microstrip antennas. It is also possible to employ this concept in a variety of ways to increase the impedance bandwidth. Some of the implementations of this concept employ two or more resonant elements, with slightly different resonant frequencies, proximity coupled to each other. Coupling is controlled to increase the bandwidth. The impedance locus of such multiple resonant antennas consists of two or more closely spaced closed loops.

Some of the most common implementations of broadbanding through parasitic coupling are described next.

9.5.1 Broadbanding Using Stacked Elements

The exploded view of a typical stacked patch microstrip antenna is shown in Figure 9.16. The effect of stacking of patches was first studied in 1978 [28] soon after the initial studies on microstrip antennas. Unlike the aperture-coupled configuration shown in the figure, the bottom patch can be fed by a coaxial probe [29, 30] or by a microstrip line. The upper patch is proximity

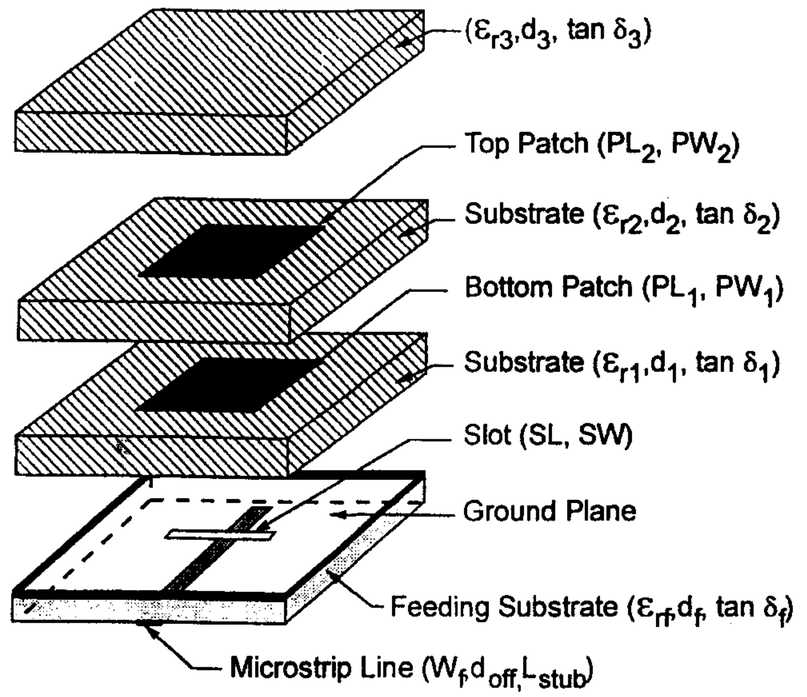

Figure 9.16 Exploded view of a typical aperture-coupled stacked patch microstrip antenna.

coupled to the excited bottom patch. The size of the upper patch is slightly different from that of the lower patch to obtain a slightly different resonant frequency.

A number of variables are used in the dual-patch configuration, for example, substrate thicknesses d_1 and d_2; dielectric constants ϵ_{r1} and ϵ_{r2}; offsets between the centers of patches; patch sizes; and feed location. These variables can be adjusted for various applications. For dual-frequency applications, the size of the two patches is determined by the two frequencies of operation. For broadband operation, the various parameters are optimized for maximum bandwidth. For offset elements, a shift in the x and y directions has a significant effect on impedance bandwidth and the radiation patterns.

A study showed that although offset patches give rise to a wider bandwidth, the structural asymmetry gives rise to beam squint in the E plane [31]. Impedance bandwidths of 10% to 29% have been achieved with probe-fed stacked patches [29, 30, 32], and 18% to 67% for aperture-coupled stacked patches [33–36]. The larger bandwidth in each case corresponds to a relatively thicker substrate. It is possible to use three stacked patches, but the improvement in bandwidth over that obtained from a properly optimized two-element design may not be considerable. A study of the effect of patch shape in a multilayer

configuration has been carried out [37]. Equilateral triangular patches are found to give poor cross-polar level in the radiation patterns.

The stacked patch configuration has a number of attractive features, including these:

- Since stacking of patches does not increase the surface area occupied by the element, compared to coplanar parasitic elements discussed in this chapter, the stacked element can be used in an array configuration without the need for increased element spacing and the associated grating lobe problem.
- The radiation patterns and the phase center of the stacked element remains symmetrical over its operating band. This is an important consideration for its use in reflector feed, and for array applications.

Analysis

The stacked patch configuration has been analyzed using the integral equation approach [35], the lossy transmission line model [38], and the cavity model [39]. The coupling mechanism between the stacked patches can be better understood in terms of the field distribution between them or the current distributions on the patch metalization.

The approximate electric current distributions for two stacked rectangular patches is shown in Figure 9.17 for the even and odd modes. At the lower frequency of 9.9 GHz, the currents are in phase on the two patches [see Figure 9.17(a)]. This mode is called the *even mode*. The odd mode occurs at a higher frequency of 11.75 GHz and the currents on the patches are out of phase in this case [see Figure 9.17(b)]. The odd-mode frequency sets an upper limit to the bandwidth of the stacked patch configuration because this mode is not suitable as a radiator.

The field distribution between the stacked patches is similar to that in a broadside coupled microstrip line. It is shown in Figure 9.18 for the even mode. The magnetic coupling between the patch resonators of a probe-fed antenna can be modeled by an equivalent circuit shown in Figure 9.19. The value of mutual inductance M can be obtained from the analysis of broadside coupled microstrip lines.

Design of Aperture-Coupled Stacked Microstrip Antennas

Simple analysis of a stacked patch antenna is not available. Therefore, the design approach given below is based on the results of a full-wave analysis presented by Targonski et al. [36] for an aperture-coupled feed. The stacked patch configuration, shown in Figure 9.16, consists of two resonant patches that are slightly different in size, with the lower patch fed by a microstrip line

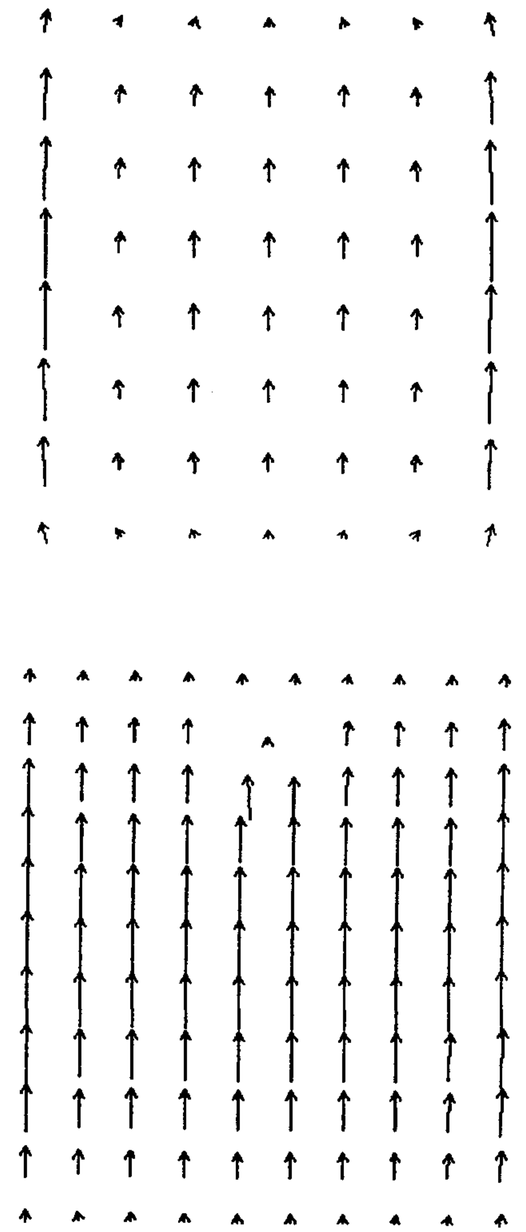

Figure 9.17 (a) Even-mode current distribution for probe-fed stacked rectangular patches at 9.9 GHz; $\epsilon_{r1} = 2.17$, $d_1 = 0.254$ mm, $\epsilon_{r2} = 1$, $d_2 = 1$ mm, $PL_1 = 10$ mm, $PW_1 = 9$ mm, $\epsilon_{r3} = 2.17$, $d_3 = 0.254$ mm, $PL_2 = 10$ mm, $PW_2 = 9$ mm. (b) Odd-mode current distribution for probe-fed stacked rectangular patches at 11.75 GHz. Dimensions are same as those in part (a).

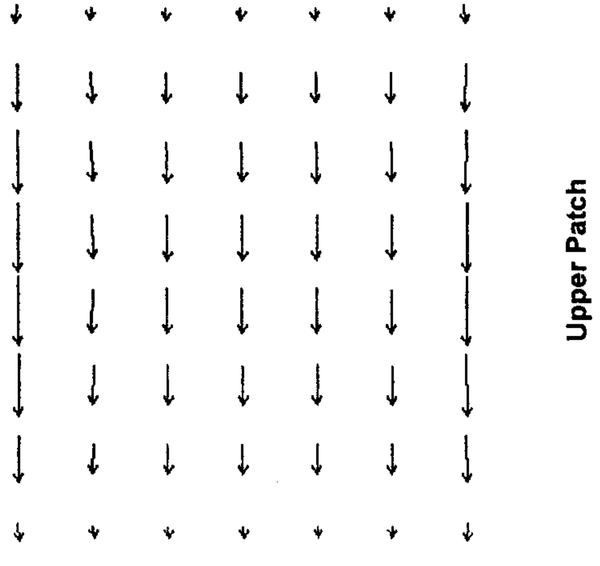

Figure 9.17 (continued).

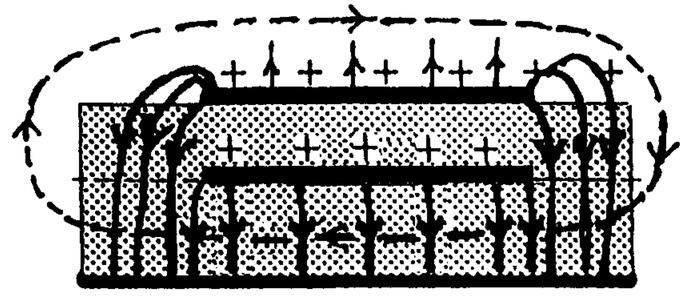

Figure 9.18 Electric and magnetic field distributions for the even mode in a stacked patch configuration. The patches are coupled through the magnetic field; ____, electric field; ----, magnetic field.

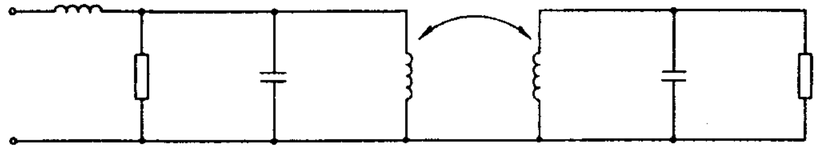

Figure 9.19 Equivalent circuit for the even mode in a probe-fed stacked patch configuration.

through a resonant slot in the common ground plane. The basic feature of this configuration is that each of the three resonators, two patches and the aperture, has its own impedance loop. There is also mutual coupling among these resonances. The resonator parameters are adjusted to bring the impedance loops closer to each other. The substrate thickness and dielectric constant between the resonators is also varied to adjust the mutual coupling between them resulting in a wide bandwidth. The design approach is presented next.

A typical impedance locus of a wide bandwidth stacked patch antenna is shown in Figure 9.20 [36]. This locus, which consists of two closed loops near the center of the Smith chart, is produced by the coupling of the individual resonances of the two patches and the aperture. The mutual coupling between the lower patch and the aperture produces a lower frequency loop in the impedance locus, and the upper frequency loop is produced by the mutual coupling of the two patches. These loops are narrow closed loops and are also positioned near each other, resulting in a dramatic increase in bandwidth. For wide-band operation, these loops should approximately encircle the center of the Smith chart and the circle having a size of no more than VSWR = 2. The design process for the antenna consists of varying the various parameters of the antenna like the size of the two patches, length of the aperture, substrate parameters between the first patch and the aperture, and that between the second patch and the first patch.

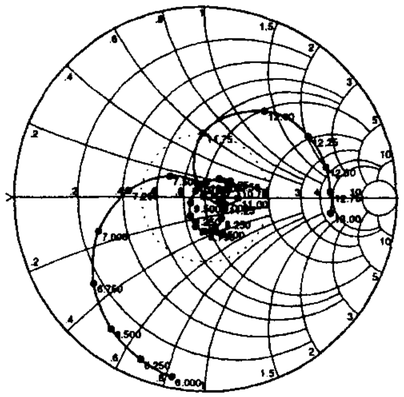

Figure 9.20 A typical impedance plot of a wide-band aperture-coupled stacked microstrip antenna. The aperture is near resonant. (From [36]. © 1998 IEEE. Reprinted with permission.)

The narrow (impedance) loops are produced by weak coupling between the resonances and therefore broader loops are the result of tight or overcoupled resonances. Coupling between the resonators can be adjusted by changing the resonator frequency and the material parameters separating them. In the discussion to follow, the substrate dielectric constant for the antenna has been fixed and only the substrate thickness is varied to vary the coupling.

Figure 9.21 shows the effect of varying the aperture length on the input impedance. Three values of aperture length are used. We can see that this change has a pronounced effect on the size of lower frequency loop representing the coupling between the lower patch and the aperture. The size of the upper loop remains almost unaffected. The increase in the length of the aperture increases the coupling (Section 9.4) and therefore increases the size of the lower frequency loop. At the same time, this operation brings the two loops together. Now fixing the other parameters of the antenna and the aperture length at 10 mm, the size of the lower square patch is changed about 9 mm.

The change in input impedance is shown in Figure 9.22 for three values of lower patch size. *This is a critical parameter because this action contributes to both mutual resonances (with the aperture below and the upper patch) and therefore affects the size of both the loops.* The effect of changing the upper patch size is shown in Figure 9.23. The similarities between Figures 9.22(a) and 9.23(c) and between Figures 9.22(c) and 9.23(a) indicate that it is the relative size of the two patches that governs the impedance behavior rather than their absolute size. When the resonances of the two patches are undercoupled as in Figures 9.22(c) and 9.23(a) (the corresponding loop size is smaller), the impedance behavior is dominated by the mutual resonance between the lower patch and the aperture. The other combination of figures represents overcoupled patches.

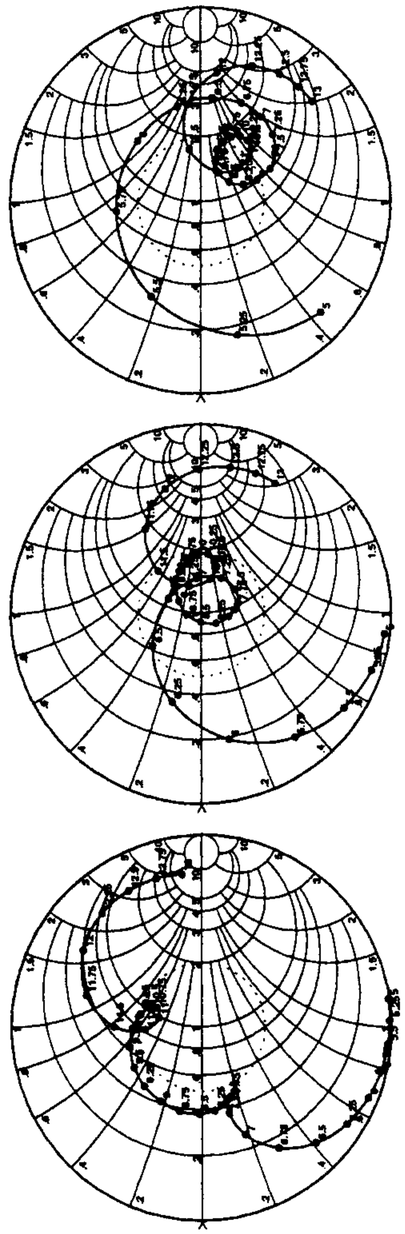

Figure 9.21 Input impedance as a function of aperture length for a stacked patch antenna: (a) SL = 8 mm, (b) SL = 10 mm, and (c) SL = 12 mm. Other parameters: feed side: W_f = 4.75 mm, L_{sub} = 3.4 mm, SW = 0.8 mm; patches: $PL_1 = PW_1$ = 9.1 mm, $PL_2 = PW_2$ = 10 mm; dielectric layers: ϵ_{rf} = 2.33, d_f = 1.6 mm, $\tan\delta_f$ = 0.0012, ϵ_{r1} = 2.2, d_1 = 3.175 mm, $\tan\delta_1$ = 0.0009, ϵ_{r2} = 1.07, d_2 = 3 mm, $\tan\delta_2$ = 0.0009; superstrate layer: ϵ_{r3} = 2.2, d_3 = 0.127 mm, $\tan\delta_3$ = 0.0009. (From [36]. © 1998 IEEE. Reprinted with permission.)

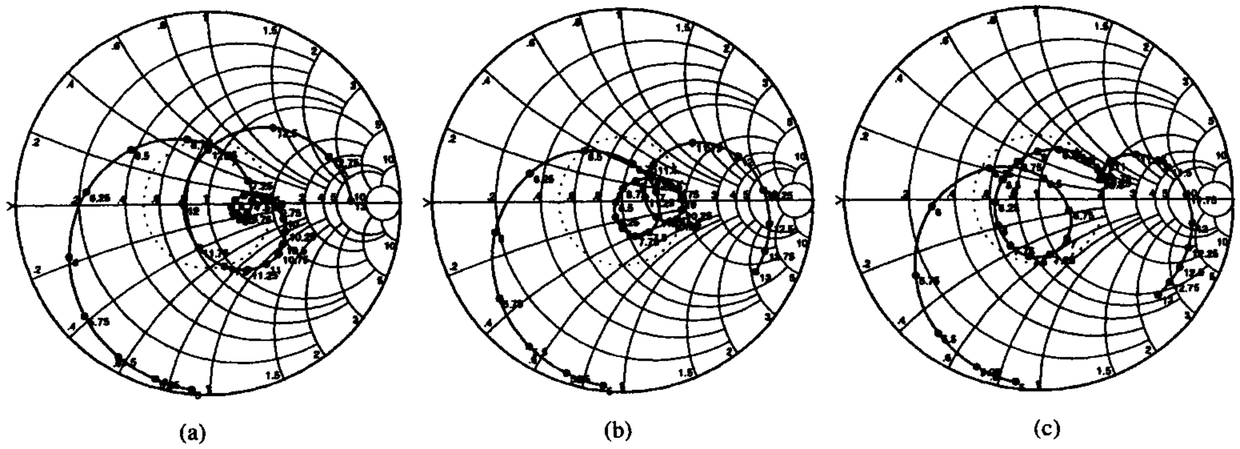

(a) (b) (c)

Figure 9.22 Input impedance as a function of lower patch size for a stacked patch antenna: (a) $PL_1 = PW_1 = 8$ mm, (b) $PL_1 = PW_1 = 9$ mm, and (c) $PL_1 = PW_1 = 10$ mm. SL = 10 mm and other parameters are same as those in Figure 9.21. (From [36]. © 1998 IEEE. Reprinted with permission.)

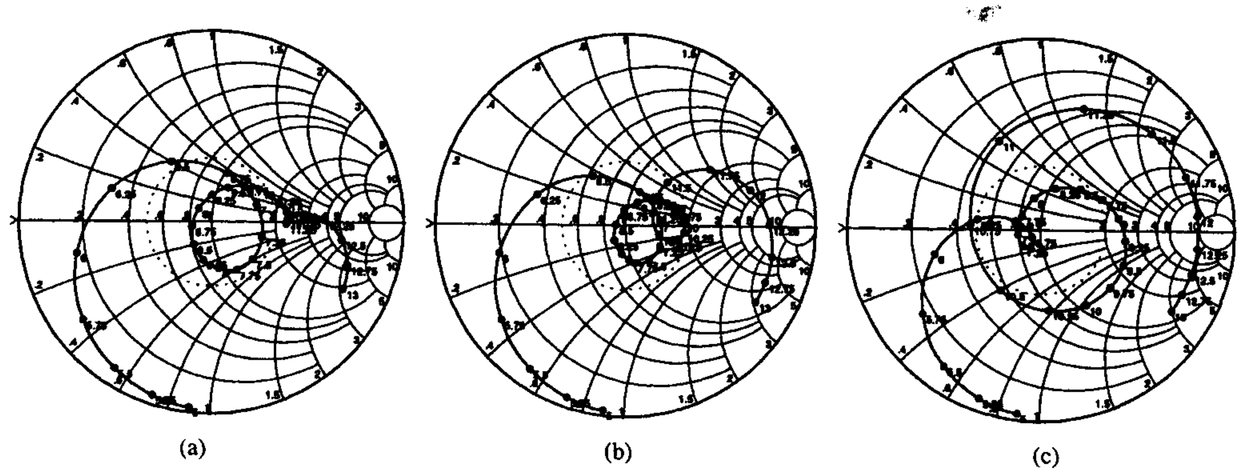

(a) (b) (c)

Figure 9.23 Input impedance as a function of upper patch size for a stacked patch antenna: (a) $PL_2 = PW_2 = 9$ mm, (b) $PL_2 = PW_2 = 10$ mm, and (c) $PL_2 = PW_2 = 12$ mm. $PL_1 = PW_1 = 9$ mm, SL = 10 mm, and other parameters are same as those in Figure 9.21. [From [36]. © 1998 IEEE. Reprinted with permission.)

Figures 9.21(b), 9.22(b), and 9.23(b) represent a proper balance between the two mutual resonances and therefore maximum bandwidth with respect to patch size and aperture size.

The substrate thickness between the lower patch and the aperture is varied in Figure 9.24. It affects the Q of the lower patch and mutual coupling between the corresponding resonances. An increase in separation decreases the mutual coupling and therefore the size of the lower frequency loop decreases. A similar effect was achieved by varying the aperture size as shown in Figure 9.21. The effect of substrate thickness between the two patches on the upper frequency loop (see Figure 9.25) can be explained similarly. Figure 9.25(a) shows that at a separation of 2 mm, the two mutual resonances are essentially decoupled. However, at a separation of 4 mm [see Figure 9.25(c)], there is a high degree of coupling between the two resonances, decreasing the size of the lower frequency loop.

Coupling of the antenna to the microstrip feed line can be addressed now. Because the size of the aperture is decided by the mutual coupling considerations between the resonators, the coupling to the feed line must be controlled in some other manner. Use of a resonant aperture gives rise to overcoupling to the feed and therefore high input impedance (see Figure 9.8). The coupling must be reduced to impedance match the antenna to the feed line. Three approaches are shown in Figure 9.26. A simple approach is to use a 50Ω feed line with an offset as shown in Figure 9.26(a). The offset is adjusted to control the coupling. However, this configuration suffers from increased cross-polarization in the radiation patterns. Another approach is based on the use of a wide-centered feed line as in Figure 9.26(b). It is based on the fact that coupling decreases with the increase in feed line width. An alternative approach is to use the dual-offset feed lines of Figure 9.26(c). The impedance of each of the feed lines at the aperture location is now 100Ω and can be obtained from the 50Ω parent feed line through a reactive power divider. Configurations (b) and (c) are symmetric in nature and therefore do not contribute to cross-polarization. Both the components of current on the wider feed line must be included in the analysis of Figure 9.26(b).

Targonski et al. have designed a 67% bandwidth linearly polarized microstrip antenna employing two stacked rectangular patches and a resonant aperture [36]. The substrates for the antenna are composed of a composite substrate of two layers between the first patch and the ground plane, one layer sandwiched between the two patches, and a superstrate layer. The optimized dimensions of this antenna are (refer to Figure 9.16 for the meaning of various parameters):

Feed parameters: W_f = 0.5 mm, d_{off} = 5.4 mm, L_{stub} = 5.8 mm;
ϵ_{rf} = 2.2, d_f = 0.635 mm, $\tan\delta_f$ = 0.0009

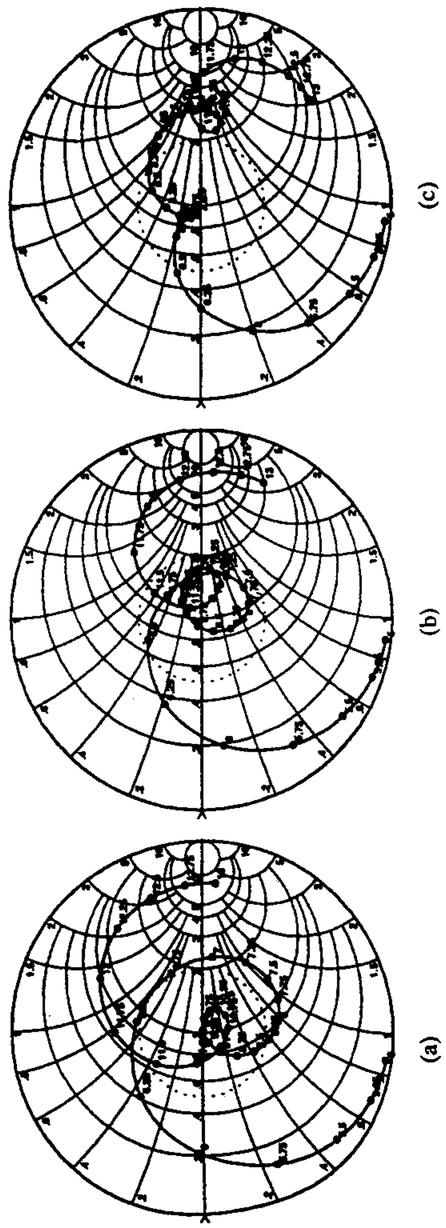

Figure 9.24 Input impedance as a function of lower substrate thickness for a stacked patch antenna: (a) d_1 = 2.5 mm, (b) d_1 = 3 mm, and (c) d_1 = 4 mm. $PL_1 = PW_1$ = 9 mm, $PL_2 = PW_2$ = 10 mm, SL = 10 mm, and other parameters are same as those in Figure 9.21. (From [36]. © 1998 IEEE. Reprinted with permission.)

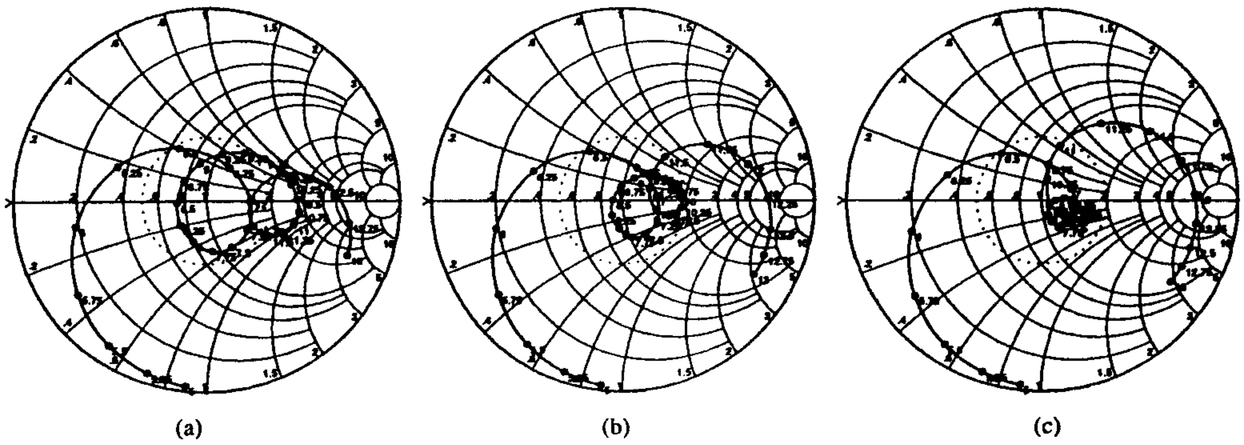

Figure 9.25 Input impedance as a function of upper substrate thickness for a stacked patch antenna: (a) d_2 = 2 mm, (b) d_2 = 3 mm, and (c) d_2 = 4 mm. $PL_1 = PW_1$ = 9 mm, $PL_2 = PW_2$ = 10 mm, d_1 = 3 mm, SL = 10 mm, and other parameters are same as those in Figure 9.21. (From [36]. © 1998 IEEE. Reprinted with permission.)

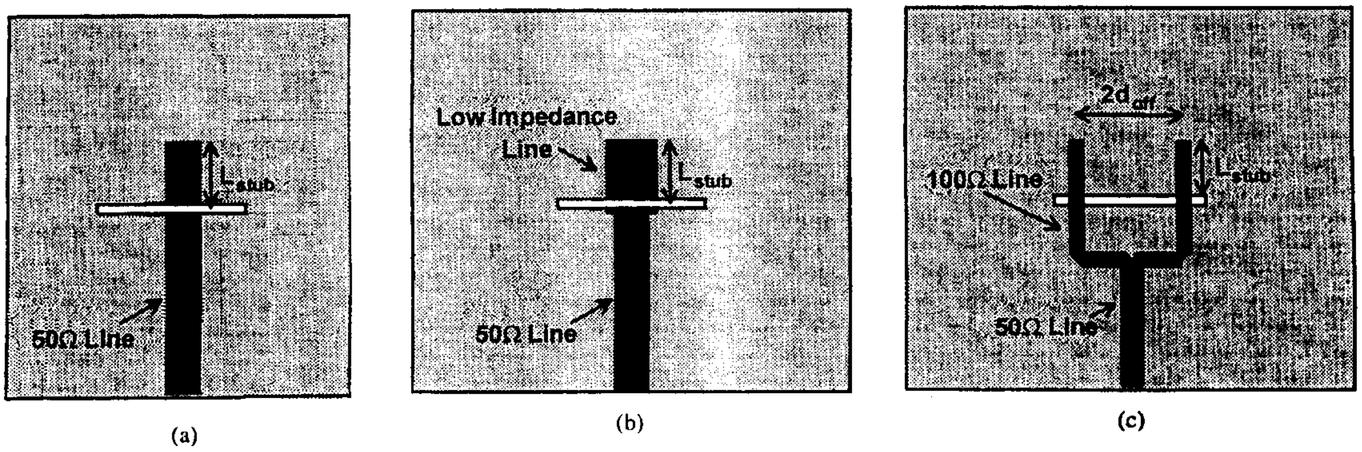

Figure 9.26 Impedance matching of the aperture-coupled stacked antenna to the microstrip feed line: (a) 50Ω feed line with an offset, (b) wide-centered feed line, and (c) dual-offset feed lines. (From [36]. © 1998 IEEE. Reprinted with permission.)

Aperture dimensions: SL = 16 mm, SW = 1 mm

Antenna substrates: composite substrate ϵ_{r11} = 1.07, d_{11} = 1.2 mm, $\tan\delta_{11}$ = 0.0009; ϵ_{r12} = 2.2, d_{12} = 3.175 mm, $\tan\delta_{12}$ = 0.0009; sandwich layer ϵ_{r2} = 1.07, d_2 = 3.1 mm, $\tan\delta_2$ = 0.0009; superstrate layer ϵ_{r3} = 2.53, d_3 = 0.508 mm, $\tan\delta_3$ = 0.003

Patch elements: PL_1 = 10.8 mm, PW_1 = 20 mm; PL_2 = 11.2 mm, PW_2 = 20 mm

Measured return loss and gain of this antenna are compared in Figures 9.27 and 9.28, respectively, against the computed values. The measured VSWR = 2 bandwidth is reported to be 69% (5.07 to 10.38 GHz) and the measured gain is greater than 6 dB over a 67% bandwidth, 5.2 to 10.4 GHz. The computed front-to-back ratio of the antenna ranged from 8 to 14 dB and the surface wave efficiency (only surface wave loss is considered) ranged from 82% to 90% over most of the band.

A probe-fed stacked patch antenna has also been studied for wide-band operation [28–30, 32]. The configuration of a probe-fed stacked patch microstrip antenna is shown in Figure 9.29. Croq et al. have compared probe-fed and aperture-coupled feeding techniques in relation to a stacked patch antenna [32]. The integral equation technique applied in spectral domain is used for analysis. The bandwidths of these antennas are found to be comparable, and determined by the Q factor of the patches and the coupling between the resonators. The main differences are in the radiation characteristics.

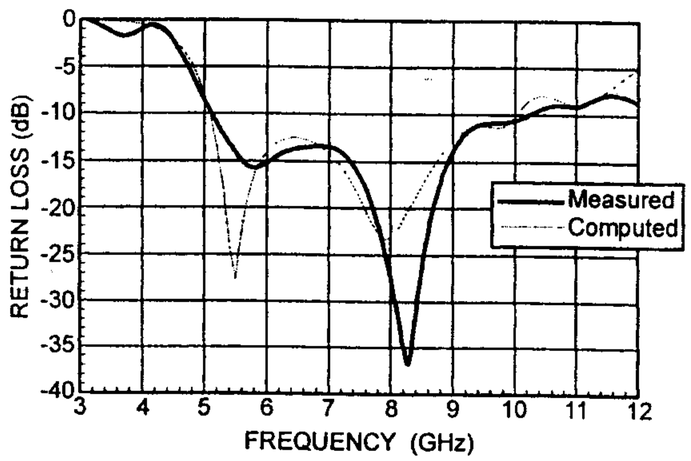

Figure 9.27 Comparison of computed and measured return loss of a stacked patch aperture-coupled microstrip antenna. (From [36]. © 1998 IEEE. Reprinted with permission.)

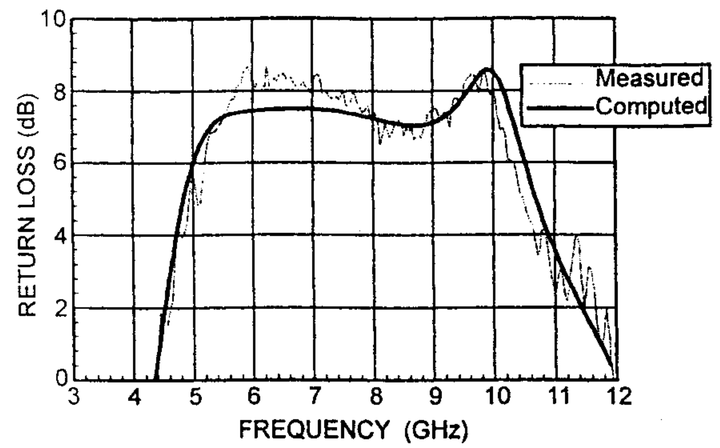

Figure 9.28 Comparison of computed and measured gain of a stacked patch aperture-coupled microstrip antenna. (From [36]. © 1998 IEEE. Reprinted with permission.)

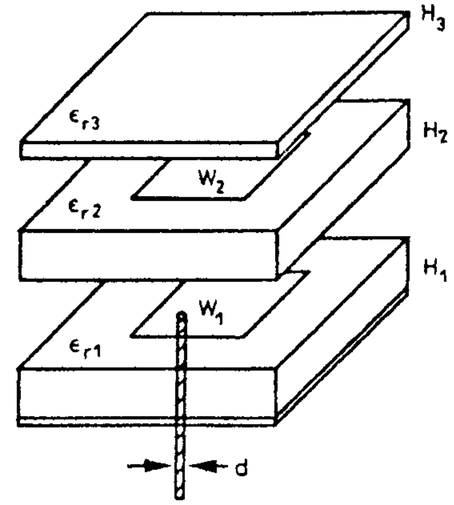

Figure 9.29 Exploded view of probe-fed stacked patch antenna.

The radiation patterns for these antennas are shown in Figure 9.30 [32]. For the antennas studied at X/Ku bands, the copolar and cross-polar patterns are distorted for the probe-fed structure. The parasitic radiation from the probe and transverse current on the patch affects cross-polarization in particular. This radiation is highly asymmetrical due to the effect of feed location and the level is also relatively higher (–26 dB over 4° angle about boresight). However, back radiation is virtually absent in probe-fed antennas. Therefore, these antennas are better suited at lower frequencies and for applications in which electromagnetic compatibility is a major constraint. The cross-polar radiation for the aperture-

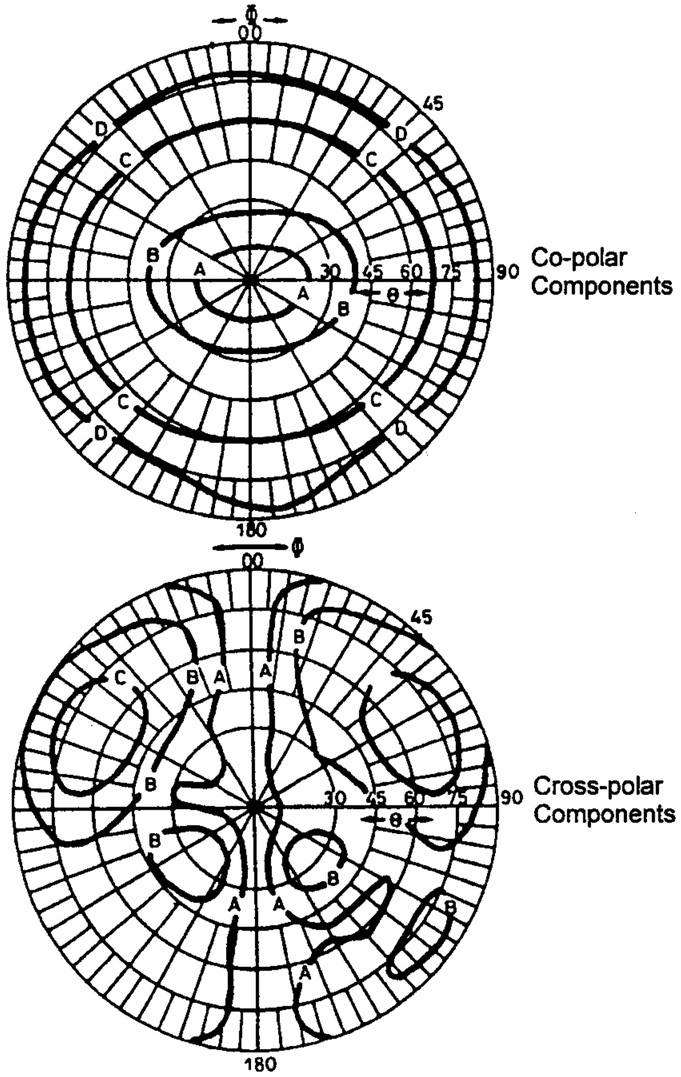

(a) Probe feed

Figure 9.30 Measured radiation patterns of stacked (square) patch antennas at 12 GHz. (a) Probe-fed antenna; W_1 = 8 mm, W_2 = 6.9 mm, $x_p = y_p$ = 2.5 mm, ϵ_{r1} = 2.2, ϵ_{r2} = 1.0, ϵ_{r3} = 2.2, H_1 = 1.53 mm, H_2 = 1.53 mm, H_3 = 3.09 mm; copolar component: A = –1 dB, B = –3 dB, C = –5 dB, D = –10 dB; cross-polar component: A = –30 dB, B = –20 dB, C = –12 dB. (b) Aperture-coupled antenna; with reference to Figure 9.16, the dimensions are SL = 6.7 mm, SW = 0.4 mm, W_f = 2.3 mm, d_{off} = 0, L_{stub} = 2.7 mm, $PL_1 = PW_1$ = 7.3 mm, $PL_2 = PW_2$ = 7 mm, ϵ_{rf} = 2.2, d_f = 0.762 mm, ϵ_{r1} = 2.2, d_1 = 1.54 mm, ϵ_{r2} = 1.0, d_2 = 2.2 mm, ϵ_{r3} = 2.2, d_3 = 1.54 mm; copolar component: A = 1 dB, B = –3 dB, C = –7 dB, D = –10 dB; cross-polar component: A = –35 dB, B = –26 dB, C = –20 dB, D = –14 dB. (From [32]. © 1993 IEE. Reprinted with permission.)

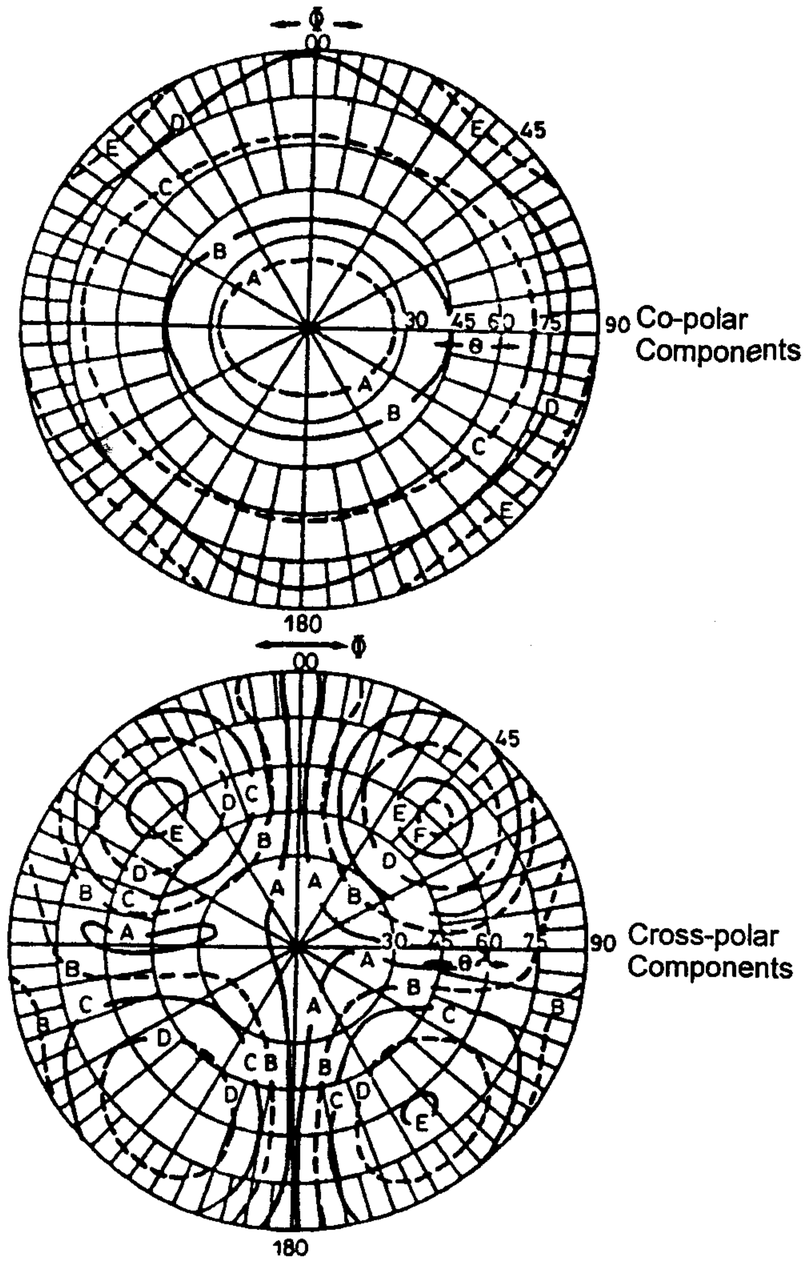

(b) Aperture coupled feed

Figure 9.30 (continued).

coupled case is lower (–35 dB around the boresight) and highly symmetrical. Generally, aperture-coupled structures should be used at frequencies higher than C band [32].

One of the main applications for dual-band or broadband multilayer structure is in global positioning systems [40]. However, because of multilayer

fabrication, these structures either are not well suited for mass manufacturing, or prevent the use of discrete components or MICs, in a microstrip edge feed.

9.5.2 Broadbanding Using Coplanar Parasitic Elements

Another configuration that has broadband performance is a set of coplanar resonators with slightly different resonant frequencies. Some of these geometries are shown in Figures 9.31 and 9.32. Only the central patch is driven by the feed line and the other patches are either gap coupled or directly coupled to the driven patch. The basic configuration of Figure 9.31(a) with two dipole gaps coupled to a radiating patch was reported in 1979 [41]. When two patches were gap coupled to the main patch along the radiating edges [see Figure 9.31(b)], a maximum bandwidth up to 5.1 times that of a single rectangular patch antenna was obtained [42]. This type of parasitic coupling along the nonradiating edges [see Figure 9.31(c)] produced 4 times the bandwidth [43]. A similar configuration consisting of short-circuited quarter-wave patches coupled to a half-wave patch along the radiating edges [see Figure 9.31(d)] yielded 5.35 times the bandwidth [44]. In another example, two $\lambda/4$ long short-circuited patches with coupling along the radiating edge [see Figure 9.31(e)] were studied. This geometry avoids the mutual coupling between the two radiating edges of a rectangular patch. The bandwidth was found to be about 2.4 times [44]. A geometry of four patches gap coupled to the four edges of a driven patch has been analyzed using a multiport network model [43]. The geometry of this antenna is shown in Figure 9.31(f). It yielded 6.7 times the bandwidth of a single patch.

The concept of gap-coupled elements was extended to gap-coupled arrays [45]. In this array, a driven patch is gap coupled to closely spaced adjacent patches, which are further coupled to additional patches, leading to a linear or planar array [see Figure 9.31(g)]. The coupling gap between the adjacent patches is used to adjust the amplitude distribution of the array and is normally very small, 0.1 to 2 times the substrate thickness. Linear (7×1) and planar configurations (5×3) of parasitically coupled patches have been experimentally developed [45]. The planar array utilizing a substrate volume of 1.57 mm $\times$ 30 mm $\times$ 30 mm at 8.55 GHz is reported to have 16% bandwidth, 9 dB gain, and -26-dB sidelobes. A linear array of seven dipoles coupled along the nonradiating edges but with optimized dipole widths and gap spacings produced about 8 times the impedance bandwidth [see Figure 9.31(h)] [46]. In another arrangement, a number of dipoles having varying lengths were excited by a slot aperture at the middle to create a stagger tuned effect [47]. These geometries are shown in Figures 9.31(i) and (j). Multifrequency operation at three different frequencies has been reported [47]. A variation of this geometry with all the

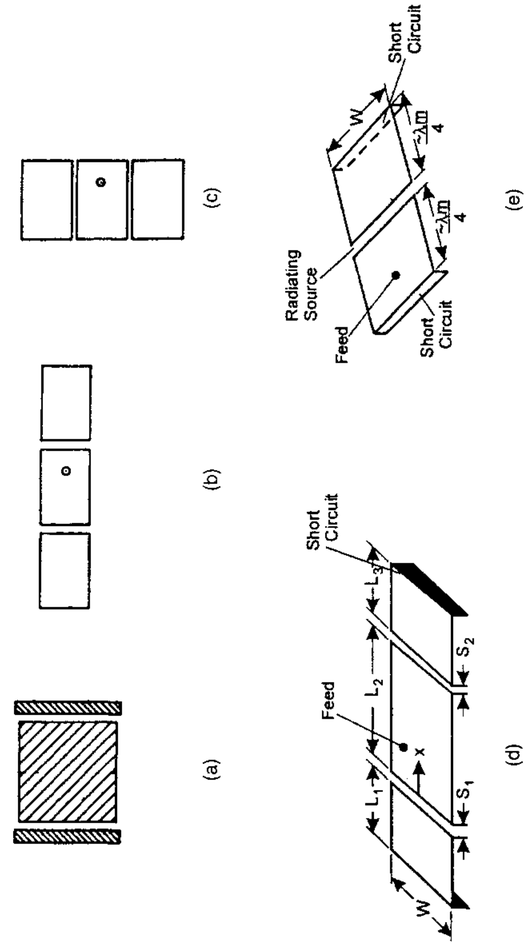

Figure 9.31 Configurations of some broadband microstrip antennas using coplanar gap-coupled resonators. (a) A driven patch antenna gap coupled to two dipoles along the radiating edges. (From [41]. © 1979 New Mexico State University. Reprinted with permission.) (b) A driven patch antenna gap coupled to two patches along the radiating edges. (From [42]. © 1984 IEEE. Reprinted with permission.) (c) A driven patch antenna gap coupled to two patches along the nonradiating edges. (From [43]. © 1985 IEEE. Reprinted with permission.) (d) A driven patch antenna gap coupled to two quarter-wave patches along the radiating edges. (From [54]. © 1993 *Electronics Letters*. Reprinted with permission.) (e) A quarter-wave patch gap coupled to a driven quarter-wave patch antenna. (From [44]. © 1980 IEE. Reprinted with permission.) (f) A driven patch antenna gap coupled to four patches along the edges. (From [43]. © 1985 IEEE. Reprinted with permission.) (g) A microstrip array antenna with a driven patch and gap-coupled parasitic patches. (h) A broadband gap-coupled linear array of seven dipoles. (From [46]. © 1990 IEEE. Reprinted with permission.) (i) Configuration of a multifrequency multiple resonator aperture-coupled antenna. (From [47]. © 1992 IEEE. Reprinted with permission.) (j) Another configuration of a multifrequency multiple resonator aperture-coupled antenna. (From [47]. © 1992 IEEE. Reprinted with permission.)

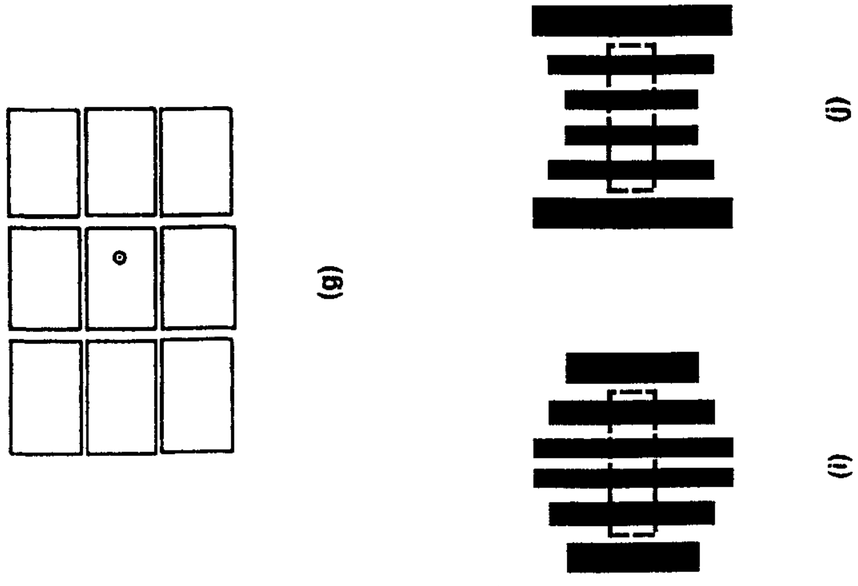

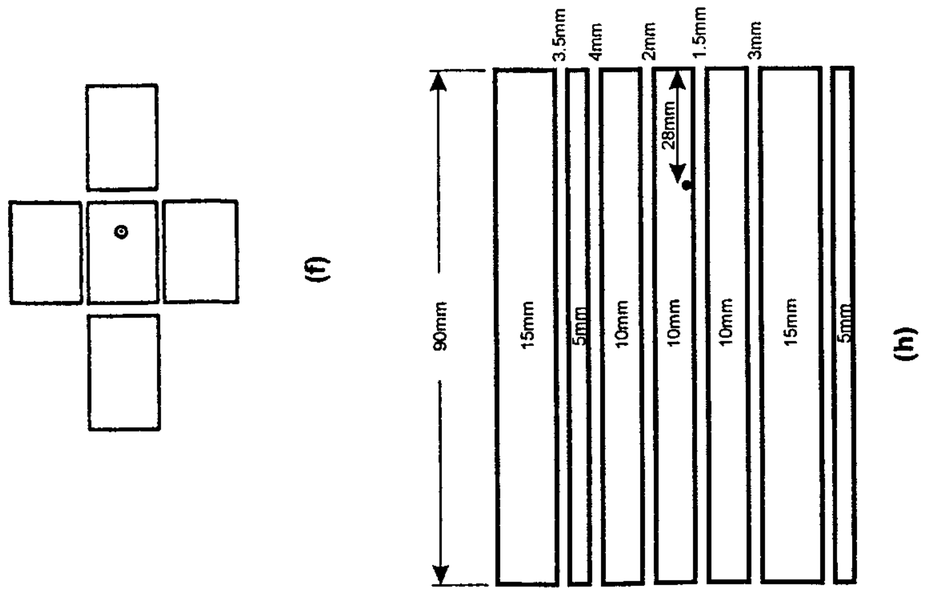

Figure 9.31 (continued).

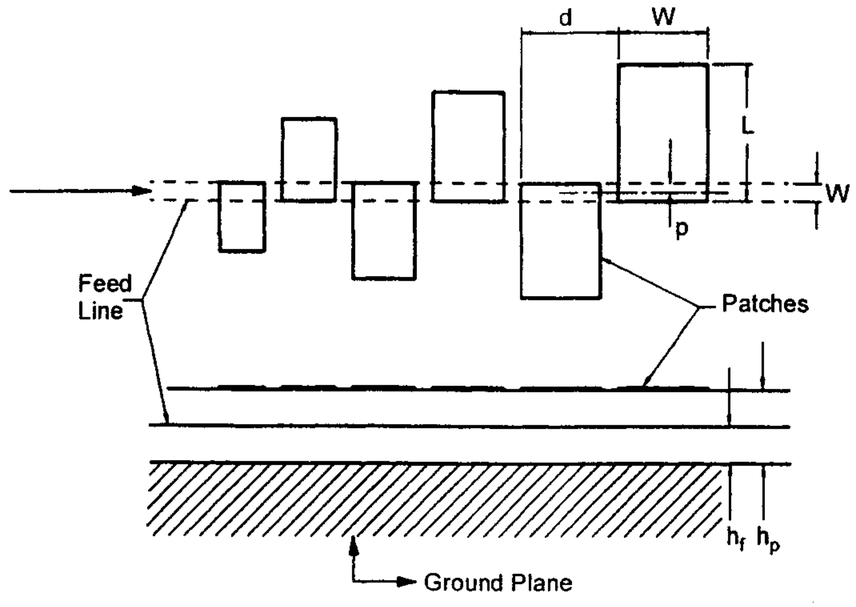

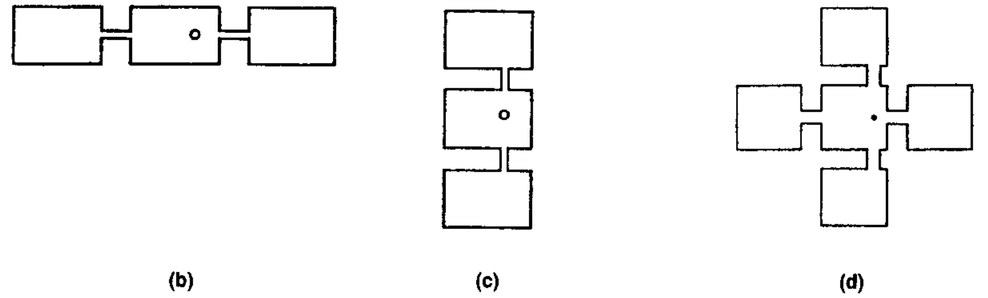

Figure 9.32 Some more configurations of broadband microstrip antennas using coplanar gap-coupled resonators. (a) Configuration of a broadband gap-coupled log-periodic microstrip array. (From [49]. © 1986 IEE. Reprinted with permission.) (b) A driven patch antenna directly coupled to two patches along the radiating edges. (From [50]. © 1985 IEEE. Reprinted with permission.) (c) A driven patch antenna directly coupled to two patches along the nonradiating edges. (From [50]. © 1985 IEEE. Reprinted with permission.) (d) A driven patch antenna directly coupled to four patches along the edges. (From [50]. © 1985 IEEE. Reprinted with permission.) (e) Microstrip disk antenna gap coupled to a shorted annular ring. (From [51]. © 1985 *Electronics Letters*. Reprinted with permission.)

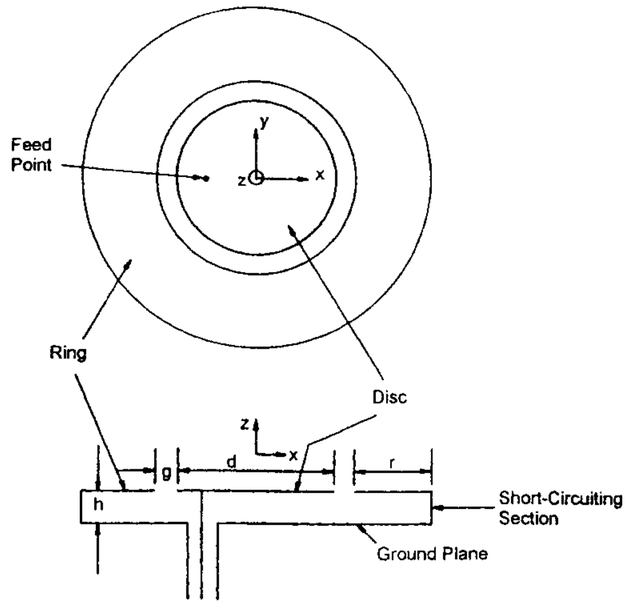

(e)

Figure 9.32 (continued).

dipoles resonating at the same frequency and aperture coupled to the feed microstrip line has also been studied [48]. The optimized bandwidth of this geometry with three dipoles in a symmetric configuration produces about 23% bandwidth for an antenna thickness of $0.083\lambda_0$. This is about 1.5 times the bandwidth of the corresponding square patch antenna. But the polarization purity of this antenna is expected to be better because of the use of strips instead of patches. Finally, the stagger tuned resonator concept can be extended to a log-periodic array of printed dipoles to achieve multioctave bandwidths [49]. The log-periodic antenna is shown in Figure 9.32(a). Directly coupled resonator configurations were also studied. These are shown in Figure 9.32(b)–(d). In these cases the outer patches are parasitic to the fed patch but are directly coupled to it. Bandwidths similar to the corresponding gap coupled geometries of Figures 9.31(b), (c), and (f) were obtained [50].

Coplanar parasitic antenna in the circular geometry has been studied. It consists of a microstrip disk gap coupled to a short-circuited annular ring on the same surface [51]. The geometry of this antenna is shown in Figure 9.32(e). This antenna can also be considered a cylindrical cavity with an annular slot. The resonant frequencies of the disk and the cavity are nearly the same. This antenna produces a circularly symmetric radiation pattern with a 10-dB beamwidth of about 160°, and is suitable for illuminating a reflector with $F/D = 0.3$. Maximum cross-polarization within the 10-dB beamwidth is

reported to be −21 dB over the band of 5 to 5.44 GHz. It is possible to achieve a 10% impedance bandwidth by adjusting the coupling gap dimension.

All the microstrip antennas with coplanar parasitic resonators suffer from an enlargement in surface area. Moreover, the radiation patterns and the phase center changed markedly with frequency, especially for wider bandwidth designs. However, a planar array with 1,280 elements has been reported [52]. This array used 256 subarrays consisting of a central driven patch surrounded on all four sides by parasitic elements [see Figure 9.31(f)]. Grating lobes in this array were avoided by using a triangular grid.

Analysis and Design

Coplanar parasitically coupled patch resonators have been analyzed using the integral equation approach [47], multiport network method [42, 43, 50], and the transmission line model [53, 54]. The basic principle underlying the operation of these antennas is the capacitive coupling between the driven patch and the parasitic patches. The loading effect produced by the parasitic patches lowers the Q, thereby increasing the impedance bandwidth.

For analysis purposes, the electric field in the coupling gap can be modeled as a π network of capacitors as shown in Figure 9.33 [53]. The radiation produced by the fields in the gap is described by a resistance across the series capacitor. The patches themselves can be represented by the transmission line model described in Chapter 2. The radiation conductance G can be taken nearly equal to the open-end conductance of a rectangular patch, as described in Chapter 2. The equations for gap capacitances are available in Appendix B [21]. The above approach has been applied to the geometry of Figure 9.31(d)

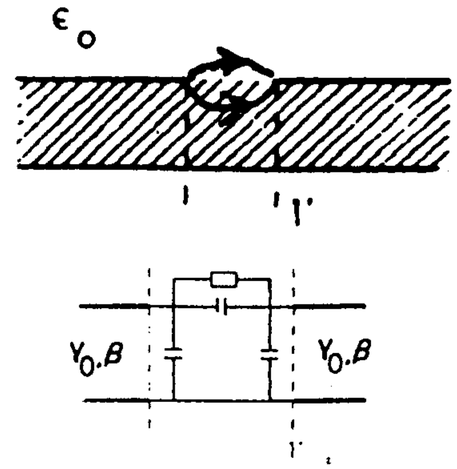

Figure 9.33 Geometry and equivalent circuit representation of a radiating gap. (From [53]. © 1990 *Electronics Letters*. Reprinted with permission.)

[54]. The transmission line equivalent circuit for this geometry is shown in Figure 9.34. The mutual coupling is represented here by a voltage-dependent current source (see Section 4.2.1). This approach can be extended to linear arrays of patch antennas. The antennas of Figures 9.31(b), (c), and (f) and Figures 9.32(b)–(d) have been analyzed using the multiport network model.

It has been suggested in [1] that the bandwidth of an antenna is governed by the volume occupied by it. With this in mind, the percentage impedance bandwidth of coplanar, coupled resonator microstrip antennas as a function of volume occupied by the antenna is plotted in Figure 9.35(a) for various antennas [48]. It is observed from this figure that antenna numbers 5, 6, and 7 have utilized the volume efficiently. Antenna number 8 consists of a number of resonators in an array configuration. The large number of parasitic resonators does not give rise to a substantial increase in bandwidth because of the weak excitation of end resonators. Antenna numbers 5 and 7 suffer from degradation of radiation patterns with frequency.

Impedance bandwidth versus normalized volume for some of the stacked patch antennas is compared in Figure 9.35(b). Both the probe-fed and aperture-coupled antenna are considered for comparison. The thickness of the substrate is included in calculating the volume of the antenna. Comparison of Figures 9.35(a) and (b) indicates that the stacked geometry can provide a larger bandwidth for the same volume. This is due to the fact that the volume in this geometry comprises larger height and lesser surface area, and larger height represents more efficient utilization of volume. However, the large bandwidth of the stacked geometry is accompanied by poor front-to-back ratio and these antennas are not amenable to mass production due to critical alignment of the patches and feed.

9.5.3 Other Multimoding Techniques

In some of the approaches discussed next, two independent modes are excited in the same patch or in the patch and the feed network. A nearly square patch

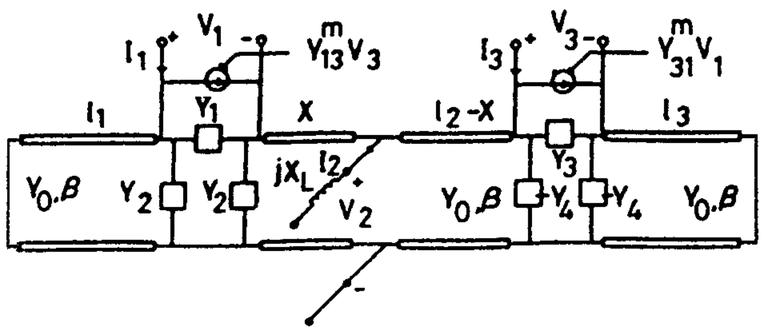

Figure 9.34 Transmission line equivalent circuit for the geometry of Figure 9.31(d). (From [54]. © 1993 *Electronics Letters*. Reprinted with permission.)

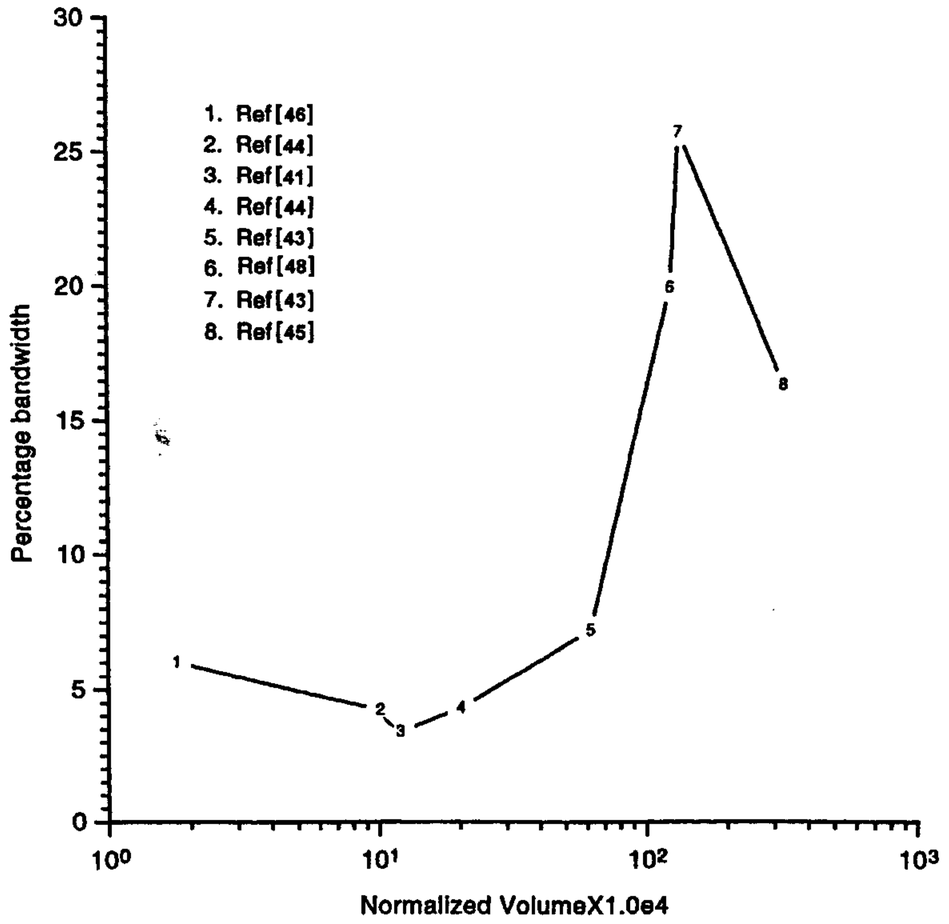

Figure 9.35 (a) Impedance bandwidth versus normalized volume $(V/\lambda_0^3) \times 10^4$ for the coplanar, coupled resonator antennas reported in the literature.
(b) Impedance bandwidth versus normalized volume $(V/\lambda_0^3) \times 10^3$ for the stacked patch resonator antennas reported in the literature.

has been used to obtain almost three times the bandwidth by exciting two modes with orthogonal polarizations [55]. To excite both the modes, the feed, in this case, is located along the diagonal [see Figure 9.36(a)]. The input impedance plot for this patch is shown in Figure 9.36(b) for L = 13.6 cm, W/L = 0.99, ρ_0/L = 0.16, and h/λ_0 = 0.0037 [55]. Elliptical and triangular patch shapes can also be used.

A rectangular patch with a U slot embedded in it (see Figure 9.37) has been found to be a broadband antenna [56–58]. The patch and the slot are designed to produce resonances close to each other. Moreover, the frequency and the Q of the resonances can be independently controlled by adjusting their length and width. In a design developed by Chow et al. [58] the 10-dB return loss bandwidth was found to be about 32% near 1.5 GHz and utilized a foam substrate of thickness 16.5 mm.

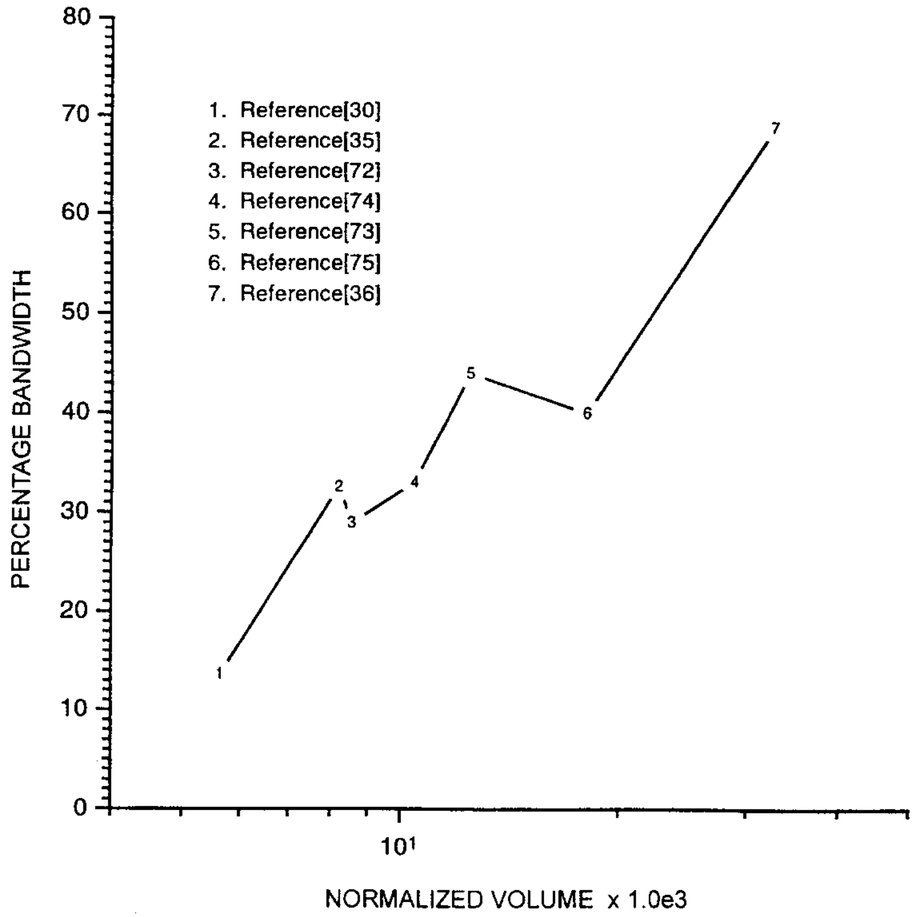

Figure 9.35 (continued).

Dubost has developed a double-folded dipole antenna with several closely spaced modes of resonance [59]. A dipole is folded at both ends and then combined with another similar dipole to yield a symmetrical structure as shown in Figure 9.38. Alternatively, this structure can be considered to be a rectangular patch loaded with an H-shaped slot. Still another description for this antenna could be in terms of a folded slot dipole [60]. The antenna is symmetrically fed across a gap by means of a strip line and is operated between the third and fourth resonances. The lossy transmission line model has been used to determine the characteristics of the antenna. A bandwidth of about 16% was achieved for a thin structure.

9.6 Other Broadbanding Techniques

In earlier sections we have described the use of substrate parameters to increase the impedance bandwidth. Staggered tuned resonators in the stacked patch

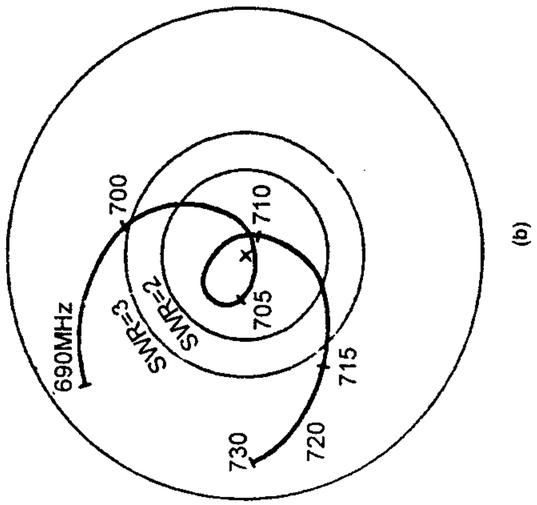

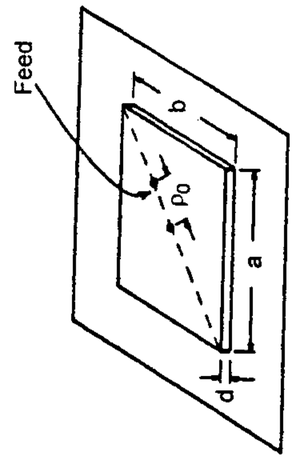

Figure 9.36 Broadband microstrip antenna utilizing two orthogonal modes in (a) a nearly square patch and (b) the input impedance plot. (From [55]. © 1981 IEEE. Reprinted with permission.)

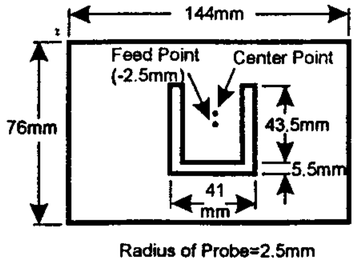

Figure 9.37 Top view of a rectangular patch with a U slot to produce dual resonance and increase in bandwidth. (From [58]. © 1998 IEEE. Reprinted with permission.)

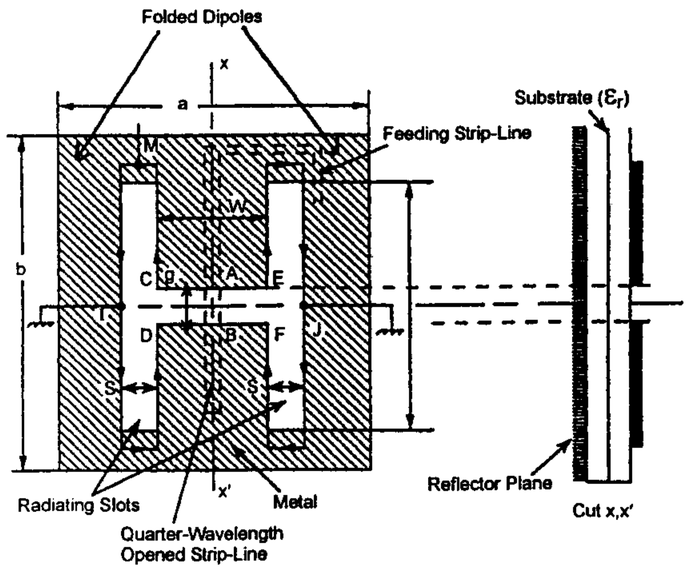

Figure 9.38 A double-folded dipole antenna with broad bandwidth. (From [60]. © 1993 *Antennas and Propagation Society Magazine*. Reprinted with permission.)

configuration and gap-coupled configuration were described in the last section. The use of more than one mode in the same patch was also described. In this section we discuss some more approaches to increase the impedance bandwidth.

9.6.1 Impedance Matching

One of the most common and direct techniques used to influence the impedance behavior is to use an impedance matching network in the feed part of the microstrip antenna. Tuning stubs and quarter-wave transformers can be used for this purpose. The matching network should be mounted as close as possible

to the radiating element for overall efficiency and bandwidth. However, the discontinuities in the matching network may also radiate, degrading the cross-polarization characteristic of the antenna. The complexity and losses of the matching network generally limit the achievable bandwidth to about 10% to 30%. Pues and Van de Capelle [61] obtained a bandwidth of about 10% to 12% using a passive coplanar matching network. Similar techniques used by Paschen [62] produced a bandwidth of more than 25%, which was sufficient to cover both GPS bands with a single radiating element.

In an ingenious approach a 3-D tapered transition has been used to increase the impedance bandwidth to about 90%. A suspended microstrip line has been used to develop this transition between the probe feed and the suspended rectangular patch [63, 64]. The geometry of this antenna is shown in Figure 9.39. The antenna and the transition do not use any dielectric material. The patch is supported in the center by a post (metallic or nonmetallic). The transition may be a uniform width metal strip inclined to the ground plane as shown in Figure 9.39(a), or it may be a tapered width strip perpendicular to the ground plane as in Figure 9.39(b). Both approaches result in a very broadband transition because of their tapered impedance nature. The advantages of this antenna include a very large VSWR bandwidth of the order of 90%, freedom from dispersion and surface wave effects, higher efficiency, and higher power handling capability because the thickness of the antenna can reach $0.25\lambda_0$ at the high-frequency end.

Various dimensions of the antenna of Figure 9.39(a) are given in Figure 9.40. The feeding strip is 27.95 mm wide, 19.30 mm long, and is connected to the patch at 8.90 mm inside the longer edge of the patch as shown. The strip makes an angle of 55° with the patch. A plastic pin 6.35 mm in diameter supports the patch. The measured and computed VSWR for this antenna are shown in Figure 9.41. The VSWR = 2 bandwidth is about 90% (2.2 to 4.3 GHz). However, there is considerable variation in radiation patterns and gain of the antenna over this bandwidth. The measured gain bandwidth (defined as the drop in gain of 1.0 dB) is about 40%. The deterioration in the performance of the antenna toward the higher frequency end is due to the excitation of higher order modes and radiation from the transition itself. The height of the element is $0.14\lambda_0$ at the lower frequency end and $0.27\lambda_0$ at the higher end.

The design of impedance matching networks is very well documented in the texts [65]. The real frequency technique [66] and the simplified real frequency technique [67] are the improved versions.

In another approach the impedance matching network is embedded in the patch itself as shown in Figure 9.42(a) [68]. The matching network is designed such that it produces a reactance behavior that is opposite to that of

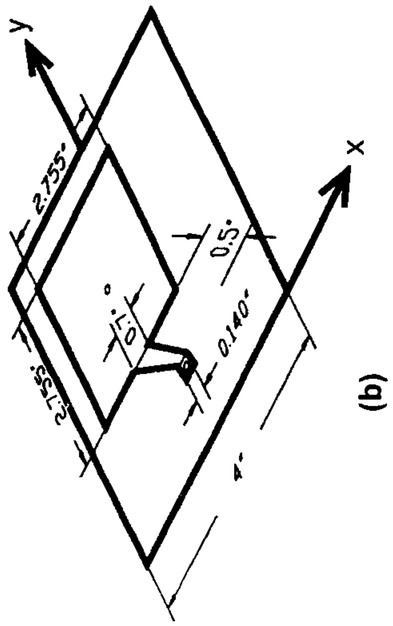

Figure 9.39 A wide-band single-layer patch antenna using 3-D tapered transition. (a) A suspended patch with an inclined 3-D transition. (From [64]. © 1998 IEEE. Reprinted with permission.) (b) A suspended patch with a vertical 3-D tapered transition. (From [64]. © 1998 IEEE. Reprinted with permission.)

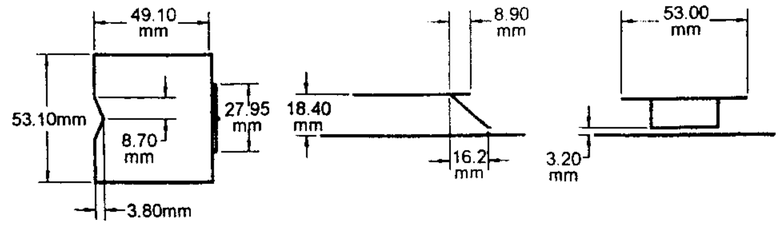

Figure 9.40 Various dimensions of the antenna shown in Figure 9.39(a). (From [63]. © 1998 IEEE. Reprinted with permission.)

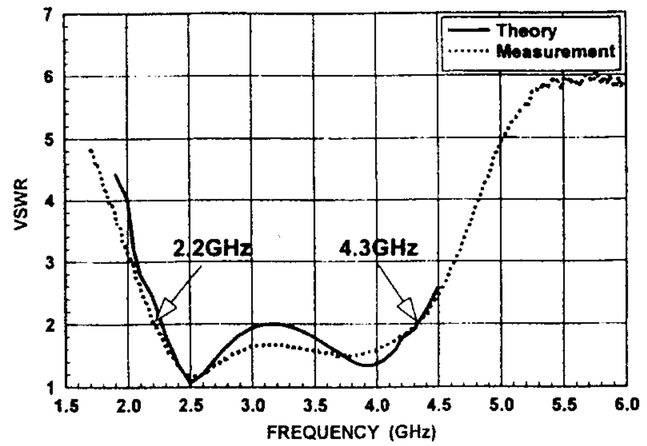

Figure 9.41 Comparison of measured and computed VSWR of the antenna shown in Figure 9.39(a). The dimensions of the antenna are given in Figure 9.40. (From [63]. © 1998 IEEE. Reprinted with permission.)

the patch at resonance; that is, the load is capacitive below resonance and inductive above the resonance frequency. The loaded patch will now have two resonances giving rise to broadband operation [see Figure 9.42(b)]. The bandwidth of the modified patch has been found to be 75 MHz compared to 20 MHz for the regular patch. The maximum cross-polarization level over the band is found to be −17 dB.

9.6.2 Resistive Loading

It has been pointed out by Pozar [1] that the impedance bandwidth of a patch antenna can be increased by introducing losses in the antenna, but at the expense of decrease in radiation efficiency. The losses can be in the form of lossy substrate materials, layer of lossy film, or a discrete chip resistor. Wong and Lin have studied the loading effect of a 1Ω chip resistor mounted at the

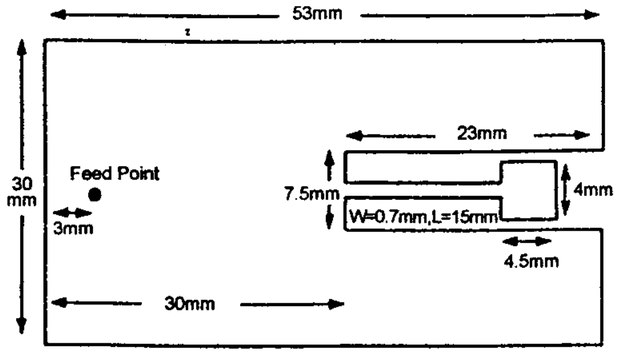

The transmission line loaded patch structure. (ϵ_r = 4.8, h = 0.52mm)

(a)

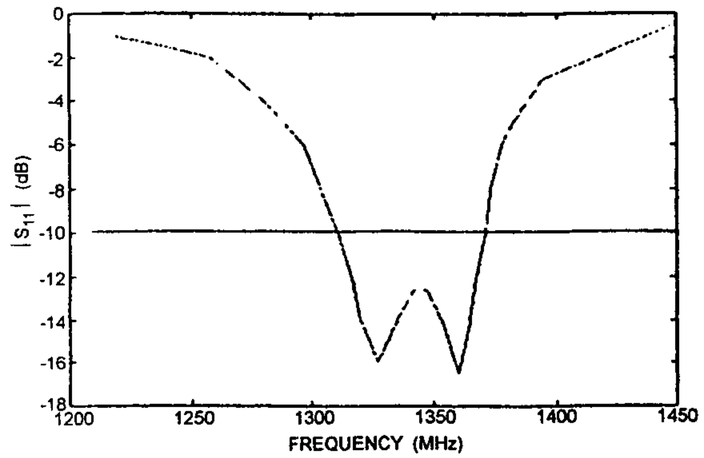

Measured $|S_{11}|$ of the loaded patch antenna

(b)

Figure 9.42 (a) The impedance matching network integrated inside the patch for improved bandwidth. The various dimensions (in millimeters) of the antenna are given in the figure and the substrate parameters are h = 0.52 mm and ϵ_r = 4.8. (From [68]. © 1998 IEEE. Reprinted with permission.) (b) Measured return loss of the loaded patch antenna of part (a). (From [68]. © 1998 IEEE. Reprinted with permission.)

edge of a rectangular patch (see Figure 9.43) [69, 70]. The 10-dB return loss bandwidth of this patch antenna is found to be about 4.9 times that of a patch without the resistor loading [70]. Moreover, the size of the patch reduces to about 0.39 times that of the unloaded patch. The reduction in antenna gain due to resistive loading is estimated to be about 2 dB. The decrease in antenna

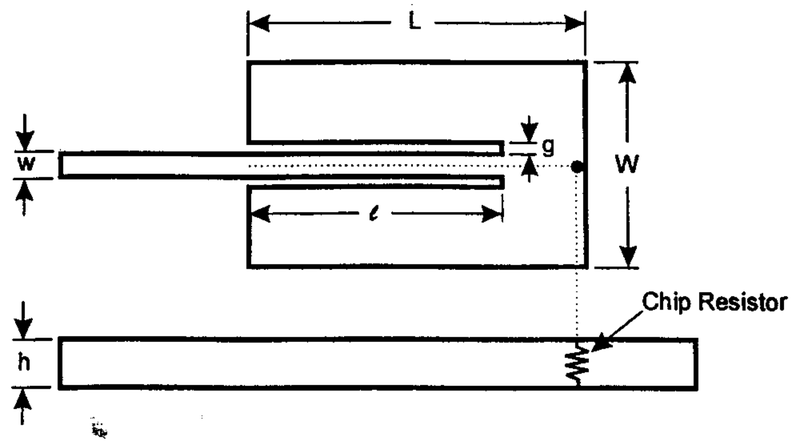

Figure 9.43 Geometry of a broadband rectangular patch antenna with a chip-resistor loading; $l = 0.79L$. (From [70]. © 1998 IEEE. Reprinted with permission.)

gain can be recovered by using a superstrate (see Chapter 10). A circular patch antenna loaded with a chip resistor has also been studied by them [70].

9.7 Multifrequency Operation

The multimoding approach discussed earlier for broadbanding of antennas can be employed for multifrequency operation also. The only difference is that the resonant modes, in this case, are so designed that instead of being close to each other (to provide coupling for broad banding), they should be well separated. The stacked patch and the coplanar parasitic configurations have been extensively used for this purpose [47]. Some additional techniques for dual-frequency operation are discussed in the next chapter.

A stacked patch antenna for dual-frequency and broadband performance has been described recently [71]. It is smaller in size due to the usage of quarter-wave patches. The geometry of this antenna is shown in Figure 9.44. The dual-band structure consists of two oppositely stacked quarter-wave elements as shown in Figure 9.44(a), whereas in the broadband antenna the short circuits are along the same plane [see Figure 9.44(b)]. The lower patches in both the cases are fed by a probe at the midpoint of the longer side. The feed point is symmetric with respect to the y axis. The ratio between the two frequencies of the dual-frequency antenna can be closely controlled within a range varying between 1.3 and 2. However, the radiation patterns are quite different at the two frequencies. The beam is located at $\theta = \pm 45°$ at the lower frequency and the broadside pattern at the upper frequency. The broadband antenna can provide a VSWR < 2 bandwidth of about 30% for a total air thickness of

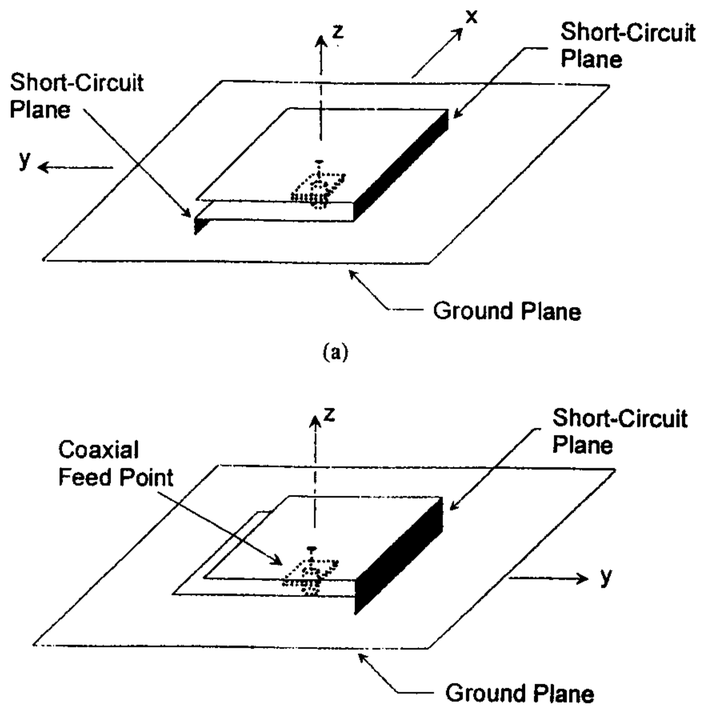

Figure 9.44 Geometry of dual-frequency and broadband stacked patch antennas utilizing quarter-wave patches: (a) Dual-frequency antenna and (b) broadband antenna. (From [71]. © 1999 IEEE. Reprinted with permission.)

16 mm at 1.8 GHz. The cross-polarization level for this antenna is very high, reaching −3 dB for $\theta = 45°$ in the $\phi = 0°$ and 180° planes. It has been suggested that these stacked configurations should find applications where wider bandwidth, dual-band operation and diversity of radiation properties are needed [71].

References

[1] Pozar, D. M., "A Review of Bandwidth Enhancement Techniques for Microstrip Antennas," in *Microstrip Antennas, The Analysis and Design of Microstrip Antennas and Arrays*, D. M. Pozar and D. H. Schaubert (Eds.), IEEE Press, New York, 1995, pp. 157–166.

[2] Sanchez-Hernandez, D., and I. D. Robertson, "A Survey of Broadband Microstrip Patch Antennas," *Microwave J.*, Sept. 1996, pp. 60–84.

[3] Zurcher, J.-F., and F. E. Gardiol, *Broadband Patch Antennas*, Artech House, Norwood, MA, 1995.

[4] Alexopoulos, N. G., et al., "Substrate Optimization for Integrated Circuit Antennas," *IEEE Trans. Microwave Theory and Techniques*, Vol. MTT-31, 1983, pp. 550–557.

[5] Pozar, D. M., "Microstrip Antennas," *Proc. IEEE*, Vol. 80, 1992, pp. 79–91.

[6] Pozar, D. M., "Considerations for Millimeter Wave Printed Antennas," *IEEE Trans. Antennas and Propagation*, Vol. AP-31, 1983, pp. 740–747.

[7] James, J. R., and P. S. Hall, Eds., *Handbook of Microstrip Antennas*, Vol. 1, Peter Peregrinus, London, UK, 1989.

[8] Pozar, D. M., "A Microstrip Antenna Aperture-Coupled to a Microstrip Line," *Electron. Lett.*, Vol. 21, 1985, pp. 49–50.

[9] Sullivan, P. L., and D. H. Schaubert, "Analysis of an Aperture-Coupled Microstrip Antenna," *IEEE Trans. Antennas and Propagation*, Vol. AP-34, 1986, pp. 977–984.

[10] Pozar, D. M., "A Reciprocity Method of Analysis for Printed Slot and Slot-Coupled Microstrip Antennas," *IEEE Trans. Antennas and Propagation*, Vol. AP-34, 1986, pp. 1439–1445.

[11] Pozar, D. M., and S. M. Voda, "A Rigorous Analysis of a Microstripline Fed Patch Antenna," *IEEE Trans. Antennas and Propagation*, Vol. AP-35, 1987, pp. 1343–1350.

[12] Targonski, S. D., and D. M. Pozar, "Design of Wideband Circularly Polarized Aperture-Coupled Microstrip Antennas," *IEEE Trans. Antennas and Propagation*, Vol. AP-41, 1993, pp. 214–220.

[13] Himdi, M., J. P. Daniel, and C. Terret, "Analysis of Aperture-Coupled Microstrip Antenna Using Cavity Method," *Electron. Lett.*, Vol. 25, 1989, pp. 391–392.

[14] Saed, M. A., "Efficient Method for Analysis and Design of Aperture-Coupled Rectangular Microstrip Antennas," *IEEE Trans. Antennas and Propagation*, Vol. AP-41, 1993, pp. 986–988.

[15] Yazidi, M. El., M. Himdi, and J. P. Daniel, "Aperture-Coupled Microstrip Antenna for Dual Frequency Operation," *Electron. Lett.*, Vol. 29, 1993, pp. 1506–1508.

[16] Himdi, M., J. P. Daniel, and C. Terret, "Transmission Line Analysis of Aperture-Coupled Microstrip Antenna," *Electron. Lett.*, Vol. 25, 1989, pp. 1229–1230.

[17] Yazidi, M. El., M. Himdi, and J. P. Daniel, "Transmission Line Analysis of Nonlinear Slot Coupled Microstrip Antenna," *Electron. Lett.*, Vol. 28, 1992, pp. 1406–1408.

[18] Ittipiboon, A., et al., "A Modal Expansion Method of Analysis and Measurement on Aperture-Coupled Microstrip Antenna," *IEEE Trans. Antennas and Propagation*, Vol. AP-39, 1991, pp. 1567–1574.

[19] Bhattacharyya, A. K., Y. M. M. Antar, and A. Ittipiboon, "Spectral Domain Analysis of Aperture-Coupled Microstrip Patch Antennas," *IEE Proc.*, Vol. 139, Pt. H, 1992, pp. 459–464.

[20] Das, B. N., and K. K. Joshi, "Impedance of a Radiating Slot in the Ground Plane of a Microstripline," *IEEE Trans. Antennas and Propagation*, Vol. AP-30, 1982, pp. 922–926.

[21] Gupta, K. C., et al. *Microstrip Lines and Slotlines*, 2nd ed., Artech House, Norwood, MA, 1996.

[22] Zurcher, J.-F., "The SSFIP: A Global Concept for High-Performance Broadband Planar Antennas," *Electron. Lett.*, Vol. 24, 1988, pp. 1433–1435.

[23] Gronau, G., and I. Wolff, "Aperture Coupling of Rectangular Microstrip Resonator," *Electron. Lett.* Vol. 22, 1986, pp. 554–556.

[24] Harrington, R. F., *Time Harmonic Electromagnetic Fields*, McGraw-Hill, New York, 1968.

[25] Croq, F., and A. Papiernik, "Large Bandwidth Aperture-Coupled Microstrip Antenna," *Electron. Lett.*, Vol. 26, 1990, pp. 1293–1294.

[26] Hall, R. C., "Full-Wave Aperture-Coupled Patch Antenna," *Electron. Lett.*, Vol. 29, 1993, pp. 2073–2074.

[27] Simons, R. N., and R. Q. Lee, "Coplanar Waveguide Aperture-Coupled Patch Antennas With Ground Plane/Substrate of Finite Extent," *Electron. Lett.*, Vol. 28, 1992, pp. 75–76.

[28] Long, S. A., and M. D. Walton, "A Dual-Frequency, Stacked Circular Disc Antenna," *IEEE Antennas and Propagation Symp. Digest*, 1978, pp. 260–263.

[29] Chen, C. H., et al., "Broadband Two-Layer Microstrip Antenna," *IEEE Antennas and Propagation Symp. Digest*, 1984, pp. 251–254.

[30] Lee, R. Q., et al., "Characteristics of a Two-Layer Electromagnetically Coupled Rectangular Patch Antenna," *Electron. Lett.*, Vol. 23, 1987, pp. 1070–1072.

[31] Damiano, J. P., et al., "Dual-Frequency and Offset Multilayer Microstrip Antennae," *8th IEE Int. Conf. Antennas and Propagation*, 1993, pp. 732–735.

[32] Croq, F., G. Kossiavas, and A. Papiernik, "Stacked Resonators for Bandwidth Enhancement: A Comparison of Two Feeding Techniques," *IEE Proc.*, Vol. 140, Pt. H, 1993, pp. 303–308.

[33] Tsao, C. H., et al., "Aperture-Coupled Patch Antennas With Wide-Bandwidth and Dual Polarization Capabilities," *IEEE Antennas and Propagation Symp. Digest*, 1988, pp. 936–939.

[34] Ittipiboon, A., et al., "Slot-Coupled Stacked Microstrip Antennas," *IEEE Antennas and Propagation Symp. Digest*, 1990, pp. 1108–1111.

[35] Croq, F., and D. M. Pozar, "Millimeter-Wave Design of Wide-Band Aperture-Coupled Stacked Microstrip Antennas," *IEEE Trans. Antennas and Propagation*, Vol. AP-39, 1991, pp. 1770–1776.

[36] Targonski, S. D., R. B. Waterhouse, and D. M. Pozar, "Design of Wide-Band Aperture-Stacked Patch Microstrip Antennas," *IEEE Trans. Antennas and Propagation*, Vol. AP-46, 1998, pp. 1245–1251.

[37] Damiano, J. P., et al., "Study of Multilayer Microstrip Antennas With Radiating Elements Of Various Geometry," *IEE Proc.*, Vol. 137, Pt. H, 1990, pp. 163–170.

[38] Dubost, G., and A. Zerguerras, "Transmission Line Model Analysis of Arbitrary Shape Symmetrical Patch Antenna Coupled With a Director," *Electron. Lett.*, Vol. 26, 1990, pp. 952–954.

[39] Gomez-Tagle, J., and C. G. Christodoulou, "Extended Cavity Model Analysis of Stacked Microstrip Ring Antennas," *IEEE Trans. Antennas and Propagation*, Vol. AP-45, 1997, pp. 1626–1635.

[40] Mittra, R., et al., "Microstrip Patch Antennas for GPS Applications," *IEEE Antennas and Propagation Symp. Digest*, 1993, pp. 1478–1481.

[41] Schaubert, D. H., and F. G. Farrar, "Some Conformal Printed Circuit Antenna Designs," *Proc. Workshop Printed Circuit Antenna Tech.*, New Mexico State University, Las Cruces, NM, Oct. 1979, pp. 5/1–21.

[42] Kumar, G., and K. C. Gupta, "Broadband Microstrip Antennas Using Additional Resonators Gap Coupled to The Radiating Edges," *IEEE Trans. Antennas and Propagation*, Vol. AP-32, 1984, pp. 1375–1379.

[43] Kumar, G., and K. C. Gupta, "Nonradiating Edges and Four Edges Gap Coupled Multiple Resonator Broadband Microstrip Antennas," *IEEE Trans. Antennas and Propagation*, Vol. AP-33, 1985, pp. 173–178.

[44] Wood, C., "Improved Bandwidth of Microstrip Antennas Using Parasitic Elements," *Proc. IEE*, Vol. 127, Pt. H, 1980, pp. 231–234.

[45] Entsehladen, E., and U. Nagel, "Microstrip Patch Array Antenna," *Electron. Lett.*, Vol. 20, 1984, pp. 931–933.

[46] Aanandan, C. K., P. Mohanan, and K. G. Nair, "Broadband Gap Coupled Microstrip Antenna," *IEEE Trans. Antennas and Propagation*, Vol. AP-38, 1990, pp. 1581–1586.

[47] Croq, F., and D. M. Pozar, "Multifrequency Operation of Microstrip Antennas Using Aperture-Coupled Parallel Resonators," *IEEE Trans. Antennas and Propagation*, Vol. AP-40, 1992, pp. 1367–1374.

[48] Reddy, V. S., and R. Garg, "A Broadband Coupled Strips Microstrip Antenna," private communication.

[49] Hall, P. S., "Multioctave Bandwidth Log-Periodic Microstrip Antenna Array," *Proc. IEE*, Vol. 133, Pt. H, 1986, pp. 127–136.

[50] Kumar, G., and K. C. Gupta, "Directly Coupled Multiple Resonator Wideband Microstrip Antennas," *IEEE Trans. Antennas and Propagation*, Vol. AP-33, 1985, pp. 588–593.

[51] Prior, C. J., and P. S. Hall, "Microstrip Disc Antenna With Short-Circuited Annular Ring," *Electron. Lett.*, Vol. 21, 1985, pp. 719–721.

[52] Miller, P. A., et al., "A Wide Bandwidth Low Sidelobe Low Profile Microstrip Array Antenna for Communication Applications," *ISAP Proc. Digest*, 1989, pp. 525–528.

[53] Cho, Y. K., J. P. Hong, and H. Son, "New Radiating Edges Coupling Model for the Gap Between Two Rectangular Microstrip Patch Antennas," *Electron. Lett.*, Vol. 26, 1990, pp. 1295–1297.

[54] Cho, Y. K., et al., "Improved Analysis Method for Broadband Rectangular Microstrip Antenna Geometry Using E-Plane Gap Coupling," *Electron. Lett.*, Vol. 29, 1993, pp. 1907–1909.

[55] Yano, S., and A. Ishimaru, "Broadbanding of Microstrip Antennas by Orthogonal Polarizations," *IEEE Antennas and Propagation Symp. Digest*, 1981, pp. 363–365.

[56] Huynh, T., and K. F. Lee, "Single-Layer Single Patch Wideband Microstrip Antenna," *Electron. Lett.*, Vol. 31, 1995, pp. 1310–1312.

[57] Lee, K. F., et. al., "Experimental and Simulation Studies of the Coaxially Fed U-Slot Rectangular Patch Antenna," *Proc. IEE, Microwaves, Antennas and Propagation*, Vol. 144, 1997, pp. 354–358.

[58] Chow, Y. L., et al., "A Design Theory on Broadband Patch Antennas With Slot," *IEEE Antennas and Propagation Symp. Digest*, 1998, pp. 1124–1127.

[59] Dubost, G., *Flat Radiating Dipoles and Applications to Arrays*, Research Studies Press, New York, 1981.

[60] Daniel, J. P., et al., "Research on Antennas and Arrays: Structures Rayonnantes," *Antennas and Propagation Society Magazine*, Vol. 35, Feb. 1993, pp. 14–38.

[61] Pues, H. F., and A. R. Van de Capelle, "An Impedance Matching Technique for Increasing the Bandwidth of Microstrip Antennas," *IEEE Trans. Antennas and Propagation*, Vol. AP-37, 1989, pp. 1345–1354.

[62] Paschen, D. A., "Practical Examples of Integral Broadband Matching of Microstrip Antenna Elements," *Proc. 1986 Antenna Applications Symp.*, 1986, pp. 199–217.

[63] Herscovici, N., "A Wide-Band Single-Layer Patch Antenna," *IEEE Trans. Antennas and Propagation*, Vol. AP-46, 1998, pp. 471–474.

[64] Herscovici, N., "New Considerations in the Design of Microstrip Antennas," *IEEE Trans. Antennas and Propagation*, Vol. AP-46, 1998, pp. 807–812.

[65] Johnson, R. C., and H. Jasik (Eds.), *Antenna Engineering Handbook*, 2nd ed., McGraw-Hill, New York, 1984, Chap. 43.

[66] Carlin, H. J., and J. J. Comiak, "A New Method of Broadband Equalization Applied to Microwave Amplifiers," *IEEE Trans. Microwave Theory and Techniques*, Vol. MTT-27, 1979, pp. 93–99.

[67] An, H., et al., "Broadband Microstrip Antenna Design With the Simplified Real Frequency Technique," *IEEE Trans. Antennas and Propagation*, Vol. AP-42, 1994, pp. 129–136.

[68] Fayyaz, N., and S. S. Naeini, "Bandwidth Enhancement of a Rectangular Patch Antenna by Integrated Reactive Loading," *IEEE Antennas and Propagation Symp. Digest*, 1998, pp. 1100–1103.

[69] Wong, K. L., and Y. F. Lin, "Small Broadband Rectangular Microstrip Antenna With Chip-Resistor Loading," *Electron. Lett.*, Vol. 33, 1997, pp. 1593–1594.

[70] Wong, K. L., and Y. F. Lin, "Microstrip-Line-Fed Compact Microstrip Antenna With Broadband Operation," *IEEE Antennas and Propagation Symp. Digest*, 1998, pp. 1120–1123.

[71] Zaid, L., et al., "Dual-Frequency and Broadband Antennas With Stacked Quarter-Wavelength Elements," *IEEE Trans. Antennas and Propagation*, Vol. AP-47, 1999, pp. 654–660.

[72] Au, T. M., and K. M. Luk, "Effect of Parasitic Elements on the Characteristics of Microstrip Antenna," *IEEE Trans. Antennas and Propagation*, Vol. AP-39, 1991, pp. 1247–1251.

[73] Barilese, B., and C. Peixeiro, "Wide-Band Microstrip Patch Antenna Elements," *IEEE AP-S Int. Symp. Digest*, 1998, pp. 1104–1107.

[74] Zurcher, B., J.-F. Zurcher, and F. Gardiol, "Broadband Microstrip Radiators: The SSFIP Concept," *Electromagnetics*, Vol. 9, 1989, pp. 385–393.

[75] Reddy, V. S., and R. Garg, "Design of Large Bandwidth Multilayered Aperture Coupled Microstrip Antenna," *Proc. National Conf. Commun., NCC-99*, Kharagpur, India, 1999, pp. 793–798.

10

Loaded Microstrip Antennas and Applications

10.1 Introduction

Modern communication systems, such as those for satellite links (GPS, vehicular, etc.), for mobile communication, and for emerging applications, such as wireless local-area networks (WLANs), often require compact antennas at low cost. Further, due to their lightness, microstrip antennas are well suited for airborne applications, such as synthetic aperture radar (SAR) systems and scatterometers. In addition to compactness, the antenna may be required to provide circular polarization as in satellite links. In some applications, operation at two or more discrete bands and an arbitrary separation of bands is desired. Further, all bands may be required to have the same polarization, radiation pattern, and input impedance characteristics.

It may not be possible to achieve these objectives from the basic microstrip antennas having regular shapes that have been discussed in earlier chapters. The range of applications of microstrip antennas and their performance can be improved considerably by suitably loading them. Some examples of loaded microstrip antennas were given in Chapters 4, 8, and 9, where loading of the basic shape was used to obtain circular polarization, frequency tuning, broadbanding, impedance matching, higher gain, and so on. It is the goal of this chapter to discuss loading in a general way to obtain characteristics such as size reduction, dual-frequency operation, polarization control, radiation pattern control, and frequency agility.

A survey of various papers published on the applications of microstrip antennas shows that shorts, stubs, and slot loadings have been used for the

most part. Therefore, we consider only the effect of these loadings although loading can take various forms such as stub loading, slot or notch loading, short circuits or vias, parasitic coupling, substrate loading, superstrate cover, resistors, capacitors, and diodes.

A microstrip antenna can easily be made to resonate at many frequencies associated with various modes. The characteristic of each mode is different and is determined by the resonant frequency, radiation pattern, polarization, bandwidth, and so on. For a given feed location, if the patch is now loaded with a short, the field and current distributions for various modes will be disturbed and therefore their characteristics will change. This change will depend on the amount of load and the mode under consideration. For example, a short placed at the nodal line of a mode will hardly affect its characteristics, whereas another mode with electric field maximum at the short will experience the maximum change. If used properly, the loading effect can be used to obtain a desirable change in the antenna characteristics.

First, we discuss some applications of loaded microstrip antennas to realize polarization diversity, frequency agility, and radiation pattern control. Next, loading will be used to reduce the size of circularly polarized antennas, and dual-frequency operation antennas. Various types of compact antennas are listed. The planar inverted-F antenna, a compact antenna suggested for mobile handsets, is described in detail.

10.2 Polarization Diversity Using Microstrip Antennas

Polarization diversity [1] of reception is important to counter the effect of fading in communications, especially in mobile communications. The polarization of a microstrip antenna can be selected by making a proper choice for the feed location. For example, the square microstrip antenna shown in Figure 10.1 [1] can be used to transmit or receive vertical polarization or horizontal polarization depending on which feed is used and which shorting posts are not used. The two polarizations are associated with the modes (1, 0) and (0, 1) excited by the respective feeds. Simultaneous operation in two polarizations at the same frequency is possible if both feeds are used. If the square patch is replaced by a rectangular patch antenna, then it is possible to have dual-frequency and dual-polarization operation. The square patch antenna of Figure 10.1 when loaded with posts as indicated can be used for generating desired circular polarization by a proper selection of feed. The posts located along the diagonal help in the excitation of both the modes with a single feed. Proper location of the posts ensures equal amplitude and a phase difference of 90° for the two modes.

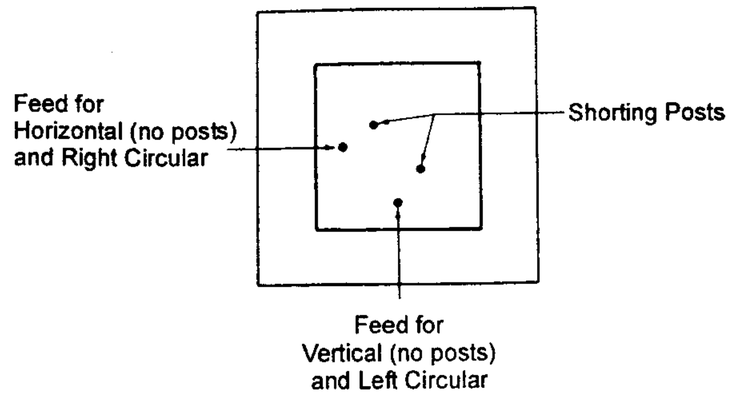

Figure 10.1 Dual-feed antenna for horizontal and vertical, or left- or right-hand circular polarizations. (From [1]. © 1981 IEEE. Reprinted with permission.)

It is also possible to obtain four different polarizations—horizontal, vertical, right-hand circular, and left-hand circular—with a single feed. This is shown in Figure 10.2 for a square patch antenna. The feed is located along the diagonal and the shorting pins are located along the center lines. The polarization of the signal is decided by the selection of the shorting pins, and can be explained on the basis of change in resonant frequency produced by the loading effect of the short.

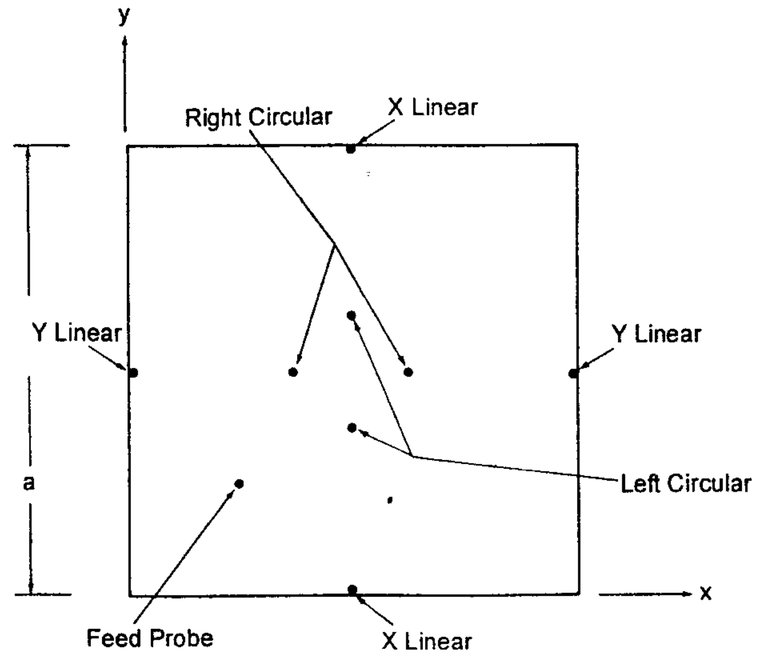

Figure 10.2 Single-feed square patch antenna with four pairs of posts for obtaining four different polarizations. (From [1]. © 1981 IEEE. Reprinted with permission.)

The square patch, without shorting pins, supports both the (1, 0) and (0, 1) modes with x-oriented and y-oriented polarizations. The resonant frequency for both the modes is the same. Because the feed probe is located along the diagonal, both the modes are excited with equal amplitude and phase. By adding shorting pins along the center line $x = a/2$ (see Figure 10.2), the resonant frequency of the (0, 1) or y-oriented mode can be raised without affecting the other mode. Therefore, the mode with desired polarization (x or y) can be selected by shifting the resonant frequency of the undesired mode far above that of the desired mode. The required large frequency shift is obtained by placing the shorting pins at or near the edges of the patch as shown in the figure.

Circular polarization is obtained by exciting both the x- and y-polarized modes with equal amplitude and 90° phase difference. This can be accomplished by raising the resonant frequency of one mode slightly above the other and operating at a frequency midway between the two frequencies. Then the input impedance of one mode is inductive and the other mode is capacitive. By adjusting the difference between the resonant frequencies, both the modes can be excited with equal amplitude and 90° phase difference.

The pair of posts inside the patch raises the resonant frequency of one of the modes only. Figure 10.3 [1] shows the measured axial ratio of a typical patch antenna as the separation between a pair of shorting posts is varied.

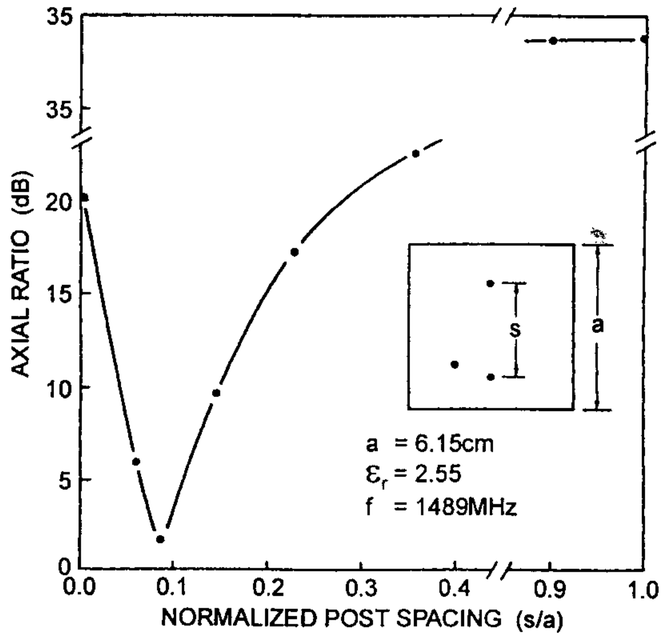

Figure 10.3 Measured axial ratio as a function of post spacing s/a for a square patch antenna on a 1.6-mm Teflon fiberglass substrate. (From [1]. © 1981 IEEE. Reprinted with permission.)

When $s/a = 0$, the posts are at the center and they do not affect either mode. Because both the modes are excited with equal amplitude by the diagonal feed, the polarization is linear oriented along the feed diagonal. When $s/a = 0.09$, the resonant frequencies of the two modes are offset enough to obtain a phase difference of about 90° and the antenna is circularly polarized. As the posts are moved further apart, that is, as they approach the respective edge, the resonant frequency of the vertically polarized mode is further increased and the polarization of the antenna becomes horizontal linear with large axial ratio as shown in the figure. The input impedance of the antenna changes with the movement of the posts, but the VSWR remains good for all senses of polarization. The change in the resonant frequency of a mode with short circuit loading is discussed in Section 10.5.

Although one post is sufficient to raise the resonant frequency of any mode, two symmetrically located posts are used so that the antenna structure is symmetric with respect to loading, and the cross-polarized component in the radiation pattern due to loading is minimized. The shorting posts can be realized by microwave switching diodes for precise control of the resonant frequency and polarization switching applications.

10.3 Frequency Agile Microstrip Antennas

Frequency agile microstrip elements are elements whose resonant frequency can be adjusted over a wide range without any variation in the input impedance or radiation pattern. The resonant frequency of a microstrip antenna can be changed in a number of ways. These include mechanical tuning and electronic tuning. In principle, any reactive loading of the patch antenna will give rise to a change in the resonant frequency. Some of the techniques that have been used are shorting pins or posts, stubs, variable dielectric layer thickness, varactor diodes, and optical control. Pins, posts, stubs, and so on give rise to mechanical tuning, whereas varactor and switching diodes embedded in the patch and optical control of PIN diode impedance can be used for electronic tuning or frequency agility of the patch antenna. Mechanical tuning of antennas was described in Chapter 4. The frequency agile antennas or electronic tuning is described next.

10.3.1 Varactor-Tuned Microstrip Antennas

Fixed or variable capacitors can be used to change the resonant frequency of a patch antenna. Capacitive loading lowers the resonant frequency. The use of varactor diodes to obtain frequency agile microstrip antennas was first reported in 1982 by Bhartia and Bahl [2]. In this approach, two varactor

diodes are embedded in the patch such that the symmetry of the patch is retained, which is essential to minimize the cross-polarization component in the radiation pattern. Configuration of this type of antenna is shown in Figure 10.4(a). A frequency tuning range of about 30% was achieved depending on the diode characteristics and the position of the diode in the patch.

The mechanism responsible for the change in resonant frequency with the applied reverse bias to the diodes can best be explained by means of the

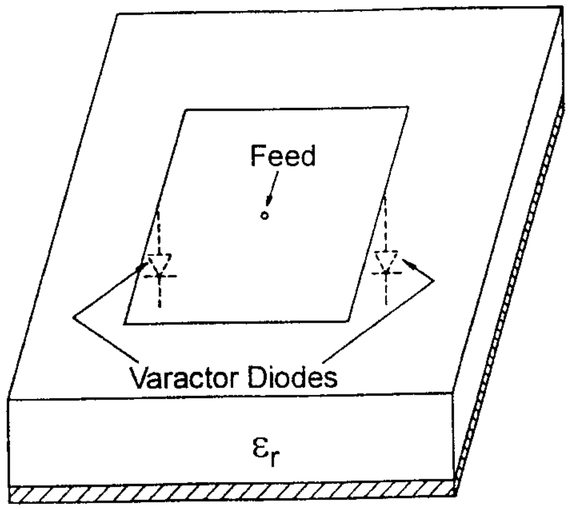

(a)

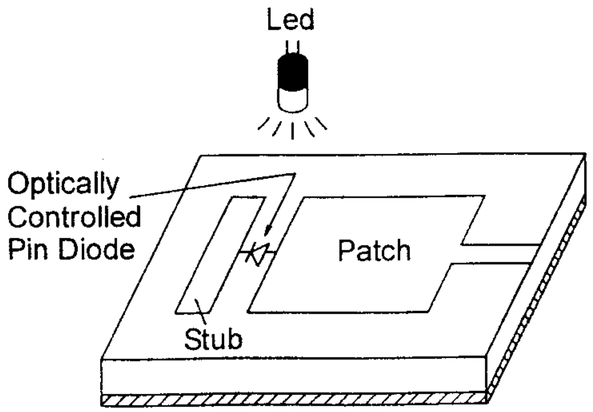

(b)

Figure 10.4 Electronic and optical tuning of microstrip antennas. (a) Electronic tuning using varactor diodes. (b) Optical tuning using PIN diodes. (From [7]. © 1986 IEEE. Reprinted with permission.)

tank circuit of the patch. Consider the equivalent circuit of the diode loaded patch as shown in Figure 10.5 [3]. Here, R_{pat}, L_{pat}, and C_{pat} represent the lumped element equivalent circuit parameters of the patch, and L_{feed} is the feed inductance associated with the probe feed. The equivalent circuit parameters of the diode are represented by L_p, R_s, C_j, and C_p. The junction capacitance C_j of the diode is used to tune out tank circuit inductance and therefore the resonant frequency of the antenna can be changed. As the reverse bias level of the diode is increased, the junction capacitance C_j decreases and the resonant frequency of the loaded patch increases, until it equals that of the unloaded patch. The tuning curve, which is nonlinear with bias, is shown in Figure 10.6 [4]. Further studies have shown that the efficiency of this type of antenna becomes a function of the bias to the diodes [5] because of the power dissipated in the diodes. The efficiency varies from 95% at high reverse bias to about 30% at low bias. As a direct consequence of the reduced efficiency of the antenna, the radar cross-section of the patch decreases.

The varactor loaded patch antenna can be designed to operate at two vastly different frequencies. In a particular design by Waterhouse and Shuley the rectangular microstrip patch was designed to resonate at 2.1 GHz [6]. The varactor diodes were placed at $0.3L$ and $0.7L$, where L is the resonant length of the patch corresponding to 2.1 GHz. The loading by varactor diodes resulted in dual-frequency operation of the antenna as explained in Section 10.5. The lower resonant frequency could be tuned between 350 and 650 MHz as the varactor bias changed from −2.5 to −17V. A varactor loaded patch has been used as an element in scanning arrays [3]. The full-wave integral equation

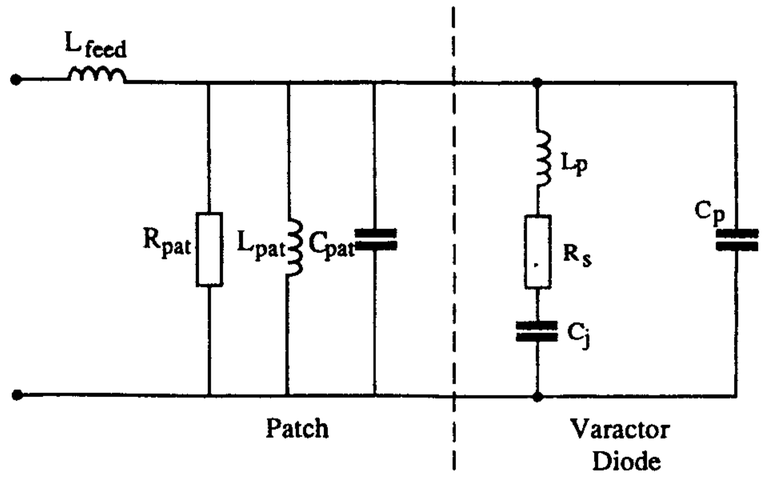

Figure 10.5 Simple equivalent circuit of a probe-fed microstrip patch antenna loaded with a varactor diode. (From [3]. © 1993 IEEE. Reprinted with permission.)

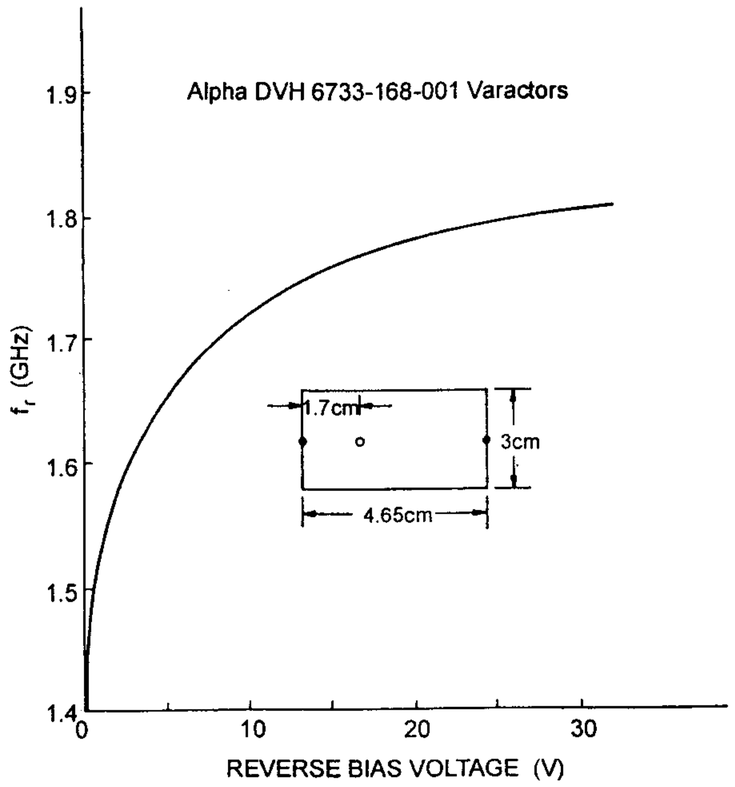

Figure 10.6 Tuning curve of a varactor loaded rectangular microstrip antenna. (From [4]. © 1982 IEEE. Reprinted with permission.)

approach has been used to accurately predict the impedance and radiation characteristics of a diode loaded patch [3].

10.3.2 Optical Tuning of Patch Antennas

Patch antennas can be optically tuned over a narrow frequency range of about 100 MHz. A schematic of this approach is shown in Figure 10.4(b) [7]. The antenna consists of a patch and a stub joined by an optically controlled PIN diode. When the PIN diode is reverse biased, it acts as an open circuit and the resonant frequency of the antenna corresponds to that of the patch alone. By forward biasing the PIN diode to the level of the short circuit, the patch and the stub act in tandem and the combination resonates at a lower frequency. By properly illuminating the PIN diode with light, the diode impedance can be varied from a high value to a low value. The gradual change in diode impedance with light intensity can be used to tune the antenna. It was found experimentally that an illumination of 1 W/cm^2 resulted in a 15-MHz downward shift in resonant frequency.

10.4 Radiation Pattern Control of Microstrip Antennas

In general, a microstrip antenna produces a symmetrical elevation pattern with beam in the zenith. This is because ordinarily, a single mode is dominant. Some applications require an omnidirectional radiation pattern with the maximum gain in the horizon. Higher order modes in a circular patch or an annular ring can be used to obtain maximum gain in the horizon. Guo et al. [8] have used the (0, 2) mode of the circular patch. But the size of the antenna may be too large for the 450-MHz band. Zhou has proposed a pin loaded annular ring compact antenna [9]. The geometry of this antenna is shown in Figure 10.7(a). The antenna is designed on a substrate with $\epsilon_r = 2.0$. The outer diameter of the ring is 11 cm and the inner diameter is 5.5 cm. Without the shorting pins, the antenna would resonate at 1.8 GHz, which is 4 times the desired frequency of 450 MHz. Pin 1 is closer to the feed probe and its diameter is used to control the input impedance. The resonant frequency is adjusted by moving pin 2 on the opposite side of the feed point. Measured radiation patterns at 450 MHz are plotted in Figure 10.7(b) for a ground plane diameter of 90 cm [9]. We can see that the radiation pattern resembles a dipole pattern and the maximum radiation is toward the horizon with omnidirectional radiation. The maximum gain above the ground plane is 2 dBi.

Other possible applications of loaded microstrip antennas include wide-angle impedance control to improve the scanning range of phased arrays. Waterhouse has studied several shorted patch configurations consisting of multiple posts to design an array to obtain minimal scan impedance variation for scan angles up to 80° in all the three planes, even when thick substrates are used [10]. A hybrid configuration consisting of three switching diodes is also proposed.

Surface wave effects in microstrip antennas can be suppressed considerably by surrounding the antenna by photonic bandgap (PBG) structures [11]. The PBG structures are basically periodically loaded substrates. To save substrate area, microstrip antennas can also be designed on PBG substrates [12]. PBG structures and their advantages are described in Chapter 1.

10.5 Loading Effect of a Short

We know that the size of a rectangular patch can be reduced to half by placing a short circuit at the zero electric field line, the other half being absent. This antenna is called a *short-circuited quarter-wave patch*, as discussed in Chapter 4. The introduction of shorts in this case does not load the antenna because they are being placed at the zero electric field position. Further reduction in

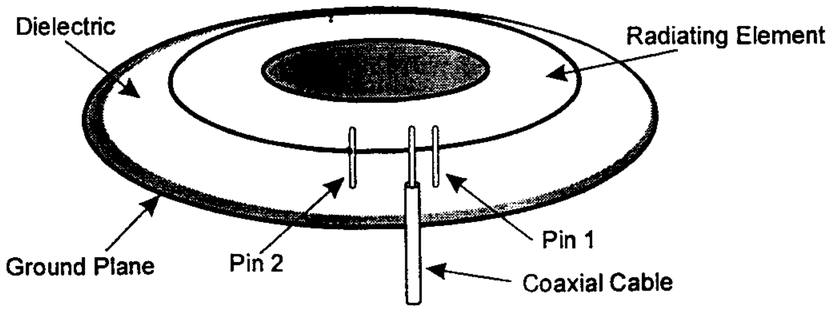

(a)

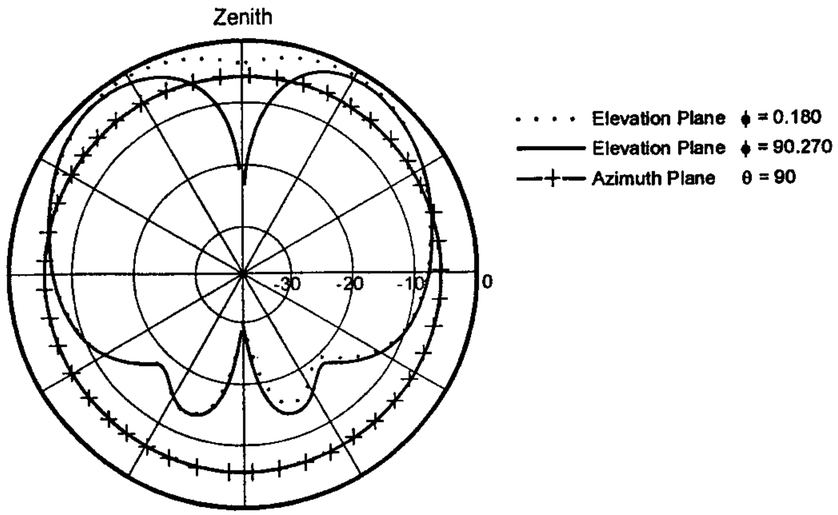

(b)

Figure 10.7 (a) Geometry of a shorting pin loaded annular ring microstrip antenna. (b) Measured radiation patterns of the antenna in part (a). (From [9]. © 1998 IEEE. Reprinted with permission.)

size can be achieved by placing the shorts at other positions. Loading by an electrical short has been used frequently as a convenient means of reducing the size of the antenna, for dual-frequency operation, for change of polarization, and so on. The field disturbances produced by a short are very complex in nature and cannot be described simply as a perturbation effect. However, the effect on input impedance *in certain cases* can be described by a shunt inductor. Depending on the application, the shorting pin may be located at the edge or at the center line of the patch. A single shorting pin at a corner of a rectangular patch gives rise to the maximum reduction in the size of the antenna.

The simplest way to realize a short in a patch antenna is by inserting a via hole or a metal pin joining the patch metalization and the ground plane at the desired location. For increased loading effect, one can use a large number of pins close together or a metal strip usually at the periphery of the patch. Microwave switching diodes may be used for electronic control.

10.5.1 Shorting Pin at the Radiating Edge

A schematic of a microstrip antenna with probe feed and a shorting pin/post is shown in Figure 10.8 [13]. The probe feed is described by its radius r_p and is located at (x_p, y_p). The shorting pin has the radius r_{ps} and is located at (x_{ps}, y_{ps}). The rectangular patch antenna is described by the dimensions $W \times L$, and the disk by radius R. The substrate parameters are h and ϵ_r. The analysis of the post loaded microstrip antenna has been carried out using the transmission line model [1, 14], cavity model [15, 16], multiport network model [17], integral equation approach [18], and FDTD technique [19, 20]. In the transmission line model of a shorted rectangular patch, the post is modeled as a shunt inductor. The models yield reasonably accurate results

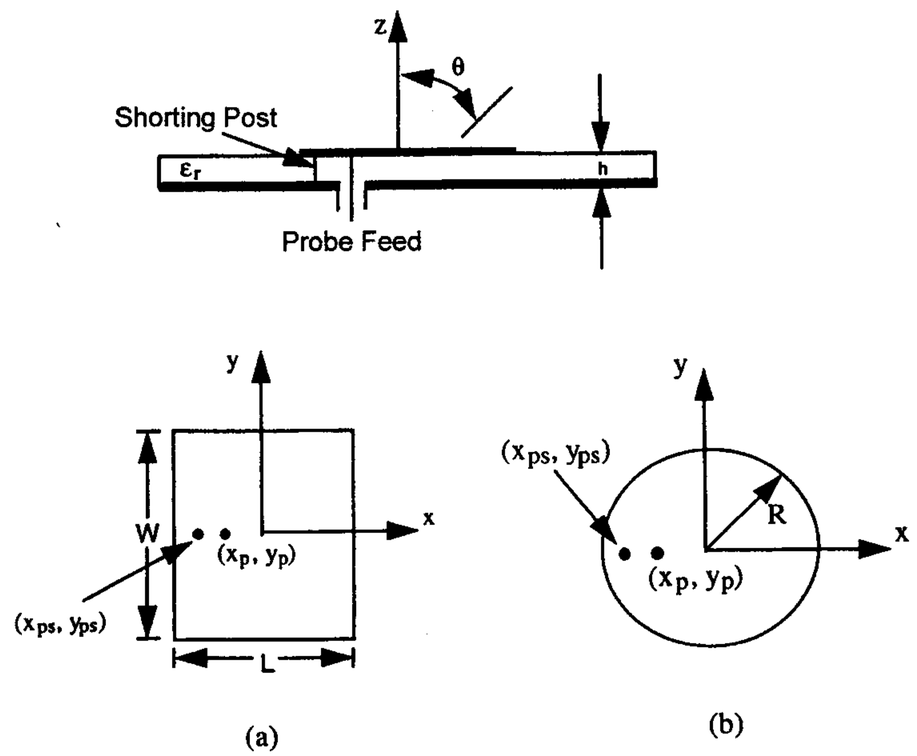

Figure 10.8 Schematic of a microstrip antenna with a shorting pin: (a) Rectangular patch and (b) circular disk. (From [13]. © 1998 IEEE. Reprinted with permission.)

when the loading effect is minor and the post is not in very close to the feed. The reason for the failure of the models is that the field distribution in a post loaded patch is complex and some of the assumptions of the model break down if the post is located at the periphery or close to the feed [16].

Full-wave techniques are capable of analyzing all situations. Attachment modes are used at the patch-post junction and the probe-patch junction to describe the current distribution in the integral equation approach [13]. The FDTD technique is better suited to analyze the loading effect of a short because it is model free and can include the effects of finite sized ground plane and substrate. Next, we give the results obtained from the full-wave approach.

We assume that the post is located on the radiating edge of the rectangular patch antenna, $x = L/2$, because one can achieve higher loading effect at these positions. Consider a square patch with $L = W = 46.5$ mm, $h = 1.6$ mm and $\epsilon_r = 4.3$, $\tan\delta = 0.02$. The resonant frequency for the unloaded patch is approximately 1.55 GHz. Let the diameters of the shorting pin and probe feed be 1 mm and located at (22.75 mm, 0), (20.75 mm, 0), respectively. For the computation of data the post was modeled as a shunt inductor with an inductance of 0.36 nH. Two resonant frequencies are observed for this configuration. The computed values are 461.5 MHz and 1.701 GHz, and the measured values are 462 MHz and 1.677 GHz [17]. When the post is moved to the corner of the patch at (22.75 mm, 22.75 mm) and the feed moved to (17.75 mm, 22.75 mm), the computed resonant frequencies changed to 369.5 MHz and 1.708 GHz, respectively. The measured frequencies are 381 MHz and 1.717 GHz [17]. The decrease in resonant frequency for the lower resonance is about 20%.

The variation of lower resonant frequency with the offset of the post from the center line ($y = 0$) is plotted in Figure 10.9. It shows that this resonant frequency decreases as the short approaches the corner of the patch. The resonant frequency is least when the short is located at the corner, that is, maximum reduction in the size of the antenna is achieved in this position of the short. Approximately, the resonant frequency is now determined by the perimeter of the patch rather than the length L. The approximate expression for the resonant frequency is given by

$$f_r = \frac{1}{4}\frac{c}{\sqrt{\epsilon_r}(L + W)} \tag{10.1}$$

That is, the resonant length of the patch corresponding to the lower resonance is approximately equal to $2(L + W)\sqrt{\epsilon_r}$ instead of $L\sqrt{\epsilon_{re}}/2$ for the TM_{10} mode. The quadrature current distribution on the patch metalization is shown in Figure 10.10 for this case. The patch currents in phase with the

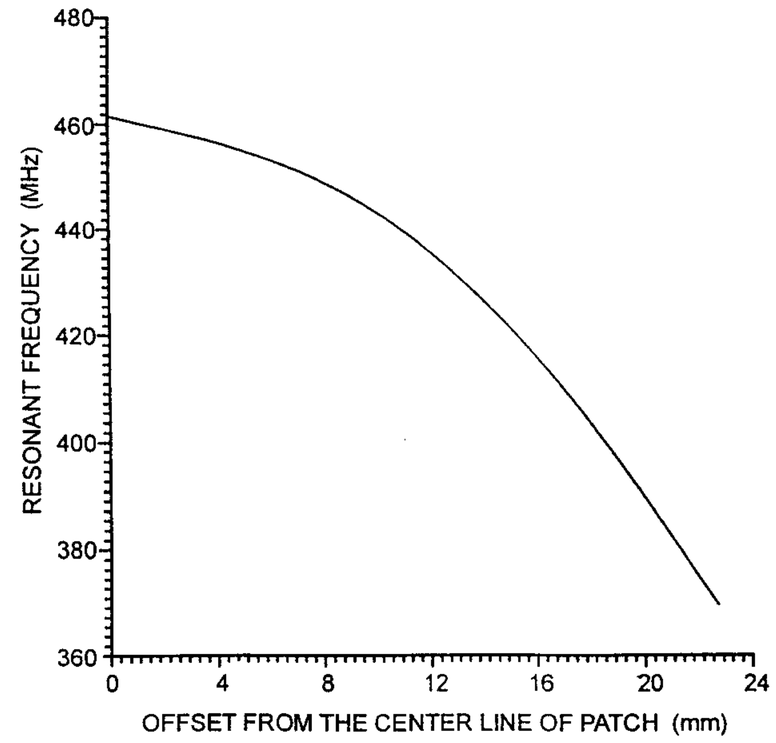

Figure 10.9 Variation of lower resonant frequency of a post loaded microstrip antenna. The post is located on a radiating edge. $L = W = 4.65$ cm, $h = 1.6$ mm, $\epsilon_r = 4.3$, $\tan\delta = 0.02$, post inductance = 0.36 nH, probe diameter = 1 mm, post diameter = 1 mm.

probe currents are very small. We can see from Figure 10.10 that the current distribution is very much different than that of the TM_{10} mode. It is maximum at the short and decreases away from it. Since the input resistance is defined as the ratio of voltage and current at the feed, it is expected that the input resistance will be minimum near the short position and increase away from it.

Variation of input resistance with increased separation between the short and feed is plotted in Figure 10.11. We can see that the input resistance increases away from the short and therefore the feed should be located close to the short for 50Ω input resistance.

The impedance (VSWR < 2) bandwidth of the antenna is plotted in Figure 10.12 as a function of the short position on the radiating edge. The bandwidth of the antenna increases from 6 to 8.8 MHz as the electrical thickness of the substrate increases with the increase in resonant frequency. The E_θ and E_ϕ radiation patterns of the antenna in the $\phi = 0°$ plane are plotted in Figure 10.13 for the post at the corner of the patch. The radiation patterns in the

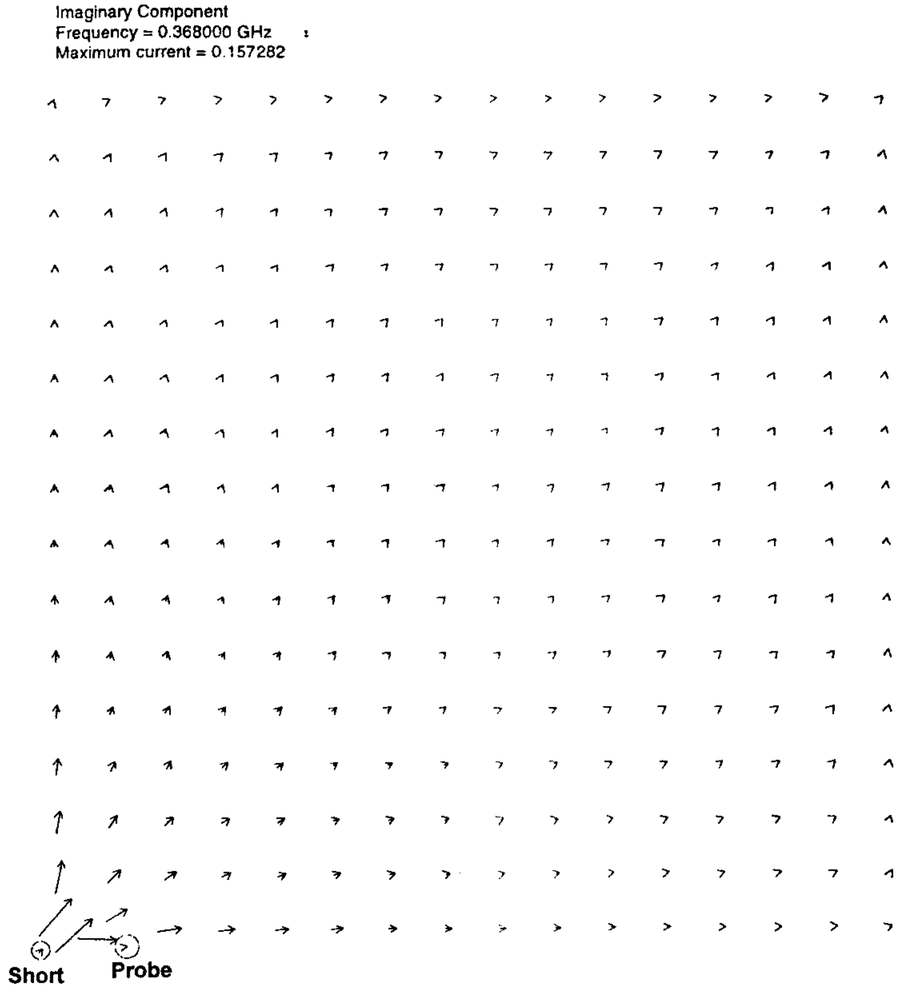

Figure 10.10 Variation of quadrature current on the patch when the post is located at the corner. Other parameters are the same as in Figure 10.9.

$\phi = 90°$ plane are similar to those in the $\phi = 0°$ plane because of the square patch geometry. The cross-polar level is found to be as high as the copolar level when the post is located at the corner. The high value of the cross-polar component is related to the patch current distribution of Figure 10.10. Variation of cross-polar level with the position of post is plotted in Figure 10.14. The cross-polar component is found to decrease as the post approaches the center line. Note that the substrate used in the example is lossy, $\tan\delta = 0.02$; otherwise, for low loss substrates, the variations of antenna characteristics with post position are much larger.

Analysis of the results presented above shows that loading by a post can be used to reduce the size of a microstrip antenna. However, the size reduction is accompanied by reduced gain and bandwidth, increased resonant resistance

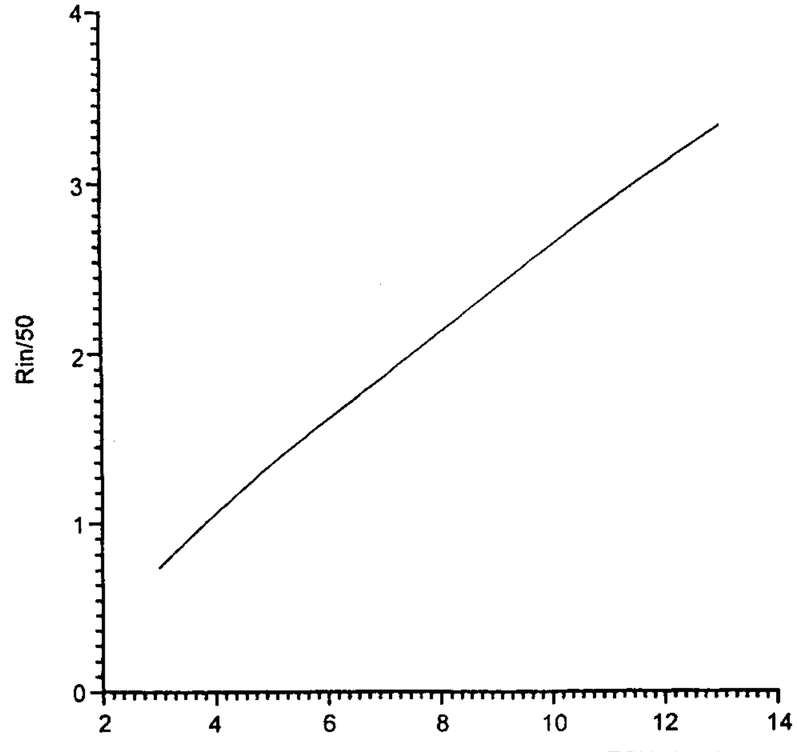

Figure 10.11 Variation of input resistance with feed location when the post is located at the corner. Other parameters are the same as in Figure 10.9.

and cross-polar level, and tight tolerance for the feed position. The compact patch antennas described in Section 10.6 try to overcome these deficiencies. The various approaches used include thicker substrate for increasing the bandwidth, aperture coupling of feed to overcome impedance mismatch between the feed line impedance and antenna impedance, use of a superstrate to increase the gain of the antenna, and so on. Parametric study of a disk with a single post was carried out in [13] and yields valuable insight into the design of an antenna. Techniques to improve mechanical tolerances are also described. A summary of these results is given in Table 10.1. These conclusions are true, independent of the patch shape.

10.5.2 Shorting Pin on the Center Line of the Patch

The geometry of a rectangular patch antenna with a shorting pin on the center line $y = 0$ is shown in Figure 10.15(a). This loading suppresses the excitation of $(0, n)$, $n = 2, 4, 6, \ldots$, modes because the pin is located at the maximum electric field position corresponding to these modes. For the same reason, the

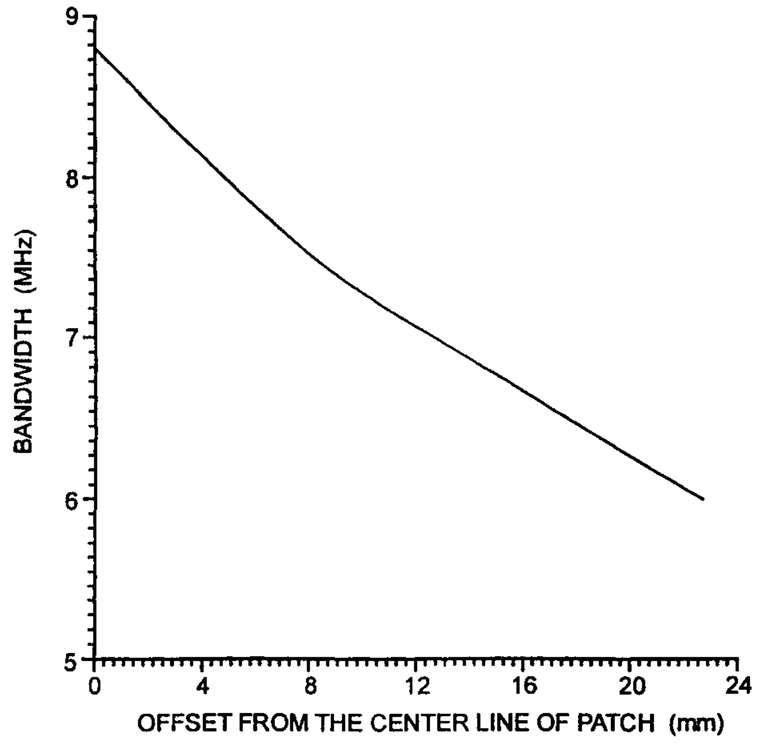

Figure 10.12 Variation of impedance bandwidth with the position of the short on the radiating edge. Other parameters are the same as in Figure 10.9.

feed probe is also located on the line of symmetry. This type of loading produces two lowest resonant frequencies with the same polarization and can be excited with good matching using a single probe feed [15].

The variation of two frequencies and frequency ratio with shorting pin position is shown in Figure 10.15(b) for a typical rectangular patch antenna [15]. The 10-dB return loss bandwidth of the antenna is found to lie between 1.4% and 1.8%, respectively. The size reduction of the antenna at the lowest frequency is roughly 2.6. A frequency ratio between 2.0 and 3.2 has been obtained with reduced antenna size and gain, and higher cross-polarization level in the H plane. The reduction in size and gain and the increase in cross-polarization level are the characteristic features of loading by a short as described earlier. The cross-polarization level can be reduced by symmetrical loading of the patch, that is, a pair of pins symmetric with respect to the y axis are used as in Figure 10.3. A simplified transmission line model without mutual coupling between the radiating ends was used by Schaubert to explain the lower resonant frequency [1]. The model was refined by Sengupta to better explain the resonant frequency [14].

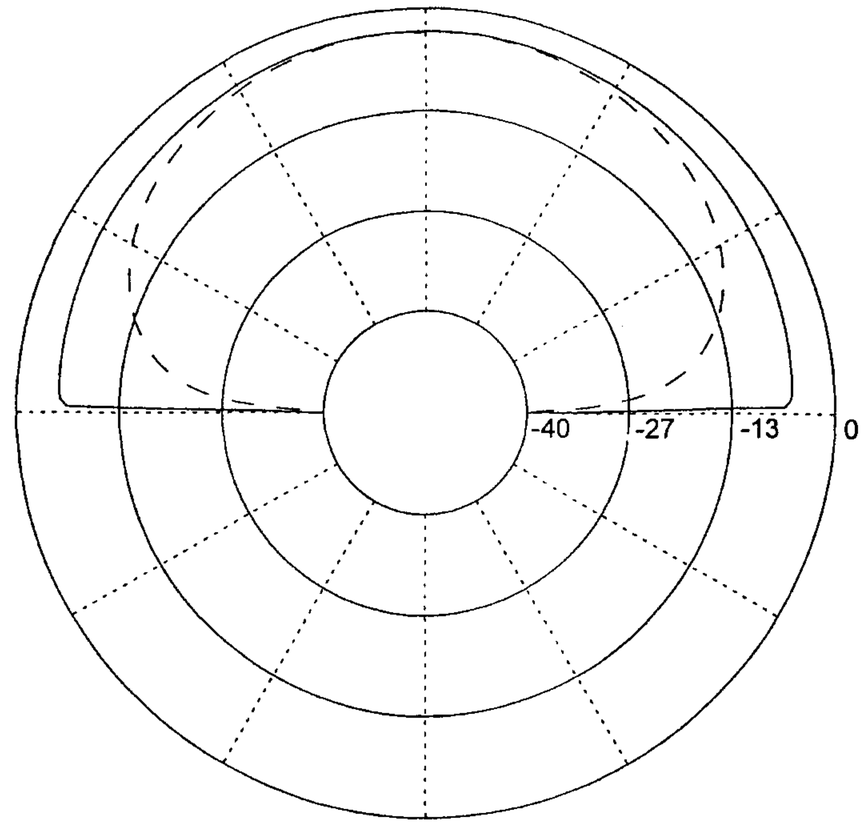

Figure 10.13 E_θ and E_ϕ radiation patterns of the patch antenna (in the $\phi = 0°$ plane) with a short at a corner. Antenna parameters are the same as in Figure 10.9 and f = 368 MHz; ____, E_θ; ----, E_ϕ.

10.6 Compact Patch Antennas

10.6.1 Compact Linearly Polarized Antennas

One of the aims of reducing the size of the antenna is for use in telephone handsets for mobile communications. Geometries of some compact microstrip antennas are given in Figures 10.16 and 10.17. Data for these antennas and their performance are listed in Table 10.2 [21–32]. The data given in the parentheses refer to the unloaded antenna.

We can see from Table 10.2 that various techniques have been explored to develop a compact antenna without sacrificing the gain or cross-polarization performance. In this respect, a triangular patch antenna with a short at the tip provides the most compact antenna with a relatively better cross-polarization level. The gain of the antenna can be improved by superstrate loading. However,

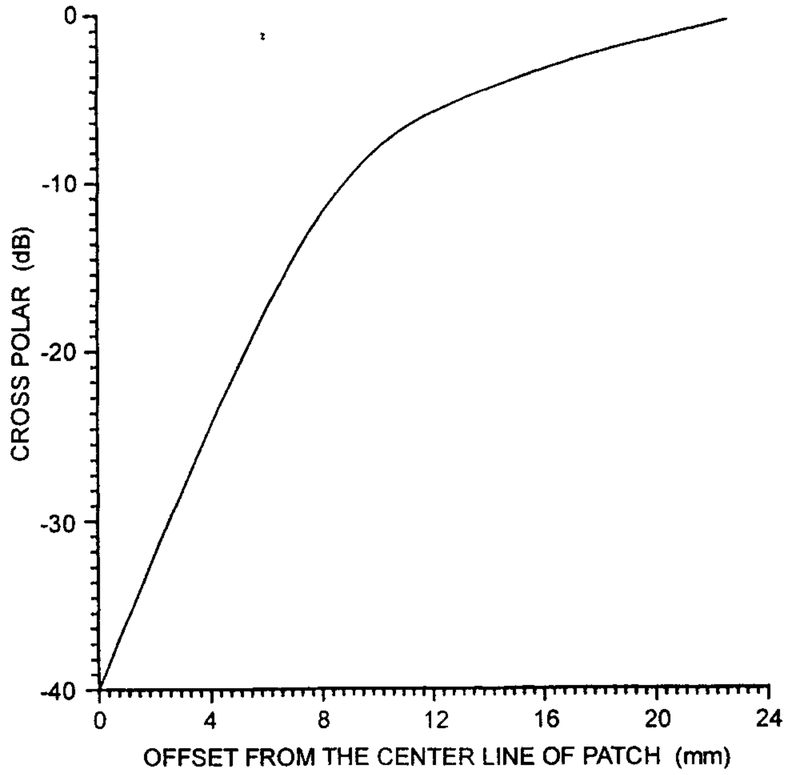

Figure 10.14 Variation of cross-polarization level with the position of short. Antenna parameters are the same as in Figure 10.9.

Table 10.1
Effect of Change in Parameters on the Design of a Shorted Disk

Parameter	Action	Consequences
Substrate ϵ_r	↓	↑Δ, ↑R, ↑BW
Substrate h	↑	↑Δ, ↓R, ↑BW
x_{ps}/R	↑ (But ≤ 1)	↓Δ, ↓R
r_{0s}	↑ (Keeping r_0 constant)	↑Δ, ↑R
r_0	↑ (Keeping r_{0s} constant)	↓Δ, ↓R
Cover layer	Add	↑Δ, ↓R

BW, Bandwidth; Δ, distance between probe and post; R, radius of disk; r_0 is the radius of the probe; r_{0s} is the radius of the short; x_{ps} is the location of short. From [13].

a chip resistor loaded antenna can yield a compact antenna with good bandwidth, but at the cost of decreased gain. It is possible to reduce cross-polarization in some antennas by symmetric loading [33].

It has been pointed out that for the application of mobile communication handsets, cross-polarization is not a major concern because most of these fields

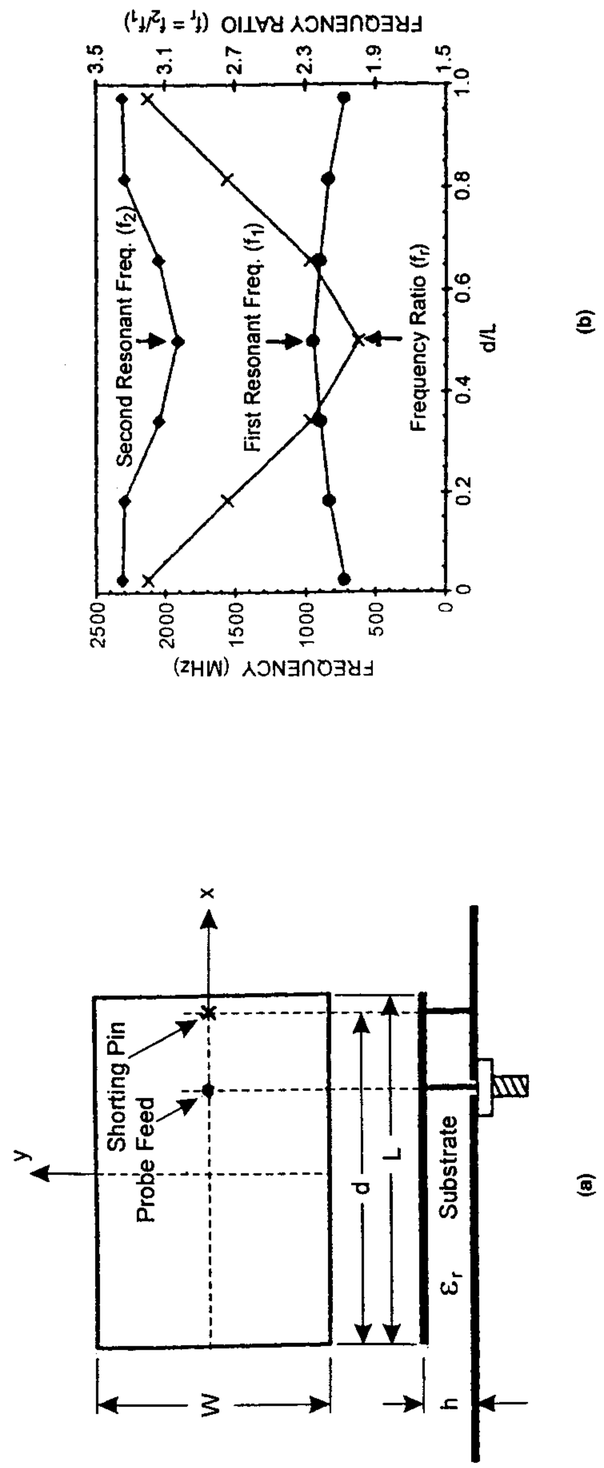

Figure 10.15 (a) Geometry of a rectangular microstrip antenna with a shorting pin on the center line. (b) Variation of first two resonant frequencies and frequency ratio versus shorting pin position. L = 37.3 mm, W = 24.87 mm, h = 0.762 mm, ϵ_r = 4.4. (From [15]. © 1997 *Electronics Letters*. Reprinted with permission.)

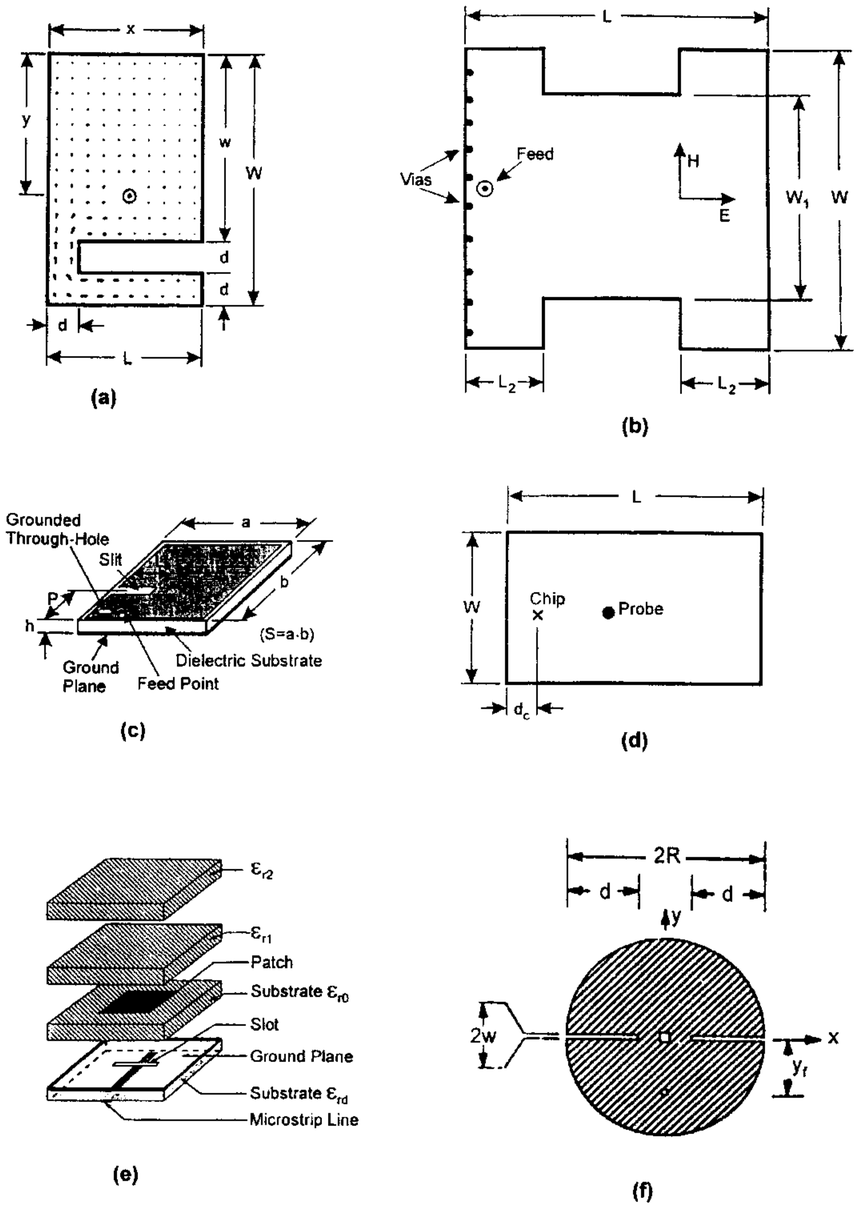

Figure 10.16 Some of the compact linearly polarized microstrip antennas.

will diffract off the edges of the small ground plane within the handset [13]. Dual-frequency antennas, described in Section 10.8, can also be used as compact antennas for operation at a single frequency.

10.6.2 Compact Circularly Polarized Antennas

Circular polarization is a requirement for satellite communications, and compactness is a desirable feature for mobile or airborne applications. Compact

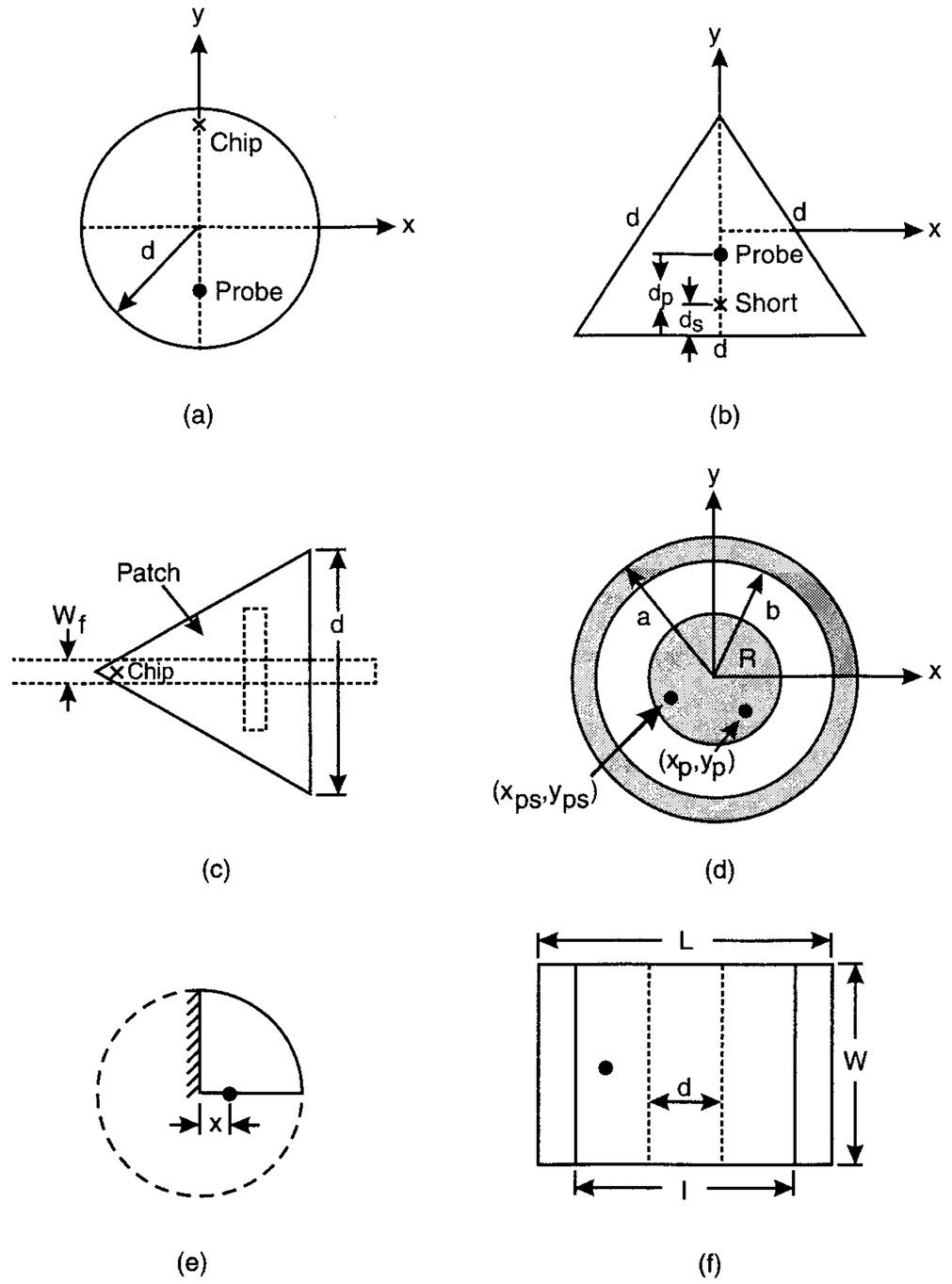

Figure 10.17 Top view of some more compact linearly polarized microstrip antennas.

circularly polarized antennas can be realized by starting with the circularly polarized configurations (see Chapter 8) and loading them with shorts and/or slots. Further compactness can be achieved by using a single feed, thereby eliminating the need for an external polarizer such as a 90° hybrid coupler.

Table 10.2
Performance of Various Types of Compact Linearly Polarized Microstrip Antennas (All Dimensions in Millimeters)

Antenna Type	Figure	Feed Type and Position	Type and Amount of Loading	Patch Dimensions	Resonant Frequency	10-dB Return Loss BW	H-Plane Cross-Polarization Level	Gain
C-shaped patch [21]	10.16(a)	Probe, $x = 12.5$, $y = 31.25$	Slit size: 12.5×50	62.5×62.5 (114.5×114.5); $\epsilon_r = 10.1$, $\tan\delta = 0.0005$; $h = 0.8$, $d = 12.5$	413 MHz	Slightly lower	< -25 dB	—
H-shaped patch with a shorted edge [22]	10.16(b)	Probe	Two slits	$L = 9.55$, $W = 11$; $\epsilon_r = 2.2$, $h = 0.508$; $W_1 = 1$, $L_1 = L_2 = 2.5$	2.6 GHz (5 GHz for the quarter-wave patch)	0.39% (0.77%)	< -17 dB	—
Rectangular patch [23]	10.8(a)	Probe	Post diam = 1	24×24; $\epsilon_r = 3.6$, $\tan\delta = 0.003$, $h = 5$	879 MHz	30 MHz	—	−1 dB compared to dipole
Rectangular patch [23]	10.16(c)	Probe	Post + Slit post diam = 1	24×24; $\epsilon_r = 3.6$, $\tan\delta = 0.003$, $h = 2.5$, $P = 5$, $L_s = 10$	820 MHz	5.5 MHz	—	—
Rectangular patch [24]	10.16(d)	Probe	1Ω Resistor	11.5×8 (46.7×30); $\epsilon_r = 3$, $h = 1.524$	1.84 GHz	7.91% (1.07%)	—	−10.8 dB compared to unloaded
Rectangular patch [24]	10.16(d)	Probe	1Ω Resistor + high ϵ_r superstrate	10.6×8 (46.7×30); $\epsilon_r = 3.79$; $h = 1.524$, 3.05	1.84 GHz	6.52% (1.07%)	—	−1.9 dB compared to unloaded
Rectangular patch [25]	10.16(e)	Aperture coupling	Two high ϵ_r superstrates	19.5×13.5, $\epsilon_r = 10.5$, 38, 38, 80; $h = 0.635$, 0.67, 1.34, 3.35	1.66 GHz	2.58%	—	5.3 dBi

Table 10.2 *(continued)*
Performance of Various Types of Compact Linearly Polarized Microstrip Antennas (All Dimensions in Millimeters)

Antenna Type	Figure	Feed Type and Position	Type and Amount of Loading	Patch Dimensions	Resonant Frequency	10-dB Return Loss BW	H-Plane Cross-Polarization Level	Gain
Circular patch [26]	10.16(f)	Probe	Two equal colinear slits	$R = 20$, $\epsilon_r = 2.5$, $\tan\delta = 0.0018$, $h = 1.52$; $2w = 0.7$, $d = 18$	1.543 GHz (2.66 GHz)	8.3 MHz (46 MHz)	—	−1.15 dBi (6.3 dBi)
Circular patch [13]	10.8(b)	Probe, diam = 0.65 $x = 6.2$, $y = 0$	Post, diam = 1.2 $x = 8.3$, $y = 0$	$R = 10.65$ $\epsilon_r = 1.07$, $\tan\delta = 0.015$, $h = 10$	1.9 GHz	6.8%	Poor	—
Circular patch [27]	10.17(a)	Probe, $x = 0$, $y = -11.5$	1Ω chip resistor	$d = 21.97$ (73.5)	542 MHz	11.5% (1.9% at 1.9 GHz)	—	Lower
Triangular patch [28]	10.17(b)	Probe (diam = 0.6), $d_p = 12.75$	Post diam = 0.26, $d_s = 13.25$	$d = 15.3$ (59.9), $\epsilon_r = 3$, $h = 0.762$	1.93 GHz	—	Poor	—
Triangular patch [29]	10.17(c)	Aperture coupling	Post	$d = 50$, $\epsilon_r = 4.4$, 4.4; $h = 1.6$, 1.6	501 MHz (1866 MHz)	1.6% (4.0%)	Poor	—
Triangular patch [29]	10.17(c)	Aperture coupling	1Ω chip resistor	$d = 50$, $\epsilon_r = 4.4$, 4.4; $h = 1.6$, 1.6	435 MHz (1866 MHz)	7.6% (4.0%)	Poor	—
Annular ring coupled to a disk [30]	10.17(d)	Probe (diam = 0.65), $x = 4.1$, $y = 0$	Post (diam = 0.65), and superstrate; $x = 5.3$, $y = 0$	$R = 8.2$ (30), $a = 25.8$, $b = 9.6$, $\epsilon_r = 2.2$, 2.2; $\tan\delta = 0.001$, $h = 6.096$, 0.254	1.9 GHz	10.1% (4.7%)	< -20 dB	6.2dBi (7.1 dBi)
90° circular sector [31]	10.17(e)	Probe, $x = 3$	One edge shorted	$a = 30$, $\epsilon_r = 2.33$; $h = 1.59$, $\tan\delta = 0.006$	1.761 GHz (1.866 GHz)	14 MHz (25 MHz)	< -10 dB	—
Dual-patch, with a slot in the lower patch [32]	10.17(f)	Probe feeding of lower patch	Upper patch shorted to lower patch via two vertical walls	$l = 45$, $W = 31$, $L = 51$, $\epsilon_r = 1$, 1; $h = 2$, 2; $d = 6$	1.61 GHz (2.635 GHz)	5% (1.25% for a single layer patch)	−15 dB	−2 dBi

Many designs of single-feed circularly polarized compact microstrip antennas have been reported. Geometries of some of these antennas are shown in Figure 10.18, and a brief description of some of these antennas is given below.

(a) Loaded Square Ring: The design of a square ring antenna is based on the fact that this configuration supports two degenerate modes with orthogonal polarizations, like a square patch antenna [34]. The size of this antenna is smaller because the average circumference of the antenna equals one wavelength, that is, the size of this antenna can be reduced to nearly a quarter-wave. The degeneracy of the modes is lifted either by using a nearly square ring [34] or by loading the square ring. The loaded ring antenna described in [35] employs a narrow slit of size 6.5×1 mm^2 in one of the arms [see Figure 10.18(a)]. For the substrate with $\epsilon_r = 4.4$ and $h = 1.6$ mm, the inner dimension of the antenna is 22 mm and the outer dimension is 30 mm. The center frequency of the antenna is 2180 MHz with the 3-dB axial ratio bandwidth of 21 MHz. For comparison, the nearly square patch of size 30 mm would have a center frequency of 2318 MHz.

(b) Slit Loaded Square Patch: In this antenna, the square patch is loaded with two pairs of slits to reduce the antenna size [see Figure 10.18(b)]. For a square patch antenna with $L = 30$ mm, $\epsilon_r = 4.4$, and $h = 1.6$ mm the resonant frequency is 2,318 MHz. When this antenna is loaded with a pair of slits of size 10×1 mm^2 and 9.2×1 mm^2, the frequency of operation decreases to 1849 MHz, that is, about a 20% reduction in frequency with a 36% reduction in size [36]. The 3-dB axial ratio bandwidth is found to be nearly 24 MHz. Coaxial probe feed is used for excitation. A similar antenna with a superstrate loading is described in [37].

(c) Short Loaded Rectangular Patch: The geometry of a nearly square patch with four symmetric shorts is shown in Figure 10.18(c) [38]. The antenna was fed by a probe along the diagonal. The return loss plot shows two resonances near 2.5 GHz. This antenna was a part of a self-diplexing stacked patch antenna for satellite mode handset.

(d) Circular Patch Integrated With Hybrid Feed: The geometry of this antenna is shown in Figure 10.18(d). In this case, compactness has been achieved by integrating the branch-line coupler feed with the microstrip disk [39]. The antenna was designed to operate at 10 GHz on a substrate with $\epsilon_r = 2.33$ and $h = 31$ mil. The two-port feed network is capable of transmitting and receiving left- and right-hand circularly polarized signals. The isolation between transmit/receive ports was found to be greater than 20 dB over a 200-MHz bandwidth.

(e) Slit Loaded Circular Disk: A circular disk loaded with four slots [see Figure 10.18(e)] has been developed by Bokhari et al. [26] for circular polarization. This configuration is similar to that of the slit loaded square

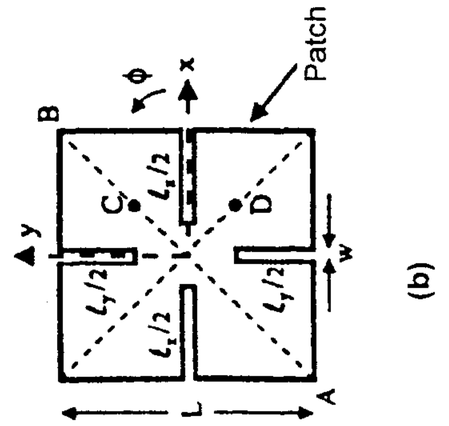

Figure 10.18 Top view of some compact circularly polarized microstrip antennas.

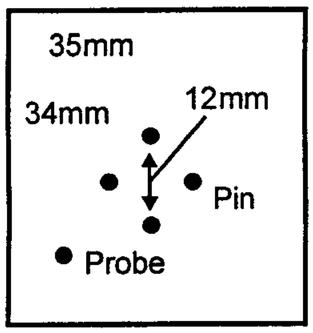

(c)

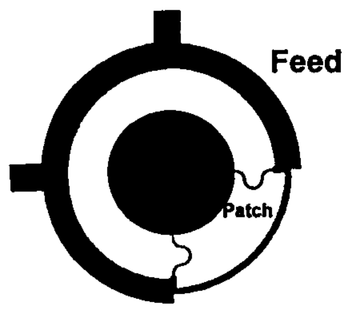

(d)

Figure 10.18 (continued).

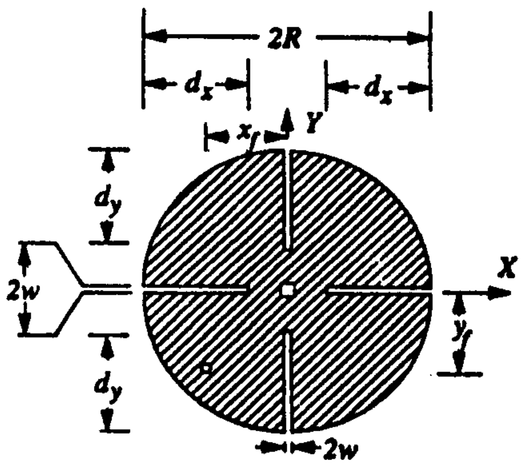

(e)

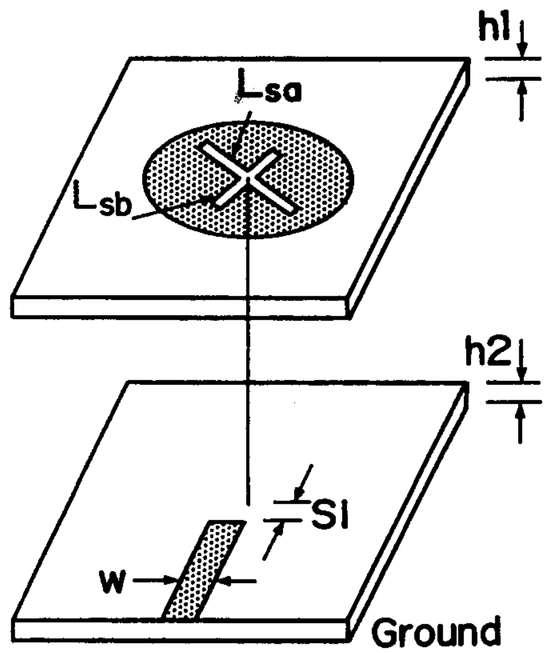

(f)

Figure 10.18 (continued).

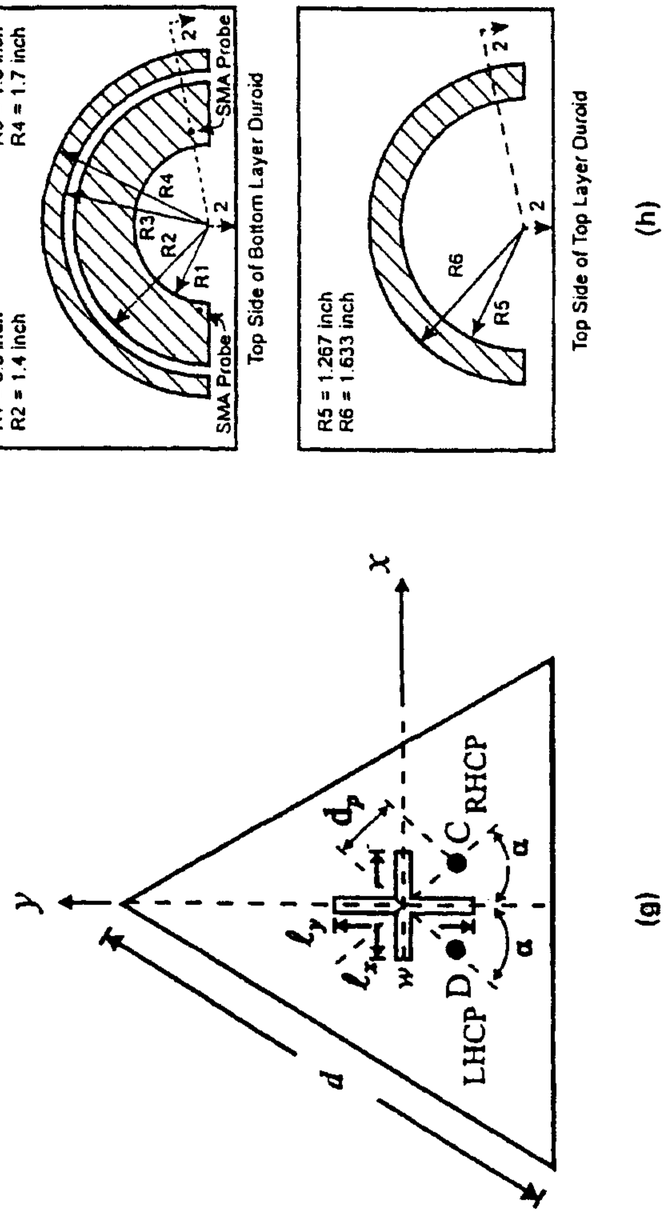

Figure 10.18 (continued).

patch antenna of Figure 10.18(b). The parameters used are R = 20 mm, ϵ_r = 2.5, $\tan\delta$ = 0.0018, h = 1.52 mm, W = 0.7 mm, with slit lengths of d_x = 12.4 mm, d_y = 6.5 mm. The measured resonant frequency for the antenna is about 0.8 times the resonant frequency of unloaded disk. A simple mechanical tuning mechanism for the axial ratio is also described.

(f) Circular Disk With a Cross-Slot: A circular disk loaded with a cross-slot of unequal slot lengths [see Figure 10.18(f)] has been reported by Iwasaki [40]. The slots cross each other orthogonally at the center of the disk. The degenerate modes of the circular disk experience unequal loading due to unequal slot lengths. The difference in slot lengths can be adjusted to obtain a 90° phase difference at the operating frequency. The resonant frequency of the patch decreases monotonically with increasing slot length. Therefore, resonant frequency can be controlled by changing the slot length. Compact antennas are notorious for impedance matching of the feed. Therefore, a proximity coupled microstrip feed is used in this antenna. A circularly polarized antenna operating at 980 MHz using ϵ_r = 2.6, $h_1 = h_2$ = 1.6 mm, L_{sa} = 61 mm, and L_{sb} = 60.5 mm, nearly equal to the diameter of the patch was tested. The size of the antenna was reduced by about 36% compared to the circular disk without cross-slots. The gain was about 7 dB lower. The boresight axial ratio was 0.5 dB, and an approximate 3-dB axial ratio was obtained in the ±45° range.

(g) Triangular Patch With Cross-Slot: An equilateral triangle supports two degenerate orthogonal (TM_{10} dominant) modes. Circular polarization from this antenna can be obtained by perturbing one of these modes. A narrow slot embedded in the patch, with the slot oriented parallel to the bottom side of the patch and the slot center at the null voltage point of the dominant mode, can be used to perturb the modes [41]. The dimensions of the slot can be adjusted to introduce 90° phase difference. This principle has been extended to the cross-slot loading of a triangular patch to develop a compact circularly polarized antenna. This antenna is shown in Figure 10.18(g). Like in the circular patch of Figure 10.18(f), the slot lengths l_x and l_y are adjusted to realize a 90° phase difference. The antenna is fed by a coaxial probe at a point such that the line joining the feed point and the center of the cross-slot are inclined to the y axis at an angle $\alpha = \tan^{-1}(l_x/l_y)$ [see Figure 10.18(g)]. The feed point C gives rise to RHCP and feed point D produces LHCP if $l_y > l_x$. The performance of the antenna is summarized in Table 10.3. Antenna 3 corresponds to an antenna size reduction of about 17% compared to the antenna without the cross-slot.

(h) Traveling-Wave Curved Microstrip Antenna: In this antenna, leaky wave over a half-circle curved microstrip line is employed to obtain circular polarization [42]. The antenna shown in Figure 10.18(h) has a two-layer

Table 10.3
Performance of the Compact Circularly Polarized Triangular Patch Loaded With Cross Slot. (From [65].)

	l_x, l_y, (mm)	d_p (mm)	Center Frequency	CP Bandwidth
Antenna 1	6.5, 10.4	9.0	1916 MHz	22 MHz (1.15%)
Antenna 2	11, 14	7.5	1880 MHz	19 MHz (1.01%)
Antenna 3	17.8, 18	1.5	1768 MHz	16 MHz (0.91%)

d = 48 mm, h = 1.6 mm, w = 1 mm, ϵ_r = 4.4.

geometry with the lower microstrip fed by a probe, and the upper microstrip coupled through a long narrow slot in the lower microstrip as shown. The antenna displays better than a 6-dB axial ratio between 4.5 and 4.8 GHz. The substrate parameters are ϵ_r = 2.2 and h = 62 mil.

10.7 Planar Inverted-F Antenna

A planar inverted-F antenna (PIFA) is a post loaded rectangular microstrip antenna fed by a probe. It is called an inverted-F antenna because the side view of this antenna shown in Figure 10.19 for air dielectric resembles the letter F with its face down. This antenna has been suggested for mobile telephone handsets because of its compactness and low profile [43]. The size of PIFA with the post located at a corner of a rectangular plate can be determined approximately from [23]

$$f_r = \frac{c}{4(L + W)} \tag{10.2}$$

where c is the velocity of light, L and W are the dimensions of the element, and f_r is the operating frequency. The size of the antenna can be further

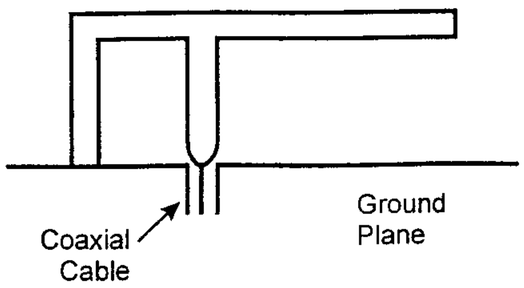

Figure 10.19 Side view of a planar inverted-F antenna (PIFA).

reduced by loading it. Rowell and Murch have developed a capacitively loaded PIFA suitable for digital communication systems (DCSs) [20]. The antenna has a VSWR < 2 bandwidth of 178 MHz centered at 1.795 GHz. The capacitive load is 1.478 pF and the total volume of the antenna is 640 mm^3. We saw earlier in Section 10.5 that a reduction in the size of the antenna is accompanied by an increased impedance level. The resulting impedance matching problem in this case is addressed by using a novel feed [44], in which the probe is top loaded by a disk having a size much smaller than that of the antenna. The disk electromagnetically couples to the radiating top plate. The area of the disk, its distance from the top plate, and the location of the probe are designed to achieve impedance match. The capacitively loaded PIFA is shown in Figure 10.20. The capacitive load is realized by folding the open end of the PIFA toward the ground plane and attaching a plate (parallel to the ground plane) to produce a parallel plate capacitor. Input impedance variations of a PIFA antenna for 1- and 2-mm separations between the radiating plate and the feed disk are shown in Figure 10.21 [20]. The input impedance is seen to decrease drastically with the separation distance.

The PIFA antenna is generally mounted on a small conducting box to simulate the metallic cover of a handset suitable for mobile telephone applications (see Figure 10.20). The analysis and design of the mounted PIFA antenna can be carried out using the FDTD technique described in Chapter 3. Some of the other analysis techniques fail to integrate the effect of the box on the

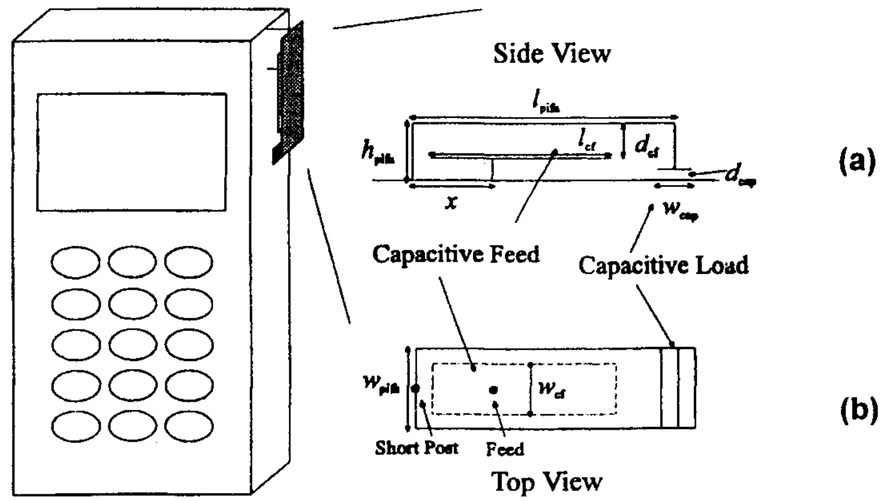

Figure 10.20 A capacitively loaded PIFA mounted on a handset: (a) Side view and (b) top view of a capacitively loaded PIFA antenna. (From [20]. © 1997 IEEE. Reprinted with permission.)

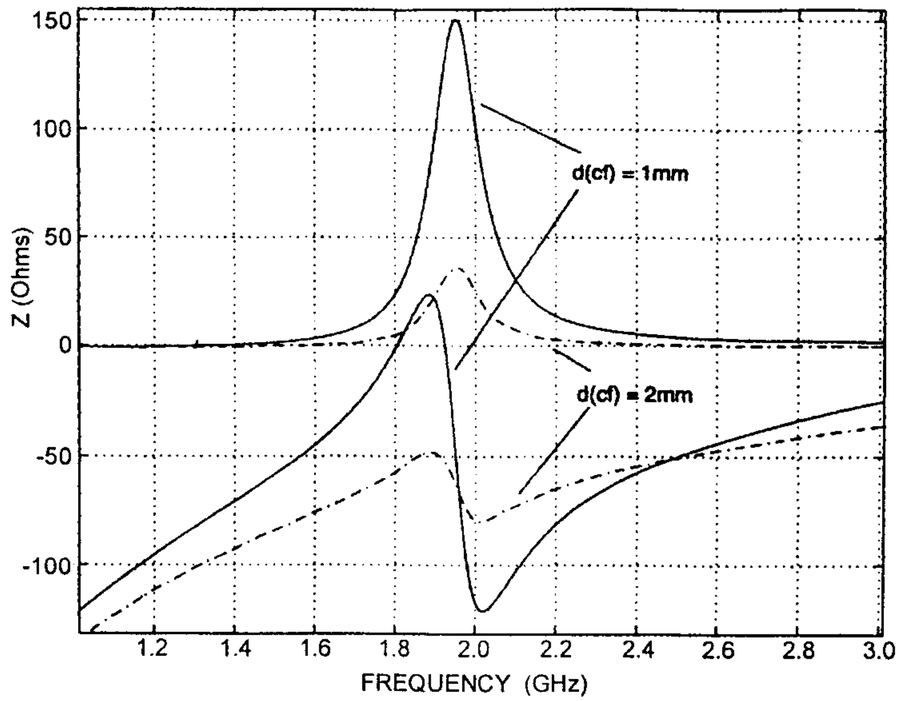

Figure 10.21 Input impedance curves for two values of d_{cf} between the antenna plate and the feed disk. l_{pifa} = 25 mm, w_{pifa} = 10 mm, h_{pifa} = 5 mm, d_{cap} = 0.5 mm, w_{cap} = 4 mm, x = 5.6 mm, l_{cf} = 23 mm, w_{cf} = 10 mm, and ϵ_r = 1. The post and the probe are centered along the y axis. The size of the box is 80 mm × 40 mm × 10 mm. (From [20]. © 1997 IEEE. Reprinted with permission.)

antenna characteristics. It has been found that the radiation pattern of the antenna remains relatively unaffected by the addition of the disk on the probe. The capacitive load has a minor effect on the radiation patterns. The radiation patterns with and without the capacitive load are shown in Figure 10.22. Due to capacitive load, the H-plane pattern has become more uniform by eliminating two notches, and the E-plane pattern is less uniform due to an additional notch. The dimensions of the final antenna for operation at 1.795 GHz are:

$$l_{\text{pifa}} = 20 \text{ mm}, w_{\text{pifa}} = 8 \text{ mm}, h_{\text{pifa}} = 4 \text{ mm}, l_{cf} = 18.4 \text{ mm}, w_{cf} = 8 \text{ mm}, d_{cf} = 2 \text{ mm}, d_{\text{cap}} = 0.4 \text{ mm}, w_{\text{cap}} = 0.5 \text{ mm}, x = 5.6 \text{ mm}, \text{and } \epsilon_r = 1$$

The size of the box used is $80 \times 40 \times 10$ mm^3.

The antenna of Figure 10.20 has been modified to operate in the 900-MHz band. The configuration of the new PIFA antenna is shown in

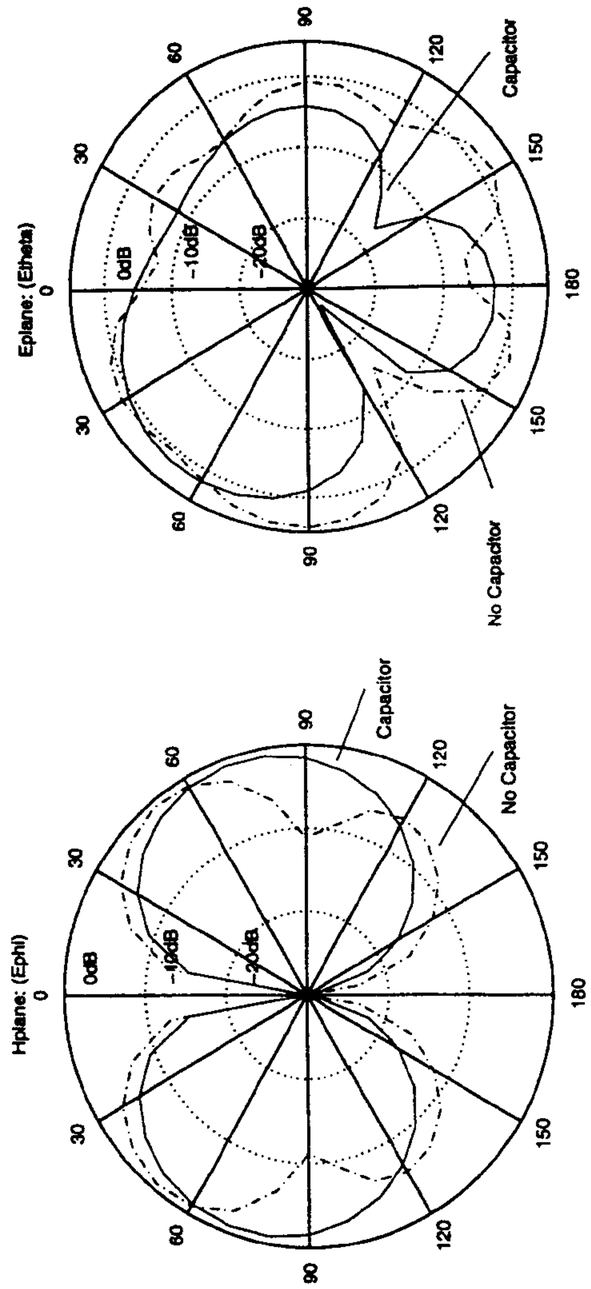

Figure 10.22 Radiation patterns of the PIFA antenna with and without the capacitive load. The antenna dimensions are the same as in Figure 10.21. (From [20]. © 1997 IEEE. Reprinted with permission.)

Figure 10.23 [45]. A slit and dielectric loadings have been added to the antenna of Figure 10.20 so that the final size of the antenna meets the size requirement for the handset. The step-by-step design approach given below consists of starting with conventional PIFA (the capacitive load, capacitive feed, the slit, and the dielectric are removed) and the loads are then added one by one [45].

1. For $(l_{\text{pifa}}, w_{\text{pifa}}) = (25, 26)$ mm, $h_{\text{pifa}} = 4$ mm, and $d_{\text{short}} = w_{\text{pifa}}/2$, and the probe feed directly connected to the top plate, the resonant frequency from the FDTD analysis is 2.2 GHz.
2. By offsetting the shorting pin from $d_{\text{short}} = w_{\text{pifa}}/2 = 13$ mm to 5 mm, the resonant frequency decreases to 1.95 GHz.
3. Capacitive load is added next. Although capacitive loading can be used to reduce the frequency straight to 900 MHz, in the design preferred by authors of [45], the equivalent capacitance used is 0.5 pF, realized using $w_{\text{cap}} = 4$ mm, $d_{\text{cap}} = 2$ mm. A disk loaded probe feed is also added at this stage with $l_{cf} = 13$ mm, $w_{cf} = w_{\text{pifa}}$, $d_{cf} = 2$ mm to provide a good match to 50Ω. The new resonant frequency is 1.64 GHz.
4. The slit is now added to the antenna top plate to reduce the frequency further. With the addition of the slit, the effective length of the antenna

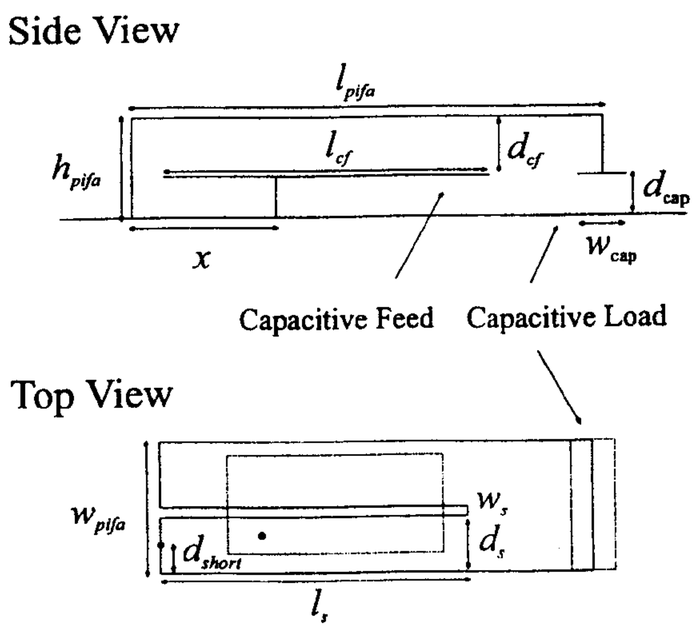

Figure 10.23 Configuration of slit loaded PIFA for operation in the 900 MHz band. (From [45]. © 1998 IEEE. Reprinted with permission.)

increases because the current has to flow around the slit. For every 5-mm increase in slit length, the resonant frequency is found to decrease by approximately 3%. If a slit of size 24 mm × 1 mm is placed along the center of the top plate, the resonant frequency will reduce to 1.4 GHz.

5. Finally, the antenna is filled with a dielectric with $\epsilon_r = 2.1$ for easier construction. The new resonant frequency becomes 940 MHz.

The impedance bandwidth of the new PIFA is found to be about 7%.

10.8 Dual-Frequency Microstrip Antennas

In many applications, operation in two or more discrete bands with an arbitrary separation of bands is desired. In such cases, a patch antenna capable of operating in multiple bands is highly desirable. One of the implementations could be in the form of two or more patches placed side by side (see Figure 9.31) or stacked on top of each other (see Figure 9.16), or simultaneous excitation of natural modes of the antenna. But for most applications, all bands may be required to have the same polarization, radiation pattern, and bandwidth characteristics. It is also desirable to have one input port and an arbitrary separation of the frequency bands. All of these requirements impose severe constraints on the use of natural modes. Here, we describe some techniques to achieve dual-frequency operation by modifying the natural modes. Compact dual-frequency antennas are described in the next section. An excellent review of dual-frequency antennas is given in [46], and a review of techniques for dual and circularly polarized microstrip antennas is available in [47].

An annular ring radiates in the broadside direction when excited in the (1, 1), (1, 2), or (1, 3) mode. The frequencies for these modes can be adjusted by choosing the inner and outer radii. However, the ratio of the two frequencies is somewhat limited [48]. A change in the resonant frequency of a natural mode can be achieved by properly loading the mode. Therefore, it is possible to practically tune the operating frequencies of these modes independent of each other.

Wang and Lo have used shorting pins and slots in a rectangular patch to obtain dual-frequency operation [48]. The (0, 1) and (0, 3) modes of the rectangular patch are used because these modes have the same polarization and a broadside radiation pattern. In the unloaded state, the frequency ratio of these modes is nearly 3. The concept used by them is based on the fact that shorting pins placed at the nodal line of (0, 3) mode will not have much effect

on the modal field distribution for this mode but can have a strong effect on the (0, 1) modal field. These pins thus *raise* the (0, 1) modal frequency. Similarly, if the slots are cut in the patch where the magnetic field of the (0, 3) mode is maximum, they can have a strong effect on the (0, 3) modal field without disturbing much the (0, 1) modal field. Thus, the operating frequency of the (0, 3) mode can be lowered. By using both pins and slots, the frequency ratio can be varied between 1.31 and 3.02. A top view of this dual-frequency antenna is shown in Figure 10.24 [48]. The feed probe is symmetrically placed with respect to the nonresonant dimension so that even modes like (2, 0), (4, 0), and so on are not excited. The cavity model was used to design the antenna. The rectangular patch parameters are L = 194 mm, W = 146 mm, ϵ_r = 2.62, $\tan\delta$ = 0.001, h = 1/16 in., and x_0 = 97, y_0 = 0.

Table 10.4 summarizes the design for six cases. From these results, it is seen that in general the slots can lower f_H and shorting pins can raise f_L, resulting in a variation in frequency ratio from 3.02 to 1.31. The radiation patterns for both bands remained primarily the same as that of the unloaded patch, that is, the radiation pattern at the upper frequency is a three-lobed pattern. The input impedance can vary widely with the feed position, and it is not difficult to obtain impedance matches for both the bands. The antenna described next features similar radiation patterns at the upper and lower frequencies.

10.8.1 Dual-Frequency Slotted Patch Antennas

It is possible to achieve dual-frequency operation of a patch antenna by loading with slots only. Unlike the insertion of a post in the substrate, the fabrication

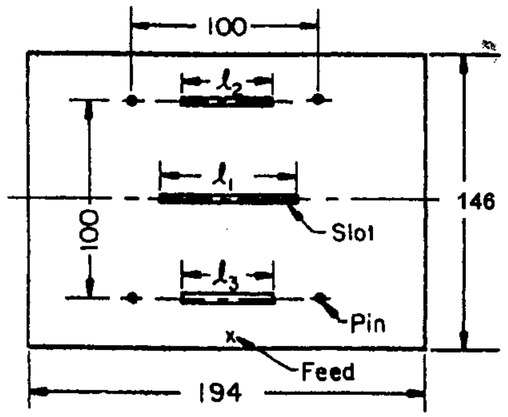

Figure 10.24 Top view of a dual-frequency microstrip antenna loaded with shorting pins and slots. All dimensions are in millimeters. (From [48]. © 1984 IEEE. Reprinted with permission.)

Table 10.4
Resonant Frequencies of a Dual-Mode Antenna Employing Slots and Pins

	Case	f_L (MHz)	f_H (MHz)	f_H/f_L
A.	One slot: l_1 = 10 mm at (97, 73)	628	1900	3.02
B.	One slot: l_1 = 30 mm at (97, 73)	596	1700	2.85
C.	Three slots: l_1 = 70 mm, l_2 = l_3 = 30 mm at (97, 24), (97, 73), and (97, 122)	555	1420	2.55
D.	Three slots l_1 = l_2 = l_3 = 70 mm at the same locations as in case C	553	1310	2.36
E.	Same as case D plus four pins as shown in Figure 10.24	698	1087	1.56
F.	Same as case E plus six pins at (37, 24), (97, 24), (157, 24), (37, 122), (97, 122), and (157, 122)	890	1181	1.31

L = 194 mm, W = 146 mm. From [48].

process of a slot is compatible with antenna fabrication technology. The loading effect of a slot is maximum when inserted at the location of maximum magnetic field.

The configuration of a rectangular patch antenna with a pair of symmetrical slots in the patch metalization is shown in Figure 10.25 [49]. The antenna is aperture coupled to the microstrip feed line. The physical behavior of the slotted antenna can be understood by starting from the cavity model description of the unslotted rectangular patch. The excited modes in the antenna depend on the type and position of the feed. By choosing aperture coupling with a centered slot, the even modes are not excited. Actually, only the (1, 0) mode

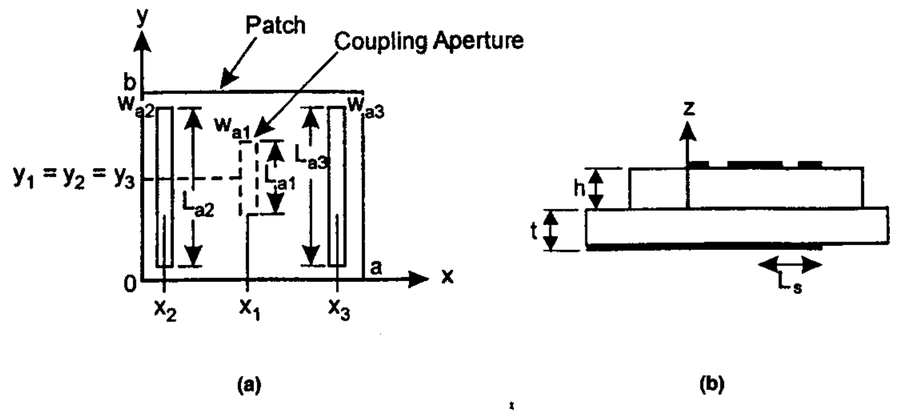

Figure 10.25 Configuration of a slot loaded patch for dual-frequency operation (From [49]. © 1993 *Electronics Letters*. Reprinted with permission.)

is employed in practice because the (2, 0) mode produces a broadside null in the radiation pattern whereas the (3, 0) mode produces grating lobes.

When the patch is loaded by the two slots close to the radiating edges, the slots do not significantly change the (1, 0) resonant frequency and the associated radiation patterns because the slots are near the current minimum. However, they strongly interact with the (3, 0) mode. As a result, the *middle current lobe* of this mode gets flattened and the outer current lobes also get significantly modified. This implies that the current distribution becomes similar to that of the (1, 0) mode and a similar radiation pattern is expected. The slot loading lowers the resonant frequency for the (3, 0) mode.

The frequency ratio depends on the number of slots, their position and the slot length. The ratio of the resonant frequencies of a patch antenna as a function of slot position is shown in Figure 10.26(a) [49]. The slot widths have been fixed at 1 mm, and slot lengths at 46 mm. We can see from this figure that slots located near the radiating edges of the patch give rise to the lowest frequency ratio, that is, the loading effect of the slot is maximum at the position of maximum magnetic field. The effect of slot length on the frequency ratio is shown in Figure 10.26(b) [49]. The loading effect of the slot increases with the slot length. Symmetric slots produce lower values of frequency ratio and low cross-polarization.

Figure 10.27 shows the current distributions at the lower and upper resonant frequencies when the loading effect is maximum. As expected from physical considerations, the loading slots induce minor perturbations of the

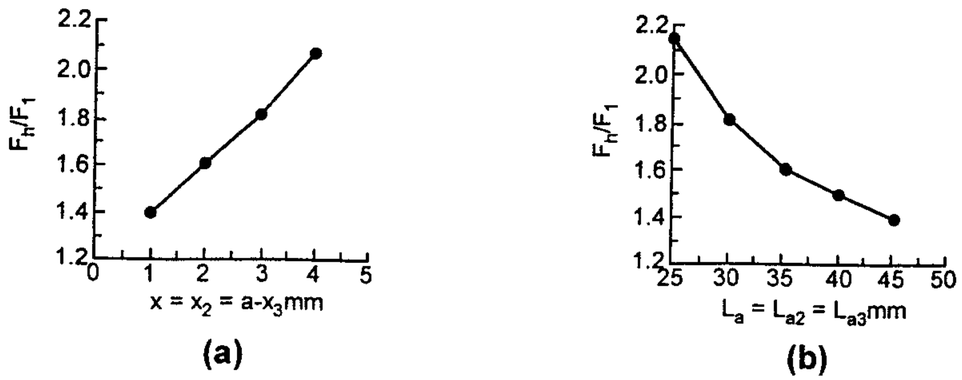

Figure 10.26 (a) Variation of ratio F_h/F_l with slot position; $L = W = 47$ mm, $\epsilon_{r1} = 2.2$, $h = 1.6$ mm, $L_{a2} = L_{a3} = 46$ mm, $W_{a2} = W_{a3} = 1$ mm, $\epsilon_{r2} = 2.55$, $t = 0.8$ mm; microstrip feed line: $W_s = 2.2$ mm, $L_s = 20.6$ mm, $W_{a1} = 1$ mm, $L_{a1} = 15$ mm, $x_1 = y_1 = 23.5$ mm. (b) Variation of ratio F_h/F_l with slot length; $x_2 = 1.5$ mm, $x_3 = 45.5$ mm, $y_2 = y_3 = 23.5$ mm. Other parameters are the same as in part (a). (From [49]. © 1993 *Electronics Letters*. Reprinted with permission.)

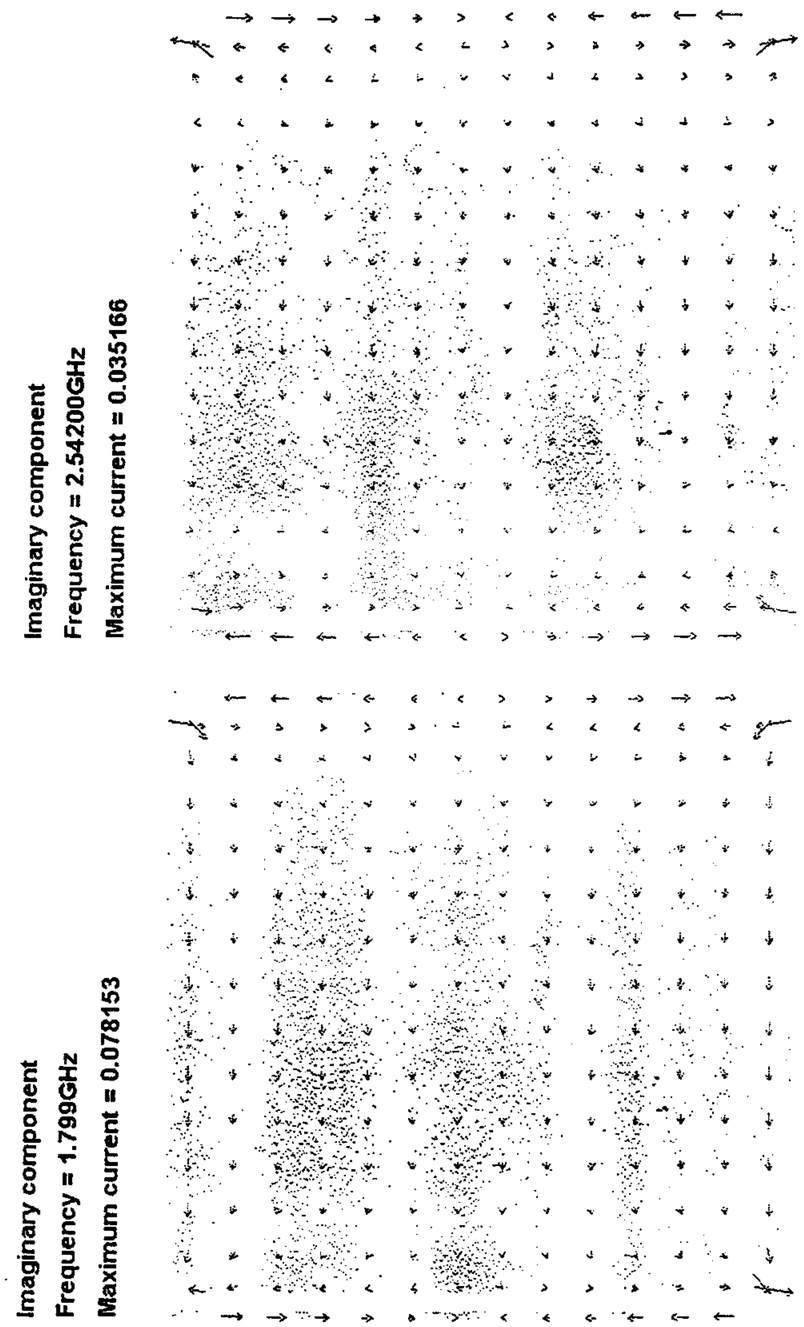

Figure 10.27 In-quadrature current distribution on the slot loaded patch of Figure 10.25. Antenna parameters are the same as in Figure 10.26(a) and $x_2 = 1.5$ mm, $x_3 = 45.5$ mm, $y_2 = y_3 = 23.5$ mm. (a) At $f = 1.799$ GHz and (b) at $f = 2.542$ GHz.

(1, 0) mode [see Figure 10.27(a)]. On the other hand, there is a strong influence of the slots on the current distribution near the (3, 0) mode resonant frequency [see Figure 10.27(b)], making this distribution very similar to that of the (1, 0) mode. As a consequence, the copolar radiation patterns at the upper and lower frequencies are almost the same. Radiation patterns at the upper frequency are shown in Figure 10.28. A similar study was carried out by Maci et al. [50], and they have obtained frequency ratios between 1.4 and 2.1.

Slot loading along the nonradiating edges has also been used to obtain single-feed dual-frequency operation. The geometry of this antenna is shown in Figure 10.29 [51]. The slots employed are step slots whose step ratio W_2/W_1 is varied in order to vary the frequency ratio. The frequency ratio can be varied between 1.23 and 1.63. For a typical antenna with L = 38 mm, W = 25 mm, h = 1.6 mm, ϵ_r = 4.4, l_s = 18 mm, W_1 = 1 mm, $d_L = d_W$ = 1 mm, d_p = 2.2 mm, and W_2 = 10 mm, the two frequencies are 1480 and 2414 MHz, and the impedance bandwidths are 1.35% and 1.33%, respectively. The polarization is the same for both modes and radiation patterns are also similar, with maximum in the broadside direction. The difference in gain for the two modes is about 2.5 dB in the broadside.

10.8.2 Dual-Frequency Dual-Linearly Polarized Microstrip Antennas

Dual polarization is an increasingly important requirement. Optimized patch geometry now allows isolation of the order of −40 dB to be achieved for linear polarization.

If two orthogonal linear polarizations at separate frequencies are required, the simplest antenna for this is a rectangular patch antenna fed at the diagonal for exciting the (1, 0) and (0, 1) modes. The frequencies of these modes are determined by the respective lengths of the patch. Impedance matching at the two frequencies can be easily achieved, otherwise an inclined slot in the ground plane can be used [52]. Use of separate feed points located along the perpendicular center lines of the antenna exciting the orthogonal modes (see Figure 10.2) can also be used for increased isolation. However, the beamwidths for these modes are governed by the dimensions of the patch.

This limitation can be overcome by using stacked rectangular patches with independent feeds as shown in Figure 10.30 [53]. The upper feed passes through the lower element at a voltage null. If the frequency separation is greater than the individual-patch bandwidth, the isolation is primarily determined by the frequency separation-to-patch bandwidth ratio [47]. For closely spaced frequencies, such as those used at L-band for satellite communication systems, square or circular patches can be used. In this case, isolation is dependent on the geometry and is a critical guide to the quality of the antenna. Isolation

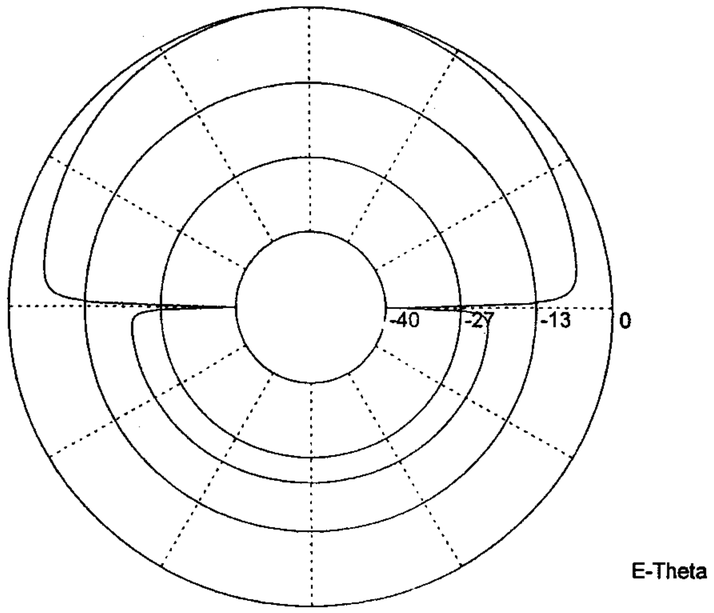

Figure 10.28 Radiation patterns at f = 2.542 GHz for the slot loaded patch antenna of Figure 10.25: (a) $\phi = 0°$ plane and (b) $\phi = 90°$ plane.

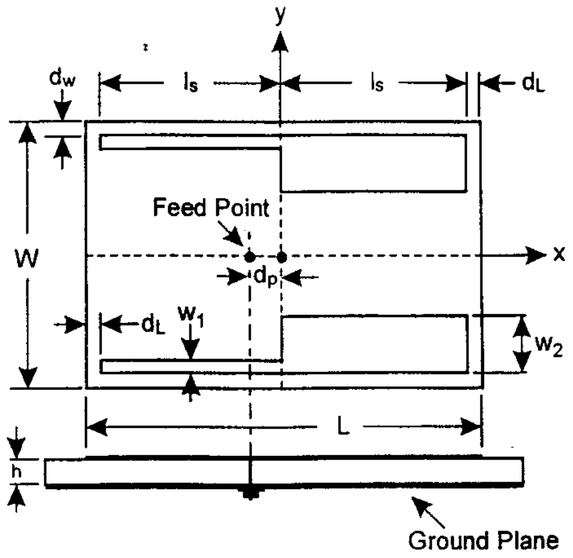

Figure 10.29 Top view of single-feed dual-frequency rectangular microstrip antenna with a pair of step slots. (From [51]. © 1999 *Electronics Letters*. Reprinted with permission.)

depends on the Q factor of the patch and the feed geometry. For example, for a circular patch, the isolation decreased from −50 to −28 dB as the substrate thickness was increased from 3.2 to 12.3 mm (lower Q) [53]. In general, increase in feed port size increases coupling, giving decreased isolation [47]. However, isolation can be improved by optimizing the feed position [54]. Isolation for dual-linear polarization using a circular patch is shown in Figure 10.31 and compared with dual-circular polarization [55]. It is seen that isolation degrades from about 20 dB for dual-linear polarization to less than 10 dB for dual-circular polarization. The use of notched or slotted patches increases coupling.

Figure 10.25 can also be modified to obtain dual-polarization behavior. The modification consists of introducing slots along the other edges also. A configuration for this antenna and its modified form, called a slotted cross-patch, are shown in Figure 10.32 [46, 56]. The modes are excited by separate feeds, and isolation between the ports was found to be better than 35 dB [46].

An unslotted circular patch microstrip antenna with two input ports, for dual-frequency or dual-polarization operation, has been reported by Murakami et al. [57]. The modes used are the degenerate (1, 1) modes of the circular patch. The microstrip feeds are coupled to these modes in the patch through rectangular slots whose axes are perpendicular to each other. The slot dimensions are selected for maximum isolation between the two modes of operation. A top view of the antenna is shown in Figure 10.33. The asymmetric loading

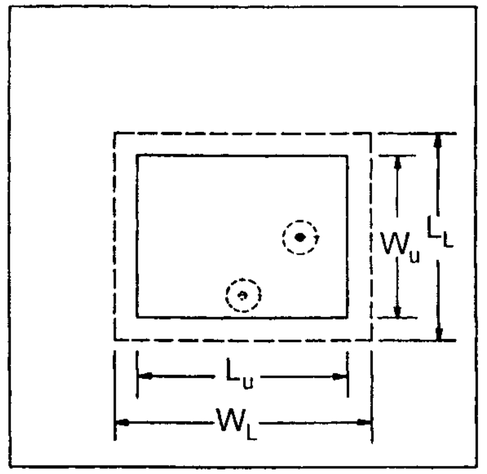

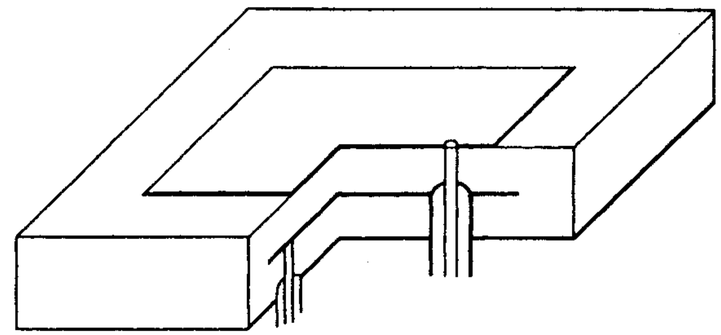

Figure 10.30 Stacked patch configuration for realizing orthogonal linear polarizations at two frequencies. (From [53]. © 1989 Peter Peregrinus. Reprinted with permission.)

of the patch through the coupling slots lifts the degeneracy of the (1, 1) modes. The frequency difference between the two modes was 100 MHz and an isolation greater than −35 dB between the two ports was achieved at a frequency near 1.55 GHz. Isolation of about −40 dB has been achieved for an etched cross-patch in which a gridded structure is used to polarize the surface currents in the direction of resonance [58].

10.8.3 Dual-Frequency Circularly Polarized Microstrip Antennas

Current global positioning satellite (GPS) receivers operate at the L1 frequency of 1575 MHz. For applications such as surveying systems employing differential GPSs for maximum positioning accuracy, an antenna operating at both the L1 and L2 frequencies of 1575 and 1227 MHz is required. The bandwidth

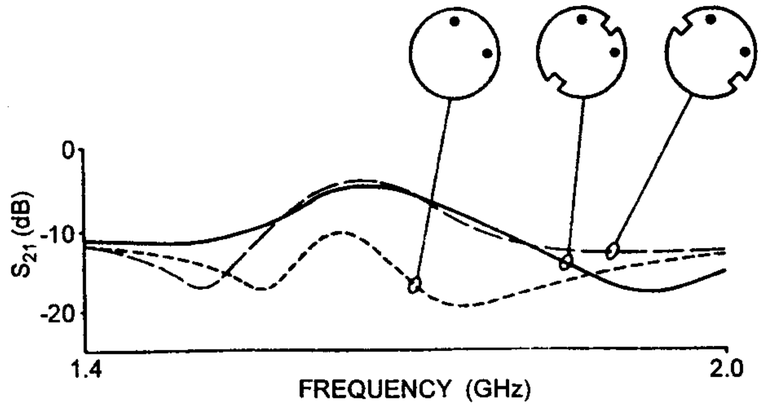

Figure 10.31 Comparison of isolation between orthogonal feed ports of a circular patch for dual-linear and dual-circular polarizations. (From [55]. © 1992 IEE. Reprinted with permission.) Patch diameter = 40 mm, h = 0.79 mm, ϵ_r = 2.3.

required is approximately 40 MHz about both frequencies. These antennas typically use a circularly polarized microstrip antenna.

Pozar [59] has used stacked square patches to obtain dual-frequency operation. Circular polarization is achieved by aperture coupling the lower patch by a crossed slot. This is shown in Figure 10.34 [59]. The crossed slot is fed by an external polarizer with a microstrip feed network using a number of power splitters. This type of feeding is necessary to obtain a large 3-dB axial ratio bandwidth and a large frequency separation of about 350 MHz between the L1 and L2 frequencies.

Karamakar and Bialkowski [60] have reported a right-hand circularly polarized microstrip antenna covering the receiving frequency band of 1545 to 1559 MHz and the transmitting frequency band of 1646 to 1661 MHz by a broadband antenna. Three different configurations have been tried. The single-feed aperture-coupled circular patch with perturbation strips shown in Figure 10.35(a) does not meet the axial ratio bandwidth requirement. The cause for limited bandwidth is the single feed. This problem has been solved using two different approaches. In the first approach, another patch is stacked on top of the first patch, resulting in single-feed aperture-coupled stacked circular patches with perturbation strips [see Figure 10.35(b)]. In the alternative approach, two orthogonal apertures fed by a 3-dB branch line hybrid coupler are used as a feed network for the circular patch. This configuration is called a dual-feed aperture-coupled circular patch and is shown in Figure 10.35(c). The last two antenna configurations meet the bandwidth requirement of 8% at 1.6 GHz in addition to 9-dBi gain across the specified band. The isolation and axial ratio, as a function of frequency for the dual-feed configuration, is shown in Figure 10.36 [60]. In Figure 10.36(a), d is the distance between the

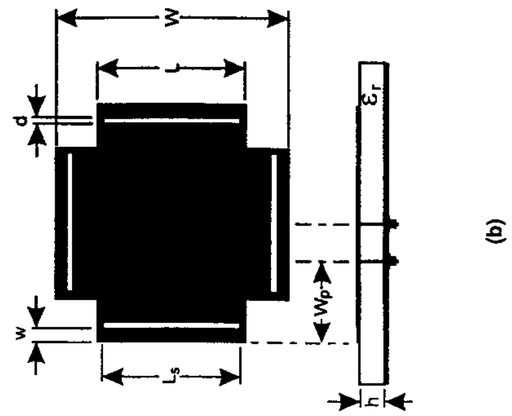

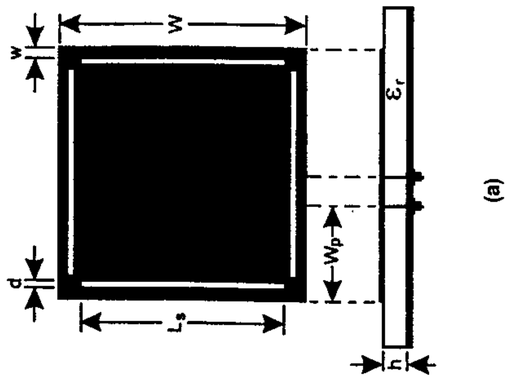

Figure 10.32 Top view of (a) slotted-square and (b) slotted cross-patch antennas for dual-frequency and dual-polarization operation. (From [46]. © 1997 IEEE. Reprinted with permission.)

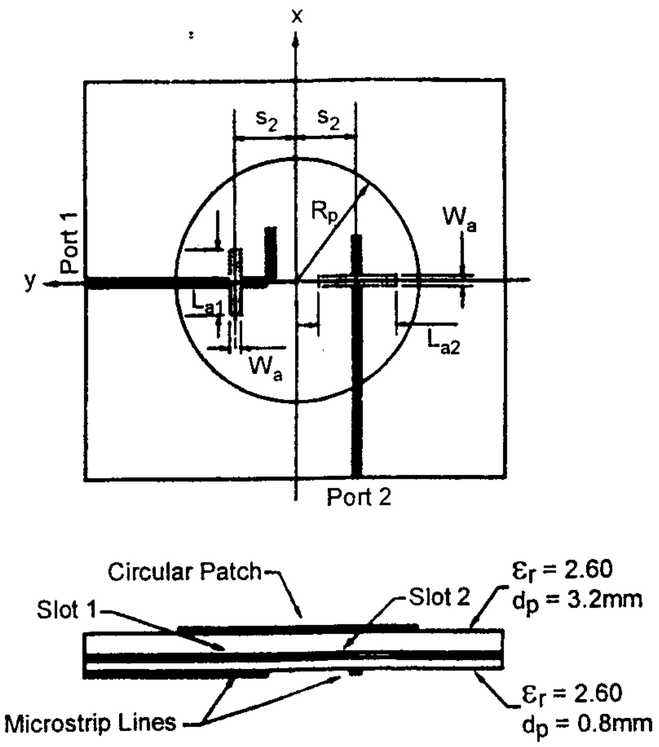

Figure 10.33 Top view of two feeds, dual-frequency, orthogonal polarization circular patch microstrip antenna. (From [57]. © 1993 *Electronics Letters*. Reprinted with permission.)

nearest corners of orthogonal rectangular apertures. The larger value of d yields larger isolation and axial ratio behavior follows the isolation behavior.

10.8.4 Dual Circularly Polarized Microstrip Antennas

Dual-circular polarization has been realized in a number of ways. Analysis of nearly equilateral triangular patch antennas shows that there are a number of feed points available for either hand of circular polarization at different frequencies [61]. Figure 10.37 [61] shows that Γ_1 and Γ_2 loci can be used for RHCP and LHCP, respectively, at 1583.8 MHz, whereas Γ_3 and Γ_4 loci are suitable for LHCP and RHCP, respectively, at 1564.2 MHz. The frequency spacing can be controlled to some degree by the aspect ratio a/b. Similar characteristics can be obtained from a rectangular patch loaded with stubs [62]. Alternatively, a stacked structure using the circular patch and a short-circuited annular ring of Figure 10.38 [63, 64] can be used. By rotation of the patch with respect to the ring, isolation of about −50 dB can be achieved over a narrow range of frequencies.

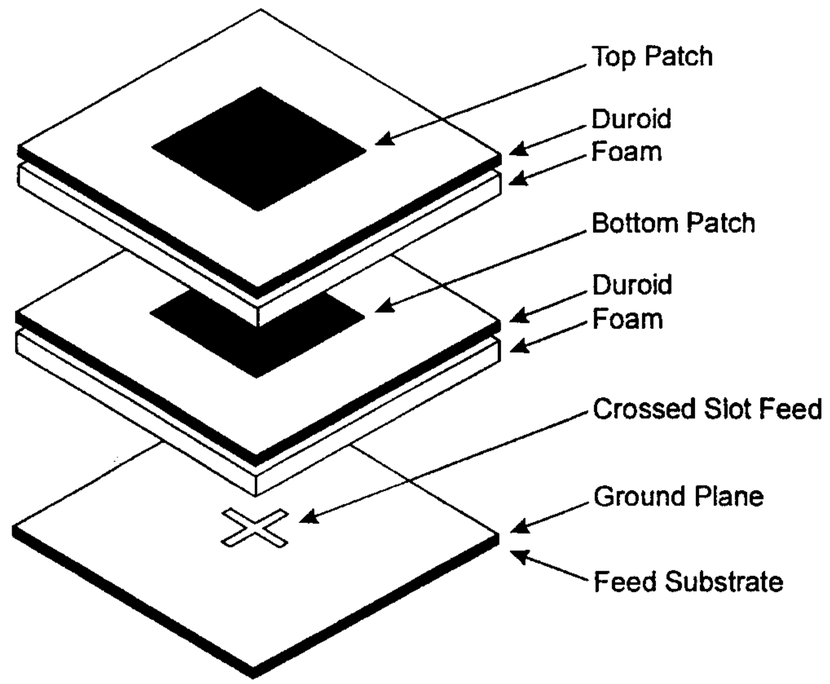

Figure 10.34 Geometry of an aperture coupled stacked-patch circularly polarized dual-frequency antenna. (From [59]. © 1997 IEEE. Reprinted with permission.)

10.9 Dual-Frequency Compact Microstrip Antennas

A number of approaches have been reported to achieve compact dual-frequency microstrip antennas. These include: loading of rectangular [15], circular [65], and triangular patches by shorting pins [66], loading by crossed slots [67, 68], and the use of a rectangular ring [69]. The concept behind the realization of dual-frequency operation is that loading in any form disturbs the field distribution and therefore the resonant frequency for various modes of the patch. The frequency ratio between the desired modes can be adjusted by suitably locating the load and the amount of load. Frequency tuning can be obtained independently of the frequency ratio by changing the dimensions of a rectangular patch.

10.9.1 Pin-Loaded Dual-Frequency Antennas

A dual-frequency rectangular patch antenna with a pin on the center line was described in Section 10.5. A frequency ratio between 2.0 and 3.2 was achieved. The dual-frequency behavior of an equilateral triangular patch with pin loading is shown in Figure 10.39 [66]. The shorting pin and the probe feed are again located on the symmetry line of the antenna. The frequency ratio for this

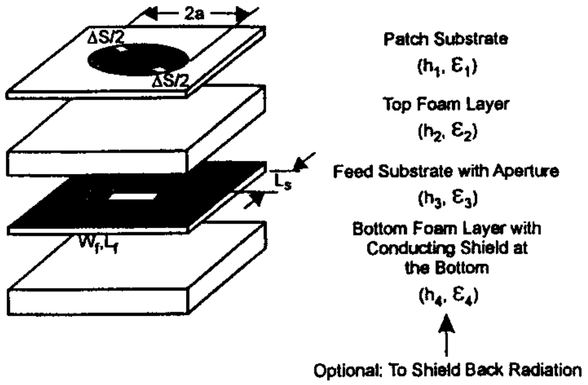

(a)

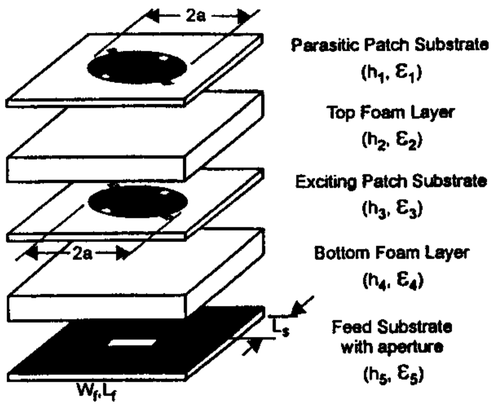

(b)

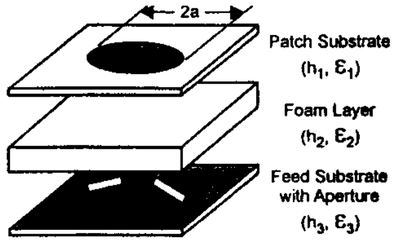

(c)

Figure 10.35 Three configurations for dual-frequency circularly polarized microstrip antennas: (a) Single-feed aperture-coupled circular patch antenna, (b) single-feed aperture-coupled stacked circular patches, and (c) dual-feed aperture coupled circular patch. (From [60]. © 1999 IEEE. Reprinted with permission.)

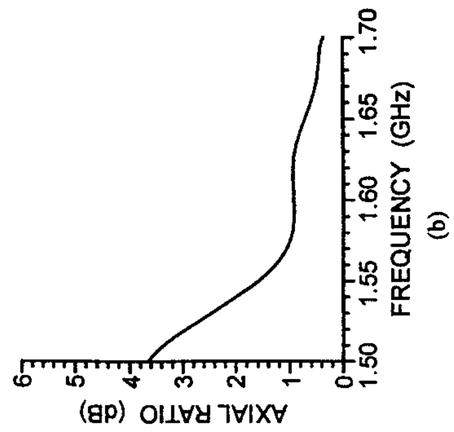

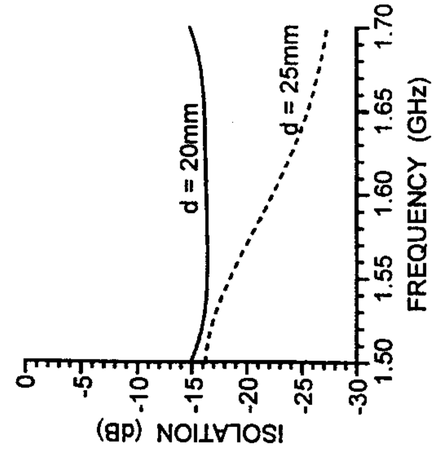

Figure 10.36 Variation of isolation and axial ratio with frequency for the antenna configuration of Figure 10.35(c). a = 42 mm, h_1 = 0.785 mm, ϵ_{r1} = 2.2, h_2 = 9 mm, ϵ_{r1} = 1.47, L_a = 39 mm, W_a = 4 mm, stub length L_s = 10 mm. (a) Isolation and (b) axial ratio. (From [60]. © 1999 IEEE. Reprinted with permission.)

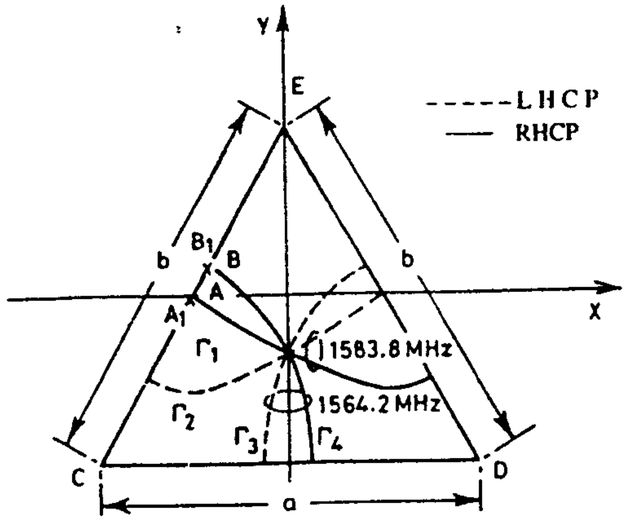

Figure 10.37 Feed location loci for circular polarization in equilateral triangle microstrip antenna. b/a = 0.98, a = 76 mm, h = 3.2 mm, ϵ_r = 2.55. (From [61]. © 1987 IEE. Reprinted with permission.)

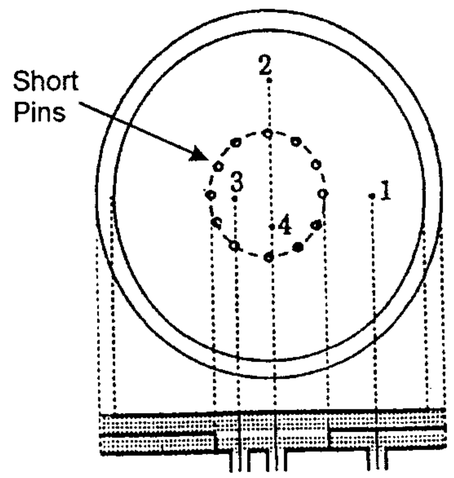

Figure 10.38 Dual-circular polarization from a circular patch stacked on a shorted annular-ring. (From [63]. © 1992 IEEE. Reprinted with permission.)

geometry can be tuned from 2.5 to 4.9. Therefore, a higher frequency ratio can be achieved by the use of a triangular geometry. Other antenna characteristics are similar to that of a loaded rectangular patch. The dual-frequency behavior of a pin loaded circular patch antenna is shown in Figure 10.40 [65]. The shorting pin is placed on the line joining the patch edge and the center, and the feed is placed on the same line about the pin. The frequency ratio obtained is between 2.55 and 3.83. The size reduction of the antenna at the lowest

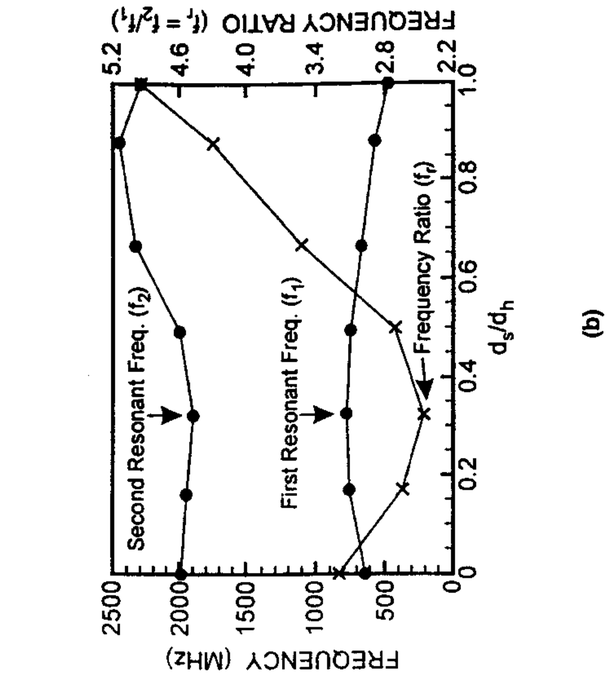

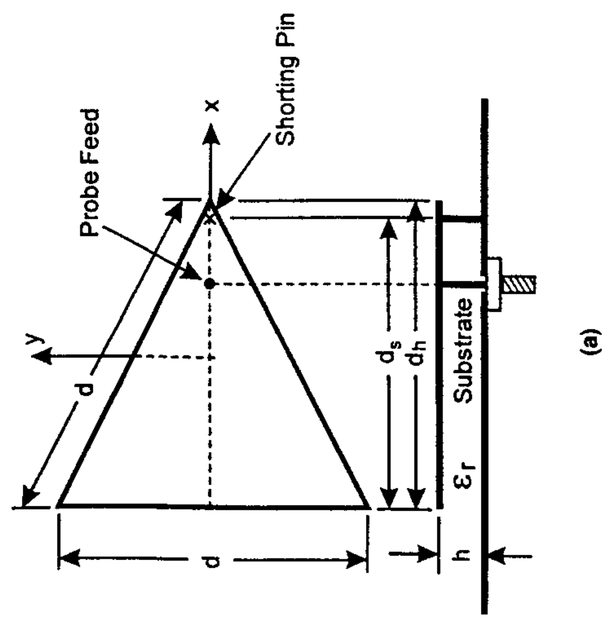

Figure 10.39 (a) The geometry of a dual-frequency triangular microstrip antenna with a shorting pin. (b) Variation of resonant frequencies and frequency ratio versus shorting pin position. d = 50 mm, h = 0.762 mm, ϵ_r = 4.4. (From [66]. © 1998 IEEE. Reprinted with permission.)

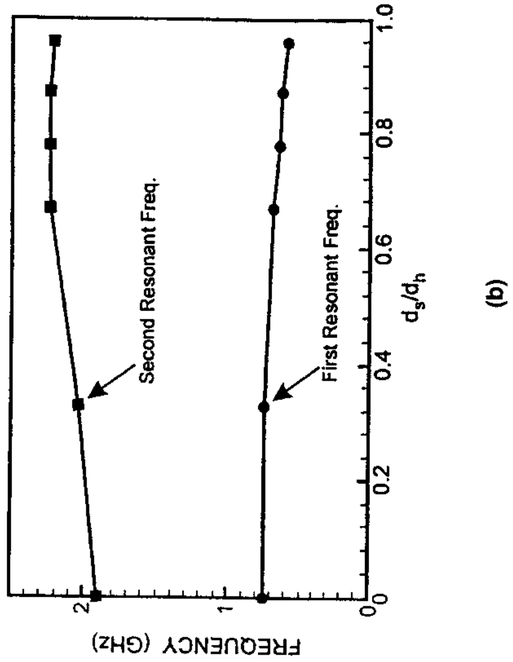

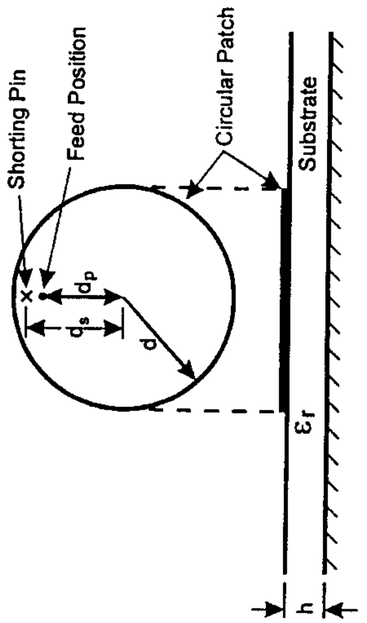

Figure 10.40 (a) Geometry of a dual-frequency circular microstrip antenna with a shorting pin. (b) Variation of resonant frequencies versus shorting pin position. d = 21.86 cm, h = 1.6 mm, ϵ_r = 4.4, radius of the short = 0.32 mm. (From [65]. © 1997 *Electronics Letters.* Reprinted with permission.)

frequency is roughly 3.3. The 10-dB return loss bandwidth varies between 1.5% and 1.7%. The radiation patterns for the loaded disk are similar to that of a loaded rectangular patch.

10.9.2 Slot-Loaded Dual-Frequency Antennas

Loading by cross slots has been used to obtain dual-frequency, dual-polarization operation of a rectangular patch [67]. The modes utilized for this purpose are (1, 0) and (0, 1), because these modes can provide orthogonal linear polarizations. The top view of a rectangular patch with centered crossed slots is shown in Figure 10.41(a). The loading can be varied by varying the slot lengths. The modes in the slotted patch are excited by an inclined aperture in the ground plane of the patch [see Figure 10.41(b)]. Performance of this antenna can be ascertained from Table 10.5.

The antenna size reduction at the lowest frequency is about 40% and the cross-polar performance is better than that of pin loaded antennas. A similar antenna with probe feed has also been studied [68]. In another attempt, a square slot has been etched from the center of a rectangular patch as shown in Figure 10.42 [69]. The rectangular ring antenna so obtained is electrically smaller than the rectangular patch employed [70]. The ring antenna has lower resonant frequencies because the surface currents have to travel along the slot perimeter to reach the other end, which is a longer distance. The first two modes of the ring are excited by feeding along the diagonal of the ring. The

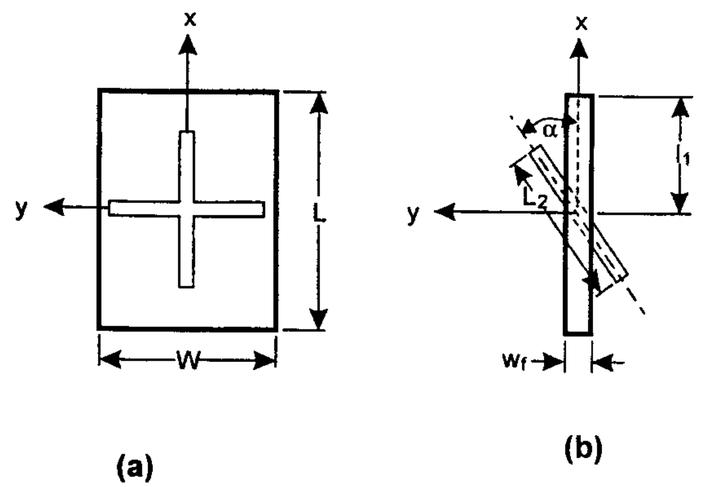

Figure 10.41 (a) Top view of a rectangular microstrip antenna with cross-slot to obtain dual-frequency operation. (b) Microstrip feed line with an inclined slot for coupling. (From [67]. © 1998 *Electronics Letters.* Reprinted with permission.)

Table 10.5
Resonant Frequencies for a Dual-Frequency Antenna for Various Cross-Slot Lengths

Cross-Slot Length l, (mm)	Coupling Slot Size $(mm)^2$	Tuning Stub Length (mm)	f_1 (MHz), BW (%)	f_2 (MHz), BW (%)	Frequency Ratio
26	1.2 × 25.5	26.16	1389, 1.51	1804, 1.55	1.299
22	1.2 × 23.5	24.06	1529, 1.63	1963, 1.68	1.284
16	1.2 × 21.0	21.92	1676, 1.85	2135, 2.20	1.274
8	1.2 × 19.0	18.25	1773, 1.97	2271, 2.33	1.281
0	1.2 × 18.5	18.25	1799, 2.05	2306, 2.40	1.282

$h = t = 1.6$ mm, $\epsilon_{ra} = \epsilon_{rf} = 4.4$, $L = 37.7$ mm, $W = 28.4$ mm, $L/W = 1.327$, slot width $w = 1$ mm, $w_f = 3$ mm, $\alpha = 37°$. From [67].

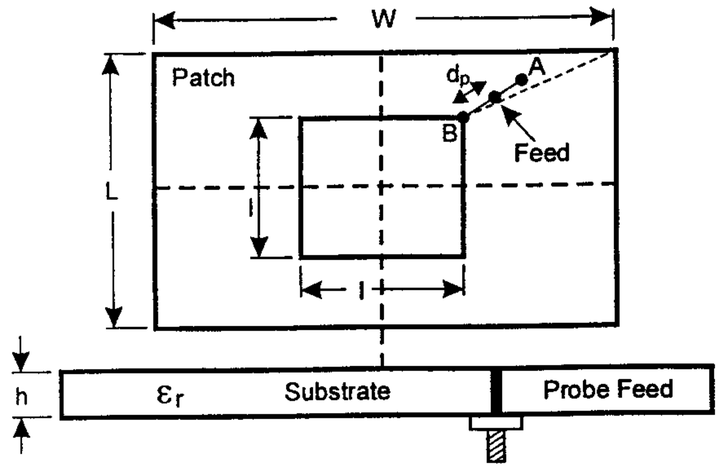

Figure 10.42 Top view of a rectangular ring microstrip antenna. The ring is excited along the diagonal for dual-frequency operation. (From [69]. © 1998 *Electronics Letters*. Reprinted with permission.)

performance of the ring antenna as a function of the size of the slot is given in Table 10.6.

From Table 10.6, we can see that the frequency ratio is slightly lower than the aspect ratio = 1.32 of the rectangular patch. The radiation patterns of the ring antenna at two frequencies are shown in Figure 10.43. The cross-polar behavior is observed to be good. Another variation of the ring antenna is obtained when the central square slot is rotated by 45° [69]. This antenna can accommodate a larger slot size and therefore larger reduction in size before running into impedance matching problems. The radiation patterns remain unchanged with the rotation of the slot.

Table 10.6
Resonant Frequencies for a Rectangular Ring Antenna for Various Slot Lengths

Slot Length l (mm)	f_1 (MHz), BW (%)	f_2 (MHz), BW (%)	Frequency Ratio	d_p (mm)
0.0	2115, 1.9	2698, 2.2	1.276	6
2.5	2094, 1.9	2675, 2.1	1.277	5
7.5	2034, 1.8	2587, 2.1	1.272	2
9.0	1932, 1.8	2475, 2.0	1.281	0

$h = 1.6$ mm, $\epsilon_r = 4.4$, $L = 33.2$ mm, $W = 25.5$ mm, $L/W = 1.32$. From [69].

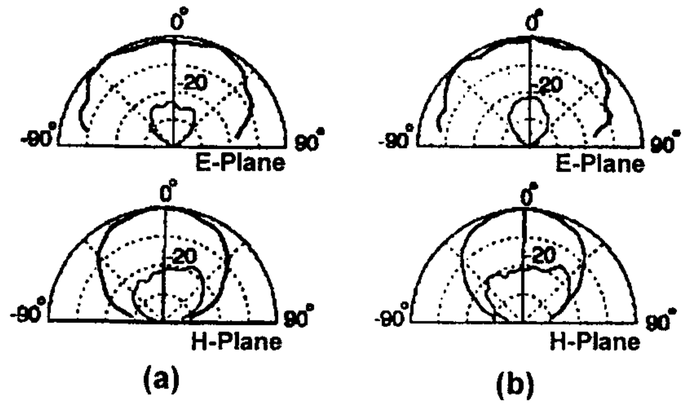

Figure 10.43 E- and H-plane radiation patterns of a rectangular ring microstrip antenna. $L = 33.2$ mm, $W = 25.5$ mm, $h = 1.6$ mm, $\epsilon_r = 4.4$, $l = 9$ mm; ____, copolarization; ____, cross-polarization. (a) $f = 1932$ MHz and (b) $f = 2478$ MHz. (From [69]. © 1998 *Electronics Letters*. Reprinted with permission.)

A dual-frequency compact antenna capable of receiving both linearly and circularly polarized radiation has been reported [71]. It generates linear polarization at the lower frequency and circular polarization at the upper frequency. The antenna is shown in Figure 10.44. It consists of a square patch with two symmetrical shorting pins. It is possible to generate circular polarization by using two shorting pins in a square patch as described in Section 10.1. A mode with linear polarization will also be produced in this antenna due to pin loading [72]. The frequency of this mode is far below the fundamental mode of the patch antenna. A reduction factor of 5 in area has been achieved at the lower frequency end. Other characteristics of the antenna shown in Figure 10.44 are given in Table 10.7 [71].

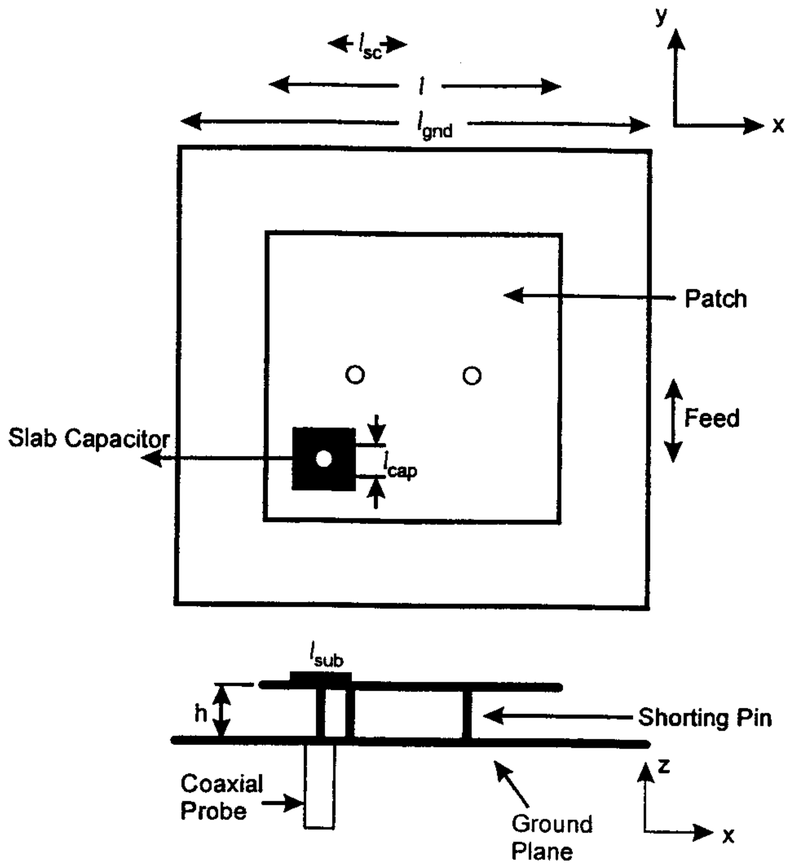

Figure 10.44 Single-feed, dual-frequency, dual-polarization square microstrip antenna. l_{sc} = 18 mm, l = 72 mm, l_{grid} = 140 mm, l_{cap} = 6 mm, l_{sub} = 10 mm, feed = 14 mm, h = 8 mm, ϵ_r = 1. (From [71]. © 1999 *Electronics Letters.* Reprinted with permission.)

10.9.3 Dual-Frequency PIFA

The PIFA antenna introduced in Section 10.7 can also be modified for the dual-frequency operation. Two configurations for dual-band operation are available, having either one or two input ports. Both are described next.

A two-port PIFA is shown in Figure 10.45 [73]. It consists of two separate radiating elements, with the rectangular element being used at 1.8 GHz and the L-shaped element at 900 MHz. The size of this structure is almost the same as that of a single rectangular element at 900 MHz. The two radiating elements are grounded to the case of the handset and probe feed near the shorting pins. The shorting pins are placed back to back to minimize coupling between the two antennas. The antenna is mounted on the side of the metal case to maximize the bandwidth [74].

Table 10.7
Characteristics of a Dual-Band, Dual-Polarization Microstrip Patch Antenna

Characteristic	f_1 = 0.85 GHz	f_2 = 1.848 GHz
Polarization	Linear	Circular
Radiation pattern	Omnidirectional, dipole like	Omnidirectional, hemispherical
Return loss (dB)	−24.21	−10.76
Gain (dB)	−0.36	8.94
−10-dB bandwidth	2%	—
5-dB axial ratio bandwidth	—	4%
Cross-polarization (dB)	−10	—
Axial ratio (dB)	—	0.62
5-dB axial ratio beamwidth	—	80° (*yz* plane) 60° (*xz* plane)

From [71].

The analysis and design of the antenna are carried out using the FDTD technique to include the effect of the handset on antenna characteristics. The size of the element operating at 1.8 GHz can be determined approximately from (10.2). The element at 900 MHz can also be designed using (10.2) because the field distribution in the L-shaped element is nearly the same as in the rectangular shaped patch.

The FDTD simulated electric field distributions underneath the antenna at 900 MHz and 1.76 GHz are shown in Figure 10.46 [73]. The results show that the electric field is zero at the position of shorting pins and the edge effect is pronounced. The magnitude of electric field at the nonresonant element is much lower than at the resonant one as expected. This indicates that mutual coupling is poor between the two elements at both frequencies. This observation was confirmed by the measurement of mutual coupling between the ports, which is shown in Figure 10.47 [73]. The measured coupling is less than −17dB at both resonant frequencies. Low coupling ensures that less power is lost in the second antenna while the desired antenna is radiating. The VSWR < 2 bandwidth was found to be 63 MHz at 900 MHz and 110 MHz at 1.8 GHz. Measured and computed radiation patterns of the antenna in the *z-x* plane are plotted in Figure 10.48 [73]. Approximately omnidirectional patterns, desirable for handset antennas, are obtained at both frequencies.

The antenna performance was also studied with respect to the frequency ratio. For these computations, the overall size of the antenna and the gap between the two elements were fixed, as shown in the inset of Figure 10.49. The resonant frequencies of the elements were varied by increasing the size of

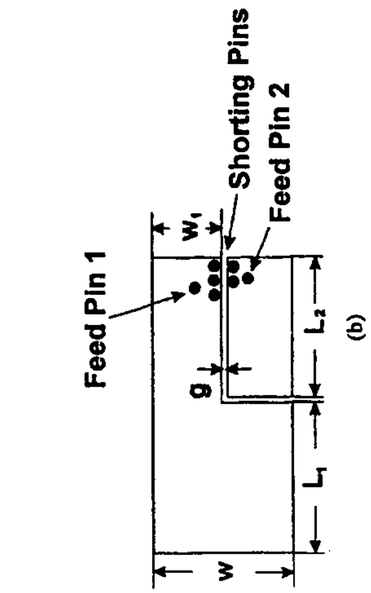

Figure 10.45 Dual-frequency, two-port PIFA antenna: (a) Mounted on a conducting telephone case and (b) top view of the antenna. (From [73]. © 1997 IEEE. Reprinted with permission.)

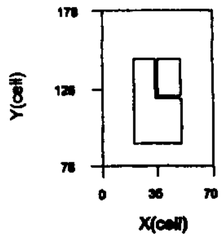

Antenna Layout in the FDTD Computation Space

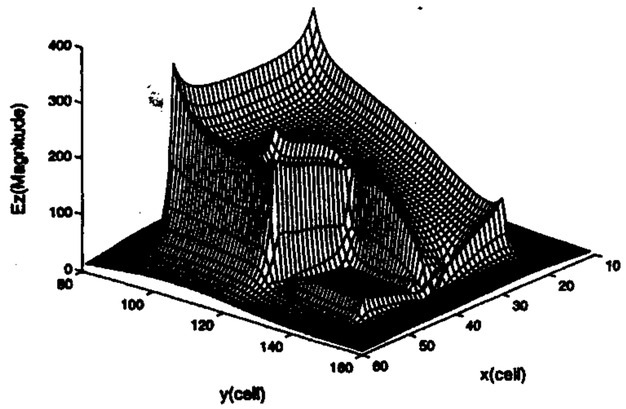

(a)

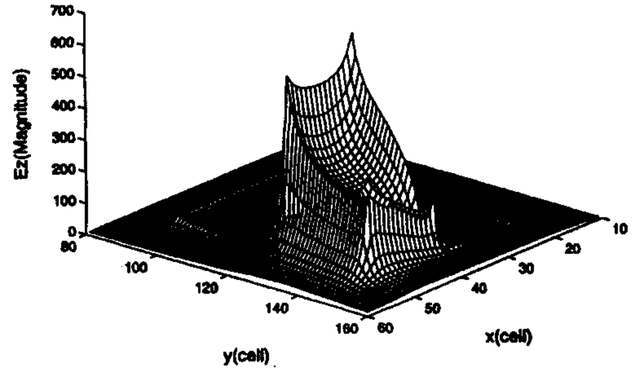

(b)

Figure 10.46 Computed electric field distribution in the antenna of Figure 10.45. (a) Field distribution at 900 MHz. (b) Field distribution at 1.76 GHz. Antenna details: a = 62 mm, b = 138 mm, c = 30 mm, h = 9 mm, W = 30 mm, W_1 = 14.5 mm, g = 2 mm, L_1 = 29 mm, L_2 = 23 mm, ϵ_r = 1. FDTD details: Δx = 1 mm, Δy = 1 mm, Δz = 2.2 mm and Gaussian pulse excitation. (From [73]. © 1997 IEEE. Reprinted with permission.)

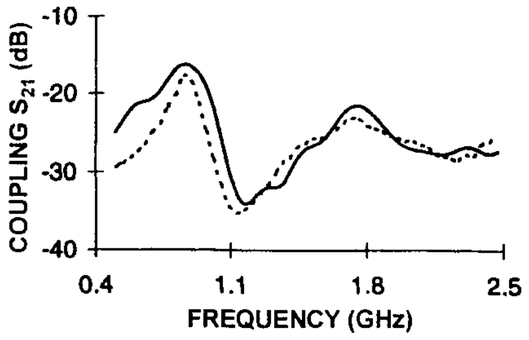

Figure 10.47 Measured and computed mutual coupling between the two antennas as a function of frequency. Other details as in Figure 10.46. ____, FDTD; ...., measured. (From [73]. © 1997 IEEE. Reprinted with permission.)

one element and decreasing the size of the other by the same amount. The bandwidth of the L-shaped element as a function of frequency ratio is shown in Figure 10.49, where we can see that the bandwidth of the L-shaped element increases with frequency ratio. This is expected, because the electrical size of the antenna increases with frequency. Many other studies are reported in the paper.

In some applications, it is desirable to have one input port instead of two. The configuration of this antenna is shown in the inset of Figure 10.50. It is obtained from the two-port configuration of Figure 10.45 by electrically shorting the two radiating elements using common shorting pins. The new antenna was fabricated on a substrate with $\epsilon_r = 2.2$ and thickness of 1.143 mm. The measured return loss for the antenna is shown in Figure 10.50 [73]. It shows two resonances with greater than 17-dB return loss, and the frequency ratio is 1.8.

The simulated electric field distribution underneath the antenna at the resonant frequencies is shown in Figure 10.51. The results show that the magnitude of electric field at the nonresonant element is three or four times lower than that of the resonant one, indicating a mutual coupling of about −10 dB. These dual-frequency antennas are suitable for GSM and DCS 1800 systems.

The dual-frequency single-patch antennas can achieve a limited value of frequency ratio and compromise other antenna characteristics. For a large value of frequency ratio or improved performance at a number of frequencies, multiple patch configurations, as described in Chapter 9, can be used. A triple-frequency antenna with a single feed is described in [75]. A stacked patch antenna for dual-frequency and broadband performance is described in Section 9.7.

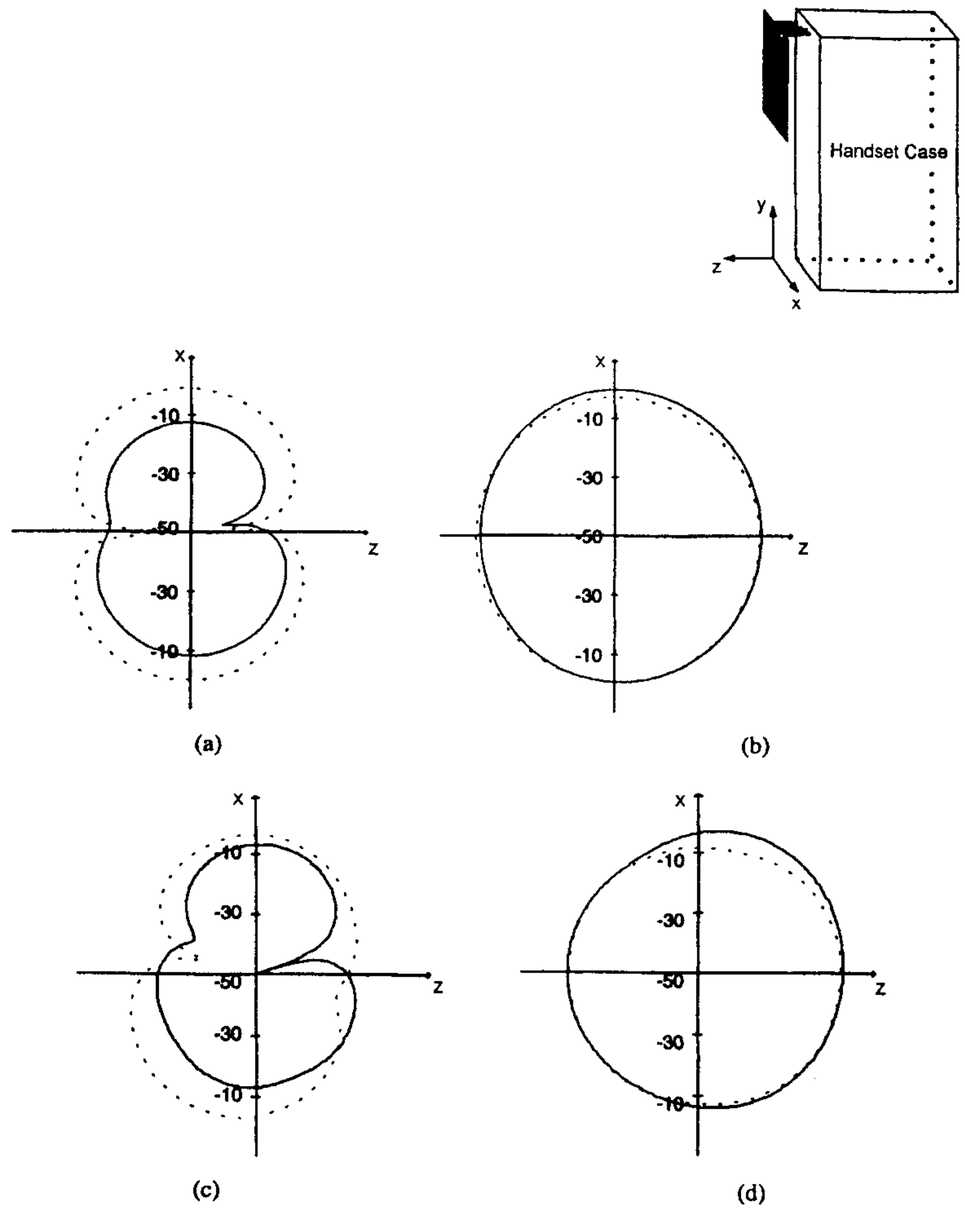

Figure 10.48 Comparison of measured and computed radiation patterns in the *x-z* plane. Other details as in Figure 10.46. ____, measured; ...., computed. (a) Horizontal polarization at 900 MHz, (b) vertical polarization (*y* directed) at 900 MHz, (c) horizontal polarization at 1.7 GHz, and (d) vertical polarization (*y* directed) at 1.76 GHz. (From [73]. © 1997 IEEE. Reprinted with permission.)

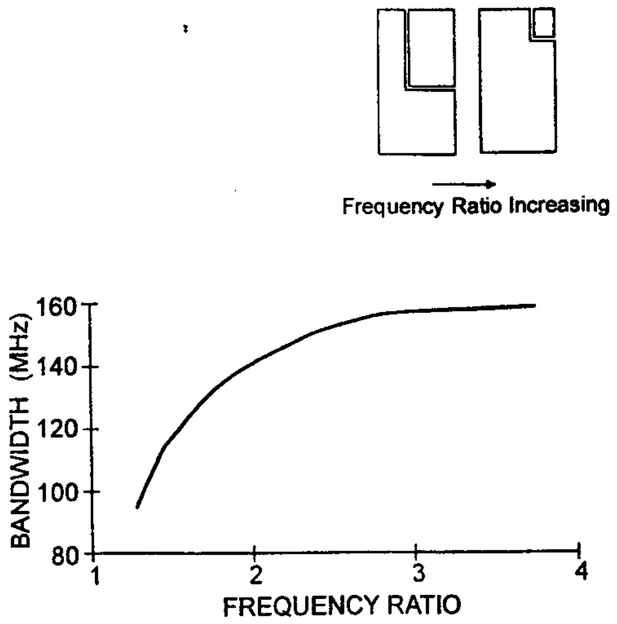

Figure 10.49 Bandwidth of the L-shaped element as a function of frequency ratio. (From [73]. © 1997 IEEE. Reprinted with permission.)

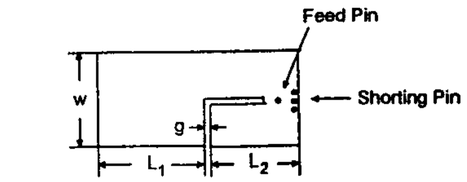

Dual-Band Inverted-F Antenna with a Single Feed

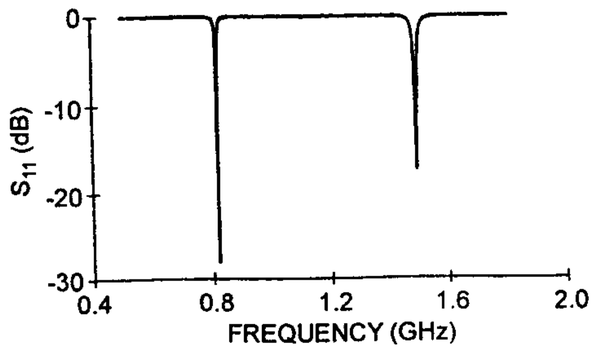

Figure 10.50 Measured return loss of a single-feed, dual-band PIFA antenna. $W = 28.5$ mm, $g = 1$ mm, $L_1 = 25$ mm, $L_2 = 14$ mm. (From [73]. © 1997 IEEE. Reprinted with permission.)

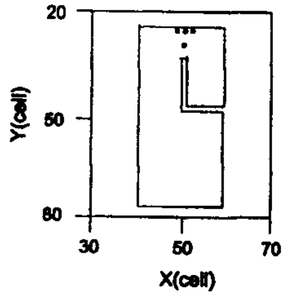

antenna layout in the FDTD computation space

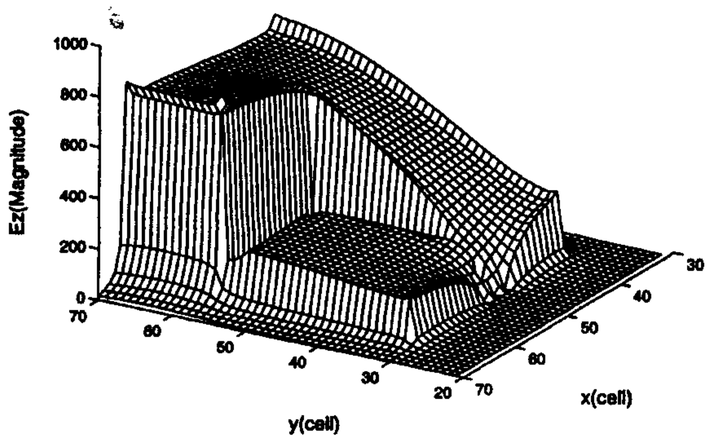

(a)

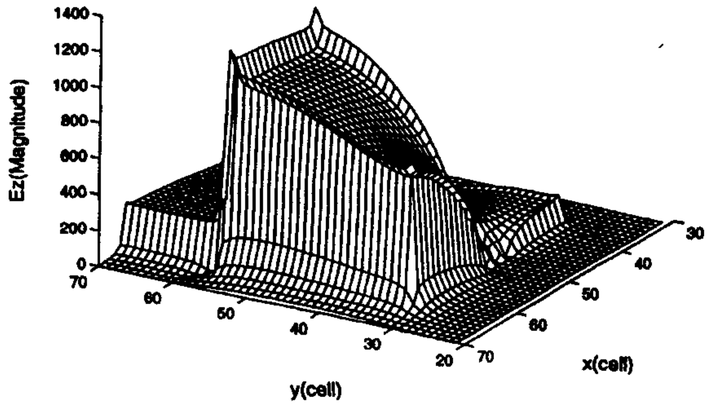

(b)

Figure 10.51 Computed electric field distribution in the one-port antenna. Field distribution (a) near 800 MHz and (b) near 1.5 GHz. Antenna details: $a = 62$ mm, $b = 138$ mm, $c = 30$ mm, $h = 1.143$ mm, $W = 28.5$ mm, $g = 1$ mm, $L_1 = 25$ mm, $L_2 = 14$ mm, $\epsilon_r = 2.2$. FDTD details: $\Delta x = 1$ mm, $\Delta y = 1$ mm, $\Delta z = 0.57$ mm and Gaussian pulse excitation. (From [73]. © 1997 IEEE. Reprinted with permission.)

References

[1] Schaubert, D. H., et al., "Microstrip Antennas With Frequency Agility and Polarization Diversity," *IEEE Trans. Antennas and Propagation*, Vol. AP-29, 1981, pp. 118–123.

[2] Bhartia, P., and I. J. Bahl, "Frequency Agile Microstrip Antennas," *Microwave J.*, Oct. 1982, pp. 67–70.

[3] Waterhouse, R. B., and N. V. Shuley, "Scan Performance of Infinite Arrays of Microstrip Patch Elements Loaded With Varactor Diodes," *IEEE Trans. Antennas and Propagation*, Vol. AP-41, 1993, pp. 1273–1280.

[4] Bhartia, P., and I. J. Bahl, "A Frequency Agile Microstrip Antenna," *IEEE AP-S Int. Symp. Digest*, 1982, pp. 304–307.

[5] Aberle, J. T., et al., "Scattering and Radiation Properties of Varactor-Tuned Microstrip Antennas," *IEEE AP-S Symp. Digest*, 1992, pp. 2229–2232.

[6] Waterhouse, R. B., and N. V. Shuley, "Dual Frequency Microstrip Rectangular Patches," *Electron. Lett.*, Vol. 28, 1992, pp. 606–607.

[7] Daryoush, A. S., K. Bontzos, and P. R. Herczfeld, "Optically Tuned Patch Antenna for Phased Array Applications," *IEEE AP-S Int. Symp. Digest*, 1986, pp. 361–364.

[8] Guo, Y. J., et al., "A Circular Patch Antenna for Radio LANs," *IEEE Trans. Antennas and Propagation*, Vol. AP-45, 1997, pp. 177–178.

[9] Zhou, G., "Shorting-Pin Loaded Annular Ring Microstrip Antenna," *IEEE AP-S Int. Symp. Digest*, 1998, pp. 900–903.

[10] Waterhouse, R. B., "The Use of Shorting Posts To Improve the Scanning Range of Probe-Fed Microstrip Patch Phased Arrays," *IEEE Trans. Antennas and Propagation*, Vol. AP-44, 1996, pp. 302–309.

[11] Gonzalo, R., P. de Maagt, and M. Sorolla, "Enhanced Patch-Antenna Performance by Suppressing Surface Waves Using Photonic-Bandgap Substrates," *IEEE Trans. Microwave Theory and Techniques*, Vol. MTT-47, 1999, pp. 2131–2138.

[12] Gauthier, G. P., A. Courtay, and G. M. Rebeiz, "Microstrip Antennas on Synthesized Low Dielectric-Constant Substrates," *IEEE Trans. Antennas and Propagation*, Vol. AP-45, 1997, pp. 1310–1314.

[13] Waterhouse, R. B., S. D. Targonski, and D. M. Kokotoff, "Design and Performance of Small Printed Antennas," *IEEE Trans. Antennas and Propagation*, Vol. AP-46, 1998, pp. 1629–1633.

[14] Sengupta, D. L., "Resonant Frequency of a Tunable Rectangular Patch Antenna," *Electron. Lett.*, Vol. 20, 1984, pp. 614–615.

[15] Wong, K.-L., and W.-S. Chen, "Compact Microstrip Antenna With Dual-Frequency Operation," *Electron. Lett.*, Vol. 33, 1997, pp. 646–647.

[16] Richards, W. F., and Y. T. Lo, "Theoretical and Experimental Investigations of a Microstrip Radiator With Multiple Lumped Linear Loads," *Electromagnetics*, Vol. 3, 1983, pp. 371–387.

[17] Srinivasan, V., R. Kapur, and G. Kumar, "MNM for Compact Dual Frequency Rectangular Microstrip Antenna," *Proc. APSYM-98*, Cochin, India, 1998, pp. 88–91.

[18] Waterhouse, R. B., "Small Microstrip Patch Antenna," *Electron. Lett.*, Vol. 31, 1995, pp. 604–605.

[19] Liu, Z. D., and P. S. Hall, "Dual-Band Antenna for Hand Held Portable Telephones," *Electron. Lett.*, Vol. 32, 1996, pp. 609–610.

[20] Rowell, C. R., and R. D. Murch, "A Capacitively Loaded PIFA for Compact Mobile Telephone Handsets," *IEEE Trans. Antennas and Propagation*, Vol. AP-45, 1997, pp. 837–842.

[21] Kossiavas, G., et al., "The C-Patch: A Small Microstrip Element," *Electron. Lett.*, Vol. 25, 1989, pp. 253–254.

[22] Singh, D., P. Gardner, and P. S. Hall, "Miniaturised Microstrip Antenna for MMIC Applications," *Electron. Lett.*, Vol. 33, 1997, pp. 1830–1831.

[23] Ogawa, K., and T. Uwano, "A Diversity Antenna for Very Small 800-MHz Band Portable Telephones," *IEEE Trans. Antennas and Propagation*, Vol. AP-42, 1994, pp. 1342–1345.

[24] Huang, C.-Y., et al., "Gain-Enhanced Compact Broadband Microstrip Antenna," *Electron. Lett.*, Vol. 34, 1998, pp. 138–139.

[25] Lo, T.-K., et al., "Miniature Aperture Coupled Microstrip Antenna of Very High Permittivity," *Electron. Lett.*, Vol. 33, 1997, pp. 9–10.

[26] Bokhari, S. A., et al., "A Small Microstrip Patch Antenna With a Tuning Option," *IEEE Trans. Antennas and Propagation*, Vol. AP-44, 1996, pp. 1521–1527.

[27] Chen, H.-T., "Compact Circular Microstrip Antenna With Embedded Chip Resistor and Capacitor," *IEEE AP-S Int. Symp. Digest*, 1998, pp. 1356–1359.

[28] Wong, K.-L., and S.-C., Pan, "Compact Triangular Microstrip Antenna," *Electron. Lett.*, Vol. 33, 1997, pp. 433–434.

[29] Lu, J.-H., and K.-P. Yang, "Slot-Coupled Compact Triangular Microstrip Antenna With Lumped Load," *IEEE AP-S Int. Symp. Digest*, 1998, pp. 916–919.

[30] Waterhouse, R. B., "Printed Antenna Suitable for Mobile Communication Handsets," *Electron. Lett.*, Vol. 33, 1997, pp. 1831–1832.

[31] Satpathy, S. K., K. P. Ray, and G. Kumar, "Compact Shorted Variations of Circular Microstrip Antenna," *Electron. Lett.*, Vol. 34, 1998, pp. 137–138.

[32] Chair, R., K. M. Luk, and K. F. Lee, "Small Dual Patch Antenna," *Electron. Lett.*, Vol. 35, 1999, pp. 762–764.

[33] Waterhouse, R. B., "Small Printed Antenna With Low Cross-Polarised Fields," *Electron. Lett.*, Vol. 33, 1997, pp. 1280–1281.

[34] Palanisamy, V., and R. Garg, "Analysis of Circularly Polarized Square Ring and Crossed-Strip Microstrip Antennas," *IEEE Trans. Antennas and Propagation*, Vol. AP-34, 1984, pp. 1340–1346.

[35] Chen, W.-S., and H.-D. Chen, "Single-Feed Circularly Polarized Square-Ring Microstrip Antenna With a Slit," *IEEE AP-S Int. Symp. Digest*, 1998, pp. 1360–1363.

[36] Wong, K.-L., and J.-Y. Wu, "Single-Feed Small Circularly Polarized Square Microstrip Antenna," *Electron. Lett.*, Vol. 33, 1997, pp. 1833–1834.

[37] Huang, C.-Y., and J.-Y. Wu, "Compact Microstrip Antenna Loaded With Very High Permittivity," *IEEE AP-S Int. Symp. Digest*, 1998, pp. 680–683.

[38] Yawata, M., and H. Arai, "Self-Diplexing Stacked Patch Antenna for Satellite Mode Handset System," *IEEE AP-S Int. Symp. Digest*, 1998, pp. 2124–2127.

[39] Ortiz, S., and A. Mortazawi, "A Compact Circularly Polarized Microstrip Transmit-Receive Antenna for LAN Applications," *IEEE AP-S Int. Symp. Digest*, 1998, pp. 2104–2107.

[40] Iwasaki, H., "A Circularly Polarized Small-Size Microstrip Antenna With a Cross Slot," *IEEE Trans. Antennas and Propagation*, Vol. AP-44, 1996, pp. 1399–1401.

[41] Lu, J.-H., C.-L. Tang, and K.-L. Wong, "Single-Feed Slotted Equilateral-Triangular Microstrip Antenna for Circular Polarization," *IEEE Trans. Antennas and Propagation*, Vol. AP-47, 1999, pp. 1174–1178.

[42] Lee, C. S., and V. Nalbandian, "Circularly Polarized Traveling-Wave Microstrip Antenna," *IEEE AP-S Int. Symp. Digest*, 1998, pp. 908–911.

[43] Fujimoto, K., et al., *Small Antennas*, Research Studies Press, New York, 1987.

[44] Vandenbosch, G. A. E., and A. R. Van de Capelle, "Study of the Capacitively Fed Microstrip Antenna Element," *IEEE Trans. Antennas and Propagation*, Vol. AP-42, 1994, pp. 1648–1652.

[45] Rowell, C. R., and R. D. Murch, "A Compact PIFA Suitable for Dual-Frequency 900/1800-MHz Operation," *IEEE Trans. Antennas and Propagation*, Vol. AP-46, 1998, pp. 596–598.

[46] Maci, S., and G. Biffi Gentili, "Dual-Frequency Patch Antennas," *IEEE Antennas and Propagation Magazine*, Vol. 39, Dec. 1997, pp. 13–20.

[47] Hall, P. S., "Review of Techniques for Dual and Circularly Polarised Microstrip Antennas," in *Microstrip Antennas: The Analysis and Design of Microstrip Antennas and Arrays*, D. M. Pozar, and D. H. Schaubert (Eds.), IEEE Press, New York, 1995, pp. 107–116.

[48] Wang, B. F., and Y. T. Lo, "Microstrip Antennas for Dual-Frequency Operation," *IEEE Trans. Antennas and Propagation*, Vol. AP-32, 1984, pp. 938–943.

[49] Yazidi, M. El, M. Himdi, and J. P. Daniel, "Aperture Coupled Microstrip Antenna for Dual Frequency Operation," *Electron. Lett.*, Vol. 29, 1993, pp. 1506–1508.

[50] Maci, S., G. B. Gentili, and G. Avitabile, "Single-Layer Dual Frequency Patch Antenna," *Electron. Lett.*, Vol. 29, 1993, pp. 1441–1443.

[51] Lu, J.-H., "Single-Feed Dual-Frequency Rectangular Microstrip Antenna With Pair of Step-Slots," *Electron. Lett.*, Vol. 35, 1999, pp. 354–355.

[52] Antar, Y. M. M., A. I. Ittipiboon, and A. K. Bhattacharyya, "A Dual-Frequency Antenna Using a Single Patch and an Inclined Slot," *Microwave and Optical Tech. Lett.*, Vol. 8, 1995, pp. 309–310.

[53] James, J. R., and P. S. Hall (Eds.), *Handbook of Microstrip Antennas*, Vol. 1, Peter Peregrinus, London, UK, 1989.

[54] Murakami, Y., W. Chujo, and M. Fujise, "Mutual Coupling Between Two Ports of Dual Slot Coupled Circular Patch Antennas," *IEEE AP-S Int. Symp. Digest*, 1993, pp. 1469–1472.

[55] Hall, P. S., "Dual Polarisation Antenna Arrays With Sequentially Rotated Feeding," *IEE Proc.*, Vol. 139, Pt. H, 1992, pp. 465–471.

[56] Piazzesi, P., S. Maci, and G. Biffi Gentili, "Dual-Band Dual-Polarization Patch Antennas," *Int. MiMiCAE J.*, Vol. 5, 1995, pp. 375–384.

[57] Murakami, Y., et al., "Dual Slot-Coupled Microstrip Antenna for Dual Frequency Operation," *Electron. Lett.*, Vol. 29, 1993, pp. 1906–1907.

[58] Habib, L., G. Kossiavas, and A. Papiernik, "Cross Shaped Patch With Etched Bars for Dual Polarisation," *Electron. Lett.*, Vol. 29, 1993, pp. 916–918.

[59] Pozar, D. M., and S. M. Duffy, "A Dual-Band Circularly Polarized Aperture-Coupled Stacked Microstrip Antenna for Global Positioning Satellite," *IEEE Trans. Antennas and Propagation*, Vol. AP-45, 1997, pp. 1618–1624.

[60] Karamakar, N. C., and M. E. Bialkowski, "Circularly Polarized Aperture-Coupled Circular Microstrip Patch Antennas for L-Band Applications," *IEEE Trans. Antennas and Propagation*, Vol. AP-47, 1999, pp. 933–940.

[61] Suzuki, Y., N. Miyano, and T. Chiba, "Circularly Polarised Radiation From Singly Fed Equilateral-Triangular Microstrip Antenna," *IEE Proc. H*, Vol. 134, 1987, pp. 194–198.

[62] Murakami, Y., et al., "Dual Band Circularly Polarised Stub Loaded Microstrip Antenna," *Int. Symp. on Antennas and Propagation, ISAP92*, 1992, pp. 793–796.

[63] Nakano, M., et al., "Double Layered Self Diplexing Antenna Using Ring Patch Antenna and Its Feed Circuits," *IEEE AP-S Int. Symp. Digest*, 1992, pp. 483–486.

[64] Chujo, W., et al., "Improvement of the Isolation Characteristics of a Two Layer Self Diplexing Array Antenna Using a Circularly Polarised Ring Patch Antenna," *IEICI Trans.*, Vol. E76-B, 1993, pp. 755–758.

[65] Tang, C.-L., H.-T. Chen, and K.-L. Wong, "Small Circular Microstrip Antenna With Dual Frequency Operation," *Electron. Lett.*, Vol. 33, 1997, pp. 1112–1113.

[66] Pan, S.-C., and K.-L. Wong, "Design of Dual-Frequency Microstrip Antennas Using a Shorting Pin Loading," *IEEE AP-S Symp. Digest*, 1998, pp. 312–315.

[67] Yang, K.-P., and K.-L. Wong, "Inclined-Slot-Coupled Compact Dual-Frequency Microstrip Antenna With Cross-Slot," *Electron. Lett.*, Vol. 34, 1998, pp. 321–322.

[68] Wong, K. L., and K. P. Yang, "Small Dual-Frequency Microstrip Antenna With a Cross-Slot," *Electron. Lett.*, Vol. 33, 1997, pp. 1916–1917.

[69] Chen, W.-S., "Single Feed Dual Frequency Rectangular Microstrip Antenna With Square Slot," *Electron. Lett.*, Vol. 34, 1998, pp. 231–232.

[70] Palniswamy, V., and R. Garg, "Rectangular Ring and H-Shaped Microstrip Antennas: Alternatives to Rectangular Patch Antenna," *Electron. Lett.*, Vol. 21, 1985, pp. 874–876.

[71] Lee, E., P. S. Hall, and P. Gardner, "Compact Dual-Band Dual-Polarisation Microstrip Patch Antennas," *Electron. Lett.*, Vol. 35, 1999, pp. 1034–1036.

[72] Delaveaud, Ch., Ph. Leveque, and B. Jecko, "New Kind of Microstrip Antenna: Monopolar Wire Patch Antenna," *Electron. Lett.*, Vol. 30, 1994, pp. 1–2.

[73] Liu, Z. D., P. S. Hall, and D. Wake, "Dual-Frequency Planar Inverted-F Antenna," *IEEE Trans. Antennas and Propagation*, Vol. AP-45, 1997, pp. 1451–1458.

[74] Taga, T., and K. Tsunekawa, "Performance Analysis of a Built-In Planar Inverted-F Antenna for 800 MHz Band Radio Units," *IEEE J. Select. Areas Commun.*, Vol. SAC-5, 1987, pp. 921–929.

[75] Croq, F., and D. M. Pozar, "Multifrequency Operation of Microstrip Antennas Using Aperture Coupled Parallel Resonators," *IEEE Trans. Antennas and Propagation*, Vol. AP-40, 1992, pp. 1367–1374.

11

Active Integrated Microstrip Antennas

11.1 Introduction

Active integrated antennas are antennas in which the active devices are integrated directly in the antenna structure. The whole system is treated together with the antenna simultaneously serving the function of load as well as radiator. This is in contrast to a conventional antenna subsystem design in which each component is designed separately and then connected via transmission lines. By directly integrating active devices into antenna elements, feed line losses can be significantly reduced. This is particularly important as the operating frequency increases. Further advantages include size and weight reductions, enhanced reliability, and lower manufacturing costs.

Active integrated antennas have many potential applications in radar and communications. They can be used as modules for a high-gain phased array and in a spatial power combiner to overcome limited output power from a solid-state device. They also have strong potential for commercial applications in wireless communications and radar and as low-cost and compact transceivers and sensors.

Various antennas have been integrated to active devices [1–4]. However, only the integration of microstrip patches with active devices is treated in this chapter. Classification of active antennas and their design methodologies are discussed together with some design samples.

11.2 Classification of Active Integrated Microstrip Antennas

Active integrated antennas can be classified by the function of active devices they integrate. The basic functions of these devices in active integrated antennas

are RF signal generation, RF signal amplification, or frequency conversion. Depending on the function of the active device, the active integrated antennas can be classified into the oscillator type, the amplifier type, and the frequency conversion type [1–4]. These basic units can be combined in an active integrated antenna to perform a more complicated function, for example, as transceivers or transponders, as required by the intended applications.

11.2.1 Oscillator Type

When an active device is integrated with a microstrip antenna for the purpose of generating a steady-state oscillation, it is classified as an *oscillator-type active integrated microstrip antenna*. The oscillator type converts dc power to RF power using the negative resistance characteristics of an active device. This type of active antenna has been developed for sensor applications [5, 6]; however, much of its progress has been generated by the interest in the potential for spatial power combiner applications to overcome the power limitations of solid-state sources at high frequency.

The oscillator consists of an active device in conjunction with a microstrip antenna that simultaneously serves as a load determining the frequency of oscillation and a radiating element of the generated RF power into free space. A proper selection of an operating point of the active device is important for the operational performance. The active elements can be two terminal devices, for example, IMPATT diodes and Gunn diodes, or they can be three terminal devices, for example, MESFET, HEMT, and HBT. Two examples using a diode and a transistor are illustrated in Figure 11.1. Figure 11.1(a) shows a patch antenna integrated with a Gunn diode. A dc bias and matching circuits are also shown in the configuration. Figure 11.1(b) is a schematic diagram of a patch integrated with a FET in a parallel feedback topology [7]. The examples clearly demonstrate that the patch antennas are integral parts of the active device circuits, which have to be considered simultaneously during the design process.

In general, both advantages and disadvantages are associated with each type of solid-state source. Two-terminal devices are suitable for high-power applications at millimeter-wave frequencies, but have the disadvantage of low DC-to-RF efficiency, thus requiring a better process for heat dissipation in circuit design. Higher DC-to-RF efficiency and low-noise figure can be achieved by using three-terminal devices. Circuit design is more complicated, but integration with planar circuit structure, either in a hybrid or monolithic approach, is easier. Transistor oscillators are also more flexible, allowing for better control of oscillation frequencies, temperature stability, and output noise. The power

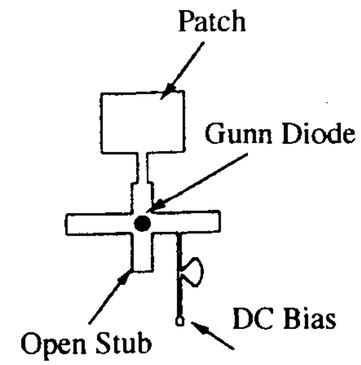

(a)

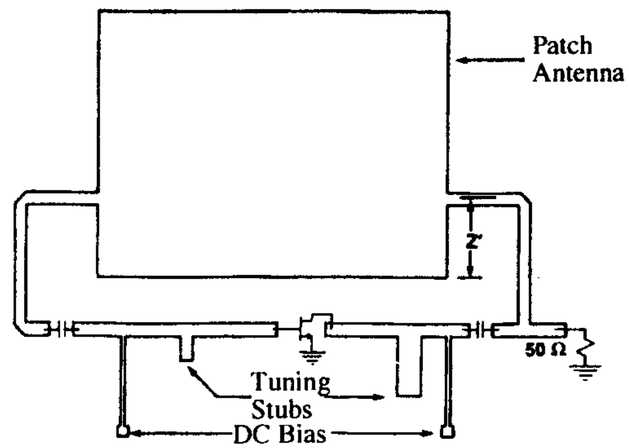

(b)

Figure 11.1 Oscillator-type active integrated antennas: (a) Patch integrated with a Gunn diode. (From [4]. © 1994 IEEE. Reprinted with permission.) (b) Patch integrated with a FET. (From [7]. © 1991 *Microwave Journal*. Reprinted with permission.)

versus frequency performance for typical commercial Gunn and IMPATT diodes and transistors are shown in Figure 11.2 [8, 9].

11.2.2 Amplifier Type

The integration of a two-port active device with a passive microstrip antenna at the input or the output port for the purpose of signal amplification is classified as being of the amplifier type. When the antenna is at the input port,

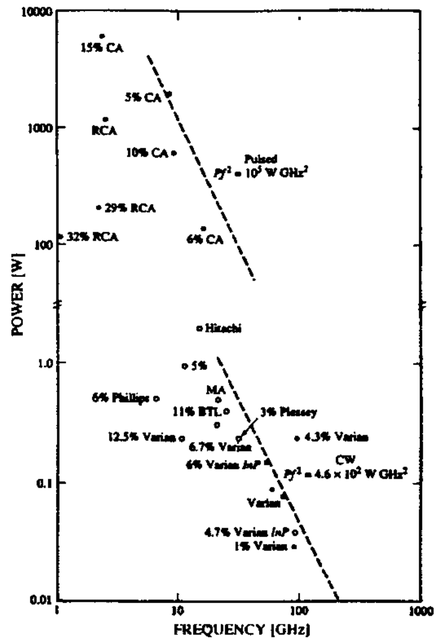

(a)

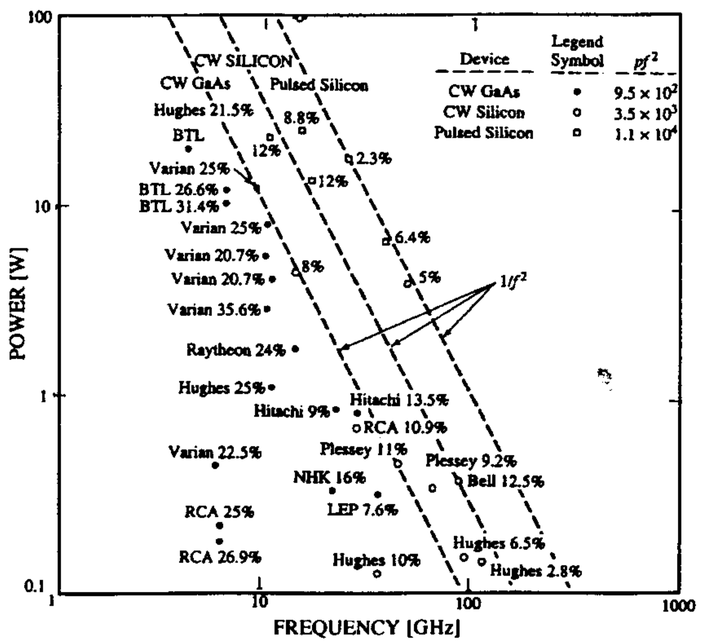

(b)

Figure 11.2 Power versus frequency performance: (a) Gunn diodes. (From [8]. © 1998 John Wiley & Sons. Reprinted with permission.) (b) IMPATT diodes. (From [8]. © 1998 John Wiley & Sons. Reprinted with permission.) (c) Transistors. (From [9]. © 1992 *Microwave Journal*. Reprinted with permission.)

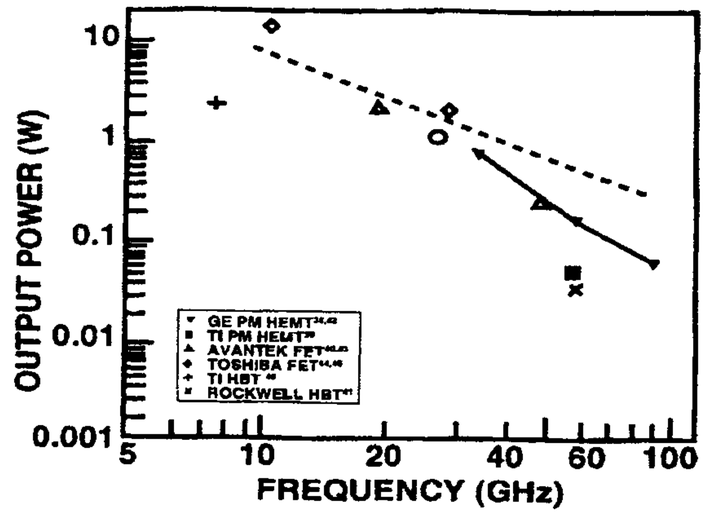

(c)

Figure 11.2 (continued).

it is considered to be a source impedance for the device. The integrated active antenna works as a receiver. The low-noise amplifier design technique is usually applied in order to achieve the required noise performance. When the antenna is placed at the output port, it acts as a device load impedance. In this case, the integrated active antenna functions as a transmitter. An amplifier design technique for achieving gain bandwidth performance is generally applied. Examples of transmit and receive active integrated microstrip antennas are shown in Figure 11.3. Figures 11.3(a) and (b) show relative locations of a patch to a FET when the active integrated antennas operates as a transmitter and a receiver, respectively.

The advantages of incorporating an amplifier with a passive antenna structure include gain and bandwidth enhancement and improvement of noise performance. Active microstrip antennas using FETs are compatible with microwave integrated circuit (MIC) and monolithic microwave integrated circuit (MMIC) technologies, allowing easy integration, which leads to compactness and potentially low costs of fabrication. Interest in this type of active microstrip antennas is growing because of its potential applications in large phased arrays and in spatial power combining amplifiers [1–4, 10–12].

11.2.3 Frequency Conversion Type

When a microstrip antenna is integrated with an active device for the purpose of frequency translation either up or down, it is classified as the frequency conversion type. The conversion efficiency is an important performance parame-

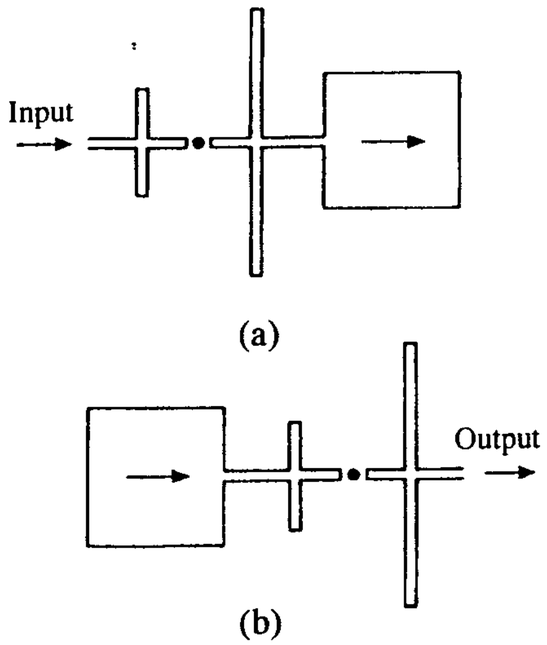

Figure 11.3 Amplifying active integrated microstrip antennas: (a) Transmitting case and (b) receiving case. (From [10]. © 1993 *Electronics Letters*. Reprinted with permission.)

ter. The active devices are biased to operate in a nonlinear region. This type of active antenna can be used as oscillator/modulator in a compact transmitter application or as an oscillator/mixer in a receiver application. Two-terminal devices, for example, Gunn diodes, and three-terminal active devices, for example, HEMT or MESFET, can be used. The advantages of three-terminal devices are conversion gain and compatibility with MIC and MMIC technologies at the cost of increased circuit complexity. Applications for this type of active antennas include short-distance communications, microwave identification systems, and local-area networks.

Various design configurations have been reported in the literature for receiver, modulator, and sensor applications [13–15]. Topologies of using separated devices for local oscillator (LO) and mixers and self-oscillating mixers, in which a single device both produces the LO power and mixes the LO with the RF signal, have been demonstrated with excellent results [16, 17].

Examples of frequency conversion-type antennas are shown in Figures 11.4(a) and (b). In Figure 11.4(a), a patch antenna forms part of the feedback loop for a FET oscillator, which is biased for a class C operational characteristic. A modulating signal is applied to vary the drain voltage, which in turn controls the output level of the oscillator. The patch radiates this amplitude-modulated

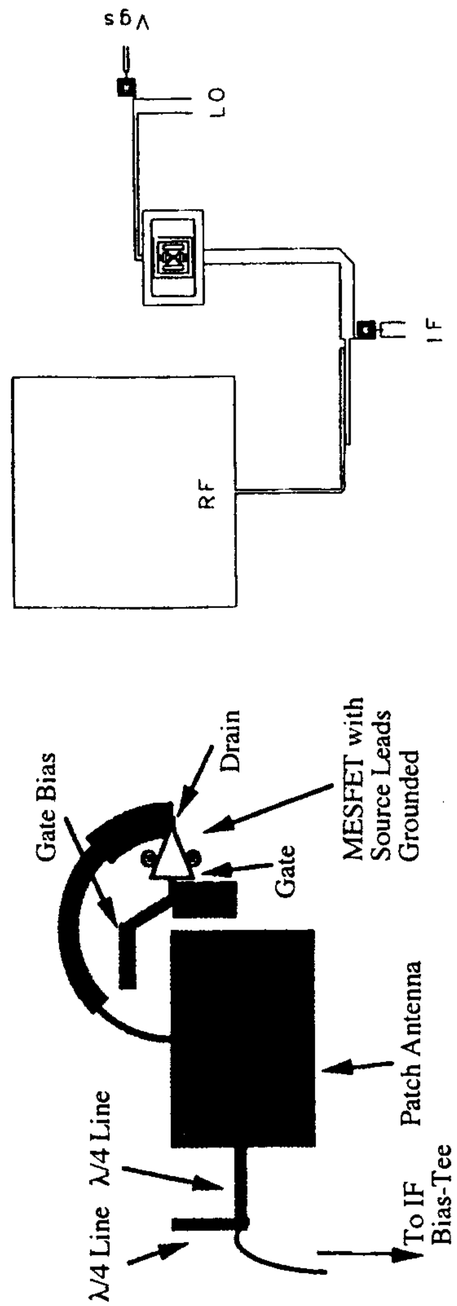

Figure 11.4 (a) An oscillator/modulator active integrated microstrip patch antenna. (From [14]. © 1994 IEEE. Reprinted with permission.) (b) An integrated patch antenna receiver. (From [13]. © 1994 IEEE. Reprinted with permission.)

RF signal of the oscillator. Figure 11.4(b) is a receiver schematic showing the RF signal from a patch and LO for a generation of IF signal.

In the following sections, the basic design principles for each group are discussed and design samples are presented. The complete theory for each design principle is beyond the scope of this book and will be left to more advanced texts [18–22].

11.3 Theory and Design of Active Integrated Microstrip Antenna Oscillators

An active integrated microstrip antenna oscillator converts dc to radiated RF power. It consists of two main parts, an active element and a passive microstrip antenna. An active element utilizes a variety of solid-state two-terminal or three-terminal devices. A passive microstrip antenna serves the functions of a radiator and the active device load to initiate and maintain oscillation. It can also become part of the active device dc bias circuit. It is important that the dc bias circuit be RF isolated. In general, the DC-to-RF conversion efficiency is low (see Figure 11.2), hence a large portion of the dc power is dissipated in the form of heat. Depending on the level of power requirement, proper heat sinking of the device may be required.

The theory behind microwave oscillators is well developed and is published in many available textbooks, for example, [18–20]. The theory will be applied to the design of active integrated microstrip antenna oscillators. The operation and design of one-port active device oscillators is first discussed. It is followed by two-port active device oscillator designs. IMPATT and Gunn diodes are usually utilized in one-port oscillators, whereas FET or bipolar (HBT) diodes are chosen for the latter.

11.3.1 One-Port Active Integrated Microstrip Antenna Oscillators

A general RF equivalent circuit for a one-port device oscillator is shown in Figure 11.5. Z_D is the impedance of the device at the fundamental oscillating frequency and Z_C is the driving-point impedance presented to the terminals of the device. The term Z_C includes the microstrip antenna impedance and a matching network. Terms Z_C and Z_D can be written as

$$Z_C = R_C + jX_C \tag{11.1}$$

$$Z_D = R_D + jX_D \tag{11.2}$$

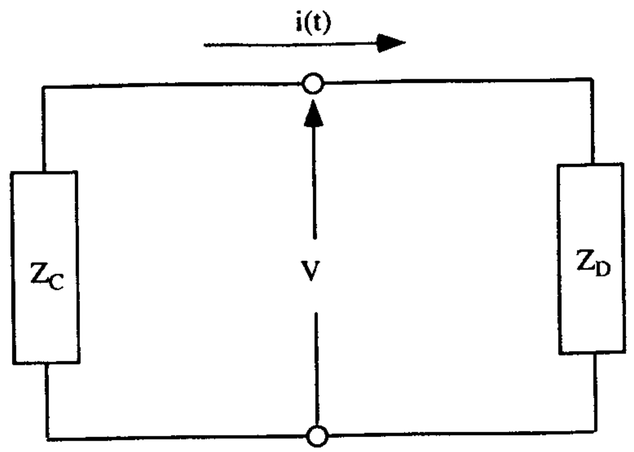

Figure 11.5 Schematic diagram of one-port negative-resistance oscillators.

Applying the voltage law to the circuit in Figure 11.5 gives

$$(Z_D + Z_C)I = 0 \tag{11.3}$$

If the circuit is capable of generating a steady-state oscillation, the current I is nonzero. Hence, (11.3) gives

$$R_D + R_C = 0 \tag{11.4}$$

$$X_D + X_C = 0 \tag{11.5}$$

In terms of the reflection coefficients Γ_C and Γ_D, (11.3) implies that

$$\Gamma_C \cdot \Gamma_D = 1 \tag{11.6}$$

Because $R_C > 0$ for a passive load, (11.4) requires that $R_D < 0$, which is obtainable from a device operating as a negative resistance under a proper bias condition. Equations (11.4) and (11.5) are the steady-state oscillating conditions. More rigorous derivations can be found in [19, 23]. For oscillations to build up and stabilize at a steady-state value, it is required, at the small signal level, that [18, 24]

$$|R_D| > R_C \tag{11.7}$$

Equations (11.7) and (11.4) simply state that initially the energy generated by the device is more than the dissipated energy at the load. This allows the

oscillation to build up until it reaches the steady state where the energy produced by the device is equal to the energy dissipated in the load R_C. This is possible because $|R_D|$ varies with both the amplitude of the RF current I and frequency. The oscillating frequency f_0 at the steady-state can be determined from (11.5), which is the condition of the circuit at resonance.

11.3.2 Active Patch Antennas Integrated With Diodes

In this section the design sample of a rectangular patch antenna integrated with a Gunn diode [7] is first discussed. The schematic diagram of the antenna configuration and its equivalent transmission line model are shown in Figure 11.6. Generally, the design goal for this type of integrated antenna is to produce the highest radiated power possible. The antenna design procedure can be summarized below.

1. Determine the antenna dimensions at the desired operational frequency. For a quick calculation, various design equations published in the texts on microstrip antennas [25, 26] can be applied. Commercially available numerical tools such as @ENSEMBLE can also be used for a more accurate result.
2. Match the device impedance to the antenna impedance. If it is necessary, a matching circuit can be utilized. A selection of a circuit topology usually depends on degradation effects on the copolar and cross-polar radiation patterns, the complexity of a device integration, and physical sizes of a device and a patch.
3. Provide a dc bias circuit that is well isolated from the RF circuit. Considerations should also be given to its physical realization and minimal degradation on the antenna radiating characteristics.
4. Heat dissipation and hermetic sealing may have to be considered depending on the power level and the intended applications. Heat dissipation is important at high frequencies where devices are less efficient and circuit dimensions are small.

Design Samples

The dimensions of the patch antenna, Figure 11.6 (a), operating at f_0 can be calculated from

$$L = \frac{c}{2f_0\sqrt{\epsilon_e}} - 2\Delta l \tag{11.8}$$

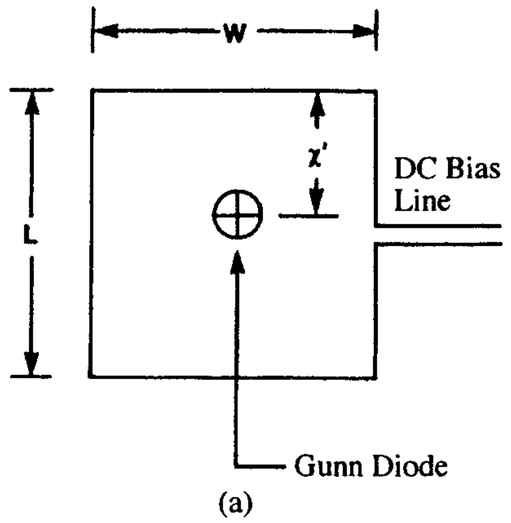

(a)

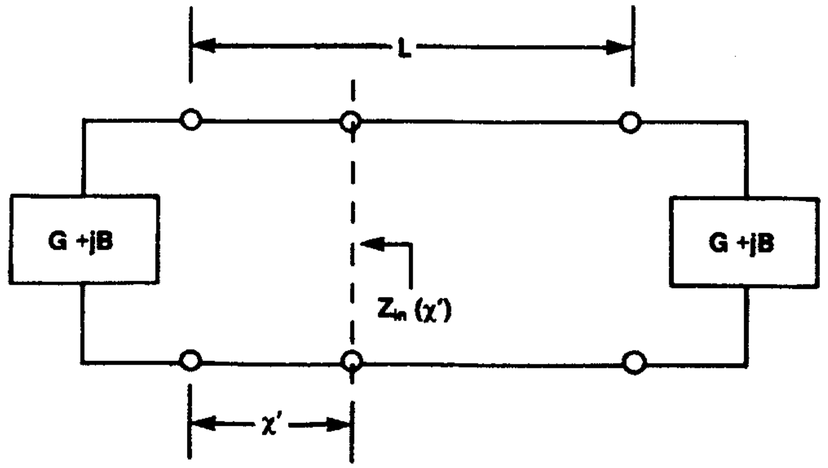

(b)

Figure 11.6 An active patch antenna integrated with a Gunn diode: (a) Schematic diagram and (b) transmission line model. (From [7]. © 1991 *Microwave Journal*. Reprinted with permission.)

where c is the velocity of light, L is the length of the patch antenna, and ϵ_e is the effective dielectric constant of the microstrip, given by

$$\epsilon_e = \frac{\epsilon_r + 1}{2} + \frac{\epsilon_r - 1}{2}\left(1 + \frac{10h}{W}\right)^{-0.5} \tag{11.9}$$

and Δl is the line extension, given by

$$\Delta l = 0.412h\frac{(\epsilon_e + 0.3)\left(\frac{W}{h} + 0.264\right)}{(\epsilon_e - 0.258)\left(\frac{W}{h} + 0.813\right)} \tag{11.10}$$

where h is the substrate thickness, W is the patch width, and ϵ_r is the dielectric constant of the substrate. Using the transmission line model, the input impedance of the patch antenna at a point x' is given by

$$Z_{\text{in}}(x') = \frac{1}{2G}\left[\cos^2(\beta x') + \frac{G^2 + B^2}{Y_0^2}\sin^2(\beta x') - \frac{B}{Y_0}\sin(2\beta x')\right] \tag{11.11}$$

where β is the propagation constant of the microstrip line, Y_0 is the characteristic admittance of the microstrip line, and G and B are the total antenna conductance and the radiating edge susceptance, respectively. Equation (11.11) can be further simplified for the practical case of $G/Y_0 << 1$ and $B/Y_0 << 1$ to

$$Z_{\text{in}}(x') = \frac{\cos^2(\beta x')}{2G} \tag{11.12}$$

The total conductance G includes both self-conductance G_r and mutual conductance G_m and, for the dominant mode, it is given by

$$G = G_r - G_m \tag{11.13}$$

$$G_m = \frac{1}{120\pi^2}\int_0^{\pi}\frac{\sin^2\left(\frac{\pi W}{\lambda_0}\cos\theta\right)\sin^3(\theta)}{\cos^2(\theta)}J_0\left(\frac{2\pi L}{\lambda_0}\sin(\theta)\right)d\theta \tag{11.14}$$

$$G_r = \begin{cases} \dfrac{W^2}{90\lambda_0^2}, & W < 0.35\lambda_0 \\ \dfrac{W}{120\lambda_0} - \dfrac{1}{60\pi^2}, & 0.35\lambda_0 \le W \le 2\lambda_0 \\ \dfrac{W}{120\lambda_0}, & 2\lambda_0 < W \end{cases} \tag{11.15}$$

where J_0 is the Bessel function of the first kind and λ_0 is the free-space wavelength. From the oscillation condition, R_{in} will be set equal to $|R_d|$ of a Gunn diode with a typical value of 8Ω. This allows the calculation of position x' for the diode location from (11.12) since, at resonance, $Z_{\text{in}}(x') = R_{\text{in}}(x')$.

$$x' = \frac{\lambda g}{2\pi}\arccos\sqrt{2|R_d|(G_r - G_m)} \tag{11.16}$$

One of the diode terminals is connected to the patch at x' and the other terminal is connected to the patch ground plane. A dc bias, which is well isolated from RF, is accomplished by using a $\frac{\lambda_g}{4}$ high-impedance microstrip line with one end attached to the low-impedance point on the nonradiating edge of the patch. The other end of the high-impedance line is terminated in a low-impedance pad, which is connected to a dc voltage source. For the antenna to oscillate, the dc bias voltage must be set greater than the threshold voltage where the device behaves as a negative resistance.

Measured results of the active antennas confirm that the antenna oscillates and generates RF power. Its output power and oscillating frequencies vary with dc bias voltage as illustrated in Figure 11.7. A 3-dB power variation tuning range of 839 MHz was achieved from 9.278 to 10.117 GHz, which is equivalent to a 9% bandwidth. The antenna radiation patterns (see Figure 11.8) show very little change as the bias voltage is varied. The beamwidths of ±45 degrees are observed for all cases. The small pattern irregularities with a peak at

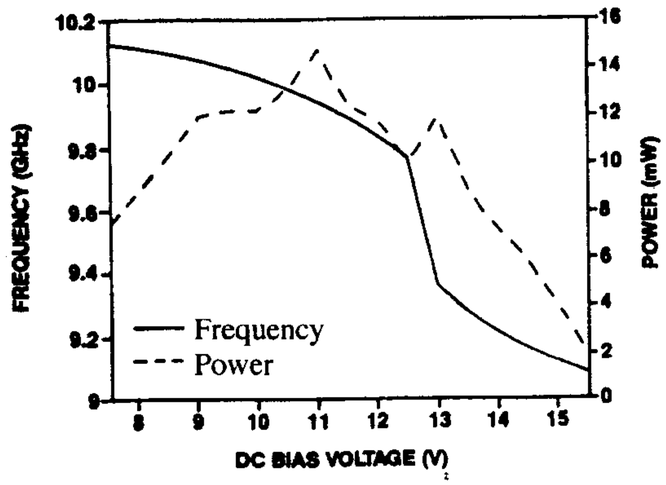

Figure 11.7 Radiated power and frequency of operation versus diode bias voltage. (From [7]. © 1991 *Microwave Journal*. Reprinted with permission.)

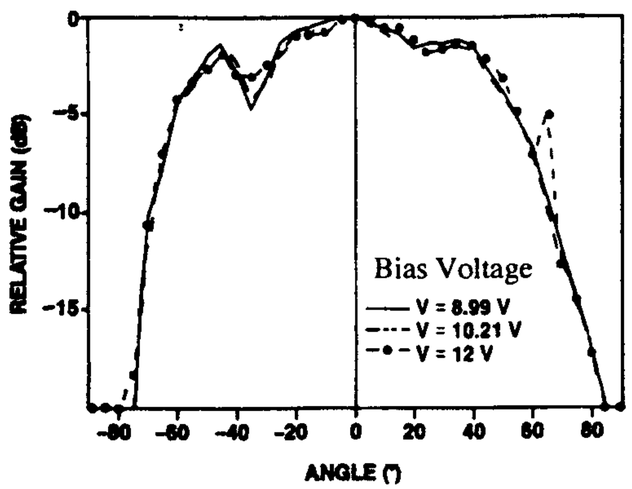

Figure 11.8 Active patch antenna H-plane pattern for different values of diode bias voltage. (From [7]. © 1991 *Microwave Journal*. Reprinted with permission.)

−60 degrees has been attributed to experimental setup. The results on the cross-polar pattern are not reported.

Following a similar procedure, the integration of a circular patch with an IMPATT diode can be designed [27]. The active antenna schematic diagram is shown in Figure 11.9. The circular patch antenna was fabricated on RT/Duroid 5880, 0.031 in. thick and with a 2.2 dielectric permittivity. The antenna dimension operating in the TM_{11} mode at the required operating frequency is determined from

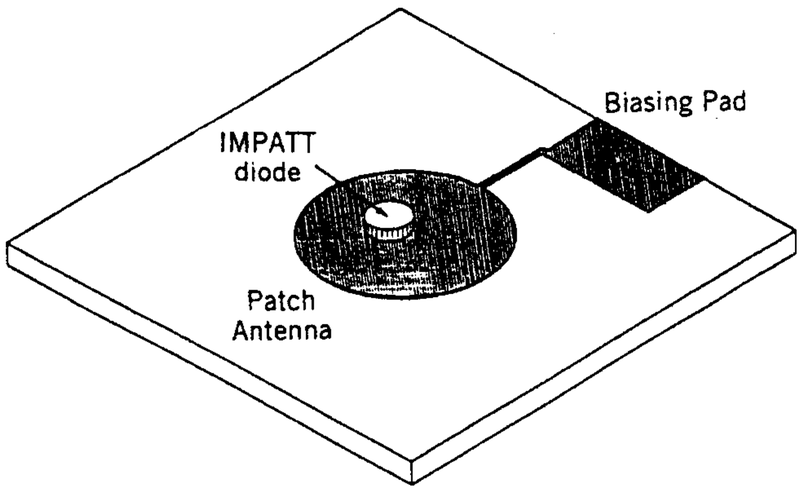

Figure 11.9 A circular patch antenna integrated with an IMPATT diode. (From [2]. © 1996 John Wiley & Sons. Reprinted with permission.)

$$a = \frac{K}{\left[1 + \frac{2h}{\pi K \epsilon_r}\left(\ln\left(\frac{\pi K}{2h}\right) + 1.7726\right)\right]^{0.5}} \tag{11.17}$$

where

$$K = \frac{8.794}{f_0\sqrt{\epsilon_r}} \tag{11.18}$$

and f_0 is the resonating frequency in gigahertz. The disk input resistance, $R_{\text{in}}(a_0)$, at a radial distance a_0 can be written as

$$R_{\text{in}}(a_0) = \frac{1}{G_r}\left(\frac{J_1(ka_0)}{J_1(ka)}\right)^2 \tag{11.19}$$

$$G_r = \frac{(k_0 a)^2}{480}\int_0^{\pi/2} [\{J_0(k_0 a\sin\theta) - J_2(k_0 a\sin\theta)\}^2 + \cos^2\theta\{J_0(k_0 a\sin\theta) + J_2(k_0 a\sin\theta)\}^2]\sin\theta d\theta \tag{11.20}$$

where k_0 and k are the propagation constants in free space and in the substrate, respectively. The location of the IMPATT diode can be found by matching the antenna input impedance to the IMPATT diode impedance, which is 1Ω. Equations (11.19) and (11.20) can be used to determine the value of a_0. For biasing, a dc circuit consists of a high-impedance microstrip transmission line connecting a low-impedance pad to a low-impedance point on the patch. The bias circuit acts as a low-pass filter, which isolates a dc source from RF.

The antenna radiation patterns are shown in Figure 11.10. It is reported that the integrated IMPATT diode/patch exhibited very high overall efficiency with an effective radiated power (ERP) on the boresight of $14.1W$ (+41.5 dBm) at 6.8 GHz.

Other topologies for matching low impedance of a diode to a patch have also appeared in the literature [2, 28]. Bartolic reported the integration of packaged Gunn diodes with modified rectangular patches using various forms of impedance inverters [28]. One of the configurations is shown in Figure 11.11 with the measured input impedance of the patch shown in Figure 11.12. At 9.13 GHz, the antenna input impedance is matched to the Gunn diode impedance. Figures 11.13(a) and (b) show the measured results of the EIRP

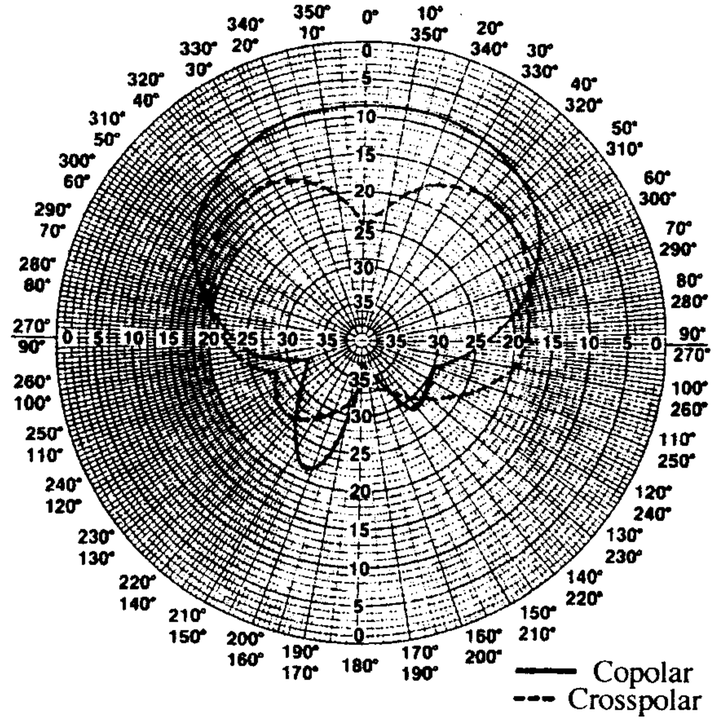

Figure 11.10 Copolar and cross-polar H-plane radiation patterns. (From [27]. © 1987 *Microwave Journal*. Reprinted with permission.)

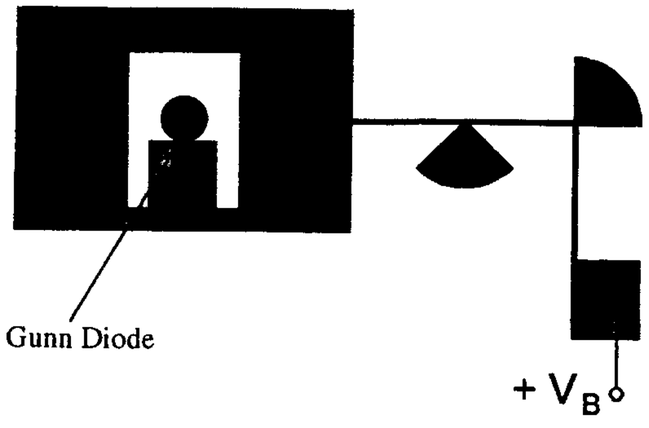

Figure 11.11 A rectangular patch with the impedance inverter integrated with a Gunn diode. (From [28]. © 1996 IEEE. Reprinted with permission.)

and of free-running oscillating frequency as a function of the dc bias voltage. The measured E- and H-plane radiation patterns in Figure 11.14 show lower cross-polarization levels in comparison to a similar unmodified active patch antenna.

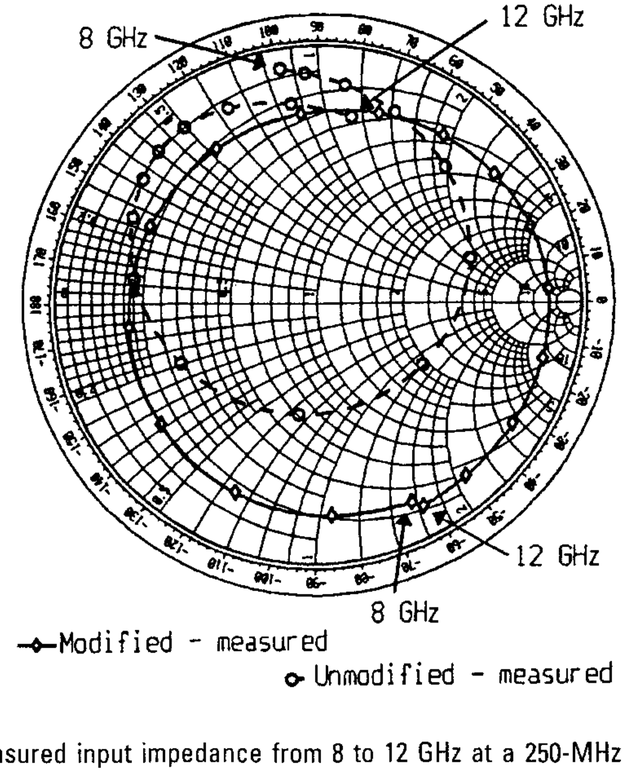

Figure 11.12 Measured input impedance from 8 to 12 GHz at a 250-MHz increment. (From [28]. © 1996 IEEE. Reprinted with permission.)

A 60-GHz band active microstrip patch antenna using a packaged Gunn diode is shown in Figure 11.15 [2, 29]. The high input impedance at the radiating edge of the patch is matched to the Gunn diode impedance using a microstrip impedance transformer. Measured dc bias tuning characteristics in Figure 11.16 indicate that the maximum power of 9.26 mW was generated at 63.24 GHz and 3V dc bias. The reported H-plane pattern appears overly directive with a 10-dB beamwidth of 30°.

11.3.3 Active Patch Antennas Integrated With Two-Port Devices

Oscillator-type integrated patch antennas can also be realized with two-port active devices. Various types of transistors such as FET, HEMT, BJT, and HBT can be selected depending on a number of factors including frequency of operation, noise figure, and power capacity. Oscillator active antennas can be realized with feedback amplifier and two-port negative resistance topologies.

Two-Port Negative Resistance Oscillator Active Patch Antennas

A general block diagram of a two-port negative resistance oscillator is illustrated in Figure 11.17. The diagram consists of input and output networks and a

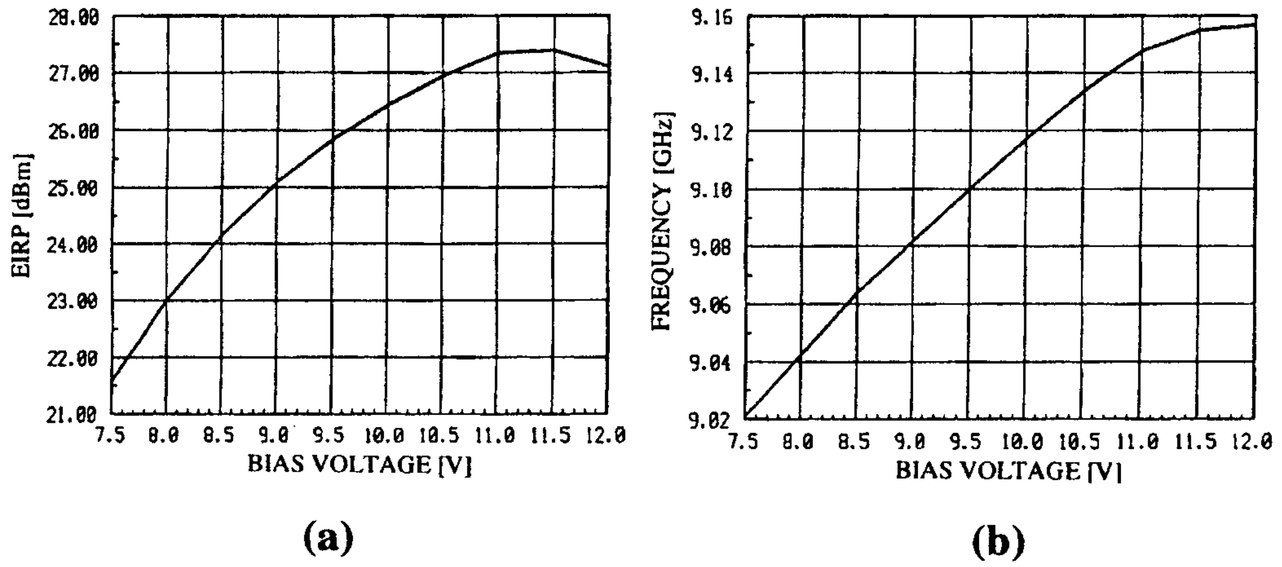

Figure 11.13 (a) EIRP versus diode bias voltage. (b) Oscillating frequency versus diode bias voltage. (From [28]. © 1996 IEEE. Reprinted with permission.)

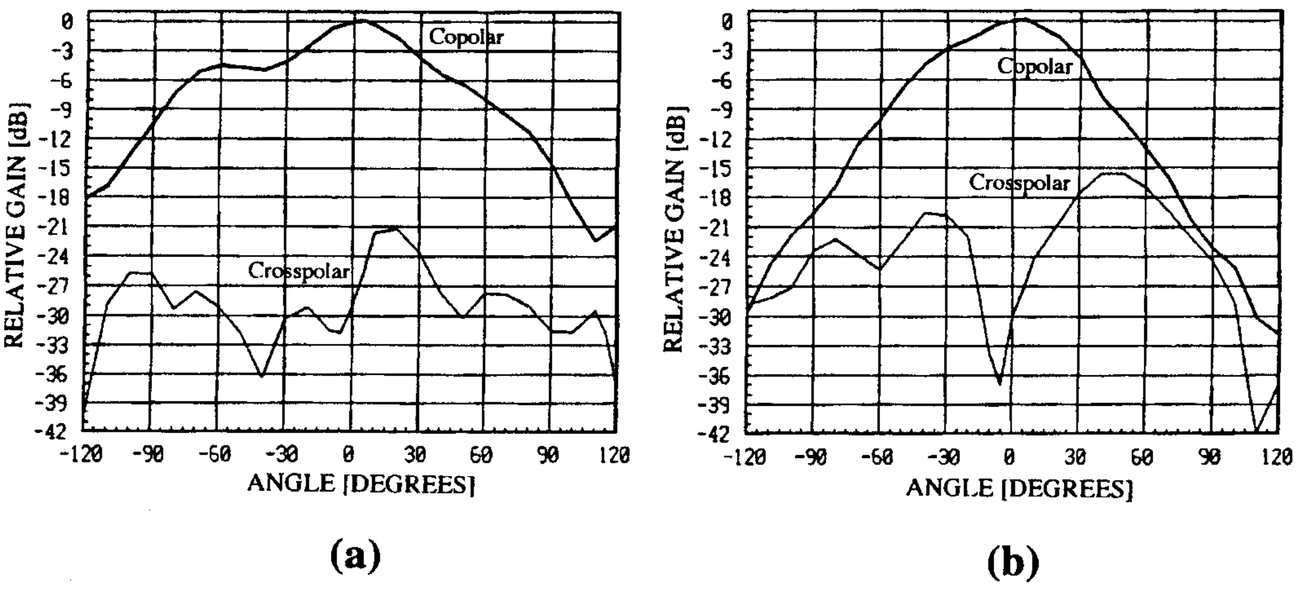

Figure 11.14 Measured radiation patterns of the active integrated patch antenna: (a) E plane and (b) H plane. (From [28]. © 1996 IEEE. Reprinted with permission.)

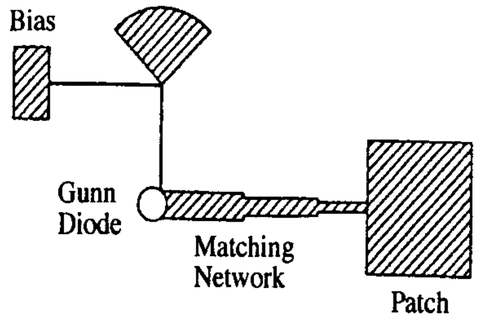

Figure 11.15 A 60-GHz–band oscillating active microstrip patch antenna. (From [29], © 1994 *Electronics Letters*, and [2], © 1996 John Wiley & Sons, Inc. Reprinted with permission.)

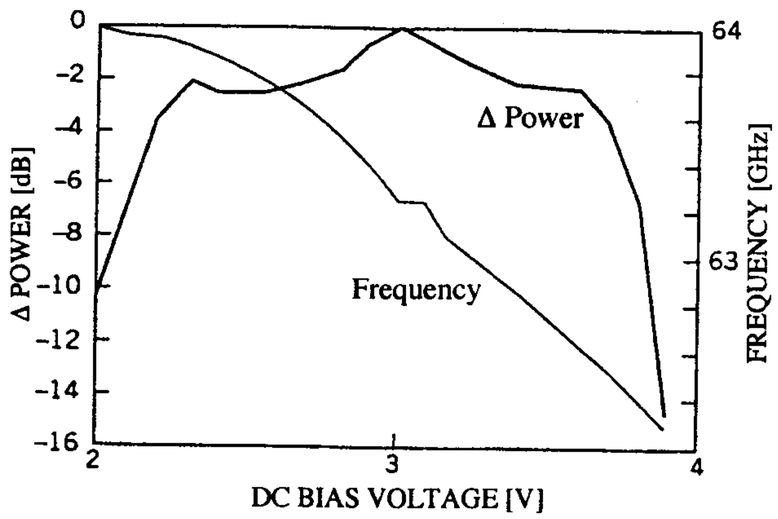

Figure 11.16 Measured dc bias tuning characteristics. (From [29], © 1994 *Electronics Letters*, and [2], © 1996 John Wiley & Sons, Inc. Reprinted with permission.)

transistor with its feedback to enhance the instability if necessary. The oscillating conditions can be derived using the S parameter approach [18, 20, 30–33].

The two-port scattering matrix of the network in Figure 11.17 can be written as

$$\begin{pmatrix} S_{11}\Gamma_S - 1 & S_{12}\Gamma_S \\ S_{21}\Gamma_L & S_{22}\Gamma_L - 1 \end{pmatrix} \begin{pmatrix} a_1 \\ a_2 \end{pmatrix} = \begin{pmatrix} 0 \\ 0 \end{pmatrix} \tag{11.21}$$

A nontrivial solution exists if its determinant vanishes. This leads to the well-known steady-state oscillation conditions:

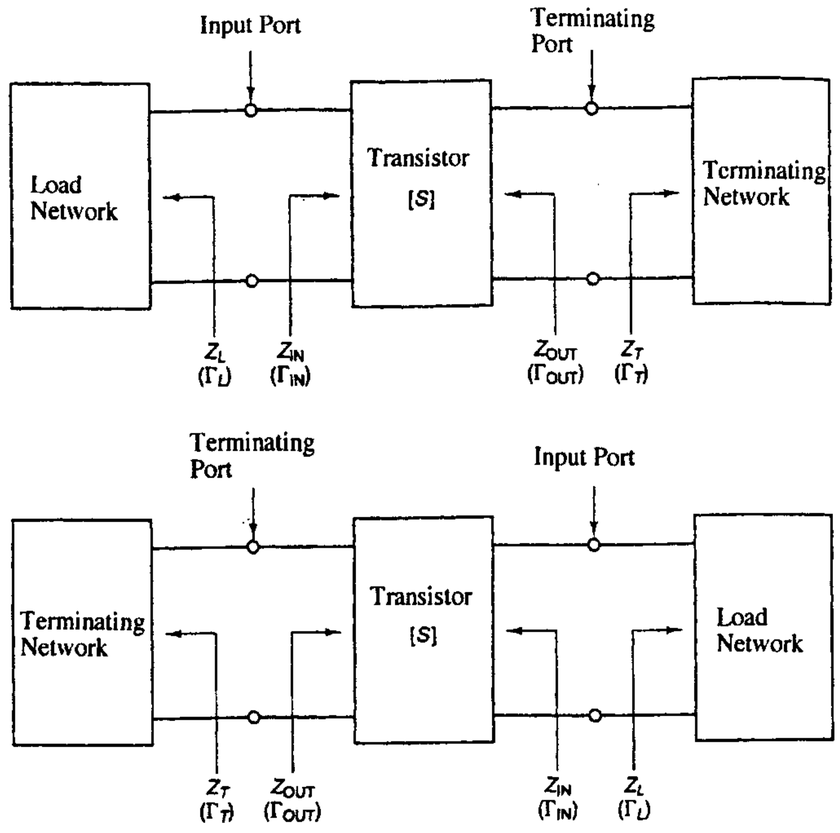

Figure 11.17 Schematic diagrams of two-port transistor oscillator. (From [18]. © 1997 Prentice Hall, Inc. Reprinted with permission.)

$$\frac{1}{\Gamma_S} = \Gamma_{\text{in}} = S_{11} + \frac{S_{12}S_{21}\Gamma_L}{1 - S_{22}\Gamma_L} \tag{11.22}$$

$$\frac{1}{\Gamma_L} = \Gamma_{\text{out}} = S_{22} + \frac{S_{12}S_{21}\Gamma_S}{1 - S_{11}\Gamma_S} \tag{11.23}$$

It can be proven that these conditions are simultaneously satisfied. Thus, when port 1 oscillates, port 2 will also oscillate. At start-up of oscillation, using the small-signal S parameters of a device, it is required that [20, 31]

$$\left|\frac{1}{\Gamma_{\text{in}}}\right| < \Gamma_S \tag{11.24}$$

$$\text{Phase}\left(\frac{1}{\Gamma_{\text{in}}}\right) = \text{phase}^{*}(\Gamma_S)$$

$$\left|\frac{1}{\Gamma_{\text{out}}}\right| < \Gamma_L \tag{11.25}$$

$$\text{Phase}\left(\frac{1}{\Gamma_{\text{out}}}\right) = \text{phase } (\Gamma_L)$$

at the input and the output ports, respectively. These conditions allow the oscillation to build up until it reaches a steady state where (11.22) and (11.23) are satisfied. This is possible because of the variation of S parameters with power level as oscillation approaches steady state. Coefficients Γ_S and Γ_L are passive network reflection coefficients in unstable regions of the active device, which can be identified from stability circle plots. The device output and input stability circles are given by [8, 18]

$$C_L = \frac{(S_{22} - \Delta S_{11}^*)^*}{|S_{22}|^2 - |\Delta|^2}, \text{ (center)} \tag{11.26}$$

$$R_L = \left|\frac{S_{12}S_{21}}{|S_{22}|^2 - |\Delta|^2}\right|, \text{ (radius)} \tag{11.27}$$

$$C_S = \frac{(S_{11} - \Delta S_{22}^*)^*}{|S_{11}|^2 - |\Delta|^2}, \text{ (center)} \tag{11.28}$$

$$R_S = \left|\frac{S_{12}S_{21}}{|S_{11}|^2 - |\Delta|^2}\right|, \text{ (radius)} \tag{11.29}$$

where

$$\Delta = S_{11}S_{22} - S_{12}S_{21} \tag{11.30}$$

For a single frequency operation, the start-up oscillation conditions should only be satisfied at the required frequency of oscillation. Otherwise the oscillator can oscillate at any one or all of the frequencies simultaneously where the conditions are met. This requirement is accomplished by ensuring that the phases of $1/\Gamma_{\text{in}}$ and Γ_S are changing in opposite angular directions with changing frequency [34].

Design Procedure

Oscillator active patch antennas can be designed based on the operational principle as described above. A patch antenna can be on either side of a two-port active device. In the design, a potentially unstable transistor at the desired frequency of oscillation will be used as a two-port active device. This can be determined by the calculation of stability factor K from the S parameters. The transistor configuration may need to be changed and feedback may have to be added to produce the desired instability with a small K factor that accepts a wider range of passive load terminations. Using the linear design approach [19], a design procedure can be summarized as follows:

1. Select a transistor configuration with a high degree of instability as determined from a stability factor K using small signal S parameters:

$$K = \frac{1 - |S_{11}|^2 - |S_{22}|^2 + |\Delta|^2}{2|S_{12}S_{21}|} \tag{11.31}$$

   Positive feedback can be used to enhance transistor instability. Small K will offer more design flexibility because a wider range of passive terminations can be accommodated.

2. Design an input network with Γ_S in the unstable region to produce a large magnitude of Γ_{out}. Γ_S is also selected to satisfy the start-up criteria requirement at the desired frequency where

$$|\Gamma_S| > \left|\frac{1}{\Gamma_{\text{in}}}\right| \tag{11.32}$$

$$\text{Phase } (\Gamma_S) = \text{phase}\left(\frac{1}{\Gamma_{\text{in}}}\right)$$

3. Design an output network with a reflection coefficient Γ_L to meet the start-up condition for oscillation at the desired frequency. For a stable oscillation where the conditions of oscillations are met at a single frequency, it is required that the phase variations of Γ_L and $1/\Gamma_S$ be in opposite angular directions with changing frequency.
4. A patch is designed to resonate at the required operating frequency. It is also designed to provide the required Γ_L by properly selecting a feed position. The patch will serve as the required output network for a transistor.

The design process can be repeated if necessary so that all conditions are satisfied and to ensure a stable oscillation.

Design Samples

The design outlined above can be applied to the design of a compact oscillator integrated microstrip patch antenna as shown in Figure 11.18 [35]. The oscillator circuit utilizes a series feedback common emitter configuration as depicted in Figure 11.19. The value of the capacitor C is chosen to give large Γ_S, which

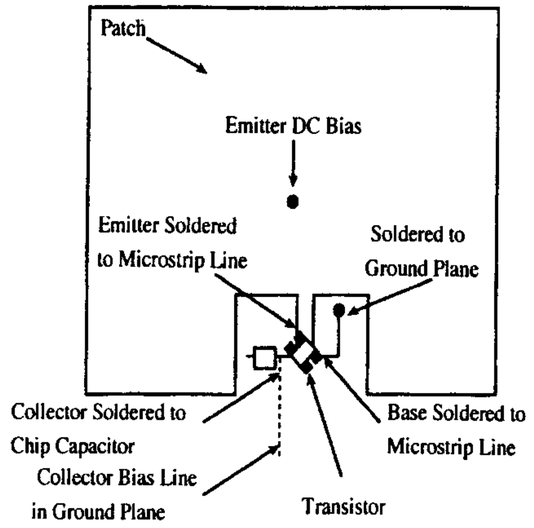

Figure 11.18 An oscillating active patch antenna integrated with a transistor. (From [35]. © 1994 *Microwave Journal*. Reprinted with permission.)

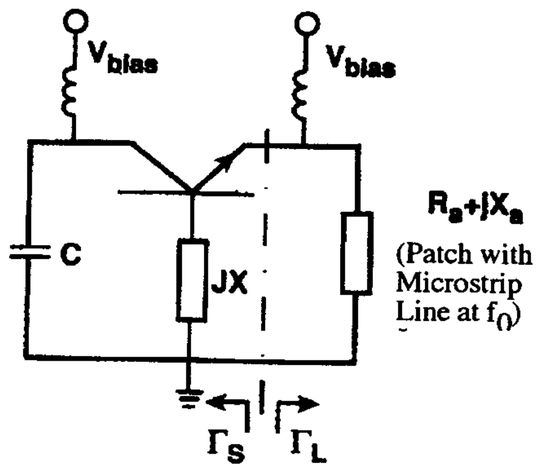

Figure 11.19 Series feedback oscillator circuit. (From [35]. © 1994 *Microwave Journal*. Reprinted with permission.)

indicates the operation in the source instability region. The antenna impedance is chosen to generate Γ_L, as illustrated in Figure 11.20, which shows $1/\Gamma_S$ and Γ_L having contradirectional phase variation versus frequency for a stable oscillation [34, 35].

The antenna input impedance, which produces the required Γ_L, is achieved by the inset feed as shown in Figure 11.21 by properly selecting the inset width S and depth X. As the oscillation builds up, Γ_S decreases to finally satisfy the steady-state oscillation condition (11.22) at the required operating frequency. The measured E- and H-plane patterns in Figure 11.22 show negligible variations of the copolar radiation but a higher cross-polarization level.

Another FET oscillator active integrated patch antenna that uses the linear design approach has been reported by Forma and Laheurte [36]. The circuit implementation utilizes a coplanar waveguide (CPW) instead of a microstrip line due to advantages of a small number of soldering points and requiring no via holes. The general design approach follows the design procedure described earlier. However, S parameters are modified by replacing a small-signal S_{21} with a large-signal S_{21} so as to obtain a maximum oscillator output power [37].

Referring to the configurations of the active oscillator antennas, Figures 11.23(a) and (b) show a CPW-fed straight slot and a CPW-fed slot loop,

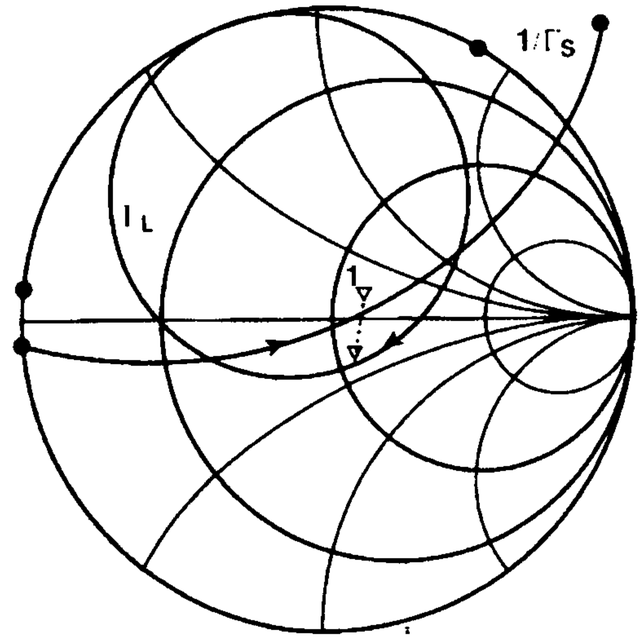

Figure 11.20 Measured reflection coefficients of the patch (Γ_L) and the amplifier ($1/\Gamma_S$). (From [35]. © 1994 *Microwave Journal*. Reprinted with permission.)

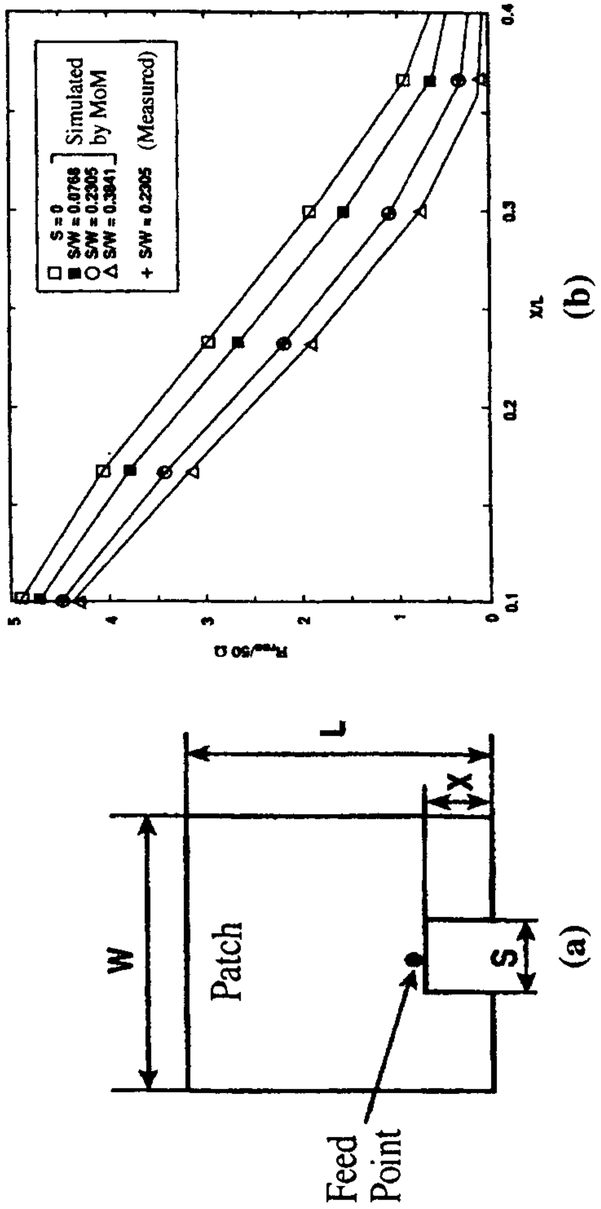

Figure 11.21 (a) A patch geometry and (b) normalized resonant input resistance for a patch with $W = L = 60$ mm, $\epsilon_r = 2.2$, $h = 1.6$ mm, and $\tan\delta = 0.001$. (From [35]. © 1994 *Microwave Journal*. Reprinted with permission.)

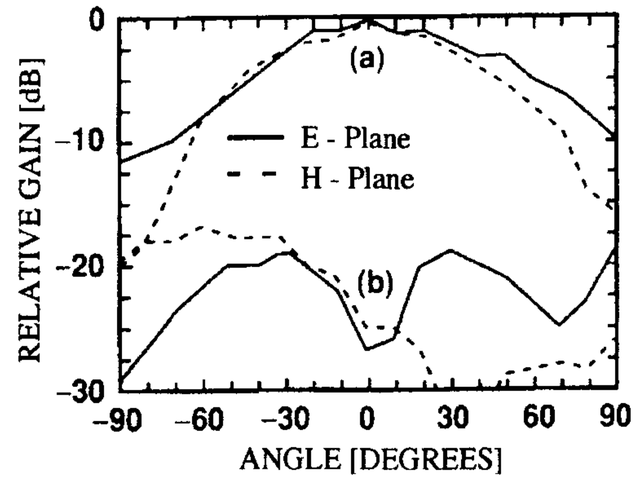

Figure 11.22 Measured (a) copolar and (b) cross-polar radiation patterns. (From [35]. © 1994 *Microwave Journal*. Reprinted with permission.)

respectively. The circuits are fabricated on a 1.524-mm-thick Duroid substrate with $\epsilon_r = 2.2$. The layout in Figure 11.23(a) consists of a straight slot fed patch with the following dimensions in millimeters: $L_p = 22$, $L_a = 15$, $l_a = 1$, $d = 5.5$, $L_d = 6$, $L_s = 17$, $L_g = 9$, $W = 2.5$, and $G = 0.25$. The circuit requires only a single dc power supply at the drain with $V_{gs} = 0$ V, $V_{ds} = 2$ V, and $I_{ds} = 125$ mA. For a slot loop case, the dimensions are $L_p = 20$, $l_a = 1$, $L_a = 12$, $D = 10$, $L_s = 17$, $L_d = 6$, $L_g = 9$, $W = 2.5$, and $G = 0.25$ mm. The main advantage of the slot loop configuration is a simpler realization of a biasing circuitry. The centered square loop performs both functions of the coupling element for the microstrip patch antenna and the isolation for dc bias. The oscillation characteristics of the two designs are listed in Table 11.1.

The measured radiation patterns in Figure 11.24 show the cross-polar levels to be below −17 dB in both cases.

Examples of other reported topologies of active integrated patch oscillators are shown in Figure 11.25 using a common source configuration [38] and in Figure 11.26 for a series feedback arrangement [39]. A narrow slot on a patch of a common source configuration in Figure 11.25 serves both functions of feedback capacitance and bias isolation. It was reported that the E-plane radiation pattern was affected by slot radiation. The design procedure outlined above can still be applied to both configurations.

The design approach as described earlier is based on the linear analysis where small-signal S parameters are used in the determination of all the oscillation conditions. It is simple, but it is unable to predict a steady-state output power level for the oscillator. For the series feedback arrangement shown in

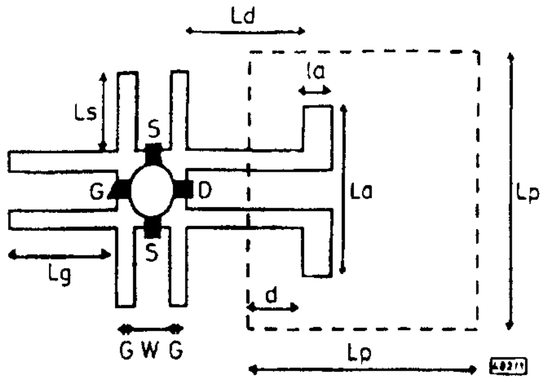

(a)

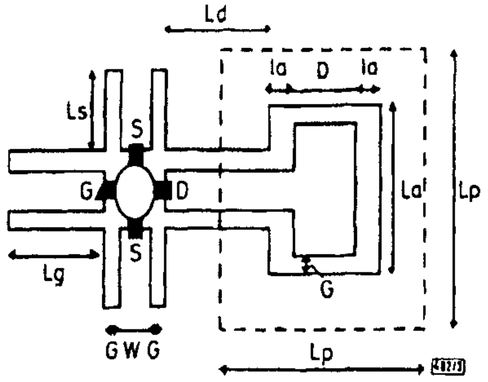

(b)

Figure 11.23 Coplanar waveguide-fed oscillating microstrip antennas: (a) Straight slot and (b) slot loop. (From [36]. © 1996 *Electronics Letters*. Reprinted with permission.)

Table 11.1
Characteristics of 3.97- and 4.01-GHz Oscillators

	Slot Loop Feed	Straight Slot Feed
Free-running frequency (GHz)	3.97	4.01
Measured radiated power (mW)	26	30
DC-to-RF efficiency (%)	10.4	12.0
Sensitivity $\Delta_f/\Delta V_{ds}$ (MHz)	20	5

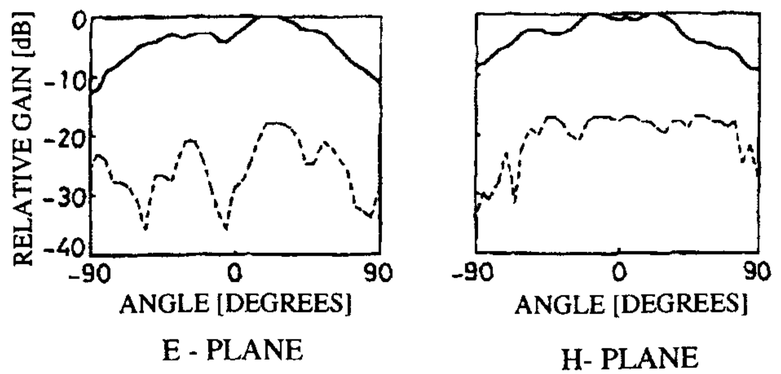

(a)

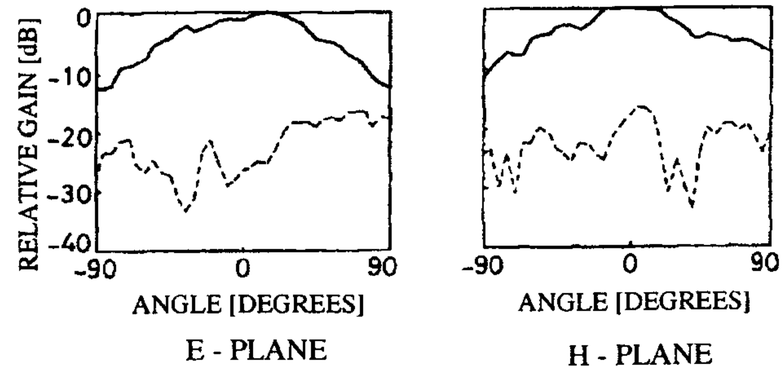

(b)

Figure 11.24 Measured radiation patterns for E and H planes: (a) straight slot fed and (b) slot loop fed. (From [36]. © 1996 *Electronics Letters*. Reprinted with permission.)

Figure 11.26, Fusco [39] used a full FET model to optimize complex terminal voltages V_1 and V_2 at the desired oscillating frequency for the maximum $P_{\text{add}}(\omega)$, which is defined as

$$P_{\text{add}}(\omega) = -\frac{1}{2}\text{Re}[V_1(\omega)I_1^*(\omega) + V_2(\omega)I_2^*(\omega)] \tag{11.33}$$

Evaluation of the required circuit lumped elements can be obtained from the synthesis equations:

$$X_1 = \frac{-\text{Re}[V_1(I_1 + I_2)]}{\text{Im}[I_1(I_1 + I_2)^*]} \tag{11.34}$$

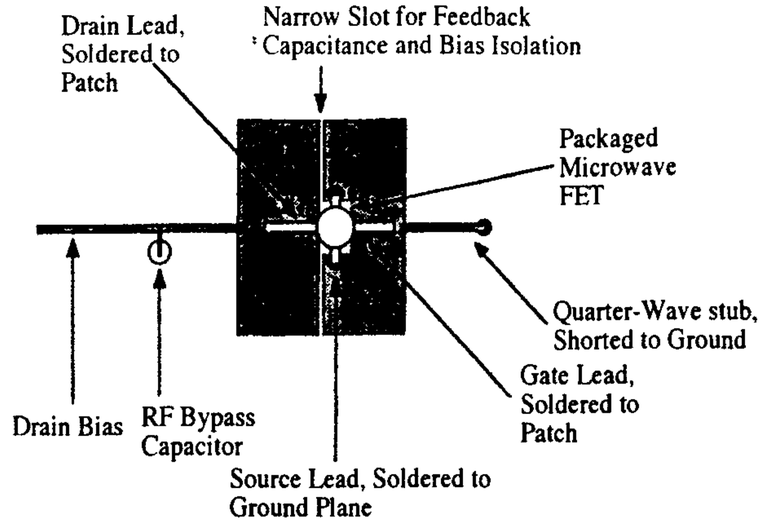

Figure 11.25 A hybrid patch antenna integrated with a FET in a common source configuration. (From [38]. © 1990 *Electronics Letters*. Reprinted with permission.)

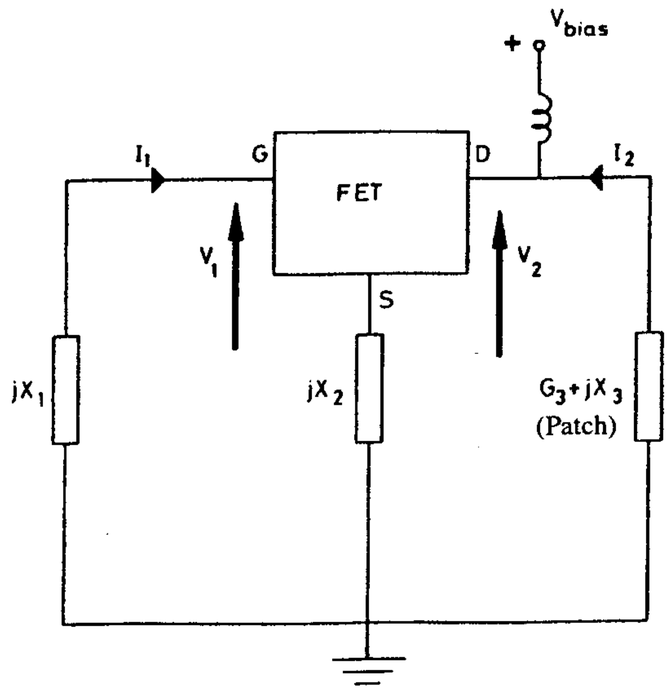

Figure 11.26 A series feedback integrated active microstrip antenna. (From [39]. © 1992 *Electronics Letters*. Reprinted with permission.)

$$X_2 = \frac{\mathrm{Re}[V_1 I_1]}{\mathrm{Im}[I_1^*(I_1 + I_2)]} \tag{11.35}$$

$$X_3 = \frac{-\mathrm{Im}(V_2 I_2^*)}{|I_2|^2} - \frac{X_2 \mathrm{Re}[(I_1 + I_2) I_2^*]}{|I_2|^2} \tag{11.36}$$

$$G_3 = \left[-jX_3 - \frac{V_2}{I_2} - jX_2 \frac{(I_1 + I_2)}{I_2} \right]^{-1} \tag{11.37}$$

Assuming a lossless embedding network, this design provides the maximum possible output power of the oscillator. Figure 11.27 shows frequency pushing characteristics and variation of the normalized (to the output power of 8 mW at 9.635 GHz) output power level against bias voltage. Alternatively, the Volterra series design technique [40] has been applied by Huang and Chu [41] to overcome the limitation of the linear design. The oscillating antenna topology depicted in Figure 11.28 consists of a slot-fed patch integrated with MESFET using a shunt feedback configuration. The measured results of oscillating frequency and antenna radiated power are 2.730 GHz and 8.4 dBm, respectively. These values are very close to the theoretical prediction of 2.707 and 2.713 GHz for oscillating frequency calculated at the input and output ports. The calculated radiated power is found to be 8.8 dBm.

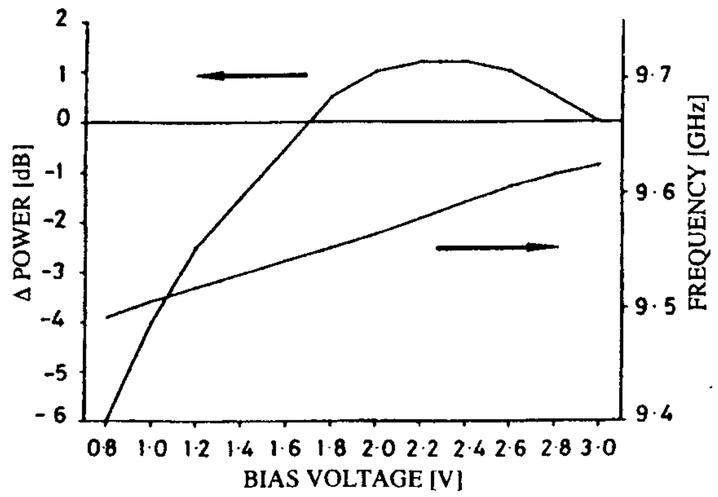

Figure 11.27 Variation of the output power and oscillating frequency versus bias voltage. (From [39]. © 1992 *Electronics Letters*. Reprinted with permission.)

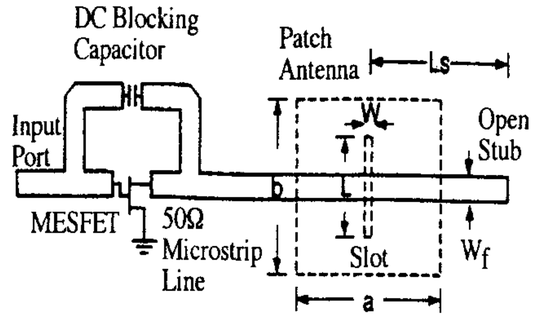

Figure 11.28 A slot-coupled patch antenna loaded with a MESFET oscillator. (From [41]. © 1995 IEEE. Reprinted with permission.)

Feedback Active Patch Antenna Oscillators

In the previous section, an active integrated antenna oscillator is realized with the transistor operating in its unstable region with a patch acting simultaneously as a terminating load for the output port and a radiator. In this section, an alternative type of active antenna oscillator that uses amplifiers and their positive feedback circuit is described.

Referring to the block diagram of a feedback oscillator in Figure 11.29, the closed loop gain $A_C(j\omega)$ of an amplifier with a positive feedback can be written as

$$A_C(j\omega) = \frac{A(j\omega)}{1 - B(j\omega)\,A(j\omega)} \tag{11.38}$$

where $A(j\omega)$ and $B(j\omega)$ are the open-loop amplifier gain and the transfer function of a feedback network, respectively. The amplifier will oscillate when

$$1 - B(j\omega)\,A(j\omega) = 0 \tag{11.39}$$

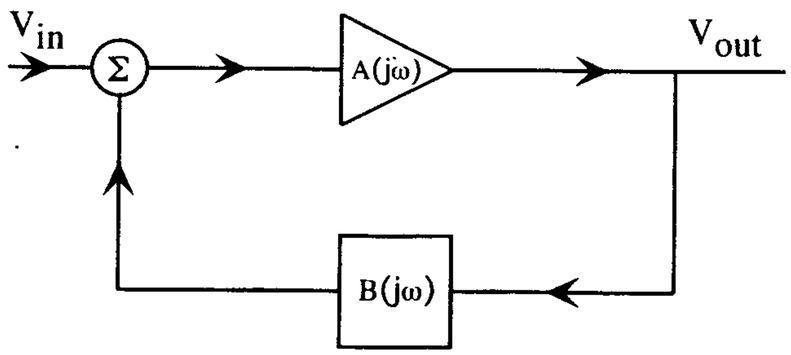

Figure 11.29 Block diagram of a feedback oscillator.

That is, the phase of the loop gain must be zero and the amplitude of the loop gain must be unity. This is a steady-state oscillation condition. For start-up conditions, it is required that [33]

$$|B(j\omega)||A(j\omega)| > 1 \tag{11.40}$$
$$\text{Phase}(B(j\omega)) + \text{phase}\ (A(j\omega)) = 0$$

Under the conditions given, any disturbance in the circuit will start oscillation, which grows in amplitude. The growth, however, will be limited by amplifier capabilities. As the oscillation increases, the loop gain will decrease to unity at which a steady-state oscillation is obtained. The oscillating frequency will be determined by the phase characteristics of the feedback loop.

Design Procedure

In this topology, a patch antenna is placed in the feedback circuit of an amplifier. The patch will act simultaneously as a radiator and a frequency selective network resonating at the desired oscillating frequency. Following the oscillation principles as described above, the design procedure can be summarized as follows:

1. Design an amplifier with matching networks and a positive feedback loop at the desired oscillating frequency. The feedback loop consists of a transmission line and a frequency selective network that resonates at the oscillating frequency. The loop gain and phase must satisfy start-up conditions for oscillation as given in (11.40). Phase of the feedback loop can be adjusted by a feedback line.
2. Design a patch for operation at the oscillating frequency. Determine the input and the output locations on the patch to provide a load requirement on the feedback line. Note that the antenna input impedance will be modified by a load seen by the antenna at the output port.
3. Design steps can be repeated if necessary to meet oscillation conditions.

Design Samples

Feedback active integrated patch oscillators were designed by Chang et al. [42] using a design procedure similar to that outlined above. The FET active patch configuration is shown in Figure 11.1(b). The active patch oscillator generates a power output of 17 mW at 5.7 GHz. The E- and H-plane radiation patterns are adversely affected by exposed oscillator circuit components, as shown in Figure 11.30. Razban et al. [43] realized similar active integrated antenna

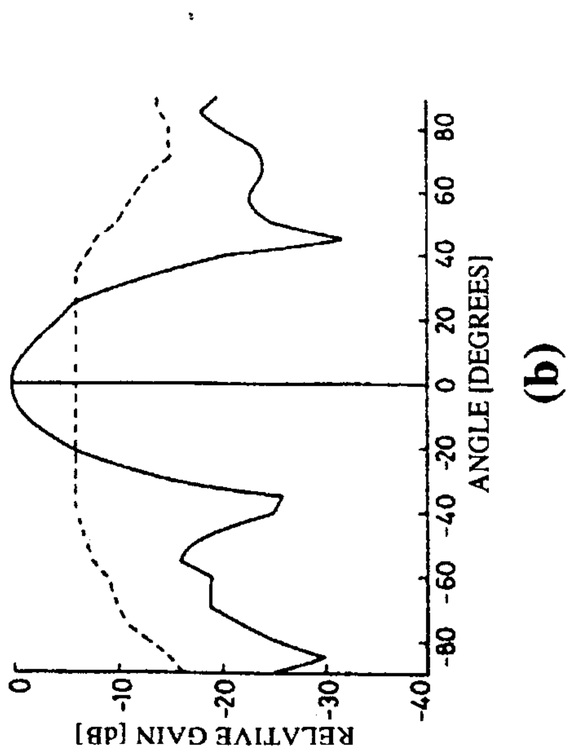

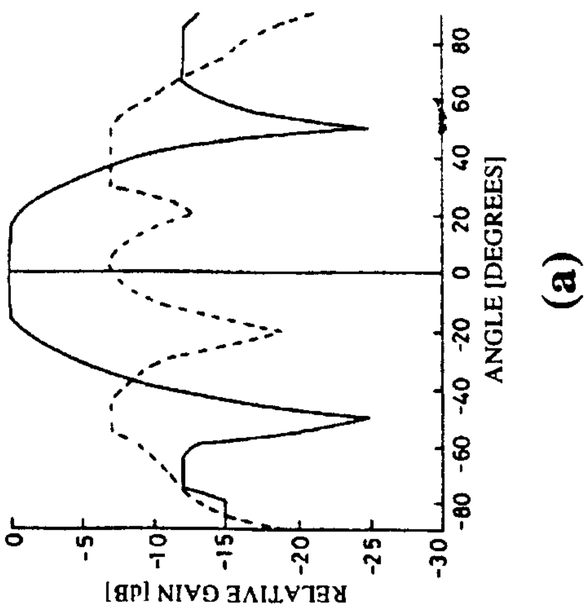

Figure 11.30 Measured radiation patterns of FET oscillating active patch antenna: (a) E plane and (b) H plane. (From [42]. © 1988 *Electronics Letters*. Reprinted with permission.)

oscillators using the strip line technology of Figure 11.31. The bias circuit comprises quarter-wavelength high-impedance lines and low-impedance pads to provide DC-to-RF isolation. Two capacitors isolate the feedback loop from dc and separate the input and output bias voltages. The feedback is realized with a 50Ω transmission line. Two design steps were used: (1) an oscillator design and (2) patch integration.

In the oscillator design, the patch is replaced by an equivalent 50Ω load representing the patch resistance. The oscillator circuit is optimized for $|S_{11}| << 1$ at the input for a good match and $|S_{21}| >> 1$ with zero phase shift at the output to satisfy the start-up condition (11.40) [see Figure 11.32(a)]. If it is necessary, the length of the feedback line can be used to adjust for a zero phase shift. For the patch integration, the 50Ω load resistor is then removed and, at exactly the same location, the 50Ω patch input is connected. The 50Ω patch output is connected to the other end of the feedback 50Ω line after a section of the line with an electrical length equivalent to the electrical distance between the input and output of the patch including the length of connecting pins is removed. The final structure of the active integrated patch oscillator is shown in Figure 11.32(b). The measured results show that the active antenna oscillates at 1 GHz. The radiation patterns were not reported. However, since the active circuit components and the patch are isolated from each other by the ground plane except through connecting pins, the circuit should have minimal effects on the radiation patterns.

Fusco and Burns [44] derived synthesis equations for a configuration of a feedback active integrated antenna oscillator, as illustrated in Figure 11.33, in terms of the optimum input and output complex voltages V_1 and V_2. In the design, V_1 and V_2 are optimized for maximum added power (11.33) at

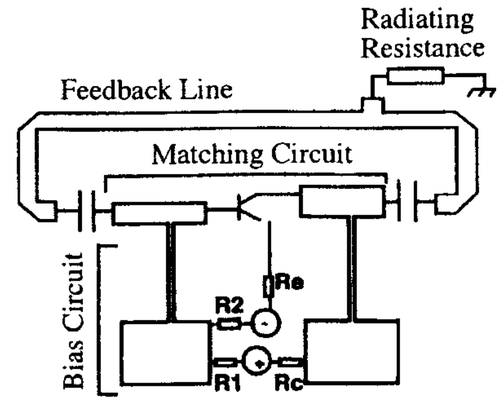

Figure 11.31 An oscillating active patch antenna using strip line technology. (From [43]. © 1993 *Microwave Journal*. Reprinted with permission.)

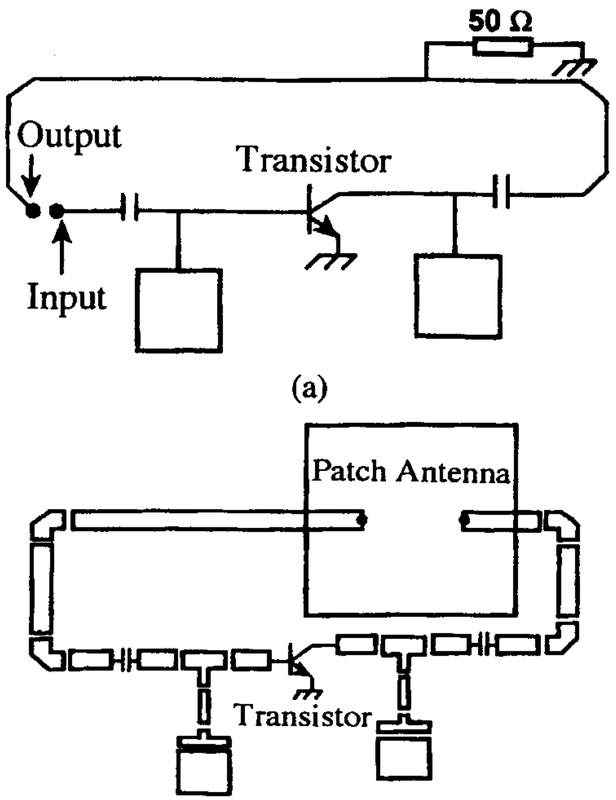

Figure 11.32 The final structure of the oscillating antenna illustrating a patch integration. (From [43]. © 1993 *Microwave Journal*. Reprinted with permission.)

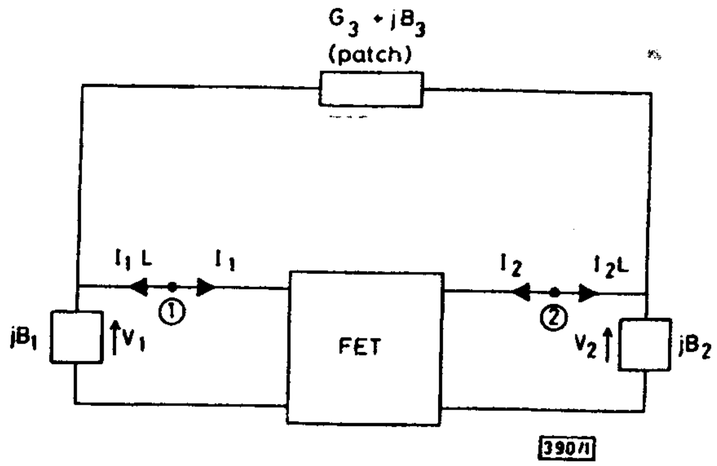

Figure 11.33 A feedback active integrated patch antenna oscillator. (From [44]. © 1990 *Electronics Letters*. Reprinted with permission.)

the desired operating frequency, which corresponds to the maximum possible output power of the oscillator [45]. These relationships are

$$B_1 = C_2 + C_4 + V_{gr}B_2 \tag{11.41}$$

$$B_2 = \frac{(C_1 + C_3)}{V_{gi}} \tag{11.42}$$

$$B_3 = \frac{V_{gi}C_1 - (1 - V_{gr})[C_4 + V_{gr}B_2]}{(1 - V_{gr})^2 + V_{gi}^2} \tag{11.43}$$

$$G_3 = \frac{(C_1 - V_{gi}B_3)}{(1 - V_{gr})} \tag{11.44}$$

$$C_1 = \mathrm{Re}\left(\frac{I_1}{V_1}\right),\ C_2 = \mathrm{Im}\left(\frac{I_1}{V_1}\right) \tag{11.45}$$

$$C_3 = -\mathrm{Re}\left(\frac{I_2}{V_1}\right),\ C_4 = -\mathrm{Im}\left(\frac{I_2}{V_1}\right) \tag{11.46}$$

$$V_g = \frac{V_2}{V_1} = V_{gr} + jV_{gi} \tag{11.47}$$

where I_1 and I_2 are related to V_1 and V_2 through two-port characterization of a FET.

Active integrated antenna oscillators do not have to be limited to the topologies discussed above. Other possible configurations consist of series and shunt feedback combinations. For practical applications, consideration may include compact size, fabrication complexity, and minimal interference of oscillator circuit to antenna radiation characteristics. Design procedures as given by Johnson [37] or Choo et al. [45] can be applied to determine the optimum embedding elements for oscillator circuits. The technique employed by Razban [43] can be used for antenna integration.

In other reported design variations, a single patch is integrated to multiple FETs for power output enhancement. Birkeland and Itoh [46] demonstrated two- and four-FET integration with a single patch oscillating in the push-pull mode as shown in Figure 11.34. Some slight degradation in the E-plane pattern of the single patch with two FETs was reported. The cross-polar patterns were found to be 18 dB below the main lobe, indicating the well-balanced oscillation

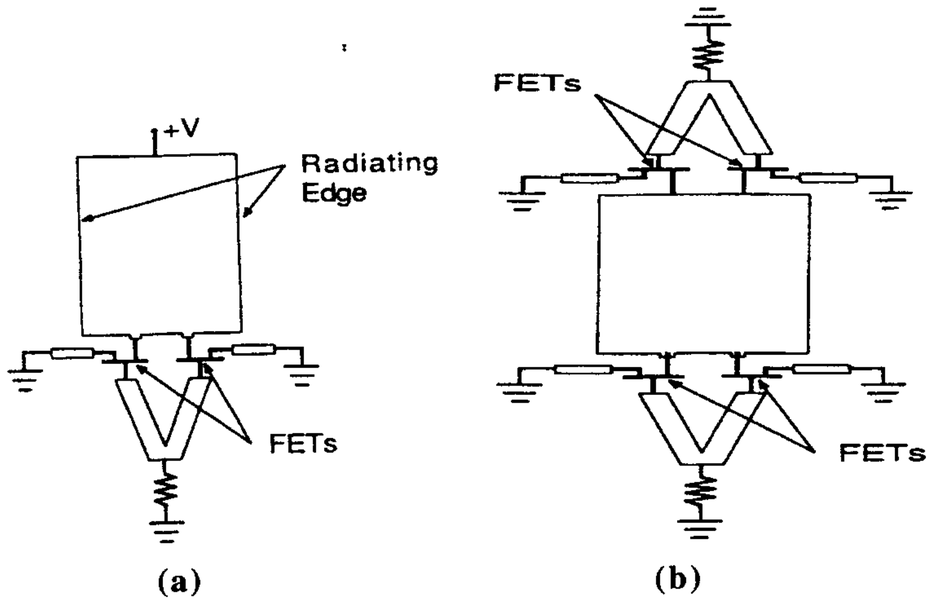

Figure 11.34 (a) The push-pull oscillator and (b) the four-FET oscillator. (From [46]. © 1990 IEEE. Reprinted with permission.)

of the FETs. These designs were developed to enhance the output power of a given number of patches in spatial power combining arrays.

Several factors must be taken into consideration when designing active integrated antenna oscillators. These factors include conversion efficiency, stability of oscillation, and spectral purity of the output. Conversion efficiency is defined as the ratio of RF output power to dc input power. For the same dc input power, a lower value of conversion efficiency indicates more energy dissipated in the form of heat. A stable oscillator ensures that the oscillation will return to its steady state after experiencing a slight operational disturbance. Thermal stability is necessary to minimize the fluctuations of an oscillator output power level and frequency because the device impedance is a function of temperature. Spectral purity is influenced by interaction of noise with the circuit and device. In applications, an oscillator can be injection locked by an external RF signal for synchronization and for improvement of spectral purity.

11.4 Theory and Design of Active Integrated Microstrip Antenna Amplifiers

In the previous section, solid-state devices are integrated with microstrip patches to produce oscillation by operating the active devices in their unstable regions. This is in contrast to the operation of amplifier-type active integrated microstrip antennas where stability of devices is prerequisite to avoid potential oscillation. The purpose of direct integration of a patch with an amplifier is to produce signal amplification for transmission or reception depending on the patch location, that is, whether it is at the output or the input port. This, in effect, enhances the realized gain of a patch through amplification by the integrated amplifier.

For transmission applications, the design goal is to achieve high gain over a broad bandwidth. For reception applications, the goal is to achieve good noise performance and reasonable gain flatness. Advantages of direct integration of a patch to an amplifier include low feed loss and compact antenna module for applications in active phased arrays and mobile and satellite communications. Various CAD software packages are available for microwave amplifier design and they are recommended for better accuracy such as HP EEsof for linear and nonlinear microwave circuit design. However, the analytical design approach discussed later has the advantages of illustrating the operating principles of the amplifier.

11.4.1 Analysis and Design of Active Integrated Microstrip Antenna Amplifiers

In general, design of active integrated microstrip antenna amplifiers still follows the design procedure of microwave transistor amplifiers with a microstrip patch acting as a load for the transmitting case and as a source impedance for the receiving case. The basic design principles of microwave amplifiers based on the transistor S parameters concerning the gain, stability, and noise figure are briefly reviewed below. Detailed discussions on the subject can be found in more advanced texts, for example, [18, 47].

A general block diagram of a microwave amplifier circuit is shown in Figure 11.35. For transmitting antennas, Z_S is the complex source impedance and Z_L is the input impedance of a microstrip antenna. For receiving cases, Z_S and Z_L are the input impedance of a patch and a complex load impedance.

Gain

The transducer power gain G_T is defined as the ratio of power delivered to the load Z_L to power available from the source [8, 18]. Gain G_T can be expressed in terms of S parameters Γ_L and Γ_S as

$$G_T = \frac{1-|\Gamma_S|^2}{|1-\Gamma_{in}\Gamma_S|^2}|S_{21}|^2\frac{1-|\Gamma_L|^2}{|1-S_{22}\Gamma_L|^2} \tag{11.48}$$

$$G_T = \frac{1-|\Gamma_S|^2}{|1-S_{11}\Gamma_S|^2}|S_{21}|^2\frac{1-|\Gamma_L|^2}{|1-\Gamma_{out}\Gamma_L|^2}$$

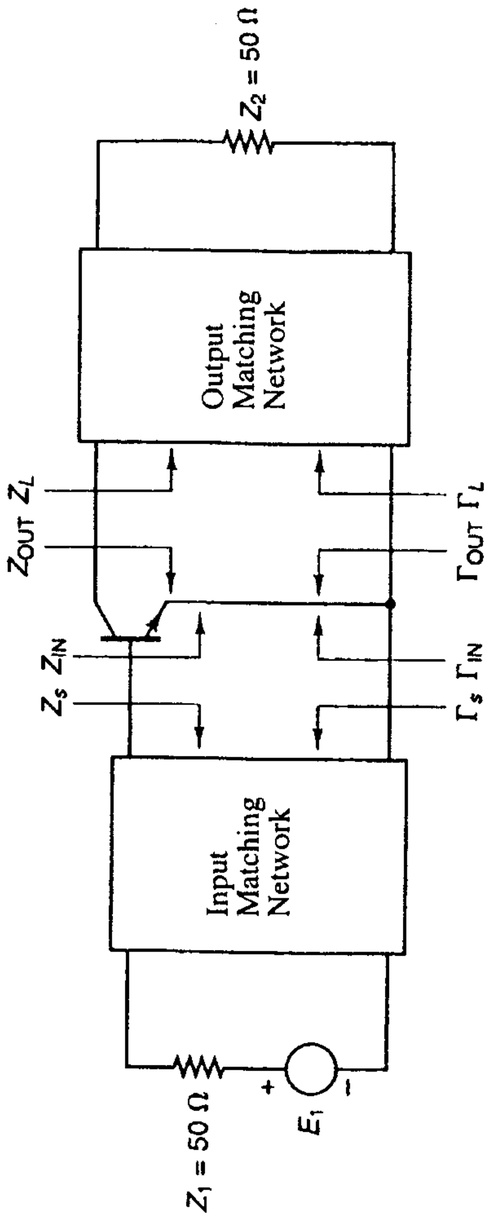

Figure 11.35 Block diagram of a microwave amplifier circuit. (From [18]. © 1997 Prentice Hall, Inc. Reprinted with permission.)

where

$$\Gamma_{in} = S_{11} + \frac{S_{12}S_{21}\Gamma_L}{1 - S_{22}\Gamma_L} \tag{11.49}$$

$$\Gamma_{out} = S_{22} + \frac{S_{12}S_{21}\Gamma_S}{1 - S_{11}\Gamma_S} \tag{11.50}$$

The realized gain of an active antenna can be defined, following the standard gain measurement, as [48]

$$G_a(\theta, \phi) = G(\theta, \phi) \tag{11.51}$$

where $G(\theta, \phi)$ is the gain of a passive radiator.

Stability

An amplifier is said to be unconditionally stable if $|\Gamma_{in}| < 1$ and $|\Gamma_{out}| < 1$ for all passive source and load impedances. However, if $|\Gamma_{in}| < 1$ and $|\Gamma_{out}| < 1$ are true for a certain range of passive source and load impedances, an amplifier is said to be conditionally stable. $|\Gamma_{in}| = 1$ defines the output stability circle on the Γ_L plane and $|\Gamma_{out}| = 1$, the input stability circle on the Γ_S plane. The expressions for radii and centers of stability circles are given by

$$r_L = \left| \frac{S_{12}S_{21}}{|S_{22}|^2 - |\Delta|^2} \right| \tag{11.52}$$

$$C_L = \frac{(S_{22} - \Delta S_{11}^*)^*}{|S_{22}|^2 - |\Delta|^2}$$

$$r_S = \left| \frac{S_{12}S_{21}}{|S_{11}|^2 - |\Delta|^2} \right| \tag{11.53}$$

$$C_S = \frac{(S_{11} - \Delta S_{22}^*)^*}{|S_{11}|^2 - |\Delta|^2}$$

where Δ is defined in (11.30). These circles identify the regions on the Smith chart where Γ_L and Γ_S must be located for stable operation of an amplifier.

In designing an amplifier, the stability of a transistor has to be checked. The necessary and sufficient conditions for a transistor to be unconditionally stable are [18]

$$K = \frac{1 - |S_{11}|^2 - |S_{22}|^2 + |\Delta|^2}{2|S_{12}S_{21}|} > 1 \qquad (11.54)$$

$$|\Delta| < 1$$

If a transistor is unconditionally stable, the stability circles need not be plotted. A potentially unstable transistor can be stabilized by series or shunt resistive loadings at the expense of gain and noise performance [18].

11.4.2 Specified Gain Active Integrated Microstrip Antenna Amplifier Design

For a transmitting active antenna, the design goal is to achieve either the maximum obtainable gain or gain over a broad bandwidth. However, only a constant gain design procedure is discussed in this section. It is then followed by a design procedure for a receiving case where the design objective is usually to obtain the desired gain at a minimum noise figure.

Constant Gain Design

An amplifier with a specified gain is much simpler to design when a transistor is a unilateral device where $|S_{12}|$ is negligibly small. Under this assumption, Γ_{in} and Γ_{out} are decoupled from a load and a source, respectively. The transducer power gain G_T, (11.48), is reduced to the unilateral power gain G_{TU} and is given by

$$G_{TU} = \frac{1 - |\Gamma_S|^2}{|1 - S_{11}\Gamma_S|^2}|S_{21}|^2\frac{1 - |\Gamma_L|^2}{|1 - S_{22}\Gamma_L|^2} \qquad (11.55)$$
$$= G_S G_0 G_L$$

where G_S, G_0, and G_L are defined as effective gain factors for the input matching network, the transistor, and the output matching network, respectively. The error bound of using G_{TU} instead of G_T is determined from

$$\frac{1}{(1+U)^2} < \frac{G_T}{G_{TU}} < \frac{1}{(1-U)^2} \qquad (11.56)$$

where

$$U = \frac{|S_{12}||S_{21}||S_{11}||S_{22}|}{(1 - |S_{11}|^2)(1 - |S_{22}|^2)} \qquad (11.57)$$

and U is known as the unilateral figure of merit. The error bound can be used to justify whether a unilateral assumption is acceptable.

Normalized gain factors g_S and g_L are defined as

$$g_S = \frac{G_S}{G_{S\max}} = \frac{1 - |\Gamma_S|^2}{|1 - S_{11}\Gamma_S|^2}(1 - |S_{11}|^2) \qquad (11.58)$$

$$g_L = \frac{G_L}{G_{L\max}} = \frac{1 - |\Gamma_L|^2}{|1 - S_{22}\Gamma_L|^2}(1 - |S_{22}|^2) \qquad (11.59)$$

where $G_{S\max}$ is obtained when $\Gamma_S = S_{11}^*$ and $G_{L\max}$ when $\Gamma_L = S_{22}^*$. For specified values of G_S and G_L, Γ_S and Γ_L in (11.58) and (11.59) represent circles on the Smith chart with centers and radii given by

$$C_S = \frac{g_S S_{11}^*}{1 - (1 - g_S)|S_{11}|^2} \qquad (11.60)$$

$$R_S = \frac{\sqrt{1 - g_S}(1 - |S_{11}|^2)}{1 - (1 - g_S)|S_{11}|^2}$$

$$C_L = \frac{g_L S_{22}^*}{1 - (1 - g_L)|S_{22}|^2} \qquad (11.61)$$

$$R_L = \frac{\sqrt{1 - g_L}(1 - |S_{22}|^2)}{1 - (1 - g_L)|S_{22}|^2}$$

A constant gain circle design is equivalent to determining matching networks Γ_S and Γ_L to provide proper mismatches for a generation of the required gain G_{TU}. The design procedure can be summarized as follows:

1. Characterize the transistor. Calculate the error bound to check if a unilateral assumption is acceptable.
2. Check transistor stability by calculating the K and Δ factors. If the transistor is potentially unstable, stability regions for Γ_S and Γ_L can be identified by plotting the output and the input stability circles on the Smith chart. Only values of Γ_S and Γ_L in the stability regions are used in the amplifier design.
3. Plot circles of Γ_S and Γ_L on the Smith chart that correspond to fixed values of G_S and G_L. Γ_S and Γ_L can be selected from G_S and G_L circles that produce the desired G_{TU}.

4. Design input and output matching networks to provide the required Γ_S and Γ_L. The patch antenna input impedance acts as a load to the output matching network. For a compact design, a patch feed structure can be modified to provide the required impedance. The patch is designed to resonate at the desired operating frequency.

When a unilateral assumption is not acceptable, a more complicated bilateral design using constant available power gain circles may have to be applied. Detailed discussion of this procedure can be found in [18]. The other design technique for a stable broadband microwave amplifier using the simplified real frequency technique has also been discussed in [49, 50].

Design Samples

A schematic diagram of the integrated active microstrip patch antenna amplifier, which can be designed using the procedure outlined above, is shown in Figure 11.36 [51]. The microstrip antenna is a probe-fed square patch. It was fabricated on a 3M Cu-clad of thickness 0.5 mm with ϵ_r = 2.17. The patch was located above the ground plane with an Eccofoam spacer of 6.35-mm thickness and ϵ_r = 1.03. The patch was designed to resonate at the fundamental frequency of 3.3 GHz. A probe feed was used to couple energy from the amplifier output port to the patch. The amplifier circuit consisted of a FET, input and output T-type microstrip matching networks, and the patch acting as a load at the output.

To improve stability, the FET input and output were terminated with a resistor in parallel. An et al. [51] applied a microwave CAD package to optimize the amplifier input and output matching networks. Measured transmission performance of the active and the passive patch antennas in Figure 11.37 shows that the amplifier provides extra gain of 9.5 dB at the center frequency of 3.3 GHz. The gain flatness of ±0.45 dB over 24% of the center frequency was

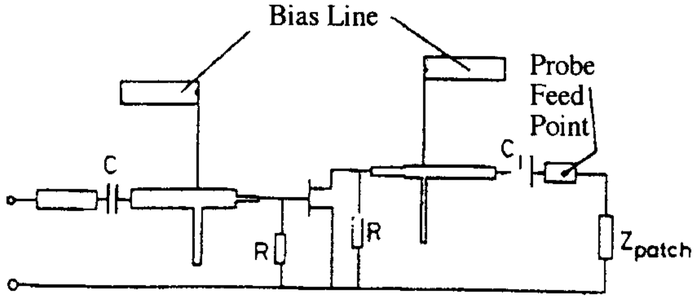

Figure 11.36 Circuit diagram of an amplifying active integrated patch antenna. (From [51]. © 1991 *Electronics Letters*. Reprinted with permission.)

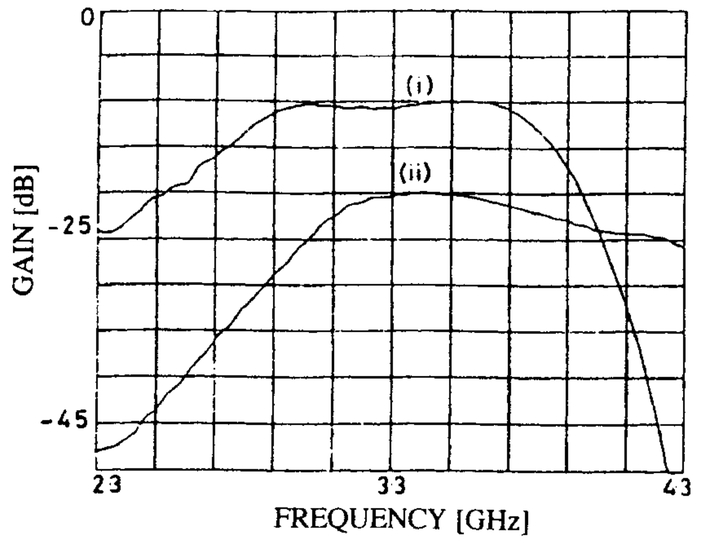

Figure 11.37 Gain versus frequency characteristics: (i) active patch and (ii) passive patch. (From [51]. © 1991 *Electronics Letters*. Reprinted with permission.)

achieved. The active antenna radiation patterns were not given but they were reported to be very similar to the passive case.

An alternative topology of a C-band slot coupled active integrated microstrip patch antenna with a FET amplifier realized on a coplanar waveguide (CPW) was demonstrated by Giauffret et al. [52] as shown in Figure 11.38. This design took advantage of a CPW, which allows easy integration of a FET and a bias circuit without the need for via holes because the line and the ground plane are on the same level. A FET was inserted into a series gap with the gate and drain connected to the center strip of the CPW. Detailed discussion of the input and output matching networks of the amplifier were not reported except for the utilization of the open-circuited stub tuner to compensate for the antenna mismatch. Measured results in Figure 11.39 validate the gain increase for the active over the passive antennas. The increase of 7 dB in the cross-polarization level due to the radiation of the transistor and its circuitry has also been observed.

Other topologies have been reported in which multistage amplifiers are utilized for more gain enhancement. An et al. [48] discussed the active integrated microstrip antenna using multistage amplifiers. A sequential design approach based on the simplified real frequency technique was applied to determine lossless matching networks of amplifiers. A schematic diagram of the active integrated microstrip antenna with two-stage amplifier is shown in Figure 11.40. The measured transducer power gain with a mean value of 24 dB was achieved with the gain flatness of ±0.7 dB over the frequency band of 2.85 to 3.6 GHz or 24.5% as compared to 12% bandwidth for the passive patch.

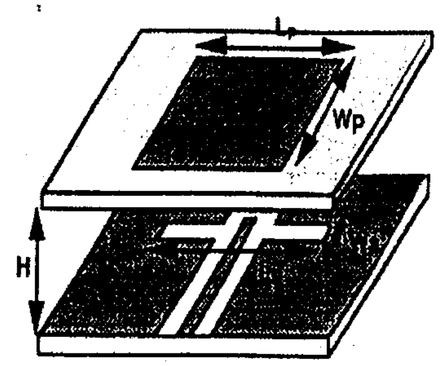

(a)

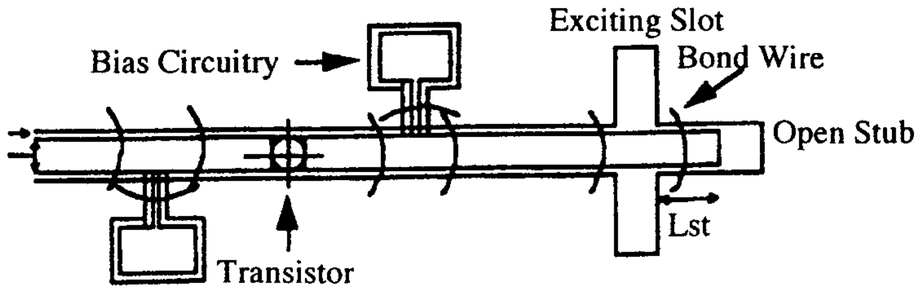

(b)

Figure 11.38 (a) CPW-fed microstrip antenna and (b) layout of the active circuit. (From [52]. © 1994 *24th European Microwave Conference Proceedings*. Reprinted with permission.)

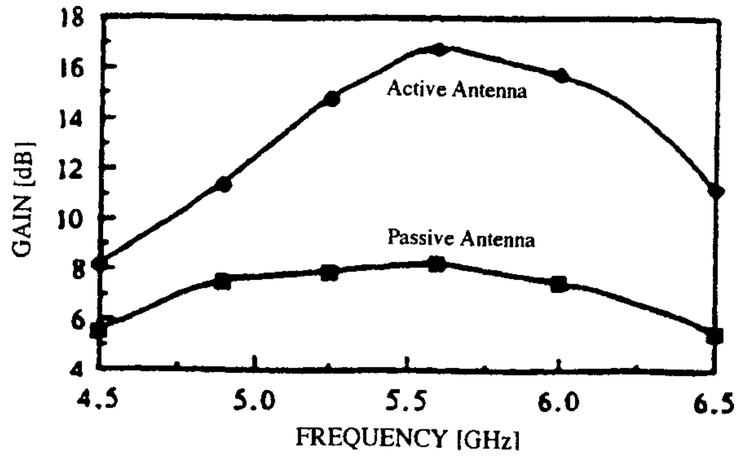

Figure 11.39 Measured gain of the passive and active antennas. (From [52]. © 1994 *24th European Microwave Conference Proceedings*. Reprinted with permission.)

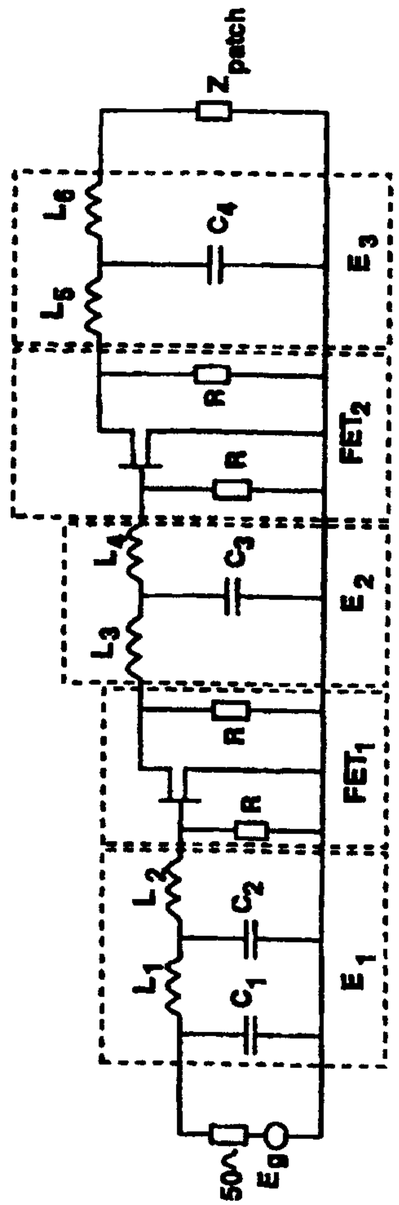

Figure 11.40 Active integrated microstrip antenna with two-stage amplifier. (From [48]. © 1994 IEEE. Reprinted with permission.)

11.4.3 Low-Noise Active Integrated Microstrip Antenna Amplifier Design

In receiving applications of active integrated microstrip antenna amplifiers, a low-noise figure is usually the design objective since it has the dominant effect on the noise performance of the overall system. Usually, it is not possible to achieve the minimum noise figure and the maximum gain simultaneously. Design trade-offs have to be made between gain and noise figures, which can be done by using constant gain and constant noise figure circles.

Constant Noise Figure Circles

The noise figure F of a two-port amplifier can be expressed in terms of the source reflection coefficient Γ_S and Γ_{opt} as

$$F = F_{min} + \frac{4R_N}{Z_0} \frac{|\Gamma_S - \Gamma_{opt}|^2}{(1 - |\Gamma_S|^2)|1 + \Gamma_{opt}|^2} \tag{11.62}$$

where F_{min}, R_N, and Γ_{opt} are known as the noise parameters of the device. They can be supplied by the manufacturer or can be determined experimentally. Equation (11.62) is rearranged to show Γ_S in terms of F and noise parameters as

$$\frac{|\Gamma_S - \Gamma_{opt}|^2}{1 - |\Gamma_S|^2} = \frac{F - F_{min}}{4R_N/Z_0}|1 + \Gamma_{opt}|^2 = N \tag{11.63}$$

where N is the noise figure parameter. In the complex Γ_S plane, (11.63) represents circles of constant noise figure with centers and radii given by

$$C_F = \frac{\Gamma_{opt}}{N + 1} \tag{11.64}$$

$$R_F = \frac{\sqrt{N(N + 1 - |\Gamma_{opt}|^2)}}{N + 1}$$

Typical constant gain circles G_S, (11.60), and constant noise figure circles, (11.64), in the Γ_S plane are shown in Figure 11.41.

It is evident from Figure 11.41 that the maximum gain and the minimum noise figure cannot be obtained simultaneously. Design compromises have to be made between the noise figure and gain.

The general design procedure for low-noise active integrated microstrip antenna amplifiers still follows the outline described for the constant gain design. However, in the Γ_S plane, a set of constant noise figure circles has to be plotted together with a set of constant gain circles, G_S. Γ_S, which results in the required noise figure and gain, can then be selected from the plot. Note that a patch acts as a source for receiving applications.

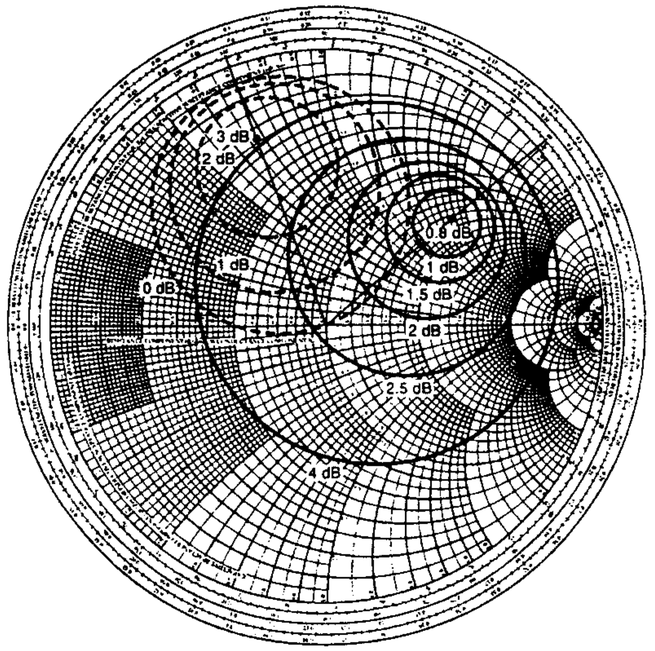

Figure 11.41 Typical constant gain circles (dashed curves) and constant noise figure circles (solid curves). (From [18]. © 1997 Prentice Hall, Inc. Reprinted with permission.)

Design Samples

A design sample for a receiver patch antenna integrated with a low-noise amplifier transistor [53] is shown in Figure 11.42. The configuration was proposed by Robert et al. for a compact, conformal active antenna design. A circuit block diagram of this active antenna is depicted in Figure 11.43. A proper value of Γ_S is selected from constant noise figure and constant gain circle plots. Referring to Figure 11.44, $\Gamma_S = \Gamma_{opt}$ is chosen for the minimum noise figure design, which corresponds to the minimum noise figure of 1.8 dB. The required Γ_S was realized by modifying the antenna structure to accommodate an inset feed as shown in Figure 11.42. This approach results in a compact design since the transistor can be directly connected to the patch without the need for a matching network. The active integrated antenna achieved the measured noise figure of 1.9 dB and the amplifier gain of 8.5 dB. The measured E- and H-plane radiation patterns (see Figure 11.45) were not affected by the patch modification.

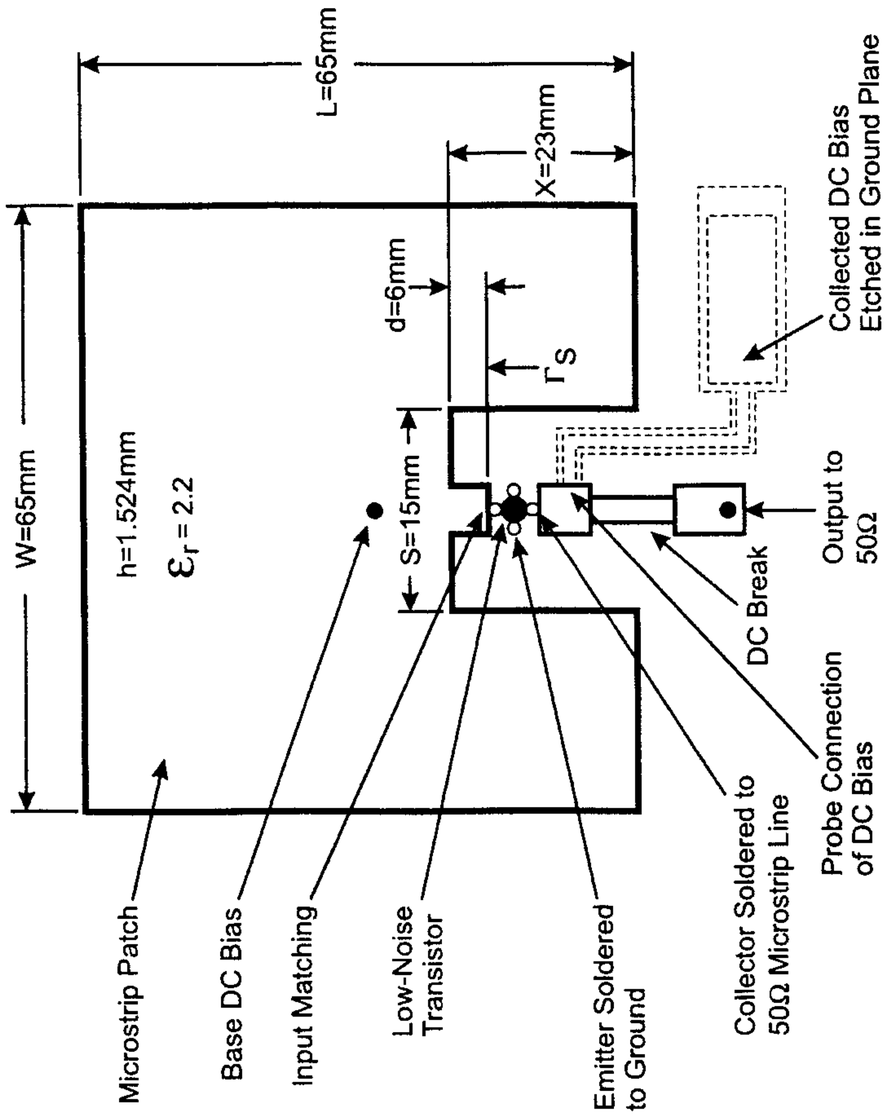

Figure 11.42 A low-noise amplifier integrated patch antenna. (From [53]. © 1993 *Microwaves & RF*. Reprinted with permission.)

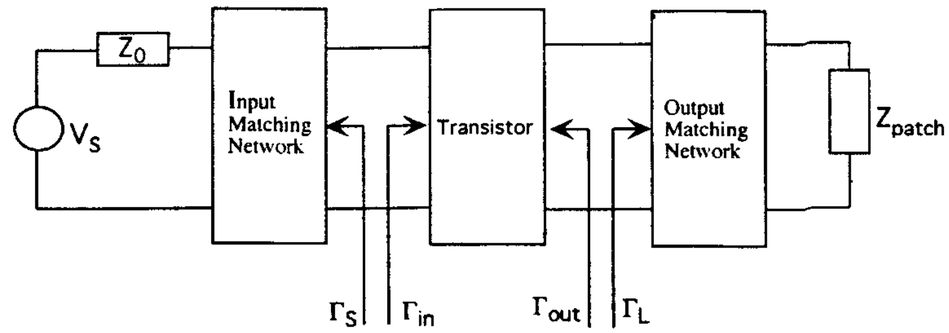

Figure 11.43 A circuit block diagram of the low-noise amplifier integrated patch antenna.

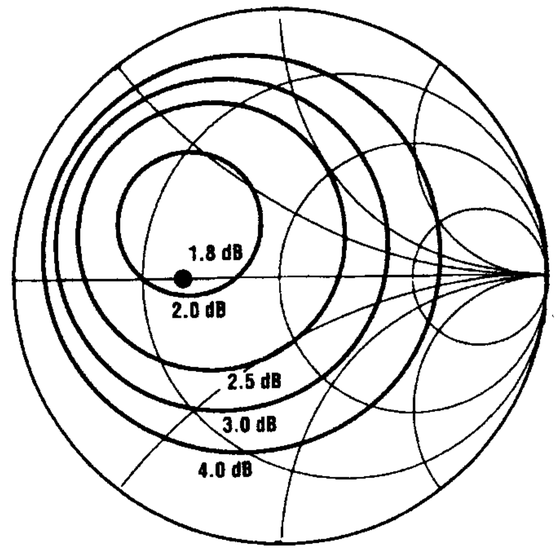

Figure 11.44 Constant noise figure circles of a bipolar transistor for a low-noise amplifier design. (From [53]. © 1993 *Microwaves & RF*. Reprinted with permission.)

11.5 Frequency Conversion Active Integrated Microstrip Antenna Theory and Design

Frequency conversion occurs when two signals, the RF and LO signals, are mixed by a nonlinear active device. The applied LO signal causes periodic variation of device junction characteristics, which is exploited for frequency conversion. The up or down frequency conversion of the RF signal can be selected depending on applications. Factors that are of concern are conversion gain, noise figure, and RF-to-IF isolation. Diodes and transistors have been used in the design of mixers. Advantages of transistors include conversion gain and monolithic compatibility.

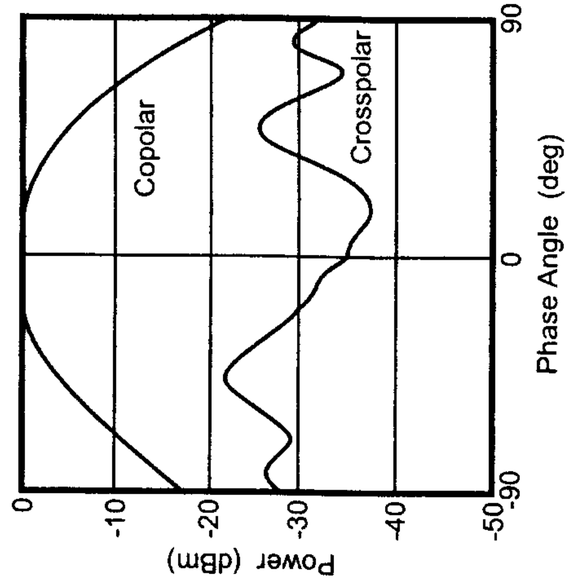

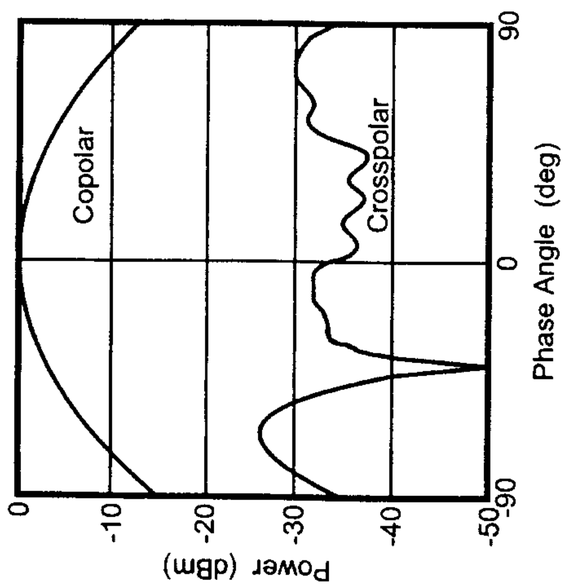

Figure 11.45 Measured radiation patterns: (a) E plane and (b) H plane. (From [53]. © 1993 *Microwaves & RF*. Reprinted with permission.)

There are various types of mixers [22, 54–56]. In this section, only the design for transconductance mixers [54, 57] that are amenable for direct integration with a patch to form a frequency conversion-type active antenna is given. Discussion is mainly confined to FET self-oscillating mixers [58, 59] where the FET simultaneously functions as an oscillator and a mixer. This results in compactness at the expense of slightly inferior performance to the case when a separate local oscillator is used. Design of self-oscillating mixers using diodes can be found in the literature [5, 6].

11.5.1 Operational Principle of Transconductance Mixers

A model of a FET transconductance mixer is shown in Figure 11.46 [53]. Under the small-signal assumption, the drain current i_d is approximated from a Taylor series expansion about the operating point by neglecting higher order terms, as

$$i_d(t) = g_m(t)v_g(t) \tag{11.65}$$

where $g_m(t)$ is the transconductance waveform and $v_g(t)$ is the gate voltage. For a fixed value of gate-source bias, LO signal on the gate-source terminals results in a periodic transconductance function $g_m(t)$ with the same period of oscillation as the LO (see Figure 11.47). Fourier series expansion of $g_m(t)$ gives

$$g_m(t) = \sum_{n=-\infty}^{\infty} g_n \exp(jn\omega_0 t) \tag{11.66}$$

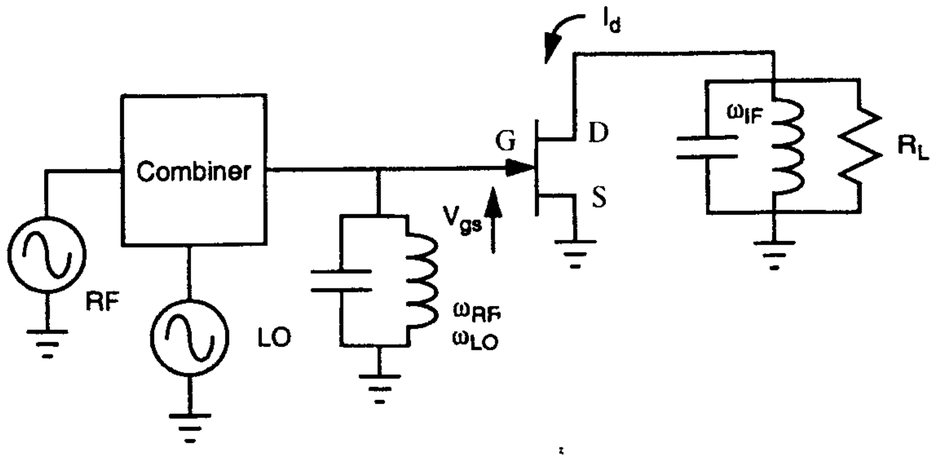

Figure 11.46 A model of a FET transconductance mixer. (From [54]. © 1998 Artech House. Reprinted with permission.)

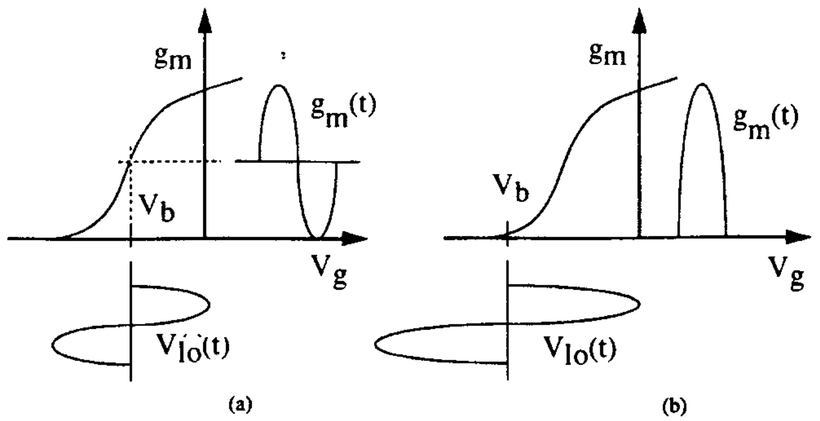

Figure 11.47 Transconductance waveforms: FET biased in the (a) active region and (b) near pinch-off. (From [54]. © 1998 Artech House. Reprinted with permission.)

where ω_0 denotes the LO frequency. When a small RF signal $v_g(t) = V_g \exp(j\omega_s t)$ is applied to the gate, the drain current $i_d(t)$ becomes

$$i_d(t) = V_g \sum_{n=-\infty}^{\infty} g_n \exp(j(n\omega_0 + \omega_s)t) \tag{11.67}$$

Hence, $i_d(t)$ contains all side-band frequency components $|\omega_s \pm n\omega_0|$ where n takes on all integer numbers. For up or down conversion applications, the sideband components $|\omega_s \pm \omega_0|$ are usually the desired outputs that have to be maximized for a good conversion gain. This requirement can be satisfied by a gate bias near pinch-off where transconductance g_1 is largest and most sensitive to bias modulation by the LO [57]. The drain bias should be at the level that keeps a FET in current saturation. The conversion efficiency is further improved by conjugate matching of the input RF signal at the gate.

11.5.2 Self-Oscillating Mixer Active Integrated Microstrip Antennas

A general schematic of a self-oscillating mixer (SOM) is shown in Figure 11.48. The circuit consists of an injection RF source, input and output matching networks, a FET performing both functions of the LO and the mixer, loads Y_{L1} and Y_{L2} and an IF filter. A microstrip antenna is included in Y_{L1} for a receiving case and in Y_{L2} for a transmitting case.

When the injection source is connected to the oscillator input, it is called *transmission-type locking*. Otherwise, it is known as *reflection-type locking* when the injection source is at the output. In designing self-oscillating mixers, the frequency of the injecting RF signal is required to be out of the locking range

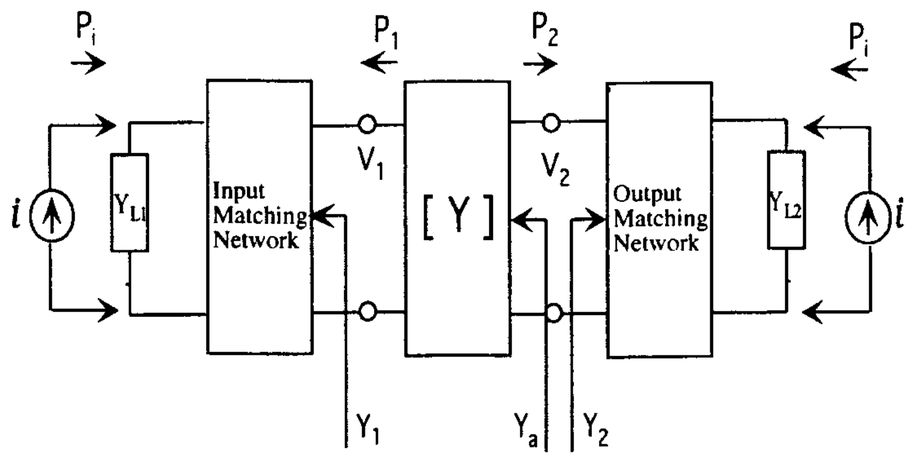

Figure 11.48 General two-port oscillator with injection current sources.

to prevent the LO from being injection locked to the RF signal, thus depriving the mixer of the LO power. The transmission-type locking range $(\omega_0 \pm \Delta\omega)$ is determined by [58]

$$\Delta\omega = \frac{\omega_0}{Q_{\text{ext}}} \frac{G_s}{G_p} \left(\frac{P_i}{P_2}\right)^{1/2} \frac{1}{|\sin\theta|} \tag{11.68}$$

$$G_s = \left|\frac{Y_{21}}{Y_{12}}\right| \tag{11.69}$$

$$G_p = \left(\frac{P_2}{P_1}\right)^{1/2} \tag{11.70}$$

where P_1 and P_2 are the free-running output power from port 1 and port 2, respectively, P_i is the available power from the injection source, Q_{ext} is the external Q of the load G_L, and θ is the angle made by loci $-Y_a$ and Y_2, device line and load, respectively as indicated in Figure 11.48. For a reflection type, the locking range can also be found from (11.68) without a factor (G_s/G_p). A self-oscillating mixer may not generate sufficient LO power at a bias condition where the transconductance g_1 is strongest. Moreover, small oscillating power also increases the locking range $\Delta\omega$ for a fixed injected power P_i.

A general design procedure follows the outline of active integrated antenna oscillators. However, the bias condition has to be selected to provide good LO power and efficient mixing.

Design Samples

The concept of a self-oscillating mixer active integrated patch antenna was applied by Cha et al. to develop a new small planar transponder for potential applications in communications and contactless ID systems [60]. The basic building blocks of the transponder consist of a SOM active patch antenna receiver and an amplifier-type active integrated patch antenna transmitter.

The SOM active patch receiver down-converted RF to IF, which was then amplified and reradiated by the active patch transmitter. The design of an active patch oscillator follows the design procedure as described in Section 11.3.3. The FET was drain-biased and gate-biased near pinch-off so that the active patch functioned as a self-oscillating mixer. The patch oscillator was designed to resonate at 14 GHz. The patch simultaneously acted as the RF injection source and the source impedance for the oscillator circuit. The locking range condition must be checked to prevent the oscillator from being injection locked to the RF. The self-oscillating mixer down-converted 14 GHz RF injected at the gate to 8 GHz IF, which was extracted from the drain.

All harmonics resulting from the nonlinear mixing process were suppressed by an IF bandpass filter. The IF signal was then radiated by the amplifier-type active patch antenna, which provided a gain of 9.5 dB before transmission. The design procedure of the active integrated patch amplifier was described in Section 11.4.2. The transmitting patch was designed to resonate at 8 GHz and served as a load for the amplifier. The measured power spectrum validated the transponder design.

References

[1] York, R. A., and Z. B. Popovic (Eds.), *Active and Quasi-Optical Arrays for Solid-State Power Combining*, John Wiley & Sons, New York, 1997.

[2] Navaro, J. A., and K. Chang, *Integrated Active Antennas and Spatial Power Combining*, John Wiley & Sons, New York, 1996.

[3] Mortazawi, A., T. Itoh, and J. Harvey (Eds.), *Active Antennas and Quasi-Optical Arrays*, IEEE Press, New York, 1998.

[4] Lin, J., and T. Itoh, "Active Integrated Antennas," *IEEE Trans. Microwave Theory and Techniques*, Vol. MTT-42, 1994, pp. 2186–2194.

[5] Kwok, S. P., and K. P. Weller, "Low Cost X-Band MIC BARITT Doppler Sensor," *IEEE Trans. Microwave Theory and Techniques*, Vol. MTT-27, 1979, pp. 844–847.

[6] Armstrong, B. M., et al., "Use of Microstrip Impedance-Measurement Technique in the Design of a BARITT Diplex Doppler Sensor," *IEEE Trans. Microwave Theory and Techniques*, Vol. MTT-28, 1980, pp. 1437–1442.

[7] Navaro, J. A., K. A. Hummer, and K. Chang, "Active Integrated Antenna Elements," *Microwave J.*, Vol. 35, Jan. 1991, pp. 115–126.

[8] Pozar, D. M., *Microwave Engineering*, 2nd ed., John Wiley & Sons, New York, 1998.

[9] Wiltse, J. C., and J. W. Mink, "Quasi-Optical Power Combining of Solid-State Sources," *Microwave J.*, Vol. 36, Feb. 1992, pp. 144–156.

[10] Hall, P. S., "Analysis of Radiation From Active Microstrip Antennas," *Electron. Lett.*, Vol. 29, No. 1, 1993, pp. 127–129.

[11] Whicker, L. R., "Active Phased Array Technology Using Coplanar Packaging Technology," *IEEE Trans. Antennas and Propagation*, Vol. AP-43, 1995, pp. 949–952.

[12] Sanzgiri, S., et al., "A Hybrid Tile Approach for Ka Band Subarray Modules," *IEEE Trans. Antennas and Propagation*, Vol. AP-43, 1995, pp. 953–959.

[13] Dahlgren, U., et al., "An Integrated Millimeterwave BCB Patch Antenna HEMT Receiver," *IEEE MTT-S Int. Microwave Symp. Digest*, 1994, pp. 661–664.

[14] Martinez, R. D., and R. C. Compton, "A Quasi-Optical Oscillator/Modulator for Wireless Transmission," *IEEE MTT-S Int. Microwave Symp. Digest*, 1994, pp. 839–842.

[15] Angelov, I., H. Zirath, and J. Svedin, "A New Mixer for Sensor Applications," *IEEE MTT-S Int. Microwave Symp. Digest*, 1998, pp. 1051–1054.

[16] Montiel, C. M., L. Fan, and K. Chang, "A Novel Active Antenna With Self-Mixing and Wideband Varactor-Tuning Capabilities for Communication and Vehicle Identification Applications," *IEEE Trans. Microwave Theory and Techniques*, Vol. MTT-44, 1996, pp. 2421–2430.

[17] Lin, S., Y. Qian, and T. Itoh, "A Quasi-Optical Subharmonic Self-Oscillating Mixer," *Proc. 28th European Microwave Conf.*, 1998, pp. 412–414.

[18] Gonzalez, G., *Microwave Transistor Amplifiers: Analysis and Design*, 2nd ed., Prentice Hall, Upper Saddle River, NJ, 1997.

[19] Holzman, E. L., and R. S. Robertson, *Solid-State Microwave Power Oscillator Design*, Artech House, Norwood, MA, 1992.

[20] Bahl, I., and P. Bhartia, *Microwave Solid State Circuit Design*, John Wiley & Sons, New York, 1988.

[21] Bhartia, P., and I. J. Bahl, *Millimeter Wave Engineering and Applications*, John Wiley & Sons, New York, 1984.

[22] Maas, S. A., *Microwave Mixers*, 2nd ed., Artech House, Norwood, MA, 1993.

[23] Kurokawa, K., "Some Basic Characteristics of Broadband Negative Resistance Oscillator Circuits," *Bell System Tech. J.*, Vol. 48, 1969, pp. 1937–1955.

[24] Chang, K., *Microwave Solid-State Circuits and Applications*, John Wiley & Sons, New York, 1994.

[25] Bahl, I. J., and P. Bhartia, *Microstrip Antennas*, Artech House, Dedham, MA, 1980.

[26] James, J. R., and P. S. Hall (Eds.), *Handbook of Microstrip Antennas*, Peter Peregrinus, London, UK, 1989.

[27] Perkins, T. O., III, "Active Microstrip Circular Patch Antenna," *Microwave J.*, Vol. 30, Mar. 1987, pp. 109–117.

[28] Bartolic, J., D. Bonefacic, and Z. Sipus, "Modified Rectangular Patches for Self-Oscillating Active-Antenna Applications," *IEEE Antennas and Propagation Magazine*, Vol. 38, Aug. 1996, pp. 13–21.

[29] Sanchez-Hernandez, D., and I. Robertson, "60 GHz-Band Active Microstrip Patch Antenna for Future Mobile Systems Applications," *Electron. Lett.*, Vol. 30, No. 9, 1994, pp. 677–678.

[30] Basawapatna, G. R., and R. B. Stancliff, "A Unified Approach to the Design of Wide-Band Microwave Solid-State Oscillators," *IEEE Trans. Microwave Theory and Techniques*, Vol. MTT-27, 1979, pp. 379–385.

[31] Medley, M. W., Jr., *Microwave and RF Circuits: Analysis, Synthesis, and Design*, Artech House, Norwood, MA, 1993.

[32] Howald, R., "A 24 GHz HEMT Microstrip Oscillator Using Linear and Nonlinear CAD Techniques," *Microwave J.*, Vol. 37, Mar. 1994, pp. 80–93.

[33] Martin, J. L. J., and F. J. O. Gonzalez, "Accurate Linear Oscillator Analysis and Design," *Microwave J.*, Vol. 39, June 1996, pp. 22–37.

[34] Boyles, J. W., "The Oscillator as a Reflection Amplifier: An Intuitive Approach to Oscillator Design," *Microwave J.*, Vol. 29, June 1986, pp. 83–98.

[35] Razban, T., et al., "A Compact Oscillator Integrated in a Microstrip Patch Antenna," *Microwave J.*, Vol. 37, Feb. 1994, pp. 110–115.

[36] Forma, G., and J. M. Laheurte, "CPW-Fed Oscillating Microstrip Antennas," *Electron. Lett.*, Vol. 32, No. 2, 1996, pp. 85–86.

[37] Johnson, K. M., "Large Signal GaAs MESFET Oscillator Design," *IEEE Trans. Microwave Theory and Techniques*, Vol. MTT-27, 1979, pp. 217–227.

[38] York, R. A., R. D. Martinez, and R. C. Compton, "Active Patch Antenna Element for Array Applications," *Electron. Lett.*, Vol. 26, No. 7, 1990, pp. 494–495.

[39] Fusco, V. F., "Series Feedback Integrated Active Microstrip Antenna Synthesis and Characterisation," *Electron. Lett.*, Vol. 28, No. 1, 1992, pp. 89–91.

[40] Bussgang, J. J., L. Ehrman, and J. W. Graham, "Analysis of Nonlinear Systems With Multiple Inputs," *Proc. IEEE*, Vol. 62, No. 8, 1974, pp. 1088–1119.

[41] Huang, C., and T. Chu, "Radiating and Scattering Analyses of a Slot-Coupled Patch Antenna Loaded With a MESFET Oscillator," *IEEE Trans. Antennas and Propagation*, Vol. AP-43, No. 3, 1995, pp. 291–298.

[42] Chang, K., K. A. Hummer, and G. K. Gopalakrishnan, "Active Radiating Element Using FET Source Integrated With Microstrip Patch Antenna," *Electron. Lett.*, Vol. 24, No. 21, 1988, pp. 1347–1348.

[43] Razban, T., M. Nannini, and A. Papiernik, "Integration of Oscillators With Patch Antennas," *Microwave J.*, Vol. 36, 1993, pp. 104–110.

[44] Fusco, V. F., and H. O. Burns, "Synthesis Procedure for Active Integrated Radiating Elements," *Electron. Lett.*, Vol. 26, No. 4, 1990, pp. 263–264.

[45] Choo, E. B. L., J. A. C. Stewart, and V. F. Fusco, "Computer-Aided Design of Nonlinear Optimum Output Power MESFET Oscillator," *Microwave and Optical Technology Lett.*, Vol. 1, No. 8, 1988, pp. 277–281.

[46] Birkeland, J., and T. Itoh, "Spatial Power Combining Using Push-Pull FET Oscillators With Microstrip Patch Resonators," *IEEE MTT-S Int. Microwave Symp. Digest*, 1990, pp. 1217–1220.

[47] Ha, T. T., *Solid-State Microwave Amplifier Design*, John Wiley & Sons, New York, 1981.

[48] An, H., B. Nauwelaers, and A. Van De Capelle, "Broadband Active Microstrip Antenna Design With the Simplified Real Frequency Technique," *IEEE Trans. Antennas and Propagation*, Vol. AP-42, No. 12, 1994, pp. 1612–1619.

[49] Jung, W. L., and J. Wu, "Stable Broad-Band Microwave Amplifier Design," *IEEE Trans. Microwave Theory and Techniques*, Vol. MTT-38, No. 8, 1990, pp. 1079–1085.

[50] Jung, W. L., and J. Chiu, "Stable Broad-Band Microwave Amplifier Design Using the Simplified Real Frequency Technique," *IEEE Trans. Microwave Theory and Techniques*, Vol. MTT-41, No. 2, 1993, pp. 336–340.

[51] An, H., B. Nauwelaers, and A. Van De Capelle, "Broadband Active Microstrip Array Elements," *Electron. Lett.*, Vol. 27, No. 25, 1991, pp. 2378–2379.

[52] Giauffret, L., and J. Laheurte, "A CPW-Fed Active Microstrip Antenna Working in the C-Band," *Proc. 24th European Microwave Conf.*, 1994, pp. 1814–1818.

[53] Robert, B., T. Razban, and A. Papiernik, "Patch Antenna Integrates a Low-Noise Amp," *Microwaves & RF*, Vol. 32, Aug. 1993, pp. 121–126.

[54] Maas, S. A., *The RF and Microwave Circuit Design Cookbook*, Artech House, Norwood, MA, 1998.

[55] Maas, S. A., "Theory and Analysis of GaAs MESFET Mixers," *IEEE Trans. Microwave Theory and Techniques*, Vol. MTT-32, No. 10, 1984, pp. 1402–1406.

[56] Camacho-Penalosa, C., and C. S. Aitchison, "Analysis and Design of MESFET Gate Mixers," *IEEE Trans. Microwave Theory and Techniques*, Vol. MTT-35, No. 7, 1987, pp. 643–652.

[57] Pucel, R. A., D. Masse, and R. Bera, "Performance of GaAs MESFET Mixers at X Band," *IEEE Trans. Microwave Theory and Techniques*, Vol. MTT-24, No. 6, 1976, pp. 351–360.

[58] Tajima, Y., "GaAs FET Applications for Injection-Locked Oscillators and Self-Oscillating Mixers," *IEEE Trans. Microwave Theory and Techniques*, Vol. MTT-27, No. 7, 1979, pp. 629–632.

[59] Hwang, V. D., and T. Itoh, "Quasi-Optical HEMT and MESFET Self-Oscillating Mixers," *IEEE Trans. Microwave Theory and Techniques*, Vol. MTT-36, No. 12, 1988, pp. 1701–1705.

[60] Cha, K., S. Kawasaki, and T. Itoh, "Transponder Using Self-Oscillating Mixer and Active Antenna," *IEEE MTT-S Int. Microwave Symp. Digest*, 1994, pp. 425–428.

12

Design and Analysis of Microstrip Antenna Arrays

12.1 Introduction

In certain applications, desired antenna characteristics may be achieved with a single microstrip element as discussed in the previous chapters. However, as in the case of conventional microwave antennas, characteristics such as high gain, beam scanning, or steering capability are possible only when discrete radiators are combined to form arrays. The elements of an array may be spatially distributed to form a linear, planar, or volume array. A linear array consists of elements located finite distances apart along a straight line. Similarly, a planar array has elements distributed on a plane and a volume array has elements that are distributed in three dimensions. In practice, the array type is usually chosen depending on the intended application.

Many excellent texts are available on array theory [1–8]; hence, theory is not discussed here. Instead, this chapter concentrates on analysis and design of microstrip patch arrays. Various types of array feed systems are first discussed and then followed by some analysis and design procedures for microstrip arrays.

12.2 Parallel and Series Feed Systems

In general, radiation characteristics of an array can be determined once the aperture distribution is known. The amplitude and phase distribution at each element is usually determined from the intended application, for example, low sidelobe and beam direction. The means of excitation of the radiating elements

are thus an essential and important factor which must be carefully considered so that the required distribution is realized.

Existing methods that have been employed to feed microstrip arrays can be categorized into parallel and series feeds, which refers to geometries rather than to actual equivalent circuits. The parallel or corporate feed has a single input port and multiple feed lines in parallel constituting the output ports. Each of these feed lines is terminated at an individual radiating element. The second type of feed system is the series feed. It usually consists of a continuous transmission line from which small proportions of energy are progressively coupled into the individual element disposed along the line by various means including proximity coupling, direct coupling, probe coupling, or aperture coupling. The series feed constitutes a traveling-wave array if the feed line is terminated in a matched load, or a resonant array if the termination is an open or a short circuit. Both types of feeds can be realized as either coplanar with the radiating elements or in a separate transmission line layer.

The feed networks in general have certain undesirable characteristics that must be carefully monitored in order to minimize any adverse effects on array performance. These characteristics include conductor and dielectric losses, surface wave loss, and spurious radiation due to discontinuities such as bends, junctions, and transitions. These losses constitute the overall insertion loss of the feed affecting the maximum obtainable gain of the array.

12.2.1 Parallel Feed for One and Two Dimensions

One-Dimensional Parallel Feed

The fundamental configuration of a one-dimensional parallel feed consists of a branching network of two-way power dividers as illustrated in Figure 12.1.

A corporate feed is the most widely used parallel feed configuration. For a uniform aperture distribution, the power is equally split at each junction; however, different power divider ratios can be chosen to generate a tapered distribution across the array. If the distances from the input port to each radiating element are identical, the beam position is independent of the frequency and the feed is broadband. By incorporating proper progressive phasers or line extensions as shown in Figure 12.2, the beam direction can be controlled. The disadvantage of this type of feed is that it requires long transmission lines between the radiating elements and the input port, hence, the insertion loss of the feed network can be prohibitively large, thereby reducing the overall efficiency of the array.

In the design, all radiating elements are usually identically matched to the feed lines by appropriate feed coupling design or by using quarter-wave transformers. For a symmetrical corporate feed network, the number of radiating

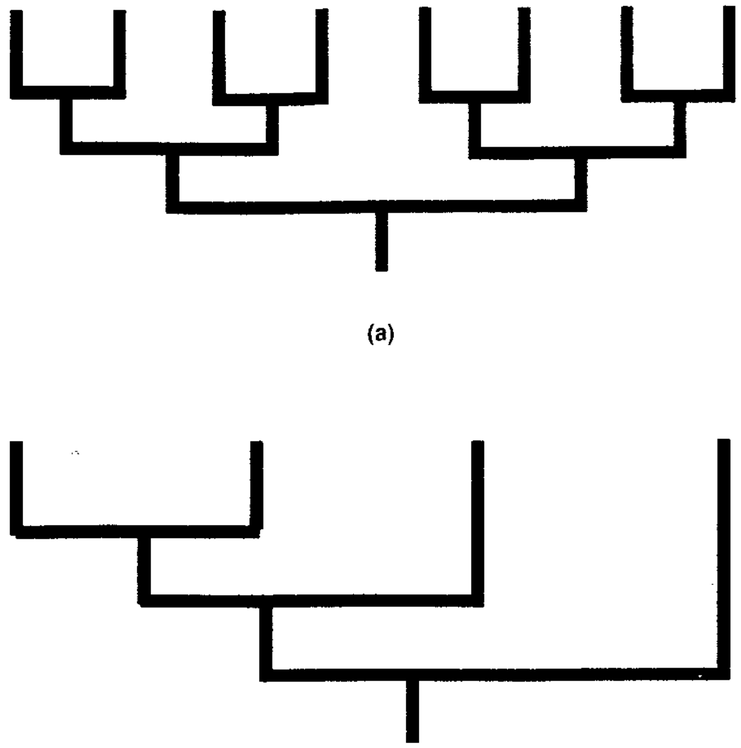

Figure 12.1 Basic one-dimensional parallel feed networks: (a) Symmetrical configuration and (b) asymmetrical configuration.

elements is 2^n where n is an integer; otherwise, an asymmetrical feed configuration as shown in Figure 12.1(b) has to be used. The symmetry of a corporate feed network allows the use of identical power dividers to provide uniform aperture distribution, thereby reducing the number of different power dividers needed. In practice, the T-junction or its modified configuration is the most widely used divider. Quarter-wave transformers are generally employed to obtain impedance match at the junction.

Two-Dimensional Parallel Feed

One-dimensional parallel feed can be arranged to form a two-dimensional parallel feed as shown in Figure 12.3. The basic subarray configuration can be extended to larger arrays with specifically 2^n elements per side to maintain a symmetrical configuration. If there is an odd number of elements per side, the symmetry is lost. Different power divider ratios are then required to provide uniform aperture distribution.

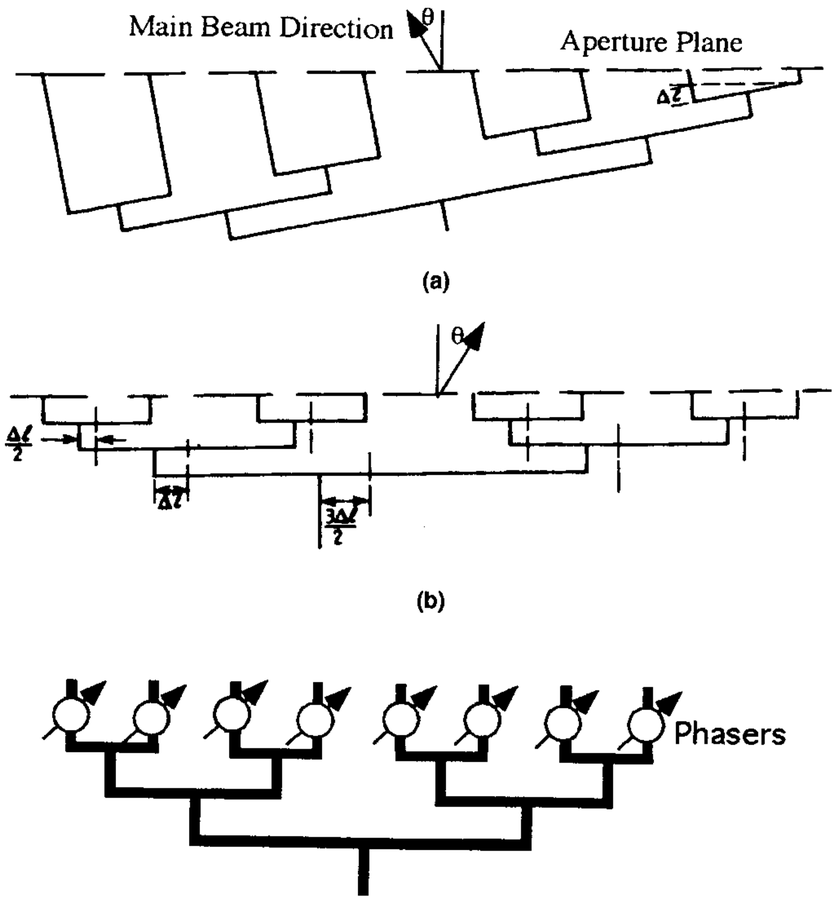

Figure 12.2 Parallel feed networks for radiating inclined beams by using (a) line extension, (b) offset power divider, and (c) phasers. (From [12]. © 1989 Peter Peregrinus. Reprinted with permission.)

A two-dimensional parallel feed structure has been used in the design of microstrip patch arrays on a thin substrate at 35, 38, and 60 GHz as shown in Figure 12.4 [9, 10]. The overall array efficiency for the 35-GHz 4 × 4 element array was measured at 77% [9]. The losses were attributed to dielectric loss, copper loss, and feed system mismatches.

12.2.2 Series Feeding of Microstrip Arrays

Typical series-fed microstrip arrays are shown in Figure 12.5 for two types of radiating element arrangements, referred to as *transposed* and *untransposed* arrays [10, 11]. In the untransposed array of Figure 12.5(a), the element spacing for the boresight beam is λ_g. However, for the case of the transposed array [see

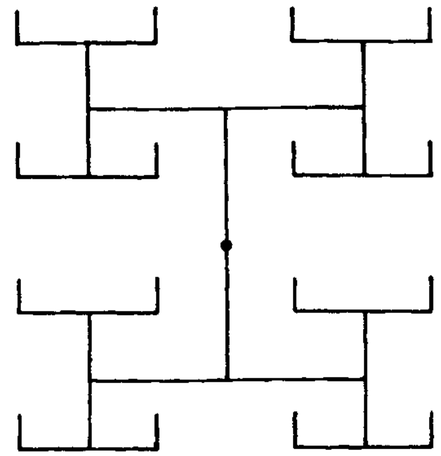

Figure 12.3 Two-dimensional parallel feed network. (From [12]. © 1989 Peter Peregrinus. Reprinted with permission.)

Figure 12.5(b)], there is a phase change of 180° on the radiated fields between adjacent elements due to the effect of the coupling mechanism. Consequently, the element spacing of $\lambda_g/2$ will produce a boresight beam [12–14]. As a result, the transposed array can provide beams over a much wider range of scanned angles without producing grating lobes.

It is clear from Figure 12.5 that the number of feed lines is smaller than with the parallel-fed configuration, which may be attractive when the overall array efficiency needs to be maximized. The disadvantages of this type of feed are narrow bandwidth and inherent beam shift with frequencies due to the insertion phase shift of the patch in the series configuration. However, by appropriate adjustment of the parameters of the array, the beam squint can be kept low.

Resonant Arrays

The equivalent circuit of a resonant feed array in Figure 12.6 represents radiating elements periodically spaced along a feed line that is terminated in an open or a short circuit at one-half or a quarter-guide wavelength beyond the last radiating element, respectively. Hence, the terminating load always appears as the open circuit at the last element. The element spacing can be either λ_g or $\lambda_g/2$ depending on whether the element arrangement is of the untransposed or the transposed type. The resonant feed is only useful in generating a broadside beam. The VSWR bandwidth is very narrow because of its resonant nature. Small reflections from the radiating elements will add up and result in high return loss due to element spacing of either λ_g or $\lambda_g/2$ for the resonant array.

In designing this type of array, the input admittance of the array is set equal to the characteristic admittance of the feed line [12, 13], that is,

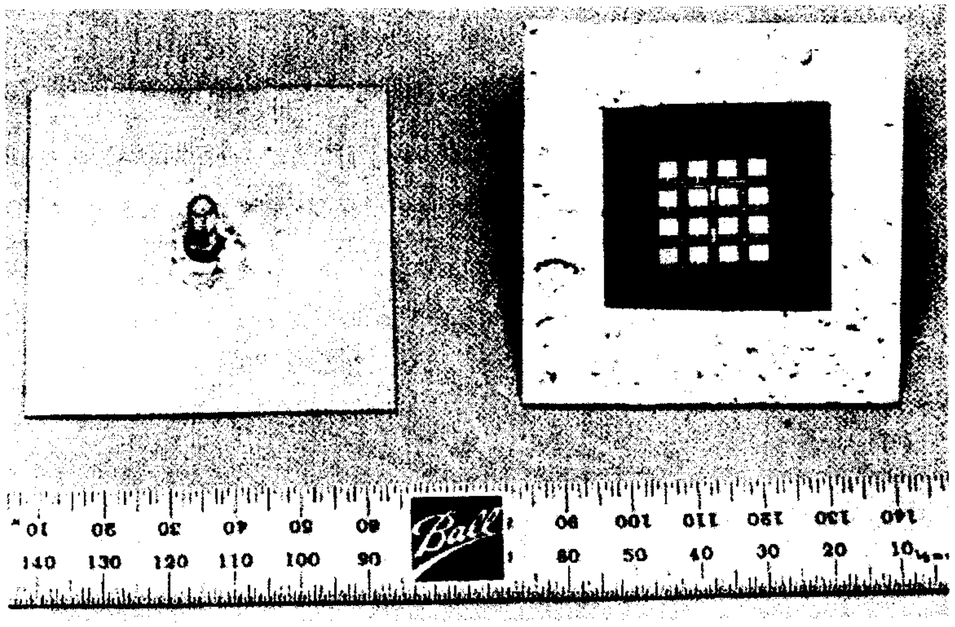

(a)

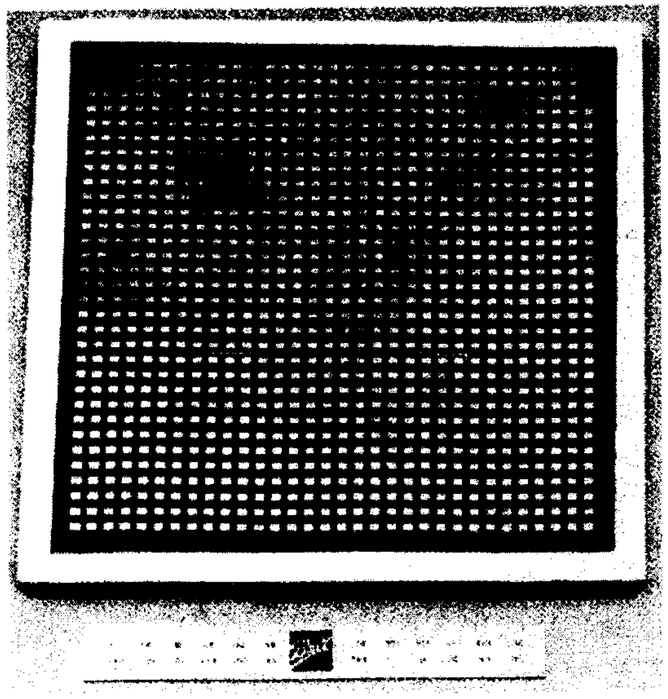

(b)

Figure 12.4 Microstrip antenna arrays using two-dimensional parallel feed configurations: (a) 35-GHz 4 × 4 element array and (b) 38-GHz 32 × 32 element array. (From [9]. © 1981 IEEE. Reprinted with permission.)

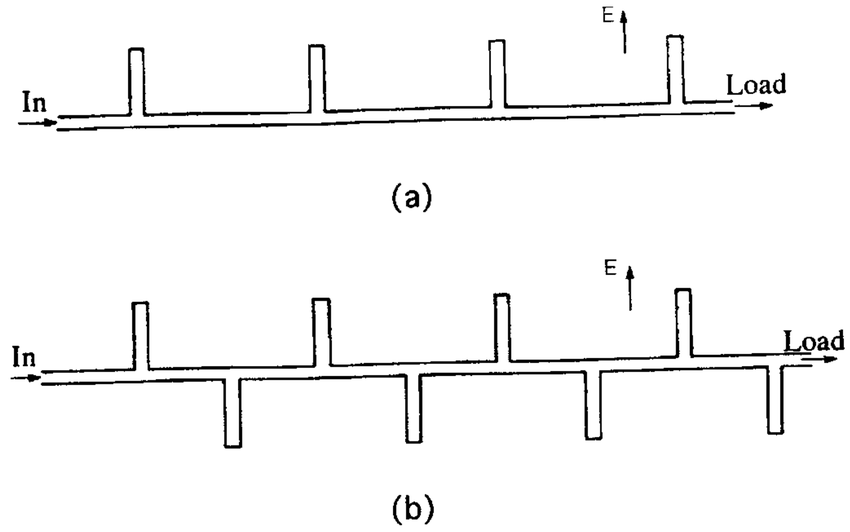

Figure 12.5 One-dimensional series feed arrays: (a) Untransposed configuration and (b) transposed configuration. (From [12]. © 1989 Peter Peregrinus. Reprinted with permission.)

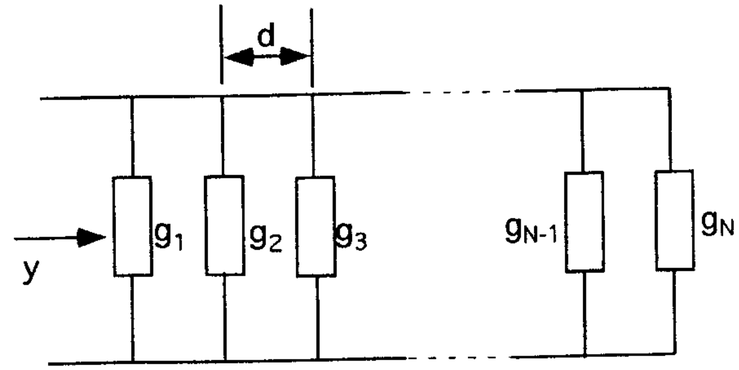

Figure 12.6 Resonant array circuit.

$$y = \sum_{n=1}^{N} g_n + j0 = 1 \tag{12.1}$$

where y is the normalized input admittance of the array, g_n is the normalized radiation conductance of the nth element, and N is the total number of radiating elements in the array. The total input admittance in (12.1) is simply the sum of the element admittance due to the element spacing of $\lambda_g/2$ or λ_g. The relative conductance values can be freely chosen to obtain the required aperture distribution, provided that they are realizable and (12.1) is satisfied.

Traveling-Wave Arrays

A series feed array is of the traveling-wave type when the feed line is terminated in a matched load to absorb the residual energy after the last element. Alternatively, the array can be designed where the last radiating element also serves as a matched load for better operational efficiency, as shown in Figure 12.7 [15]. Similar to the resonant case, radiating elements along the feed line can be arranged in the untransposed or the transposed type with element spacing of λ_g or $\lambda_g/2$, respectively, for a broadside beam. These spacings can lead to a large VSWR at the input due to an in-phase combining of the reflections caused by each element along the line. To avoid large VSWR, elements are spaced slightly different from λ_g or $\lambda_g/2$. Since the wave on the feed line is a traveling wave, the beam peak is squint with a change in frequency. When the loss along the line is negligible, the normalized conductance at the nth element can be derived from the equivalent circuit in Figure 12.8 and is given by [13, 14]

$$g_n = \frac{F_n}{\frac{1}{1-L}\sum_{m=1}^{N} F_m - \sum_{m=1}^{n} F_m} \tag{12.2}$$

where F_n is the desired array excitation power distribution such as Taylor line source distribution, N is the total number of elements, and L is the fraction of input power dissipated in the matched load, that is,

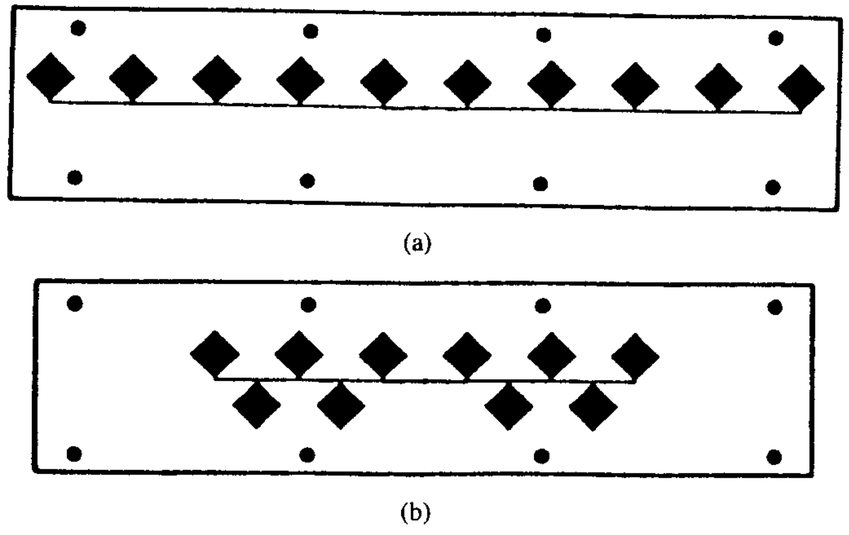

Figure 12.7 Traveling-wave linear arrays of corner-fed square patches: (a) Untransposed configuration and (b) transposed configuration. (From [15]. © 1989 Peter Peregrinus. Reprinted with permission.)

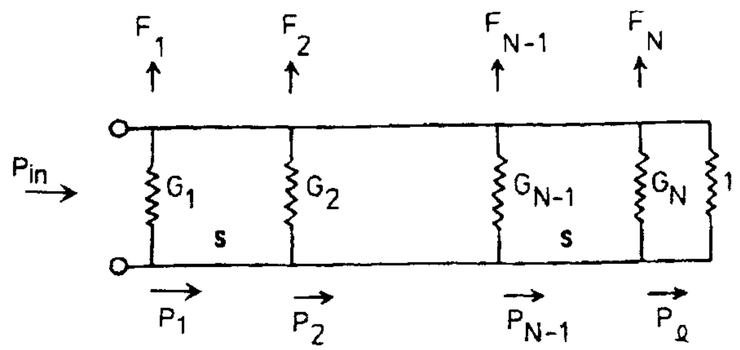

Figure 12.8 Equivalent circuit representation of traveling-wave coupling. (From [13]. © 1983 Peter Peregrinus. Reprinted with permission.)

$$L = \frac{P_{\text{load}}}{P_{\text{in}}} \tag{12.3}$$

In practice, L is usually chosen to be 5% to 10%. If the choice of L results in g_n being unrealizable from any particular element, then considerably more power may have to be dissipated in the load. In actual design, g_n as obtained in (12.2) includes self- and mutual conductance of the element.

12.3 Mutual Coupling

Radiation conductance and susceptance of microstrip radiating elements obtained from models as given in previous chapters can be used in designing series arrays. For series feed arrays comprising a small number of elements, Metzler found that they may be adequately modeled by cascaded elements interconnected by high-impedance lines [16, 17]. However, measured results showed anomalies in terms of increased sidelobes and unpredictable beam positions due to the omission of mutual coupling between radiators. Therefore, it is important to consider the effects of mutual coupling for a more accurate design.

Several approaches have been successfully applied for the determination of mutual coupling for microstrip antennas. Metzler [16, 17] utilized the experimental procedure as described by Zucker [18] to generate empirical design curves for the conductance of the radiator in the presence of mutual coupling effects. The method requires the insertion loss measurement of several samples of traveling-wave arrays of N (at least 20) *identical* elements with different parameters such as the width of a patch for each array. The normalized radiation conductance can then be calculated from

$$10 \log_{10}(1 + g) = \frac{\text{Insertion loss in dB}}{N} \tag{12.4}$$

Alternatively, analytical techniques, including the moment method [19], the transmission line model [20], and the cavity model [15], can also be applied to determine mutual admittance between microstrip patch radiating elements. Mutual impedance between microstrip dipoles has also been analyzed using a moment method [21], and is included in Chapter 6 as Figure 6.18. The mutual coupling data have been presented in Chapter 2 as Figures 2.16 and 2.17 for the E plane and H plane, respectively.

12.4 Design of Linear Arrays

This section deals with fixed beam array design. Linear arrays are usually utilized when the beamwidth in a particular plane has to meet certain specifications. Depending on the allowable surface wave excitation as well as the mounting requirements, the most convenient radiating elements for linear arrays are (1) open-circuited microstrip stubs, (2) printed dipoles, and (3) rectangular and circular microstrip patches.

12.4.1 Linear Array Design With Microstrip Patches

General design principles for microstrip patch linear arrays using corporate and series feeds are discussed in this section. Examples are also given to illustrate the basic design procedure.

Corporate-Fed Arrays

In the corporate feed configuration, the antenna elements are fed by 1:n power divider network with identical path lengths from the feed point to each element. The advantages of this topology include design simplicity, flexible choice of element spacing, and broader bandwidth, and they are amenable to integration with other devices such as amplifiers and phase shifters. The disadvantage of this type of array is that it requires more space for the feed network. For large arrays, the length of feed lines running to all the elements is prohibitively long, which results in high insertion loss. The insertion loss is even more pronounced at millimeter-wave frequencies, thereby adversely degrading the gain of the array.

At higher frequencies, the feed lines laid on the same plane as the patches will also radiate and interfere with the radiation from the patches, thus further

increasing the mutual coupling and cross-polarization of the array. Various corporate feed loss calculations can be found in [22].

Design of a symmetrical corporate-fed array as shown in Figure 12.9 for a uniform aperture distribution can be summarized as follows:

1. Antennas are matched to the feed lines through appropriate dimensioning of coupling structures or by using quarter-wave transformers.
2. Each pair of feed lines from neighboring elements is connected to a T-junction, which is matched to the input line, if necessary through a quarter-wave transformer.
3. Repeat step 2 until the last stage is reached in which the line is connected to the feed point of the array.

In the design, realizable high characteristic impedance feed lines should be used to minimize feed line degradation [22]. The number of different power dividers should also be kept to a minimum to reduce optimization complexity.

The example in Figure 12.9 shows a corporate-fed linear array [23]. The patch element with a 200Ω input resistance at the edge is connected to the feed line with 200Ω characteristic impedance. The 200Ω lines from neighboring elements are joined at a T-junction and transformed through a 140Ω quarter-wave transformer back to a single 200Ω line as illustrated in Figure 12.9. It is clear that all the T-junctions at this level are matched.

In the next step, neighboring pairs of 200Ω lines are again joined at the next level T-junction and similarly transformed through a 140Ω quarter-wave transformer back to a single 200Ω line as indicated in Figure 12.9. The process is continued until the final pair of the feed line is joined at the last T-junction and transformed through a 71Ω quarter-wave transformer to match with the

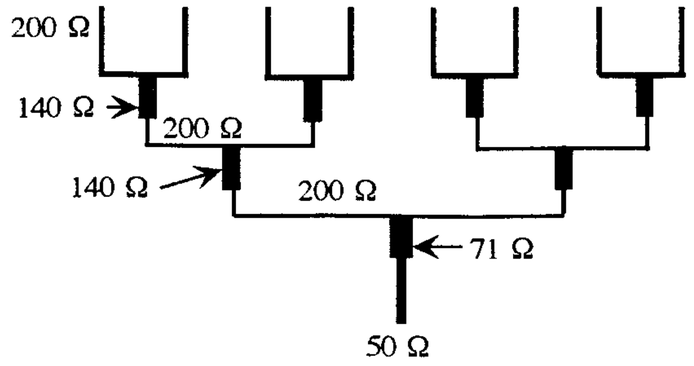

Figure 12.9 Eight-element linear array with corporate feed configuration.

50Ω line of the array feed. In this example, all of the quarter-wave transformers are 140Ω except for the final stage, which is 71Ω.

Series-Fed Arrays

Series-fed microstrip patch arrays, as shown in Figure 12.10, are formed by interconnecting all the elements with high-impedance transmission lines and feeding the power at the first element. Because the feed arrangement is compact, the line losses associated with this type of array are lower than those of a corporate-fed type. Linear arrays are frequently designed with series feed, either in the resonant or nonresonant mode.

The main limitation in series-fed arrays is the large variation of the impedance and beam-pointing direction over a band of frequencies. The main beam direction and the scan sensitivity can be calculated from the following equations [24]:

$$d\sin\theta + \sqrt{\epsilon}l = \lambda = \frac{c}{f} \tag{12.5}$$

$$\frac{\partial\theta}{\partial f} = -\frac{c}{df^2\cos\theta} \tag{12.6}$$

where d is the element spacing, l is the length of the transmission line joining the successive elements, c is the velocity of light, f is the operating frequency, and θ is the beam-pointing angle measured from the boresight direction. Such a configuration can also be used as a frequency scanned array.

For the low sidelobe design, the radiation resistance offered by each patch is chosen according to the required amplitude distribution. This can be achieved by varying the nonresonant width of the rectangular patch element. A chain of series-fed arrays can be accurately designed by using the cavity model for each patch. All parameters of the array, such as the input VSWR and bandwidth, can be estimated by using this model. An example of such an array at 40 GHz is discussed by Menzel [25].

The design of series-fed arrays of both the resonant and nonresonant types is centered around:

Figure 12.10 Linear microstrip patch array with series feed configuration.

1. Estimation of input impedance over the band of frequencies about the resonance (input characteristics);
2. Determination of both amplitude and phase excitation at each element of the array (radiation characteristics).

Input Impedance of Series-Fed Antenna Arrays

Each element in the series-fed array as shown in Figure 12.10 can be considered to be a two-port microstrip rectangular element with ports located on its nonresonant edges. For such a configuration, the input impedance of the antenna at the feed for a given loading Z_L can be represented as [26]

$$Z_{\text{in}} = Z_{11} - \frac{Z_{12}^2}{Z_{22} + Z_L} \tag{12.7}$$

where Z_{ij} are the impedance matrix parameters of the two-port rectangular element and can be determined from [10, 26]

$$Z_{ij} = -j\omega\mu_0 h \sum_{m,n} \frac{\psi_{mn}(x_i, y_i)\psi_{mn}(x_j, y_j)}{k^2 - k_{mn}^2} \left[\frac{\sin\left(\frac{m\pi w_f}{2a}\right)}{\frac{m\pi w_f}{2a}} \right]^2 \tag{12.8}$$

where w_f is the effective width of the feed strip (see Appendix B). Other quantities in (12.8) are defined in Section 4.2.2. For $i = j$, this represents the self-impedance at the single input port.

After determining the effective loss tangent δ_{eff} [27], the Z matrix for a two-port microstrip patch can be determined with appropriate locations of the two ports on the periphery of the patch element. Effective values of the patch dimensions are used for the evaluation of the impedance matrix in the above calculations. This results from the fact that the patch can be treated as a cavity with effective patch dimensions equal to $a \times b$. The effective widths are determined from equations of Appendix B or [28]. The input impedance of the entire series-fed antenna structure is then determined by starting from the input impedance of the last element, which, after transferring through the connecting line, acts as a load Z_L of the next element. The process is then repeated until the input impedance of the array is obtained.

Excitation Across the Array

The excitation at each element is determined from the available and the radiated power of the element [10]. Reflection at each junction must be taken into

account in the calculation of power available to each radiator. The amplitude distribution at each element can be determined from its radiated power. This is calculated by determining the normalized radiation conductance as

$$g_r = \frac{Z_0}{R_{\text{rad}}} \tag{12.9}$$

where R_{rad} is the radiation resistance of the patch element, and Z_0 is the characteristic impedance of the feed line. From the input impedance evaluation at each element, the reflection coefficient at the nth junction can be determined from

$$\Gamma_n = \frac{Z_{\text{in}n} - Z_{fl}}{Z_{\text{in}n} + Z_{fl}} \tag{12.10}$$

where $Z_{\text{in}n}$ is the input impedance at the nth junction, and Z_{fl} is the feed line or interconnection line impedance. The power radiated by the nth element in the series-fed array can be calculated from the general expression

$$V_{rn}^2 = P_{rn} = g_n(1 - g_{n-1})(1 - g_{n-2}) \ldots \tag{12.11}$$
$$(1 - g_1)(1 - |\Gamma_1|^2)(1 - |\Gamma_2|^2) \ldots (1 - |\Gamma_n|^2)$$

where g_r and Γ for a given element are obtained from (12.9) and (12.10), respectively. This type of excitation provides a natural exponential taper due to series feeding. The reverse traveling wave from the last element toward the generator can be assumed to be small in the calculation of the power radiated by each element.

The relative phase distribution across the array is determined from the insertion phase due to the patch and connecting line. From the wavelength in the patch and the feed line, the electrical length and hence the relative phase can be estimated at each element of the series-fed array. Once the amplitude and phase at each element are known, the radiation pattern is found from the standard equations for array factor and element pattern.

12.4.2 Linear Array Design With Capacitively Coupled Fingers

In another array configuration, rectangular patches are fed by means of capacitive coupling along the resonant edges as shown in Figure 12.11. The coupling to each element is adjusted by the gap between the main transmission line and the length of the resonant edge of the radiating element. This type of

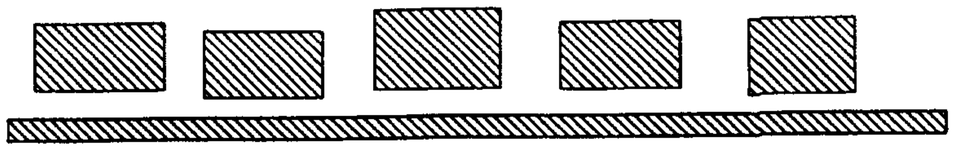

Figure 12.11 Linear array of capacitively coupled microstrip patches.

configuration results in a longitudinally polarized end-fed array. In the resonant array configuration, the element spacing is λ_g for a broadside beam array. The center points of the elements are adjusted to coincide with the voltage maxima of the transmission line feeder so that each element appears as a small load.

The main disadvantage of the capacitively coupled structure is small VSWR bandwidth and potential of grating lobes problem due to λ_g element spacing. By tapering the width of the rectangular element such that it forms a diamond-shaped patch, it was found that the bandwidth and coupling parameters improve when the taper angle is approximately 20°. Such an array with tapered elements is called the Lozenge array (see Figure 12.12) [10].

12.4.3 Design of Comb-Line Arrays With Microstrip Stubs

The basic radiating element in the comb-line array of Figure 12.13 is the open-circuited microstrip stub. A comb-line array can be designed either in the resonant or nonresonant traveling-wave configuration. In the traveling-wave array, a predetermined amount of power is dissipated in the matched termination. This array is useful in obtaining greater bandwidth at the expense of lower efficiency owing to power dissipation in the matched load.

A comb-line array is formed by connecting a number of open-circuited microstrip stubs at right angles to the main microstrip feeder. Each stub radiates from its open-circuited end and forms a T-junction with the main feeder. Depending on the type of the array, the feeder can be terminated in a matched load, short circuit, or open circuit.

The required aperture distribution along the array determines the necessary impedance loading on the main line due to the stubs, which can be realized by varying the stub width. The length of the stub is normally chosen to be $\lambda_g/2$ so that its resistance at the feeder is the same as the radiation resistance

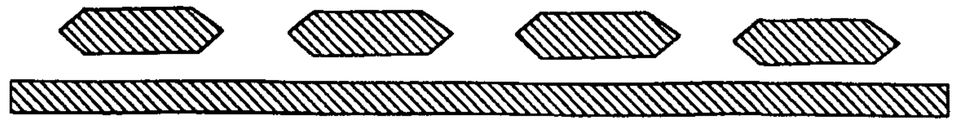

Figure 12.12 Configuration of microstrip Lozenge array.

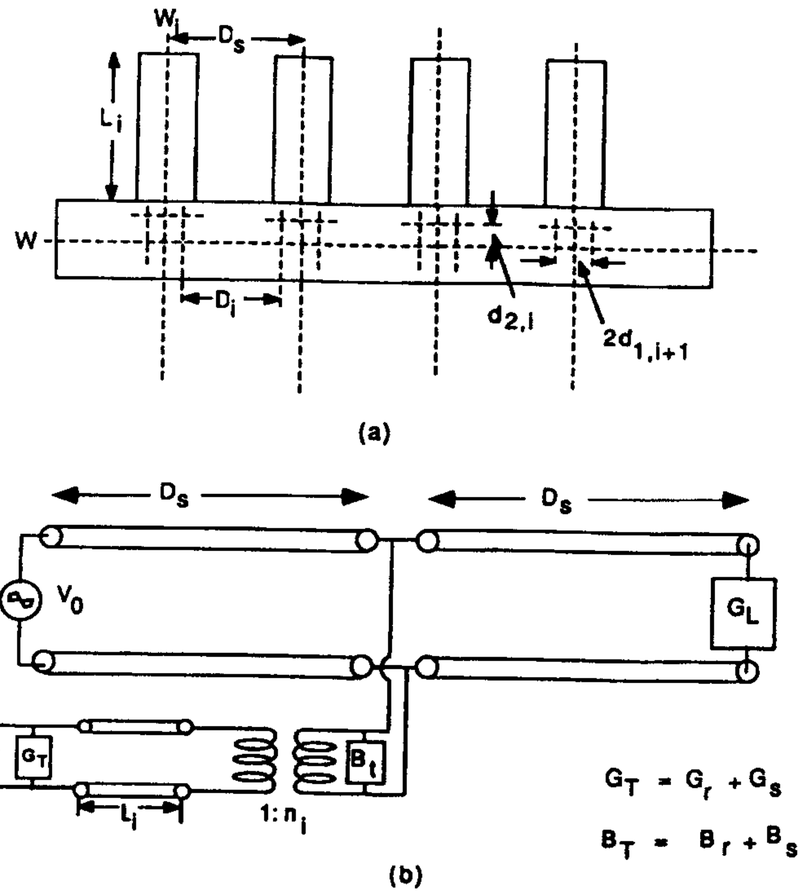

Figure 12.13 (a) Basic configuration of comb-line array and (b) equivalent circuit.

at the open end of the stub. For a nonresonant array, the relative phase between successive fingers is frequency dependent, which results in beam direction variation with frequency. The value of the squint can be calculated from the electrical separation between the elements.

Referring to Figure 12.13(a), there are N open-circuited stub radiators connected to the feeder. Each stub has a width W_i and length L_i. The equivalent circuit of a single stub along with the connecting line lengths is shown in Figure 12.13(b) with the two admittances $G_r + jB_r$ and $G_s + jB_s$ representing the open-circuited stub radiation and the surface wave, and B_t denoting the T-junction susceptance. These equivalent circuit parameters can be determined for given specifications. The ABCD transmission matrix representation in the equivalent circuit includes the line losses and associated phase due to the connecting lines. The transmission matrix of a line of length L, propagation constant γ, and characteristic impedance Z_0 is given by [28, 29]:

$$A(W, L) = \begin{bmatrix} \cosh \gamma L & Z_0 \sinh \gamma L \\ \dfrac{\sinh \gamma L}{Z_0} & \cosh \gamma L \end{bmatrix} \tag{12.12}$$

The steps in the design process are summarized next [10].

Design Steps

1. Select a substrate material having a low loss tangent and low value of relative permittivity. To ensure that the higher order modes are not excited in the strip, the propagation constant k_z can be found for all the higher order modes at the frequency of operation. The propagation constant becomes zero at the cutoff frequencies of all higher order modes. This provides a reasonable check on the excitation of the mode. The propagation constant k_z is given by

$$k_z^2 = k^2 - k_y^2 = (2\pi f)^2 \mu_0 \epsilon_0 \epsilon_r - \left(\frac{m\pi}{W_e}\right)^2, \qquad m = 1, 2, 3, \ldots \tag{12.13}$$

where W_e is the effective width of the microstrip line.

2. The stub spacing can be calculated from the allowable squint specification θ_q from the following equation:

$$D_i = \frac{\lambda_0}{1 + \sin \theta_q} \tag{12.14}$$

3. The aperture distribution can be obtained from the sidelobe and beamwidth specifications. If the sidelobe level is not a major concern, uniform amplitude distribution simplifies the design and gives a sidelobe level around 13.5 dB below the main beam. For a lower sidelobe, an amplitude distribution based on the Taylor line source can be chosen. The conductance at each stub can be calculated from (12.2) and (12.3).
4. *Translation of the required conductance at each stub into a set of physical parameters:* Various factors contribute to the total conductance of a stub, including radiation at the open-circuited end, surface wave, T-junction radiation, and stub mutual coupling. The equivalent circuit

in Figure 12.13(b) has been applied by James and Hall [29] to account for these factors excluding stub mutual coupling. Detailed discussion can also be found in [10]. Note that the susceptance arising at junction B_t could be tuned out by trimming the length of each stub.

5. After determining the width of each stub for the required conductance, the input VSWR can be calculated following the ABCD transmission matrix formulation for the array; that is, transmission matrices of various stubs and line lengths are multiplied together to obtain the overall ABCD matrix. The input impedance is then given by

$$Z_{\text{in}} = \frac{A(1, 1)Z_L + A(1, 2)}{A(2, 1)Z_L + A(2, 2)} \tag{12.15}$$

where Z_L is the load termination.

6. The overall array pattern can be obtained from standard pattern multiplication of the array factor and the element pattern.

Alternative arrangements of comb-line arrays have also been introduced to eliminate some of the problems experienced by the conventional configuration. The transposed array in Figure 12.14(a), where a phase change of 180° occurs between adjacent elements, allows elements to be spaced closer together

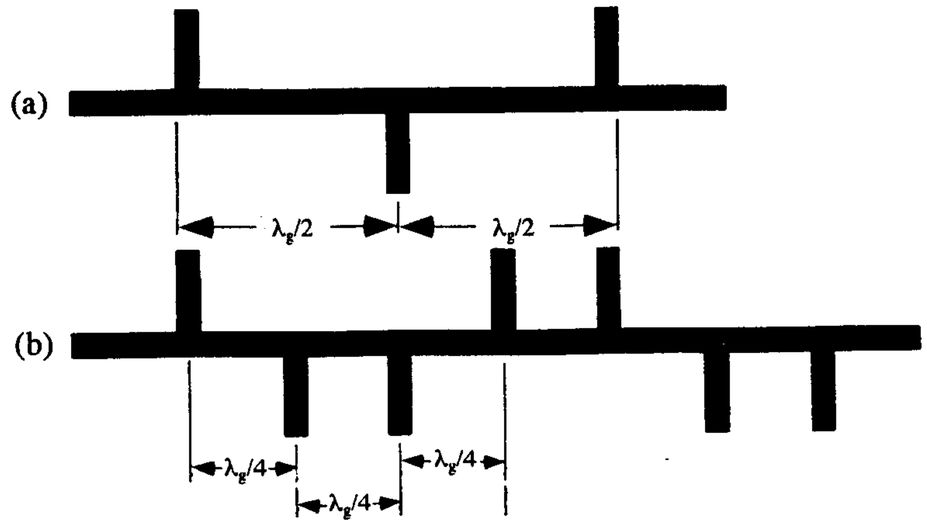

Figure 12.14 Transposed arrangement of microstrip comb-line array: (a) Cophase configuration and (b) quadrature phase configuration. (From [29]. © 1977 IEE. Reprinted with permission.)

at $\lambda_g/2$ to avoid the grating lobe problem. A quadrature phase stub configuration in Figure 12.14(b) was found to function well in removing beam squint and maintaining a good VSWR at the expense of a slight increase in sidelobe level due to aperture phase error of ±45° [29].

12.5 Design of Planar Arrays

Planar array configurations are extensively used in both communication and radar systems where a narrow pencil beam is required. Individual elements can be positioned along a rectangular grid to form a planar array for better control of beam shape and position in space. Planar arrays of printed radiating elements are potentially good candidates for low-cost scanning array applications. They are also very likely to be utilized in active integrated phased arrays.

Planar arrays can be formed by stacking linear array columns with a corporate feed arrangement. The two broad categories of planar arrays are (1) very large arrays where the infinite array solution can be applied and (2) finite arrays where every element is subjected to edge effects. In this section, analysis and design considerations of infinite arrays of patches and printed dipoles are given. Finite arrays are also discussed.

12.5.1 Infinite Arrays of Printed Dipoles

The diagram of an infinite planar array with printed dipoles is shown in Figure 12.15. The element positions are identified with integers m and n in the x and y directions, respectively. The interelement spacings in these directions are denoted by d_x and d_y. Without loss of generality, the printed dipoles are assumed to be center fed and oriented in the x direction. By periodicity, the solution for a dipole in a unit cell is the same for all dipoles in the infinite array.

The unknown current distribution of a dipole in a single unit cell is solved by applying the moment method to the integral equation constructed from the Green's function of an infinite phased array of infinitesimal dipoles on a grounded slab, which is obtainable from Floquet's expansion of the Green's function of a single infinitesimal dipole [30]. This results in the usual matrix equation $[Z][I] = [V]$ where $[I]$, the vector of expansion mode coefficients of the dipole current, can be determined for a given $[V]$. The generalized impedance matrix element Z_{ij} can be expressed as

$$Z_{ij} = \frac{j\eta_0}{k_0 d_x d_y} \sum_{m=-\infty}^{\infty} \sum_{n=-\infty}^{\infty} Q(k_x, k_y) F_i^*(k_x, k_y) F_j(k_x, k_y) \tag{12.16}$$

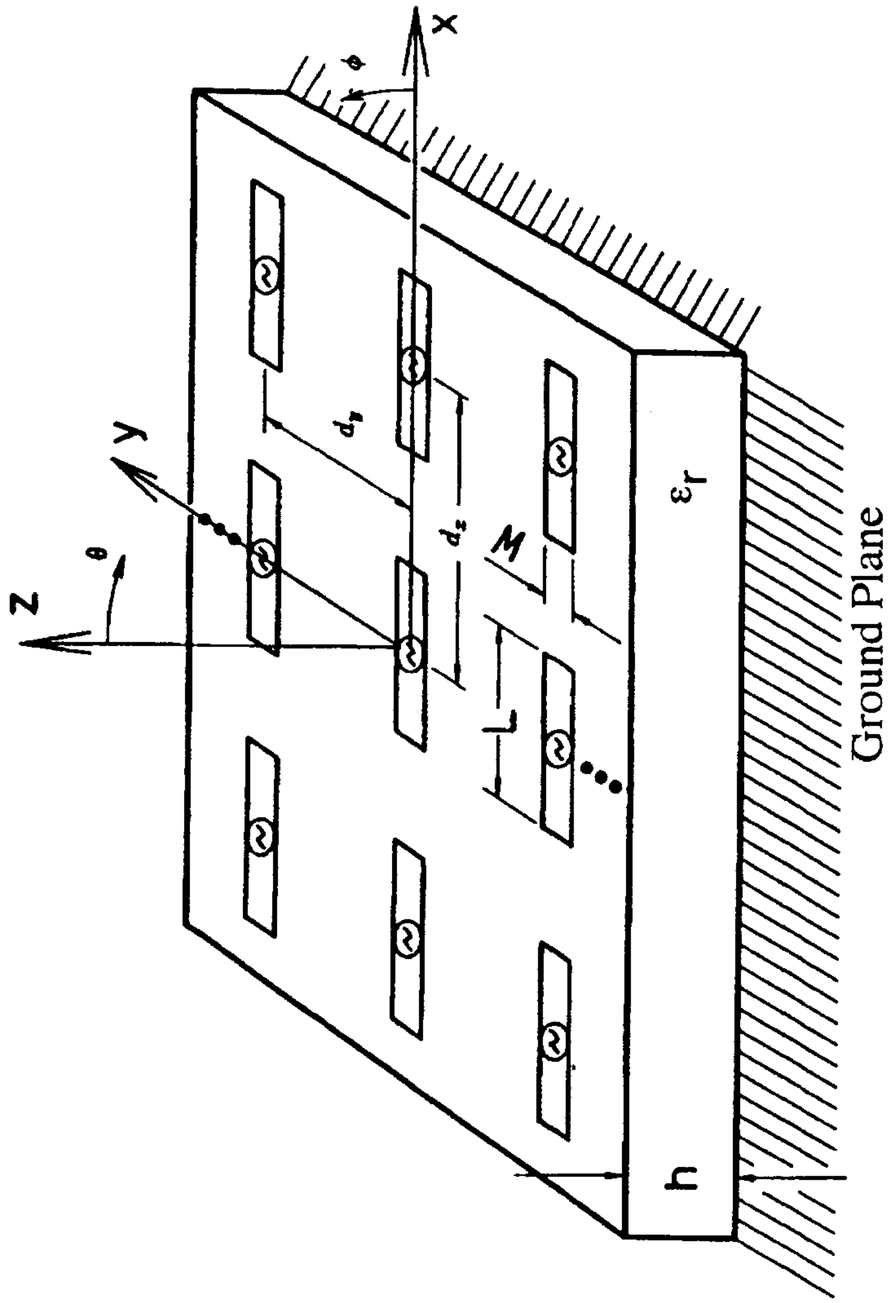

Figure 12.15 Infinite planar array of printed dipoles.

where

$$Q(k_x, k_y) = \frac{(\epsilon_r k_0^2 - k_x^2)k_2 \cos k_1 h + j(k_0^2 - k_x^2)k_1 \sin k_1 h}{T_e T_m} \sin k_1 h \qquad (12.17)$$

$$k_x = \left(\frac{2\pi m}{d_x} + k_0 \sin\theta_0 \cos\phi_0\right), \qquad k_y = \left(\frac{2\pi n}{d_y} + k_0 \sin\theta_0 \sin\phi_0\right)$$

and T_e, T_m, and so on have been derived in Appendix 3A of Chapter 3. The scan angle (θ_0, ϕ_0) is also taken into account in the solution above. The zeros of the T_m and T_e functions represent transverse magnetic (TM) and transverse electric (TE) surface waves, respectively, of the grounded dielectric slab. The value $F_i(k_x, k_y)$ is defined as the Fourier transform of the expansion mode of current J_i for unit cell $m = n = 0$:

$$F_i(k_x, k_y) = \int_{x_i - l_i}^{x_i + l_i} \int_{-W/2}^{W/2} J_i(x_0, y_0)\, e^{-jk_x x_0} e^{-jk_y y_0} dx_0 dy_0$$

$$J_i(x_0, y_0) = \frac{\sin k_e(l_i - |x_0 - x_i|)}{W \sin k_e l_i}; \quad |x_0 - x_i| < l_i, \quad |y_0| < \frac{W}{2} \qquad (12.18)$$

$$k_e = k_0 \sqrt{\frac{(\epsilon_r + 1)}{2}}$$

where l_i and x_i are the half-length and the center of the ith expansion mode, respectively, and W is the width of the dipole. After the unknown coefficients I_i are determined, the input impedance Z_{in} is obtained from the relation

$$Z_{\text{in}} = -\sum_j I_j V_j^e \qquad (12.19)$$

where

$$V_j^e = \frac{-j\eta_0}{d_x d_y k_0} \sum_m \sum_n [Q_{zx}\hat{x} + Q_{zy}\hat{y}] \cdot \overline{F}_j^* e^{jk_x x_p} \qquad (12.20)$$

At the scan angle (θ_0, ϕ_0) where the input impedance $Z_{\text{in}}(\theta_0, \phi_0)$ of the dipole produces a severe mismatch, the array will be unable to radiate a significant portion of the input power, which is consequently trapped in the nonradiating surface wave. The angle (θ_0, ϕ_0) is referred to as scan blindness

of the array. At the scan blindness, the active reflection coefficient $|R(\theta_0, \phi_0)|$ is very close to unity where $R(\theta_0, \phi_0)$ is defined as [7, 31–33]

$$R(\theta_0, \phi_0) = \frac{Z_{\text{in}}(\theta_0, \phi_0) - Z_{\text{in}}(0, 0)}{Z_{\text{in}}(\theta_0, \phi_0) + Z_{\text{in}}^*(0, 0)} \tag{12.21}$$

$Z_{\text{in}}(0, 0)$ is the input impedance when the beam is at broadside and the array is assumed matched for maximum array gain. It is found that the blindness angles can be estimated from the propagation constants of surface waves as determined from the zeros of T_e and T_m [30]. Generally, scan blindness will occur if the following conditions are satisfied:

1. A Floquet mode propagation constant β equals a surface wave propagation constant β_{sw}. This condition may be satisfied in the visible space for certain element spacings.
2. The TM (TE) surface wave pole is not canceled by a zero value for k_x (k_y). If cancellation occurs, this means that a particular TM or TE surface wave cannot be excited due to the array polarization mismatch.

Condition 1 can be expressed as

$$\left(\frac{\beta_{\text{sw}}}{k_0}\right)^2 = \left(\frac{k_x}{k_0}\right)^2 + \left(\frac{k_y}{k_0}\right)^2 \tag{12.22}$$

$$= \left(\frac{m}{d_x/\lambda_0} + \sin\theta_0 \cos\phi_0\right)^2 + \left(\frac{n}{d_y/\lambda_0} + \sin\theta_0 \sin\phi_0\right)^2$$

The reflection coefficient in (12.21) has also been used in determining the active element pattern $f(\theta,\phi)$ of a two-dimensional infinite array which is defined as [7, 32]:

$$f(\theta, \phi) = (1 - |R(\theta, \phi)|^2) \cos\theta \tag{12.23}$$

Design Considerations

The main considerations in the design of planar arrays are as follows:

1. Selection of the interelement spacings to avoid the grating lobes in the visible region;
2. Selection of the substrate thickness, dielectric constant, and interelement spacings to eliminate scan blindness from the required scan volume.

Studies on several infinite dipole arrays are available in [30]. Some of the results are given here as an illustrative example of scan blindness occurrence.

A dipole array is designed with grid spacings $d_x = d_y = 0.5\lambda_0$, dipole length $L = 0.39\lambda_0$, dipole width $W = 0.002\lambda_0$, on a substrate with thickness $h = 0.19\lambda_0$, and permittivity $\epsilon_r = 2.55$. The propagation constants of the first three surface wave modes as a function of the substrate thickness h/λ_0 are plotted in Figure 12.16. At $h = 0.19\lambda_0$, the substrate is seen to support only TM_0 surface wave with $\beta_{\text{sw}}/k_0 = 1.283$. From (12.22), two possible solutions in the principal planes are:

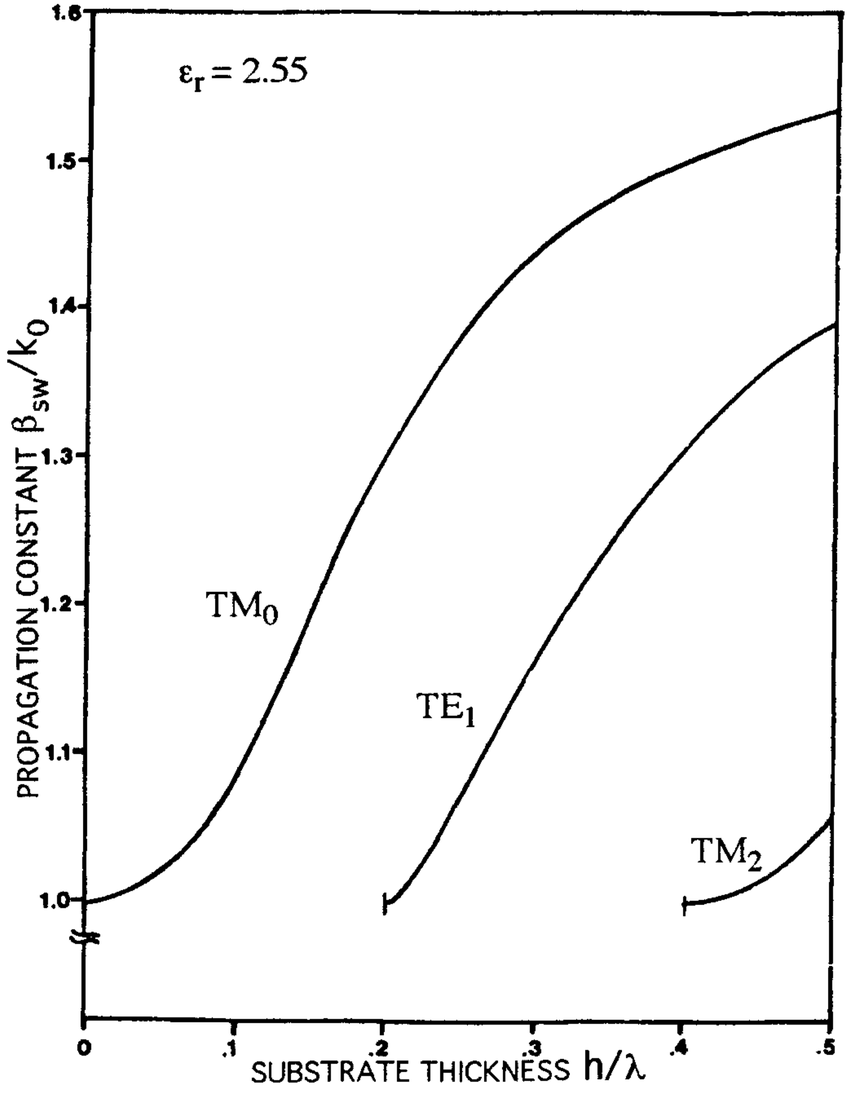

Figure 12.16 Normalized surface wave propagation constants for a ground substrate versus normalized substrate thickness. (From [30]. © 1984 IEEE. Reprinted with permission.)

1. $m = -1$, $n = 0$, $\sin\theta_0 = 0.717$ in the E plane $\phi_0 = 0°$
2. $m = 0$, $n = -1$, $\sin\theta_0 = 0.717$ in the H plane $\phi_0 = 90°$

Solution 1 in the E plane results in $k_x = (-2\pi/d_x + 0.717)$, which differs from zero. Hence, the second condition is satisfied. Scan blindness is possible at $\theta_0 = 45.8°$. However, solution 2 in the H plane makes $k_x = 0$, which exactly cancels the TM surface wave. Hence, the second condition is not satisfied and scan blindness does not occur in the H plane. In Figure 12.17, $|R(\theta_0, \phi_0)|$ versus scan angle θ_0 confirms the occurrence of scan blindness. The D plane in Figure 12.17 denotes a diagonal scan ($\phi = 45°$).

12.5.2 Infinite Arrays of Rectangular Microstrip Patches

The geometry of an infinite array of probe-fed rectangular microstrip patches is shown in Figure 12.18. This element is one of the most widely used, particularly in integrated phased arrays. The approach in general is very similar to that of an infinite dipole array; however, the Green's function is more complicated due to the current distribution that exists along the length and width of the patch. By applying the moment method, the unknown expansion coefficients I_j for current distribution on a patch can be determined from the following set of linear equations [32]:

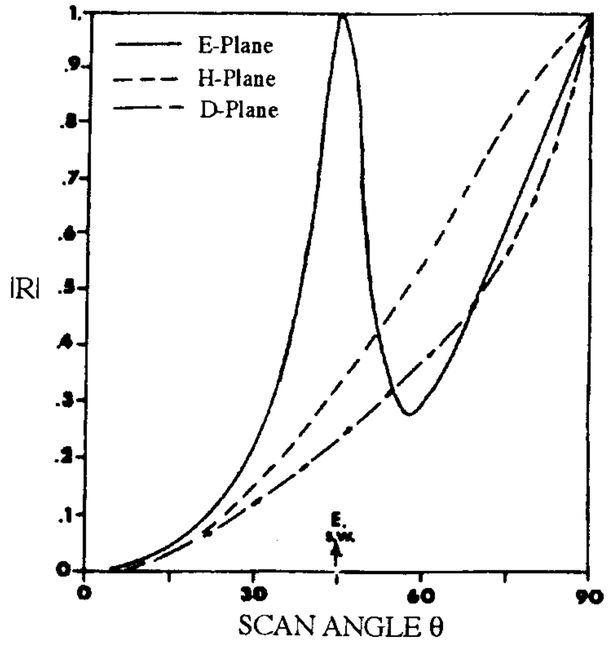

Figure 12.17 Magnitude of reflection coefficient versus scan angle for infinite printed dipole array with $d_x = d_y = 0.5\lambda$, $L = 0.39\lambda$, $W = 0.002\lambda$, $h = 0.19\lambda$, $\epsilon_r = 2.55$, and $Z_{in}(0,0) = 75\Omega$. (From [30]. © 1984. Reprinted with permission.)

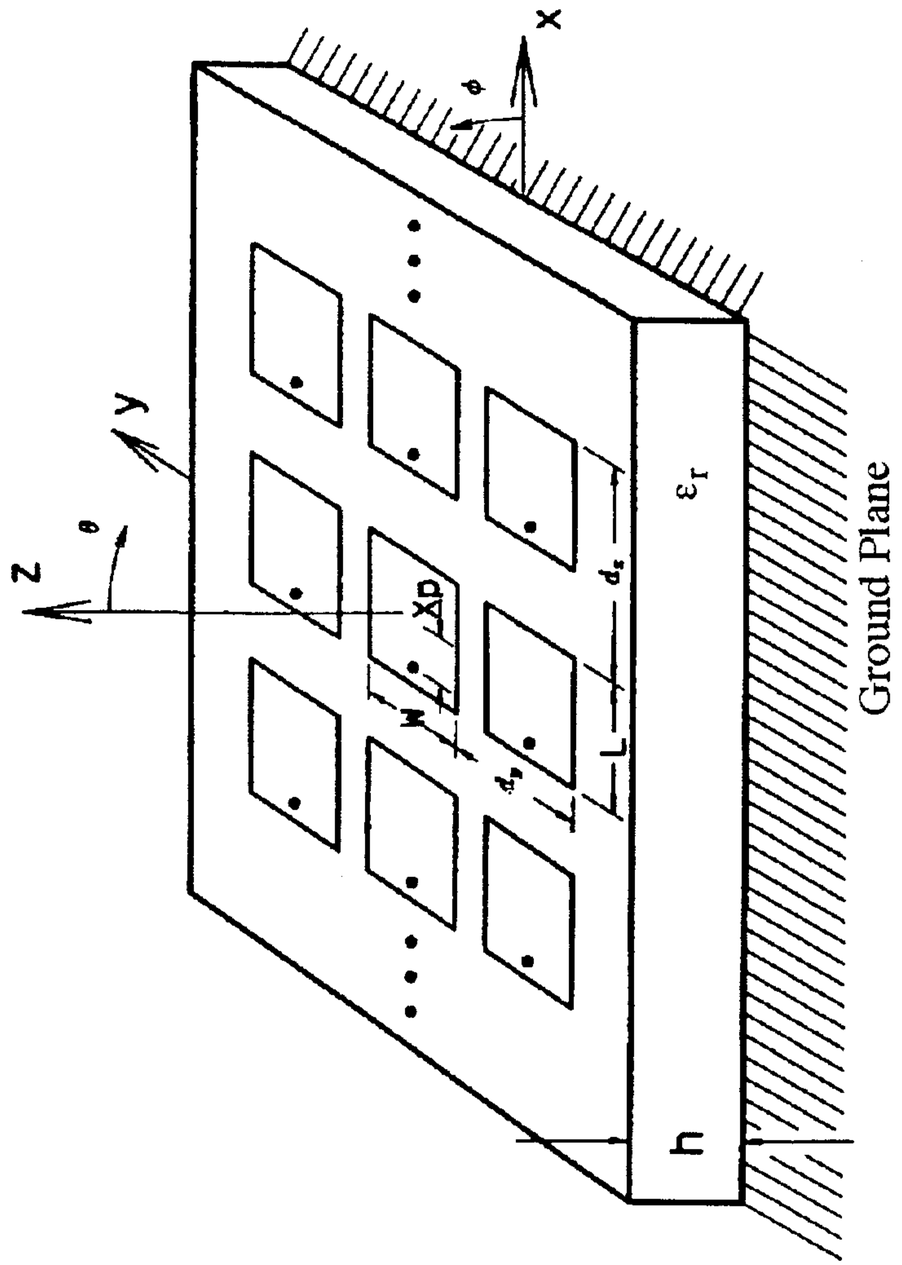

Figure 12.18 Infinite planar array of microstrip patches.

$$\sum_j Z_{ij} I_j = V_i \qquad \text{for all } i \tag{12.24}$$

where for a probe of unit current at $(x_p, 0)$, it is found that

$$Z_{ij} = \frac{j\eta_0}{d_x d_y k_0} \sum_m \sum_n \bar{F}_i \cdot \overline{\overline{Q}} \cdot \bar{F}_j^*$$

$$V_i = \frac{-j\eta_0}{d_x d_y k_0} \sum_m \sum_n \bar{F}_i \cdot [\hat{x} Q_{xz} + \hat{y} Q_{yz}] e^{-jk_x x_p} \tag{12.25}$$

$$\bar{F}_i(k_x, k_y) = \iint_S \bar{J}_i(x, y) e^{jk_x x} e^{jk_y y} dx\, dy$$

The integration is performed over the patch surface S and $\bar{J}_i(x, y)$ is an expansion mode representing surface current distribution in either the $\hat{x}$ or the $\hat{y}$ direction. Entire domain basis functions can be used for the $\hat{x}$-directed and the $\hat{y}$-directed current modes as given by

$$\bar{J}_i(x, y) = \hat{x} \sin\frac{k\pi}{L}\left(x + \frac{L}{2}\right) \cos\frac{l\pi}{W}\left(y + \frac{W}{2}\right) \tag{12.26}$$

$$\bar{J}_i(x, y) = \hat{y} \cos\frac{k\pi}{L}\left(x + \frac{L}{2}\right) \sin\frac{l\pi}{W}\left(y + \frac{W}{2}\right)$$

where k, l are integer indices accounting for the number of variations in the x, y directions, respectively. The dyad $\overline{\overline{Q}}$ in (12.25) is defined as

$$\overline{\overline{Q}} = \hat{x} Q_{xx} \hat{x} + \hat{x} Q_{xy} \hat{y} + \hat{y} Q_{yx} \hat{x} + \hat{y} Q_{yy} \hat{y}$$

$$Q_{xx} = \frac{(\epsilon_r k_0^2 - k_x^2) k_2 \cos k_1 h + j k_1 (k_0^2 - k_x^2) \sin k_1 h}{T_e T_m} \sin k_1 h$$

$$Q_{yy} = \frac{(\epsilon_r k_0^2 - k_y^2) k_2 \cos k_1 h + j k_1 (k_0^2 - k_y^2) \sin k_1 h}{T_e T_m} \sin k_1 h$$

$$Q_{xy} = Q_{yx} = \frac{-k_x k_y [k_2 \cos k_1 h + j k_1 \sin k_1 h] \sin k_1 h}{T_e T_m}$$

$$Q_{xz} = Q_{zx} = \frac{-j k_x k_2 \sin k_1 l_p}{k_1 T_m}$$

$$Q_{yz} = Q_{zy} = \frac{-j k_y k_2 \sin k_1 l_p}{k_1 T_m} \tag{12.27}$$

where l_p is the probe length, and T_e, T_m, and so on have been defined in Appendix 3A of Chapter 3.

In (12.24), k_x and k_y represent the spatial harmonic propagation constants, which take the discrete values of

$$k_x = \left(\frac{2\pi m}{d_x} + k_0 \sin\theta_0 \cos\phi_0\right) \tag{12.28}$$

$$k_y = \left(\frac{2\pi n}{d_y} + k_0 \sin\theta_0 \sin\phi_0\right)$$

where (θ_0, ϕ_0) represents a scan angle.

The scan reflection coefficient of the array $R(\theta, \phi)$ can then be calculated from (12.21). The array blindness occurs at the locations where $|R(\theta, \phi)|$ is very close to unity. Alternatively, the scan blindness can be approximately determined from the condition when a Floquet mode propagation constant β equals the surface wave propagation constant β_{sw} of the unloaded dielectric substrate similar to the case of printed dipole arrays [32]. It is interesting to note that there is no blind spot for an H-plane scan for arrays of printed dipoles aligned along the x axis. However, due to the two-dimensional nature of surface current distribution for the case of microstrip patch arrays, the TM surface wave mode can still be resonated for the H-plane scan, which results in a blind spot. The rest of the design considerations are still similar to those for infinite arrays of printed dipoles.

Studies on several infinite rectangular microstrip patch arrays are available in [32]. Some of the results are given here as an illustrative example of scan blindness occurrence.

A microstrip patch array is designed with grid spacings $d_x = 0.51\lambda_0$, $d_y = 0.5\lambda_0$, patch length $L = 0.28\lambda_0$, and width $W = 0.3\lambda_0$, on a substrate with thickness $h = 0.06\lambda_0$ and permittivity $\epsilon_r = 2.55$. Referring to Figure 12.16, the substrate is seen to support only a TM_0 surface wave with $\beta_{sw}/k_0 = 1.028$ at $h = 0.06\lambda_0$. From (12.22), two solutions obtained in the two principal planes are:

1. $m = -1$, $n = 0$, $\theta_0 = \sin^{-1} = 0.9328 = 68.9°$ in the E plane $\phi_0 = 0°$
2. $m = 0$, $n = -1$, $\theta_0 = \sin^{-1} = 0.972 = 76.4°$ in the H plane $\phi_0 = 90°$

In Figure 12.19, $|R(\theta_0, \phi_0)|$ versus scan angle θ_0 confirms the occurrence of scan blindness.

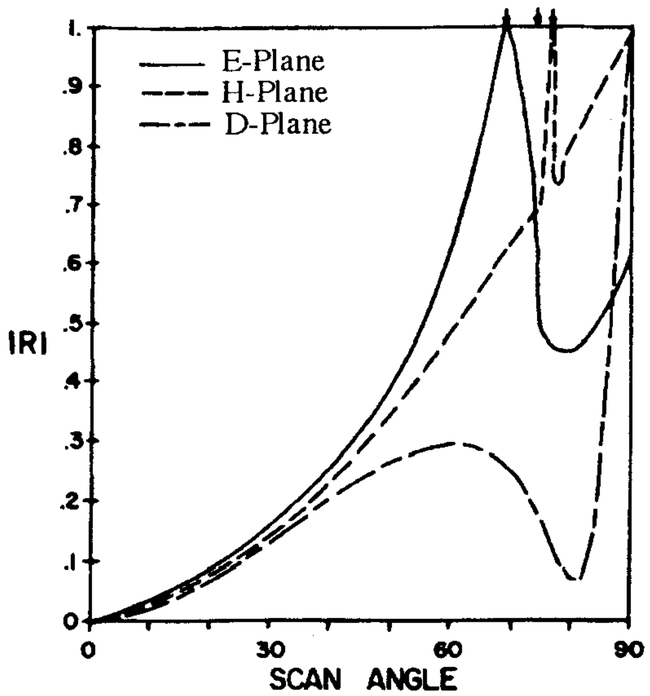

Figure 12.19 Magnitude of reflection coefficient versus scan angle for infinite microstrip array with $d_x = 0.51\lambda$, $d_y = 0.5\lambda$, $L = 0.28\lambda$, $W = 0.3\lambda$, $h = 0.06\lambda$, $\epsilon_r = 2.55$, $x_p = 0.14\lambda$, and $Z_{in}(0,0) = 86\Omega$. (From [32]. © 1984 IEEE. Reprinted with permission.)

12.5.3 Finite Planar Arrays of Printed Dipoles

It is known that isolated printed antenna elements can convert a significant amount of the input power into surface waves. However, for infinite arrays, surface waves cannot exist except at the blindness angles where all the input power is converted to surface waves, resulting in no radiation from the array. Logically, this leads to an interesting question about the role of surface waves on a finite size array. To answer this question, a finite size array is analyzed element-by-element using the moment method in the spectral domain [33].

The geometry of a finite array of printed dipoles is shown in Figure 12.20. The dipoles are assumed to be narrow, and hence there are only the x-directed currents. The Green's functions and other related equations are identical to those discussed in the previous section. By applying the Galerkin moment method to an electric field integral equation formed by enforcing the boundary condition of vanishing total tangential electric field on the dipole surfaces, the resulting matrix equation is obtained [33]:

$$\{[Z] + [Z_T]\}[I] = [V] \tag{12.29}$$

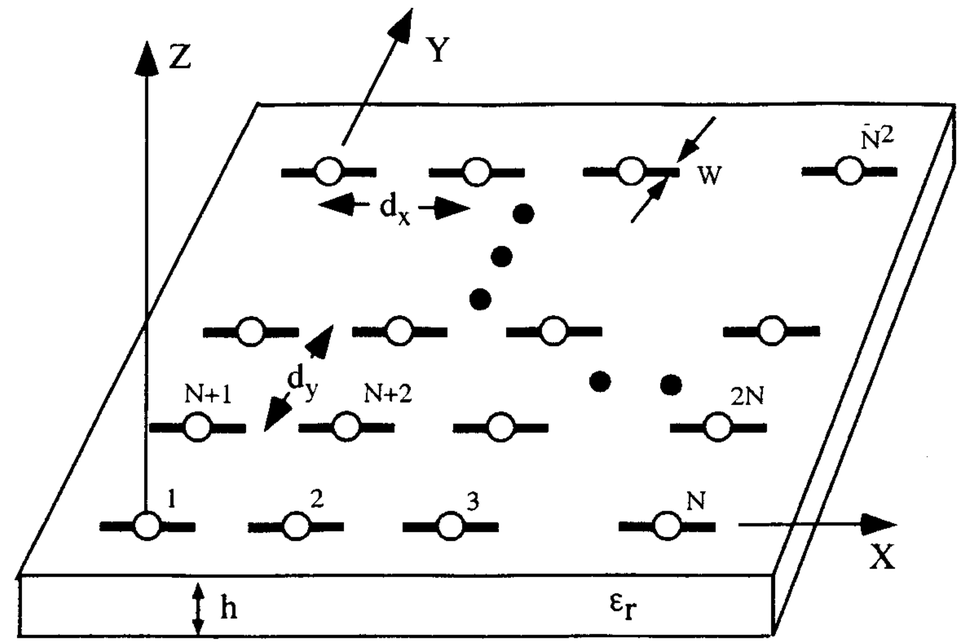

Figure 12.20 Configuration of $N \times N$ planar array of printed dipoles on a grounded substrate. (From [33]. © 1985 IEEE. Reprinted with permission.)

where $[I]$ is the unknown vector of expansion mode coefficients of the electric surface current density on the dipoles, $[V]$ is the voltage excitation vector, and $[Z_T]$ is a diagonal matrix representing the generator terminating impedances, which depend on the type of excitations. In the forced excitation, constant driving voltages are applied to elements regardless of scan angles. This type of excitation corresponds to $[Z_T] = [0]$. In the case of free excitation, the constant available power type of feed, $[Z_T] \neq [0]$. Here $[Z]$ is the impedance matrix of the array with Z_{mn} elements given by

$$Z_{mn} = \frac{j\eta_0}{4\pi^2 k_0} \int_{-\infty}^{\infty} \int_{-\infty}^{\infty} Q(k_x, k_y) F_m(k_x, k_y) F_n^*(k_x, k_y)\, dk_x dk_y \tag{12.30}$$

where $F_n(k_x, k_y)$ is the Fourier transform of the expansion mode on dipole n. $F_n(k_x, k_y)$ and $J_n(x, y)$ are defined in (12.18), whereas $Q(k_x, k_y)$ and other related equations are given in (12.17). Since (12.29) is formulated for the whole array, the order of the linear system of equations is $N \times N \times M$ for an $N \times N$ array with M expansion modes on each dipole. For a printed dipole array, a single expansion mode is found to be a very good approximation [33].

The voltage vector elements in $[V]$ for one expansion mode per dipole can be written as

$$V_n = \exp[jk_0(x_n \sin\theta_0 \cos\phi_0 + y_n \sin\theta_0 \sin\phi_0)] \tag{12.31}$$

where (x_n, y_n) is the location of the center of the nth dipole, and (θ_0, ϕ_0) represents a beam scanning direction. The active reflection coefficient $R^n(\theta, \phi)$ at the nth dipole can be calculated from (12.21) using the input impedance, which is given by

$$Z_{\text{in}}^n(\theta, \phi) = \frac{V_n}{I_n} \tag{12.32}$$

The $R^n(\theta, \phi)$ term is defined such that the array is conjugate matched to the broadside scan impedance [7, 34]. As an illustrative example, Figure 12.21 compares the active reflection coefficient $R^n(\theta, \phi)$ for the center element

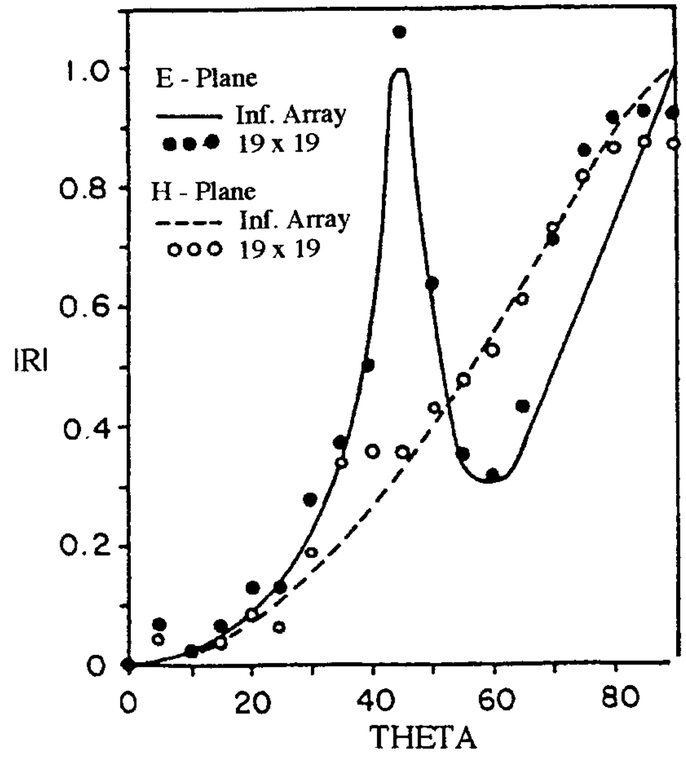

Figure 12.21 Magnitude of reflection coefficient versus scan angle for the center element of 19×19 array and infinite array with $d_x = d_y = 0.5\lambda$, $L = 0.39\lambda$, $W = 0.01\lambda$, $h = 0.19\lambda$, and $\epsilon_r = 2.55$. (From [33]. © 1985 IEEE. Reprinted with permission.)

of a 19×19 dipole array with $|R(\theta, \phi)|$ of an infinite array of similar dipoles on a substrate with $\epsilon_r = 2.55$ and thickness $h = 0.19\lambda_0$. The infinite array shows a scan blindness at $\theta = 45.8°$ in the E plane because $|R| = 1$. However, at the same scan angle, $|R^n|$ for the center element of the finite array is greater than unity, which indicates that this dipole is delivering power to its generator. This power is being transferred from other dipoles in the array. This is possible since the input impedance varies across the finite array as observed from the results in Figure 12.22, which demonstrates the variation of $|R^n|$ with the element position, particularly near a scan blindness at $\theta = 45.8°$.

The example suggests strong effects of surface waves and mutual coupling in the array. Because the surface wave power does not radiate in the desired direction, it represents power lost in the array. Hence, the array performance can be described in terms of radiation efficiency η which is defined as [33]

$$\eta = 1 - \frac{P_{\text{sw}}}{P_{\text{in}}} \tag{12.33}$$

where P_{in}, the total input power to the array, and P_{sw}, the surface wave power, can be calculated from (3.24) and (3.25).

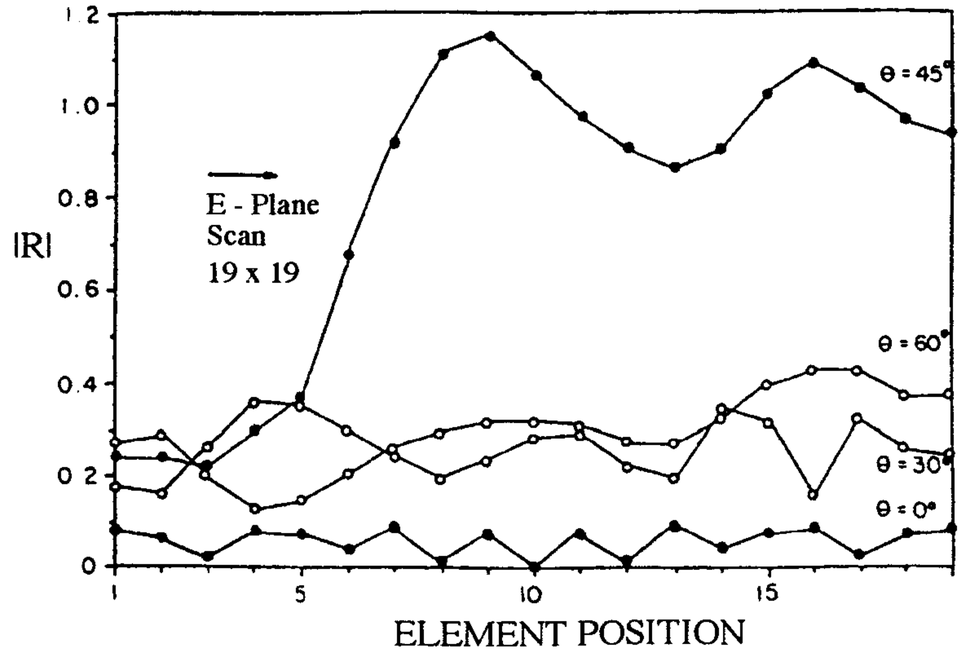

Figure 12.22 Magnitude of reflection coefficient versus element position across the E plane for 19×19 array with $d_x = d_y = 0.5\lambda$, $L = 0.39\lambda$, $W = 0.01\lambda$, $h = 0.19\lambda$, and $\epsilon_r = 2.55$. (From [33]. © 1985 IEEE. Reprinted with permission.)

Figure 12.23 shows efficiency plots versus E-plane scan angle for various array sizes of dipoles similar to those described in Figure 12.21. Efficiency increases with the array size at all scan angles except those near 45.8° where the efficiency rapidly decreases with the increasing array size. For the infinite array, the efficiency becomes zero at the 45.8° angle, which is the blindness angle. A similar trend can also be observed from studies on several other arrays available in [33].

It can be generally concluded that the ability of the array to radiate is adversely degraded near the scan blindness angle even for relatively small arrays. It is probably prudent in array design to limit the maximum scan angle to about 10° less than the scan blindness angle.

12.6 Monolithic Integrated Phased Arrays

Even though phased array antennas possess many desirable features such as pattern control, electronically scanned beam, and low profile, cost has been a major drawback and limits their use in many applications. The cost of a large

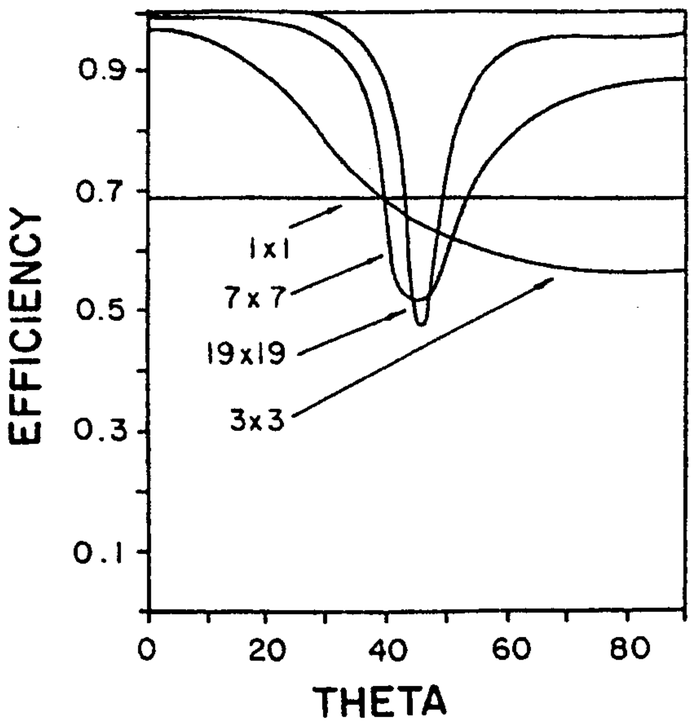

Figure 12.23 Efficiency versus E-plane scan angle for various dipole array sizes. (From [33]. © 1985 IEEE. Reprinted with permission.)

phased array is directly related to the number of elements, which is typically of the order of 1,000 to 10,000 or even more. Hence, special methodologies are needed for fabricating, assembling, and mounting array elements for cost reduction.

The concept of a monolithic array is very promising for achieving the goal of lowering per-element costs through the process to allow for the fabrication and assembly of elements, active and passive devices, and controller circuits all in the same step. Devices can be integrated close to radiating elements, thus minimizing circuit losses, which can be prohibitive for very large arrays. Integration of active devices such as amplifiers close to radiating elements can further enhance the array efficiency. Monolithic arrays have the potential to be more reliable and repeatable since the array is not produced element by element. Figure 12.24 demonstrates basic subsystems and essential technologies required for the production of integrated phased arrays. Microstrip antennas are very attractive candidate radiating elements since they are compatible with monolithic integrated circuit technology. General design considerations for integrated phased array are given in the following section.

12.6.1 Design Considerations

General design considerations for integrated phased arrays can be summarized as follows:

1. The first consideration involves substrate selection. A high-permittivity substrate such as GaAs is a preferred choice for active devices; however, a radiating element performs better in terms of radiation efficiency and bandwidth on a low ϵ_r substrate. One of the design options is to use two layers of substrate where the lower ϵ_r is for radiating elements and the higher ϵ_r for active device mounting and feed circuits.
2. Considerations of scan blindness will determine the choice of substrate permittivity and thickness and possibly element spacing, which should be selected in such a way that the resulting blind angle is outside the specified maximum scan angle. Figure 12.25 illustrates scan blindness versus substrate permittivity for various element spacings and substrate thickness [35].
3. Array feed network selection has to be considered with regard to spurious feed radiation, complexity, and availability of substrate real estate. Spurious radiation can adversely interfere with the main array radiation, resulting in sidelobe and cross-polarization level degradation. The radiation should be kept to a minimum by using an efficient feed system or by isolating the feed network from the radiating elements.

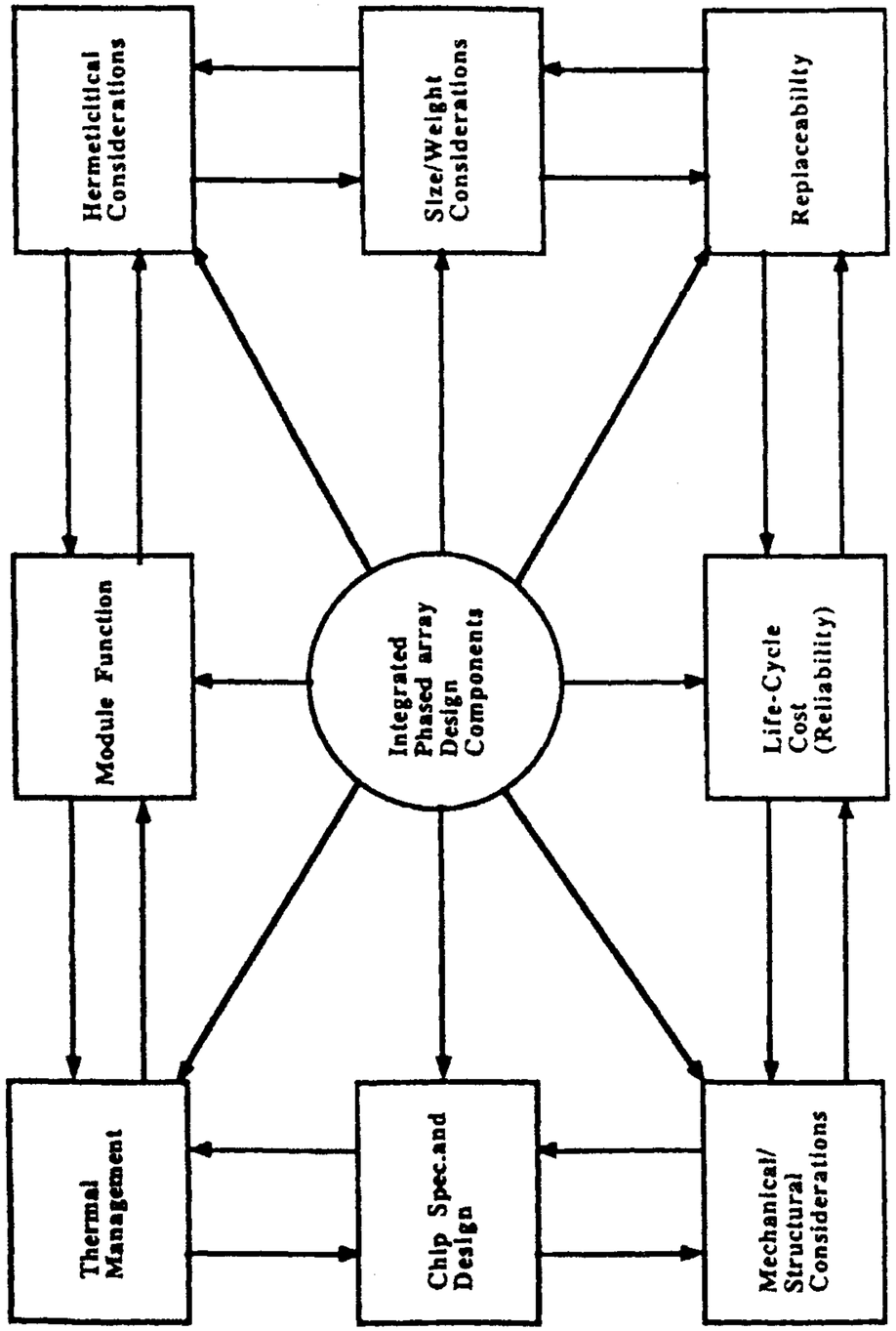

Figure 12.24 Basic subsystem and technology requirements for integrated phased array.

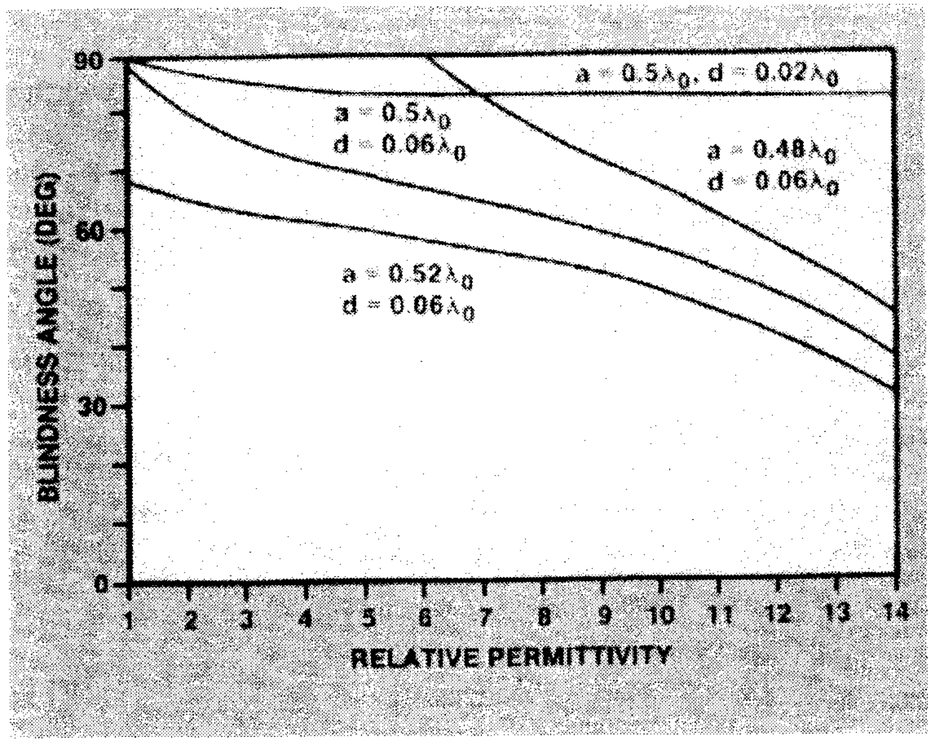

Figure 12.25 Scan blindness angle versus relative permittivity for infinite printed dipole array with various element spacings and substrate thickness. (From [35]. © 1985 *Microwave Journal*. Reprinted with permission.)

4. Thermal management must be included in the array design consideration. Heat dissipation requirements can put a severe constraint on the possible choice of array configurations since cooling systems must share limited available space with other components.
5. A large array will involve a number of array components. For reliability and repeatability, array architectures should be considered that would allow as much of the fabrication and assembly processes to be automated as possible.

12.6.2 Array Architectures

In general, array architectures can be classified into brick and tile configurations as shown in Figure 12.26 [36]. The brick concept uses array depth to accommodate feed circuit modules, which are orthogonally arranged to the plane of radiating aperture. Each module contains various components, which may include power dividers, amplifiers, phase shifters, control circuits, and cooling systems. Elements such as horizontal dipoles and end-fire tapered slot antennas are suitable with the brick concept. The brick is also compatible with monolithic

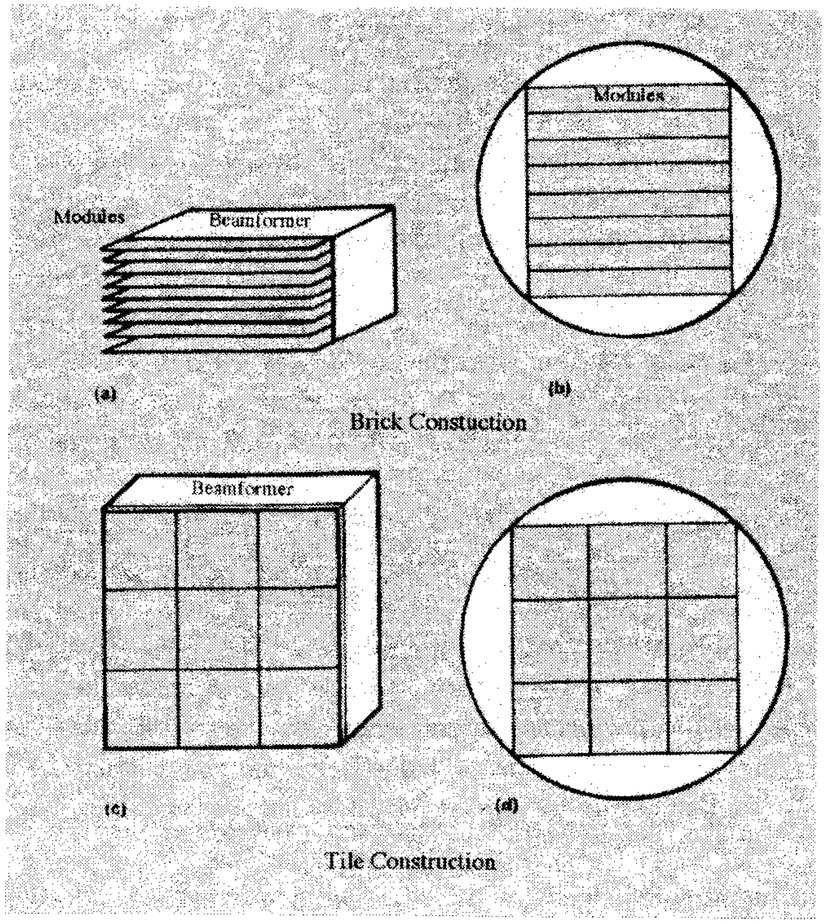

Figure 12.26 Brick and tile concepts of monolithic array: (a, c) Aperture and (b, d) GaAs wafer. (From [36]. © 1987 *Microwave Journal.* Reprinted with permission.)

integrated circuit technology for low-cost fabrication. A dipole array with a brick configuration is shown in Figure 12.27(a) [7].

In the tile concept, radiating elements are located in the same plane as feed circuits. However, multilayer configurations, in which radiating elements, RF power division, and control circuits are on separate layers, are more likely to be utilized due to real estate problems in accommodating feed networks. Multilayer arrangements may pose problems such as board alignment, good vertical coupling between boards, thermal expansion, and heat removal. Suitable radiating elements include microstrip patches, printed dipoles, and slot antennas.

Monolithic integrated circuit technology is also compatible with the tile arrangement for low-cost fabrication. Examples of microstrip arrays with tile construction are shown in Figures 12.27(b) and (c) for multilayer and a single-layer configurations, respectively [7, 35]. Other examples of the tile construction

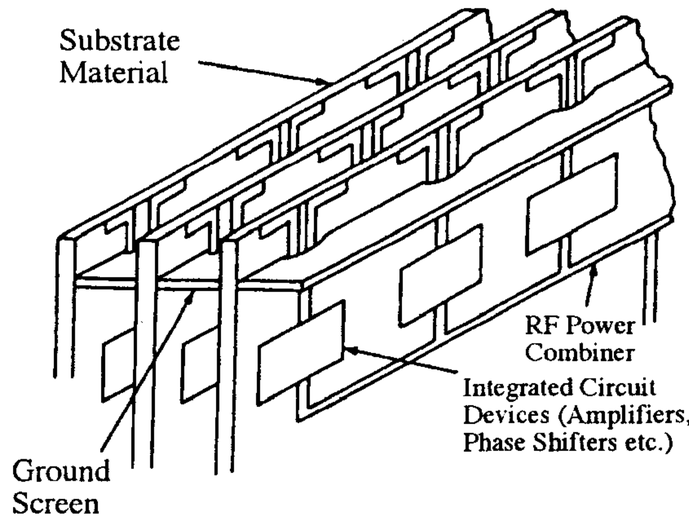

(a)

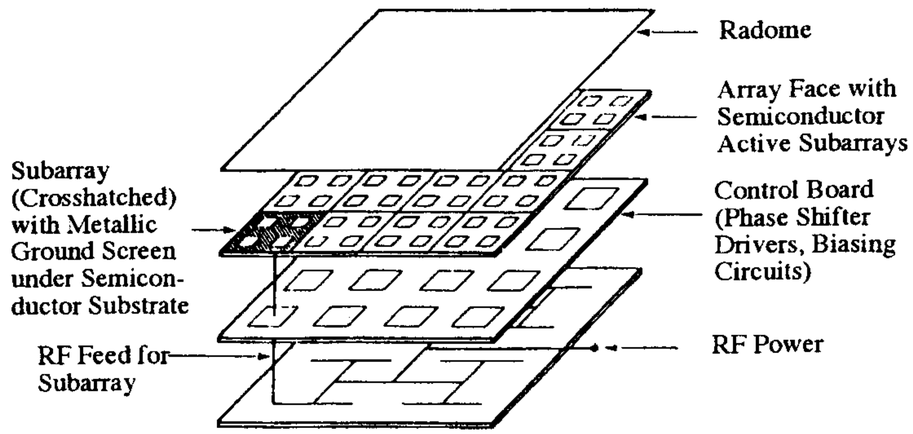

(b)

Figure 12.27 Basic monolithic array configurations: (a) Dipole array with brick architecture. (From [7]. © 1994 Artech House. Reprinted with permission.) (b) Multilayer microstrip array with tile architecture. (From [7]. © 1994 Artech House. Reprinted with permission.) (c) Single-layer microstrip array with tile architecture. (From [35]. © 1986 *Microwave Journal.* Reprinted with permission.)

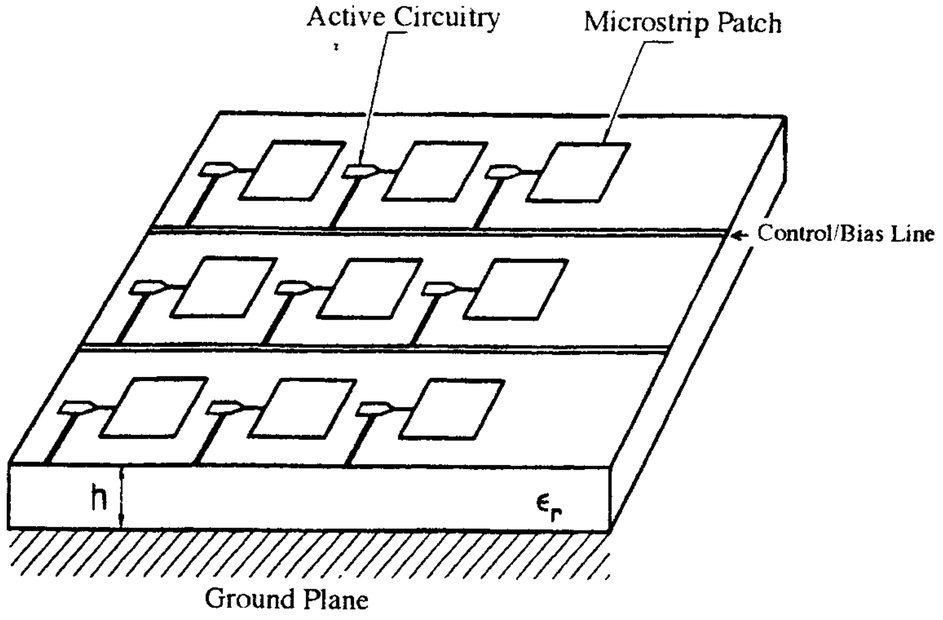

(c)

Figure 12.27 (continued).

can also be found in [37], which describes the development of monolithic phased arrays for EHF satellite terminals.

References

[1] Collin, R. E., and F. J. Zucker, *Antenna Theory—Part 1*, McGraw-Hill, New York, 1969.

[2] Hansen, R. C. (Ed.), *Microwave Scanning Antennas*, Vols. I–III, Academic Press, New York, 1966.

[3] Amitay, N., V. Galindo, and C. P. Wu, *Theory and Analysis of Phased Array Antennas*, Wiley-Interscience, New York, 1972.

[4] Oliner, A. A., and G. H. Knittel, *Phased-Array Antennas*, Artech House, Dedham, MA, 1972.

[5] Ma, M. T., *Theory and Applications of Antenna Arrays*, Wiley-Interscience, New York, 1974.

[6] Brookner, E. (Ed.), *Practical Phased-Array Antenna Systems*, Lex Book, Lexington, MA, 1997.

[7] Mailloux, R. J., *Phased-Array Antenna Handbook*, Artech House, Norwood, MA, 1994.

[8] Hansen, R. C., *Phased Array Antennas*, Wiley-Interscience, New York, 1998.

[9] Weiss, M. A., "Microstrip Antennas for Millimeter Waves," *IEEE Trans. Antennas and Propagation*, Vol. AP-29, 1981, pp. 171–174.

[10] Bhartia, P., K. V. S. Rao, and R. S. Tomar, *Millimeter-Wave Microstrip and Printed Circuit Antennas*, Artech House, Norwood, MA, 1991.

[11] Skidmore, D. J., and G. Morris, "The Design and Performance of Covered Microstrip Serpent Antennas," *IEEE Int. Conf. on Antennas and Propagation*, London, UK, 1983, pp. 454–458.

[12] Owens, R. P., "Microstrip Antenna Feeds," in *Handbook of Microstrip Antennas*, Vol. 2, J. R. James and P. S. Hall (Eds.), Peter Peregrinus, London, UK, 1989.

[13] Hansen, R. C., "Linear Arrays," in *The Handbook of Antenna Design*, Vol. 2, A. W. Rudge et al. (Eds.), Peter Peregrinus, London, UK, 1983.

[14] Kummer, W. H., "Feeding and Phase Scanning," in *Microwave Scanning Antennas*, Vol. III, R. C. Hansen (Ed.), Academic Press, New York, 1966.

[15] Penard, E., and C. Terret, "Design and Technology of Low-Cost Printed Antennas," in *Handbook of Microstrip Antennas*, Vol. 1, J. R. James and P. S. Hall (Eds.), Peter Peregrinus, London, UK, 1989.

[16] Metzler, T., "Microstrip Series Arrays," *IEEE Trans. Antennas and Propagation*, Vol. AP-29, 1981, pp. 174–178.

[17] Metzler, T., "Microstrip Series Arrays," *Proc. Workshop on Printed Circuit Antenna Technology*, Las Cruces, NM, Oct. 1979, pp. 20-1–20-16.

[18] Zucker, F. J., "Surface- and Leaky-Wave Antennas," in *Antenna Engineering Handbook*, H. Jasik (Ed.), McGraw-Hill, New York, 1961.

[19] Pozar, D. M., "Input Impedance and Mutual Coupling of Rectangular Microstrip Antennas," *IEEE Trans. Antennas and Propagation*, Vol. AP-30, 1982, pp. 1191–1196.

[20] Van de Capelle, A., "Transmission-Line Model for Rectangular Microstrip Antennas," in *Handbook of Microstrip Antennas*, Vol. 1, J. R. James and P. S. Hall (Eds.), Peter Peregrinus, London, UK, 1989.

[21] Katehi, P. B., D. R. Jackson, and N. G. Alexopoulis, "Microstrip Dipoles," in *Handbook of Microstrip Antennas*, Vol. 1, J. R. James and P. S. Hall (Eds.), Peter Peregrinus, London, UK, 1989.

[22] Hall, P. S., and C. M. Hall, "Coplanar Corporate Feed Effects in Microstrip Patch Array Design," *IEE Proc.*, Vol. 135, Pt. H, 1988, pp. 180–186.

[23] Ashkenazy, J., P. Perlmutter, and D. Treves, "A Modular Approach for Design of Microstrip Array Antennas," *IEEE Trans. Antennas and Propagation*, Vol. AP-31, 1983, pp. 190–193.

[24] Lalezari, F., and C. D. Massey, "MM-Wave Microstrip Antennas," *Microwave J.*, Vol. 30, 1987, pp. 87–96.

[25] Menzel, W., "A 40 GHz Microstrip Array Antenna," *IEEE MTT-S Int. Symp. Digest*, 1980, pp. 225–226.

[26] Richard, W. F., Y. T. Lo, and D. D. Harrison, "An Improved Theory for Microstrip Antennas and Applications," *IEEE Trans. Antennas and Propagation*, Vol. AP-29, 1981, pp. 38–46.

[27] James, J. R., P. S. Hall, and C. Wood, *Microstrip Antenna: Theory and Design*, Peter Peregrinus, London, UK, 1981.

[28] Gupta, K. C., R. Garg, and R. Chadha, *Computer Aided Design and Microwave Circuits*, Artech House, Dedham, MA, 1981.

[29] James, J. R., and P. S. Hall, "Microstrip Antennas and Arrays, Part 2: New Array-Design Technique," *IEE Proc. Microwaves, Optics and Acoustics*, Vol. 1, Sept. 1977, pp. 175–181.

[30] Pozar, D. M., and D. H. Schaubert, "Scan Blindness in Infinite Phased Arrays of Printed Dipoles," *IEEE Trans. Antennas and Propagation*, Vol. AP-32, 1984, pp. 602–610.

[31] Oliner, A. A., and R. G. Malech, "Radiating Elements and Mutual Coupling," in *Microwave Scanning Antennas*, Vol. II, R. C. Hansen (Ed.), Academic Press, New York, 1966.

[32] Pozar, D. M., and D. H. Schaubert, "Analysis of an Infinite Array of Rectangular Microstrip Patches With Idealized Probe Feeds," *IEEE Trans. Antennas and Propagation*, Vol. AP-32, 1984, pp. 1101–1107.

[33] Pozar, D. M., "Analysis of Finite Phased Arrays of Printed Dipoles," *IEEE Trans. Antennas and Propagation*, Vol. AP-33, 1985, pp. 1045–1053.

[34] Pozar, D. M., "General Relations for a Phased Array of Printed Antennas Derived From Infinite Current Sheets," *IEEE Trans. Antennas and Propagation*, Vol. AP-33, 1985, pp. 498–504.

[35] Pozar, D. M., and D. H. Schaubert, "Comparison of Architectures for Monolithic Phased Array Antennas," *Microwave J.*, Vol. 29, 1986, pp. 93–104.

[36] Kinzel, J. A., B. J. Edward, and D. Rees, "V-Band, Space-Based Phased Arrays," *Microwave J.*, Vol. 30, 1987, pp. 89–102.

[37] McIlvenna, J. F., "Monolithic Phased Arrays for EHF Communications Terminals," *Microwave J.*, Vol. 31, 1988, pp. 113–125.

Appendix A

Substrates for Microstrip Antennas

A.1 Substrate Characteristics for Microstrip Antenna Design

The first step in designing an antenna is to choose an appropriate substrate. The substrate in microstrip antennas is principally needed for the mechanical support of the antenna metalization. To provide this support, the substrate needs to consist of a dielectric material, which may affect the electrical performance of the antenna, circuits, and transmission line. A substrate must, therefore, simultaneously satisfy the electrical and mechanical requirements, which is sometimes difficult to meet.

Substrate choice and evaluation are an essential part of the design procedure. Many substrate properties need to be considered: The dielectric constant and loss tangent and their variation with temperature and frequency, homogeneity, isotropicity, thermal coefficient and temperature range, dimensional stability with processing and temperature, humidity and aging, and thickness uniformity of the substrate are all of importance. Similarly, other physical properties, such as resistance to chemicals, tensile and structural strengths, flexibility, machinability, impact resistance, strain relief, formability, bondability, and substrate characteristics when clad, are important in fabrication.

The large range of PTFE (polytetrafluoroethylene), polystyrene, polyolefin, polyphenylene, alumina, sapphire, quartz, ferrimagnetic, rutile, and semiconductor substrates available permits considerable flexibility in the choice of a substrate for particular applications. There is no ideal substrate; rather, the choice depends on the application. For instance, conformal microstrip antennas require flexible substrates, whereas low-frequency applications require high dielectric constants to keep the size small. Microstrip patch antennas use

low dielectric constant substrates, whereas tapered slot antennas may require high dielectric constant materials.

The various substrates can be grouped in five categories: ceramic, semiconductor, ferrimagnetic, synthetic, and composite [1]. The main characteristics of these groups are described next.

A.1.1 Ceramic Substrates

The most commonly used ceramic substrate for microstrip circuits is alumina (Al_2O_3). It has desirable electrical characteristics such as low loss and less dispersion with frequency. However, it is hard and brittle and therefore difficult to process mechanically. For example, it is difficult to drill a hole through the substrate. Moreover, its maximum size is limited by the fabrication process to about 4 in. × 4 in. Sapphire is the monocrystalline form of alumina. It exhibits better electrical characteristics than alumina, but it is highly anisotropic in nature and very expensive. It can be used for low-loss applications at millimeter-wave frequencies. Characteristics of alumina and sapphire are listed in Table A.1.

A number of other ceramic materials are available with ϵ_r ranging between 20 and 150. A high dielectric constant is useful to attain important size reductions at low microwave frequencies (below 1 GHz). The use of ceramic materials as substrates is limited to microwave circuits because these materials cannot be manufactured in large dimensions.

A.1.2 Semiconductor Substrates

Semi-insulating or high-resistivity semiconductors like Si or GaAs can be used for passive circuits and antennas. However, the size of available semiconductor substrates is too small to be used at microwave frequencies for antennas, the notable exception being monolithic integrated antennas at millimeter waves [2]. Characteristics of high resistivity GaAs and Si substrates are listed in Table A.1.

A.1.3 Ferrimagnetic Substrates

The use of ferrite substrates has become very popular [3]. These substrates are anisotropic in nature. The ferrite and YIG substrates have relative permittivity value in the 9 to 16 range and generally have low dielectric loss ($\tan\delta$ for ferrite at 10 GHz is 0.001). The resonant frequency of a microstrip patch deposited on a ferrite substrate depends on the biasing magnetic field. Thus, wide-band tunability (almost 40% in some cases) [4] can be realized by varying

Table A.1
Characteristics of Laminates at 10 GHz

Laminate/Substrate	Dielectric Constant	Loss Tangent	Dimensional Stability	Chemical Resistance	Temperature Range (°C)	Relative Cost
Ceramic substrates						
Alumina	9.8	0.0004	Excellent	Excellent	To +1600	Medium to high
Sapphire	9.4, 1.6	0.0001	Excellent	Excellent	–24 to +370	Very high
Semiconductor substrates						
Semi-insulating GaAs ($>10^3$ Ω-m)	13.0	0.0006	Excellent	Excellent	–55 to +260	Very high
Silicon ($>10^3$ Ω-m)	11.9	0.0004	Excellent	Excellent	–55 to +260	High
Ferrimagnetic substrates						
Ferrite	9.0 to 16.0	≈ 0.001	Excellent	Excellent	–24 to +370	Medium
Synthetic substrates						
PTFE (Teflon)	2.1	0.0004	Poor	Excellent	–27 to +260	Medium
Polypropylene	2.18 ± 0.05	0.0003	Poor	Good	–27 to +200	Medium
Polyphenylene oxide (PPO)	2.55	0.0016	Good	Poor	–27 to +193	Medium
Cross-linked polystyrene	2.54	0.0005	Good	Good	–27 to +110	Medium
Irradiated polyolefin	2.32	0.0005	Poor	Excellent	–27 to +110	Low
Composite material substrates						
PTFE-glass, woven web	2.17 to 2.55	0.0009 to 0.0022	Excellent	Excellent	–27 to +260	Medium
PTFE-glass, random fiber	2.17 to 2.35	0.0009 to 0.0015	Fair	Excellent	–27 to +260	Medium to high
PTFE-quartz, reinforced	2.47	0.0006	Excellent	Excellent	–27 to +260	High
PTFE-ceramic, composite	10.2	0.002	Excellent	Good	–15 to +170	High
Cross-linked polystyrene-glass, reinforced	2.62	0.001	Good	Good	–27 to +110	Low

Table A.1 *(continued)*
Characteristics of Laminates at 10 GHz

Laminate/Substrate	Dielectric Constant	Loss Tangent	Dimensional Stability	Chemical Resistance	Temperature Range (°C)	Relative Cost
Cross-linked polystyrene-quartz	2.6	0.0005	Good	Good	–27 to +110	Medium to high
Cross-linked polystyrene-quartz, woven	2.65	0.0005	Good	Good	–27 to +110	Medium to high
Cross-linked polystyrene-ceramic, powder filled	3 to 15	0.0005 to 0.0015	Fair to good	Fair	–27 to +110	Medium to high
Teflon-glass, reinforced	2.55	0.0015	Good	Excellent	–27 to +260	Medium
Teflon-ceramic, reinforced	2.3	0.001	Fair to good	Excellent	–27 to +260	Medium to high
Teflon-quartz, reinforced	2.47	0.0006	Good	Excellent	–27 to +260	High
Teflon-ceramic, filled	10.3	0.002	Good	Excellent	–27 to +260	Low
Irradiated polyolefin-glass, reinforced	2.42	0.001	Fair	Excellent	–27 to +100	Medium
Polyolefin-ceramic, powder filled	3 to 10	0.001	Poor	Excellent	–27 to +100	High
Glass-bonded mica	7.5	0.002	Excellent	Excellent	–27 to +593	Medium to high
Silicon resin-ceramic, powder filled	3 to 25	0.0005 to 0.004	Fair to good	Good	–27 to +268	Medium
Polyester-ceramic powder-filled glass, reinforced	6	0.017	Excellent	Excellent	–27 to +205	Medium
Polymethacrylate foam, Rohacell 51	1.07	0.0009	—	—	—	—

the bias on the ferrite material without seriously affecting the radiation characteristics of the antenna.

Magnetic superstrates are also frequently used in combination with dielectric substrates to tailor the performance of a single element or an array (especially the latter) to the desired specifications.

A.1.4 Synthetic Substrates

A number of pure organic materials are commonly used as substrates. These include PTFE or Teflon, polystyrene, polyolefin, and polyphenylene. These materials possess low loss and low permittivity suitable for microstrip antennas. However, their mechanical properties are less than desirable, because these materials are soft and unstable with temperature. The most common of these synthetic substrates is PTFE or Teflon, polystyrene, polyphenylene, and polypropylene. The characteristics of some of these substrates are listed in Table A.1 [5, 6].

A.1.5 Composite Material Substrates

Substrate manufacturers have tried to combine the characteristics of various basic materials to obtain the desired electrical and mechanical properties. The resulting materials are called composite materials. By adding fiberglass (woven or random), quartz, or ceramic in suitable proportion to the organic or synthetic materials, the mechanical properties are modified and the permittivity adjusted. A very wide variety of products is now available with a permittivity range of 2.1 to 10 and $\tan\delta$ from 0.0005 to 0.002 at 10 GHz. Some of these materials are listed in Table A.1. All of these substrates are available in large sizes (up to 1m or more), with good mechanical properties allowing for machining, and antenna fabrication possible with standard printed circuit techniques. The dielectric constants of some well-known composite material substrates suitable for microstrip antennas are listed in Table A.2 [1].

A.1.6 Low-Cost Low-Loss Substrates [7]

Traditional microstrip antennas at microwave frequencies use substrates such as PTFE, quartz, and honeycomb for good radiation efficiency. These offer excellent electrical performance, but the resulting substrate costs are often too high for commercial civilian applications such as data transmission, mobile communication, direct broadcasting satellite reception, and so on. The price of a mass-produced printed antenna is directly related to the substrate and connector costs. Epoxy/glass (FR4) is a widely used material for low-frequency

Table A.2
Dielectric Constant of Some Composite Material Substrates (f = 10 GHz)

Material	ϵ_r	$\tan\delta$	Material	ϵ_r	$\tan\delta$
RT/Duroid 5870	2.33 ± 0.02	0.0012	Arlon DiClad 527	2.5 ± 0.04	0.0019
RT/Duroid 5880	2.2	0.0009	Arlon DiClad 870	2.33 ± 0.04	0.0012
RT/Duroid 6002	2.94	0.0012	Arlon DiClad 880	2.20 ± 0.04	0.0009
RT/Duroid 6006	6.0 ± 0.15	0.0019	Arlon DiClad 810	10.5 ± 0.25	0.0015
RT/Duroid 6010.5	10.5 ± 0.25	0.0024	Arlon Epsilam-10	102 ± 0.25	0.002
Ultralam 2000	2.5 ± 0.05	0.0022	Arlon CuClad 250	2.4–2.6	0.0018
RO 3003	3.0 ± 0.04	0.0013	Arlon CuClad 233	2.33 ± 0.02	0.0014
TMM-3	3.25	0.0016	Arlon CuClad 217	2.17 ± 0.02	0.0008
TMM-4	4.5	0.0017	Arlon IsoClad 917	2.17 ± 0.02	0.0011
TMM-6	6.5	0.0018	Arlon IsoClad 933	2.33 ± 0.02	0.0014
TMM-10	9.8	0.0017	Epoxy FR4 GE313	4.4	0.01
Trans-Tech D-MAT	8.9–14	<0.0002	Trans-Tech D-450	4.5	<0.0004
Trans-Tech S-145	10.0	<0.0002	Trans-Tech S8400	10.5	<0.0001

From [1].

and digital circuit boards. Its low cost, easy availability, and ease of fabrication are its strengths. Its high loss tangent and relatively variable dielectric constant limits its usage to frequencies below about 1 GHz or so. Recently, substrate manufacturers have introduced new materials that provide good electrical performance at reasonable prices. Table A.3 lists some of these new substrates. The loss tangents are comparable to other standard microwave materials. The

Table A.3
New Low-Cost Substrates for Microstrip Antennas at Low Frequencies

Material	Dielectric Constant at 1 GHz	Loss Tangent at 1 GHz	Manufacturer
R03003	3.00	0.0013	Rogers Corp
R03006	6.15	0.0013	Rogers Corp
R03010	10.2	0.0013	Rogers Corp
R04003	3.38	0.0022	Rogers Corp
TLC-32	3.2	0.003	Taconic Plastics
HT-2	4.3	0.0033	Hewlett-Packard
Polyguide	2.32	0.0005	Shawinigan Research
Epoxy/glass (FR4)	4.4	0.01	—

From [7].

cost for the new materials is three or more times less than for the traditional microwave substrates and, in some cases, approaches that of epoxy/glass. For comparison epoxy/glass (FR4) is also listed. Its high-loss tangent should be noted.

A.1.7 Substrate Anisotropy

Anisotropy is defined as the dependence of the substrate dielectric constant on the orientation of the applied electric field. To obtain desired electrical and mechanical properties in a substrate, suitable filler materials are generally added during the process of substrate manufacturing. These fillers have a tendency to assume preferred orientations. This may lead to anisotropic effects in some of the substrates used in practice. The PTFE-based composites display a mild anisotropy.

The value of the dielectric constant quoted by the manufacturer is generally for the case when the applied electric field is along the thickness of the sheet, which is usually sufficient information for most microstrip antenna work. The designer should, however, carefully check for the anisotropic effects in the substrate material, and evaluate the effects of anisotropy on the design.

Mathematically, the permittivity of an anisotropic substrate can be represented by a second rank tensor, or dyadic, of the form

$$\epsilon = \begin{pmatrix} \epsilon_{xx} & \epsilon_{xy} & \epsilon_{xz} \\ \epsilon_{yx} & \epsilon_{yy} & \epsilon_{yz} \\ \epsilon_{zx} & \epsilon_{zy} & \epsilon_{zz} \end{pmatrix} \tag{A.1}$$

For a biaxially anisotropic substrate, one can transform (A.1) into

$$\epsilon = \begin{pmatrix} \epsilon_x & 0 & 0 \\ 0 & \epsilon_y & 0 \\ 0 & 0 & \epsilon_z \end{pmatrix} \tag{A.2}$$

whereas for a uniaxially anisotropic substrate, one can write

$$\epsilon = \begin{pmatrix} \epsilon_x & 0 & 0 \\ 0 & \epsilon_x & 0 \\ 0 & 0 & \epsilon_z \end{pmatrix} \tag{A.2}$$

where the z direction is taken along the thickness of the substrate. Most of the PTFE-based composite substrates are mildly uniaxially anisotropic with

$\epsilon_z/\epsilon_x < 1$. The anisotropy ratio defined as $(\epsilon_x + \epsilon_y)/2\epsilon_z$ is plotted in Figure A.1 for woven and nonwoven glass-PTFE substrates as a function of nominal value of ϵ_r. This graph shows that the random glass-microfiber-PTFE (nonwoven) structure is less anisotropic than a woven-fabric structure [8].

It has been shown [3, 9, 10] that the resonant frequency of an antenna element may be seriously affected if the dielectric anisotropy is not included in the design. For instance, the resonant length of a rectangular patch of width $0.23\lambda_0$ on an Epsilam-10 material having $\epsilon_x = 13.0$, $\epsilon_z = 10.2$ is plotted in Figure A.2 versus the substrate thickness [3]. The curve for $\epsilon_x = 10.2$ in this figure is the result of assuming an isotropic substrate with $\epsilon_r = 10.2$. The curve for $\epsilon_x = 13.0$ is obtained when the effect of uniaxial anisotropy is included.

Clearly the effect of the anisotropy is to decrease the resonant length, or to increase the effective dielectric constant of the substrate in this case. The change in resonant length increases with the increase in substrate thickness. Also, the shift in resonant frequency due to anisotropy of the substrate can be almost as high as the bandwidth of the antenna [9]. The implication of this assumption is that an antenna designed for a specific operating frequency may actually resonate outside the desired frequency range if the designer fails to include the effects of substrate anisotropy.

Substrate dimensions and dielectric constant are functions of substrate temperature, so operating temperature range must be considered in the design. For example, the variations of ϵ_r and the loss tangent ($\tan\delta$) with temperature for copper clad GX-060-45 [5], which is a PTFE-based laminate, are shown in Figures A.3 and A.4. These figures clearly show that, if changes in ϵ_r and

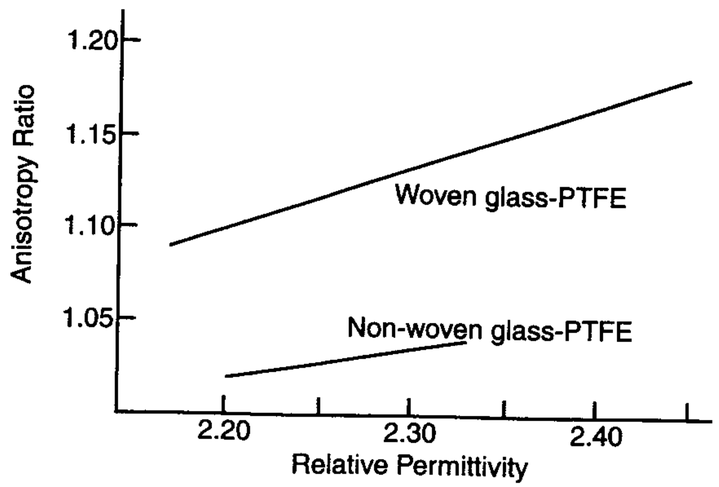

Figure A.1 Anisotropy ratio $(\epsilon_x + \epsilon_y)/2\epsilon_z$ plotted versus nominal ϵ_r for woven and nonwoven glass-PTFE composite substrates. (From [8]. © 1989 Peter Peregrinus. Reprinted with permission.)

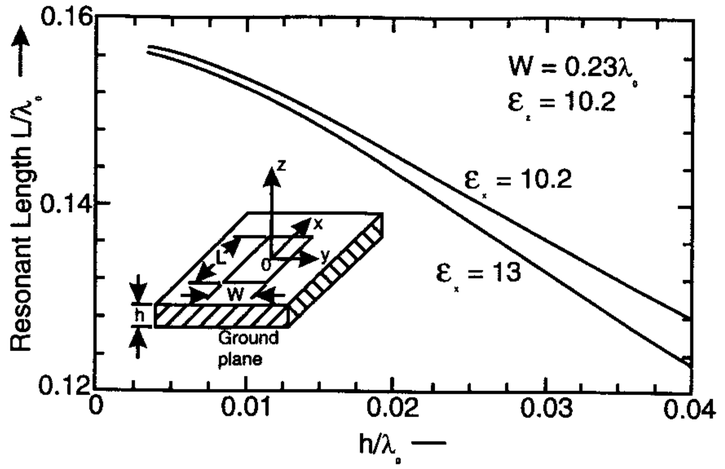

Figure A.2 Effect of anisotropy on the resonant length of a rectangular microstrip patch. (From [3]. © 1987 IEEE. Reprinted with permission.)

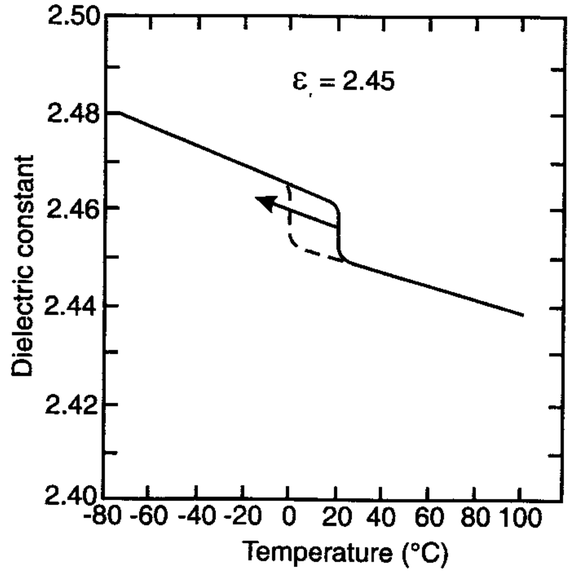

Figure A.3 Variation of the dielectric constant with temperature for GX-060-45 substrate. (From [5]. © 1979 New Mexico State University. Reprinted with permission.)

$\tan\delta$ over the operating temperature range of the antenna are not taken into consideration in design, the performance will be degraded because the bandwidth of these antennas is narrow. Applications where this consideration is important are high-speed missiles, rockets, and weaponry.

Dielectric constant and loss tangent are also functions of frequency. Thus, the values at 10 GHz listed in Table A.1 cannot be expected to be true at 1 GHz or 100 MHz. For most of the substrates listed, the changes are generally

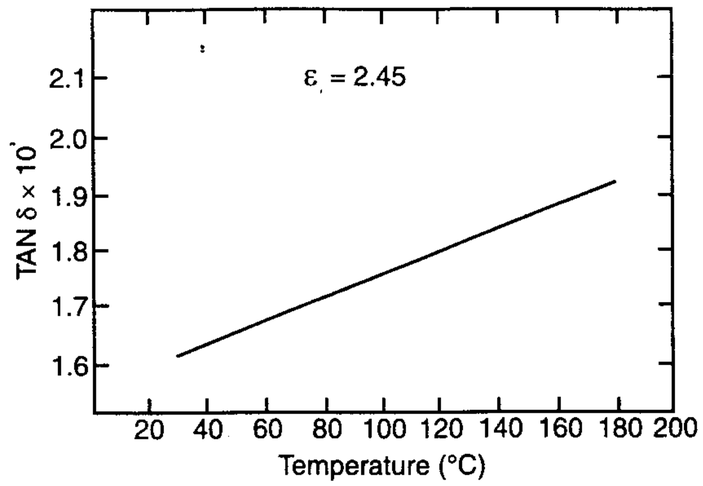

Figure A.4 Variation of the loss tangent with temperature for GX-060-45 substrate. (From [5]. © 1979 New Mexico State University. Reprinted with permission.)

small, of the order of 10%, with the greatest change occurring in $\tan\delta$, which may change by orders of magnitude.

For some special applications, antenna stability may be affected by environmental factors such as vibration, heat, aging, water absorption, and ultraviolet radiation exposure. Most of the substrates listed in Table A.1 are not significantly affected by these factors. Finally, for a conformal design, a soft substrate is required [11].

A.2 Desirable Substrate Characteristics for Antenna Fabrication

Apart from the electrical and physical properties listed in the preceding section, a successful antenna design involves consideration of the properties critically involved in the antenna production process. Chemical resistance, strain relief, machinability, and bondability are significant.

During fabrication, the antenna chemicals must be selected for cleaning, photoresist, resist removal, etching, and plating. It is important that the substrate be nonreactant, nonabsorbent, and, in general, be chemically inert to the materials mentioned here. Chemicals or water used should not be trapped in the material. Exposure to strong plating/etching solutions should not cause degradation of the metal/dielectric bond. Thus, data on the chemical resistance of the substrate must be obtained before fabrication starts. Generally this is not a problem, because substrate manufacturers recommend suitable chemicals for the above purposes.

Laminating a metal foil to a dielectric substrate often involves increasing the temperature of the substrate. Subsequent cooling results in a strain being set up in the substrate, due to the different thermal expansion coefficients of the metal foil and the dielectric laminate. The strain can be larger in the foil or the substrate, depending on the ratio of their thicknesses. Strain relieving techniques depend on the substrate, and may often be accomplished by adjustment in dimensions in the artwork for the photoresist etching mask.

In other cases, where artwork adjustment is expensive, a double mask procedure can be used. In this procedure, first an oversize mask pattern is employed, which allows exposure of most of the copper foil to be removed but protects enough to allow for strain relief errors. A second mask is then employed to obtain the exact pattern after the circuit has been etched and strain relieved.

Material hardness must be considered whenever substrates are machined. Speeds of cutting and tool feed rates must suit the substrates involved. If care is not exercised, the material may be scraped rather than cut, and will tend to deform and slide around the finite-sized radius of the cutting edge. Incorrect usage of cutting tools causes tool wear and tends to increase the radius of the edge. In the case of excessive tool wear, the cutting speed should be decreased and the tool feed rate increased. The same considerations apply to other machine practices that might be performed on substrates, for example, drilling, milling and routing, sawing, and turning.

For conformal antennas on nonplanar surfaces, formability becomes an important consideration. When the substrate is bent, it is stretched on one side and compressed on the other. Nonwoven fiber substrates sustain this type of distortion without permanent stress, since the fibers are discontinuous in the polymer matrix. However, continuous filament or woven structure substrates will be subjected to high stress. Best results in forming are obtained if the elastic deformation limit is not exceeded and time is allowed for stress relaxation.

A comprehensive study on technological aspects of microwave substrates is available in [8].

As discussed in Chapter 4, microstrip antennas are often coated with a dielectric material for environmental protection. In such cases, bonding may be desirable and coating materials of the proper combination of electrical characteristics, melting point, and adhesion must be chosen. Generally, substrate manufacturers are willing to provide information on bonding materials as well as the techniques to be used for proper bonding.

A wide range of substrate materials is available that use copper, aluminum, or gold cladding. Laminates are usually available in 1/32-, 1/16-, or 1/8-in thicknesses, and more recently in 5-, 10-, 25-, 50-, 75-, and 100-mil thicknesses,

or thicknesses at increments of 5 mil. The cladding material is usually designated in terms of weight per square yard, such as 14g (1/2 oz), 28g (1 oz), 57g (2 oz), and so on, for copper cladding. Typical cladding thicknesses corresponding to the ounce designations are given in Table A.4. Thinner cladding is essential for better fabrication tolerances, whereas thicker clads ease soldering. For high-power applications of microstrip antennas, a thick cladding is desirable.

Table A.4
Standard Copper Foil Weights and Foil Thickness (t)

Foil weight,				
g	14	28	57	112
oz	0.5	1	2	4
Foil thickness,				
mm	0.01778	0.03556	0.07112	0.14224
in	0.0007	0.0014	0.0028	0.0056

References

[1] Zurcher, J.-F., and F. E. Gardiol, *Broadband Patch Antennas*, Artech House, Norwood, MA, 1995, Chap. 8.

[2] Rebeiz, G. M., et al., "Integrated Horn Antennas for Millimeter Wave Applications," *IEEE Trans. Antennas Propagation Magazine*, Vol. 34, 1992, pp. 7–16.

[3] Pozar, D. M., "Radiation and Scattering From a Microstrip Patch on a Uniaxial Substrate," *IEEE Trans. Antennas and Propagation*, Vol. AP-35, 1987, pp. 613–621.

[4] Pozar, D. M., and V. Sanchez, "Magnetic Tuning of a Microstrip Antenna on a Ferrite Substrate," *Electron. Lett.*, Vol. 24, 1988, pp. 729–731.

[5] Nowicky, T. E., "Microwave Substrates Present and Future," *Proc. Workshop on Printed Circuit Antenna Technology*, New Mexico State University, Las Cruces, NM, Oct. 1979, pp. 26.1–26.12.

[6] Vossberg, W. A., "Stripping the Mystery From Strip-Line Laminates," *Microwaves*, Vol. 7, Jan. 1968, pp. 1–5.

[7] Sainati, R. A., *CAD of Microstrip Antennas for Wireless Applications*, Artech House, Norwood, MA, 1996, Chap. 3.

[8] Traut, G. R., "Advances in Substrate Technology," in *Handbook of Microstrip Antennas*, J. R. James and P. S. Hall (Eds.), Peter Peregrinus, London, UK, 1989.

[9] Pozar, D. M., "Considerations for Millimeter Wave Printed Antennas," *IEEE Trans. Antennas and Propagation*, Vol. AP-31, 1983, pp. 740–747.

[10] Alexopoulos, N. G., "Integrated-Circuit Structures on Anisotropic Substrates," *IEEE Trans. Microwave Theory and Techniques*, Vol. MTT-33, 1985, pp. 847–881.

[11] Woermbke, J. D., "Better Your MIC Designs With High-K Substrates," *Microwaves*, Mar. 1979, pp. 66–68.

Appendix B

Design of Planar Transmission Lines and Discontinuities

Planar transmission lines form the feed network for microstrip and other printed antennas. The same antenna can be fed by different types of transmission lines. The feed network for an array may consist of a number of power splitters, phase shifters, and attenuators. Each of these components involves a number of discontinuities—intentional or otherwise. The antenna itself may include some discontinuities such as an open end, gap, or short. Design equations for most of the planar transmission lines are included here for easy reference. Equivalent circuits for most of the commonly occurring microstrip discontinuities are given. Closed-form expressions for the lumped equivalent circuit parameters are also given wherever available.

B.1 Microstrip Line Design

The numerical methods for the characterization of a microstrip line involve extensive computations. But closed-form expressions are available that have accuracies compatible with various types of errors such as tolerances in microstrip parameters (ϵ_r, h, and W) and measurement errors. These expressions are presented here. The characteristics included are impedance, guide wavelength, transmission loss, power handling capability, and the quality factor Q. The dominant mode of propagation in a microstrip line is quasi-TEM. Quasi-static analysis of the transmission structure is carried out to determine the capacitance per unit length, C. This information is then used to determine the characteristic impedance and effective dielectric constant of the line using the following relations:

$$, \quad Z_0 = (c\sqrt{CC_a})^{-1} \tag{B.1}$$

$$\epsilon_{re} = C/C_a \tag{B.2}$$

where C_a is the capacitance per unit length of the structure with the dielectric replaced by air and c is the velocity of light in free space.

Characteristic Impedance, Z_0

The characteristic impedance of a microstrip line as shown in Figure B.1 is [1–3] ($t = 0$ assumed)

$$Z_0 = \frac{\eta_0}{2\pi\sqrt{\epsilon_{re}}} \ln\{F_1/u + \sqrt{1 + 4/u^2}\} \tag{B.3}$$

where

$$F_1 = 6 + (2\pi - 6) \times \exp\{-(30.666/u)^{0.7528}\}$$

$$\eta_0 = 120\pi\,\Omega \quad u = W/h$$

and

$$\epsilon_{re} = \frac{\epsilon_r + 1}{2} + \frac{\epsilon_r - 1}{2}\left(1 + \frac{10}{u}\right)^{-ab} \tag{B.4}$$

in which

$$a = 1 + \frac{1}{49}\ln\left\{\frac{u^4 + (u/52)^2}{u^4 + 0.432}\right\} + \frac{1}{18.7}\ln\left\{1 + \left(\frac{u}{18.1}\right)^3\right\}$$

$$b = 0.564\left(\frac{\epsilon_r - 0.9}{\epsilon_r + 0.3}\right)^{0.053}$$

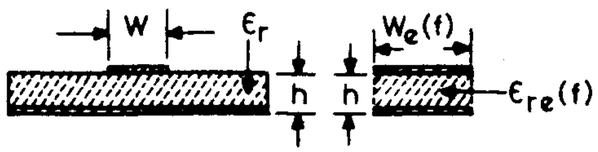

Figure B.1 Configuration of a microstrip line and its planar waveguide model.

Here W is the width of the strip conductor, h is the substrate thickness, and ϵ_{re} is the zero frequency value of the effective dielectric constant of the microstrip line. The maximum relative error in Z_0 obtained from (B.3) is less than 1%. The accuracy of the ϵ_{re} expression is better than 0.2% for $\epsilon_{re} \le 128$ and $0.01 \le u \le 100$ [3].

The synthesis expressions for Z_0 follow. For $Z_0\sqrt{\epsilon_{re}} > 89.91$, that is, $A > 1.52$,

$$\frac{W}{h} = \frac{8\exp(A)}{\exp(2A) - 2} \tag{B.5}$$

for $Z_0\sqrt{\epsilon_{re}} \le 89.91$, that is, $A \le 1.52$

$$\frac{W}{h} = \frac{2}{\pi}\left\{B - 1 - \ln(2B - 1) + \frac{\epsilon_r - 1}{2\epsilon_r}\left[\ln(B - 1) + 0.39 - \frac{0.61}{\epsilon_r}\right]\right\} \tag{B.6}$$

where

$$A = \frac{Z_0}{60}\left\{\frac{\epsilon_r + 1}{2}\right\}^{1/2} + \frac{\epsilon_r - 1}{\epsilon_r + 1}\left\{0.23 + \frac{0.11}{\epsilon_r}\right\}$$

$$B = \frac{60\pi^2}{Z_0\sqrt{\epsilon_r}}$$

Again the accuracy of (B.5) and (B.6) is better than 1%. The effect of strip metal thickness t on Z_0 can be included by replacing u with u' in (B.3); u' is defined as [4, p. 160]

$$u_0' = u + \frac{1}{\pi}\frac{t}{h}\ln\left(1 + \frac{4\exp(1)}{t/h \times \coth^2\sqrt{6.517u}}\right) \quad \text{for } \epsilon_r = 1 \tag{B.7a}$$

$$u_z' = u + \frac{u_0' - u}{2}\left(1 + \frac{1}{\cosh\sqrt{\epsilon_r - 1}}\right) \quad \text{for } \epsilon_r > 1 \tag{B.7b}$$

Based on the above equations, the characteristic impedance and effective dielectric constant of a microstrip line with $t > 0$ and $\epsilon_r > 1$ are given by

$$Z_{0t} = Z_0(u_z') \tag{B.8a}$$

and

$$\epsilon_{ret} = \epsilon_{re}(u_z') \tag{B.8b}$$

Guide Wavelength, λ

The guide wavelength is required for the design of microstrip circuits and antennas. It is defined as

$$\lambda = v_p/f \tag{B.9}$$

where f is the frequency of operation, and v_p is the phase velocity in the microstrip line given by

$$v_p = c/\sqrt{\epsilon_{re}(f)} \tag{B.10}$$

and c is the velocity of light. The value of $\epsilon_{re}(f)$ is always lower than the dielectric constant ϵ_r of the substrate, as it takes into account the fields external to the substrate. From (B.9) and (B.10)

$$\lambda = \lambda_0/\sqrt{\epsilon_{re}(f)} \tag{B.11}$$

where λ_0 is the free-space wavelength. The effective dielectric constant $\epsilon_{re}(f)$ is given by [5]

$$\epsilon_{re}(f) = \epsilon_r - \frac{\epsilon_r - \epsilon_{re}}{1 + P(f)} \tag{B.12a}$$

where

$$P(f) = P_1 P_2 \{(0.1844 + P_3 P_4) f_n\}^{1.5763}$$

$$P_1 = 0.27488 + u\{0.6315 + 0.525/(1 + 0.0157 f_n)^{20}\} - 0.065683 \exp(-8.7513u)$$

$$P_2 = 0.33622\{1 - \exp(-0.03442\epsilon_r)\}$$

$$P_3 = 0.0363 \exp(-4.6u)\{1 - \exp[-(f_n/38.7)^{4.97}]\}$$

$$P_4 = 1 + 2.751\{1 - \exp[-(\epsilon_r/15.916)^8]\}$$

$$f_n = fh \text{ (in GHz.mm)} = 47.713 k_0 h \tag{B.12b}$$

The frequency f is in gigahertz and the thickness h is in millimeters. The accuracy of (B.12a) is suggested to be 0.6% up to 60 GHz for $1 \le \epsilon_r \le 20$, $0.1 \le W/h \le 100$, and $0 \le h/\lambda_0 \le 0.13$ [5].

Planar Waveguide Model

The planar waveguide model of a microstrip line was developed for analyzing discontinuities in microstrip circuits [6]. Since then it has found many other applications. In the planar waveguide model, the microstrip line is modeled as a parallel plate waveguide of finite plate width, with perfect magnetic conductors at the side walls and perfect electric conductors at the top and bottom. This is shown in Figure B.1. The waveguide is of height h, equal to the microstrip substrate thickness. It is filled with a dielectric of relative permittivity ϵ_{re}. This ensures that the planar waveguide and the corresponding microstrip line have the same phase velocity. The plate width for the planar waveguide W_e is determined to ensure that both have the same characteristic impedance Z_0, that is,

$$Z_0 = \frac{\eta_0}{\sqrt{\epsilon_{re}}} \frac{h}{W_e} \tag{B.13}$$

An expression for the effective width W_e as a function of the microstrip physical parameters can be determined by comparing (B.3) and (B.13). Effective dielectric constant ϵ_{re} can be obtained from either (B.4) or (B.12). A frequency-dependent expression for W_e is also available [7]:

$$W_e(f) = W + \frac{W_e(0) - W}{1 + (f/f_{c1})^2} \tag{B.14}$$

where $W_e(0)$ is the quasi-static value of W_e defined in (B.13), and f_{c1} is the cutoff frequency of the TE_{10} mode in the planar waveguide model:

$$f_{c1} = \frac{c}{2W_e(0)\sqrt{\epsilon_{re}}} \tag{B.15}$$

The frequency-dependent value of characteristic impedance $Z_0(f)$, based on planar waveguide model, is defined as [7]

$$Z_0(f) = \frac{\eta_0}{\sqrt{\epsilon_{re}(f)}} \frac{h}{W_e(f)} \tag{B.16}$$

Very accurate expressions for $Z_0(f)$ based on the power-current definition were obtained by Jansen and Kirschning [8].

Losses

As for other transmission lines, the attenuation constant α of a microstrip line is one of its important characteristics. The loss in a microstrip line is due to its conductor loss α_c and the substrate dielectric loss α_d. An accurate and simple expression for conductor loss is derived using (B.3) with strip thickness t and the incremental inductance rule [2, 9]. This expression for α_c (dB/unit length) is

$$\alpha_c = \begin{cases} 1.38A\dfrac{R_s}{hZ_{0t}}\dfrac{32-(u_0')^2}{32+(u_0')^2} & \text{for } W/h \le 1 \\ 6.1\times 10^{-5}A\dfrac{R_sZ_{0t}\epsilon_{ret}}{h}\left[u_0'+\dfrac{0.667u_0'}{u_0'+1.444}\right] & \text{for } W/h \ge 1 \end{cases} \tag{B.17}$$

where

$$A = 1+\frac{1}{u_0'}\left\{1+\frac{1.25}{\pi}\ln\frac{2h}{t}\right\}$$

and $R_s = \sqrt{\pi f\mu_0\rho}$, where ρ is the resistivity of the strip conductor. The expression for dielectric loss (dB/unit length) is given by [2, 10]

$$\alpha_d = \begin{cases} 4.34\eta_0\sigma\dfrac{\epsilon_{re}(f)-1}{(\epsilon_r-1)\sqrt{\epsilon_{re}(f)}} \\ 27.3\dfrac{\epsilon_r}{\epsilon_r-1}\dfrac{\epsilon_{re}(f)-1}{\sqrt{\epsilon_{re}(f)}}\dfrac{\tan\delta}{\lambda_0} \end{cases} \tag{B.18}$$

where $\sigma = \omega\epsilon_0\epsilon_r\tan\delta$ is the conductivity of the dielectric substrate.

In addition to the dielectric loss and conductor loss, one should consider radiation loss also for high-Q circuits. However, radiation loss for a microstrip line becomes significant for frequencies higher than [11]

$$f\,(\text{in GHz}) > 2.14\frac{\sqrt[4]{\epsilon_r}}{h\,(\text{in mm})} \tag{B.19}$$

Power Handling Capability

There is a widespread impression that microstrip lines are suitable only for low-power components. Although microstrip lines are not as well suited for high-power applications as waveguides or coaxial lines of comparable cross sections, they could certainly be used for several medium-power applications. A 50Ω microstrip on a 25-mil-thick alumina substrate can handle a few kilowatts of power.

The power handling capacity of a microstrip, like that of any other dielectric filled transmission line, is limited by heating caused because of ohmic and dielectric losses and by dielectric breakdown. An increase in temperature due to conductor and dielectric losses limits the average power of the microstrip line, while the breakdown between the strip conductor and ground plane limits the peak power.

Average Power Handling Capability, P_{av}

The *average power handling capability* (APHC) of a microstrip is determined by the temperature rise of the strip conductor and the supporting substrate. The parameters that play major roles in the calculation of average power capability are (1) transmission line losses, (2) thermal conductivity of the substrate material, (3) surface area of the strip conductor, and (4) ambient temperature. Therefore, dielectric substrates with low-loss tangent and large thermal conductivity will increase the average power handling capability of microstrip lines.

The maximum average power P_{av} for a given line can be calculated from [2, 12]

$$P_{av} = (T_{max} - T_{amb})/\Delta T \tag{B.20}$$

with the rise in temperature

$$\Delta T = \frac{0.2303h}{K}\left(\frac{\alpha_c}{W_e}+\frac{\alpha_d}{2W_e(f)}\right)\quad (^\circ\text{C/W}) \tag{B.21}$$

where W_e has been defined in (B.13), and

$$W_e(f) = W+\frac{W_e-W}{1+(f/f_p)^2} \tag{B.22}$$

$$f_p = \frac{Z_0}{2\mu_0 h} \tag{B.23}$$

T_{max}: maximum operating temperature for the substrate
T_{amb}: ambient surrounding temperature
α_c (dB/unit length): conductor loss in the strip conductor
α_d (dB/unit length): dielectric loss of the substrate
K = thermal conductivity of the substrate material

The properties of various substrates are given in Table B.1. For polystyrene, the maximum operating temperature is 100°C, whereas for the rest of the dielectrics it is much more than 100°C. For T_{max} = 100°C, T_{amb} = 25°C, and Z_0 = 50Ω, values of APHC for various substrates at 2 and 10 GHz are calculated and listed in the same table. Among the dielectrics considered, APHC is the lowest for polystyrene and maximum for BeO.

Peak Power Handling Capability, P_p

The calculation of peak power handling capability of microstrip lines is more complicated. The peak voltage that can be applied without causing dielectric breakdown in a microstrip line determines the peak power handling capability (PPHC) of the microstrip line. If Z_0 is the characteristic impedance of the microstrip line and V_0 is the maximum voltage the line can withstand, the maximum peak power is given by

Table B.1
Properties of Various Dielectric Substrates and the APHC

Material	ϵ	$\tan\delta$ at 10 GHz	K (W/cm/°C)	Dielectric Strength (kV/cm)	APHC at 2.0 GHz	APHC at 10.0 GHz
Polystyrene	2.53	4.7×10^{-4}	0.0015	280	0.321	0.124
Quartz (fused)	3.8	1.0×10^{-4}	0.01	10×10^3	1.200	0.523
Si ($\rho = 10^3\Omega$-cm)	11.7	50×10^{-4}	0.9	300	3.19	2.23
GaAs ($\rho = 10^7\Omega$-cm)	12.3	16×10^{-4}	0.3	350	3.55	1.47
Sapphire	11.7	1×10^{-4}	0.4	4×10^3	11.65	5.10
Alumina	9.7	2×10^{-4}	0.3	4×10^3	12.12	5.17
BeO	6.6	1×10^{-4}	2.5	—	174.5	75.7

From [2].

$$P_p = \frac{V_0^2}{2Z_0} \tag{B.24}$$

Thick substrates can support higher voltages (for the same breakdown field). Therefore, low-impedance lines and lines on thick substrates have higher peak power handling capability.

The sharp edges of the strip conductor serve as field concentrators. The electric field tends to a large value at the sharp edges of the microstrip conductor if it is a flat strip and decreases as the edge of the conductor is rounded off more and more. Therefore, thick and rounded strip conductors will increase breakdown voltage.

The dielectric strength of the substrate material, as well as that of the air, plays an important role. The breakdown strength of dry air is approximately 30 kV/cm. Thus, the maximum electric field (tangential) near the strip edge should be less than 30 kV/cm. To avoid air breakdown near the strip edge, the edge of the strip conductor is painted with a dielectric paint, which has the same dielectric constant as that of the substrate and is lossless. The dielectric strength of various dielectrics is also given in Table B.1. Of the dielectric materials considered, fused quartz has the maximum dielectric strength, while polystyrene has the minimum.

In some cases, connectors or launchers determine the PPHC of the microstrip line. The 3-mm subminiature connectors and their transitions will break down before the line itself [13]. N-type connectors and transitions have higher PPHC. An additional factor that may reduce PPHC is the effect of internal mismatches. Data for PPHC are not readily available. Howe [13] has reported successful operation of microstrip lines up to 10 kW at S-band and 4 kW at X-band.

B.2 Suspended and Inverted Microstrip Line Design

The cross sections of suspended microstrip line and inverted microstrip line are shown in Figure B.2. These transmission lines provide a higher Q (500 to 1,500) than the conventional microstrip line.

Expressions for the characteristic impedance and effective dielectric constant for the transmission lines with thin metal strip are given in [2, p. 116; 14]. Equation (B.3) applies for characteristic impedance.

For the suspended microstrip $u = W/H$, and $u = W/(H - h)$ for the inverted microstrip line. All the variables are defined in Figure B.2.

For a suspended microstrip the effective dielectric constant ϵ_{re} is obtained from

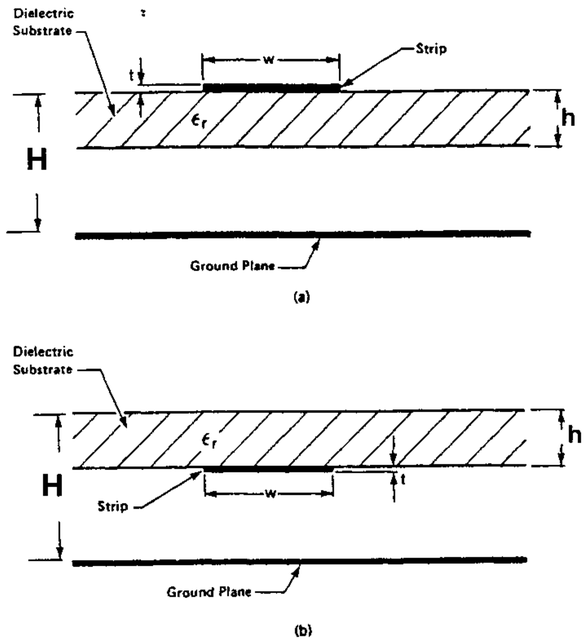

Figure B.2 Multilayered microstrip line configurations: (a) Suspended microstrip line, (b) inverted microstrip line, and (c) microstrip line with a superstrate.

$$\sqrt{\epsilon_{re}} = \left[1 + \frac{h}{H-h}\left(a - b\ln\frac{W}{H-h}\right)\left(\frac{1}{\sqrt{\epsilon_r}} - 1\right)\right]^{-1}$$

$$a = \left(0.8621 - 0.125\ln\frac{h}{H-h}\right)^4 \qquad \text{(B.25)}$$

$$b = \left(0.4986 - 0.1397\ln\frac{h}{H-h}\right)^4$$

and for an inverted microstrip the effective dielectric constant is given by

$$\sqrt{\epsilon_{re}} = 1 + \frac{h}{H-h}\left(\overline{a} - \overline{b}\ln\frac{W}{H-h}\right)(\sqrt{\epsilon_r} - 1)$$

$$\overline{a} = \left(0.5173 - 0.1515\ln\frac{h}{H-h}\right)^2 \qquad \text{(B.26)}$$

$$\overline{b} = \left(0.3092 - 0.1047\ln\frac{h}{H-h}\right)^2$$

The accuracy of (B.25) is within 1% for $1 < W/(H-h) \leq 8$, $0.2 \leq h/(H-h) \leq 1$, and $\epsilon_r \leq 6.0$. For $\epsilon_{re} \approx 10$, the error is less than 2%.

B.3 Design of Microstrip Line With a Superstrate

For certain feed designs like proximity coupling of antennas, it is convenient to fabricate the antenna using two dielectric layers. Also, a superstrate layer is used in antennas to protect them against the environment or to increase the gain. In such instances, it is necessary to include the effect of these layers to determine the resonant frequency. Quasi-static analysis of a multilayered microstrip line has been presented by Svacina [15]. Zhong et al. [16] have developed a closed-form expression for the resonant frequency of a rectangular patch operated in TM_{10} mode. Conformal transformation is used to determine the effective dielectric constant of the multilayered microstrip line of which the rectangular patch is a section. A cross section of a microstrip line with a superstrate layer and two substrate layers is shown in Figure B.2(c). The expression for ϵ_{re} for the multilayered microstrip line obtained as [16]:

$$\epsilon_{re} = \epsilon_{r1}\epsilon_{r2}\frac{(q_1 + q_2)^2}{\epsilon_{r1}q_2 + \epsilon_{r2}q_1} + \epsilon_{r3}\frac{(1 - q_1 - q_2)^2}{\epsilon_{r3}(1 - q_1 - q_2 - q_3) + q_3} \qquad \text{(B.27a)}$$

where q_1, q_2, and q_3 are the filling fractions defined for $W/h_{12} \geq 1$ as

$$q_1 = \frac{h_1}{2h_{12}}\left\{1 + \frac{\pi}{4} - \frac{h_{12}}{W_e}\ln\left[\frac{2W_e}{h_1}\sin\left(\frac{\pi h_1}{2h_{12}}\right) + \cos\left(\frac{\pi h_1}{2h_{12}}\right)\right]\right\}$$

$$q_2 = 1 - q_1 - \frac{h_{12}}{W_e}\ln\left(\frac{\pi W_e}{h_{12}} - 1\right)$$

$$q_3 = 1 - q_1 - q_2 - \frac{h_{12} - v_e}{2W_e}\ln\left(\frac{2W_e}{2h_{13} - h_{12} + v_e}\cos\left[\frac{\pi v_e}{2h_{12}}\right] + \sin\left[\frac{\pi v_e}{2h_{12}}\right]\right)$$

in which

$$W_e = W + \frac{2h_{12}}{\pi}\ln\left[17.08\left(\frac{W}{2h_{12}} + 0.92\right)\right]$$

$$v_e = \frac{2h_{12}}{\pi}\tan^{-1}\left[\frac{2\pi}{\pi W_e - 4h_{12}}(h_{13} - h_{12})\right]$$

Various thicknesses h_1, h_2, and so on are defined in Figure B.2(c). Dispersive behavior of a multilayered microstrip line is given by an equation similar to (B.12), that is,

$$\epsilon_{re}(f) = \epsilon_r' - \frac{\epsilon_r' - \epsilon_{re}}{1 + P(f)} \tag{B.27b}$$

Here, ϵ_r' represents the equivalent relative permittivity of the multilayered microstrip line, and is defined as

$$\epsilon_r' = \frac{2\epsilon_{re} - 1 + A}{1 + A}$$

$$A = \left(1 + \frac{12h_{12}}{W}\right)^{-1/2}$$

The factor $P(f)$ in (B.27b) is identical to that in (B.12), but (ϵ_r', u') is used in place of (ϵ_r, u) with

$$u' = W_e/h_{12}$$

Accuracy of the above model is found to be good provided

$$h_1/\lambda_{d1} + h_2/\lambda_{d2} + h_3/\lambda_{d3} \leq 0.1$$

where λ_{di} is the wavelength in the ith dielectric layer.

B.4 Parallel Strips Line Design

A parallel strips line is a balanced line. It can be used as a feed line for the center-fed double-sided printed dipole. A cross section of this type of line is shown in Figure B.3. The field distribution in this line remains unchanged if

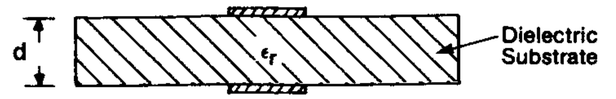

Figure B.3 Cross section of a parallel strips transmission line.

an infinite sized perfect electric conductor is inserted at any plane inside the substrate and parallel to the strips. Placing this conductor at a distance $d/2$ from either strip will convert the parallel strips' geometry into a combination of two identical microstrip lines placed back to back. Therefore, the design of the parallel strips line is simply related to the design of the microstrip line.

The characteristic impedance of a parallel strips line with dielectric separation d is twice the characteristic impedance of a microstrip line with dielectric thickness $h = d/2$ (both with the same strip width and dielectric constant), that is,

$$Z_{0\,\text{parallel-strips}} = 2Z_{0\,\text{microstrip}}(h = d/2) \tag{B.28a}$$

$$\epsilon_{re\,\text{parallel-strips}} = \epsilon_{re\,\text{microstrip}}(h = d/2) \tag{B.28b}$$

B.5 Strip Line Design [17–20]

The cross section of a strip line is shown in Figure B.4. This transmission line can be aperture coupled to the microstrip antenna by cutting a slot in the common ground plane of the antenna and the strip line. Being a completely shielded line, spurious radiation is negligible.

The dominant mode of propagation is TEM, and the design data can be obtained entirely from an electrostatic analysis. The design for the strip line is considerably simplified when the metal thickness t of the strip is assumed to be zero. This results in the following equation for the characteristic impedance [17]:

$$Z_0\sqrt{\epsilon_r} = 30\pi\frac{K'(k)}{K(k)}, \quad k = \tanh(\pi W/2b) \tag{B.29a}$$

$$\epsilon_{re} = \epsilon_r \tag{B.29b}$$

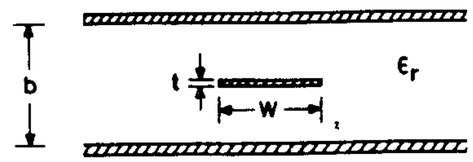

Figure B.4 Cross section of a strip line.

An accurate but simple expression of the ratio K/K' is available in the literature [21] and is included here for the readers' convenience.

$$\frac{K(k)}{K'(k)} = \begin{cases} \dfrac{\pi}{\ln[2(1+\sqrt{k'})/(1-\sqrt{k'})]} & \text{for } 0 \le k \le 1/\sqrt{2} \quad \text{(B.30a)} \\ \dfrac{1}{\pi}\ln[2(1+\sqrt{k})/(1-\sqrt{k})] & \text{for } 1/\sqrt{2} \le k \le 1 \quad \text{(B.30b)} \end{cases}$$

$$k' = \sqrt{1-k^2} \tag{B.31}$$

Expressions (B.30a) and (B.30b) are accurate to within 3 parts per million. The ratio K/K' varies from 0 to ∞ as k varies from 0 to 1.

The following expression can be used when the strip thickness t cannot be ignored [19].

$$Z_0\sqrt{\epsilon_r} = 30\ln\left\{1 + \frac{4}{\pi}\frac{b-t}{W'}\left[\frac{8}{\pi}\frac{b-t}{W'} + \sqrt{\left(\frac{8}{\pi}\frac{b-t}{W'}\right)^2 + 6.27}\right]\right\} \tag{B.32}$$

where

$$\frac{W'}{b-t} = \frac{W}{b-t} + \frac{\Delta W}{b-t} \tag{B.33}$$

with

$$\frac{\Delta W}{b-t} = \frac{x}{\pi(1-x)}\left\{1 - \frac{1}{2}\ln\left[\left(\frac{x}{2-x}\right)^2 + \left(\frac{0.0796x}{W/b + 1.1x}\right)^m\right]\right\} \tag{B.34}$$

in which

$$m = 2\left[1 + \frac{2}{3}\frac{x}{1-x}\right]^{-1} \quad \text{and} \quad x = t/b \tag{B.35}$$

For $W'/(b-t) < 10$, (B.32) to (B.35) are stated to yield data that are accurate to within 0.5%.

Synthesis Equations for Strip Lines

For computer-aided design and optimization, synthesis equations are needed; that is, strip width W for a given impedance line should be expressed in terms of parameters b, ϵ_r, and t. For zero-thickness strips, W/b is obtained from (B.29a) as

$$\frac{W}{b} = \frac{2}{\pi}\tanh^{-1}(k) \tag{B.36}$$

where

$$k = \begin{cases} \left[\dfrac{e^{\pi/x} - 2}{e^{\pi/x} + 2}\right]^2 & \text{for } 0 \le x \le 1 \quad \text{(B.37a)} \\ \sqrt{1 - \left[\dfrac{e^{\pi x} - 2}{e^{\pi x} + 2}\right]^4} & \text{for } x \ge 1 \quad \text{(B.37b)} \end{cases}$$

with $x = Z_0\sqrt{\epsilon_r}/(30\pi)$.

The synthesis equation for W/b (with $t \neq 0$) is obtained from (B.32) and is given below [19]:

$$\frac{W}{b} = \frac{W_0}{b} - \frac{\Delta W}{b} \tag{B.38}$$

with

$$\frac{W_0}{b} = \frac{8(1-x)}{\pi}\frac{\sqrt{e^A + 0.568}}{e^A - 1}, \quad A = \frac{Z_0\sqrt{\epsilon_r}}{30}$$

and

$$\frac{\Delta W}{b} = \frac{x}{\pi}\left\{1 - \frac{1}{2}\ln\left\{\left(\frac{x}{2-x}\right)^2 + \left(\frac{0.0796x}{W_0/b - 0.26x}\right)^m\right\}\right\}$$

The quantities x and m were defined earlier in (B.35). An expression for the conductor loss can be derived from the impedance expression for $t \neq 0$ case. The dielectric loss is given by

$$\alpha_d = 27.3\sqrt{\epsilon_r}\tan\delta/\lambda_0 \quad \text{(dB/unit length)} \tag{B.39}$$

B.6 Slot Line Design

The cross section of a slot line is shown in Figure B.5. Expressions for the characteristic impedance and guide wavelength of a slot line on high ϵ_r substrate have been obtained [2, 22] by curve-fitting the results based on Cohn's analysis [23]. The expressions given below have an accuracy of about 2% for the following range of parameters:

$$9.7 \leq \epsilon_r \leq 20$$

$$0.02 \leq W/h \leq 1.0$$

$$0.01 \leq h/\lambda_0 \leq (h/\lambda_0)_c$$

where $(h/\lambda_0)_c$ is the cutoff value for the TE_0 surface wave mode on the grounded substrate and is given by

$$(h/\lambda_0)_c = 0.25/\sqrt{\epsilon_r - 1} \tag{B.40}$$

The expressions obtained [2, p. 282] follow. For $0.02 \leq W/h \leq 0.2$:

$$\lambda_s/\lambda_0 = 0.923 - 0.448\log\epsilon_r + 0.2W/h - (0.29W/h + 0.047)\log(h/\lambda_0 \times 10^2) \tag{B.41a}$$

$$Z_{0s} = 72.62 - 35.19\log\epsilon_r + 50\frac{(W/h - 0.02)(W/h - 0.1)}{W/h} + \log(W/h \times 10^2)[44.28 - 19.58\log\epsilon_r] - [0.32\log\epsilon_r - 0.11 + W/h(1.07\log\epsilon_r + 1.44)] \times (11.4 - 6.07\log\epsilon_r - h/\lambda_0 \times 10^2)^2 \tag{B.41b}$$

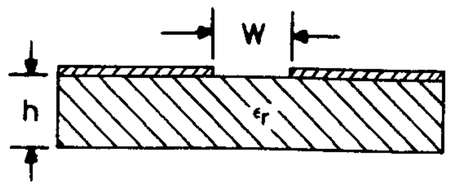

Figure B.5 Cross section of a slot line.

For $0.2 \leq W/h \leq 0.1$:

$$\lambda_s/\lambda_0 = 0.987 - 0.483\log\epsilon_r + W/h(0.111 - 0.0022\epsilon_r) - (0.094W/h + 0.121 - 0.0032\epsilon_r)\log(h/\lambda_0 \times 10^2) \tag{B.42a}$$

$$Z_{0s} = 113.19 - 53.55\log\epsilon_r + 1.25W/h(114.59 - 51.88\log\epsilon_r) + 20(W/h - 0.2)(1 - W/h) + [0.15 + 0.23\log\epsilon_r + W/h(-0.79 + 2.07\log\epsilon_r)] \times [10.25 - 5\log\epsilon_r + W/h(2.1 - 1.42\log\epsilon_r) - h/\lambda_0 \times 10^2]^2 \tag{B.42b}$$

The logarithms in (B.41) and (B.42) are to the base 10. Expressions with 1% accuracy for dielectric constant values of 9.7 and 20.0 are also available [2, p. 283].

High ϵ_r substrates are used for circuit applications to confine the fields near the slot. Slot lines on low ϵ_r substrates have interesting applications in antennas. Janaswamy and Schaubert [24] have obtained closed-form expressions for low ϵ_r substrates by curve-fitting the numerical results obtained from Galerkin's method in the Fourier transform domain. These expressions are as follows and are valid for the range of parameters [24] given:

$$2.22 \leq \epsilon_r \leq 9.8$$

$$0.0015 \leq W/\lambda_0 \leq 1.0$$

$$0.006 \leq h/\lambda_0 \leq 0.06$$

1. For $0.0015 \leq W/\lambda_0 \leq 0.075$ and $2.22 \leq \epsilon_r \leq 3.8$:

$$\frac{\lambda_S}{\lambda_0} = 1.045 - 0.365\ln\epsilon_r + \frac{6.3\epsilon_r^{0.945}(W/h)}{238.64 + 100W/h} - \left[0.148 - \frac{8.81(\epsilon_r + 0.95)}{100\epsilon_r}\right] \times \ln(h/\lambda_0) \tag{B.43a}$$

average error = 0.37%, max error = 2.2% (at one point)

$$Z_{0S} = 60 + 3.69\sin\left[\frac{(\epsilon_r - 2.22)\pi}{2.36}\right] + 133.5\ln(10\epsilon_r)\sqrt{W/\lambda_0}$$
$$+ 2.81[1 - 0.011\epsilon_r(4.48 + \ln\epsilon_r)](W/h)\ln(100h/\lambda_0) \quad \text{(B.43b)}$$
$$+ 131.1(1.028 - \ln\epsilon_r)\sqrt{h/\lambda_0}$$
$$+ 12.48(1 + 0.18\ln\epsilon_r)\frac{W/h}{\sqrt{\epsilon_r - 2.06 + 0.85(W/h)^2}}$$

average error = 0.67%, max error = 2.7% (at one point)

2. For $0.0015 \le W/\lambda_0 \le 0.075$ and $3.8 \le \epsilon_r \le 9.8$:

$$\frac{\lambda_S}{\lambda_0} = 0.9217 - 0.277\ln\epsilon_r + 0.0322(W/h)\left[\frac{\epsilon_r}{0.435 + W/h}\right]^{1/2} \quad \text{(B.44a)}$$
$$- 0.01\left[4.6 - \frac{3.65}{\epsilon_r^2(9.06 - 100W/\lambda_0)\sqrt{W/\lambda_0}}\right] \times \ln(h/\lambda_0)$$

average error = 0.6%, |max| error = 3% (at three points, occurs for $W/h > 1$ and $\epsilon_r > 6.0$)

$$Z_{0S} = 73.6 - 2.15\epsilon_r + (638.9 - 31.37\epsilon_r)(W/\lambda_0)^{0.6}$$
$$+ (36.23\sqrt{\epsilon_r^2 + 41} - 225)\frac{W/h}{W/h + 0.876\epsilon_r - 2} \quad \text{(B.44b)}$$
$$+ 0.51(\epsilon_r + 2.12)(W/h)\ln(100h/\lambda_0)$$
$$- 0.753\epsilon_r(h/\lambda_0)/\sqrt{W/\lambda_0}$$

average error = 1.58%, max error = 5.4% (at three points, occurs for $W/h > 1.67$)

3. For $0.075 \le W/\lambda_0 \le 1.0$ and $2.22 \le \epsilon_r \le 3.8$:

$$\frac{\lambda_S}{\lambda_0} = 1.194 - 0.24\ln\epsilon_r - \frac{0.621\epsilon_r^{0.835}(W/\lambda_0)^{0.48}}{1.344 + W/h} \quad \text{(B.45a)}$$
$$- 0.0617\left[1.91 - \frac{\epsilon_r + 2}{\epsilon_r}\right]\ln(h/\lambda_0)$$

average error = 0.69%, max error = −2.6% (at two points, for $W/\lambda_0 > 0.8$)

$$Z_{0S} = 133 + 10.34(\epsilon_r - 1.8)^2 + 2.87[2.96 + (\epsilon_r - 1.582)^2]$$
$$\times [\{W/h + 2.32\epsilon_r - 0.56\}\{(32.5 - 6.67\epsilon_r)(100h/\lambda_0)^2 - 1\}]^{1/2} \text{(B.45b)}$$
$$- (684.45h/\lambda_0)(\epsilon_r + 1.35)^2 + 13.23[(\epsilon_r - 1.722)W/\lambda_0]^2$$

average error = 1.9% |max error| = 5.4% (at three points, for $W/\lambda_0 > 0.8$)

4. For $0.075 \le W/\lambda_0 \le 1.0$ and $3.8 \le \epsilon_r \le 9.8$:

$$\frac{\lambda_S}{\lambda_0} = 1.05 - 0.04\epsilon_r + 1.411 \times 10^{-2}(\epsilon_r - 1.421)$$
$$\times \ln[W/h - 2.012(1 - 0.146\epsilon_r)] \quad \text{(B.46a)}$$
$$+ 0.111(1 - 0.366\epsilon_r)\sqrt{W/\lambda_0}$$
$$+ 0.139(1 + 0.52\epsilon_r\ln(14.7 - \epsilon_r))(h/\lambda_0)\ln(h/\lambda_0)$$

average error = 0.75%, |max error| = 3.2% (at two points, for $W/\lambda_0 = 0.075$, $h/\lambda_0 > 0.03$)

$$Z_{0S} = 120.75 - 3.74\epsilon_r + 50[\tan^{-1}(2\epsilon_r) - 0.8]$$
$$\times (W/h)^{[1.11 + (0.132(\epsilon_r - 27.7)/(100h/\lambda_0 + 5))]} \quad \text{(B.46b)}$$
$$\ln[100h/\lambda_0 + \sqrt{(100h/\lambda_0)^2 + 1}]$$
$$+ 14.2(1 - 0.458\epsilon_r)(100h/\lambda_0 + 5.1\ln\epsilon_r - 13.1) \times (W/\lambda_0 + 0.33)^2$$

average error = 2.0%, |max error| = 5.8% (at two points, occurs for $W/\lambda_0 < 0.1$)

In the above equations λ_S is the guide wavelength in the slot line and $\beta_S = 2\pi/\lambda_S$.

B.7 Coplanar Waveguide Design

Cross sections of various types of coplanar waveguides (CPW) are shown in Figure B.6 [2]. The expressions for the characteristic impedance and effective dielectric constant given below are based on the quasi-static analysis, and the method used is the conformal transformation.

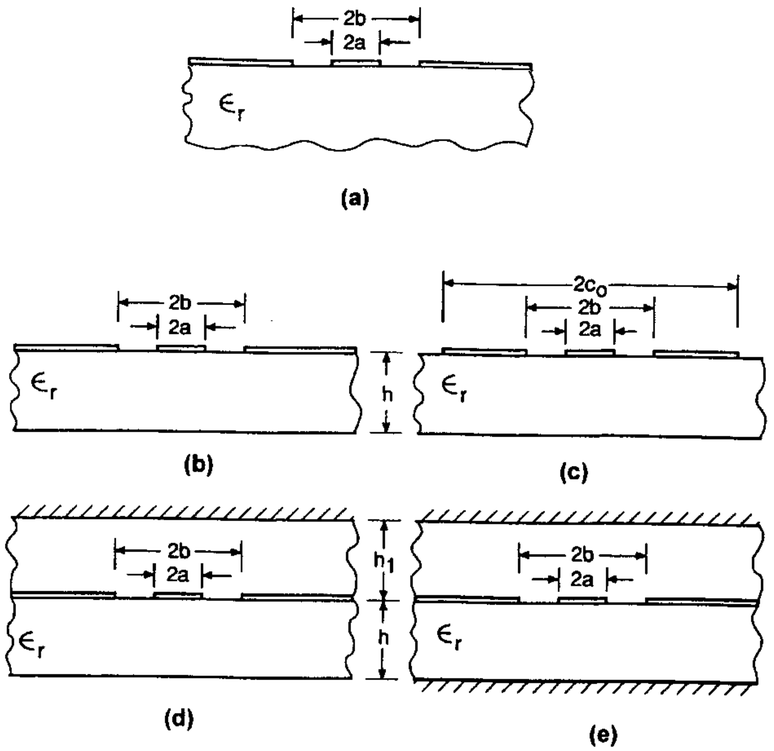

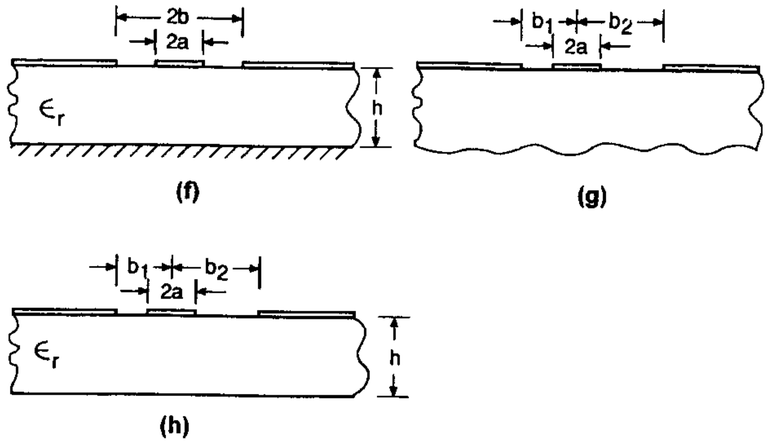

Figure B.6 Various types of coplanar waveguide configurations.

The underlying assumption in the analysis is that all the interfaces in the structure, including slots, can be replaced by magnetic walls. For analysis purposes, the transmission line structure is divided into two halves: the upper half, which is above the metalization, and the lower half, which is below the metalization. Capacitance per unit length for each half is determined by transforming it into a parallel plate geometry using conformal transformation.

These capacitances yield the characteristics of the line, as in the case of a microstrip line. The closed-form expression for the effective dielectric constant of the CPW is represented as

$$\epsilon_{re} = 1 + q(\epsilon_r - 1) \tag{B.47}$$

where q is called the filling fraction. Expressions for q are given below for the various geometries.

B.7.1 CPW With an Infinitely Thick Substrate [Figure B.6(a)]

$$q = 0.5 \tag{B.48a}$$

$$Z_{0cp} = \frac{30\pi}{\sqrt{\epsilon_{re}}} \frac{K'(k_1)}{K(k_1)}, \quad k_1 = \frac{a}{b} \tag{B.48b}$$

B.7.2 CPW With Finite Dielectric Thickness [Figure B.6(b)]

$$q = \frac{1}{2} \frac{K(k_2)}{K'(k_2)} \frac{K'(k_1)}{K(k_1)}, \quad k_2 = \frac{\sinh(\pi a/2h)}{\sinh(\pi b/2h)} \tag{B.49a}$$

$$Z_{0cp} = \frac{30\pi}{\sqrt{\epsilon_{re}}} \frac{K'(k_1)}{K(k_1)} \tag{B.49b}$$

The aspect ratio k_1 has been defined in (B.48b).

B.7.3 CPW With Finite Dielectric Thickness and Finite Width Ground Planes [Figure B.6(c)]

$$q = \frac{1}{2} \frac{K(k_4)}{K'(k_4)} \frac{K'(k_3)}{K(k_3)}, \quad k_3 = \frac{a}{b} \sqrt{\frac{1 - b^2/c_0^2}{1 - a^2/c_0^2}} \tag{B.50a}$$

$$k_4 = \frac{\sinh(\pi a/2h)}{\sinh(\pi b/2h)} \sqrt{\frac{1 - \sinh^2(\pi b/2h)/\sinh^2(\pi c_0/2h)}{1 - \sinh^2(\pi a/2h)/\sinh^2(\pi c_0/2h)}} \tag{B.50b}$$

$$Z_{0cp} = \frac{30\pi}{\sqrt{\epsilon_{re}}} \frac{K'(k_3)}{K(k_3)} \tag{B.50c}$$

B.7.4 CPW With Finite Dielectric Thickness and a Cover Shield [Figure B.6(d)]

$$q = \frac{K(k_2)/K'(k_2)}{K(k_1)/K'(k_1) + K(k_5)/K'(k_5)}, \quad k_5 = \frac{\tanh(\pi a/2h_1)}{\tanh(\pi b/2h_1)} \tag{B.51a}$$

$$Z_{0cp} = \frac{60\pi}{\sqrt{\epsilon_{re}}} \frac{1}{K(k_1)/K'(k_1) + K(k_5)/K'(k_5)} \tag{B.51b}$$

B.7.5 Conductor-Backed CPW With a Cover Shield [Figure B.6(e)]

$$q = \frac{K(k_6)/K'(k_6)}{K(k_5)/K'(k_5) + K(k_6)/K'(k_6)} \tag{B.52a}$$

$$Z_{0cp} = \frac{60\pi}{\sqrt{\epsilon_{re}}} \frac{1}{K(k_5)/K'(k_5) + K(k_6)/K'(k_6)} \tag{B.52b}$$

B.7.6 Conductor-Backed CPW [Figure B.6(f)]

$$q = \frac{K(k_6)/K'(k_6)}{K(k_1)/K'(k_1) + K(k_6)/K'(k_6)} \tag{B.53a}$$

$$Z_{0cp} = \frac{60\pi}{\sqrt{\epsilon_{re}}} \frac{1}{K(k_1)/K'(k_1) + K(k_6)/K'(k_6)} \tag{B.53b}$$

B.7.7 Asymmetric CPW Without Dielectric Substrate [Figure B.6(g)]

$$q = 1 \tag{B.54a}$$

$$Z_{0cp} = 60\pi \frac{K'(k_7)}{K(k_7)}, \quad k_7 = \sqrt{\frac{2a(b_1 + b_2)}{(a + b_1)(a + b_2)}} \tag{B.54b}$$

$$k_7' = \sqrt{\frac{(b_1 - a)(b_2 - a)}{(b_1 + a)(b_2 + a)}} \tag{B.54c}$$

B.7.8 Asymmetric CPW With Finite Dielectric Thickness [Figure B.6(h)]

$$q = \frac{1}{2} \frac{K(k_8)}{K'(k_8)} \frac{K'(k_7)}{K(k_7)}, \quad k_8^2 = \frac{2(k_{1\epsilon} + k_{2\epsilon})}{(1 + k_{1\epsilon})(1 + k_{2\epsilon})} \tag{B.55a}$$

$$k_{1\epsilon} = \frac{\sinh(\pi a/2h)}{\sinh(\pi b_1/2h)} \tag{B.55b}$$

$$k_{2\epsilon} = \frac{\sinh(\pi a/2h)}{\sinh(\pi b_2/2h)} \tag{B.55c}$$

$$Z_{0cp} = \frac{30\pi}{\sqrt{\epsilon_{re}}} \frac{K'(k_7)}{K(k_7)} \tag{B.55d}$$

B.8 Coplanar Strips Design

Cross sections of various types of coplanar strips (CPS) [2] lines are shown in Figure B.7. CPS is a balanced transmission line like slot line and has been used for feeding the printed dipole. Due to fabrication tolerances we may end up with a CPS in which the two strips do not have the same width. This line is called an *asymmetric CPS*. Sometimes, it is desirable to use an asymmetric CPS to adjust the characteristic impedance by changing the width of one of the strips while keeping the width of the other strip and the slot width fixed. Asymmetric CPS geometries are also shown in Figure B.7.

CPS can also be analyzed using the conformal mapping method. Since coplanar strips and coplanar waveguide geometries are complementary to each other in the metalization plane, the transformation used for CPW can also be applied to the CPS. Results for the various CPS geometries are given next. Use is made of (B.47) to calculate ϵ_{re} for CPS also.

B.8.1 Symmetric CPS With Infinitely Thick Substrate [Figure B.7(a)]

$$q = 0.5 \tag{B.56a}$$

$$Z_{0cs} = \frac{120\pi}{\sqrt{\epsilon_{re}}} \frac{K(k_1)}{K'(k_1)}, \quad k_1 = \frac{a}{b} \tag{B.56b}$$

B.8.2 Asymmetric CPS With Infinitely Thick Substrate [Figure B.7(b)]

$$q = 0.5 \tag{B.57a}$$

$$Z_{0cs} = \frac{60\pi}{\sqrt{\epsilon_{re}}} \frac{K'(k_2')}{K(k_2')} \quad k_2' = \sqrt{\frac{W_1}{W_1 + S} \frac{W_2}{W_2 + S}} \tag{B.57b}$$

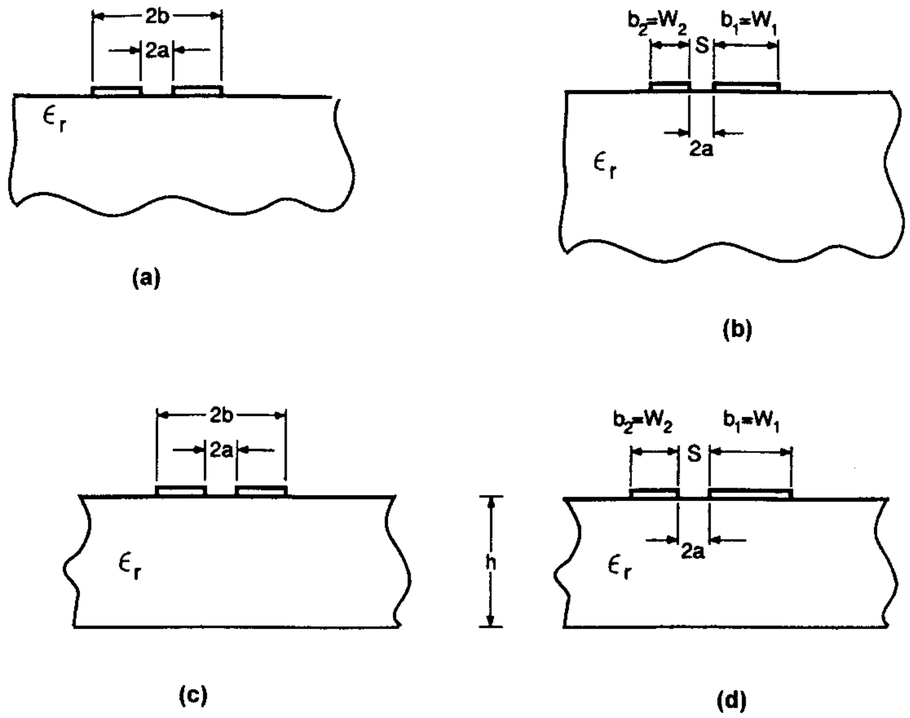

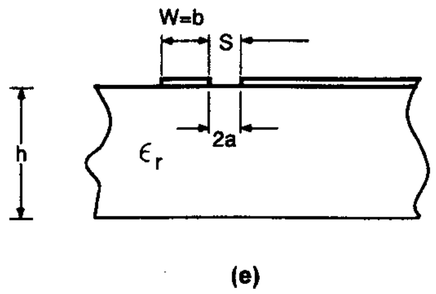

Figure B.7 Various types of coplanar strip configurations.

B.8.3 Asymmetric CPS With Finitely Thick Substrate [Figure B.7(c)]

$$q = \frac{1}{2}\frac{K(k_4)}{K'(k_4)}\frac{K'(k_3)}{K(k_3)} \tag{B.58a}$$

with $k_3 = k_2'$ and insert of (B.57b)

$$k_4 = \sqrt{\frac{\sinh(\pi W_1/2h)}{\sinh(\pi(W_1+S)/2h)}\frac{\sinh(\pi W_2/2h)}{\sinh(\pi(W_2+S)/2h)}} \tag{B.58b}$$

$$Z_{0cs} = \frac{60\pi}{\sqrt{\epsilon_{re}}}\frac{K'(k_3)}{K(k_3)} \tag{B.58c}$$

B.8.4 Symmetric CPS With Finite Dielectric Thickness [Figure B.7(d)]

Conformal transformation analysis of symmetric CPS with finite dielectric thickness has been reported. But the values of ϵ_{re} and Z_{0s} do not agree with the results of numerical analysis. It has been found that (B.49a) for q of CPW gives good agreement for $h/b > 1$ because of the complementary nature of CPS and CPW. The expression for the characteristic impedance of a CPS is

$$Z_{0cs} = \frac{120\pi}{\sqrt{\epsilon_{re}}}\frac{K(k_1)}{K'(k_1)}, \quad k_1 = \frac{a}{b} \tag{B.59}$$

B.8.5 Asymmetric CPS With an Infinitely Wide Strip [Figure B.7(e)]

$$q = \frac{K(k_7)}{K'(k_7)}\frac{K'(k_6)}{K(k_6)} \tag{B.60a}$$

with

$$k_6 = \sqrt{\frac{W}{W+S}} \quad \text{and} \quad k_7 = \sqrt{\frac{\sinh(\pi W/2h)}{\sinh(\pi(W+S)/2h)}e^{-\pi S/2h}} \tag{B.60b}$$

$$Z_{0cs} = \frac{60\pi}{\sqrt{\epsilon_{re}}}\frac{K'(k_6)}{K(k_6')} \tag{B.60c}$$

A procedure for the synthesis of coplanar lines is given in [2]. The effect of dispersion and nonzero metalization thickness on the characteristics has been determined. Dielectric, conductor, surface wave, and radiation losses have been expressed in closed form [2].

B.9 Coupled Microstrip Lines Design

The geometry of symmetric coupled microstrip lines is shown in Figure B.8. This geometry supports two modes, called the *even* and *odd* modes. The effective dielectric constants and the characteristic impedances for these modes are functions of substrate parameters, and W and S.

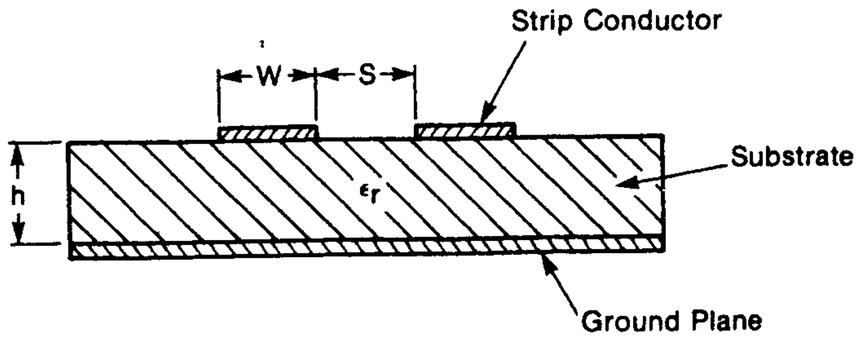

Figure B.8 Cross section of coupled microstrip lines.

Accurate closed-form expressions for the static effective dielectric constants and characteristic impedances are available [25]. These are given next.

For the even mode:

$$\epsilon_{re}^{e}(0) = \frac{\epsilon_r + 1}{2} + \frac{\epsilon_r - 1}{2}\left(1 + \frac{10}{v}\right)^{-a_e b_e} \tag{B.61a}$$

with

$$v = \frac{u(20 + g^2)}{10 + g^2} + ge^{-g}$$

$$a_e = 1 + \frac{1}{49}\ln\left[\frac{v^4 + (v/52)^2}{v^4 + 0.432}\right] + \frac{1}{18.7}\ln\left[1 + \left(\frac{v}{18.1}\right)^3\right]$$

$$b_e = 0.564\left(\frac{\epsilon_r - 0.9}{\epsilon_r + 3}\right)^{0.053}$$

and

$$Z_{0e} = Z_0 \frac{\sqrt{\epsilon_{re}(0)/\epsilon_{re}^{e}(0)}}{1 - Q_4\sqrt{\epsilon_{re}(0)} \times Z_0/377} \tag{B.61b}$$

with

$$Q_1 = 0.8695u^{0.194}$$

$$Q_2 = 1 + 0.7519g + 0.189g^{2.31}$$

$$Q_3 = 0.1975 + \left[16.6 + \left(\frac{8.4}{g}\right)^6\right]^{-0.387} + \frac{1}{241}\ln\left[\frac{g^{10}}{1 + (g/3.4)^{10}}\right]$$

$$Q_4 = \frac{2Q_1}{Q_2} \cdot \frac{1}{u^{Q_3}e^{-g} + (2 - e^{-g})u^{-Q_3}}$$

Here $u = W/h$ and $g = S/h$. The error in ϵ_{re}^{e} is within 0.7% and Z_{0e} is within 0.6% over the following range of parameters [25]:

$$0.1 \le u(= W/h) \le 10 \quad 0.1 \le g(= S/h) \le 10 \quad 1 \le \epsilon_r \le 18 \tag{B.62}$$

For the odd mode:

$$\epsilon_{re}^{o}(0) = \epsilon_{re}(0) + [0.5(\epsilon_r + 1) - \epsilon_{re}(0) + a_o]e^{-C_o(gd_o)} \tag{B.63a}$$

with

$$a_o = 0.7287\{\epsilon_r(0) - 0.5(\epsilon_r + 1)\}(1 - e^{-0.179u})$$

$$b_o = \frac{0.747\epsilon_r}{0.15 + \epsilon_r}$$

$$C_o = b_o - (b_o - 0.207)e^{-0.414u}$$

$$d_o = 0.593 + 0.694e^{-0.562u}$$

and

$$Z_{0o} = Z_0 \frac{\sqrt{\epsilon_{re}(0)/\epsilon_{re}^{o}(0)}}{1 - Q_{10}\sqrt{\epsilon_{re}(0)} \cdot Z_0/377} \tag{B.63b}$$

with

$$Q_5 = 1.794 + 1.14\ln\left[1 + \frac{0.638}{g + 0.517g^{2.43}}\right]$$

$$Q_6 = 0.2305 + \frac{1}{5.1}\ln[1 + 0.598g^{1.154}] + \frac{1}{281.3}\ln\left[\frac{g^{10}}{1 + (g/5.8)^{10}}\right]$$

$$Q_7 = \frac{10 + 190g^2}{1 + 82.3g^3}$$

$$Q_8 = \exp\{-[6.5 + 0.95\ln(g) + (g/0.15)^5]\}$$

$$Q_9 = \ln(Q_7)(Q_8 + 1/16.5)$$

$$Q_{10} = Q_4 - \frac{Q_5}{Q_2}\exp\left[\frac{Q_6\ln(u)}{u^{Q_9}}\right]$$

The error in $\epsilon_{re}^{o}(0)$ is stated to be of the order of 0.5%, and Z_{0o} is in error of the order of 0.6% for the range of parameters specified in (B.62).

In the closed-form expressions given above, $\epsilon_{re}(0)$ is the static effective dielectric constant, Z_0 is the static characteristic impedance for a microstrip line of width W, and $\epsilon_{re}^{e,o}(0)$ represents the static effective dielectric constant for a coupled microstrip line.

The expressions for $\epsilon_{re}^{e,o}(0)$ and $Z_{0(e,o)}$ can also be used to obtain capacitances (per unit length) for the even and odd modes. The relationship between these quantities is given as

$$C_{e,o}\frac{1}{c}\frac{\sqrt{\epsilon_{re}^{e,o}(0)}}{Z_{0(e,o)}} \tag{B.64a}$$

$$C_{e,o}^{a} = \frac{1}{c}\frac{1}{Z_{0(e,o)}\sqrt{\epsilon_{re}^{e,o}(0)}} \tag{B.64b}$$

Design equations for the asymmetric coupled microstrip lines are not available.

B.10 Coupled Strip Lines Design

The cross section for parallel coupled strip lines is shown in Figure B.9. The even and odd mode analysis of this geometry is carried out by placing perfect

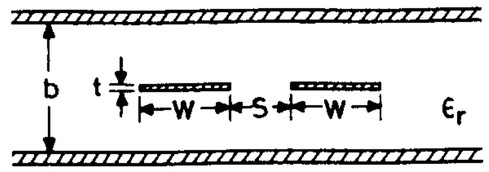

Figure B.9 Cross section of coupled strip lines.

magnetic and electric walls, respectively, at the plane of symmetry of the structure. The uncoupled one-half of the structure is then analyzed for capacitance per unit length. The procedure now followed is identical to that used for the strip line (uncoupled) case.

For zero thickness ($t = 0$) coupled strip lines, exact formulas for even and odd mode impedances have been derived using a conformal mapping procedure [20, 26]. These are given as

$$Z_{0e}\sqrt{\epsilon_r} = 30\pi\frac{K'(k_e)}{K(k_e)} \tag{B.65a}$$

$$Z_{0o}\sqrt{\epsilon_r} = 30\pi\frac{K'(k_o)}{K(k_o)} \tag{B.65b}$$

The ratio $K'(k)/K(k)$ has been defined in (B.30), and

$$k_e = \tanh\left(\frac{\pi}{2}\frac{W}{b}\right)\tanh\left(\frac{\pi}{2}\frac{W+S}{b}\right), \quad k_e' = \sqrt{1-k_e^2} \tag{B.66a}$$

$$k_o = \tanh\left(\frac{\pi}{2}\frac{W}{b}\right)\coth\left(\frac{\pi}{2}\frac{W+S}{b}\right), \quad k_o' = \sqrt{1-k_o^2} \tag{B.66b}$$

Synthesis

For the synthesis of coupled strip lines the following formulas can be used [20]:

$$\frac{W}{b} = \frac{2}{\pi}\tanh^{-1}\sqrt{k_e k_o} \tag{B.67}$$

and

$$\frac{S}{b} = \frac{2}{\pi}\tanh^{-1}\left(\frac{1-k_o}{1-k_e}\sqrt{\frac{k_e}{k_o}}\right) \tag{B.68}$$

with

$$k_{e,o} = \begin{cases} \left(\dfrac{e^{\pi/x} - 2}{e^{\pi/x} + 2}\right)^2 & \text{for } 0 \le x \le 1 \quad \text{(B.69)} \\ \sqrt{1 - \left(\dfrac{e^{\pi x} - 2}{e^{\pi x} + 2}\right)^4} & \text{for } 1 \le x \le \infty \quad \text{(B.70)} \end{cases}$$

with $x = \dfrac{Z_{0e}\sqrt{\epsilon_r}}{30\pi}$ or $\dfrac{Z_{0o}\sqrt{\epsilon_r}}{30\pi}$ for the even and odd modes, respectively.

B.11 Characterization of Discontinuities in Microstrip Lines

Various types of discontinuities occurring in microstrip circuits are shown in Figure B.10. The approximate equivalent circuits are also shown there. These discontinuities have been studied extensively and a detailed review is given in [2]. Closed-form expressions for these discontinuities (wherever available) and the ranges of their validity are included here. Some of these closed-form expressions are based on full-wave analysis data. Some of the discontinuities, such as step-in-width, T-junction, and bend, are commonly used in power splitters and other portions of the feed network. Other discontinuities, like open ends, gaps, and shorts, are a part of the antenna.

B.11.1 Open Ends [Figure B.10(a)]

An empirical expression for the open-end effect of a microstrip line has been derived by curve-fitting the numerical results based on hybrid-mode full-wave analysis [27]. According to this, the open-end reactance can be expressed in the form of an equivalent additional line length Δl_{oc} given as

$$\frac{\Delta l_{oc}}{h} = \xi_1 \xi_3 \xi_5 / \xi_4 \quad \text{(B.71)}$$

where

$$\xi_1 = 0.434907 \frac{\epsilon_{re}^{0.81} + 0.26}{\epsilon_{re}^{0.81} - 0.189} \times \frac{(W/h)^{0.8544} + 0.236}{(W/h)^{0.8544} + 0.87}$$

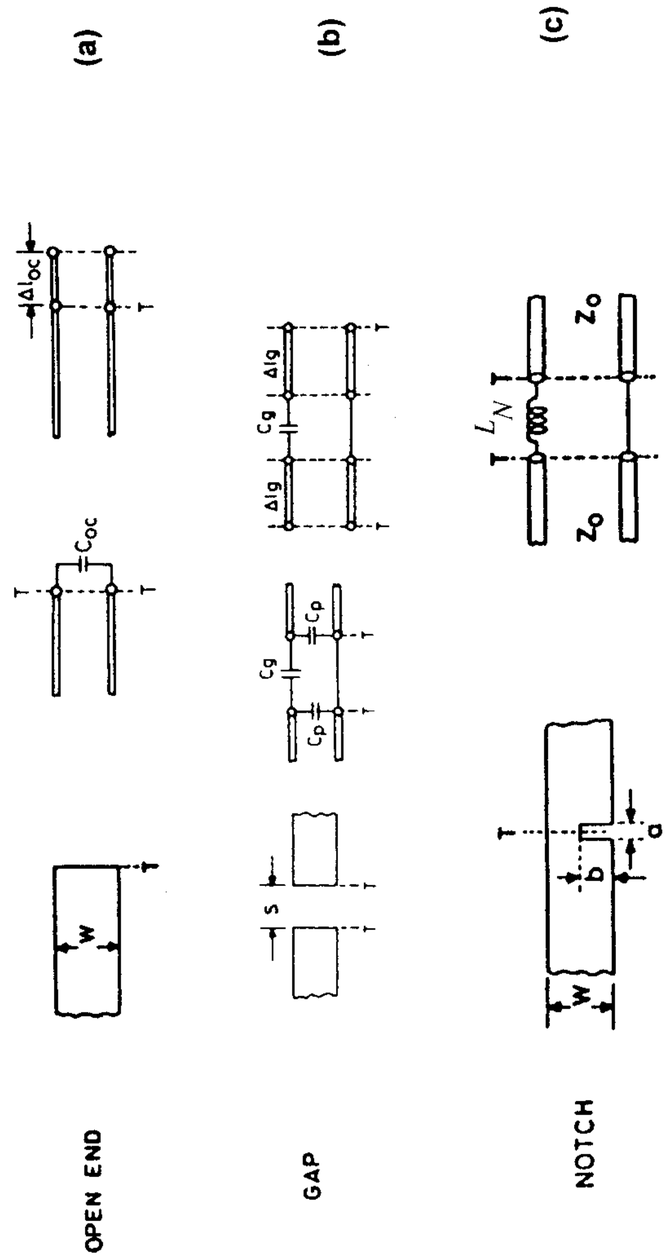

Figure B.10 Lumped equivalent circuit models for various types of microstrip discontinuities.

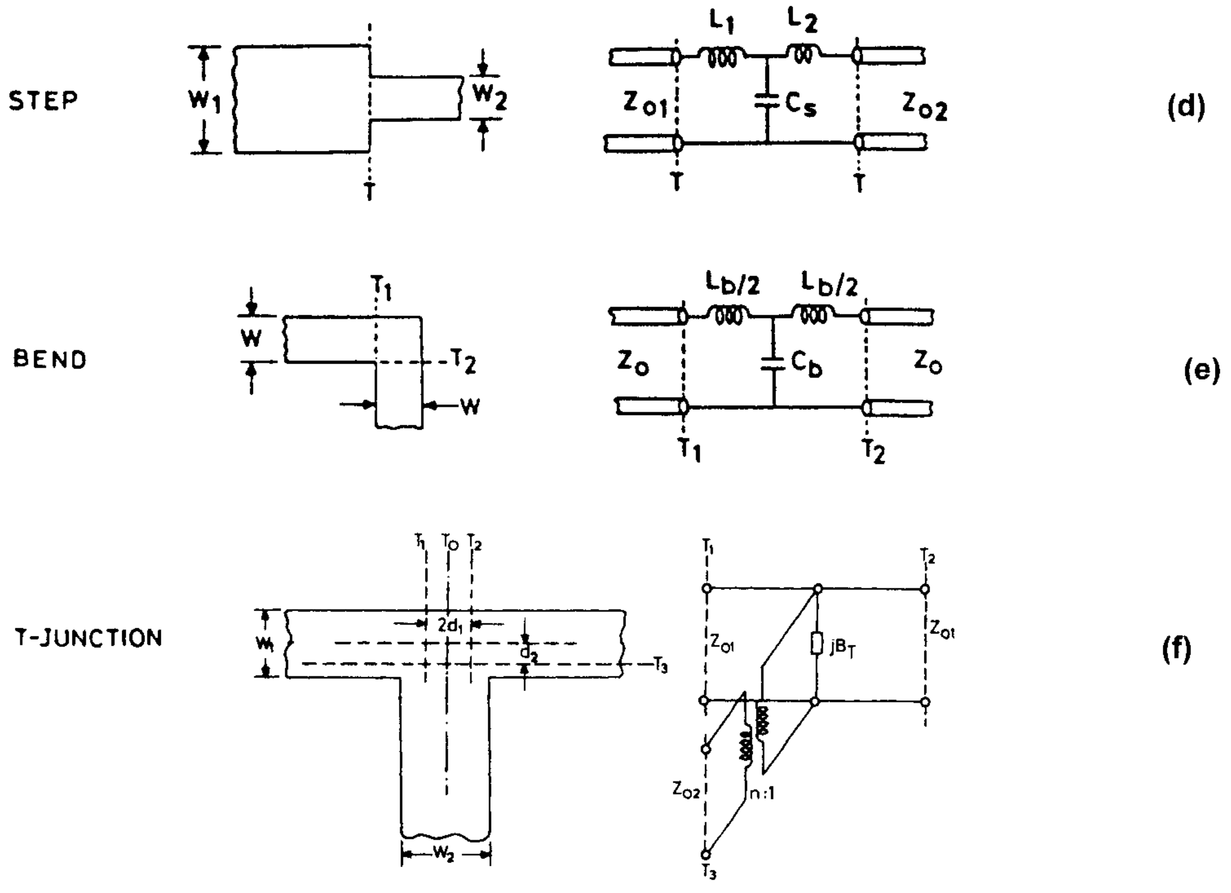

Figure B.10 (continued).

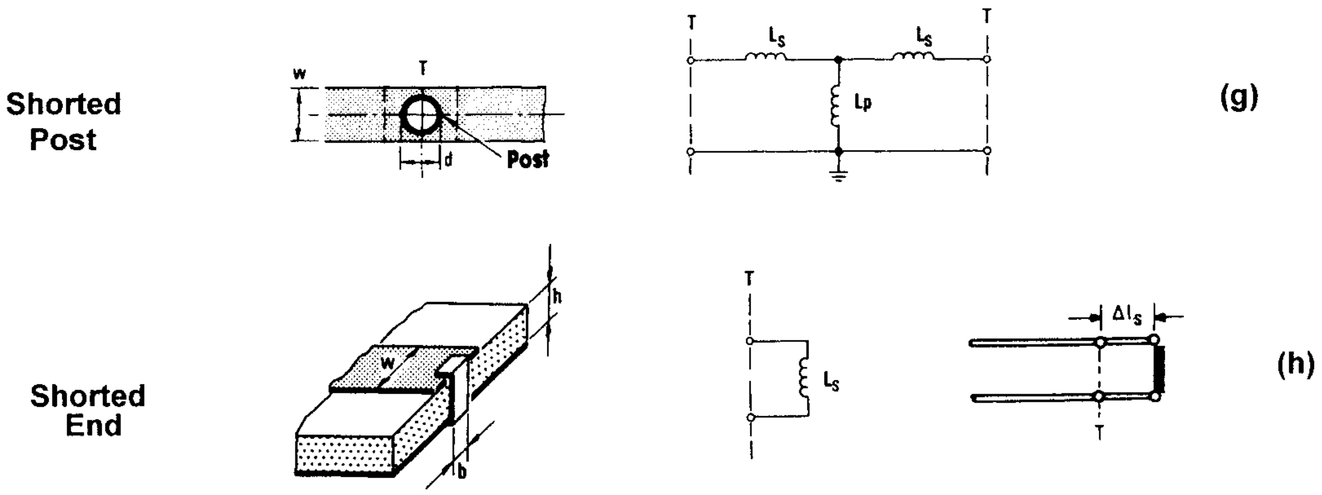

Figure B.10 (continued).

$$\xi_2 = 1 + \frac{(W/h)^{0.371}}{2.358\epsilon_r + 1}$$

$$\xi_3 = 1 + \frac{0.5274 \arctan[0.084(W/h)^{1.9413/\xi_2}]}{\epsilon_{re}^{0.9236}}$$

$$\xi_4 = 1 + 0.0377 \arctan[0.067(W/h)^{1.456}] \times \{6 - 5\exp[0.036(1 - \epsilon_r)]\}$$

$$\xi_5 = 1 - 0.218\exp(-7.5W/h)$$

The preceding expression has an accuracy better than 0.2% for the range $0.01 \le W/h \le 100$ and $\epsilon_r \le 128$. The additional line length Δl_{oc} can be converted into an equivalent open-end capacitance as

$$\frac{C_{oc}}{W} = \frac{\Delta l_{oc}}{h}\frac{\sqrt{\epsilon_{re}}}{cZ_0 W/h} \tag{B.72}$$

The effect of dispersion on Δl_{oc} has been analyzed by Itoh [28]. At millimeter wavelengths the value of Δl_{oc} is considerably smaller than that computed by using the quasi-static approximation. However, for frequencies up to about 10 GHz, the quasi-static approach gives reasonably good results. For thicker substrates and for wider microstrip lines used in microstrip antennas, radiation from an open end becomes significant. The associated radiation conductance is quantified in Chapter 4.

B.11.2 Gaps in Microstrip Lines [Figure B.10(b)]

The characterization of a gap discontinuity in a microstrip line is useful in the analysis of gap coupled microstrip antennas. The equivalent capacitances C_p and C_g are related to C_{even} and C_{odd} by [2, 29]

$$C_{\text{even}} = 2C_p \tag{B.73}$$

$$C_{\text{odd}} = 2C_g + C_p \tag{B.74}$$

where, for $\epsilon_r = 9.6$ and $0.5 \le W/h \le 2$

$$\frac{C_{\text{odd}}}{W} = \left(\frac{S}{W}\right)^{m_o}\exp(k_o) \quad (\text{pF/m}) \tag{B.75}$$

$$\frac{C_{\text{even}}}{W} = 12\left(\frac{S}{W}\right)^{m_e}\exp(k_e) \quad (\text{pF/m}) \tag{B.76}$$

In the above, C_{even} and C_{odd} are the equivalent circuit parameters for the gap when it is excited symmetrically and antisymmetrically, respectively. The expressions for m_e, m_o, k_e, and k_o are given next:

$$\left.\begin{aligned} m_o &= [0.619\log(W/h) - 0.3853]W/h \\ k_o &= 4.26 - 1.453\log(W/h) \end{aligned}\right\} \quad (0.1 \le S/W \le 1.0) \tag{B.77}$$

$$m_e = \begin{cases} 0.8675 & k_e = 2.043(W/h)^{0.12} \quad \text{for } 0.1 \le S/W \le 0.5 \quad \text{(B.78a)} \\ \dfrac{1.565}{(W/h)^{0.16}} - 1 & k_e = 1.97 - \dfrac{0.03}{W/h} \quad \text{for } 0.5 \le S/W \le 1.0 \quad \text{(B.78b)} \end{cases}$$

The values of C_{even} and C_{odd} for other values of ϵ_r in the range $2.5 \le \epsilon_r \le 15$ can be calculated by scaling according to the relations [30]

$$C_{\text{odd}}(\epsilon_r) = 1.1C_{\text{odd}}(9.6)(\epsilon_r/9.6)^{0.8} \tag{B.79a}$$

$$C_{\text{even}}(\epsilon_r) = 1.167C_{\text{even}}(9.6)(\epsilon_r/9.6)^{0.9} \tag{B.79b}$$

The accuracy of these expressions is within 7% for the above-mentioned set of parameters.

For the alternative equivalent circuit of Figure B.10(b), the line length Δl_g can be obtained from the capacitance C_p as follows:

$$\frac{\Delta l_g}{h} = \frac{C_p}{W}\frac{cZ_0 W/h}{\sqrt{\epsilon_{re}}} \tag{B.80}$$

B.11.3 Notch [Figure B.10(c)]

A notch or a narrow transverse slit in the strip conductor of a microstrip line can be introduced to realize a series inductance. The value of the series inductance L_N can be obtained from the approximate relation [31]

$$\frac{L_N}{h}\,(\text{nH/mm}) = 2\left(1 - \frac{Z_0\sqrt{\epsilon_{re}}}{Z_0'\sqrt{\epsilon_{re}'}}\right)^2 \qquad \text{(B.81)}$$

where ϵ_{re} and ϵ_{re}' are the effective dielectric constants for microstrip lines with widths W and $(W - b)$, respectively, and Z_0 and Z_0' are the corresponding impedances. The substrate thickness h is measured in millimeters. The expression for L_N above is valid for $0 \le b/W \le 0.9$ and $a \le h$.

B.11.4 Steps in Width [Figure B.10(d)]

Steps in width exist at the junctions of two microstrip lines that have different impedances. This type of discontinuity is encountered when designing matching transformers, couplers, filters, and transitions. The discontinuity capacitance C_S represents the fringing field capacitance at the junction, and can be approximated by an equivalent line length Δl_S. Because discontinuity effects are small, the change in lengths can be approximated by $\Delta l_{oc}(1 - W_2/W_1)\,f(\epsilon_r)$ [31] where Δl_{oc} is the open-circuit line extension calculated from (B.80) for line width W_1 and the function $f(\epsilon_r)$ has the form [32]

$$f(\epsilon_r) = 1.25 + 0.19\tan^{-1}(6.16 - \epsilon_r) \qquad \text{(B.82)}$$

A closed-form expression for C_S is given as [28]

$$\frac{C_S}{\sqrt{W_1 W_2}}\,(\text{pF/m}) = (10.1\log\epsilon_r + 2.33)\frac{W_1}{W_2} - 12.6\log\epsilon_r - 3.17 \qquad \text{(B.83)}$$

This expression yields an error of less than 10% for $\epsilon_r \le 10$; $1.5 \le W_1/W_2 \le 3.5$.

The inductances L_1 and L_2 are obtained from the total discontinuity inductance L_S as

$$L_1 = \frac{L_{w1}}{L_{w1} + L_{w2}} L_S \qquad \text{(B.84a)}$$

$$L_2 = \frac{L_{w2}}{L_{w1} + L_{w2}} L_S \qquad \text{(B.84b)}$$

where, in general, L_w is the inductance per unit length of the microstrip of width W given by

$$L_w = \frac{Z_0\sqrt{\epsilon_{re}}}{c} \qquad \text{(H/unit length)} \qquad \text{(B.85)}$$

The expression for inductance L_S is given by [29]

$$\frac{L_S}{h}\,(\text{nH/m}) = 40.5\left(\frac{W_1}{W_2} - 1.0\right) - 75\log\frac{W_1}{W_2} + 0.2\left(\frac{W_1}{W_2} - 1.0\right)^2 \qquad \text{(B.86)}$$

Equation (B.86) has an error of less than 5% for $W_1/W_2 \le 5$ and $W_1/h = 1.0$. A more general expression for L_S is given as

$$L_S\,(\text{nH}) = 0.000987h\left(1 - \frac{Z_{01}}{Z_{02}}\sqrt{\frac{\epsilon_{re1}}{\epsilon_{re2}}}\right)^2 \quad (h \text{ is in } \mu\text{m}) \qquad \text{(B.87)}$$

B.11.5 Bends in Microstrips [Figure B.10(e)]

A microstrip bend can be formed by two lines of equal or unequal impedances and is normally used for introducing flexibility in the layout of the circuit. The equivalent circuit of a microstrip bend with lines of equal impedances is shown in Figure B.10(e). The most common form of microstrip bend used in circuits and investigated analytically is the right-angled bend.

Closed-form expressions for right-angled bend discontinuities are given as [29]

$$\frac{C_b}{W}\,(\text{pF/m}) = \begin{cases} \dfrac{(14\epsilon_r + 12.5)W/h - (1.83\epsilon_r - 2.25)}{\sqrt{W/h}} + \dfrac{0.02\epsilon_r}{W/h} & \text{for } (W/h < 1) \\ (9.5\epsilon_r + 1.25)W/h + 5.2\epsilon_r + 7.0 & \text{for } (W/h \ge 1) \end{cases} \qquad \text{(B.88)}$$

$$\frac{L_b}{h}\,(\text{nH/m}) = 100(4\sqrt{W/h} - 4.21) \qquad \text{(B.89)}$$

Equation (B.88) is accurate to within 5% for $2.5 \le \epsilon_r \le 15$ and $0.1 \le W/h \le 5$. The accuracy of (B.89) is about 3% for $0.5 \le W/h \le 2.0$.

B.11.6 Symmetric T-Junctions [Figure B.10(f)]

The T-junction is perhaps the most important discontinuity in a microstrip line because it is found in most circuits such as impedance networks, stub

filters, and branch-line couplers. A symmetric microstrip T-junction and its equivalent circuit are shown in Figure B.10(f). The main arm has the characteristic impedance Z_{01}, and the side arm is characterized by Z_{02}. Use of the planar waveguide model in the analysis gives the following expressions for the symmetric case [33]:

$$\frac{d_1}{D_2} = 0.055\left[1 - 2\frac{Z_{01}}{Z_{02}}\left(\frac{f}{f_{p1}}\right)^2\right]\frac{Z_{01}}{Z_{02}} \tag{B.90}$$

$$\frac{d_2}{D_1} = 0.5 - \left[0.05 + 0.7\exp\left(-1.6\frac{Z_{01}}{Z_{02}}\right) + 0.25\frac{Z_{01}}{Z_{02}}\left(\frac{f}{f_{p1}}\right)^2 - 0.17\ln\frac{Z_{01}}{Z_{02}}\right]\frac{Z_{01}}{Z_{02}} \tag{B.91}$$

$$n^2 = 1 - \pi\left(\frac{f}{f_{p1}}\right)^2\left[\frac{1}{12}\left(\frac{Z_{01}}{Z_{02}}\right)^2 + 0.5 - \frac{d_2}{D_1}\right)^2\Bigg] \tag{B.92}$$

$$\frac{B_T}{Y_{02}}\frac{\lambda_1}{D_1} = 5.5\frac{\epsilon_r + 2}{n^2\epsilon_r}\left[1 + 0.9\ln\frac{Z_{01}}{Z_{02}} + 4.5\frac{Z_{01}}{Z_{02}}\left(\frac{f}{f_{p1}}\right)^2 - 4.4\exp\left(-1.3\frac{Z_{01}}{Z_{02}}\right) - 20\left(\frac{Z_{02}}{\eta_0}\right)^2\right]\frac{d_1}{D_2} \tag{B.93}$$

where D, f_p, and λ are the equivalent parallel plate line width, first higher order mode cutoff frequency, and guide wavelength of the microstrip line, respectively. Subscripts 1 and 2 represent series and shunt lines. Expressions for D and f_p are given as

$$D = \eta_0 h/(\sqrt{\epsilon_{re}}Z_0) \qquad \eta_0 = 377\Omega \tag{B.94a}$$

$$f_p\ (\text{GHz}) = 0.4Z_0/h \qquad (h \text{ is in mm}) \tag{B.94b}$$

It has been suggested that for moderate nonsymmetry, the results for the symmetrical case can be extended to the nonsymmetrical case.

B.11.7 Short-Circuited Posts in Microstrips [Figure B.10(g)]

Short circuits in microstrip lines are used in bandpass filters and quarter-wave stubs, and to obtain ground points on the upper surface of the substrate. The geometry of a short-circuiting post and its equivalent circuit are shown in Figure B.10(g). The post diameter is d and the strip width is W. For $d/W \ll 1$, the series inductance L_S can be ignored and the shunt inductance L_p takes on the inductance of a circular wire [4, p. 302]. The expression for the wire inductance is given as [34, p. 48]

$$L_p\ (\text{nH}) = 0.2h[\ln(4h/d) + d/(2h) - 1] \quad (h \text{ and } d \text{ are in mm}) \quad d/W \ll 1 \tag{B.95a}$$

The series resistance R associated with the loss in the wire is given as

$$R = 2.63 \times 10^{-3}(h/d)\sqrt{\rho f/\rho_{Cu}} \qquad (f \text{ is in GHz}) \qquad d/W \ll 1 \tag{B.95b}$$

where ρ is the resistivity of the post metal and $\rho_{Cu} = 1.72 \times 10^{-4}\Omega \cdot m$.

B.11.8 Shorted Ends [Figure B.10(h)]

A microstrip line short circuit achieved by means of a metal ribbon at the end of the line is shown in Figure B.10(h). The ribbon of width b, length h, and thickness t is bonded to the strip as well as the ground. The equivalent circuit of this short is described either by the ribbon inductance L_S or by an equivalent line length extension Δl_S [4, p. 306]. The expression for the ribbon inductance is given as [34, p. 5]

$$\frac{L_S}{h}\ (\text{nH/mm}) = 0.2\left\{\ln\frac{2h}{b + t} + 0.2235\frac{b + t}{h} + 0.5\right\} \tag{B.96}$$

(h, b, and t are in mm)

The corresponding line length is obtained by using (B.85)

$$\Delta l_S = \frac{cL_S}{Z_0\sqrt{\epsilon_{re}}} \tag{B.97}$$

The series resistance R due to loss in the ribbon is given as [4]

$$R = 4.13 \times 10^{-3} \frac{h}{b + t} \sqrt{f(\text{GHz})\, \rho/\rho_{Cu}} \tag{B.98}$$

The range of applicability of (B.96) in terms of ratio b/h is not known.

B.12 Open-End Discontinuity in Coupled Microstrip Lines

Similar to the open end in a microstrip line, the open end in coupled microstrip lines is capacitive in nature, and can be characterized in the form of an additional line length $\Delta l_{o,e}$ for each mode. Closed-form expressions for $\Delta l_{o,e}$ have been reported [2, p. 516]. These are given as [25]

$$\Delta l_e = \Delta l_{oc}(u, \epsilon_r) + [\Delta l_{oc}(2u, \epsilon_r) - \Delta l_{oc}(u, \epsilon_r) + 0.0198h \times g^{R_1}] \times \exp(-0.328 g^{2.244}) \tag{B.99a}$$

$$\Delta l_o = \Delta l_{oc}(u, \epsilon_r)(1 - e^{-R_4}) + hR_3 \times e^{-R_4} \tag{B.99b}$$

with

$$u = W/h \quad \text{and} \quad g = S/h$$

$$R_1 = 1.187[1 - \exp(-0.069u^{2.1})]$$

$$R_2 = 0.343u^{0.6187} + \frac{0.45\epsilon_r}{1 + \epsilon_r} \times u^{[1.357 + 1.65/(1 + 0.7\epsilon_r)]}$$

$$R_3 = 0.2974(1 - e^{-R_2})$$

$$R_4 = (0.271 + 0.0281\epsilon_r) \times g^{[1.167\epsilon_r/(0.66 + \epsilon_r)]} + \frac{1.025\epsilon_r}{0.687 + \epsilon_r} g^{[0.958\epsilon_r/(0.706 + \epsilon_r)]}$$

The quantities $\Delta l_{oc}(u, \epsilon_r)$ and $\Delta l_{oc}(2u, \epsilon_r)$ represent open-end extension values for a single line with widths W and $2W$, respectively. The range of applicability of (B.96) is again defined by (B.62), and the associated accuracy is about 5%. It is found that line length extension Δl_e decreases asymptotically to $\Delta l_{oc}(u, \epsilon_r)$ as the spacing S/h is increased.

References

[1] Bahl, I. J., and R. Garg, "Simple and Accurate Formulas for Microstrip With Finite Strip Thickness," *Proc. IEEE*, Vol. 65, 1977, pp. 1611–1612.

[2] Gupta, K. C., et al., *Microstrip Lines and Slot Lines*, 2nd ed., Artech House, Norwood, MA, 1996.

[3] Hammerstad, E., and O. Jensen, "Accurate Models for Microstrip Computer-Aided Design," *1980 IEEE MTT-S Intl. Microwave Symp. Digest*, pp. 407–409.

[4] Hoffmann, R. H., *Handbook of Microwave Integrated Circuits*, Artech House, Norwood, MA, 1987.

[5] Kirschning, M., and R. Jansen, "Accurate Model for Effective Dielectric Constant of Microstrip With Validity Up to Millimeter-Wave Frequencies," *Electron. Lett.*, Vol. 18, 1982, pp. 272–273.

[6] Kompa, G., and R. Mehran, "Planar Waveguide Model for Calculating Microstrip Components," *Electron. Lett.*, Vol. 11, 1975, pp. 459–460.

[7] Owens, R., "Predicted Frequency Dependence of Microstrip Characteristic Impedance Using the Planar-Waveguide Model," *Electron. Lett.*, Vol. 12, 1976, pp. 269–270.

[8] Jansen, R., and M. Kirschning, "Arguments and an Accurate Mathematical Model for the Power Current Formulation of Microstrip Characteristic Impedance," *Arch. Elek. Ubertragung.*, Vol. 37, 1983.

[9] Wheeler, H. A., "Formulas for the Skin Effect," *Proc. IRE*, Vol. 30, 1942, pp. 412–424.

[10] Schneider, M. V., "Microstrip Lines for Microwave Integrated Circuits," *Bell Syst. Tech. J.*, Vol. 48, 1969, pp. 1421–1444.

[11] Hammerstad, E. O., and F. Bekkadal, *Microstrip Handbook*, ELAB Report STF44 A74169, Norwegian Institute of Technology, Trondheim, Norway, 1975.

[12] Bahl, I. J., and K. C. Gupta, "Average Power-Handling Capability of Microstrip Lines," *IEE J. Microwaves, Optics and Acoustics*, Vol. 3, 1979, pp. 1–4.

[13] Howe, H., Jr., "Strip Line Is Alive and Well. . . .," *Microwave J.*, Vol. 14, July 1971, p. 25.

[14] Pramanick, P., and P. Bhartia, "CAD Models for Millimeter-Wave Finlines and Suspended Substrate Microstrip Lines," *IEEE Trans. Microwave Theory and Techniques*, Vol. MTT-33, 1985, pp. 1429–1435.

[15] Svacina, J., "A Simple Quasi-Static Determination of Basic Parameters of Multilayer Microstrip and Coplanar Waveguide," *IEEE Microwave Guided Wave Lett.*, Vol. 2, 1992, pp. 385–387.

[16] Zhong, S.-S., G. Liu, and G. Qasim, "Closed Form Expressions for Resonant Frequency of Rectangular Patch Antennas With Multidielectric Layers," *IEEE Trans. Antennas and Propagation*, Vol. AP-42, 1994, pp. 1360–1363.

[17] Cohn, S. B., "Characteristic Impedance of Shielded Strip Transmission Line," *IRE Trans.*, Vol. MTT-2, 1954, pp. 52–55.

[18] Cohn, S. B., "Problems in Strip Transmission Lines," *IRE Trans.*, Vol. MTT-3, 1955, pp. 119–126.

[19] Wheeler, H. A., "Transmission Line Properties of a Strip Line Between Parallel Planes," *IEEE Trans. Microwave Theory and Techniques*, Vol. MTT-26, 1978, pp. 866–876.

[20] Gupta, K. C., R. Garg, and R. Chadha, *Computer-Aided Design of Microwave Circuits*, Artech House, Dedham, MA, 1981, Chap. 3.

[21] Hilberg, W., "From Approximations to Exact Relations for Characteristic Impedances," *IEEE Trans. Microwave Theory and Techniques*, Vol. MTT-17, 1969, pp. 259–265.

[22] Garg, R., and K. C. Gupţa, "Expressions for Wavelength and Impedance of Slot Line," *IEEE Trans. Microwave Theory and Techniques*, Vol. MTT-24, 1976, p. 532.

[23] Cohn, S. B., "Slot Line on a Dielectric Substrate," *IEEE Trans. Microwave Theory and Techniques*, Vol. MTT-17, 1969, pp. 768–778.

[24] Janaswamy, R., and D. H. Shaubert, "Characteristic Impedance of a Wide Slotline on Low Permittivity Substrates," *IEEE Trans. Microwave Theory and Techniques*, Vol. MTT-34, 1986, pp. 900–902.

[25] Kirschning, M., and R. H. Jansen, "Accurate Wide-Range Design Equations for Parallel Coupled Microstrip Lines," *IEEE Trans. Microwave Theory and Techniques*, Vol. MTT-32, 1984, pp. 83–90; see also corrections, *IEEE Trans.* Vol. MTT-33, 1985, p. 288.

[26] Cohn, S. B., "Shielded Coupled-Strip Transmission Line," *IRE Trans.*, Vol. MTT-3, 1955, pp. 29–38.

[27] Kirschning, M. R., R. H. Jansen, and N. H. L. Koster, "Accurate Model for Open End Effect of Microstrip Lines," *Electron. Lett.*, Vol. 17, 1981, pp. 123–125.

[28] Itoh, T., "Analysis of Microstrip Resonators," *IEEE Trans. Microwave Theory and Techniques*, Vol. MTT-22, 1974, pp. 946–952.

[29] Garg, R., and I. J. Bahl, "Microstrip Discontinuities," *Int. J. Electron.*, Vol. 45, 1978, pp. 81–87.

[30] Yu, C.-C., and K. Chang, "Transmission-Line Analysis of a Capacitively Coupled Microstrip-Ring Resonator," *IEEE Trans. Microwave Theory and Techniques*, Vol. MTT-45, 1997, pp. 2018–2024.

[31] Hoefer, W. J. R., "Equivalent Series Inductivity of a Narrow Transverse Slit in Microstrip," *IEEE Trans. Microwave Theory and Techniques*, Vol. MTT-25, 1977, pp. 822–824.

[32] Rizzoli, V., F. Mastri, and D. Masotti, "Modeling the Microstrip Impedance Step From Direct Measurements in the 1–27 GHz Band," *Microwave and Opt. Tech. Lett.*, Vol. 4, 1991, pp. 562–566.

[33] Hammerstad, E., "Computer-Aided Design of Microstrip Couplers With Accurate Discontinuity Models," *IEEE MTT-S Int. Microwave Symp. Digest*, 1981, pp. 54–56.

[34] Terman, F. E., *Radio Engineers Handbook*, McGraw-Hill, New York, 1950.

About the Authors

Ramesh Garg received a M.Sc. (Hons.) degree in physics from Panjab University, Chandigarh, India, in 1968 and a Ph.D. from the Indian Institute of Technology (IIT), Kanpur, India, in 1975. From 1975 to 1981, he was with the Advanced Centre for Electronic Systems at the IIT Kanpur, as a research engineer, working on transmission lines for microwave integrated circuits and computer-aided design.

Since 1981, Dr. Garg has been with the IIT Kharagpur (India), first as an assistant professor with the Radar and Communication Centre and now as a professor with the Department of Electronics and Electrical Communication Engineering. He was a visiting assistant professor at the University of Houston (University Park), from 1985 to 1987, and a research associate at the University of Ottawa (Canada) in 1994. His research activities have been primarily in the areas of microwave integrated circuits, leaky wave antennas, Gunn circuits, and microstrip antennas. He has published more than 50 papers in reference journals and conferences. He is a coauthor of the book *Computer-Aided Design of Microwave Circuits* (Artech House) and *Microstrip Lines and Slotlines* (Artech House).

Dr. Garg was a recipient of the outstanding paper award at the 1976 IEEE (India Section) Annual Convention. He has also received the Best Paper Award from the Institution of Electronics and Telecommunication Engineers (IETE), India, and the 1987 IIT Kharagpur Silver Jubilee Research Award. He was chairman of the IEEE Kharagpur Section in 1991. He is a Senior Member of the IEEE and a Fellow of the IETE, India.

Apisak Ittipiboon is a research scientist at the Communications Research Centre of Industry Canada in Ottawa. He holds a Ph.D. in electrical engineering

from the University of Manitoba. He has conducted research and development on novel printed antennas, dielectric resonator antennas, active phased arrays, and low-profile high-gain antennas. His interests include applied electromagnetics, millimeter-wave technology and devices, and mobile/wireless communications.

Dr. Ittipiboon has published more than 100 technical papers and holds several patents for antennas and microwave components. He has served as a reviewer for several journals and chaired technical sessions at conferences.

Inder Bahl received a Ph.D. in electrical engineering from the Indian Institute of Technology, Kanpur, India, in 1975. From 1969 to 1981, Dr. Bahl held positions at IIT Kanpur, the University of Ottawa, and the Defence Research Establishment Ottawa, Canada. He joined the ITT Gallium Arsenide Technology Center in 1981 and has been working on microwave and millimeter-wave GaAs ICs. In his present capacity as an executive scientist at M/A-COM, Dr. Bahl's interests are in the areas of device modeling, high-efficiency high-power amplifiers, 3-D MMICs, and the development of MMIC products for commercial and military applications.

Dr. Bahl is the author/coauthor of more than 130 research papers. He coauthored books such as *Microstrip Lines and Slotlines* (Artech House), *Microstrip Antennas* (Artech House), *Millimeter Wave Engineering and Applications* (John Wiley), *Microwave Solid State Circuit Design* (John Wiley), *Microwave and Millimeter-Wave Heterostructure Transistors and Their Applications* (Artech House), *Gallium Arsenide IC Applications Handbook* (Academic Press), and *RF and Microwave Coupled-Line Circuits* (Artech House). Dr. Bahl also contributed chapters to several handbooks. He holds 15 patents in the areas of microstrip antennas and microwave circuits. Dr. Bahl is an IEEE Fellow and a member of the Electromagnetic Academy.

Prakash Bhartia obtained his M.Sc. and Ph.D. degrees in electrical engineering from the University of Manitoba in Winnipeg. He served as an associate professor and assistant dean of engineering at the University of Regina until 1977. In that year he joined the Department of National Defence in Ottawa and served in a number of director-level positions. In 1992 he was appointed director general of the Defence Research Establishment Atlantic in Halifax and in 1998 as the director general of the Defence Research Establishment Ottawa, in which position he currently serves.

Dr. Bhartia has had considerable consulting experience with many companies while serving at the university and is the author of more than 150 papers in the areas of radar, microwave, and millimeter-wave circuits, components, and transmission lines. He is also the coauthor of a number of books, including

Microstrip Antennas (Artech House), *Millimeter Wave Engineering and Applications* (John Wiley), *E-Plane Integrated Circuits* (Artech House), *Microwave Solid State Circuit Design* (John Wiley), *Millimeter Wave Microstrip and Printed Circuit Antennas* (Artech House), *Microstrip Lines and Slotlines* (Artech House), and *RF and Microwave Coupled-Line Circuits*. He has also contributed chapters to other books and holds a number of patents. Dr. Bhartia is a Fellow of the Royal Society of Canada, a Fellow of the IEEE, and a Fellow of the Institution of Electrical and Telecommunications Engineers.

Index

Absorbing boundary conditions, 205–14
  analysis and design, 697–700
  analytical, 208–9
  computational expenses and, 220
  material, 209–10
  perfectly matched layer, 210–14
  stimulation methods, 207–8
  See also Finite-difference time-domain (FDTD) approach
Absorbing sheets method, 209
Active integrated antenna amplifiers, 661–63, 696–709
  defined, 661–63, 696–97
  gain, 699
  low-noise, 663, 706–9
  microwave circuit block diagram, 697–98
  radiation patterns, 710
  receiving case, 664
  reception applications, 697
  specified gain, 700–705
  stability, 699–700
  transmission applications, 697
  transmitting case, 664
  See also Active integrated antennas
Active integrated antenna oscillators, 660–61, 666–96
  60-GHz-band, 678
  configurations, 695–96
  defined, 660
  elements, 660
  feedback, 690–96
  four-FET oscillator, 696
  illustrated, 661
  one-port, 666–68
  patch integrated with diodes, 668–75
  patch integrated with FET, 661
  patch integrated with Gunn diode, 661
  patch integrated with two-port devices, 675–96
  push-pull oscillator, 696
  solid-state advantages/disadvantages, 660
  with strip line technology, 693
  two-port negative resistance, 675–79, 675–90
Active integrated antennas, 659–714
  amplifier type, 661–63
  basic functions, 659–60
  classification of, 659–66
  frequency conversion type, 663–66
  introduction to, 659
  oscillator/modulator, 665
  oscillator type, 660–61
  series feedback, 688
Active microstrip antennas, 222
  FDTD analysis, 198
  series feedback integrated, 688
  slot, 464
Active patch antenna integrated with diodes, 668–75
  circular, with IMPATT diode, 672
  design procedure, 668

design samples, 668–75
diode bias voltage, 671
EIRP vs. diode bias voltage, 676
Gunn diode, 669
H-plane radiation patterns, 672, 674
input impedance, 675
radiated power, 671
radiation patterns, 677
Active patch antenna integrated with two-port devices, 675–96
design procedure, 681–82, 691
design samples, 682–90, 691–96
feedback oscillator, 690–96
negative resistance oscillator, 675–90
Admittance
aperture, 110–18
boundary condition, 333–34
edge, 329–37
mutual, 118–21, 139
patch, 540
probe, 122–24
radiation, 137–40
wall, 138
Air gaps
circular disk antennas with, 356–57
circular ring antennas with, 386–88
mechanical tuning with, 306
thickness, 357, 386
Analytical ABC, 208–9
first-order, 208
for normally incident wave, 208
See also Absorbing boundary conditions
Analytical models, 73–150
aperture admittance, 110–18
aperture model, 476–78
cavity model, 76, 90–102
for coaxial probe, 121–25
comparison, 126–28
good, characteristics, 74
importance of, 73
introduction to, 73–78
multiport network model (MNM), 103–8
mutual admittance, 118–21
objectives, 73–74
radiation fields and, 108–10
solutions, 74
transmission line model, 76, 78–90
Anisotropic perfectly batched layer, 213
Anisotropic substrate, 765–68
biaxially, 765
defined, 765
permittivity, 765
uniaxially, 765
See also Substrates
Anisotropy
defined, 765
effects, 767
ratio, 766
Annular ring antennas
bandwidths, 538
calculation, 378
radiation, 625
shorting pin loaded, 600
See also Ring antennas
Annular slot antennas, 470–80
bandwidth, 477–78
cavity-backed, 477
circular polarization, 476
with coordinate system, 473
defined, 470
elements, 470
E-plane radiation patterns, 476
far-field radiation pattern, 472
geometry, 470, 473
H-plane radiation patterns, 476
radiation patterns, 475
radiation power patterns, 475
with reactive loading, 478
slot loading effect, 476–80
without load, 480
See also Slot antennas
Antenna fields, 75
Aperture
admittance, 110–18
conductance, 111–16
length, 558, 559
model, 76–78
proximity effect, 185
susceptance, 116–18
uniform field distribution, 111
width of, 76
Aperture-coupled microstrip antennas, 183, 539–40
analysis, 539
aperture length, 549

aperture shapes, 543, 545
bandwidth, 551
characteristic impedance, 539
dual-feed, circular patch, 634
elements, 539
equivalent circuit, 541, 546
exploded view, 540
impedance locus, 549
input impedance, 542, 543
input impedance, as function of frequency, 549
resonant frequency, 548
resonant resistance, 549, 550
series resonance behavior, 549, 551
stacked patches configuration, 552–70
wide-band, 558
Aperture-coupled microstrip feed, 28–29, 182–85
bandwidth, 28, 29
configuration, 26
equivalent circuit, 29
mathematical model, 182–85
proposal, 539
radiation, 28
See also Feeding techniques
Aperture coupling
antenna fabrication and, 268
modal expansion model of, 544–51
shapes, 543, 545
transmission line model, 540–44
Aperture field
Fourier transform of, 112, 113
magnetic, 113
Applications, 54–68
DBS, 62
GPS, 60–61
microstrip applicators for medicine, 67–68
mobile communications, 57, 65–66
radar, 66–67
satellite communications, 57–65
types of, 57
Arrays, 719–56
cavity model and, 97
circular-patch, 62
coaxial feed, 19
comb-line, 733–37
of composite elements, 501
corporate-fed, 728–30
cylindrical, 402
elements, spatial distribution of, 719
feed systems, 719–22
finite, 746–50
infinite, 737–46
introduction to, 719
linear, 570, 728–37
linearly polarized patches, 498–500
Lozenge, 733
monolithic integrated phased, 750–56
mutual coupling, 727–28
parallel feed, 720–22
planar, 570, 737–50
radiation characteristics, 719
resonant, 723–25
sequentially rotated, 525–30
series feeding of, 722–27, 730–32
square, 62, 528–29
transposed, 722–23
traveling-wave, 501–3, 520–24, 726–27
untransposed, 722
Yagi, 60
Asymmetric CPS, 793–95
with finitely thick substrate, 794–95
with infinitely thick substrate, 793–94
with infinitely wide strip, 795
See also Coplanar strips (CPS)
Asymmetric CPW, 792–93
with finite dielectric thickness, 792–93
without dielectric substrate, 792
See also Coplanar waveguides (CPW)
Average power handling capability (APHC), 777–78

Bandwidth, 306
annular ring, 538
annular slot antenna, 477–78
aperture-coupled microstrip antenna, 551
axial ratio, 283
center-fed dipole, 412
circular ring antenna, 383
dual-frequency PIFA, 652
end-fed dipole, 412
enhancement techniques, 524–30
half-power, 534

impedance, 283, 314, 349–51, 366, 388, 391, 535, 576, 603; 625
increasing, 284–85
microstrip dipole, 419–20
printed dipole, 406, 419–20
rectangular patch antenna, 282–85
substrate dielectric constant effect on, 286
substrate parameters effect on, 534–38
variation, 283–84, 288
VSWR, 279–80, 283, 297, 360, 420
Basis functions, 174–79
for calculating input impedance, 430
charge density, 195
computation time, 176
entire domain, 174
number of, effect of, 179
pulse-pulse, 176
PWL-pulse, 176
roof-top, 176, 195
subdomain, 174–75
for unknown current, 191
Beamwidth
circular disk antenna, 342, 364
dual-linearly polarized antenna, 630
half power, 276, 484
increasing, 276
linear TSAs (LTSAs), 483
rectangular patch antenna, 276
tapered slot antenna (TSA), 481–83
Bends, 16
Bessel-Fourier transform, 189
Bessel function, 319, 342, 452, 542
Boundary admittance, 334–35
Boundary conditions, 258, 337
absorbing, 205–14
admittance, 333–34
magnetic field, 319
in space domain, 236
Bow-tie antennas, 402
CPW-fed slot, 468–70, 472
double-sided, 402
radiation patterns, 416, 418
Broadbanding, 533–86
with coplanar parasitic elements, 570–76
impedance matching, 580–83
introduction, 533–34
multifrequency operation, 585–86
resistive loading, 583–85
with stacked elements, 552–70
through parasitic coupling, 552–76
Capacitance, 262
edge, 117
gap, 575
parallel plate, 117
Capacitive loading, 595
Capacitively coupled fingers, 732–33
defined, 732–33
disadvantage, 733
illustrated, 733
See also Linear arrays
Capacitively coupled slot antenna, 464
Cavities
interior region of, 91
lossy, 90, 257
magnetic wall of, 327
patch, 92, 258
Cavity-backed annular slot antenna, 477
Cavity model, 90–102
aperture fields ratio, 377
application to patch shapes, 96
array applications and, 97
circular disk antenna, 318–29
circular polarization prediction, 96
circular ring antenna, 366–68
comparison, 126, 127
conductor loss, 328
defined, 76, 90
dielectric loss, 95, 328
effective dielectric constant, 148
effective loss tangent, 94–95
effective permittivity, 148–49
eigenfunctions, 144–48
equivalent dimensions, 149–50
generalized, 97–102
input impedance, 94, 260–61
radiation loss, 328
rectangular patch antenna, 257–64
semicircular disk antennas, 360–61
stored energy, 95
triangular patch antenna, 431–32
See also Analytical models
Center-fed dipoles
bandwidth, 412
defined, 399

illustrated, 400
input impedance, 417
input resistance, 412
radiation resistance, 413
resonant resistance, 415
variation of VSWR, 420
See also Dipoles
Ceramic substrates, 760
Chain antenna, 504, 522
Characteristic impedance, 221
aperture-coupled microstrip antenna, 539
illustrated, 222
parallel strip line, 783
of segment patch, 279
symmetric T-junctions, 808
Characteristics calculations, 40–43
dissipated power, 41
input impedance, 42–43
radiated power, 40–41
stored energy, 41–42
Circular disk antennas, 317–60
with air gap, 356–57
analysis, 317–39
aperture fields ratio, 379
beamwidth, 342, 364
boundary admittance, 334–35
cavity electric field, 319
cavity model, 318–29
with coaxial feed, 332
computer-aided design, 359–60
configuration, 318, 325
conical pattern shape, 346
cross section, 357, 387
with cross-slot, 617, 619
design considerations, 339–60
dielectric cover effects, 357–58
directivity, 344–46, 379
disk metalization, 336
disk radius, 339–42
effective permittivity, 356
effect of finite substrate and ground plane size, 347–49
feed point location, 352–54
fields and currents, 318–20
fields excited by feed source, 325–27
gain, 344–46
generalized transmission line model, 337–39
geometry, 318
impedance bandwidth, 349–51
input impedance, 327–29, 330, 335–37
magnetic current distribution, 322
for microstrip feed, 354
mode matching with edge admittance, 329–37
on alumina substrate, 345
polarization, 354–56
quality factor, 349–51
radiated power, 342–44
radiation efficiency, 351–52
radiation fields, 320–24
radiation patterns, 342–49
radiation resistance, 342–44
RCS, 358–59
rectangular antennas vs., 364–66
resonant frequency, 324–25
slit loaded, 614, 617, 619
substrate selection, 339–42
superstrate effects, 357–58
transmission line equivalent circuit, 338
Circular electric current sheet, 34
far field, 38–40
far-zone vector potential, 38
illustrated, 34
Circularly polarized antennas, 493–530
arrays of composite elements, 501
bandwidth enhancement techniques, 524–30
chain, 504, 522
compact, 610–20
crank-type, 504, 521–22
dual, 636–37
dual-frequency, 633–36
dual-orthogonal fed patch, 494–96
elliptical patch, 495
introduction to, 493
linearly polarized patch arrays for, 498–500
microstrip spiral, 500–501
pentagonal patch, 495, 499
rampart line, 502, 504, 521–22
ring, 495
singly fed, 496–98, 503–15
square-loop line, 504, 523–24
square patch, 495

traveling-wave arrays, 501–3
triangular, 495, 499
types of, 493–503
See also Circular polarization
Circularly polarized circular antennas, 513–15
analysis, 514
circular CP elements, 515
equivalent circuit, 514
feeding system, 515
schematic diagrams, 515
standard patch, 515
See also Circularly polarized antennas
Circular patch antennas, 222
array, 62
for automobiles, 65–66
with four probe feeds, 61
integrated with hybrid feed, 614, 616
with PBG lattice, 55
radiation pattern, 65–66
unslotted, 632
Circular patches
surface electric current of TM mode of, 78
surface magnetic current for TM mode of, 77
two-port, 98
Circular polarization, 289, 356
annular slot, 476
cavity model and, 96
from circular disk, 356
dual, 498, 636–37
horizontal, 593
left-hand, 593
microstrip antenna perturbations for, 505
microstrip patch, 494–500
obtaining, 497, 594
patch design procedure, 512–13
perfect, 493
radiation, 498–500
radiation condition, 510–12
right-hand, 593
vertical, 593
See also Polarization
Circular ring antennas, 366–88
with air gap, 386–88
bandwidth, 383
cavity model analysis, 368
computed/measured input impedance comparison, 383, 384
copper loss, 380
current distributions, 371
with dielectric cover, 386
dielectric loss, 380
effective loss tangent, 381
eigenfunctions for, 145, 147
features, 366–68
field patterns, 371
fields and currents, 368–70
geometry, 86, 368
GTLM application to, 86–88
impedance bandwidth, 366, 385, 388
input impedance, 88, 381–85
input resistance, 383, 385
parallel plate model, 372
radiated power, 380
radiation fields, 375–80
radiation resistance, 381
resonant frequencies, 370–75, 388
with superstrate, 386
total energy stored, 380–81
wall admittance, 87–88
See also Ring antennas
Circular sector antennas, 360–66, 388
analysis, 388
eigenfunctions, 145, 147, 363, 388
geometry, 388
GTLM analysis, 363
impedance bandwidth, 388
rectangular patch antenna comparison, 388
See also Ring antennas
Cladding material, 769–70
Coaxial feed, 16–19
advantages, 19
array, 19
circular disk antenna with, 332
input power computation and, 42
modeling, 18–19
probe, 17–18
See also Feeding techniques
Coaxial probe model, 121–25
junction configuration, 123
reactance, 121
Colinear dipoles, 425
Comb-line arrays, 733–37
aperture distribution, 735
array pattern, 736
configuration, 734
design steps, 735–37

equivalent circuit, 734
formation, 733
stub spacing, 735
transposed arrangement, 736
traveling-wave configuration, 733
See also Linear arrays
Compact circularly polarized antennas, 610–20
circular disk with cross-slot, 617, 619
circular patch integrated with hybrid feed, 614, 616
loaded square ring, 614, 615
performance, 620
realization, 611
short loaded rectangular patch, 614, 616
slit loaded circular disk, 614, 617, 619
slit loaded square patch, 614, 615
traveling-wave curved microstrip antenna, 618, 619–20
triangular patch with cross-slot, 618, 619
See also Circularly polarized antennas
Compact dual-frequency antennas, 637–53
PIFA, 646–53
pin-loaded, 637–43
slot-loaded, 643–46
Compact linearly polarized antennas, 607–10
annular ring, 613
circular patch, 613
circular sector, 613
C-shaped patch, 612
dual-patch, 613
geometries, 610, 611
H-shaped patch, 612
performance, 612–13
rectangular patch, 612
top view of, 611
triangular patch, 613
Compact patch antennas, 607–20
circularly polarized, 610–20
linearly polarized, 607–10
Composite material substrates, 763
defined, 763
dielectric constant of, 764
See also Substrates
Computer-aided design
circular disk antennas, 359–60
rectangular patch antennas, 297–99
Conductance
aperture, 111–16
load, 110–11
mutual, 118–19, 670
radiation, 111, 115, 116
resonant radiation, 278, 343
self-, 118, 670
total, 670
Conductor-backed CPW, 792
Conformal antennas, 769
Conformal transformation, 268
Continuity equation, 239
Coplanar gap-coupled resonators, 570–76
analysis, 575–76
in circular geometry, 574
concept, 570
configurations, 571–72, 573–75
design, 576
equivalent circuit, 575
gap capacitances, 575
geometry, 575
impedance bandwidth, 576
Coplanar microstrip feeds, 19–27
defined, 19–24
designing, 27
edge-coupled, 24
fabricating, 27
gap-coupled, 22, 24
mathematical model, 182
modeling, 24–27
Coplanar strips (CPS), 793–95
asymmetric, with finitely thick substrate, 794–95
asymmetric, with infinitely thick substrate, 793–94
asymmetric, with an infinitely wide strip, 795
design, 793–95
geometry, 403
symmetric, with finite dielectric thickness, 795
symmetric, with infinitely thick substrate, 793
Coplanar waveguide (CPW) feed, 29–31, 402
advantages, 31
configurations, 30
defined, 29
loop antenna, 467
slot antenna, 467
See also Feeding techniques

Coplanar waveguides (CPW)
analysis assumptions, 790
asymmetric, 792–93
conductor-backed, 792
cross sections, 789–90
design, 789–93
effective dielectric constant, 791
filling fraction, 791
with finite dielectric thickness, 791
with finite dielectric thickness and cover shield, 792
with finite dielectric thickness and finite width ground planes, 791
with infinitely thick substrate, 791
Corporate-fed arrays, 728–30
advantages, 728
configuration illustration, 729
defined, 728
insertion loss, 728
symmetrical, 729
See also Linear arrays
Coupled microstrip lines, 795–98
asymmetric, 798
cross section, 796
design, 795–98
discontinuities in, 810
even mode, 795, 796–97
odd mode, 795, 797–98
symmetric, 795
Coupled strip lines, 798–800
cross section, 799
synthesis, 799–800
zero thickness, 799
CPW-fed oscillating antennas, 686
CPW-fed slot antennas, 463–70
aperture, 463, 467
bow-tie, 468–70, 472
capacity coupled, 464
center-fed, 464
configurations, 471
folded-slot, 465–67
illustrated, 464
inductively coupled, 464
offset-fed, 464
for power combining, 468
transition, 463
unidirectional, 467–68
See also Slot antennas
Crank-type microstrip line antenna, 504, 521–22
Cross-polar components, 289–90
in E plane, 355
in H plane, 355
level, 290
minimizing, 289
variation of, 290
Cross-shaped patch, 97, 99
Current density, 4, 5

Dielectric anisotropy, 766
Dielectric constant
effective, 220, 221
effect on impedance bandwidth, 535
Dielectric cover
circular disk antennas, 357–58
circular ring antennas, 386
rectangular patch antennas, 292–93
Dielectric loss, 163
cavity model, 95
determining, 41
strip line, 785
Dipoles, 9–13, 222
alternative approach for input impedance, 413–15
center-fed, 399
colinear, 425
configurations, 11–13
defined, 9
double-folded, 578, 580
end-fed, 411, 412
feed design considerations, 403–9
feed mechanism, 9
finite planar array of, 746–50
half-length, 409
horizontal electric (HED), 187, 226, 240
infinite arrays of, 737–42
input impedance, 409–16
input resistance, 409
microstrip, 399
moment method approach for input impedance, 416
mutual coupling between, 422–25
mutual impedance between, 424
printed, 399
radiation patterns, 416
radiation resistance, 414

resonant length, 416–19
scalar potential, 239
separation distance between, 419
stacked, 419
surface current, 239
symmetrical cylindrical, 413–15
Direct broadcast satellite (DBS) application, 62
Directive gain, 277, 287, 292
Directivity
circular disk antenna, 344–46, 379
defined, 276, 344
maximum, 345
rectangular patch antenna, 276–77
resonant frequency vs., 346
tapered slot antenna (TSA), 481
variation, 288
Discontinuities, 800–810
bends in microstrips, 807
from branch point, 241
in coupled microstrip lines, 810
gaps in microstrip lines, 804–5
lumped equivalent circuit models for, 801–3
of magnetic fields, 140
in microstrip lines, 800–810
notch, 805–6
open ends, 800–804
of patches, 108
short-circuited posts in microstrips, 809
shorted ends, 809–10
steps in width, 806–7
symmetric T-junctions, 807–8
voltage, 447, 449–50
Discrete Fourier transform (DFT), 217
Discretization of current, 162
Disk radius
effective, 340
as function of frequency, 341
metalization, 340
See also Circular disk antennas
Disks
eigenfunctions for, 145, 146
elliptical, modeled as circular, 150
with narrow slot, 145, 147–48
Dispersion, 292
defined, 203
diagram, 52, 53, 204
due to discretization, 205
effective permittivity and, 269
effects, 268
numerical, 203–5
Dissipated power calculation, 41
Double-folded dipole antenna, 578
Dual circularly polarized antennas, 636–37
feed location loci for, 640
realization, 636
stacked on shorted annular ring, 640
See also Circularly polarized antennas
Dual-frequency circularly polarized antennas, 633–36
compact, 637–53
configuration illustrations, 638
configurations, 634
defined, 634
geometry, 637
isolation and axial ratio with frequency for, 639
slotted cross-patch, 635
slotted-square, 635
top view, 636
See also Circularly polarized antennas
Dual-frequency microstrip antennas, 625–53
circularly polarized, 633–37
dual-linearly polarized, 630–33
implementations, 625
PIFA, 646–53
pin-loaded, 637–43
resonant frequencies, 627
shorting pins and, 625
single-feed, 630
slot-loaded, 643–46
slot loaded patch configuration, 627
slotted patch, 626–30
top view of, 626
Dual-frequency PIFA, 646–63
bandwidth, 652
electric field distribution, 649, 653
mutual coupling, 650
radiation patterns, 651
return loss, 652
two-port, 646, 648
See also Planar inverted-F antenna (PIFA)
Dual-linearly polarized antennas, 630–33
beamwidths, 630

defined, 630
stacked patch configuration, 633
Dual-orthogonal fed circularly polarized patch antennas, 494–96, 515–20
180-degree hybrid, 518
configurations, 496
defined, 515–16
design procedure, 520
illustrated, 495
power-divider circuits, 494
quadrature hybrid, 516–17
T-junction power divider, 519–20
Wilkinson power divider, 518–19
See also Circularly polarized antennas

Edge admittance
mode matching with, 329–37
network (EAN), 105–8
Edge capacitance, 117
Edge susceptance, 116–18
Effective loss tangent
cavity model, 94–95, 328
circular ring antenna, 381
series-fed antenna arrays, 731
Eigenfunctions, 258
for circular ring, 145, 147
for circular sector, 145, 147, 363, 388
for disk, 145, 146
for disk with narrow slot, 145, 147–48
orthonormalized, 259
for rectangle, 144, 145
for right-angle isosceles triangle, 145, 146
for thirty-/sixty-degree triangle, 145, 146
for triangle, 144, 145
Electric-field Green's functions, 159, 186, 188, 230
Electric surface current model, 273–75
Electromagnetic coupling, 28, 383
Electromagnetics, 358
End-fed dipoles
bandwidth, 412
impedance transformation of, 411
radiation resistance, 413
See also Dipoles
Entire domain basis functions (EB)
defined, 174
illustrated, 175
for rectangular patch, 174
set, 174
use of, 174
See also Basis functions
Equivalent circuits
aperture-coupled microstrip antenna, 541, 546
aperture-coupled microstrip feed, 29
circularly polarized circular antenna, 514
comb-line array, 734
feeding techniques, 21–26
GTLM, 140
lumped, frequency variation of, 454
for microstrip discontinuities, 801–3
microstrip-fed slot antennas, 446–47
microstrip feeds, 21–26
microstrip patch antenna with perturbation, 509
nonuniform transmission line, 134–37
of radiating gap, 575
transmission line, of circular disk antenna, 338
transmission line, of rectangular patch feed, 541
traveling-wave coupling, 727
Equivalent current densities, 6–7
Even mode
current distribution, 555–56
defined, 554
electric/magnetic field distributions, 557
equivalent circuit, 557
See also Stacked patch configuration
Excitation
across array, 731–32
for circuit modeling problems, 214–15
current, 259, 361
for eigenvalue problems, 214
electric fields, 220
Gaussian pulse, 220
source, 215
tapered slot antenna (TSA), 486–87
voltage shape, 216

Fabrication
antenna chemicals and, 768
desirable substrate characteristics for, 768–70
errors, 299
tolerance, 301

Far-zone fields, 168–69
Far-zone vector potential, 36, 38
Fast Fourier transform (FFT), 217
Feedback active patch antenna oscillators, 690–96
block diagram, 690
defined, 690–91
design procedure, 691
design samples, 691–96
FET active patch configuration, 691
final structure, 694
illustrated, 694
with strip line technology, 693
See also Active integrated antenna oscillators
Feed inductance, 264
Feeding phase shift, 528
Feeding techniques, 14–31
aperture-coupled microstrip feed, 28–29
coaxial feed/probe coupling, 16–19
comparison, 32
coplanar waveguide feed, 29–31
equivalent circuits, 21–26
gap-coupled, 22, 24
microstrip (coplanar) feeds, 19–27
noncoplanar, 27–31
proximity (electromagnetically) coupled microstrip feed, 28
selection, 16, 538–51
Feed point location, 287–89, 297
change in, 287
circular disk antenna, 352–54
determination, 289
input impedance variance and, 352
rectangular patch antenna, 287–89
Feed reactance, 264
Ferrimagnetic substrates, 760–63
FETs
active microstrip antennas using, 663
hybrid patch antenna integrated with, 688
oscillating active patch antenna, 692
patch integration with, 661
transconductance mixer, 711
Finite-difference time-domain (FDTD) approach, 74, 158, 197–224
3-D, 214
absorbing boundary conditions, 205–14
active microstrip antenna analysis with, 198
advantages, 198
applications of, 221–24
complex antenna analysis with, 198
computer resource requirements, 198
defined, 197–98
excitation and source modeling, 214–17
extraction of frequency-domain characteristics from time-domain data, 217–19
formulation of, 199–202
Green's function and, 158
numerical dispersion, 203–5
numerical techniques vs., 198
propagation in microstrip line, 220–21
source plane representation, 215
stability criteria, 203
truncation of domain by exterior region, 207
Yee's cell geometry in, 200
See also Full-wave analysis
Finite planar arrays, 746–50
defined, 746
efficiency vs. E-plane scan angle, 750
geometry, 746, 747
impedance matrix, 747
reflection coefficient vs. scan angle, 748, 749
scan blindness, 749
single expansion mode, 747
voltage vector elements, 748
See also Planar arrays
Folded-slot antenna, 465–67
Four-FET oscillator, 696
Fourier cosine series, 333
Fourier transform, 163, 227, 235
of aperture field, 112, 113
of basis current density, 231
of boundary conditions in space domain, 236
discrete, 217
fast, 217
Maxwell's equations, 227
Four-slot radiation models, 79

Frequency agile microstrip antennas, 595–98
  defined, 595
  optical tuning, 598
  varactor-tuned, 595–98
Frequency conversion active integrated antennas, 663–66, 709–14
  applications, 709
  defined, 663–64, 709
  examples, 664–65
  mixers, 709–14
  oscillator/modulator, 665
  self-oscillating mixer, 712–14
  transconductance mixer, 711–12
  See also Active integrated antennas
Fringing fields, 266
Full-wave analysis, 157–246, 602
  accuracy, 158
  benefits, 157–58
  completeness, 158
  computation cost, 158
  FDTD, 197–224
  features, 158
  MPIE, 186–97
  spectral-domain, 158, 159–86
  types of, 158–59
  versatility, 158

Gain
  active integrated antenna amplifier, 699
  directive, 277, 287
  high, 481
  polygonal ring antenna, 391
  rectangular patch antenna, 276–77
  of rectangular patch as function of ground plane size, 295
  stacked patch aperture-coupled antenna, 567
Galerkin procedure, 192, 231, 787
Gap-coupled microstrip feed, 22, 24
Gaps in microstrip lines, 804–5
Gaussian pulse, 216
  bandpass, 216
  excitation, 220
Generalized cavity model, 97–102
  comparison, 127
  electric field determination, 98
  input impedance, 102
  multiport connection method, 100–101
  resonant frequency, 101–2
  segmentation, 98–100
  See also Cavity model
Generalized transmission line model (GTLM), 85–88
  accuracy, 88
  application of, 85, 128
  application to circular ring microstrip antenna, 86–88
  circular disk antenna, 337–39
  circular sector antenna, 363
  comparison, 127
  defined, 85
  equivalent circuit of patch antenna, 140
  input impedance, 140–42
  introduction to, 128–31
  nonuniform transmission line equivalent circuit, 134–37
  radiation admittance, 137–40
  theoretical background, 128–44
  transmission line equations, 132–34
  transmission model vs., 85
  variation of fields, 85
  See also Transmission line model
Geometrical theory of diffraction (GTD), 296
Global positioning system (GPS) application, 60–62
  bandwidth requirement, 633–34
  dual-band/broadband multilayer structure for, 569–70
  operation frequency, 633
Green's functions, 40, 93, 98
  dyadic, 162
  electric field, 159, 186, 188, 230
  FDTD approach and, 158
  free-space, 143, 383, 384
  half-plane, 482
  for magnetic field, 143
  for multilayered geometry, 231
  obtaining, 226
  potential, derivation of, 234–40
  potential, in space domain, 189–90
  potential, in spectral domain, 187–89
  for a segment, 102

  in space domain, 230
  spectral-domain full-wave analysis and, 159, 184
  of stratified media, 143
Ground planes
  effect, 376
  extension, 295
  finite size, effects of, 293–96, 347–49
  finite width, 791
  resonant frequency and, 295
  size, resonant frequency and, 295–96
Gunn diodes, 668
  active patch antenna integrated with, 669
  patch integration with, 661
  power vs. frequency performance, 662
  rectangular patch with impedance inverter integrated with, 674

Half-wave rectangular patch antennas
  Q factor, 310
  radiation resistance, 309
Hankel function, 246
Hankel integral transform, 189
Helmholtz equations, 234–35, 237, 238
Horizontal electric dipole (HED), 187
  geometry of, 226
  y-directed, 240
H-shaped patch, 97
Huygen field equivalence principle, 4

IMPATT diodes
  circular patch antenna integrated with, 672
  impedance, 673
  location of, 673
  power vs. frequency performance, 662
Impedance bandwidth, 283
  circular disk antenna, 349–51
  circular ring antenna, 366, 385, 388
  circular sector antennas, 388
  coplanar gap-coupled resonator, 576
  dielectric constant effect on, 535
  loaded microstrip antenna, 603
  patch antenna, 534
  planar inverted-F antenna (PIFA), 625
  polygonal ring antenna, 391
  stacked patch antennas, 314
  substrate thickness and, 535
Impedance matching, 580–83
  of aperture-coupled stacked antenna, 565
  design, 581
  embedded in patch, 581–82, 584
  network, 580–81
  quarter-wave transformers for, 580
  tuning stubs for, 580
  See also Broadbanding
Impedance matrix
  block submatrices, 232
  efficient computation of, 196–97
  elements, 194, 231–32
  evaluation, 196
  multiport, 104
Impedances
  computing, 218–19
  matching, 16
  mismatched, 605
Inclined slot, 453–55
  equivalent circuit, 453
  geometry, 453, 457
Inductance
  feed, 264
  series, 282
Inductively coupled slot antenna, 464
  electric/magnetic fields, 465
  illustrated, 464
Infinite arrays of printed dipoles, 737–42
  current distribution, 738
  design considerations, 740–42
  diagram, 738
  element positions, 737
  grid spacings, 741
  reflection coefficient vs. scan angle, 742
  scan blindness, 740
  studies, 741
  See also Planar arrays
Infinite arrays of rectangular patches, 742–46
  defined, 742
  geometry, 742, 743
  grid spacings, 745
  integration, 744
  reflection coefficient vs. scan angle, 746
  scan blindness, 745
  scan reflection coefficient, 745
  studies, 745
  See also Planar arrays

Input impedance, 19
  active patch antenna integrated with diodes, 675
  aperture-coupled microstrip antenna, 176, 542, 543
  aperture length effect on, 558, 559
  basis functions for calculating, 430
  calculation, 42–43
  cavity model, 94, 260–61
  center-fed dipole, 417
  circular disk antenna, 327–29, 330, 335–37
  circular ring antenna, 381–85
  circular ring microstrip antenna, 88
  dipole, 409–16
  feed point location and, 352
  frequency vs., 124–25
  as function of dipole length, 409, 410
  as function of frequency, 297
  as function of frequency and feed position, 433
  as function of lower patch size, 560
  as function of lower substrate thickness, 563
  as function of upper patch size, 561
  as function of upper substrate thickness, 564
  generalized cavity model, 102
  GTLM, 140–42
  linear TSAs (LTSAs), 483–84
  moment method approach, 416
  parallel R-L-C network, 263
  patch length and, 298
  PIFA antenna, 621
  probe-fed patch microstrip antenna, 257, 263
  rectangular patch antenna, 178, 255
  ring antenna, 366
  semicircular disk antenna, 365
  series-fed array, 731
  shorting pins and, 600
  slot antenna, 444, 469
  spectral-domain full-wave analysis, 164–66
  tapered slot antenna (TSA), 481, 483–86
  total, 142
  triangular patch antenna, 430–32
  two-port negative resistance active patch antenna oscillator, 683
Input power, 285, 351
Input resistance, 298, 352, 354
  circular ring antenna, 383, 385
  dipole, 409
  triangular patch antenna, 434
  two-port negative resistance active patch antenna oscillator, 684
Integrations, 171–73, 323
  alternative path of, 243
  numerical, 171, 172–73
  over interval, 171–73
International Maritime Satellite System (INMARSAT), 58
Inverted microstrip line, 779–81

Junctions, 16

Known expansion functions, 231

Land mobile systems, 65–66
Leap frog algorithm, 201
Linear arrays, 570, 728–37
  with capacitively coupled fingers, 732–33
  comb-line, 733–37
  corporate-fed, 728–30
  design of, 728–37
  excitation across, 731–32
  with microstrip patches, 728–32
  relative phase distribution, 732
  with sequential feeding, 527
  series-fed, 730–31
Linearly polarized patches, 498–500
  arrangement, for circular polarization, 500
  arrays, 498–500
Linear TSAs (LTSAs), 480–84
  beamwidth, 483
  dielectric supported, 482
  input impedance, 483–84
  opening angles, 481
  Zucker's curve, 482
  See also Tapered slot antennas (TSA)
Load admittance, 110
Load conductance, 110–11
Loaded microstrip antennas, 591–653
  forms, 592

  frequency agile, 595–98
  impedance bandwidth, 603
  introduction to, 591–92
  loading effect of shorts, 599–607
  lower resonant frequency variation, 603
  polarization diversity, 592–95
  radiation pattern control, 599
  short, rectangular patch, 614
  slit, circular disk, 614, 617, 619
  square patch, 614, 615
  square ring, 614, 615
Load susceptance, 110
Local oscillator (LO), 664
Log-periodic antenna, 574
Loop antenna
  configurations, 467
  far-field pattern, 470
  radiation efficiency, 468
Lorentz gauge condition, 187, 234, 237
Lossy cavities, 90, 257
Lossy transmission line model, 88–90
  comparison, 127
  defined, 88–90
  radiation admittance, 90
  See also Transmission line model
Low-cost low-loss substrates, 763–65
Low earth-orbiting satellite systems, 60
Low-noise active integrated microstrip antenna amplifier, 706–9
  bipolar transistor for, 709
  circuit block diagram, 709
  constant noise figure circles, 706–7
  defined, 706
  design samples, 707–9
  illustrated, 708
  See also Active integrated antenna amplifiers
Low-sidelobe case, 481
Lozenge array, 733

Manpack radar, 66
Marine radar, 66
Material ABC, 209–10
Mathematical model of excitation, 179–85
  aperture-coupled microstrip feed, 182–85
  microstrip edge feed, 180–82
  probe feed, 180
  See also Excitation
Matrix elements
  impedance, 194
  numerical evaluation of, 169–73
Maxwell's equations, 131, 158
  curl, 199, 203, 213
  differential form, 200
  divergence, 199
  source-free, 226
Mechanical tuning
  with an adjustable air gap, 306
  rectangular patch antenna, 302–6
  scheme illustrations, 304–5
  with shorting posts or pins, 303–6
  with stubs, 303
Medicine patch applicators, 67–68
Method of moments, 163
  defined, 163
  integral equation solution with, 191–97
  results, 163
Microstrip antennas
  active, 198
  advantages, 2
  analysis steps, 160
  analytical models for, 73–150
  aperture-coupled, 539–40
  applications, 54–68
  broadbanding of, 533–86
  center positions loci, 408
  characteristics calculations, 40–43
  charge distribution, 4
  circular disk, 317–60
  circularly polarized, 493–530
  circular sector, 360–66
  comparison, 16
  configurations, 2, 8–14
  current density, 4, 5
  dipoles, 9–13, 399–425
  dual-frequency, 625–53
  full-wave analysis, 157–246
  general network model, 262
  inhomogeneous dielectric, 7
  limitations, 2–3
  loaded, 591–653
  maturation of, xxi
  miniaturization, 47–48
  patch, 4, 8–9
  probe-fed, 256–57
  radiation mechanism, 3–8

radiation pattern control, 599
rectangular, 253–314
ring, 366–94
semicircular disk, 360–66
slot, 13, 14, 441–88
stacked, 222
structure complication, xxii
traveling-wave, 13–14, 15
triangular patch, 425–36
wide-band, 524–25
Microstrip bends, 807
Microstrip circuits, xxi
Microstrip dipoles
bandwidth, 419–20
defined, 399
design of, 416–22
effective dielectric constant, 419
feeds for, 406–9
illustrated, 402
microstrip patches vs., 403
proximity-coupled, 419
proximity coupling, 407
radiation efficiency, 421–22
resonant length, 416–19
resonant resistance, 421
superstrate, 408
See also Dipoles
Microstrip edge feed, 180–82
Microstrip-fed slot antennas, 441–63
center-fed, 443
cross polarization, 442
cylindrical, 463
defined, 441–42
design of, 455–57
determination of network quantities, 447–53
discontinuity voltage, 449–50
equivalent circuit, 446–47
inclination angle effect, 458
inclined slot, 453–55
introduction to, 441
narrow slot, 447
off-center, 445–46, 455
offset, geometry, 462
radiation conductance, 447–49
radiation patterns, 457–63
results, 453
return loss, 459
series impedance, 455, 456
turns ratio, 450–53
See also Slot antennas
Microstrip lines
average power handling capability (APHC), 777–78
bends in, 807
characteristic impedance, 772–74
configuration, 772
coupled, design, 795–98
coupled, open-end discontinuity, 810
design, 771–79
discontinuities, characterization of, 800–810
gaps in, 804–5
guide wavelength, 774–75
inverted, 779–81
losses, 776
maximum average power, 777
notch, 805–6
numerical methods for characterization, 771
open ends, 800–804
peak power handling capability (PPHC), 778–79
planar waveguide model, 775–76
power handling capability, 777
short circuits in, 809
shorted ends in, 809–10
steps in width, 806–7
with superstrate, 781–89
suspended, 779–81
symmetric T-junctions, 807–8
See also Planar transmission lines
Microstrip patch antennas (MPA), 8–9
aperture-coupling, 182–85
circular, 55
circularly polarized, 494–500
configurations with separable geometry, 128, 129
defined, 8
dual-orthogonal fed circularly polarized, 494–96
effective permittivity, 148–49
equivalent dimensions, 149–50
gain, 8
geometry of, 222–23
linearly polarized arrays, 498–500

magnetic wall model, 92
microstrip line-fed, 223
patch energization, 4
PBG, 51–54
with perturbation, 509
possible geometries, 10
proximity coupling, 182
radiation characteristics, 8
radiation conductance, 447
radiation patterns, 80
rectangular, 54
return loss, 224
shapes, 9
singly fed circularly polarized, 496–98
stacked, 96
stored energy, 41–42
time-domain response, 225
Microstrip patches. *See* Patches
Microstrip radiators, 1–68
applications, 54–68
feeding techniques and modeling, 14–31
introduction to, 1–8
photonic bandgap structures, 47–54
surface waves, 43–47
Microstrip reflectarray, 62–65
defined, 62
forms, 64
photograph, 64
Microstrip spiral antennas, 500–501
Microstrip traveling-wave antennas (MTAs)
configurations, 15
defined, 13
main beam, 13
use of, 13–14
See also Traveling-wave arrays
Microwave integrated circuits (MICs), 663
Microwave monolithic integrated circuits (MMICs), 29
Mixed-potential integral equation (MPIE) analysis, 186–97
applications, 197
efficiency, 186
integral equation solution, 191–97
numerical efficiency, 197
performance, 197
results for potentials, 190–91
in space domain, 189, 442
starting point, 186
See also full-wave analysis
Mixers
design of, 710
transconductance, 711–12
types of, 711
Mobile communications, 57, 65–66
antennas for land mobile systems, 65–66
antennas for pedestrians, 66
antenna types, 57
See also Applications
Mobile Satellite (MSAT) system, 58
Modeling
coaxial feed, 18–19
coplanar microstrip feeds, 24–27
FDTD excitation/source, 214–17
Moment method solution, 231–34
basis currents, 233
impedance matrix, 232
for input impedance, 416
known expansion functions, 231
matrix equation, 231
voltage vector, 232–33, 234
Monolithic integrated phased arrays, 750–56
advantages, 751
architectures, 753–56
array feed network selection, 751
brick construction, 754
components, 753
concept, 751
configurations, 755–56
cost, 751
design considerations, 751–53
dipole array with brick architecture, 755
multilayer array with tile architecture, 755
scan blindness, 751
single-layer array with tile architecture, 756
substrate selection, 751
subsystem and technology requirement, 752
thermal management, 753
tile construction, 754
See also Arrays

Monolithic microwave integrated circuits (MMICs), 663
Multifrequency operation, 585–86
  geometry, 586
  radiation patterns, 585
  See also Broadbanding
Multimoding techniques, 551–78
  antenna with two independent modes, 576, 579
  broadbanding with coplanar parasitic elements, 570–76
  broadbanding with stacked elements, 552–70
  double-folded dipole antenna, 578
  rectangular patch with U slot, 577, 580
Multiport impedance matrix, 104
Multiport network model (MNM), 94, 103–8
  advantages, 108
  applications, 108
  comparison, 127
  EAN, 105–8
  illustrated, 103
  MCN, 105–8
  number of ports, 103
  rectangular patch antenna, 103
  rectangular patch antenna incorporating mutual coupling, 106
  See also Analytical models
Mutual admittance, 118–21
  closed-form expressions, 118
  stationary expression, 143
  between two walls, 139
  wall, 142–44
Mutual conductance, 118–19
Mutual coupling
  arrays, 727–28
  in broadside direction, 422
  calculation of, 422
  determination geometry, 119
  between dipoles, 422–25
  dual-frequency PIFA, 650
  MNM incorporating, 106
  results comparison, 108
  transmission line model with, 81, 82–85
Mutual coupling network (MCN), 105–8
  calculation, 120
  between patches, 107
Mutual susceptance, 120–21

Newton-Raphson procedure, 360
Noncircular ring antennas, 389–94
  polygonal ring, 389–91
  properties, 389
  square ring, 389, 390
  types of, 389
  See also Ring antennas
Noncoplanar microstrip feeds, 27–31
Nonuniform transmission line
  equivalent circuit, 134–37
  section illustration, 136
Normalization conditions, 258
Notches, 805–6
Numerical dispersion
  defined, 203
  determining, 204
  minimizing, 204–5
  See also Dispersion

Odd mode
  current distribution, 555–56
  defined, 554
  See also Stacked patch configuration
Off-centered microstrip-fed slot antenna, 445–46
  results, 453
  top/side views, 445
One-port active integrated antenna oscillators, 666–68
  reflection coefficients, 667
  schematic diagram, 667
Optical-tuned microstrip antennas, 598
  defined, 598
  illustrated, 596
Organization, this book, xxii–xxv
Oscillator/modulator active integrated antenna, 665

Parallel feed, 720–22
  asymmetrical configuration, 721
  one-dimensional, 720–21
  for radiating inclined beams, 722
  symmetrical configuration, 721
  two-dimensional, 721–22, 723, 724
Parallel plate model, 372, 373

Parallel R-L-C network, 261, 263
Parallel strip line, 782–83
  characteristic impedance, 783
  cross section of, 783
  defined, 782
  design, 782–83
Parseval's theorem, 448
Partial differential equations, 199
Patch applicators, 67–68
  defined, 67
  illustrated, 67
Patches
  admittance, 540
  cavities, 92, 258
  circular, 77, 78, 98
  CP, 512–13
  cross-shaped, 97
  discontinuity, 108
  equivalent current densities on, 6
  half-wave, 307
  H-shaped, 97
  length, 266, 297, 298
  linear array design with, 728–32
  MCN between, 107
  metalization, 4
  quarter-wave, 307, 308–11
  radiation, 269
  rectangular, 7, 76–77, 174, 178, 291–92, 577, 580, 600, 674, 742–46
  resonant length of, 602
  shape selection, 538
  shorting pin on center line of, 605–7
  size, 265–69
  suspended, 582
  width, 265–66
Peak power handling capability (PPHC), 778–79
Pedestrians, antennas for, 66
Perfectly matched layer ABC, 210–14
  anisotropic, 214
  defined, 210
  finite thickness, 211
  interface, 211–12
  oblique incidence of waves, 213
  region portions, 210, 211
  See also Absorbing boundary conditions
Perfectly matched uniaxial medium, 214
Periodic loading, 50–51
Photonic bandgap structures, 47–54, 599
  defined, 48
  dispersion diagram, 52, 53
  measured *S* parameters, 51
  patch antenna design, 51–54
  periodic loading types, 50–51
  transmission coefficient, 49, 51
Piecewise sinusoidal (PWS) pulse functions, 175
PIN diodes, 598
Pin-loaded dual-frequency antennas, 637–43
  behavior, 640
  circular, 642
  frequency ratio, 640
  geometry, 641, 642
  triangular, 641
  See also Compact dual-frequency antennas
Planar arrays, 737–50
  categories, 737
  design of, 737–50
  finite arrays of printed dipoles, 746–50
  formation, 737
  infinite arrays of printed dipoles, 737–42
  infinite arrays of rectangular patches, 742–46
  uses, 737
  See also Arrays
Planar inverted-F antenna (PIFA), 66, 620–25
  applications, 620
  capacitively loaded, 621
  defined, 620
  design approach, 624–25
  for digital communication system (DCSs), 621
  dual-frequency, 646–53
  impedance bandwidth, 625
  input impedance curves, 622
  input impedance variations, 621
  mounting, 621
  radiation patterns, 622, 623
  side view, 620
  size determination, 620
  size reduction, 620–21
  slit loaded, 624

Planar transmission lines, 771–810
coplanar strips, 793–95
coplanar waveguide, 789–93
coupled microstrip lines, 795–98
coupled strip lines, 798–800
microstrip line, 771–79
parallel strips line, 782–83
slot line, 786–89
strip line, 783–85
suspended and inverted, 779–81
Planar waveguide model, 775–76
Polarization
associated with modes, 592
changing, 289
circular, 289, 356, 476, 493
circular disk antenna, 354–56
cross, 289, 355
diversity, 592–95
rectangular patch antenna, 289–90
selection, 592
square patch support, 594
Polygonal ring antennas, 389–91
analysis, 389–91
arrangement, 394
center-driven, 393
end-driven, 392
features, 389
gain, 391
geometry, 389, 391
impedance bandwidth, 391
radiation patterns, 389–91, 392–93
See also Noncircular ring antennas; Ring antennas
Potential Green's functions
derivation of, 234–40
in space domain, 189–90
in spectral domain, 187–89
Potentials
far-field approximation for, 245
scalar, 190, 239–40
vector, 190, 237
Power dividers, 516
characteristics, 519
quadrature hybrid, 516–17
ring hybrid, 517, 518
schematic diagrams, 517
T-junction, 517, 519–20
Wilkinson, 517, 518–19
Poynting vector
over aperture area, 113
over hemisphere above disk, 342
over hemisphere above patch, 277
over large hemisphere, 334
Printed dipoles, 399
bandwidth, 406, 419–20
cross section of CPS line, 404
cross section of parallel strips line, 404
design of, 416–22
double-sided, 401
feeds for, 403–6
finite planar arrays of, 746–50
folded, 405
illustrated, 400–401
infinite arrays of, 737–42
length, 406
microstrip to slot line cross-junction transition, 404
minimum width, 405
radiation efficiency, 421–22
resonant length, 416–19
resonant resistance, 421
suspension, 405
See also Dipoles
Printed slot antennas. *See* Slot antennas
Printed strip lines, 405
Probe admittance, 122–24
Probe coupling, 16–19
Probe-fed patch microstrip antennas, 255, 256–57
illustrated, 257
input impedance, 257, 263
Probe feed, 180, 360
Probe inductance, 20
Propagation
constant, 218
in microstrip line, 220–21
time-domain, 225
Proximity-coupled microstrip dipole, 419
Proximity-coupled microstrip fed antenna, 197
Proximity coupling
antenna fabrication and, 268
microstrip dipole, 407
patch antenna, 406
Push-pull oscillator, 696

Quality factor
circular disk antenna, 349–51

half-wave patch antenna, 310
quarter-wave patch antenna, 310
rectangular patch antenna, 279–82
variation, with resonant frequency, 351
Quarter-wave patch
E-plane patterns, 310
geometry, 308
H-plane patterns, 311
with shorting pins, 308–11
TM_{10} mode for, 311
Quarter-wave rectangular patch antennas, 306–14
defined, 306–7
Q factor, 310
quarter-wave patch with continuous patch, 307
quarter-wave patch with shorting pins, 307
radiation resistances, 309
with shorting pins, 308–11
stacked, 311–14
See also Rectangular patch antennas

Radar antennas, 66–67
manpack, 66
marine, 66
SAR, 67
secondary surveillance, 66–67
See also Applications
Radar cross section (RCS)
analysis, 291, 358
calculation, 358, 359
of circular disk antenna, 358–59
control, 358
measured, 358, 359
peak value, 358–59
of rectangular patch, 291–92
variation of, 291–92
Radiated power
active patch antenna integrated with diodes, 671
calculation, 40–41
circular disk antenna, 342–44
in radiation efficiency, 285, 351
rectangular patch antenna, 277–79
Radiation admittance, 137–40
Radiation conductance, 111
approaches, 115
microstrip-fed slot antenna, 447–49
microstrip patch antenna, 447
for slot on grounded substrate, 116
Radiation efficiency
aspect ratio, 285
calculation, 352
circular disk antenna, 351–52
defined, 285, 351
as function of resonant frequency, 286
input power, 285
loop antenna, 468
microstrip dipole, 421–22
microstrip dipole vs. substrate thickness, 422
printed dipole, 421–22
radiated power, 285
rectangular patch antenna, 285–87
resonant frequency vs., 353
spectral-domain full-wave analysis, 164–66
variation of, 286, 288
Radiation fields, 31–43
analytical models and, 108–10
circular disk antenna, 320–24
circular ring antenna, 375–80
determination of, 33–40
magnetic current, 375
rectangular slot analysis, 110
vector potentials and, 33–40
Radiation patterns
active integrated antenna amplifier, 710
active patch antenna integrated with diodes, 672, 674, 677
annular slot antenna, 472, 475
aperture-coupled stacked antenna, 568–69
based on electric surface current model, 273–75
based on two-slot model, 270–73
bidirectional, 462
bow-tie antenna, 416, 418
circular disk antenna, 342–49
circular patch antenna, 65–66
comparison, 56
computed, in elevation plane, 347
control, 599
dipole, 416
dual-frequency PIFA, 651
E-plane, 272, 274, 275, 461, 476

of FET oscillating active patch antenna, 692
ground plane and substrate effect, 110
higher order mode, 346–47
H-plane, 273, 274, 275, 461, 476
importance of, 269
of matched offset-fed resonant slot, 461
microstrip-fed slot antenna, 457–63
multifrequency operation and, 585
nonradiating slots, 270
planar inverted-F antenna (PIFA), 622, 623
rectangular patch antenna, 269–79, 293, 294
rectangular ring antenna, 645
semicircular disk antenna, 362, 364
slot loaded patch antenna, 631
spectral-domain full-wave analysis, 166–69
stacked quarter-wave antenna, 311–12
substrate loaded patch, 110
tapered slot antenna (TSA), 481
for TM_{10} mode, 166–69, 181
triangular patch antenna, 432–33, 435
two-port negative resistance active patch antenna oscillator, 685
for *y*-directed current, 169
Radiation resistance, 287
center-fed dipole, 413
circular disk antenna, 342–44
circular ring antenna, 381
dipole, 414
end-fed dipole, 413
half-wave patch antenna, 309
numerically computed, 279, 280
quarter-wave patch antenna, 309
rectangular patch antenna, 277–79
variation of, 288, 345
Rampart-line antenna, 502, 504, 521–22
defined, 502
illustrated, 504, 521
Razor testing, 192
Reactance, 263
feed, 264
probe feed, 360
Reaction theorem, 448
Reciprocity, 139
relationship, invoking, 450
theorem, 233
Rectangular magnetic current sheet, 34
far fields, 36–38
far-zone vector potential, 36
illustrated, 34
two-dimensional, 36
vector electric potential, 36–37
vector magnetic potential, 36–37
Rectangular microstrip antennas, 253–314
geometry, 254
introduction to, 253–54
radiation characteristics, 254
Rectangular patch antennas
bandwidth, 282–85
beamwidth, 276
broadband, geometry, 585
cavity model analysis, 257–64
with chip-resistor loading, 585
circular sector ring antennas vs., 388
computer-aided design, 297–99
design considerations, 265–99
directivity, 276–77
effects of dielectric cover, 292–93
effects on finite ground plane size, 293–96
electric field distribution, 271
element width and length, 265–69
exterior fields, 258
feed point location, 287–90
field distribution, 258
gain, 276–77
geometry, 161
input impedance, 255
interior fields, 258
losses, 279–82
magnetic current source distribution, 270, 271
mechanical tuning, 302–6
MNM, 103
MNM incorporating mutual coupling, 106
models for, 254–64
with multilayered dielectric substrate, 269
on normally biased ferrite substrate, 498
PBG substrate, 54
performance, 264
polarization, 289–90

power radiation, 261
probe-fed, 256
probe reactance, 121
proximity coupling, 406
Q factor, 279–82
quarter-wave, 306–14
radiated power, 277–79
radiation efficiency, 285–87
radiation field in principle planes, 270
radiation pattern, with cover layer, 293
radiation pattern based on electric surface current model, 273–75
radiation pattern based on two-slot model, 270–73
radiation patterns, 269–79
radiation patterns, with superstrate, 294
radiation resistance, 277–79
radiation variation, 536, 537
reactive loading, 303
resonant frequency, 263, 267
with shorting pin, 609
with shorting pin on center line, 605–7
substrate selection, 265
with superstrate, 293
tolerance analysis, 299–302
transmission line model, 255–57
two-slot model, 272
See also Microstrip patch antennas (MPA)
Rectangular patches
effective dimensions, 76–77
entire domain basis functions, 174
with impedance inverter integrated with Gunn diode, 674
infinite arrays of, 742–46
input impedance, 178
with magnetic current density distribution, 7
microstrip dipole vs., 403
RCS, 291–92
shorting pin at corner of, 600
short loaded, 614, 616
with U slot, 577, 580
Rectangular ring antennas, 643–45
radiation patterns, 645
resonant frequencies, 645
top view, 644
See also Ring antennas
Rectangular-type circularly polarized antennas, 505–13
circular polarization radiation condition, 510–12
CP patch with single-point feed design, 512–13
type A patch, 507–9
type B patch, 509–10
See also Circularly polarized antennas
Reflection coefficients, 182
finite planar array, 748, 749
infinite arrays of printed dipoles, 742
infinite arrays of rectangular patches, 745, 746
one-port active integrated antenna oscillator, 667
simultaneous tuning, 303
two-port negative resistance active patch antenna oscillators, 683
Reflection-type locking, 712
Resistive loading, 583–85
defined, 583–84
geometry, 585
Resonance approximation, 323
Resonant arrays, 723–25
circuit illustration, 725
designing, 723–25
Resonant frequencies, 217–18, 268
aperture-coupled microstrip antenna, 548
capacitive loading and, 595
changing, 303
circular disk antenna, 324–25
circular ring antenna, 370–75, 388
directive gain variation with, 287
directivity vs., 346
discrepancy, 299
disk radius as function of, 341
dual-mode antenna, 627
for feed locations, 263
fractional change in, 301, 387
generalized cavity model, 101–2
ground plane size and, 295–96
for higher-order modes, 430
input impedance evaluation and, 102
mean ring radius vs., 375
of microstrip ring structures, 374
Q factor variation with, 351

radiation efficiency as function of, 286
radiation efficiency vs., 353
radiation resistance as function of, 345
rectangular patch antenna, 263, 267
rectangular ring antenna, 645
ring antenna, 643
separation of posts vs., 305
simultaneous tuning of, 303
TM_{10} mode, 429
triangular patch antenna, 429–30
VSWR bandwidth variation with, 352
Resonant resistance
aperture-coupled microstrip antenna, 549, 550
of microstrip dipole vs. substrate thickness, 421
value, 421
Return loss
dual-frequency PIFA, 652
microstrip-fed slot antenna, 459
microstrip patch antenna, 224
Ring antennas, 366–94
annular, 366–88
circular, 366–88
circularly polarized, 495
geometries, 367
input impedance, 366
with noncircular shapes, 389–94
properties, 366
radiation pattern, 376
rectangular, 643, 644
resonant frequencies, 643
shape types, 366
Ritz-Galerkin method, 506
Roof-top testing, 196

Satellite communications, 57–65
antenna types, 57
circular polarization requirement, 610
DBS application, 62
GPS applications, 60–61
INMARSAT, 58
low earth-orbiting systems, 60
MSAT, 58
Yagi array for, 60
See also Applications
Scalar potentials, 190, 239–40
dipole, 239
electrostatic dipole, 240
modulus of, 191
normalized, variation of, 191
numerical evaluation, 240–46
phase of, 191
testing function, 196
See also Potentials; vector potentials
Scan blindness, 741, 742, 745, 749, 751
Secondary surveillance radar, 66–67
Segmentation, 98–100
Self-admittance, 142–44
Self-conductance, 118
Self-oscillating mixers (SOMs), 712–14
active patch receiver, 714
defined, 712
design procedure, 713
design samples, 714
reflection-type locking, 712
schematic, 713
transmission-type locking, 712
Semicircular disk antennas, 360–66
cavity model analysis, 360–61
electric field, 361
excitation current, 361
field distribution, 361
geometry, 361
input impedance, 365
magnetic current distribution, 362
metalization, 360
modes, 361
radiation patterns, 362, 364
Semiconductor substrates, 760
Sequentially fed disk antennas, 530
Sequentially rotated arrays, 525–30
basic operation, 525–30
configurations, 527
defined, 525
total radiated fields, 526
See also Arrays
Series-fed arrays, 722–27
configuration illustration, 730
effective loss tangent, 731
input impedance, 731
limitations, 730
linear, 730–31
low sidelobe design, 730
nonresonant, 730–31
one-dimensional, 725
radiating element arrangements, 722
resonant, 723–25, 730–31
transposed, 722
traveling-wave, 726–27
untransposed, 722
See also Arrays
Series feedback oscillator circuit, 682
Series impedance, 455, 456
Series resistance, 455
Short-circuited posts, 809
Shorted ends, 809–10
Shorting pins, 599–607
antenna schematic with, 601
at center line of patch, 605–7
at corner of rectangular patch, 600
for dual-frequency operation, 625
field disturbances, 600
geometry, 600
input impedance and, 600
at radiating edge, 601–5
rectangular microstrip antenna with, 609
Shorts
defined, 599
impedance bandwidth and, 603
input resistance variation and, 605
lower resonant frequency variation and, 603
quadrature current variation on patch and, 604
realization of, 601
Singly fed circularly polarized antennas, 496–98, 503–15
amplitude/phase of orthogonal modes for, 497
circular, 513–15
configurations, 496, 506
illustrated, 495
rectangular-type, 505–13
See also Circularly polarized antennas
Slot antennas, 13, 13–14, 14, 222, 441–88
active, 464
annular, 463–70
bidirectional radiators, 13
capacitively coupled, 464
comparison with microstrip antennas, 487–88
CPW-fed, 463–70
defined, 13
feed structures, 14
folded, 465–67
inductively coupled, 464, 465
input impedance, 469
input impedance, reducing, 444
microstrip, 441–63
radiation fields, 457
radiation pattern, 469
series resistance, 455
shapes, 14
tapered, 480–87
unidirectional, 13
Slot line
cross section, 786
design, 786–89
Slot-loaded dual-frequency antennas, 643–46
dual-polarization square, 645, 646
rectangular ring, 643–45
resonant frequencies, 644
size reduction, 643
top view, 643
See also Compact dual-frequency antennas
Slot loaded patch antenna, 626–30
configuration of, 627
in-quadrature distribution, 629
middle current load, 628
radiation patterns, 631
top view, 632
Space domain
Fourier transform of boundary conditions, 236
Green's functions in, 230
MPIE in, 442
potential Green's functions in, 189–90
S-parameter determination, 219
Specified gain active integrated antenna amplifier, 700–705
active circuit layout, 704
C-band slot coupled, 703
circuit diagram, 702
constant gain design, 700–702
CPW-fed, 704
design goal, 700
design procedure, 701–2
design samples, 702–5

gain vs. frequency characteristics, 703
measured gain, 704
normalized gain factors, 701
stability improvement, 702
topologies, 730
two-stage, 705
See also Active integrated antenna amplifiers
Spectral domain
derivation fields, 240
derivation of Green's functions in, 224–31
electric field components in, 159–61
potential Green's functions in, 187–89
Spectral-domain full-wave analysis, 158, 159–86
applications, 185–86
basis functions, 173–79
defined, 159
dielectric loss, 163
Green's function and, 159, 184
input impedance, 164–66
mathematical model of excitation, 179–85
numerical evaluation of matrix elements, 169–73
radiation efficiency, 164–66
radiation patterns, 166–69
See also Full-wave analysis
Square arrays, 528–29
construction, 528
patch, 62
with recurrent arrangement of linear sequential arrays, 529
Square-loop microstrip line antenna, 504, 523–24
design equation, 523
illustrated, 504
Square patch antenna
axial ratio, 594
polarization support, 594
single-feed, 593
slit loaded, 614, 615
Square ring antenna, 389
directivity variation, 390
loaded, 614, 615
Stability analysis, 203
Stacked patch configuration, 552–70
analysis, 554
computed/measured gain comparison, 567
design, 554–70
for dual-frequency performance, 585
even-mode current distribution, 555–56
exploded view, 553
impedance locus, 557
impedance matching, 565
input impedance as function of lower patch size, 560
input impedance as function of lower substrate thickness, 563
input impedance as function of upper patch size, 561
input impedance as function of upper substrate thickness, 564
odd-mode current distribution, 555–56
for orthogonal linear polarizations of two frequencies, 633
probe-fed, 567
radiation pattern, 568–69
wide-band, 558
See also Aperture-coupled microstrip antennas
Stacked quarter-wave antennas, 311–14
coupling, 311
geometry, 312
impedance bandwidths, 314
radiation patterns, 311–12
with short circuits, 313
See also Quarter-wave rectangular patch antennas
Stepped impedance transformers, 16
Steps in width, 806–7
Stored energy
calculation, 41–42
cavity model, 95
Strip line
cross section, 783
design, 783–85
dielectric loss, 785
parallel, 782–83
synthesis equations, 785
TEM mode, 783
Stubs, 16
Subdomain basis functions, 174, 174–75
for arbitrary current distribution, 174

current density, 175
defined, 174
deployment, 184
illustrated, 177
roof-top, 180
See also Basis functions
Substrates, 759–70
alumina, 345
anisotropy, 765–68
categories, 760
ceramic, 760
characteristic comparison, 761–62
characteristics, 759–68
choice of, 759
cladding material, 769–70
composite material, 763
desirable characteristics for antenna fabrication, 768–70
Duroid, 374
effect on wall admittance, 383
evaluation of, 759
ferrimagnetic, 760–63
finite size effect, 347–49
lossy dielectric, 280
low-cost low-loss, 763–65
multilayered dielectric, 269
optimum thickness, 423
PBG, 599
properties, 299
selection, 265, 280–81, 339
semiconductor, 760
synthetic, 763
Substrate thickness, 265, 283, 341, 352
effect on impedance bandwidth, 535
lower, 563
upper, 564
Superstrate
circular disk antennas, 357–58
circular ring antennas, 386
defined, 358
microstrip dipole, 408
microstrip line design with, 781–82
rectangular patch antennas, 293–94
Surface
charge density, 239
current density, 451
impedance, 163
wave poles, 170
Surface waves, 43–47
effects in microstrip antennas, 599
features, 43
first mode on lossless two-layer medium, 49
phase velocity, 44
power, 281–82
power increase, 538
propagation of, xxi, 44
Susceptance
aperture, 116–18
edge, 116–18
load, 110
mutual, 120–21
Suspended microstrip line, 779–80, 779–81
Symmetrical cylindrical dipoles, 413–15
length, 413
radius, 413
results, 415
See also Dipoles
Symmetric CPS
with finite dielectric thickness, 795
with infinitely thick substrate, 793
See also Coplanar strips (CPS)
Symmetric T-junctions, 807–8
Synthetic aperture radar (SAR), 67, 591
Synthetic substrates, 763

Tapered slot antennas (TSA), 480–87
air dielectric, 481
beamwidth, 481–83
characteristics, 481
CWSA, 480
directivity, 481
elements, 480
excitation, 486–87
illustrated, 480
input impedance, 481, 483–86
invention of, 480
linear (LTSA), 480–84
metalization, 482
with microstrip feed, 486, 487
single-element, applications, 485–86
slot width, 481
symmetric radiation patterns, 481
Vivaldi, 480
See also Slot antennas
Taylor approximation, 45

TEM mode approximation, 88
TE modes
  cutoff frequency, 44
  dispersion relations, 44
  with electric boundary conditions, 426
Test functions, 163
T-junction power divider, 519–20
  characteristics, 519
  defined, 519
  schematic diagram, 517
  See also Power dividers
TM_{10} mode
  for quarter-wave patch, 311
  radiation patterns, 166–69, 181
  resonant frequency, 429
TM modes, 4
  cutoff frequency, 44
  dispersion relations, 44
  electric field distribution for, 5, 426
  field patterns, 428
  longitudinal electric surface current distribution, 185
  in lossless substrates, 45
  magnetic field distribution for, 426
  patch length, 167
  radiation patterns, 166–69, 181
  surface wave, 45
Tolerance analysis
  for first-order change in resonant frequency, 300
  rectangular patch antenna, 299–302
Transconductance mixers, 711–12
  model illustration, 711
  waveforms, 712
  See also Mixers
Transistors
  two-port negative resistance active patch antenna oscillator integrated with, 682
  unconditionally stable, 700
Transitions, 16, 582
Transmission line
  equations, 132–34
  nonuniform, 134–37
  in u direction, 132–34
  in v direction, 134
Transmission line model, 78–90
  accuracy, improving, 90
  of aperture coupling, 540–44
  comparison, 127
  defined, 76
  generalized, 85–88, 128–44
  illustrated, 81
  lossy, 88–90
  with mutual coupling, 81, 82–85
  rectangular patch antenna, 255–57
  simple, 80–82
  three-port equivalent network for, 84
  See also Analytical models
Transmission-type locking, 712
Transposed arrays, 722–23
Traveling-wave arrays, 501–3, 520–24
  chain antenna, 522
  comb-line, 733
  crank-type microstrip line antenna, 521–22
  defined, 501–2, 520–21
  dipole, 503
  equivalent circuit representation, 727
  linear, 726
  rampart line antenna, 521–22
  slot, 503
  square-loop-type antenna, 523–24
  See also Arrays; Circularly polarized antennas
Traveling-wave modes, 184
Triangles
  eigenfunctions for, 144, 145
  equilateral, 425
  patches, 425
  right-angle isosceles, 145, 146
  sixty-degree, 145, 146
  thirty-degree, 145, 146
Triangular patch antennas, 425–36
  cavity model analysis, 431–32
  with cross-slot, 618, 619
  design of, 433–34
  equilateral, 426, 433–34
  field patterns, 428
  field representation, 425–29
  geometry, 426
  input impedance, 430–32
  input resistance, 434
  radiation patterns, 432–33, 435
  resonant frequency, 429–30
  size reduction, 425

  total Q factor vs. resonant frequency, 436
Turns ratio, 450–53
Two-port negative resistance active patch antenna oscillators, 675–90
  coplanar waveguide-fed, 686
  defined, 675–78
  design procedure, 681–82
  design samples, 682–90
  E-plane radiation pattern, 687
  H-plane radiation pattern, 687
  input impedance, 683
  input network, 681
  input resistance, 684
  integrated with transistor, 682
  output network, 681
  patch geometry, 684
  radiation patterns, 685
  reflection coefficients, 683
  scattering matrix, 678
  schematic diagrams, 679
  start-up of oscillation, 679
  See also Active integrated antenna oscillators

Unidirectional slot antennas, 467–68
Unknown complex coefficients, 231
Untransposed arrays, 722

Varactor-tuned microstrip antennas, 595–98
  illustrated, 596
  operation frequencies, 597
  tuning curve, 598
Vector potentials, 190, 237
  asymptotic behavior of, 245
  electric, 33, 36–37, 321
  far-zone, 36, 38
  magnetic, 33–35, 36–37
  numerical evaluation, 240–46
  radiation field formulation and, 33–40
  See also Potentials; Scalar potentials
VSWR bandwidth, 279–80, 283, 297, 360
  variation, of center-fed dipole, 420
  variation with resonant frequency, 352

Wall admittance
  active, 138
  determining, 138
  mutual, 142–44
  self-, 142–44
  substrate effect on, 383
Wide-band microstrip antennas, 524–25
Wiener-Hopf technique, 115, 117
Wilkinson power divider, 518–19
  characteristics, 519
  defined, 518
  equal-split, 519
  schematic diagram, 517
  See also Power dividers
Wireless local-area networks (WLANs), 591